

13th International Conference on Plasma Surface Engineering

September 10 - 14, 2012, in Garmisch-Partenkirchen, Germany

Editors

J. Bradley, Liverpool (UK)
A. Cavaleiro, Coimbra (P)
Th. Czerwiec, Nancy (F)
P. Eklund, Linköping (S)
U. Helmersson, Linköping (S)
G.J. van der Kolk, Venlo (NL)
W. Möller, Dresden (GER)
L. Nielsen, Aarhus (DK)
C. Oehr, Stuttgart (GER)
R. Tietema, Venlo (NL)
J. Vlcek, Plzen (CZ)

Copyright

The publishers will keep this document online on the Internet – or its possible replacement –from the date of publication barring exceptional circumstances.

The online availability of the document implies permanent permission for anyone to read, to download, or to print out single copies for his/her own use and to use it unchanged for non-commercial research and educational purposes. Subsequent transfers of copyright cannot revoke this permission. All other uses of the document are conditional upon the consent of the copyright owner. The publisher has taken technical and administrative measures to assure authenticity, security and accessibility. According to intellectual property law, the author has the right to be mentioned when his/her work is accessed as described above and to be protected against infringement.

For additional information about Linköping University Electronic Press and its procedures for publication and for assurance of document integrity, please refer to its www home page: http://www.ep.liu.se/.

To the Reader

At the conference, the following published articles are non-refereed extended abstracts from a subset of the presentations. The role of the editors was to make an initial selections of submitted short abstracts only and do not take any responsibility for the correctness and/or scientific quality of the content of the published extended abstracts.

Linköping University Electronic Press Workshop and Conference Collection, No. 2
Linköping University Electronic Press
Linköping, Sweden, 2013
URL: http://www.ep.liu.se/wcc_home/default.aspx?issue=002

© The Authors, 2013

Table of Contents

Influence of Atmospheric Plasma Jet Pre-Treatments of TiO2 Electrodes on Dye Adhesion and DSSC Cell
Stephen Sheehan, Mahfujir Rahman and Denis Downling.....1

Study of the chemical etching of carbon surfaces facing argon/hydrogen plasmas in a helicon type reactor
Xavier Glad, Thomas Bieber, Ludovic de Poucques, Robert Hugon and Mohammed Belmahi.....6

Development and Application of New Multicomponent Electrode Materials for Deposition Technologies
Evgeny Levashov, Yuri Pogozhev, Dmitry Shtansky, Alexander Kudryashov, Philipp.....10

Spotless arc activated high-rate deposition using novel dual crucible technology for titanium dioxide
Bert Scheffel, Christoph Metzner, Thomas Modes.....14

Surface Interaction and Processing Using Polyatomic Cluster Ions
Gikan Takaoka, H. Ryuto, M. Takeuchi.....18

Hierarchical simulation of microcrystalline PECVD silicon film growth and structure
Dimitrios Tsalikis, Chunggi Baig, Vlasis Mavrantzas, Eleftherios Amanatides and Dimitrios Mataras.....22

Multifunctional coatings on fabrics by application of a low-pressure plasma process
Joëlle Levalois-Grützmacher, Marie-Jérôme Tsafack, Kanchit Kamlangkla and Katrin Prinz.....26

Hierarchical, Plasma Nanotextured, Superamphiphobic Polymeric Surfaces
Kosmas Ellinas, Katerina Tsougeni, Angeliki Tserepi and Evangelos Gogolides.....30

On the deposition rate during High-Power Impulse Magnetron Sputtering.
Stephanos Konstantinidis.....34

ION Flux–Film Structure Realtionship During Reactive Magnetron Sputtering of Tungsten
Axel Hemberg, Stephanos Konstantinidis, Jean-pierre Dauchot and Ryne Snyder.....36

Thermal and electrical characterization of thin carbon nanotubes films
Mireille Gaillard, Èliane Amin-Chalhoub, Nadjib Semmar, Agnés Petit, Anne-Lise Thomann and Chantal Boulmer-Leborgne.....39

Influence of the nano-structure and composition of titanium nitride based substrate on the carbon
M. Morales, S. Cucatti, J.J.S. Acuña, L.F. Zagonel, O. Antonin, M.C. Hugon, N. Marsot, B. Bouchet-Fabre, T. Minea and F. Alvarez.....43

Fabrication of heterostructured M@M´Ox Nanorods by low temperature PECVD
Manuel Macias-Montero, Ana Borras, Angel Barranco, Jose Cotrino, Juan Espinos and Agustin R. González-Elipe.....47

Plasma polymers used for controlled interphase in polymer composites
Vladimir Cech, Adam Babik, Antonin Knob and Erik Palesch.....51

Study of the transition between capacitive and inductive modes on propanethiol plasma polymer
Damien Thiry, Nikolay Britun, Stephanos Konstantinidis, Jean-Pierre Dauchot, Maxime Guillaume, Jérôme Cornil and Rony Snyders 56

Mechanical properties of plasma polymer films controlled by RF power
Erik Palesch, Sona Kontarova and Vladimir Cech 60

Plasma deposition of hydrophobic coatings on structured surfaces for condensation and heat transfer
D. Gloess, P. Frach, M.Maicu, E. Holst, R. Schmittgens, G. Gerlach, C.H. Lu, T. Roch, M. Bieda, A. Lasagni and M. Beckmann 64

Tribological Characterization and Wear Mechanisms of Novel Oxynitride PVD Coatings Designed for Applications at High Temperatures
Jiri Nohava, Pascal Dessarzin, Pavla Karvankova and Marcus Morstein 58

General Regularities and Differences of Nanostructured Coatings Based on Nitrides of Zr, Ti, Hf, V, Nb Metals and Their Combinations
A. D. Pogrebnjak, V. M. Beresnev, A. A. Andreev, O. V .Sobol, D. A. Kolesnikov, F. F. Komarov, S. S. Mel'nik, M. V. Kaverin and A .P. Shypylenko 72

Composition of Plasmapolymeric Coatings Using O2/HMDSO Gas Mixtures and Application on Elastomers for Tribological Improvement
Dominik Paulkowski, Klaus Vissing and Ralp Wilken 76

High Power Density Pulse Magnetron Sputtering - Process and Film Properties
Peter Frach, Christian Gottfried, Fred Fietzke, Heidrun Klostermann, Hagen Bartzsch and Daniel Gloess 80

Crystallinity control of sputtered ZnO films by utilizing buffer layers fabricated via nitrogen mediated crystallization
N. Itagaki, K. Oshikawa, K. Matsushima, I. Suhariadi, D. Yamashita, H. Seo, K. Kamataki, G. Uchida, K. Koga and M. Shiratani 84

The Effect of Nitrogen Partial Pressure and Substrate Temperature on the Characteristics of Photocatalytic N:TiO2 Thin Films deposited by Filtered Vacuum Arc Deposition
Eda Goldenberg, L. Burstein, Ines Chayun-Zucker, Rudi Avni and Raymond L. Boxman 88

Effect of Xe+ ion bombardment induced patterns in stainless steel on plasma nitriding processes
Silvia Azevedo dos Santos Cucatti, E.A. Ochoa, M. Morales, R. Droppa Jr, J. Garcia, H.C. Pinto, L.F. Zagonel, D. Wisnivesky and F. Alvarez 92

Investigations on the active screen plasma nitriding process
Kristian Börner, Igor Burlacov, Heinz-Joachim Spies, Horst Biermann, Spetham Hamann and Jürgen Röpcke 96

Control of nanoparticle formation in reactive plasmas and its application to fabrication of green energy devices
Masaharu Shiratani, G. Uchida, K. Katamaki, H. Seo, N. Itagaki and K. Koga 100

Towards deeper understanding of a HiPIMS discharge by time-resolved optical plasma
Nikolay Britun, Maria Palmucci, Stephanos Konstantinidis and Rony Snyders 104

Study of the ionisation in a nickel plasma by Inductively Coupled Impulse Sputtering (ICIS)
Daniel A.L. Loch and Arutiun P. Ehiasarian 108

Nanoparticle Synthesis in a Plasma Downstream Reactor – From Plasma Parameters to Nanoparticle Properties
Christian Roth, Gina Oberbossel and Philip Rudolf von Rohr 112

Silicon dioxide coating of titanium dioxide nano particles from dielectric barrier discharge in a gaseous mixture of silan and nitrogen
Sebastian Dahle, Lienhard Wegewitz, Fei Qi, Alfred P. Weber and Wolfgang Maus-Friedrichs 116

High Power Pulsed Hollow Cathode for Nanoparticle Synthesis
Daniel Söderström, Iris Pilch, Nils Brenning and Ulf Helmersson 118

Performance of atmospheric plasma sprayed HA coatings under dry and wet fatigue conditions
James Nicholas Barry, Alun J. Carr and Denis P. Dowling 122

Comparison of microbiological effects in long fine-lumen tubes by low and atmospheric pressure plasmas
Uta Schnabel, Manfred Stieber and Jörg Ehlbeck 126

Tribological properties of laser textured and DLC coated surfaces with solid lubricants
Jussi Oksanen, Timo Hakala, Sanna Tervakangas, Jukka Kolehmainen and Jari Koskinen 130

Zr-DLC coatings - analysis of the friction and wear mechanisms
Tomas Vitu, Bernando Joao Vitor Pimentel, A. Escudeiro, Albano Cavaleiro and Tomas Polcar 132

Control of Deposition Profile and Properties of Plasma CVD Carbon Films
Kazunori Koga, Tatsuya Urakawa, Giichiro Uchida, Kunihiro Kamataki, Yenwoon Seo, Nahi Itagaki, Masaharu Shiratani, Yuuichi Setsuhara, Makoto Sekine and Masaru Hori 136

Plasma surface modification of diamond-like carbon films to graphene
Savcho Tinchev 140

Composite layers "MgAl intermetalic layer / PVD coating" obtained by hybrid surface treatment method on the AZ91D magnesium alloy
Jerzy Smolik, Adam Mazurkiewicz and Jaroslaw Mizera 144

Plasma processing of scaffolds: perspectives for Tissue Engineering
Francesca Intranuovo, Roberto Gristina, Marco Domingos, Guiseppe Camporeale, Eloisa Sardella, Paulo Bartolo and Pietro Favia 146

Formation of pH-responsive polymer composite membranes by plasma-induced graft polymerization method
Liubov Kravets, Sergey Dmitriev and Gheorghe Dinescu 149

Interpretation of optical emission in a strongly inhomogeneous PIAD environment
Jens Harhausen, Ralf-Peter Brinkmann, Rüdiger Foest, Sergey Gorchakov, A. Ohl and Benjamin Schröder 153

The Study about Surface Modification of Steel by Water Plasma
Jung-Hyun Kong, Tomonori Takeda, Masahiro Okumiya, Yoshiki Tsunekawa, Masashi Yoshida and Sang Gweon Kim 157

Study of the growth kinetics, microhardness and morphology of PEO coatings formed on Al 2024 alloy in alkaline-silicate electrolytes using different current waveforms
Alexander Grigorievitch Rakoch, Gérard Henrion, Vasilij Leonifovich Kovalyov, Alexandre Nominé and Ilya Vyacheslavovich Bardin 161

Scuffing propagation of heavily-loaded, lubricated, coated friction joints
Remigiusz Michalczewski, Witold Piekoszewski, Waldemar Tuszyński and Marian Szczerek 165

Progress in Quantitative Adhesion Testing of Films and Coatings by means of Centrifuge Technology – Present State of the Art
Uwe Beck, Stefan Hielscher, Matthias Weise, Renate Mix, Dietmar Lerche and Uwe Reitz 169

Nano-Impact Tests on Micro-Blasted Coatings for Assessing Their Brittleness
Konstantinos-Dionysios Bouzakis, Stefanos Gerardis, Georgios Skordaris and Emmanouil Bouzakis 173

Optical Layer Systems for Product Authentication:Interference, Scattering, Light Diffusion and Ellipsometric Encoding as Public, Hidden and Forensic Security Features
D. Hönig, S. Schneider, R. Domnick, M. Belzner, U. Beck, A. Hertwig, R. Stephanowitz and M. Weise 177

Wide-angle broadband AR coating by combining interference layers with a plasma-etched gradient layer
Ulrike Schulz, Peter Munzert, Christiane Präfke, Friedrich Rickelt and Norbert Kaiser 181

Sensitization of Er3+ Emission in Er- and Yb-doped Si Thin Films by Laser Ablation
Shinji Kawai 184

Synthesis and characterization of La2NiO4-δ coatings deposited by reactive magnetron sputtering using plasma emission monitoring
Fondard Jérémie, Briois Pascal, Billard Alain and Bertrand Ghislaine 188

Silicon carbide surface micromachining using plasma ion etching of sacrificial layer
Norbert Kwietniewski, Andy Zhang, Jang-Kwon Lim, Mietek Bakowski, Mariusz Sochacki and Jan Szmidt 192

Rapid Stripping of Brass-plating on Fine Saw Wire by Triangle-type Multiple Magnetron Plasmas
H. Fujiyama, K. Miyazaki, N. Matsuo, Y. Kobayashi, M. Shinohara and S. Nishiyama 195

Scaling laws governing the NF3 cleaning plasma in a large area reactor
G. F. Leu, C. Goury, P. Modrzynski, M. Klindworth and C. Ellert 199

Cleaning of Organic Contamination from EUV Optics Surfaces Using Hydrogen-based Plasmas
N. Skoro and E. Gogolides 203

Influences of surface-active substances on specific power inputs and on surface roughnesses of the metal product under plasma vacuum arc treatment
V.N. Arustamov, Kh.B. Ahsurov, Kh.Kh.Kadirov and I.Kh.Khudaykulov 207

Plasma etching of aluminum nitride thin films prepared by magnetron sputtering method
Piotr Firek, Bartłomiej Stonio, Rafał Chodun, Jan Szmidt and Krzysztof Zdunek 211

On the Injected Gas/Electric Power Relation for Deposition Efficiency Control During the Gims Deposition
Krzysztof Zdunek, Katarzyna Nowakowska-Langier, Rafal Chodun and Jerzy Dora 215

Influence of the Ion Beam Current on Microstructures and Optical Properties of Al2O3 Thin Films by Oxygen Ion Beam Assisted Pulse Reactive Magnetron Sputtering
Zhimin Wang, Jinxiao Wang, Yi Wang, Kai Zhao, Xiaomei Su, Hu Wang and Yudong Feng 219

Formation of plasma technological influence of vacuum arc on the internal surfaces of metal pipes and putting of the protecting coatings
V.N. Arustamov, Kh.B. Ashurov, Kh.Kh. Kadirov and I.Kh. Khudaykulov 223

Features of DC magnetron sputtering of mosaic copper-graphite targets
Valery Mitin, Yury Mankelevich, Alexander Pal, Tatyana Rakhimova, Alexey Ryabinkin, Alexander Serov, Alexey Mitin and Nikolay Krasnobaev 227

Sn Thin Film Deposition using a Hot Refractory Anode Vacuum Arc
I. I. Beilis, Y. Koulik and R. L. Boxman 231

Hydrophilization treatment of polyimide using Ar-O2 mixture gas surface wave plasma – Oxygen radical density and plasma parameter dependence
Yoshinari Hirukawa, Shigeru Ono and Suzuki Syuichi 235

In-situ FTIR-ATR spectroscopic investigations of atmospheric-pressure plasma modification of polyolefin thin films
Zohreh Khosravi, Alena Hinze and Claus-Peter Klages 239

Functional coatings for polymer composites
A.Babik, L. Hoferek, D. Janova and V. Cech 243

Applications of Low Pressure Plasma in High-tech Textiles
Rubel Alam, Gaffar Hossain, Günter Grabher and Mokbul Hossain 247

Poly(acrylic) nanocoatings deposited by AP-PECVD processes on paper substrates for packaging applications
José Manuel García, Jordi Mota, Laia Crespo, Meritxell Martínez, Laurent Aubouy and Llorenç Bautista 251

Atmospheric Plasma surface treatment of Styrene-Butadiene Rubber
Cátia A. Carreira, Ricardo Silva, Vera V. Pinto, Maria José Ferreira, Fernando Sousa, Fernando Silva and Carlos M. Pereira 255

Formation of plasma-generated nanostructures on polymer surfaces for various polymer types
P. Munzert, C. Praefke, U. Schulz and N. Kaiser 258

Plasma Directed Assembly: Process Issues, Materials and Applications
Dimitrios Kontziampasis, Athanasios Smyrnakis, Vassilios Constantoudis and Evangelos Gogolides 262

DC Discharge Plasma Polymerization of 1-Naphthylamine
M. Yablokov, A. Gilman, N. Surin, M. Augustyniak-Jablokow, K. Tadyszak and A. Kuznetsov 266

Polymerization of Acrylic Acid by a 4kJ plasma focus device
Morteza Habibi, Reza Amrollahi and MHS Alavi 270

Characterization of Nanostructured TiN and ZrN thin films elaborated by reactive magnetron sputtering
Chahinez Saied and Abdelouahad Chala 274

The Improved Friction Properties of Bonded MoS2 Films by MAO Treating of Al Substrates
Hu Hanjun, Zhou Hui, Zheng Yugang, Sang Ruipeng, Zhang Kaifeng and Wan Zhihua 279

Self-lubricating W-S-C-Cr tribological coatings deposited by r.f. magnetron sputtering
Joao Vitor Pimentel, Manuel Evaristo, Tomas Polcar and Albano Cavaleiro 283

Wear Properties of AISI 4140 Steels Modificated By Using Pulse Plasma Technique
Y.Y.Özbek and M.Durman 287

Atmospheric pressure plasma treatments inside meander-like cavities
Antje Quade, Katja Fricke and Klaus-Dieter Weltmann 291

Optimization of APS Process Parameters Using a Designof Experiment for CSZ (CeO2 Stabilized Zirconia) Coatings
Ekrem Altuncu and Fatih Uste 295

Microstructure and Mechanical Behaviour Relationship of Plasma Sprayed Mullit+YSZ Coatings
Yıldız Yaralı Özbek, Ekrem Altuncu and Fatih Üstel 299

The effectiveness of prevailing plasma spray conditions in the synthesis of protective coatings
Vitas Valinčius, Viktorija Grigaitienė, Pranas Valatkevičius and Liutauras Marcinauskas 303

A Comparative Study of Wear Effect on the Microstructures Behavior of CoNiCrAlY Coatings fabricated by APS, HVOF and CGDS Coatings
Mustafa Sabri Gok, Abdullah Cahit Karaoğlanlı, Azmi Erdoğan and Ahmet Türk 307

Oxygen effect in Magnetron Sputtered Aluminum doped Zinc oxide films
Saad Rahmane, Mohamed Abdou Djouadi, Mohamed Salah Aida and Nicolas Barreau 311

Photocatalytic, hydrophilic titanium dioxide prepared by direct current magnetron sputtering
Falk Bernsmann and Udo Grabowy 317

Photocatalytically Active Titania Produced by MOCVD Plasma Process
Eva Maria Moser, Sidney Chappuis and Javier Olleros 321

Plasma Nitriding Performed under Atmospheric Pressure using Pulsed-Arc Plasma Jet
R. Ichiki, H. Nagamatsu, Y. Yasumatsu, M. Yoshida, S. Akamine and S. Kanazawa 325

Effect of Plasma Nitriding and Nitrocarburising Process on the Corrosion Resistance of Grade 2205 Duplex Stainless Steel
Subroto Mukherjee, Alphonsa Joseph, Ghanshyam Jhala, Satyapal M, A. S. Khanna, Pratipal Rayjada, Narendra Chauhan and Raja V. S. 329

Wear Properties of Plasma Nitrided Inconel 718 Superalloy
Halim Kovacı, Hojjat Ghahramanzadeh ASL, Çiğdem Albayrak and Akgün Alsaran 333

Effects of ion-beam bombardment and nitridation on physical/mechanical properties of 100Cr6 TiN coated steels
R. Droppa Jr, H. Pinto, J. Garcia, E. Ochoa, M. Morales, S. Cucatti and F. Alvarez 338

Mechanism of Ti99.2 titanium unconventional ion nitriding
Tadeusz Fraczek, Jerzy Michalski, Michal Olejnik and Jaroslaw Jasinski 342

Evaluation of the Mechanical Behaviour of a DLC Film on Plasma Nitrided AISI 420 with Different Surface Finishing
Sonia Brühl, Raúl Charadia, Eugenia Dalibón, Vladimir Trava Airoldi, Amado Cabo 346

Nanocomposite Nitrid Thin films for hard coatings : Applications in wear and corrosion
Abdelouahad Chala, Chahinez Saied and Hanane Ghelloudj 350

Wear behaviour of PN+CrN, PN+CrAlN and PN+TiCrAlN layer composite during ball-on-disk tests in higher temperature
Joanna Kacprzyńska, Jerzy Smolik and Adam Mazurkiewicz 356

Chromium and Chromium nitride thin films deposited by HiPIMS using short pulses
Axel Ferrec, Frédéric Schuster, Pierre-Yves Jouan and Mohamed Abdou Djouadi.....360

Effect of low temperature air plasma treatment on physico-chemical properties of kaolinite
Lubomir Lapcik, Ivo Krasny, Ivana Kupska and Barbora Lapcikova.....364

Biocompatible thin films obtained from Heparim-methane plasma process
R. P. Mota, I. A. Perrenoud, R. Y. Honda, M. A. Algatti, M. E. Kayama, K. G. Kostov, T. Sadahito China and N. C. Cruz.....368

Analysis of the aging of cell-adhesive plasma-polymer coatings on titanium surfaces
F. Hempel, J. Schäfer, H. Rebl, J.B. Nebe, K.-D. Weltmann and B. Finke.....372

Comparison of surface properties of DLC and ultrananocrystalline diamond films with respect to their bio-applications
Miroslav Jelinek, Alexandra Voss, Tomáš Kocourek, Mahsa Mozafari, Veronika Vymetalová, Marketa Zezulová, Petr Písarí, Cyril Popov and Jan Mikšovský.....376

New methods for reprocessing of medical devices based on plasma treatment
Jörg Ehlbeck, Uta Schnabel, Manfred Stieber, Jörn Winter, Martin Polak, Udo Krohmann and Klaus Dieter Weltmann.....380

Fabrication and plasma modification of polymer scaffolds for regenerative and replacement medicine
Victor N. Vasilets Valentina A. Surguchenko and Viktor I. Sevastianov.....384

The Corrosion Properties of Zirconium and Titatium Loadbearing Implant Materials with Protective Oxide Coatings
Anna Zykova, Vladimir Safonov, Jerzy Smolik, Renata Rogowska, Vladimir Luk'yanchenko, Oleg Vyrva and Stas Yakovin.....388

High rate PECVD of a-C:H coatings in a hollow cathode arc plasma
Burkhard Zimmermann, Fred Fietzke, Heidrun Klostermann, Jan Lehmann, Frans Munnik and Wolfhard Möller.....392

Growth of Carbon Materials on Gold Substrate by Plasma Enhanced CVD
Jirí Sperka, Lenka Zajícková, Ondrej Jasek, Annapurna Pamreddy, Josef Have, Jan Schäfer and Rüdiger Foest.....395

Cr-DLC films deposited by dual pulsed laser ablation
Petr Písařík, Miroslav Jelínek, Tomáš Kocourek, Jan Mikšovký amd Karel Jurek.....399

Comparison of the wear particle size distribution of different a-C coatings deposited by vacuum
Ying Ren, Ingo Erdmann, Victoria Khlopyanova, Friederike Deuerler and Volker Buck.....403

Oxidation behaviour of RuAl thin films: influence of diffusion barrier
M. A. Guitar and F. Mücklich.....407

Production and Characterization of Self-Healing Properties of B4C+SIC Added TBC
Fatih Üstel, Ahmet TÜRK and Garip Erdogan.....409

Effects of Production Method and Heat Treatment on the AdhesionStrength and Microstructural Behavior of MCrAlY Coatings
H. Dikici, A. C. Karaoglanli, T. Grund c, T.Lampke and Y. Kucuk.....416

Oxidation Behavior of Thermal Barrier Coatings With Cold Gas Dynamic Sprayed CoNiCrAlY Bond Coats
A. C. Karaoglanli,A. Turk, Đ. Ozdemir and F.Ustel.....420

Thermal stability of TiZrAlN films deposited by a reactive magnetron sputtering method
G. Abadias, I. A. Saladukhin, V.V. Uglov and S. V. Zlotski 424

Lifetime Assessment and Shock Behavior of TBC in Gas Turbine Blades: Experimental and Numerical Investigations
Yaşar Kahraman and İmdat Taymaz 427

Novel Nanometer Thin Films On Magnesium Alloy Prepared By Ultra-Shallow Nitrogen Implantation Using PECVD Method
Marcin Grobelny, Małgorzata Kalisz, Robert Mroczyński and Magdalena Szymańska 431

Effect of nitrogen incorporated into oxide layer, formed on the magnesium alloys by using r.f. PECVD process, on their corrosion resistance.
Małgorzata Kalisz, Marcin Grobelny and Barbara Dytkowicz 435

Application of the dusty plasma technology for diamond ceramics production
Alexander Pal, Evgeny Ekimov, Alexander Ivanov, Nikolay Borovikov, Andrey Rusinkevich, Alexey Ryabinkin, Alexander Serov, Andrey Starostin, Vladimir Fortov and Elena Gromnitskaya 439

Effect of the rapid thermal annealing on the structure and optical properties of TaOxNy thin films deposited by reactive magnetron sputtering
F. Zoubian, E. Tomasella, A. Bousquet, J. Cellier and T. Sauvage 443

The Structure-Phase Compositions of Ni - Cr and Co–Cr Based Powder Alloys Coatings Deposited by Plasma-Detonation on Steel Substrates
Darya L. Alontseva, Alexander D. Pogrebnjak and Galina Klassen 447

Synthesis of intermetallic compounds in the surface layer of eutectic silumin by dense plasma impact
Nikolai Cherenda, Natalya Bibik, Vladimir Uglov, Valentin Astashynski and Anton Kuzmitski 451

Evaluation of the PVD and CVD coatings' structure using the modified method of spherical metallographic microsection (Baltest-M).
Marek Betiuk 455

Measurements of SiH4/H2 VHF Plasma Parameters with Heated Langmuir Probe
Tsukasa Yamane, Sachiko Nakao, Yoshiaki Takeuchi, Hiroshi Muta, Ryuta Ichiki, Kiichiro Uchino and Yoshinobu Kawai 459

Systematic evaluation of thin electrically insulating layers on common engineering materials
F. Schmaljohann, D. Hagedorn andF. Löffler 463

Ultra-shallow fluorine implantation from r.f. plasma as a method for improvement of electro-physical properties of MIS structures with PECVD gate dielectric layers
M. Kalisz and R. Mroczyński 467

Laminated Composite on the Basis of Plasma Modified PTFE Films and Thin Aluminum Layers
M. Yablokov, A. Gilman, A. Kechek'yan and A. Kuznetsov 471

The formation of superhard coatings ≥ 48 GPa in Ti-Hf-N (Fe) and analysis of their structure and properties.
A. D. Pogrebnjak, A. G. Ponomarev, M. V. Kaverin, D. A. Kolesnikov, V. M. Beresnev, F.F. Komarov and S. S. Mel'nik 475

Electrochemical and mechanical properties of low friction nc-CrC/a-C:H and nc-WC/a-C:H coatings on construction materials deposited by magnetron sputtering.
Marcin Grobelny, Dariusz Rudnik, Marcin Makowka, Katarzyna Włodarczyk-Kowalska, Piotr Nolbrzak and Wojciech Pawlak.....479

Effect of time in plasma electrolytic oxidation process on titanium substrate with addition nano alpha alumina powder in electrolyte and investigate wear behavior of coating
S. Sarbishei, M.A. Faghihi-Sani, M. Mohammadi and F.Einkhah.....483

Fatigue Behavior of Coated and Uncoated.Cemented Carbide Inserts Inverstigated by Impact test at the Cutting Edge Vicinity
K.-D. Bouzakis, M. Batsiolas, G. Skordaris, N. Michailidis and F. Stergioudi.....487

Influence of post deposition Plasma surface Treatments of TiO_2 Electrodes with respect to DSSC Cell performance

S. Sheehan[1], M. Rahman[1], K. Ravindranathan Thampi[1], D. P. Dowling[1,2*]

[1]School of Chemical and Bioprocess Engineering, University College Dublin, Ireland
[2]School of Mechanical & Materials Engineering, University College Dublin, Ireland
Tel: +353 (0)1 716 1747 Fax: +353 (0)1 283 0534 E-mail: denis.dowling@ucd.ie

1. Introduction

Dye-sensitized solar cells (DSSC) based on nanocrystalline TiO_2 were invented by O'Regan and Gratzel in 1991. DSSC are third generation, thin film solar cells. They are photoelectrochemical devices whose operating principle closely resembles the photosynthesis reaction of green plants. There is increasing interest in dye-sensitized solar cells (DSSCs) due to their relatively low cost and ease of manufacture. However, the performance of the DSSC solar cell in many cases is limited by the presence of oxygen vacancy (- Ti^{3+} defects site) along with surface contamination in the TiO_2 electrode. To improve current density and the overall efficiency of the DSSCs surface contamination and surface defects need to be reduced. This study investigated the influence of plasma surface treatments of nanocrystalline TiO_2 films on photovoltaic performance of the corresponding DSSCs. Two surface treatments, PlasmaTreat™ an atmospheric air plasma system and a Microwave (MW) plasma system were used for the first time to study the effect of plasma surface treatment of TiO_2 on DSSC performance.

2. Experimental

The TiO_2 layer was deposited and sintered by SolarPrint™. The plasma surface treatments of TiO_2 layer deposited onto a conducting (FTO) glass substrate were carried out using an air plasma jet system called PlasmaTreat™ and an oxygen plasma using a circumferential antennaplasma (CAP) microwave system.. For the PlasmaTreat™ system, percentage plasma cycle time (PCT) was varied from 20 – 90 and the overall treatment time (from 15 to 45 seconds) was varied for the MW plasma system. The morphological and crystallographic properties of the sintered TiO_2 layer both before and after plasma treatment were investigated using SEM, optical profilometry and X-ray diffraction techniques. Subsequent to the TiO_2 plasma surface treatment, a ruthenium based dye (N719) was applied to the coating on the plasma surface treated coatings. The level of dye adsorption on the treated and non-treated TiO_2 coatings were assessed using UV-Vis spectroscopy. This analysis was performed by desorbing the dye from a fixed area of TiO_2 coated glass in a buffer alkaline solution.

3. Results and Discussion

The performance of each cell was assessed using IV, IPCE and UV-Vis dye adsorption measurement. It can be seen in Figure 1 that the highest efficiency was recorded for TiO_2 samples treated with in the PlasmaTreat™ system using 50% PCT and in the MW system treated for 30 seconds. Compared to control samples, the PlasmaTreat system treated samples using 50% PCT exhibited an

increase of 5.9% Voc, 8.7% increase in Jsc, 19% increase in IPCE and a 19.3% increase in efficiency. Likewise a 30 sec MW plasma treated sample showed a 5.9% increase in Voc, 19.8% increase in Jsc, 30% increase in IPCE and a 22.9% increase in efficiency when compared to control samples.

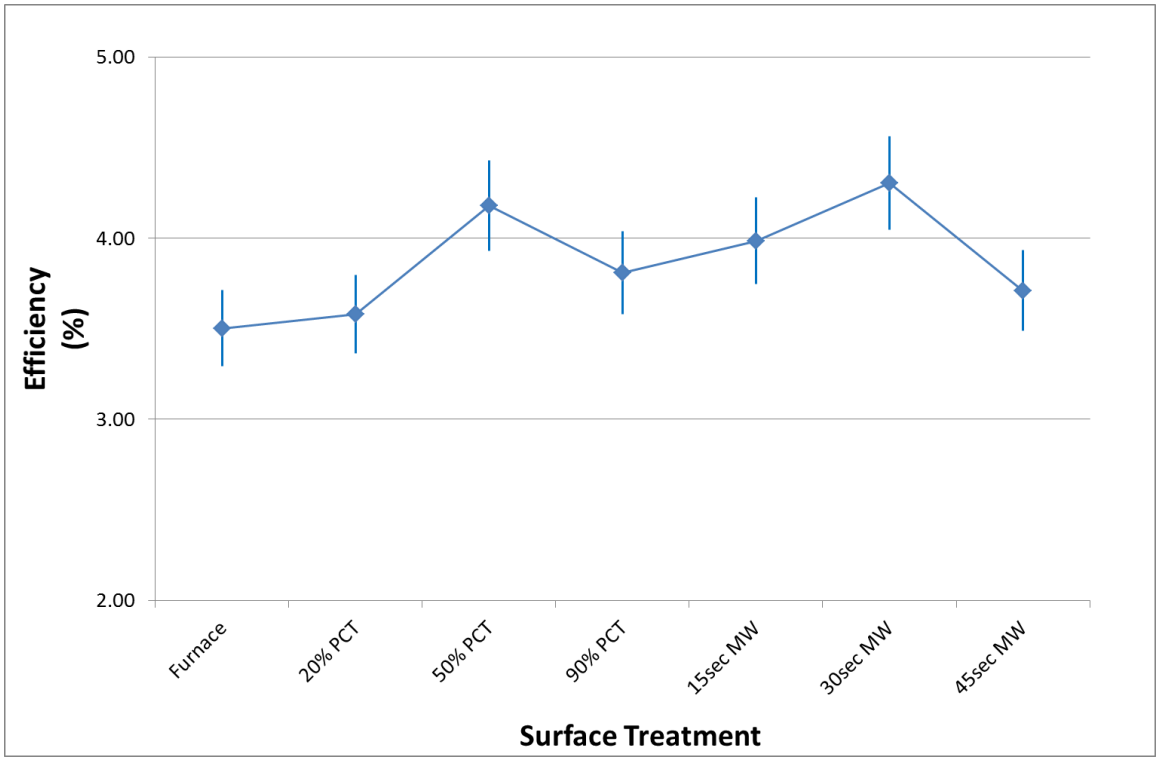


Figure 1 Efficiency of corresponding DSSC cells after various surface treatments

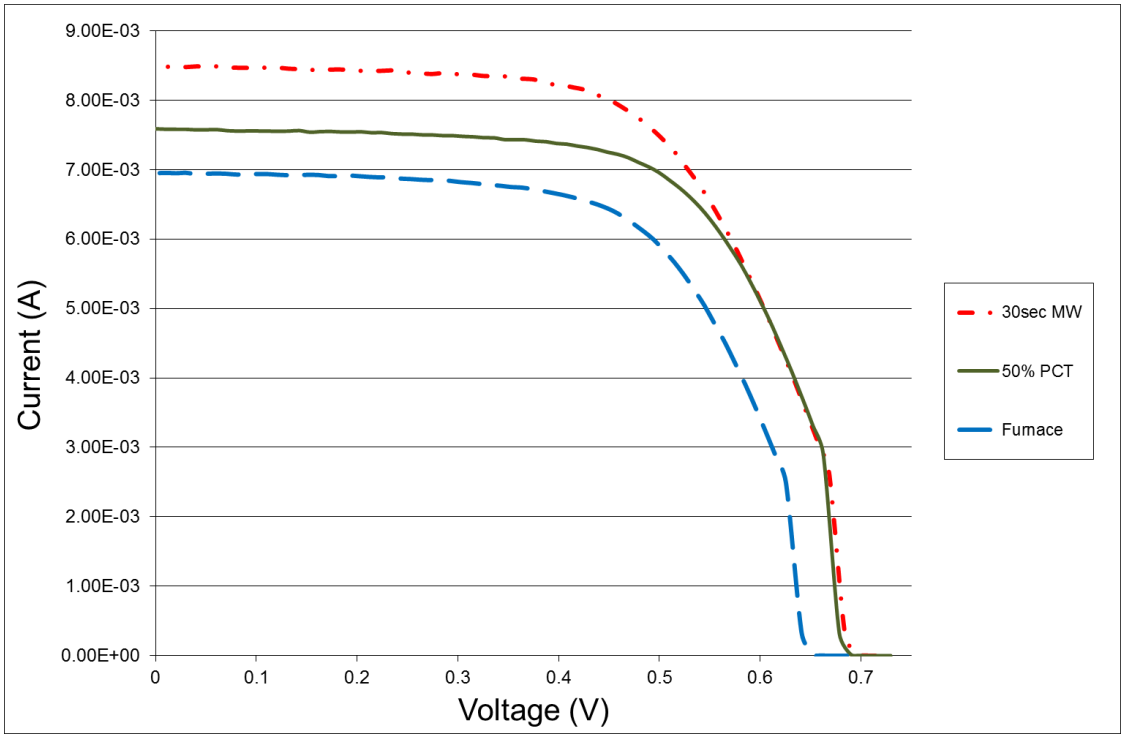


Figure 2 Current/Voltage curves of two best performing samples as compared to furnace treated samples

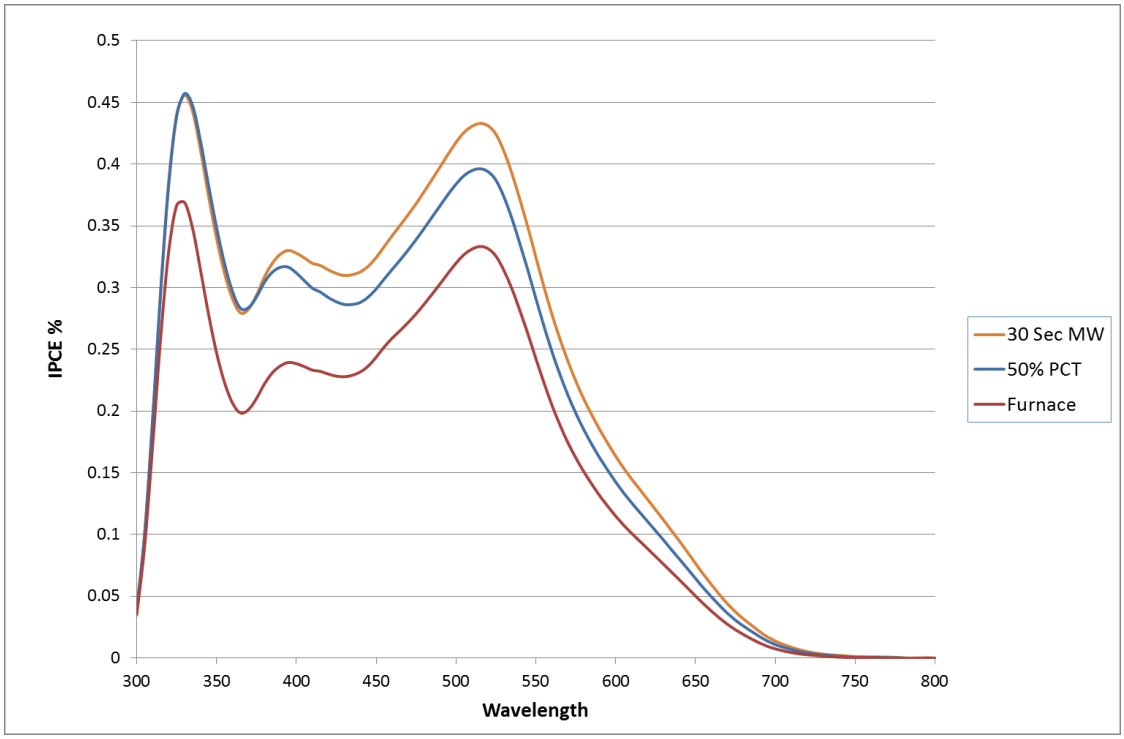


Figure 3 IPCE measurements of two best performing samples as compared to furnace treated samples

4. Conclusion

This study demonstrated that MW and PlasmaTreat™ processes could be used as a means of post deposition plasma surface treatment of TiO_2 electrode for improving overall DSSC cell efficiency. A 22.9% and 19.3% improvement of efficiency was observed for MW and PlasmaTreat™ samples respectively. A possible explanation for the enhanced level of efficiency after plasma activation is the increased level of dye adsorption as confirmed by UV-Vis spectroscopy, reduction of oxygen deficiency site and removal of aqueous and organic contaminants from the TiO_2 surface. Detailed characterization studies of the plasma treated TiO_2 electrodes are currently ongoing to find out the mechanism behind the increase in DSSC cell efficiency.

Study of the chemical etching of carbon surfaces facing argon/hydrogen plasmas in a helicon type reactor

X. Glad*[1,2], T. Bieber[1,2], L. de Poucques[1,2], R. Hugon[1,2], M. Belmahi[1,2], J.-L. Vasseur[1,2], J. Bougdira[1,2].
[1]Université de Lorraine, Institut Jean Lamour, Vandoeuvre-lès-Nancy, F-54506, France.
[2]CNRS, Institut Jean Lamour, Vandoeuvre-lès-Nancy, F-54506, France.

Abstract—The study of the chemical erosion by atomic hydrogen of graphite in the purpose of characterizing etching and re-deposition growth kinetics is presented. Carbon samples undergo plasma treatment under different time-exposures and gas mixtures at 10 mTorr, determined as the optimal pressure. The etching outcomes are analyzed via mass loss and structure comparison (SEM, micro-Raman spectroscopy) in order to evaluate the impact of the different experimental conditions, *i.e.* pressure, gas mixture, RF power coupling mode and erosion duration.

Index Terms—Atomic hydrogen source, Carbon chemical etching, Carbon dust, Langmuir probe, ITER.

1 Introduction

In the path to achieving controlled nuclear fusion as a secure and sustainable energy source, one of the remaining obstacles to overcome is the chemical and physical erosions of the reactor walls by the scrape-off-layer. Indeed, carbon erosion and re-deposition obtained in tokamaks induce important issues such as fusion plasma energy losses by radiation, deconfinement and tritium retention to an unacceptably large amount in the divertor region [1]. A better understanding of the process is essential in order to improve the quality of the carbonaceous compound and limit it from polluting the fusion reaction, especially in ITER.

Laboratory plasmas permit to approach the conditions of tokamak edge plasmas, *i.e.* equivalent electron temperature (< 5 eV) and density ($\sim 10^{12}$ cm^{-3}), low pressure, incomplete ionization [2]. On that account, this work focuses on the study of the chemical erosion by atomic hydrogen of different carbon surfaces (graphite and N11 carbon-fiber-composite used in Tore Supra†) in the purpose of characterizing erosion (etching and re-deposition growth) kinetics. Therefore the influence of different experimental parameters, such as pressure, gas mixture, RF power coupling mode and experiment duration, are investigated.

*. *Corresponding author:*
xavier.glad@ijl.nancy-universite.fr

†. Previous results demonstrated similar results for these two compounds, thus, in this work, only graphite will be studied [3].

2 Experimental set-up

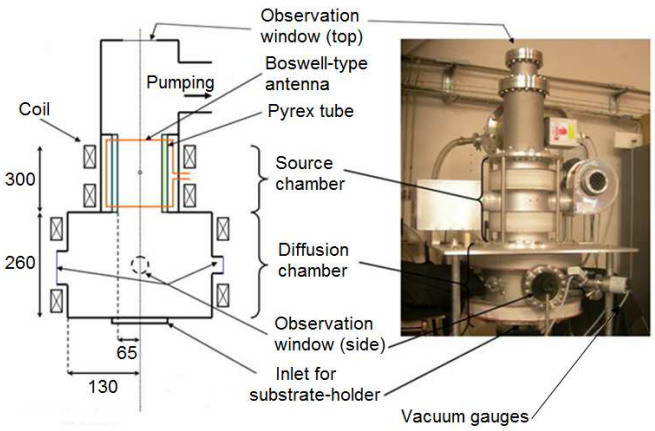


Figure 1: Sketch and photography of the experimental apparatus. Dimensions are given in mm.

Experiments were conducted in a helicon-type reactor presented in Fig. 1. The apparatus is divided in source and diffusion chambers. The former consists of a pyrex tube surrounded by a double saddle type antenna [4] connected to a 13.56 MHz 2 kW RF power supply (P_{RF}) via a Pi matching network. Consequently, the plasma is created in the source chamber and diffuses to the stainless steel

diffusion chamber. This transport is influenced by the pressure p inside the vessel.

Two different gas mixtures are used, pure argon and pure hydrogen for physical and chemical etching, respectively. Two sets of copper coils generate downward static magnetic fields up to 200 G in the source chamber (B_s) and up to 100 G in the diffusion one (B_{diff}). Erosion experiments, whose duration t_{exp} may vary, are performed on graphite samples lying on a heating substrate-holder able to reach a temperature T_{sh} of 650 °C.

To study plasma-surface interactions, several diagnostics are carried out for plasma and carbon samples characterizations. Electron density is determined by Langmuir probe measurements via the SmartSoft software from Scientific Systems. The carbon samples are 2×2 cm^2 squares of 125 µm thickness extracted from graphite sheets distributed by the company GoodFellow. One sample is used per etching experiment. The erosion outcomes are studied with mass loss, leading to an estimated erosion rate, and structure comparison. The latter is achieved via Scanning Electron Microscopy (SEM). Furthermore, the re-deposited carbon structures are analyzed by means of micro-Raman spectroscopy.

3 Results and discussion

3.1 Infuence of the pressure

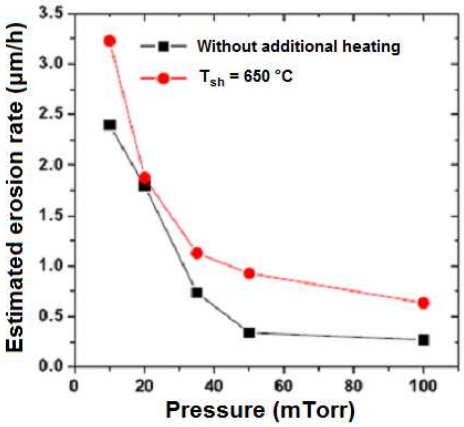
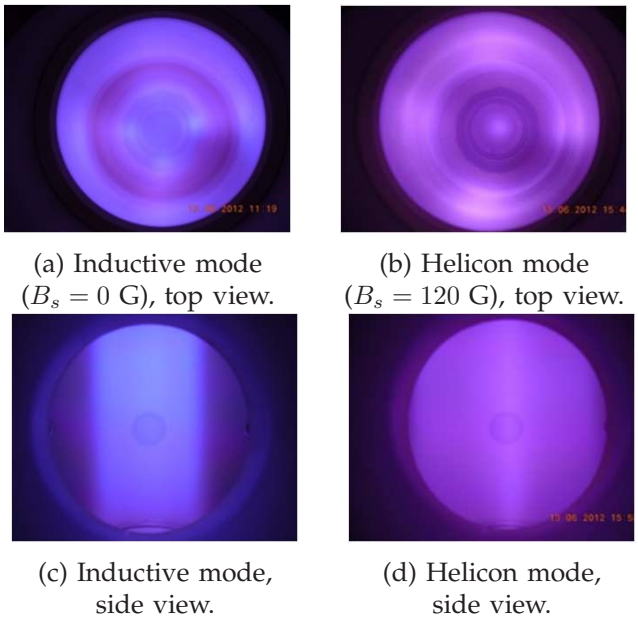


Figure 2: Erosion rate on graphite samples as a function of the pressure p. Pure hydrogen, $P_{RF} = 900$ W, $B_s = 0$ G, $B_{diff} = 100$ G, $t_{exp} = 4$ h, $T_{sh} = 650$ °C. [3]

A preliminary work was achieved in order to obtain the highest erosion rate, thus the strongest atomic hydrogen flux upon the graphite sample. Pressure being one of the main plasma parameters, its effect was examined. As seen in Fig. 2, erosion rate is inversely proportional to the pressure, the increasing pressure limiting the transport of the plasma. Due to the instability of a pure hydrogen discharge below 10 mTorr, this latter value has been determined as the optimal pressure. Moreover, such a low pressure permits to obtain the helicon mode in our experimental conditions.

One has to notice that, as previously obtained [5], the effect of the substrate-holder temperature is not to neglect, therefore, all experiments were done at $T_{sh} = 650$ °C.

3.1.1 Description



(a) Inductive mode ($B_s = 0$ G), top view.

(b) Helicon mode ($B_s = 120$ G), top view.

(c) Inductive mode, side view.

(d) Helicon mode, side view.

Figure 3: RF modes distinction, plasma pictures from the top and the side windows. Pure argon, $P_{RF} = 1800$ W, $B_{diff} = 100$ G, $p = 10$ mTorr.

The helicon reactor exhibits four modes, including inductive and helicon ones which both present the highest electron density (above 10^{11} cm^{-3} at 900 W). The inductive mode exists for high power, low pressure and $B_s < 20$ G and is described by a very bright and wide plasma column (Fig. 3a and 3c). Helicon mode is characterized by a thin and bright plasma column‡ and only appears at low pressure and high power for certain (n_e/B_s) couples [6] (Fig. 3b and 3d). The helicon mode was explained by F.F. Chen as the constructive interference between the incident helicon waves and its own reflection [7].

‡. The faint peripheral plasma seen in the pictures is due to the TG mode that always coexists with the helicon mode in our experimental conditions.

Additional details about the four available modes can be found in [8].

3.1.2 Physical erosion rate in pure argon

Erosion rate was evaluated in pure argon for the two previously described modes in order to determine the most suited one for carbon etching. One can notice that without any addition of H_2, the etching is only physical. Experiments lasted for 4 hours (t_{exp}) in the conditions described in the Fig. 3.

The results show an erosion rate of $0.5\ \mu\mathrm{m}\cdot\mathrm{h}^{-1}$ in inductive mode and $0.9\ \mu\mathrm{m}\cdot\mathrm{h}^{-1}$ in helicon one. The latter mode generating a very confined plasma due to helicon wave propagation, these results seem to show that the helicon column presents very strong electron and ion densities, especially at its very centre. Indeed, a specific and very localized topography can be seen on the sample at a position matching the plasma column centre.

Compared with pure hydrogen plasma which gave $3.2\ \mu\mathrm{m}\cdot\mathrm{h}^{-1}$ in the same conditions but less RF power (Fig. 2), argon physical etching is considerably less effective. One has to notice that experiments were conducted without bias voltage on the samples, therefore the latter were at floatting potential. In light of these results, the effects of the presence of H_2 in the gas mixture has been analyzed.

3.1.3 Addition of H_2

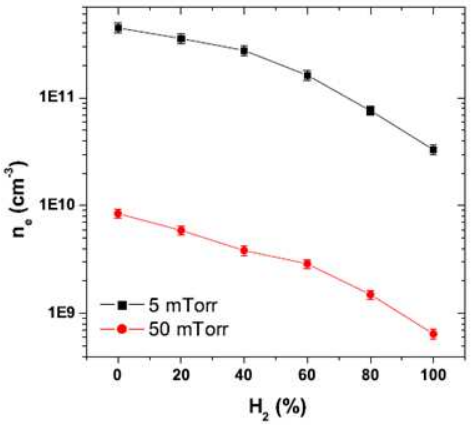


Figure 4: Electron density n_e as a function of H_2 proportion in a Ar/H_2 gas mixture for two different pressures. $P_{RF} = 800$ W, $B_s = 0$ G, $B_{diff} = 80$ G.

The addition of a molecular gas, H_2, in a pure atomic plasma, Ar, completely depletes the electron density as seen in Fig. 4. It is well known that electron energy dissipates to excite vibrational and rotational levels of the hydrogen molecule [9].

Such an effect has drastic consequences on the helicon mode. Indeed, the latter is impossible to obtain above a certain hydrogen percentage which could be in line with the assumption that the helicon mode does not appear below an electron density threshold. Taking these results into account, following etching experiments were carried out in inductive mode.

3.2 Chemical erosion kinetics in a pure hydrogen plasma

The mass loss was estimated on graphite samples for different t_{exp} at 1800 W in inductive mode, as depicted in Fig. 5.

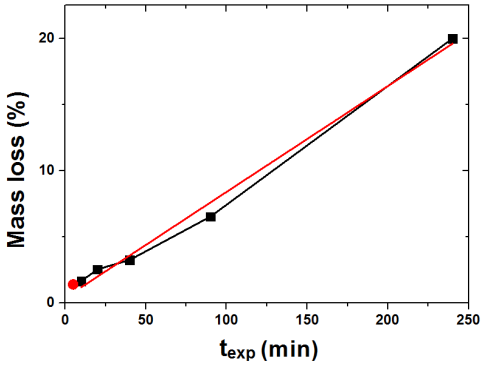
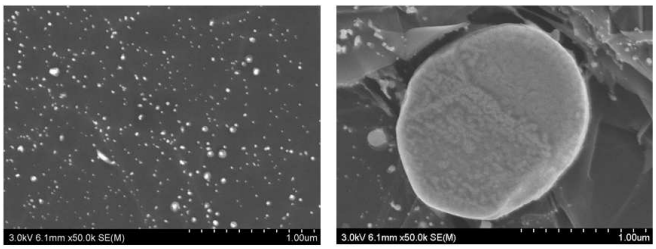


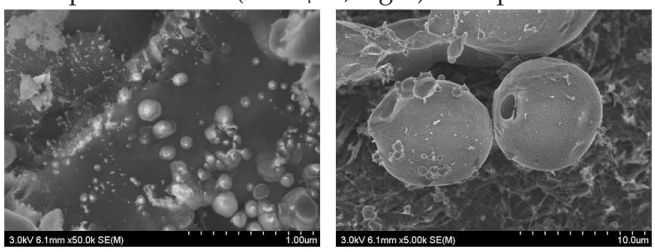
Figure 5: Mass loss percentage on graphite samples as a function of the experiment duration. Pure hydrogen, $P_{RF} = 1800$ W, $B_s = 0$ G, $B_{diff} = 100$ G, $p = 10$ mTorr, $T_{sh} = 650\,^{\circ}\mathrm{C}$.

At first glance, the mass loss is propotional to the experiment duration which could mean that the two erosion processes, etching and re-deposition, maintain the same contribution to the mass change in time. Calculations from the fit give a constant erosion rate of $6.0\ \mu\mathrm{m}\cdot\mathrm{h}^{-1}$ for each sample. This value is in good agreement with the estimated individual values varying from 4.8 to $6.3\ \mu\mathrm{m}\cdot\mathrm{h}^{-1}$. The only critical point is seen for $t_{exp} = 5$ min which presents an erosion rate almost twice higher than in other experiments ($10\ \mu\mathrm{m}\cdot\mathrm{h}^{-1}$). This phenomenon could be explained by the topography of the untreated samples, the very first minutes of plasma exposure smoothing the sample surface layers leading to a high mass loss and thus, an elevated etching rate. After this smoothing, the bulk of the sample, denser, seems to undergo the etching.

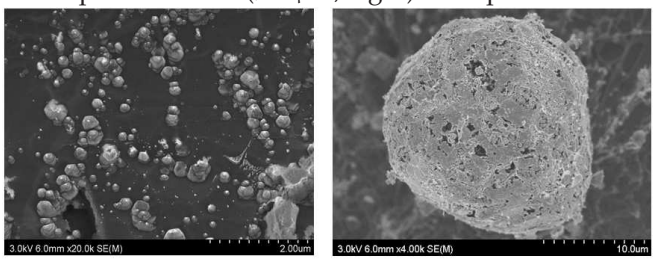
SEM micrographs, as depicted in Fig. 6, exhibits a characteristic topography. After 5 minutes,



(a) $t_{exp} = 5$ min: heaps (zoom: x50k, left) and spherical dust ($\varnothing 1.6$ µm, right) re-deposition.



(b) $t_{exp} = 90$ min: heaps (zoom: x50k, left) and spherical dust ($\varnothing 9$ µm, right) re-deposition.



(c) $t_{exp} = 4$ hour: heaps (zoom: x20k, left) and spherical dust ($\varnothing 21$ µm, right) re-deposition.

Figure 6: SEM micrographs of graphite samples according to their plasma exposure time. Pure hydrogen, $P_{RF} = 1800$ W, $B_s = 0$ G, $B_{diff} = 100$ G, $p = 10$ mTorr, $T_{sh} = 650\,^{\circ}$C.

re-deposition can already be observed (up to $\varnothing 1.6$ µm). The spherical re-deposited structures grow with the exposition time, up to $\varnothing 11$ µm and $\varnothing 35$ µm for 90 min and 4 hours, respectively. It seems that the heaps (left pictures in Fig. 6) are created by surface re-deposition. By contrary, the spherical dusts could undergo volume growth in gaseous phase before being deposited on the sample and gain in size by contribution of CH radicals clusters. In any case, one could suggest that radicals resulting from the etching would be deposited preferentially on the already present structures. This could explain why, even though the etching rate is important, massive structures are observed.

Moreover, the latter seem to consist mainly of amorphous carbon. This assumption has been strengthened by the micro-Raman spectrographs which present a clear increase of the disordered carbon D peaks after plasma treatment.

These porous carbon dusts look similar to those obtained in tokamaks, which are the core of the tritium retention issue.

4 Conclusion

The erosion rate of graphite samples was studied varying experimental parameters in order to determine the suited conditions to improve carbon etching, approaching the scrape-off-layer conditions. Re-deposition was analyzed via scanning electron microscope which revealed characteristic structures found on N11 CFC tiles of tokamaks.

It was shown that, in our conditions, the highest etching rate is obtained at 10 mTorr in a hydrogen inductive discharge. However, helicon mode in Ar and Ar/H_2 gas mixtures needs further investigations.

The erosion rate do not seem to have any dependence with the experiment duration. Nonetheless, this parameter has a strong influence on the re-deposition observed via SEM. Additional diagnostics, such as micro-Raman spectroscopy and TEM, should help examine the re-deposited structures detected in hydrogen inductive and argon helicon discharges. High resolution OES, Langmuir probe and TALIF measurements will be performed to characterize plasma species, such as electrons, H, C, C_2, CH and C_xH_y, in order to find correlations and explain fundamental processes responsible of plasma/surface interactions. The aim is to understand these interactions in an attempt to limit them, as well as dust transport, in fusion plasma.

References

[1] G. Federici *et al.*, *Nucl. Fusion* 41 (2001) 1967-2137.
[2] J.P. Harpe, D.A. Petti, H.-W. Bartels, *Fusion Engineering and Design* 63-64 (2002) 153-163.
[3] T. Bieber, *PhD Thesis*, Université de Lorraine, France (2012).
[4] R.W. Boswell, *Phys. Lett. A* 33 (1970) 457-458.
[5] C.M. Donnelly, R.W. McCullough, J. Geddes, *Diamond and Related Materials* 6 (1997) 787-790.
[6] K.K. Chi, T.E. Sheridan and R.W. Boswell, *Plasma Sources Sci. Technol.* 8 (1999) 421-431.
[7] F.F. Chen, *Phys. Plasmas* 10 (2003) 2586-2592.
[8] T. Bieber, S. Bardin, L. de Poucques, F. Brochard, R. Hugon, J.-L. Vasseur and J. Bougdira. *Plasma Sources Sci. Technol.* 20 (2011) 015023.
[9] H. Tawara, Y. Itikawa, H. Nishimura, and M. Yoshino, *J. Phys. Chem. Ref. Data* 19 (1990) 617-636.

DEVELOPMENT AND APPLICATION OF NEW MULTICOMPONENT ELECTRODE MATERIALS FOR DEPOSITION TECHNOLOGIES

E.A. Levashov*, Yu.S. Pogozhev, D.V. Shtansky, A.E. Kudryashov, Ph.V. Kiryukhantsev-Korneev

National University of Science and Technology "MISIS", Leninsky Prospect, 4, Moscow 119049, Russia, levashov@shs.misis.ru

The synthesis of advanced multicomponent nanostructured films by PVD and pulsed electrospark deposition (PED) requires the development of multicomponent electrodes. Self-propagating high-temperature synthesis (SHS) is a promising method for electrodes fabrication, which provides a highly dense, exhibits required mechanical, thermal, and electrical properties needed for such composite materials. The control of chemical composition of targets facilitates the deposition of multicomponent films with required composition.

During the last decade various SHS- composite targets have been developed and synthesized for hard tribological films (TiB_x, $TiSi_x$, TiBN, TiCrB, TiSiB, TiAlBN, TiAlSiB, TiCrSiCN, TiSiBN, TiCrAlC, CrAlBSi, oth.) and for biological films ($TiC_{0.5}$+CaO, $TiC_{0.5}$+ZrO_2, $TiC_{0.5}$+CaO+TiO_2, $TiC_{0.5}$+$Ca_{10}(PO_4)_6(OH)_2$, Ti_5Si_3+ZrO_2, (Ti,Ta)C+$Ca_3(PO_4)_2$, (Ti,Ta)C+CaO) [1-4]. In order to enhance the toughness and thermal-resistance (resistance to thermal-cycling during high-power magnetron sputtering) needed for PVD targets, functionally graded targets have been developed and manufactured. As an example, Fig. 1 shows three layers functionally graded target with $TiC_{0.5}$ -Ti_3PO_x-CaO working layer, TiB-Ti intermediate layer, and Ti bottom layer.

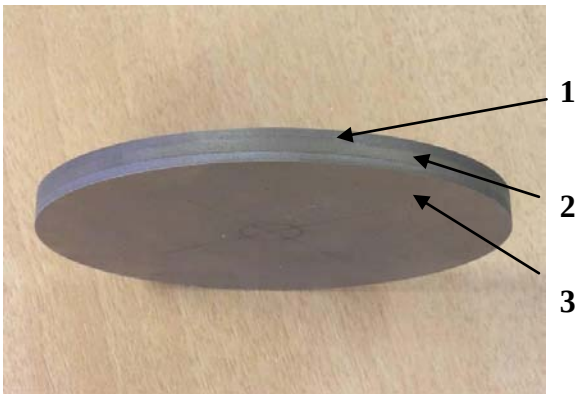


Fig. 1. Functionally graded target with $TiC_{0.5}$–$Ca_3(PO_4)_2$ working layer (1), $TiC_{0.5}$ intermediate layer (2) and Ti bottom layer (3).

In the case of multicomponent target uniform flow of both metal and non metal atoms and ions is realized from the target to substrate. SHS- targets can be especially benefit for the deposition of multifunctional nanostructured films in which both metallic (Ti, Ta, Al, Mo, Cr, Ca) and nonmetallic (Si, B, C, P, O, N) elements.

Taking into account the demand for composite targets for ion-plasma technologies for the deposition of functional nanostructured coatings, this work is a review of recently obtained results on synthesis in the combustion mode of a series of chemical classes of systems. The experimental results for self-propagating high-temperature synthesis are presented. The described ceramics becomes often to be implemented in technology of magnetron sputtering of thin films and coatings characterized by high mechanical properties, high heat resistance to high-temperature oxidation, and thermal stability. Some of considered classes of ceramics are advanced as a biocompatible material for medicine.

The second part of the work is focused on the development of electrodes for PED. Three groups of electrodes are presented: *dispersive-hardening ceramic materials* with effect of simultaneous strengthening of carbide grains and metallic binder by precipitations; *nanoparticles disperse-strengthened composite materials* with nanoparticles based on refractory compounds; *MAX- phases based materials; nanostructured cemented carbides*.

Recent studies concerning ceramic materials with the effect of dispersion hardening by nanoparticles in order to controlling the distribution of alloying elements within carbide grains are reviewed. Combination of the force SHS-pressing followed by annealing makes it possible to synthesize composite materials with desirable structure and properties. Some service properties are increased due to nanosized precipitations to be formed result in concentration separation of supersaturated solid solutions. Composite ceramic materials based on Ti-xC, Ti-Me–xC (Me= Zr, Nb, Ta, Mo) systems were produced by SHS. Contents of third elements are varied from 5 to 25 at.%. Composition and structure of carbide grains and intergranular phase just after combustion process is not equilibrium: supersaturated solid solutions are formed because of high temperature gradient and combustion velocity. Precipitations are appeared result in concentration separation of supersaturated solid solution. Carbide grains content precipitations sized 20-200 nm based on solid solution (Ti-Me).

Precipitations are formed as a results of concentration separation of supersaturated solid solution via two possible schemes [5]:

$(Ti, Me)_{x+y}C = (Ti, Me)_xC + y(Me\text{-}Ti)$, where Me = Nb, Ta, Zr (less 6%)

or

$(Ti, Me)_{x+y}C = (Ti, Me)_xC + (Me, Ti)_yC$, where Me = Mo, W

Also mixed mechanism was experimentally observed:

$(Ti, Zr)_{x+y}C = (Ti, Zr)_xC + y(Zr\text{-}Ti) + z(Zr, Ti)_zC$.

The SHS was successfully used to fabricate MAX-phases in the systems Ti_3AlC_2, Ti_2AlC, Cr_2AlC. A complex study on structure, phase composition, and chemical and mechanical properties of ceramic materials based on the $M_{n+1}AX_n$-phases has been recently presented [6].

PED- coatings deposited on Ti-, Ni-, Fe- alloy substrates with successful combination of hardness, elastic recovery, adhesion strength, heat resistance, and reduced friction coefficient were obtained. Coatings thickness (more than 50 μm) at density till 100%, lower roughness (less than 0.1 μm) were achieved due to high energy expended to erosion of nanostructured anode at high frequency and relatively lower pulse discharge energy. It was shown that MAX- phase based electrodes application and optimization of PED frequency-energy parameters allows depositing coatings with amount of hexagonal phase till 50%.

REFERENCES

1. Levashov E.A., Pogozhev Yu.S., Kurbatkina V.V., Lin G., Kimura T., Susana M.M., Rivera T., oth. Advances in Ceramics – Synthesis and Characterization, Processing and Specific Application. Edited by Costas Sikalidis, Published by INTECH, ISBN 978-953-307-505-1, 2011, p. 3-41.

2. Levashov E.A., Kurbatkina V.V., Rogachev A.S., Kochetov N.A., Patsera E.I., Sachkova N.V. Characteristic properties of combustion and structure formation in the Ti–Ta–C system. Russian J. Non-Ferrous Metals 2008 , 49(5), p.404–413.

3. Levashov E.A., Rogachev A.S., Kurbatkina V.V., Epishko Yu.K., Kochetov N.A. Combustion and structure formation in the Ti-Ta-C-$Ca_3(PO_4)_2$ system. Int. J. SHS 2007, 16(4), p. 218-224.

4. Levashov E.A., Larikhin D.V., Shtansky D.V., Rogachev A.S., Grigoryan H.E., Moore J.J. Self-propagating high-temperature synthesis of functionally graded PVD targets with a ceramic working layer of TiB_2-TiN or Ti_5Si_3-TiN. J. Mater. Synth. Process, 2002, 10(6), p. 319-330.

5. Levashov E.A., Kurbatkina V.V., Zaitsev A.A., Rupasov S.I., Patsera E.I., Chernyshev A.A., Zubavichus Ya.V., Veligzhanin A.A. Structure and Properties of Precipitation-Hardening Ceramic Ti-Zr-C and Ti-Ta-C Materials. The Physics of Metals and Metallography, 2010, vol. 109, No. 1, pp. 95-105.

6. E.A. Levashov, Yu.S. Pogozhev, D.V. Shtansky, M.I. Petrzhik, Russ. J. Non-Ferrous Met., 2008, No. 3, p. 13-28.

Spotless arc activated high-rate deposition using novel dual crucible technology for titanium dioxide coatings

Bert Scheffel, Thomas Modes, Christoph Metzner,
Fraunhofer Institute for Electron Beam and Plasma Technology (FEP)

Introduction

For deposition of thin oxide coatings there are a lot of qualified PVD processes today. If high productivity or large-area coating is necessary for economic reasons processes with high deposition rate are reasonable. Using electron beam (EB) evaporation all inorganic materials can be evaporated with high rates. Microstructure of coatings deposited by EB-evaporation depends on substrate temperature during layer growth and melting temperature of coating material. Particularly in case of high melting materials columnar and porous microstructure is obtained. For large area coating several plasma sources have been developed in order to enhance energy of condensing particles and to get denser layer microstructure [1].

Spotless arc Activated Deposition (SAD) combines electron beam high-rate evaporation using axial gun and a spotless arc discharge burning in metal vapor on hot evaporating cathode [2]. The SAD process is suitable for evaporation of high-melting metals like titanium, zirconium or tantalum providing high deposition rate up to 2000 nm/s. Moreover plasma-activation enables reactive mode of operation and deposition of oxides, nitrides or other compounds with a high rate in the range of 20 to 100 nm/s. A Spotless arc is an arc discharge burning in metal vapor which is obtained if the cathode temperature is high enough to enable high thermionic electron emission current density. Spotless mode results in relatively low cathodic arc current density and droplets known from arc evaporators with cold cathode are completely avoided [3]. Nevertheless high DC arc current up to 2000 A is possible.

Recent work has shown that SAD process is well suited for deposition of titanium dioxide coatings based on evaporation of titanium and reactive processing in oxygen atmosphere [4]. TiO_2 layers were deposited at very high deposition rates between 40 and 70 nm/s. Depending on process conditions amorphous coatings or crystalline phases were obtained. Coatings consisting of anatase phase show very good properties concerning photoinduced superhydrophilicity and photocatalysis. Transparent layers with high refractive indexes in the range of 2.30 and 2.58 could be reached.

SAD processing with dual crucible

High current arc discharge burning in metal vapor needs a good contact of vapor cloud to an anode. In case of titania deposition anode needs to be coated with understoichiometric titanium oxide coatings in order to maintain electrical conductivity. Therefore anode has to be positioned in the near of evaporation source. A water-cooled anode is well qualified to meet the requirements regarding high arc current, vapor condensation and thermal load during EB and plasma process. However, it has been found that coatings deposited on water-cooled anode will peel off from the anode after some hours of operation time. Therefore long-term stability of SAD process with water-cooled anode is limited. Some industrial applications demand long-term stability of high-rate and large-area coating processes over 100 h.

Limitation of long-term stability of SAD process caused by coatings deposited at anode equipment could be overcome by introduction of a novel dual crucible technology. The process has been

engineered for high-rate electron beam evaporation and is well matched to large area coating. For homogeneous coatings over wide strip width two or several dual crucibles have to be used.

The new process is based on two evaporating electrodes. While evaporating metal within the first crucible acts as cathode, evaporating metal of the second crucible forms the anode of the arc discharge. Both electrodes are in a good contact to vapor and reactive gas but plasma process can't be disturbed by coating of electrodes anymore. In figure 1 schematic of the process and electrical circuitry as well as a picture of plasma process with a laboratory type of dual crucible are shown.

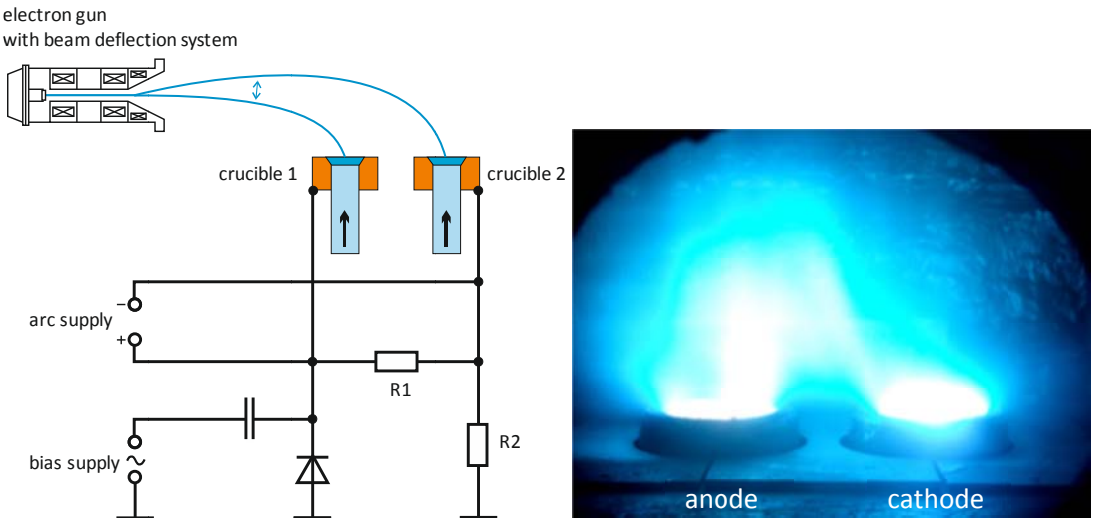


Figure 1 Schematic of SAD process with dual crucible and electrical circuitry for biasing (left)
Dual crucible during SAD process with titanium ingots, arc current 250 A DC (right)

Dual crucible consists of two water-cooled crucibles each equipped with an independently motor-driven rod-feed system from below. Titanium rods of a diameter of 65 mm can be moved with constant speed into the titanium melt heated by electron beam. A static magnetic field bends the electron beam from beam generation direction to the titanium surfaces. Electron beam is generated by an electron gun of axial type and is deflected by an integrated fast magnetic beam deflection system. Deflection pattern on surface, jumping beam frequency and duty cycle can be defined within wide ranges and define power density distribution and mean power for each crucible. Both crucibles are electrically insulating fastened from each other and from ground potential. Resistors R1 and R2 were dimensioned so that losses of arc and bias current are negligible but crucible potentials are shifted towards ground potential.

A bias supply delivers a sinus ac current in mid-frequency range (25 kHz) for pulsed plasma biasing method. The alternating voltage is rectified by a Villard circuit. Resulting pulsed positive voltage is applied to one of the crucibles with respect to ground potential. In this way plasma potential can be periodically shifted with respect to substrate potential if substrate is at ground potential. For large area coating of metal substrates, e.g. metal strip, it is a big advantage if substrate can be kept at ground potential. Nevertheless positively charged ions will be accelerated to high energy in the plasma sheath near the substrate surface.

The arc discharge burns between the two evaporating titanium melts. There are several possibilities for arrangement of crucibles and electron gun and for circuitry of arc supply: with or without magnetic beam bending, parallel or perpendicular arrangement of crucibles related to magnetic field lines, DC or AC arc supply, Cathode of DC arc discharge = crucible 1 or crucible 2. Moreover jumping beam

frequency and arc AC frequency can be synchronized or not. Also phase relation plays a role if same frequencies are used (e.g. deflected EB always meets cathode or EB always meets anode).

All main options have been approved. Favorable option is an arrangement of crucibles as shown in figure 1 - at which a line linking the crucibles is perpendicular to field lines of magnetic bending field (not shown) - and DC arc discharge with crucible 2 acting as cathode. Low energy plasma electrons have to drift perpendicularly to the magnetic field resulting in increased arc voltage and ionization rate. In this configuration plasma is not only generated at cathode (as in case of water-cooled anode) but also at the anode. Moreover plasma jets are formed in the region between anode and cathode having their roots at the electrodes. Anodic and inter-electrode phenomena of the magnetized plasma are not well understood up to now. Additional plasma generation at the anode is a very welcome effect compensating the loss of ionization degree that can be expected if a water cooled anode is replaced by an evaporating anode. Arc discharge can be sustained in a wide range of evaporation of anode. The arc discharge extinguishes if heating of anode or cathode is switched off. Degree of flux ionization calculated by relation of ion saturation current density (assuming singly charged ions) and deposition rate is in the range of 10 to 30 %.

High-rate deposition of titanium dioxide coatings

An oxygen flow in the range of 3000 to 6000 sccm was necessary to obtain stoichiometric and transparent titanium dioxide layers. Coating thickness was measured in situ using light reflection spectroscopy. Dynamic deposition rate of oxide layers was between 500 and 1000 nm m/min corresponding to a stationary deposition rate between 40 and 80 nm/s. Optical properties concerning absorption and refractive index of the TiO_2 coatings were investigated by ellipsometry, analysis of phase composition phase was done by x-ray diffraction. The layers are practically free of absorption in the visible range of spectrum. The refractive index is drastically influenced by substrate temperature and plasma parameters. Layers deposited with plasma activation have a significant higher refractive index between 2.30 and 2.58, even at low substrate temperature.

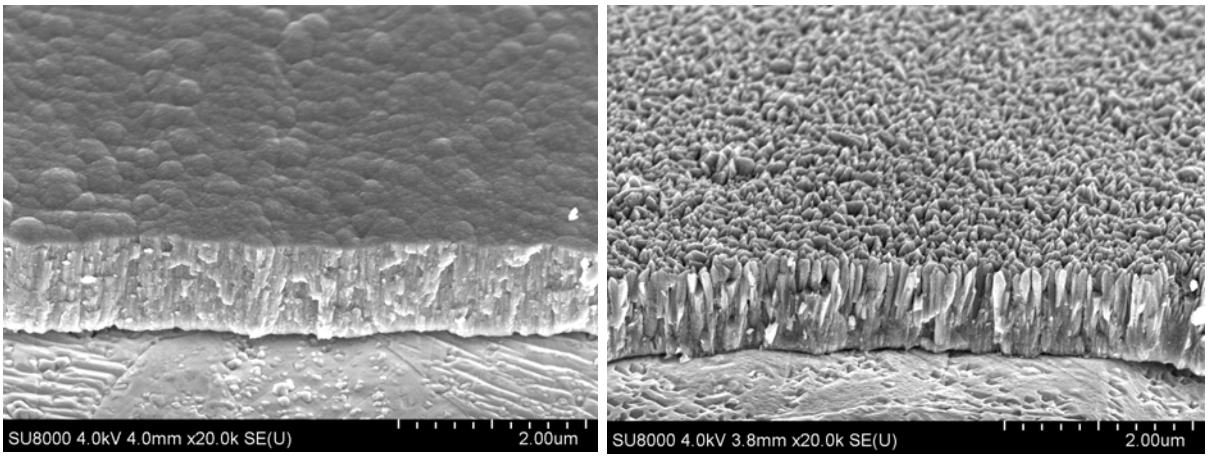


Figure 2 Titanium dioxide coatings on steel strip, SEM images of cross fracture, amorphous (left) and anatase phase (right)

Depending on substrate temperature, oxygen partial pressure and plasma parameters amorphous, anatase-phase or rutile-phase can be obtained. Amorphous and anatase-phase coatings were deposited at a substrate temperature below 150°C and above 200°C respectively. SEM images of cross fractures of such coatings are shown in figure 2. Associated XRD diagrams are given in figure 3. XRD diagram of anatase layer does not show any traces of rutile phase crystallites.

In order to check long-term stability of the process titanium dioxide coatings were deposited on continuously moved 250 mm wide stainless steel strip. Liquid titanium level was kept constant by adapted speed of rod feed of each crucible. Process and coating parameters could be kept constant without problems over many hours. The process stability was only limited by the length of the titanium rods of 230 mm. Total process duration of 30 h was achieved by some process interruptions and re-load titanium rods.

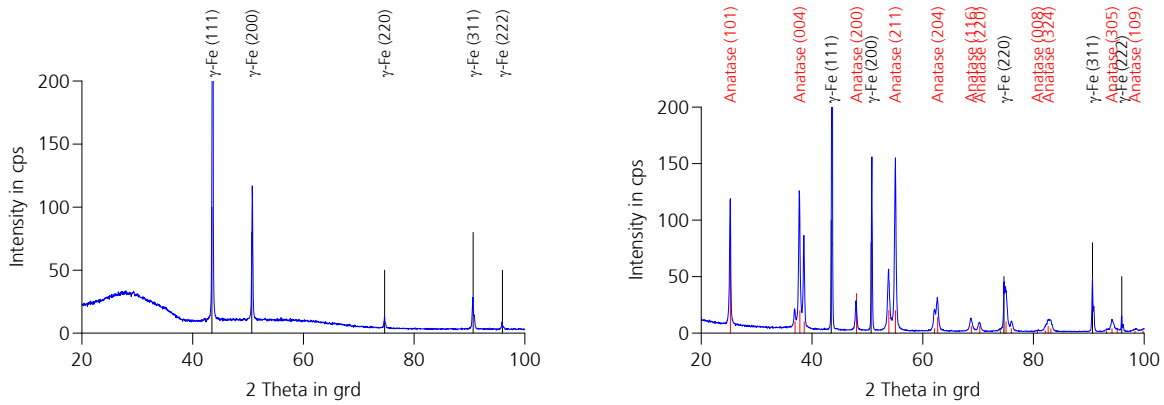


Figure 3 Titanium dioxide coatings on steel strip, XRD diagrams, amorphous (left) and anatase phase (right)

Acknowledgement

The project was funded by the European Union and the Free State of Saxony (funding reference 14274/2473). We gratefully acknowledge co-operational research with the company Von Ardenne Anlagentechnik GmbH.

Literature

[1] A. Anders, Surface & Coatings Technology 200 (2005) 1893 – 1906

[2] K. Goedicke, B. Scheffel, S. Schiller, Surface & Coatings Technology 68/69 (1994) 799-803

[3] A. I. Vasin, A. M. Dorodnov, V. A. Petrosov, Sov. Tech. Phys. Lett. 5 (12) (1979), 634-636

[4] T. Modes, B. Scheffel, C. Metzner, O. Zywitzki, E. Reinhold, Surface & Coatings Technology 200 (2005) 306– 309

Surface interaction and processing using polyatomic cluster ions

G. H. Takaoka, H. Ryuto, and M. Takeuchi

Photonics and Electronics Science and Engineering Center, Kyoto University,
Nishikyo, Kyoto 615-8510, Japan
Corresponding author: gtakaoka@kuee.kyoto-u.ac.jp

Abstract

We developed two types of polyatomic cluster ion sources, one of which was a liquid cluster ion source using organic materials with a high-vapor pressure. Vapors of liquid material such as ethanol and water were ejected through a nozzle into a vacuum region, and liquid clusters were produced by an adiabatic expansion phenomenon. Another type was a cluster ion source using ionic liquids with a relatively low-vapor pressure. Positive and negative cluster ions were produced by a high-electric field emission. In addition, the interaction of polyatomic cluster ions with solid surfaces such as Si(100), SiO_2, glass, and PMMA surfaces was investigated, and chemical sputtering was predominant for the Si(100) surfaces irradiated by ethanol cluster ion beams. Also, the irradiation damage of the Si(100) surfaces by ethanol and water cluster ion beams was smaller than that by Ar monomer ion irradiation at the same acceleration voltage. With regard to surface modification, PMMA surfaces were chemically modified by water cluster irradiation. Also, glass surfaces changed to electrically conductive surfaces by ionic liquid cluster ion irradiation. Furthermore, to demonstrate engineering applications of high-rate sputtering and low-damage irradiation by ethanol cluster ion beams, micro-patterning was performed on the Si surfaces.

Key words: Cluster, Polyatomic ion, Ionic liquid, Sputtering, Micro-patterning, Surface modification

Experimental

Liquid materials served as a source for the production of polyatomic clusters. They are more appropriate than gaseous materials, as they tend to have more radicals in their polyatomic molecules than gaseous materials. Liquid cluster ion sources for a high-vapor pressure of materials were developed. The details of the source were described elsewhere [1,2]. The liquid materials were heated up to 150℃, and the vapors were ejected through a nozzle into a vacuum region. The time of flight (TOF) measurement showed that the cluster size was distributed between a few hundreds and a few tens of thousands, and the average size (peak size) was approximately 500 to 1000 molecules for ethanol clusters and approximately 2500 molecules for water clusters, respectively. It should be noted that both water clusters and ethanol clusters might have the hydrogen bonding ability. It is different from that of gas clusters, which are loosely-coupled each other by a van der Waals force. Therefore, these liquid clusters might be stronger in the intermolecular force than gas clusters [3].

The polyatomic ion source for ionic liquids was also developed. Ionic liquid used was 1-butyl-3-methylimidazolium hexafluorophosphate (BMIM-PF_6). A high-electric field method was employed for the ion-emission from a sharp tip made of carbon rod [4]. The diameter of the rod was 0.3 mm. As a tip designed, for example, a needle with a radius of 80 μm was employed. The TOF measurement showed that the peak mass number was approximately 5000 for positive and negative ions. The molecular weight of cation ($C_8H_{13}N_2$) and anion (PF_6) is 139.22 and 144.96, respectively. By assuming that singly charged ions were extracted, ionic liquid cluster ions with a size of approximately 18 molecules were produced. It should be noted that they might have the ionic bonding ability.

Results and discussion

Polyatomic clusters produced by an adiabatic expansion phenomenon were ionized by an electron bombardment. The electron voltage for ionization (Ve) was 200 V, and the electron current for ionization (Ie) was 250 mA. The polyatomic cluster ions such as ethanol and water cluster ions were accelerated toward a substrate. Various kinds of substrates such as Si(100), SiO_2, glass, and PMMA substrates were irradiated at different acceleration voltages. The irradiation damage by polyatomic cluster ion beams was investigated using the Rutherford backscattering spectrometry (RBS) method.

Figure 1 shows the number of displaced atoms for the Si(100) surfaces irradiated at different acceleration voltages by ethanol and water cluster ions. The ion dose was 1.0×10^{15} ions/cm^2, and the cluster size used was larger than 100 molecules per cluster. The number of displaced atoms increases with increasing acceleration voltage. The number is less than that for argon (Ar) monomer ion irradiation at the same acceleration voltage. The incident energy of a molecule is the accelerating energy divided by the cluster size, and this is very low for cluster ion irradiation. Therefore, irradiation damage caused by ethanol and water cluster ion beams is less than that of Ar monomer ion beams. In addition, at an acceleration voltage of 1 kV the number of displaced atoms by ethanol cluster ion irradiation is the same as that of the Si(100) surface prior to irradiation. Because the incident energy of an ethanol molecule is less than 10 eV, a damage-free surface can be obtained using the low-energy-irradiation effect of the ethanol cluster ion beams.

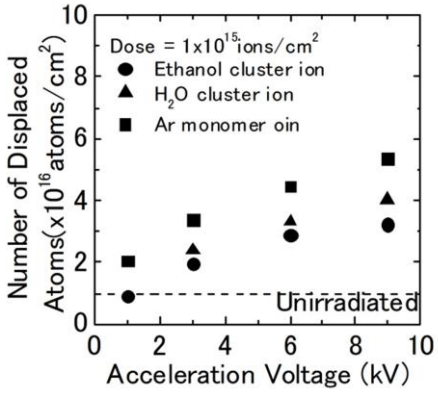


Fig.1 Number of displaced atoms for Si(100) Surfaces at different acceleration voltages.

In order to investigate the irradiation damage of Si(100) surfaces by ethanol cluster ion beams, the ellipsometry measurement was performed [5]. Figure 2 shows the values of Delta and Psi measured for Si(100) surfaces irradiated by ethanol cluster ions and Ar monomer ions at different acceleration voltages. The ion dose was 1.0×10^{15} ions/cm^2. For the ethanol cluster ion irradiation, the thickness (T_{ox}) of oxide layer increases with increasing acceleration voltage, and it is approximately 9.5 nm at an acceleration voltage of 9 kV. With regard to damage thickness (T_d), it is less than 1.0 nm. The total thickness of the oxide and damage thickness corresponds to the damage thickness measured by the RBS channeling. This indicates that the damage layer induced by the ethanol cluster ion irradiation is very thin, and that the oxide layer is thicker than the damage layer. The oxygen as a constituent atom of the ethanol molecule might contribute to the oxide layer formation. At an acceleration voltage of 1 kV, the damage layer thickness by ethanol cluster ion irradiation is extremely thin, although the oxide layer thickness is approximately 1.5 nm. On the other hand, for the Ar monomer ion irradiation, the damage layer thickness increases with increasing acceleration voltage. The oxide layer is thinner than the damage layer, and it is similar to the natural oxide layer formed on the unirradiated surface.

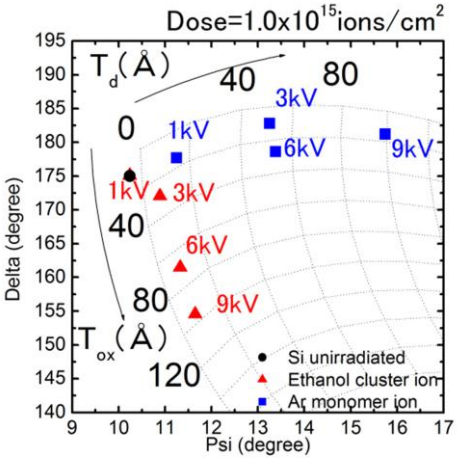


Fig.2 Values of Delta and Psi for Si(100) surfaces irradiated at different acceleration voltages.

It is well known that the wet process using organic liquid materials has been applied to the surface treatment for solid surfaces. However, etching by organic liquid materials, such as ethanol, is not achieved even at elevated temperatures. Figure 3 shows the dependence of sputtered depth for Si(100) substrates and SiO_2 films on acceleration voltage for ethanol and water cluster ions. The ion dose was 1.0×10^{16} ions/cm^2. As shown in the figure, the sputtered depth increases with increasing acceleration voltage. For the case of water cluster ions, the sputtered depths of Si and SiO_2 are almost the same. This is ascribed to the physical sputtering by the water cluster ion irradiation. With regard to Si(100) surface, the surface oxidation occurs rapidly after bombardment of the water cluster ions. The OH radicals and oxygen atoms produced after the bombardment have important roles in the oxidation due to the implantation and/or diffusion processes. For the bombardment of water cluster ions after the oxide layer formation, the incident energy is used for physical sputtering of the silicon oxide layers. Hereby, the sputtered depth of Si surfaces is similar to that of SiO_2 surfaces.

In contrast, the sputtered depths of Si(100) and SiO_2 by the ethanol cluster ion irradiation are much different, as shown in the figure. When the acceleration voltage is 9 kV, the sputtered depth is 475 nm for Si(100) and 47 nm for SiO_2, respectively. The sputtering ratio of Si(100) to SiO_2 is approximately 10. Taking account of the sputtered depth and the ion dose, the sputtering yield can be calculated by estimating the density of Si such as 2.42 g/cm^3. The sputtering yield of Si at an acceleration voltage of 9 kV for the ethanol cluster ions is 246 atoms-per-ion, which is approximately 100 times larger than that by Ar ion beam sputtering. After bombardment of the ethanol cluster ions, hydrogen atoms are produced, and they react with the Si surface atoms. The selectivity arises from the volatility of the reaction products and the difference in binding energy among the materials [6,7]. This suggests that chemical reactions between Si(100) and ethanol produce silicon hydride which is the dominant etching material for Si(100) surfaces.

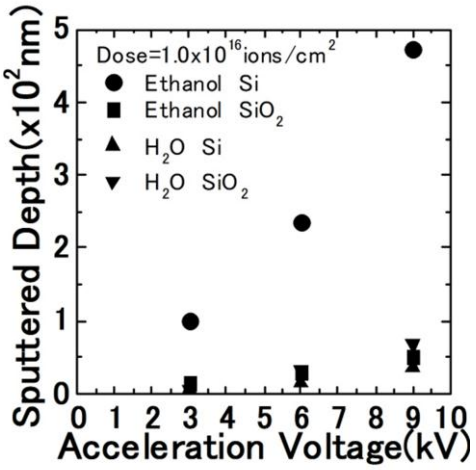


Fig.3 Dependence of sputtered depth for Si(100) and SiO_2 surfaces on acceleration voltage for ethanol and water cluster ions.

Polymethyl methacrylate (PMMA) is a polymer with a molecular structure of $CH_3CCH_2COOCH_3$. PMMA has attracted interest as an organic glass, and it has been used in various kinds of chemical devices such as microreactors. Figure 4 shows the sputtering yield for PMMA surfaces irradiated at different acceleration voltages by ethanol and water cluster ion beams. Taking account of the sputtered depth and the ion dose, the sputtering yield was calculated by first estimating the density of PMMA to be 1.19 g/cm^3. As shown in Fig. 4, the sputtering yield increases with increasing acceleration voltage, and the yield was found to be 206 molecules-per-ion for water cluster ion irradiation and 134 molecules-per-ion for ethanol cluster ion irradiation at an acceleration voltage of 9 kV. The high sputtering yield of PMMA substrates occurs because of the ejection of sputtered particles as a monomer unit due to the cluster ion irradiation.

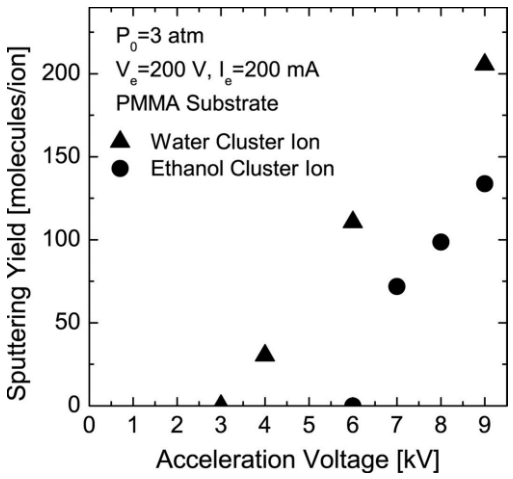


Fig.4 Sputtering yield for PMMA surfaces irradiated at different acceleration voltages by ethanol and water cluster ion beams.

In particular, water cluster ion irradiation exhibits higher sputtering yields than ethanol cluster ion irradiation at different acceleration voltages. For PMMA substrates irradiated by water cluster ions, it is thought that the chemical erosion of the substrate surfaces occurs through the exchange of the CH_3 radical in $COOCH_3$ with an H atom of the water cluster, or through the exchange of an OCH_3 radical with an OH radical [3]. Therefore, the PMMA surface changes to a polymethacrylic acid surface, which has a melting point lower than room temperature and is dissolvable in water. The impact of water cluster ions on the changed surface enhances the ejection of methacrylic acid molecules in the monomer state from the surface. Thus, the high sputtering yield of PMMA surfaces is achieved by both the chemical erosion of the surface and the momentum transfer of the incident energy of the water cluster ion irradiation.

To demonstrate an engineering application of high-rate sputtering and low-damage irradiation by ethanol cluster ion beams, a patterning process was performed on the Si(100) surface with a photo resist mask. Line, circle, and square mask patterns were commercially available and the line width was in the range of 0.5 μm to 3 μm. The diameter of the circle and the edge length of the square were both 60 μm, and the spacing for the circle and square patterns was 10 μm. The thickness of the photo resist film coated on the Si(100) substrate was approximately 1 μm. Figure 5 shows the scanning electron microscope (SEM) images for the lines, circles, and squares patterned with ethanol cluster ion beams.

The acceleration voltage was 9 kV, and the ion dose was 5.0×10^{15} ions/cm^2. After the ethanol cluster ion irradiation, the photo resist film on the Si(100) surface was removed with acetone. As shown in the above figure, the pattern edge is sharp, and the sputtered surface (bright area) is a flat plane. The micropattern has been clearly prepared by the ethanol cluster ion beam. Moreover, the measured sputtered depth was approximately 0.22 μm, which increased with increasing ion dose. A sputtered depth of 0.75 μm was obtained at an ion dose of 2×10^{16} ions/cm^2, and the maximum depth available was limited by the resist film thickness.

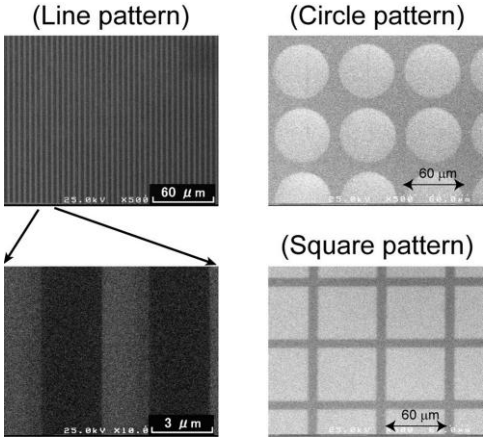


Fig.5 SEM images for the lines, circles and squares patterns on Si surfaces.

Figure 6 shows (a) SEM and (b) atomic force microscope (AFM) images of glass substrates deposited by positive ions of ionic liquids. The extraction voltage applied to the tip was 6kV. As shown in the figure, the SEM images of glass substrates are observed clearly without charge-up of electron beams. This is due to the deposition of ionic liquids exhibiting electrically conductive property. Furthermore, the glass surface becomes rough after deposition. According to AFM measurement, the surface roughness (Ra) is 0.53 nm. It is larger than the surface roughness of the unirradiated glass, such as 0.4 nm. Also, the deposited film was transparent, and the transmittance was larger than 95 %. Furthermore, the X-ray photoelectron spectroscopy (XPS) measurement showed that the composition of the deposited films was the same as ionic liquid (BMIM-PF_6). This is due to the deposition of ionic liquid clusters, which include both cations and anions.

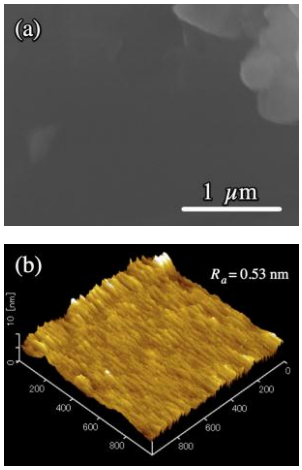


Fig.6 (a)SEM and (b)AFM images for ionic liquid films deposited on glass substrates.

In summary, polyatomic molecular ions exhibit unique features, one of which is that it can transfer energy and mass as well as fragment radicals toward substrate surfaces. These radicals play an important role in chemical erosion and sputtering, which results in high rate sputtering and low irradiation damage of the substrate surfaces. In addition, a cluster state of polyatomic molecules has several unique features, for example, the clusters enable a link between the atomic state and bulk state. The physical and chemical properties of clusters are different to those of the bulk state. Based on these features of polyatomic cluster ions, we focused on liquid materials such as ethanol, water, and ionic liquid, and produced polyatomic cluster ions by exploiting an adiabatic expansion phenomenon or by using a high-electric field emission of ions. The interactions of liquid cluster ions with solid surfaces were investigated in order to clarify the physics and chemistry of polyatomic cluster ion beams. Applications of the materials processing methods were demonstrated with polyatomic cluster ion beams, including high-rate sputtering of surfaces, micro-patterning, and surface modification.

References

[1] G.H. Takaoka, H. Noguchi, K. Nakayama, Y. Hironaka and M. Kawashita, Nucl. Instrum. Methods **B237** (2005) 402.
[2] G.H. Takaoka, "*Chemical Reactions on Surfaces*" (Eds. J.I. Duncan and A.B. Klein) (Nova Science Publishers, Inc., New York, 2008) Chap. 3.
[3] G.H. Takaoka, H. Ryuto and M. Takeuchi, J. Mater. Res. **27**(5) (2012) 806.
[4] G.H. Takaoka, M. Takeuchi and H. Ryuto, Rev. Sci. Instrum., **81** (2010) 02B302.
[5] J.L. Buckner, D.J. Vitkavage and E.A. Irene, J. Appl. Phys. **63** (1988) 5288.
[6] J.W. Coburn and H.F. Winters, J. Vac. Sci. Technol. **16** (1979) 391.
[7] H.F. Winters and J.W. Coburn, Surf. Sci. Rep. **14** (1992) 161.

Hierarchical simulation of microcrystalline PECVD silicon thin film growth and structure

D. Tsalikis[1], Ch. Baig[2], V. G. Mavrantzas[1], E. Amanatides[1], and D. Mataras[1]

[1]University of Patras, Department of Chemical Engineering, 1 Karatheodori Street, Patras GR 26504
[2]School of Nano-Bioscience and Chemical Engineering, UNIST (Ulsan National Institute of Science & Technology), Ulsan, South Korea 689-798

We have designed and implemented a hierarchical simulation methodology capable of addressing the growth rate and microstructural features of thin silicon films deposited through PECVD (Plasma Enhanced Chemical Vapor Deposition). Our main objective is to elucidate the microscopic mechanisms as well as the interplay between atomic level and macroscopic design parameters associated with the development of nano- or micro-scale crystalline regions in the grown film. The ultimate goal is to use multi-scale modeling as a design tool for tackling the issue of local crystallization and its dependence on operating variables. At the heart of our simulation approach is a very efficient, large-scale kinetic Monte Carlo (kMC) algorithm which allows generating samples of representative Si films based on a validated chemistry model. In a second step, the generated film is subjected to an atomistic simulation study which restores the molecular details lost or ignored in the kMC model. The atomistic simulations are computationally very demanding; they are, however, an important ingredient of our work: we use it to back-map the coarse grained model employed in the kMC simulations to an all-atom model which is further relaxed through detailed NPT molecular dynamics (MD) or Monte Carlo simulations. This tunes local structure thus also important morphological details associated with the presence of crystalline and amorphous regions (and the intervening interfacial domains) in the grown film.

The kMC algorithm is based on a carefully chosen set of reacting or active radicals (species) in the gas phase impinging the film and a detailed set of surface reactions. Inputs for species fluxes are taken from a well-tuned plasma fluid model that includes a detailed gas phase chemistry reaction scheme [1,2]. The growth mechanism consists of various surface kinetic events including radical-surface and adsorbed radical-radical interactions, radical-surface diffusion, and surface dissociation reactions. The very fast surface diffusion is decoupled from the rest of the kMC events and is treated deterministically in our work. For a three-dimensional Si(001)-(2x1):H crystalline lattice, our kMC algorithm allows us to simulate film growth over several seconds, resulting in thickness on the order of tens of nanometers. In the following pages we provide more details about the implementation of our kMC algorithm along with validation results.

The n-fold kinetic Monte Carlo method

For the temporal evolution of the reactive surface species, we have used the classic n-fold MC scheme,[3] over a diamond lattice structure. The substrate surface corresponds to a Si(001)-(2×1):H surface and contains 16384 (128x128) Si atoms. The simulation cell has dimensions 22.6nm×23nm and periodic boundary conditions are applied along the (xy) plane perpendicular to film growth. In order to generate a list of all possible events at each time step we developed a kMC propagator, which keeps track of the coordination of all surface Si atoms up to the next-nearest neighbor for each site. The identification of all possible events on all surface sites is carried out through

a parallel implementation that does not demand the exchange of any piece of information between the surface sites.

Decoupled diffusion

In out computational experiments of Si film growth under specific conditions (dilution ratios in SiH_4 varying from 1 to 6%), the surface diffusion reactions are extremely faster than any other reaction in the system. For example, for a brute force kMC simulation the vast majority of computational time (≈99.996%) is spent on tracking the very fast surface diffusive motion of the adsorbed radicals. Therefore we decided to decouple the diffusion reactions from the rest of the kMC events by approximating it as a a Markovian random walk, i.e. by considering the trajectory of the absorbed radicals on the xy plane as a sequence of successive random steps.

Flow chart of the kMC algorithm

1. Initialize computations at time t=0
2. Determine the list of all possible events and select one of them
3. Update system topology and propagate time
4. Identify what type of radicals are adsorbed
5. Choose randomly an absorbed radical and identify its type i^{type}.
6. Choose randomly a new position from its first-neighboring available
7. Propagate time $t=t+dt^{itype}$
8. Repeat steps 5, 6 and 7 n^{type} times for each type of adsorbed radicals
9. Go to step 2
10. Propagate system until a specific film thickness is obtained

Surface Diffusion Verification

Parameters dt^{itype} and n^{type} are system specific and of significant importance, since they control the diffusive motion of the adsorbed radicals. To ensure that the proposed method samples correctly the diffusive motion tracked deterministically, the random walk time step dt^{itype} is adjusted so that the resulting mean square displacement (msd) is identical to that obtained through a brute force application of the kMC algorithm (that is with diffusion being treated as the rest of the reaction events). For all types of diffusive radicals, the self-diffusivity D_s^{itype} is computed from the computed msd via the Einstein equation as:

$$D_s = \frac{1}{4}\lim_{t\to\infty}\frac{\partial\left\langle r(t)^2\right\rangle}{\partial t} \quad (1)$$

where $<r(t)^2>$ is given by the following formula :

$$\left\langle r(t)^2\right\rangle = \frac{\sum_{i=1}^{N}\left(r_i(t+\tau)-r_i(\tau)\right)^2}{N} \quad (2)$$

and $r(t)$ is the unwrapped (true) particle position of site i at time t. For a two-dimensional lattice one, can approximate the self-diffusivity via the following equation:

$$D_s = \frac{1}{4}\frac{L^2}{dt} \quad (3),$$

where L is the distance between two neighbouring sites and dt the time needed for a jump between two neighbouring sites. Combining equations 1 and 3 results in:

$$dt = \frac{L^2}{\lim_{t\to\infty} \frac{\partial \left\langle r(t)^2 \right\rangle}{\partial t}} \quad (4),$$

from which we determine the value of dt^{itype}. Using this time step in the kMC algorithm ensures a self-consistent treatment of the diffusive motion in the simulations.

The time that adsorbed radicals are allowed to diffuse with a predefined diffusivity between two successive kMC steps is governed by n^{type}. This quantity is of great importance because it determines the diffusion time for each radical and hence the structural properties of the resulting films. The identification of the appropriate value of n^{type} is accomplished by requiring the concentration profiles of the most important structural quantities (dangling bonds and hydrogen content of the corresponding brute force kMC simulations) to be correctly computed in the course of the hybrid simulations. As we can see in Figures 1, 2 and 3 the concentration profiles of all quantities obtained by both methods are in very good agreement. In typical PECVD simulations, the system size increases rapidly with time so that calculations become quickly too slow. Our massively parallel kMC code performs extremely well (see in Figure 4) even when the system size has been increased by more than 30 times.

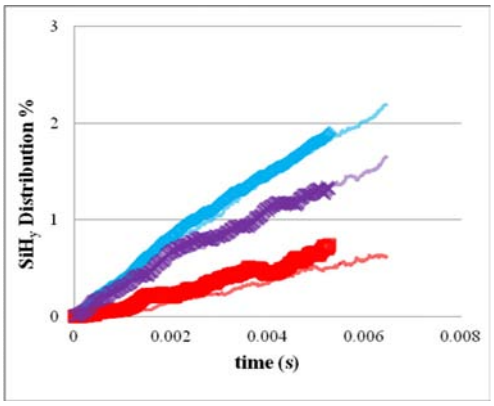


Fig. 1. Time evolution of surface coverage of hydride species. The open symbols correspond to brute force kMC simulation while the noisy lines to the proposed methodology. Red, blue, and purple colors correspond to y=0, 1, and 3, respectively.

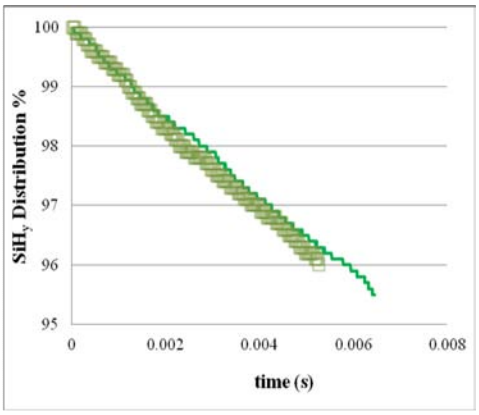


Fig. 2. Time evolution of surface coverage of hydride species. The open symbols correspond to brute force kMC simulation while the noisy lines to the proposed methodology for y=2.

The method has been validated by carrying out several computational experiments over a wide range of dilution ratios and by comparing the numerical results for the growth rate, hydrogen bonding and roughness with data from experimental measurements such as ellipsometry, Raman Spectroscopy, FTIR Spectroscopy and Atomic Force Microscopy, where good agreement has been observed in most cases which should be attributed to the accuracy of the rather detailed and rich (it involves 5 species and 29 reactions) phenomenological chemical (kinetic) model adopted. All kMC simulations have been conducted under industrially

relevant conditions of thin film Si deposition (Pressure=4 mbar. Power = 500 W, Total Flow rate =1 slm, Silane fraction=1 - 6 %).

Currently, the 3-d structures generated with kMC are used as input into large-scale all-atom MD simulations for times up to several nanoseconds to allow the system further relax towards the preferred morphological state at the conditions of the computational experiment. This will allow us to obtain predictions for other industrially relevant quantities and observables (such as the hydrogen content which is experimentally accessible by FTIR and Raman spectroscopy), thus opening the way to fully understanding the conditions and the underlying complex molecular mechanisms responsible for the growth of micro- or nanocrystalline films.

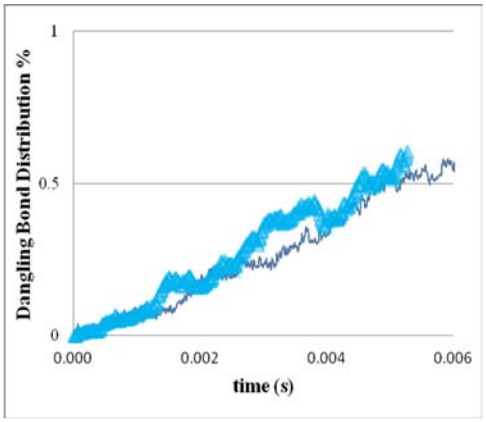


Fig. 3. Evolution of surface coverage of dangling bonds. Open symbols correspond to the brute force kMC simulation while the noisy lines to the kMC methodology.

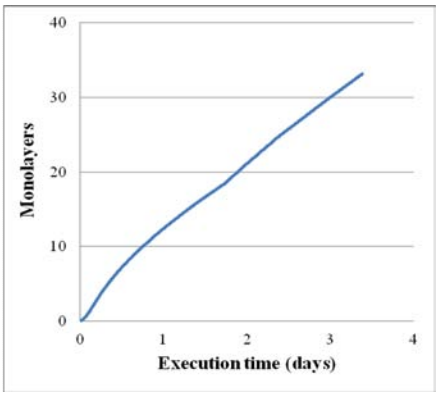


Fig. 4. Evolution of system size with execution time at T=180^{o}C (dilution ratio=3% SiH_4).

ACKNOWLEDGMENT

We acknowledge financial help from the European Commission through the PEPPER project (FP7/2007-2013, grant agreement nr 249782).

References

[1] E. Amanatides, S. Stamou, D. Mataras, J. Appl. Phys. 90, 5786 (2001)

[2] B. Lyka, E. Amanatides and D. Mataras, Jap. J. Appl. Phys. 45 (2006) 8172-8176

[3] A.B. Bortz, M. H. Kalos and J.L. Lebowitz, *J. Comp. Physiol*. 17, 10 (**1975**)

Multifunctional coatings on fabrics by application of a low-pressure plasma process

Joëlle Levalois-Grützmacher, Marie-Jérôme Tsafack, Kanchit Kamlangkla, Katrin Prinz

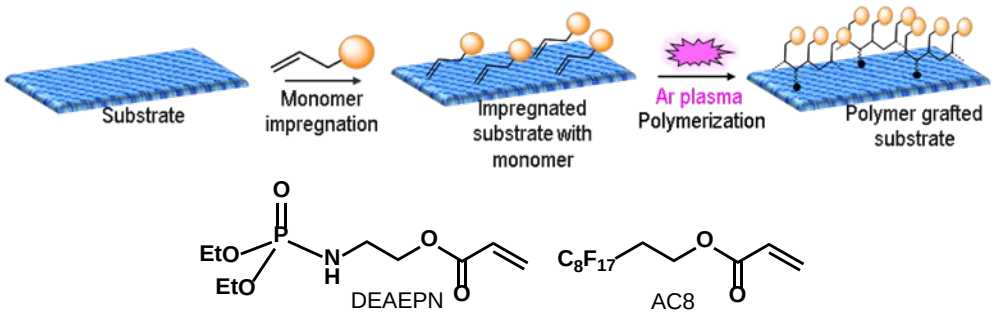
ETHZ, Swiss Federal Institute of Technology, Zurich, Switzerland

Abstract

Nowadays, there is an increased demand to produce highly-performant fabrics combining multiple properties such as flame retardancy, hydrophilicity/hydrophobicity, antibacterial, UV resistance, etc. In order to produce a wash-resistant-flame-retardant-water-repellent-dyed multifunctional coating on natural fabrics like cotton and silk, various protocols involving the Ar plasma-induced graft-polymerization (PIGP) process of suitable monomers were investigated. The burning behaviour of treated fabrics is discussed using LOI measurements. The water repellent behaviour is evaluated by means of Schmerber pressures ($P_{Sch.}$) and dyeing properties by spectrophotometric measurements. The wash-resistance of the coatings was tested by using an accelerated laundry method. The obtained results have shown that for each protocol, the flame retardant monomer is compatible with a water repellent or a dyeing treatment.

1. Introduction

The challenge to confer wash-resistant flame retardant properties to textiles remains[1]. This is even more relevant when textiles of natural origin like cotton or silk fabrics are concerned. Indeed, the flame retardant finishing could only be applied by surface modification technologies. Among all of them, the plasma induced graft polymerization (PIGP) process we have developed and refined in our laboratory over the last years has proven to be an efficient tool for that purpose[2-6]. The substrate is immersed into a solution containing a monomer (acryloyl- or methacryloyl derivative) bearing the requested property. Under Ar plasma the monomer is simultaneously grafted and polymerized onto the surface of the substrate (scheme 1). The thin homogeneous layer of grafted polymer onto the surface exhibit excellent wash-fastness properties thanks to the covalent bonding created during this process between the polymeric layer and the substrate. By using this process, we were already able to confer excellent wash-resistant-flame retardant behaviour to cotton and silk[6] fabrics without altering their bulk properties. The flame retardant monomer used for this application which has been synthesized in our laboratory is the diethyl(acryloyloxyethyl)phosphoramidate (DEAEPN) (scheme 1). However it was of interest to know whether this new property conferred to cellulosic fabrics allows further treatment like a water repellent treatment or a dyeing process. Therefore the FR-cotton fabrics obtained by this process where submitted either to a water repellent treatment or a dyeing process. In both cases, the added functionality has been evaluated by the relevant technique and the flammability of the bi-functional fabric has been further assessed as well as the durability of the new finishing.



Scheme 1: PIGP process and flame retardant (DEAEPN) and water repellent (AC8) monomers used in this study

2. Experimental

The textiles (twill woven bleached cotton 210 g/m^2) were kindly supplied by EMPA Testmaterialien AG (Switzerland) or obtained from TESTEX Prüfmaterialien (Germany). The synthesis of the monomer diethyl(acryloyloxyethyl)phosphoramidate (DEAEPN) is depicted elsewhere[2-6]. The photoinitiator Irgacure 819 was obtained from BASF AG Schweiz. EGDA (ethyleneglycoldiacrylate) and 1,1,2,2, tetrahydroperfluorodecylacrylate (AC8) were purchased from Aldrich and used as received. Solvents, chemicals and textile auxiliaries were obtained from the usual laboratory suppliers (Fluka, Baker and Merck) and were purified prior to use, if necessary, by standard methods. Remazol brilliant Blue R was used (Dyestar Textilfarben GmbH&CO) for reactive dyeing experiments.

PIGP on cotton textiles: The PIGP process which takes place in a Europlasma DC300PC MW-generator (2.46 GHz) is described elsewhere[2-4]. The samples (50 mm x 100 mm) were weighed and then impregnated at RT with 0.7 ml of an ethanol solution containing up to 30% on the weight of the fabric (w_{of}) of monomer, 10% on the weight of the monomer (w_{om}) of cross-linking agent (EGDA) and 5% w_{om} of photoinitiator. After padding and drying in air the fabrics were placed on a glass plate and exposed to a MW argon plasma treatment (F_{Ar} = 125 sccm; P = 100 W; p = 500 mT; t = 20 min). Then after several cycles of washing (Soxhlet ethanol, water) the samples were dried at room temperature and stored under standard conditions for at least 24 hours before measurements.

Dyeing experiments: A Polymat 1000 (Ahiba) was employed for dyeing experiments with a rotation rate of 40 rpm. A liquor-to-goods ratio of 25:1 was used with 50 g/L Na_2CO_3 and dyed in different shades for 60 min at 60 °C followed by soaping (liquor-to-goods ratio 40:1, 1 g/L Nekanil 910, 98 °C, 30 min).

Water repellent treatment: Two different procedures were followed involving the low pressure plasma process: (i) the FR-cotton fabrics are submitted to a CF_4 plasma treatment (F_{CF4} = 36 sccm, working pressure = 0.66 mb, P = 300 W). (ii) PIGP process of a perfluorinated acrylate monomer (AC8) (F_{Ar} = 125 sccm. P = 100 W; p = 500 mT; t = 5 min; [AC8] = 50g/L) on FR-cotton fabrics

3. Results and discussion

3.1. Combination of dyeing and flame retardant finishing

In dyeing processes the affinity of the dyestuff to the fibres is plays a important role and is sensitive to any surface modifications. Therefore it has to be investigated to ensure whether the flame retardant finishing by PIGP can be integrated into the whole textile finishing process. Reactive[5] dyes are one of the most applied in the cotton finishing processes, therefore they were employed in this study. Figure 1 presens the spectrophotometric measurements obtained for FR-cotton with increasing amounts of DEAEPN add-on and deeply dyed with Remazolbrilliant blue, 3% w_{of}.

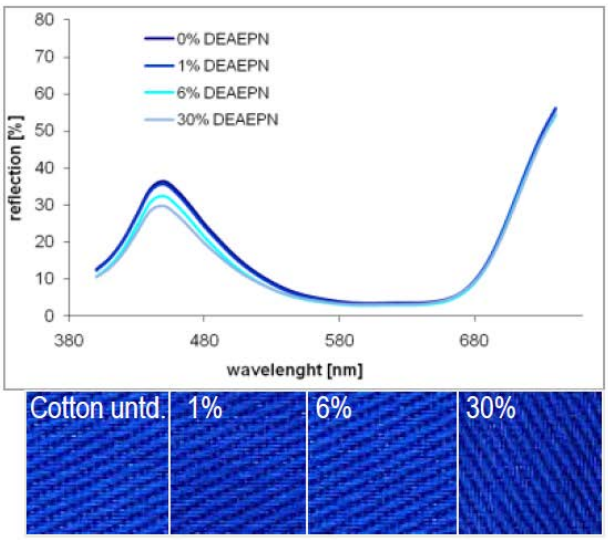


Figure 1: Spectrophotometric results and photographs of 3%w_{of} RB blue dyed FR treated cotton with various amount of grafted FR-polymer.

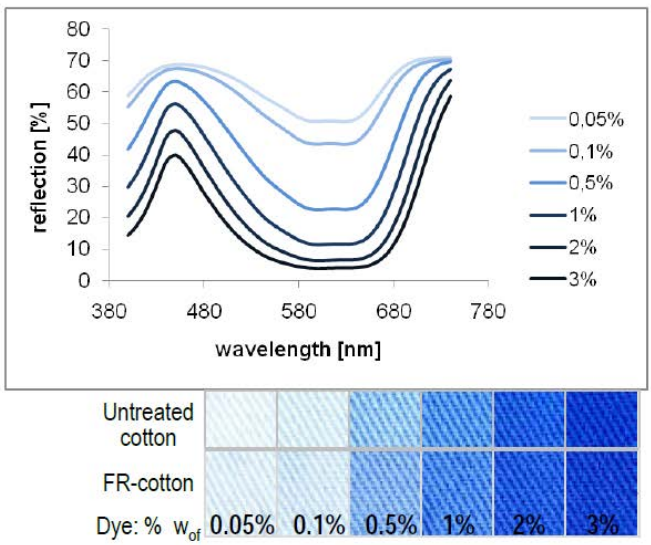


Figure 2: Reflexion curves and photographs of different RB blue dyed shades on untreated and FR-treated cotton (DEAEPN: 17.5% w_{of}).

At a first glance, a good match of the reflection curves can be seen at low amount of grafted flame retardant (< 6%). However, while reaching high degree of grafting (30%) a slight decrease of the absorption is observed in the blue range region. The samples become darker. Nevertheless, this deviation is hardly visible from human eyes. This indicates that the presence of the flame retardant polymer on the surface of the cellulosic fabric allows a post dyeing treatment. A good diffusion of the dye into the pores of the cotton fabric is maintained and sufficient cellulosic-OH groups remain for the reactivity with the dye.

In a second step the colour shade was varied by using increasing amount of RB blue dye (0.05 to 3% w_{of}) on flame retardant finished cotton (17.5% w_{of}). The results presented in figure 2 indicate that even for high FR-grafting excellent colour shades are possible with respect to the original colour and correlate with the amount of dye. The affinity of the dyestuffs is not influenced by the thin polymer film.

LOI measurements performed on the dyed fabrics have indicated that the dyeing process does not alter the flame retardant properties of the fabric even after several cycles of washing and soaping.

3.2. Flame retardant and water repellent cotton fabrics

(i) CF_4 plasma treatment of flame retarded cotton fabrics with DEAEPN

Perfluorocarbon plasmas are well known to be effective for waterproofing polymeric substrates[7]. Virgin and FR-cotton fabrics were submitted to a CF_4 plasma (F_{CF4} = 36 sccm, working pressure = 0.66 mb, P = 300 W) during 5 minutes. Before and after the plasma treatment, the Schmerber pressures ($P_{Sch.}$) were measured. The results obtained are given in Table 1.

Cotton fabric	LOI_1	P_{sch1}	P_{sch2}	LOI_2
Untreated	19.0	0	2	19.0
DEAEPN (200g/L)	27.5	0	2	27.5

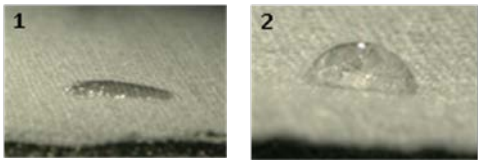


Table 1: LOI and Schmerber pressures (P_{Sch}) before (LOI_1/P_{Sch1}) and after (LOI_2/P_{Sch2}) the CF_4 plasma treatment on untreated- and FR-cotton fabrics and photographs of droplets of water on FR-cotton before (1) and after (2) CF_4 plasma treatment.

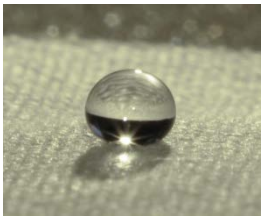
Before the CF_4 plasma treatment, the FR-cotton fabrics are totally absorbent ($P_{Sch.1}$ = 0 mb). After the CF_4 plasma treatment, the $P_{Sch.}$ values of the FR-sample increases slightly up to 2 mb. Droplets of water remain but do not roll on the surface of the treated fabrics. However, by heating the fabrics during 1h at 100°C in an oven, P_{Sch} double from 2 to 4 mb. The droplets of water slightly roll on the surface of the fabrics. This is due to the increase of the chain mobility with the temperature as already observed[7]. Interestingly, LOI values are the same before and after the CF_4 plasma.
CF_4 plasma treatment of flame retarded (FR) fabrics leads to a decrease of the surface energy of the treated fabrics compared to the untreated ones. However this can be attributed only to a simple surface fluorination, since there is no noticeable difference in IR and weight measurements between FR-cotton samples before and after the CF_4 plasma exposure. This CF_4 plasma treatment is not sufficient to impart a good water repellent character.

(ii) Plasma-induced graft polymerization of AC8 on FR-cotton fabrics

In this approach the (AC8)[2, 7] monomer is grafted and polymerized via the PIGP process onto the surface of FR-cotton. The amount of grafted polymer the $P_{Sch.}$ values and the corresponding LOI values are listed in Table 2.

Cotton	$\%G_{FR}$	LOI_1	P_{sch1}	$\%G_{FR+AC8}$	LOI_2	P_{sch2}
Untreated	-	19	0	3.03	19	11
DEAEPN	24	26.5	0	29.36	27	15

Table 2: Grafting percentage (%G), LOI and Schmerber pressures (P_{Sch}) before (LOI_1/P_{Sch1}) and after (LOI_2/P_{Sch2}) the PIGP of AC8 on untreated- and FR-cotton fabrics. Photograph of the water-repellent-FR-cotton fabric.



The results clearly indicate that both the degree of grafting and the $P_{Sch.}$ values increase after the PIGP of AC8 on the FR-cotton fabrics. This indicates the presence of a fluorinated polymer on the surface of the fabrics. The droplets of water roll onto the surface of the double-layer treated fabrics. This observation confirms the good water repellent character of the cotton textiles. The LOI of the flame retarded fabrics remain almost the same after water repellent treatment.

From these results, it can be concluded that it is possible to confer good water repellent properties to FR-cotton fabrics with only 3% of grafted polyAC8 using the PIGP procedure. This occurs without affecting the flame retardant character of the fabrics.

4. Conclusion

From these results we have shown that the Plasma Induced Graft Polymerization process of a flame retardant monomer can be easily integrated in a cotton fabric finishing process as it is totally compatible with reactive dyeing process and water repellent treatment. Moreover, the flame retardant properties are not affected by these post plasma treatment and exhibits excellent wash-fastness properties after 50 cycles of laundry[8].

References

1. A. R. Horrocks and D. Price, *"Advances in fire retardant materials"* Woodh. Publ. Limit. (2008), ISBN: 9781845692629
2. F. Hochart, R. De Jaeger, J. Levalois-Grützmacher, Surf. Coat. Technol. 165 (2003) 201.
3. M.J. Tsafack, J. Levalois-Grützmacher, Surf. Coat. Technol. 201 (2007) 5789.
4. K. Kamlangkla, S. Hodak, J. Levalois-Grützmacher, Surf. Coat. Technol. 205 (2011) 3755.
5. G. Ebner and D. Schelz, *Textilfärberei und Farbstoffe.* Berlin : Springer Verlag (1989) 226-230.
6. Y. Iriyama, T. Yasuda, D. L. Cho, H. Yasuda, J. Appl. Polym. Sci. 39 (1990) 249
7. U. Vorher, M. Müller, C. Oehr, Surf. Coat. Technol. 98 (1998) 1128.
8. W. F. McSherry, G. L. Drake, A.B. Cooper, A. R. Markezich, Am. Dyest. Rep. 63 (1974) 52.

Hierarchical, Plasma Nanotextured, Superamphiphobic Polymeric Surfaces

K. Ellinas, K. Tsougeni, M. Vlachopoulou A. Tserepi, E. Gogolides,

Abstract
A facile, mass production amenable, rapid method for making superamphiphobic / amphiphobic surfaces by random plasma nanotexturing of polymers in plasmas is presented. Plasma etched and simultaneously randomly roughened (nanotextured) polymethylmethacrylate (PMMA) Polyether-ether-ketone (PEEK), Cyclic-olefin-copolymer (COC) and Polydimethylsiloxane (PDMS) substrates show hierarchical roughness and complex high-aspect-ratio morphology. Here, they are investigated as superamphiphilic surfaces after plasma etching or superamphiphobic surfaces, after plasma deposition of a thin fluorocarbon film following plasma etching. We show that polymer surfaces etched in oxygen (PMMA, PEEK, COC) or SF_6 (PDMS) plasma for few minutes (with texture height< 600nm) exhibit excellent superamphiphobic behaviour, while surfaces treated for longer time show porous-like filamental morphology (filaments several microns height), which is coalesced and stabilized upon wetting, allowing their potential long-term use. Superamphiphobic / amphiphobic behaviour is observed in all cases

1.Introduction

Wetability (amphiphilicity or amphiphobicity) is a fundamental property of a surface, being affected by both the chemical composition and the surface morphology [1,2]. Superamphiphobic surfaces (on which water or other liquid drops roll and have a large contact angle (typically>150^o) with a very small contact angle hysteresis (typically<10^o)) are being extensively studied, due to their potential practical application as self-cleaning, anti-icing, anti-fogging, anti-fouling, low adhesion, and drag reduction surfaces [3].

Several techniques to produce superamphiphobic surfaces have been exploited [4,5], including stochastic or biomimetic bottom-up approaches [6,7]. Using these approaches hydrophobicity can be easily achieved, while amphiphobicity needs a more careful design. Plasma processing induces roughening of polymers at the nanoscale, and thus plasma-induced polymer nano-roughness control may lead to new nano-manufacturing processes and products. If a morphology containing ordered micron or submicron posts is desired, colloidal lithography may be used in combination with plasma processing to create ordered micro-scale structures, while simultaneously nanotexturing these structures during plasma etching. The combination of colloidal lithography and plasma etching results in a hierarchical (triple-scale) topography (ordered micro posts with random dual scale texture of a few hundred nano and a few tens nano) with controllable undercut profiles which enhance oleophobicity [10].

In this work, we present our technology for manufacturing stochastic or quasi-ordered, hierarchical superamphiphobic, amphiphobic and superamphiphilic polymer surfaces using plasma etching.

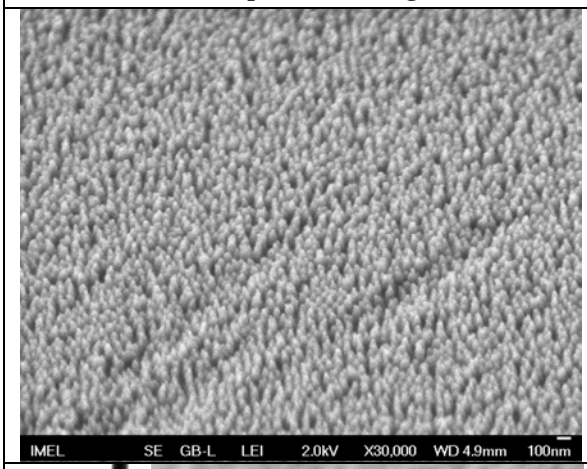
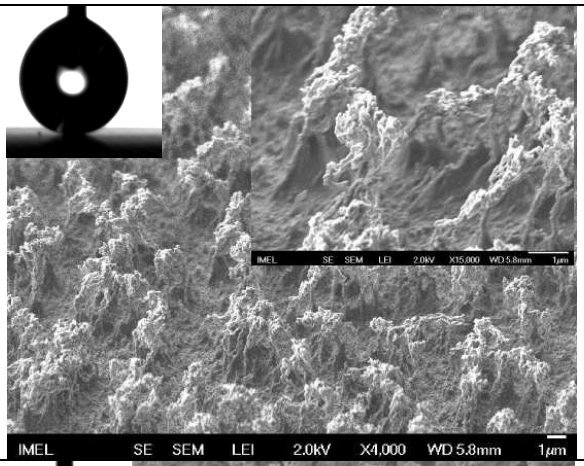
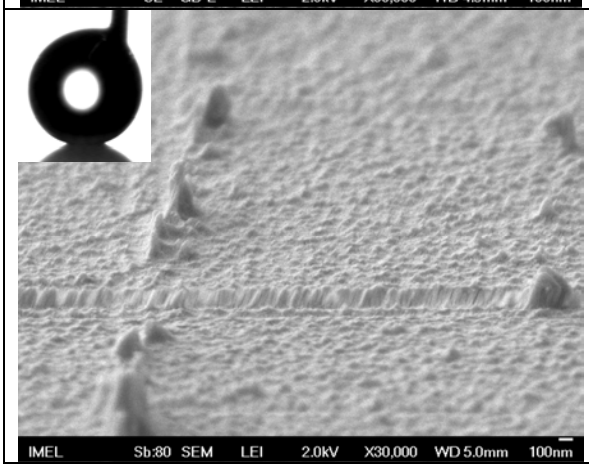
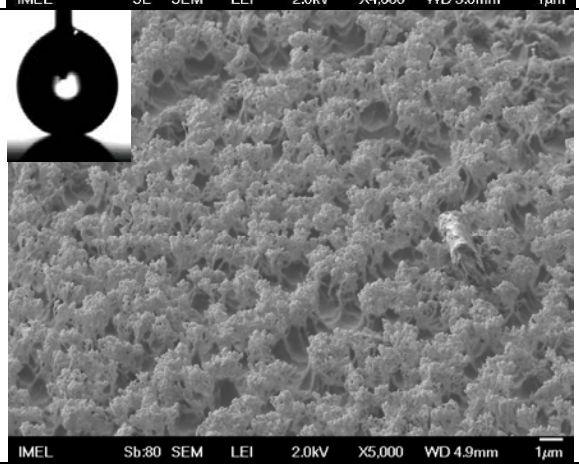
2.Results and discussion

2.1 Stochastic random topography

All plasma processes were performed in our Micromachining Etching Tool (MET) by Alcatel, equipped with a helicon source (at 13.56 mHz) providing RF power up to 2,000 W. Typical values are 1,900 W, 0.75 Pa, 100 sccm, –100 V, 15°C. Surfaces after plasma etching become amphiphilic. The same reactor was also used

for conformal deposition of a thin fluorocarbon film after plasma etching using C_4F_8 gas at conditions (900 W,0 V, 5.33 Pa C_4F_8, deposition rate 30 nm min^{-1}) that conformally deposits a thin fluorocarbon (FC) film after plasma etching to render the surface amphiphobic.

We begin with a brief description of what plasma nanotexturing actually is. When a polymer surface is etched and a few micrometres of material have been removed, nanotexture (nanoroughness) may develop on its surface, and roughness may increase linearly with time. Starting from a flat surface, within minutes, one can get a rough quasi-ordered surface. For longer plasma etching time order is reduced and the surface becomes filamental (right column fig1). X-ray photoelectron spectroscopy (XPS) analysis reveals relatively large surface concentration of aluminium present in oxide form, coming from sputtering of the alumina dielectric dome, and the anodized aluminium clamping ring of our etch tool . This 'hard' etch inhibitor creates micromasking and leads to the development of nanotexture. In nanoscience terminology the plasma directs the assembly of a rough nanotexture on the top surface of the polymer. The XPS results suggest that nanotexture is a result of plasma–wall interactions [8]. Oxygen is used to nanotexture PMMA, COC, PEEK, and SF_6 is used to nanotexture PDMS. We note that the nanotexture is dual scale comprising approximately 600nm heigh, 200nm wide and 50nm wide columnar structures for 1min plasma treatment.

1min plasma etching	**10min plasma etching**	
		**PMMA**
		**COC**

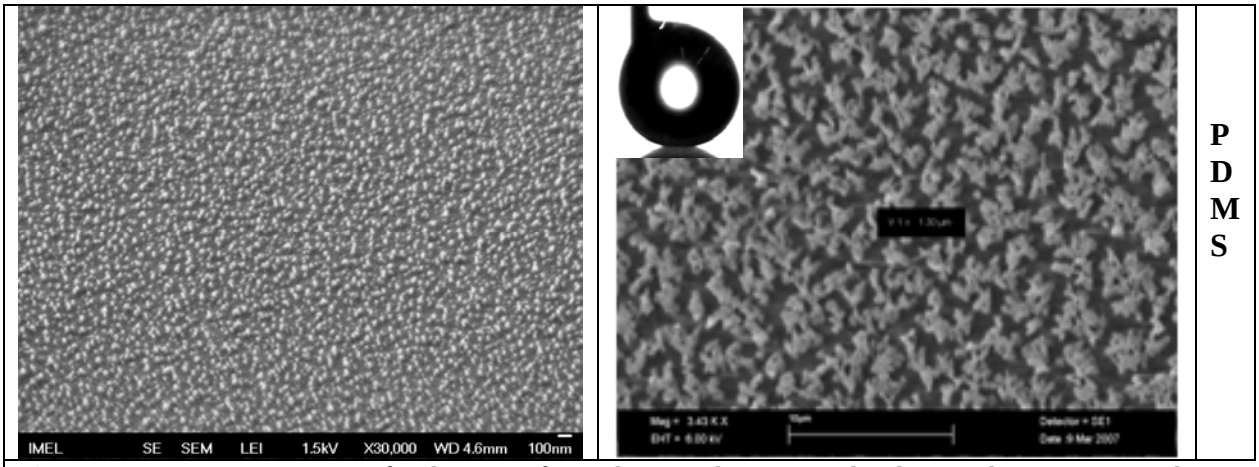


Figure 1. SEM, AFM images of polymer surfaces showing the quasi ordered to random nanotextured topography created after plasma treatment in various polymers after 1min (left column) and after 10 min (right column). Notice how the small order present in the 1min etched surfaces is decreased as etching time increases. 5μl water droplets on such surfaces after plasma fluorocarbon deposition is also shown. Water contact angle measurements for all surfaces are between155^0-165^0.

All surfaces are hydrophobic after 1 min of plasma treatment, while longer treated surfaces for more than 4 min exhibit amphiphobic properties: water contact angle is larger than 160^0, while for other liquids contact angles are larger than 130^0. For long plasma treatments the resulting filamanetal nanostructures are not mechanically stable. To stabilise the surface before hydrophobization we immerse the surface into water; upon drying the nanofilaments coalescence in shorter more compact hierarchical microhills, due to capillary forces. The wetted-dried surface is mechanically stable [9].

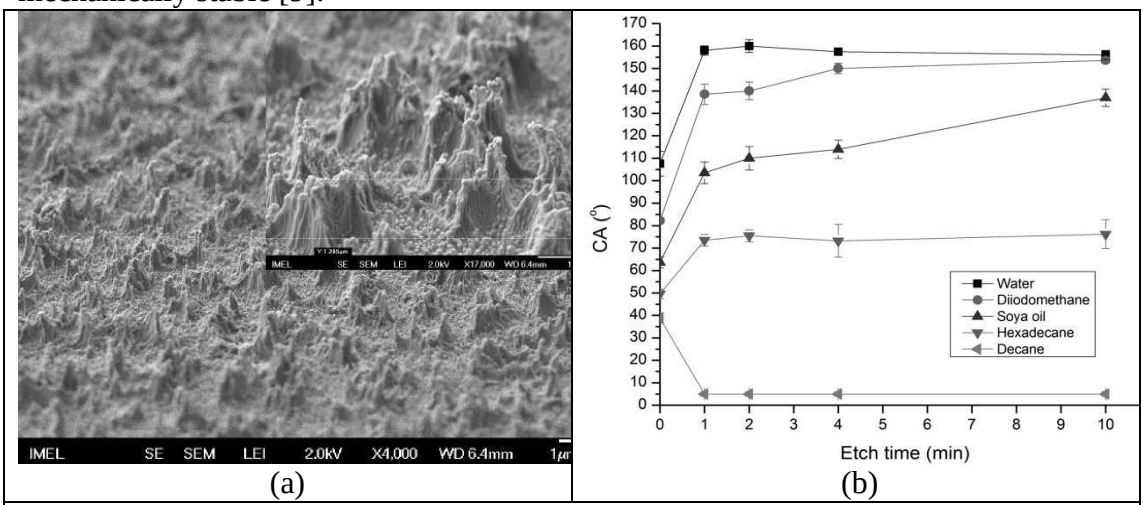


Figure 2. (a) PMMA 10 min treated surface after wetting and drying, where the coalescence of filamental structures occurs leaving behind hierarchical microhills, (b) Static contact angle for various liquids versus etching time of PMMA. Data are taken after wetting-drying of fibrous structures to cause coalescence, and coating with fluorocarbon plasma-deposited film. Water and diiodomethane roll on the surface, while oils stick.[9]

2.2 Deterministic quasi-ordered topography

Uniform, self-assembled, closely packed arrays of PS spheres (1&3 μm) are fabricated after spinning the colloidal particles (fig 3a), followed by plasma etching with a moderate bias voltage and duration (fig3 b, c) resulting in undercut hierarchical pillars (fig3c) that exhibit superamphiphobic behavior for various test liquids (fig3d).

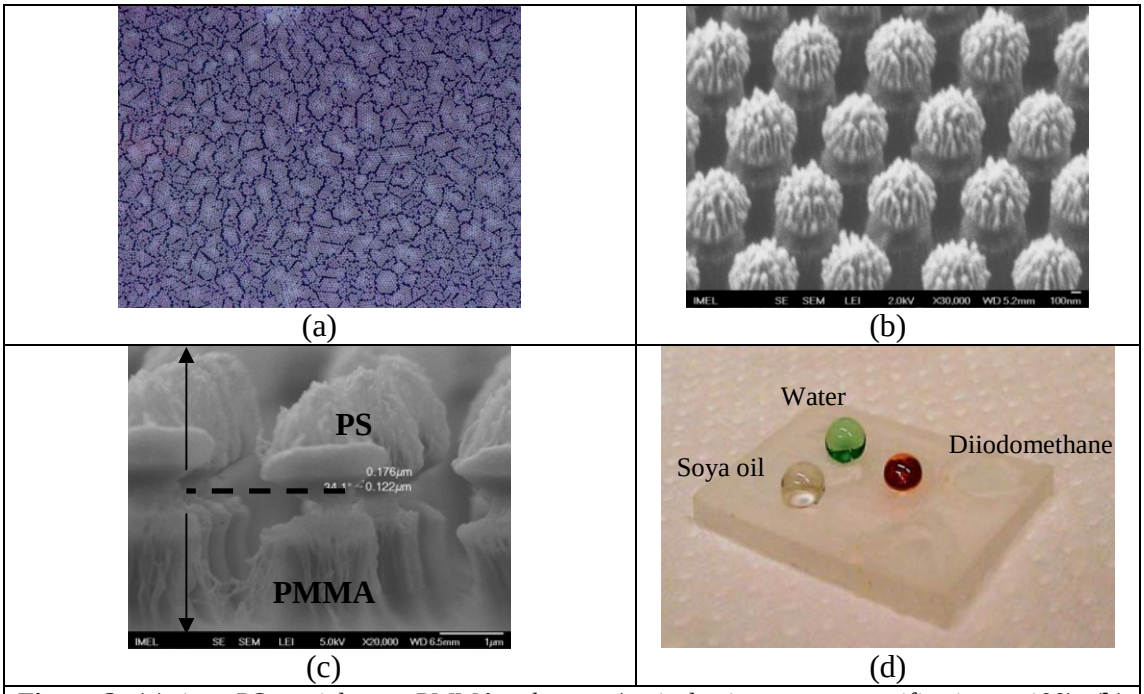


Figure 3. (a) 1μm PS particles on PMMA substrate (optical microscope magnification × 100), **(b)** Hierarchical (triple-scale) roughness micro-pillars produced by the combination of colloidal lithography of 1μm particles followed by plasma etching and dual-scale nano-roughness on the top of the pillars formed during plasma etching (tilt 40^0). **(c)** Undercut, reentrant topography of a PMMA surface after 3μm PS colloidal microparticle lithography followed by a two-step etching process in Oxygen plasma. The first anisotropic etching step (3.5min) produces the column, while the second isotropic etching (2.5 min) step enhances the re-entrant shape of the pillar, by etching isotropically both the PMMA and the bottom PS hemisphere. Notice the top nanotexture on the top half PS hemisphere, **(d)** Fluorocarbon coated, Oxygen plasma treated superamphiphobic PMMA surface at optimal conditions [10]

These surfaces are truly multiscale with roughness in the micron, hundred-nanometer, and ten nanometer range. In addition these surfaces have micron scale order (coming from the colloidal lithography) and nanoscale randomness coming from plasma nanotexturing, resulting in ordered superamphiphobic surfaces, exhibiting excellent wetting repellent properties [10].

3 .Conclusions

In conclusion, plasma etching and nanotexturing technology is an attractive path to micro- or nano-structured polymeric surfaces of polymers with varying degrees of order. 'Smart' amphiphobic surfaces may be fabricated either as open surfaces or as embedded in polymeric microsystems to produce new 'smart' devices. Applications in fluid control (e.g. producing slip-less flow) on surfaces, anti-icing, protein and/or cell adsorption / antifouling are some of the applications of such surfaces.

References

1. Wenzel, R.N. (1936) *Ind. Eng. Chem.*, Vol. 28, p.988.
2. Cassie, A.B.D. and Baxter, S. (1944) *Trans. Faraday Soc.*, Vol. 40, p.546.
3. Bhushan, B.; Jung, Y. C., *Progress in Materials Science* 2011**,** 56, (1), 1-108.
4. Ma, M.; Hill, R., *Current Opinion in Colloid & Interface Science* 2006**,** 11, (4), 193-202.
5. Roach, P.; Shirtcliffe, N. J.; Newton, M. I.,. *Soft Matter* 2008**,** 4, (2), 224.
6. Steele, A.; Bayer, I.; Loth, E. *Nano Letters* 2009, *9*, 501-505.
7. Hsieh, C. T.; Wu, F. L.; Chen, W. Y. *Mater Chem Phys* 2010, *121*, 14-21.
8. Gogolides E., Constantoudis V., Kokkoris G., Kontziampasis D., Tsougeni K., Boulousis G., Vlachopoulou M., Tserepi A., J. Phys. D: Appl. Phys. 44 (2011) 174021.
9. Gnanappa A.K., Papageorgiou D.P., Gogolides E., Tserepi A., Papathanasiou, A.G., Boudouvis, A.G., Plasma Process. Polym. 2012, 9, 304–315.
10. Ellinas, K., Tserepi, A., Gogolides E., Langmuir, 2011, 27 (7), pp 3960–3969.

On the deposition rate during High-Power Impulse Magnetron Sputtering.

Stephanos Konstantinidis

Stephanos.konstantinidis@umons.ac.be

Chimie des Interactions Plasma – Surface, CIRMAP, Université de Mons, 23 place du Parc, 7000 Mons.

For several years, the High-Power Impulse Magnetron Sputtering (HiPIMS) technology has attracted much attention as it enables the synthesis of functional thin films with enhanced or new properties [1]. During the high-power plasma pulse, typically characterized by peak current densities of the order of sev. A/cm^2 and a target voltage in the kV range, the sputtered film forming species are ionized and the film growth process is assisted by a flux of ions whose trajectory and energy can be controlled by an appropriate biasing of the substrate. The major drawback of this technology is the decrease of the deposition rate as compared to the rates achieved during DC magnetron sputtering discharge, in the same working conditions.

One reason for the reduced deposition rate is the propensity of the HiPIMS discharge to transit from the argon-driven sputter regime towards the self-sputtering mode, where metal ions are used to sputter the target. The later situation is detrimental to the deposition rate as some of the film-forming species do not reach the substrate and the erosion rate of the target is reduced. In this contribution, where short (< 50µs) high-power pulses are used (see e.g. Fig 1), we first analyze the influence of the exchange of momentum occurring between the sputtered atoms (Cu, Ti or W) and the argon background gas, i.e. the sputtering wind [2], on this transition and consequently on the decrease of deposition rate.

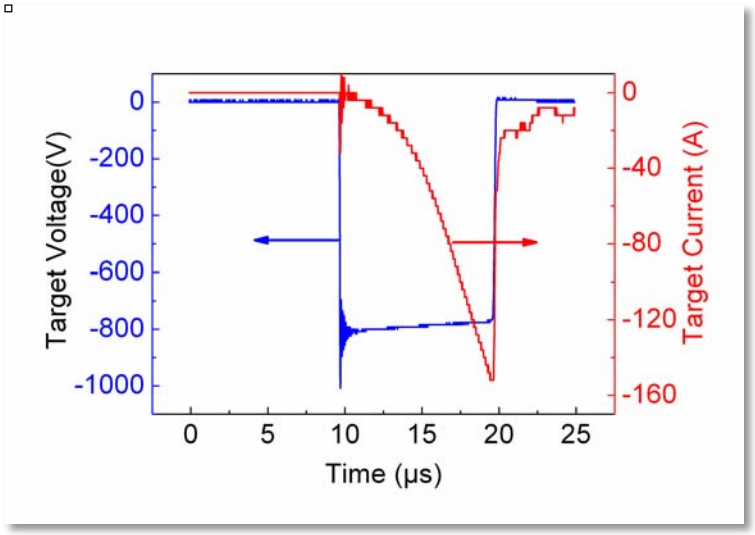


Fig 1: Typically current – voltage waveform during a short high-power plasma pulse.

Secondly, we show it is possible to increase the deposition rate, above the DCMS threshold, in the case of a reactive Ar/O_2 process used for the growth of tungsten oxide thin films provided that the HiPIMS deposition experiment is performed at high oxygen content (> 80 %) [3]. This situation is represented in Fig 2.

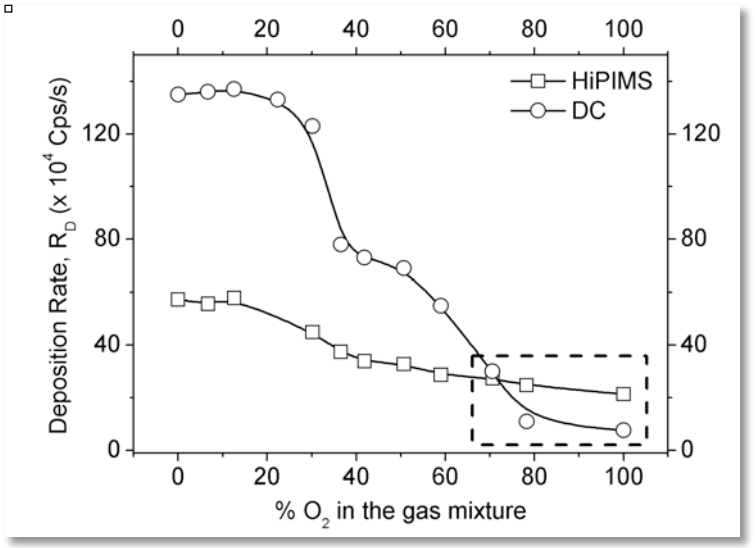


Fig. 1: Deposition rates obtained from X-Ray Fluorescence measurements for the DC and HiPIMS reactive discharges as a function of the oxygen content in the gas mixture (from [3]).

References :

[1] K. Sarakinos, J. Alami, and S. Konstantinidis, Surf. Coat. Technol. **204**, 1661 (2010).

[2] D.W. Hoffman, J. Vac. Sci. Technol. A **3**, 561 (1985).

[3] A. Hemberg, J.-P. Dauchot, R. Snyders, and S. Konstantinidis, J. Vac. Sci. Technol. A **30**, 040604 (2012).

ION FLUX–FILM STRUCTURE RELATIONSHIP DURING REACTIVE MAGNETRON SPUTTERING OF TUNGSTEN.

Axel Hemberg[1], Stephanos Konstantinidis[2], Jean-pierre Dauchot[2], Rony Snyders[1, 2]

[1]Materia Nova Research Center, Parc Initialis, B-7000 Mons, Belgium

[2]Chimie des Interactions Plasma Surface (ChIPS), CIRMAP, Université de Mons, 23 Place du Parc, B-7000 Mons, Belgium

Semiconducting metal oxides such as WO_3 are widely used as sensitive layer in gas sensors applications. It has been demonstrated that the sensor performances are strongly dependent on the microstructure of the layer: grain size, phase constitution, material density, ...[1-4] These features can be controlled by varying the energy and flux of the ions impinging the growing films in magnetron processes. [5-8]

In this work, we aim evaluating the effect of ion bombardment during WO_3 thin films growth by reactive magnetron sputtering on the crystallographic and microstructural properties of the material. The ion bombardment was modified by using two distinct strategies: (i) the use of two magnetic configurations (a balanced magnetic field, BM, and a strongly unbalanced one, UBM) of the magnetron using a pulsed magnetron discharge (PDMS).[9] and (ii) the use, for a UBM configuration, of different electrical sources allowing different degree of ionization of the plasma, namely a conventional DC source, a PDMS source, a high power impulse source (HiPIMS) and a modulated plasma source (MPP).

The effects of these different parameters on the chemical, crystallographic and microstructural properties of the deposited films were evaluated by XPS, XRD and TEM/AFM, respectively.

Our results allow the different ion bombardment regimes to be correlated with the structural properties of the films (grains size, texture, etc.). In order to understand our observations, plasma diagnostic through energy-resolved mass spectrometry measurements were performed.

In all cases, depositions without intentional heating of the substrate lead to XRD amorphous thin films. All the depositions were therefore performed at 550°C which was identified as the "ideal" temperature in order to get a sufficient crystallization of the deposited material.

By comparing the two magnetic field configurations (BM and UBM) using the PDMS source, the main observations are that in all cases, the films crystallize in the low temperature stable monoclinic phase of WO_3. Nevertheless, due to the increased ion bombardment enabled by the UBM configuration, the texturation of the films changes from (002) in the BM case to (200) for the UBM configuration. Concerning the grain size, it appears that the UBM conditions lead to significantly smaller grains. These results are correlated with the ion flux towards the growing films which was measured to be at least 2 times higher in the UBM case while the deposition rate and the mean energy of the bombarding ions remains similar.

When comparing different sputtering sources for the UBM case, the situation becomes more complicated. Indeed, for the MPP case, the films features look like those observed when the BM configuration is used with the PDMS source. For the HiPIMS deposited films, we observe a modification of the crystalline structure since the films crystallize in the high temperature orthorhombic phase of WO_3. If the latter situation is expected, we expected a similar situation for MPP which is also a highly ionized physical deposition method (IPVD).

The analysis of the plasma phase during these depositions reveals that both MPP and HiPIMS discharges are effectively IPVD methods.

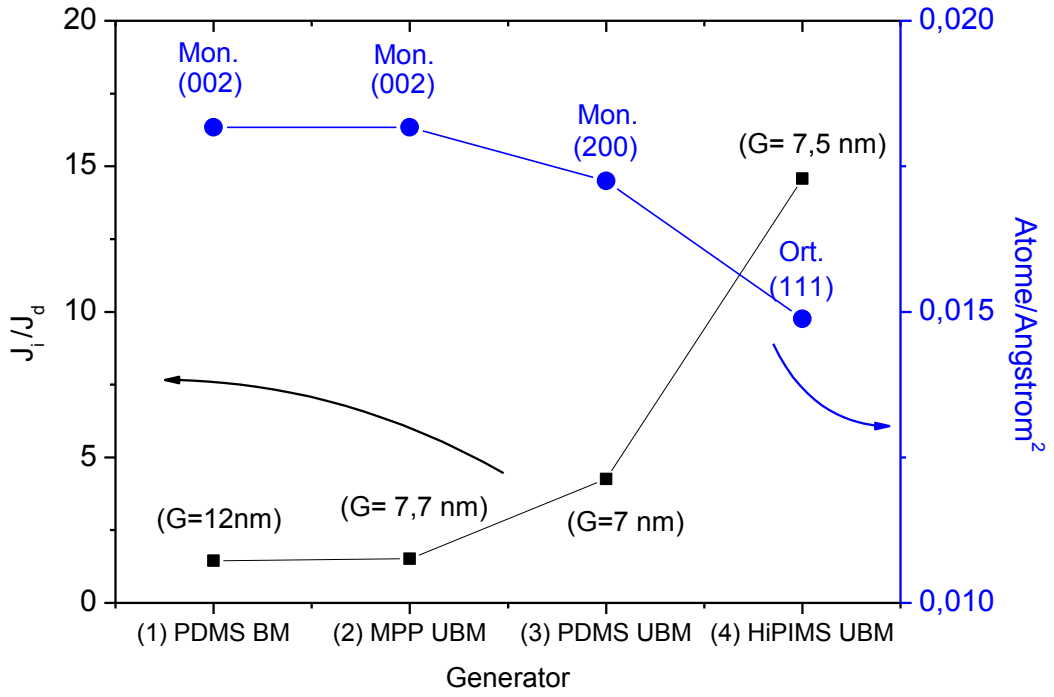


Figure 1: Evolution of J_i/J_d and plane density as a function of the deposition conditions: PDMS (balanced and unbalanced), HiPIMS and MPP discharges. G is the grain size.

In order to understand these data, it has been necessary to consider not only the ion fluxes towards the growing film but also the ratio between the ions and deposition (neutral+ions) fluxes: (J_i/J_d). Indeed, it is accepted that this quantity is a key parameters controlling the diffusion process on the surface during the thin film growth and therefore, the growth mechanism and the phase constitution of the material.[6] In this work, it has been roughly estimated by dividing the ion fluxes measured by mass spectrometry by the deposition rate (expressed as a quantity of matter). **Figure 1** shows the evolution of this parameter as a function of the synthesis method used in this work.

These results show a global view of the energy provided to the growing films during the different processes. It appears that, even if the ion flux is lower in MPP, due to the high deposition rate of the process, the J_i/J_d ratio is significantly lower than in HiPIMS. On the other hand, the PDMS-UBM combination allows a low value of this ratio to be reached.

When looking at the crystallographic properties of the deposited films as a function of the source used (**Fig. 1**), a correlation is observed with, at low J_i/J_d value, the synthesis of the room temperature monoclinic phase with a strong (002) texturation and at high J_i/J_d value, the synthesis of the high temperature orthorhombic phase. In that case, by playing with the pulse length in HiPIMS, it is even possible to modify the texturation from the (001) plane to the (111) plane due to higher energy provided to the films.

Concerning the grain size (G) of the material which is important for the efficiency of thin films based MOS-based gas sensors, we observe a reduction of the latter as the ratio increases as revealed by **Figure 1**. This can be understood by the limited growth of the grains due to the strong bombardment when the ion flux increases.

We have therefore established that it is possible to finely control the crystallographic and microstructural properties of WO_3 thin films deposited by reactive magnetron sputtering by playing either with the magnetic configuration of the magnetron and/or with the electrical source used to sputter the W target. In order to understand the evolution of these data, it is necessary to consider the energy provided per depositing atom. This parameter can be roughly deduced by combining the data provided by energy-resolved mass spectrometry measurements and the deposition rate data.

[1] G. Korotcenkov, Mater. Sci. Eng. R **61** (2008) 1
[2] G. Korotcenkov, Sensor. Actuat. B-Chem. **107** (2005) 209
[3] W.T. Moon, K.S. Lee, Y.K. Jun, H.S Kim, S.H. Hong, Sensor. Actuat. B-Chem. **115** (2006) 123
[4] Scott C. Moulzolf, S.A. Ding, R.J. Lad, Sensor. Actuat. B-Chem. **77** (2001) 375
[5] K. Sarakinos, J. Alami, S. Konstantinidis, Surf. Coat. Techno. **204** (2010) 1661
[6] I. Petrov, P. B. Barna, L. Hultman, J. E. Greene, J. Vac. Sci. Technol. A **21** (2003) 117
[7] S. Mahieu, P. Ghekiere, D. Depla, R. De Gryse, Thin Solid Films **515** (2006) 1229
[8] A. Anders, Thin Solid Films **518** (2010) 4087
[9] A. Hemberg, S. Konstantinidis, F. Renaux, J.P. Dauchot, R. Snyders Eur. Phys. J. Appl. Phys.**56**, 24016 (2011)

Thermal characterization of thin carbon nanotubes films

Mireille Gaillard, Éliane Amin-Chalhoub, Nadjib Semmar, Agnès Petit,
Anne-Lise Thomann and Chantal Boulmer-Leborgne

GREMI, UMR7344, 14 rue d'Issoudun, BP6744, 45067 Orléans cedex2, France

Résumé

Carbon nanotubes (CNTs) are grown with a three steps process combining pulsed laser deposition and radio frequency plasma enhanced chemical vapor deposition techniques. The result is a dense thin film made of vertically aligned and multi-walled CNTs. To characterize the thermal properties of the film by pulsed photothermal method, it is necessary to deposit on the top a metallic thin layer of 600 nm acting as a photothermal transducer. The thermal conductivity and volumetric heat capacity of the CNTs film are identified. They are found to be respectively 180 $Wm^{-1}K^{-1}$ and 5×10^4 $JK^{-1}m^{-3}$. The thermal resistance between the CNTs film and the metallic transducer is identified as well : 1×10^{-7} Km^2W^{-1}.

Introduction

One of the great challenge for futur microelectronics components is to manage the heat within circuits. This point is of special concern, because of the continuous components size decrease. This trend leads to a continuous current density increase through connexions between components and between external circuit and components [1, 2]. It becomes then crucial to efficiently evacuate the heat to avoid the damages due to either electromigration or thermomigration within the electrical connectors. For this reason, new materials are looking for since some years by microelectronic industries. Among the possible ways, carbon nanotubes (CNTs) are seen as potential substitutes thanks to their unusual thermal properties along with their electrical ones [3]. To answer the question "Can carbon nanotubes be used as heat sink ?" their thermal properties must be measured. For this goal, we prepared vertically aligned carbon nanotubes films [4] and characterized their structure by electronic microscopy and their thermal properties by pulsed photothermal method.

Growth of CNTs films

The growth of the CNTs films is a three-step process which takes place in the same reactor without venting the chamber between steps. First, the catalyst thin film (less than 10 nm) is deposited at room temperature by pulsed laser deposition (PLD). We first optimized the catalyst film thickness in order to obtain sufficiently high and dense CNTs films [5].
In the second step, the catalyst film is annealed to the CNTs growth process temperature (550-700°C) in order to get nanoparticles which will catalyze the CNTs growth. Then, the temperature is kept constant under a pressure of 1 Pa for 15 min.
Finally, the carbon-containing gas mixture is introduced for the growth of the CNTs by plasma enhanced chemical vapor deposition (PECVD) technique at a pressure of 150 Pa. The mixture is composed of ethylene (C_2H_4)/hydrogen (H_2) in the ratio of 1 :2. A RF plasma is created, its power is kept at 25 W.
The CNTs obtained with this technique are vertically aligned perpendicular to the substrate surface, with a diameter distribution between 5 and 20 nm and form a porous film of few to several tens of μm in height

(see Fig. 1) and whose porosity has been evaluated to 70% (Fig. 1(right)). Moreover, catalyst can be found within the body of the CNTs, especially at the top.

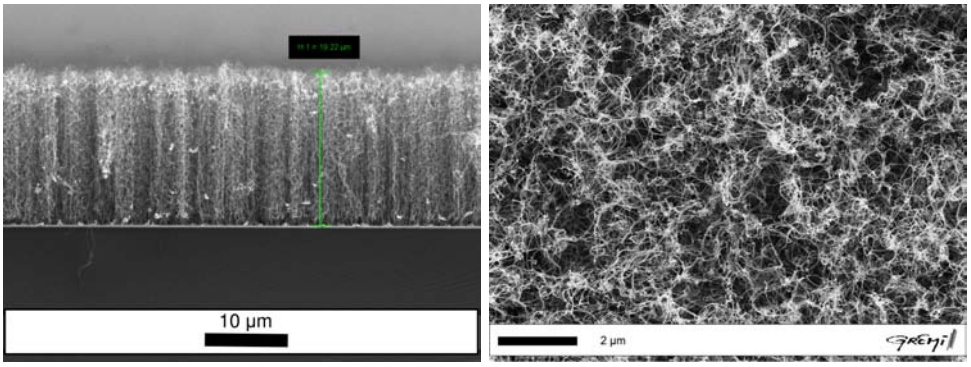


FIGURE 1 – SEM images of CNTs film obtained by PLD-PECVD groth process. Cross-sectional view (left) and top view (right).

Thermal characterization setup

The thermal characterization is done with the pulsed photothermal method (PPT) : the sample surface is heated up with an UV KrF laser. This allows to heat only the extreme surface of the sample (several tens of nanometers) which is really suitable for the thermal characterization of thin films [6]. The only stringent condition is that of a homogeneous absorption of the laser beam energy.
Thermal properties of thin films are determined from the time relaxation of the surface temperature after one laser pulse. In order to deduce the surface temperature from the electrical signal of the IR detector, a calibration process is necessary for each sample. In fact, the emissivity of each surface depends on the nature of the material, its surface state and its thickness. For the calibration, a resistive heater and a K-type thermocouple are in contact with the back side of the sample. The sample is heated by this resistance, and once the thermal steady state is reached, the thermal radiations emitted from its front surface are measured by the IR detector and can be plotted versus thermocouple temperature values [7].

Deposition of a metallic transducer : a metallic thin layer on the top of CNTs films

The use of the pulsed-photothermal method is possible only if the laser beam energy is homogeneously absorbed by the sample surface. For porous and complex surface as is the top of the CNTs films, this condition is not met. When the laser beam heats the surface, it interacts with carbon material and air between CNTs. To force the homogeneous heat transfer from laser beam to CNTs, the deposition of a metallic thin film, which acts as a transducer, on the CNTs surface is required : this metallic thin layer absorbs the UV beam energy, becomes a uniform heat source, and transmits the photon energy toward the substrate by phonon vibrations [6]. The transducer must thus be chosen according to following requirements : non-transparent medium at 248 nm, good and thermally stable emissivity in IR and chemically and mechanically stable when irradiated.
Furthermore, CNTs emit non-thermal IR photoluminescence signal under UV excitation [8, 9] which is added with the thermal one and lead to wrong properties identification. The metallic transducer then prevents the photoluminescent signal by blocking the direct UV excitation of CNTs.
According to previous conditions, titanium, tungstene or nickel layers can be used. They can be deposited by magnetron sputtering technique [10]. As seen on the Fig. 2 for the Ti example, the metallic thin layer does

wrap around the upper part of the CNTs ; with the proper deposition conditions it is seen as a homogeneous film by the laser beam and can be used as a transducer.

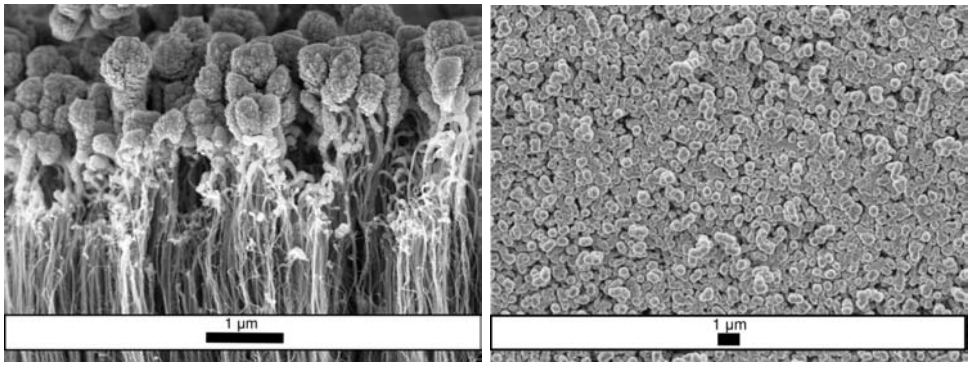


FIGURE 2 – SEM images of CNTs + 600 nm Ti film : cross-section of the upper part (left) and top view (right).

Thermal Properties

After a calibration step (thermal properties of metals onto silicon substrate), the thermal properties are determined for a sample composed of a 600 nm thick film of metal deposited on a CNTs film of 20 μm in height. Typical surface temperature evolution of transducer/CNTs sample is given in Fig. 3, normalised to the relaxation temperature. The transducer temperature rises up to about 250°C. When using log-log scale, it appears that the temperature relaxation occurs with two different slopes. The first slope (first tens of ns) corresponds to the transducer relaxation and the second slope to the CNTs film relaxation. The

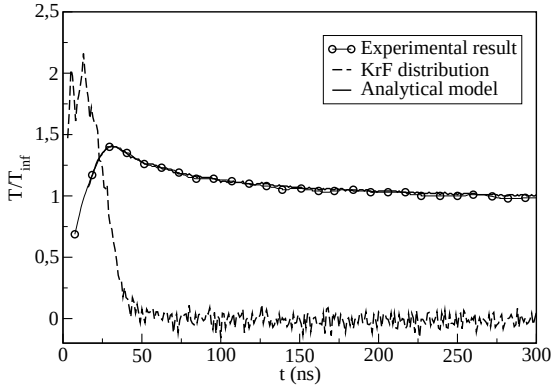


FIGURE 3 – Experimental (point) and analytical (line) curves of the normalised temperature temporal relaxation T/T_{inf} in semi-log scale. Real laser beam shape (dotted line) used during experiments. See text for T_{inf} definition.

thermophysical properties of the CNTs carpet as well as of the thermal transducer obtained from these curves are listed in Table 1. The values of the thermal contact resistance, R_{th}, and the volumetric heat capacity, ρc_p, explain well the slow temperature relaxation.

Conclusion

Vertically aligned multi-walled CNTs are grown thanks to PLD catalyst deposition and then RF PECVD growth process. The SEM images show that the films obtained are composed of vertically aligned CNTs of several μm in height. Actually, the films are porous media as the typical porosity is estimated around

	Ti	CNT
κ ($\mathrm{Wm^{-1}K^{-1}}$)	22 ± 2.2	180 ± 5
ρc_p ($\mathrm{JK^{-1}m^{-3}}$)	$(1.4 \pm 0.14)\times 10^6$	$(5 \pm 0.5)\times 10^4$
R_{th} ($\mathrm{Km^2W^{-1}}$)	$(1 \pm 0.5)\times 10^{-7}$	

TABLE 1 – Thermophysical properties of Ti transducer and CNTs carpet : thermal conductivity, κ, and volumetric heat capacity, ρc_p as well as thermal contact resistance, R_{th}, between these two medias, determined by the model.

70% at least and can be considered as composite films made of multi-walled CNTs of various diameter with catalyst particles inside.
These porous media is characterized with the PPT method in order to estimate its thermal properties as conductivity and volumetric heat capacity. To apply this technique with porous objects, it is necessary to deposit a thin metallic layer on the top of the CNTs film. Then, it is possible to obtain the thermal contact resistance between the CNTs film and this metallic layer.
These porous nanomaterials are found to be good thermal conductors, compare to known and used connectors. Moreover, their properties are independant of the location at which the thermal properties are evaluated (the probed depth within the CNTs film) wich means that the entangled shape of the top of CNTs film does not influence their thermal properties. This confims that they can be used where thermal conductivity and heat sink effect are requested.

Acknowledgement

The French Agency ANR is acknowledged for its financial support through the NanothermIC P3N project. And STMicroelectronics-Tours company to provide all the substrates.

Références

[1] E. Pop, *Nano Res.* **3**, 147 (2010).

[2] Y. Sun, L. Zhu, H. Jiang, J. Lu, W. Wang, and C. Wong, *J. Electr. Mat.* **37**, 1691 (2008).

[3] P. Ajayan, and O. Zhou, *Carbon nanotubes*, Springer, Berlin, 2001, pp 391-425 : Applications of carbon nanotubes.

[4] M. Gaillard, H. Mbitsi, A. Petit, E. Amin-Chalhoub, C. Boulmer-Leborgne, N. Semmar, E. Millon, J. Mathias, and S. Kouassi, *J. Vac. Sci. Technol. B* **29**, 041805 (2011).

[5] M. Gaillard, C. Boulmer-Leborgne, N. Semmar, E. Millon, and A. Petit, *Appl. Surf. Scie.* p. in press (2012).

[6] E. Amin-Chalhoub, N. Semmar, L. .Coudron, G. Gautier, C. Boulmer-Leborgne, A. Petit, M. Gaillard, J. Mathias, and E. Millon, *J. Phys. D : Appl. Phys.* **44**, 355401–9 (2011).

[7] J. Martan, N. Semmar, C. Leborgne, E. L. Menn, and J. Mathias, *Applied Surface Science* **247**, 57–63 (2005).

[8] Y. Yan-Hong, M. Run-Cai, B. Jin-Tao, and H. Xun, *Chin. Phys. Soc* **15**, 2761–04 (2006).

[9] J. Riggs, Z. Guo, D. Carroll, and Y. Sun, *J. Am. Chem. Soc.* **122**, 5879–5880 (2000).

[10] V. Dolique, A.-L. Thomann, P. Brault, Y. Tessier, and P. Gillon, *Materials Chemistry and Physics* **117**, 142–147 (2009).

Influence of the structure and composition of titanium nitride based substrate on the carbon nanotubes grown by CVD

M. Morales[1], S. Cucatti[1], J.J.S. Acuña[2], L.F. Zagonel[3], O. Antonin[4], M.C. Hugon[4], N. Marsot[4], B. Bouchet-Fabre[5], T. Minea[4], and F. Alvarez[1]

[1]UNICAMP, Inst. de Fisica "Gleb Wataghin"13081-970 Campinas, SP, CP 6165, Brazil
[2] UFSC, Laboratório Central de Microscopia Eletrônica, 88040-970 - Florianopolis, SC – Brazil
[3] Electron Microscopy Laboratory, Brazilian Nanotechnology National Laboratory, R. Giuseppe Maximo Scolfaro, 10000, Campinas ,Brazil
[4]Laboratoire de Physique des Gaz et des Plasmas, Bat 210, Université Paris Sud-XI, 91405, Orsay, France.
[5]Laboratoire Francis Perrin, CEA-Saclay/CNRS,IRAMIS/SPAM, F-91191 Gif sur Yvette Cedex, France
Alliance Concept, Cran-Gevrier, France

Corresponding author: mmorales@ifi.unicamp.br

Abstract

We present a study of the influence of the substrate nano-structure and composition on the morphological properties of the carbon nanotubes (CNTs) by sequentially growing in situ TiN_x:O_y film, dispersed nickel catalyst particles, and CNTs obtained by CVD. The results show that the stoichiometry and the nanostructures of the substrate intervene in the growing process. Particular attention is pay to the influence of oxygen on the CNT growths. The results show that O prevents the coarsening of the catalyst nickel particles, avoiding the surface diffusion mobility of the precursor atoms involved in the nanotubes growth (Ostwald ripening)[1]. The dependence of the size and density of the CNTs on the amount of O present in the substrate are reported and discussed. The experimental findings show that, besides acting as diffusion barrier between the catalyst particles and the silicon, the substrate also influences the kinetics of growth of carbon nanotubes.

Key words: Structured TiNx:Oy, Carbon nanotubes, Barrier (buffer) layer

Experimental

The non-stoichiometric TiN_x:O_y films were grown on crystalline silicon by Ti ion beam sputtering at 500°C followed by nickel nano-particles deposition at 750°C.The CNTs are grown immediately after the catalyst deposition by feeding acetylene gas and maintaining the substrate at 700°C. *In situ* X-ray photoelectron spectroscopy (XPS) system allows compositional and structural analysis of the samples. The phases of the TiN_x:O_y were analyzed by X-ray diffraction. The quite aligned CNTs were studied by scanning and transmission electron microscopy techniques showing different population density, morphology and diameter as a function of the O substrate content.

Results and discussion

The XPS technique probe up to ~50 Å depth[2]. As the influence of the buffer layer on CNTs grows depend on surface phenomena the probed region is giving a valuable information for our purposes. The XPS spectra of the studied samples showed the bands associated to electrons in Ti2p, N1s and O1s bonds. From the XPS spectra (not shown) were identified the bands associated to electrons in $Ti2p_{3/2}$-N ($Ti2p_{1/2}$-N) bonds, located at ~455 eV[3] (~461,2 eV). The band corresponding to electrons associated to titanium oxide for $Ti2p_{3/2}$-O ($Ti2p_{1/2}$-O) is located at ~457 eV[4] (~463,6 eV). The bands associated to N electrons are located in Ti-N (~397 eV) [3,5] and N-O-Ti (~400 eV) [6]. Finally, the band associated to O electrons are located at O1s-N-Ti (~532 eV)[5] and O1s-Ti (~530 eV)[5,7].

One of the main purposes of the work is studying the possible influence on the CNTs growing of the

buffer layer composition and structure. Therefore, the relative atomic composition of the TiN_x:O_y buffer layers were obtained from the XPS spectra. Figure 1 shows the concentration of oxygen present in the thin films as a function of the ratio of gas $[H_2]/[N_2+Ar]$ used during the films deposition. This concentration shows the reduction effect of hydrogen during the films deposition. This result was important controlling the oxygen content in the buffer layer.

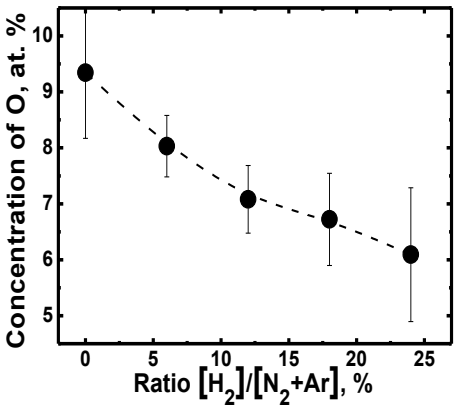


Figure 1. Concentration of O as function of the gaseous mixture $[H_2]/[N_2+Ar]$ used during the films growing.

The X-ray difractograms of the studied samples are shown in Figure 2. The crystalline evolution of the compound is revealed by the dependence of the microstructure of the buffer layer on the material composition. The difractograms show the main reflections associated to the (111) and (200) crystalline orientations of TiN of the studied samples. Also, an ill-defined reflection associated to the (220) TiN orientation is barley observed[8]. The reflection from the (300) crystalline orientation in the Ti_2O_3 compound is clearly displayed in the difractogram[9]. These plots show that the crystalline orientations associated with reflections (111) and (200) of TiN do not strongly depend on oxygen. Meanwhile, the reflection associated with the (300) crystalline orientations in Ti_2O_3 clearly depend on oxygen content, i.e., increasing hydrogen during the deposition process reduce the presence of oxygen in the film.

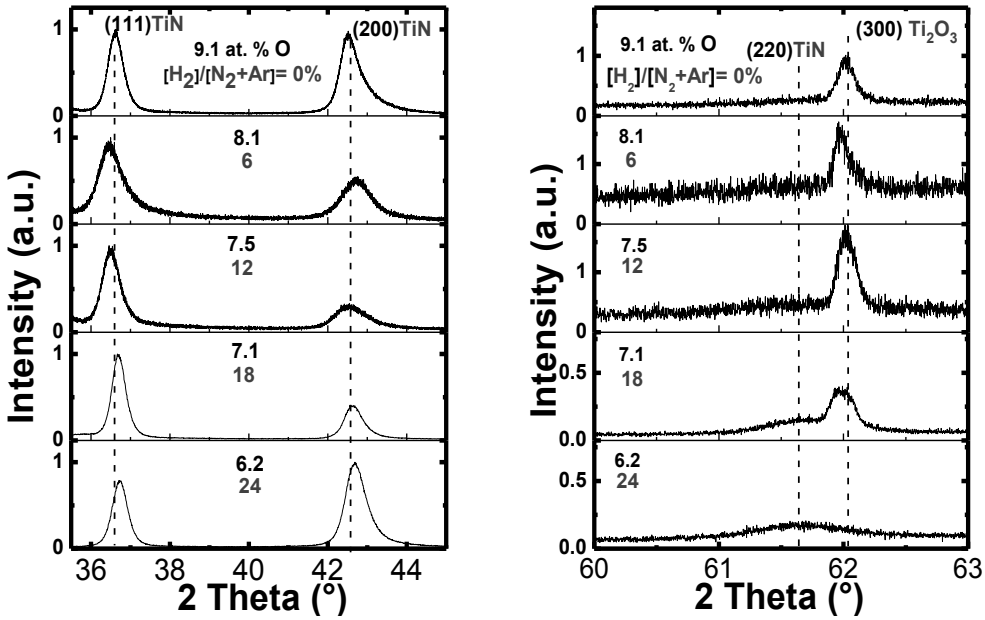


Figure 2. X-ray difractograms of the studied TiN_x:O_y films. The relative O concentrations as well as the gaseous mixture used in the deposition of the samples are indicated. For the sake of clarity, in the right panel, the difractograms corresponding to oxygen concentration is expanded.

A set of micrographs for the CNTs grew on the different prepared buffer layers were obtained. Figure 3a. shows a typical "carpet" of carbon nanotubes grown on one of the studied buffer layer, manifesting homogeneity in all film. We remark that in the scale of this micrograph all the samples look similar.

Figures 3b, c, d, e and f show a blow up of the CNTs deposited on different buffers layers. By a systematic counting on these set of micrograph were estimated the density and diameter distribution of the CNTs obtained in each studied substrate. Figure 4a shows the number of nanotubes per unit of area as a function of the concentration of oxygen. This plot shows that increasing O in the buffer layers leads to a higher density of CNTs in almost a factor five.

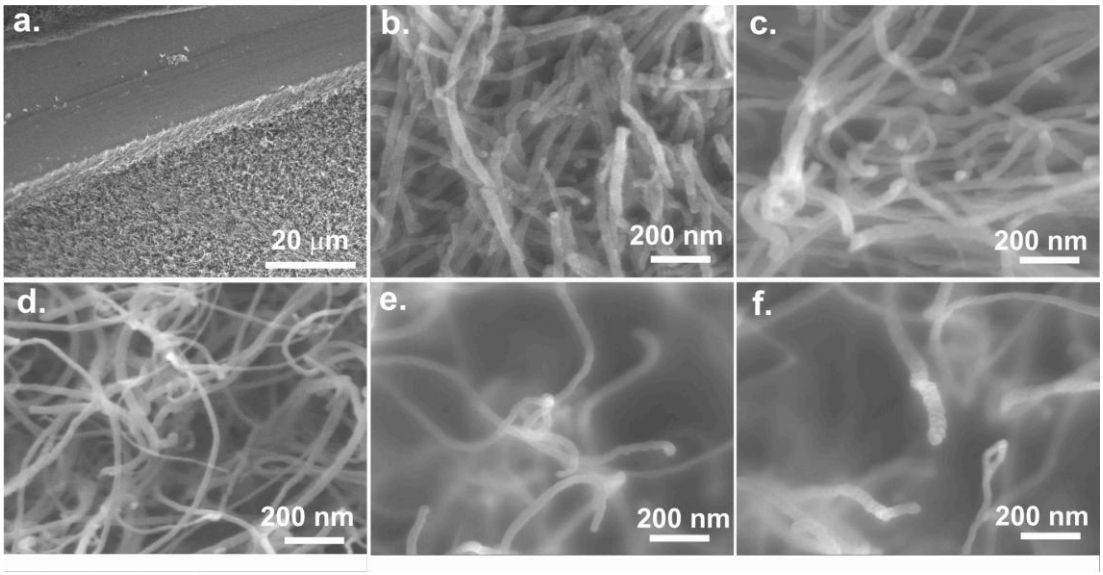


Figure 3. a) SEM top view images of CNTs a) carpet of CNTs; b, c, d, e and f) CNTs grown on different substrates different stoichiometry containing 9.1, 8.1, 7.5, 7.2, 6.2 oxygen at. %, respectively.

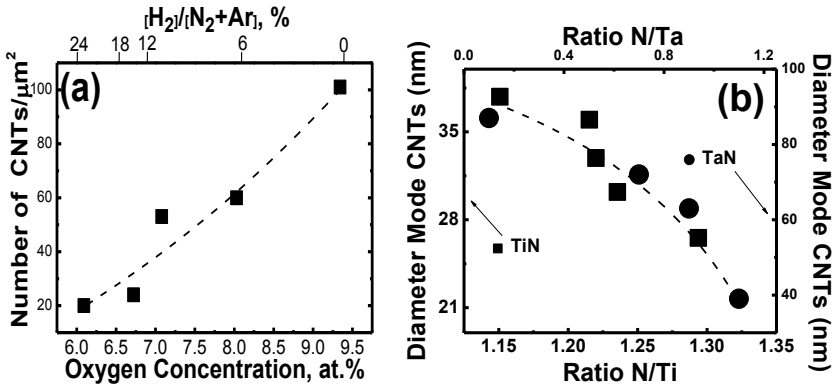


Figure 4 a) Density of CNTs as a function of oxygen concentration (bottom axis) and gaseous mixture (top axis); b) diameter mode of the CNTs grown on the studied substrates as a function s N/Ti (black). With comparison purposes, the experimental data obtained in previous work realized on tantalum nitride substrate[10] are also indicated (filled circles).

The dependence of the CNTs density on oxygen could be explained as a consequence of the inhibition phenomenon known as Ostwald ripening[1,11]. Roughly speaking, this effect consists in the growing of bigger particles at expenses of smaller ones (ripening) by surface migration of the catalyst particles. Our results suggest that the presence of Ti_2O_3 diminishes the catalyst particles surface mobility preventing Ni particles coalescence, i.e., the original number of catalyst particles remains constant. An interesting work regarding with the interaction nickel-titanium oxides films was reported by Dumesic and coworkers[12]. In an experiment realized at equivalent temperatures to the one used in our experiments (750 ^{0}C), these authors showed that, in the *presence of hydrogen*,

the Ni particles reduces the titania film and migrate, coalescing after meeting other catalyst particle. Therefore, we can assume that reducing the Ti_2O_3 phase in the buffer layers will favor the catalyst particles mobility and coalescence, i.e., the number of seeds will diminishes.

Consequently, a smaller CNTs density is expected, as it is experimentally found. Finally, in order to compare with previous results obtained in samples grown on TaN reported by Bouchet, et al.[10] we have plotted the mode of the diameter CNTs as a function of the ratio N/Ti and N/Ta (Figure 4b). As noted, the same trend is obtained in both cases suggesting that the behavior of the metal nitrides of compounds belonging to the p-block metal of the periodic table behaves similarly.

Conclusions

Different concentrations of oxygen were study in order to identify structural changes in the TiN_x:O_y substrates and its influence on the CNTs growth. The Ti_2O_3 phase present in the films is controlled by the presence of hydrogen in the gaseous mixture used during growth. This phase affects the catalyst particle surface diffusion mobility, preventing nickel coalescence. As the nanotubes growing depend on the density of nickel seeds, the density of CNTs is also dependent on the presence of the Ti_2O_3 phase, i.e., by reducing this phase the CNTs density diminishes. The diameter mode as a function of the N/Ti ratio shows a similar trend that the one observed in experiment performed on tantalum nitride buffer layers, suggesting that metal compound from the p-block of the periodic table behave similarly regarding with the CNTs growing process. Finally, this work shows the importance of the substrate structure and composition on the CNTs growth, showing that it is acting not only as diffusion barrier preventing silicide formation but also intervening on the kinetic of the process.

[1] P. B. Amama, C. L. Pint, L. McJilton, S. M. Kim, E. A. Stach, P. T. Murray, R. H. Hauge and B. Maruyama. Role of Water in Super Growth of Single-Walled Carbon Nanotube Carpets, Nano Lett, 9 (2009), pp. 44-49

[2] D. Briggs and M. P. Seah. Practical Surface Analysis, 2nd ed. John Wiley & Sons, New York, 1 (1993)

[3] Ch. Cardinaud, G. Lemperiere, M.C. Peignon, P.Y. Jouan. Characterisation of TiN coatings and of TiN/Si interface by x-ray photoelectron spectroscopy and Auger electron spectroscopy, Appl Surf Sci, 68, (1993), 595-603

[4] A. Luches, A. Perrone. B. Dubreuil, B. Rousseau, C. Boulmer-Leborgne, G. Blondiaux, H. Estrade, J. Hermann, J. L. Debrun, M. L. Degiorgi, M. Martino, P. Brault. Direct carbitation of titanium as a result of multipulse UV-laser irradiation of titanium samples in an ambient methane gas, Appl Surf Sci, 54 (1992), pp. 349-352

[5] Ju.F. Huravlev, M.V. Kuznetsov, V.A. Gubanov. XPS analysis of adsoption of oxygen molecules on the surface of Ti and TiNx films in vacuum, J Electron Spectrosc Relat Phenoma, 38 (1992), pp. 169-176

[6] N. Jiang, H.J. Zhang, S.N. Bao, Y.G. Shen, Z.F. Zhou. XPS study for reactively sputtered titanium nitride thin films deposited under different substrate bias, Physica B, 352 (2004), pp. 118–126

[7] A. Trenczek-Zajac, M. Radecka, K. Zakrzewska, A. Brudnik, E. Kusior, S. Bourgeois, M.C. Marco de Lucas, L. Imhoff. Structural and electrical properties of magnetron sputtered Ti(ON) thin films: The case of TiN doped in situ with oxygen, J Power Sources, 194 (2009), pp. 93-103

[8] M. Popović, M. Novaković and N. Bibić. Structural characterization of TiN coatings on Si substrates irradiated with Ar ions, Mat Charac, 60 (2009), pp. 1463-1470

[9] M. A. Afifi, M.M. Abdel-Aziz, I.S. Yahia, M. Fadel, L.A. Wahab. Transport properties of polycrystalline TiO2 and Ti2O3 as semiconducting oxides, Journal of Alloys and Compounds, 455 (2008), pp. 92-97

[10] B. Bouchet-Fabre, A. Fadjie Djomkam, M. Delmas, C. Jin, O. Antonin, M.C. Hugon, M. F. Mayne-L'Hermite, F. Alvarez, T. Minéa. Tantalum based coated substrates for controlling the diameter of carbon nanotubes Carbon, 47 (2009), pp. 3424-3426

[11] W. Ostwald. Lehrbuch der Allgemeinen Chemie, Leipzig, Germany , 2, (1896)

[12] J.A.Dumesic, S. A. Stevenson, R. D. Sherwood, and R. T. Baker, J. of Catalysis, 99, 79 (1986)

Fabrication of heterostructured M@M´Ox Nanorods by low temperature PECVD

Manuel Macias-Montero, Ana Borras,* Angel Barranco, Jose Cotrino, Juan Espinos, Agustin R. González-Elipe
Nanotechnology on Surfaces Laboratory, Materials Science Institute of Seville (ICMS, CSIC-US), C/ Americo Vespucio 49, 41092, Sevilla, Spain
anaisabel.borras@icmse.csic.es

Abstract

In this communication we report on the fabrication of two different heterostructured core@shell 1D materials by low temperature (135 ^{o}C) plasma enhanced chemical deposition: Ag@TiO_2 and Ag-NPs@ZnO nanorods (NRs). The controlled formation of these heterostructures on processable substrates such as Si wafers, fused silica and ITO is demonstrated. The NRs are studied by SEM, HAADF-STEM, TEM, XRD and in situ XPS in order to fully describe their microstructure and inner structure, eventually proposing a growth mechanism. The first type of nanostructures consists on a silver wire surrounded by a TiO_2 shell that grows following the volcano-like mechanism. The Ag-NPs@ZnO nanostructures are formed by supported ZnO nanorods decorated with Ag nanoparticles (NPs). The 3D reconstruction by HAADF-STEM electron tomography reveals that the Ag NPs are distributed along the hollow interior of highly porous ZnO NRs. The aligned Ag-NPs@ZnO-NRs grow by a combination of different factors including geometrical distribution of precursor, plasma sheath and differences in the silver/silver oxide densities. Tuning the deposition angle, Ag-NPs@ZnO-NRs depicting different tilting angles can be homogeneously grown allowing the formation of zig-zag nanostructures. The as prepared surfaces are superhydrophobic with water contact angles higher than 150º. These surfaces turn into superhydrophilic with water contact angles lower than 10º after irradiation under UV light. In the case of the AgNPs@ZnO NRs such modification can be also provoked by irradiation with VIS light. The evolution rate of the wetting angle and its dependence on the light characteristics are related with the nanostructure and the presence of silver embedded within the NRs.

Introduction

The growing interest in nanostructured and porous thin films and in supported 1D nanostructures such as nanowires (NWs), nanofibres (NFs), nanoribbons, nanorods (NRs), etc, has fostered the development of new procedures of surface and thin film tailored fabrication. Wet chemical and electrochemical routes [13], vapour phase condensation methods (e.g. vapour–liquid–solid (VLS) methods) [2], solution-phase methods [3], template-directed synthesis [4] or physical vapour deposition approaches [5] are currently used for the synthesis of these types of nanostructured materials.

Plasma deposition and, in general, plasma processing have also been successfully used for the surface nanostructuring of materials, either by etching [6] or, to a much lesser extent, by plasma-

[1] Yang P, Yan R and Fardy M 2010 Nano Lett. 10 1529
[2] Barth S, Hernandez-Ramirez F, Holmes J D and Romano-Rodriguez A 2010 Prog. Mater. Sci. 55 563
[3] Macak J M, Tsuchiya H, Ghicov A and Schmuki P 2005 Electrochem. Commun. 7 1133
[4] Wacaser B A, Dick K A, Johansson J, Borgstrom M T, Deppert K and Samuelson L 2009 Adv. Mater. 21 153
[5] Peng P, Milliron D J, Hughes S M, Johnson J C and Alivisatos A P 2005 Nano Lett. 5 1809
[6] Gogolides E, Constantoudis V, Kokkoris G, Kontziampasis D, Tsougeni K, Boulousis G, Vlachopoulou and Tserepi A 2011 J. Phys. D: Appl. Phys. 44 174021
[7] Borras A, Groening O, Koeble J and Groening P 2009 Adv. Mater. 21 4816
[8] Mieszawska A J, Jalilian R, Sumanasekera G U and Zamborini F P 2007 Small 3 722
[9] Rao C N R and Govindaraj A 2009 Adv. Mater. 21 4208

enhanced chemical vapour deposition (PECVD) of 1D nanostructures such as carbon nanotubes, oxide nanofibres (NFs) or nanorods [7, 8]. The main advantage of PECVD techniques in comparison with thermal CVD or other liquid-phase or chemical methods is that it operates at low temperatures and does not produce any substantial amount of waste materials.

Probably, the most typical example of plasma synthesis of 1D nanostructures is the formation of deposited carbon nanotubes (CNTs) [9, 10]. In this case, the formation of nanostructures does not occur at low temperatures and metal particles acting as seeds are needed to catalyze the nanotube growth by favoring the preferential arrangement and diffusion of the carbon species arriving at the surface from the plasma phase. Previously, we have shown that supported core@shell Ag@TiO_2 NFs form at low temperatures when titanium oxide is deposited by PECVD on silver metal foil previously treated with oxygen plasma [11, 12].

The outstanding properties of Ag/ZnO heterostructures have prompted us to fully develop a robust methodology for their fabrication on processable substrates, as well as to propose a model accounting for their growth by plasma deposition

Experimental

Silver deposited on fused silica and silicon wafers have been used as substrates. The silver was deposited by DC sputtering from a metal wire in Ar atmosphere, controlling the equivalent layer thickness (ELT).

These silver-covered substrates were placed in a plasma deposition chamber. The sample holder was heated by irradiation with quartz lamps up to a maximum temperature of 405 K. The plasma reactor used for deposition of ZnO consisted of a stainless steel chamber supplied with a microwave plasma source (SLAN, from Plasma Consult, GmbH, Germany) in a remote configuration. Details about this reactor can be found elsewhere [13]. For the deposition of ZnO, the reactor was supplied with oxygen (5×10^{-3} mbar) and excited with a microwave power of 400 W. Diethylzinc (ZnEt2), used as the precursor of zinc, was dosed directly into the deposition chamber from a stainless steel bottle that was heated at 308 K. Substrates and precursor dispenser were separated by a distance of 5 cm, much larger than the mean free path of the gas particles at the working pressure during our experiments. The plasma source fed with oxygen was located above the dispenser tube, while the pumping system was located at the bottom, thus defining a preferential top-down direction for the gas species in the chamber. As we will show below, this configuration is critical in the formation of tilted nanostructures.

Results

Characteristic SEM and STEM images of the Ag-NPs@ZnO nanorods are gathered in Figure 1.There it is show that the layer consists of a continuous set of separated and vertically aligned NRs supported on the silicon substrate, with typical surface densities of the order of 10^9 NRs cm^2 (Fig. 1b). A statistical analysis of the images renders a mean diameter of 40 nm and a height of 900 nm for the NRs, i.e., an aspect ratio of 20. Both the diameter and length of the NRs are controlled by the experimental parameters, particularly the deposition time. The number of NRs is determined by both the distribution of silver particles on the substrate and the precursor arrival rate to the surface.

The internal microstructure of the nanorods was determined by HAADF-STEM electron tomography [14].

[10] Sharma S C and Tewari A 2011 Phys. Plasmas 18 063503
[11] Borras A, Barranco A, Yubero F and Gonzalez-Elipe A R 2006 Nanotechnology 17 3518
[12] Borras A, Barranco A, Espinos J P, Cotrino J, Holgado J P and Gonzalez-Elipe A R 2007 Plasma Proc. Polym. 4 515
[13] Barranco A, Cotrino J, Yubero F, Espinos J P, Clerc C and Gonzalez-Elipe A R 2001 Thin Solid Films 401 150
[14] Macias-Montero M, Borras A, Saghi Z, Romero-Gomez P, Sanchez-Valencia J R, Gonzalez J C, Barranco A, Midgley P, Cotrino J and Gonzalez-Elipe A R 2012 J. Mater. Chem. 22 134
[15] Gonzalez-Garcia L, Gonzalez-Valls I, Lira-Cantu M and Barranco A 2011 Energy Environ. Sci. 4 3426
[16] X. Feng, L. Feng, M. Jin, J. Zhai, L. Jiang and D. Zhu, J. Am. Chem. Soc., 2004, 126, 62.

A characteristic example of the internal microstructure of these NRs can be seen in figure 1(d) where it is appreciated a hollow structure with porous walls and an approximately 15 nm wide channel extending all along its length. It is also apparent that in the interior of this channel there are partially percolated silver nanoparticles of different sizes and shapes. Owing to this internal microstructure, we will consider these nanostructures as hollow nanorods rather than as compact nanofibres as was the case in our previous works on Ag@TiO_2 structures [11, 12]. GAXRD analysis of these NRs revealed that they consist of a crystalline wurzite ZnO phase. Further HRTEM characterizations have demonstrated the preferential orientation of the ZnO along the (002) direction [14].

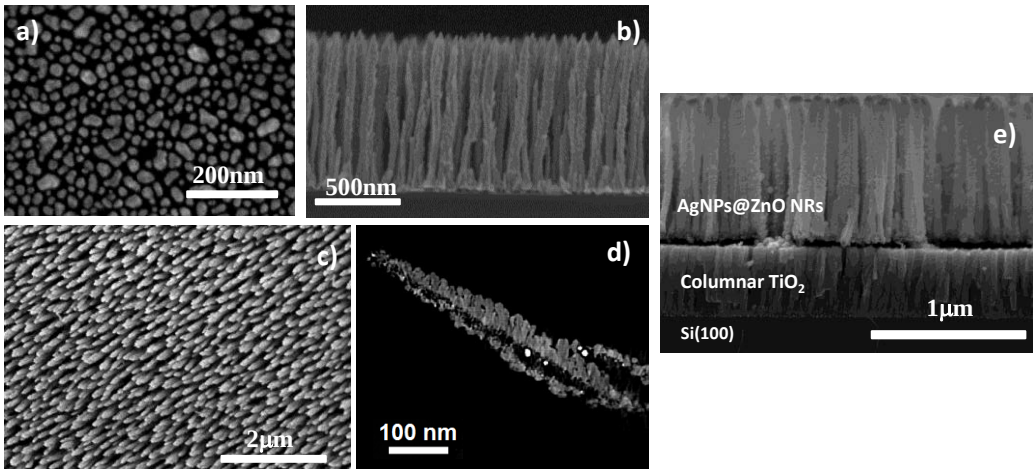


Figure 1. (a) SEM image of the silver oxide NPs developed after heating in O_2 at 135 ºC. (b) Cross-section and (c) norma SEM views at two different amplification scales of the Ag-NPs@ZnO nanorods obtained after deposition of ZnO at 135 ºC. (d) Vertical orthoslice through one of the formed Ag-NPs@ZnO nanorods after 3D reconstruction by HAADF-STEM. Bright spots along the inner channel of the rod correspond to the silver nanoparticles. (e) Cross-section SEM micrograph of the Ag-NPs@ZnO NRs grown on plasma made columnar TiO_2 previously coated with a silver layer.

This methodology is compatible with the fabrication of two-oxide heterostructured systems. Figure 1(e) shows an example of the formation of Ag-NPs@ZnO NRs on TiO_2 nanocolumns previously decorated with a silver coating. The method provides the formation of a high density and homogeneous NR layer similar to those presented in Figure 1(b-c) on the top of the mesoporous TiO_2 film. The fabrication of this type of heterostructured multilayers might be of special interest in applications such as microfluidics and nanosensoring.

Formation of tilted nanocolumnar structures is a common feature of oxide thin films prepared by physical evaporation at glancing angle (GLAD) [15^3]. This method is a line-of-sight procedure where shadowing is the main factor controlling the formation of the tilted nanocolumns. To control the orientation of the zinc oxide NRs with respect to the substrate, we have carried out a series of experiments by modifying the deposition geometry. Figure 2 shows three different cross-section micrographs corresponding to samples grown onto horizontal or 60^o oriented substrates as indicated in the schemes. At first glance it is apparent that the deposition geometry is crucial for the orientation of the NRs and that, by its adjustment, it is possible to obtain zigzag or even more complex structures. Zigzag structures were obtained by performing a first deposition with the substrate at 60^o and a second deposition with the substrate in a symmetrically mirrored orientation.

Previous works have demonstrated that ZnO-NR surfaces become superhydrophilic (i.e. WCA < 10^o) under UV irradiation because the surface of this material becomes photon activated and the water may then smoothly spread over the whole internal surface of the wire structure [16]. A similar behavior is depicted by the system Ag-NPs@ZnO-NRs where the conversion from a

[17] V. Rico, C. Lopez, A. Borras, J. P. Espinos and A. R. Gonzalez-Elipe, Sol. Energy Mater. Sol. Cells, 2006, 90, 2944.
[18] W. Lu, S. Gao and J. Wang, J. Phys. Chem. C, 2008, 112, 16792 13 D. Lin, H. Wu, R. Zhang and W. Pan, Chem. Mater., 2009, 21, 3479
[20] R. Georgekutty, M. K. Seery and S. C. Pillai, J. Phys. Chem. C, 2008, 112, 13563.
[21] M. K. Seery, R. george, P. Floris and S. C. pillai, J. Photochem. Photobiol., A, 2007, 189, 258.

superhydrophobic to superhydrophilic state under UV illumination is completed after 8 min of irradiation. In agreement with ref. [16] and [17] the surface recovered its superhydrophobic character after keeping the samples in the dark. A similar superhydrophobic– superhydrophilic conversion was found when this surface was irradiated with visible light. The WCA decreases under the visible illumination until reaching a superhydrophilic state. Visible light activation of ZnO can be surprising since this material is a band gap semiconductor which requires UV photons (E = 3.2 eV) for excitation. However it is already established that the deposition of noble metals on semiconductors promotes an enhancement in their photocatalytic activity by indirect influence on the interfacial charge transfer process [18-21].

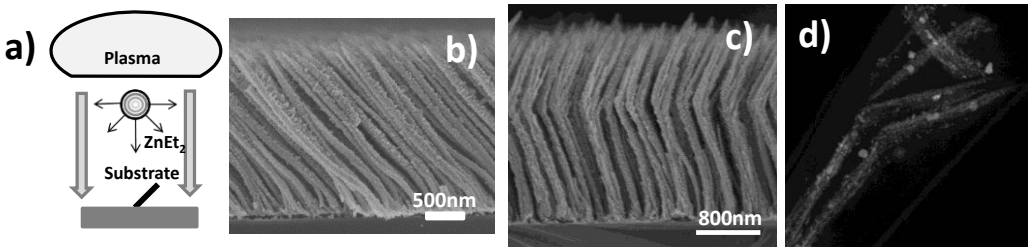


Figure 2. (a) Schematic showing the geometry of the ZnO deposition; (b) cross-section micrographs of Ag@ZnO NRs prepared by placing the substrates at the position and angle with respect to the sample holder indicated by the schematic in (a). The zigzag microstructure in (c) is obtained by first placing the substrates first in the position in (a) and then symmetrically. (d) HAADF-STEM micrograph of the zigzag NRs in (c) showing the distribution of silver nanoparticles along the microstructure.

Discussion

The scheme in Figure 3 shows a pictorial description of the nanorod formation under our experimental conditions. According to it (step i), some nuclei of the oxidized silver layer act as nucleation points of the NRs. Once these NR nuclei precursors have been formed, mobilization of silver or silver oxide in the interior of the NRs contributes to have a silver core within a NR which grows preferentially in length (step ii). The preferential linear growth of the NRs must be related with the presence of some small silver/silver oxide particles at the NR tip where, simultaneously, they react with the $ZnEt_2$ precursor and favor the confinement of the electrical field lines of the plasma sheath. As a result, sharp NR tips are produced and the hollow structure is preserved below the silver NP at the tip. After this initial nucleation, silver continues moving through the interior of the growing NRs until most silver has been removed from the substrate layer to decorate the ZnO phase (steps iii and iv). At this stage, the growth mechanism is no longer controlled by the silver located at the tip and different ZnO nanostructures can then be obtained.

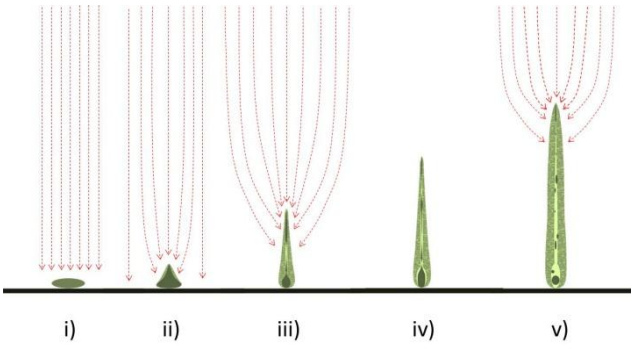


Figure 3. Model of the growth mechanism proposed for the formation of the Ag-NPs@ZnO NR. Grey features correspond to silver or silver oxide clusters, green to the ZnO and blue arrows to the electric field lines.

We thank the Junta de Andalucía (Projects P09-CTS- 5189, TEP5283 and FQM-6900) and the Ministry of Economy and Competitiveness (Projects CONSOLIDER CSD2008-00023, MAT2010-21228, and MAT2010-18447) for financial support. We also thank Dr. Zineb Saghi from University of Cambridge for the HAADF-STEM reconstruction.

Plasma polymers used for controlled interphase in polymer composites

Vladimir Cech, Adam Babik, Antonin Knob, Erik Palesch

Institute of Materials Chemistry, Brno University of Technology
Purkynova 118, CZ-61200 Brno, Czech Republic

The performance of fiber-reinforced composites is strongly influenced by the functionality of composite interphases. Sizing, i.e. functional coating (interlayer), is therefore tailored to improve the transfer of stress from the polymer matrix to the fiber reinforcement by enhancing fiber wettability, adhesion, compatibility, etc. The world market is dominated by glass reinforcement in unsaturated polyester. However, commercially produced sizing (wet chemical process) is heterogeneous with respect to the thickness and uniformity, and hydrolytically unstable. Companies search for new ways of solving the above problems. One of the alternative technologies is plasma polymerization. Plasma polymer films of hexamethyldisiloxane, vinyltriethoxysilane, and tetravinylsilane, pure and in a mixture with oxygen gas, were engineered as compatible interlayers for the glass fiber/polyester composite. The interlayers of controlled physico-chemical properties were tailored using the deposition conditions with regard to the elemental composition, chemical structure, and Young's modulus in order to improve adhesion bonding at the interlayer/glass and polyester/interlayer interfaces and tune the cross-linking of the plasma polymer. The optimized interlayer enabled a 6.5-fold increase of the short-beam strength compared to the untreated fibers. The short-beam strength of GF/polyester composite with the plasma polymer interlayer was 32% higher than that with commercial sizing developed for fiber-reinforced composites with a polyester matrix. The progress in plasmachemical processing of composite reinforcements enabled us to release a new conception of composites without interfaces.

Keywords: thin films, plasma polymerization, glass fiber, polymer composites, interface/interphase

1. Introduction

The development of high-performance fiber-reinforced plastics (FRP) is linked to an effort to improve the properties of reinforcing fibers and polymer matrices. The effort results in special materials such as high-modulus or high-strength fibers of stable mechanical properties and polymers of high thermal or chemical resistance. However, new materials with outstanding properties are very expensive. Another way to improve composite performance is advancement in engineered interfaces [1] or, more properly termed, composite interphases [2]. The composite interphase is a 3D region in composite material that can be found between the fiber surface and the matrix. In simple terms, the interphase comprises an interlayer (thin film), which is coated onto reinforcing fiber, and a modified matrix, which is affected by the presence of the coated fiber (Fig. 1). The concept of the interphase was schematically illustrated in Ref. 3.

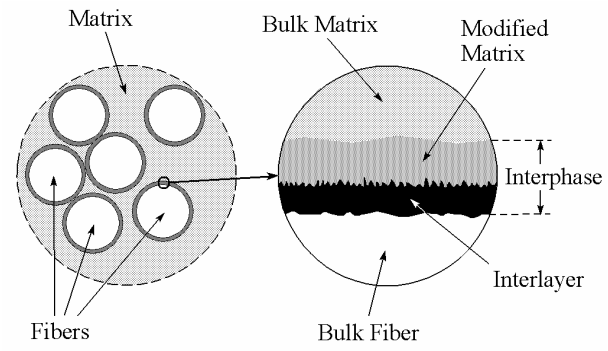


Fig. 1. A schematic illustration of a composite interphase.

The interlayer should improve compatibility and form a strong but tough link between the fiber and the matrix, which are of distinct physical and chemical properties. Theoretical and experimental studies have shown that composite interphases can markedly influence the performance of composites with respect to their strength and toughness [4,5]. The aim of this paper was to highlight plasma polymerization [6-8] as a technology capable of preparing thin films of controlled properties [9], which could improve composite performance markedly via the controlled interphase.

2. Wet chemical process

The performance of fiber-reinforced composites is strongly influenced by the functionality of composite interphases [1]. The world market is dominated by glass reinforcement in unsaturated polyester, which comprises almost 90% of the total market. Approximately 1.8×10^6 t of E-glass fiber is manufactured annually for use in composites and 50% goes into continuous and long-fiber reinforced thermosets [10]. Sizing, i.e. functional coating, is therefore tailored to improve the transfer of stress from the matrix to the fiber reinforcement by enhancing fiber wettability, adhesion, compatibility, etc. Commercially produced sizing is heterogeneous with respect to the thickness and uniformity [11], the molecules of silane coupling agents have a tendency towards self-condensation, forming siloxane oligomers rather than complete bonding with the glass surface [12,13], and the low density of siloxane bonds with the surface decreases if water molecules diffuse to the interface since this type of bond is hydrolytically unstable [14]. Only 10–20% of the total sizing is bonded to the fiber surface and this amount is directly related to the composite interfacial strength [15]. Technological centers in glass companies search for new ways of solving the above problems. One of the alternative technologies is the low-temperature plasma technique.

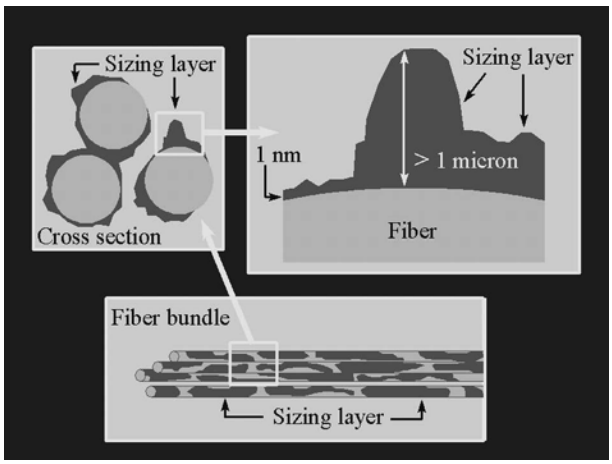


Fig. 2. Scheme of the nonuniform distribution of sizing layers that is characteristic of commercial glass fiber products (adapted from [11]).

3. Plasmachemical processes

Low temperature plasma may be used as a gentle but powerful tool for surface treatment and coating of fibers, which retain their mechanical properties. Plasma surface modification of fibers and its application in FRP has been widely used since the 1980s, see the reviews in Refs. 16 and 17. Plasma treatment (surface etching and/or functionalization) and plasma polymerization (film coating) have remained very popular up to today. Oxygen plasma is often used for surface treatment of carbon [18,19], polyamide [20], polyethylene terephthalate (PET) [21], poly(p-phenylene-2,6-benzo-bisoxazole (PBO, Zylon) [22], poly(p-phenylene terephthalamide) (PPTA, Kevlar) [23], and sisal [24] fibers, carbon nanotubes [24,25], polyamide [26] and carbon [27,28] nanofibers. The oxygen plasma may increase the surface roughness and introduce functional groups, such as –OH, C–O, C=O, and O–C=O, into the surface layer of material, which results in an improvement of wettability. Argon, air, CO_2, H_2O, and NH_3 plasmas may also be used for plasma treatment [19,21,27,29].

4. Plasma polymerization

Most researches employ the plasma-treatment technique as described above to increase the wettability and the roughness of fiber surface, and consequently the fiber/matrix adhesion, which supports composite strength enhancement, but at the expense of composite toughness [17]. An effective solution how to simultaneously improve the composite strength and toughness is the coating technique (plasma polymerization) [5]. Thin polymer films prepared by the plasma-polymerization technique may be formed as homogeneous with respect to thickness, uniformity, composition and structure. Plasma polymerization, as a film-coating technique, offers a greater range of surface modifications for e.g. glass [30-32] and carbon [19,33,34] fibers or silica particles [35].

The composite interface/interphase is specific to each fiber-matrix system [3]. An RF helical coupling pulsed-plasma apparatus [25] can be used for continual or static surface modification (treatment and coating) of fibers. Plasma polymer films of hexamethyldisiloxane (HMDSO), vinyltriethoxysilane (VTES), and tetravinyl-silane (TVS), pure or in a mixture with oxygen gas, were engineered as compatible interlayers for the glass fiber/polyester composites. Thin and ultrathin films were deposited on planar glass, silicon substrates, and glass fiber (GF) bundles to characterize their physical and chemical properties.

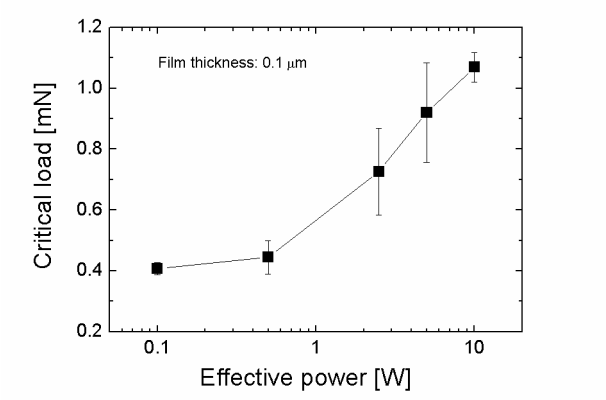


Fig. 3. Adhesion of pp-TVS film on glass substrate.

As an example, we can demonstrate physical and chemical properties of plasma-polymerized tetravinyl-silane (pp-TVS) films. The pp-TVS films with a thickness of 0.1 µm were deposited on planar glass substrates. The adhesion of films was evaluated by scratch test. The test consists of drawing a tip over a film under increasing normal loads. The value of the load at which adhesion failure is detected is known as the critical load. The failure events were examined by atomic force microscopy (AFM). The critical load increased significantly with enhanced power, used for film deposition, as can be seen in Fig. 3. The critical load was almost three times higher for the film deposited at 10 W than that for the film deposited at 0.1 W.

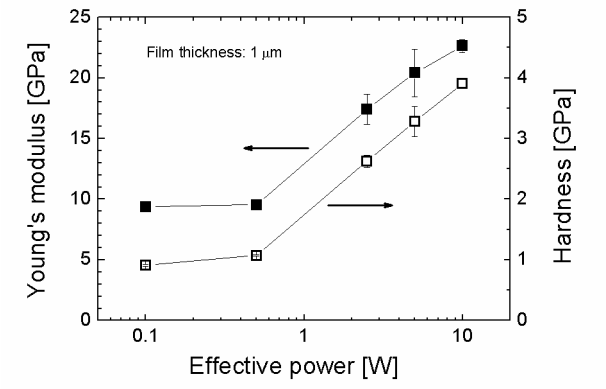


Fig. 4. Young's modulus and hardness of pp-TVS film as a function of the effective power.

Nanoindentation measurements enabled to characterize selected mechanical properties of 1 µm-thick films deposited on silicon wafers (Fig. 4). The Young's modulus (full symbol) increased form 9.4 to 23 GPa with power enhanced by two orders of magnitude (0.1 – 10 W). A similar trend was observed

for hardness and the values increased from 0.9 to 3.9 GPa with enhanced power. The mechanical parameters (Young's modulus and hardness) of pp-TVS films increased with enhanced power due to a higher cross-linking of plasma polymer network [36]. Monomer molecules are more activated and fragmented forming a higher density of free radicals, if the plasma energy (power) increases, and the reactive species result in a highly cross-linked polymer.

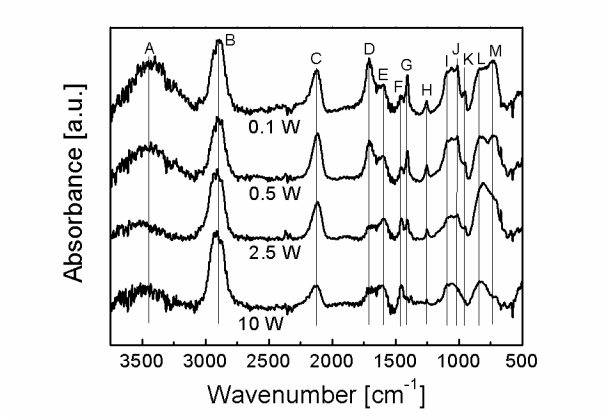


Fig. 5. FTIR spectra corresponding to pp-TVS film deposited at different effective powers.

Typical infrared spectra of pp-TVS films deposited at different powers are given in Fig. 5. The intensity and area of absorption bands A, D, and I, corresponding to species such as OH, C=O, and Si–O–C, respectively, descended with enhanced power and the trend was in good agreement with a descent of oxygen concentration in plasma polymer revealed by Rutherford Backscattering Spectrometry measurements [37]. The SiH (band C), SiC (band M), and CH_x species (band B) in the plasma polymer film were identified as responsible for post-deposition oxidation (ageing) of the deposited material [37]. A decrease of bands C, H, L, and M assigned to species containing silicon atoms was observed as well and the trend corresponded to an increase of C/Si ratio with enhanced power. An occurrence of vinyl groups in plasma polymer was evident from IR spectra corresponding to pp-TVS films deposited at lower power ($\leq$ 2.5 W). The concentration of vinyl groups decreased with enhanced power as a descent of bands E, J, and especially G, K indicated. The vinyl groups are responsible for chemical bonding to polyester resin (matrix) at the matrix/interlayer interface.

The results of the Owens-Wendt-Kaelble geometric mean method are given in Fig. 6, where the total surface free energy and its polar and dispersion components are plotted as a function of the effective power. The total surface free energy (full symbol) increased from 40 mJ m^{-2} up to a saturated value of 49 mJ m^{-2} reached at a power of 5 W. The values of the dispersion component (empty symbol) were responsible for the increase of the surface free energy due to decreased concentration of vinyl groups in plasma polymer with enhanced power. The polar component (half symbol) of value about 4 mJ m^{-2} was approximately independent of the power.

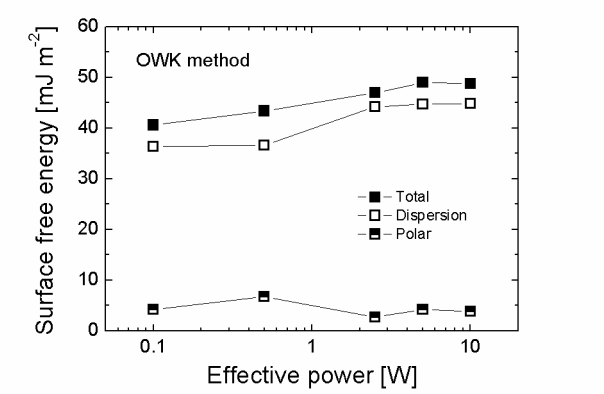


Fig. 6. Surface free energy of pp-TVS film depending on the effective power.

The plasma polymer films were deposited on bundles of unsized glass fibers. Free radicals diffuse into the central part of the bundle and form a thin film even on surface of central fibers during the plasmachemical deposition. However, the deposition rate decreases in radial direction into the fiber bundle due to the shadowing effect of surrounding fibers and thus the film thickness of coating on central fibers is lower with respect to that on surface fibers. Unsized, industrially sized (wet chemical process), and plasma polymer coated glass fibers were embedded into unsaturated polyester resin and cured to form GF/polyester composite.

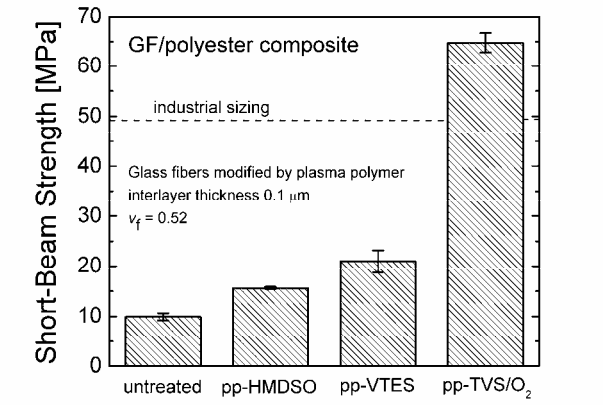


Fig. 7. Short-beam strength of GF/polyester composite for different surface modifications of glass fibers. The volume fraction of fibers was 0.52.

Short-beam composites were evaluated in a three-point bending test according to ASTM D 2344/D 2344M - 00 [38] to compare their performance (Fig. 7). The interlayers of controlled physicochemical properties were tailored using the deposition conditions with regard to the elemental composition, chemical structure, and Young's modulus in order to improve adhesion bonding at the interlayer/glass and polyester/interlayer interfaces and tune the cross-linking of the plasma polymer. The optimized interlayer, using pp-TVS/O_2 film, enabled a 6.5-fold increase of the short-beam strength compared to the untreated fibers. The short-beam strength of GF/polyester composite with the plasma polymer interlayer was 32% higher than that with industrial sizing developed for fiber-reinforced composites with a polyester matrix [39].

The progress in plasmachemical processing of composite reinforcements enabled us to release a new conception of composites without interfaces [9].

5. Composites without interfaces

A region of the modified matrix (spontaneous interphase) could be formed around the fiber if untreated (unsized) fiber is embedded into the polymer matrix and a composite is formed. A simple schema of the elastic modulus profile across such an interphase is shown in Fig. 8(a). The Young's modulus, E, of the fiber often differs from that of the matrix by one order or more, e.g. E_{GF} = 73 GPa for glass fiber and E_{PES} = 4 GPa for polyester matrix. Adhesion bonding between the fiber surface and the modified matrix has to be strong to ensure stress transfer from the matrix to the fiber. We can then expect the modulus of the modified matrix affected by the fiber surface to be higher than that of the bulk matrix. Regardless of this, the fiber/matrix interface is very sharp and the modulus change very high, resulting in high stress concentration under both mechanical and thermal loading. Formation of a strong bond at the interface is possible using a gentle plasma treatment of the fiber surface. Thus the enhanced surface roughness and wettability together with new functional groups result in high interfacial shear strength, while the mechanical properties of the fiber are retained. However, an increase in the shear strength is inevitably accompanied by a loss in the impact fracture toughness, with the result that the composite material is too brittle to be applicable. It is very difficult to control interfacial bonding with respect to bond strength and/or bond density by technology.

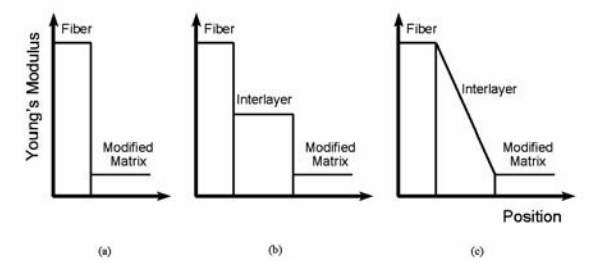


Fig. 8. Schematic illustration of the elastic modulus profile across the interphase: (a) without interlayer, (b) homogeneous interlayer, (c) gradual interlayer.

The fiber-coating method for toughening composites seems to be one of the most effective methods for achieving simultaneous high strength and high toughness when an appropriate interlayer material is chosen [1,3]. Thus, an interlayer is inserted between the fiber and the matrix (Fig. 8(b)), and the film must be strongly bonded at both interfaces to form a strong but tough link between the fiber and the matrix. It is evident that the specific composite system with an interlayer material of a modulus comparable to that of the fiber or matrix results in similar disadvantages to the composite system without an interlayer. Therefore, we can expect that the interlayer modulus should be lower than that of the fiber. Some theoretical and experimental studies have shown that the coated material should be ductile or flexible [5]. Even though we do not know fully in advance which coating material is most suitable for a specific composite system; the variables that affect the properties of FRP have been identified as follows: interlayer modulus, interlayer thickness, matrix modulus, coating material (composition) and interaction at the interfaces [5].

In general, utilization of an interlayer with the modulus about that of the matrix or even lower results in problems with a strong mismatch at the fiber/interlayer interface. A simple gradual interlayer could suit better, see Fig. 8(c). In that case, there is no mismatch at either interface and the interlayer material is not so stiff. A more sophisticated modulus profile can be suggested to ensure a strong but tough composite using a functionally gradual nanostructured interlayer, see Fig. 9 (solid line). Preparation of an interlayer with chemical and physical properties continuously varying from those of the fiber to those of the matrix without any interface could be an ambitious aim. Such an interlayer could eliminate problems with a modified matrix, whose properties are controlled only with difficulty.

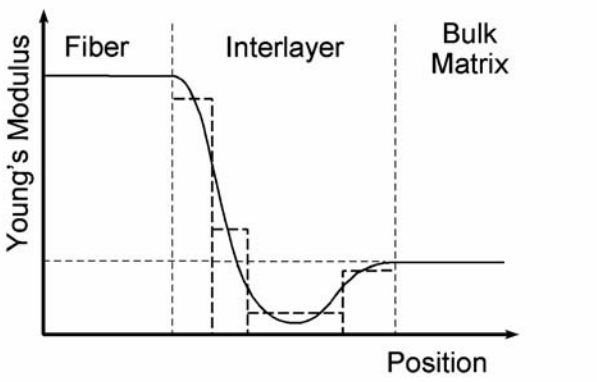


Fig. 9. Schematic illustration of the elastic modulus profile across the interphase with a functionally gradual nanostructured interlayer prepared layer by layer (dashed line) or in one deposition (solid line).

Structured films (multilayers) can be prepared using the "bottom-up" method. Thus a nanostructured interlayer can be prepared layer by layer (Fig. 9, dashed line), where the film thickness of an individual layer could be only a few tens of nanometers, and the individual layers must be bonded to each other using strong chemical bonds. We could construct a functionally gradual nanostructured interlayer without interfaces if a coating technology were available that could prepare film of continuously varying properties in one deposition. Such a nanotechnology could be valuable for the formation of the controlled interphase. Plasma polymerization has technological potential to fabricate nanostructured thin films of controlled properties in one deposition.

Acknowledgements: This work was supported in part by the Czech Science Foundation, grants no. P106/11/0738 and P205/12/J058, the Czech Ministry of Education, grant no. ME09061 and the Technology Agency of the Czech Republic, grant no. TA01010796.

References

1. J.-K. Kim and Y.-W. Mai, *Engineered Interfaces in Fiber Reinforced Composites.* Elsevier, Amsterdam (1998).
2. L.T. Drzal, M.J. Rich and P.F. Lloyd, *J. Adhesion* 16 (1983) 1.
3. J.-K. Kim and Y.-W. Mai, *Compos. Sci. Technol.* 41 (1991) 333.
4. L. J. Broutman and B. D. Agarwal, *Polym. Eng. Sci.* 14 (1974) 581.
5. M. Labronici and H. Ishida, *Compos. Interfaces* 2 (1994) 199.
6. H. Yasuda, *Plasma Polymerization*. Academic Press, Orlando (1985).
7. H. Biederman and Y. Osada, *Plasma Polymerization Processes*. Elsevier, New York (1992).
8. N. Inagaki, *Plasma Surface Modification and Plasma Polymerization*. Technomic Publ., Lancaster (1996).
9. V. Cech, in: S. Zhang (Ed.), *Nanostructured Thin Films and Coatings*, Volume 1, CRC Press, New York, 2010, p. 481.
10. M.G. Bader, The composite market. in: A. Kelly, C. Zweben (Eds.) *Comprehensive Composite Materials.* Amsterdam: Elsevier, 2000, Volume 6.
11. D.W. Dwight, Glass fiber reinforcements. in: A. Kelly, C. Zweben (Eds.) *Comprehensive Composite Materials.* Amsterdam: Elsevier, 2000, Volume 1.
12. G.M. Nishioka, *J. Non-Cryst. Solids* 120 (1990) 102.
13. W. Wang, A.T. Dibenedetto, *J. Adhesion* 68 (1998) 183..
14. E.P. Plueddemann, *Silane Coupling Agents.* New York: Plenum Press, 1991.
15. J.L.Thomason, *Composites* 26 (1995) 487.
16. R. Li, L. Ye and Y.-W. Mai, *Composites Part A* 28 (1997) 73.
17. V. Cech, New progress in composite interphases: a use of plasma technologies, in: *Proceedings of FRC 2000*, Newcastle upon Tyne 2000, pp.246.
18. S. J. Park and B. J. Kim, *Mater. Sci. Eng. A* 408 (2005) 269.
19. H. M. Kang, N. I. Kim and T. H. Yoon, *J. Adhes. Sci. Technol.* 16 (2002) 1809.
20. J. Yip, K. Chan, K. M. Sin and K. S. Lau, *Polym. Int.* 53 (2004) 634.
21. M. O. H. Cioffi, H. J. C. Voorwald, L. R. O. Hein and L. Ambrosio, *Composites Part A* 36 (2005) 615.
22. J. M. Park, D. S. Kim and S. R. Kim, *J. Colloid Inter. Sci.* 264 (2003) 431.
23. E. Couto, I. H. Tan, N. Demarquette, J. C. Caraschi and A. Leao, *Polym. Eng. Sci.* 42 (2002) 790.
24. Y. S. Song and J. R. Youn, *Polymer* 47 (2006) 1741.
25. V. Chirila, G. Marginean and W. Brandl, *Surf. Coat. Technol.* 200 (2005) 548.
26. Q. F. Wei, W. D. Gao, D. Y. Hou and X. Q. Wang, *Appl. Surf. Sci.* 245 (2005) 16.
27. V. Bruser, M. Heintze, W. Brandl, G. Marginean and H. Bubert, *Diamond Relat. Mater.* 13 (2004) 1177.
28. W. Brandl, G. Marginean, V. Chirila and W. Warschewski, *Carbon* 42, 5 (2004).
29. X. W. Yuan, K. Jayaraman and D. Bhattacharyya, *J. Adhes. Sci. Technol.* 16 (2002) 703.
30. F. M. Zhao, S. A. Hayes, E. A. Patteson and F. R. Jones, *Composites Part A* 37 (2006) 216.
31. V. Cech, R. Prikryl, R. Balkova, J. Vanek and A. Grycova, *J. Adhes. Sci. Technol.* 17 (2003) 1299.
32. D. J. Marks and F. R. Jones, *Composites Part A* 33 (2002) 1292.
33. A. Bismarck, M. Pfaffernoschke, J. Springer and E. Schulz, *J. Therm. Comp. Mater.* 18 (2005) 307.
34. C. Auclair-Daigle, M. N. Bureau, J. G. Legoux and L. H. Yahia, *J. Biomed. Mater. Res. Part A* 73 (2005) 398.
35. N. I. Kim, H. M. Kang and T. H. Yoon, *J. Adhes. Sci. Technol.* 18 (2004) 1325.
36. V. Cech, J. Vanek, A.A. Goruppa, F.R. Jones, *J. Mater. Sci.* 40 (2005) 5099.
37. J. Studynka, V. Cech, *Thin Solid Films* 519 (2011) 2168.
38. ASTM D2344. *Standard Test Method for Short-Beam Strength of Polymer Matrix Composite Materials and Their Laminates.* American Society for Testing and Materials, West Conshohocken (2001).
39. V. Cech, *Compos. Interfaces* 14 (2007) 321.

Study the effect of the inductive to capacitive transition on propanethiol plasma polymers properties: correlation between film and plasma chemistry

Damien Thiry[1], Nikolay Britun[1], Stephanos Konstantinidis[1],
Jean-Pierre Dauchot[1], Maxime Guillaume[2], Jérôme Cornil[2] and Rony Snyders[1,3]

1) *Chimie des Interactions Plasma Surface (ChIPS), CIRMAP, Université de Mons, 23 Place du Parc, B-7000 Mons, Belgium*
2) *Service de Chimie des Matériaux Nouveaux (CMN), CIRMAP, Université de Mons, 23 Place du Parc,B-7000 Mons, Belgium*
3) *Materia Nova Research Center, Parc Initialis, B-7000 Mons, Belgium*

Inductively coupled plasma (ICP) discharges using a coil as an electrode, which normally exhibit two modes of operation, are commonly used for plasma polymerization.[1-3] At low power, these discharges are characterized by rather low electron density and faint light emission which are common features of the capacitive mode (E). In this case, the discharge is maintained by the electrostatic field developed between the coil extremities. Increasing the power up to a transition value ($P_{tr.}$) results in a shift to the inductive mode (H). In this regime, the plasma is generated by the induced electrical field produced by the oscillating magnetic field as RF current is flowing through the coil. This mode requires sufficiently high electron densities to support the induced currents in the discharge. In H mode, the plasma has about one order of magnitude higher electron density and much stronger light emission. It was shown that these plasma features change abruptly for a power value equal to $P_{tr.}$.[4,5]

The E-H transition was the topic of both theoretical and experimental studies related to Ar, N_2, Ar/ N_2, O_2, Ar/ O_2, H_2 and Ar/H_2 plasmas used mainly for materials etching required e.g. in semiconductor processing, or in biological sterelization.[6,7] Nevertheless, it has received little attention in the plasma polymer field. However, we demonstrated recently the importance of the E-H transition on propanethiol plasma polymers films (Pr-PPF) [8] which could be used as a support for DNA immobilization or gold nanoparticles due to the great affinity between thiol and gold. [9,10] It was shown that the chemical composition of the layers and the chemical stability of the coatings are strongly affected by the mode operation of the coil.

Due to the different chemical properties observed for layers synthesized in E and H mode, one could expect major changes on the plasma chemistry and hence in the growth mechanism involved in each mode. Therefore, in this work, with the aim to gain more understanding on the effect of the E-H transition on the plasma chemistry, mass spectrometry measurements in RGA (“Residual Gas Analysis”) mode were performed.

These data are correlated with the chemical composition of the layers evaluated by *in-situ* and *ex-situ* XPS measurements. The E-H transition as a function of power (P_{RF}) and pressure (p) was observed by using optical emission spectroscopy (OES).[6] The evolution of the deposition rate (R_D) is also monitored using mechanical profilometry since it provides information on the growth mechanism of the layer. Moreover, as a theoretical support to our understanding of the mass spectrometry data, DFT ("Density Functionnal Theory") calculations were performed. Based on this approach, different fragmentation pathways in the plasma have been identified depending on the operation mode of the discharge.

The E-H transition was detected by measuring the mean intensity of the acquired emission spectra. For $P_{RF} = P_{tr.}$, the mean intensity increases markedly and is attributed to the E-H transition (Figure 1 (a)). The $P_{tr.}$value increases as a function of p which is in good agreement with literature data for molecular gas like H_2, O_2 and N_2.[11]Actually, for the discharge to shift from E to H mode, a minimal electron density is required to sustain the induced electrical field. While increasing p, electrons loss more energy through collisional processes including dissociation reactions and rotational/vibrational/electronic excitations. Therefore, a higher power has to be dissipated into the discharge to generate enough ions-electrons pairs allowing the discharge to shift from E to H mode.

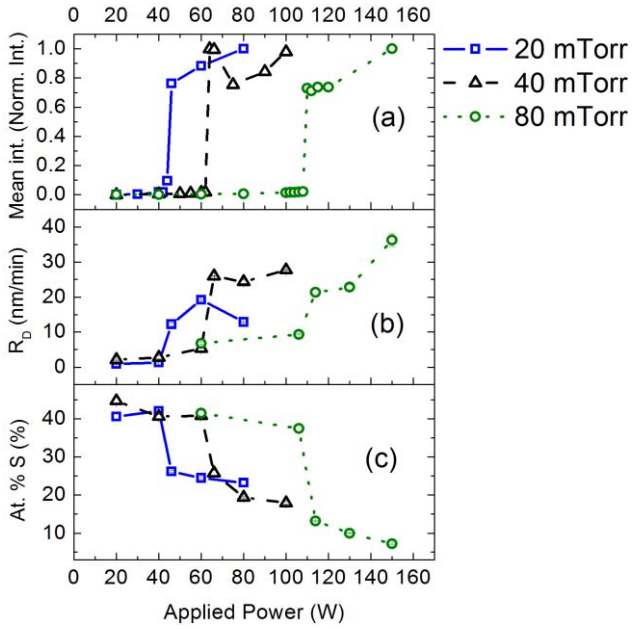


Figure 1 : Evolution of the mean intensity (a), the deposition rate (b) and the atomic sulfur content (c) as a function of the P_{RF} for a p of 20, 40 and 80 mTorr.

Concerning the evolution of R_D for the three p considered in this work, a transition from low to high values appears for $P_{RF} = P_{tr.}$ (Figure 1(b)). That could be explained by the large increase in the concentration of film forming species resulting from the higher number of fragmentations reaction as the electron density in the H mode is higher.

For each p, the evolution of the atomic sulfur content (at.%S) also reveals a strong discontinuity for $P_{RF} = P_{tr.}$ namely a significant lowering (by 40% to 75%) when transiting from the E to the H mode (Figure 1 (c)). This phenomenon could be attributed to the extended fragmentation of the precursor in the H mode which would leads to the loss of S-based fragments by pumping as it is often observed in plasma polymerization.[2]

Moreover, surprisingly, in the E mode, the at.%S is found to be much higher (~40%) than in the precursor (25%). This is quite unusual since most of the time, the plasma polymerization process leads to the loss of functionalities due to fragmentation of the precursor and subsequent pumping of stable molecules.[2] We attribute this observation to the presence, in the plasma polymer network, of unbounded stable molecules presenting a high S/C ratio (e.g H_2S, CS_2). This phenomenon is not observed for films prepared in the H mode probably because, in that case, the energy brought to the film by ions and photons is much

higher and lead to the desorption of the trapped sulfur based molecules. Furthermore, the energy of ions and UV photons is high enough to break the organic chemical bonds at the plasma/growing film interface. That could also result in a higher release of the sulfur-containing molecules from the growing film which would additionally decrease the at.%S.

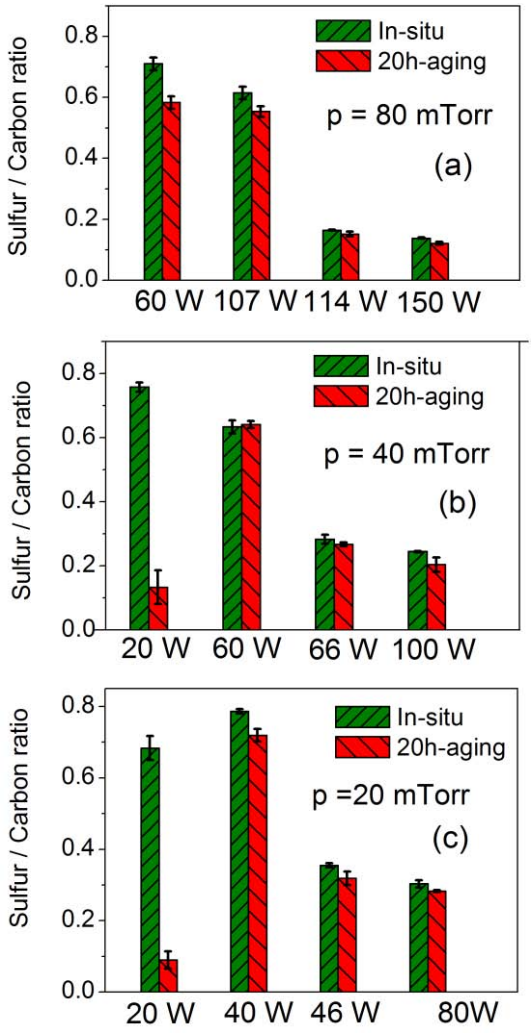


Figure 2 : The evolution of the S/C ratio measured by XPS (i) *in-situ* and (ii) after aging in the air during 20h as a function of P_{RF} for the films synthesized at a p of 80mTorr (a), 40mTorr (b) and 20 mTorr (c).

Based on these observations and in order to study the chemical stability of the coatings, the S/C ratio of E- and H- mode prepared films were measured by XPS after 20h aging in air, and compared with the initial S/C values measured *in-situ*. The data indicate, whatever the p and for the lower P_{RF} used in the E mode, a large decrease of the S/C ratio likely due to the release of the trapped sulfur-molecules in the air supporting our previous explanation. Still in E mode but close to the transition, the behavior is different with the disappearance of the aging effect and as a consequence, a high sulfur content in the films even after aging. This could be explained by the increase of the cross-linking density with P_{RF} at a fixed p as previously reported for allylamine plasma polymers[3]. In H mode, whatever the P_{RF}, the Pr-PPF present a lower at.%S which is stable under aging suggesting that in this case, all sulfur atoms are covalently bonded to the film.

Aiming to identify the trapped sulfur molecules and to gain more understanding about the effect of the E-H transition on the plasma chemistry, mass spectrometry measurements in RGA mode were performed (Data not shown). In E mode, H_2S molecules are detected in a large amount in the mass spectra. Being stable, these molecules do not take part to the growth of the film but could be trapped after adsorption explaining the extra sulfur content. Based on DFT calculations, the formation of these molecules is explained trough (i) rearrangement reaction of the precursor induced by electron impact and (ii) an exothermic addition reaction between the precursor and hydrogen atom.

By comparing the mass spectra from E to H mode, the main modifications consist in (i) the complete disappearance of the precursor signal in H mode due to the strong fragmentation and (ii) the important production of CS_2 molecules. In addition to reactions at the growing film interface involving sulfur species, gas phase reactions, supported by DFT calculations were also considered to explain the important presence of these molecules. From theoretical data, it was shown that different reactions pathways leading to the formation of the CS_2

molecules are highly exothermic. At the same time, the concentration of CS_2 in the gas as a function of the process parameters was correlated to the at.%S measured in the synthesized layers. Higher is the CS_2 proportion in the plasma, lower is the at.%S in the films.

The whole set of our data clearly demonstrate that both plasma and film chemistries are strongly influenced by the plasma mode when using an ICP coil. All our findings show that the E-H transition plays a key role defining the growth mechanism of sulfur-based plasma polymers using ICP discharges.

References

1. R. Jafari, M. Tatoulian, and F. Arefi-Khonsari, Reactive & Functional Polymers **71**, 520 (2011).
2. L. Denis, F. Renaux, D. Cossement, C. Bittencourt, N. Tuccitto, A. Licciardello, M. Hecq, and R. Snyders, Plasma Process. Polym. **8**, 127 (2011).
3. L. Denis, D. Thiry, D. Cossement, P. Gerbaux, F. Brusciotti, I. Van De Keere, V. Goossens, H. Terryn, M. Hecq, and R. Snyders, Prog. Org. Coat. **70**, 134 (2011).
4. M. A. Lieberman and A. J. Lichtenberg, *Principles of Plasma Discharge and Materials Processing* (Wiley, New York, Second Edition, 2005) chapter 12.
5. M.M Turner, and M.A Lieberman, Plasma Sources Sci. Technol. **8**, 313 (1999).
6. K. N. Ostrikov, S. Xu, and A.B.M Shafiul Azam, J. Vac. Sci. Tech. A. **20**, 251 (2002).
7. A.A Bol'shakov, B.A Cruden, R. Mogul, M.V.V.S. Rao, S. P. Sharma, B. N. Khare, and M.Meyyappan, AIAA Journal **42**, 823 (2004)
8. D. Thiry, N. Britun, S. Konstantinidis, J.P Dauchot, L. Denis, and R. Snyders, Appl. Phys. Lett. **100**, 071604 (2012).
9. W. C. E. Schofield, J. McGettrick, T. J. Bradley, J. P. S. Badyal, and S. Przyborski, J. Am.Chem.Soc. **7**, 2280 (2006).
10. V. Švorčík, A. Chaloupka, K. Záruba, V. Král, O.Bláhová, A.Macková, and V. Hnatowicz, Nuclear Instruments and Methods in Physics Research Section B **267**, 2484 (2009).
11. Y. W. Lee, H.L. Lee, and T.H. Chung, J. Appl. Phys. **109**, 113302 (2011).

Mechanical properties of plasma polymer films controlled by RF power

Erik Palesch, Sona Kontarova, Vladimir Cech
Institute of Materials Chemistry, Brno University of Technology
Purkynova 118, CZ-61200 Brno, Czech Republic

Abstract
This study deals with plasma polymer films deposited on silicon substrates using tetravinylsilane monomer. The deposition technique was plasma-enhanced chemical vapour deposition. Nanoindentation was used as a method to investigate mechanical properties of samples prepared at different RF powers. The Young's modulus and hardness of thin films were estimated from load-displacement curves. The nanoscratch test was employed to determine the critical normal load needed for film delamination, as a parameter describing adhesion to the substrate. AFM images of scratches were carried out to correlate the data with nature and shape of scratches.

Keywords
Thin films, plasma polymer, mechanical properties, nanoindentation, nanoscratch test

1. Introduction
Thin polymer films prepared by plasma-enhanced chemical vapour deposition (PECVD) using organosilicon precursors are quite popular materials in many technological areas nowadays. Such films has found their use as corrosion protective layers [1], gas barrier coatings [2], low-k dielectrics [3], and as functional interlayers in glass fiber reinforced polymer composites [4]. In many of their applications, mechanical properties of the films are essential. They can be effectively controlled by choosing appropriate fabrication variables, such as power, monomer flow rate or pressure, during deposition process [4].

Nanoindentation proved itself to be one of the most important methods when characterizing mechanical properties of materials in form of thin films [5]. One cycle of nanoindentation measurement consists of loading segment, when indenter is sinking into the sample causing both elastic and plastic deformation, and unloading segment, when mostly recovery of elastic deformation occurs. In cyclic nanoindentation, the sample is reloaded immediately to higher depths/loads than in previous loading cycle. The reloading path should not overlap with the unloading path of the previous loading cycle, resulting in hysteresis loops. The cyclic nanoindentation is a rapid way to construct depth dependencies of mechanical parameters [6].

The nanoscratch test is extended feature of the nanoindentation device. Scratch is done by moving the indenter laterally while continuously penetrating into the sample. By recording the lateral force, normal force and normal displacement signal, one is able to investigate adhesive properties of the thin film.

In this study, we examined mechanical properties of single layer a-SiC:H films deposited from tetravinylsilane on silicon substrates by PE-CVD at different powers. Cyclic nanoindentation, nanoscratch test and atomic force microscopy (AFM) were methods used for determining the Young's modulus, E, hardness, H, and critical normal load for delamination, F_c.

2. Experimental

2.1 Sample preparation
Thin a-SiC:H films characterized in this work were prepared in plasma reactor working with capacitively-coupled plasma designed for deposition onto flat substrates. The monomer used was tetravinylsilane (TVS, Sigma-Aldrich, 97 %). The plasma polymer was deposited on double-sided polished silicon substrates with dimensions 10 × 10 × 0.6 mm (ON SEMICONDUCTOR CZECH REPUBLIC s.r.o). Before deposition, substrates were pre-activated with help of Ar plasma (5 W, 10 sccm, 5 Pa). The deposition of plasma-polymerized (pp) TVS films was performed at powers in range 10 - 70 W, system pressure was 3 Pa, and monomer flow rate was 3.8 sccm. The reaction chamber was flushed with argon gas for 1 hour after plasma polymerisation. Samples were held inside reactor till next day to prevent reactions with air and so to prevent thin film modification. The plasma reactor was equipped with *in situ* spectroscopic ellipsometer UVISEL (Jobin-Yvon), thus we were able to measure the thickness of films. Samples intended for indentation testing were deposited with a thickness of 1 μm to prevent substrate influence. Samples used for scratch testing had a thickness of about 100 nm.

2.2 Nanoindentation

Mechanical properties of samples were investigated using nanoindentation head TriboScope TS-70 (Hysitron, Minneapolis, USA) attached to Ntegra Prima scanning probe microscope (NT-MDT, Zelenograd, Russia). The head consists of the three-plate capacitive transducer capable of moving the indenter in both vertical and horizontal directions with high accuracy and sensitivity. The force and displacement resolution of this device are <1 nN and 0.0004 nm, respectively. Three-sided pyramidal Berkovich type indenter with curvature radius of 150 nm was used. Hardness and Young's modulus of thin films were evaluated from load-displacement curves of cyclic nanoindentation measurement using the widely known Oliver Pharr method [5].

2.3 Nanoscratch test

Nanoscratch tests were performed with the same equipment as the nanoindentation tests. We looked for the critical normal load for delamination as an indication of thin film failure. It is found in the normal force vs lateral force plot as the point where lateral force response abruptly changes for the first time. Material of thin film is removed from the substrate. This event could happen several times after initial delamination as the normal force is increasing during progressive load scratch test.

2.4 Atomic force microscopy (AFM)

For surface analysis of scratches, a scanning probe microscope Ntegra Prima (NT-MDT) was used in scanning-by-sample configuration. Semi-contact mode of atomic force microscopy measurements was employed to acquire topography maps of scratched areas. Also, amplitude images (feedback error signal) were recorded together with topography images to better observe outlines of scratches and smooth surface features. A cantilever NSG10 with a resonance frequency of 190 - 325 kHz was used for measurements. The curvature radius of tip apex is approx. 10 nm. We investigated scratch images for thin film failure points and they were used for comparison with the data obtained by nanoscratch test.

3. Results and Discussion

3.1 Nanoindentation measurements

Five samples were investigated to characterize their mechanical properties. The films were prepared at powers 10, 20, 25, 50 and 70 W. Deposited films with a thickness of approximately 1 μm were homogeneous, isotropic materials, according to ellipsometric spectroscopy, X-Ray photoelectron spectroscopy and Rutherford backscattering spectroscopy [7, 8]. The depth profiles of mechanical properties, the Young's modulus and hardness (Fig. 1), were constructed for all the samples using cyclic nanoindentation. Each cyclic nanoindentation consisted of 25 cycles. Measurements were performed four times for each sample, thus we were able to evaluate average value of the Young's modulus and hardness, together with the standard deviation.

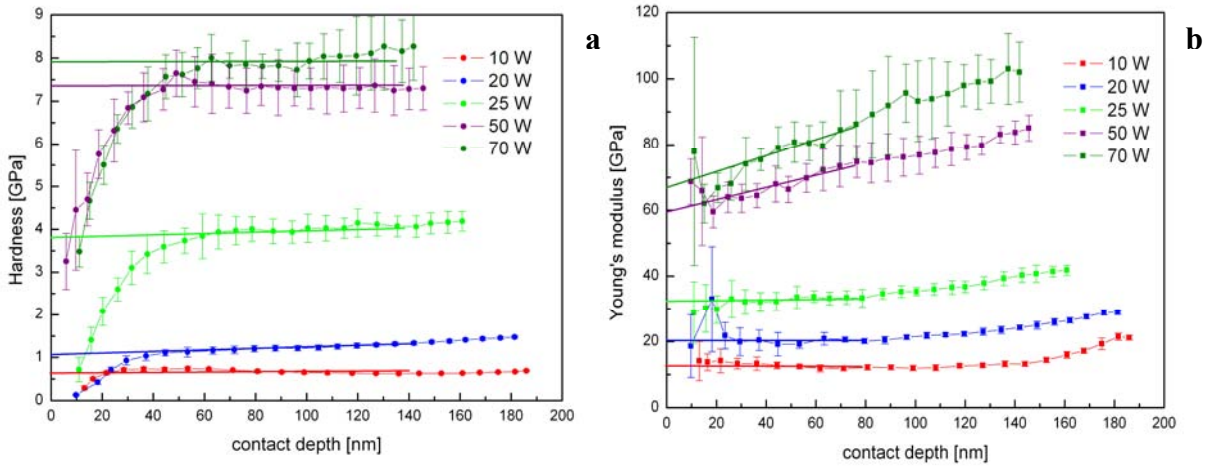


Fig. 1: Depth profiles of hardness (a) and Young's modulus (b) for samples prepared at different power

Hardness values are quite stable for all depths greater than 50 nm. For lower depths measured values of hardness are not reliable because unlike modulus, hardness is not defined when creating tip area calibration function. It is computed value dependent on the contact area of the probe, which in case of very low contact depths doesn't have perfect pyramidal shape for Berkovich indenter. Thus for hardness, the contact area calibration is not sufficient for low penetration depths.

There is an increasing trend in modulus profiles, when the contact depths are significantly greater than 100 nm. In case of stiffer films (50 W, 70 W) the profiles increase from the very beginning. The reason for this behaviour is the stiff silicon substrate (E = 170 GPa, H = 11 GPa), which affects the measurements. The 10% rule says that modulus values are not significantly influenced by the substrate in depths till 10% of film thickness. However, as observed in one of our previous studies [9], this rule is not valid for a-SiC:H films prepared at higher powers, like in this case of 50 or 70 W. We evaluated the Young's modulus and hardness by extrapolating linear part of each profile to zero contact depth (Fig. 1). As it is evident from the graphs, both the Young's modulus and hardness increased with enhanced power. The trend is the same for modulus as for hardness (Fig. 2). Enhancement of power for plasma deposition causes more intense fragmentation of monomer molecules (tetravinylsilane in this case) and it will increase the cross-linking of resulting polymer. The more cross-linked polymer, the stiffer it will be, what corresponds to higher values of Young's modulus and hardness.

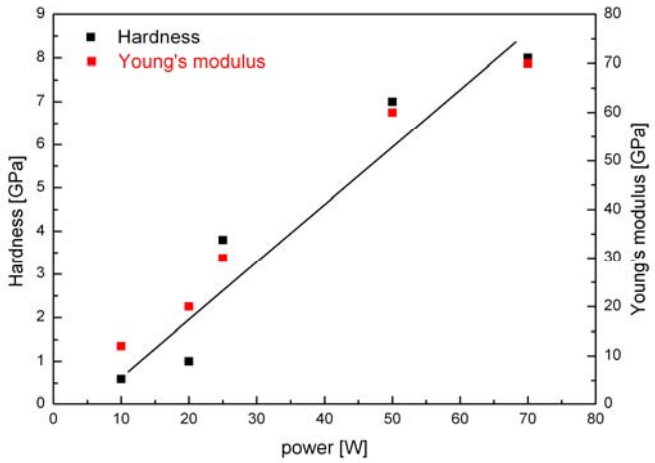


Fig. 2: Effect of power on hardness and Young's modulus

3.2 Nanoscratch test

For nanoscratch test, four samples were prepared at powers 10, 25, 50 and 70 W, all with thickness approx. 100 nm. Such a thickness enabled us to utilize a maximum load of 10 mN.

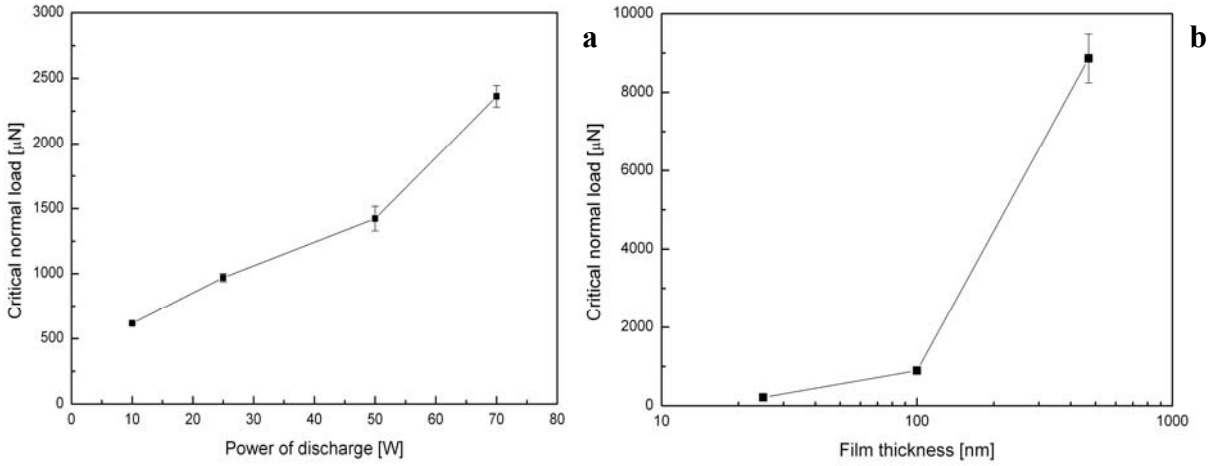


Fig. 3: (a) plot of critical normal load for delamination vs power of discharge, (b) effect of film thickness on critical normal load.

Every scratch was 10 μm long and it took 30 seconds to perform scratch. A peak normal load for each sample was chosen to initiate delamination approximately in the half of the scratch path. Results of samples prepared at different powers are graphically presented in Fig. 3a. We evaluated the critical normal load from lateral force vs normal force plots constructed from acquired data. Each sample was measured five times, so we obtained averaged values together with standard deviation (Fig. 3a). Like in the case of the Young's modulus and hardness, the critical normal load showed increasing trend when increasing the power. The trend of this dependence is quite linear in the range of powers we used for deposition. The critical normal load is the parameter characterizing adhesive properties of the film. The nanoscratch data were correlated with AFM images of scratch path. For this purpose, we used semicontact mode of atomic force microscope to obtain topography images of scratches, like that showed in Fig. 4, which is a representative scratch made in sample prepared at 70 W. Scratches in other samples had similar appearance. The point of film failure is obvious from AFM image and it correlates well with an abrupt change of the lateral force. The critical normal load for delamination was rising with enhanced power.

Besides this experiment, three samples with increasing thickness of 25, 100 and 470 nm were investigated for the critical normal load. All these samples were prepared at power of 10 W. Figure 3b shows that there is a

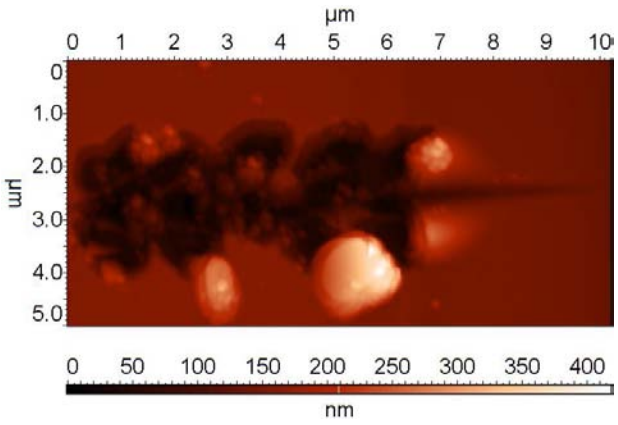


Fig. 4: AFM topography image of scratch in 70 W sample

significant increase of the critical load with enlarged thickness of the film. Such behaviour is expected as long as the residual stress in the film is not increased with the film thickness [10]. Increasing trend was also found out in the study of amorphous carbon coatings [11].

4. Conclusions

Pp-TVS films with the thicknesses from 25 nm to 1 µm were deposited by PECVD working in continual regime. The Young's modulus and hardness were determined using cyclic nanoindentation. For samples prepared at powers in range 10 – 70 W, we found out an influence of the power on measured mechanical properties, resulting in an increase of Young's modulus and hardness with enhanced power due to an increased polymer cross-linking. The same increasing trend was found for the critical normal load, parameter characterizing adhesion of the film to the substrate, evaluated from nanoscratch tests performed on samples with a thickness of 100 nm and prepared at above mentioned range of powers. The thickness dependence of critical normal load was examined, showing an increased F_c value for a thicker film.

Acknowledgements: This work was supported in part by the Czech Science Foundation, grants no. P106/11/0738, P205/12/J058 and 104/09/H080, the Czech Ministry of Education, grant no. ME09061 and the Technology Agency of the Czech Republic, grant no. TA01010796.

References

[1] C. Petit-Etienne, M. Tatoulian, I. Mabille, E. Sutter, F. Arefi-Khonosari, Plasma Process. Polym. 4 (2007) S562.
[2] A. Francescangeli, F. Palumbo, R. d'Agostino, C. Defranoux, Plasma Process. Polym. 6 (2009) 132.
[3] A.M. Coclite, A. Milella, F. Palumbo, F. Fracassi, R. d'Agostino, Plasma Process. Polym. 6 (2009) 512.
[4] V. Cech, in: S. Zhang (Ed.), Nanostructured Thin Films and Coatings, Volume 1, CRC Press, New York, 2010, pp. 481.
[5] W.C. Oliver, G.M. Pharr, J. Mater. Res. 7 (1992) 1564.
[6] R. Trivedi, V. Cech, Surf. Coat. Technol. 205 (2010) S286.
[7] V. Cech, J. Studynka, B. Cechalova, J. Mistrik, J. Zemek, Surf. Coat. Technol. 202 (2008) 5572.
[8] V. Cech, J. Zemek, V. Perina, Plasma Process. Polym. 5 (2008) 745.
[9] R. Trivedi, L. Hoferek, V. Cech, Surf. Coat. Technol. 205 (2011) S470.
[10] P.J. Burnett, D.S. Rickerby, Thin Solid Films 157 (1988) 233.
[11] B.K. Gupta, B. Bhushan, Thin Solid Films 270 (1995) 391.

Plasma deposition of hydrophobic coatings on structured surfaces for condensation and heat transfer applications

D. Gloess[1], P. Frach[1], M.Maicu[1], E. Holst[2], R. Schmittgens[2], G. Gerlach[2], C.H. Lu[4], T. Roch[3], M. Bieda[3], A. Lasagni[3], M. Beckmann[4]

[1] Fraunhofer-Institut für Elektronenstrahl und Plasmatechnik (FEP),Winterbergstraße 28, 01277 Dresden, Germany

[2] Technische Universität Dresden, Institut für Festkörperelektronik (IFE), 01062 Dresden, Germany

[3] Fraunhofer-Institut für Werkstoff und Strahltechnik (IWS),Winterbergstraße 28, 01277 Dresden, Germany

[4] Technische Universität Dresden, Institut für Energietechnik (IET), 01062 Dresden, Germany

Keywords:

condensation, plasma deposition, direct laser interference patterning, hydrophobic coating

1. Introduction

The control of vapor condensation processes by suitably prepared surfaces is a prominent research area with important applications in the industry. For example, it is well known that the efficiency of condensation heat exchangers can be significantly increased when the vapor condenses to form droplets on the surface, instead of a closed film which does not wet the surface [1, 2]. In the present work, hydrophobic thin films are deposited via plasma CVD processes on metallic surfaces to investigate the condensation of water vapor on these surfaces. The drop-wise condensation on the coated surfaces is analyzed by optical microscopy and the effect on the heat transfer is measured by heat flux measurements.

In order to show the potential of the deposition process for industrial applications and to investigate the effect of drop-wise condensation on heat transfer, copper (Cu) substrates were coated with a plasma polymer film using an organosilicon monomer (Hexamethyldisiloxane, HMDSO) as a precursor. In addition, the effect of surface roughness on the drop-wise condensation is presented because the static contact angle of water on hydrophobic surfaces depends strongly on surface topography.

2. Methodology, Results and Discussion

a) Plasma polymerization by PECVD

The plasma polymerization process is schematically shown in Fig.1. The PECVD unit consists of a RF capacitively coupled discharge, fed by a 60 MHz generator [3]. Beside the monomer HDMSO, Argon was used as inert gas. In the plasma region the monomer precursor is transformed into reactive species which polymerize as a thin film on the substrate. The film thickness was varied between 10 and 100 nm by adjusting pulse and deposition time.

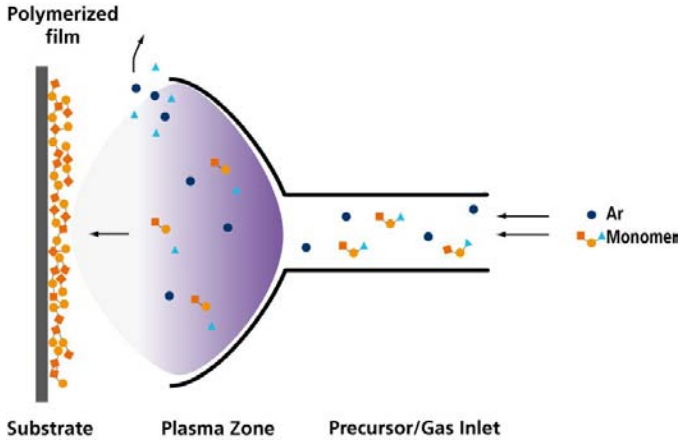


Fig.1. Scheme of the PECVD process for plasma polymerization.

b) Surface structuring by Direct Laser Interference Patterning (DLIP)

Patterning of surfaces and controlling the surface energy can be used to further enhance the efficiency of condensation heat exchangers, e.g. by defining droplet growth sites on the surface or by directing the drop movement. Direct Laser Interference Patterning (DLIP) is presented as an efficient structuring method for heat exchanger surfaces. Surface geometries for enhanced droplet removal are presented and the effect of the drop-wise condensation process is demonstrated.

In order to fabricate the structures shown in Fig. 2, a q-switched Nd-YAG-Laser (pulse width: 10 ns, pulse repetition rate: 10 Hz) at 355 nm wavelength was used. The primary beam was split into two laser beams, which were then recombined to interfere on the substrate surface (Fig. 3). The pitch P is determined by the angle θ between the two beams and the laser wavelength λ:

$$P = \frac{\lambda}{2\sin\theta}.$$

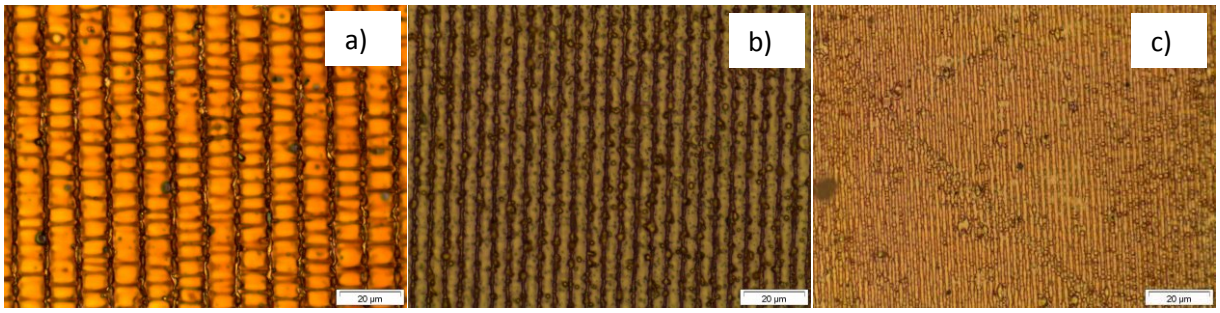


Fig.2. Structured copper surfaces with different pitches: a) 10 µm, b) 5 µm, and c) 2 µm.

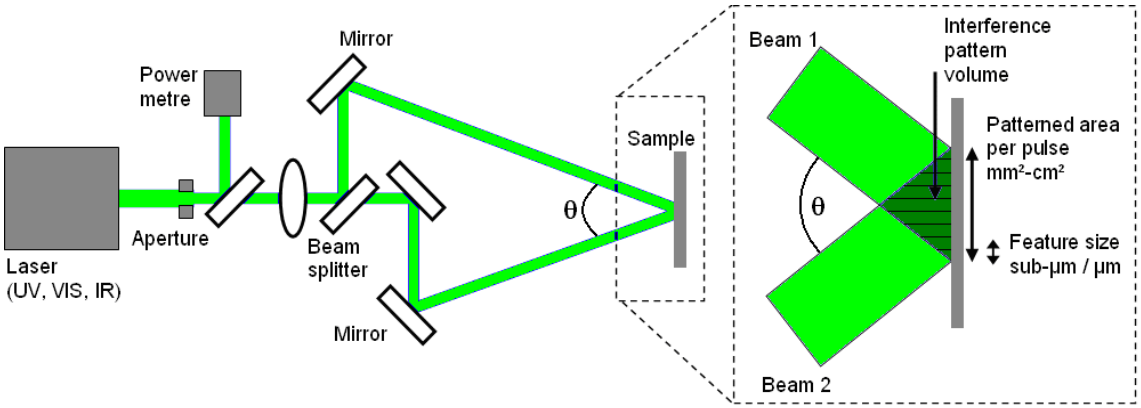


Fig.3. Scheme of the experimental setup for DLIP.

c) Heat transfer coefficient measurements

The extent of the condensation on structured and non-structured surfaces, as well as the influence of the hydrophobic coatings, was evaluated by calculating the heat transfer coefficient ***α*** (also ***h***) for all samples. The experiments are based on the measurement of the heat flow transfer through the sample. The heat flow was determined by monitoring the steam-to-metal surface temperature difference ΔT with thermocouples placed on both sides of the metallic samples [1].

The plots in Fig. 4 show the results of the heat flow transfer measurements, that were obtained for three different samples (substrate: Cu): (1) surface structured (P=2 µm)/coated with a hydrophobic film, (2) surface structured/uncoated, (3) surface unstructured/coated with a hydrophobic film. In addition, the theoretical curve based on the Nusselt theory for laminar films is included (4) to facilitate the comparison to samples (1) to (3). It is evident, that the laser structured Cu surface together with a post-deposited PECVD hydrophobic film result in higher values for α and an improved heat transfer.

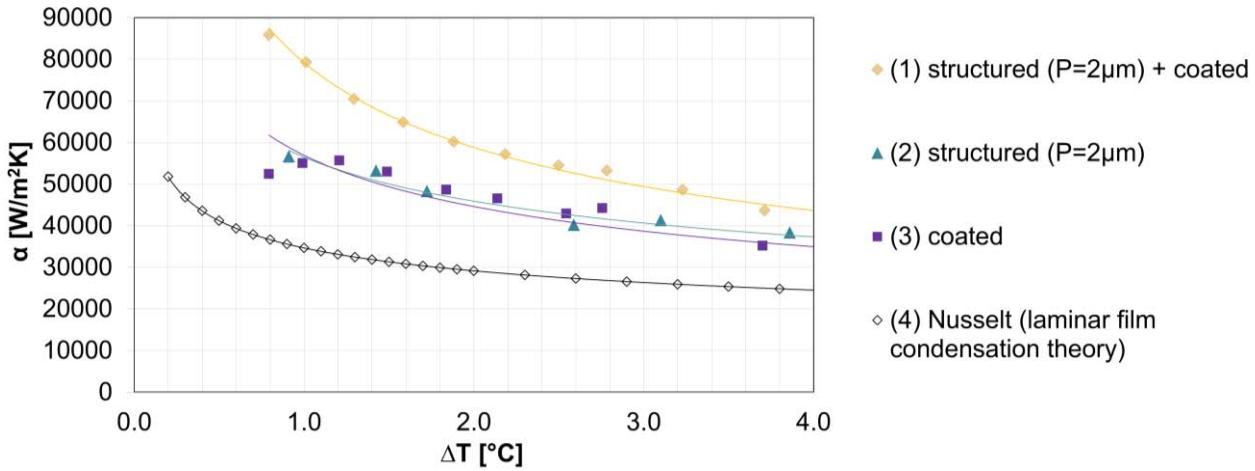


Fig.4. Heat transfer coefficients α versus the subcooling temperature ΔT measured for Cu samples with and without plasma polymer coating and laser patterns.

Moreover, water contact angles measurements show increasing values in the order: uncoated (~90°) < coated (~105°) < structured and coated (119...130° for P=2...5 µm) Cu substrates. No drifts in the contact angles were observed for all samples even after boiling tests (Fig. 5), which proves the high stability and durability of the films to some extreme conditions under those commercial condensation heat exchangers would run.

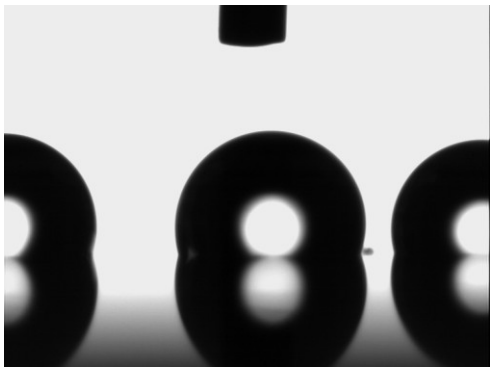


Fig.5. Image of the contact angle measurement for a Cu sample coated with a plasma polymer film and submitted to boiling test.

3. Conclusions

The potential of a PECVD deposition process to create hydrophobic films based on organosilicon monomers has been successfully proven. The plasma polymer coated surfaces yielded higher contact angles than uncoated surfaces and are also characterized by a higher heat transfer coefficient ***α*** (***h***). Furthermore, structuring the Cu surface by Direct Laser Interference Patterning before the film deposition proved to be an effective method to enhance the drop-wise condensation and consequently improve the heat transfer. The combination of both technologies to modify surfaces and consequently enhance the efficiency of condensation heat exchangers shows a great potential for industrial applications.

Acknowledgement

This work has been partially supported by a Grant-in-Aid for Technology Funding by the European Regional Development Fund (ERDF) and the State of Saxony (Grant no. 14256/2423).

References

[1] S.S. Finnicum, J.W. Westater, Int. J. Heat Mass Transfer. 32, No. 8 (1989) 1541-1549.

[2] B.-J. Chung et al., Journal of Mechanical Science and Technology 22 (2008) 127-133.

[3] R. Schmittgens, M. Wolf, E. Schultheiss, Plasma Processes and Polymers 6 (2009) 912.

Tribological Characterization and Wear Mechanisms of Novel Oxynitride PVD Coatings Designed for Applications at High Temperatures

J. Nohava; CSM Instruments, Switzerland

P. Dessarzin; PLATIT AG, Switzerland

P. Karvankova; PLATIT AG, Switzerland

M. Morstein; PLATIT AG, Switzerland

Introduction

In recent years, newly developed protective coatings for cutting tools have become more and more wear and abrasion resistant to the extreme environments associated with modern machining processes. On these new coatings the common pin on disk tribological tests have failed, resulting in practically no wear or strongly heterogeneous wear. For efficient tribological testing and determination of wear resistance of the new hard coatings it is therefore crucial to establish a valid set of room temperature and high-temperature wear test conditions. After a large number of preliminary tests performed on a state-of-the-art high-temperature pin on disc tester we identified optimized conditions for characterization of these new types of hard coatings. The investigated coatings comprised AlTiN-based reference, nanostructured Al-Cr-based nitride, oxynitride and oxide coatings deposited using an industrial rotating cathodes arc PVD process on cemented carbide. The nitrogen in the coating was progressively substituted by oxygen up to 100 at.% to create oxide structure in order to avoid oxidation of the coatings at high temperatures. These new oxide coatings are known to withstand extremely high temperatures in dry milling and turning of high-strength materials while exhibiting high wear resistance. However, characterization of their wear resistance by the common tribological tests had proven to be very difficult and new testing procedures had to be established.

Materials and experimental details

Four types of coatings were used in this study: AlTiN-based and AlCrN nitride coatings, AlCrON oxynitride coating and α-$(Al,Cr,X)_2O_3$ oxide coating. All coatings were deposited using π Technology: LARC® Lateral- and CERC® Central Rotating Arc Cathodes (Platit AG, Switzerland) in N_2/O_2 atmosphere (oxynitride and oxide coatings) at 4 Pa pressure and bias voltage from -30 V to -100 V using medium frequency. During the deposition the substrates from WC-Co (Extramet, Switzerland) in form of cylinders with 50 mm diameter and 10 mm thickness were heated to 550°C. The stack of layers was (from the substrate toward the top surface): TiN adhesion layer, AlTiN, nACo nanocomposite layer and top layer. The top (functional) layer, crucial for the wear properties, was AlCrN, $AlCrO_xN_{1-x}$ or α-$(Al,Cr,X)_2O_3$ (see Table 1). The AlTiN reference sample contained only the TiN and AlTiN layers without any additional top layer. The thickness of the whole coatings was ~4 μm.

Table 1 – Oxygen content and temperature for which the coating was designed.

Coating denomination	Oxygen content	Designed for temperature
AlTiN	0 at. %	up to 600°C
AlCrN	0 at. %	600°C
AlCrON	70 at. %	600°C-800°C
α-$(Al,Cr,X)_2O_3$	99.8 at. %	800°C-1000°C

The wear tests were performed by pin on disk method on THT 800 instrument (CSM Instruments, Switzerland) at temperatures of 24°C, 600°C and 800°C. The normal load was 7 N (10N respectively for 24°C), the counterbody was alumina ball with 6 mm diameter and the linear velocity was 20 cm/s. The pin on disk tests were performed with 32'000 laps and the total duration of the tests varied between 120 minutes and 240 minutes depending on the radius of the wear track. Scanning electron microscopy (SEM) images, energy dispersive X-ray spectroscopy (EDX) and focused ion beam (FIB) cuts was done on Lyra3 scanning electron microscope (Tescan, Czech Republic).

Results

The results of the tribological tests at room temperature, 600°C and 800°C are summarized in Fig. 1. The AlTiN based reference coating performed well only at room temperature but its coefficient of friction varied strongly at 600°C and 800°C indicating severe wear. Optical images and SEM observation of the AlTiN wear track at 600°C and 800°C revealed areas with catastrophic failure. The AlCrN and AlCrON coatings showed better stability of the coefficient of friction and better wear resistance up to 600°C but they failed during tribological tests at 800°C. The α-$(Al,Cr,X)_2O_3$ oxide coating, on the other hand, presented practically no signs of wear even at 800°C. Furthermore, the coefficient of friction of this new oxide coating decreased to ~0.3 at 800°C (compared to ~0.6 at 600°C) indicating excellent wear resistance and negligible degradation of this coating at high temperatures (see Fig. 1, 800°C, blue line).

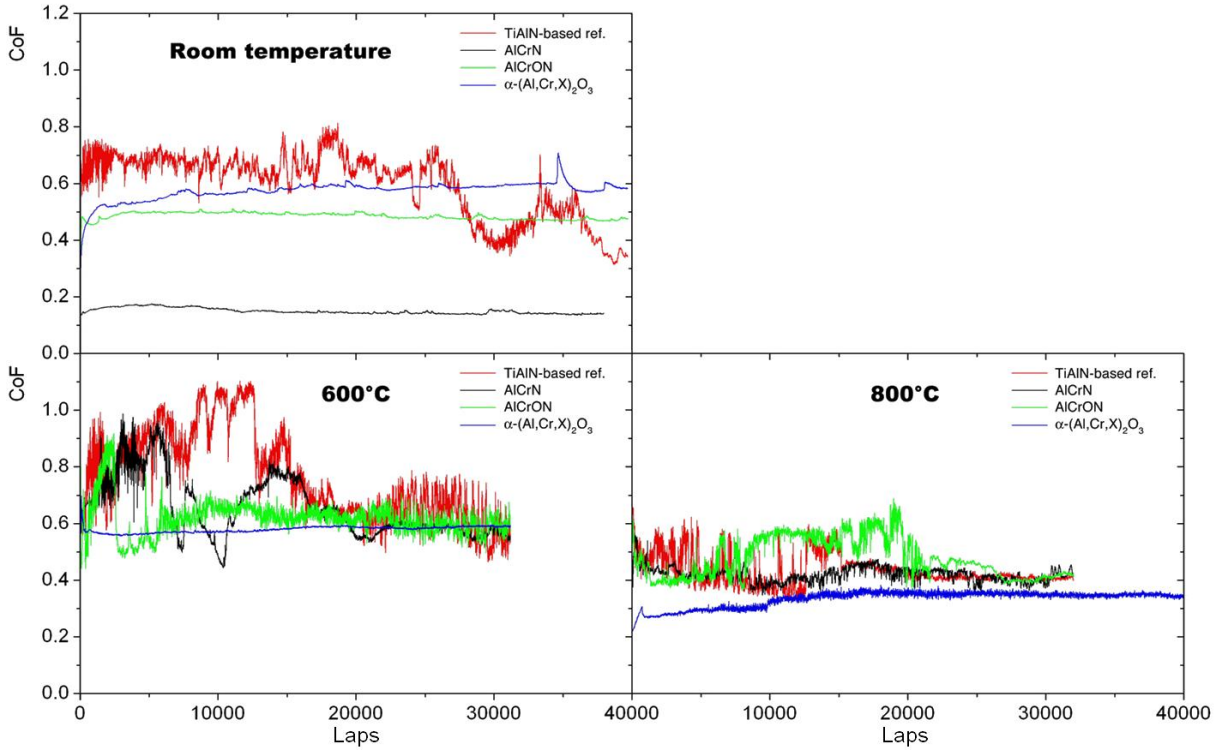


Figure 1 – Comparison of coefficient of friction of all tested samples at 24°C, 600°C and 800°C. Note excellent stability and low value of coefficient of friction of the α-$(Al,Cr,X)_2O_3$ oxide coating (blue line).

The evaluation of the wear rate at room temperature via profile of the wear track revealed low wear for the AlTiN coating and almost non-measurable wear for all other coatings. At 600°C the AlTiN-based coating showed moderate wear. The wear rates for AlCrN and AlCrON were higher at 600°C and even higher at 800°C compared to room temperature.

The α-$(Al,Cr,X)_2O_3$ oxide coating, on the other hand, showed minor wear with very little traces of interaction with the alumina counterpart at 600°C and 800°C – see Fig. 2. As noted above, also the coefficient of friction at 800°C on this coating was very stable. Surprisingly enough, the wear track profiles in some areas on the AlTiN and AlCrN coatings at 800°C did not show a typical 'worn-out' profile but rather a large material build-up. Figure 2 shows the relatively 'low' wear rate of the AlTiN coating at 800°C whereas the build-up rate was the highest on this coating. Nevertheless, both wear rate and build-up rate were significantly higher than that of the oxide coating.

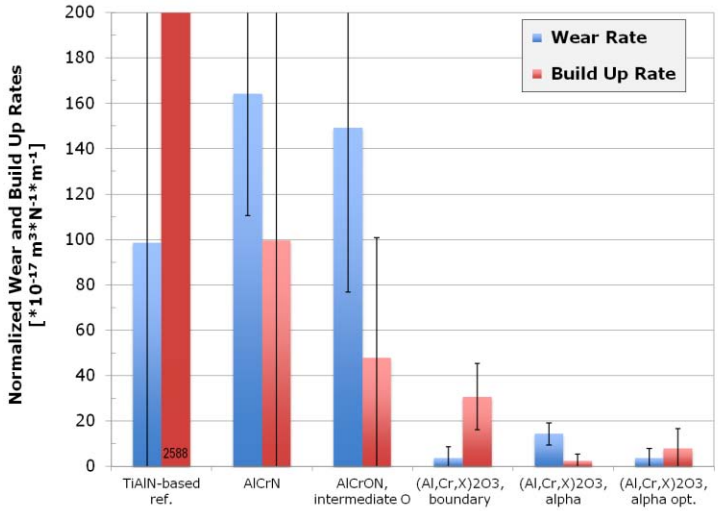


Figure 2 – Wear and build up rates of all tested coatings. Apart from the α-$(Al,Cr,X)_2O_3$ oxide coating (alpha opt.) also two other variations of oxide coating are included.

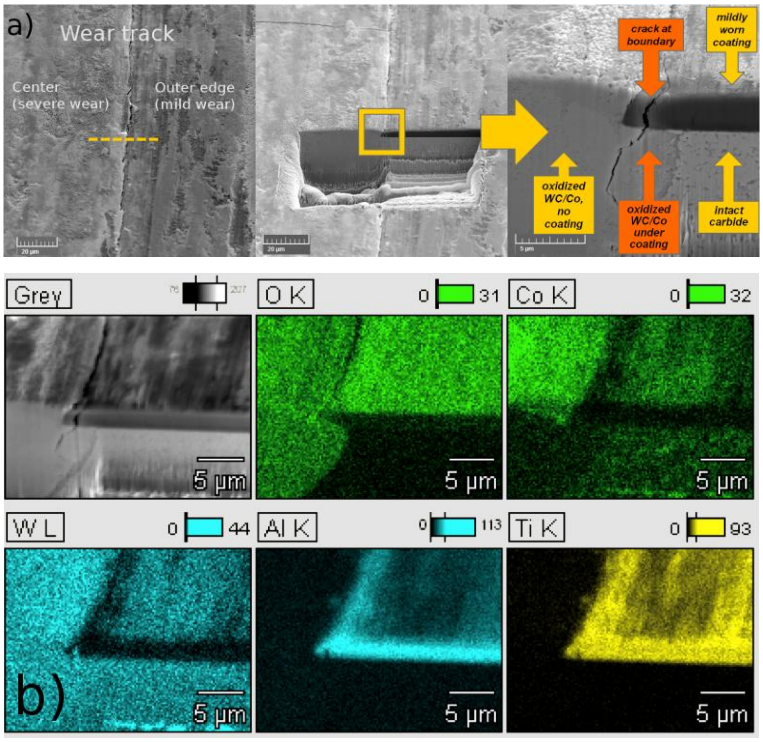


Figure 3 – a) SEM micrograph (secondary electrons) of the wear track on the TiAlN coating after 800°C pin on disk test, showing the position of the FIB cut. b) EDX in the FIB cut showing strong oxidation of the WC-Co substrate.

Discussion

Although the AlTiN, AlCrN and AlCrON coatings showed good wear resistance at room temperature and at 600°C, they all failed during tribological tests at 800°C. AlTiN, AlCrN and AlCrON showed signs of severe wear including catastrophic failure in several regions. EDX analysis of the worn surface and also FIB cuts in the wear track revealed oxidation of the substrate in the regions of severe wear. The FIB cuts of the wear track on AlTiN coating tested at 800°C revealed oxidation of the substrate also beneath the coating in regions where the coating was not completely removed. This indicates insufficient resistance of the AlTiN coating to oxidation at high temperatures.

SEM analysis of the wear tracks revealed that the wear on samples with low oxygen content was governed by an abrasive mechanism with limited micro-scale cohesive fracture. EDX mapping showed that oxidation played a negative role for AlTiN and AlCrN coatings while $AlCrO_xN_{1-x}$ coating remained relatively intact at 600°C. The α-$(Al,Cr,X)_2O_3$

oxide coating retained high wear resistance up to 800°C. The EDX and SEM images showed that the wear mechanisms especially at high temperatures are very complex and characterization of wear resistance cannot be based only on the wear track profile and simple calculation of volume of material removal. To further elucidate these wear mechanisms, FIB cuts were performed in the wear track of the AlTiN and the α-$(Al,Cr,X)_2O_3$ oxide coating after the 800°C pin on disk tests. Figure 3a shows this FIB cut in the AlTiN wear track and Fig. 3b shows corresponding EDX analysis in this area. The oxidation of the substrate in the wear track lead to the growth of the material in the wear track thus almost completely filling up the cavity created by the wear test. This process resulted in erroneously low wear rate and in build-up of the WC-Co oxides on the periphery of the wear track. The evaluation of wear rate especially at high temperature tribological tests requires therefore a more complex analysis than simple measurement of the profile of the wear track. In contrast, the α-$(Al,Cr,X)_2O_3$ oxide coating showed practically neither wear nor material build-up thus confirming excellent oxidation and wear resistance of this new type of coating.

Conclusions

This work presents a thorough study of tribological behavior of new types of hard coatings designed for use at high temperatures. The novel α-$(Al,Cr,X)_2O_3$ oxide coating confirmed its excellent wear resistant properties and oxidation resistance at temperatures up to 800°C. The AlTiN, AlCrN and AlCrON coatings showed good wear resistance at room temperature, acceptable wear resistance at 600°C; at 800°C all these coatings exhibited severe wear. The superior wear resistance of the oxide coating was due to high oxygen content in this coating which hindered high temperature oxidation and subsequent catastrophic degradation of the coatings with lower oxygen content.

GENERAL REGULARITIES AND DIFFERENCE OF NANOSTRUCTURED COATINGS BASED ON NITRIDES OF Zr, Ti, Hf, V, Nb METALS AND THEIR COMBINATIONS

A.D.Pogrebnjak[1], V.M.Beresnev[2], A.A.Andreev[3], O.V.Sobol[4], D.A.Kolesnikov[5], F.F.Komarov[6], S.S.Mel'nik[7], M.V.Kaverin[1], A.P.Shypylenko[1]

[1.] Sumy State University, Str. R-Korsakov 2, 40007 Sumy, Ukraine; e-mail: alexp@i.ua
[2.] Kharkov National University, Kharkov, Ukraine
[3.] Kharkov Phisico-Technical Institute, Kharkov, Ukraine
[4.] Kharkov Polytechnical University, Kharkov, Ukraine
[5.] Belgorod State University, Belgorod, Russia
[6.] Belarus State University, Minsk, Belarus
[7.] Institute of Applied Physics, Sumy, Ukraine

Abstract

Using the vacuum-arc source with the HF discharge, nano-structured hard and super-hard coatings based on Ti-Hf-N(Fe), Ti-Hf-Si-N, Ti-Zr-Si-N, and (Ti, Zr, Hf, Nb, V)N of 1.2μm to 2.5μm thickness were manufactured. The coatings were studied using the proton micro-beam μ-PIXE, RBS, SIMS, SEM with EDS, XRD, and tested for adhesion resistance, wear, and nano-hardness. It was found that a concentration of Ti, Zr, Hf, V, and Nb metals as well as a bias potential applied to a substrate and residual pressure in a chamber (N or Ar/N) affected the formation regularities of solid solutions and quasi-amorphous phases based on α-Si_3N_4. Hardness of the resulting coatings reached 48GPa to 52GPa, their elastic modulus was 420GPa to 535GPa. The friction coefficient was 0.12 to 0.2, and temperature resistance was as high as 1300^{o}C.[1]

Coating structures varied from a columnar to a nanosized one. Grain sizes of the phases of the solid solutions were from 4nm to 10nm or 12nm. Those of α-Si_3N_4 inter-layer were from 0.8nm to 1.2nm.

Keywords: super-hardness, adhesion, friction, nano-grains, thermal stability

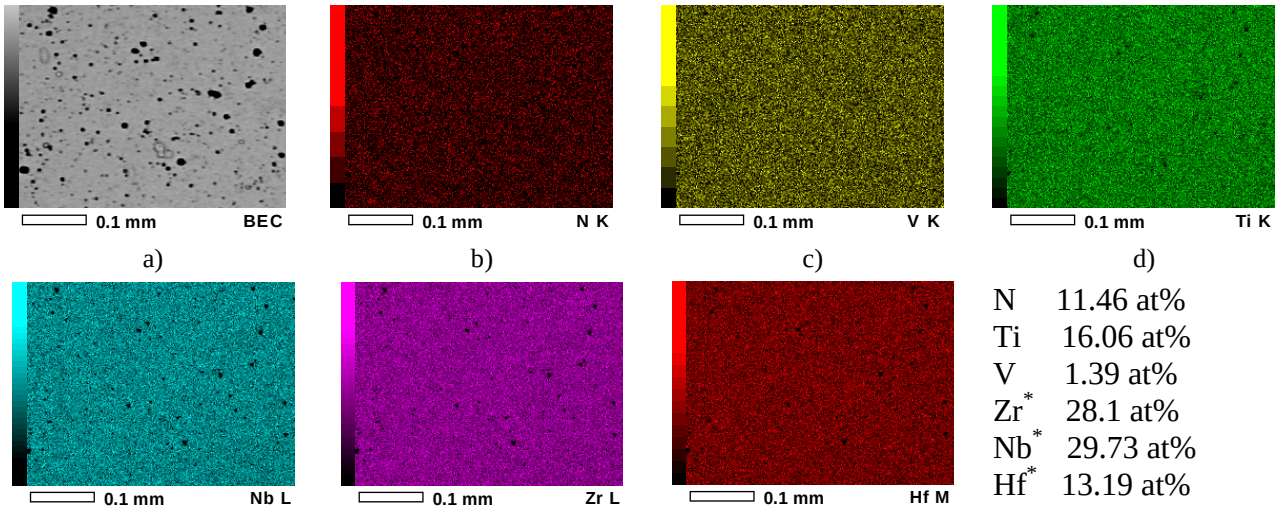
I Introduction

The purpose of the given work is creation of the new multycomponent nanostructure coatings based on (Ti-Zr-Hf-V-Nb)N using the cathode vacuum-arc deposition, investigation of its structure, morphology, physical-mechanical and frictional properties. As the cathode we used material, melted from the powder with (Ti; Zr; Hf; V; Nb)N composition on the device, being well described in the work [1,2].

For element and composition analysis we used such methods, as scanning electron microscopy with microanalysis (EDS), on Jeol 7000 F, Japan; RBS analysis on ion accelerator 4.5 MeV Tandentron, NIMS, and on another ion accelerator, Van de Graaff, Dresden, with ion energy 2MV, and we built element profiles through the coating thickness and detected stoichiometry of the coating. We investigated structure and phase composition using XRD analysis in sliding geometry on the device XPert PANanalitical (Holland), U = 40kV, I = 40 mA, cathode – copper. Also, on the samples with coatings we made cross-sections (using ion-beam) in order to analyze its structure, thickness and

coating morphology. Nanohardness and elasticity modulus were detected using nanoindentor Nanoindentor II GSM, frictional characteristics were explored using equipment Revetest, Belgorod State University, Russia. On separate samples with coatings we obtained profiles of defects through the coating thickness using slow beam of positrons at the Halle University, Germany. Deposition of the sample was held in the chamber with a residual pressure of P = 8×10^{-4} to 5×10^{-3} Pa, potential applied to the steel substrate U = 40 - 200 V, with concentration of coating elements changes, for example, for N from 8.4 to 16 at.%, for Ti from 14.8 to 27 at.%, for V from 1.4 to 5.6 at.%, for Zr from 13 to 28 at.%, for Nb from 13 to 29.7 at.%, and for Hf from 13 to 37 at.%.

As the example, on the fig. 1 we presented map of the (Ti-Zr-Hf-V-Nb)N coating surface in the element contrast. Sample spectrum was shown on the insertion. Analysis of defects through the coating thickness was shown on the fig. 2a. It is obvious, that positron beam energy is enough for penetration through the coating thickness. Annealing with the step 150^0C up to the temperature of 600^0C, spinodal segregation ending on the boundaries of the grains showed, that some part of positrons actually annihilates on the vacancy defects, laying on the grains boundaries. Further XRD analysis showed, that in the system, made of Hf-Ti-Si-N, an amorphous α-Si_3N_4 phase was formed with the high weighting ratio in comparison with the coating, which was obtained using the deposition method (under room temperature). From theoretical works [3] it is well-known, that maximum hardness and plasticity of nanocomposite coatings is reached when interphase boundary between nanograins is 1 ML or less, and volume fraction of the interphase boundary is 30-50%.



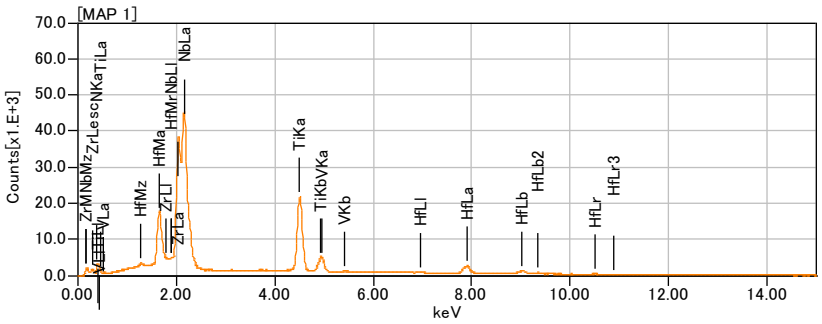


Fig. 1. Element composition of the coating made of (Ti-Zr-Hf-V-Nb)N in contrast of elements (colored images MAP); a), b), c), d), e), f), g) – energy-dispersive spectrum, obtained on the coating; h) – concentration of elements in the coating, measured in atomic percent.; i) – EDS spectrum of the coating.

From the results presented on Fig. 2 a, b it is clearly seen that the defect profiles (S-parameter) vary significantly for different deposition conditions (for example see samples 504 and 508). At the same time, annealing in vacuum chamber with a sufficiently high residual atmosphere pressure leads to even greater changes (S-parameter) at a depth of coating.

In case of sample 504, the value of S-parameter decreases from (0,58 ÷ 0,56) to (0,52 ÷ 0,51) after annealing and only approaching to the energy (12,5 ÷ 15) keV of positron analyzing the magnitude of S-parameter increases to 0.53. In case of sample 508 (Fig. 2b) S-parameter before annealing does not show any defects in depth and it's value is minimal, i.e. 0.49. But after annealing up to 600ºC, it's value increases significantly to 0.53 in the surface layer of coating, and then increases with depth from the positron energy (10 – 17) keV, while the value of S-parameter increases further and becomes maximum, approaching 0.59 (the maximum possible value).

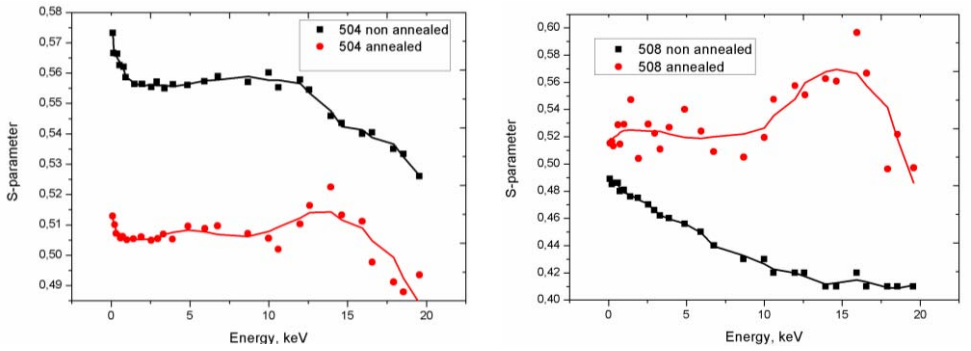


Fig. 2a, b Dependence of S-parameter of Doppler broadening of the annihilation peak measured at a depth of coating (Ti,Zr,Hf,Nb,V)N (samples 504 (a) and 508 (b)) before and after annealing up to 600ºC (50 mbar).

According to Fig.3, in direct-flow mode without separation the non-textured polycrystalline coatings are formed. Rather high intensity of the peaks at XRD-patterns of (Ti,Hf)N solid solutions is attributed to relatively large concentration of hafnium, which has larger reflectance value than titanium.

In case of beam separation the coatings have different texturation. At low substrate potential (100 V) coatings have [110] texture, and coatings consist of textured and non-textured crystallites. The volume content of textured crystallites is about 40% of total amount of the crystallites, and their lattice parameter enlarged in comparison to non-textured crystallites. We suppose that the increased lattice parameter may be caused by the inhomogeneous distribution (mainly in the lattice sites of the textured crystallites) of the hafnium atoms in coating.[4,5,6]

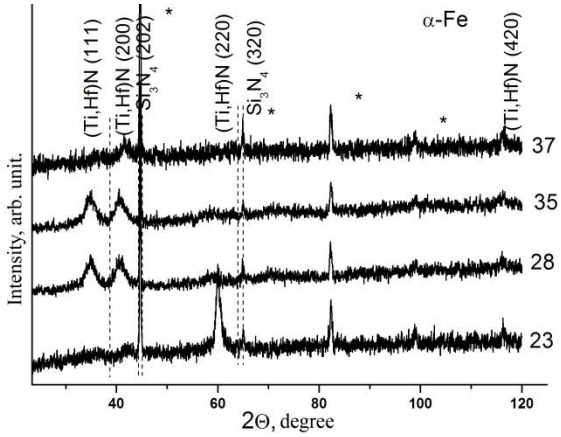


Fig. 3 XRD spectra of the coatings deposited on a steel substrate at modes (1-(23) – 100V, separated, 2-(28)-200V, non separated, 3 (35)-100V, non separated, 4 (37)-200V, separated).

Conclusion

Thus, in the work we studied the processes of impurities segregation on the boundaries of nanograins after finishing of the process of spinodal segregation. We used the unique methods of analysis: SEM with EDS, XRD, Nanoindentor, Test "Revest", Positron Microbeam (Positron Annihilation), Microbeam (PIXE, RBS) Finally, we obtained solid multycomponent nanostructure coatings (Ti-Zr-Hf-V-Nb)N with high physical and mechanical properties.

The work was performed within the framework of F41.20-2011 GFFR project of Ukraine and T11K-058 BR FFRC project of Belarus

References

1. J. Musil, J. Sklenka, R. Cerstvy. Hard and Superhard Nanocomposite Coatings. – Surf. and Coat. Tech. N125, 2000, 322 – 330 p.

2. A.D. Pogrebnjak, A.P. Shpak, N.A. Azarenkov, V.M. Beresnev. Structure And Properties Of Hard And Superhard Nanocomposite Coatings. – Usp. Fizich. Nauk, N179 (1), 2009, 35 – 64 p.

3. A.D. Pogrebnjak, A.G. Ponomarev, A.P. Shpak, Yu.A. Kunitskij. Application Of Micro-Nanoprobes To The Analysis Of Small-Size 3D Materials, Nanosystems Ad Nanoobjects. – Usp. Fizich. Nauk, N182 (3), 2012, 287 – 321 p.

4. V.M. Beresnev, O.V. Sobol', A.D. Pogrebnjak and others. Features of the structurally-phase state of multycomponent coatings on basis of Zr-Ti-Si-N system, formed by the method of vacuum-arc deposition. – Probl. of Atom. Sci. and Tech., N6, 2009, 162 – 168 p.

5. J. Musil. Transparent Zr-Al-O Oxide Coatings with Enhanced Resistance to Cracking. – Surf. and Coat. Tech., N206, 2012, 2105 – 2109 p.

6. S. Veprek. The Search for Novel, Superhard Materials. – J. Vac. Sci. Tech., N17, 1999, 2401 – 2420 p.

Composition of plasmapolymeric coatings using O2/HMDSO gas mixtures and application on elastomers for tribological improvement

Dr. Dominik Paulkowski, Dr.-Ing. Klaus Vissing, Dr. Ralph Wilken

Fraunhofer IFAM, Wiener Str. 12, 28359 Bremen

The composition of plasmapolymeric coatings (SiOx) using O2/HMDSO gas mixtures in a plasma enhanced chemical vapour deposition (PECVD) process can be widely tailored varying the mixing ratio of the process gases as well as the applied power in the deposition process. This article demonstrates the changing properties of those coatings and its capability for reduction of friction regarding elastomers for the application on seals[1]. A reduced friction of sealing rings in an automobile realizes the reduction of CO2 emission due to energy saving.

On the one hand the deposition process was varied regarding the mixing ratio of the process gases oxygen (O2) and Hexamethyldisiloxan (HMDSO) from 1:5 to 18:1 as well as the applied power from 500 W to 1500 W. On the other hand the friction of three different types of elastomers plasmapolymeric coated as well as uncoated was investigated. These three substrate types were acrylic rubber (ACM), fluoric rubber (FKM/FPM), and nitrile rubber (NBR).

The studied coated and uncoated elastomers were tested as flat plates. The friction of elastomers was investigated using an Universal Material Tester (UMT3) system[2] with oscillating Pin-on-plate contact geometries (Figure 1). The tribological tests were done in ambient conditions with a velocity of 200 mm/s and a stroke length of 11 mm. The counterparts in the tribological tests were on the one hand a 440C steel ball with a diameter of 9.5 mm and on the other hand an end plane of a steel rolling bearing with diameter of 6 mm. In the case of the steel ball a normal force of 4.7 N was used. Using the rolling bearing a normal force of 10.6 N was applied. The used normal forces represent an initial Hertzian pressure of 1.5 MPa and 0.5 MPa, respectively.

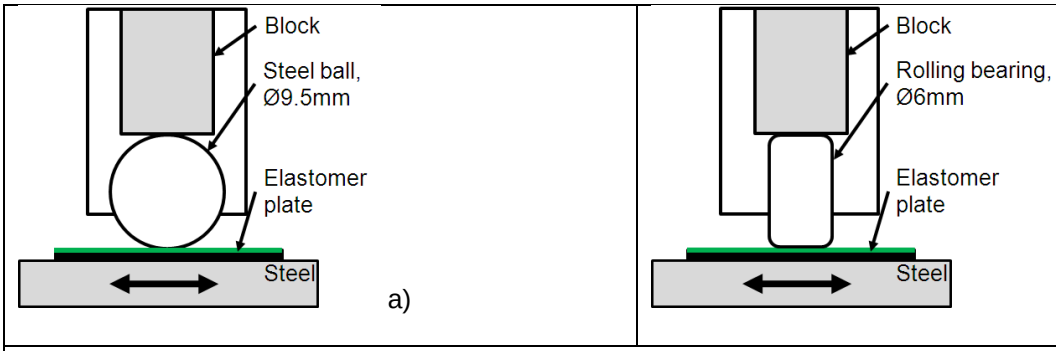


Figure 1: a) steel ball and b) steel pin in contact with coated or uncoated elastomer plate.

[1] Patent “Dichtungsartikel”: DE 10 2008 002 515 A1.
[2] Universal Material Tester (UMT3), Bruker formally Center for Tribology Inc., 1717 Dell Ave., Campbell, CA 95008

Determine the nanohardness and the Young's modulus of the coatings nanoindentation experiments were done. The force-indentation depth curves were evaluated using the model of Oliver and Pharr[3]. Investigating in the chemical composition mircoelementary analysis (µAnalyse[4]) techniques as well as IR spectroscopy (Bruker Equinox 55 spectrometer, detection angle 75 ° at IRRAS configuration, at least 32 scans, 4cm^{-1} resolution) was used determining the bond configuration. The surface energy was calculated according to Wu[5].

The nanohardness of the coatings was tailored to slightly higher values to increase the wear resistance of the elastomeric substrates. As a result, it was found that the Young's modulus and the nanohardness of the plasmapolymeric coatings were increasing at increasing amount of O_2 content (Figure 2a). These mechanical properties saturated at higher O_2 contents due to a transition to a SiO_2 network.

The surface energy of the samples could be tailored varying the mixing ratio of the process gases in the deposition process (Figure 2b). The surface energy was increasing at increasing O_2 content as well as a decreasing amount of methyl groups (compare Figure 3).

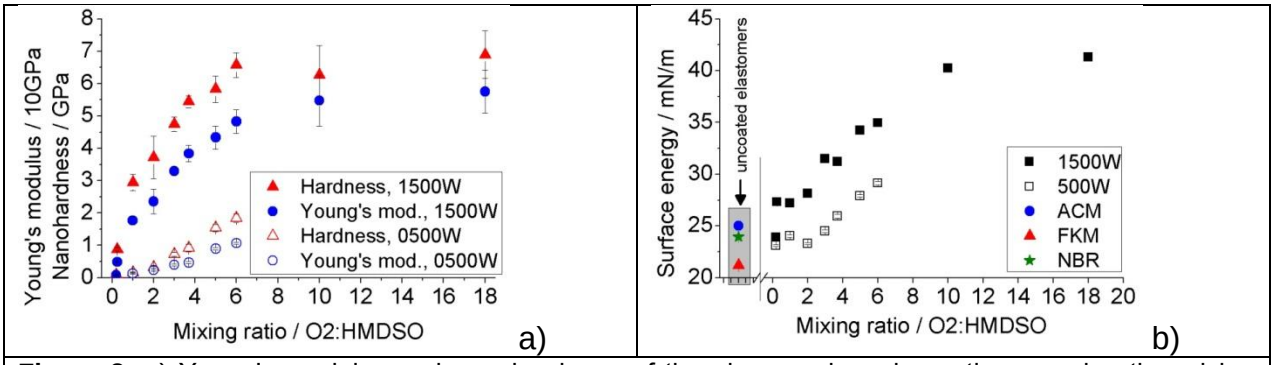


Figure 2: a) Young's modulus and nanohardness of the plasmapolymeric coatings varying the mixing ratio of the process gases. b) Surface energy of elastomeric substrates and plasmapolymeric coatings. The surface energy of the plasmapolymeric coating could be tailored varying the mixing ratio of the process gases.

Regarding the six methyl groups in the precursor HMDSO it was obvious to investigate in associated bonds. On the one hand the mass-% content of C as well as H was determined using µAnalyse. On the other hand the bond configuration was investigated using IR spectroscopy. It was found that the mass-% content of C as well as H was decreasing with increasing amount of O_2 content due to the decreasing amount of HMDSO content (Figure 3).

[3] W. C. Oliver, G. M. Pharr, An improved technique for determining hardness and elastic modulus using load and displacement sensing indentation experiments, J. Material Res. (1992) Vol. 7, No. 6, 1564-1583
[4] Mikroanalytisches Labor Pascher, An der Pulvermühle 1, 53424 Remagen
[5] S. Wu, Calculation of interfacial tension in polymer systems, Journal of Polymer Science Part C: Polymer Symposia (1971), Vol. 34, Issue 1, 19-30

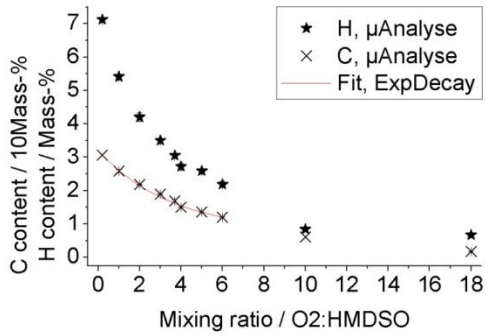


Figure 3: C as well as H content of the plasmapolymeric coatings. The contents can be tailored varying the mixing ratio of the process gases.

The determined IR spectra of each plasmapolymeric coating version are shown in Figure 4a. A pure HMDSO spectrum was determined using an ATR-crystal configuration additionally. In Figure 4b depicted peak positions are listed to demonstrate peak shifts. As a very brief conclusion regarding these spectras and all determined coating properties of the plasmapolymers above it is obvious that there was a smooth transition in the composition from polymer-like structure to SiO_2 network and furthermore a densification in the SiO_2 network.

The transition from polymer-like structure to SiO_2 network was observed regarding bonds of CH_x, Si-CH_x, and Si-O-Si. Due to missing Si-H bonds and the measured C as well as H content regarding the mixing ratio of the process gases it is obvious that the C and H was mainly bond as CH_x. Therewith the CH_x content was decreasing increasing the amount of O_2 content.

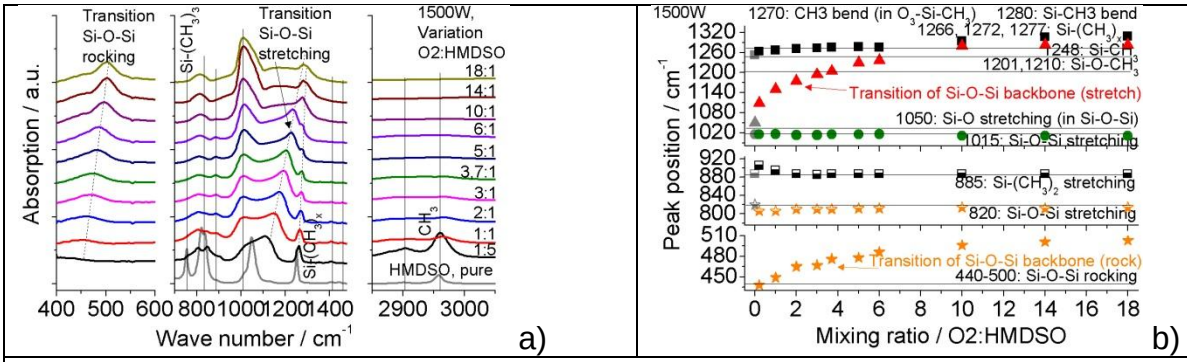


Figure 4: a) Depicted FTIR spectra of the plasmapolymeric coatings as well as pure HMDSO. b) Shifting of peak position varying the mixing ratio of the plasmapolymeric coatings.

The investigations in the tribological improvement of the elastomers due to the applied plasmapolymeric coatings showed a reduction of friction (Figure 5). It was found that the coefficient of friction µ could be reduced by 86 % of the uncoated elastomers from 1.24 to 0.17 using plasmapolymeric coatings at dry friction (Figure 5a). In the past an improvement of dry friction by 84 % of the uncoated elastomers from 1.24 to 0.20 using plasmapolymeric coatings applied by classical bar electrodes was shown[6]. Up to four times higher deposition rates of the large scaled electrode in the actual article

[6] Dominik Paulkowski, Klaus Vissing, Tribological improvement of elastomers using plasmapolymeric coatings, 15/1-15/14, Proceedings of Tribologie Fachtagung 2011, GfT, Göttingen

demonstrates the increased cost effectiveness of the deposition process. The significant tribological improvement and the decreased deposition time are fulfilled basic demands from the applied plasmapolymeric coatings.

Regarding sealing rings in automobiles or other elastomer devices a reduction in friction of lubricated contacts is required. It was found that the coefficient of friction μ could be reduced by 43 % from 0.14 to 0.08 at oil lubricated contact (Figure 5b) and up to 71 % from 0.80 to 0.23 at grease lubricated contact (Figure 5c-d). The nanohardness as well as the Young's modulus, the surface energy and the chemical composition of the plasmapolymeric coatings exhibit a clear dependency. That means the wear resistance could be tailored in relation to the damping behavior of the elastomers.

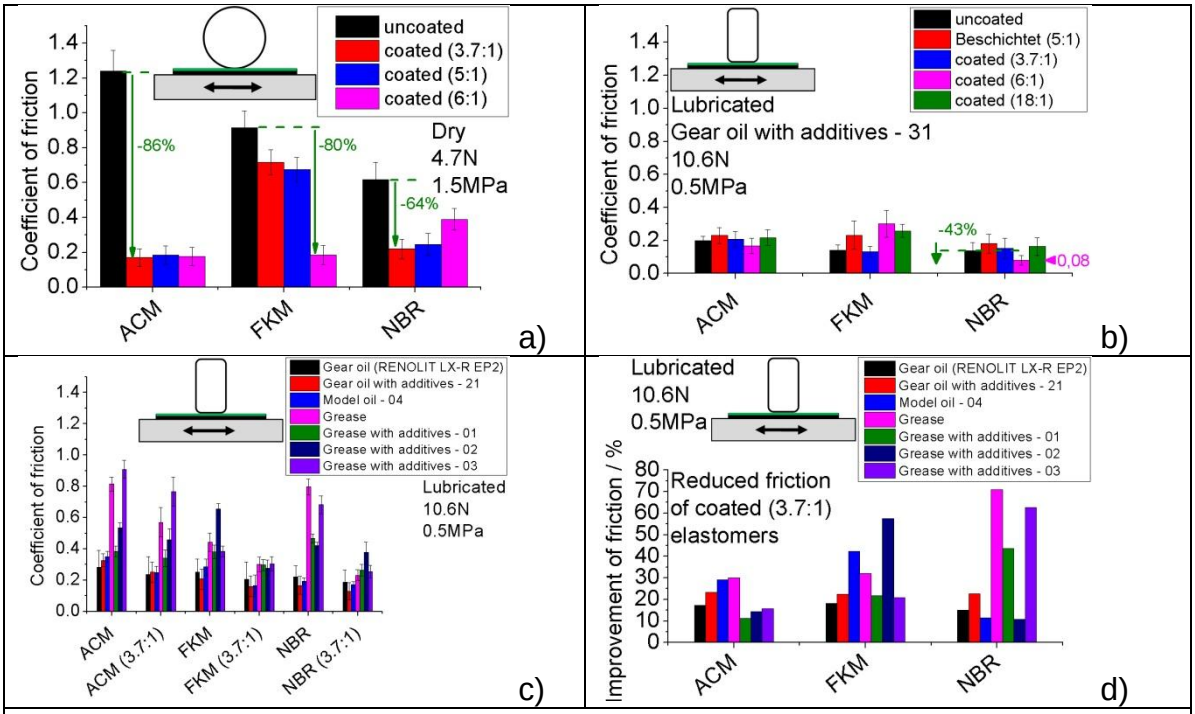


Figure 5: Coefficient of friction of uncoated as well as plasmapolymeric coated elastomeric substrates. The contact geometry in each case is drafted in the diagrams. a) Dry, c-d) lubricated friction. In a) and b) the reduction of friction was listed directly, in d) the improvement of c) due to the plasmapolymeric coating is listed.

It has to be noticed that the friction results revealed differences between the three coated elastomeric substrates ACM, FKM as well as NBR (Figure 5). The three elastomeric samples were chosen due to identical 75-Shore-A hardness. The main difference was the relatively higher friction of the plasmapolymeric coatings on FKM in relation to ACM or NBR. Several reasons had been discussed by the authors in the past[6].

The authors acknowledge the financial support of the Bundesministerium für Wirtschaft und Technologie (BMWi) and the participating companies. The support code was 0327499A.

High Power Density Pulse Magnetron Sputtering - Process and Film Properties

Peter Frach*, Christian Gottfried, Fred Fietzke, Heidrun Klostermann, Hagen Bartzsch, Daniel Gloess

Fraunhofer-Institut für Elektronenstrahl- und Plasmatechnik FEP, Dresden
*corresponding author: Tel.: 0351-2586-370; Fax 0351-2586-55-370;

Abstract. In this paper specific advantages and disadvantages of different pulse magnetron sputtering processes (unipolar and bipolar pulse sputtering at high and very high power density including HIPIMS) as well as current and potential fields of application will be discussed.
On the examples of Ti and TiO_2 the typical effects and their influence on film properties occurring during the transition from classical medium frequency pulse magnetron sputtering to high energy pulse sputtering (HIPIMS) and the influence on film properties will be described. The discharge current density was varied between 0.2 and 3.5 A/cm^2. Aspects of energy feed-in, magnetron design and methods of reactive process control in the transition mode will be considered. Ideas for upscaling of the HIPIMS process will be discussed. Furthermore the influence of increasing ionisation on the occurrence of crystalline phases and on mechanical, optical and photocatalytic properties of the layers will be presented.

Keywords: HIPIMS, HPPMS, high power density pulse magnetron sputtering,TiO_2, reactive sputtering

1. Introduction

Since the idea of high power pulsed magnetron sputtering (HPPMS or HIPIMS) was born more than 10 years ago [1], there has been ever increasing interest within the scientific community to use this new technology, to carry out extensive R&D, and to clarify the mechanisms involved [2]. In some areas, the technology has attained special technical significance, for example for the coating of deep trenches in microelectronics by "Highly Ionized Metal Sputtering" [3]. First investigations regarding industrial use for hard coatings have been presented. In contrast, no applications for large surfaces have been developed, so far. In industry a certain reticence to use the technology, and to transfer the acquired knowledge to real processes, has prevailed.

HIPIMS, like conventional PMS, implies feeding energy pulses into a magnetron discharge – albeit with much higher power densities and hence drastically reduced values for the pulse-pause ratio and pulse frequency. Typically conventional PMS has power / current densities on the target during the pulse-on-time in the range 5 ... 50 W/cm^2 / < 0.5A/cm^2 for pulse-pause ratios of 1:1 and pulse frequencies between 20 kHz and 200 kHz. The relevant values for HIPIMS are 0.5 ... 5 kW/cm^2 / > 0.5A/cm^2 at pulse-pause ratios of 1:10 ...1:1000, in a frequency range of 50 Hz to 500 Hz. The high power density in the pulse leads to a high degree of ionization of the layer-forming particles, allowing the deposition of layers which are exceptionally dense, smooth, and homogenous. Besides this advantage, there are a number of disadvantages and in particular the drastically reduced deposition rate and the much higher tendency for arc discharges. Furthermore there are problems of up-scaling towards larger magnetron size due to limitations regarding powering and arc management.

In order to build up a knowledge base at Fraunhofer FEP for evaluating this technology and its potential for industrial use, the HIPIMS generator TruePlasma HighPulse 4008 (Trumpf Hüttinger Elektronik) with performance parameters 20 kW DC, 2 kV / 4 kA pulse at max. 500 Hz , was compared with established MF pulse generators under a wide range of conditions (coating plant, magnetron type, target material, pressure, gas composition). The discharges themselves, the possibilities of reactive process control and also the properties of the deposited layers were evaluated.

2. Experimental

Two different sputtering systems were used for this investigation.

System 1 is the Double Ring Magnetron sputter source DRM 400 on the Cluster 300 plant [4, 5]. The inner target of the DRM 400 was powered against the anode (Fig. 1a). The experiments in the unipolar HIPIMS mode were carried out using the TruePlasma HIPIMS generator. The relatively small target size of 116 cm^2 allowed to achieve a maximum power density up to 4kW/cm^2. For comparison the pulse unit UBS-C2 of Fraunhofer FEP was used for the normal unipolar pulse mode. Amongst the materials which were studied, comparative tests were carried out with a Ti target, with and without reactive gas.

System 2 is a Double Magnetron System DMS 500 with two 120 x 500 mm^2 rectangular targets in the batch coating plant UNIVERSA. The DMS 500 was powered by a voltage-fed rectifier made by MagPuls (60 kW DC, 1 kV / 1 kA pulse at max. 50 kHz). The power was introduced in the bipolar pulse mode, where the polarity of the two magnetrons is switched in each half cycle (Fig. 1b). By varying the duty cycle between 90% and 14%, the

current densities in the pulse changed between 0.2 and 1.2 A/cm^2, i.e. between normal bipolar pulse mode to bipolar HIPIMS-mode.

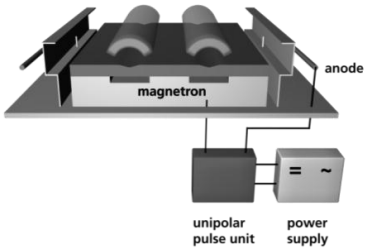


Figure 1a. Schematic of the unipolar powering configuration of the inner target of the DRM 400 against the anode in the normal pulse and in the HIPIMS mode

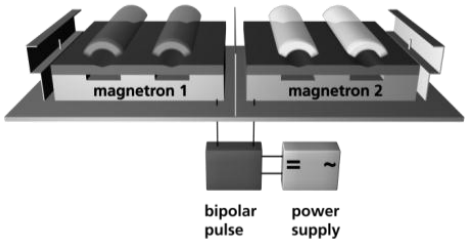


Figure 1b. Schematic of the bipolar powering configuration of the two targets of the DMS 500 in the normal pulse and in the HIPIMS mode

3. Results and discussion

3.1. Ti and TiO_2 layers deposited with DRM400 (system 1)

The DRM 400 has moveable magnet systems so that the dependence of the energy input in HIPIMS mode on the magnetic field strength could be studied in detail. It was found that the power density on the target is strongly dependent on the magnetic field strength for sputtering in pure argon (Fig. 2). The maximum power density in the pulse increases from 2.4 kW/cm^2 to 4 kW/cm^2 (67% increase) when the magnetic field strength is increased by 15%, only. To achieve high power densities, strong magnetic fields are therefore favorable.

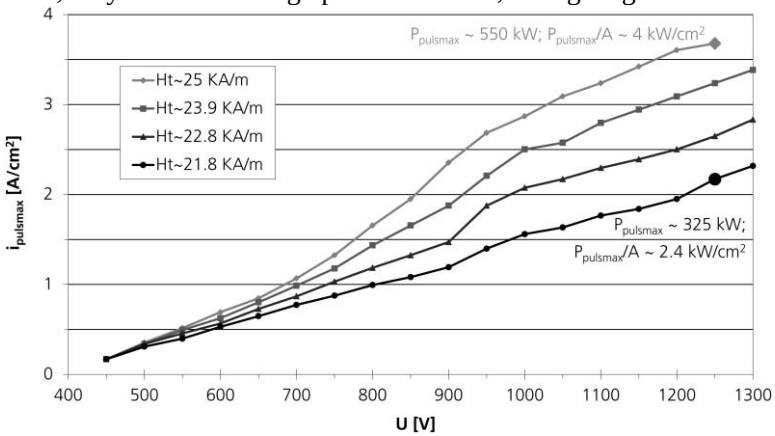


Figure 2. Maximum discharge power density $i_{pulsmax}$ in the pulse for a Ti target (magnetron DRM 400) as a function of the discharge voltage U at different magnetic field strengths (p = 1 Pa Ar, f = 12 Hz, t_{on} = 200 µs). The values in the figure for pulse power density $P_{pulsemax}/A$ of 2.4kW/cm^2 and 4kW/cm^2 correspond to the enlarged data points of the lower and the upper curve, respectively

In the HIPIMS mode, the Ti coating rates are only between 10 to 14% of the coating rates in normal pulse mode at the same average power. This could be confirmed in the reactive mode for TiO_2-films (about 17%, see Tab. 1). Furthermore, it was found that the thermal substrate load per unit layer thickness was comparable to that of the PMS process. The temperature of glass substrates started at room temperature and raised to about 190°C±5°C for normal pulse mode and HIPIMS mode after depositing 1 µm Ti-layer. The deposition time in the HIPIMS mode was by a factor of about 7 longer than in the unipolar pulse mode. As a consequence of this, the substrate temperature would be much higher in the HIPIMS mode if the deposition rate could be improved using higher power level or more process stations. This needs be considered in the case of temperature sensitive substrates.

The following results were achieved from experiments in reactive mode with a Ti target in argon-oxygen atmosphere. In HIPIMS mode, the reactive process showed hysteresis, similar to the normal PMS process. It has been operated in the transition mode using optical plasma emission spectrometry as described below.

The maximum achievable coating rate for stoichiometric TiO_2 in the HIPIMS mode is significantly lower than that of normal PMS. It is only 5% (fully reactive) to 17% (highest rate for stoichiometric films in the transition mode) of the deposition rate in normal pulse mode. The TiO_2 layers deposited in the HIPIMS mode are much finer grained than those deposited in the normal pulse mode. Starting from the substrate, they grow first in amorphous phase and then in the crystalline rutile form. Similar behavior was observed for TiO_2 layers deposited in normal bipolar pulse mode or in pulse packet mode [6]. The TiO_2 layers deposited in the HIPIMS mode have, however, a higher hardness of up to 20 GPa compared to a maximum of 16 GPa for those deposited in pulse packet mode. They also have a somewhat higher refractive index n than the layers deposited in normal pulse mode [7].

Table 1. Layer properties for different pulse modes and different reactive working points for TiO_2 deposition

unipolar pulse mode	working point	layer thickness [nm]	deposition rate [nm/min]	hardness [GPa]	n @ 550 nm	k @550 nm
normal	stoichiometric	560	110.0	~7.0	2.480	$< 10^{-5}$
HIPIMS	substoichiometric	848	28.0	20.0	2.552	$4.70 \cdot 10^{-3}$
HIPIMS	fully reactive	180	6.0	16.5	2.514	$4.20 \cdot 10^{-3}$
HIPIMS	stoichiometric (transition mode)	675	18.4	19.1	2.565	$2.95 \cdot 10^{-3}$

3.2. TiO_2 layers deposited with DMS 500 (system 2)

The experiments with DMS 500 were carried out to investigate the properties of the process and of the films during gradual transition between normal pulse mode and HIPIMS mode. By varying the duty cycle between 90% and 14% the current densities in the pulse changed from 0.2 to 1.2 A/cm^2 (Tab. 2). The value of 0.5 A/cm^2 was reached at a duty cycle of about 33%, i.e. the discharge is in the HIPIMS mode for smaller duty cycle. The optical plasma intensity of different lines was investigated in dependence on duty cycle (Fig. 3) showing a monotonous variation. It is assumed that the reduction of Ar I-line might be due to gas rarefaction effects. The reduction of Ti I-line corresponds to the deposition rate reduction.

Table 2. Duty cycle, frequency and current densities of Ti layers deposited with DMS 500

Duty cycle [%]	90	50	33	20	14
frequency [kHz]	10	5	3.3	2	1.4
current density [A/cm^2]	0.2	0.3	0.55	0.8	1.2

The reactive process was controlled using the plasma control unit S-PCU (Fraunhofer FEP) having closed feedback system for the piezo valve of the oxygen gas inlet. A spectrometer inside S-PCU was used and 2 lines were chosen: Ti 500 nm and O_2 777 nm. The intensity ratio of these two lines was used as control value for the reactive gas flow. By controlling the process in this way, the discharge can be stabilized within any desired working point and stoichiometric TiO_2 layers can be deposited in both normal pulse mode and in HIPIMS mode. Reduced hysteresis was observed for lower duty cycles (Fig. 4), but the hysteresis does not disappear.

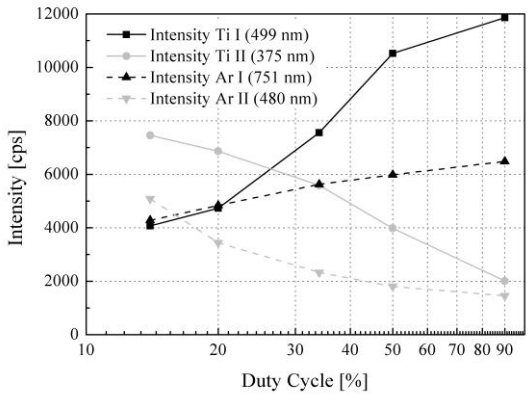


Figure 3. Optical plasma intensity vs. duty cycle for Ar I and II as well as for Ti I and II

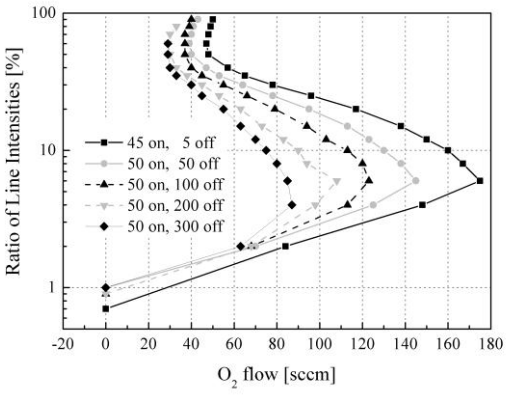


Figure 4. Ratio of line intensities (in %) vs. oxygen flow within the hysteresis region of the reactive sputtering process of TiO_2 for different parameters of duty cycle

Rotating substrates (X5CrNi18.10) were coated with TiO_2 at different duty cycles. At high duty cycle (normal pulse mode) clear facetted anatase crystallites were found (Fig. 5). At small duty cycle a reduction of crystal size and a growing rutile fraction as a second phase with lower roughness were observed.

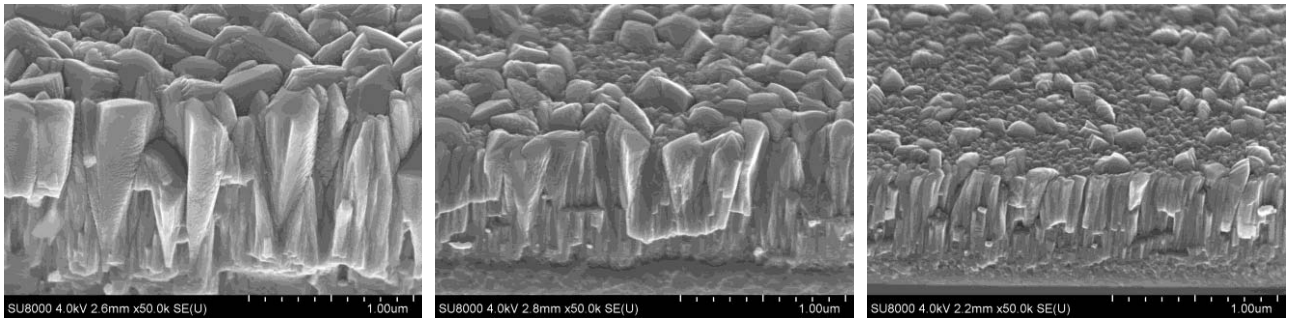


Figure 5 a-c. SEM images of TiO_2-layers at different duty cycle (left: 90%, middle: 34%, right: 14%)

Keeping the total power constant, the deposition rate decreased to about one third at a duty cycle of 14% (Fig. 6). The Ti I-line intensity behaves in the same way representing the number of sputtered Ti atoms in the plasma. The roughness reduces to about 53%, which corresponds to the change of microstructure and apparent roughness in the SEM images. The hardness rises from 8.7 GPa (typical value for anatase) at 90% duty cycle to 16 GPa (typical value for rutile) at 14% duty cycle. The elastic modulus correlates well with the hardness and changes from 160 GPa to 210 GPa, respectively. Furthermore the refractive index increases from 2.35 to 2.65 as a consequence of the growing fraction of rutile phase in the film. Another indication of the reduced anatase fraction is the decreasing photocatalytic activity derived from methylene blue decomposition measurements [to be published elsewhere].

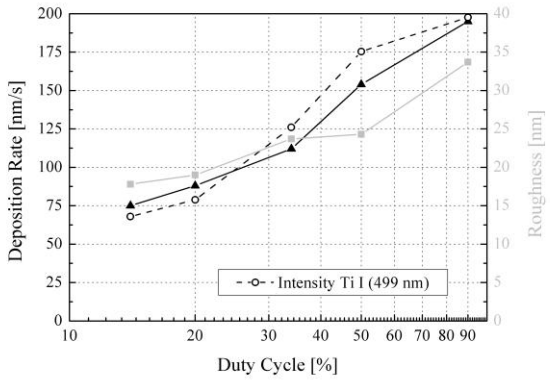


Figure 6. Deposition rate, roughness and Ti I-line intensity vs. duty cycle

4. Summary

The studies on TiO_2 have shown that HIPIMS is a promising technology for achieving layer properties that cannot be achieved using other sputtering techniques. These properties include a higher hardness and fine crystallinity. The disadvantages of the technique are in particular the strongly reduced coating rate at higher power density and the worse process stability. Given the current state of HIPIMS generators, laboratory scale process development should ensue. For the further development of the technology, suitable magnetron sputter sources with a high magnetic field and power supplies with sufficient performance to allow up-scaling of the process are required. This will then enable HIPIMS processes to be developed for industrial applications.

References

[1] Vladimir Kouznetsov, Karol Macak, Jochen M. Schneider, Ulf Helmersson, Ivan Petrov, "A novel pulsed magnetron sputter technique utilizing very high target power densities", Surface and Coatings Technology 122 (1999) 290–293

[2] K. Sarakinos, J. Alami, S. Konstantinidis, "High power pulsed magnetron sputtering: A review on scientific and engineering state of the art", Surface and Coatings Technology 204 (2010) 1661–1684

[3] Ulf Helmersson, Martina Lattemann, Johan Bohlmark, Arutiun P. Ehiasarian,Jon Tomas Gudmundsson: Ionized physical vapor deposition (IPVD), "A review of technology and applications", Thin Solid Films 513 (2006) 1–24

[4] H. Bartzsch, P. Frach, K. Goedicke, Chr. Gottfried, "Different pulse techniques for stationary reactive sputtering with double ring magnetron", Surface and Coatings Technology 120–121 (1999) 723–727

[5] Hagen Bartzsch, Peter Frach, Klaus Goedicke, „Abscheidung optisch, elektrisch und akustisch wirksamer Schichten mit dem Doppel-Ring-Magnetron", Vakuum in Forschung und Praxis 15 (2003) Nr. 3 122–126

[6] O. Zywitzki T. Modes, P. Frach, D. Glöss "Effect of structure and morphology on photocatalytic properties of TiO_2 layers", Surface & Coatings Technology 202 (2008) 2488–2493

[7] M. Vergöhl, S. Bruns,"Properties of TiO_2 Films Deposited by Bipolar Reactive HiPiMS", Conference Proceedings of International Conference on Coatings on Glass ICCG 8, Braunschweig, pp. 301-305, 2010

Crystallinity control of sputtered ZnO films by utilizing buffer layers fabricated via nitrogen mediated crystallization

N. Itagaki*[1,2], K. Oshikawa[1], K. Matsushima[1], I. Suhariadi[1], D. Yamashita[1], H. Seo[1], K. Kamataki[1], G. Uchida[1], K. Koga[1], M. Shiratani[1]

[1]Grad. Sch. of Information Sci. and Electrical Eng., Kyushu Univ., Motooka 744, Nishi-ku, Fukuoka 819-0395, JAPAN;

[2]PRESTO, Japan Sci. and Technol. Agency, 5 Sanbancho, Chiyoda-ku, Tokyo 102-0075, Japan

ABSTRACT

High quality ZnO:Al (AZO) films have been obtained by utilizing buffer layers fabricated via nitrogen mediated crystallization (NMC), where sputtering method is employed for preparation of both buffer layers and AZO films. Introduction of small amount of N_2 ($N_2/(Ar+N_2)$ = 16%) to the sputtering atmosphere of NMC-ZnO buffer layers drastically improves the crystallinity of buffer layers and thus AZO films. The most remarkable effect of the buffer layers is a significant reduction in the resistivity at high base pressure of background gases. The resistivity of conventional AZO films increases from 2.0 mΩ•cm to 70.0 mΩ•cm with increasing the base pressure from 3×10^{-5} Pa to 1×10^{-3} Pa, while the resistivity of AZO films with NMC buffer layers increases from 0.5 mΩ•cm to 2.0 mΩ•cm, where the thickness of AZO film is 88 nm. Furthermore, AZO films with a sheet resistance of 10 Ω/□ and an optical transmittance higher than 80% in a wide wavelength range of 400–1100 nm have been obtained.

Keywords: zinc oxide, transparent conducting oxide, nitrogen mediated crystallization, magnetron sputtering, buffer layer

1. INTRODUCTION

Oxide semiconductors have attracted much attention because of their advantages such as high transparency and wide-ranging conductivity [1, 2]. ZnO is one of the most fascinating oxide with a wide application range. The low electrical resistivity, the high transparency to visible lights, and the material abundance make ZnO a great potential alternative to indium-doped tin oxide (ITO) for transparent conductive oxide (TCO). The resistivity of ZnO-based TCO, however, is higher than that of ITO especially at high base pressure of background gases [3-5]. Since the crystallinity of ZnO films strongly affects both the carrier density and the mobility, fabrication methods of high crystalline ZnO films have been required.

Many efforts have been devoted so far to improve the crystallinity of ZnO films. Introduction of the buffer layers is one of the promising methods to obtain high quality films. Nakamura et al. have studied the effects of low temperature (LT) ZnO homo-buffer layers on the qualities of ZnO films, which were deposited by PLD on c-plane sapphire substrate[6]. In the same way, high quality epitaxial ZnO layers have been obtained at reducing growth temperature by using ultra violet assisted deposition techniques[7].

Recently, we have developed a novel fabrication method of ZnO buffer layers crystallized via nitrogen-atom mediation (NMC) [8-11], which enable us to make high-quality ZnO films, especially when a sputtering method is employed for film preparation. In the case of a conventional sputtering, ZnO is immediately crystallized once it is deposited on a substrate even at room temperature because of its low crystallization temperature. Furthermore, a lot of high energetic species incoming to the substrate enhance high-density and randomly-orientated nucleation at initial stage of deposition, which causes the reduction in grain size and the large crystal mosaics. On the other hand, in the case of NMC method, the nucleation density can be reduced since the adsorbed nitrogen atoms on the growth surface disturb the crystallization of ZnO, as a result, ZnO films with well-aligned crystal orientation and large grain size are obtained.

In this paper, we study the effects of NMC buffer layers on the properties of ZnO:Al (AZO) films, which are discussed with comparison to those of ZnO films fabricated without NMC layers. Furthermore, we report the dependence of electrical properties of AZO films with NMC buffer layers on the base pressure during AZO film deposition.

2. EXPERIMENT

NMC buffer layers were deposited on quartz glass substrates by radio-frequency (RF) magnetron sputtering at 300°C. The used targets were ZnO (2 inches in diameter; purities > 99.99 %) and the applied RF powers were 100 W. Ar-N_2 mixed gas was used and the total pressure was 0.3 Pa. The flow rates of Ar and N_2 were 4.5-24.5 sccm and 0.0-20.0 sccm, respectively. According to X-ray diffraction (XRD) analysis, as-deposited ZnON films were confirmed to have ZnO crystal grains. In this experiment, the thickness of NMC buffer layers was 5 nm.

AZO films were deposited on NMC buffer layers by RF magnetron sputtering with AZO targets (2wt.% Al_2O_3). The used gas was Ar and the total pressure was 0.3 Pa, where the base pressure was varied from 3×10^{-5} Pa to 1×10^{-3} Pa. The substrate temperature was kept at 200°C and no post annealing of AZO was performed. For a comparison, AZO films deposited directly on quartz glass substrates were fabricated under the same deposition conditions as AZO films mentioned above. The crystal structures of the films were examined by XRD and the optical transmittance spectra were measured with UV-Visible spectrophotometer. The electrical properties of AZO films were evaluated by 4 point probe measurements and hall-effect measurements.

3. RESULTS AND DISCUSSION

XRD measurement reveals that all AZO films show a strong peak at 34.4° that corresponds to the (002) plane of ZnO wurtzite structure, indicating that the films are strongly orientated along the c-axis. Here, the film thickness of AZO and NMC buffer layer are 100 nm and 5 nm, respectively. Both the crystal orientation and the grain size of the NMC buffer layers, however, highly depend on the N_2/Ar flow rate ratio. Introduction of small amount of N_2 (N_2/Ar = 4/20.5 sccm) drastically improves the crystallinity of the buffer layers. FWHM of XRD patterns for 2θ-ω and ω scan of (002) plane are 0.25° and 2.6°, being significantly small compared with 0.92° and 3.5° for the buffer layers fabricated without N_2. On the other hand, a further increase in N_2/Ar flow rate ratio deteriorates the crystallinity, because excess N atoms in the films disarrange the crystal structure of ZnO. As a result, AZO films with high crystallinity have been successfully fabricated by utilizing the NMC-buffer layers deposited at N_2/Ar = 4/20.5 sccm. The crystal grain size of 100-nm-thick AZO films on the NMC-buffer layers is 60 nm, which is about 5 times larger than that of conventional AZO films. From these results, we conclude that utilizing NMC buffer layer fabricated at adequate Ar/N_2 flow rate ratio is very promising to obtain well-orientated AZO films with high crystallinity.

The effects of the NMC buffer layers on the electrical properties of AZO films have been also investigated by measuring the resistivity, hall mobility and carrier density of the films. Figure 2 shows the resistivity of 88-nm-thick AZO films prepared on 5-nm-thick buffer layers, which is plotted against the base pressure during AZO film deposition. The deposition rates of AZO films were 21.0 nm/min and 26.5/min, which were controlled by changing the RF power. For all base pressures, the resistivity of AZO films with NMC-ZnO buffer layer is lower than the films prepared

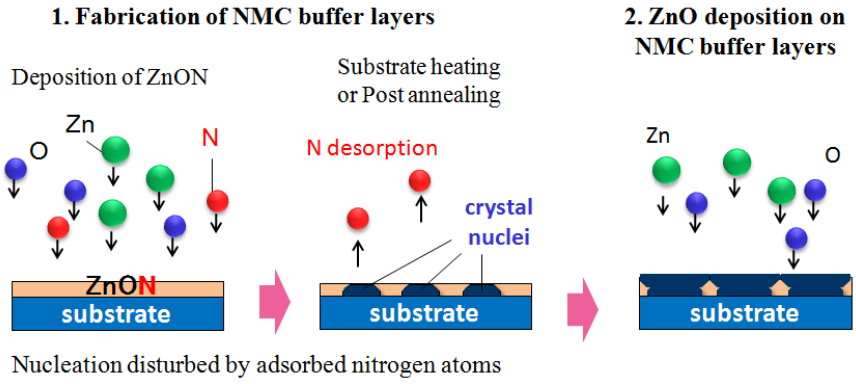


Figure 1. Flow chart of our fabrication method utilizing buffer layers prepared by NMC method.

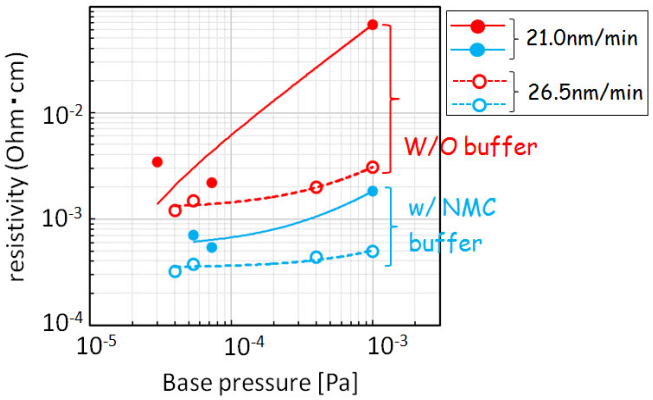


Figure 2. Resistivity of AZO films prepared on NMC buffer layers with a thickness of 5 nm as a function of base pressure during AZO deposition. The deposition rates of AZO films were 21.0 nm/min and 26.5 nm/min, which were controlled by changing the RF power.

by conventional sputtering without NMC layer. It was found from the hall-effect measurement that the decrease in the resistivity by using buffer layer is attributed to increase in both the carrier mobility and the carrier density of the films. The most remarkable effect of NMC-ZnO buffer layers is a significant reduction in the resistivity at high base pressure. As shown in Fig. 2, the resistivity of AZO films fabricated by conventional sputtering increases substantially with increasing the base pressure, while the resistivity of AZO films with NMC buffer layers does not change much. In the case of conventional sputtering, the excessive nucleation with various orientations is induced by high energy of impingement of the sputtered species and/or the fragments from plasma at the initial stage of the deposition. As a result, the AZO films have small grain size and low degree of c-axis orientation. Furthermore, it has been reported that the residual water vapor in background gases deteriorates the crystallinity of transparent-conducting-oxide films, leading to a decrease in the grain size, which is caused by the absorption of H_2O molecules at the growing film surface[5,13]. This decrease in the grain size results in low carrier mobility of AZO films. The residual water also induces the decrease in the oxygen vacancies that generate electron carriers via water oxidation of AZO films[5]. These are the reasons why the resistivity is high and increases much with increasing the base pressure in the case of conventional sputtering. On the other hand, in the case of NMC method, the excessive nucleation can be suppressed and the films with high crystallinity are grown from the early stage of deposition. As a result, the crystallinity of AZO films deposited on the NMC buffer layers is high independent of the base pressure and thus low resistivity is observed even at high base pressure. Since the dopant-activation efficiency depends on the degree of c-axis orientation in AZO films, the significant improvement of resistivity at high base pressure can be also accompanied by an enhancement in the orientation degree of the AZO films by using the NMC-ZnO buffer layers[14]. As a result, highly conducting AZO films with a small thickness, that is, high transparency, have been obtained. Figure 5 shows the optical transmittance AZO films with a sheet resistance of 10 Ω/□. Here, the film thickness of AZO films with and without NMC-ZnO buffer layers is 400 nm and 1000 nm, respectively. We observed that the films with NMC-ZnO buffer layers has high transmittance (>80%) in a wide wavelength range of 400–1100 nm.

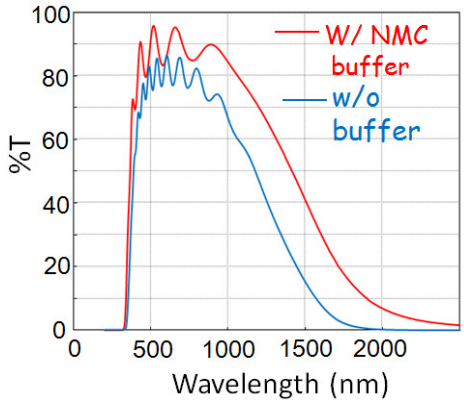


Figure 3. Optical transmittance of AZO film with a sheet resistance of 10 Ω/□. The film thickness of AZO films with and without NMC-ZnO buffer layers is 400 nm and 1000 nm, respectively.

4. CONCLUSIONS

Effects of NMC-ZnO buffer layers on the properties of AZO films have been studied, where sputtering method is employed for preparation of both buffer layers and AZO films. As a result, high quality AZO films have been obtained by utilizing NMC buffer layers. The crystal grain size of AZO films with NMC-buffer layers is about 3 times larger than that of conventional films, which is considered to be due to the low nuclei density of NMC-buffer layers. The most remarkable effect of NMC-ZnO buffer layers is a significant reduction in the resistivity at high base pressure. The resistivity of conventional AZO films increases from 2.0 mΩ•cm to 70.0 mΩ•cm with increasing the base pressure from 3×10^{-5} Pa to 1×10^{-3}

Pa, while the resistivity of AZO films with NMC buffer layers increases from 0.5 mΩ•cm to 2.0 mΩ•cm, where the thickness of AZO film is 88 nm. Furthermore, AZO films with a sheet resistance of 10 Ω/□ and an optical transmittance higher than 80% in a wide wavelength range of 400–1100 nm have been obtained. From these results, we conclude that our method described here is full of promise for fabrication of ZnO-based transparent conducting films.

REFERENCES

[1] Kumomi, H., Yaginuma, S., Omura, H., Goyal, A., Sato, A., Watanabe, M., Shimada, M., Kaji, N., Takahashi, K., Ofuji, M., Watanabe, T., Itagaki, N., Shimizu, H., Abe, K., Tateishi, Y., Yabuta, H., Iwasaki, T., Hayashi, R., Aiba, T., and Sano, M., "Materials, Devices, and Circuits of Transparent Amorphous-Oxide Semiconductor", J. Display Technol. **5**(12), 531-540 (2009).

[2] Itagaki, N., Iwasaki, T., Kumomi, H., Den, T., Nomura, K., Kamiya, T. and Hosono, H. "Zn–In–O based thin-film transistors: Compositional dependence", phys. stat. sol. (a) **205** (8), 1915-1919 (2008).

[3] Imanishi, Y., Taguchi, M., and Onisawa, K., "Effect of sublayer surface treatments on ZnO transparent conductive oxides using dc magnetron sputtering", Thin Solid Films **518** (11), 2945-2948 (2010).

[4] Minami, T., and Miyata, T., "Present status and future prospects for development of non- or reduced-indium transparent conducting oxide thin films", Thin Solid Films **517** (4), 1474-1477 (2008).

[5] Kim, D. K., and Kim, H. B., "Dependence of the properties of sputter deposited Al-doped ZnO thin films on base pressure", J. Alloys Compd. **522**, 69-73 (2012).

[6] Nakamura, T., Yamada, Y., Kusumori, T., Minoura, H., Muto, H., "Improvement in the crystallinity of ZnO thin films by introduction of a buffer layer", Thin Solid Films **411**(1), 60-64 (2002).

[7] Craciun, V., Perriere, J., Bassim, N., Singh, R. K., Craciun, D., Spear, J., "Low-temperature growth of epitaxial ZnO films on (001) sapphire by Ultraviolet-Assisted Pulsed Laser Deposition", Appl. Phys. **A69** (7), S531-S533 (1999).

[8] Itagaki, N., Kuwahara, K., Nakahara, K., Yamashita, D., Uchida, G., Koga, K., and Shiratani, M., "Highly Conducting and Very Thin ZnO:Al Films with ZnO Buffer Layer Fabricated by Solid Phase Crystallization from Amorphous Phase", Appl. Phys. Express **4** (1), 011101 (2011).

[9] Itagaki, N., "Novel fabrication method for oxide semiconductors via atomic-additive mediated crystallization", Proc. IEEE Region 10, 998-1001(2010).

[10] Itagaki, N., and Kuwahara, K., "Novel fabrication method of ZnO films utilizing solid-phase crystallized seed layers", Proc. MRS **1315**, mm02-09 (2011).

[11] Kuwahara, K., Itagaki, N., Nakahara, K., Yamashita, D., Uchida, G., Kamataki, K., Koga, K., and Shiratani M., "High quality epitaxial ZnO films grown on solid-phase crystallized buffer layers", Thin Solid Films **520**, 4674-4677 (2012).

[12] Itagaki, N., Kuwahara, K., Matsushima, and K., Oshikawa, K., "Novel fabrication method for ZnO films via nitrogen-mediated crystallization", Proc. SPIE photonics west **8263**, 826306 (2012).

[13] Song, P.K., Watanabe, M., Kon, M., Mitsui, A., and Shigesato, Y., "Electrical and optical properties of gallium-doped zinc oxide films deposited by dc magnetron sputtering", Thin Solid Films **411**, 82–86 (2002).

[14] Lin, K. M., Chen, H. C., Chen, Y. Y., and Chou, K. Y., "Influences of preferred orientation growth on electrical properties of ZnO:Al films by sol–gel method", J. Sol–Gel Sci. Technol. **55**(3), 369-276 (2010).

The Effect of Nitrogen Partial Pressure and Substrate Temperature on the Characteristics of Photocatalytic N:TiO_2 Thin Films deposited by Filtered Vacuum Arc Deposition

E. Goldenberg[*1], L. Burstein[2], I. Chayun-Zucker[1], R. Avni[1], R.L Boxman[1]

[1]*Electrical Discharge and Plasma Laboratory, Tel Aviv University, POB 39040, Tel Aviv 69978, Israel*

[2]*Wolfson Applied Materials Research Center, Tel Aviv University, POB 39040, Tel Aviv 69978, Israel*

[*] Corresponding author. Tel: +972-3-640-8176 Fax: +972-3-641-0189 E-mail:edacetinorgu@gmail.com

Abstract

Nitrogen doped Titanium Oxide (N:TiO_2) thin films were deposited using filtered vacuum arc deposition, and their structure, composition and morphology were studied as functions of the total pressure, N_2/O_2 gas ratio and the substrate temperature. The film structure, surface morphology, and composition were determined by XRD, AFM and XPS. The optical characterization of the films was determined with spectrophotomery and ex-situ variable angle spectroscopic ellipsometry (VASE). In addition to the effects of other deposition conditions such as arc current, total deposition pressure, and post-deposition annealing on the film characteristics, photocatalytic activity was also determined as a function of deposition parameters and results were discussed.

Keywords: Titanium Oxide, Photocatalytic Coatings, FVAD, Structure, Optical Characterization

Introduction

Most photocatalytic materials respond to only ultra-violet (UV) radiation. A major challenge is to increase the photocatalytic spectral range to include visible (VIS) light, which composes the largest part of solar radiation, since only a small percent of solar energy (5-7%) is in the UV region [1]. In the recent years, Titanium dioxide (TiO_2) as a photocatalyst has been practically applied in hospitals and houses [2]. TiO_2 which has a band gap of 3.2 eV (anatase phase) is superior to other semiconductor oxides due to its high chemical stability, low cost and non-toxicity [3,4]. However, un-doped TiO_2 shows photocatalytic activity only under UV light irradiation (λ<384 nm) [2,5].

One of the approaches to activate photocatalysis with VIS- light is to shift the optical band gap of TiO_2 into the VIS spectrum by doping. Because it is non-toxic, N:TiO_2 is very attractive [6-8]. In recent years, TiO_2 and N:TiO_2 thin films have been deposited by un-filtered and filtered vacuum arc deposition (FVAD), utilizing the relatively high deposition rate of this method (up to ~10 nm/s), producing thin films characterized by high adhesion, high density and stability. The published work on FVAD of TiO_2 thin films focused mainly on their structural, compositional and optical properties, and their correlation with deposition parameters (arc current, oxygen pressure and substrate bias and substrate temperature). However, the effects of deposition parameters and nitrogen doping on the composition, structure, morphology, and photocatalytic activity of FVAD N:TiO_2 thin films has not been reported. Upgrading TiO_2 films for VIS–light driven photocatalytic application motivates interest in the growth mechanism and requires more detailed knowledge of the film structure and composition.

The objective of the present work was to determine of the effects of nitrogen partial pressure and substrate temperature on the

structure, composition, morphology, and the optical properties of FVAD N:TiO_2 thin films for its future application as a VIS-light activated photocatalyst.

Experimental Details

A Ti cathode was used to deposit N:TiO_2 films by FVAD. The deposition system included a vacuum arc plasma source, and a magnetic quarter-torus macro-particle filter. This system was previously described by Ben-Shalom *et al* [9] and Kaplan *et al* [10]. The arc current was 150 or 200 A, and the total pressure in the deposition chamber was 1.06 or 1.33 Pa. The N_2/N_2+O_2 gas ratio was varied between experiments from 0 to 69 %. Film deposition times were 150, 180 or 240 s. The films were deposited on 25×76×1 mm glass microscope slide substrates at room temperature (RT), 300 or 500 ^oC. All of the films were annealed in a nitrogen (N_2) atmosphere at 400±2 ^oC for 1 h (preceded by a 20 min heating period and followed by a 40 min cooling period).

The PCA was evaluated by measuring the decomposition of a model pollutant known as Methylene Blue (MB), in an aqueous solution on the basis of the decomposition rate of MB under light irradiation for up to 4 h at the peak absorption of MB at 664 nm. The results were presented as percentage removal (100×(Co-Ct)/Co) where Co and Ct are the concentrations initially and after time t of irradiation respectively. The effect of deposition parameters on photocatalytic activity was evaluated.

Results

Film Microstructure, Morphology and Composition

The XRD patterns of the TiO_2 thin films deposited in a pure oxygen environment indicated that films were polycrystalline in the anatase phase, while films deposited in an atmosphere in which the N_2 fraction was greater than 9% were amorphous, for substrate temperatures up to 500°C. Annealing at 400^oC in N_2 for one hour generated polycrystalline films with anatase phase independent of %N_2 fraction during deposition. The grain size of the annealed films deposited with some N_2 in the deposition atmosphere decreased from 64 to 44 nm, when the N_2 fraction was increased from 9% to 50%. Increase of the average grain size with the total gas pressure, substrate temperature, and by annealing can be attributed to grain growth and improved crystallinity.

AFM analysis of films deposited in a 41% N_2 atmosphere indicated that the surface roughness increased from 0.5 up to 3.2 nm when the substrate temperature was increased from RT to 500°C, and it was higher for films deposited at 23% N_2 partial pressure (~5.7 nm) compared to films deposited on RT substrates at 23% N_2. In addition, the average grain size of the films increased with substrate temperature and with annealing, up to 54.2 nm and 36.3 nm, respectively. Furthermore, the surface roughness decreased with the increased N_2%, except for films deposited at 200 A arc current and which were also crystalline. This decrease might be explained by the amorphous phase formation with increased N_2% and also the increase in ion flux and plasma density which plays a key role also in surface modification of TiO_2 films deposited by FVAD.

XPS analysis indicated that all films deposited in 0% N_2 were stoichiometric TiO_2. N content in the films increased with $\%N_2$ in the deposition atmosphere, however the N-content in the film, 1 3 at.% N, was much less than that in the gas mixture (9-69%N_2). Annealing decreased the N-content in these films to <1 at.%. In addition, the XPS revealed that all N:TiO_2 films had two main N 1s components, at 396-397 eV and at 399-400 eV, associated with substitutional and interstitial nitrogen, respectively. The N 1s peaks around 396 and 397 eV might indicate that there are multiple nitrogen states connected to these peaks, and the binding energy of N 1s at ~397 eV is associated with Ti-N bonding and indicates a substitution of O atoms by N atoms.

Film Optical Properties

Optical transmission spectroscopy and ellipsometry indicated that the average film transmission (T%) was approximately 80% in the visible spectrum for films deposited at lower N_2 partial pressures (<41%), and it decreased to ~50% for higher $\%N_2$ (see Fig.1).

The deposition rate varied between 0.8 and 4 nm/s. The refractive indices of the films were in the range 2.48 - 2.78, and the extinction coefficients were ~10^{-3} - 0.5. The absorption edge of the films shifted to longer wavelengths with increased substrate temperature and $\%N_2$, from ~380 nm up to ~485 nm for films deposited with 41% N_2 and a substrate temperature of 500°C.

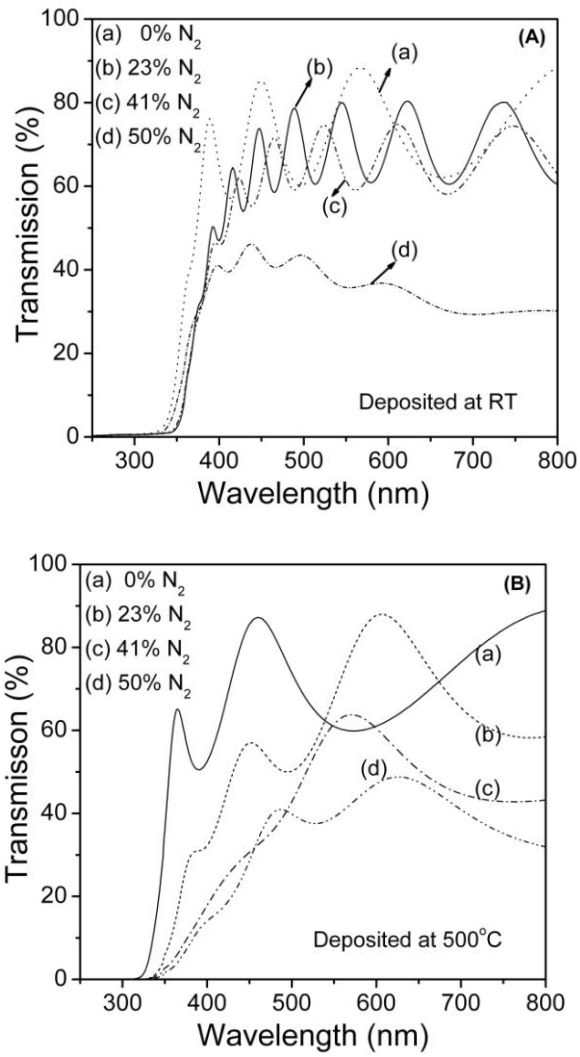


Figure 1. Typical transmission spectra for N:TiO_2 samples deposited at: a) RT and b) 500°C substrate temperatures for different nitrogen partial pressures.

Photocatalytic Properties

MB could be successfully degraded by N:TiO_2 films at RT. The arc current, total gas pressure, deposition time and $\%N_2$ had a minor effect on the PCA, but increasing the substrate temperature from RT to 500 °C increased the MB removal from 20% to 35% removal and the post-deposition annealing significantly increased the MB removal from 20% to 50% removal (see Figs. 2 and 3). The increased MB removal in annealed films is attributed to crystallization of the thin films in the anatase phase. PCA was found to be correlated with the

396 397 eV to 399 400 eV peak intensity ratio. The choice of substrate significantly affected both MB adsorption and PCA.

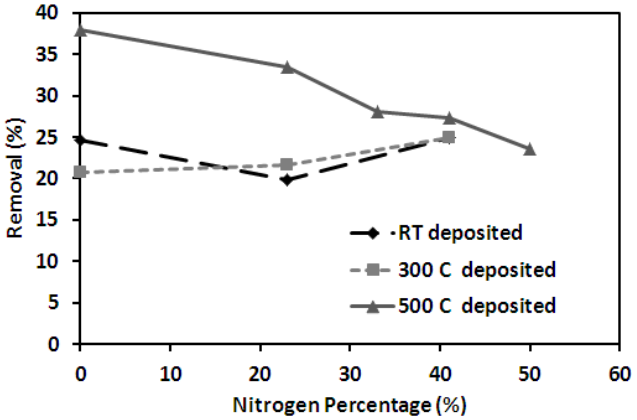


Figure 2. Removal percentage as a function of $\%N_2$ for films deposited at 1.06 Pa, 150 A, at various substrate temperatures

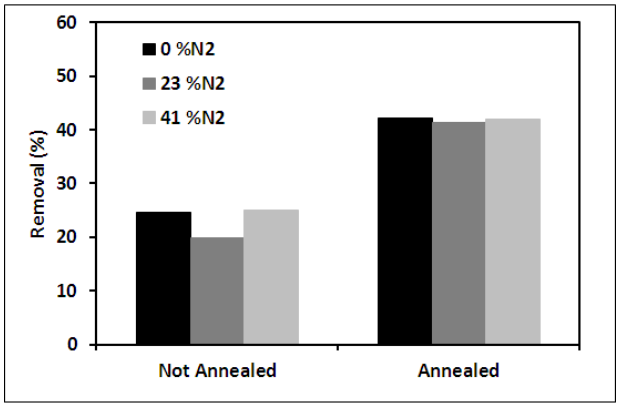


Figure 3. Removal percentage for films deposited at RT, 1.06 Pa, 150 A, at various $\%N_2$ with and without annealing in a nitrogen environment for one hour at 400°C

Conclusions

As-deposited TiO_2 thin films were crystalline, the addition of nitrogen with various percentages of the total gas pressure during the deposition produced amorphous N:TiO_2 thin films. Annealing them at 400°C for 1 h in N_2 transformed them to polycrystalline. The crystallinity and the grain size of these films increased with annealing. As-deposited N:TiO_2 films had 1-3 at.$\%N_2$ while annealing decreased the $\%N_2$ to <1 at.$\%N_2$. The O:Ti ratio in the films varied between 2.2 to 2.7. Two main N 1s XPS peaks were observed at ~396-397 eV and ~399-400 eV for all N:TiO_2 samples. The intensity ratio of the N 1s peak at 396-397 eV to N 1s peak at 399-400 eV increased with the total pressure, $\%N_2$ and by the annealing. The absorption edge of the deposited films shifted to longer wavelengths in the VIS spectrum with $\%N_2$ >23%, and the strongest shift up to 490 nm was observed for films deposited on 500°C substrates.

In order to achieve high PCA, the photocatalytic N:TiO_2 thin film should be crystalline with large grain size and surface roughness and high 396-397 eV to 399 400 eV XPS nitrogen peak intensity ratio.

References

[1] D. Reyes-Coronado, G. Rodriguez-Gattorno, M. E. Espinosa-Pesqueira, C. Cab, R. de Coss, G. Oskam, Nanotechnology 19(14) (2008) 145605.
[2] A. Fujishima, X. Zhang, C. R. Chimie 9 (2006) 750–760
[3] S. Rehman, R. Ullah, A. M. Butt, N. D. Gohar, J. Hazard. Mater. 170 (2009) 560.
[4] M. A. Fox and M. Dulay, Chem. Rev. 83 (1995) 341357.
[5] K. Hashimoto, H. Irie, A. Fujishima, Jpn. J. Appl. Phys., 44(12) (2005) 8269
[6] J. Zhang, Y. Wu, M. Xing, S. A. K. Leghari, S. Sajjad, Energy Environ. Sci. 3 (2010) 715
[7] N. Serpone, J. Phys. Chem. B 110 (2006) 24287-24293
[8] K. Balasubramanian, X. F. Han, K. H. Guenther, Appl. Opt. 32(28) (1993) 5594.
[9] A. Ben-Shalom, L. Kaplan, R. L. Boxman, S. Goldsmith, M. Nathan, Thin Solid Films 236 (1993) 20.
[10] L. Kaplan, I. Rusman, R. L. Boxman, S. Goldsmith, M. Nathan, E. Ben-Jacob, Thin Solid Films 290-291 (1996) 355.

Effect of Xe^+ ion bombardment induced patterns in stainless steel on plasma nitriding processes.

S. Cucatti[1], E.A. Ochoa[2], M. Morales[1], R. Droppa Jr[3], J. Garcia[4], H.C. Pinto[5], L.F. Zagonel[6], D. Wisnivesky[7], F. Alvarez[1]

[1] Instituto de Física, UNICAMP, Campinas, Brazil [2] Departamento de Física, PUCRJ, Rio de Janeiro, Brazil [3] Universidade Federal do ABC, UFABC, Santo André, SP, Brazil [4] Sandvik Machining Solutions, Stockholm, Sweden [5] Escola de Engenharia de São Carlos, EESC., USP, São Carlos, SP, Brazil [6] Brazilian Synchrotron Light Laboratory, LNLS, Campinas, SP, Brazil [7] Plasma-LIITS, Equipamentos e Processos, Campinas, SP, Brazil

Abstract

The texturing of surfaces is an important method applied in various technological areas of research. Much of the current interest on surface modifications stems from the possibility of obtaining special optical, magnetic, tribological, and mechanical properties in a variety of materials. The texturization of steel surface by ionic bombardment (atomic attrition) is an interesting route to modify plasma nitriding process. The observed changes in plasma nitriding are attributed to several causes such as increasing surface nitrogen retention, stress, and creation of lattice defects, altogether improving nitrogen diffusion.[1] In this paper we report the effect of Xe^+ ion bombardment on the surface of the steel (SS 316L and AISI 4140). The bombardment effect on plasma pulsed nitriding process is also reported.

Experimental

Rectangular samples of 20x10 mm and 2 mm thick, from the same source of SS 316L (C: <0.08, Si: <0.5 P: 0.05, S: 0.03, Mn: 1.6, Mo: 2.1, Ni: 12.0, Cr: 17.0, Fe: balanced in wt. %) were study. The samples were mirror polished using standard metallurgical techniques. The Xe^+ ion bombardment was performed at room temperature, during 30 minutes using a Kaufman source 3 cm diameter beam. Details of the apparatus are described elsewhere.[2] The ion beam energy and current density were fixed at 1 keV and 0.37mA/cm^2, respectively. According with TRIM ion bombarding simulations, the stopping distance of the ions is between ~11 to 18 Å.[1,3] The background chamber pressure is ~10^{-7} mbar, and the working pressure during Xe^+ bombardment (1.40±0,02)x10^{-3} mbar. Five impinging ion bombardment angles (θ = 0º, 15º, 30º, 45º and 60º) were selected for the study. Samples of AISI 4140 steel (C: 0.4, Si:0.25, P:0.04, S:0.04, Mn: 0,85, Mo: 0.20, Cr: 1, Fe: balanced in w%) were also studied (20x10 mm, 3 mm thick, mirror polished). These samples were partially covered with a silicon wafer during the pre-bombardment treatment, i.e., the screened part of the sample was not bombarded and the other part suffered the texturization. Afterwards, these samples were 20 hs nitrided in a commercial pulsed plasma vacuum furnace (Plasma-LIITS, Campinas São Paulo, Brazil) at 380ºC, ~1.2 Torr chamber pressure, gaseous mixture of nitrogen and hydrogen (20% = $[N_2]/[H_2+N_2]$). Therefore, the two regions (i.e., the pre- and not bombarded parts of the sample) few millimeters apart were analyzed to study the effect on nitriding produced by the initial state of the surface.

Results and discussion

II.1. Bombarding effect on the material surface

As reported for other authors, the analysis of images obtained by scanning electron microscopy (SEM-FEG) and atomic force microscopy (AFM) show that the noble gases ion bombardment evidenced the crystalline grains and stimulated the formation of quite regular patterns. In metals, these patterns depend on the crystalline orientation of the grains rather that the direction of the ion beams (Figures 1, 2). This behavior is explained by the roughening instability model due to Ehrlich-Schwoebel diffusion barriers in metal.[4] Roughly speaking, the regular pattern stems from essentially two mechanisms inducing surface instability. The first one is related to the surface curvature dependence of the ion sputtering and the second one is due to the presence of an energy barrier to diffusing adatoms to descend step edges.

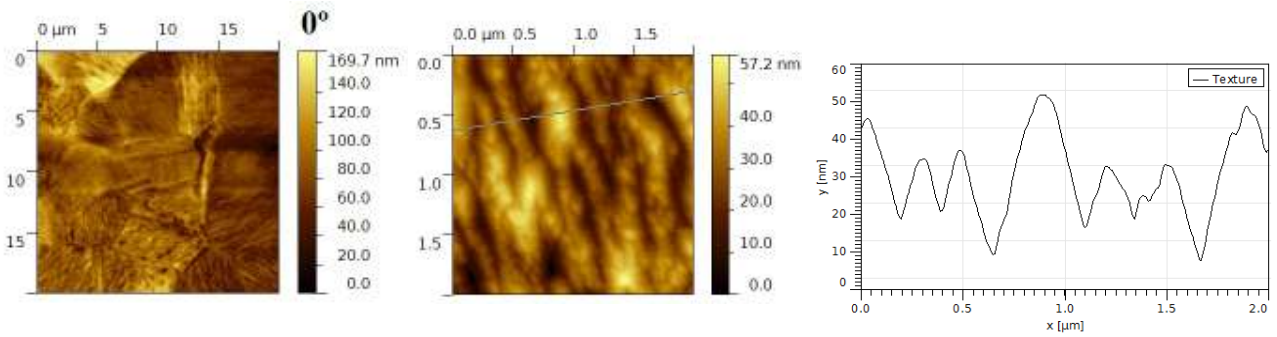


Figure 1: AFM pictures from SS316 of the perpendicularly bombarded sample (1 keV). (a) an overview of several grains with different patterns orientations; (b) grain pattern detail; (c) profile along the line indicated in (b).

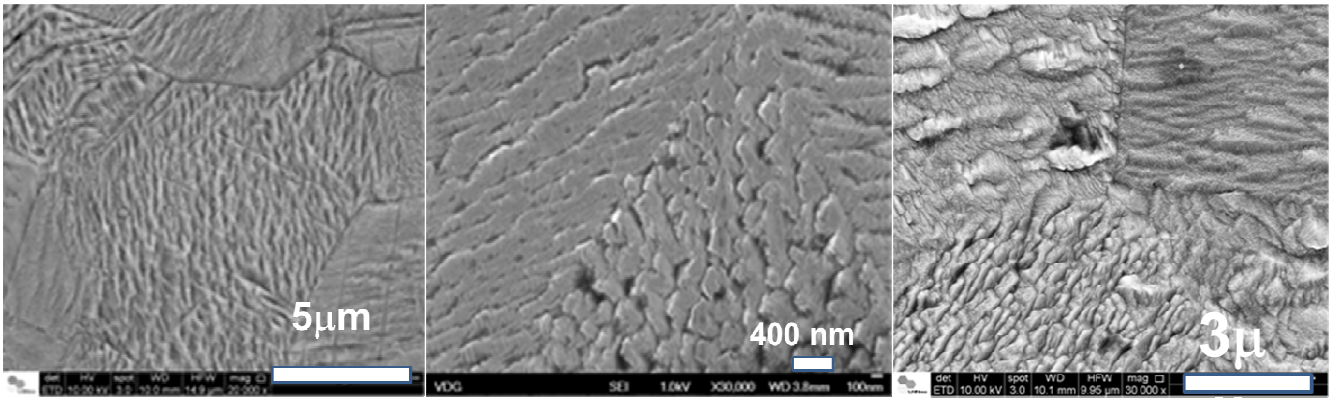


Figure 2: SEM-FEG images from SS316 a different ion beam impinging angles (1 keV**):** (a) perpendicularly; (b) 30º; (c) 60º.

Figure 2 shows the micrographs corresponding to bombarded samples at different magnifications and incident bombarding angles. For limitation of space only a selected group of pictures are displayed. The varieties of patterns and grains borders evidenced by the ionic bombarding are vividly illustrated in the pictures. Figure 3 shows the RMS roughness vs. impinging ion beam angle measured along several grains of the studied samples. The increasing slope of the curve on the incident ion beam impinging angles is related with the sputtering yield (Figure 3). In order to obtain information about the residual stress induced by the bombardment treatment, grazing X-ray diffraction (GIXD) were performed at θ = 0.5º, 1º and 5º incident angles corresponding to 0.5, 1 and 4.5 µm depth penetration of the radiation, respectively. As shown in Figure 4 left, the austenitic stainless steel SS316L studied samples show a γ(220) preferred orientation. The shifting of the γ(111) reflection on depth in the pristine sample stems from polishing procedure and is indicative of compressive stress. Also, the α (110) reflection is present only at the surface and disappears after the bombardment

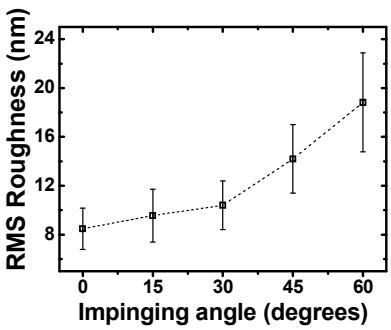


Figure 3: RMS roughness obtained in the studied samples.

(Figure 4, middle). The origin of this subtle thin phase is uncertain but probably comes from the polishing procedure. The ion bombarding modify both the positions and width of the γ (111) reflection peak, indicating stress and disorder, respectively. These effects are a consequence of the energy transferred by the projectile (knock-on) and the occupancy of small spaces by the massive Xe atoms (misfitting).[1,5,6,7] Figure 4, right shows the peak position shifts and width corresponding to the (111) reflection as a function of the sample depth. As noted, the peak position is changing a little bit. On the other hand, the width of the lines is wider suggesting an increasing disorder up to ~ 5 μm depth.

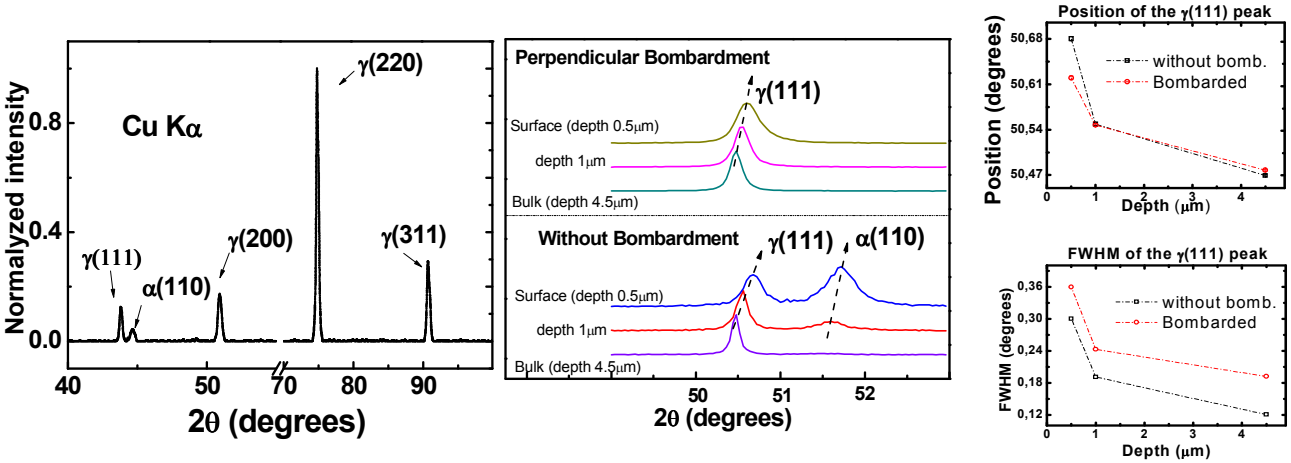


Figure 4: Left: X-ray diffraction of the SS316L sample. Middle: pristine sample and bombarded sample at three x-ray angles. Right: Peak and width evolution as a function of depth.

II.2. Effect of bombarding on pulsed plasma nitriding process

In this section we shall discuss the influence of the texture and related stress generated in the material by the ion bombardment on the plasma nitriding process. As explained in section II, the samples were prepared by partially screening the material surface during bombardment pretreatment in such a way that only a portion of the sample is texturized, as it is schematically indicated in Figure 5, top. After nitriding, a cross-section sample was sliced, mirror polished, attacked with Nital solution (5%) was studied, and its morphology scrutiny by electron microscopy (SEM-FEG, Figure 5, bottom).

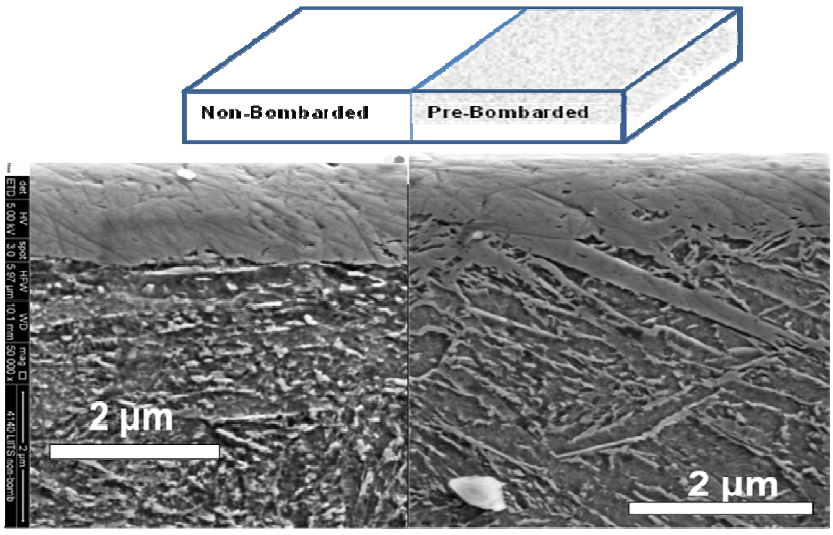


Figure 5. Top: in order to guarantee exactly equal starting condition, the sample left side was screened during the Xe^+ bombarding preparation, as schematically indicated in the sketch before nitriding. Bottom: SEM-FEG images of nitrided

sample after chemical etching (Nital Solution). Bottom left (right): SEM cross section micrograph of the non (pre) bombarded and posterior nitrided sample.

As observed in the micrographs, the microstructure nitride region is well different in the two regions of the studied sample. The diffusion region in the non-pre-bombarded sample shows fragmented and discontinues small nitride particles precipitates. On the other hand, the pre-bombarded region of the sample shows longer shaped needles extending few microns. This effect suggests that the bombardment is creating channels where nitrogen can easily diffuse for relative long distance, i.e., an effective larger nitrogen diffusion coefficient allows nitrogen moving faster into the material. Also, the increasing area due to the texturization is probably increasing nitrogen retention on the surface. The thicker white layer observed in the no pre-bombarded region of the sample is probably due to same reason, i.e., a smaller diffusion coefficient in this part of the sample result in a piling up of nitrogen at the surface of the material surface and consequently, a thicker white layer is formed. Nevertheless, more work is necessary in order to confirm this hypothesis.

II.3. Conclusions

The effect of the Xe^+ ion beam bombardment incident angle on the surface texture and strain of the surface of SS316L steel is reported. The generation of characteristic patterns depends on the crystalline orientation of the constitutive grains of the steel. The heavy ion bombardment induces effects at distance orders of magnitude larger than the stopping region of the projectiles. Plasma nitriding experiments show that the pre-bombarded samples present a peculiar microstructure forming long nitrides needles probably due to the presence of diffusion channels. On the contrary, the non-pre-bombarded samples show small, fragmented precipitates suggesting a smaller effective diffusion coefficient.

Acknowledgements

This work is part of the Master degrees requirements of S.C. The authors are grateful to C. Piacenti for technical help. Part of this work was supported by FAPESP, project 05/53926-1. SC is a FAPESP fellow. FA and EAO are CNPq fellows. The DRX were performed at the Brazilian Synchrotron Light Laboratory (LNLS).

References

[1] E. A. Ochoa, C. A. Figueroa, T. Czewiec, and F. Alvarez, Appl. Phys. Lett. **88**, 254109 (2006)
[2] P. Hammer, N. M. Victoria, and F. Alvarez, J. Vac. Sci. Technol. A **16**, 2941 (1998)
[3] J.P.B. Biersack, G. L. Haggmark, Nucl. Instrum. Methods 174 (1980) 257.
[4] See W. L. Chana and E. Chason, J. of Applied Phys.**101** (121301) 2007 and references there in.
[5] C.A Davis, Thin Sol. Films 226. 30 (1993)
[6] Seitz and Koelher, Sol. Stat. Phys., AP, 2, 1956
[7] J.D.Kamminga,Th.H. de Keijser, and R. Delhez, J. Appl. Phys., 88, 11, 6332 (2000)

Investigations on the active screen plasma nitriding process

K. Börner[1], I. Burlacov[1], H.-J. Spies[1], H. Biermann[1], S. Hamann[2], J. Röpcke[2]

[1] TU Bergakademie Freiberg, Institute of Materials Engineering, Gustav-Zeuner-Str.5, 09599 Freiberg, Germany

[2] INP Greifswald, Felix-Hausdorff-Str. 2, 17489 Greifswald, Germany

Corresponding author: boerner@ww.tu-freiberg.de

Abstract

This study presents the mechanism of nitrogen transfer in a large scale active screen plasma nitriding (ASPN) unit. The active screen provides a homogeneous temperature distribution within the workload as well as an arcing tendency is reduced, since the plasma is moved from the treated work pieces to the active screen. In order to study the mechanisms in detail, plasma diagnostics is necessary. The applied diagnostic methods for analyses of the excited process gas synthesised by the active screen include mass spectrometry and infrared diode laser spectroscopy (TDLAS). Together with a metallurgical characterisation of nitrided steels a better understanding of the chemical phenomena in the N_2-H_2 plasmas is achieved. Various N_2/H_2 gas mixtures and variable bias activation powers at the pressure of 200 Pa were investigated. It was found that even during heating up in nitrogen free process gas exited nitrogen (atomic or molecular) releases from the active screen. Infrared diode laser spectroscopy has been used as a diagnostic methode to measure the concentrations of the stable NH_3 molecules downstream the plasma source. The ammonia production turns out to depend on the mixtures of N_2-H_2 and the current input of the bias activation. The results are discussed with the plasma parameters measured by the electrostatic probe. Thus, a contribution to the interpretation of the mass transfer in ASPN process has been realised.

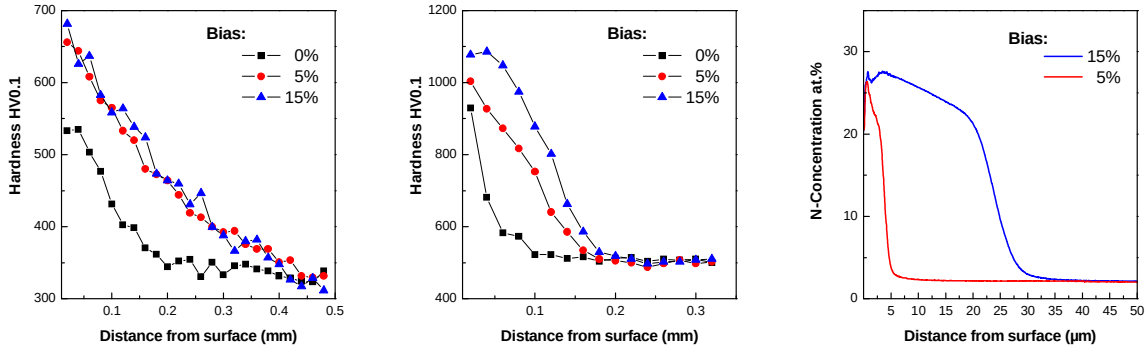
Experimental

In the presented study a large scale active screen plasma nitriding (ASPN) unit is investigated, which are used for improving the wear, fatigue and load bearing properties of ferrous engineering components [1]. The work pieces to be treated are surrounded by large metal screen (0,8m diameter and 0,75m hight) on which a cathodic potential is applied. The N_2/H_2 glow discharge at the active screen radiates the heat and provides a reactive process gas. To supply a homogeneous temperature distribution in particular heavily loaded chamber a relative low bias voltage is subjected. Experiments were conducted to examine the influence of the process parameter on the nitride layer formation. Samples of hardened and tempered low alloy steel were nitrided at 580℃ for 4 hours in 200 Pa N_2/H_2 gases. Here the results of common engineering steels (42CrMo4, X38CrMo5.1) are present. The plasma diagnostics were carried out using mass spectroscopy (Balzers QMS 200), infrared diode laser spectroscopy (TDLAS), and an electric probe technique.

Results

The introduction of nitrogen into the substrate surface produces a compound layer on the surface, on top of a nitrogen diffusion zone. In this work also the structure of nitride-containing cover layer on the

compound layer under consideration of the process parameters are investigated with scanning electron microscope. The results of investigations show that the bias power enhances the growth of nitride cover layer. Such processes were also observed during formation of compound layer during gas nitriding and described by a parabolic law of diffusion controlled layer growth [2]. Figure 1 shows hardness profiles and the nitrogen concentration profiles/compound layer thickness after active screen plasma nitriding with different bias power. Nitrogen content in the process gas and the bias power enhance the nitriding results. The expected nitriding case depth can be reached at bias power at the level of 5% or 15% of the active screen power. Increasing bias power produces thicker compound layers. Therefore active screen nitriding process is particularly suitable to create uniform and very thin γ´ compound layers with a deep decarburization of the nitrogen diffusion zone.



a) b) c)

Figure 1: Influence of bias on the hardness profile of steels 42CrMo4 (a) and X38CrMoV5-1 (b) as well as the nitrogen concentration profile of the compound layer, steel 42CrMo4 (c)

The understanding of ion nitriding process, mechanism of nitrogen atom production and transfer from the media to the component surface is not complete and still in the focus of investigation of many research groups worldwide [3-6]. In the past many models have been proposed for the plasma nitriding of ferrous materials. A very common approach of “sputtering and deposition” mechanism, suggested by Kölbel cannot explain the mass transfer [7]. The high reactivity of active nitrogen species was mentioned for the first time in the literature 100 years ago. That is why R.J. Strutt designated as active nitrogen [8]. Several studies have been carried out using different plasma diagnostic methods to analyse ionized species [9] and the adsorption of neutral atoms/molecules [10]. Ricard et al [11] demonstrates that the N^+_2, the vibrational N_2 and the N neutral species are most relevant.

To study the plasma processes involved in plasma nitriding at the industrial scale ASPN unit we used quadruple mass spectrometry (QMS). The signal intensity increases compared with the measurement without discharge at the active screen. The peak intensity for N^+ (m/z 14) and N^+_2 (m/z 28) were chosen to represent the major products in a N_2/H_2 process gas. The peak intensities decreased with increasing H_2 composition. It was found that even during heating up in nitrogen free process gas exited nitrogen (atomic or molecular) releases from the active screen. The ion stimulated desorption of neutral gas from active screen at temperature up to 400 ℃ due to preceding exposures to nitrogen gas has been studied. The gas species desorbing during Ar^+ ion bombardement are a result of prefential sputtering [12] and the metastability of iron nitride.

As already described above there is a mass transfer of nitrogen without a bias activation. Therefore the knowledge of the electron energy is necessary to explain the excitation processes which occur. One of the most direct ways to measure local properties of plasma is with electrostatic probes. This study used a time resolved Langumir probe method.

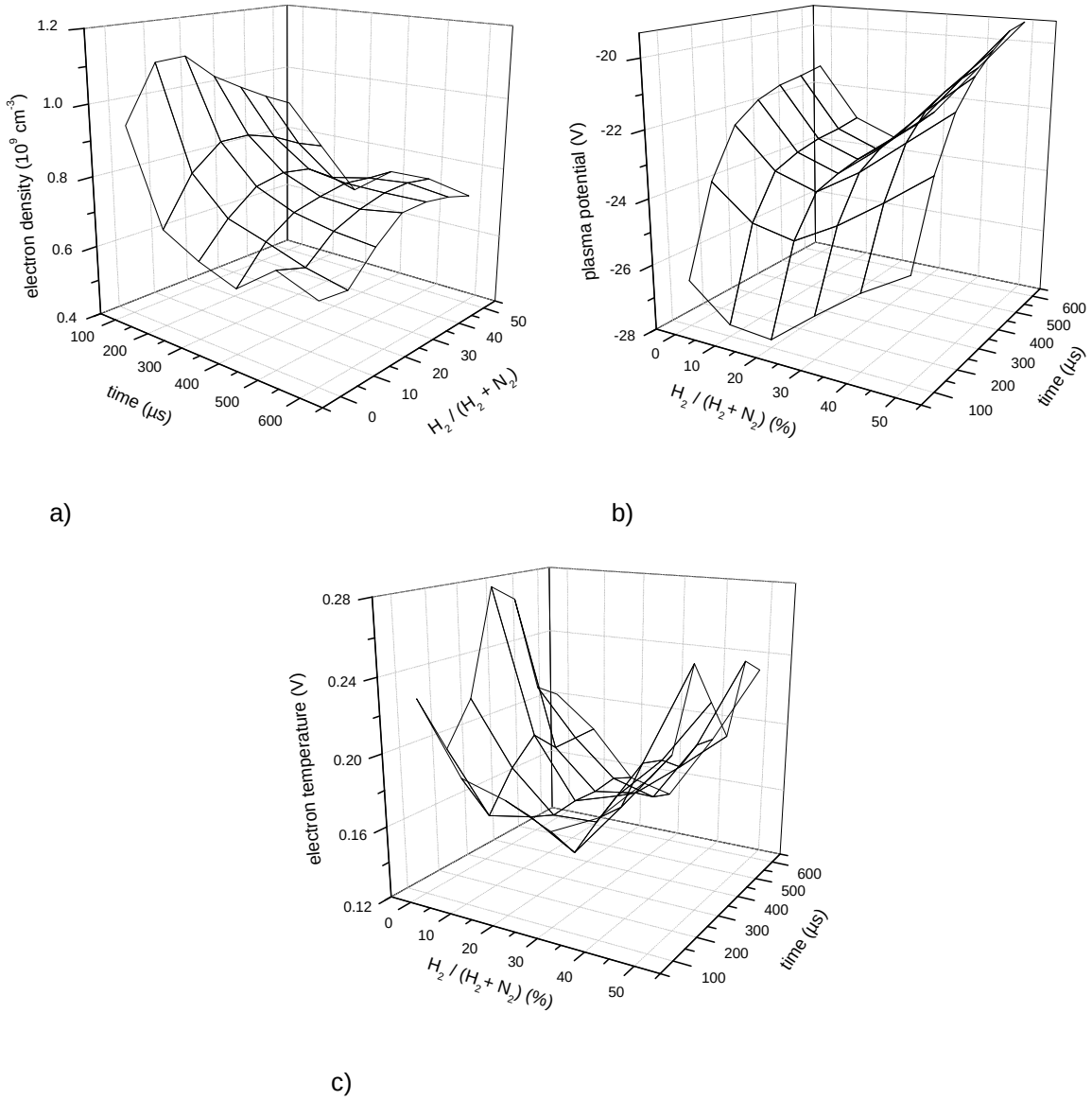


Figure 2: Temporal distribution of electron density (a) plasma potential (b) and electron temperature (c) during the on phase in dependence of the composition of the N_2/H_2 process gas

A characteristic time dependence of the charge-carrier density during the pulse on time containing maximum values of almost $1.0 \cdot 10^9$ cm^{-3} was found. Furthermore, the increase of the plasma parameters by varying the hydrogen content was monitored in the process gas. Floating and plasma potential indicate 20% admixture of H_2 a minimum. At this proportion of hydrogen in the process gas positive ions is accelerated most strongly to the substrate. The electron density in Figure 2 a shows between 15 - 25% hydrogen content, a slight maximum, while the electron temperature (Figure 2 c) in this area has a minimum. Maximum mean electron energy is due to the quasi-neutrality in the plasma

also an ion peak, so more particles are available for charge exchange. Regardless of the process gas composition average electron temperature of <0.3 V can be detected.

The qualitative measurements of quadruple mass spectrometry (QMS) should be complemented by the possibility of determining the absolute concentrations of stable molecules through the mid infrared tunable diode laser absorption (TDLAS). Though the study of the plasma chemically reactions of active nitrogen we investigated the efficiency of ammonia generation generated from mixtures of N_2 and H_2 under various plasma conditions. The main result of the preliminary investigation on the reactions of the dissociated species and the NH_3 - production rate is that it can be initiated depending on the gas composition, but above all as a function of bias power, a concentration of 1% NH_3. The determined maximum is at a hydrogen content of 50% and is an indicator of increased responsiveness due to adjusting glow discharge conditions.

References

[1] Georges, J., US Patent 5,989,363, (1999).

[2] Pietzsch, S.; Böhmer, S.: Growth of nitride cover layers on Compound layers of iron. Materials Science Forum Vols. 163-165 (1994), 259-264

[3] Walkowicz, J.; Smolik, J.; Miernik, K.: Research on physico-chemical bases of the ion nitriding process control with the use of plasma spectroscopic diagnostics. Vacuum 56 (2000), 63-69

[4] Li, C. X.; Bell, T.; Dong, H.: A Study of Active Screen Plasma Nitriding. Surface Engineering 2002 Vol. 18 No. 3, 174-181

[5] Zhao, C.; Li, C.; Dong, H.; Bell, T.: Study on the active screen plasma nitriding and its nitriding mechanism. Surface and Coatings Technology 201 (2006), 2320–2325

[6] Hubbard, P.; Partridge, J.G; Doyle, E. D.; McCulloch, D.G; Taylor, M.B; Dowey, S.J.: Investigation of nitrogen mass transfer within an industrial plasma nitriding system I: The role of surface deposits. Surface and Coatings Technology 204 (2010), 1145–1150

[7] Kölbel, J.: Die Nitridschichtbildung bei der Glimmentladung. Forschungsbericht des Landes NRW; Nr.1555; Köln, Opladen, Westdeutscher Verlag, 1965.

[8] Strutt, R. J.: Proceedings of the Royal Society of London, A85 (1911), 223.

[9] Hudis, M.: Study of ion-nitriding. Journal of Applied Physics 44 (1973), 1489-1496

[10] Michel, H.; Czerwiec, T.; Gantois, M.; Ablitzer, D.; Ricard, A.: Progress in the analysis of the mechanisms of ion nitriding. Surface and Coatings Technology 72 (1995), 103-111.

[11] Michel, H.; Czerwiec, T.; Gantois, M.; Ablitzer, D.; Ricard, A.: Progress in the analysis of the mechanisms of ion nitriding. Surface and Coatings Technology 72 (1995), 103-111

[12] Erlandsson, R.: Ion induced desorption from stainless steel studied with isotope techniques. Applications of Surface Science 6 (1980), 473-488

Acknowledgements

The authors appreciate German Research Foundation (DFG) for financial support in the frame of grant BI 418/20-1.

Control of nanoparticle formation in reactive plasmas and its application to fabrication of green energy devices

M. Shiratani

Graduate School of Information Science and Electrical Engineering, Kyushu University, Fukuoka, Japan

G. Uchida, K. Kamataki, H. Seo, N. Itagaki, K. Koga

Center of Plasma Nano-interface engineering, Kyushu University, Fukuoka, Japan

Abstract

We are developping “plasma nano-factories” which are bottom-up guided assembly processes and miniature versions of macroscopic conventional factories. Here, we report plasma-based control of the size, size distribution, and structure of nanoparticles, their agglomeration and transport as well as sticking. We apply nano-particle films to green energy devices such as low energy consumption LSI’s, solar cells, and Li ion batteries. Our results show that core-shell nanoparticles are effective for improving performances of these devices.

1. Introduction

Recent developments in nanomaterials have led to new opportunities of applying them to an increasing number of applications in electronics, optoelectronics, medical components *et al* [1-11]. One of our interests has been concerned with energy conversion devices using Si nanoparticles, because the technologically important and abundant material Si is the backbone of the electronics industry. To realize the green energy devices using nanoparticles, we develop a “plasma nano-factories” which is a miniature version of macroscopic conventional fabrication, based on the knowledge of nanoparticle formation in reactive plasma [12-16]. A plasma nano-factories produces nanoblocks and radicals (adhesives) in reactive plasmas, transports nanoblocks toward a substrate and arranges them on the substrate as shown in Fig. 1 [17-22]. There are three advantages of a nano-factories in plasma: controlled agglomeration and transport of nanoblocks as well as parallel processing over large area at relatively low temperature. First, we describe fabrication of core-shell Si nanoparticle films using SiH_4/H_2 and CH_4 or N_2 double multi-hollow discharge plasma CVD. Then, we show application of Si nanoparticles to next generation solar cells and lithium ion batteries [23-25].

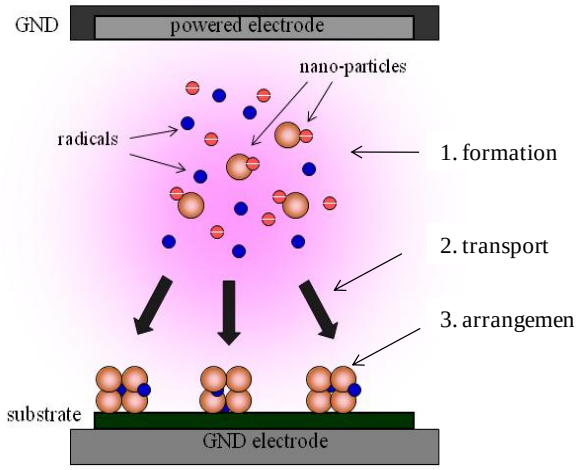


Figure 1. Concept of plasma nano-factories.

2. Deposition of core-shell nanoparticles films

Production of Si nanoparticles and surface treatment by hydrocarbon or nitrogen radicals were carried out using a multi-hollow discharge plasma CVD method as shown in Fig. 2, where two discharge plasmas of SiH_4/H_2 (plasma 1) and CH_4 or N_2 (plasma 2) were independently generated in a vacuum chamber. The multi-hollow electrode consisted of a powered electrode and two grounded electrodes of 30 mm diameter, and discharges were sustained in eight small holes of 5 mm diameter. Plasma 1 was generated by applying an rf power of 30 W to the powered electrode at SiH_4 and H_2 flow rates of 2 and 448 sccm, respectively. Si nanoparticles were nucleated, grown in SiH_4/H_2 plasma produced inside small holes, and transported downstream by a strong SiH_4/H_2 neutral gas flow. Si nanoparticles about 4 nm in average size were produced at the gas pressure of 5 Torr. The nanoparticle size can be controlled by changing pressure. Hydrocarbon or nitrogen radicals, which were produced in CH_4 and N_2 plasma at a CH_4 and N_2 flow rate of 2 and 100 sccm, respectively, were irradiated to the surface of Si nanoparticles during their transport downstream. Si nanoparticle films were deposited on substrates located downstream 67 mm from the multi-hollow electrodes, and the substrate temperature was 180°C.

Nitrogen content in Si nano-particle films was evaluated by measuring N-Ka fluorescence intensity obtained from X-ray fluorescence (XRF) measurements. As is found in Fig. 3 (a), Nitrogen content increases with approaching to the position of the N_2 discharge, whereas Si content is almost constant (see Fig. 3(b)). Double multi-hollow discharge plasma CVD method realizes combinatorial deposition of nitridated Si nano-particle films.

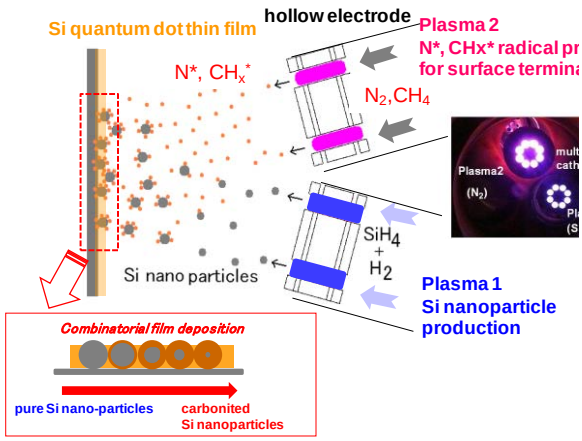


Figure 2. Schematic of experimental apparatus of double multi-hollow discharge plasma CVD.

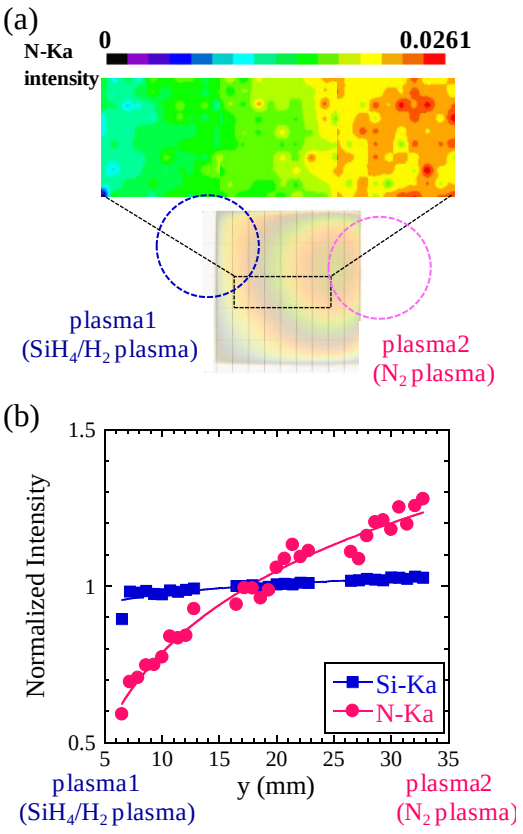


Figure 3. (a) Two-dimensional distribution of N-Kα fluorescence intensity obtained from X-ray fluorescence (XRF) measurement. (b) Substrate position dependence of N-Kα and Si-Kα fluorescence intensities from XRF.

3. Application to green devices

(1) Application to quantum-dot sensitized solar cells

SiN-Si and SiC-Si core-shell nanoparticle films were employed as sensitizers for TiO_2 photoelectrodes as shown in Fig. 4. Polysulfide electrolyte solution was used to fill the space between the TiO_2 electrode and an Au-coated FTO counterelectrode. The short-circuit current density of Si QD sensitized solar cells increases by a factor of 2.5 by irradiation of CH_4 plasma to Si nanoparticle surface. We also have measured incident photon-to-current conversion efficiency (IPCE) in the near-ultraviolet range using quartz-glass plates as front panels of QD sensitized solar cells. IPCE gradually increases by light irradiation in a wavelength range less than 600 nm around optical band-gap (E_g) of Si nanoparticle films, and then steeply increases below 280 nm around $2E_g$. This rapid increase of IPCE under short incident light may be attributed to the theoretically predicted multiple exciton generation (MEG), the creation of more than two electron-hole pairs from one high-energy photon, in nanoparticle QDs.

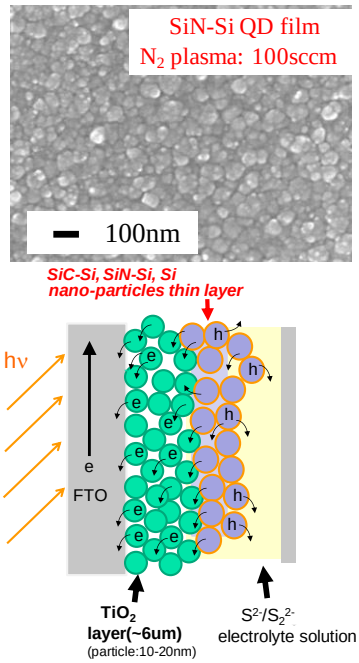


Figure 4. (a) SEM image of SiN nanoparticle films. (b) Cell structure of quantum-dot sensitized solar cells.

(2) Application to lithium ion batteries

SiC-Si core-shell nanoparticle films were used as an anode material as shown in Fig. 5, because Si has the high charge-discharge capacity up to 4200 mAh/g. The electrolyte was 1M $LiPF_6$ in ethylene carbonate (EC)/ dimethylene carbonate (DMC) (1:2). For measurements of anode properties, a Li metal sheet of 1 mm in thickness was used as a cathode. Li intercalation capacity was measured with a constant current of 0.1 mA/mg. Charge-discharge capacity of the SiC nano-composite anode of the first cycle was 3000 mAh/g, which is 9 times higher than the capacity of Li ion batteries using the conventional graphite anode.

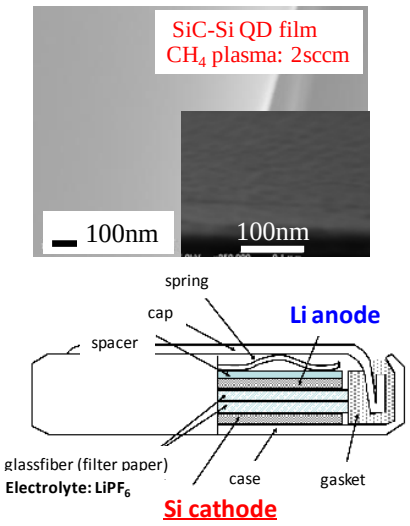


Figure 5. (a) SEM image of SiC nanoparticle films. (b) Cell structure of Li ion batteries.

4. Conclusions

We successfully developed quantum-dot sensitized solar cells and Li ion batteries using Si nanoparticles. We found that core-shell structure of Si nanoparticles is effective for improving the device performances, and observed a drastic increase in the short-circuit current density of Si QD sensitized solar, and in the charge-discharge capacity of Li ion batteries.

Acknowledges

This work was partly supported by the New Energy and Industrial Technology Development Organization (NEDO), the Ministry of Education, Culture, Sports, Science and Technology in Japan (MEXT), the Japan Society for the Promotion of Science (JSPS), Photovoltaic Power Generation Technology Research Association (PVTEC), and the Japan Science and Technology Agency (JST). We acknowledge stimulating discussions with Prof. T. Ishihara (Kyushu Univ.), Dr. M. Kondo (AIST), Dr. Y. Takeuchi (MHI), and Mr. T. Higuchi (PVTEC).

Referances

[1] D. Majumder, *et al.*, IETE Tech. Rev., 24 (2007) 9.
[2] P. Rutkevych, *et al.*, Phys. Plasmas, 14 (2007) 0435025.
[3] C. Joachim, *et al.*, Nature, 408 (2000) 541.
[4] V. Gill, *et al.*, Int. J. Solids Structures, 45 (2008) 943
[5] I. Ennen, *et al.*, J. Appl. Phys., 102 (2007) 013910.
[6] N. Khanduja, *et al.*, Appl. Phys. Lett., 90 (2007) 083105.
[7] A. Nel, *et al.*, Science, 311 (2006) 622.
[8] X. Wang, *et al.*, Aerosol Sci. Technol., 39 (2005) 624.
[9] A. Heeren, *et al.*, Microelectron. Eng., 84 (2007) 1706.
[10] J. W. G. Wildoer, *et al.*, Nature, 391 (1998) 59.
[11] V. Balzani. *et al.* Nanotoday, 2 (2007) 18.
[12] M. Shiratani, *et al.*, J. Phys. D: Appl. Phys., 44 (2011) 174038.
[13] K. Ostrikov, Rev. Mod. Phys., 77 (2005) 489.
[14] M. Meyyappan, *et al.*, Plasma Source Sci. Technol., 12 (2003) 205
[15] T. Okada, *et al.*, Chem. Phys. Lett., 417 (2006) 288.
[16] M. Mozetic, *et al.*, Adv. Mater., 17 (2005) 2138.
[17] M. Shiratani, *et al.*, Faraday Discuss., 137 (2008) 127.
[18] S. Iwashita, *et al.*, Plasma Sources Sci. Technol., 21 (2012) 032001.
[19] K. Kamataki, *et al.*, Appl. Phys. Exp., 4 (2011) 105001.
[20] K. Kamataki, *et al.*, J. Inst., 7 (2012) C0417.
[21] S. Iwashita, *et al.*, Jpn. J. Appl. Phys., 47 (2008) 6875.
[22] W. M. Nakamura, *et al.*, Surf. Coat. Technol., 105 (2010) 5241.
[23] T. Ishihara, *et al.*, Electrochem. Solid-State Lett., 10 (2007) A74.
[24] G. Uchida, *et al.*, Phys. Status Solidi C, 1-4 (2011) 20100229.
[25] G. Uchida, *et al.*, Jpn. J. Appl. Phys., 51 (2012) 01AD01.

Towards deeper understanding of an HiPIMS discharge by time-resolved optical plasma diagnostics

N. Britun[1], M. Palmucci[1], S. Konstantinidis[1], and R. Snyders[1,2]

[1] *Chimie des Interactions Plasma Surface, CIRMAP, Université de Mons, Place du Parc 23, B-7000 Mons, Belgium.*

[2] *Materia Nova Research Center, Parc Initialis, Avenue N. Copernic 1, B-7000 Mons, Belgium.*

Keywords: HiPIMS, OES, ROAS, LIF, plasma diagnostics, temperature, velocity

As a promising pulsed sputter deposition technique, High-Power Impulse Magnetron Sputtering (HiPIMS) required an extensive time-resolved plasma characterization. Being essentially non-intrusive, optical plasma diagnostics methods posses in particular the time- and space- resolution(s) which normally exceed the typical needs of a typical HiPIMS geometry [1] and, therefore, can be readily applied for characterization of the high-power pulsed discharges.

Our recent progress on time-resolved study of a HiPIMS discharge is presented in this work. The selected Optical Emission Spectroscopy (OES), Resonance Optical Absorption Spectroscopy (ROAS), and Laser-Induced Fluorescence (LIF) results are reported. Several parameters, such as the absolute densities of the sputtered species, gas temperature, velocity distribution function of the sputtered species are described.

The schematic representation of the studied magnetron discharge system for the implementation of LIF diagnostics [2] is given in Fig. 1. The analyzed plasma regions in case of LIF are nearly cylindrical with the width of about 5 mm and length of about 10 cm. For OES and ROAS diagnostics the probed plasma volume had the width of about 1 cm and was located at about 5 cm above the magnetron target.

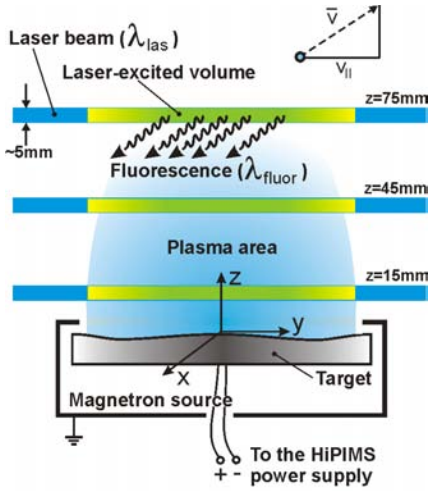


Fig. 1. Schematic representation of the HiPIMS plasma together with the probed volume by LIF.

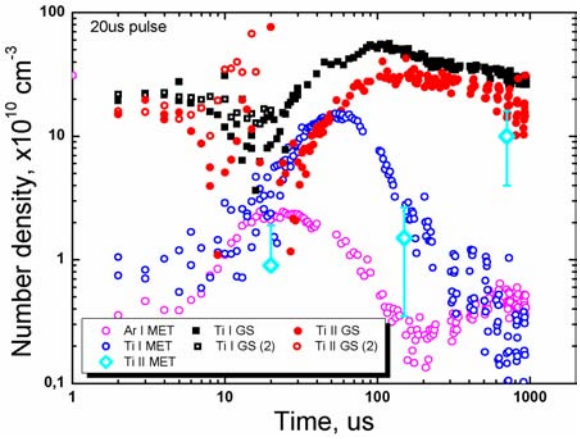


Fig. 2. Time-resolved evolution of the absolute densities during the HiPIMS on- (20 μs) and off- (980 μs) time measured by ROAS.
Pressure = 20 mTorr.

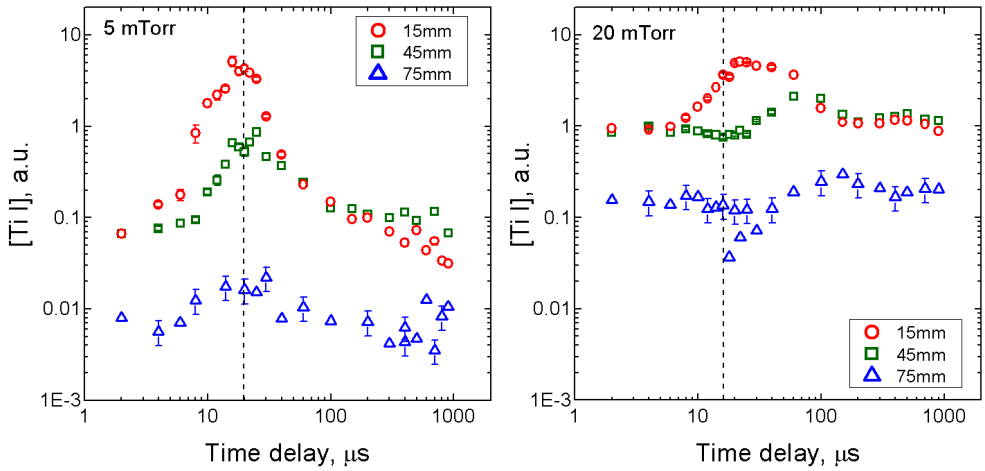


Fig. 3. Time-evolution of the Ti sputtered atoms density measured by LIF in a HiPIMS plasma at three different distances from the magnetron target. Dashed lines indicate end of the pulse.

Results obtained by ROAS [3] during sputtering of Ti in Ar demonstrate the large differences in the absolute densities for Ti, Ti^{+}, Ti^{met} and Ar^{met}, as shown in Fig. 2. Such an integrated time-resolved representation indicates a highly non-uniform time-evolution of the sputtered Ti, its ions as well as the metastables of Ti and Ar, which are supposed to play an important role in HiPIMS plasmas. The arrival time (to the probed volume) for all the measured species during the HiPIMS pulse is found to be different, as it can be seen from Fig. 2. In addition, this is accompanied by the population inversion of the ground and metastable states energy sublevels during the pulse [3] (not shown). These results are in agreement with the Ti ground state density recently measured by LIF [4] at different distances from the magnetron target (Fig. 3). Here we can clearly observe a "wave" of the sputtered species propagating away from the magnetron target at high pressure, as well as the rarefaction of the Ti density during the 20 μs plasma pulse (Fig. 3(b)). These effects are absent, however, at low pressure (Fig. 3(a)).

Along with the above described measurements, the gas temperature (T_{gas}) associated with the thermalized species during the pulse is determined based on the rotational band analysis of N_2^+ (391.4 nm) assuming partial bulk gas thermalization [5]. T_{gas} is found to grow linearly during the HiPIMS pulse being mainly a function of the energy E_P delivered per pulse. The minimum and maximum gas temperatures attained during the HiPIMS plasma pulse measured in this way are presented in Fig. 4. As it can be seen, gas temperature depends strongly on the target material, and increases linearly with increasing of E_P for heavier target atoms (W), whereas it saturates quickly for the lighter ones (Ti).

In addition, LIF spectroscopic diagnostics applied for time-resolved characterization of the velocity distribution of the sputtered Ti atoms in HiPIMS reveals a rapid increase of the full width at half maximum (FWHM) of the velocity distribution function (vdf) during the plasma pulse following by a fast decrease of the vdf's FWHM during the plasma off-time [2, 6], as it is summarized in Fig. 5 for 15 mm of the distance from the target. After taking into account possible valuable broadening mechanisms (such as Stark, Zeeman, instrumental, etc.), the described vdf behaviour was finally attributed to the Doppler-shift phenomenon in plasma, i.e. to the rapid broadening (on-time), or relaxation (off-time) of the vdf of sputtered species likely accompanying by either rarefaction [7] (on-time) or refilling [8] (off-time) effects in the bulk gas.

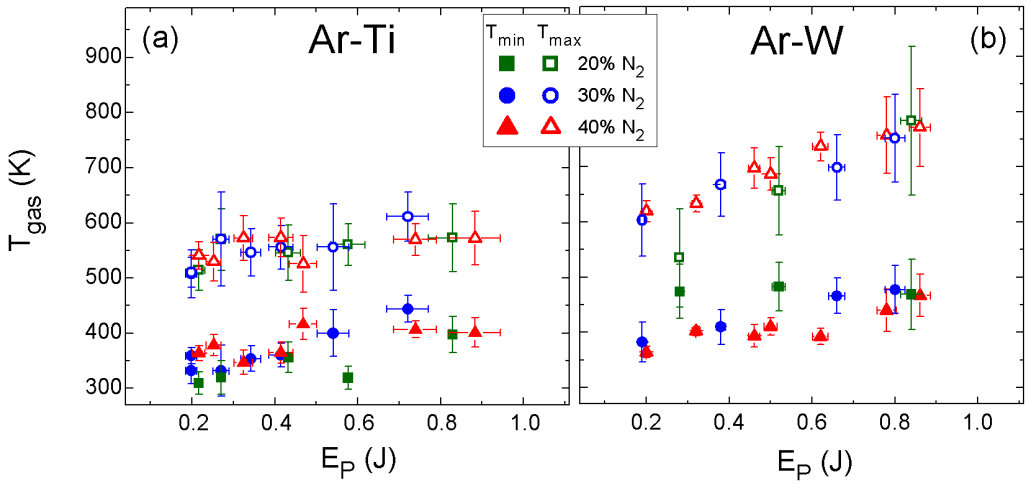


Fig. 4. T_{gas} attained at the beginning (T_{min}) and at the end (T_{max}) of the HiPIMS plasma pulse calculated based on the linear fits of the T_{gas} time-evolution during the pulse. The results are presented for Ti (a) and W (b) sputtering at various E_p values and different N_2 contents. Pulse duration is 20 μs. Ar pressure is 20 mTorr.

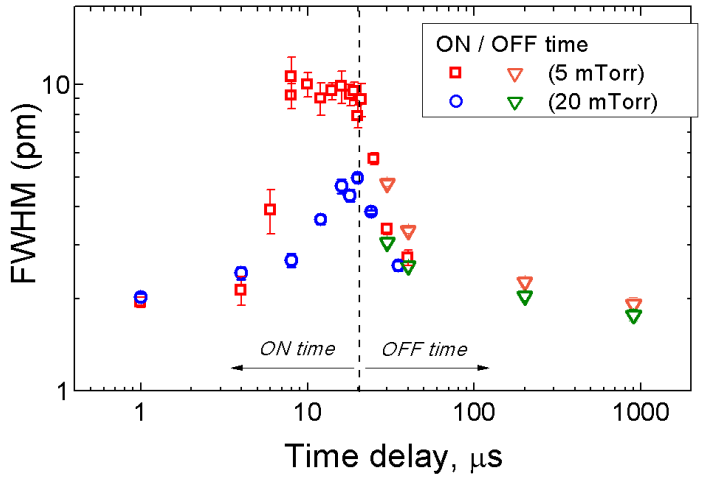


Fig. 5. The time-resolved evolution of FWHM of the Ti absorption line measured by LIF after the deconvolution with the side broadening effects determined at two gas pressures. The maximum attained broadening corresponds to about 5 km/s of the velocity component parallel to the magnetron target.

As we can observe in Fig. 5, the FWHM saturates in the second part of the plasma pulse forming a plateau (where FWHM is about 10 pm). This effect is also visible at somewhat larger distances from the target. Based on the FWHM data shown in Fig. 5, it should be noted that, the high broadening values obtained during the plasma pulse at 15 mm are, in our opinion, mainly due to the intensive bulk gas rarefaction in the second half of the plasma pulse which allows observing the "initial" velocity of the sputtered species without their considerable deceleration by collisions with the bulk Ar. At the same time, at higher distances from the target (or at higher pressure) the maximum attainable FWHM values decreases considerably.

Summarizing the diagnostics results, the following time- and space- resolved picture of a HiPIMS discharge can be deduced:

During the plasma pulse, Ti and Ti^+ species are produced first and they are keeping their ground state and metastable sublevels population inverted due to rather high level of the gas excitation. This is following by an increase of the density of Ti and finally Ar metabstables, which also experience the population inversion when reach their maxima.

At the same time, during the HiPIMS pulse, the velocity distribution gets essentially broadened presumably due to the bulk gas rarefaction, and rapidly shrinks far away from the target as well as right after the plasma pulse with a faster-than-exponential decay, which is due to the collisional relaxation of the vdf enhanced additionally by the refilling effect. These effects, as expected, are especially prominent at low pressure and in the vicinity of the magnetron target (z = 15 mm).

The gas temperature associated with the thermalized bulk Ar species in the discharge (measured by the rotational structure of the added nitrogen) increases linearly during the plasma pulse proportionally to the total energy E_P delivered during the pulse. After the HiPIMS pulse ends, both the ballistically moving and thermalized heated species rapidly dissipate their energy, and the gas cools down to nearly the room temperature during the off-time. The bulk gas temperature is found to be also different for heavy and light sputtered particles due to the different ways of the energy transfer to the bulk gas. Observed “bulk temperature” trends reflect the overall gas heating and relaxation channels in HiPIMS as a function of the applied power, distance from target, sort of the sputtered species, etc.

References:

[1]. K. Macak, V. Kouznetsov, J. Schneider, U. Helmersson, and I. Petrov, J. Vac. Sci. Technol. A **18(4)** (2000) 1533.

[2]. M. Palmucci, N. Britun, et.al., Time-evolution of the velocity distribution of high power impulse magnetron sputtered atoms, (*in preparation*).

[3]. N. Britun, M. Palmucci, S. Konstantinidis, R. Snyders, Proc. of the 11-th Int’l Symposium for Sputtering (ISSP-2011), Kyoto July 6-8 2011, p. 198.

[4]. N. Britun, M. Palmucci, et al., Combined time- and space- resolved LIF-ROAS study of a HiPIMS discharge, (*in preparation*).

[5]. N. Britun, M. Palmucci, et al., Thermalization particularities in a high-power pulsed magnetron plasma, (*in preparation*).

[6]. N. Britun, M. Palmucci, and R. Snyders, Appl. Phys. Lett., **99** (2011) 131504.

[7]. D. Horwat, A. Anders: J. Appl. Phys. **108** (2010) 123306.

[8]. T. Kubart, M. Aiempanakit, J. Andersson, et.al., Surf. Coat. Technol. **205** (2011) S303.

Study of the ionisation in a nickel plasma by Inductively Coupled Impulse Sputtering (ICIS)

Daniel A. L. Loch, Arutiun P. Ehiasarian
HIPIMS Technology Centre, Sheffield Hallam University, Howard St., Sheffield, S1 1WB, UK

Abstract

Inductively coupled impulse sputtering (ICIS) removes the need for a magnetron, while delivering equal or higher ion to neutral ratios compared to other ionised PVD technologies such as high power impulse magnetron sputtering (HIPIMS). This is especially advantageous for the sputtering of magnetic materials, as these would shunt the magnetic field of the magnetron, thus reducing the efficiency of the sputtering and ionisation process. ICIS produces highly ionised metal-dominated plasmas inside a high power pulsed RF coil with a magnet free high voltage pulsed DC powered cathode.

ICIS processing with Ti and Cu has been attempted before; however operation with magnetic target materials has not been attempted so far. The paper aims to clarify the effects of power and pressure on the deposition flux and structure of deposited Ni films.

The setup comprises of a 13.56 MHz pulsed RF coil operating at a frequency of 500 Hz and a pulse width of 150 µs, which results in a duty cycle of 7.5 % . A pulsed DC voltage of 1900 V was applied to the cathode to attract Argon ions and initiate sputtering.

Optical emission spectra (OES) for argon and nickel species sputtered at a constant pressure of 14 Pa, show a linear intensity increase for peak RF powers of 1000 W - 4800 W. Ni neutral line intensity increased linearly exhibiting two different slopes for powers below 2000 W and those above 2000 W RF - power.

The influence of pressure on the process was studied at a constant peak RF power of 3000 W for pressures of 3.2 – 26 Pa.

The intensity of nickel neutrals rises linearly for pressures of 3.2- 26 Pa and saturates for pressures from 12 – 21.4 Pa. Argon neutrals rise linearly with increasing pressure. Ni ions have not been visible in the OES spectra and analysis into the ion to neutral ratios will be conducted by other techniques.

From the Ti process we know, that the intensity of neutrals and ions increases linearly with power and pressure. Intensity modelling is also conducted for the Ni process. The deposition rate for Ni is 50 nmh^{-1} for a RF-power of 3000 W and a pressure of 14 Pa.

The microstructure of the Ni coatings shows columnar dendritic growth. Bottom coverage of unbiased vias with width 0.300 µm and aspect ratio of 3.3:1 was 15 % and for an aspect ratio of 1.5:1 was 47.5 %. Parameters for this coating are mean values from a power and pressure matrix. To investigate ionisation influence, coatings have also been deposited at higher power and pressure.

The current work has shown that the concept of combining a RF powered coil with a magnet-free pulsed DC powered cathode works very well for the sputtering of hard magnetic material in very stable plasma.

Keywords: ICIS, Ionised PVD, Magnet-free sputtering, deposition on high aspect ratio vias

1 Introduction

Deposition of thin films of magnetic material is of great importance for various applications such as data recording [1] and magnetic microelectromechanical systems (MagMEMS) [2].

Magnetron-based sputtering techniques suffer from low target utilisation rates of 40% [3] and short service intervals for magnetic materials as targets need to be thin.

A high degree of ionisation of sputtered species is preferable, as this allows deposition on structured surfaces because ions follow the electric field lines that are created by the potential difference between the plasma bulk and substrate surface. This makes it possible to deposit even coatings on sidewalls and the bottom of high aspect ratio features of the substrate.[3]

Inductively Coupled Impulse Sputtering (ICIS) is a new development which aims to solve the previously mentioned issues by eliminating the need for a magnetron. ICIS is based on an experimental development by Yukimura and Ehiasarian [4], which utilises high pulsed RF-power in

the coil and high pulsed DC voltage on the target to generate a plasma and attract argon (Ar) to initiate sputtering
In this work ICIS technology was adapted to work inside a deposition system and uses a 13.56 MHz RF-power supply.
In the current work the plasma composition and ionisation is studied by Optical Emission Spectroscopy (OES), the coating microstructure and thickness by Scanning Electron Microscopy (SEM) and the coating chemical composition and contamination by sputtered RF coil material by Energy - Dispersive X-ray spectroscopy (EDX).
A model [5] based on the optical emission of DC and RF magnetron discharges is used to explain the connection between the intensity (I(λij)) and power (P) for highly ionised magnetron plasma processes. Dony et.al. explain the dependence of the optical emission of the plasma to the power on the cathode. As with ICIS the plasma is generated inside the induction coil, in this study we correlate the optical emission of the plasma to the power applied to the coil. As the model is based on magnetron processes, it is very useful to compare the ionisation efficiency of ICIS with conventional magnetron processes.

2 Experimental Details

The experimental ICIS system (shown schematically in Fig.1) consists of a UHV chamber (Kurt J. Lesker CMS - 18), Hüttinger PFG 5000 RF power supply (13.56 MHz), a Hüttinger HIPIMS power supply HMP6/16, a 2-turn 80 mm diameter solid rod copper coil and a magnet free 75 mm diameter cathode.
The plasma discharge is created within the RF powered coil. When the plasma has ignited, pulsed DC power is applied to the cathode. RF and DC power pulses are synchronised by a pulse generator.
In the current study a pressure - RF-power matrix was used to examine the influences of working pressure and RF- power on the ionisation of the discharge and deposition properties. The pulsed DC parameters were kept constant at 1900 V. The working pressure was varied from 2.96 - 21.4 Pa and the RF power was varied between 1000 W - 4800 W. The repetition frequency was 500 Hz with a pulse width of 150 µs. The substrate was silicon dioxide (SiO_2), an insulator, with vias, held at floating bias voltage. Temperature on the substrate at the beginning of the process was between 20 - 28 ºC and during deposition rose by approx. 5 ºC within one hour.

2.1 Plasma and Coating Characterisation Techniques

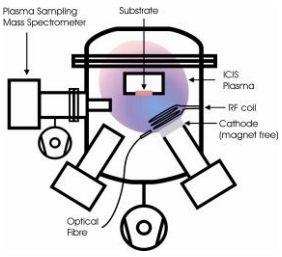


Figure 1 Experimental setup of the ICIS deposition system with the assembly of the inductive coil, magnet-free cathode and OES location.

Plasma composition analysis was carried out by OES monochromator (Jobin Ivon Triax 320) with quartz optical fibre and collimator *in vacuo*. The comparison of the excitation efficiency of ICIS with conventional RF-ICP magnetron sputtering is realised by fitting the OES results for increasing RF-Power to a model for ionisation by electron and Penning collisions developed for RF-coil enhanced magnetron sputtering. [5]

Scanning electron microscopy (SEM) (FEI NovaSEM 200) was used to examine the coating properties and to determine the structure and bottom coverage, i.e. the ratio of the coating thickness on the bottom and top surfaces of vias.

2.2 Modelling of the Excitation Properties

The results showed an increase in metal excitation and ionisation as a function of power. The relation between emission intensity and RF power in the coil is expressed by a power law with exponent β, which is derived from the slope in a log - log graph: $I_{Ar} = P^{\beta}$ (1).
As the excitation of Ar is predominantly by electron collision the intensity is proportional to the electron density, $I_{Ar} \propto n_e$ (2).
For the intensity of Ar neutrals and metastables we obtain the following equation:
$\log(I_{Ar}) = \beta \log P$(3), where I is the intensity of Ar for a certain wavelength, β is the slope and P is

the power applied to the RF-coil.
For the excitation of metal neutrals the intensity is $I_{Me} = K_{Me} \cdot n_{Me} \cdot n_e \cdot C^{Me}$(4). K_{Me} and C^{Me} are constants. From the definition of the sputtering yield, $n_{Me} = \varepsilon \gamma_e n_{Ar^+}$ (5) where ε is a constant and γ_e is the sputtering coefficient and because plasma is considered to be quasineutral, $n_{Ar^+} \approx n_e$(6), it can be concluded that $I_{Me} \propto {n_e}^2$ (7). Following from equations (1) and (2) for metal neutrals we get $I_{Me} = \left(P^{\beta}\right)^2$ (8). For Ni neutrals we get: $\log(I_{Ni^0}) = 2\beta \log P$ (9). As a further electron collision is necessary to ionise the excited metal atoms for Ni ions the equation is: $\log(I_{Ni^{1+}}) = 3\beta\, logP$ (10). This means that the slopes of Ni neutrals are expected to be twice as steep and three times steeper for Ni ions as those of Ar neutrals.

3 Results and Modelling

3.1 Optical Emission Measurement

OES results for a ICIS 3000 W Ni plasma in fig.3 show strong emission from Ni neutrals. Ni ions which were expected at 333.188 nm were below the detection limit of the OES. Most Ni ions can be expected at lower wavelengths very much further in the ultraviolet spectrum. Further experiments are intended to detect these.

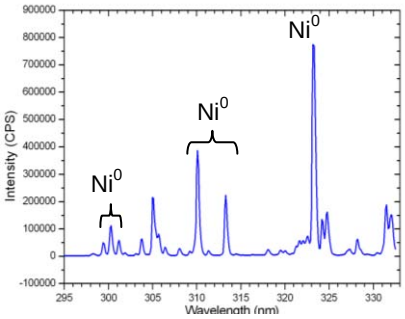


Figure 2 OES Measurement of a ICIS Ni Plasma at 3000 W RF-Power

3.2 Modelling the Influence of Power on Ionisation

As has been discussed, according to the prediction model the intensity of the sputtered species rises linearly with increasing RF-Power in a logarithmic graph. Fig. 4 shows measured OES intensities against RF coil power in a logarithmic graph. As no intensities for Ni ions were measured the graphs only contain the data for Ar and Ni neutrals. For the ICIS of Ni plasma there are two distinct slopes for powers below and above 2000 W respectively. For powers below 2000 W the slope is three times higher for Ni neutrals compared to Ar neutrals. According to the model a factor of 2 is to be expected. The reasons for this behaviour need to be examined further. For powers above 2000 W the slopes of Ar and Ni neutrals react as predicted by the model.

Table 1: Comparison of the slopes of Ar and Ni neutrals in ICIS plasma.

1.Ar 750slope:	0.53	2.Ar 750slope:	0.41
1.Ni 341 slope:	1.40	2.Ni 341 slope:	0.79
1.Ni 345 slope:	1.41	2.Ni 345 slope:	0.74
1.Ni 346 slope:	1.32	2.Ni 346 slope:	0.66

Figure 4 describes the influence of pressure on the ionisation at a constant power. It can be seen that for higher pressures the intensity of Ni neutrals reduces. Similar studies with ICIS of Ti showed that the reduction of neutrals is accompanied by an increase in Ti ion intensity, due to an increased efficiency of ionisation at higher pressures.
It can be expected that this effect would be valid in Ni and the reduction might be attributed to an increasing ionisation. Even though the intensity from Ni ions was not measurable, this indicates that the ionisation processes are more efficient at higher pressures. This could be attributed to a reduction in mean free path of collisions between Ni atoms and Ar atoms. This has two consequences. One is the reduction of energy of Ni atoms leading to longer transit times

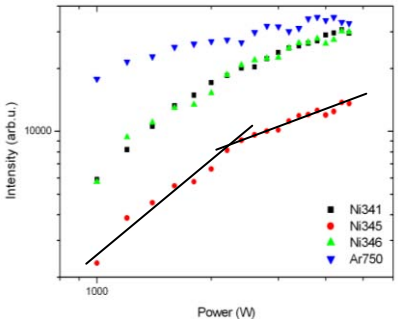


Figure 3 Measured results for Ar and Ni neutrals for a constant pressure of 12 Pa with varying RF-Power. The black lines highlight the different slopes below and above 2000 W

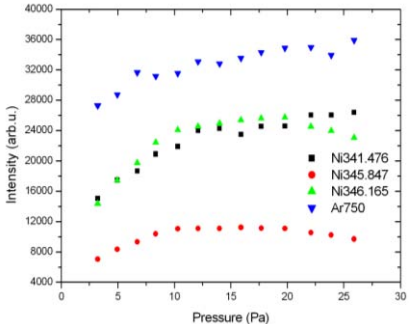


Figure 3 Measured results for Ar and Ni neutrals for a constant RF-Power of 3000 W and varying pressure.

through the ionisation zone of the RF coil. Another consequence is the greater frequency of collisions with Ar metastables. Both of these consequences result in a higher probability of ionisation through a Penning process.

3.3 Coating properties

The cross section image (Fig. 5) of a high aspect ratio(AR) via 2:1 coated by ICIS of Ni at RF-power of 4000 W and low pressure (6.4 Pa) being conditions that would result in a medium ionisation degree of the sputtered material. The films exhibit dense columnar dendritic growth. The bottom-coverage (BC) for these process settings and AR is 21.2 % with a floating bias. The deposition rate was approx. 125 nm/h.

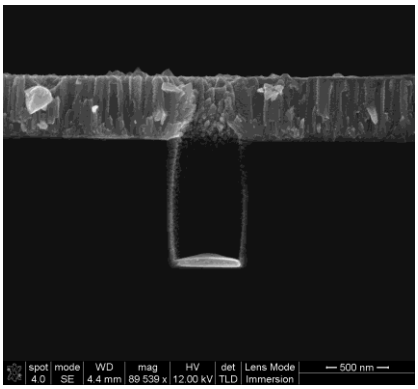


Figure 5 SEM cross section of Ni coated high aspect ratio vias deposited with 4000 W RF-Power at 6.4 Pa.

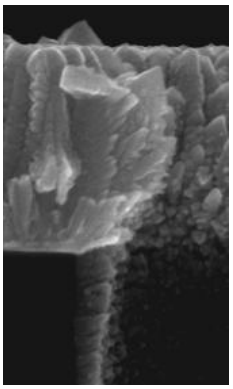


Figure 5a Close up of the corner of the via from figure 5. Dendritic growth of the Ni coating can be seen along with the perpendicular growth on the sidewalls.

In fig. 5a it can clearly be seen, that the growth of columns on the sidewalls is perpendicular to the substrate surface and homogeneously level over the whole depth of the feature.
The accumulation of material at the bottom of the structure indicates the deposition of ions. The overall distribution of the deposit indicates that the majority of the deposited species were metal ions. The dense structure of the bottom coating and no visible separation between the sidewall and bottom as well as the even sidewall coverage suggest only modest resputtering.

4 Conclusion

Successful deposition of magnetic material has been demonstrated by ICIS achieving high degrees of ionisation. While ions have not been detected by OES measurements there are numerous indicators that the sputtered target material does indeed get ionised. These are the deposition into high aspect ratio structures with good sidewall and bottom coverage, the horizontal orientation of columns on the sidewalls of vias and the reduced intensity of metal neutrals at higher pressures.
Further calculations of the excitation in ICIS processes has shown to be comparable to magnetron based systems but further work needs to be completed to measure the actual ionisation and to explain the higher excitation rate at lower powers.

References

[1] WHITE, R.M. (1990). The Materials Aspect of Magnetic Recording. *Journal of Magnetism and Magnetic Materials.* **88**, 165 - 176.
[3] GIBBS, M.R.J. et.al. (2004). Magnetic Materials for MEMS applications. *J. Phys. D: Appl. Phys* . **37**, R237 - R244.
[3] CHAPMAN, Brian (1980). Glow Discharge Processes: Sputtering and Plasma Etching. *Wiley-Interscience; 1 edition.*
[4] ROSSNAGEL, Steve (2000). Ionisation by Radio Frequency Inductively Coupled Plasma. *Thin Films*,**VOL.27**, 37-65.
[5] YUKIMURA, Ken and EHIASARIAN, Arutiun P. (2009). Generation of RF plasma assisted high power pulsed sputtering glow discharge without using a magnetic field. *Nuclear instruments and methods in physics research section B: Beam interactions with materials and atoms,* **267** (8-9), 1701-1704.
[6] DONY, M.F; RICARD, A.; DAUCHOT, J.P.; HECQ, M.; WAUTELET, M. (1995). Optical diagnostics of d.c. and r.f. argon magnetron discharges. *Surface and Coatings Technology,* **74-75**, 479-484.

Nanoparticle Synthesis in a Tubular Plasma Reactor – From Plasma Parameters to Nanoparticle Properties

Extended abstract for
Keynote Lecture KN1600, at the PSE conference 2012, Garmisch-Partenkirchen
held on Wednesday, September 12, 16:45 – 17:15

Christian Roth, Gina Oberbossel, Philipp Rudolf von Rohr
ETH Zurich, Institute of Process Engineering, Zurich, Switzerland

1 Introduction

In the presented study a tubular plasma reactor is investigated, which is normally used for the continuous plasma surface modification of fine-grained powders. The plasma reactor basically consists of a 1.5 m long glass tube with a gas and precursor feed unit at its top and a particle-gas separation unit at the lower end. The power is coupled inductively into the plasma via a coil which is wrapped around the reactor tube.

Substrate powders normally pass the discharge tube with high velocity and are functionalized on their way through the plasma in approximately 0.1 s. Possible plasma surface functionalization processes for powders are illustrated in Figure 1.1. The wettability of powders is increased by the formation of polar groups on the surface [1]. Films are deposited on particle surfaces to protect the substrate from harsh environments [2] or for catalytic applications [3]. In recent years, also a new plasma process, which increases the flowability of fine-grained powders, gained increasing attention. Nanostructured SiO_x is formed in the plasma and directly deposited on the substrate particle surface [4]. These nanoparticle structures increase the surface roughness of the substrate particles. Thus, the interparticle van der Waals forces are reduced, which leads to a major improvement of the powder flowability [5]. This process shows promise for companies dealing with cohesive granular materials.

The feasibility of this process was shown in the past, but at the same time the need for fundamental research in this field was recognized. Which ion density is required to yield in an effective surface modification? What is the thermal load of a substrate particle during the treatment? Which precursor should be used for a maximum improvement of the flowability?

In order to answer such questions, we measured axial profiles of plasma parameters in this continuous reactor and studied the nanoparticle synthesis in detail. No substrate powder was fed during these investigations to facilitate probe measurements and to focus on the produced nanoparticles.

Silica-like nanoparticles were produced from the four organosilicon monomers hexamethyldisiloxane (HMDSO), tetramethyldisiloxane (TMDSO), tetraethyl orthosilicate (TEOS), and tetramethyl orthosilicate (TMOS) in argon-oxygen gas mixtures. The chemical composition and morphology of the emerging particles and its production rate were studied as a function of process pressure (100 – 400 Pa), plasma power (200 – 350 W), gas velocity (5 – 16 m/s) and gas composition. Langmuir double probe and calorimetric probe measurements allowed determining the axial profiles of electron temperature, positive ion density, and energy influx along the vertical axis of this tubular reactor.

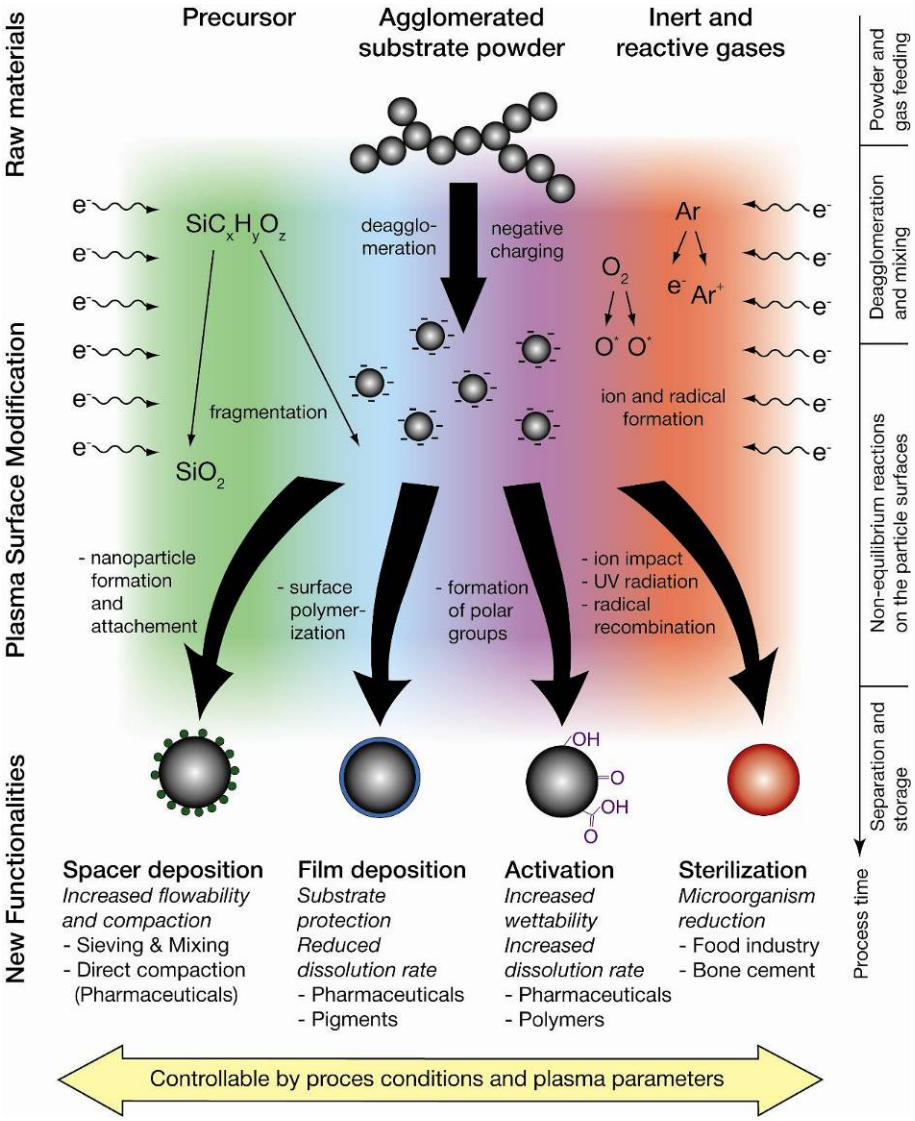


Figure 1.1: Overview of plasma-assisted surface modification processes for fine-grained powder substrates.

2 Experimental

The process scheme for the nanoparticle production in the tubular plasma reactor is shown in Figure 2.1. The plasma chamber (1) consists of a 1.5 m long double wall glass reactor with an inner diameter of 40 mm. Thus, a high surface-to-volume-ratio of 100 m^{-1} is provided. The gap between inner and outer glass tube was flushed with deionized water (2) of 20 °C to ensure a constant reactor temperature.

The discharge was driven with radio frequency (RF) of 13.56 MHz. The RF-generator (3) was connected over a matching network (4) with the water cooled copper coil (5) on the outside of the cooling jacket. The flow rates of oxygen, argon and the organosilicon monomers were adjusted by flow controllers. The liquid monomers were fed through a controlled evaporation mixing device (6) and stored under a 2 bar argon atmosphere (7) to prevent monomer degradation.

Below the plasma zone the produced nanoparticles were separated from the gas stream by a downcomer (8), cyclone (9) and filter unit (10) and collected in the solid collection vessels (11). Since the produced silica structures are very small, all powder was collected from the polyester filter. A constant pressure in the reactor was maintained during the process by a butterfly control valve (12) in front of the two stage roots and rotary vane vacuum pump (13).

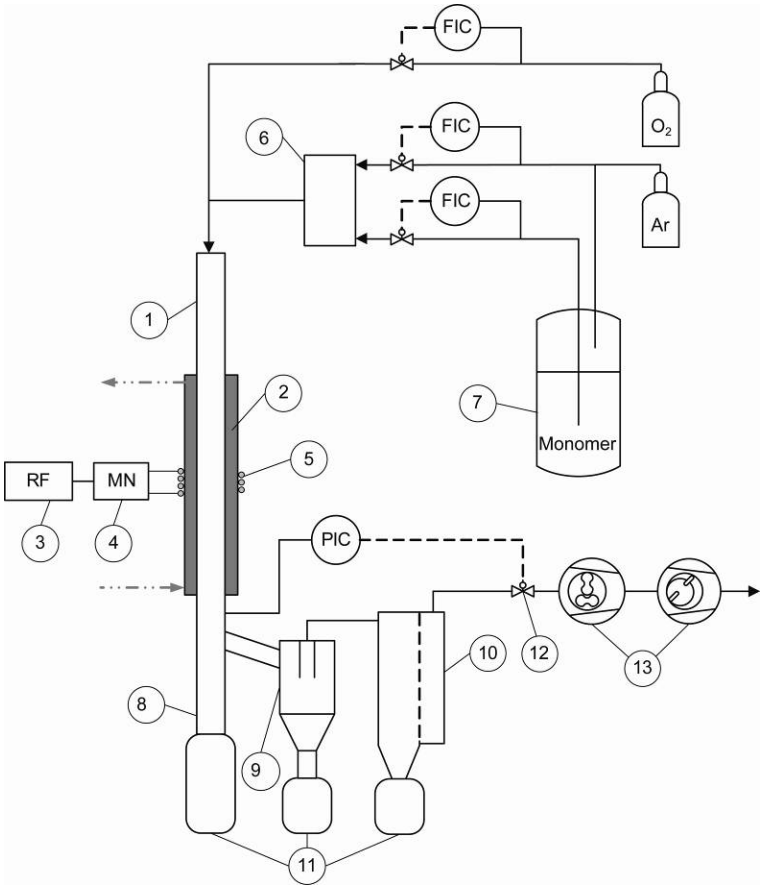


Figure 2.1: Process scheme of the tubular plasma reactor adapted for nanoparticle production, PIC:flow indicator controller, PIC: pressure indicator controller, numbers are indicated in the text, taken from [6].

3 Analytical methods

The plasma was characterized by a tailor-made Langmuir double probe and a calorimetric energy influx probe. In addition, photographs of the discharge were taken to discuss characteristic differences in optical emission of the plasma as a function of the process parameters. The morphology of the emerging nanoparticles was investigated by transition electron microscopy (TEM). For the determination of the mass production rate of nanoparticles the filter weight was measured before and after each experiment. Information about the bond structure of the produced particles was gained by Fourier transform infrared (FTIR) spectroscopy, whereas the chemical composition of the particles was studied by X-ray photoemission spectroscopy (XPS).

4 Results

The electron temperature reached its maximum in the domain of the inductive coil and values up to 17 eV were measured. The positive ion density featured as well maximum values in the region of the helical coil. Densities up to approximately $2 \cdot 10^{11}$ cm^{-3} were found and the positive ion density as well as the energy influx rose with increasing plasma power. The measured energy influx was additionally strongly influenced by the mean gas velocity in the reactor.

The carbon content of the orthosilicate derived particles was generally lower compared to disiloxane derived particles. Furthermore, the carbon content decreased with rising oxygen to monomer ratio, plasma power, and process pressure. The conversion from monomer to nanoparticles was favoured by high pressure, short residence time, and high monomer content in the process gas. The morphology of the produced amorphous particles was similar to fumed silica, with primary particles in the size range of 10 nm, building hard-agglomerates of several

hundred nanometres during the synthesis. Finally, an adapted particle growth model for a continuous plasma reactor, illustrated in Figure 4.1, was introduced which explains the influence of the different process parameters on the particle evolution.

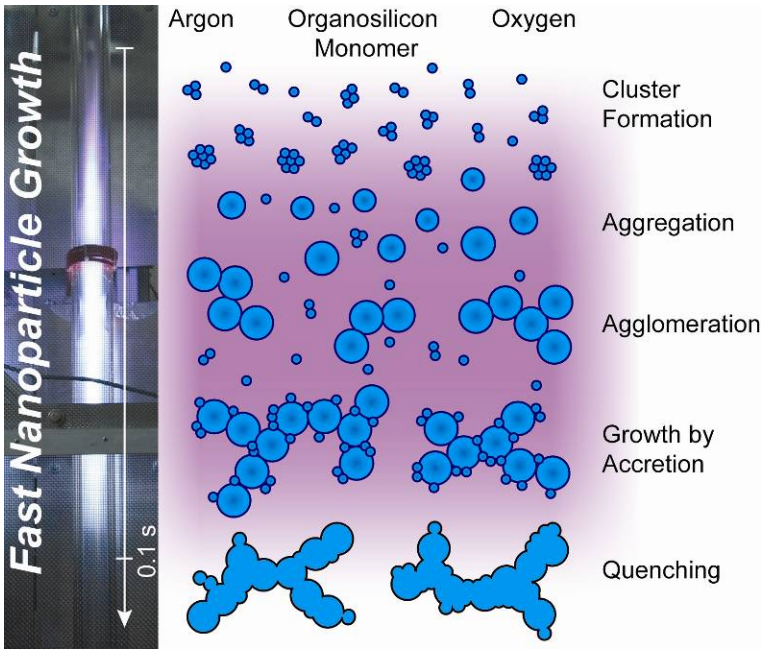


Figure 4.1: Adapted particle growth model for this tubular plasma reactor, taken from [6].

5 References

[1] Arpagaus C, Rossi A and Rudolf von Rohr P. Short-time plasma surface modification of HDPE powder in a plasma downer reactor - process, wettability improvement and ageing effects. *Applied Surface Science*, 252(5): 1581-95, 2005.

[2] Karches M, Morstein M and von Rohr P R. Encapsulation of abrasive particles by plasma CVD. *Surface & Coatings Technology*, 169: 544-8, 2003.

[3] Karches M, Morstein M, von Rohr P, Pozzo R L, Giombi J L and Baltanas M A. Plasma-CVD-coated glass beads as photocatalyst for water decontamination. *Catalysis Today*, 72(3-4): 267-79, 2002.

[4] Spillmann A, Sonnenfeld A and Rudolf von Rohr P. Flowability modification of lactose powder by plasma enhanced chemical vapor deposition. *Plasma Processes and Polymers*, 4: S16-S20, 2007.

[5] Roth C, Künsch Z, Sonnenfeld A and Rudolf von Rohr P. Plasma surface modification of powders for pharmaceutical applications. *Surface & Coatings Technology*, 205(S2): S597-600, 2011.

[6] Roth C, Oberbossel G, Buitrago E, Heuberger R and Rudolf von Rohr P. Nanoparticle synthesis and growth in a continuous plasma reactor from organosilicon precursors. *Plasma Processes and Polymers*, 9(2): 119-34, 2012.

Topic:

***(3) Films and coatings* – Nano Films –** Nanostructures and nanoparticles

Title: **Silicon dioxide coating of titanium dioxide nanoparticles from dielectric barrier discharge in a gaseous mixture of silane and nitrogen**

Sebastian Dahle[12*], Lienhard Wegewitz[13], Fei Qi[4], Alfred P. Weber[4], Wolfgang Maus-Friedrichs[1]

[1] Institut für Physik und Physikalische Technologien, Technische Universität Clausthal, Leibnizstrasse 4, D-38678 Clausthal-Zellerfeld, Germany

[2] Hochschule für Angewandte Wissenschaft und Kunst, Fakultät für Naturwissenschaften und Technik, Von-Ossietzky-Straße 99, D-37085 Göttingen, Germany

[3] Clausthaler Zentrum für Materialtechnik, Technische Universität Clausthal, Leibnizstrasse 4, D-38678 Clausthal-Zellerfeld, Germany

[4] Institut für Mechanische Verfahrenstechnik, Technische Universität Clausthal, Leibnizstrasse 19, D-38678 Clausthal-Zellerfeld, Germany

[*] Corresponding author: Tel: +49-5323-72-2745 Fax: +49-5323-72-3600
e-mail: s.dahle@pe.tu-clausthal.de

Keywords: Metastable Induced Electron Spectroscopy, Ultraviolet Photoelectron Spectroscopy, X-ray Photoelectron Spectroscopy, Atomic Force Microscopy

ABSTRACT

Titanium dioxide nanoparticles are used commonly in various applications due to their high catalytic activity. Many of these applications require subsequent treatments after the deposition of the TiO_2 particles. Some of these include thermal processing at high temperatures, e.g. roof tiles. For all of these applications, the crystal structures as well as the microscopic properties are essential. Thus, sintering severely affects the catalytic activity in most of the cases. During thermal processing, the nanoparticles transform from the catalytical highly active anatas structure to the substantially less active rutil structure. This structural change has been found to be significantly retarded when coating the TiO_2 nanoparticles with a closed film of SiO_2. During the thermal treatment, these films break open, revealing the underlying TiO_2 [i]. Thus, the film thickness has to be appropriate for the designated treatment subsequent to the nanoparticle deposition.

In this study, we present an approach of SiO_2 film deposition making use of silane gas. Pure silane gas is highly demanding on safety standards and technical installations, since it acts self-igniting and highly explosive when getting in contact with air or any oxygen containing gas. Thus, diluted process gases are used for most technical implementations, which contain just about 3% silane in 97% helium, neon, argon, hydrogen or nitrogen. While noble gases and hydrogen are used as dilution for a wide range of applications, the process gas consisting of nitrogen and silane is only implemented for silicon nitride deposition. Nevertheless, this gas should be the most suitable for many applications

regarding economics and handling. Closed films produced by dielectric barrier discharges in such mixtures of gases consist of mainly non-stoichiometric silicon nitride, while the other diluted process gases produce metallic silicon films. The deposition of silicon dioxide films is rather complicated, since the silane reacts instantaneously with every oxygen-rich gas. Thus, both gases must not get in contact until they have arrived in front the surface that is to be coated. Most of the existing work found in the literature focuses on the implementation of this condition, to merge the silane and the oxygen right at the surface being coated. Taking a quite different approach, we divided the film deposition into two steps: In the first step, a silicon nitride film was deposited from the process gas with the silane diluted in nitrogen employing a dielectric barrier discharge plasma. As a second step, the silicon nitride film has been tried to convert into silicon dioxide by means of a second plasma discharge using either oxygen for a process gas or even environmental air.

All studies have been carried out in an ultra high vacuum apparatus, while the plasma treatments have been carried out up to atmospheric pressure. During the investigations we employed Metastable Induced Electron Spectroscopy (MIES), Ultraviolet Photoelectron Spectroscopy (UPS) and X-ray Photoelectron Spectroscopy (XPS), as well as Atomic Force Microscopy (AFM). The microscopic measurements showed the deposited film to enclose the particles in a Frank van der Merwe – type growth mode. Film thicknesses determined by increased particle diameters in AFM were in good accordance to calculated film thicknesses from XPS peak intensity attenuation. Spectroscopic results show a formation of a silicon nitride film with substoichiometric nitrogen content, though free of oxynitrides. Surface impurities and adsorbates from the ex-situ preparation procedure were strongly removed and seemed to notably increase the growth rate. The second step gained a transformation of the film up to 98% silicon dioxide according to XPS. Remaining carbon impurities from the initially uncleaned surface were removed by both of the oxidizing plasmas. The transformation was found to be even more effective for the air plasma treatment than for the oxygen plasma treatment at a comparable oxygen partial pressure.

---

[i] Qi F, Moiseev A, Deubener J, Weber A (2911) J. Nanopart. Res. 13:1325-1334.

High Power Pulsed Hollow Cathode for Nanoparticle Synthesis

Daniel Söderström[1], Iris Pilch[1], Nils Brenning[2], and Ulf Helmersson[1]

[1]Linköping University, Plasma & Coatings Physics, Linköping, Sweden
[2]Royal Institute of Technology, School of Electrical Engineering, Division of Space & Plasma Physics, Stockholm, Sweden

Abstract

Copper nanoparticles were synthesized using a novel method based on sputtering material from a hollow cathode using high power pulses. The high power pulses provide a supersaturated vapor with a high degree of ionization from which the nanoparticles are formed in the gas phase. By adjusting the pulse parameters, the plasma environment and thus the nanoparticle growth can be affected. It was found that the nanoparticle size can be influenced by varying, e.g., the pulse frequency or the pulse power. The results using the high power pulsed hollow cathode are compared to nanoparticles synthesized with a dc discharge using the same setup.

Introduction

The large interest in materials in the form of nanoparticles (NPs) stems from the unique properties they have compared to bulk quantities, e.g high surface-to-volume ratio [1,2] and plasmonic effects [3,4]. This has led to a demand for NPs with well-defined characteristics, e.g. sizes with narrow size distributions. The challenge is to develop a technique that can meet the demands. Today, there exist several techniques to synthesize NPs, e.g. milling, wet chemistry, flame synthesis, and plasma-based methods. Plasma-based methods provide an elegant method to create non-agglomerated NPs from a wide selection of materials in a controlled environment. The material from which the NPs should be synthesized can in the plasma-based methods be provided either chemically, i.e. in a reactive process [5], or physically in a sputtering process [6]. Using a physical method, any material that can be sputtered can in principle be used to synthesize NPs.

NPs in a non-equilibrium plasma will, when they reach a size of about 10 nm, be negatively charged due to the higher mobility of the electrons compared to the positive ions. This is the reason why the NPs will not be agglomerated in the plasma, which is a large benefit.

The NPs form in the plasma by a supersaturated vapor. Three-body collisions form small clusters that grow by colliding with each other or with single atoms or ions. As the NPs grow, they get negatively charged and coalescence between NPs is prevented. They can now only grow by collecting atoms or ions. Due to the attractive force between positive ions and the negatively charged NPs, the collision cross-section for positive ions is at least one order of magnitude larger than for neutrals. It is therefore of benefit to have a large fraction of the NP building material in ionized form. Achieving a high plasma density also leads to a higher density of sputtered material, which promotes NP formation.

In our novel method to synthesize NPs, we use high power pulses similar to what is used in high power impulse magnetron sputtering [7], to achieve a high plasma density. To further enhance the plasma density and to keep the plasma focused, we use a hollow cathode.

In this study, we have used a copper hollow cathode to synthesize copper NPs, and studied the effect of pulse power and pulse frequency on the size of the NPs. The results from the pulsed power method has also been compared to the results from running the same set-up with DC power.

Method

The copper hollow cathode (length 54 mm, outer diameter 12 mm, and inner diameter 5 mm) was mounted at the center of the top lid of a stainless steel chamber with a diameter of 290 mm and a height of 430 mm. A sketch of the setup can be seen in figure 2. The cathode is water cooled with a gas inlet from above. Outside the orifice of the hollow cathode a stainless steel grounded anode shaped as a ring with a diameter of 30 mm is placed. The anode ring was kept at a distance of 45 mm from the cathode during the experiments. A volume outside the hollow cathode, including the anode ring, is enclosed by a stainless steel mesh cage that prevents the plasma from escaping to other grounded structures.

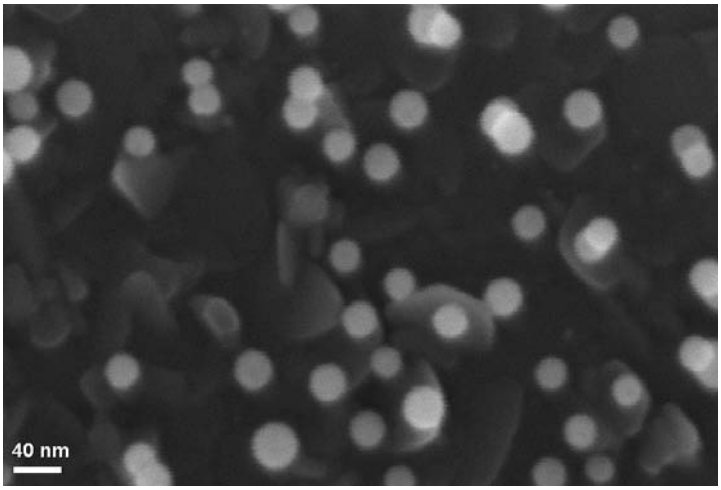


Figure 1: Example scanning electron microscope image of copper nanoparticles. The background shows the titanium film on the silicon substrate.

Below and outside the mesh cage, 160 mm from the hollow cathode, a rotatable substrate table with space for up to six substrates is mounted. The substrates are 10x10 mm silicon pieces with a 200 nm layer of titanium on them. To attract the negatively charged NPs to the substrates, a bias voltage of +10 V was applied to the substrates by a clamp to the substrate surface.

The chamber was pumped down by a turbomolecular pump backed by an oil-sealed pump to a base pressure of $4x10^{-6}$ Torr. Argon was used as sputtering gas, and the working pressure was set to 0.8 Torr (107 Pa), yielding an argon gas flow of 60 sccm. The high power pulses were delivered by a pulsing unit built in-house, fed by a DC power supply (Advanced Energy MDX-1K).

The dependence on the pulsing parameters were studied by varying the pulse frequency while keeping the pulse power (i.e. the energy per pulse) constant, and by keeping the time-average power constant, i.e. by decreasing the pulse power as the frequency is increased. The effect of varying pulse power was studied by keeping the frequency constant and equal to 700 Hz.

A series of experiments with DC power were also performed and compared to the pulsed power results. The setup during the DC experiments was the same as during the pulsed power experiments.

The synthesized NPs, collected on the titanium-coated silicon pieces were analyzed using a scanning electron microscope. An example of spherical copper NPs synthesized with the pulsed power process is shown in figure 1. Micrographs at different magnifications were run through a Matlab script which identified single NPs and calculated their size distributions. The mean size and standard deviation were calculated by fitting a log-normal distribution to the result.

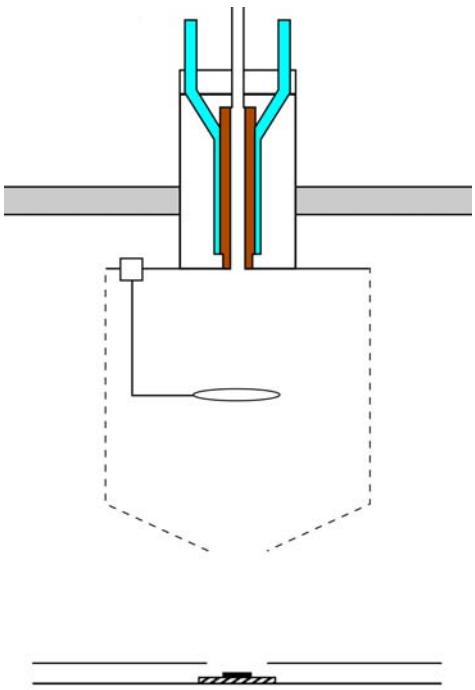


Figure 2: Schematic drawing of the experimental setup. Ar sputter gas flows through the hollow cathode,which is cooled by circulating water. The anode ring, mesh cage, and substrate table are seen below the hollow cathode.

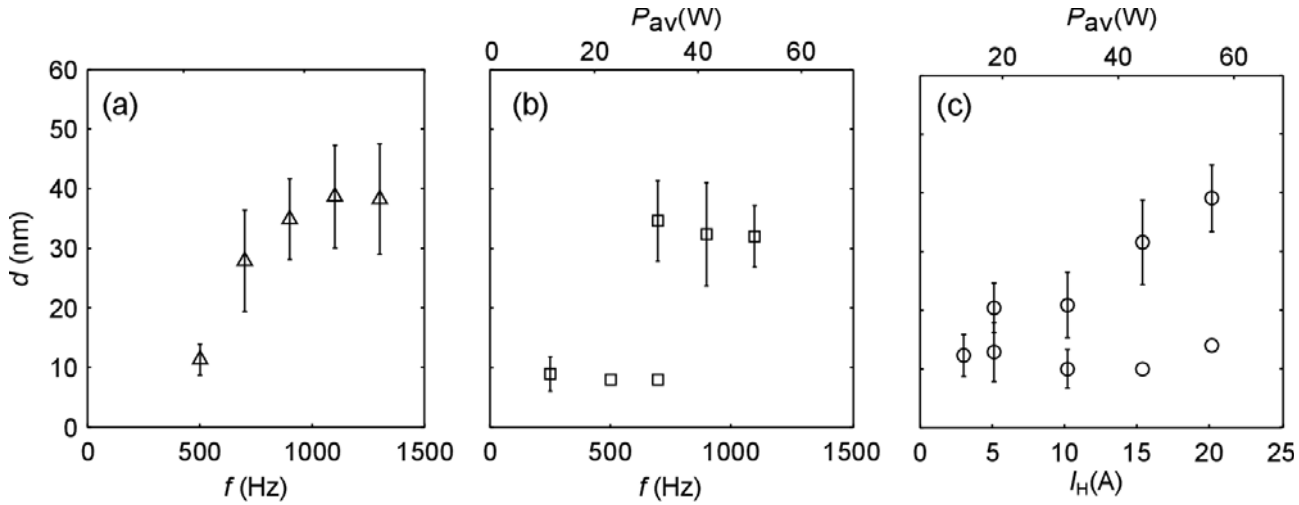


Figure 3: Mean nanoparticle diameters synthesized with the pulsed hollow cathode at (a) constant average power (30 W), (b) constant energy per pulse, and (c) constant pulse frequency (f=700 Hz). The error bars indicate the standard deviation of the fitted log-normal distribution. Points without error bars did not have enough statistics to estimate a standard deviation.

Results and discussion

The results from the pulsed power experiments are shown in figure 3. The NP size increases both with frequency and average power.

A step can be seen in the NP size when the frequency is increased with constant pulse power (the peak current in the pulse was kept at I = 10 A) in figure 3 (b). Assuming that the sputtered material per pulse is the same, the increase in NPs size with frequency can be explained by an overlap of material and plasma from consecutive pulses. Since the shape of the current curve is constant when the frequency is changed, a plasma overlap within the hollow cathode can be excluded. Even when the frequency is changed with constant average power (figure 3 (a)) the NP sizes increases. As the frequency is increased the power per pulse, and thus the amount of sputtered material and the ionization per pulse, is lowered to keep the average power constant. This shows that the material and plasma overlap is important, since sputtered material that is refilled to a region where NPs already exist mainly attaches to the NPs rather than form new NPs and a re-ionization by consecutive pulses charges already present NPs which can grow by the effect discussed in the introduction.

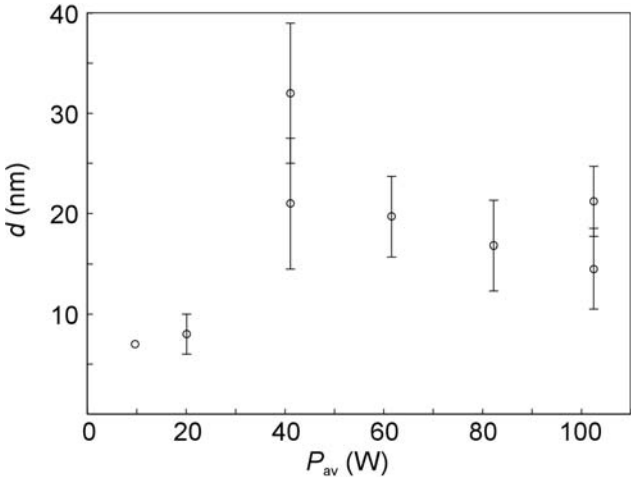


Figure 4: Mean nanoparticle diameters synthesized with the DC hollow cathode at different discharge powers. The error bars indicate the standard deviation of the fitted log-normal distribution. Points without error bars did not have enough statistics to estimate a standard deviation.

As the peak current in the pulses was changed at constant frequency (f=700 Hz), two size populations could be observed, see figure 3 (c). The amount of smaller NPs decreased as the peak current increased. Since the frequency, 700 Hz, is in the range where a sharp rise in NP sizes occurs, it is natural that we have two size populations of smaller and larger NPs. As the peak current, and thus the power in the pulse, increases, more material is sputtered and the ionization degree increases, which increase the NP sizes.

When the process was run with DC power, the synthesized NPs were generally smaller compared to the pulsed process at the same average power, as can be seen in figure 4. The size has a maximum around 40 W and decreases towards higher power. This has also been seen in other studies [8]. The NP formation is dependent on the surrounding gas temperature, and an elevated gas temperature is expected to heat the NPs so that they evaporate and are reduced in size. Since the gas temperature in the discharge would increase with deposited power, a reduction of NP sizes should be seen as the power is increased.

In the DC case we lack the effect of providing material at high density in pulses, and the degree of ionization should be lower compared to the pulsed case. Judging from the results of the pulsed process, where those two parameters are important, the continuous power deposition in the DC case leads to a different type of NP growth. The reduction of NP sizes as the average power is increased can not be seen from the results for the pulsed process. More experiments are needed to fully understand this process.

Summary

A novel plasma-based NP synthesis process utilizing high power pulses has been developed. The high power pulses were applied to a copper hollow cathode, which leads to a high density plasma and a high sputtered material density. The pulse parameters frequency and pulse energy were varied. It was found that the NP sizes generally increase with average power. The same trend was seen for constant average power when the frequency was increased, showing that overlapping pulses are important for the NP growth.

The pulsed process was compared to a DC process using the same experimental setup. The results from the DC experiments show that the NP size in this case in general are smaller than the NPs synthesized by the pulsed process at the same average power. The sizes also show a maximum at a certain power with decreasing sizes towards higher powers, which can be caused by an increasing gas temperature at higher powers leading to a higher evaporation rate of the NPs.

References

[1] B. R. Cuenya, Thin Solid Films 518, 3127, 2010.
[2] A. Z. Moshfegh, Journal of Physics D: Applied Physics 42, 233001, 2009.
[3] S. Linic, P. Christopher, et al., Nature Materials 10, 911, 2011.
[4] E. A. Coronado, et al., Nanoscale 3, 4042, 2011.
[5] M. Adachi, et al., Journal of Nanoparticle Research, vol. 5, no. 1/2, pp. 31-37, Apr. 2003.
[6] K. Ostrikov and A. B. Murphy, Journal of Physics D: Applied Physics, vol. 40, no. 8, pp. 2223-2241, Apr. 2007.
[7] U. Helmersson, et al., Thin Solid Films 513, 1, 2006.
[8] K. Ishii, K. et al., Journal of Vacuum Science & Technology A: Vacuum, Surfaces, and Films, vol. 17, no. 1, p. 310, 1999.

Performance of atmospheric plasma sprayed HA coatings under dry and wet fatigue conditions

J. N. Barry, A. J. Carr, D. P. Dowling

School of Mechanical and Materials Engineering, University College Dublin, Belfield, Dublin 4;

Email: denis.dowling@ucd.ie

Keywords: Mechanical Fatigue, Biomimetic testing, Plasma Spray, Bio-medical Coatings

Abstract

Hydroxyapatite (HA) is widely used as a bio-medical coating on press-fit (cementless) orthopaedic implants to enhance the biological response of the device. Presently atmospheric plasma spray (APS) is the most widely applied technology for the deposition of such bio-medical coatings. There have been concerns however, regarding the high deposition temperatures to which the HA precursor powder is exposed during APS processing, as this can result in changes to the HA powder's crystallinity. Furthermore, concerns have been raised regarding the affect these crystalline alterations may have on the solubility of the deposited HA coating, and thus, the affect they may have on the integrity of the coating at the metal interface. The aim of this study is to evaluate the fatigue performance of APS HA coatings, carried out under both dry and wet fatigue conditions. The wet fatigue conditions were facilitated using a Simulated Body Fluid (SBF) solution, which enabled the *in vitro* simulation of the HA coating response in a typical *in vivo* environment. SEM and XRD examination of both the reference (as received) and dry samples demonstrated the coating properties were almost identical after 10 million cycles, while the evaluation of the wet samples suggested complete failure of the HA coating had occurred during testing. In conclusion, HA coating delamination during the wet fatigue testing was attributed to significant weakening of the coating, due to material loss from dissolution as a result of exposure to the SBF solution. Significantly the dissolution was found to occur both at the interface and within the coating.

Introduction

The commercial success of the atmospheric plasma spray (APS) deposition technology in the application of HA coatings is due to its high deposition rates, large coating thickness, reasonable chemical and microstructure control, mid-level deposition cost and ability to coat complex shapes. Concerns however, have been raised regarding the change in HA crystalline phase during the high temperature (≈5700 °C) APS deposition process [1]. Crystalline HA coatings have shown lower dissolution rates and enhanced long term fixation in-vivo [1, 2]. Furthermore, there are concerns regarding the effect that this enhanced dissolution may have on the integrity between the metal interface and the plasma spray coating [2].

In recent years, explanted APS HA coated devices, have shown signs of severe coating delamination [3] and third body wear [4]. The issue of delamination has been attributed to the continuous loading and unloading (or fatigue loading) of the device during normal implanted function, however, ISO standard fatigue tests performed on APS HA coatings, have shown little or no coating failure after 10

million cycles [5]. Significantly these standards require the fatigue tests be performed only in atmospheric conditions. While these conditions are suited for replication, they do not however represent the biological conditions that the implant is exposed to during normal implanted function.

This paper evaluates the long term fatigue performance of APS HA coatings carried out under both dry (atmospheric) and wet fatigue conditions. Both the dry and wet fatigue tests were performed to a modified ISO standard. In the case of the wet tests, the APS HA coating is exposed to a Simulated Body Fluid (SBF) solution during testing. The SBF solution is designed to mimic the ion concentration and pH conditions that an implanted coated device would be exposed to during normal implanted function [6]. The properties of the samples were evaluated post fatigue testing using a range of characterisation techniques. The aim of this study was to determine if the wet conditions, rather than the dry conditions, would better represent the long term response of the APS HA coatings observed during normal implanted function.

Materials & Methods

The fatigue studies were carried out using titanium alloy (grade V) cylindrical substrates machined to the dimensions detailed in Figure 1. The APS HA coatings were deposited by APS Materials Inc. (Waterford, Ireland), a commercial atmospheric plasma spray deposition company. The fatigue tests were performed using a rotating cantilever bending machine (or Wöhler tester) [7], which operates at 4700 rpm, and with an adjustable cantilever length set to 70mm.

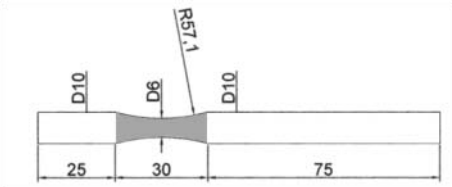


Figure 1: Fatigue substrate dimensions, with the coated section indicated in grey

Fatigue Limit

The fatigue limit is defined as the maximum value of applied alternating stress that a test sample can indefinitely endure without failure. The fatigue limit is integral to this study, as the purpose of this study is to evaluate the fatigue performance of the APS HA coatings and not that of the substrate. Knowing the fatigue limit will prevent failure of the substrate and determine the maximum fatigue stress possible to be imparted on the APS HA coatings. Through experimentation the fatigue limit of the titanium substrates was estimated to be 550 MPa, which fits well with literature [8-10].

Dry fatigue testing

The dry fatigue tests were performed under atmospheric conditions, and involved mounting the APS HA samples on the tester with the required cantilever load positioned 70mm from the centre of coated section (grey area in Figure 1). The APS HA samples were then tested to 10 million cycles, at 4700 rpm. The load was calculated as that required to develop a stress amplitude equivalent to 90 % the

fatigue limit, or 495MPa. The use of only 90 % of the fatigue limit gave further assurance that the substrates would not prematurely fail due to fatigue, and also guaranty a high level of stress could be imparted on the APS HA coating.

Wet fatigue testing

The wet fatigue tests were performed under the same fatigue parameters as the dry tests. An additional soft polymer enclosure, encapsulating the APS HA coating, facilitated the exposure of the SBF solution to the coating for the full period of testing. To insure retention of the SBF solution during the high speed testing, the soft polymer enclosure was sealed using a cyanoacrylate adhesive.

Following testing, the substrates were ultrasonically cleaned in deionised water and dried at 50 °C for 1.5 hours prior to evaluation. The surface roughness (R_a) of the HA coatings was determined using optical profilometry. Scanning Electron Microscopy (SEM) analysis was performed to examine the coating morphology and cross-section. The chemical elements present at the coated interface were determined using Energy Dispersive X-ray spectroscopy (EDX). The crystallographic structure present at the coated interface was determined using X-ray diffraction (XRD).

Results & Discussion

SEM micrographs of the tested samples established that the morphology (Figure 2) of both the reference and dry samples were almost identical. Conversely, there appeared to be little or no coating present in the micrographs of the wet samples.

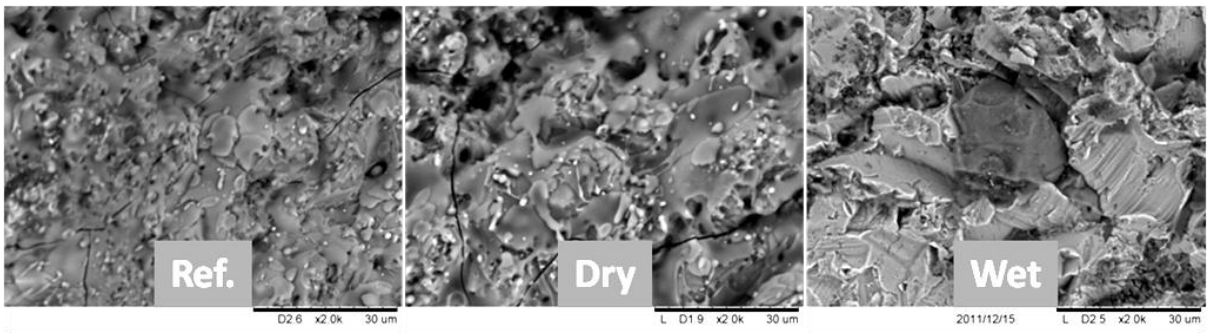


Figure 2: SEM morphological micrographs (×2000) of the Ref (as received), Dry tested and Wet tested samples.

Further investigation using XRD (Figure 3) reflected these findings, with the wet sample's spectra showing no XRD peaks related to HA and three large peaks associated with the substrate material. Furthermore, EDX analysis of the wet samples only detected trace elements of Ca and P (constituent of HA). Cross-sectional micrographs of the tested samples, verified that no HA coating was present on the wet tested samples, but significantly found that minor coating splintering had occurred in the case of the dry samples.

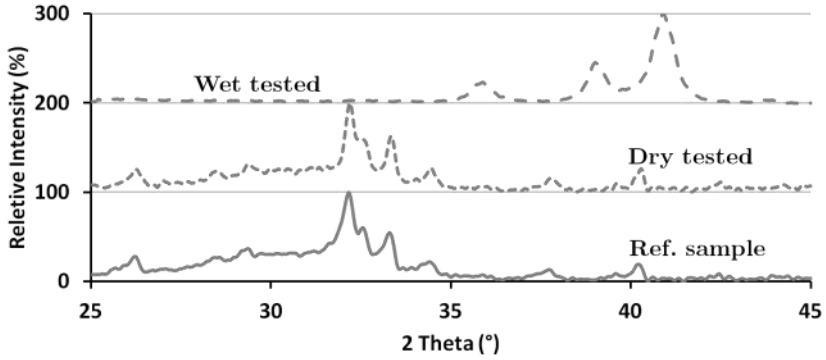


Figure 3: XRD evaluation of the Ref (as received), Dry tested and Wet tested samples.

These findings indicate that complete delamination of the APS HA coatings has occurred during wet fatigue tests, while the same fatigue parameters under dry conditions resulted in only some splinters but no coating delamination. The disparity in results for the dry and wet fatigue test conditions are due in part to the inherent HA dissolution that occurs in the presence of the SBF solution. Importantly, this dissolution would also be expected to occur within the body. An examination of the literature regarding explanted APS HA coated devices would further suggest that the tests performed with the SBF solution provide a more accurate representation of the implanted device environment. Therefore, this fatigue test methodology should provide a more accurate assessment of the long term performance of APS HA coatings in the body.

Acknowledgement

This work is supported by the Science Foundation Ireland under grant No. 08/SRC/I1411

References

1. Hench, L. and J. Wilson, *An introduction to bioceramics*1993: World Scientific Pub Co Inc.
2. Xue, W.C., et al., *In vivo evaluation of plasma sprayed hydroxyapatite coatings having different crystallinity.* Biomaterials, 2004. **25**(3): p. 415-421.
3. Heimann, R.B., *Thermal spraying of biomaterials.* Surface and Coatings Technology, 2006. **201**(5): p. 2012-2019.
4. Brown, T., et al., *2009 Nicolas Andry Award: Clinical Biomechanics of Third Body Acceleration of Total Hip Wear.* Clinical Orthopaedics and Related Research®, 2009. **467**(7): p. 1885-1897.
5. Clemens, J.A., et al., *Fatigue behavior of calcium phosphate coatings with different stability under dry and wet conditions.* J Biomed Mater Res, 1999. **48**(5): p. 741-8.
6. Kokubo, T., et al., *Solutions able to reproduce in vivo surface-structure changes in bioactive glass-ceramic A-W3.* Journal of biomedical materials research, 1990. **24**(6): p. 721-734.
7. Knez, M., et al., *A rotating bending approach for determination of low-cycle fatigue parameters.* International Journal of Fatigue, 2010. **32**(10): p. 1724-1730.
8. Callister, W., *Materials Science and Engineering: An Introduction, 7th Eds*, 2008, Wiley, 832p.(ch2) Callister WD and Reth isch DG.
9. Rack, H.J. and J.I. Qazi, *Titanium alloys for biomedical applications.* Materials Science and Engineering: C, 2006. **26**(8): p. 1269-1277.
10. Niinomi, M., *Mechanical properties of biomedical titanium alloys.* Materials Science and Engineering: A, 1998. **243**(1–2): p. 231-236.

Comparison of microbiological effects in long fine-lumen tubes by low and atmospheric pressure plasmas

Uta Schnabel, Manfred Stieber, Jörg Ehlbeck

Leibniz-Institute for Plasma Science and Technology e.V. (INP), Felix-Hausdorff-Straße 2, D-17489 Greifswald, Germany

Inadequate cleaning and disinfection of reprocessed endoscopes have been reasonable factors of infectious complications during endoscopic procedures. The decontamination of long fine-lumen tubes as occurred in endoscopes by low and atmospheric pressure plasmas is shown. Furthermore, the antimicrobial effect of different plasma setups is comparable due to a new established and standardized contamination and recovery procedure.

Key words: bacterial spores; non-thermal plasma; polytetrafluoroethylene (PTFE); decontamination; multicentre trials

Introduction

Minimal invasive treatment using tubes such as catheters and endoscopes is well-established. Since the introduction of flexible endoscopy into medical practice, many cases of infectious complications involving bacteria, fungi and viruses have been linked to endoscopic procedures. Inadequate cleaning and disinfection during the reprocessing of the instruments have been reasonable factors as well as insufficient final rinsing and incomplete drying of the endoscope or contaminated flushing equipment for the air/ water-channel. Flexible endoscopes are thermo-labile and cannot withstand heat sterilization processes. Common disinfection processes like ethylene oxide or hydrogen peroxide vapour as well as formaldehyde are more or less effective, but require long contact and aeration times. Furthermore, these processes use toxic and explosive substances. Therefore, the development of new methods for the sterilization of thermo sensitive devices especially with long fine lumen is very important. A promising possibility is the decontamination by plasma discharge treatment. Various plasma setups have been developed. However, due to the complexity of plasma techniques and technologies, setups and parameters, it is impossible to compare their antimicrobial efficacy by single experiments. A standardization of microbiological parameters is necessary to attribute the observed effects solely to the plasma efficacy.

This work is based on round robin tests with and without plasma treatment by three institution (the Fraunhofer IGB Stuttgart, Germany; the HygCen GmbH Schwerin, Germany and the INP Greifswald, Germany) and the publications by Maucher et al. (2011) and Schnabel et al. (2012).

Materials and Methods

Endospores of *B. atrophaeus* (ATCC 9372) and of *G. stearothermophilus* (ATCC 7953) as standardized biological indicator for sterilization processes were chosen.

Corresponding author: Uta Schnabel
e-mail: uta.schnabel@inp-greifswald.de
Tel.: +49-3834-5543875; fax: +49-3834-554301

Polytetrafluoroethylene (PTFE) tubes (Saint-Gobain Performance Plast, Germany) with an inner diameter of 2 mm, outer diameter of 3 mm, and a length of 1–1.2 m (1 m length was used as positive reference, without plasma treatment, or 1.20 m, according to the required length for the used plasma treatment composition) were used as test tubes.

The contamination of the test tubes with endospores and the recovery of reference bacteria and of survival bacteria after plasma plasma treatment was realized by a newly developed cycle method. This so called IGB-cycle method is described in Maucher et al. (2011). The defined endospore suspension with 10^8–10^9 cfu ml^{-1} was pumped for a period of 5 minutes (flow rate of 15 ml min^{-1}) for contamination or 50 ml tryptic soy broth for 20 min (flow rate of 30 ml min^{-1}) for recovery from a storage flask through the test tube and back to the flask. Venting was assured by a filter. After plasma treatment, the collected suspension contains the endospores detached from the test tube and suspended in the broth. The resulting amounts of colony forming units (cfu) were quantified according to, for instance, EN 14561 and TS/ISO 15883-5.

The INP decided to use a coaxial DBD setup. The setup consists of a grounded, metallic inner and a spiral outer electrode for the presented studies described in Schnabel et al. (2012). The inner electrode is moved in translatory motion to avoid local damages of the tube wall. The microbial decontamination was done with moistened air (1.5 slm and a relative humidity of 65%). The high voltage was generated by a car ignition coil from the amplified sine-wave signal of a signal generator (‘‘AFG 3022 B’’ Tektronix, Cologne, GmbH Germany). The process parameters for the decontaminating plasma treatment of three tubes were an Uss of 9.0 kV, a f of 3.0 kHz and a P of 8.0 W. The all in all treatment time for the decontamination of the specimen was 14 min and the inner temperature ranged from 50 to 60 °C.

The decontamination of the specimen at Fraunhofer IGB has been done using low pressure plasma glow discharge. The plasma treatments have been done with a coaxial arrangement of the electrodes with or without an inner electrode as described in Schnabel et al. (2012). The grounded electrode is a wire of stainless steel (diameter 0.8mm) and located along the axis within the lumen of the contaminated PTFE tube. This specimen is located within a conduit of polymethylmethacrylate (PMMA). The inner diameter of this conduit (6mm, wall thickness 1mm) is slightly larger than the outer diameter of the specimen. The hot electrode does consist of an adhesive copper strip (supplier 3M Deutschland GmbH, width 10 mm), which is wounded in a helical manner around the PMMA conduit. The power source is a RF generator (ENI) HPG-2 with 190 kHz. The vacuum is created at one end of the specimen by a rotary vane pump (Alcatel 2012A) resulting in a residual pressure of 2 mbar. The other end is connected to massflow controllers (MKS). The pressure (Vacubrand DVR5) at the entrance of gas flow into the specimen is 15 mbar, at the exit 4 mbar. The applied powers and treatment times have been at 15 W and 20 min.

Results and Discussion

The focus was on the comparability of the antibiological efficacy affected by different plasma techniques conducted by different laboratories. Furthermore, the recovery of plasma treated specimen by three different laboratories was compared. Overall six comparative experiments were carried out. The contamination of all test tubes was performed according to the IGB-cycle-method described above. HygCen performed the contamination for the experimental series 2, 3, and 6. IGB performed the contamination in series 5 and INP in series 4. The recovery experiments were done by all participating laboratories using the earlier explained recovery procedure. The plasma treatment was realized by the working groups of the IGB (low pressure plasma) and of the INP (atmospheric pressure plasma).

The round robin tests 1–3 are preliminary performed to investigate different microbial techniques for contamination and recovery of bacterial load in long fine lumen tubes. During these tests a standardized procedure was established for the comparability of antimicrobial efficacy of different plasma techniques independent on performer, microorganism, and laboratory. The first round robin test showed strong differences in contamination and recovery as measured by the participating laboratories. The second experimental series showed significant improvement in the uniformity of the results. The detected residues of the plasma treated specimen were comparable for each plasma configuration itself and for both techniques. The final standardization was reached by the third test. Moreover, the results for the plasma treated specimen showed a rising decontamination by plasma with reductions of 3.0–4.3 $\log_{10}$ cfu per specimen.

Finally, the establishment of the IGB-cycle-method for untreated and plasma treated specimen was received within three experimental series. The used conditions led to the best comparable results and furthermore to an upward decontamination of *B. atrophaeus* endospores in long fine lumen tubes. To verify the reproducibility of the methodology, the round robin tests 4–6 were performed to show the possibility of standardization of the IGB-cycle-method. Therefore, the microbial contamination was done by the INP (4th series), the IGB (5th series), and with endospores of *G. stearothermophilus* (6th series, contamination by HygCen).

The treatment with plasma resulted in *B. atrophaeus* endospore reductions from 3.2 $\log_{10}$ cfu per specimen as a minimum to 6.2 $\log_{10}$ cfu per specimen as a maximum. A reduction factor of 5.3 $\log_{10}$ cfu per specimen for the inactivation of spores of the biological indicator *G. stearothermophilus* could be achieved. Both plasma techniques lead to very good decontamination results that lay underneath the detection limit of 0 cfu per specimen.

Six series of experiments were required to assure a widespread standardization in the problematic areas related to verification of decontamination performance. The first important step is the procedure used to prepare the contaminating agent and the condition of the specimen. Secondly, the methodology used for contamination and its uniformity must be investigated. Finally the procedure for recovery has to be adjusted to assure reproducible and quantifiable results.

The advantage of our experimental workflow is the comparability of the microbicidal efficacy of different plasma setups by a standardized contamination and recovery used for all compared specimen. The problem of comparability of various plasma techniques was described by Ehlbeck et al. (2011).

Conclusion

Due to the complexity of plasma techniques and technologies, setups, and parameters, it is impossible to compare their antimicrobial efficacy by single experiments. A standardization of microbiological parameters is necessary to attribute the observed effects solely to the plasma efficacy. Therefore the specimen, microorganism, load, contamination, and recovery method as well as initial concentration must be well defined. Moreover, the commonly used and established challenge test is not suitable for non-thermal plasma decontamination investigations. In this work we showed a new and innovative procedure for the investigation of plasma techniques used for decontamination of long fine lumen of thermo-labile tubes and the possibility to get comparable results which rely on the antimicrobial effects of plasma. Furthermore three new plasma setups for the decontamination of PTFE-tubes were developed. Moreover, the effort which is needed to achieve comparable results in the round robin tests demonstrated the difficulties to compare microbiological results of different research groups in literature. Beside the standardized testing procedures also the amount and kind of data describing the test procedures is insufficient for comparability. Therefore, more work is needed to ensure in future the correct evaluation of data of different researchers.

Acknowledgements: We thank the Ministry of Education and Investigation of Germany (project EndoPlas 13N9320 to 13N929 as well as 13N9582) for financial support.

References

Ehlbeck, J., Schnabel, U., Polak, M., Winter, J., von Woedtke, Th., Brandenburg, R., von dem Hagen, T. and Weltmann, K.-D. (2011) Low temperature atmospheric pressure plasma sources for microbial decontamination. *J. Phys. D: Appl. Phys.* 44: 013002 (18pp)

Maucher, T., Schnabel, U., Volkwein, W., Koehnlein, J., Winter, J., Weltmann, K.-D., Trick, I. and Oehr, C. (2011) Assembly of Standardized Test Specimen for Microbial Quantification of Plasma Sterilization Processes of fine PTFE Tubes as used in Thermo Sensitive Medical Devices like Flexible Endoscopes. *Plasma Process. Polym.* 8, 200-207

Schnabel, U., Maucher, T., Köhnlein, J., Volkwein, W., Niquet, R., Trick, I., Stieber, M., Müller, M., Werner, H.-P., Ehlbeck, J., Oehr, C. and Weltmann, K.-D. (2012) Multicentre Trials for Decontamination of Fine-Lumen PTFE Tubes Loaded with Bacterial Endospores by Low and Atmospheric Pressure Plasma. *Plasma Process. Polym.* 9, 37-47

Tribological properties of laser textured and DLC coated surfaces with solid lubricants

J. Oksanen, T.J. Hakala, P. Laakso, S. Tervakangas, J. Kolehmainen, and J. Koskinen

Abstract

Hydrogen free diamond-like carbon coatings (DLC), i.e. tetrahedral amorphous carbon (ta-C) films, have high hardness and low coefficient of friction at ambient temperature and humid conditions. However, the coefficient of friction and wear rate in sliding contacts against steel surfaces increase severely at elevated temperatures. Adding solid lubricant into micro-reservoirs produced by Laser Surface Texturing (LST) has been reported to decrease the coefficient of friction of sliding surfaces. In this study, incorporation of MoS_2 and WS_2 solid lubricants onto laser textured and ta-C coated steel surface by burnishing was demonstrated to provide improved tribological properties such as low friction and high wear resistance at elevated temperature with an extended lifetime of the surfaces.

Introduction

Diamond-like carbon (DLC) films have been of interest due to their unique mechanical, chemical and tribological properties. Hydrogen free tetrahedral amorphous carbon (ta-C) films have high hardness and low coefficient of friction at ambient temperature and humid conditions. However, these tribological properties become remarkably deteriorated at elevated temperatures.

Solid lubricants are extensively used for reducing friction and wear in severe conditions, as in vacuum and high temperatures, where fluid lubricantion is not possible. Transition metal dichalcogenides (TMD) such as molybdenum disulphide (MoS_2) and tungsten disulphide (WS_2) are well known for their lubricating behavior [Winer, 1967].

Surface texturing as a method to improve the tribological properties of mechanical components is already well known for the last decade [Etsion, 2005]. The fundamental idea of LST is the controlled preparation of small dimples or grooves to act as lubricant reservoirs.

Solid lubricant addition onto surface micro-pits produced by LST has been reported to decrease the coefficient of friction of sliding surfaces [Rapoport *et al*., 2008]. The LST increased significantly the wear life of a burnished solid lubricant layer when compared to a non-textured surface.

Attempts of improving tribological properties of hydrogenated DLC by surface texturing have been reported [Dumitru *et al*., 2003] but no solid lubricants have been utilized in these studies.

The aim of this work was to improve the tribological properties of ta-C films at elevated temperatures by MoS_2 and WS_2 addition on LST surfaces.

Materials and Methods

Polished stainless steel (AISI 316, surface roughness less than 0,01 μm) disks were laser surface textured by picosecond laser. Dimples of 50 μm diameter and 5-10 μm depth with a spatial period of 50 μm yielding a dimple density of 28% were processed on the whole substrate surface.

LST steel substrates were coated with 1 μm thick ta-C film in DIARC filtered cathodic arc coating equipment.

MoS_2 and WS_2 solid lubricants were added on separate ta-C coated LST surfaces by burnishing technique using commercially available powders with an average particle size less than 2 μm. The burnishing process was done in lab conditions by applying a sliding pressure with a hard plate to the powder against the sample surface.

The tribological experiments were carried out by using a pin-on-disc (POD) tribometer developed at VTT. Tests were carried out with a sliding velocity of 0.05 m/s and a normal load of 10 N. At room temperature, 2 N load was used to avoid high Hertzian contact pressures at the beginning of the sliding. Stainless steel (AISI 316) spheres with 10 mm diameter were used as a counter body. In order to study the tribological properties of the samples at elevated temperatures, test temperature was varied from ambient room temperature to 350°C. Temperature steps were room temperature, 100°C, 200°C, 250°C, 300°C, and 350°C. The test was performed so that the temperature was increased into the next step after every 30 minutes of sliding and stopped when the coefficient of friction (COF) started to oscillate and increase remarkably. The sliding track was not changed between the different steps. COF for every temperature step was calculated as an average value of COF acquired during the test time of 10-30 minutes. As a reference, flat ta-C sample without any solid lubricant addition was also tested in the same manner.

Results

LST treated steel substrate resulted in a surface with evenly distributed dimples. Only small, approximately a few hundred nanometer high dimple bulges, which were removed after a short post-polishing process, were formed. After the coating process, the LST top surface had a whole ta-C film while the rough surfaces of the dimple bottoms were only partially coated.

Fig. 1 shows SEM images of burnished solid lubricants on ta-C coated LST surfaces. In the burnished surfaces, the dimples were filled with powder and also a few microns thick solid lubricant layer was formed on the areas around the dimples. Both lubricants were noticed to be rather adhesive on ta-C thus the burnishing method was noted to be a feasible method.

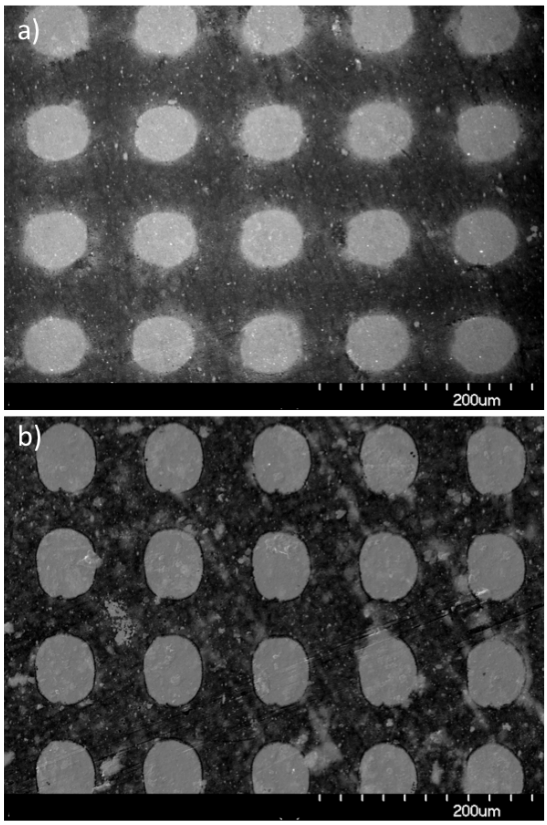


Figure 1. Burnished a) MoS_2 and b) WS_2 on ta-C coated LST steel surface.

The average COF values for ta-C coated LST surfaces with solid lubricants at different temperatures are shown in Fig. 2.

Burnished MoS_2 resulted to oscillation of COF values at room temperature (0.15-0.25). At 100°C, friction and oscillation decreased significantly. Lowest friction values of 0.02 was at 250°C but already at 300°C values increased and began to oscillate. At 350°C, friction increased severely and the coating broke down.

Burnished WS_2 had lower and more stable coefficient of friction than MoS_2 at room temperature (0.15) and COF decreased even further at 100°C. Interestingly the lowest coefficient of friction was approximately 0.05 at 300°C. At 350°C, the friction curve started to oscillate and slowly crept upwards as sliding continued, which indicated that the temperature was too high for WS_2 to operate properly. It seems that WS_2 addition provided better protection for ta-C at higher temperatures than MoS_2.

The reference ta-C film showed low friction values at ambient temperature but already at 100°C COF increased dramatically and the coating broke down after couple of minutes.

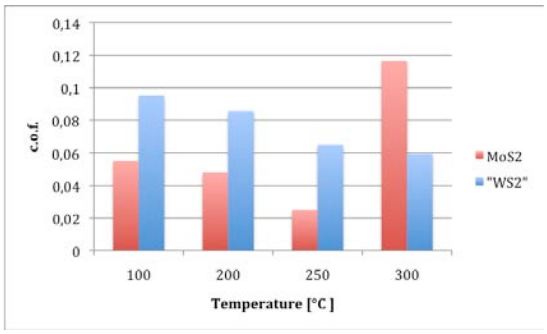


Figure 2. The average coefficient of friction values for ta-C coated LST surfaces with MoS_2 and WS_2 addition at different temperatures.

Discussion

The present study demonstrates possibilities for enhancing the tribological properties, such as low friction and wear resistance, of ta-C type DLC coatings in sliding contacts by a combination of laser surface texturing and solid lubricant.

Results showed that MoS_2 and WS_2 addition by burnishing did not improve the tribological properties of ta-C at room temperature but already at 100°C both solid lubricants provided a good protection for ta-C by reducing coefficient of friction remarkably compared to bare ta-C coating. It should be noted though that the solid lubricants used here would most probably oxidize if exposed to elevated temperatures for longer periods. This might have detrimental effect on their tribological properties.

Acknowledgements

The authors want to thank The MATERA Plus program for funding the research and Raimo Penttilä for laser texturing.

References

Winer W.O., Molybdenum disulphide as a lubricant: a review of fundamental knowledge. Wear, 10 (1967) pp. 422-52.

Etsion I., State of the art in laser surface texturing, ASME J. Tribol. 125 (2005) 248–253.

Rapoport L., Moshkovich A., Perfilyev V., Lapsker I., Halperin G., Itovich Y., Etsion I., Friction and wear of MoS_2 films on laser textured steel surfaces, Surface & Coatings Technology, Vol. 202, 2008, pp. 3332-3340.

Dumitru G., Romano V., Weber H.P., Pimenov S., Kononenko T., Hermann J., Bruneau S., Gerbig Y., Shupegin M., Laser treatment of tribological DLC films, Diamond and Related Materials, Vol. 12, 2003, pp. 1034–1040.

Zr-DLC coatings - analysis of the friction and wear mechanisms

T. Vitu[1], B.J.V. Pimentel[2], A. Escudeiro[3], A. Cavaleiro[3], T. Polcar[2,4]
[1]Faculty of Transportation Sciences, CTU in Prague, Czech Republic
[2]Faculty of Electrical Engineering, CTU in Prague, Czech Republic
[3]SEG-CEMUC - Department of Mechanical Engineering, University of Coimbra, Portugal
[4]nCATS, School of Engineering Sciences, University of Southampton, UK
e-mail: vitu@fd.cvut.cz

Introduction

In the last few decades, the amorphous or nanostructured carbon structures prepared by several deposition techniques are a subject of considerable research interest due to their excellent properties, such as high hardness and chemical inertness, wear resistance or low friction [1,2]. There have been also attempts to improve the mechanical, chemical or tribological properties of carbon coatings by addition of other elements. Generally, specific chemical composition of the modified films strongly affects the surface energy, and may modify various physical properties and decrease compressive stress, making some metal-doped carbon films suitable for large variety of practical applications [3].

Our work was focused on the structural, chemical and tribological properties of Zr-doped DLC coatings with controlled composition. The main attention was paid to the determination of the wear mechanisms, characterization of the worn surfaces and wear debris and formation of a tribolayer affecting the tribological process. The as-deposited coatings and worn surfaces were studied using 3D optical profilometry, Raman spectroscopy, X-Ray diffraction (XRD) and Scanning electron microscopy (SEM).

Experimental Details

Two d.c. magnetron sputtering deposition configurations were used to obtain both non-hydrogenated (Ar atmosphere) and hydrogenated DLC structure (reactive CH_4/Ar atmosphere). The coating structures were deposited using four targets - two of them were of pure carbon, one target was composite carbon with pellets of zirconium located in the erosion zone, fourth target was of Ti due to the adhesion interlayer deposition. The composite Zr/C target power was changed in order to obtain the structures with different zirconium content.

The coatings were studied from the structural, morphological and chemical point of view. The coatings composition was studied by Electron probe micro-analysis (EPMA). The XRD enabled to comprehend the coatings structure, Raman spectroscopy (λ = 532 nm) was used for detailed analysis of as-deposited, as well as worn areas and testing counter-parts. The tribological tests were performed by pin-on-disc Tribometer CSM at room temperature against 100Cr6 bearing balls with a diameter of 6 mm. The wear rates were observed using

3D non-contacting profilometer.

Results and discussion

The Zr-DLC(-H) coatings composition obtained by EPMA clearly proved that introducing of Zr/C composite target power led to the increasing zirconium content from 0 to 4.5 at.% approx. The Raman spectra of as-deposited Zr-DLC(-H) coatings are shown in Fig. 1.

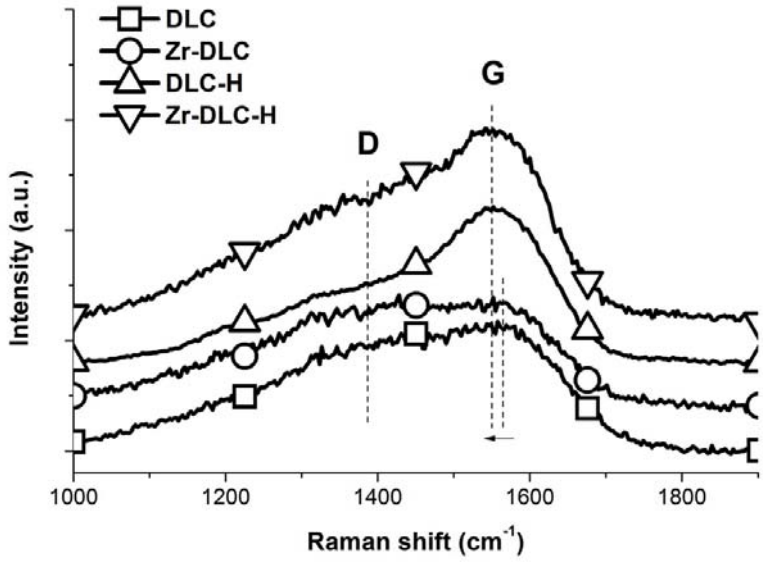


Fig. 1 Raman spectra of as-deposited Zr-DLC(-H) coatings

All Raman spectra clearly showed main carbon D and G peaks. With the incorporation of the Zr into the films, the G peak position shifted slightly towards lower wavenumbers. This G peak shift was associated with carbon bonds disordering and fragmentation [4]. Generally, the G peak position was slightly lower for hydrogenated coatings regarding on the Zr content in the film. Moreover, both the D and G peak appeared more pronounced compared to the corresponding hydrogen-free samples.

The hydrogenated films exhibited slight background photoluminescence effect. The I_D/I_G ratio determined from peak areas clearly supported the conclusions given by the G peak analyses. First, the incorporation of Zr dopants caused significant I_D/I_G ratio growth for both the hydrogen-free and hydrogenated coatings. Second, the hydrogenation of the DLC and Zr-DLC films resulted in the lower I_D/I_G ratio. More pronounced D peaks corresponded to the higher degree of C-C bonds fragmentation and decreasing of the specific size of carbon clusters. Lower I_D/I_G ratio could be also an indirect proof of the increasing sp^3/sp^2 fracture [5]. The friction curves of the Zr-DLC(-H) coatings were relatively stable with significant running-in stage (Fig. 2). The average friction coefficient varied from about 0.07 (hydrogenated Zr-DLC) to 0.24 (non-doped coatings).

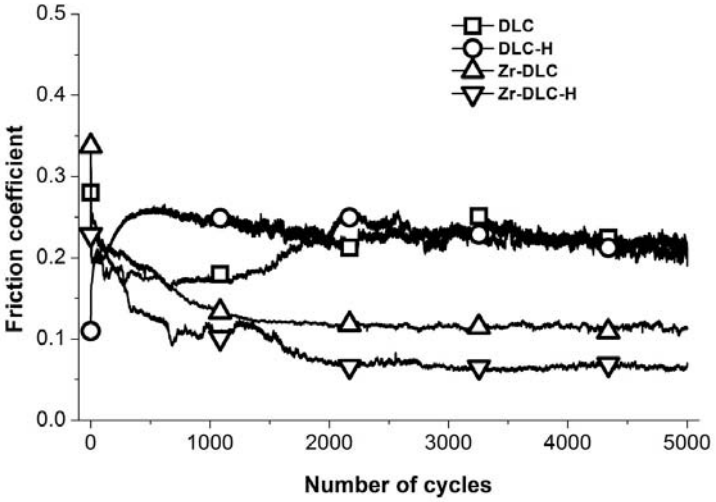


Fig. 2 Typical friction curves of Zr-DLC(-H) coatings at room temperature

The contacting area on the steel ball contained a mixture of iron oxides and graphitized carbon structure (Fig. 3). Although the free unworn surface of the 100Cr6 steel ball could not prove any vibration spectra, the contacting surface showed several driving effects - presence of iron oxides, slight photoluminescence effect and the G peak position shift towards higher wave numbers compared to as-deposited coating.

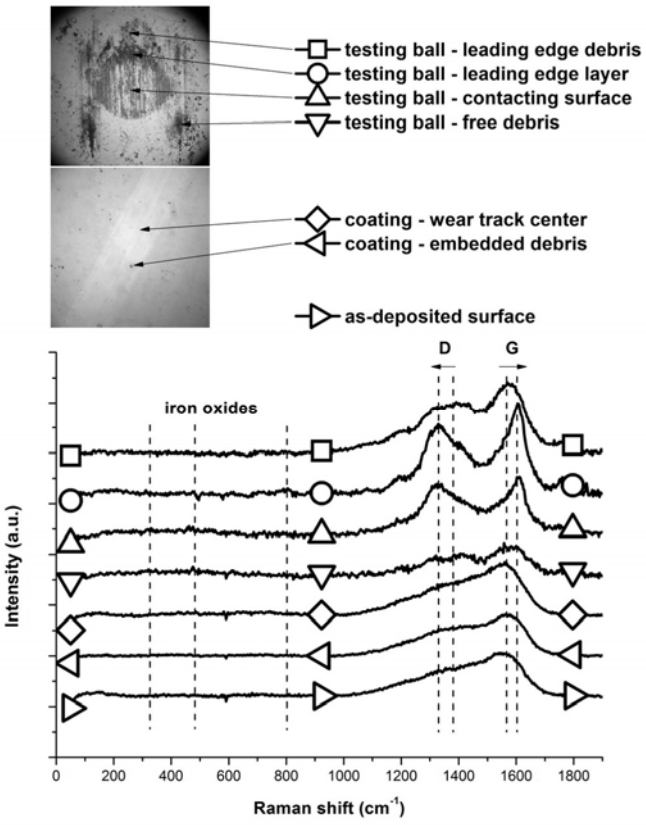


Fig. 3 Raman analysis of the ball vs. Zr-DLC-H contact

The tribolayer on the ball surface was formed from a mixture of iron oxides and reordered C-C structure. Moreover, the thin layer formed at the leading edge exhibited Raman spectra similar to the pure graphite. This could be explained by strong graphitization of the outer coating surface during the friction process. The graphitic interlayer formation, as well as iron oxides presence was significantly dependent on coating composition.

Conclusions

It was showed that the wear processes taking place at the contact interface were significantly dependent on the coatings composition. Fundamental relations between as-deposited coating properties, wear track surface properties, tribolayer properties, and tribological tests conditions has been described.

Acknowledgement

This work was supported by the Czech Science Foundation; project Nr. P108/10/P446.

References

[1] A. Cavaleiro, J. Th. M. De Hosson, Nanostructured coatings, 2006, Springer Publishing, New York, ISBN: 978-0387-25642-9

[2] J. Robertson, Materials Science and Engineering R 37 (2002) 129-281

[3] K. Bewilogua, C.V. Cooper, C. Specht, J. Schröder, R. Wittorf, M. Grischke, Surface and Coatings Technology 127 (2000) 224-232

[4] C. Casiraghi, F. Piazza, A.C. Ferrari, D. Grambole, J. Robertson, Diamond & Related Materials 14 (2005) 1098-1102

[5] A. C. Ferrari, Diamond and Related Materials 11 (2002) 1053-1061

Control of Deposition Profile and Properties of Plasma CVD Carbon Films

Kazunori Koga[1], Tatsuya Urakawa[1], Giichiro Uchida[1],
Kunihiro Kamataki[2], Yenwoon Seo[1], Naho Itagaki[1,5], Masaharu Shiratani[1,6],
Yuuichi Setsuhara[3,6], Makoto Sekine[4,6], and Masaru Hori[4,6]

[1]*Graduate School of Information Science and Electrical Engineering, Kyushu University, 744 Motooka, Nishi-ku, Fukuoka 819-0395, Japan,*

[2]*Faculty of Arts and Science, Kyushu University, 744 Motooka, Nishi-ku, Fukuoka 819-0395, Japan*

[3]*Joining and Welding Research Institute, Osaka University, Osaka, Japan,*

[4]*Dept. of Electrical Engineering and Computer Science, Nagoya University, Nagoya, Japan,*

[5]*PRESTO, Japan Science and Technology Agency, Tokyo 102-0075, Japan*

[6]*CREST, Japan Science and Technology Agency, Tokyo 102-0075, Japan*

We have succeeded to deposit anisotropic and top surface deposition profile on substrates with trenches using H-assisted plasma CVD of Ar + H_2 + C_7H_8 at a low substrate temperature of 100 ^oC. For the anisotropic deposition profile, carbon is deposited without being deposited on side-wall of trenches. For the top surface deposition profile, carbon is deposited at only top surface. The optical emission measurements and evaluation of deposition rate have revealed that a high flux of H atmos is the key to the deposition profile control. The mass density of the films and their Raman spectrum have shown that their structure is a-C:H.

Keywords: carbon film, deposition profile, plasma CVD, trench

1. Introduction

Wide interest in carbon films such as diamond-like carbon (DLC) and hydrogenated amorphous carbon (a-C:H) stems from their attractive properties such as biocompatibility, chemical inertness, high mechanical hardness, optical transparency and wide band gap [1-6] and hence have widespread applications as protective coatings in several areas such as car parts, micro-electromechanical systems (MEMS) and as magnetic storage disks [5]. DLC films first reported in the 70s were deposited by ion beam deposition [7, 8], and a-C:H films introduced in the beginning of 80s were deposited by rf plasma CVD [9]. Since then a-C:H films deposited by rf plasma CVD have been studied intensively by many researchers [10]. In addition, the most widely used technique for DLC films deposition is rf plasma CVD. The plasma CVD has the advantage of being possible to deposit at a low substrate temperature compared with thermal CVD methods. The advantages allow us to make protective coatings on polymer such as PMMA (poly(methyl methacrylate)) employed for photoresist films.

Deposition profile control of carbon films on fine structures is one of the concerns for MEMS and ultra large scale integration (ULSI) applications. So far, we have succeeded in controlling deposition profile of Cu films on trench, and have realized sub-conformal, conformal and anisotropic deposition, for which Cu is filled without being deposited on side-wall of trenches, using a H-assisted plasma CVD method [11-16]. We have applied the method to carbon film deposition on trenched substrates in order to control deposition profile [17-21]. In this paper, we have examined effects of Ar gas addition to H_2+Toluene (C_7H_8) plasma on deposition profile

control at a low substrate temperature of 100°C using the H-assisted plasma CVD method.

2. Experimental

Experiments were performed using the H-assisted plasma CVD reactor, in which a capacitively-coupled main discharge and an inductive-coupled discharge for an H atom source were sustained as shown in Fig. 1. For the main discharge, a mesh powered electrode of 85 mm in diameter and a plane substrate electrode of 85 mm in diameter were placed at a distance of 33 mm. The main discharge is mainly used for producing carbon containing radicals as precursors for carbon deposition. The excitation frequency of the main discharge was 28 MHz and the supplied power P_m was below 45W. The discharge of the H atom source was sustained with an rf induction coil of 100 mm in diameter placed at 65 mm above the substrate electrode of the main discharge. The H atom source can generate a high flux of H atoms toward the substrate. The excitation frequency is 13.56 MHz and the supplied power P_H = 500 W. C_7H_8 was used for ingredient molecules for carbon film deposition. It vaporized at 150°C, and supplied with H_2. The C_7H_8 flow rate was 0.63 sccm. Ar diluted H_2 gas was introduced from the top of the reactor. The total flow rate of H_2 and Ar was 90 sccm. The total pressure was 13 Pa. The trench substrate set on a substrate electrode. The trenches were fabricated with SiO_2 on crystalline silicon wafers and were covered by WN layer. The aspect ratio which is defined as a ratio of the depth of the trenches and their width was between 0.7 and 5. An rf bias voltage of 400 kHz was applied to the substrate for controlling kinetic energy of ions incident on it. The bias voltage was -7 V. Since the plasma potential which was measured by Langmuir prove was 25 V, the ion energy E_i was 32 eV.

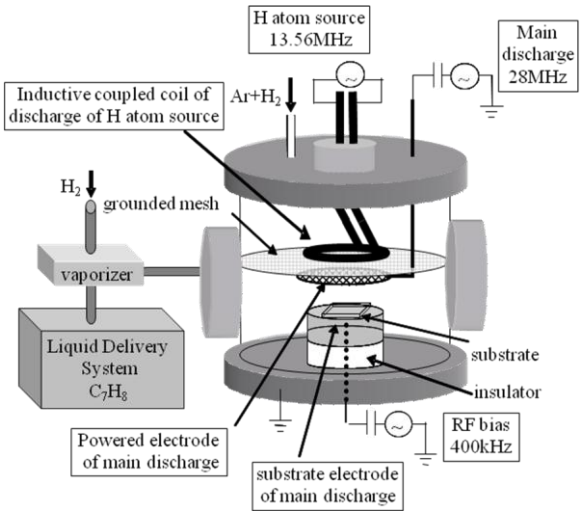


Fig. 1. H-assisted plasma CVD method.

3. Results and Discussion

The flux of H atoms towards the substrate is an important factor for the carbon film deposition. The deposition rate is reduced by etching by H atoms. To study effects of Ar dilution on the H atom generation, we have measured optical emission intensity of H_α at 20 mm above the center of the substrate electrode. Figure 2 shows dependence of the H_α intensity on a flow rate ratio R= $[H_2]/([H_2]+[Ar])$. The intensity has a maximum value around R= 22 %. It indicates that generation of the H atoms is enhanced by Ar dilution. To evaluate the deposition profile control, we have evaluated a ratio of the deposition rate ratio at side wall of the trenches and that at top $DR_{sidewall}/DR_{top}$ ant a ratio of the deposition rate at bottom and that at top DR_{bottom}/DR_{top}. Figure 3(a) and 3(b) shows dependence of $DR_{sidewall}/DR_{top}$ and DR_{bottom}/DR_{top} on an aspect ratio of the trenches as a parameter of R, respectively. The deposition rate at the top is constant irrespective of the aspect ratio, whereas the deposition rates at the sidewall and bottom tend to decrease with increasing the aspect ratio.

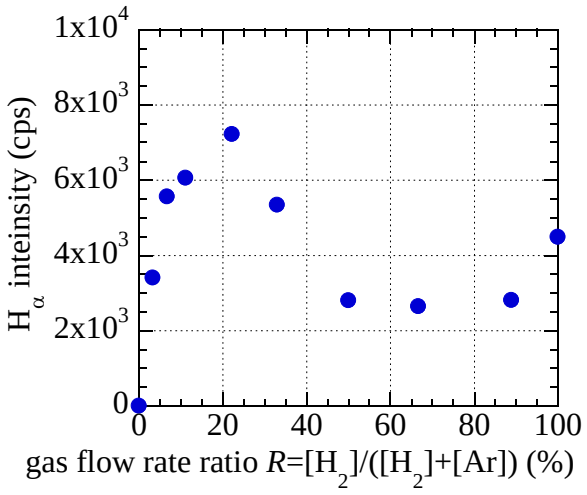


Fig. 2. Dependence of H_α intensity on gas flow rate ratio R.

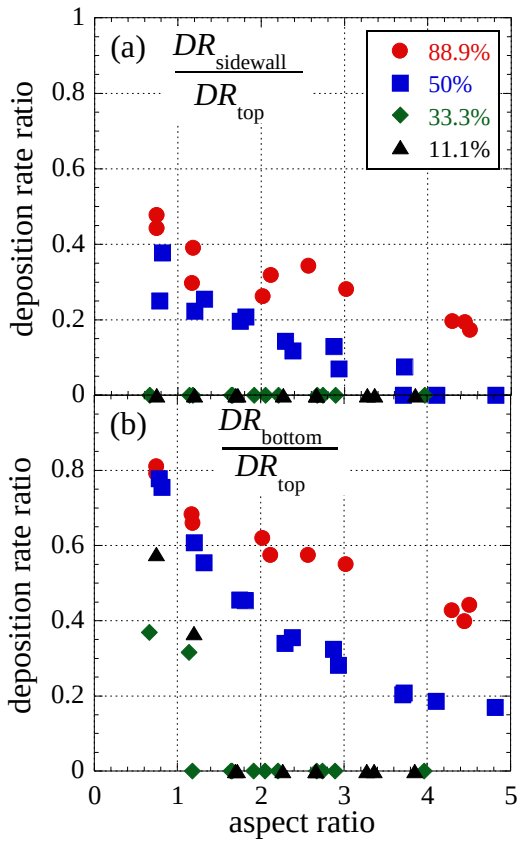


Fig. 3. Dependence of deposition rate ratio on aspect ratio of trenches as a parameter of R.

Thus, the deposition rate ratio decreases with increasing the aspect ratio. This is because the incident deposition radical flux per surface area in a trench decreases with increasing the aspect ratio. The deposition rate ratio tends to decrease with decreasing the *R*. The $DR_{sidewall}/DR_{top}$ is smaller than DR_{bottom}/DR_{top}. The decrease in the deposition rate ratio for the side wall is larger than that for the bottom. No deposition takes place at the sidewall of trenches of all aspect ratio in Fig. 3(a) for the gas flow ratio *R* = 33.3 % 11.1 %. In other words, we have succeeded in deposition carbon films on trenched substrates in an anisotropic way. Figure 4(a) shows a cross-section SEM image of the anisotropic deposition profile. For *R*= 33.3 % and 11.1 %, the carbon films does not deposit at both of the sidewall and bottom for the aspect ratio > 1.6. We have realized top surface deposition. Figure 4(b) shows a SEM image of top surface deposition profile.

Experimental deposition profiles are determined by the balance between deposition of carbon containing radicals and etching by H atoms. When the etching rate surpasses the deposition rate of carbon containing radicals, no deposition takes place there. Irradiation of ions induces structural modification at the film surface [22]. The etching rate for the modified hard films is significantly lower than that for the unmodified films. Therefore etching rates at the top and bottom is lower than that at sidewall, because ion fluxes on the top and bottom are higher than that on the sidewall. Moreover, incident deposition radical flux per surface area at the sidewall and bottom is lower than that at the top. Because of the lower incident deposition radical flux per surface area and the higher etching rate, the deposition rate at the sidewall is the lowest. The etching rate at the top is lower than that at bottom, because ion fluxes on the top is higher than that on the bottom. Thus, the deposition rate at the bottom is lower than that at the top. We can realize anisotropic and top surface deposition with increasing H atom flux to suppress sidewall and bottom deposition. Therefore, a high H atom flux is the key to anisotropic and top surface deposition.

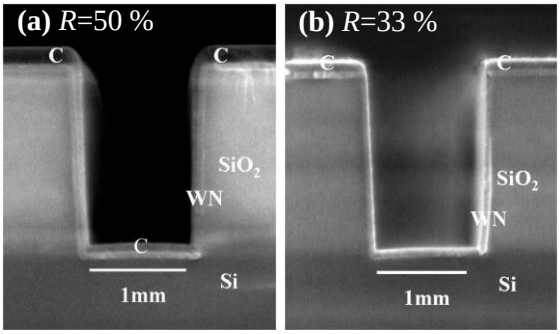


Fig. 4. Cross-section SEM images of (a) anisotropic deposition profile for *R*= 50 % and (b) top surface deposition profile for *R*= 33.3 %.

The hardness of the carbon films is important to employ this deposition profile control to fabricate protection layer in fine structures. We have evaluated properties of the films deposited for *R*= 33%. Table 1 shows the film density, peak intensity ratio of G band and D band in Raman spectrum and etch selectivity of the films for SiLK films which is used as low-k materials for dielectric layer in ULSI. The films density of 1.54 g/cm^3 and the Raman peak ratio of 1.93 show that the deposited film is a-C:H films. The films have a moderate value of the etch

Table 1. Film properties of the carbon films deposited for R= 33.3 %.

Film properties for *R*= 33 %	
Mass density (g/cm^3)	1.54
Raman peak ratio of G band and D band	1.93
Etch selectivity for SiLK^{TM}	0.88

selectivity of 0.88. To improve the hardness of the films, we have found that the E_i is an important parameter [20, 21]. For E_i= 100 eV, the film density and the etch selectivity have maximum values. The film density and the etch selectivity for E_i= 100 eV is 2.27 g/cm^3 and 4.4, respectively [20, 21]. The results indicate our deposition profile control method is useful for depositing protection layer in fine structures.

4.Conclusions

We have studied the aspect ratio dependence of deposition rate ratio as a parameter of *R*. The following conclusions are obtained in this study.

1) Optical emission intensity of H_α in the main discharge region has a maximum value for *R*= 22 %. The generation of H atoms is enhanced by Ar dilution. A high H atom flux is the key to anisotropic and top surface deposition.

2) We have succeeded to deposit anisotropic and top surface deposition profile on substrates with submicron wide trenches using H-assisted plasma CVD of Ar + H_2 + C_7H_8 at a low substrate temperature of 100 ^oC.

3) The films deposited for R= 33.3 % are a-C:H films and has a moderate etching selectivity for SiLK films of 0.88. To improve the film hardness, the ion energy is important. For E_i=100eV, the etch selectivity increases to 4.4.

Acknowledgements

This work was partly supported by JST, CREST and MEXT.

References

[1] J. Robertson, Mater. Sci. and Eng., R **37**, 129-281 (2004).

[2] J. Robertson, Prog. Solid State Chem., **21**, 199 (1991).

[3] J. Robertson, Surf. Coatings Technol., **50**, 185 (1992).

[4] A.A. Voevodin and M.S. Donley, Surf. Coatings Technol., **82**, 199 (1996).

[5] J. Robertson, Phys. Stat. Sol. (a), **205**, 2233 (2008)

[6] J. Robertson, Jpn. J. Appl. Phys. **50** (2011) 01AF01.

[7] S. Aisenberg and R. Chabot, J. Appl. Phys., **42**, 2953 (1971).

[8] S. Aisenberg and R.W. Chabot, J. Vac. Sci. Technol., **10**, 104 (1973).

[9] K. Enke, H. Dimigen, and H. Hübsch, Appl. Phys. Lett., **36** (4), 291 (1980).

[10] K. Holmberg and A. Matthews, Coatings Tribology, Tribology Series, **28**, 440 (1994).

[11] M. Shiratani, H. J. Jin, K. Takenaka, K. Koga, T. Kinoshita, and Y. Watanabe, Sci. Technol. Adv, Mater., **2**, 505 (2001).

[12] K. Takenaka, M. Shiratani, M. Takeshita, M. Kita, K. Koga, and Y. Watanabe, Pure Appl. Chem., **77**, 391 (2005).

[13] K. Takenaka, M. Kita, T. Kinoshita, K. Koga, M. Shiratani, and Y. Watanabe, J. Vac. Sci. Technol., A**22**, 1903 (2004).

[14] K. Takenaka, K. Koga, M. Shiratani, Y. Watanabe, and T. Shingen, Thin Solid Films, **506-507**, 197 (2006).

[15] J. Umetsu, K. Koga, K. Inoue, H. Matsuzaki, K. Takenaka, and M. Shiratani, Surf. Coat. Technol., **202**, 5659 (2008).

[16] J. Umetsu, K. Inoue, T. Nomura, H. Matsuzaki, K. Koga, M. Shiratani, Y. Setsuhara, M. Sekine, and M. Hori, Proceedings of 30th International Symposium on Dry Process, (Tokyo, Japan), 35 (2008).

[17] T. Nomura, K. Koga, M. Shiratani, Y. Setsuhara, M. Sekine, and M. Hori, MRS Proceedings, **1222**, DD05-16 (2009).

[18] J. Umetsu, K. Inoue, T. Noumra, H. Matsuzaki, K. Koga, M. Shiratani, Y. Setsuhara, M. Sekine, and M. Hori, J. Plasma Fusion Res. SERIES **8** (2009) 1443.

[19] T. Noumra, T. Urakawa, Y. Korenaga, D. Yamashita, H. Matsuzaki, K. Koga, M. Shiratani, Y. Setsuhara, M. Sekine, and M. Hori, Tencon IEEE Region 10 Conference Proc. (2010) 2213.

[20] T. Urakawa, H. Matsuzaki, D. Yamashita, Giichiro Uchida, K. Koga, M. Shiratani, Y. Setsuhara, M. Sekine, and M. Hori, Surface and Coatings Technology (2012) submitted.

[21] T. Urakawa, R. Torigoe, H. Matsuzaki, D. Yamashita, G. Uchida, K. Koga, M. Shiratani, Y. Setsuhara, K. Takeda, M. Sekine, and M. Hori, Jpn. J. Appl. Phys. (2012) submitted.

[22] W. Jacob, Thin Solid Films, **326**, 1 (1998).

Plasma surface modification of diamond-like carbon films to graphene

S.S. Tinchev
Institute of Electronics, Bulgarian Academy of Sciences, Sofia 1784, Bulgaria,
stinchev@ie.bas.bg

Graphene, the first 2D atomic crystal ever know possess interesting electrical properties, especially high carrier mobility, which promise its bright future in electronics. However, there is still no suitable technology for fabrication of graphene for general electronic applications. Today the most successfully fabrication technology is CVD on metals followed by a transfer process on insulated substrates as needed usually in electronics. This process is quite successful – up to 30-inch graphene sheets were fabricated and successfully transferred to plastic substrates [1]. Although such technology is suitable for transparent electrodes, a general applicable technology for fabrication of graphene on insulating substrates is needed. Here one should mentioned that the fabrication of graphene from SiC by thermal decomposition [2] is not an alternative because the high temperatures ($\geq$ 1300°C) needed to sublimate Si atoms make this technology incompatible with the existing silicon electronics.

Recently [3] we proposed an idea for fabrication of graphene on the top of insulating amorphous carbon films by low-energy ion modification. In this low-temperature process the surface of the amorphous carbon could crystallize to graphene as a result of point defect creation and enhanced diffusion caused by the ion bombardment. Different ions can be used to modify diamond-like carbon films, for example carbon and hydrogen ions as inherent to the starting material (a-C:H) in our experiments. We choose argon ions, which are widely used in the microelectronic technology and as a noble gas should not react with the carbon. To estimate the necessary energy and doses of the ions in order to modify only some monolayers on the surface of the amorphous carbon films the Monte Carlo SRIM-2008 program [4] was used. We found [3] that for energy of the argon ions 1 keV the dose should be ~ 4.5×10^{15} Ar^+/cm^2 in order to break all bonds of the surface of the amorphous carbon films. This estimated value is in good agreement with the experimental value found in the literature [5].

In our first experiments [3] the films were modified in DC magnetron system at unipolar pulsed discharges. Pulse biasing of the magnetron is needed because the diamond-like carbon films are highly insulating and ion bombardment with DC voltage would cause charging of the film. The reason for use magnetron in the film modification was the possibility for easy production of argon ions with low energy and high ion density. However, this choice has also a drawback. To achieve the necessary dose of about 4.5×10^{15} Ar^+/cm^2 it was found that the modification time should be shorter then 1 s. Although these first experiments were quite successful, the short modification time was difficult to control and to vary in order to optimize the technology.

Therefore another system was built later [6]. It is a simple diode system. Both electrodes are cooper strips fixed on an alumina substrate and the samples could be placed on/or near the cathode. The results presented in this paper were obtained for samples placed directly on the cathode. The cathode and samples were not cooled because to our estimations it should not be significant heating during the ion bombardment. The voltage amplitude was 400 V, pulse frequency of 66 kHz and pulse time of 10 μs. The system was evacuated by a combination of diffusion and a mechanical pump. During the modification the pressure of the chamber was $3x10^{-1}$ Torr.

Fig. 1 shows the calculated profile of the vacancies produced in amorphous carbon films for 400 eV argon ion modification. As expected only 1 nm of the surface of the film (about 3 monolayers) will be modified. One can see in Fig. 1 also the profile of the implanted argon ions – the curve “Ion range” with maximum at about 1.6 nm. Obviously the argon ions are implanted far behind the modified surface region and they should not introduce additional effects. The

calculated necessary dose for this ion energy is nearly the same as calculated in [3], about 4.5 × 10^{15} Ar^{+}/cm^{2}.

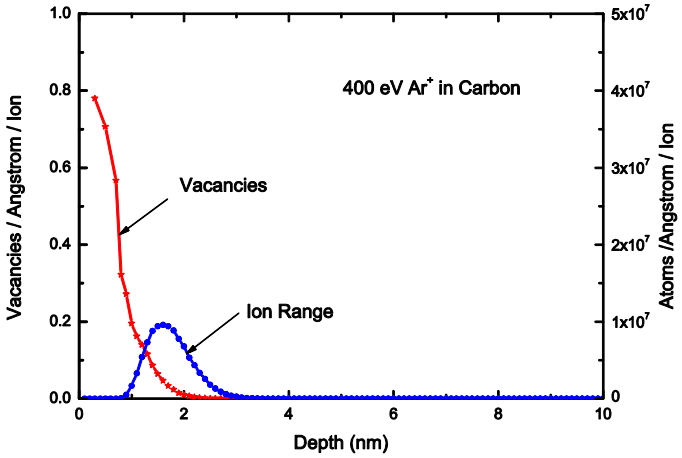


Fig. 1. Calculated vacancies profile and argon ion distribution for 400 eV Ar^{+} plasma treatment of amorphous carbon.

Here one significant remark should be made. Usually in plasma-based implantation systems (as actually our system is) the ion dose incident in the sample is measured by integrating the current induced in the sample by the ion beam. However, because our samples are highly insulating, there is problem to measure the sample current. Due to the difficulties associated with dose measurements, in this paper we will give only the irradiation times instead of the ion doses.

Raman spectra of the samples were measured before and after sample modification at room temperature. Raman spectra were obtained using laser with 633 nm wavelength and laser power smaller then 0.9 mW in order to prevent modification of the films by the laser irradiation. Raman spectra of the plasma treated (but not annealed) samples show only small differences in comparison with the non implanted samples. This can be expected because at room temperature the diffusion coefficient of the carbon is not high enough for its crystallization. Obviously an annealing should be made after the plasma treatment. Fig. 2 shows Raman spectra of the samples after annealing at 350ºC for 6 hours. This temperature was chosen as maximal temperature, which cannot affect the underplaying amorphous carbon. In Fig. 3 it is demonstrated that without plasma treatment an annealing of a sample does not change significant the Raman spectrum. In our first experiments [3] the annealing temperature was some lower - 300ºC. Later we have found that it can be increased to 350ºC.

Obviously the most significant changes of the Raman spectra after annealing were the splitting of the broad amorphous spectrum into two distinct D- and G-peaks. This is typical for partial crystalline carbon with small crystalline size. Without plasma treatment such partial crystallization of amorphous carbon can be achieved by annealing at temperatures 800–900ºC. It is well known that in the graphite or graphene presence of the D peak indicates the presence of disorder. However, in amorphous carbons the development of a D peak indicates ordering. The D-peak intensity rises with increasing plasma treatment time, i.e. the crystallization is enhanced. However, its position remained stable, as Fig. 4 presents. In contrast to this, the G-peak shows an upshift (~ 12 cm^{-1}) from 1572 cm^{-1} to 1584 cm^{-1}, close to the typical G-peak of graphene. As the plasma treatment time increased, the G-peak narrowed, indicating again enhanced ordering (crystallization) of the modified amorphous carbon.

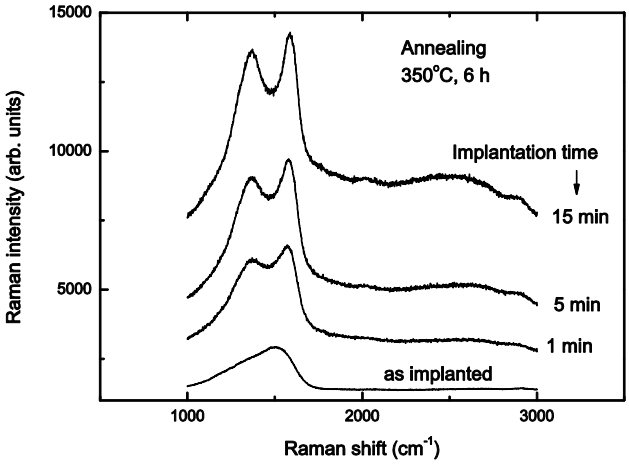


Fig. 2. Raman spectra of samples modified for different times and annealed at 350ºC for 6 hours.

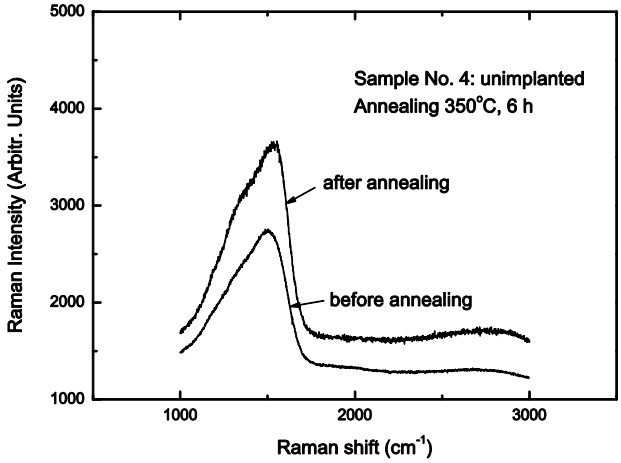


Fig. 3. Raman specra of unmodified sample before and after annealing at 350ºC for 6 hours.

The I_D/I_G ratio widely used for characterization of carbon materials is shown also there. In this paper we refer to I_D/I_G as the ratio of peak heights. With increasing implantation time this ratio rises up to ~ 0.96 indicating sp^2 cluster size of about 1.5 nm [7]. However, such conclusions should be made very carefully because interpretation of Ramen signal of such complicated system like graphen on amorphous carbon is not easy.

The single and sharp second order Raman band (2D) is widely used as a simple and efficient way to confirm the presence of single layer graphene. In the Raman spectra of our samples in the 2D band region one can recognize a peak at 2700 cm^{-1} which is however, not sharp as expected. These broad Raman spectra are typical for defected graphene [8-10]. With increasing modification time (ion dose) this peak rises and two other small peaks at about 2000 cm^{-1} and 2900 cm^{-1} can be seen. The peak at 2900 cm^{-1} can be identified as D + D' combination [8]. At the moment the origin of the peak at about 2000 cm^{-1} is not clear.

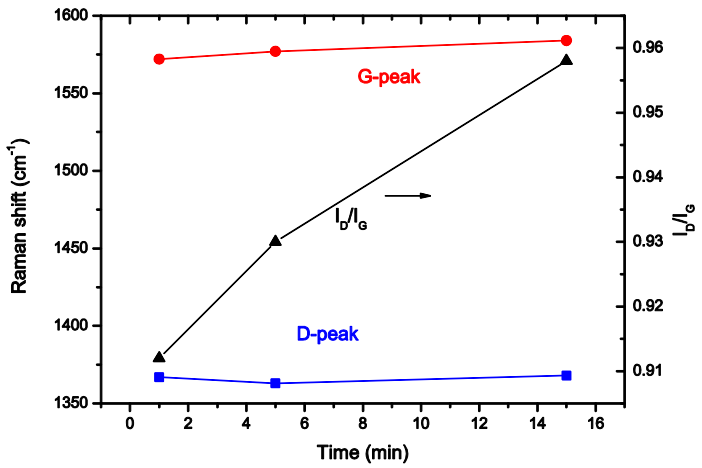


Fig. 4. D-peak and G-peak positions vs. plasma treatment time. Sown is here also the intensities ratio of D-peak and G-peaks.

In conclusion surface modification by low energy pulsed argon plasma was used to fabricate graphene on the top of insulating diamond-like carbon films. It is shown that by following low temperature thermal annealing at 350°C is possible to achieve partial crystallization of amorphous carbon to graphene. The observed Raman spectra are typical for defected graphene – splitted D- and G-peaks and a broad 2D-peak. This result is very encouraging and we hope that by improving this technology it will be possible to fabricate defect-free graphene, which can be used in electronics without transfer to other substrates.

Acknowledgement:

The author would like to thank Dr. Evgenia Valcheva for the Raman measurements.

References:

1. Sukang Bae, Hyeongkeun Kim, Youngbin Lee, Xiangfan Xu, Jae-Sung Park, Yi Zheng, Jayakumar Balakrishnan, Tian Lei, Hye Ri Kim, Young Il Song, Young-Jin Kim, Kwang S. Kim, Barbaros Ozyilmaz, Jong-Hyun Ahn, Byung Hee Hong and Sumio Iijima, Nature Nanotechnology **5**, 574 (2010).

2. Walt A. de Heer, Claire Berger, Ming Ruan, Mike Sprinkle, Xuebin Li, Yike Hu, Baiqian Zhang, John Hankinson, and Edward Conrad, PNAS **41**, 16900 (2011).

3. S.S. Tinchev, Applied Surface Science **258**, 2931(2012).

4. www.SRIM.org

5. I.A. Faizrakhmanov, V.V. Bazarov, V.A. Zhikharev, A.L. Stepanov, I.B. Khaibullin, Vacuum **62,** 15 (2001).

6. S.S. Tinchev, Low temperature crystallization of diamond-like carbon films to graphene by low energy plasma surface treatment, arXiv:1207.0837.

7. A. C. Ferrari, and J. Robertson, Physical Review B **61**, 14 095 (2000).

8. T. Gokus, R.R. Nair, A. Bonetti, M. Boehmler, A. Lombardo, K.S. Novoselov, A.K. Geim, A.C. Ferrari, ACS Nano **3,** 3963 (2009).

9. C.N.R. Rao, K.S. Subrahmanyam, H.S.S. Ramakrishna Matte, B. Abdulhakeem, A. Govindaraj, B. Das, P. Kumar, A. Ghosh, D.J. Late, Sci. Technol. Adv. Mater. **11**, 054502 (2010).

10. Andrea C. Ferrari, Solid State Communications **143**, 47 (2007).

Composite layers “MgAl intermetalic layer / PVD coating” obtained by hybrid surface treatment method on the AZ91D magnesium alloy

Jerzy Smolik [1], Adam Mazurkiewicz [1], Jarosław Mizera [2]

[1)] Institute for Sustainable Technologies – National Research Institute,
Pułaskiego 6/10, 26-600 Radom, Poland
[2)] Warsaw University of Technology, Faculty of Materials Engineering,
Wołoska 141, 02-507 Warsaw, Poland

Extended Abstract

The magnesium alloys are very interesting construction materials in aviation, automotive and machine industries as well as in production of portable electric devices. Their low densities from 1.75 to 1.85 g/cm3 and high specific strength give a chance of considerable reduce of energy. The main inconvenient feature of magnesium alloys which make difficult their applications is very small corrosion and tribology resistance.

This paper presents the technological process of creation of the composite layers consist of “intermetalic layer MgAl – PVD coating” on AZ91D magnesium alloy intended for anticorrosion and anti-wear applications. The investigated composite layers were obtained with the use of the hybrid surface treatment technology, which consist of diffusion treatment in Al powder followed by electron beam deposition method. In order to present the technical realization of hybrid technology the authors designed an original technological process implemented in the hybrid multisource device (Fig.1), produced at the Institute for Sustainable Technologies – National Research Institute in Radom (Poland).



Fig.1. The hybrid multisource device produced at the Institute for Sustainable Technologies – National Research Institute in Radom.

The device has been equipped with two arc sources with the cathode diameter of ϕ=80 mm and with the 60kW electron gun with the dynamic electron beam deflection circuit and steering system. The device is equipped with modern, reliable power systems, substrate

polarization system, multichannel process gases dosing system as well as the systems of monitoring and measuring substrate temperature and atmospheric gas pressure.

The Al_2O_3 ceramic coatings was obtained on the AZ91D magnesium alloy with the intermetalic layer MgAl on the surface. The properties of the designed and created composite layers like as microstructure (optical microscopy technique), phase structure (X-ray diffraction), chemical composition (GDOES method) were investigated (Fig.2).

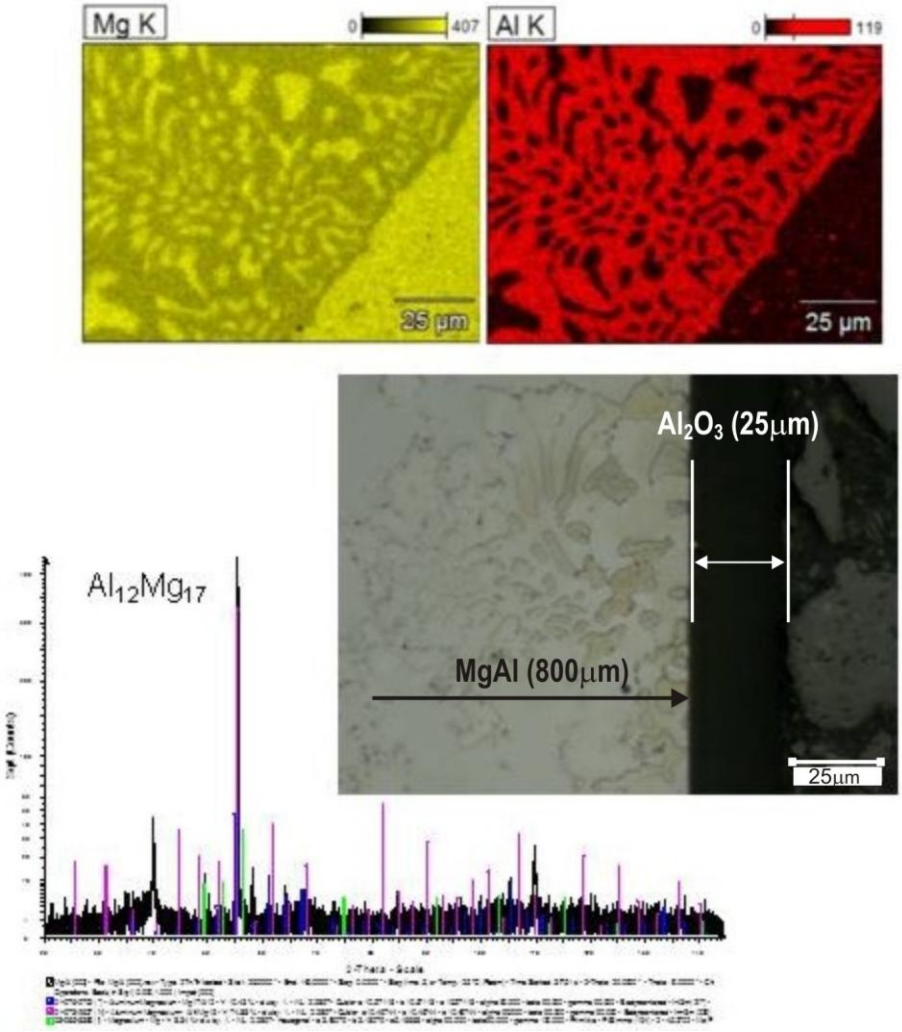


Fig.2. The Al_2O_3 ceramic coatings obtained on the AZ91D magnesium alloy with the intermetalic layer MgAl on the surface.

The paper also demonstrates the results of adhesion (Scratch test), mechanical properties (Nano Hardness Tester), corrosion investigations (electrochemical corrosion test method) as well as tribology investigations (ball-on-disk method) carried out for AZ91D magnesium alloy covered by investigated composite layers.

The obtained results proved that hybrid surface treatment technology – diffusion treatment in Al powder + electron beam deposition, which was developed by authors, enable to significant increase of corrosion and tribology resistance of AZ91D magnesium alloy.

Plasma processing of scaffolds: perspectives for Tissue Engineering

F. Intranuovo[1], R. Gristina[2], M. Domingos[3], G. Camporeale[1], E. Sardella[2], P.J. Bartolo[3], P. Favia[1,2,4]

[1]*Department of Chemistry, University of Bari "Aldo Moro", Bari, Italy*
[2]*Institute of Inorganic Methodologies and Plasma (IMIP) CNR, Bari, Italy*
[3] *Centre for Rapid and Sustainable Product Development, Polytechnic Institute of Leiria, 2430-028 Marinha Grande, Portugal*
[4]*Plasma Solution Srl, Spin off of the University of Bari, Italy*

intranuovo@chimica.uniba.it

Keywords: plasma deposition, plasma treatment, wettability, porosity, cell affinity

Since the mid-1980s, Tissue Engineering has been proposed as a potential tool in addressing the repair, replacement, and/or regeneration of vital organs. Thus this field is now an interesting alternative to artificial prosthesis and confronts the transplantation crisis, i.e., the shortage of donor tissues and organs available for transplantation[1].

This new emerging field is based on the use of cells (particularly stem cells) seeded in a three-dimensional (3D) scaffold (most often made og a biodegradable polymer), that provides the initial structural integrity and organizational backbone for cells to assemble into a functional tissue[2]. Thus, scaffolds, characterized by high porosity, proper pore size, shape, surface area, suitable biodegradability and biocompatibility, stiffness and mechanical integrity, are required. These 3D structures have to allow the necessary support for cell attachment, proliferation, differentiation, leading to a correct tissue regeneration in advanced applications.

Nowadays, several fabrication techniques have been employed to realize scaffolds with suitable biocompatibility[3-5]. For instance, Solvent Casting/Particulate Leaching (SC/PL) is the most easy, low time-consuming and cheap conventional scaffolding technique, used by material engineers. It allows the control of micro-structural characteristics such as total porosity and total pore size[6]. Another known conventional technique includes the supercritical carbon dioxide ($scCO_2$) as porogen, that is advantageous because it does not require organic solvents and leaching process to eliminate the porogen[7]. Also, with this technique it is possible to control the total porosity and pore size, even if the pores are randomly distributed inside the scaffold.

Unlike conventional machining, computer-aided technologies, like Solid Free-Form fabrication (SFF) and Rapid Prototyping (RP), are able to build scaffolds by selectively adding materials, layer-by-layer, as specified by a computer program, creating a highly reproducible architecture along the 3D construct[8].

Surface properties influence cell-material interactions in the tissue engineered structures. Generally, when cells are seeded *in vitro* into 3D scaffolds, cell adhesion is favoured at the peripheries of the constructs, resulting in poorly populated inner parts, because the external surfaces of the scaffolds are more accessible than the inner ones. Thus, by controlling scaffold surface chemistry by some surface modification techniques, it should be possible to control adsorption of proteins from the cell culture medium and, in turn, to enhance cell

adhesion and motility, inside/outside the scaffolds, in a homogeneous way[9].

Cold plasma processes at low and atmospheric pressure can be used to tailor the surface composition of scaffolds . Recent advances in radiofrequency plasma processes (RF, 13.56 MHz) Glow Discharges for biomedical applications, include the achievement of functional surfaces for direct cell growth and biomolecules immobilization, the deposition of non-fouling coatings, the deposition of nano-composite bacterial resistant coatings and the synthesis of nano-structured surfaces[10,11]. Even though many approaches for the modification of surface chemistry of polymers have been described, it remains an interesting challenge to understand their efficiency and penetration when applied to complex 3D structures.

Recently, we have described low pressure plasma modification processes applied to poly-(lactic acid, PLA) scaffolds, fabricated with a conventional scCO_2 technique, using allyl amine/hexane plasma depositions. This technique is based on the generation of gas bubbles within a polymer and the use of supercritical CO_2 as porogen, through a three phases cycle (plasticization, nucleation and vitrification). The low pressure plasma depositions were able to create chemical gradients (hydrophobic outside and hydrophilic inside the scaffolds) attracting cells inside the polymeric structures[12].

A low pressure O_2/H_2 plasma treatment has been applied to polycaprolactone (PCL) scaffolds, produced by means of SC/PL technique. This scaffolding technique consists of dispersing a porogen (NaCl crystals at proper diameter range and NaCl/polymer composition ratio) within a polymeric solution, fixing the structure and removal of the porogen, to result in a porous scaffold. We observed that by varying the plasma parameters (e.g. pressure, power, gas feed composition), the hydrophilicity of the scaffolds varied in a controlled way, obtaining different water absorption kinetics, that could address the behaviour of different cell lines[13].

Further, ethylene/N_2 mixtures were used to plasma deposit cell-adhesive coatings to increase the affinity of osteoblast-like cells of PCL scaffolds produced with the same SC/PL technique[14]. Good nitrogen content penetration was achieved inside the porous constructs, with a good adhesion of osteblast-like cells.

The same low pressure plasma deposition has been applied to PCL scaffolds fabricated with a Fused Deposition Modeling (FDM) technique, by means of the BioCell Printing instrument[8]. This technique is based on the extrusion of a thermoplastic material through a nozzle, where the filament material is supplied by an extrusion head, controlled by a computer, that follows a programmed path which is based on a pre-defined CAD model. The plasma depositing species were able to uniformly coat the PCL filaments of these scaffolds, from the top to the bottom surfaces. Osteoblast-like cells followed the nitrogen-based thin film, adhering on all the scaffold thickness[15].

Although in the biomedical field at low pressure plasma processes are utilized more often rather than atmospheric pressure, the latter are gaining popularity, especially in the field of Plasma Medicine. This emerging area is based on the use of atmospheric plasmas directly on living tissues, wound healing, cancer treatments and other therapeutic purposes[16]. Among the atmospheric pressure plasma sources, Dielectric Barrier Discharges (DBD) are mostly utilized in this field. Few works have been devoted to the application of these plasmas to tissue engineered scaffolds. Safinia *et al.* treated poly-(lactic/glycolic acid) scaffolds with an air atmospheric pressure plasma process, grafting O- and N-containing chemical groups on the scaffold surfaces, improving wettability and affinity with eukaryotic cells[17]. In our laboratory, we have applied air plasma DBD treatments on 2D polystyrene substrates and PCL scaffolds fabricated with the SC/PL technique. Increased hydrophilicity was assessed after the plasma treatments and for 2D substrates, the behavior of osteoblast-like and NHDF fibroblast cells was also studied.

References

[1] Lanza R, Langer R, Vacanti J editors. Principles of Tissue Engineering – 3rd edition. China: Elsevier Academic Press; 2007.
[2] W.F. Liu and C.S. Chen, MaterialsToday, 8, 12 (2005).
[3] P.X. Ma, MaterialsToday, 7, 5 (2004).
[4] D. Li and Y. Xia, Adv. Mater., 16, 14 (2004).
[5] K.F. Leong *et al.*, Journ. of the Mechanic. Behav. of Biomed. Mater., 1, 2, 140 (2008).
[6] A.G. Mikos *et al.*, Journ. of Biotechnology, 3, 2 (2000).
[7] J.J.A. Barry, M.M.C.G. Silva, V.K. Popov, K.M. Shakesheff, S.M. Howdle, Phil. Trans. R. Soc. A 364 (2006) 249.
[8] Bártolo P., Domingos M., Gloria A., Ciurana J., CIRP Annals Manufacturing Technology, 60(1), 271-274, 2011.
[9] J.J.A. Barry *et al.*, Adv. Mater., 18, 1406 (2006).
[10] P. Favia *et al.*, S. Guceri and Smirnov Editors (2008) NATO-ASI series.
[11] F. Intranuovo, P. Favia, E. Sardella, C. Ingrosso, M. Nardulli, R. d'Agostino, R. Gristina. Biomacromolecules. 2011, 12, 380-387.
[12] F. Intranuovo, D. Howard, L. White, R.K. Johal, A.M. Ghaemmaghami, P. Favia, S.M. Howdle, K.M. Shakesheff, M.R. Alexander. Acta Biomaterialia 2011, 7 (9), 3336-3344.
[13] unpublished results
[14] F. Intranuovo, E. Sardella, R. Gristina, M. Nardulli, L. White, D. Howard, K.M. Shakesheff, M.R. Alexander, P. Favia. Surface Coating and Technology 2011, 205, S548–S551.
[15] M. Domingos, F. Intranuovo, A. Gloria, R. Gristina, P. Favia, P.J. Bártolo. Improved osteoblast cell affinity on plasma-modified 3D extruded PCL scaffolds. Submitted
[16] G. Fridman, G. Friedman, A. Gutsol, A.B. Shekhter, V.N. Vasilets, A. Fridman. Plasma Processes and Polymers 5:503-533, 2008.
[17] L. Safinia, K. Wilson, A. Mantalaris, A. Bismark. Macromolecular Bioscience 7:315-327, 2007.

Formation of pH-responsive polymer composite membranes by plasma-induced graft polymerization method

[1]Liubov Kravets, [1]Sergey Dmitriev, [2]Gheorghe Dinescu

[1]Joint Institute for Nuclear Research, Flerov Laboratory of Nuclear Reactions, Joliot-Curie Str. 6, 141980 Dubna, Russia
[2]National Institute for Laser, Plasma and Radiation Physics, Atomistilor Str. 111, 77125 Magurele, Bucharest, Romania

E-mail: kravets@lnr.jinr.ru

Abstract. The structure and the transport properties of polymer composite membranes consisting of a porous substrate and a polymer layer obtained by plasma-induced graft polymerization method were studied. It has shown that the presence of the polymer layer on the surface of porous substrate leads to changing its transport properties – the water permeability of the formed composite membranes substantially depends on the solution pH. These changes are caused by convertible conformational transitions of macromolecules of the grafted polymer layer from an expanded state into a compact one which is in turn caused by the degree of ionization of the functional groups on the surface of this layer.

Keywords: polymer composite membranes, plasma-induced graft polymerization, pH-responsive membranes

Introduction

The intense interest has been aroused recently in problem of obtaining the so-called 'smart' or 'intelligent' membranes, that is, such membranes whose transport properties can be adjusted by changing of external conditions. These investigations are of major practical and scientific importance as they allow one not only to gain a wide spectrum of membranes with unique properties, but also to discover synthesis opportunities for membranes that imitate the biological ones. In order to create membranes with controllable transport properties, one can use the ability of the macromolecules of the surface layer in response to environmental stimuli such as temperature [1, 2], solution pH [3], electric [4] and magnetic [5] fields, solvent composition [6] and pressure [7] to make reversible conformational transitions from hydrated (swollen) state to dehydrated (compact) ones. One of the approaches is the preparation of hydrogel membranes by traditional methods of polymerization or copolymerization [4-6]. Another direction in this field consists in the modification of the surface of the industrially produced membranes. The research in this direction is related to a goal-directed formation of a membrane surface with tailored chemical structure. For this purpose, various physicochemical methods are employed: chemical [1], plasma-induced [2] or radiation-induced [3] graft polymerization of monomers, plasma [7] deposition of thin polymeric layers on the surface of membranes.

In the present paper we report on the transport properties of polymer composite membranes consisting of a porous substrate – a poly(ethylene terephthalate) track membrane (PET TM) and a polymer layer obtained by plasma-induced graft polymerization of 2-methyl-5-vinylpyridine (MVP) and acrylic acid (AA).

Experiments

The object of the investigation was PET TM with a thickness of 9.5 μm and an effective pore diameter of 215 nm (pore density of 2×10^8 cm^{-2}). In order to produce the membrane, the PET film was irradiated with krypton positive ions, accelerated at ~3 MeV/nucleon in the cyclotron U-400, and then subjected to the physicochemical treatment on a standard procedure [8]. The treatment of the membrane samples

by plasma was performed at the plasma-chemical set-up realizing a RF-discharge in parallel plate configuration at the frequency of 13.56 MHz at the air pressure in the vacuum chamber of 0.13 Pa and discharge power of 70 W. The treatment time was 2 min. Details on the treatment procedure and the scheme of the plasma reactor set-up have been described previously [9]. Only one side of the membrane was subjected to the plasma treatment. The graft polymerization of MVP was conducted using a 10% water solution of monomer at the temperature of 70°C for 1 h. The graft polymerization of AA was conducted from gas phase for 4 h. For this purpose membrane was placed over the 25% water solution of AA with temperature of 75°C. To suppress a homopolymerization process, divalent copper ions were introduced in the solution. After the graft polymerization, membranes were washed with distilled water using ultrasonic cleaner until the pH of the wash remained unchanged.

The characteristics of the initial and plasma modified membranes were determined through a series of complementary procedures given in [10]. The amount of the grafting polymer on the membrane surface was defined by the gravimetric method. The change of the membrane thickness was measured with an electronic counter of thickness 'Tesa Unit' (Austria). The gas flow rate through the membranes was defined at a pressure drop of 10^4 Pa. On the basis of the values obtained in these experiments an effective pore diameter was determined. For calculation we used the Hagen-Poiseuille equation. The water contact angle (as sessile drop method) was determined with a horizontal microscope equipped with a goniometer. Permeability experiments for water solution were carried out with the help of the standard filtration installation FMO-2 (Russia) at the pressure drop of 7×10^4 Pa on membrane samples with the area of 254 mm^2. pH of the solutions was varied by introducing the relevant quantity of hydrochloric acid or sodium hydroxide.

Results and Discussion

It is known that the main contribution introduced the delay of ions by membranes is provided by the electrochemical mechanism connected to the presence of ionized functional groups on the pore surface. The interaction of these groups of polymeric chains of the membrane matrix with the flow of molecules of a sliding phase and the change of local states of the segments of these chains causing various conformation and structural modifications, explain the change of the transport characteristics of the membrane and, first of all, its permeability. Obviously, these changes will appear to a greater degree when the changes in the value of the surface pore charge and the conformation mobility of their surface macromolecules are more essential. So, the treatment of PET TM in the air plasma results in changing its hydrodynamic characteristics. The water permeability of the modified membrane to the greater degree depends upon pH of the filtrated solution (Figure 1a). It is stipulated by increasing of the content of carboxylic groups in the surface layer of the membranes and greater conformational mobility of macromolecules of this layer [10]. Increase of the density of negative charge at the expense of increasing the concentration of the COOH-groups and increasing the degree of their dissociation at high values pH of the solution determines decreasing the water permeability in alkaline medium. But we did not observe the full contraction of the membrane pore in this case.

Table 1. Change of the membrane characteristics in the process of graft polymerization

Parameter	Initial membrane	Membrane with grafted polymer layer	
		PMVP	PAA
Grafting yield, %	—	7.2	7.4
Thickness, μm	9.5	10.5	10.1
Effective pore diameter, nm	215	160	190
Water contact angle, deg	65	45	20

The graft polymerization of MVP or AA induced by the air plasma on the PET track membrane surface leads to the formation of the composite membranes the water permeability of which can be controlled by changing the solution pH. These results can be explained by conformation transition of macromolecules of the grafted polymer layer from an expanded state 'coil' into a compact state 'globule', and vice versa. So, the research on water permeability dependence on the solution pH of the membrane with a grafted layer of poly(2-methyl-5-vinylpyridine) (PMVP) with a grafting yield of 7.2% demonstrates its abnormal behavior (Figure 1b). Note the effective pore diameter decreases in this case down to 160 nm (Table 1). This membrane is not penetrative in the region pH from 1 up to 3. If increasing pH, one can observe a linear increase of the water flow rate. Such a behavior of the membrane is explained by various conformational states of grafted PMVP macromolecules which cause changing the pore diameter. At low pH values of the solution due to protonating the nitrogen atoms of pyridine groups, the segments of the macromolecules of the grafted polymer acquire a positive charge that results in its swelling – formation of gel, causing a membrane pore contraction. The membrane pores are 'closed' in this state (Figure 2a). The macromolecules of PMVP have an extended conformation state 'coil'. Such a conformational state of macromolecules resulting from the electrostatic interaction of charged segments with water molecules is permanent. It leads to the complete contraction of pores in the acidic medium (at solution pH from 1 up to 3).

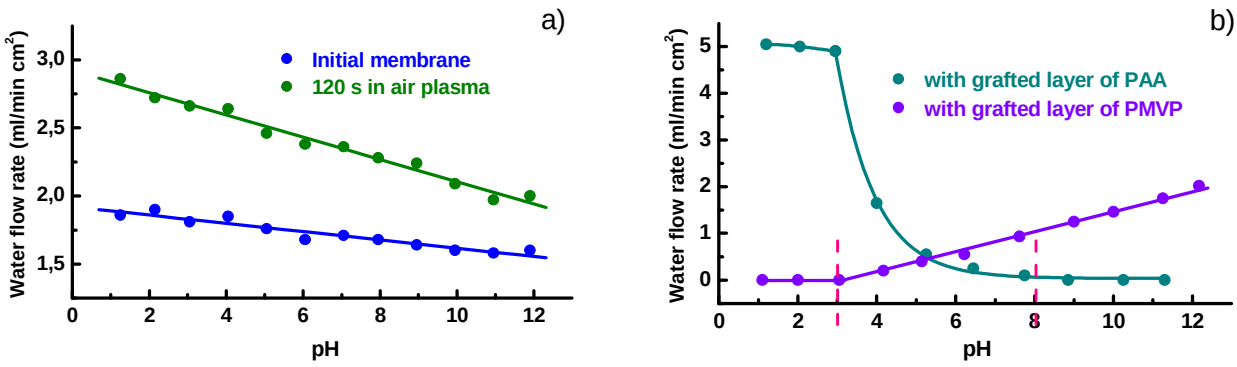


Figure 1. *pH dependence of flow rate for the: a – initial PET TM and the membrane modified by air plasma; b – composite membranes with the grafted layer of poly(acrylic acid) and poly(2-methyl-5-vinylpyridine).*

Increase of filtrate pH (the drop of ion concentration H^+ in the solution) leads to loss of the charge on the nitrogen atoms, i.e. transition of segments of the PMVP macromolecules to a neutral state. Therefore, the electrostatic interaction gets weaker. With decreasing Coulomb interaction, the non-electrostatic interaction of hydrophobic groups, in this case, of non-polar CH_3- and CH_2-groups increases. That results in a collapse of gel – transition of macromolecules in a compact conformational state 'globule'. The membrane pores are 'open' in this state (Figure 2b) that leads to increasing the membrane pore diameter, thus, its water permeability increases. The grafting of PMVP on the PET TM surface induced by plasma thus results in forming a composite mechanochemical membrane, the permeability of which is controlled by changing pH of the solution. For the membrane with a grafting yield of 7.2% at pH = 3 one can observe change-over to an operation mode of a 'chemical valve' i.e. at smaller pH values of the filtrate the membrane gets impermeable for water molecules. At higher pH values of the filtrate the membrane gets permeable for water molecules. Clearly, the boundary value of pH solution where the membrane changes for this mode will be determined by the properties of substrate and the grafted polymer layer.

The grafting of poly(acrylic acid) (PAA) on the membrane modified by plasma from a gas phase at elevated temperature results in formation of a mechanochemical membrane with 'chemical valve' too.

For the membrane that has a grafting yield of 7.4% and effective pore diameter of 190 nm (Table 1) at pH values more than 8 the full pore contraction is observed (Figure 1b) due to negative charge on the segments of the macromolecules of the grafted polymer macromolecules resulted from the dissociation of carboxyl groups. This leads to swelling the polymer layer and formation of gel. Such a conformational state of the macromolecules leads to the contraction of the membrane pores. The membrane pores are 'closed' under this condition (Figure 2a). Decrease of filtrate pH leads to loss of the charge on the segments of the grafted polymer macromolecules. That results in a collapse of gel – transition of macromolecules in a compact conformational state. The membrane pores are 'open' in this condition (Figure 2b) that leads to increasing the membrane pore diameter, thus, its water permeability increases. So, for the membrane with a grafted PAA layer change-over to an operation mode of a 'chemical valve' one can observe at pH = 8. I.e., at higher pH values of the filtrate the membrane gets impermeable for water molecules. At smaller pH values of the filtrate, the membrane gets permeable for water molecules.

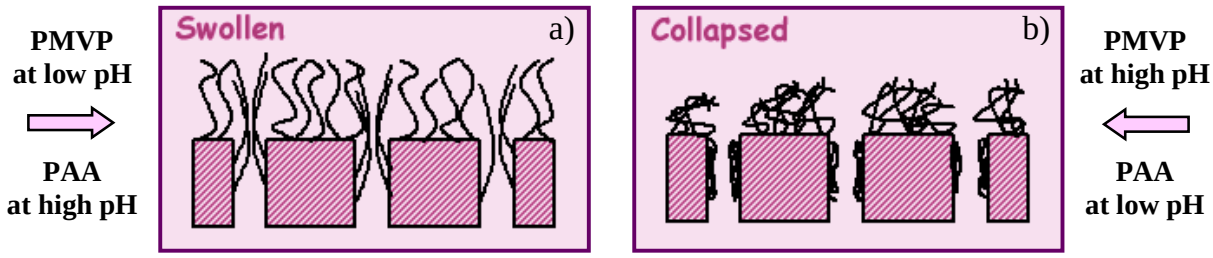


Figure 2. *Schematic illustration of changing in the conformation state of the grafted macromolecules on the track membrane surface in medium with various solution pH.*

Conclusion

The performed investigations have allowed us to make the following conclusions. The presence of the polymer layer of PMVP or PAA on the surface of PET track membrane results in changing its transport properties – the water permeability of the formed composite membranes substantially depends on the solution pH. These changes are caused by convertible conformational transitions of macromolecules of the polymer layer obtained by plasma-induced graft polymerization which is in turn caused by the degree of ionization of functional groups on the surface of this layer. Membranes with such properties can be used in biotechnology and medicine, for example, for bioseparation and biocatalysts immobilization. They also can be used for controllable drug delivery, in biosensor controls, for modeling processes of regulation in the cell, etc.

References

1. Yang B., Yang W. *J. Membr. Sci.* 218 (2003) 247.
2. Hu L., Chu L.-Y., Yang M., Yu J., Wang H.-D. *Chem. Eng. Technol.* 30 (2007) 523.
3. Tsusenda S., Endo T., Saito K., Sugita K., Horie K., Yamashita T., Sugo T. *Macromolecules* 31 (1998) 366.
4. Kim S.J., Yoon S.G., Lee S.M., Lee S.H., Kim S.I. *J. Appl. Polym. Sci.* 91 (2004) 3613.
5. Chatterjiee J., Haik Y., Chen C.-J. *J. Appl. Polym. Sci.* 91 (2004) 3337.
6. Cai W., Gupta R.B. *J. Appl. Polym. Sci.* 88 (2003) 2032.
7. Kravets L., Dmitriev S., Gilman A., Drachev A., Dinescu G. *J. Membr. Sci.* 263 (2005) 127.
8. Flerov G.N. *Vestn. Akad. Nauk SSSR* 4 (1984) 35 (in Russian).
9. Lazea A., Kravets L.I., Dmitriev S.N., Dinescu G. *Roman. Rep. Phys.* 57 (2005) 413.
10. Dmitriev S.N., Kravets L.I., Sleptsov V.V., Elinson V.M. *Desalination* 146 (2002) 279.

Interpretation of optical emission in a strongly inhomogeneous PIAD environment

J Harhausen[1*], R-P Brinkmann[2], R Foest[1], S Gorchakov[1], A Ohl[1] and B Schröder[2]

[1] *Leibniz-Institut für Plasmaforschung und Technologie e.V., Felix-Hausdorff-Strasse 2, D-17489 Greifswald, Germany*

[2] *Lehrstuhl für Theoretische Elektrotechnik, Ruhr-Universität Bochum, Universitätsstrasse 150, D-44801 Bochum, Germany*

[*] *E-mail: harhausen@inp-greifswald.de*

Preliminary remark

This extended abstract is intended to present work in progress. As this text is not subject to a rigorous review process, it is not claimed to be free of errors or to point out the final solution to the questions addressed. However, the results discussed are part of a publication in preparation. Readers are kindly invited to attend the presentation 'OR2202' on Thu, 12/09/13, or to contact the first author for questions or comments.

1 Introduction

A variety of methods exists for the production of high quality optical coatings. These are for instance magnetron or ion beam sputtering, or thermal evaporation assisted by ion or plasma ion beam sources. The choice of a particular technique is due to the specific demands for tailoring the thin film properties such as homogeneity, refractive index, absorption, mechanical stress, porosity (optical shift), etc.. To allow for economic production of complex multilayer designs, the issue of reproducibility at the highest deposition rate possible has to be faced.

The plasma ion assisted deposition (PIAD) has been invented to avoid contamination of the process environment present when gridded ion sources are employed. One example for this approach is the Advanced Plasma Source (APS)[1] which holds a considerable market share in the field of optical coatings. The APS is a hot cathode (LaB_6) DC glow discharge with an auxiliary magnetic field, typically operated with argon. A high density ($n_e \sim 10^{12}\,\mathrm{cm}^{-3}$) and high temperature ($T_e \sim 20\,\mathrm{eV}$) plasma is generated in the source region ($V \sim 0.7\,\mathrm{l}$) and expands to the chamber ($V \sim 10^3\,\mathrm{l}$) which is held at high vacuum ($p \sim 2 \cdot 10^{-2}\,\mathrm{Pa}$). The expansion induces a strong drop of the plasma potential V_p which results in an acceleration of the ions towards the substrates. The setup is outlined in figure 1. By varying the discharge voltage (V_D=50..150 V), the magnetic field (B_{max}=10..40 mT) and the gas flux (Γ_{Ar}=2..20 sccm) different characterstics of the plasma ion beam are obtained, where typical ion energies are E_i=50..150 eV. Detailed information on the APS plasma can be found in [2, 3].

As is described in the references, various probe techniques were adopted to elucidate the mechanisms of plasma beam formation in this particular PIAD setup. In an earlier work [4] the approach of optical emission spectroscopy (OES) has been pursued. This paper contains a description of the diagnostic installation allowing for tomogrgaphic reconstruction of the local optical emission near the source exit. With a simple corona model n_e and T_e could be estimated for an Ar/He mixture. The interpretation of emission close to the APS is hampered by the lack of detailed knowledge of neutral density and temperature in this region.

In this extended abstract the preparation of a more elaborate approach using collisional radiative modelling is sketched. The new aspect is the consideration of a global electron energy probability function (EEPF) based on the nonlocal approximation [5]. This concept is useful for reducing the complexity of electron kinetics by coordinate transformation from the 6D phase-space to a 1D total energy space. The analysis of OES data is not merely ment as a proof of principle. The final goal is to interpret the OES data in terms of electron parameters, as a foundation of a control scheme for the APS using non-invasive optical diagnostics. Although global parameters, such as voltages and currents can be maintained accurately, drifts in the plasma parameters which are not measured routinely in the industrial application, may lead to limitations in the reproducibility of the optical coatings. The main reason is suspected to be the alteration of the electrodes of the APS during the PIAD process.

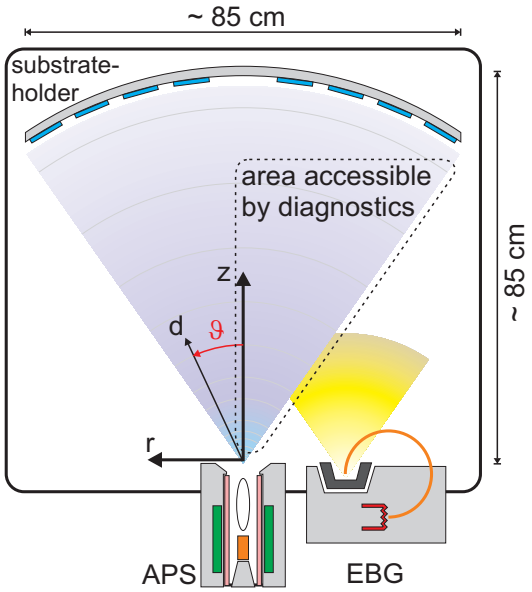


Figure 1: Scheme of the PIAD setup with plasma source (APS) and electron beam evaporator (EBG) at the bottom. The plasma diagnostics are positioned in the chamber by employing manipulators not shown in this figure. Note the indicated coordinate system.

2 Collisional radiative modelling

For argon, several approaches for collisional radiative (cr) modelling have been published, e.g. [6, 7]. Differences among the models are found in the number of species and energy levels considered, and the particular sets of cross section data adopted. Here, we use a cr-model being part of a code to resolve the electron kinetics in low pressure argon plasmas [8]. The model consideres 16 populations of argon species corresponding to the ground state $1s_1$, the first 14 excited states (in Paschen notation with increasing threshold energy: $1s_5$-$1s_2$, $2p_{10}$-$2p_1$) and the ion. In order to calculate the level/species populations, 121 cross sections for electron impact ionisation and excitation, 57 rate coefficients for quenching, 5 rate coefficients for chemoionization and 28 time constants for radiative decay are provided. Further, since the code is spatially 1D ('long discharge tube'), a radius of the plasma is defined, as well as transport parameters assigned to describe the diffusion of the ion and the metastable states ($1s_3$,$1s_5$) to the wall where the particles are neutralized or deexcited, respectively. The abundance of metastable states has a strong impact on the level populations which is one of the main problems for the development of a realistic cr-model. Here, it is aimed at finding trends based on the input data.

The code is employed to provide the argon excited states densities along the *z*-axis of the APS. As the neutral density, a fixed value of $n_0 = 2.5 \cdot 10^{12}\,\mathrm{cm}^{-3}$ is defined which is based on an estimate according to a background pressure of $p \sim 2 \cdot 10^{-2}\,\mathrm{Pa}$ in the chamber. For the model parameter tube-radius the diameter of the plasma at the particular *z*-position is considered. Although the whole process chamber is filled by the plasma, data from probes and the distribution of optical emission indicates that the plasma beam covers a cone-like region, as indicated in figure 1. At the low background pressure the mean free path of particles is quite large, so that species intersecting the plasma region from outside are assumed to be ground state neutrals originating from the vessel wall. The electron parameters are defined by the nonlocal EEPF and the ion density is set by the condition of quasi-neutrality.

3 Results and discussion

The results of the cr-model for one set of input data is presented. For brevity, we omit to state the APS configuration in detail which can be found in [3], section 4.1. Since the energy relaxation length for electrons is much larger than the dimension of the chamber, the nonlocal approximation holds. This is seen from the shape of the local EEPFs recorded along the *z*-axis. When these local EEPFs are plotted against the total energy of the electrons $E_{\mathrm{tot}} = E_{\mathrm{kin}} + E_{\mathrm{pot}}$, i.e. considering the magnitude of the local V_{p} one global EEPF containing all information can be deduced. Figure 2 shows such a nonlocal EEPF, together with the profile of $V_{\mathrm{p}}(z)$. The EEPF depicted represents the local EEPF at z=0 , if the abscissa is shifted by $+V_{\mathrm{p}}(z{=}0)$=65 V. In general, the local EEPF is obtained by shifting the energy axis by $+V_{\mathrm{p}}(z_{\mathrm{i}})$ and considering the data according to the positive half space of the energy axis which corresponds to the kinetic energy of the electrons. The shape of the nonlocal EEPF indicates that the low energy electrons are distributed likewise maxwellian, while in the high energy region, the population is depleted. Most of the

electrons are bound to the source region and only the high energy electrons a able to overcome the potential barrier towards larger distances from the source. The escaping electrons compensate the ion current to the chamber walls. Figure 3 gives an impression on the accuracy of the EEPF-model. The probe data for n_e and $T_{e,eff}(=2/3 \cdot \langle E_e \rangle)$ is well matched, albeit the high energy depletion is slightly underestimated, so that modelled and experimental values for n_e deviate at larger z-values.

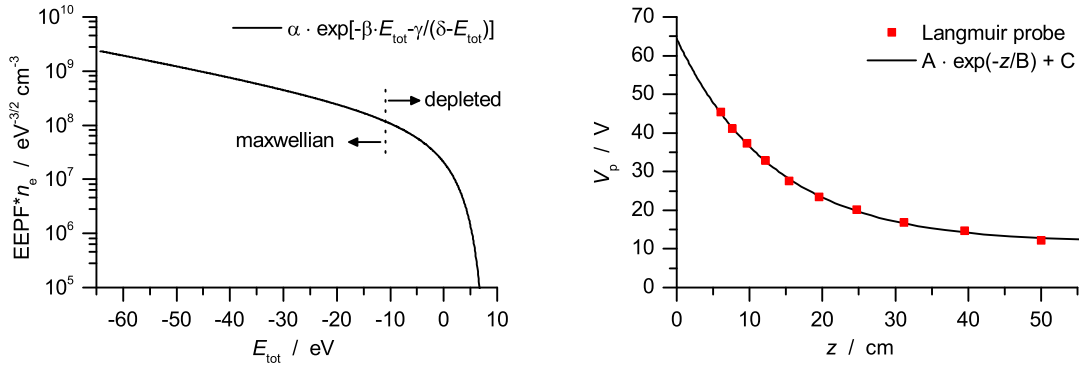


Figure 2: Models for the nonlocal EEPF (left) and for the profile of the plasma potential V_p (right) on the z-axis based on Langmuir probe data for a particular APS setting. $\{\alpha, \beta, \gamma, \delta\}$, $\{A, B, C\}$ are fitting parameters.

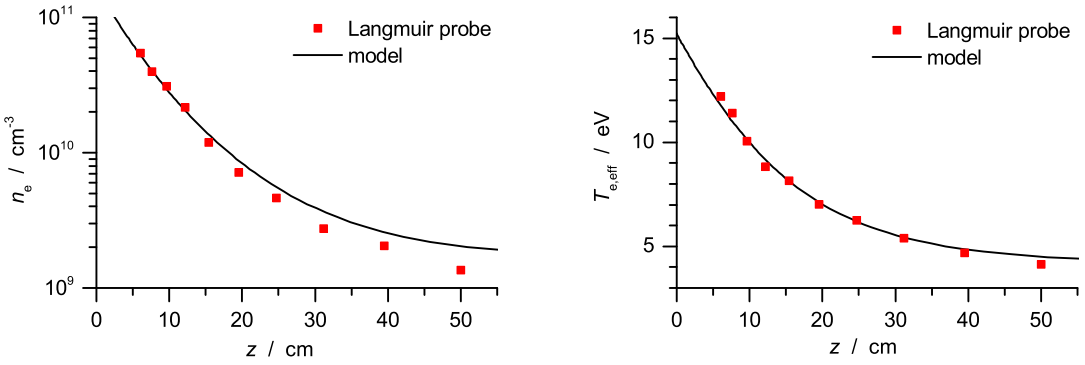


Figure 3: Electron density n_e (left) and effective electron temperature $T_{e,eff}$ (right) as determined by the Langmuir probe and the trends according to the models shown in figure 2.

The cr-code is used for a z-array which is accessible to the OES diagnostics. Figure 4 shows the resulting densities for the 1s and 2p states, where the latter are relevant for OES due to the VIS-NIR radiation. Unsurprisingly, there is a strong drop in density along the z-axis, because both n_e and $T_{e,eff}$ drop significantly. This is in agreement with the observation that the APS plasma is very bright near the source exit and the emission is barely detectable for $z > 20\,\text{cm}$. The evolution of the 1s states, i.e. the slight difference between the profile shapes of metastable and non-metastable densities has a slight impact on the population of the 2p states. Since it can hardly be resolved in the $n_x(z)$-plot, ratios of densities are shown in the right part of figure 4. Most of the 2p density ratios do not exhibit a significant variation along z. This is clear from the point of view, that the 2p states have very similar threshold energies. In principle, line ratio techniques based on very different cross sections (shape and threshold) are employed to estimate T_e . However, the ratio $2p_9/2p_4$ varies by more than a factor of two. The actual emission connected to these 2p states should give an indication, whether the approach of the cr-model is reasonable. If the experimental data deviates strongly from the predictions of the model, it is likely the abundance of metastable states which is estimated incorrectly.

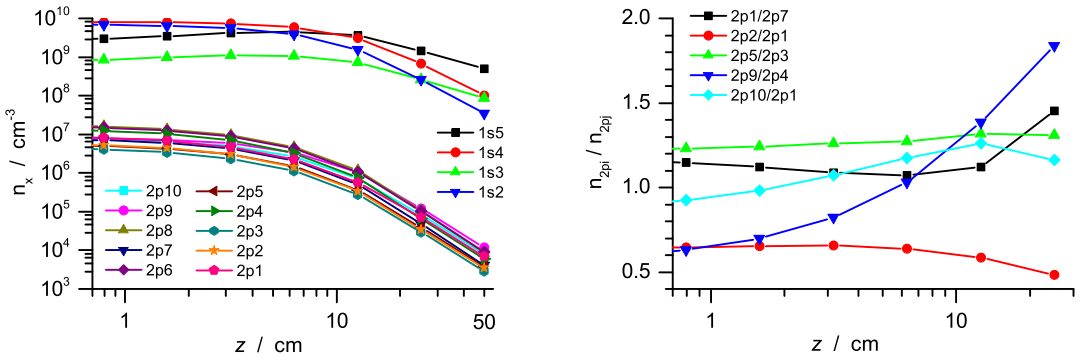


Figure 4: Left: Profiles of argon excited states densities obtained by the cr-model using the EEPF of figure 2 and further settings mentioned in the text. Right: Set of ratios of argon excited states densities.

4 Outlook

In an experimental campaign VIS/NIR line emission will be recorded and probe measurements conducted to optain the nonlocal EEPF. In order to use the cr-model reasonably, the neutral density near the APS exit will be estimated, based on the electron parameters known. The line emission predicted by the model will be compared to the experimental data. There are two approaches to check for consistency: (1) to consider the model being accurate and using as input the EEPF only to calculate the neutral density ; (2) to use the estimated neutral density, so the input to the code is EEPF and neutral density, thereby testing the reasonability of the cr-model itself.

The cr-model employed might be critizised as being too simple. Actually, emission from high lying excited neutral and ion states is observed experimentally, indicating significant densities of these states. The first goal is to examine whether global trends can be recovered from the cr-model. In order to exploit the experimental data more thoroughly, we also check whether a line ratio technique proposed for the estimation of T_e (3p states, see [9]) can be used successfully. A simple approach to monitor T_e close to the source would be a valuable tool for process optimization. Nevertheless, the ultimate goal is to determine the free parameters of the nonlocal EEPF-model by recording a proper set of argon lines during a PIAD process.

Acknowledgment

This work is funded by the German Federal Ministry of Education and Research (BMBF, Fkz. 13N10462).

References

[1] Matl K, Klug W, and Zöller A *Mat. Sci. Eng.* **A140** 523-7

[2] Schröder B, Brinkmann R P, Harhausen J, and Ohl A 2011 *J. Appl. Phys.* **110** 043305

[3] Harhausen J, Brinkmann R P, Foest R, Hannemann M, Ohl A, and Schröder B 2012 *Plasma Sources Sci. Technol.* **21** 035012

[4] Harhausen J, Meyenburg I, Ohl A, and Foest R 2011 *Surf. Coat. Tech.* **205** S407-10

[5] Kortshagen U, Busch C, and Tsendin L D 1996 *Plasma Sources Sci. Technol.* **5** 1-17

[6] Vlcek J 1989 *J. Phys. D: Appl. Phys.* **22** 623-31

[7] Bogaerts A, Gijbels R, and Vlcek J 1998 *J. Appl. Phys.* **84** 121-36

[8] Gorchakov S, Loffhagen D, and Uhrlandt D 2006 *Phys. Rev. E* **74** 066401

[9] Boffard J B, Jung R O, Lin C C, Aneskavich L E, and Wendt A E 2012 *J. Phys. D: Appl. Phys.* **45** 045201

The Study about Surface Modification of Steel by Water Plasma

J. H. Kong[a], T. Takeda[a], M. Okumiya[a], Y. Tsunekawa[a], M. Yoshida[b], S. G. Kim[c]

a: Materials Processing Laboratory, Toyota Technological Institute, 2-12-1, Hisakata, Tempaku, Nagoya, 468-8511, Japan
b: Dept. of Mechanical Engineering, Shizuoka Institute of Science and Technology, Hukuroi, 437-8555, Japan
c: Surface Technology & Heat Treatment R&D Department, Korea Institute of Industrial Technology (KITECH) 7-47, Songdo-Dong, Yeonsu-Gu, Incheon, 406-840, R. O. Korea

Abstract

Recently, a lot of research has been carried out to improve the properties of steel surface such as ion-nitriding, gas nitriding. However, they need high vacuum rate or very expensive equipment and longer treatment time. In this study, new nitriding process proposed which have extremely shorter treatment time and very simple equipment by using water plasma. For the water plasma, JIS-SCM420 specimen was used as cathode, and rolled punching stainless steel plate (SUS304) was used as anode. Voltage was applied between electrodes by DC pulsed power supply. Pulsed power supply was used to prevent discharge from concentrating on one point. Urea $(H_2N)_2C=O$ used as supply source of nitrogen and potassium hydrate (KOH) for adjusting electric conductivity. And it was put into distilled water as electrolyte. Treatment voltage was 600 V, and experiments were conducted by varying conditions such as treatment time and concentration of electrolyte. After water plasma treatment, a lot of fine discharge pores can be seen on the treated steel surface. And also, a few μm modified layer is formed on the steel surface after water plasma treatment within 5min. At the results of XRD analysis, iron nitrides are detected with Fe peaks and the hardness of nitride layer shows about 800HV.

Key words: Water plasma, Nitride layer, Urea, Potassium hydrate

1. Introduction

Steels are widely used because of good strength, toughness and workability. But steels which are used as slide parts are required additional wear resistance or fatigue resistance. To improve these mechanical properties, surface-hardening process such as carburizing, nitriding treatment has being used. For example, ion nitriding is a representative process in the most of nitriding process on nowadays. Treatment time of ion nitriding is much shorter than that of gas nitriding. In addition, harmful gases such as ammonia are not used in the treatment; therefore it is not harmful to environment as well known. [1]. However, this process needs vacuum furnace and spends more time on the pre- and post- processes for vacuuming and cooling of furnace.

Plasma which has many kind of advantage on surface modification field can be generated in a liquid by high frequency or microwave irradiation from an underwater electrode. Recently, it has been reported that in-liquid (or water) plasma can synthesize substances at a higher rate than conventional gas phase plasma [2]. In particular, it has been known that when a substrate is submerged in an organic solvent or an alcohol and plasma is generated under the substrate, diamond [3], diamond-like carbon, carbon nanotubes and SiC can be deposited on the surface of the substrate [4]. Moreover, in-liquid plasma is useful for decomposition of harmful liquids and liquids containing dissolved harmful substances [5ï 7]. And it is expected that the treatment time is also can be possible to decrease because of not needed vacuum and cooling during process. To this end the pulsed discharge of high-voltage electricity in liquids needs to be considered [8, 9].

In this study, new nitriding process that can be conducted in very short treatment time with simple equipment by using water plasma is proposed.

2. Experimental procedures

2.1 Specimen preparation

SCM420 commercial grade of bar type was used as cathode with the size of ϕ5x30mm, and SUS304 stainless steel plate (300x150x10.6mm) was used as anode after rolling and punching. Voltage was applied between SCM420 cathode and SUS304 anode electrodes by DC pulse power supply (Max 600V and 20A).

2.2 Water plasma

Pulse power supply was used to prevent discharge from concentrating on one point (pulse width: 2μs, pulse frequency: 15 kHz). Exposure area of specimen was adjusted by putting insulating tape before treatment. After preparing the specimen, the Urea ($(H_2N)_2C=O$) used as supply source of nitrogen and potassium hydrate (KOH) for adjusting electric conductivity were put into distilled water as electrolyte. Then, water plasma was performed at variety conditions such as treatment time and concentration of electrolyte under the voltage of 600V. The amount of Urea and potassium hydrate were 200g and 10~40g respectively in distilled water per 1ℓ. Fig.1 shows overview of experiment system.

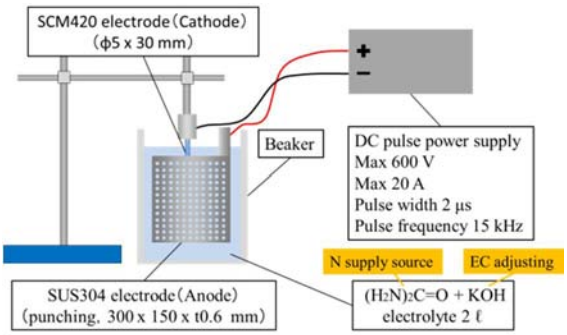


Fig.1 Overview of experiment system.

2.3 Microstructure observation and hardness test

The optical microscopy (OM) and scanning electron microcopy (SEM) (Hitachi, SU6600) were used to observe the micro-structure and morphology after water plasma. Layers were identified by an X-ray diffractometer (Rigaku, UltraX 18 TTR) using monochromatic Cu-K$_{\alpha}$ radiation. The X-ray diffraction (XRD) measurements were performed using a goniometer at a scanning range of 40°≤2θ≤80° at 40KV and 200mA with the step-size of 0.02°.

The micro hardness of the surface layer was measured using by a Vickers micro hardness tester (Akashi, HM-125).

3. Results and discussions

3.1. Changes of current during water plasma

To investigate the relationship between current density and treatment time during water plasma, the current was measured according to the treatment time. Fig.2 shows the average current as discharge time under the condition of Urea 200g/ℓ and KOH 20g/ℓ. The average current indicates around 0.6A at first and gradually decreased to about 0.25A until 360sec, after then it shows steady current state. In this result, water plasma discharge is divided into 3 regions as follows. Firstly, weak discharge generates at the edge of surface only (discharge start region). Secondly, the discharge becomes stronger and generates at all of areas (discharge intensification region). And finally, discharge becomes a little weak and stable discharge continues (discharge stability region).

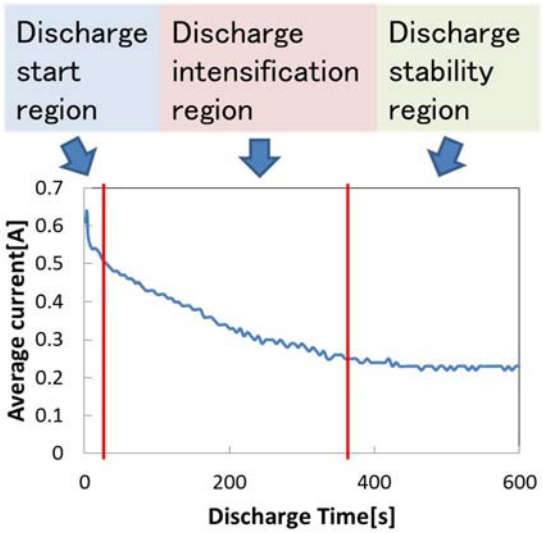


Fig.2 Changes of average currents during water plasma.

3.2. Effects of water plasma on the surface

Fig. 3 shows the changes of surface morphology after water plasma at various treatment times to investigate discharge state on the surface (Urea 200 g/ℓ, KOH 10 g/ℓ). After water plasma, discharge pores are generated on the surface area. However, most of discharge pores can be seen only at edge area of surface until 30sec. After then the time of 30sec, discharge generates all of the areas. And at the 120 sec, uniform discharge pores can be seen both area of center and edge. This tendency about the formation of discharge pores shows similar tendency compared with average current as discharge time as shown in Fig. 2.

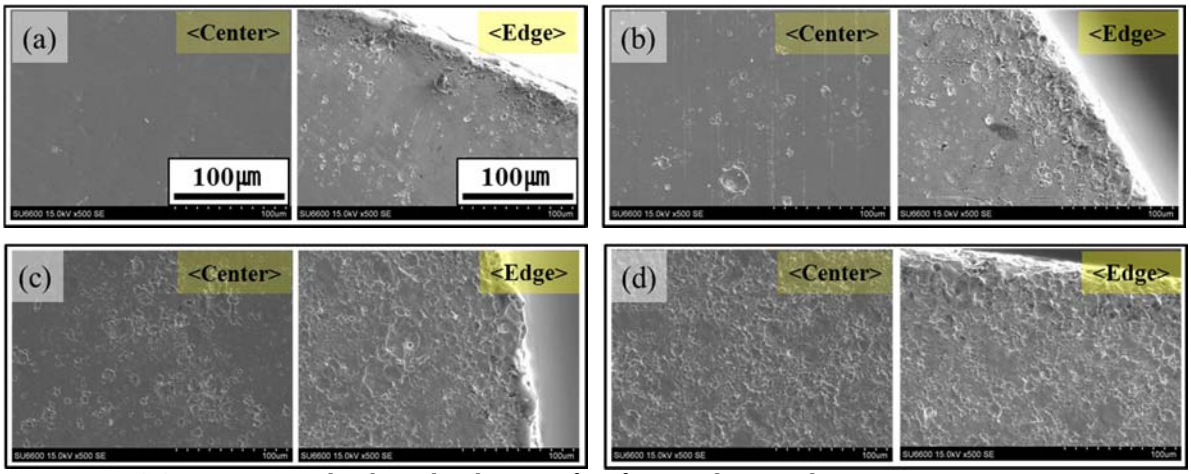


Fig.3 SEM micrographs about the changes of surface condition with respect to treatment time of (a) 10sec, (b) 30sec, (c) 60sec and (d) 120sec.

Fig. 4 shows the effects of potassium hydrate (KOH) concentration with urea 200 g/ℓ. The solution of KOH has the effect of electric conductivity. As shown in Fig. 4, discharge pores being coarsen with increasing the amount of KOH from 10g/ă to 40g/ă. It means that the high concentration of KOH have a strong discharge effect. And the edge effect also not investigated at the high concentration of KOH compared with the SEM micrographs as shown in Fig. 3. Consequently, high KOH concentrations have coarsen discharge pores by strong discharge with lack of uniformity. On the other hands, in low concentration of KOH can be possible fine discharge pores with uniform discharge except the edge effect at the short treatment time.

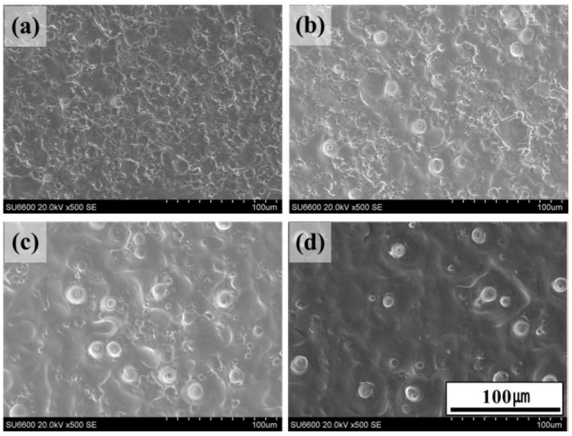


Fig. 4 SEM micrographs after water plasma at urea 200 g/ă and different KOH concentration of (a) 10g/ă, (b) 20g/ă, (c) 30g/ă and (d) 40g/ă for 30min.

3.3. Growth of modification layer

Fig.5 shows the SEM and optical micrographs on the surface area and cross-section with modified-layer respectively, after water plasma at various treatment time under the condition of urea 200 g/ℓ and KOH 20 g/ℓ.

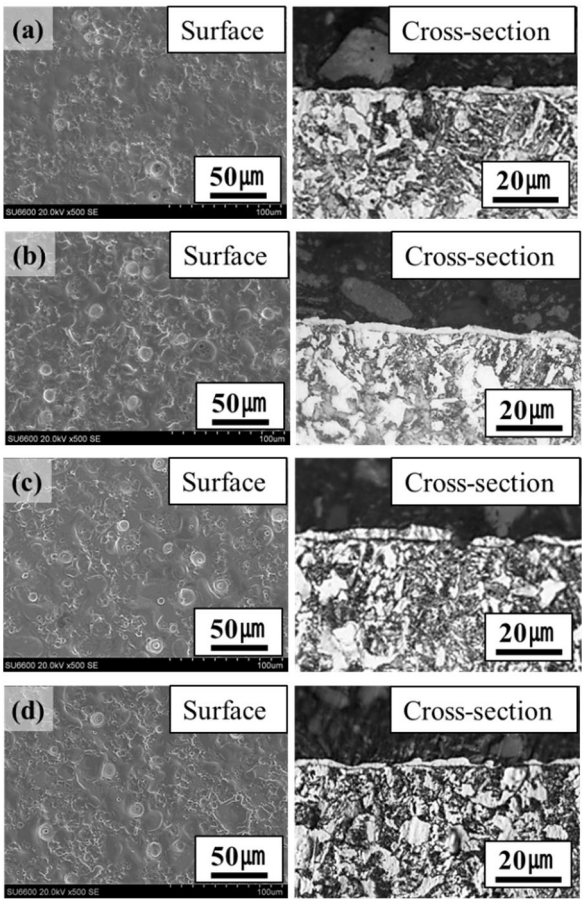


Fig.5 SEM and Optical micrographs on the surface and cross-section after water plasma under the condition of urea 200 g/ℓ and KOH 20 g/ℓ at various time of (a) 2min, (b) 5min, (c)20min and (d) 30min.

As shown in Fig. 5, a lot of fine discharge pores can be seen on the treated-surface. And

modified-layers of a few μm are also investigated at the outmost surface of cross-section. The formation of modified-layer is extremely short time compared to general surface modification process with nitriding process. The thickness of modified-layer shows 2~3μm after water plasma and it is not changed remarkably as increasing the treatment time from 2min to 30min. It is indicate that the thickness of the modified layer is not affected significantly by treatment time during water plasma.

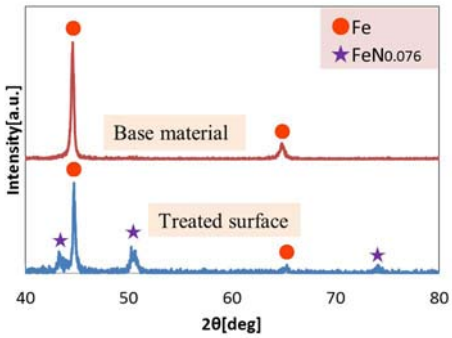


Fig.6 XRD analysis of modified-layer and SCM420 base metal after water plasma in urea 200 g/ă and KOH 20 g/ă for 5min.

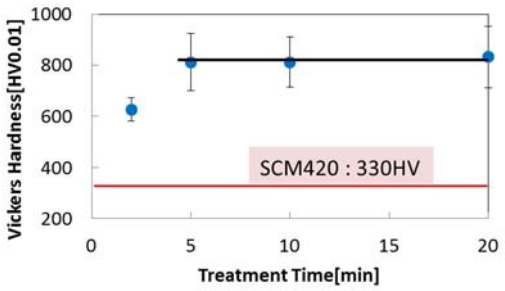


Fig.7 Hardness value of modified-layer after water plasma for various treatment time.

Fig.6 shows the results of XRD analysis of the modified-layer and SCM420 base metal after water plasma for 5min under the condition of urea 200 g/ℓ and KOH 20 g/ℓ. From the result of XRD, $FeN_{0.076}$ peaks are detected with α-Fe peaks. It means that the modified-layer is composed with iron nitrides ($FeN_{0.076}$). The hardness of nitride layer shows about 800HV at the treatment time of 5min as shown in Fig. 7. And the hardness values are also not changed as increase the treatment time. This tendency of hardness value shows similar tendency with the thickness of modified iron nitride layer. It means that the micro-arc discharge generates only at most surface without the diffusion of nitrogen ion. It is expected that the specimen is cooled by surrounding solution at the same time while the water plasma is performing. Therefore, the nitrogen cannot permeate and diffuse from surface to interior of the specimen.

4. Conclusions

After the water plasma, modified thin layer was formed in very short time by using simple equipment. It is expected that the process can be applied to thin plate or minimal parts. The obtained results are as follows;

1. Discharge of water plasma process is divided into 3 regions as follows; first: discharge start region, second: discharge intensification region and finally: discharge stability region.
2. Discharge pores were coarsening with increasing the amount of KOH during water plasma.
3. After water plasma, iron nitride ($FeN_{0.076}$) layer of a few μm(2~3μm) was formed at the outmost surface and the hardness value shows about 800HV.

Reference

[1] Hisahiko Yamanaka, Ion nitriding, Nikkan Kogyo Shinbunsha (1976)
[2] S. Nomura, H. Toyota, Appl. Phys. Lett. 83 (22) (2003) 4503ï 4505.
[3] H. Toyota, S. Nomura, Y. Takahashi, S. Mukasa, , Diamond Relat. Mater. 17 (2008) 1902ï 1904.
[4] S. Nomura, H. Toyota, S. Mukasa, H. Yamashita, T. Maehara, M. Kuramoto, Appl. Phys. Lett. 88 (21) (2006) 211503-1ï 211503-3.
[5] T. Maehara, H. Toyota, M. Kuramoto, A. Iwamae, A. Tadokoro, S. Mukasa, H. Yamashita, A. Kawashima, S. Nomura, Jpn. J. Appl. Phys. 45 (11) (2006) 8864ï 8868.
[6] T. Maehara, I. Miyamoto, K. Kurokawa, Y. Hashimoto, A. Iwamae, M. Kuramoto, H. Yamashita, S. Mukasa, H. Toyota, S. Nomura, A. Kawashima, Plasma Chem. Plasma Process. 28 (2008) 467ï 482.
[7] H. Aoki, K. Kitano, S. Hamaguchi, Plasma Sources Sci. Technol. 17 (2) (2008) 025006-1ï 025006-6.
[8] A.A. Joshi, B.R. Locke, P. Arce, W.C. Finney, J. Hazard. Mater. 41 (1995) 3ï 30.
[9] A.T. Sugiarto, M. Sato, Thin Solid Films 386 (2001) 295ï 299.

Study of the growth kinetics, microhardness and morphology of PEO coatings formed on Al 2024 alloy in alkaline-silicate electrolytes using different current waveforms

Rakoch A.G[1] , Henrion G[2], Kovalev V.L[1], Nominé A[1,2], Bardin I.V[1]

[1] NUST "MISiS" 119049, Moscow, Leninskiy prospekt 4
[2] Institut Jean Lamour - UMR CNRS 7198
Ecole des Mines de Nancy, Parc de Saurupt - CS 14234 - 54042 NANCY CEDEX

Plasma Electrolytic Oxidation (PEO) is currently widely used technique of Al-alloys surface treatment providing the obtaining of composite anticorrosive and wear resistant coatings. The microhardness of these coatings can be almost equal to the theoretical corundum microhardness thanks to the formation of high temperature α-modification of alumina in the inner part of coating. However the conditions of intensive formation of this phase of alumina in the coating have not been defined explicitly, and therefore the ways of obtaining of relatively thin (< 40 μm) and hard coatings are not established.

The purpose of the present work is to investigate the ways to intensify α-Al_2O_3 formation in the PEO-coating making vary different parameters such as current waveform and substrate temperature using a widely used commercial alloy Al 2024.

The PEO coatings were obtained using invertor based PC controlled power supply which allows to provide 50 Hz sinusoidal AC with adjustable DC offset, in an in alkaline silicate electrolytes (3g/L NaOH ; 7 g/L $Na_2O{\cdot}2{,}9SiO_2{\cdot}8H_2O$). We took as varying parameter the ratio R between positive (Q_p) and negative (Q_n) charges such as

$$R = \frac{Q_p}{Q_n}.$$

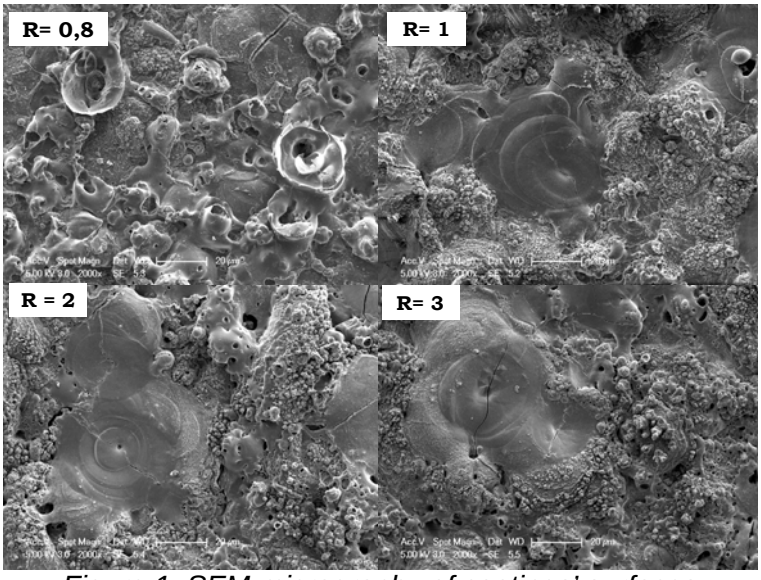


Figure 1. SEM-micrography of coatings' surfaces

The experimental results presented in figure 1 show that increasing value of R leads to the increase of dimensions of "pancakes" as well as the diameter of pore and the presence of Si-rich phase (probably SiO_2). These facts lead to increase of coating roughness as shown in figure 2. The precipitation of Si has been revealed only in the outer layer of coating. During PEO in alkaline-silicate solutions the deposition of SiO_2 on the coating surface is a result of thermo-chemical transformations of polyanions such as $n[Si_xO_y]^{2-}$ into SiO_2, and also evaporation of solvent of electrolyte in contact with plasma micro-discharges.

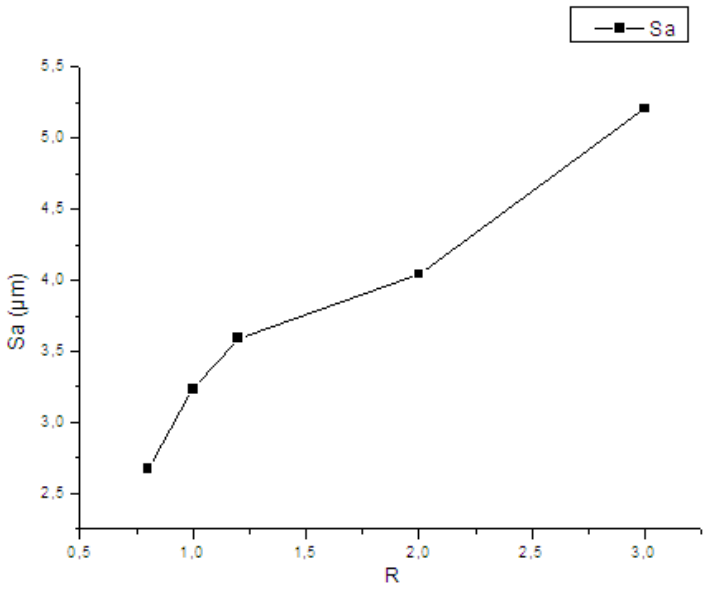


Figure 2. Influence of ratio R on coating roughness (Sa)

According to EDX analysis, the pancakes are mainly composed by Aluminium and Oxygen (obviously of Alumina) without any trace of Si (figure 3a) in contrast to the “sponge” phase that is mainly composed of Si (figure 3b).

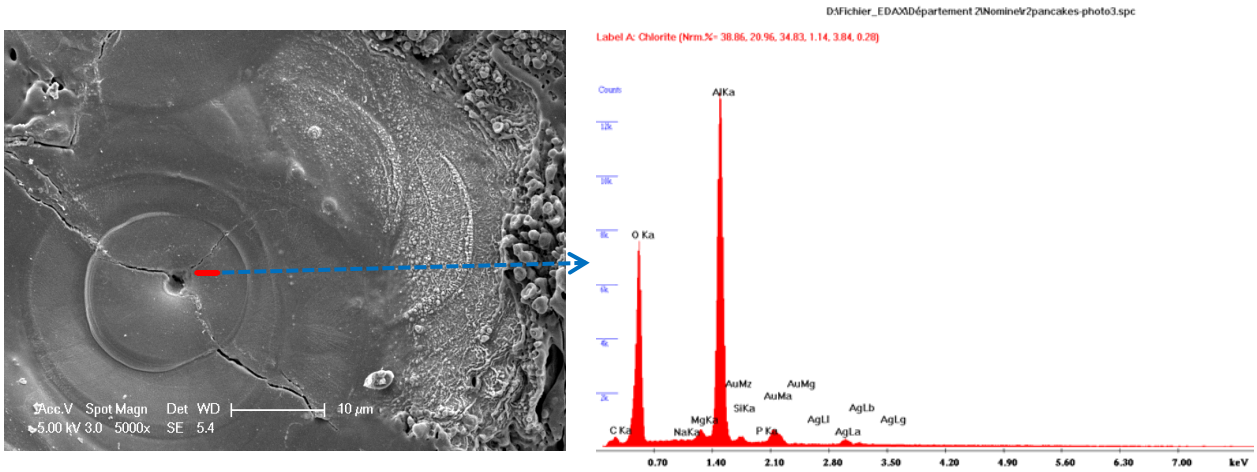


Figure 3a. EDX qualitative analysis on “pancake”

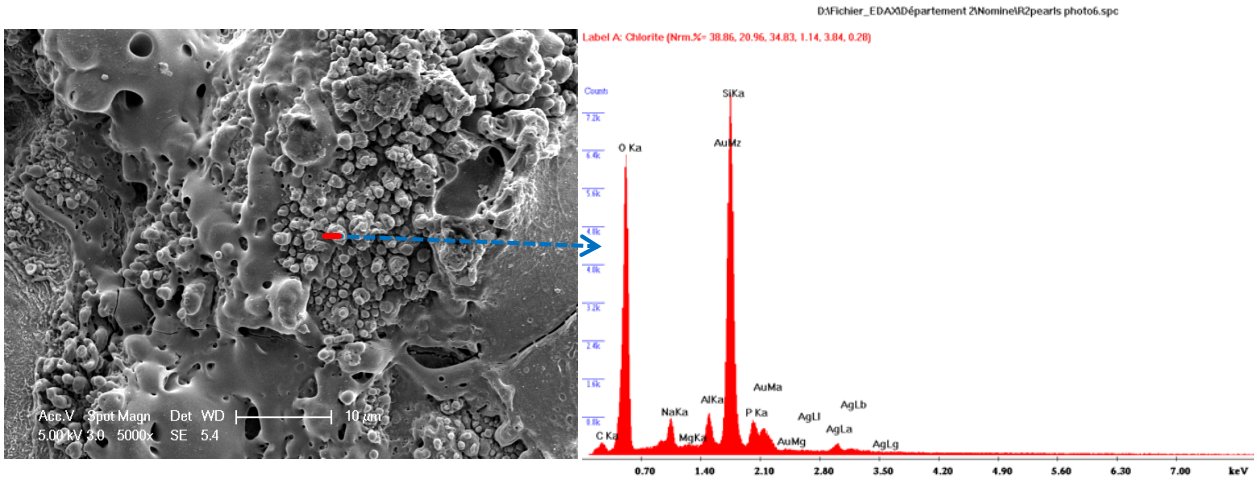
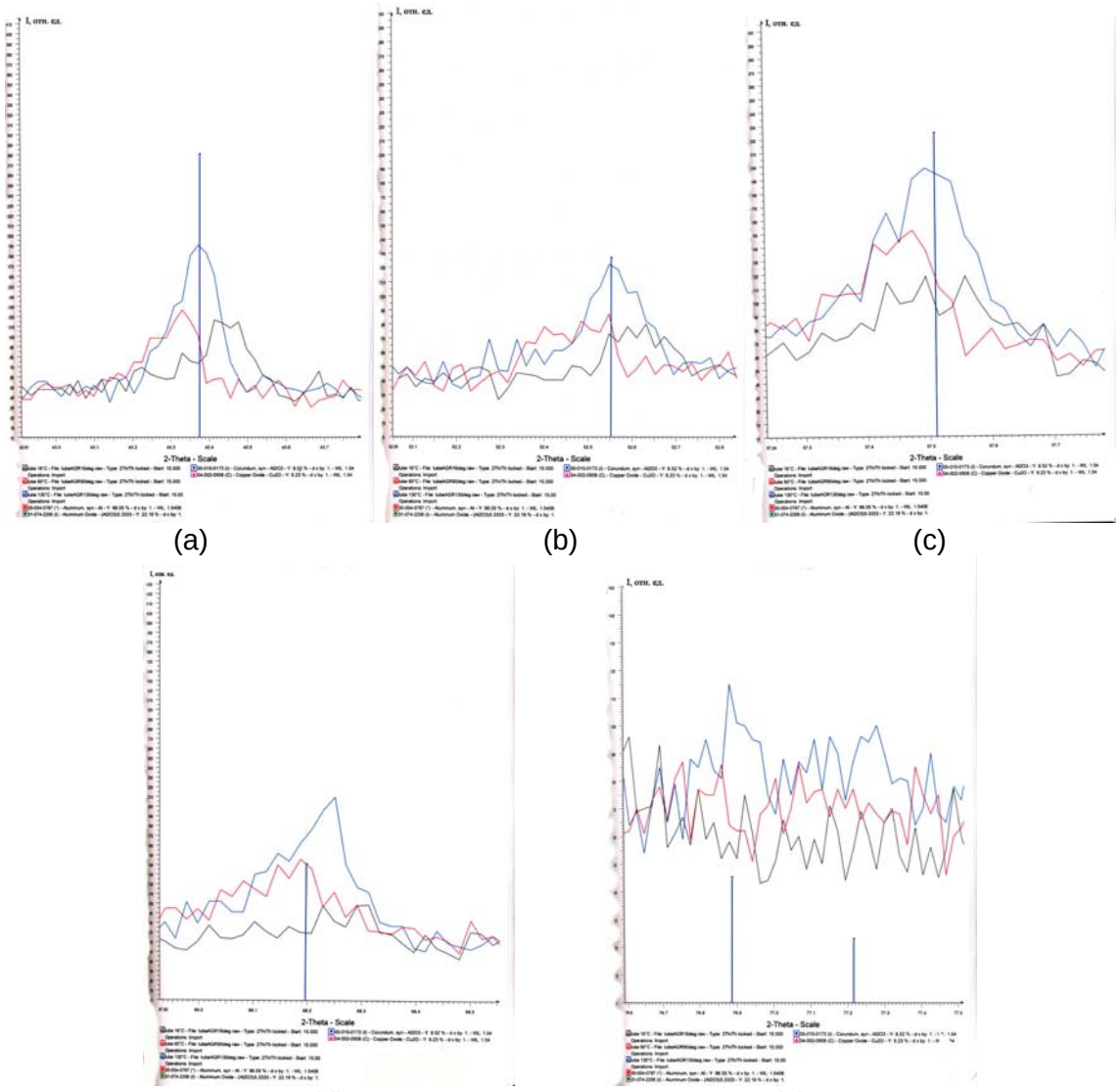


Figure 3b. EDX qualitative analysis on “sponge”

The XR analysis revealed the presence of slight amount of corundum phase in coating obtained with a current density of 15 A/dm² with R varying from 0,8 till 3. Nevertheless the increasing R value provides higher amount of α-phase in the coating (figure 4). The high temperature modification of alumina is mainly concentrated in the inner layer of coating.



(a) (b) (c)

(d) (e)

Figure 4. Relative intensity of the XR-peaks given by α-Al2O3 of the coatings obtained under different substrate temperature: 130 °C (blue line), 90 °C (red line), 16 °C (black line). The values of 2Θ angle are 43,7° (a); 52,55° (b); 57,51° (c); 68,19° (d); 76,88° and 77,21° (e)

We put forward a working hypothesis according to which the concentration of α-phase of alumina depends on a time-temperature couple: the parts of coating which are close to the microdischarges should be heated up to the temperatures more than 1200 °C and stay at this temperature for a certain time. The joint action of these factors should provide the high rates of α-alumina formation.

In witness of our working hypothesis the following experiments have been carried-out. The outer surface of the metallic tubes made out of Al 2024 and Al 6063 alloys was oxidized with an additional independent heating of substrate by means of oil (T ≈ 16…150 °C) circulating through the tubular samples and thermostat.

According to XR-data the increasing temperature of substrate leads to the higher amount of α-alumina in the PEO coating formed on the Al tubular samples. As a result the microhardness of inner coating layer increases with increasing temperature of substrate. For instance, the external additional heating of tube made out of Al 2024 up to the temperature about 150 °C allows to obtain relatively thin coating (≈ 40 μm) with microhardness (1620 ± 280

HV) almost equal to microhardness (1680 ± 250 HV) of relatively thick coating (≈ 80 μm) obtained under the same conditions but without additional external heating of a substrate. However the increasing temperature of oil circulating through the tubular samples causes the same effects of the PEO coating formed on the outer surface of tubes as the increasing value of parameter R. Obviously the increase of substrate temperature as well as the increase of R value lead to the heating of inner part of coating that results in higher amount of high-temperature modification of alumina, particularly of corundum (α-alumina). We have proposed that a coating heating is mainly contributed by 1) Joule heat and 2) low porosity of coating.

Beyond all doubt the research of temperature of microdischarges occurred on the sample surface during PEO process is of the highest scientific interest. However if the temperature of discharges overtops the melting temperature of alumina the further increase of it does not significantly accelerate α-alumina formation in the PEO coating. According to the literature data the temperature of the discharge area lies in a range from 2500 till 20000 °C, i.e. depending on time during which the parts of coating are heated up to these temperatures different amount of α-alumina can be revealed in the coating.

On the basis of our research we have suggested that in case of details the obtaining of relatively thin (< 40 μm) and hard (> 1600 HV) PEO coatings can be achieved by using of high-frequency current.

Scuffing propagation of heavily-loaded, lubricated, coated friction joints

Remigiusz Michalczewski, Witold Piekoszewski, Waldemar Tuszyński, Marian Szczerek
Institute for Sustainable Technologies – National Research Institute (ITeE-PIB)
ul. K. Pulskiego 6/10, 26-600 Radom, Poland

Keywords: low-friction coating, scuffing, wears mechanisms, four-ball tester

1. Introduction

There is great interest in improving the wear and friction of a wide variety of machine components, e.g. gear systems, gears. In modern technology, due to the increase of the unit pressure, velocities, and hence temperatures in the tribosystems of machines, a risk of a very dangerous form of wear exists. This form is scuffing.

The most effective way of to improve the mechanical properties of various engineering components is the modification of surface properties by the deposition of PVD/CVD coatings [1].

In literature, the problem concerning whether it is the most beneficial to coat only one or both of the contacting surfaces and on when and how the coatings may improve the tribological situation in heavily loaded lubricated friction joints is not solved [2, 3]. The aim of this paper was to explore the mechanisms of scuffing propagation of heavily loaded friction pair elements coated with a low-friction WC/C coating for various material combinations.

2. Experimental

WC/C coating (also denoted as a-C:H:W or W-DLC) is one of the most recommended coating for gears applications [4]. The coating was deposited in a commercial process (Oerlikon Balzers Coating Poland Ltd.). The coating consists of an elemental Cr adhesion layer adjacent to the steel substrate, followed by an intermediate transition region consisting of alternating lamellae of Cr and WC and a hydrocarbon layer doped with W. The coating was deposited using the PVD process by reactive sputtering. DLC coatings belong to the class of solid lubricant coatings due to the presence of carbon in form of graphite. A coating with a thickness of 2 µm was deposited on DIN100Cr6 (AISI52100) chrome alloy bearing steel. The hardness of the a-C:H:W coating is 10.8 GPa.

For evaluation of scuffing resistance, a four-ball tribosystem was employed. The test balls were made of chrome alloy 100Cr6 bearing steel with a diameter of 12.7 mm (0.5 in.). Surface roughness was R_a = 0.032 µm and the hardness was 60 to 65 HRC. In this method, the investigated coating can be deposited on the upper or lower balls. The four-ball tribosystem is presented in Fig. 1.

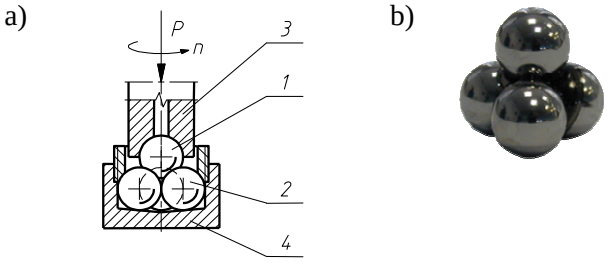


Fig. 1. Model four-ball tribosystem for testing scuffing: a) tribosystem: 1 - top ball, 2 - lower balls, 3- ball chuck, 4 - ball pot, b) photograph.

The three stationary bottom balls (2) having a diameter of 0.5 in. are fixed in the ball pot (4) and pressed against the top ball or cone (1) at the continuously increasing load P. The top ball/cone is fixed in the ball chuck (3) and rotates at the constant speed n. The tribosystem is immersed in the tested lubricant. During the run, the friction torque is observed until seizure occurs. The methods are described in detail in work [5] and patented (Polish Patent No. 179123 - B1 – G01N 33/30).

The test conditions are as follows: rotational speed: 500 rpm; speed of continuous load increase: 409 N/s; initial applied load: 0 N; maximum load: 7200 ± 100 N.

In four-ball tribosystem, the wear area of the upper ball is a track with the area larger than the wear track of all three lower balls. This means that, during the test, the wear in the contact areas of the lower balls is more intensive. This fact is critical for understanding this specific tribosystem behaviour. The tests were conducted for the following four material combinations: steel/steel tribosystem (all balls uncoated), steel/coating tribosystem (one upper ball uncoated/three lower balls WC/C coated), coating/steel tribosystem (one upper ball WC/C coated/ three lower balls uncoated), and coating/coating tribosystem (all balls WC/C coated).

To avoid any tribochemical reaction with the steel substrate, the tribosystems were lubricated with pure polyalphaolefin base oil, without any lubricating additives, denoted as PAO-8 (viscosity 7.8 mm^2/s at 100°C and viscosity index 136).

3. Results and discussions

The friction torque curves of four pairs tested are presented in Fig. 2 (darker colour is used for coated balls). The steel/steel sliding pair has shown the lowest performance level. In all cases, when a coating is applied, an increase in scuffing resistance is observed. The scuffing and seizure loads of steel/coating pair were only slightly higher. The pair that incorporate elements that are both coated has shown significantly better performance; the scuffing load is about 4 times higher than that of steel/steel or steel/coated pairs. The coating/steel pair is the best performer. The difference in tribosystem performance when one upper or lower element is coated shows the importance of the proper selection of element to coat to obtain the highest performance.

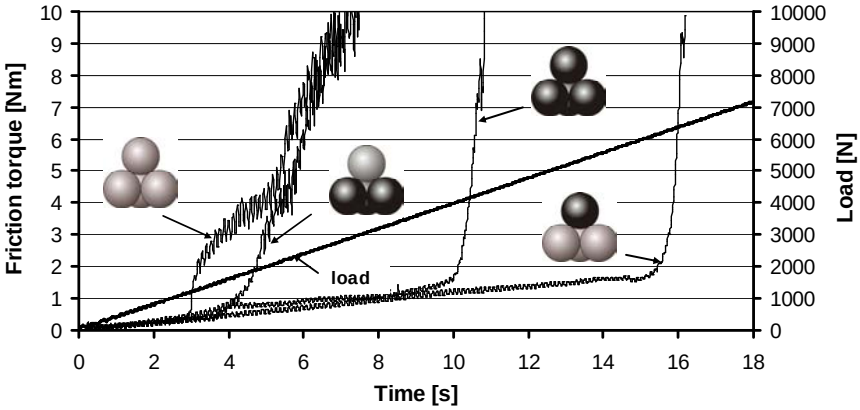


Fig. 2. Friction torque curves for various tribosystems.

The steel/coating tribosystem shows only some improvement in scuffing behaviour compared to steel/steel one. The best performance under heavily loaded lubricated conditions is achieved for the coating/steel tribosystem. The comparison of scuffing propagation for coating/coating and coating/steel tribosystems is presented below.

3.1. Coating/coating tribosystem

The schematic presentation of the main stages of coating/coating tribosystem behaviour during scuffing test is given in Fig. 3.

Initially the surfaces are separated by the lubricant film (Stage 1). Then the wear particles formed during the coating/coating micro-contacts serve as a 3rd-body abrasive and promote damage to both surfaces (Stage 2). During Stage 2, the cracks and scratches are propagated due to 3rd-body migration between balls. The surfaces become very rough. The coating is partially removed from the wear scars and the steel substrate is uncovered. However, the upper coating is only partially destroyed and can provide the transport of lubricant (oil) to the contact zone. However, at certain critical conditions, this

film can be locally removed, mainly due to high local pressures and temperatures, exposing bare metal that can cause local microscopic adhesions. During the increase in load, the steel from the lower balls is transferred to the upper one and covers the valleys. As soon as the valleys, responsible for lubricant transfer stop functioning, the steel transfer accelerates and leads to scuffing (Stage 3).

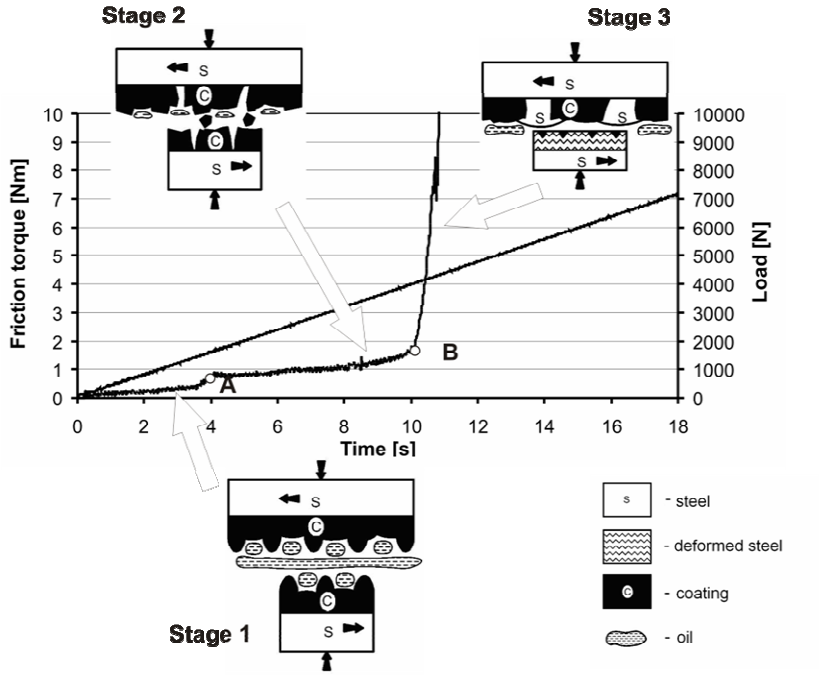


Fig. 3. The scuffing propagation in coating/coating tribosystem.

The coating/coating tribosystem exhibits only limited improvements in scuffing resistance, and the creation of a significant increase in roughness in rubbing surfaces leading to the removal of the coating material is not promising for the extension of the life of heavily loaded friction joints.

3.2. Coating/steel tribosystem

The highest scuffing resistance of the steel tribosystem was obtained when only one element, the one with a lower overlapping ratio, was coated. The schematic presentation of the main stages of coating/steel tribosystem behaviour during scuffing test is given in Fig. 4.

Stage 1 in the friction torque curve and applied load represents conditions at the beginning of the test run (low load) where the surfaces are separated by the lubricant oil corresponds to the hydrodynamic regime of lubrication. The lubricant film prevents large-scale adhesion between the sliding surfaces.

When the load increases, partial wear of the WC/C coating causes a flattening and shearing of the peaks on the coated surface. This occurs by the systematic polishing of the peaks to create a plateau that broadens as wear proceeds, until a continuous flat plateau is created. During the load increase, the contacts are on an asperity-size scale and take place during mixed lubrication regimes and cause the material transfer from coated element onto uncoated element. The lower steel balls can be deformed and can accumulate the coating particles lost by the upper ball during sliding. This enables the system to avoid the detrimental results of 3rd-body formation that were found in the case of the coating/coating pair. The enrichment of the lower steel ball by a ceramic phase lowers the friction between balls.

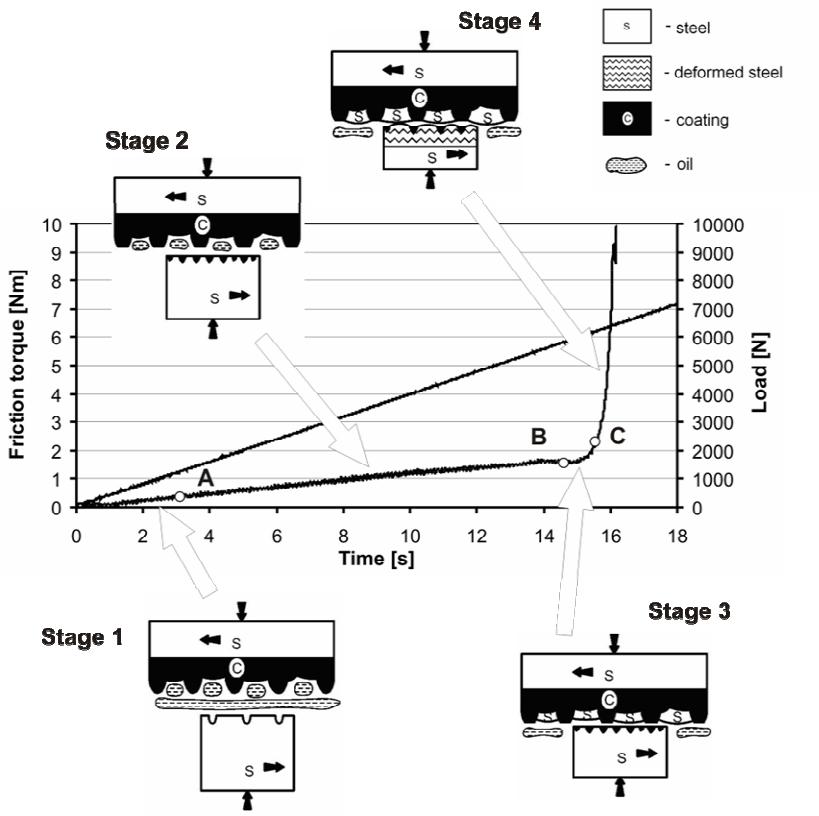


Fig. 4. The scuffing propagation in coating/steel tribosystem.

From Stage 3, the steel from the lower steel surface enriched by coating material is transferred onto coated upper ball. The transfer of steel to the upper coating starts with the filling of the valleys. The coating material is deeply included in the surface of the steel wear scar. A significant amount of graphite on the steel surface during the test of coating/steel tribosystem was detected.

4. Conclusions

The better scuffing resistance is achieved when only one specimen is coated (coating/steel tribosystem) than when all specimens are coated (coating/coating tribosystem). The description of scuffing propagation for all investigated tribosystems was done. The high scuffing resistance of coating/steel tribosystem resulted from the reducing of the adhesion between rubbing surfaces due to low chemical affinity (similarities) between the steel and the coating material and the presence of solid lubricant – graphite in the friction zone.

References

[1] Michalczewski R., Piekoszewski W., Szczerek M., Tuszynski W. *The lubricant-coating interaction in rolling and sliding contacts*, Tribology International, 42, (2009), pp. 554– 560.
[2] Kalin M., Vižintin J., *The tribological performance of DLC-coated gears lubricated with biodegradable oil in various pinion/gear material combinations*, Wear, 259 (2005), pp. 1270-1280.
[3] Podgornik B., Jacobson S., Hogmark S., *DLC coating of boundary lubricated components – advantages of coating one of the contact surfaces rather than both or none*. Tribology International, 2003, 36, pp. 843-849.
[4] Jiang J.C., Meng W.J., Evans A.G., Cooper C.V., *Structure and mechanics of W-DLC coated spur gears*, Surface & Coatings Technology, 176 (2003), pp. 50-56.
[5] Piekoszewski W., Szczerek M., Tuszynski W., The action of lubricants under extreme pressure conditions in a modified four-ball tester, Wear, 249 (2001), pp. 188–193.

Progress in Quantitative Adhesion Testing of Films and Coatings by means of Centrifuge Technology – Present State of the Art

U. Beck[1], S. Hielscher[1], M. Weise[1], R. Mix[1], D. Lerche[2], U. Rietz[2]

[1] BAM Federal Institute for Materials Research and Testing, Division 6.7,
Unter den Eichen 87, 12205 Berlin, Germany
[2] LUM GmbH, Rudower Chaussee 29, 12489 Berlin, Germany

uwe.beck@bam.de, Phone/Fax: +49 30 8104 1821/1827

1. Introduction

Standardised conventional adhesion tests are time-consuming single-sample tests. Moreover, except for the pull-off test, all these tests provide only qualitative or semi-quantitative (ranking, respectively measurement of an adhesion-correlated quantity) information on adhesion. Sometimes, adhesion is evaluated even under compressive stress conditions (e.g. cross-cut and scratch test), which itself is a contradiction to adhesive strength as defined in terms of tensile force per area.
For optical coatings [1] it has been shown that the pull-off test in a centrifuge is definitely a promising alternative with respect to the reliable, fast and quantitative determination of adhesive strength in N/mm^2. The force-controlled centrifuge test is the only multiple-sample test which provides reliable quantitative information on the adhesive strength in agreement with DIN EN 15870 and DIN EN ISO 4624 on a statistical basis for up to eight samples simultaneously tested under identical testing conditions.

2. Experimental

The desktop testing system “Adhesion Analyser LUMiFrac®“ was introduced to the public at ACHEMA 2012 [2] and is shown in Figs. 1 and 2. By means of the software SEPView® any desired load-controlled testing sequence, i.e. load ramp or load modulation, can be realised.



Fig. 1: Desktop adhesion analyser LUMiFrac®



Fig. 2: Drum rotor equipped with eight testing units

The centrifugal force acts as tensile testing force for the pull-off test within the centrifuge. As the plug-in testing unit (Fig. 3), i.e. a test stamp bonded on the sample using a guiding sleeve, is also used prior to testing as adhesive application kit, the presence of shear forces can be avoided at both testing and preparation.

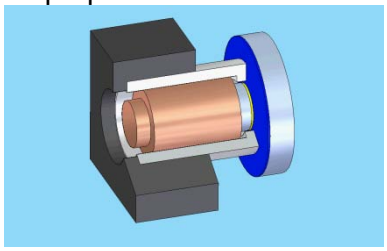


Fig. 3: Testing unit: sample (silver) with coating (blue) supported by the sleeve (grey), adhesive (yellow) connecting sample and test stamp (bright-brown), test stamp guided by the sleeve

By using test stamps made of WCu, the force range is extended to 6.5 kN corresponding to a tensile stress of roughly 80 N/mm^2 at a test stamp diameter of 10 mm. As bonding strength of adhesives is limited to approximately 30 N/mm^2 (cold-curing), respectively 100 N/mm^2 (warm-curing) this is not a severe limitation. In fact, for the lower test stamp diameters of 7 mm and 5 mm (corresponding to tensile stresses of roughly 160 N/mm^2 and 320 N/mm^2) there is no limitation at all.
Besides monolithic test stamps, modular test stamps have been investigated. One part of the test stamps functions as adhesive area usually made of stainless steel, the other part functions as mass body usually made of Cu or WCu. As a result, the cleaning effort for the reuse of test stamps is minimised and the number of material combinations is significantly higher.
Subsequent to testing, visual or microscopic inspection of the failure pattern in accordance with DIN EN ISO 10365 is recommended on both the substrate and the test stamp side. It could be shown that almost all fracture pattern, i.e. coating/substrate-related ones [substrate failure (SF), cohesive substrate failure (CSF), delamination failure (DF), partial delamination failure (pDF)] and adhesive-related ones [cohesive failure (CF), substrate-near cohesive failure (SCF), adhesive failure (AF), adhesive-cohesive failure (ACF), adhesive-cohesive failure with peeling (ACFP)], may be observed.

3. Application examples

3.1 Plasma pre-treatment of polypropylene

The effect of plasma pre-treatment of polypropylene (PP) regarding the bonding strength of adhesives is exemplarily shown in Fig. 4. According to the centrifuge test, adhesion is increased as a result of plasma pre-treatment by a factor of 10. For the pull-off test, a similar conclusion is impossible as the presence of shear forces prevents any measurement of low bonding strength values of the untreated surfaces and may generally result in apparently smaller tensile strength data as demonstrated for plasma-treated samples.

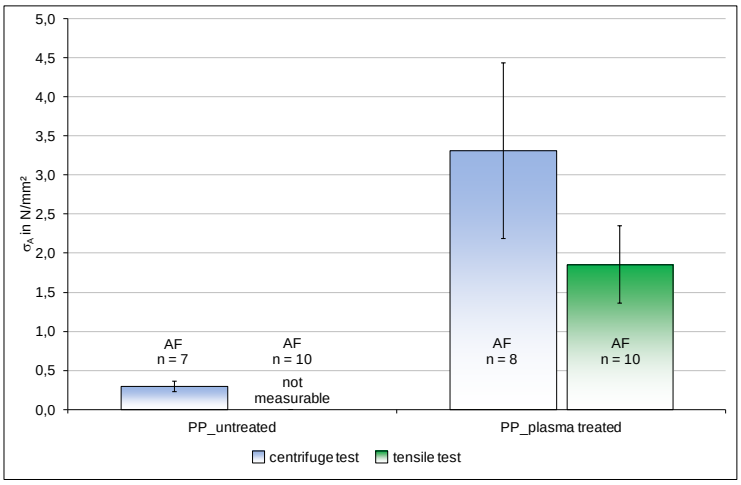


Fig. 4: Effect of pre-treatment of PP on bonding strength (3M DP 460), centrifuge vs. pull-off test

3.2 Plasma-metallised polymers

The adhesive strength of Al- and Cr-layers on polymers was investigated for polyvinylchloride (PVC) and polycarbonate (PC). Complete delamination was observed for 1 µm Cr-layers on PC already at 1.5 N/mm^2 (Fig. 5) whereas for 0.1 µm Cr-layers partial delamination occurs at only 4 N/mm^2. The thinner the Cr-layer, the lower the interfacial stress. For Al-layers, this behaviour is not as pronounced.

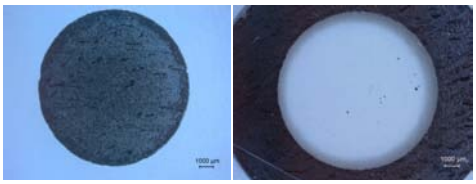


Fig. 5: DF-type failure for 1 µm Cr-layers on PC, substrate side (left) vs. test stamp side (right)

3.3 Rigid glass substrates

For glass substrates of thicknesses of 2 mm (A, B, E, F) and more than 15 mm (C, D), ACF-type failure was observed at very different tensile strength values (Fig. 6), i.e. at 10 N/mm^2 and 30 N/mm^2. This effect has to be considered for substrates without rear side reinforcement, in particular for different substrate materials or different substrate thicknesses. From the experimental point of view, it is demonstrated that adhesion is not only an interface property but also depends on plasto-elastic system features of both substrate and adhesive (Araldite 2011).

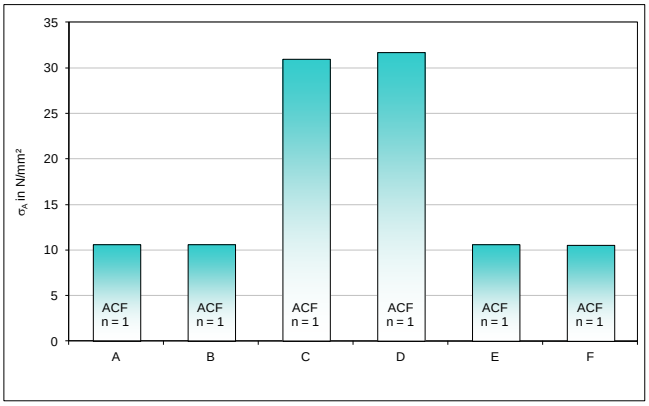


Fig. 6: Substrates without rear side reinforcement: thin (A, B, E, F) vs. thick (C, D) substrates

3.4 Flexible polymer foils

With regard to section 3.3 it is obviuos that the rear side reinforcement, e.g. by means of double-sided adhesive tape, is a prerequisite for correct measurement of flexible substrates. The effect of selective chemical reactions on plasma modified PP foils for improvement of adhesion of Al layers is described elsewhere [3]. A promising strategy is the chemical linking of functional groups by means of trialkoxysilanes. In this case, adhesive strength of Al is already beyond measurable peel strength values, i.e. no peeling of the Al-layer occurs. Within the centrifuge test, the Al-layer could easily be removed at about 2 N/mm^2, however, almost independent of the parameters of plasma treatment and the chemical modification strategy. Finally, it could be shown by XPS that the PP foil itself failed, i.e. the 2 N/mm^2 refers to the intrinsic strength of the PP foil and not to the adhesive strength of the Al-layer on PP.

3.5 Optical coatings

For optical coatings, adhesion tests according to ISO 9211-4 apply, namely the cheese cloth, the rubber, the tape and the cross-hatch (cross-cut) test. For an adhesive strength beyond several N/mm^2 it is almost impossible to discriminate adhesion by means of these tests. Fig. 7 provides one example of a protected silver mirror (CaF_2-Ag/Ta_2O_5) and shows that the centrifuge test is able to determine

adhesive strength as physical quantity to 7.5 N/mm^2 resulting from a rupture force of 600 N at a test stamp diameter of 10 mm.

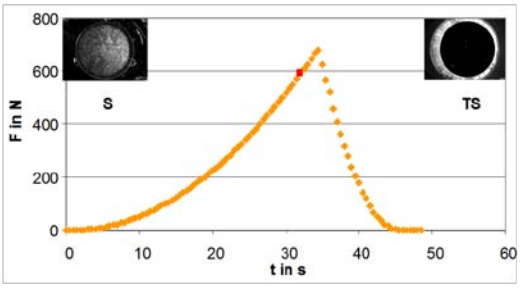


Fig. 7: Complete delamination at the CaF_2-Ag interface within the centrifuge test after 30 s

3.6 Areas of weak adhesion: TiN on 100Cr6 steel

By means of warm-curing adhesives, bonding strength can be increased to more than 100 N/mm^2. It is assumed that the adhesion of TiN and other hard coatings on steel is beyond this value. However, areas of weak adhesion, e.g. due to insufficient substrate cleaning, can be identified even for these layer/substrate systems (Fig. 8), however, adhesive-cohesive failure on the adhesive/layer interface already occurs for four samples.

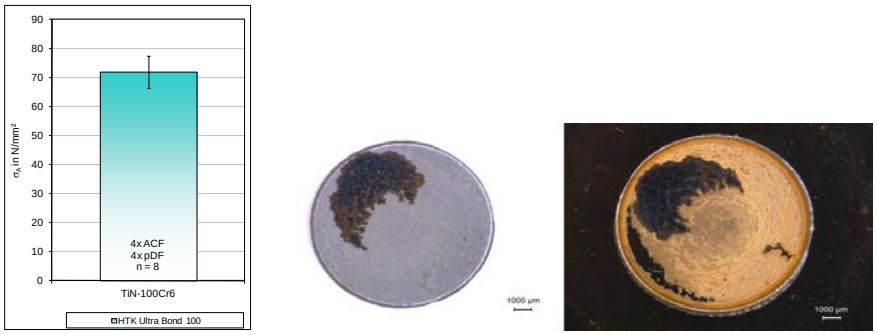


Fig. 8: ACF vs. pDF for TiN on 100Cr6 (left); pDF on test stamp (middle) and layer/substrate (right)

4. Summary and outlook

It has been shown that the pull-off test in a centrifuge has several advantages (fast and easy, no sample clamping, no shear forces, multiple sample test) and exceeds conventional tests despite the fact that in most of the cases a test stamp has to be bonded on the surface. Adhesive strength, bonding strength and composite strength as important quantities under tensile stress conditions can now be determined according to existing standards on a validated statistical basis.
Further research regarding the applicability of the centrifuge test under compressive stress conditions have already begun with regard to plasto-elastic properties, hardness in particular, densification, fatigue and others.
Of course, a new technology needs time for its dissemination, however, after several years of intense research and testing, the implementation of the new technology both to R&D and industrial QA has begun.

References

[1] U. Beck, G. Reiners, M. Weise, H. G. Niederwald, D. Lerche, U. Rietz, Surface & Coatings Technology 205 (2011) S182-S186
[2] Technical specification of Adhesion Analyser LUMiFrac, LUM GmbH
[3] R. Mix et. al., to be published

NANO-IMPACT TESTS ON MICRO-BLASTED COATINGS FOR ASSESSING THEIR BRITTLENESS

K.-D. Bouzakis, S. Gerardis, G. Skordaris, E. Bouzakis

Aristoteles University of Thessaloniki, Thessaloniki, Greece .

Fraunhofer Project Center for Coatings in Manufacturing, Aachen , Germany and Aristoteles University of Thessaloniki, Laboratory for Machine Tools and Manufacturing Engineering, Thessaloniki, Greece

Introduction

Residual compressive stresses can be induced into a PVD film up to a certain depth from the coating surface via micro-blasting [1,2]. Depending on the micro-blasting conditions, the deformed film depth varies, thus affecting the coating's performance in different applications. A method has been already introduced for determining mechanical strength properties gradation in coatings after micro-blasting [1].

Strength properties gradation and brittleness after micro-blasting

Considering these results, the grain penetration depth and moreover, the developed distribution of the improved film yield stress after micro-blasting versus the coating thickness are estimated. The induced coating residual stresses after micro-blasting may however simultaneously increase the film brittleness. For assessing the coatings' brittleness, nano-impact test was employed [3,4]. In this test, an appropriate automation enables repetitive impacts at the same position on the sample surface at a set frequency. The evolution of the indentation depth, due to the progressing film damage during the repetitive impacts, is continuously monitored. Depending on the test conditions, in brittle material cases, the cracks' formation and propagation may lead to a fast film failure.

Nano-impact test FEM simulation and comparison between calculated and experimental results

In the described investigations, nano-impact tests were carried out on variously micro-blasted cemented carbide coated inserts by a sharp cube corner diamond indenter. In a recently developed FEM model

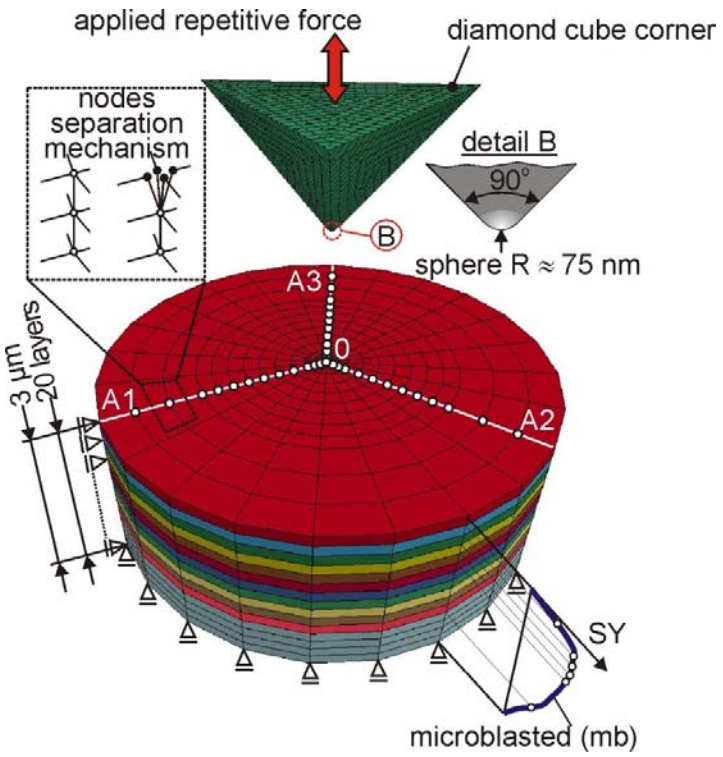


Figure 1: The developed FEM model for simulating nano-impact test on micro-blasted tools.

[4], the strength properties of the film material were uniformly distributed versus the coating thickness. Since by micro-blasting at various pressures, the attained maximum yield stress varies, depending on the depth from the coating, a new 3D-FEM model was created with a piecewise linear plasticity material law (see figure 1) [1]. Hereupon, the coating thickness was described by several material layers, with own elasto-plastic properties, developed after micro-blasting. The employed software was the LS-DYNA package. The simulation of the applied cube corner indenter geometry took place in accordance to the manufacturer specifications. The boundary conditions and the finite elements discretization network are exhibited in figure 1. The material properties and the coating thickness are variable and changeable parameters.

During the indenter penetration into the film, it is assumed that the coating at the FEM model node regions can withstand the applied load up to a maximum value, which corresponds to the coating layer rupture stress and the associated maximum plastic strain limit. Over these limits, the related nodes are disconnected from the neighboring finite elements. When all nodes of an element are disconnected, the element is released for simulating a crack formation and becomes an inactive separate entity. For minimizing the FEM calculations solving time, the nodes' ability to be disconnected is restricted to

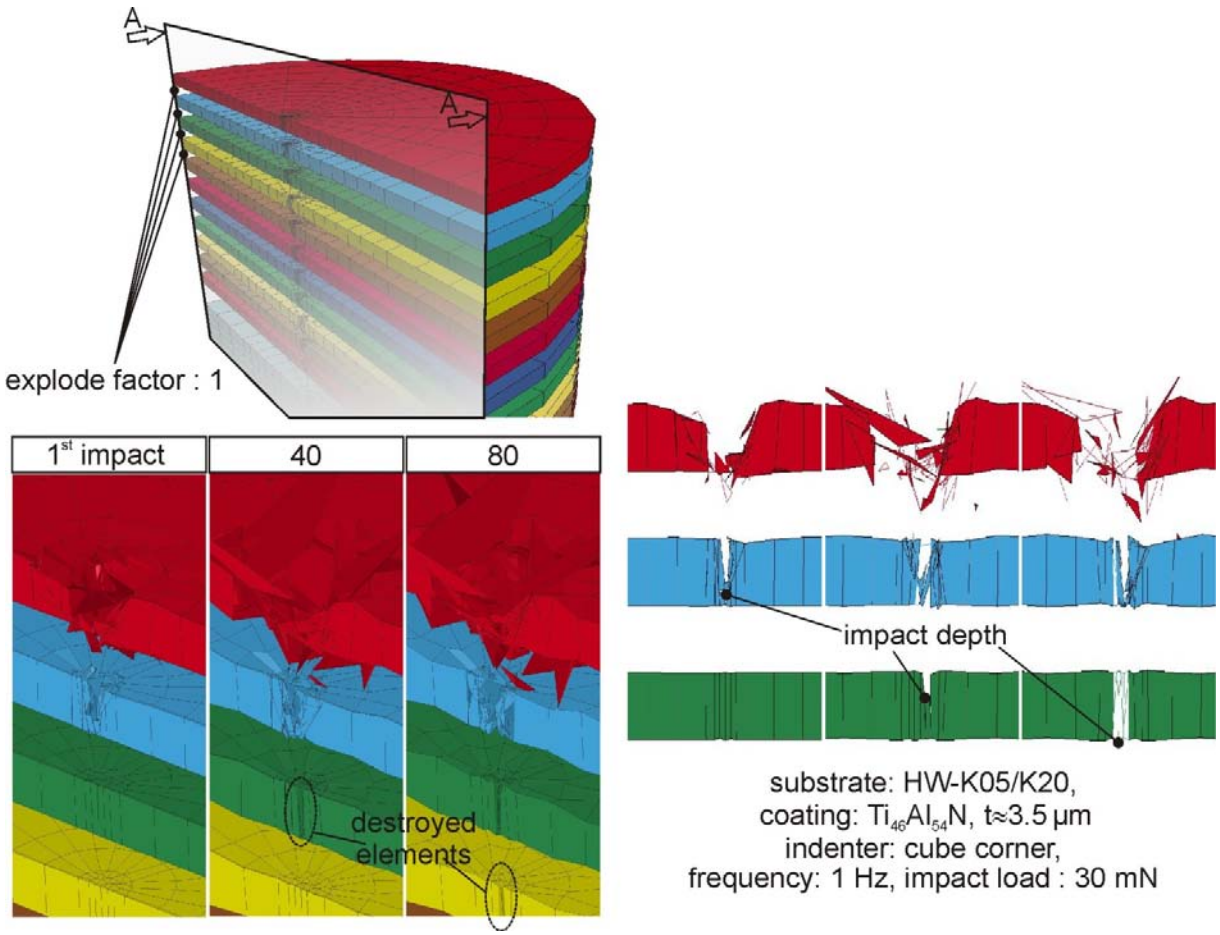


Figure 2: 3D-depiction of the crack propagation during nano-impact test on micro-blasted coatings.

those nodes, which are located on the perpendicular to the coating surface section levels OA1, OA2, OA3. The edges of the cube corner indenter lie on these levels during the indenter penetration into the film material. In this way, the stress fields developed in the coating and its fracture evolution in terms of imprint depth versus the repetitive impacts can be analytically described. A characteristic example, indicating the crack propagation and thus the impact depth versus the number of impacts is shown in figure 2. The crack propagation is implemented successively from one layer to another through the nodes' disconnections, when the developed stresses on these nodes exceed the layers' rupture stresses.

A comparison between measured and FEM calculated imprint depths on as deposited and micro-blasted coatings at impact load of 10 mN and 30 mN during the first 100 impacts is displayed in figure 3. The course of the FEM calculated imprint depths versus the number of impacts converges sufficiently with the measured results at all impact loads. In this way, micro-blasting conditions on films can be analytically optimized, for avoiding an undesired level of film brittleness.

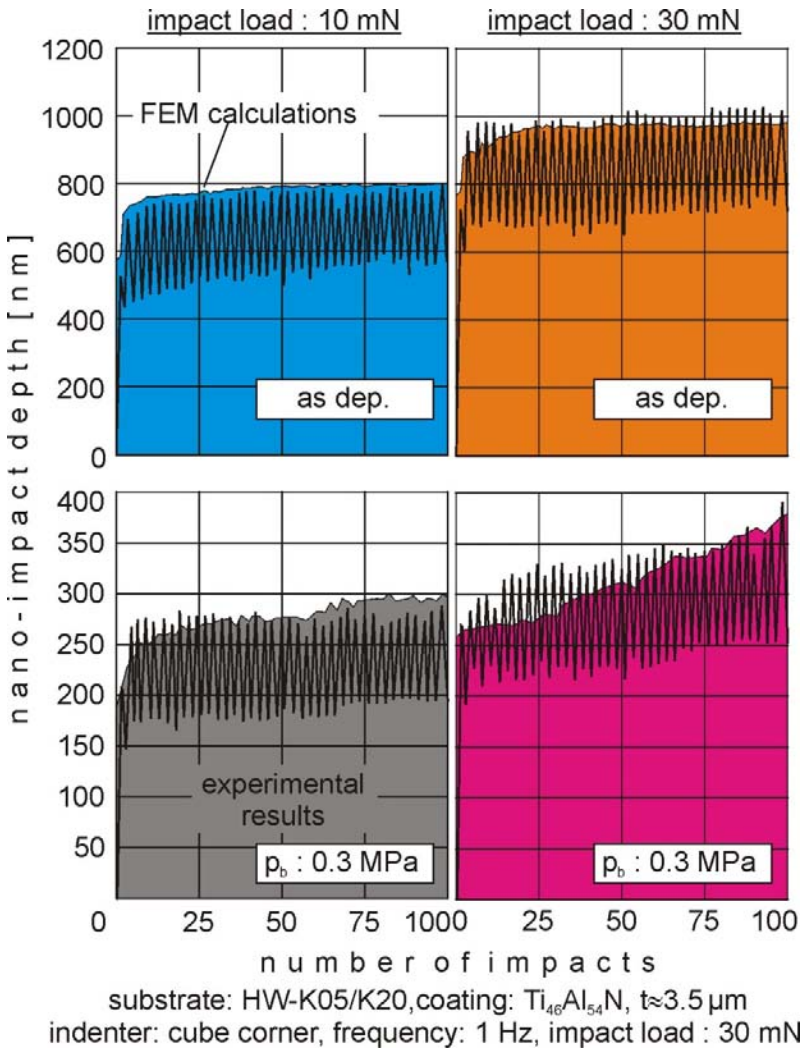


Figure 3: Comparison between experimental and FEM-calculated imprint depths versus the number of impacts

References

[1] Bouzakis, K.-D., Skordaris, Klocke, F., Bouzakis, E., Surface and Coatings Technology, 203, p.p. 2946-2953, 2009.

[2] Barbatti, C., Garcia, J., Pitonak, R., Pinto, H., Kostka, A., Di Prinzio, A., Staia, M.H., Pyzalla, A.R., , Surface and Coatings Technology 203, p.p.3708–3717, 2009.

[3] Beake, B.D., Vishnyakov, V.M., Colligon, J.S., Journal of Physics D: Applied Physics, 44/8, art. no. 085301, 2011.

[4] Bouzakis, K.-D., Gerardis, S., Skordaris, G., Bouzakis, E., Surface and Coatings Technology, 206, p.p. 1936-1940, 2011.

Optical Layer Systems for Product Authentication: Interference, Scattering, Light Diffusion and Ellipsometric Encoding as Public, Hidden and Forensic Security Features

D. Hönig[1], S. Schneider[1], R. Domnick[2], M. Belzner[2],
U. Beck[3], A. Hertwig[3], R. Stephanowitz[3], M. Weise[3]

[1] Accurion GmbH, Stresemannstraße 30, 37079 Göttingen, Germany
[2] Ara-Coatings GmbH & Co. KG, Gundstraße 13, 91056 Erlangen, Germany
[3] BAM Federal Institute for Materials Research and Testing, Division 6.7
Unter den Eichen 87, 12205 Berlin, Germany

uwe.beck@bam.de, Phone/Fax: +49 30 8104 1821/1827

1. Introduction

Embedding of information on surfaces is state of the art for identification testing in which public, hidden and forensic features are used. In many instances, the legal authentication of a product, a material or a document is required. Among the surface-based encoded labels, bar codes and data matrices are most frequently applied. They are publicly visible. The material itself is irrelevant, only a sufficient optical contrast is required.

However, a strong material dependence of the label can be achieved by means of Fabry-Perot layer stacks. Stack designs are described with regard to all three security levels: public features (e.g. color and tilt effect) perceptible by the human eye, hidden features (e.g. optical response in a given spectral range) detectable by commonly available instruments and forensic features (ellipsometric quantities Ψ and Δ as a function of wavelength λ and angle of incidence AOI) only detectable by sophisticated instruments.

Regarding material-correlated authentication, ellipsometric quantities Ψ and Δ are used as encoded forensic features for the first time [1]. Hence, Fabry-Perot layer stacks as information carriers in combination with imaging ellipsometry as optical read-out system provide all-in-one anti-counterfeiting capabilities.

2. Fabry-Perot layer stacks as information carrier

For conventional interference layers, the angle-dependent colour appearance, known as tilt effect, is mainly influenced by the thickness and the refractive index of a dielectric film on a sufficiently high reflecting substrate. Thus, for conventional interference layers, thickness and angular dependence are both unavoidable and desired design features [2-4].

Fabry-Perot layer stacks consist of at least two transparent dielectric layers embedding a semi-transparent metallic thin film in between. The entire layer stack is deposited on a highly reflecting substrate. The coloration effect is now mainly caused by multiple-beam interference within the Fabry-Perot cavity, i.e. within a semi-transparent/transparent/non-transparent metal-insulator-metal (MIM) structure. Fabry-Perot interferences are dominated by the thin semi-transparent metallic film, in particular its thickness and its morphology.

The application of Fabry-Perot stacks and their modifications results in a material-, morphology-, and design-dependence of the label. Instead of contrast in terms of grey scale, all colours (including black and white) can be realised with high brilliance. The dielectric layer on top of the semi-transparent metallic film ensures the long-term

stability of the entire layer stack in particular the protection from environmental effects. As shown in Figs. 1 and 2, the design of Fabry-Perot layer stacks can be modified in a way that the angular colour dependence known from conventional interference layers remains preserved (tilt effect) or vanishes (Aradierung®).



Fig. 1: Colour appearance of a Fabry-Perot stack (SiO_2-Cr-SiO_2 on Al) with tilt effect; dependence on AOI and design features: normal incidence (upper line), AOI = 45° (centre line) and AOI = 60° (lower line); design A (left column), design B (centre column), design C (right column)

The angle-independence of colour is achieved by specific multi-material designs and process modifications affecting the morphology of the semi-transparent metallic film.



Fig. 2: Colour appearance of Fabry-Perot stacks without any tilt effect (Aradierung®)

The light diffusion effect (LDE) as superimposed scattering effect is caused by different grain textures of the metallic interlayer and depends on the angle of incidence and the spectral range of illumination. The result is a colour change upon reflection (Ara-Authentic®) as shown in Fig. 3.



Fig. 3: LDE-effect of Fabry-Perot stacks upon reflection (Ara-Authentic®)

Thus, Fabry-Perot layer stacks and their modifications *per se* provide features of all security levels. Moreover, they are suitable for the generation of pattern such as 1D- and 2D-bar codes. This can be realised either by laser modification of the semi-transparent metallic interlayer or the bottom reflector. In case of complete or almost complete removal of the bottom reflector, effects in transmission can also be achieved.

3. Imaging ellipsometry as optical read-out technique

Regarding light intensity, ellipsometry is a standard-free phase-sensitive far-field tech A. Hertwig[3], R. Stephanowitz[3], M. Weise[3]nique with polarised light upon reflection. An ellipsometric measurement is defined as a measurement at *one* defined AOI and at *one* wavelength λ. Due to the p- and s-polarisation dependence on boundary

conditions, *two* quantities, i.e. the amplitude ratio Ψ and the phase shift Δ, can be derived. In terms of ellipsometric encoding, λ and AOI serve as external key and Ψ and Δ as optical system response of the native (as engineered) or artificial (as designed) surface. Even the interlinking of native and artificial surfaces is feasible [1]. Spectroscopic (from the UV to the NIR spectral range) and angular (typically from 30° to 80°) dependent measurements provide a huge number of external keys.
Using imaging ellipsometry based on null-ellipsometry, Ψ- and Δ-images of the surface are available from the beginning. Hence, the recognition of pattern such as 1D- and 2D-bar codes (Fig. 4) is also feasible. By an imaging microscope ellipsometer (nanofilm-ep4se), spatial resolutions down to 1 µm can be reached and hence bar code-in-bar code solutions become readable on both the macroscopic and the microscopic scale.

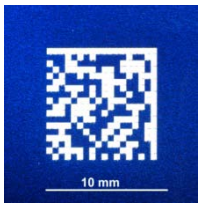


Fig. 4: Data matrix made from a Fabry-Perot stack (available as video-,Ψ- and Δ-image)

The optical system response of the native or artificial surface in Ψ and Δ is theoretically limited to 0°≤ Ψ ≤ 90° and -180° ≤ Δ ≤ +180° whereas the accuracy of measurement in Ψ and Δ is about 0.1°. This fact justifies the high surface sensitivity of ellipsometry, e.g. on native oxides, surface roughness or humidity films. For authentication, this circumstance is rather counterproductive as real surfaces are usually subject to certain variations in surface quality and hence the ellipsometric quantities vary to some extent. A sufficiently high insensitivity to these variations is therefore required. A rounding in steps of 10° for Δ should guarantee the recognition of a Δ-value as encoded. The available set of values would then amount to 360 : 10 = 36 symbols. This equals to the number of all alphanumeric signs and is more than twice as much as the hexadecimal code would require. Information storage based on the value of Δ enables designs that are not visible for the naked eye as the human eye is not sensitive to polarisation.
In contrast to native surfaces where the Ψ- and Δ-values over wavelength and angle of incidence have to be taken as given features of the surface as engineered, artificial surfaces, in particular Fabry-Perot stacks, provide for the feasibility to design layer systems with the full theoretical Δ-range, i.e. 360° either in dependence on a defined wavelength (Fig. 5) or angle of incidence range. This is the reason why Fabry-Perot stacks are the layer systems of choice regarding ellipsometric encoding.

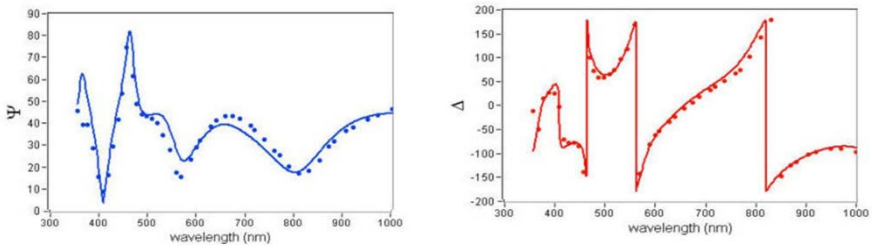


Fig. 5: Forensic features Ψ (amplitude information) and Δ (phase information) as a function of λ at given AOI

The use of λ and AOI as external keys and the application of Δ (and Ψ) as encoding table in combination with specially designed Fabry-Perot stacks might give access to a further security level *encoded forensic*. Cryptographic or steganographic features or information can be additionally implemented, also by using the ellipsometric quantities. Despite these facts, all security levels such as *public*, *hidden*, *forensic,* and *encoded forensic* can be realized at the same time with one individual Fabry-Perot layer stack in terms of PUF-functions.

4. Summary and outlook

Fabry-Perot layer systems may be carrier of public, hidden and forensic information. Physically uncloneable functions (PUFs) are realized by means of parameter-based forward stack designs, complex multi-material approaches in the deposition process and technology-dependent intrinsic preparation characteristics.

Ellipsometry is a phase-sensitive forensic measurement technique in the optical far field which assigns the ellipsometric quantities Ψ and Δ to any native and artificial surface depending on the angle of incidence (AOI) and as a function of wavelength. This can be used for ellipsometric encoding, i.e. the interlinking of information, security labels, and the product itself. The use of encoding tables for the ellipsometric quantities Ψ and Δ allow the embedding of information in dependence on the parameters AOI and wavelength as external keys.

The combination of Fabry-Perot labels as code-carriers and imaging ellipsometry as optical read-out system [5] provides a forensic all-in-one authentication system that may establish the new security level *encoded forensic.*

References

[1] patent priority: DE 2007 063 415.5, licence to Accurion GmbH
[2] J. A. Dobrowolski and D. Lowe, “Optical thin film synthesis program based on the use of Fourier transforms”, Appl. Opt. 17, 3039–3050 (1978)
[3] S. Larouche and L. Martinu; “OpenFilters: open-source software for the design, optimization, and synthesis of optical filters”, Appl. Opt., Vol. 47, No. 13, C219-C230 (2008)
[4] T. Martinuzzo; Anti-Counterfeiting Filters for Currencies, IDs and Goods, http://www.slideshare.net/ThomasUnivalor/anti-counterfeiting-filters
[5] U. Beck, A. Hertwig, R. Stephanowitz, M. Weise, D. Hönig, S. Schneider, R. Domnick, M. Belzner; ViP 08/2012, Vol. 24, No. 4

Wide-angle broadband AR coating by combining interference layers with a plasma-etched gradient layer

Ulrike Schulz*, Peter Munzert, Christiane Präfke, Friedrich Rickelt, Norbert Kaiser

Fraunhofer Institute for Applied Optics and Precision Engineering,
A.-Einstein-Str. 7, 07745 Jena, Germany

*ulrike.schulz@iof.fraunhofer.de

The realization of broadband antireflective (BBAR) properties for optical lenses is a challenging topic of optics. The performance of conventional interference stacks composed of alternating layers of high- and low- refractive-index materials is normally limited to the bandwidth of visible light and a small range of incidence angles [1]. For the requirement of a broader spectral range and an enlarged light incidence angle range up to 60°, limitations for the residual reflectance attainable are evident. A multilayer-based AR coating consisting of silica (n=1.46) and tantala (n=2.1) and optimized for bandwidth 400-800 nm and incidence angles from 0° to 60° will necessarily show a residual reflectance of about 4% at 60° incidence angle more or less independent on the number of layers and the total coating thickness. A design example is shown in Fig. 1.

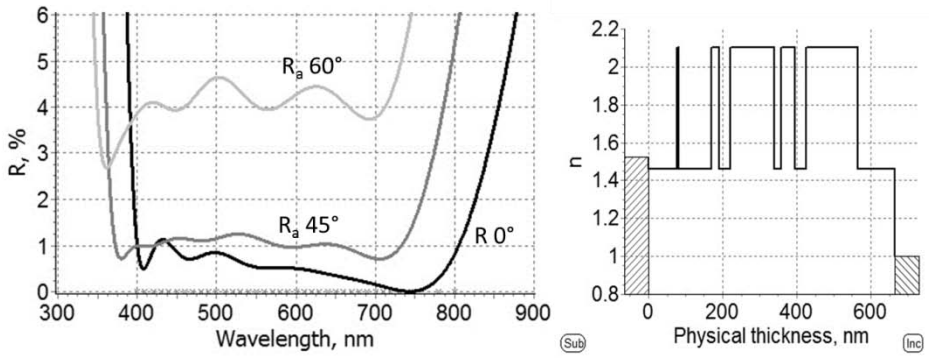


Fig. 1: Refractive index profile and calculated reflectance for a BBAR design on glass (n=1.52), optimized for incidence angles 0° to 60°.

As an alternative to multilayer coatings, a single layer with gradual decreasing effective index from the substrate surface to the ambient medium and with thickness of about 400 nm would act much better for omnidirectional antireflection [2]. However gradient layers with continuously decreasing index and sufficient thickness are hard to realize practically on glass.

An alternative method to get along with a thinner low-index top-layer is its combination with an interference stack, where high index layers are also incorporated into the multilayer. A suitable design solution for a wide range of incidence angles comprises at first a gradient layer with rising effective index starting from the substrate surface (Fig. 2). After a certain maximum a gradual layer with decreasing refractive index follows. For practical reasons the rising gradient was be replaced by discrete layers of available materials like Ta_2O_5 (n=2.1), Al_2O_3 (1.67), SiO_2 (1.46) and MgF_2 (1.38)(see Fig. 3). For this coating a low-index top-layer with a thickness of about 200 nm is needed only. This new design principle was patented by Fraunhofer IOF in 2009 [3]. Initial designs have been evaluated and implemented recently by applying plasma-etched PMMA as a top-layer [4].

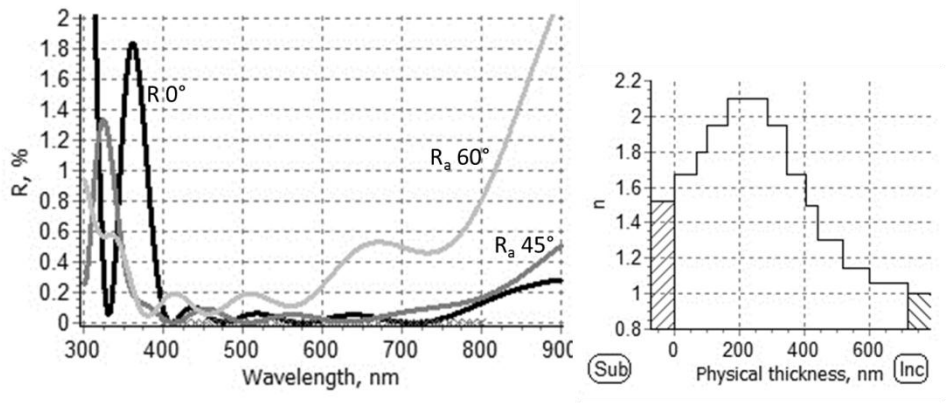


Fig. 2: Refractive index profile and calculated reflectance of BBAR design for incidence angles 0° to 60°. The design consists of a gradient with rising effective index starting from the substrate surface. After a certain maximum a graded layer with decreasing refractive index follows.

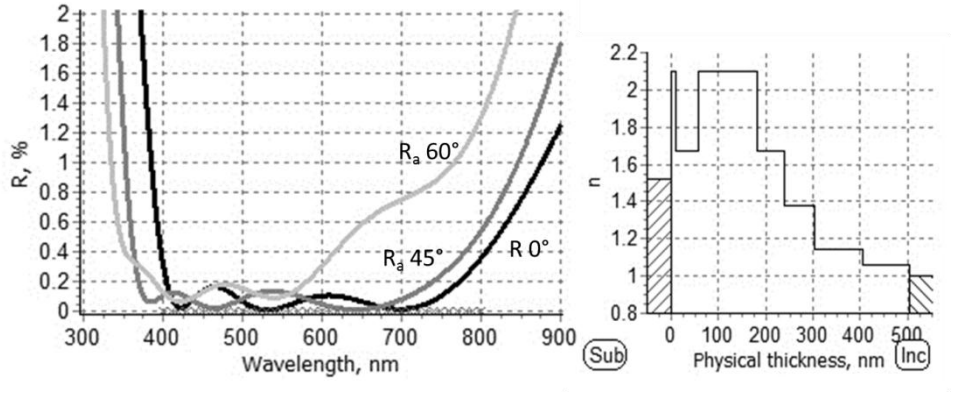


Fig. 3: Refractive index profile and reflectance of BBAR design of Fig. 2 after replacement of parts of the gradients by discrete layers of available compact materials (Al_2O_3, SiO_2, MgF_2).

Gradient layers exhibiting a low effective refractive index can be produced by plasma-etching of organic layers. The organic small-molecule materials were evaporated thermally and etched in low-pressure plasma using an Advanced Plasma Source [5]. For example, Fig. 4 shows SEM images of nanostructured layers achieved from 1,3,5-Triazine-2,4,6-triamine (melamine), N,N´-di(naphth-1-yl)-N,N´-diphenyl-benzidine (NPB) and Tris(4-carbazoyl-9-ylphenyl)amine (TCTA) thin films.

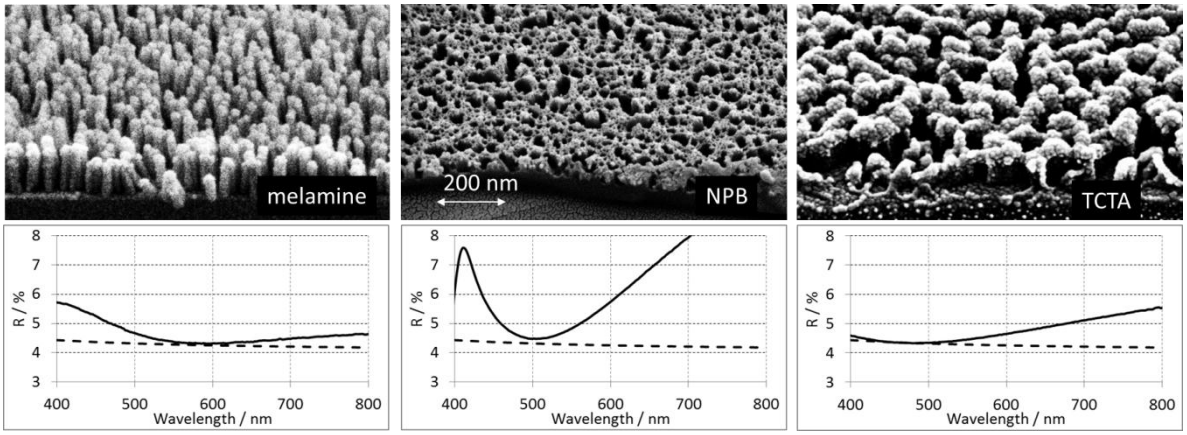


Fig. 4 SEM images and reflectance spectra of plasma-etched organic layers on glass BK7 (including backside reflectance, dotted line)

Produced as single layers on glass, all these layers exhibit an effective refractive index in the range 1.35 to 1.25. An improved antireflective performance can be expected by combining these layers with interference stacks. However, design calculations and experiments show that the optical properties of the top-layer have to be described with high accuracy because of the high error sensitivity of all the subsequent multilayers.

New broadband antireflection coatings based on this principle will be developed during the next years within in the scope of the recently started BMBF-project “FIONA” which is coordinated by the Carl Zeiss Jena GmbH [6]. Further project partners are the companies Agfa-Gevaert HealthCare GmbH, asphericon GmbH, Leica Microsystems CMS GmbH, Qioptiq Photonics GmbH & Co. KG, Leica Camera GmbH and the Fraunhofer IOF.

Acknowledgement
This research was supported by the Bundesministerium für Bildung und Forschung (BMBF, FKZ 13N12160 and FKZ 03X3028E).

References

[1] A. Dobrowolski, D. Poitras, P. Ma, H. Vakil, M. Acree,Appl. Opt. 41(2002) 3075.
[2] M. Minot, J. Opt. Soc. Am. 67 (1977)1046.
[3] U. Schulz, P. Munzert, N. Kaiser, “Reflection-reducing interference layer system and method for producing it”, WO09127581 A1, DE102008018866, US8192639B2, filed 28.09.2010.
[4] U. Schulz, C. Präfke, C. Gödeker, N. Kaiser, A. Tünnermann, Appl. Opt. 50 (2011) C31.
[5] U. Schulz, C. Präfke, P. Munzert, C. Gödeker, N. Kaiser, Optical Materials Express 1(2011) 101.
[6] www.photonikforschung.de/fileadmin/Verbundsteckbriefe/8._Plasma/Projektsteckbrief_Plasma-Fiona.pdf

Sensitization of Er^{3+} Emission in Er- and Yb-doped Si Thin Films by Laser Ablation

Shinji Kawai*
Industrial Technology Center of SAGA, Tosu, Saga 841-0052, Japan
* Corresponding author; kawai@saga-itc.go.jp
Shuji Komuro and Toru Katsumata
Sensor Photonics Research Center, Toyo University, Kawagoe, Saitama 350-8585, Japan

Keywords: rare-earth doping; ytterbium; sensitization; laser ablation

Abstract

Erbium (Er)- and ytterbium (Yb)-doped Si (Si:Er,Yb) thin films have been controllably synthesized over the Er and Yb concentrations ranging from 10^{18} to 10^{20} cm^{-3} by laser ablation technique. From the PL spectra and the concentration dependence of the intensity of Er3+ emission at 1.54 μm, Yb^{3+} acts as an efficient sensitizer of the Er^{3+}-related PL. Enhancement by a factor of 1.5 due to Yb codoping is observed from the Si:Er,Yb films.

1. Introduction

Rare-earth (RE) doping of Si and Si-related materials [1-5] has attracted much attention for the development of Si-based optoelectronic devices initiated by the report on the photoluminescence (PL) centered at around 1.54 μm of Er^{3+} ($^4I_{13/2} \rightarrow {}^4I_{15/2}$) in Si [1]. Ytterbium (Yb) is known as a sensitizer for Er^{3+} emission at 1.54 μm in Er-doped materials [2]. Since the energy level of the Yb^{3+}-$^2F_{5/2}$ state is close to that of the Er^{3+}-$^4I_{11/2}$ state, optical transitions between them are expected to raise the excitation efficiency of the Er^{3+}. Therefore, much attention has been given to Er, Yb-codoped Si and Si-related materials for Si-based optoelectronic device application. Kozanecki et al. presented that the codoping of Yb leads to the enhancement of Er^{3+}-related PL at 1.54 μm in the Er-doped SiO_2 films [2]. However, there are few studies on Er and Yb codoping of Si matrix.

In this study, we investigate the synthesis of Er- and Yb-doped Si (Si:Er,Yb) thin films by laser ablation. Laser ablation technique is simple and useful for doping the RE elements into the host materials [3]. The relationship between the Er^{3+}-related PL and the Yb doping level is discussed.

2. Experimental

The ceramic target prepared by a hot press technique from a mixture of Si, prescribed amount

1 wt % Er_2O_3, and Yb_2O_3 was used in our experiments. The Er atomic density included in the target is calculated to be 5.5×10^{19} cm^{-3}. Komuro et al. have showed that the Er atomic densities in the Er-doped Si (Si:Er) films linearly depend on those in the targets by x-ray fluorescence spectroscopy (XFS) and secondary ion mass spectroscopy (SIMS) [4, 5]. A schematic of our laser ablation chamber is shown in Fig. 1. A Q-switched YAG (QW-YAG) laser with fourth harmonics (wavelength of 266 nm; pulse duration of 5 ns; energy density per pulse of approximately 1 J/cm^2) was used to ablate the target. The background pressure of the vacuum chamber before ablation was lower than 1×10^{-7} Torr. The bulk target and Si(100) substrate were separated by the distance of approximately 40 mm in the chamber. Six targets samples with different amounts of Yb_2O_3 (0.03, 0.1, 0.3, 1, 3, and 10 wt %) were used to synthesize the Si:Er,Nd films with various Yb concentrations (1.1×10^{18}, 4.0×10^{18}, 1.1×10^{19}, 4.0×10^{19}, 1.1×10^{20}, and 4.0×10^{20} cm^{-3}). The Si:Er,Yb films with approximately 200 nm thick were synthesized on Si(100) substrates at room temperature (RT). After deposition, the Si:Er,Yb films were annealed at 800 ^{0}C for 5 min in an N_2 atmosphere to activate RE incorporation in the films. PL measurements were performed by using Ar^+ laser irradiation at 488 nm. The visible and near infrared (IR) emissions were detected by a photomultiplier tube and a liquid-N_2 cooled Ge p-i-n photodiode, respectively.

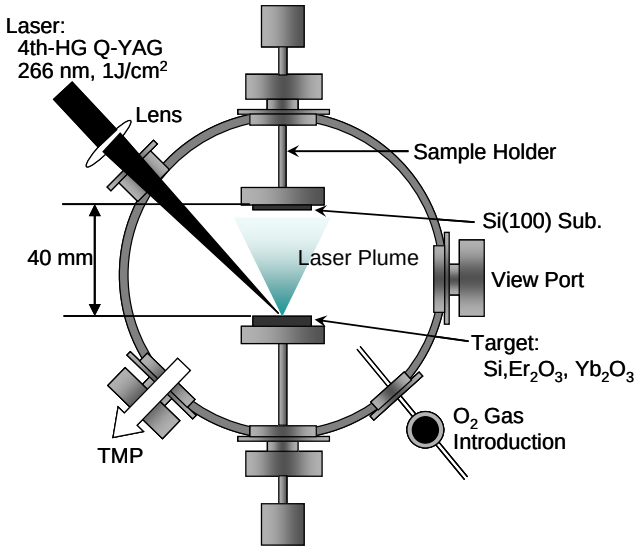


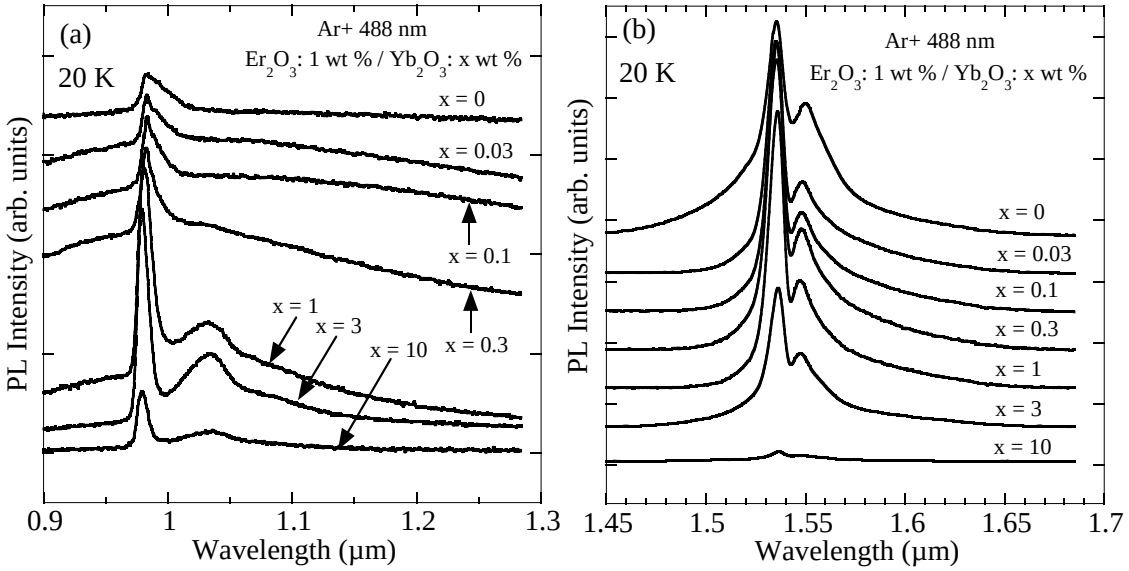
Figure 1 A schematic of our laser ablation chamber.

3. Results and discussion

In order to characterize the structure of the films, x-ray diffraction (XRD) measurements were performed. No appreciable diffraction peaks (not shown) were observed from the samples. This

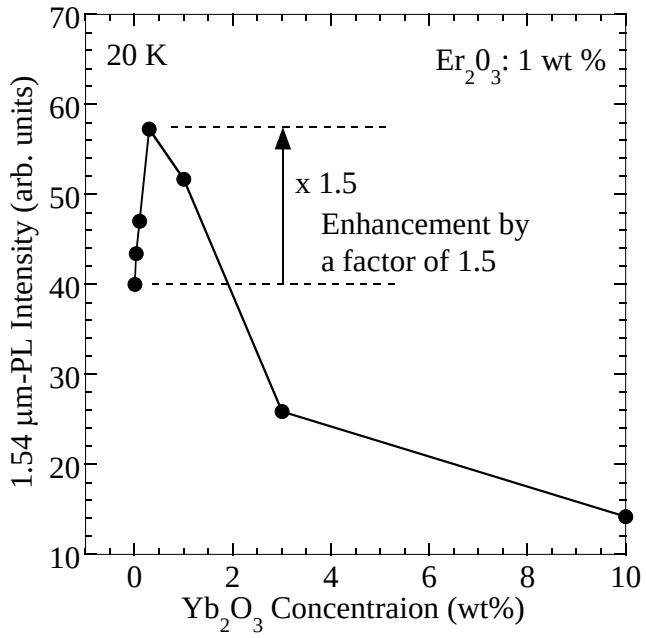
indicates that the Si:Er,Yb films consist of amorphous phase. Previously, we showed that SiOx phase is formed in the Si:Nd films synthesized by laser ablation because the broad PL peaks due to SiOx is observed at around 658 nm [5], which is consistent with the result of the present XRD measurements.

Figures 2 (a) and (b) show the PL spectra from the annealed Si:Er,Yb films at 20 K in the two near IR regions. As shown in Fig. 2 (a), the PL peak at 0.983 μm is attributed to the $^4I_{11/2} \rightarrow {}^4I_{15/2}$ transition in Er^{3+}, which is observed from the samples with 1 wt % Er_2O_3 and 0.03 – 1 wt % Yb_2O_3. In the samples with 3 and 10 wt % Yb_2O_3, the PL peak at 0.979 μm due to the $^2F_{5/2} \rightarrow {}^2F_{7/2}$ transition in Yb^{3+} is observed while the peak at 0.983 μm disappears. From Fig. 2 (b), intense and sharp PL originating from intra-4f transitions in Er^{3+} is observed from the 1 wt % Er_2O_3 and 0.3 wt % Yb_2O_3 samples.



Figures 2 (a) and (b) PL spectra at 20 K from the films with different Yb concentrations.

Figure 3 shows the Yb concentration dependence of the intensity of the 1.54 μm-PL due to the $^4I_{13/2} \rightarrow {}^4I_{15/2}$ transition in Er^{3+} at 20 K. The PL intensity increases the Yb concentration in the range from 0.03 to 0.3 wt % Yb_2O_3 while it decreases with that in the range from 1 to 10 wt % Yb_2O_3. Noted that the 1.54 μm-PL intensity for the Si:Er,Yb films with 1 wt % Er_2O_3 and 0.3 wt % Yb_2O_3 is enhanced by a factor of 1.5 higher than that for the Si:Er films with 1 wt % Er_2O_3. Therefore, it is found that for the excitation wavelength at 488 nm Yb^{3+} act as the efficient sensitizers of the Er^{3+} emission at 1.54 μm due to the $^4I_{13/2} \rightarrow {}^4I_{15/2}$ transition.



Figures 3 Yb concentration dependence of the Er3+ emission intensity at 1.54 μm.

4. Conclusions

We showed a simple and useful technique to synthesize Si:Er thin films codoped with Yb. The control of Yb codoping level ranging from 10^{18} to 10^{20} cm^{-3} in films was achieved. The sensitization of the intra-4f-shell emission of Er^{3+} due to Yb codoping was observed in the Si:Er,Yb films. Our results suggest a possibility of fabricating Si-based optoelectronic devices such as light-emitting diodes and lasers by using the Si:Er,Yb films.

Acknowledgements

One of the authors (S.K) would like to thank Prof. T. Motooka of Kyushu University for his useful discussions.

Reference

[1] H. Ennen et al., Appl. Phys. Lett. **43**, 943 (1983).

[2] A. Kozaneki at al., Appl. Phys. Lett. **73**, 2929 (1998).

[3] S. Komuro et al., Appl. Phys. Lett. **69**, 3896 (1996).

[4] S. Komuro et al., Appl. Phys. Lett. **74**, 377 (1999).

[5] S. Kawai et al., Phys. Status Solidi C **7**, 579 (2010).

Synthesis and characterization of $La_2NiO_{4-\delta}$ coatings deposited by reactive magnetron sputtering using plasma emission monitoring

Fondard Jérémie[1,2], Briois Pascal[1,2], Billard Alain[1,2], Bertrand Ghislaine[1,2]
[1]*IRTES-LERMPS, EA 7274, 90010 Belfort*
[2]*FR FCLab 3539, 90000 Belfort*
jeremie.fondard@utbm.fr

Introduction :

It is well known that the short life time and the high cost of each component of nowadays Solid Oxide Fuel Cells (SOFC) are induced by their high operating temperature. Many researches focus on the decrease of this operating temperature without reduction of the fuel cell performances (IT-SOFC). Regarding the cathode, one solution is to increase the electrocatalytic properties. Purely electronic conductor perovskite materials (for example LSM : $La_{1-x}Sr_xMnO_3$) are used in standard SOFC devices. $A_2MO_{4+\delta}$ compounds, with K_2NiF_4 structure have recently been investigated as substitutes to LSM. Indeed, these materials are mixed ionic and electronic conductors (MIECs) that moreover exhibit rather high electrocatalytic properties. It is then possible to synthesize them as dense materials for SOFC cathodes. Among these materials, lanthanum nickelates $La_2NiO_{4+\delta}$ exhibits convenient electrochemical characteristics [1- 4]. Its thermal expansion coefficient (TEC) is very close to that of the most commonly used electrolyte materials (13 10^{-6} K^{-1}, 11.9 10^{-6} K^{-1} and 11.6 10^{-6} K^{-1} for $La_2NiO_{4+\delta}$, CeO_2-Gd_2O_3 (CGO) and ZrO_2-Y_2O_3 (YSZ) respectively). Its oxygen ionic conductivity and surface exchange coefficient are interesting and seem much better than those of $La_{1-x}Sr_xMnO_3$ (LSM) and $La_{1-x}Sr_xCo_{1-y}Fe_yO_3$ (LSCF), the most commonly used cathodes [2, 5-6].
The deposition of La_2NiO_4 coatings by reactive magnetron sputtering has already successfully been performed under so called stable conditions in a laboratory vessel [7]. In this study, we investigate the feasibility of $La_2NiO_{4+\delta}$ coatings deposited by reactive magnetron sputtering under unstable conditions using Plasma Emission Monitoring (PEM) [8, 9].
The chemical composition of the coatings was measured by Scanning Electron Microscopy coupled with Energy Dispersive Spectroscopy. The influence of the La/Ni ratio on the structure was checked by X-Ray Diffraction analyses.

Experimental details

- Sputtering device:

The experimental device is a 100-litre Alcatel SCM 650 sputtering chamber pumped down via a system combining XDS35i Dry Pump and a 5401CP turbo-molecular pump. The sputtering chamber is equipped with three 200 mm diameter magnetron targets and with a 620 mm diameter rotating substrate holder parallel to the targets at a distance of about 110 mm. The distance between the targets axis and that of the substrate holder is 170 mm. The La and Ni targets are supplied thanks to a pulsed DC Advanced Energy dual generator allowing the control of the discharge current, power or voltage. The discharge current is fixed at 2.5 A on the La target and modified on the Ni target from 0.25 to 0.45 A to obtain the convenient composition of K_2NiF_4 structure. The substrates are alumina and YSZ pellets as well as glass slides positioned next to the target at 170 mm from the axis of the substrate holder. Argon and oxygen flow rates are controlled with Brooks flowmeters and the pressure is measured using a MKS Baratron gauge.

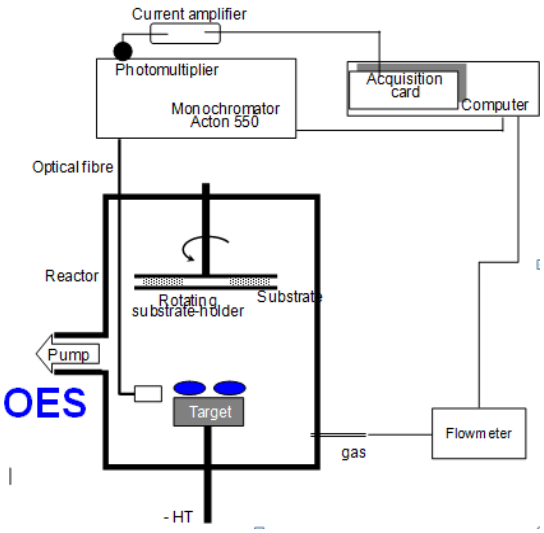


Figure 1 : Scheme of the principle of PEM

The deposition stage is monitored using a closed loop control PEM (Plasma Emission Monitoring) system (Figure 1) using optical emission spectroscopy (OES) [10]. The technique is based on the measurement of the optical intensity of the 395 nm La emission line (I^*_{La}) measured in a volume near the target. The signal is sent via an optical fiber to a Ropper Scientific SpectraPro 500i spectrometer, with a 1200 groove mm^{-2} grating and a photomultiplier tube (Hamamatsu R 636). Then, the information is transferred to a computer where a program developed under Labview® monitors the oxygen flow rate to maintain the selected intensity of the optical signal I^*_{La}.

- Stuctural Characterisation

The morphology of the coatings is characterized by Scanning Electron Microscopy (SEM) using a JEOL JSM 5800 LV equipped with Energy Dispersive Spectroscopy (EDS) for chemical measurements. The structural features of the coatings were performed in Bragg Brentano configuration X-ray diffraction using a BRUKER D8 focus diffractometer ($CoK_{\alpha 1+\alpha 2}$ radiations) equipped with the LynxEye linear detector. XRD patterns were collected at room temperature during 10 min in the [20°-80°] scattering angle range by steps of 0.019°. Coating thickness was also determined using the step method with an Altysurf profilometer from Altimet allowing an accuracy of about 20 nm. Before each measurement, the calibration of the experimental device was realised with a reference sample number 787569 accredited by CETIM organisation.

Results and discussion

- **Optimization of the regulation setpoint**

In DC mode, the optical signal of sputtered metal atoms in a pure Ar atmosphere is proportional to the square of the discharge current [11]. By fixing the discharge current of a metallic target, its physicochemical state is usually a monotonic and quite proportional function of the optical signal I^*_M measured by OES [12]. In so called unstable sputtering conditions, i.e. when the oxygen partial pressure-oxygen flow rate curve presents a hysteresis, PEM is a very suitable technique to allow high rate growth of oxide coatings [8].

In this study, the PEM setpoint of I^*_{La} was varied from 40 to 70% of the signal obtained while depositing in pure argon atmosphere. All those deposition conditions take place in the unstable sputtering domain, i.e. where a setpoint cannot be maintained without using a closed loop control system. In previous work, we have shown that increasing the setpoint decreases the coating transparency, and then the oxidation rate of the coating. Indeed, the higher is the setpoint, the higher is the sputtered flow of metal atoms and the lower is the oxygen partial pressure in the reactor. Note that coatings deposited with a setpoint of 5V, i.e. I*La of 50% allows obtaining a transparent La_2O_3 coating with the highest deposition rate.

- **Chemical and structural analyses**

The experimental parameters for the synthesis of the films are summarized in **Table 1**

Deposition parameters	values
Total pressure (Pa)	**0.3**
Ar flow rate (sccm)	**30**
Regulation voltage (V)	**5**
oxygen flow rate (sccm)	**5.5 – 6.2**
Run duration (h)	**1h30 – 2h**
Discharge current for La(A) **Frequency (Hz) – toff (µs)**	**2.5** **50 - 5**
Discharge current for Ni (A) **Frequency (Hz) – toff (µs)**	**0.25 – 0.45** **50 - 5**

Table 1: Main deposition conditions of the study

Figure 2 presents the evolution of the La/Ni atomic composition ratio measured by EDS as a function of current dissipated on the Ni target. When the current dissipated on the Ni target is 0.3 A, the metallic ratio is about 1.94. This value is close to the expected value of 2 for the La_2NiO_4 compound.

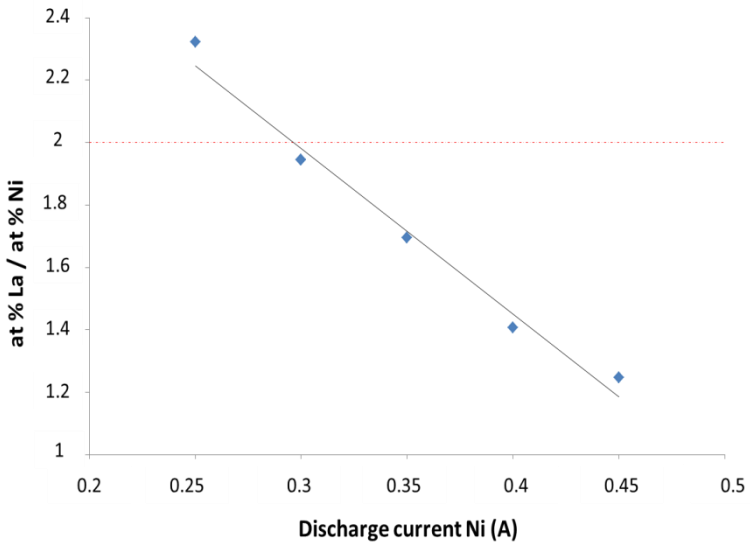


Figure 2: Evolution of atomic composition ratio La/Ni measured by EDS as a function of current dissipated on the Ni target

XRD performed on as-deposited samples shows the presence of an amorphous structure whatever the composition. In a previous study [7], we have shown that the La_2NiO_4 phase crystallization begins from 973 K and increases with the annealing temperature. At 1073 K, it was identified that most of the coating crystallized in the La_2NiO_4 structure. Hence, it was decided to perform annealing treatments for 2 h at 1173 K in order to crystallize La_2NiO_4 structure.

Figure 3 presents the evolution of the sample structure as a function of the La/Ni atomic ratio after annealing at 1173 K. When the Ni content is higher (i.e La/Ni < 2), the coating crystallizes under $LaNiO_3$ perovskite structure. The La_2NiO_4 structure appears for a La/Ni ratio around 1.7 and this structure is well defined when the ratio is close to 2. A mixture of La_2O_3 and La_2NiO_4 phases is identified when the La/Ni ratio is over 2.

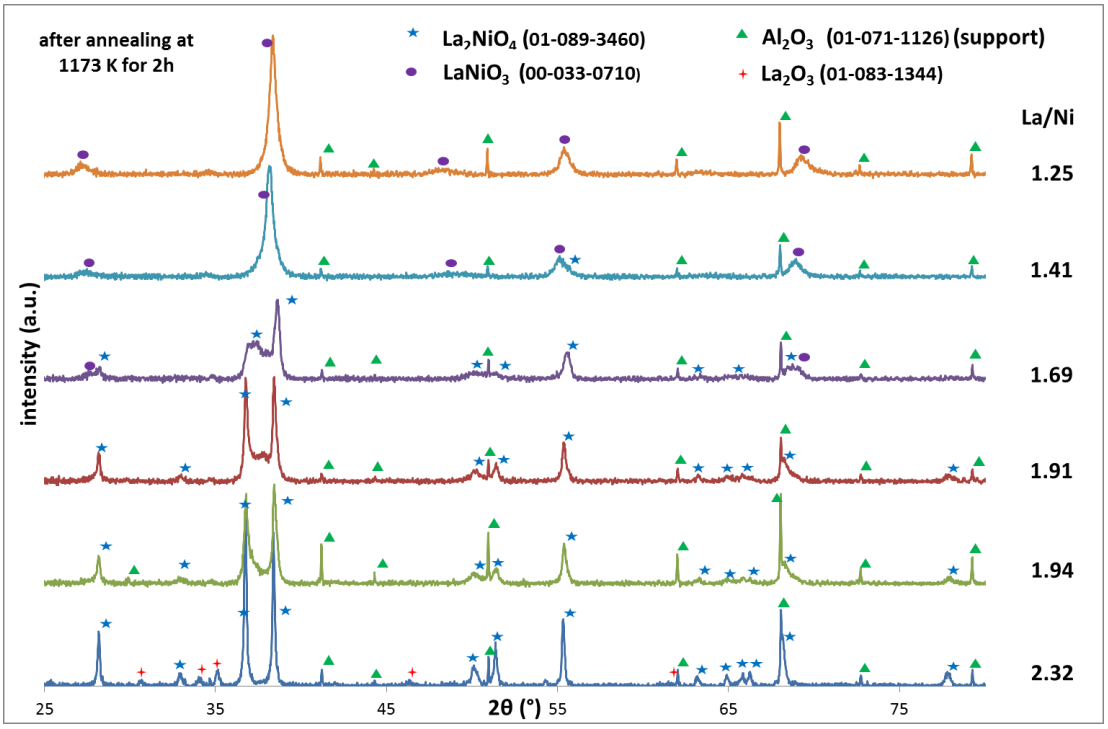


Figure 3: XRD pattern after annealing at 1173K for 2h under air as function of La/Ni atomic content ratio

Conclusion :

La-Ni-O coatings were deposited on different substrates by co-sputtering from Ni and La metallic targets in a presence of a reactive argon-oxygen mixture using plasma emission monitoring process. This technique allows the control of oxygen flow rate under unstable conditions and permits the deposition of stoichiometric coatings with high sputtering rate. The as-deposited coatings are amorphous and need an annealing treatment to crystallize on the targeted structure. At 1173 K, the different phase crystallization is completed. For 0.3 A, La_2NiO_4 phase is crystallized without phase pollution.

References :

[1]: V.V. Vashook , I.I. Yushkevich, L.V. Kokhanovsky, L.V. Makhnach, S.P. Tolochko, I.F. Kononyuk , H. Ullmann , H. Altenburg, *Solid State Ionics 119 (1999) 23–30*
[2]: E. Boehm, J.-M. Bassat, P.Dordor, F. Mauvy, J.-C. Grenier, *Ph. Stevens, Solid State Ionics 176 (2005) 2717 – 2725*
[3]: V.V. Kharton , E.V. Tsipis , E.N. Naumovich , A. Thursfield, M.V. Patrakee, V.A. Kolotygin, J.C. Waerenborgh, I.S. Metcalfe, *Journal of Solid State Chemistry 181 (2008) 1425– 1433*
[4]: A.L. Shaula, E.N. Naumovich, A.P. Viskup, V.V. Pankov, A.V. Kovalevsky, V.V. Kharton, *Solid State Ionics 180 (2009) 812–816*
[5]: R. Sayers, R.A. De Souza, J.A. Kilner, S.J. Skinner, *Solid State Ionics 181 (2010) 386–391*
[6]: H. Zhao, F. Mauvy, C. Lalanne, J.-M. Bassat, S. Fourcade, J.-C. Grenier, *Solid State Ionics 179 (2008) 2000–2005*
[7]: P. Briois, F. Perry, A. Billard, *Thin Solid Films 516 (2008) 3282–3286*
[8]: A. Billard, C. Frantz, *Surface Coatings Technology 59 (1993) 41*
[9]: S. Schiller, G. Beister, W. Sieber, *Thin Solid Films 111 (1984), p. 259-268*
[10] F. Perry, A. Billard, C. Frantz, *Surf. Coat. Technol., 94-95 (1997), 681*
[11] F. Sanchette, T. Czerwiec, A. Billard, C. Frantz, *Surf. Coat. Technol , 96 2-3 (1997), 184*
[12] A. Billard, F. Perry, C. Frantz, *Surf. Coat. Technol., 94-95 (1997), 345*

Silicon carbide surface micromachining using plasma ion etching of sacrificial layer

Norbert Kwietniewski[1], Andy Zhang[2], Jang-Kwon Lim[2], Mietek Bakowski[2], Mariusz Sochacki[1], Jan Szmidt[1]

[1] Institute of Microelectronics and Optoelectronics, Warsaw University of Technology, Koszykowa 75, 00-662 Warsaw, Poland

[2] Acreo AB, Electrum 236, SE-164 40 Kista, Sweden

Corresponding author: N.Kwietniewski@stud.elka.pw.edu.pl

Keywords: silicon carbide, plasma ion etching, etch rate, shape transfer

The perfectly-defined micrometric shapes patterned by optical lithography and selective etching seems to be a crucial step in fabrication of high voltage and MEMS devices. Wet chemical etching, reactive ion etching and chemical-mechanical processing are widely used in the semiconductor industry to achieve the required shape of the surface. The processes are well understood and successfully applied for resists or silicon oxide layer patterning [1].

High hardness and chemical stability of silicon carbide (SiC) make the etching process more difficult in comparison with other substrates processing. The shape of the etched junction termination extension (JTE) region for SiC devices often determines the breakdown voltage and reliability parameters simultaneously. Furthermore, in terms of total cost of the process simpler method of the pattering the shape of refractory materials is required. Additionally, the processing of commonly used materials such as photoresist film or deposited oxide layer by optical lithography ensures high resolution and repeatability.

In this paper we contribute to the processing methods by using a new approach define the required surface shapes. We have demonstrated the transfer of geometric shapes on top sacrificial layer to bulk SiC material using Reactive Ion Etching (RIE) and Inductively Coupled Plasma (ICP) process. The work introduces the optimization hints to assure the etch selectivity ratio 1:1 for various materials. It appears that the optimized processes lead to satisfactory selectivity ratio and make possible the transfer of sacrificial layer surface to bulk material. The idea of the process is schematically illustrated in figure 1.

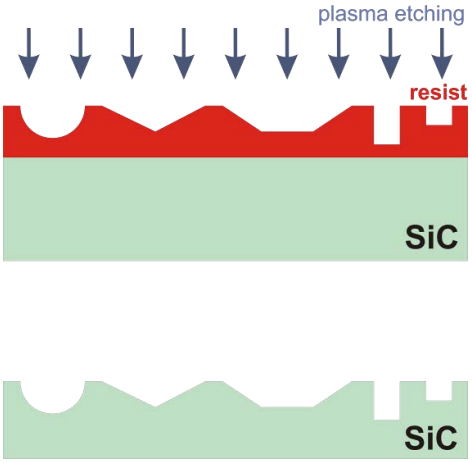


Fig. 1 The basic idea of surface shape transfer.

Unfortunately, it is not possible to obtain such etching conditions that can lead to transfer to the selectivity ratio of 1:1 in the case of resist and silicon carbide using available equipment (STS ICP DRIE from SPTS Technologies). Therefore, an additional layer of silicon dioxide was used for this purpose. The roughly the same etching rate was obtained for silicon carbide and silicon low temperature oxide (LTO) under the same process conditions. The results of our investigation are presented in figure 2 to confirm the usefulness of technology.

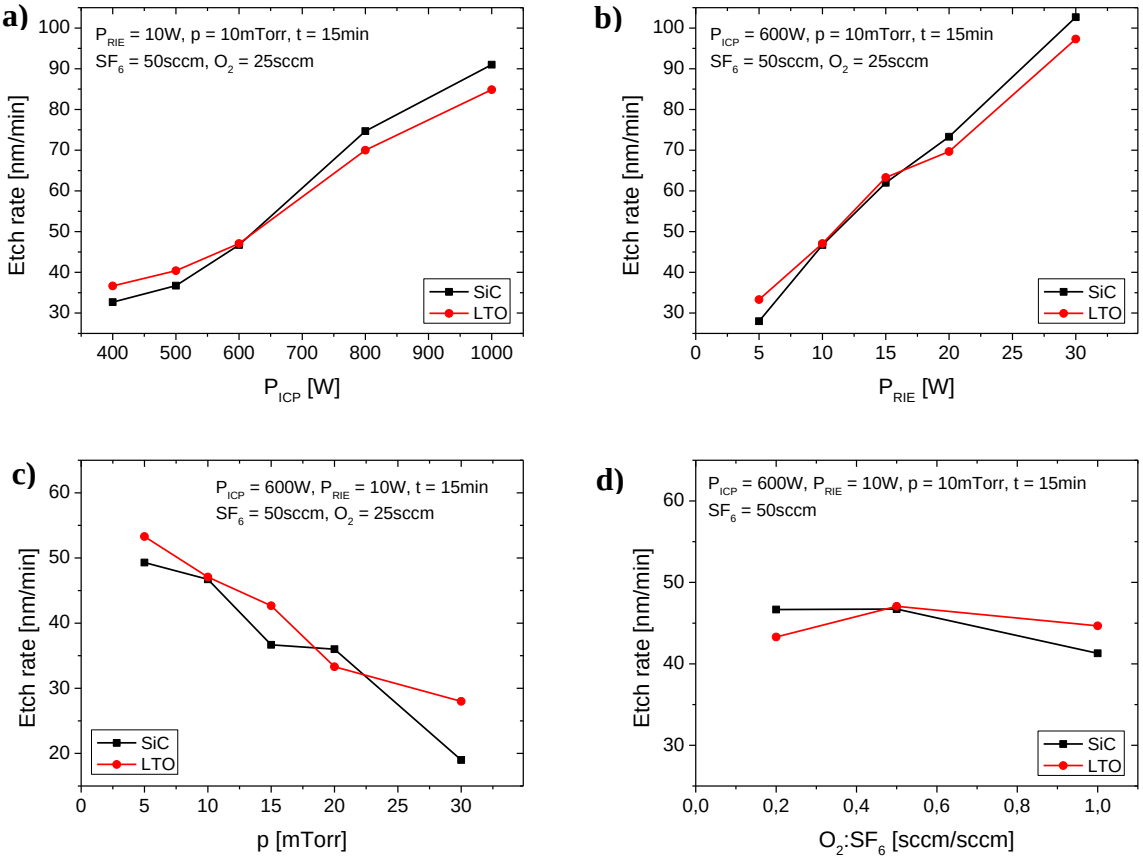


Fig. 2 Etch rate of the LTO and SiC as a function of power, pressure and gas ratio.

The concept of the surface shape transfer was used as a planarization of silicon carbide surface. Photo-benzocyclobutene-polymer resist (BCB) was used for this purpose. The BCB polymer has excellent smoothing ability on the coated surface (fig 3) [2].

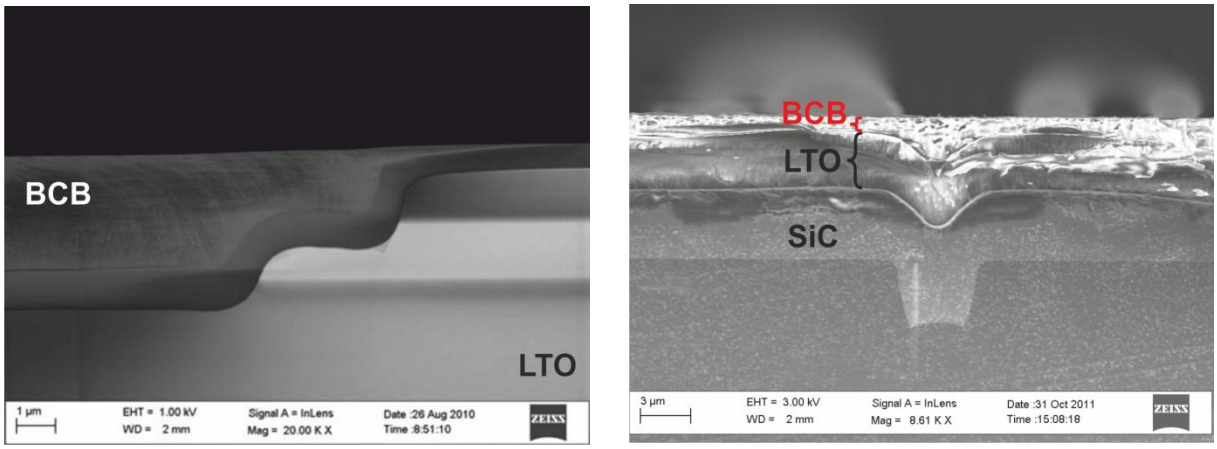
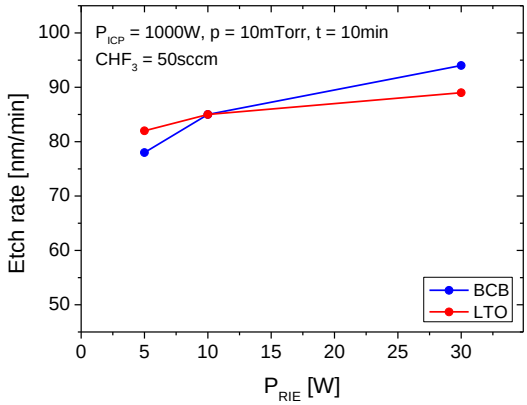


Fig. 3 SEM images of the BCB coated surface.

General idea is to transfer the flat surface of BCB to LTO and then to bulk SiC as it is shown in figure 4. In this approach it is very important to keep exactly the same etch rate for different materials. We have developed the ion etching of photo-benzocyclobutene-polymer resist (BCB) and silicon low temperature oxide (LTO) having roughly the same etch rate for the same process conditions. The results of our tests for BCB and LTO etching are presented in figures 5.



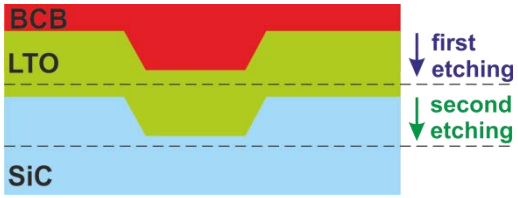


Fig. 4 Flat surface transfer idea.

Fig. 5 Etch rate of the BCB and LTO as a function of power.

Finally, we have developed technological process of plasma etching of various materials at the same etch rate. The primary shape can be transferred from the surface of one layer to another. One of the application is a planarization of SiC material using plasma etching.

References

[1] P. L. G. Ventzek, S. Rauf, T. Sparks, Plasma Etch in: R. Doering, y. Nishi (Eds), Handbook of Semiconductor Manufacturing Technology, CRC Press, New York, 2008, pp. 21.1 - 21.69

[2] http://www.microchem.com/PDFs_Dow/cyclotene_3000_dry_etch.pdf (15-07-2012)

Acknowledgements

Norbert Kwietniewski's work has been supported by the European Union in the framework of European Social Fund through the Warsaw University of Technology Development Programme.

The research was partially supported by the European Union within European Regional Development Fund, through grant Innovative Economy (InTechFun, POIG.01.03.01-00-159/08).

Rapid Stripping of Brass-plating on Fine Saw Wire by Triangle-type Multiple Magnetron Plasmas

H. Fujiyama[1], K. Miyazaki[1], N. Matsuo[1], Y. Kobayashi[1], M. Shinohara[1], and S. Nishiyama[2]

[1]*Graduate School of Engineering, Nagasaki University, Nagasaki 852-8521, Japan*

[2]*Japan Fine Steel CO. Ltd., Sanyo-Onoda 756-0063, Japan*

Email: plasma@nagasaki-u.ac.jp

ABSTRACT

To remove brass plating on fine saw wire, line-shaped magnetron plasma source has been newly developed. New type of multiple plasma sources has been developed by applying to multiple -triangle-type electrodes. The stripping effects were successfully established by using high density magnetron source with 20mm gap in an axially applied magnetic field. From the EDS analysis results of wire surface after plasma stripping during 30sec, it is clearly shown that Zn was removed after 10sec stripping and Cu after 30sec. (Fe:38.5%→97.7% , Cu:39.3%→2.43% , Zn:22.2%→ 0.03%)

Keywords: Metal sputter etching, Saw wire, Plasma stripping, Magnetron plasma

1. INTRODUCTION

Silicon wafer used crystal silicon solar cell is carved out from the silicon ingot by saw wire. Saw wire is covered with brass (Cu: 65%, Zn:35%) plated to need in wire drawing process. As a result basis of plating (especially copper) are diffused in the wafer as contamination. So the electric conductivity changes, and there is a possibility of cause to decrease solar cell efficiency. Therefore the saw wire with Cu free is strongly required.

Now, in the factory, various wet processes by ammonia, hydrochloric acid, sulfuric acid and oxygenated water have been used as a method for removing brass plating. The processes have some disadvantages that the environmental load is large and generally very expensive. In the present research, we propose to use plasma dry process for wire stripping. Dry process has some advantages that the waste liquid treatment is unnecessary, pollution policy of flue-gas treatment etc. is easy and high reaction rate is obtained at low temperature. We aim to remove brass plating on fine wire by the newly developed line-shaped magnetron plasma source. And also new type of multiple plasma sources has been developed by applying to multiple -triangle-type electrodes.

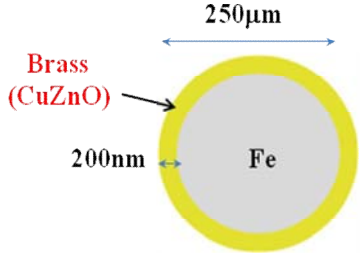


Fig.1 Brass Plating Saw Wire

2. EXPERIMENTAL

At first, it has been investigated on the electrode configuration to profit line-shaped plasma sputtering process to long and fine wire continuously. At the result, triangle-type electrode system shown in Fig.2 has been developed because of easy multination of the stripping process.

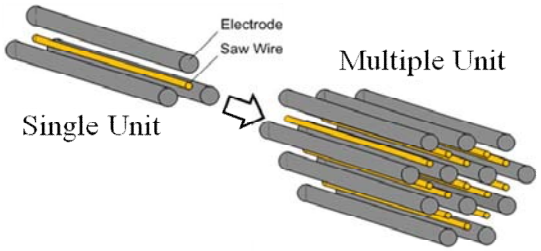


Fig.2 Easy multination of sputter etching process by the triangle-type electrode system

3. RESULTS AND DISCUSSION

3.1 Discharge Characteristics

In a magnetron discharge plasma[1], ion current density to a cathode is proportional to the magnetic flux density B^2, the gas pressure P^2 and the discharge voltage $V_d^{3/2}$:

$$J_d = A(aP^2 + bB^2)(V_d - V_0)^{3/2} \quad (1).$$

Table 1 shows the typical experimental conditions to investigate on the discharge characteristics in the single unit triangle type magnetron plasma.

Table 1 Experimental conditions

Gas	Argon
Gas Pressure [Pa]	1
Gas Flow Rate [sccm]	0.1
Gap Length [mm]	20
Wire Diameter [μm]	250

It is shown in Fig.3 that the dependence of the externally applied magnetic flux density on the discharge current into the fine wire as a cathode. The current was rapidly increased by the magnetron effect from a certain magnetic field.

The fine wire was strongly heated when the current density was more than a few mA/cm².

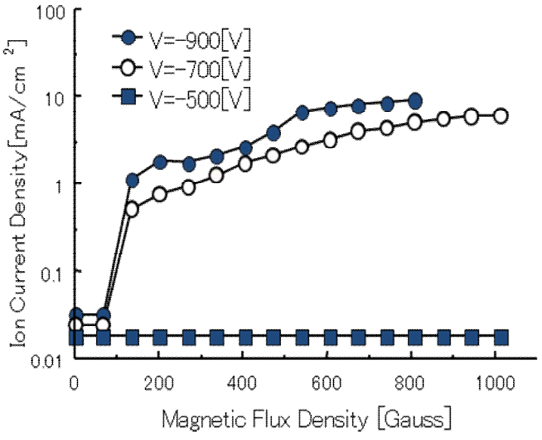


Fig.3 Discharge characteristics in single-unit coaxial magnetron plasma

3.2 Stripping Effect

The experimental results of stripping effects were successfully established by using high density magnetron plasma source with 20mm gap in an axially applied magnetic field.

Figure 4 shows the EDS analysis results of wire surface after plasma stripping during 30sec. Here, the discharge voltage was -730V, the constant discharge current density 1.5mA/cm^2 and the discharge gap length 20mm, respectively. In this figure, it is clearly shown that Zn was removed after 10sec stripping and Cu after 30sec. (Fe:38.5%→97.7% , Cu:39.3%→2.43% , Zn: 22.2%→ 0.03%)

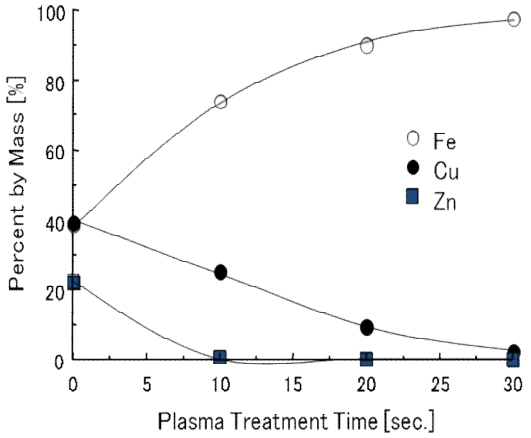


Fig.4 EDS analysis result of stripped wire

Let us estimate the required running speed for perfect removal of the brass plating. When the discharge current density was 1.5[mA/cm^2], perfect removal could be established after 25sec stripping. Therefore the stripping rate was estimated as 8nm/sec=480nm/min. This means that the required running speed of wire is 4.8 [m/min] for full removal in 2m reactor.

From these results suggest that the rapid stripping of fine wire is possible by using the developed triangle type magnetron plasmas. For the higher target voltage and current density to the wire, more rapid stripping can be realized.

3.3 Wire Temperature

Wire heating during plasma stripping is a serious problem for keeping the wire quality. In

this stripping process, before wire heating up to 500℃, perfect removal must be finished. So, high speed but low temperature process is strongly required.

Figure 5 shows the temporal variation of wire temperature measured by the electric resistivity method for the current density 1.5mA/cm^2. When the higher magnetic field, that is, for the constant current density, the higher target voltage leads to the rapid heating of the wire. The heating mechanism seems to be both Joule heating and ion kinetic energy to the wire. So, the optimum condition should be investigated.

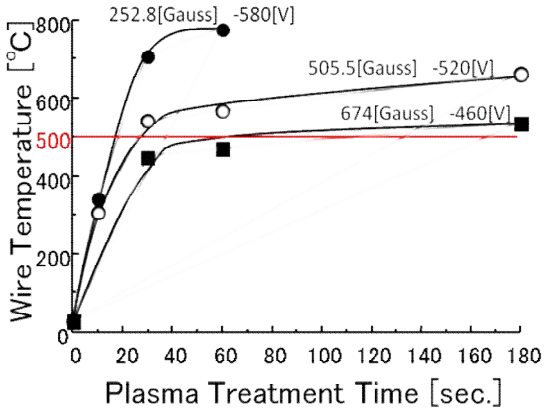


Fig.5 Wire heating during Stripping Process

3.4 Upscaling

～Idea for Multiple Unit Magnetron Plasmas～

For practical use of plasma stripper, we developed new electrode configuration for multiple wire stripping as shown in Fig.6.

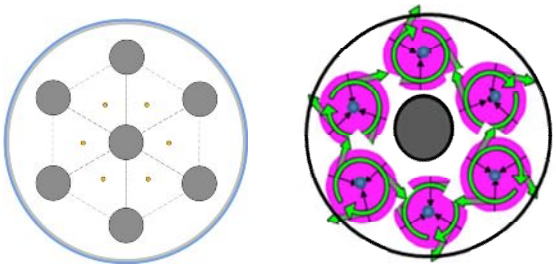


Fig.6 Concept of new electrode system (right) for multiple wire stripping:
Conventional (left), New (right)

The plasma can be generated between 6 wire cathodes and both a center rod and reactor wall as anodes. Easy maintenance and less abnormal discharge could be obtained. Photo 1 shows the cross-sectional view of magnetron plasmas for multiple unit wire stripper.

Photo 1 Cross-sectional view of plasmas for multiple units wire stripper.



Figures 7 ,8 and 9 show the dependence of magnetic flux density, Discharge voltage and gas pressure of the discharge current density in the newly developed multiple plasma stripper for the gas pressure P=0.2Pa and the gap length d=11mm. The discharge current clearly shows the magnetron property to proportional to B^2, $V^{3/2}$ and P, respectively. These results clearly shows that the newly-developed multiple line-shaped plasma has the same characteristics on the mentioned eq.(1).

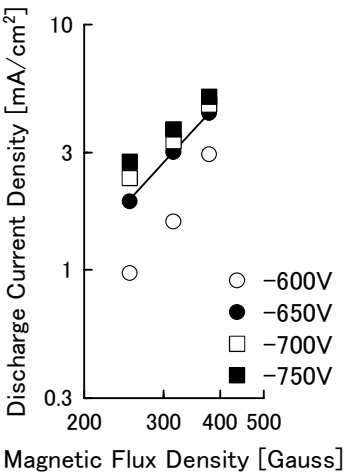


Fig.7 Dependence of magnetic flux density of the discharge current density

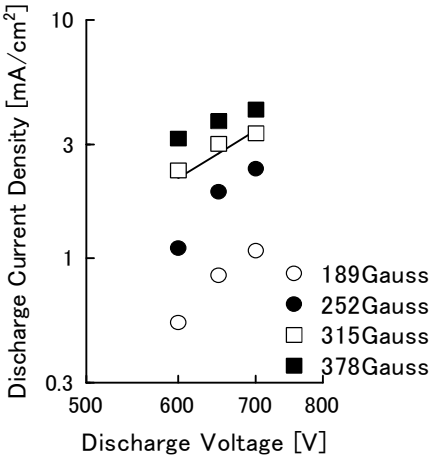


Fig.8 Dependence of discharge voltage of the discharge current density

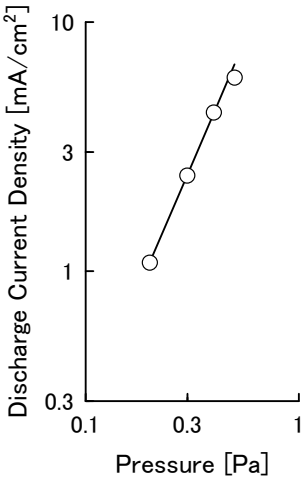


Fig.9 Dependence of gas pressure of the discharge current density

4. CONCLUSION

In order to remove brass plating on saw wire, we propose to use plasma dry process instead of wet process for wire stripping. Dry process has advantages that the waste liquid treatment is unnecessary and pollution policy of flue-gas treatment etc. become easy and high reaction rate should be obtained.

New type of line-shaped magnetron plasma source has been developed by applying magnetic field to triangle-type electrodes. For multiple wires stripping, the multiple unit magnetron plasma with new type of electrode system has been also developed.

The stripping effects were successfully established by using high density magnetron source with 10-30mm gap in an axially applied magnetic field.

Acknowledgments

This work was supported in part by the Regional Innovation Creation Research and Development Business**.**

References

[1] K. Kuwahara and H. Fujiyama: IEEE Trans. on Plasma Science, Vol.22, No.4, pp.442-448 (1994).

Scaling laws governing the NF3 cleaning plasma in a large area reactor

G. F. Leu[1], C. Goury[2], P. Modrzynski[3], M. Klindworth[2], C. Ellert[3]
.[1]OC Oerlikon Solar Ltd, Truebbach, Switzerland .[2]OC Oerlikon Solar Ltd., Truebbach, Switzerland .[3]on leave from OC Oerlikon Solar Ltd., Truebbach, Switzerland
george-felix.leu@oerlikon.com

Introduction

An important part of the thin film Silicon PECVD technology for photovoltaic industry is the Fluorine based plasma cleaning of the reactor. Precursors like CxFy, SF6, NF3 or even F2 can be used. The present paper investigates scaling laws governing the processes in NF3 plasma in a large area reactor.

Experimental device

The experimental device has been extensively described elsewhere [1], [2]. A schematic drawing of the reactor is shown in Fig. 1. The setup consists of a large area (1.4 m x 1.2 m) reactor with an inter-electrodic gap of few tens of mm, having a capacitively coupled plasma source, at 40.68 MHz in a pressure range between 0.2 mbar and few tens of mbar. SiH4/ H2 mixtures are used for deposition of a-Si/ uc-Si thin films and Fluorine containing plasmas are used for the subsequent reactor cleaning. Different discharge parameters, as for example reactor pressure, gas flows, matching box parameters, DC Bias are continuously monitored. A rest gas analyzer (RGA) was installed in the pumping lines, just upstream to the pump. Emission spectroscopy measurements were also performed.

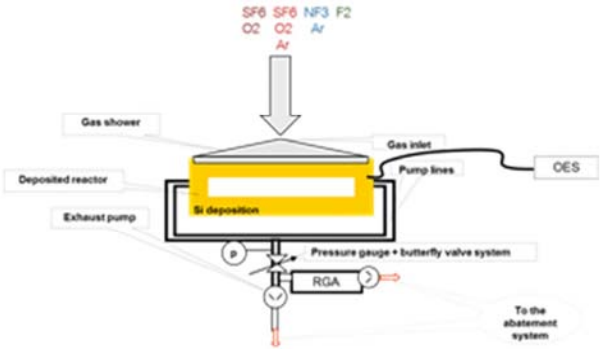


Fig. 1 Experimental device

Reactor pressure as plasma diagnostics tool

If the butterfly valve is kept in fix position, then there is a simple linear relation between the gas flow entering the pump and the reactor pressure. This feature offers the possibility of measuring the total flow at the reactor output; nonetheless some care is needed when using this method. The simple relation between outflow and pressure is valid only if no chemical reaction takes place in the pump, i.e. if no radicals but only stable molecules are present in the gas outlet. This is definitely not the case for the plasma reactor itself, but since the pumping lines are more than 8 m long and have only 0.2 m diameter, it might be true for the whole system: reactor and pumping lines.

We checked this assumption for atomic Fluorine radicals. For the given dimensions of the pumping lines and a gas flow of 5 slm, the residence time in the pumping lines is about 0.6 s. Considering the Fluorine recombination reaction at the walls F + F → F2 and using reaction time of 0.001 s [3] we notice that the reaction time is much shorter than the residence time. In this case we can consider that all of the radicals recombine in the pumping lines and therefore the reactor pressure is a measure of the total outflow entering the pump. Different scenarios (partial dissociation in reactor followed by full recombination in the pumping lines) were considered, as summarized in Table 1. In case the recombination pathway differs from the dissociation pathway and new molecules like N2, F2, N2F4 are produced, then the pressure must increase in the presence of the plasma even in case of full recombination in the pumping lines. Generally speaking, the higher the dissociation efficiency and the higher the weight of the recombination channel leading to F2 and N2 as products, the higher will be the ratio between pressure in the presence and in the absence of the plasma.

Inflow	Outflow	p_{Plasma}/p_{gas}
NF3	NF3	1
NF3	0.5 N2 + 1.5 F2	2
NF3	0.5 N2F2 + F2	1.5
NF3	0.5 N2F4+0.5F2	1

Table 1. NF3 radicals: possible scenarios

Not deposited reactor: Gas composition in the exhaust line

As seen in Figure 2.a, the pressure in the presence of the plasma increases (as expected) with both NF3 inflow and applied power. Fig2. b that all of these points “collapse” in a single parametric curve, having on x-axis a Yasuda-like parameter [4] namely the ratio between applied power and NF3 inflow. On y-axis the ratio between the pressure in presence and in absence of the plasma is depicted.

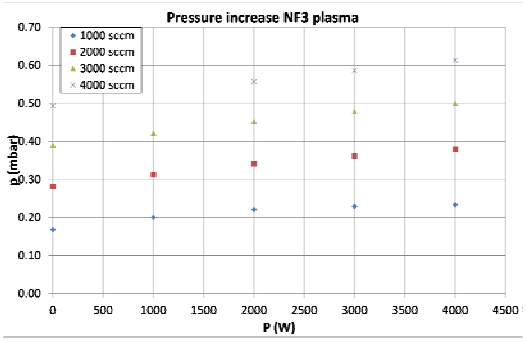


Fig. 2.a NF3 plasma: pressure vs. Flow/ Power

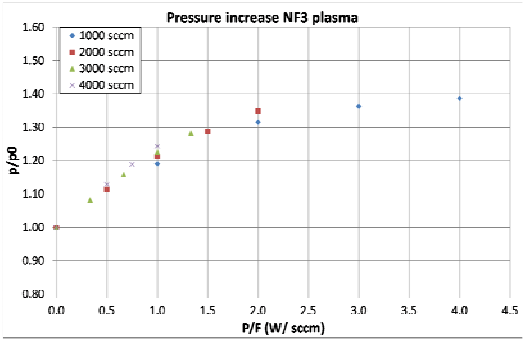


Fig. 2.b NF3 plasma: pressure vs. Flow/ Power

Parametric representation

Two regions of the parameter space can be identified: precursor rich region, for Yasuda-parameters lower than 2 W/ sccm and energy-rich for Yasuda-parameters above the said threshold.

The RGA measurements confirm the above mentioned parameterization. Fig. 3 shows for example the ratio between NF3 outflow and NF3 inflow as a function of the Yasuda-like parameter. For parameters below 2 W/ sccm increasing of Yasuda parameter leads to an increase of NF3 consumption up to 80%. Further increase of applied power (or decrease of NF3 inflow) does not lead to any supplementary increase of NF3 consumption.

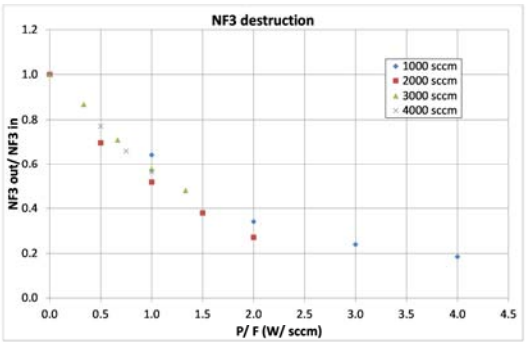


Fig. 3 NF3 destruction vs. Flow/ Power

Parametric representation

Deposited reactor: Cleaning rate

A similar parametrization can be observed when representing the cleaning rate as function of the Yasuda-parameter, as shown in Fig. 4. The cleaning rate increases with the NF3 inflow as long as the Yasuda-parameter remains below ca. 1.6 W/ sccm, and saturates or even decreases for higher flows.

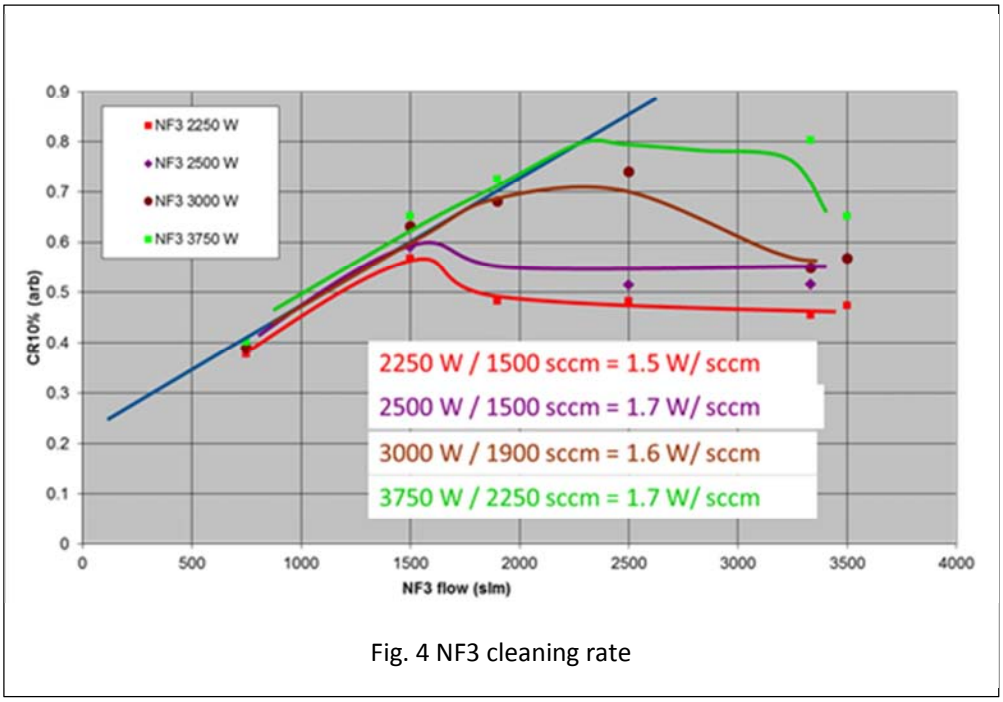


Fig. 4 NF3 cleaning rate

Optical emission spectroscopy measurements

A small amount of Ar was added to NF3 plasma in a not deposited reactor, and OES measurements were performed. Since the conditions for “corona-model” are fulfilled [5], the intensity of Ar lines is directly proportional with the electron density, and the ratio between lines of atomic Fluorine and Ar lines is proportional with the density of atomic Fluorine.

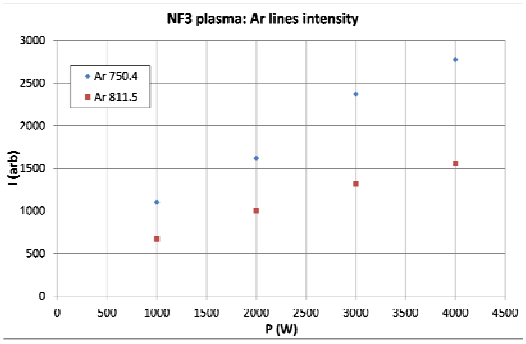


Fig. 5 OES NF3 plasma: Ar lines intensity

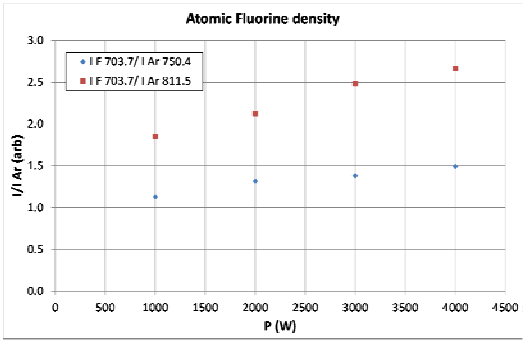


Fig. 6 OES NF3 plasma: density of atomic Fluorine

As can be seen in figures 5 and 6, none of these parameters show any saturation but a linear increase with increasing power. The results are in qualitative agreement with the conclusions global model [5]: increasing the power by constant pressure leads to a linear increase of the electron density and consequently of the density of atomic Fluorine.

Conclusions

Two types of simple scaling laws were experimentally identified in NF3 plasma used for cleaning in large area reactors:

a) the one step electron collision processes like ionization or dissociation scale linearly with the applied power
b) the multi-step molecular processes, as NF3 destruction, F2/N2 production or cleaning show a saturation region by increasing power and scale with a Yasuda-like parameter.

Reference

[1] D. Chaudhary et al, 24th European Photovoltaic Solar Energy Conference, 21-25 September 2009, Hamburg, Germany

[2] G. F. Leu et al 30th ICPIG, August 28th – September 2nd 2011, Belfast, Northern Ireland, UK

[3] S. P. Gangoli, Journal of Physics D: Applied Physics, 40, p 5140 (2007)

[4] H. Yasuda et al, Journal of Polymer science/ Macromolecular reviews, 16, 1, 199-293 (1981)

[5] M. A. Lieberman, A. J. Lichtenberg, Principles of Plasma Discharges and Materials Processing, 2nd Edition, Wiley, ISBN-13: 978-0471720010 (2006)

Cleaning of Organic Contamination from EUV Optics Surfaces Using Hydrogen-based Plasmas

N. Škoro*, E. Gogolides
nskoro@imel.demokritos.gr
Institute of Microelectronics, NCSR Demokritos, Aghia Paraskevi, Attiki 15310, Greece

The efficiency of optics used in extreme ultraviolet (EUV) range suffers from reflectivity degradation due to oxidation and carbon contamination of mirror surfaces. Therefore, an efficient cleaning procedure should be ascertained in order to facilitate applications of EUV lithography tools. Carbon contamination removal from the mirror surface has been reported in Hydrogen plasmas, and laser-induced Hydrogen plasmas in EUV tools. Here, we performed measurements in a helicon-type RF plasma reactor with hydrogen pressures similar to the ones used in laser-induced plasmas in EUV tools. The method of optical actinometry was used to determine hydrogen atom concentration and the degree of dissociation. The results are compared to those obtained by pressure-rise measurements. Preliminary results of plasma etching of thin organic films (PMMA) were also obtained to assess the cleaning efficiency.

Introduction

Extreme UV (EUV) lithography, which uses a wavelength of 13.5 nm, seems to be a promising solution for the optical lithography processes in the future, to improve attainable resolution and meet demands of shrinking feature sizes of transistors in silicon-based integrated circuit technologies [1]. The main difference between EUV lithography systems and conventional ones (using 248/193 nm radiation) is the use of reflective optical elements, such as grazing incidence and multilayer coated mirrors, since strong absorption of EUV radiation by all materials prevents the use of refractive optical components. On the other hand, normal incidence reflectivity at EUV wavelengths is only $10^{-4} – 10^{-3}$ which means that, in order to enhance the reflectivity, many layers have to be added up in phase. One of the solutions is multilayer coated mirrors, comprising a stack of materials with alternating high and low refractive index [2]. Moreover, it must be possible to apply these materials in thin smooth layers with low roughness, without intermixing or mutual reaction between them. One such combination is molybdenum-silicon, providing a reflectivity of 68% at 13.5 nm [3,4]. A special, capping layer is added on top of the multilayer stack to prevent reflectivity loss due to oxidation of the top silicon layer when exposed to air. Ruthenium is used as material for the capping layer [5], due to high resistance to oxidation, limitation of oxygen diffusion into the underlying silicon layer and high EUV reflectivity. A typical structure of a multilayer mirror is shown in Fig. 1 a).

***Table 1**. EUV-induced effects on optical surfaces [2].*

	Hydrocarbons	*Silicone*	*Oxygen (water)*
Process	*Carbon-based film deposition*	*Si-oxide-based film deposition*	*Surface oxidation*
Estimation of reflectivity loss per film thickness	*1% per 1nm*	*1% per 0.7nm*	*1% per 0.3nm*
Reversibility of the process	*Reversible*	*irreversible*	*Irreversible*

While under EUV exposure, the efficiency of EUV optics can be subject to recoverable and non-recoverable reflectivity losses [2]. Some of the effects of EUV-induced reflectivity losses are summarized in Table 1. One of the important mechanisms that can potentially threaten the mirror lifetime is carbon contamination growth on the mirror surface, which is probably the result of EUV radiation-induced dissociation of hydrocarbon molecules adsorbed on the surface [7]. The layer, which will continue to grow as long as hydrocarbon molecules and EUV radiation are supplied, drastically decreases the reflectivity of the mirrors, as shown in Fig. 1 b) [6]. Nevertheless, the removal of carbon layer without any damaging of the mirror surface restores the reflectivity of the mirror.

* On leave of absence from Institute of Physics, University of Belgrade, P. O. Box 68, Belgrade, Serbia

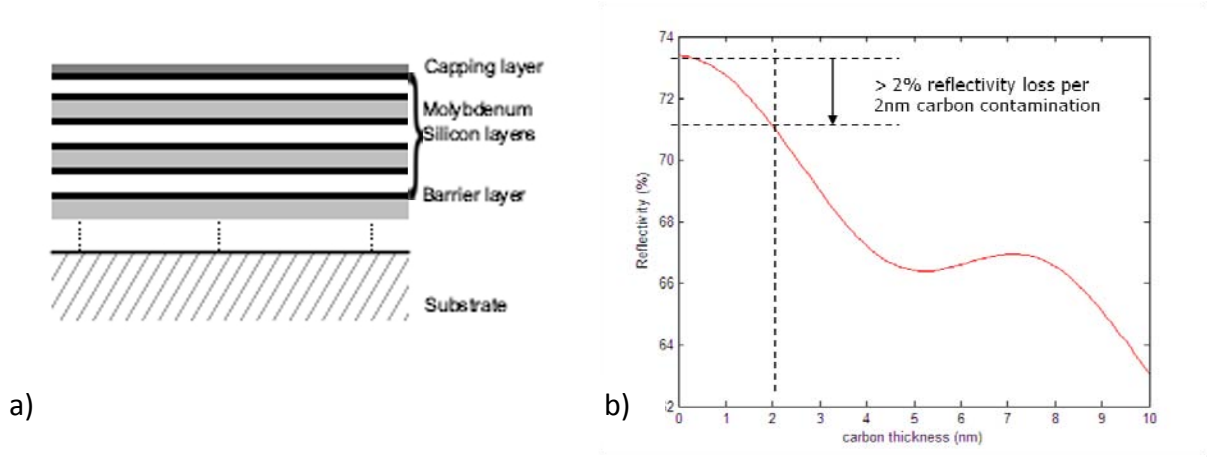


Fig.1 a) Typical structure of Mo-Si multilayer mirror with Ru capping. b) Optical simulation of EUV mirror reflectivity loss with the thickness of carbon layer deposited [6].

So far, oxygen discharges have been used for cleaning optical components involved with X-ray radiation. However, the effectiveness of oxygen cleaning is questionable for EUV optics since there is a threat of oxidation of the multilayer mirrors. Silicon-oxide is a strong EUV radiation absorber and cannot be removed from the optic surfaces, while maintaining critical optical properties [8]. Recently, several investigators have studied removal of carbon layers in hydrogen RF plasmas [1,8,9], and also as an in-situ contamination removal method using atomic hydrogen [10]. Removal of the carbon layer from the surface has been reported with a minimal change of surface properties and with H atoms playing an important role in the removal [8]. Hence, hydrogen-based plasmas appear to be a promising solution for effective removal of carbon contamination from EUV optics. We aim to explore hydrogen-based plasma conditions that will provide us with high cleaning rates and minimal increase of surface roughness. In this report, preliminary results of measurements in low pressure hydrogen plasmas are presented, aiming in determining the Hydrogen atom densities. We obtained the extent of hydrogen dissociation and processed an organic film (PMMA) in order to test etching/removal rates in the plasma.

Experimental details

Low pressure RF plasma (13.56 MHz) was created in a 95% H_2 / 5% Ar gas mixture in a helicon-type plasma reactor (Micromachining Etching Tool, MET, Adixen-Alcatel). The reactor chamber consists of two parts: the upper plasma generation (source) part comprising a quartz tube surrounded by one-turn coil-antenna, which is positioned on top of a diffusion region with a sample holder. The power was applied to the antenna while the aluminum sample holder was grounded. For the plasma characterization measurements, a blank sample holder was used. Emission from the diffusion region was guided through an optical fiber to the Spectra-Pro 500 spectrometer from Acton Research Corporation equipped with a CCD camera. To investigate etching properties, silicon wafers spin-coated with organic film were processed and measured using Woollam M2000 optical multiwavelength ellipsometer before and after etching.

Results and Discussion

In Fig. 2 a) the dependence of line peak intensities on power forwarded to plasma is shown. The maximum intensities are presented for Halpha (656.3 nm), Hbeta (486.1 nm) and Ar line (750.4 nm). The data show rise of line intensity with power.

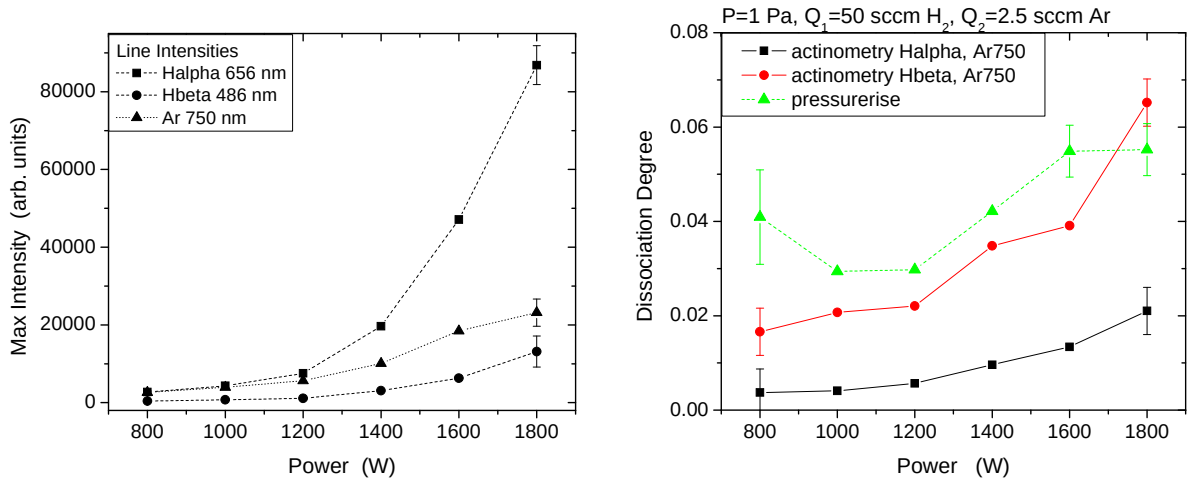


Fig. 2 *a) The dependence of peak line-intensity on power forwarded to plasma. Recordings done at p = 1 Pa and Q = 50sccm. b) Change of the dissociation degree of H_2 with power. H densities and dissociation degree were determined with actinometry measurements (shown with full lines calculated for Te = 3 eV), and pressure rise measurements (dashed line).*

Monitoring of the intensities of these lines and using optical actinometry allows the determination of H density and the dissociation degree in the plasma - an important parameter in hydrogen - containing low-temperature plasmas, when it comes to understanding the surface processes [10]. However, in order to employ this method properly, one should take into account all important kinetic processes in the plasma [11,12]. For the case of gas mixture of H_2 with Ar as actinometer gas, important processes and the data related are given in Table 2. Since the discharge pressure is below 100 Pa, the quenching can be neglected [13].

Table 2. *Processes in H_2/Ar low-pressure plasma with threshold energies and reference data.*

	Process		Eth	Ref.
1a	H atom excitation	H(n=1) + e -> H(n=3) + e	12.09	[14]
1b		H(n=1) + e -> H(n=4) + e	12.75	
2	H_2 dissociative excitation	H_2 + e -> H(n=3,4) + H(n=1) + e	16.90*	[14]
3	Ar direct excitation	Ar(3p) + e -> Ar(4p) + e	13.48	[15]
4a	Radiative de-excitation	H(n=3) -> H(n=2) + *hv (656nm)*	-	[16]
		H(n=4) -> H(n=2) + *hv (486nm)*		
4b		Ar(4p) -> Ar(4s) + *hv (750nm)*	-	[16]

*average from dissociative channels producing Hα and Hβ lines

By solving simple collision-radiative model involving reactions in Table 1, an actinometric formula consisting of a 'classical' actinometry term, describing direct electron excitation of hydrogen and argon levels, and a 'dissociative' term, describing the dissociative excitation channel in H_2, can be obtained.

In Fig. 2 b) dissociation degrees of H_2 for different powers are shown. Solid-line data is obtained from actinometry measurements, and dashed line results are from pressure-rise measurements: after ignition of the discharge, the rise in pressure can be attributed to the creation of H in the plasma, provided that the pumping speed (throttle valve position) is constant in the reactor.

Both methods predict similar increment of the dissociation extent with power. In case of actinometry data, difference between results obtained using Hα and Hβ hydrogen lines may come from the fact that the threshold energy for Hβ excitation is closer to the Ar line than Hα line threshold. As a consequence, electrons exciting monitored lines can have different energies i.e. come from different parts of electron energy distribution function. Thus, it is safer to use theHβ lines

since they are also close to the pressure-rise measurements. Both predict a small dissociation degree of H_2 and thus H densities below 10% of H_2.

To test etching–removal of organic matter in hydrogen plasma, a sample with 500 nm thick polymethylmethacrylate (PMMA) organic film was placed inside the chamber. The thickness of every sample was measured before processing and after 3 minutes of etching using multiwavelength ellipsometry. The sample holder was grounded, i.e. there was no bias applied to the samples. This means that ions reached the substrate with energy of 10 - 20eV (plasma potential). In Fig. 3, results of etching rates at different source powers forwarded to plasma are shown. An increase in etching rate with power increase is observed as a consequence of higher densities of hydrogen atoms in plasma and possibly the larger ion fluxes. Etching rates are relatively high, suggesting that cleaning could be a fast processes.

Further research will focus on hydrogen plasma characterization: obtaining the densities and fluxes of ions, which are also important for material processing. We plan to use Ion Flux and Langmuir probes. Furthermore, the method of optical actinometry will be evaluated by using measurements of hydrogen atom densities with a catalytic probe. Investigation on organic layer removal will continue using samples with a thin carbon layer. Optical damage rates will also be investigated.

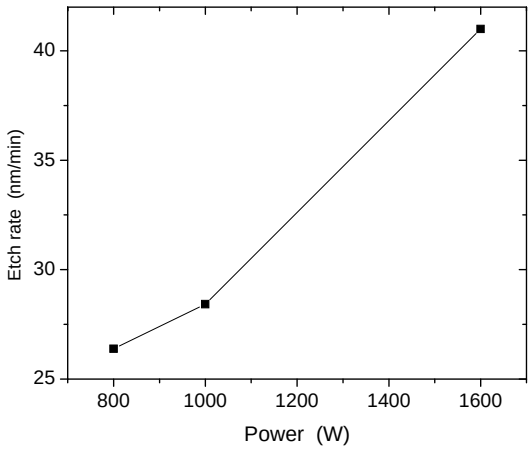


Fig. 3 *Dependence of etching rate of thin PMMA film on power forwarded to plasma. Etching conditions: p = 1 Pa of H_2 with Q = 50 sccm.*

Acknowledgement: Funding of this work comes from the EU FP7 Marie Curie Initial Training Network *Surface Physics for Advanced Manufacturing - S.P.A.M*, grant n° 215723 .

References

[1] S Wurm, C.W Gwyn, Microlithography, 2nd ed, CRC Press/Taylor & Francis Informa Group, FL (2007) Ch. 8
[2] Marc Hubertus Lorenz van der Velden, PhD, Technische Univ. Eindhoven, The Netherlands, 2008
[3] T. W. Barbee Jr., S. Mrowka, and M. C. Hettrick. Appl. Opt., 24, 883 (1985)
[4] B.L. Henke, E.M. Gullikson, and J.C. Davis, At. Data and Nucl. Data Tables, 54, 181 (1993)
[5] T.E. Madey, N.S. Faradzhev, B.V. Yakshinskiy, and N.V. Edwards, Appl. Surf. Sci., 253, 1691 (2006)
[6] B Mertens, *et al,* Microelectron. Eng., 73-74, 16 (2004)
[7] L.E Klebanoff, M.E Malinowski, W.M Clift, C Steinhaus, and P Grunow, J. Vac. Sci. Technol. A, 22, 425 (2004)
[8] S. Graham *et al*., J. Vac. Sci. Technol. B, **20**, 2393 (2002)
[9] I. Nishiyama *et al*., J. Vac. Sci. Technol. B **23**, 3129 (2005)
[10] S. Graham *et al*., Proc. of SPIE, **5037** (2003) p. 460
[11] A. Gicquel, M. Chenevier, Kh. Hassouni, A. Tserepi and M. J. Dubus, Appl. Phys. **83**, 7504 (1998).
[12] V. Schulz-von der Gathen and H. F. Doebele, Plasma Chem. Plasma Process. **16**, 461 (1996).
[13] M. J. Wouters, J. Khachan, I. S. Falconer and B. W. James, J. Phys. B: At. Mol. Opt. Phys. **32**, 2869 (1999).
[14] B. P. Lavrov B P and A. V. Pipa, Opt. Spectrosc. **92**, 647 (2002).
[15] M. Hayashi, National Institute For Fusion Science, Report No. NIFS-DATA-72 (2003).
[16] http://www.nist.gov/pml/data/asd.cfm (NIST)

INFLUENCES OF SURFACE-ACTIVE SUBSTANCES ON SPECIFIC POWER CONSUMPTION AND ON SURFACE ROUGHNESSES OF METAL PRODUCTS UNDER PLASMA VACUUM ARC TREATMENT

V.N.Arustamov, Kh.B.Ashurov, Kh.Kh.Kadirov, I.Kh.Khudaykulov

Arifov Institute of Electronics, Uzbek Academy of Sciences
Do'rmon yo'li Str. 33, 100125, Tashkent, Uzbekistan; arustamov@aie.uz

The use of the vacuum arc for cleaning of the material surfaces and for removal of various contaminations is an actual problem in view of essential advantages of this cleaning method in comparison with chemical, mechanical and other ones and, first of all, in view of absolute environmental safety of vacuum arc method [1-5]. However, in the case of vacuum arc cleaning of some kinds of the hot rolled metals covered with relative thick (6-12 microns) layers of oxide, the roughness of the surfaces after cleaning sometimes exceeds the necessary limit of 10-14 microns. Cleaning of such steels of thick layers and removal of the scale is accompanied by the large power inputs. It is a reason of necessity of improvement of plasma vacuum arc technology and of the study of the interaction mechanisms of cathode plasma of the vacuum arc with the material surfaces.

1. Introduction

It has been shown [6] that how the cathode plasma interacts with the cathode surface points to the fact that the elementary cathode spots (ECS) exist on the surface with scale in the form of compact structurally ordered groups for long lifetime; such groups were called group cathode spots (GCS). The measurements of the dependence of GCS size on current demonstrated that GCS has a configuration in which the elementary cathode spots are located along the GCS contour according to the law independent of current. This configuration is undoubtedly connected with forming a characteristic micro relief on the eroded surface in the form of an axially symmetrical columnar jut of melted metal (protrusion). Surface roughness after treatment is due to protrusion formation. The effect of a high-intensity magnetic field leads to protrusion disappearance. Assuming that the magnetic field influences the ECS formation by way of changing the density of near-surface plasma, one can suggest that it is possible to change a GCS structure and, accordingly, a surface microrelief by way of depositing substances with special characteristics on the surface [7]. More perspective are the substances with lower work function, low evaporation heat and high ionization efficiency in the gas phase. The effect of surface-active substances on surface plasma interaction with surface was experimentally studied for KOH, NaOH, $Ba(OH)\cdot 8H_2O$ и $Ba(NO_2)_2\cdot 2H_2O$. A significant increase in surface roughness and power consumption was observed. The effect of those compounds on a mechanism of vacuum arc discharge interaction with surface, on specific power consumption for vacuum arc descaling of metals and on surface roughness has been considered.

2. Effect of surface-active substances on specific power consumption and surface roughness

The samples of steels SUS304 and SUS430T were used to study the effect of special chemical compounds deposited directly before vacuum-arc treatment on roughness and specific power consumption. The chemical composition of steels is given in Table 1.

Chemical composition of steel

Table 1.

Steel quality	Components, %						
	C	Mn	P	S	Si	Cr	Ni
SUS 304	0,08	2,0	0,045	0,03	1,0	18,0-20,0	8,0-10,5
SUS 430	0,12	1,0	0,04	0,03	1,0	16,0-18,0	0,75

The KOH or NaOH water solution (10-20 weight %) was used as a chemical compound to be

deposited; these compounds were uniformly deposited on the sample surface with their further complete drying. The experiments were carried on for the cleaning rate 0.35-6 m/min and the vacuum-arc discharge currents 140-340 A, which corresponds to the surface density of charge 6 C/cm^2.

The ratios of specific charge and surface roughness for different ways of vacuum arc treatment are given in Table 2.

The dependence of specific power consumption and surface roughness on a way of vacuum arc treatment

Table 2

Compound	Steel quality	Charge density	Specific power consumption kWt/h m^2	Roughness Ra	Roughness Rmin	Decrease in specific power consumption
Без СВ	SUS304	80,91	5,82	10,2	58,5	—
KOH 10%	SUS304	39,8	2,71	5,4	31	2,1
KOH 20%	SUS304	39,3	2,57	4,3	25,4	2,3
KOH 25%	SUS304	42,5	2,8	4,0	30,7	2,1
Без СВ	SUS430	89,7	5,98	11,9	51,8	—
KOH 20%	SUS430	39,5	2.63	3,8	19,2	2,3
KOH 25%	SUS430	51,3	3,42	4,1	21,4	1,7
NaOH 10%	SUS430	45,1	2,85	7,8	34,1	2,0
NaOH 20%	SUS430	44,0	3,0	6,8	31,0	2,0
NaOH 25%	SUS430	52,6	3,65	8,3	36,5	1,6
NaOH 20%	SUS430	55,5	3,8	4,6	24,2	1,5

As seen from Table, the optimal concentration of water solution of KOH or NaOH alkali is 20%. As it should be expected, a decrease in total power consumption on steel quality and substance to be deposited is 1.5–2.4 times and the roughness 1.5–3.2 times owing to reducing the electron work function on the scale surface by the surface-active substances and increasing a flow of neutral particles evaporated from the surface, as well as owing to changing GCS structure from linear to circular.

The characteristic Talyrond traces of the SUS430 steel surface treated by the cathode spots of vacuum arc discharge are presented in Fig. 1.

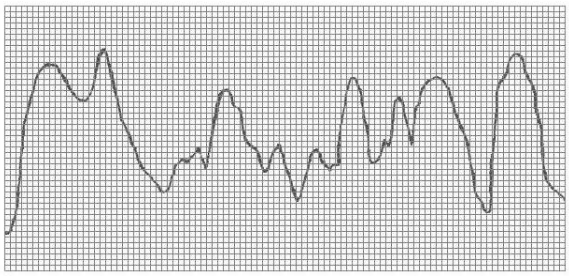


Fig. 1a

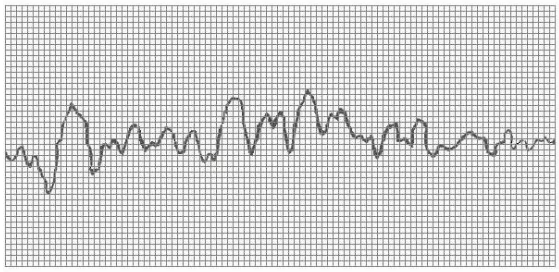


Fig. 1b

3. Experimental method and results

An experimental setup for study of the cleaning process consists of a vacuum chamber with a system of electrodes inside, a power unit of direct current for discharge, a system of vacuum pumping with a rotation pump and a system of water circulation for anode cooling. The samples were made in the form of a square 100×100×3 mm from SUS 430 steel with 5 mm scale. The sample to be tested was a cathode. Along the perimeter the sample surface was masked with a ceramic plate to avoid discharge at the sample edge. The open surface has the form of a regular square with the area 100 cm^2, 60 cm^2 and 40 cm^2.

The following substances were selected – KOH, NaOH, LiOH, $Ba(OH)_2$, KCl and NaCl. We assumed that the ECS formation probability is defined, on the one hand, by the density of near-surface plasma that is created by already existing ECSs and, on the other one, the minimal threshold density of near-surface plasma that initiates a new ECS [8]. Therefore, the substances promoting more effective plasma generation in ECS of vacuum arc discharge were selected to cover the surface. KOH and NaOH

are approximately one type with slightly different work function of metal (2.22 and 2.35 eV), similar energy of evaporation (1.4 and 1.48 eV) and boiling temperature (1570 and 1660 K). LiOH and $Ba(OH)_2$ are decomposed at rather low temperature (before the corpuscular particle flows starts to develop). However, they form stable oxides Li_2O and BaO with very low work function, high boiling temperature and rather high energy of evaporation (3.19 eV and 3.82 eV). NaCl and KCl were selected to study how Cl (gas with high affinity to electron) influences on the probability of ECS formation.

The experimental setup to study the probability of ECS formation on the surface of hot-rolled steel covered by the above-indicated substances is shown in Fig. 2. The cathode (sample) is a plate of 60×20 mm from hot-rolled steel SUS 430; this plate is divided into two identical parts with a line of 0.5 mm in thickness. One part of this plate was covered by one of the above-indicated substances the other was clean. The anode made from copper has the same form as the cathode; at the center of the anode there is a hole for an initiating electrode. The distance between the anode and cathode was 30 mm. The initiating pulse duration was 5 ms. The parameters of the discharge pulse were so that only one clearly delineated crater be formed for one pulse. The discharge pulse duration was 1 ms and the discharge current amplitude was 15 A. in that case only one GCS can be formed on the oxidized surface of SUS 430 steel. The result of cathode spot formation (discharge initiation) was registered as a separate crater of erosion on the surface. The number of craters on the every part from the separating line was counted for 30 discharges. The number of craters on the both parts without substance deposition was almost identical. The probability of CS formation on one part of the plate was defined as the ratio of the crater numbers on one part and the total number of craters on the plate. For KOH deposited on one part the probability of charge initiation and, hence, ECS formation was higher than that on the clean part. The formation probability has the maximal value for the 10% concentration of the KOH water solution, which corresponds to the surface concentration of substance 0.001 g/cm^2. As the quantity of the SAS water solution (volume units) per a surface area was always the same there is unambiguous relation between the concentration of the SAS water solution and the surface concentration of this SAS for all the experiments. The maximum of the considered dependence is a rather important experimental fact for further interpretation of the results.

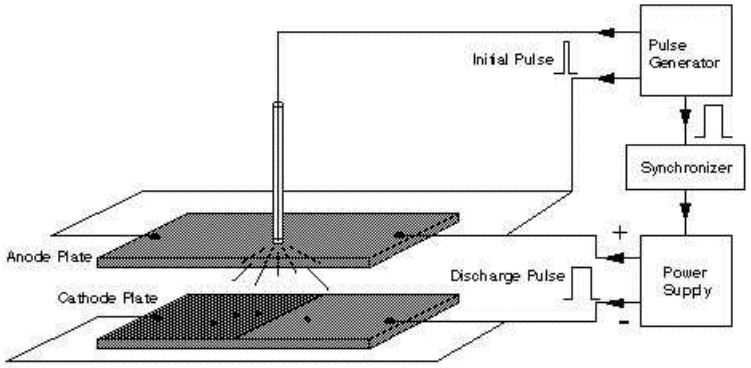


Fig. 2

The dependence of surface roughness and rate of substance removal from the surface on substance concentration have been studied for stably burning vacuum arc discharge. In this case, the power source operated in the mode of direct current. The voltage was 200 V, arc current was 55 and 100 A. the anode was a copper rod of 20 mm in diameter. The anode-cathode distance was 40 mm. The discharge was initiated with a high-voltage initiating electrode. The work pressure could be regulated from 5 to 50 Pa. It was shown that the surface roughness is almost independent of pressure within the pressure range 5–20 Pa. (Fig. 3). Moreover, the surface roughness is independent of discharge current, which is in agreement with the linear dependence of the number of cathode spots on discharge current.

It should be noted that the cleaning rate linearly depends on discharge current within the experimental range of current values. This rate was defined as follows. The samples with the exact value of the surface area to be treated were used for tests. The time of complete sample cleaning was measured for a fixed value of discharge current. The cleaning rate was defined as the ratio of cleaned surface area and time.

After descaling the surface roughness of the sample was measured with a profilometer (Mitutoyo Surftest 401). The dependences of surface roughness and cleaning rate on KOH and NaOH concentration are shown in Figs. 3b–3c. The roughness rapidly decreases with concentration increase and has the value approximately 2.5 times less than that for zero concentration. For further increase in concentration the roughness weakly increases. The maximum of cleaning rate is more pronounced for the 10% concentration of substance; this maximum is approximately 1.8 times higher than that far from the

maximum. The discharge voltage for KOH deposition is 1.5–2.0 V higher than that without KOH and has the maximal value for 10% KOH.

KCl and NaCl used instead of KOH and NaOH lead to decreasing the cleaning rate and increasing the surface roughness, as expected. The effect of different concentration of $Ba(OH)_2$ and LiOH on cleaning rate and roughness was studied as well. It has been found that $Ba(OH)_2$ does not change the cleaning rate but the roughness somewhat increases. The roughness increases more significantly for LiOH (almost in 1.6 times).

Thus, among the surface-active substances KOH, NaOH, LiOH, Ba $(OH)_2$, KCl and NaCl the most favorable results were obtained for KOH and NaOH. For the 10% concentration of SAS the surface roughness is approximately 2.5 times less than that without surface-active substances.

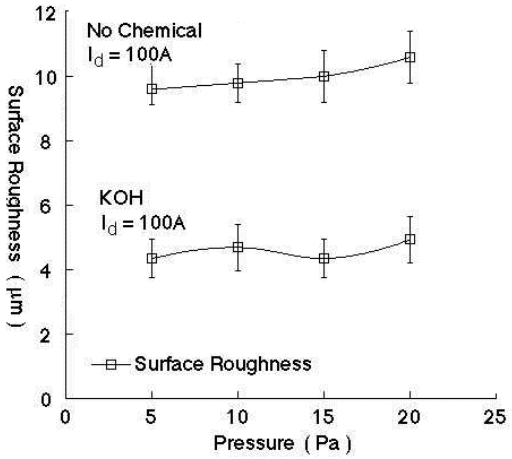


Fig. 3a

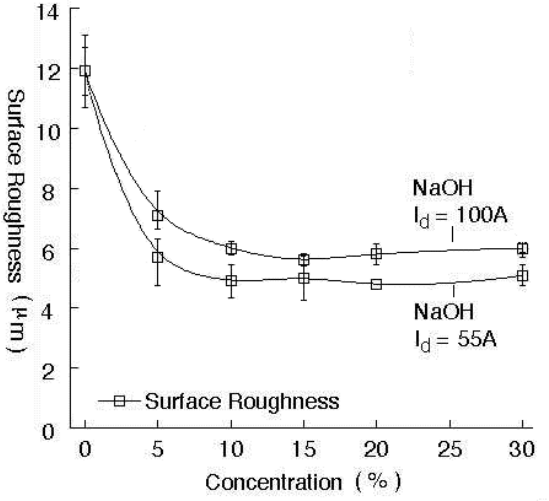


Fig. 3b

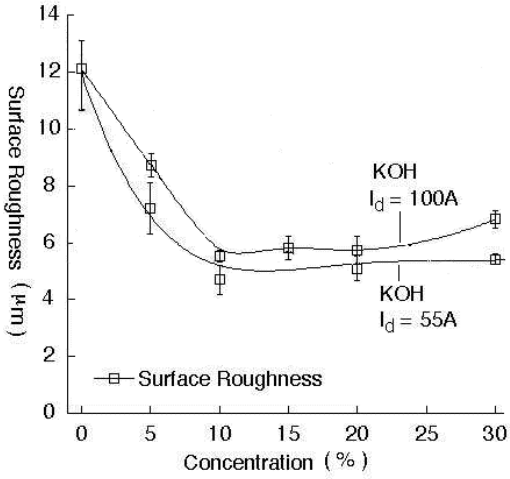


Fig. 3c

Reference

1. V.E. Bulat, A.M. Mirkarimov, R.B. Nagaibekov, S.L. Pozharov, U.Kh. Rasulev. TATF 96 Proceedings, P.155-157.
2. U.A. Arifov et.al. European Patent № 0468110. Date of filling: 24.07.90
3. S.L. Pozharov et. al. Russian Federation Patent by proposal № 93003651/12 Date of filling 21.01.93.
4. H.D. Steffens. In: “Proceedings of the Ninth International Thermal Spray Conference”, Hague, 1980, P.420
5. A. Itoh, K. Takeda, M. Ito and M. Koga. Proceedings of the National Thermal Spray Conference, Longbeach, 1990, P.20
6. W. Petasch. Surf. Coat. Technol., 1997, **97**, 176.
7. K. Kiyokawa, A Itoh., H. Matsuoka, M. Tomimatsu and K. Sugiyama. Thin Solid Films, 1999, **345**, 119.
8. S.L. Pozharov, A.M. Mirkarimov, I.V. Soldatov. JTF, 1998, **68** (11), 57.

Plasma etching of aluminum nitride thin films prepared by magnetron sputtering method

Piotr Firek[1], Bartłomiej Stonio[1], Rafał Chodun[2], Jan Szmidt[1], Krzysztof Zdunek[2]

[1]Faculty of Materials Science and Engineering, Warsaw University of Technology, Warsaw, Poland
[2]Institute of Microelectronics and Optoelectronics, Warsaw University of Technology, Warsaw, Poland .

pfirek@elka.pw.edu.pl

Introduction

Several properties of the AlN films as e.g., isomorphous crystallographic structure, high resistivity (~10^{13} Ω cm), high thermal stability (up to 2200 °C) and high thermal conductivity (~320 W/mK), make it excellent material for application in structure of HEMT, FET transistors, playing role of dielectric.
However, reaching a level of considerable maturity by technology of any electronic material, requires not only adequate methods of its synthesis but also capabilities of material processing, among others availability of means of its selective etching.

Experimental details

The AlN films were deposited using magnetron (φ = 100 mm) and pulse power supplier (f = 100 kHz, with modulation of f = 2 kHz; current 3A). Deposition processes were carried out at pulsed pressure from 10^{-3} Pa to 10^{-1} Pa and using Ar/N_2 gas mixture. The films were deposited on n-type silicon wafers located in parallel to aluminum target, with substrate-target distance at 10 cm.
Investigated in this work thin AlN films were selective etched in RF plasma environment in the 13.56 MHz OXFORD PLASMALAB 80+ setup. The influence of etching process parameters, like etching gas composition, its flow rate and RF power on etching rate was studied and discussed.
Veeco Dektak 150 profilometer was used to measure the depth of etching. To confirm the reliability of the results, all the measurement were double checked by Horiba Jobin Yvon elipsometer with wavelength range between 190 and 830 nm.

Results

Figure 1 presents the dependence of AlN layer etching rate as a function of supplying plasma power at a constant flow of working gas. As it was suspected, the higher the power, the greater the depth of etching. It can be noted that this function is in the range between 120 and 280 W and is similar to linear function.
The Figures 2 and 3 show the AlN layer etching rate as a function of the etching medium composition of the pressure of 40 mTorr. It can be noted that any maximum is not reached when 40 mTorr pressure is used. However, when the pressure was increased to 100 mTorr, the etching rate for the compound of argon and CF_4 was significantly higher. While comparing the two extreme processes that is etching in the atmosphere of Argon and in the atmosphere of CF_4, it can be concluded that etching rate in the pure Argon (physical mechanism) is 1.5 times higher than etching rate in pure CF_4 (chemical mechanism). This would comply with the frequently observed the alike effect of the strong efficiency enhancement of the plasma etching, which results from the cooperative impact of

simultaneously occurring chemical and physical material removal mechanisms, of course provided the appropriate gas mixture has been chosen [1-3]

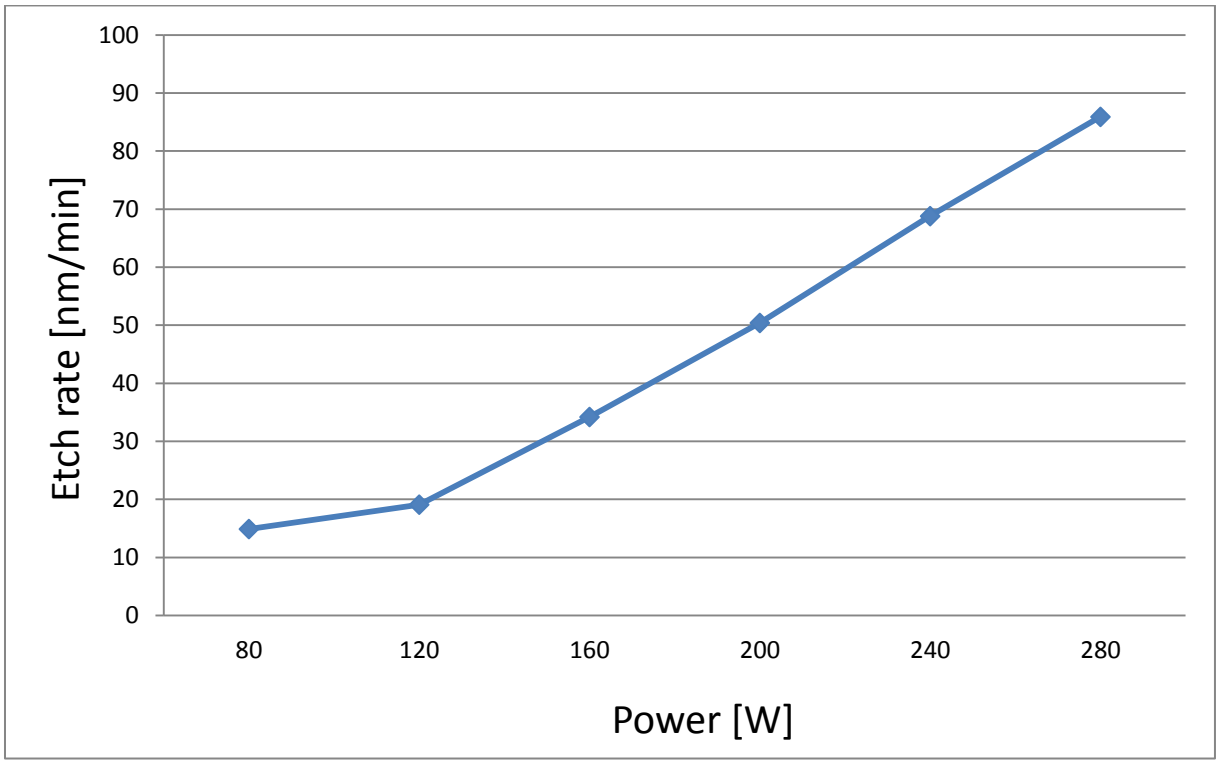


Fig. 1. The etch rate of AlN thin films as a function of RF-power (Total flow rate: 40 sccm; $CF_4/(CF_4 + Ar)$ gas-mixing ratio: 0.5; chamber pressure 40 mTorr)

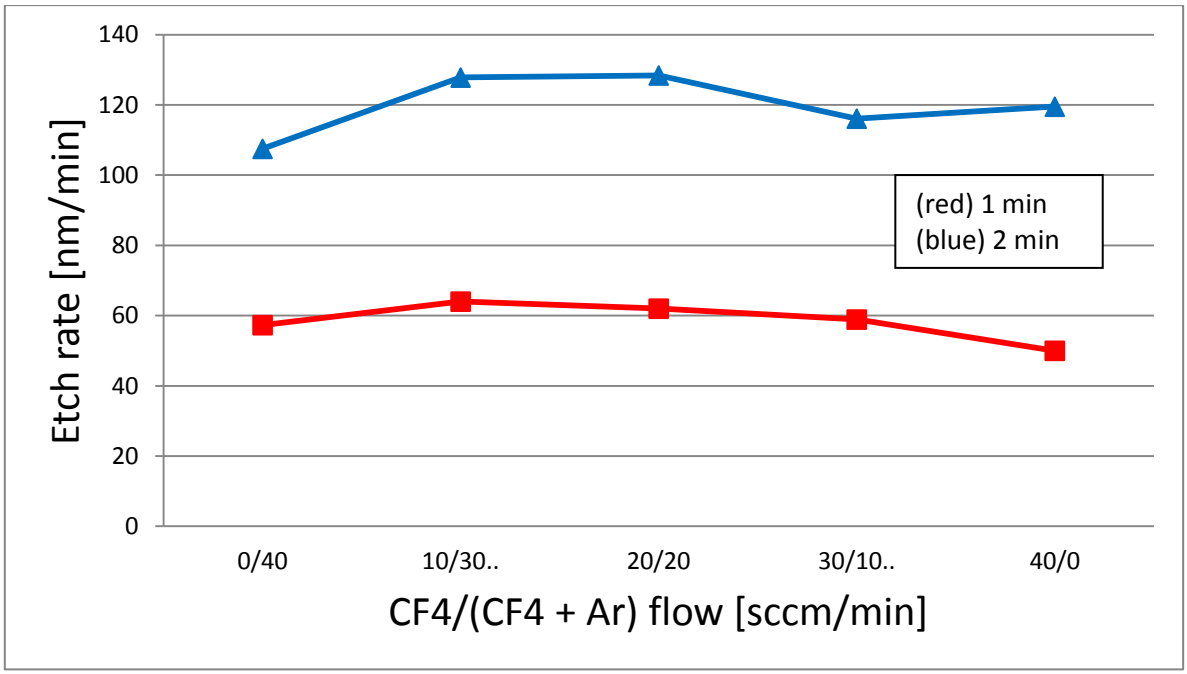


Fig. 2. The etch rate of AlN thin films as a function of $CF_4/(CF_4 + Ar)$ gas-mixing ratio (Total flow rate: 40 sccm; RF power: 280 W; chamber pressure 40 mTorr).

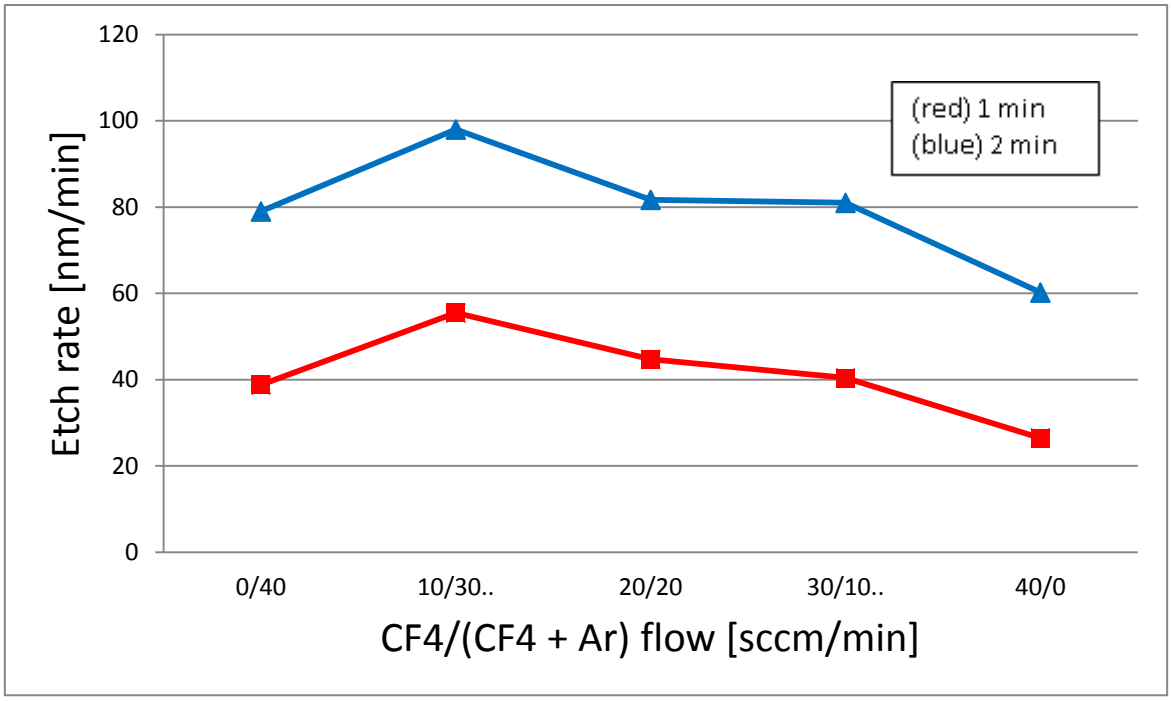


Fig. 3. The etch rate of AlN thin films as a function of $CF_4/(CF_4 + Ar)$ gas-mixing ratio (Total flow rate: 40 sccm; RF power: 280 W; chamber pressure 100 mTorr).

The influence of pressure on AlN layer etching rate is presented in Figure 4. It can be noted that characterization is convergent to linear function. It is due to the fact that with increasing pressure in the reactor chamber for plasma-assisted etching, there is a reduction of the free path of ions, electrons, and neutral particles, and thus reduces the energy of particles bombarding the substrate. It results in the decrease of layer etching rate with the pressure increase.

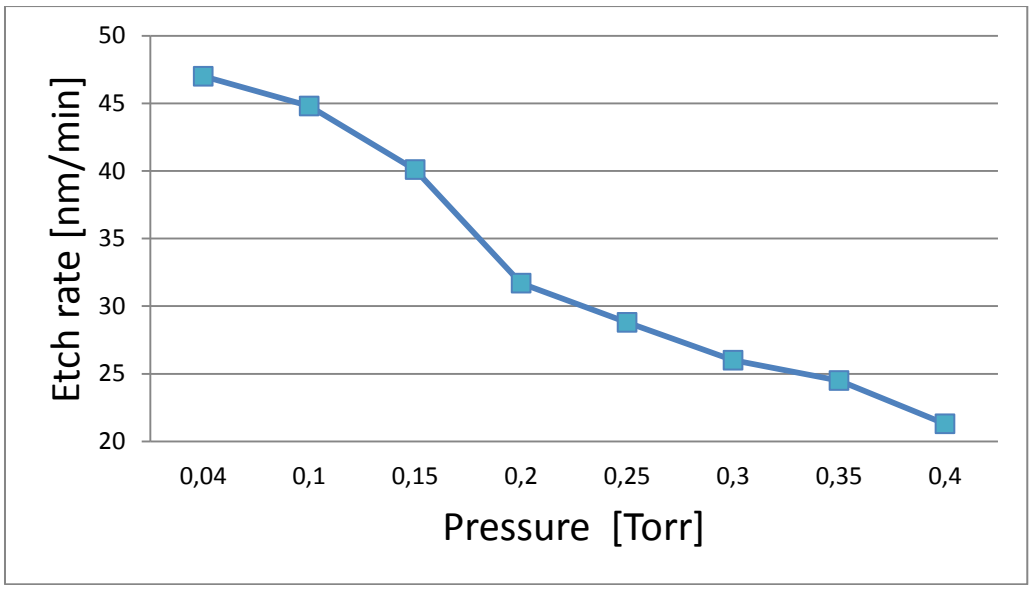


Fig. 4. The etch rate of AlN thin films as a function of chamber pressure (Total flow rate: 40 sccm; RF power: 280 W; $CF_4/(CF_4 + Ar)$ gas-mixing ratio: 0.75;).

The influence of the process time on AlN layer etching rate is presented in Figure 5. As expected, the character of this dependence is close to linear function. With the increasing of etching process, the thickness of the layer etching increases as well.

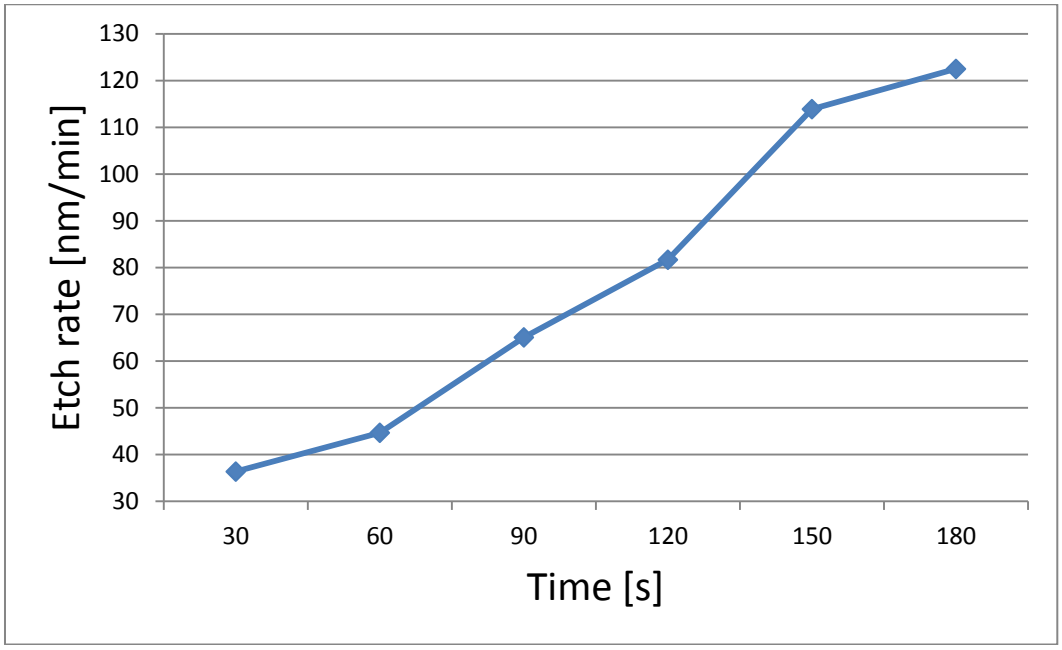


Fig. 5. The etch rate of AlN thin films as a function of time (Total flow rate: 40 sccm; RF power: 280 W; $CF_4/(CF_4 + Ar)$ gas-mixing ratio: 0.5; chamber pressure 100 mTorr).

Conclusions

The results presented in the paper confirm the feasibility of the processes of AlN layers plasma etching. Plasma etching allows for the efficient and controlled removal of AlN deposited by means of magnetron sputtering. There was approximately linear nature of the etching rate changes as a function of power, pressure and time. Appearing of an etch rate maximum for certain non-zero value of $CF_4/(CF_4 + Ar)$ gas-mixing ratio was observed. This indicates the growth of efficiency of two competing etching mechanisms: physical (due to intensified Ar ion bombardment) and chemical (due to higher fluorine atom volume density), along with increasing power. One might expect appearing of an etch rate maximum for certain non-zero value of $CF_4/(CF_4 + Ar)$ gas-mixing ratio. Mastering the process will make it possible to do MISFET structures (metal insulator semiconductor field effect transistor) and ISFET ion-sensitive structures.

References

[1] A Szczęsny, P. Śniecikowski, J. Szmidt, A. Werbowy, "Reactive ion etching of novel materials - GaN and SiC", Vacuum 70 (2003) 249–254
[2] P.-S. Kang, K.-T. Kim, D.-P. Kim, Ch.-I. Kim, A.M. Efremov, “Dry etching characteristics of $(Ba_{0.6},Sr_{0.4})TiO_3$ thin films in high density CF_4/Ar plasma”, Surface and Coatings Technology 171 (2003) 273–279
[3] S. Wolf, R.N. Tauber, “Silicon processing for the VLSI Era. Vol.1 – process technology”, Lattice Press, Sunset Beach, California, 1987.

ON THE INJECTED GAS/ELECTRIC POWER RELATION FOR BETTER CONTROL OF DEPOSITION EFFICIENCY DURING THE GIMS DEPOSITION

Krzysztof Zdunek[1,2], Katarzyna Nowakowska-Langier[2], Rafal Chodun[1], Jerzy Dora[3]

[1]Faculty of Materials Science, Warsaw University of Technology, Warsaw, Poland
[2]National Centre for Nuclear Research, Swierk/Otwock, Poland
[3]Dora Power Systems, Wilczyce/Wroclaw, Poland
contact: *zdunek@inmat.pw.edu.pl*

1. Introduction

During the last AEPSE'2011 conference [1,2] there were presented the concept as well as the first results of the use of working gas injection to control the generation of pulsed plasma. The problem was discussed on the basis of two methods: Impulse Plasma Deposition (IPD) [3] and Magnetron Sputtering (MS) *e.g.*[4,5]. The first results indicated the desirability of a deeper interest in such a way of plasma process control.

The idea of using the working gas injection instead of stationary gas flow mode assumes in the first approximation that the lack of cold gas in the chamber space prior to gas injection could next avoid the kinetic energy dissipation on collision between the plasma particles and the cold gas.

Previously presented studies [6] have shown the initial experimental results proving the positives of proposed modification of the well known methods of plasma surface deposition (in the case of IPD - possibility of exceptionally effective producing of antiabrasive layers on unheated substrates and from the other hand - the positive change in the morphology of layers as well as a different way of target erosion during the layer deposition by MS).

Lately carried out experiments [1,2] have showed that during the **GIMS** deposition of AlN coatings (**GIMS** - ***G****as* ***I****njection* ***M****agnetron* ***S****puttering*) higher amounts of Al-Al bonds have occurred in comparison with the case of continuous gas flow mode. It seems to us that the reason of that metallic "tail" could be both the diminishing of the portion of reactive gas and/or self sputtering effect of the aluminum target arising during the last phase of working gas injection. The studies describes below concerns the very last our studies on the possibilities of control the gas/electric power relation during the GIMS process.

2. Experimental procedure

The processes of AlN synthesis were performed in two modes: mode A – gas injection in its initially variant as mentioned previously [1,2] and mode B – after the just introduced modification of the gas injection procedure. The modification of the gas injection procedure consisted of using a device specially designed by us to control the gas injection/electric power phase relation (patent procedure has been just now initiated).

As described earlier in [1,2] our apparatus for AlN deposition by the GIMS was equipped with two WMK100 type magnetrons working in special dual magnetron arrangements ("gemini type") supplied by the DPS pulse power supplier operated at frequency of 70 kHz with 2 kHz

modulation. AlN layers were deposited on non-heated 2-inch Si wafer. Prior to AlN layer synthesis the aluminum target of initial thickness of about 8 mm was preliminary typically conditioned for 10-15 min by sputtering in argon (shutter) continuously dosed to the chamber and next the process of AlN layer deposition was carried in the nitrogen injected by the pulsed valve with the frequency of 10^0-10^1 Hz and the valve time "ON" duration of order of 10^{-3}-10^{-2} s. The pressure of nitrogen was periodically varied depending on the phase of gas injection. However, with an accuracy of the inertia of the pressure meter gauge in the case of mode B the plasma was excited at pressures of order of 10^{-3} Pa (!). The synthesis of AlN layers with the thickness of tenses of nanometers was carried out at an effective power of several kW, using the ratio between the circulating and effective power as one of essential parameters controlling the course of plasma process (the circulating power as an important technological parameter results from a special, novel concept of DPS magnetron power supply [7]). The distribution of particular bonds, especially Al2p orbitals of the material of AlN layers was investigated by the use of the XPS spectroscopy.

3. Results and discussion

From our earlier experiments related to the synthesis of AlN layers by magnetron sputtering [1] by the GIMS deposition came out, that after synthesis under conditions of gas injection, the presence of the Al-Al bonds has been possible (as high as even 20% in the worst case). We assumed that these bonds probably appeared as a result of target sputtering aluminum in the final stage of gas injection pulse, very close to the metallic mode of magnetron operation. In order to minimize or even to the total elimination of the unfavorable presence of Al-Al bonds we have constructed a special control system of the gas injection phase.

The procedure and some specific features of the GIMS processes realized in mode A and mode B were described above. What is worth to note in the context of GIMS is way of reactive erosion of target surface for targets exploited in the conditions of GIMS and the conditions of continuous gas flow (in the case of GIMS the target was exploited in the nitrogen atmosphere only !). The difference between targets has been shown at the fig. 1.



Fig. 1 View of the Al targets exploited in the GIMS (left photo) and under the condition of continuous working gas flow (right photo), respectively in the nitrogen only and $Ar+N_2$ atmosphere.

The comparison between the XPS studies for Al2p orbital for the layer materials produced in modes A and B has been shown in fig. 2. Deconvolution of spectra obtained for the mode A's material the presence the peak of about of 73.4 eV typical for the Al-N bonds and in addition to that also the presence of a small peak of about of 71.5 eV reflecting the binding of Al-Al (fig. 2a) *e.g.* [8]. In the case of layers produced in mod B *e.s.*with the use of the our special controller the repeatedly made XPS studies allowed us to exclude the presence of Al-Al bonds (fig. 2b).

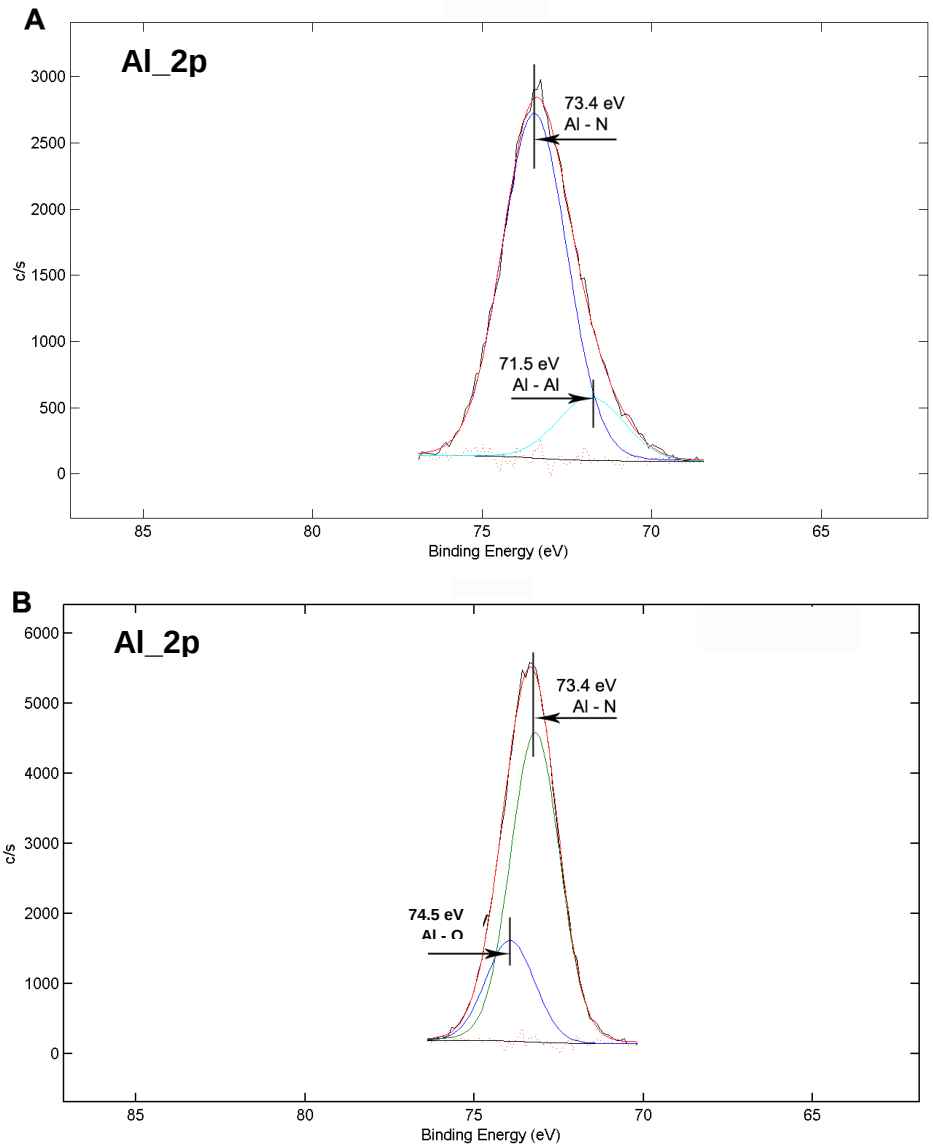


Fig. 2 XPS spectra of the Al2p orbitals for the AlN layer materials deposited in modes: A (a) and B (b)

Deconvolution of the Al2p spectra obtained for AlN layers materials produced in mode B revealed the interesting relation between the controlled gas injection phase and the relative content of the Al-N and Al-O bonds (respectively, about 73.4 eV and about 74.5 eV). The studies showed that the relative content of the "oxygen bonds" in the layer materials increases with the shortening of the individual pulse duration during the gas injection. In our opinion this probably indicates that during the AlN deposition by the GIMS technology the Al-O bond are formed in the first stage of the AlN layer synthesis as a result of binding of the residual oxygen content (chamber, target material) by a aluminum vapors. In recent years we have focused our attention on how to implement a new magnetron sputtering process. Based on our previous experience in the application of gas injection to control the production of layers by IPD, we used a similar technique in the case of MS methods. Described in this abstract studies included a successful attempt to gain better control over the phenomena associated with the synthesis of layers in a GIMS. It seems to us that we can effectively cut off the tail of aluminum vapor produced in the final phase of the individual targetu sputtering gas injection.

4. Conclusions

In recent time we have focused our attention on new magnetron sputtering (MS) technology by the use the gas injection as a tool for initiating and effective control of plasma generation process during the MS layer deposition (MS -> **GIMS**). Based on our previous experience in the application of gas injection to control the production of layers by IPD, we used a similar technique in the case of MS methods. Studies described above concerns a successful attempt to gain better control over the phenomena associated with the developed by us GIMS technique. It seems to us that by applying the specially designed controller integrated into the electric supply system of the magnetrons we can effectively cut off the tail of aluminum vapor produced in the final stage during the injection of an each individual portion of working gas during the GIMS.

Literature:

[1] K. Zdunek, K. Nowakowska-Langier, R. Chodun, J. Dora: *Gas injection as a tool for plasma process control during coating deposition*, invited lecture, AEPSE'2011, Dalian, China, 2011;
[2] K. Zdunek, K. Nowakowska-Langier, R. Chodun, J. Dora: Surf.Coat.Techn, 2012 (in press, at now available on-line);
[3] K. Zdunek: Surf. Coat. Techn., 201(2007)4813;
[4] W. M. Posadowski: Thin Solid Films, 392(2001)201;
[5] R. Arnell, P. Kelly, J. Bradley: Surf. Coat. Techn., 188/189(2004)158;
[6] K. Zdunek, K. Nowakowska-Langier, R. Chodun, M. Kupczyk, P. Siwak: Vacuum, (2010)163;
[7] W. Posadowski, A. Wiatrowski, J. Dora, Z. Radzimski: Thin Solid Films, 516(2008)4478;
[8] W.Osterle, I. Dorfel, I. Urban, T. Reier, J.W. Schultze: Surf.Coat. Techn., 102 (1998) 168;

Influence of the Ion Beam Current on Microstructures and Optical Properties of Al_2O_3 Thin Films by Oxygen Ion Beam Assisted Pulse Reactive Magnetron Sputtering

Zhimin Wang, Jinxiao Wang, Yi Wang, Kai Zhao, Xiaomei Su, Hu Wang, Yudong Feng*

Science and Technology on Surface Engineering Laboratory, Lanzhou Institute of Physics, Lanzhou 730000, China

Extended Abstract:

Al_2O_3 thin films was prepared in a self-designed ion beam assisted pulse reactive magnetron sputtering system, in which the films can be synthesized with sputtered aluminum under simultaneous oxidation with oxygen ions produced by ion source. A metallic aluminum target with the purity of 4N was employed which was a 560mm by 80mm rectangular area. The substrate holder was located 100mm away from the target surface. Argon gas of high purity (99.99%) grade was used as sputter gas and was bled to the substrate through aluminum tube. The gas mixture of oxygen and argon was imported in the ion source. Meanwhile the oxygen content was controlled by regulating the flow ratio of oxygen and argon. Prior to the deposition work, substrates were cleaned by Ar ion sputtering for 5 min to remove contaminant on the surface. During deposition, the substrate temperature was room temperature.

Fig. 1 shows the hysteresis behavior of cathode target with ion source operated at V_a=200 V, I_a=1 A and without ion beam assistance. It can be seen that the hysteresis effect still appeared in the oxygen ion beam assisted process, and thus the cathode should be operated before the transition point from the metal mode to the metastable transition mode. In ion beam oxidation process, we should carry out the research of experimental parameters on microstructures and properties of the films. In the following, we showed the influence of ion beam current on microstructures and properties of Al_2O_3 thin films with other parameters fixed.

* Corresponding author. Tel.: +86931 4585045; fax: +86931 8265391.
E-mail address: fengyd2008@gmail.com.

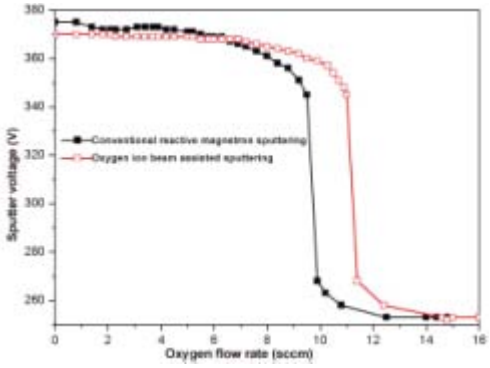


Fig. 1 Hysteresis behavior of oxygen ion beam assisted sputtering operated at V_a=200 V, I_a=1 A and conventional reactive magnetron sputtering.

XPS spectra of Al 2p photoelectrons measured from films are shown in Fig. 2 with a variation of the ion beam current from 0.25 A to 1 A. The spectrum could be separated into two Gaussian components which corresponded to metallic state at binding energy of 72.8eV and Al_2O_3 oxide state at binding energy of 74.7eV, respectively. Here it is noted that ion beam current could lead to significant influence on the composition of films. As the ion beam current increased, the intensity of aluminum form at lower binding energy wear off, and yet the intensity of Al_2O_3 form at higher binding energy strengthened, resulting that those two obvious peaks appeared in the Al 2p spectrum. And then the peak at lower binding energy gradually disappeared. In consequence, the Al 2p peak could be fitted with only one peak which shifted towards oxide state at higher binding energy with ion beam current increasing, showing that Al_2O_3 content in the film increased as the ion beam current increased. When the ion beam current increased up to 0.85 A, stoichiometrical Al_2O_3 thin films were successfully deposited. In addition, XRD measurements showed that all the Al_2O_3 films were amorphous.

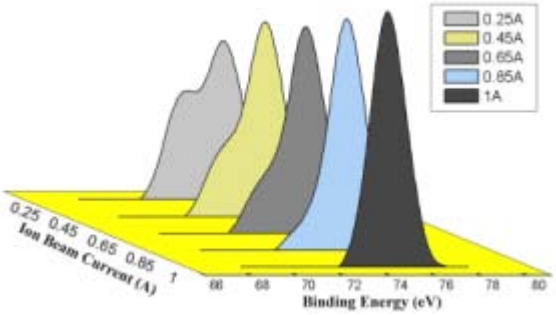


Fig. 2 XPS spectra of Al 2p photoelectrons measured from films deposited with a variation of the ion beam current from 0.25 A to 1 A.

Fig. 3 presents the transmittance spectrum of the Al_2O_3 films deposited as a function of ion beam current. It is quite obvious that the transmittance of the film deposited at lower ion beam current, i.e. ion beam current at 0.45 A, was far lower than the rest of the films deposited with higher ion beam current over the entire

spectrum. It revealed that the film deposited at lower ion beam current at 0.45 A did not entirely oxide, finally forming metal-dielectric mixture with high absorption. When the oxygen content increased to 0.85 A, the transmittance spectrum of the films was consisted with theoretical optical spectrum, indicating the film was totally stoichiometric. During the oxygen ion beam assisted process, oxygen ion was sufficient for Al oxidization to form stoichiometrical Al_2O_3 thin films with the increase of ion beam current up to 0.85 A.

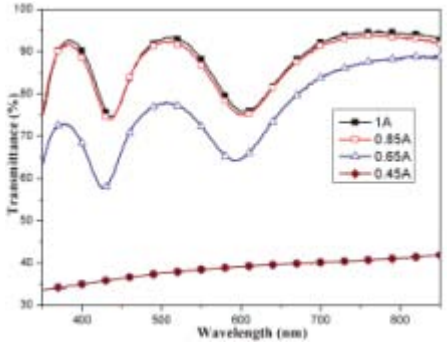


Fig. 3 Transmittance spectrum of the Al_2O_3 deposited as a function of ion beam current of the assist beam.

Fig. 4 plots the variation curve in the refraction index (n) and extinction coefficient (k) of Al_2O_3 films. It can be seen that Al_2O_3 thin films with stoichiometric at the ion beam current of 0.85 A had the highest refractive index and the lowest extinction coefficient. As the ion beam current further increased, refractive index became lower and extinction coefficient came into higher. The results could be contributed to redundant oxygen ion bombardment on growing surface, making unreactive oxygen ion covered by the following achieved Al atoms. The process increased the number of vacancies and interstitials in the film, resulting in optical property.

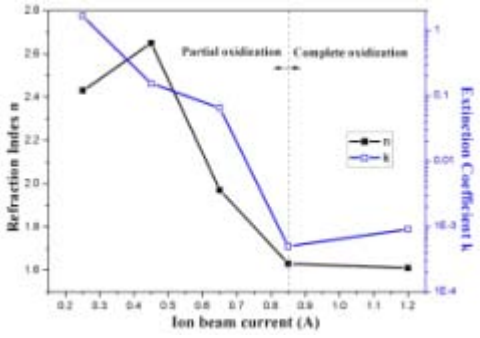


Fig. 4 Optical constants of the films with various ion beam current.

Fig. 5 presents deposition rate of the films with various ion beam current. The results show that the deposition rate was lower as the ion beam current less than 0.85 A. When the ion beam current increased up to 0.85 A, the deposition rate achieved the

maximum. As further increasing the ion beam current, the deposition rate began to saturation. Therefore, it appears to be contributed that sufficient oxygen ion could react with Al atoms to form fully oxidized thin films with the ion beam current increased above 0.85 A, when oxygen in the films gradually saturated and the thickness of films became stabilization, resulting in saturation of the deposition rate.

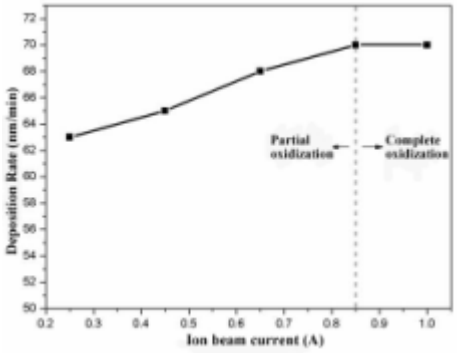


Fig. 5 Deposition rates of the films with various ion beam current.

In this paper, oxygen ion beam assisted pulse reactive magnetron sputtering has been used to deposit room temperature Al_2O_3 thin films on polyimide substrates with high deposition rate and the influence of ion beam current on microstructures, optical properties and deposition rate of Al_2O_3 thin films were investigated. The results show that the structure of the thin films deposited at various ion beam current were amorphous. Al_2O_3 thin films with stoichiometric at the ion beam current of 0.85 A had the highest refractive index and the lowest extinction coefficient. As the ion beam current further increased, refractive index became lower and extinction coefficient came into higher. The deposition rate slowly increased with the increase of ion beam current, achieved the maximum as ion beam current increased up to 0.85 A and then saturated with further increasing the ion beam current.

FORMATION OF TECHNOLOGICAL PLASMA EFFECT OF VACUUM-ARC DISCHARGE ON INNER SURFACE OF METALLIC PIPES AND DEPOSITION OF PROTECTIVE COATS ON THEM

V.N. Arustamov, Kh.B. Ashurov, Kh.Kh. Kadirov, I.Kh. Khudaykulov

Arifov Institute of Electronics, Uzbek Academy of Sciences, Uzbekistan
Durmon Yuli str. 33, 100125 Tashkent, Uzbekistan, arustamov@aie.uz

1. Introduction

In many cases of industrial applications it is economically profitable or technically necessary to combine bulk features of one material with surface features of another one in a single material. Vacuum-arc treatment of products from inexpensive materials to form new required features of surface layers is more perspective owing to its unlimited feasibility in process efficiency. Pipes are in great demand in oil-gas industries and power engineering. But there are no effective methods for pipe inner surface treatment and pipe coating deposition, which makes it impossible to use inexpensive steel pipes under conditions of aggressive liquids, high temperature, high pressure and other parameters leading to oxidation, erosion and pipe life. Therefore, development of plasma-arc technologies of pipe inner surface treatment and pipe coating deposition is very topical and actual. A specific effect of vacuum-arc discharge on material surface is due to high concentration of energy in a chaotically rapidly moving cathode spot, short-term local heating of surface and its rapid cooling. The technological effect of cathode plasma on surface is based on cathode spot movement. The effect of a plasma flow of cathode spots formed on the outer surface of a pipe cathode and controlled by a system of vacuum-arc cathode spot fixation with magnets placed inside an electrode has been considered.

A great number of studies [1,2,3] have been devoted to explaining and investigating "anomalous" movement of the cathode spots. It has been shown [2] that the cathode spot moves in the direction of the greatest action of discharge's own magnetic field and outer magnetic field. The magnets initiate an arc magnetic field [4] that confines the cathode spots and makes it possible to scan (control) them on the electrode-cathode surface and act with a plasma flow and deposit coats on inner surface of a coaxially placed pipe-product. The high efficiency of the plasma vacuum-arc method for pipe inner surface treatment and coat deposition has been found.

2. Experimental

To realize the controlled technological action and coat deposition by vacuum-arc cathode plasma flows onto the pipe inner surface in a system of coaxial electrodes, it is perspective and promising to use magnetic stabilization and cathode spot movement control. In this case the regularities of cathode spot movement in outer non-uniform magnetic field are applied. The studies of magnetic field action onto cathode spot motion along the cathode surface have shown that for the optimal ratio of magnetic field induction and distance between the magnetic system and surface the cathode spot motion into the zone of maximal magnetic field is directly restricted. The field lines are over the cathode and have the shape of arcs with their ends resting on the cathode. The cathode spot moves inside such an arc in the region where the magnetic field component perpendicular to the cathode is equal to zero (arc top). The motion takes place perpendicular to the arc plane in the direction opposite the Ampere strength. The controlling action of the arc-configuration magnetic field on the cathode spot is observed for magnetic field induction over the cathode surface $B>5\cdot10^{-4}$ Tl. The magnetic system for creating a zone of restricted motion of cathode spots makes it possible to control the cathode surface to be treated.

For the pipe inner surface to be treated by vacuum-arc discharge within the range of small diameter 30-60 mm, an electrode system "pipe-inside-pipe" is realized (Fig. 1).

A system of magnetic confinement of the cathode spots for such configuration of the electrode system is created by constant magnets magnetized in the axis direction and located along the same axis to each other with like poles inside an elongated cylindrical cathode.

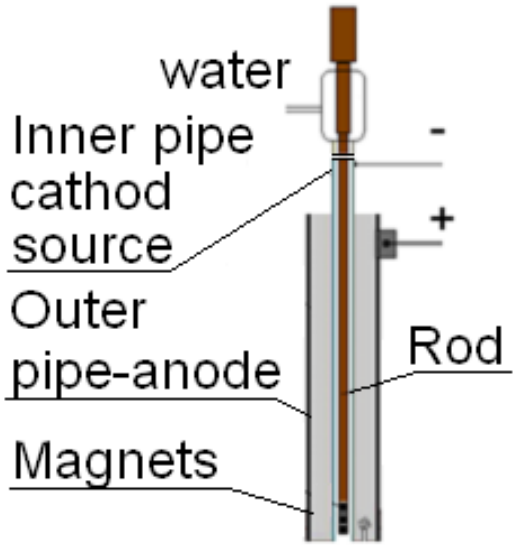


Fig. 1

Effective localization of the cathode spots by magnetic fields of two back-to-back solenoids or constant magnets is achieved by selecting a current in solenoids or constant magnets. The magnet system moving along the pipe inner surface scans the cathode spots on the outer surface of the cathode working zone. There is an arc-initiating electrode. Current is applied to the cathode-pipe at the pipe end and a product-pipe is an anode.

The magnetic cores located on the same axis between the magnets are used to strengthen the "arc" effect of the magnetic field. While arc burning both the magnetic field of the constant magnets and the magnetic field of the plasma and cathode current have an influence on cathode spot motion. The cathode spots move from the initiating electrode to current supply, having the two components of their motion – a lengthwise one in the direction of current supply (random) and an azimuthal one ensuring cathode spot rotation around the cathode axis under "arc" of the magnetic field system. To form an ion-plasma flow to be deposited on the inner surface of the outer pipe-product the magnetic system is displaced inside the cathode along the length of the product surface. A magnetic holder is shifted with a speed ensuring, on the one hand, effective containment of the cathode spots and, on the other one, homogeneous coat deposition and influence on the inner surface of pipe-product. To treat the pipes of average or large diameter it is possible to create a system of the back-to-back solenoid pairs placed along the whole length of pipe under treatment.

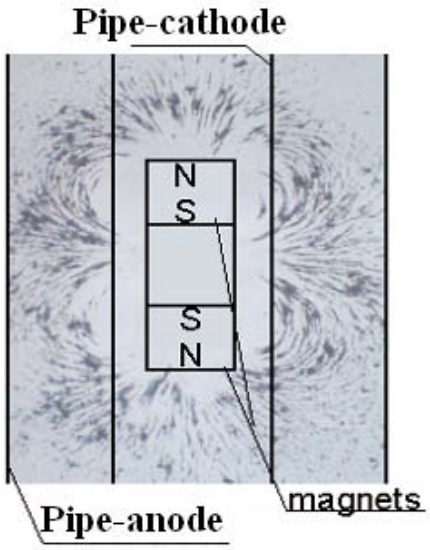


Fig. 2.

The computer programming of solenoid displacement will allow diverse variants of controlled cathode spot motion between the "arc" magnetic fields, for example a travelling wave. If the magnetic field length under the "arcs" is the same the cathode spots move from one zone into another provided that the neighboring magnets have the same value of magnetic field induction. However, a chaotic component of cathode spot motion in the regions between the trapping magnets causes some heterogeneity of the influence on the cathode surface.

The system of "arc" magnetic containment of the cathode spots and cathode surface scanning forms an intensive plasma flow for coat deposition or inner surface treatment of an external pipe (Fig. 2).

If the magnetic system is such that the vector of magnetic field induction along the length of the cathode working zone is in the plane perpendicular to the cathode axis the cathode spots move along the cathode from the initiating electrode to the opposite end in order and along a straight-line trajectory. This condition keeps the cathode spots from azimuth motion on the cathode surface.

When the magnetic field is applied an orthogonal component of magnetic field induction keeps the cathode spots from azimuth motion and a tangential one allows their lengthwise ordered motion along the straight-line trajectory.

Changes in orientation of the magnetic system relative to its axis and accordingly the cathode lead to cathode spot trajectory displacement on the cathode surface in accordance with the magnetic field pattern. For relatively small gradients of the electric field the charged particles of the plasma flow move along the magnetic lines of the outer magnetic field. Thus, the applied magnetic field specifies the direction of plasma flow motion over the cathode surface.

In any case the parameters and sizes of the magnetic system depend on a design of the vacuum-arc device and a required character of the cathode spot motion.

A design of the vacuum-arc device with the elongated cylindrical cathode 600 mm in length was developed and tested for pipes of 38 mm in diameter and 600 mm in length. Coat non-uniformity both in length and in outer side did not exceed several percents.

The experiments were carried on in the indicated electrode system in a pulse mode; the duration of vacuum-arc discharge was 1 s. It was shown that when the distance between the magnetic system axis and the cathode surface is increased the track length (L) of the cathode spots being formed on the cathode surface increases (Fig. 3). The magnetic induction values of the magnetic field on the cathode surface with distance from the magnetic system are given in Table. The magnetic induction values at B_1, B_2, B_3 of the cathode surface distant from the magnetic system are presented in Fig. 4.

Table

R (mm)	*B_1 (мTl)*	*B_2 (мTl)*	*B_3 (мTl)*	*L_{cp} (mm)*
7	0.20	0.35	0.40	6
10	0.15	0.23	0.25	9
15	0.14	0.20	0.17	15
17	0.13	0.175	0.15	20

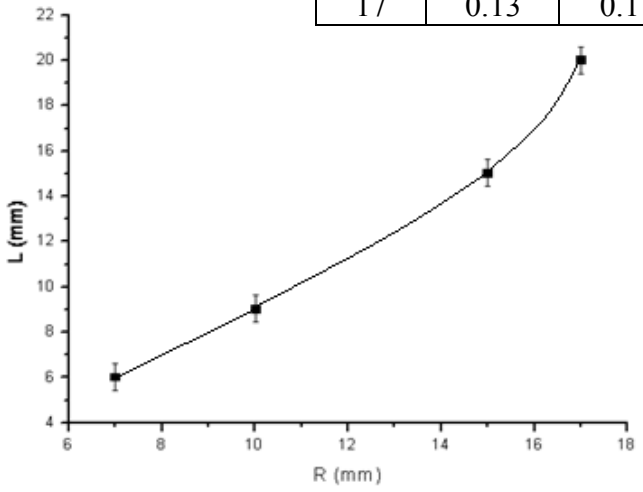


Fig.3

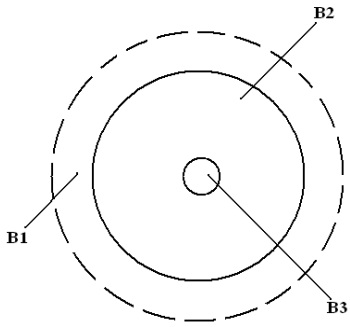


Fig.4.

3. Conclusion.

An original system of vacuum-arc cathode spot scanning on the cathode surface in a coaxial electrode system has been proposed. A magnetic field for cathode spot confinement and control on the outer surface of a cathode-pipe is created by two constant magnets magnetized in the axis direction, set coaxially relative to electrode and opposing to each other with like poles inside a cylindrical cathode. Cathode spot containment on the outer surface of the cylindrical cathode is realized by an “arc”-shaped magnetic field. The magnetic cores located between the magnets were used to enhance the “arc” features of the magnetic field. The magnetic field is oriented so that the induction vector components of the magnetic field are in the plane parallel to the cathode axis. A system of the two magnets with like poles along the cathode surface allows the cathode spots in the zone of “arc” magnetic field to be scanned on the cathode surface,

thereby ensuring plasma flow formation and cathode material deposition on the inner surface of pipe.

The proposed design of the vacuum-arc device with the elongated cylindrical cathode 600 mm in length was tested for cleaning and coat deposition on the inner surface of pipes of 38 mm in diameter and 600 mm in length. The coats have necessary density and the coat non-uniformity does not exceed 2-3 percents.

Reference

1. Vacuum arcs. Ed. J.Lafferty. Moscow, Mir, 1982, p.193.
2. Kesaev I.G. cathode processes of electric arc. Moscow, Nauka, 1968, p.244.
3. Dukhopelnikov D.V., Jukov A.V., Kostin A.A., Yurchenko A.A. Hardening Technologies and Coats, 2005, 11, 45-49.
4. Dukhopelnikov D.V., Jukov A.V., Kirillov D.V., Marakhtanov M.K. Izmeritelnaya tekhnika, 2005, 10, 42-44.

Figures:

Fig. 1. The electrode system for technological treatment of the inner surface of pipes with small diameter of about 30-60 mm by vacuum arc discharge

Fig. 2. The system of cathode spot scanning on the cathode surface

Fig. 3. The dependence of cathode spot track length on cathode-magnet distance

Fig. 4. The lines of magnetic induction in the magnetic system

Features of DC magnetron sputtering of mosaic copper-graphite targets

Valery Mitin[1], Yury Mankelevich[2], Alexander Pal[2], Tatyana Rakhimova[2], Alexey Ryabinkin[2], Alexander Serov[2], Alexey Mitin[3], Nikolay Krasnobaev[3]

[1]Naco technologies, Riga, Latvia; [2]SINP MSU, Moscow, Russian Federation; [3]VNIINM, Moscow, Russian Federation;

mitin2@mail.ru

At present materials researchers are tailoring desired properties and composition to receive new material with unique properties. Multi-element or composite materials form the cornerstone of present research activities [1, 2]. Most of multicomponent materials are fabricated as thin films by pulsed laser or magnetron sputter deposition techniques. Magnetron sputtering provides broader possibilities for complex materials engineering due to the spatial extent of the source and consequently greater area that can be homogeneously deposited. There are several possibilities to create the magnetron sputtered multicomponent coatings. First of all, a multi-source approach is widely used to deposit multi-element thin films [3]. Another way to create multicomponent thin films involves making changes at the target level. For this aim targets from an alloys [4, 5] or sintered powders [6] can be used. However, such targets have the disadvantage: their composition cannot be changed in a flexible way. Unlike them, segmented targets could easily create the necessary composition [7-10]. An alternative approach is the use of inserts. In this case, the holes drilled in the racetrack are filled with small cylindrical pieces. However the metal flux from the target can hardly be uniform. There are reasons for which sputtering of mosaic targets is problematic in reproducing the stoichiometry of a multi-element target material in the film. That is because removing a material is a ballistic process that considerably depends on many coupled processing parameters, such as the materials of target elements, the discharge power density, the target-substrate distance, the biasing voltage, the sputtering gas and the gas pressure, the electrode geometry [1]. The nonuniformity of target erosion due to the different sputter yield of the different segments should be taken into account for controlling a films composition by means of, for example, the Monte Carlo simulations [7].

It was meanwhile observed, that magnetron sputtering of metal-graphite mosaic targets after some initial transitional period resulted in an operational mode with equal erosion rates of metal and graphite elements [11]. The cause for equalization of sputtering rates of materials with highly different sputtering yields remains unclear. To clarify the problem we investigated the magnetron sputtering of the mosaic targets containing the materials with a considerably different sputtering yield, namely copper and carbon.

The Cu-C composite was chosen as a promising material. These two elements are immiscible, and therefore the composite can combine the high electrical conductivity of copper with the high characteristics of carbon, namely, a low coefficient of thermal expansion and good tribological properties. These alloys may be used in various applications from electrical contacts with friction to materials for confining plasma in nuclear fusion reactors.

The mosaic targets consisted of copper disks with cylindrical graphite inserts, placed in the racetrack region (Fig. 1). The relative area of the inserts S_{gr}/S was varied (S is the area of sputtering surface; S_{gr} is the area of the graphitic inserts). Single-component targets made with pure graphite and copper were used as well. The sputtering was performed at the discharge power density of P = 90 W/cm^2, the argon pressure of 4 mTorr, the target-substrate distance 60 mm. The time-average velocities of sputtering surface displacement of copper G_{cop} and graphite G_{gr} in the racetrack region were measured, as well as the volumes of sputtered copper V_{cop} and graphite V_{gr} and the corresponding values of discharge current I and voltage U. The structure and composition of the target after sputtering was examined with SEM having an EDX analyzer.

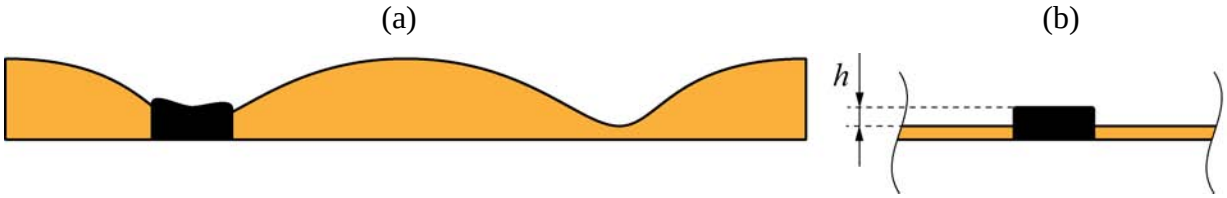


Fig. 1. Profiles of mosaic Cu-C target: radial profile (a), part of azimuth profile (b)

During about the first 60 min the values of G_{cop} and G_{gr} differed significantly, as a result the height drop h of about 1 mm between the graphite and copper surfaces was established. In the further sputtering these velocities equalized $G_{\text{cop}} = G_{\text{gr}} = G$ and the height h of the graphitic protrusion did not change during the process. The increase in the area of the graphite inserts resulted in the velocity G decrease at the same discharge power density.

Fig. 2 presents the dependencies of velocity G and of effective sputtering yield coefficients of copper Y(Cu) and graphite Y(C) sections on relative graphite surface area are presented. Effective sputtering yield coefficients Y(Cu) and Y(C) were obtained from experimental values of V_{cop} and V_{gr} and time- average ion currents on copper (I_{cop}) and graphitic (I_{gr}) parts of the sputtered target. The ion currents were corrected with allowance of ion-electron emission. When estimating the I_{cop} and I_{gr} it should to be taken into account that the ions are focussed to the nearest protruding surface by the electric fields in presheath and cathode layer. The ion path in the cathode layer is colissionless. With the cilindrical stub arised, the plasma potential distribution changes [12] and some part of the ion flow is redirected to graphite

protrusion. As a result the effective ion collection area S_{gr}^{eff} (and I_{gr} accordingly) can increase by 50% and more as compared with the geometrical area of the top of inserts, increasing the value of I_{gr}/I_{ion}. In deriving the ion current on I_{cop} and I_{gr} we took into account that centers of the graphite inserts were in the region of the maximal racetrack erosion, so the ion current density on the inserts was higher than the average one $j \approx I_{ion}/S$. The obtained values of Y(Cu) and Y(C) for various insert areas and discharge voltages are shown in Fig. 2. The value of Y(C), calculated from measured values of V_{gr} decreased significantly taking into account the ion flow redistribution. On the contrary, value of Y(Cu) increased and gave the growing dependence of Y(Cu) on the discharge voltage. But Y(C) is still remained 2.5–3 times larger than the measured effective sputtering yield of the pure graphite target.

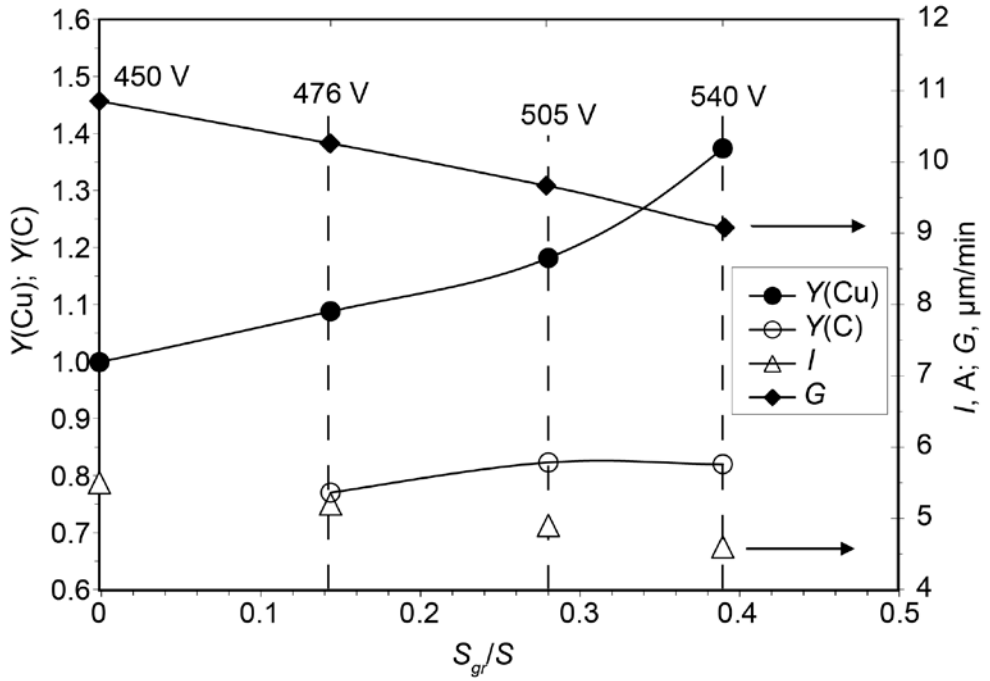


Fig. 2. The dependencies of velocity of sputtered mosaic target surface movement *G* and of effective sputtering yield coefficients Y (Cu) and Y(C) on relative graphite surface area.

SEM analysis of the sputtered target showed that sputtering surface of the inserts had an intricate micro relief. EDX analysis showed the presence of C, Cu and Ar in the sputtered graphite insert. In the regions without caverns the content of Cu was in the range of 5–12 at.%, Ar was 1–7 at.%. In the caverns the content of Cu was up to 100 at. % and Ar was up to 10 at.%. Thus during the high power sputtering the significant structure modification and composition change of target surface layer occurred. The estimation of a Cu ion fraction in the plasma n_{Cu} for our conditions and the calculation of the ion range in carbon with allowance the experimentally measured *G* value gave the relative concentration value of several percent for implanted Cu and

Ar near the surface of the carbon insert. These results give the reason to believe that during the sputtering an implantation of bombarding ions into the carbon insert and capture of the atoms (Ar and Cu) occurred. The change in the surface composition, produced by the implanted heavy inert gas atoms, has minor effects on sputtering yield because of relatively large size of these atoms. It is known that heavy atoms of high density impurities significantly increase the sputtering yield of light component by increasing the fraction of energy loss in the surface layers of the lattice [13,14**]**. According to our SRIM calculation, addition of 4–6 % of Cu atoms increases *Y*(C) by 60–90 %, and only by 15 % in case of Ar atoms impurities.

Obviously the content of copper in graphite inserts should increase with the growth of n_{Cu} and the Cu ion energy. This explains the observed relationship of the equalization of sputtering rates with the discharge power enhancement.

Thus the reasons described above are as follows: the ion flow redistribution due to graphitic insets protruding above the copper surface and the graphite sputtering yield increase due to Cu and Ar implantation can explain the effect of sputtering rate equalization for mosaic copper-graphite targets. The equalization of velocities because of ion flow redistributions should occur at sputtering of mosaic targets with small inserts of any composition.

The work was supported by RFBR grant #12-02-01177.

[1]. P.R. Willmott, Progress in Surface Science **76** (2004) 163–217.

[2]. A.D. Pogrebnyak, A.P. Shpak, N.A. Azarenkov, V.M. Bereszhnev, 2009 Phys.-Usp. **52** 29.

[3].D. Depla, W.P. Leroy, Thin Solid Films (2012), doi: 10.1016/j.tsf.2012.06.032

[4]. D.V. Shtansky et al, Int. J. of Refractory Metals & Hard Materials **28** (2010) 32–39.

[5]. Y.H. Liu, T. Fujita, A. Hirata et al., Intermetallics **21** (2012) 105-114.

[6]. S.K. Mishraet al, S & Coatings Technology (2012), doi: 10.1016/j.surfcoat.2012.03.047.

[7]. V. Abhilash, M. A. Sumesh and S. Mohan, Smart Mater. Struct. **14** (2005) S323–S328

[8]. A.A. Onoprienko et al., Surface & Coatings Technology **205** (2011) 5068–5072.

[9]. V.S. Vidyarthi, G. Suchaneck et al., Thin Solid Films **518** (2010) 4106–4112.

[10]. V. Dolique, A.-L. Thomann, P. Brault, Y.Tessier, P. Gillon,
Surface & Coatings Technology **204** (2010) 1989–1992.

[11]. S.A. Shiryaev, M.V.Atamanovet al., Technical Physics, 47 (2002), 238-243

[12]. Geha S.G., Carlile R.N., O'Hanlon J.F., and G. S. Selwyn // J. Appl. Phys. 1992. **72**, 374.

[13]. Behrisch R., Eckstein W. (Eds.) // Sputtering by particle bombardment. Berlin–Heidelberg–New York: Springer-Verlag: 2007.

[14]. Berg S. and I.V. Katardjiev // J. Vac. Sci. Technol. A. 1999. **17**, 1916.

Sn Thin Film Deposition using a Hot Refractory Anode Vacuum Arc

I. I. Beilis, Y. Koulik and R. L. Boxman

Electrical Discharge and Plasma Laboratory, School of Electrical Engineering, Faculty of Engineering,

Tel Aviv University, P.O.B. 39040, Tel Aviv 69978, Israel, beilis@eng.tau.ac.il

***Abstract*- A Hot Refractory Anode Vacuum Arc (HRAVA) starts as cathodic arc, heating the anode and depositing on it cathode material. When the anode is hot, all deposited cathode material is re-evaporated from the anode forming cleaner radially expanding plasma. It was shown that the rate of deposition reached 2-3 μm/min with significantly reduced macroparticle contamination in Sn films produced by HRAVA with current *I*=60–175 A and duration up to 180 s.**

I. INTRODUCTION

Sn thin film deposition is important in coating applications. Bimetallic Cu-Sn thin films are use in bonding components in many electrical and electronic devices to Cu conductors [1]. Bimetallic Cu-Sn thin films were prepared by consecutively depositing 560 nm of Cu and either 200 or 500 nm of Sn by e-beam evaporation onto 2.54 cm diameter fused quartz disks at a rate of ~0.5 nm/s [1]. Electroplating was used to deposit thin Sn films on copper substrates [2]. Sn thin films are needed for the anode layer of thin film Li-ion batteries due to its higher Li storage capacity in comparison than graphite anodes. Nimisha *et al* [3] fabricated Sn thin films by rf sputtering. The substrate to target distance was maintained at 5 cm with a deposition rate of 1 nm/s. Traditional deposition techniques, such as chemical vapor deposition (CVD), or pulsed laser deposition (PLD) are costly and have low-throughput.

The conventional vacuum arc plasma jet is also used for depositing coatings [4] which is related to the physical vapor deposition (PVD) techniques. The main problem with it is the generation of macroparticles (MPs) at the cathode. The Hot Refractory Anode Vacuum Arc (HRAVA) was proposed in last decade as a thin film deposition technique which produces MP-free coatings [5]. The HRAVA initially operates as a conventional cathodic vacuum arc and the cathode spot plasma jets deposit cathode material, including MPs, on a refractory anode surface while simultaneously heating the anode. When the anode reaches a sufficiently high temperature (~2000K) the previous coating and impinging cathode material from the plasma jets are re-evaporated or reflected from the hot anode. Also MPs are evaporated in the inter-electrode gap plasma. The HRAVA forms MP-free anode plasma which expands radially and can be used for depositing metallic coatings [5].

The HRAVA phenomena and deposition characteristics were investigated previously for thin film materials such Cu, Ti, Cr, Al and Zn [6,7]. Deposition rates of 1-3 μm/min were obtained with arc current in the 150-300A range.

However Sn deposition was only tested briefly [7] demonstrating relatively large rate of deposition. The details of very low melting Sn film characteristic were not investigated previously. The objective of the present work is to explicit the Sn film time evolution thickness, rate of deposition and MP contamination for different arc currents.

II. EXPERIMENTAL SETUP

Vacuum Chamber and Electrodes. A cylindrical vacuum chamber (400 mm length, 160 mm diameter), as shown schematically in **Fig. 1** was used for the experiments. The chamber was evacuated by an oil diffusion pump to 1.3×10^{-2} Pa.

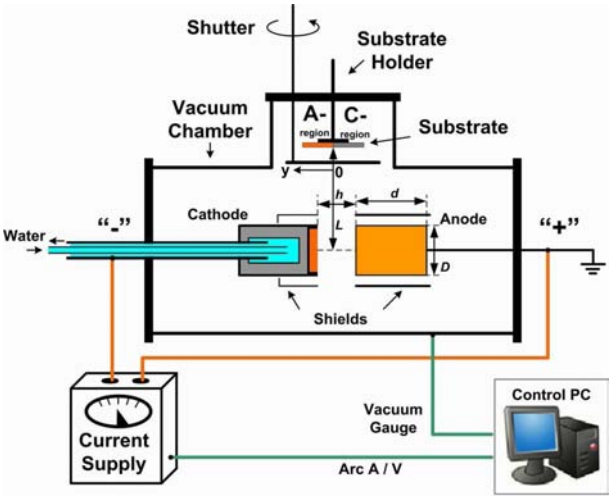


Fig. 1. Schematic diagram of the chamber, cathode-anode assembly and the substrate position with A and C regions.

During the arc, the pressure in the chamber was 5.3×10^{-2} Pa. The arc was sustained between a water-cooled Cu cup cathode filled with Sn, and a non-consumable cylindrical anode, for time

periods up to 180 s, operating with a current I=60-175 A. The Sn cathodes had a D=30 or 60 mm diameter and d=10 mm thickness.

The 30 mm diameter cathode was used with two graphite anodes, with d=9, 15 mm and D=32 mm and with gap h=10 mm. The 60 mm cathode was used with a W anode with d=10 mm, D=60 mm and h=10 and 15 mm. A D=70 mm stainless steel cylindrical radiation shield surrounded the graphite anode to reduce radiative heat loss during deposition. The W anode was used without a radiation shield. The anodes were supported by a thin tungsten rod that also connected it to the electrical circuit. The D=30 mm cathode was surrounded by a square boron nitride box-shaped shield with 65 mm sides; the cathode was recessed 3 mm behind the shield. The D=60 mm cathode was used with the boron nitride flat plte shield positioned between cathode and substrate and the cathode recessed 7 or 10 mm behind the shield for the h=15 mm case, while for the h=10 mm case no cathode shield used. The purpose of above shields was to block MP flux originating at the cathode from reaching a portion of substrate, designated the *A-region* (**Fig. 1**, see also below). The arc current was supplied by a welding power supply (Miller XMT-400 CC/CV). The anode was grounded and the chamber was floating.

Substrate preparation. The substrates were 75x25 mm glass microscope slides. The substrates were pre-cleaned by liquid detergent and water, and were then soaked in alcohol. A substrate was mounted on a holder which was movable in the radial direction, and was positioned at a distances of L=110 and 125 mm from the electrode axis (95 mm from cathode edge), facing the plasma flux emanating from the inter-electrode gap. The holder was separated from the arc plasma by a shutter which controlled the deposition onset and duration (15 s).

Coating characterization. As observed previously [5,6] the cathode shield position determined the location of a boundary between regions on the substrate with low and high MP contamination, designated as the anodic (*A*) and cathodic (*C*) regions, respectively (**Fig. 1**) [6]. The *C-region* faced the cathode and contained MPs emitted from the spots. The *A-region* faced the anode and collected anode plasma that was almost free of MPs. The MPs and deposited films in the *A-region* (about 3-5 mm from the *A-C* boundary) were characterized. The MPs were counted using an optical microscope and a digital camera, which could detect MP's larger than approximately 1-3 µm. The MP density was determined by counting the number of MPs per mm^2. The thickness was measured by profilometry of films deposited on substrates exposed to the plasma for 15 s when the shutter was open, beginning at various times from arc ignition. The deposition rate (V_{dep}) was determined as the ratio of the film thickness on the glass substrate to the exposure time. The cathode erosion rate was measured by weighing the cathode before and after arcing.

III. RESULTS AND DISCUSSION

A. Deposition Rate

Fig. 2 presents the measured Sn deposition rate dependence on time beginning from arc ignition, with I as a parameter, using a D=60 mm cathode, W anode, h=10 mm and without a cathode shield. It can be seen that V_{dep} increased with time in studied range of all arc currents. For I<100 A the V_{dep} increase was very weak, while for larger arc currents the V_{dep} increase was very significant.

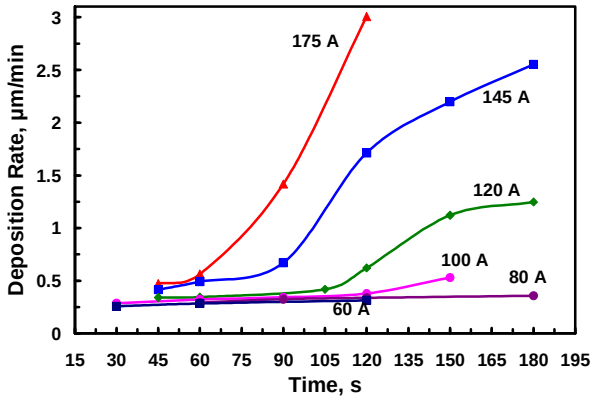


Fig. 2. Time-dependent rate of Sn film deposition, D=60 mm cathode without shield, d=10 mm W anode, h=10 mm, L=125 mm.

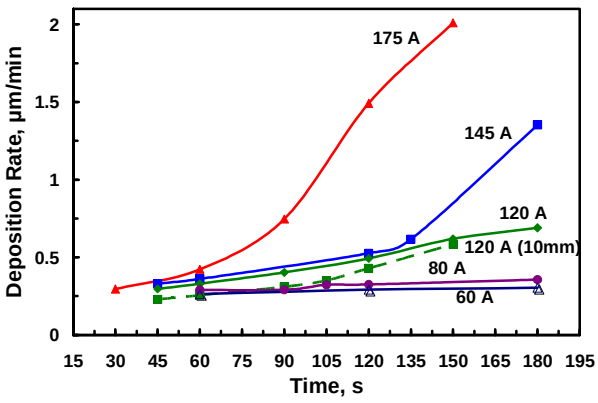


Fig. 3. Time-dependent rate of Sn film deposition, D=60 mm cathode recessed 7 mm behind shield, d=10 mm W anode, h=15 mm, L=125 mm. (The cathode recessed 10 mm behind the shield is also shown for I=120 A).

Thus, V_{dep} increased from 0.5 to 3 µm/min when the arc time increased from 45 to 105 s for I=175 A, while for I=80 A the V_{dep} was approximately constant in time.

The time dependent deposition rate for a

D=60 mm cathode with a BN cathode shield protruding for 7 mm above the cathode, W anode, and *h*=15 mm is presented in **Fig. 3**. In this case V_{dep} also increased for all investigated *I* but was lower than in the previous case without a cathode shield (V_{dep} increased from 0.3 to 2 μm/min for *I*=175 A). The case with the cathode shield protruding 10 mm above the cathode is also shown in **Fig. 3** for *I*=120 A and the deposition rate was slightly lower than for the case with the shield protruding 7 mm (~0.58 and ~0.62 μm/min respectively at 150 s).

The time dependent deposition rates for a *D*=30 mm cathode and *d*=9 and 15 mm graphite anodes are presented in **Figs. 4** and **5** respectively.

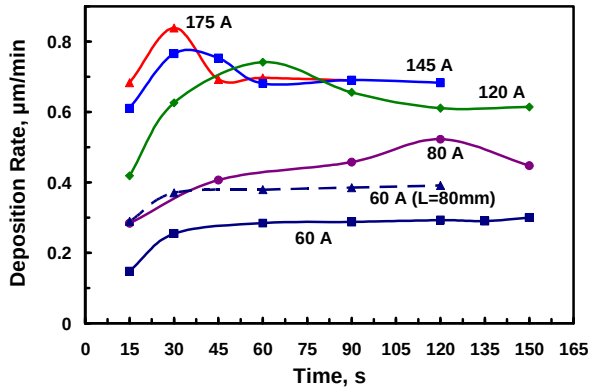


Fig. 4. Time-dependent rate of Sn film deposition, *D*=30 mm cathode recessed 3 mm behind box shield, *d*=9 mm graphite anode, *h*=10 mm, *L*=110 mm. (The case for *L*=80 mm is also shown for *I*=60 A).

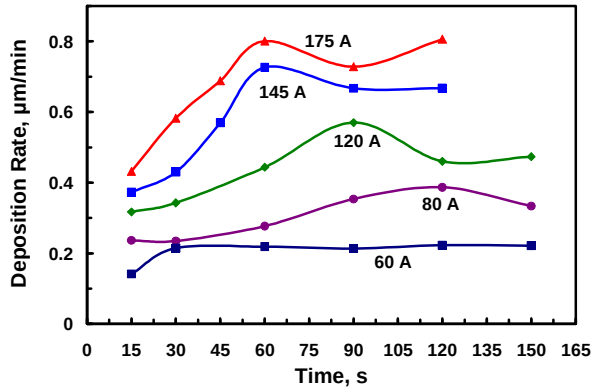


Fig. 5. Time-dependent rate of Sn film deposition, *D*=30 mm cathode recessed 3 mm behind box shield, *d*=15 mm graphite anode, *h*=10 mm, *L*=110 mm.

The BN cathode shield protruded 3 mm above the cathode and *h*=10 mm. It can be seen that V_{dep} increased with time to a peak (for *I*>80 A), and then decreased to a steady-state value. The peak value depended on the current (with *d*=9 mm, 0.74 and 0.84 μm/min for *I*=120 and 175 A respectively,) and the peak time decreased with *I* (from 60 to 30 s for *I*=120 and 175 A respectively, *d*=9 mm). At steady state with *d*=9 mm, V_{dep} increased from 0.3 to 0.7 μm/min with increasing arc current from 60 to 175 A respectively. The deposition rate for the thicker anode (*d*=15 mm) had peaks for same arc currents (**Fig. 5**) but the peaks occurred much later (90 and 60 s for *I*=120 and 175 A respectively) and the peak was wider than with the *d*=9 mm anode.

Also V_{dep} at the peak for *d*=15 mm was lower than with the *d*=9 mm anode (0.57 and 0.80 μm/min for *I*=120 and 175 A respectively, *d*=15 mm).

A V_{dep} peak was not observed with *D*=60 mm for all arc currents and was observed for smaller *D*=30 mm cathode only for *I*>80 A. Its value increased with *I* and the time appearance depended on *d*.

The observed effects can be understood, firstly, taking into account that in the HRAVA the anode heating decreased with *d* and increases with *I* [8]. Secondly, the relatively large MP production from Sn cathode spots should be noted. The measured total cathode erosion rate for Sn (~300 μg/C) with *I*=100 A, where the main part of the Sn erosion was in MP form (~200 μg/C) [4].

The reason for the peak in V_{dep} is the initial condensation of large amounts of MPs and cathode plasma on the cold anode surface. During arcing the anode is heated, and the condensed material (including MPs) was evaporated from the anode when it reached an appropriate temperature.

During the V_{dep} peak, the rate of deposition was determined by the vapor produced by the cathode spots plus the vapor generated by the evaporation of previously condensed MPs and plasma reaching the anode. Later, when the anode was sufficiently hot, and all of the condensed material on the anode completely evaporated, the lower steady state level of V_{dep} was determined by the cathode plasma jets products re-evaporated and reflected from the hot anode.

The rate of anode temperature increasing influences the rate of material evaporation from the anode. For relatively large *I* and small *D* the anode was quickly heated and therefore the vaporization was contributed stronger quickly increasing in time the anode plasma density in time and as result the V_{dep} peak appeared.

In contrast, for small *I* and large *D* the anode heating rate is weaker and therefore V_{dep} increased monotonically. As the transitory heating time is larger using thicker anodes, the V_{dep} peak for *d*=15 mm appeared later than for *d*=9 mm. Thus this result indicates when the steady-state process appeared that preferable using for engineer applications.

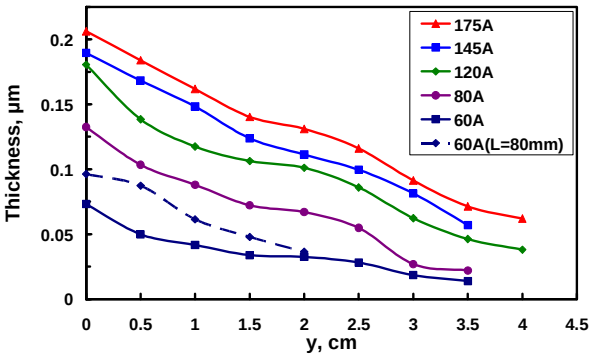


Fig. 6. Sn film thickness distribution in the A-region of the substrate in the y-direction from the A–C boundary with arc current *I* as a parameter. *D*=30 mm cathode recessed 3 mm behind box shield, *d*=9 mm graphite anode, *h*=10 mm, *L*=110 mm. (The case for *L*=80 mm is also shown for *I*=60 A).

B. Film Thickness Distribution

Fig. 6 shows the Sn film thickness distribution on the substrate in *y-direction* (parallel with the electrode axis - see **Fig. 1**), in the *A-region* (y=0 is at the *A-C boundary*) with arc current as parameter. It can be seen that the film thickness decreased with *y* in the measured range of *I* and it reached about half at *y*=2-3 cm, depending on *I*. The thickness increased with *I* relatively weaker from 120 to175 A than from 60 to 120 A.

C. MP Contamination

The MP density as a function of *I* is presented in **Fig. 7** for Sn (60 and 30 mm diameter cathodes). For comparison previously measured MP density for Al, Zn, Cu, Cr cathodes [6,9] are also presented. The substrates were exposed for 15 s after 60 s of arcing, *L*=110 mm, *h*=10 mm. The MP density for Sn is larger than for other volatile materials like Al, Zn, and increases with *I* up to 80 A, and then decreased with further increasing of *I*. The MP density for intermediate materials like Cu, Cr was significantly lower than for Sn.

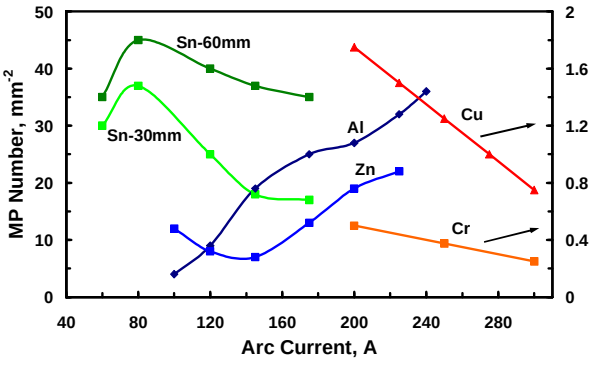


Fig. 7. Dependence of MP density on arc current for Sn (measured here), Zn and Al (left axis) and for Cu, Cr (right axis) [6,9], recessed cathodes. The substrate was exposed after 60 s for 15 s, *L*=110 mm.

Due to large difference between the very low Sn melting temperature (T_m=232C) and relatively large Sn boiling point (T_b=2687C) there is a relatively large MP fraction in the Sn cathode erosion. This fact explains the large MP contamination detected in Sn films, compared to Cu, Ti, and also to Al, Zn (*I*<150 A) for which the difference between T_m and T_b is significantly lower [9].

IV. CONCLUSIONS

1. Sn films were successfully deposited on glass substrates using HRAVA with different electrode geometries and currents.

2. V_{dep}(t) had a peak with a *D*=30 mm electrode pair and *I*>80 A, while for *D*=60 mm electrode pairs $V_{dep}(t)$ was monotonic. The peak was higher at higher current. For thicker anodes, the peak appeared at later times.

3. V_{dep} is significantly larger for larger *D* when *I*≥120 A (see Fig2 and Fig.4), due to stronger evaporation of the MPs at relatively high *I*. For this case, MP contamination decreased with *I*. Thus, V_{dep} with *D*=60 mm electrodes exceeded this rate for *D*=30 mm electrodes by a factor 2.5 (*I*=145 A, 120s, see Fig2 and Fig.4).

REFERENCES

[1] K.N. Tu and R.D. Thompson, Acta metall., **30** (1982). 947.

[2] M. Inaba, T. Uno, A. Tasaka, Journal of Power Sources **146** (2005) 473.

[3] C.S. Nimisha, G. Venkatesh, K. Yellareswara Rao, G. Mohan Rao, N. Munichandraiah, Materials Research Bulletin **47** (2012) 1950.

[4] Handbook of Vacuum Arc Science and Technology. edited by R.L. Boxman, P. Martin, D. Sanders (Noyes Publishing, Ridge Park NJ, 1995).

[5] I.I. Beilis, S. Goldsmith, R.L. Boxman, Surf. Coat. Technol., **91** (2000) 133-134.

[6] I.I. Beilis, R.L Boxman, Surf. Coat. Technol., **204** (2009), 865.

[7] I.I. Beilis, Y. Koulik, R.L. Boxman and D. Arbilly, J Mater Sci, **45** (N23) (2010) 6325.

[8] I.I. Beilis, Y. Koulik, R.L. Boxman, IEEE Trans. Plasma Sci., **39** (N6, Part 1) (2011) 1303.

[9] I.I. Beilis, Y. Koulik, R.L. Boxman and D. Arbilly, Surf. Coat. Technol., **205** (2010) 2369.

Hydrophilization treatment of polyimide using Ar-O_2 mixtue gas surface wave plasma

Oxygen radical density and plasma parameter dependence

Yoshinari Hirukawa, Shigeru Ono,Suzuki Syuichi
Tokyo City University
1-28-1 Tamatsutsumi,Setagaya-ku
Tokyo, Japan
Tel/Fax: +81-3-5707-2213, E-mail: s-ono@tcu.ac.jp

The hydrophilization treatment of polyimide is important in various applications. This paper has described the experimental research findings which explore what the parameter with large effect in the plasma treatment of polyimide is. The low pressure surface wave plasma of the argon oxygen mixed gas which can expect large homogeneity spatially was used for the experiment. The plasma state was measured by the electrostatic probe. The oxygen radical expected to be active species important for surface treatment was measured by the catalyst probe. It turned out that it depends for the water contact angle on the surface of polyimide by which plasma treatment was carried out in an oxygen radical density strongly.

Keywords-Surface wave plasma; Surface modification; Polyimide; O radical; Electron temperature; Electron density

1. INTRODUCTION

Flexible printed circuit board (FPC) is well known for wiring of electric devices, such as a cell phone and a personal computer. FPC consists of metal layer and polyimide. Polyimide has superior characteristics. So Polyimide is broadly used as base material of FPC or insulating material for electrical devices.[1,2] Process of making up FPC includes forming conductive layer on surface of polyimide. Before forming conductive layer, preliminary treatment is necessary so that give hydrophilic property to surface of polyimide.[3] As of today, chemical processing has generally used. But chemical processing has some issues including influence to environment or forming rough surface. Therefor plasma processing attracts attention.[4,5,6] Plasma processing has some advantages. First, it has no influence to environment. Second, it takes short time. Third, it doesn't roughen the surface of polyimide. The mechanism of increasing hydrophilic property caused by plasma treatment seems that functioning group including O is formed on surface of substance. So it seems that O radical in plasma contributes considerably to increasing hydrophilic property. There are many researches of the surface modification of plastic material using plasma. However there is almost no research of surface modification using surface wave plasma. Therefore we decide to conduct research using surface wave plasma. Surface wave plasma has wide processing area. But plasma parameter varies rapidly with distance from plate.

From the above, the purpose is that we investigate fundamental characteristics and look for optimum condition in surface modification of polyimide using surface wave plasma. In addition, we pay attention to plasma parameter and O radical density.

2. EXPERIMENTAL SETUP

2.1 Surface Wave Plasma Apparatus

Apparatus of generating plasma consists mainly of wave guide, microwave source and vacuum chamber. Vacuum chamber is 200mm in inner diameter and 220mm in height. Vacuum chamber has four ports for gas inflow and exhausting and pressure measurement. Pressure in chamber is evacuated with vacuum-pump. Since microwave is supplied to slot antenna on bottom of the chamber, surface wave plasma is generated.

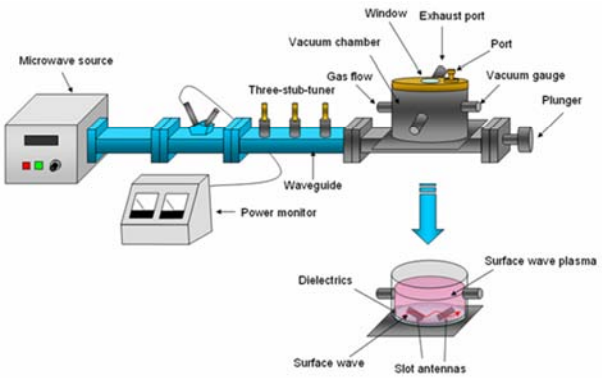


Fig.1 Surface wave plasma apparatus

2.2 Langmuir Probe Method[7,8,9]

We conducted plasma parameter measurement using Langmuir probe. Electron temperature, electron density and electron energy distribution function is derived from current-voltage characteristics. Figure2 shows schematic diagram of Langmuir probe measurement circuit.

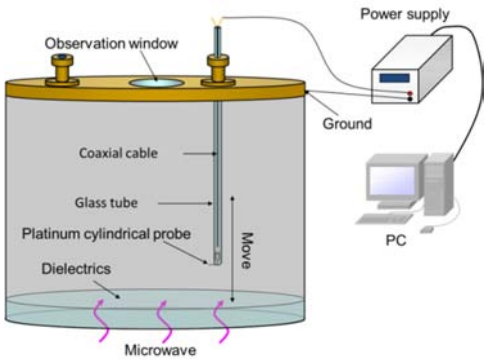


Fig.2 Langmuir probe measurement setup

2.3 Contact Angle Measurement

Hydrophilic property given by plasma treatment is evaluated with contact angle measurement. Figure3 shows an example of reduction of contact angel θ .

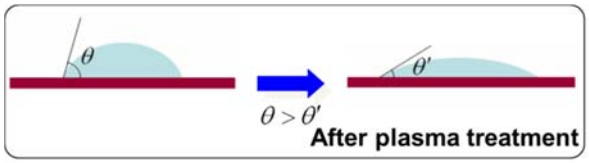


Fig.3 Solid surface and contact angle

2.4 O Radical Density Measurement Using Platinum Catalytic Probe[10]

It seems that O radical in the plasma contributes considerably to increasing hydrophilic property. When platinum is immersed in the plasma, O_2 is adsorbed on surface of platinum by dissociative adsorption. And then O radical recombines with O atom on the surface and desorbs. When it recombines to form oxygen molecule, they supplies 5.12eV to platinum. This catalytic reaction occurs considerably when temperature of platinum surface is from 800K to 900K. Figure4 shows principle of O radical density measurement of electric current heating catalytic probe.

It turns on electricity to a thin platinum wire, and heats to the temperature (800-900K) from which a catalytic reaction occurs actively. Let supply energy by turning on electricity is Energy A. Excess energy will be given to platinum if oxygen radical recombines on the platinum surface. Here, let energy which platinum was given is Energy C. The supply energy of the power source is adjusted so that the temperature of the platinum wire may become constant. The difference of the supply energy from the power source by the existence of oxygen radical is the supply energy of oxygen radical. If it thinks that oxygen radical reaches a platinum wire by thermal motion, oxygen radical density can be estimated.

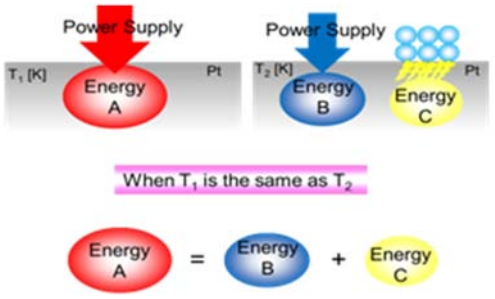


Figure.4 Principle of oxygen radical density measurement

3. RESULTS AND DISCUSSION

3.1 Plasma Parameter

Figure5 shows results of electron temperature Te and electron density Ne measurement. Experimental condition is that flow rate of Ar is 100ml/min, flow rate of O_2 is 10ml/min, power is 300W, pressures are 47Pa and140Pa. From fig.5, it found that excitation caused by surface wave occurs in a distance up to 2cm. In the position distant from the dielectrics plate, the value of the electron density in 47Pa is the value of this about 10 times in 140Pa. Figure 6 shows electron energy distribution function. Figure 6 shows that the electron with larger energy than 5.12eV exists in a range with a distance of less than 2cm.

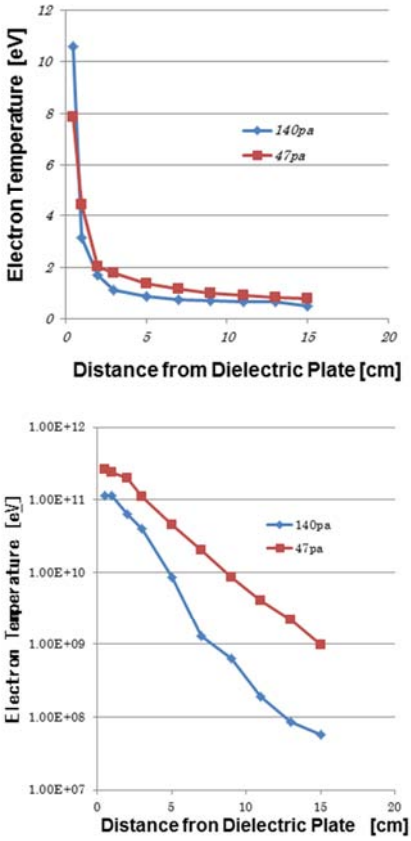


Fig.5 Variation of electron temperature (a) and electron density (b)

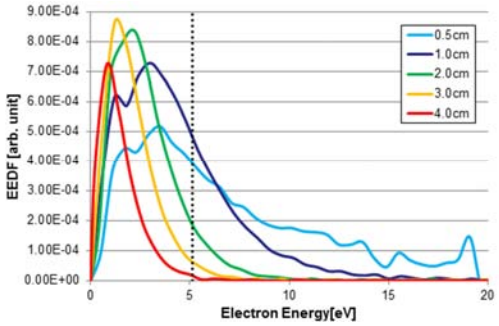


Fig.6 Electron energy distribution function

3.2 O Radical Density

Figure7 shows results of O radical density measurement. Although it seems that an oxygen radical in generated only near the dielectric plate, it turns out that the oxygen radical is diffused to a distant place as shown in fig.7. That is, the spatial distribution of the plasma differs from radical spatial distribution greatly. On condition of this experiment, the oxygen radical density in which the result of 140Pa of the result of 47Pa is also almost the same is shown.

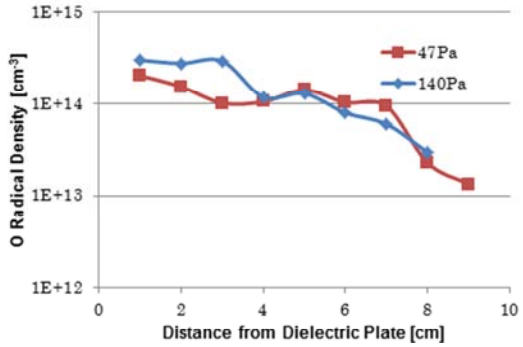


Fig7. Distance dependence of O radical density measurement

3.3 Contact angle measurement

Figure8 shows results of contact angle measurement. Generally for electroless plating, it is thought that the water contact angle of 30 degree or less is desirable. A less than 10cm region fulfills this condition from the dielectrics plate. As shown in Fig. 5, in the case of 140Pa, and the case of 47Pa, electron density differs greatly. However, both water contact angles show the value almost same as a case. On the other hand, as compared with the measurement result of the oxygen radical shown in Fig. 7, it turns out that it depends for the water angle of contact in oxygen radical density strongly.

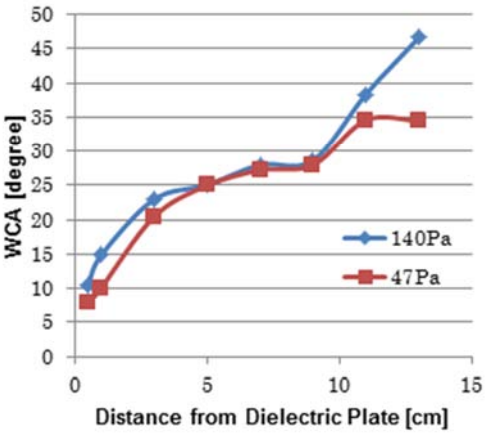


Fig.8 Results of contact angle measurement

4. SUMMARY

In this research, we conducted plasma parameter measurement of Ar-O_2 surface wave plasma, O radical density measurement, and contact angle measurement. We also evaluate hydrophilic property of polyimide surface given by plasma treatment. It found that O_2 dissociation caused by surface wave occurs in a distance up to 2cm. However O radical density distribute to more far area. Rapid lowering of the temperature and the density of the plasma is observed in the location distant from the dielectric plate in the surface wave plasma. However, hydrophilization treatment was enough performed in the considerably distant location. The reason is because the spatial distribution of the oxygen radical is larger than the spatial distribution of the plasma enough. There fact because clear from measurement of the radical density by the catalytic probe.

5. REFERENCES

1. Jiangnan Lai, et al: “Study on hydrophilicity of polymer surfacesimproved by plasma treatment”, Applied Surface Science 252 3375-3379 (2006)
2. Akihiro Uemura, Tomoya Tanabe, Satoru Iwamori: “Effect of Sputtering Condition on Thin Films Deposited by r.f. Sputtering with a Polyimide Target”, IEEJ Trans. FM, Vol.130, No.2,2010
3. Syuichi Ogasawara, “material of printed circuits and surface treatment technique” in Japanese, surface technology, Vol46, No.3, p.210-214, 1995
4. Shohei Ikari, Shuichi Ishida, Takashi Matsuoka, Tomoko Hirayama, Kiyotaka Kato : “Effect of Oxygen Plasma Treatment on Adhesionn of Copper Plating Film to Polyimide Film for Flexible Printed Circuits”, Journal of the Society of Materials Science,Japan, Vol.59, No9,pp.705-711, Sep.2010
5. Cheng Cheng, Zhang Liye, Ru-Juan Zhan: “Surface modification of polymer fibre by the new atmospheric pressure cold plasma jet”, Surface & Coatings Technology 200 6659-6665 (2006)

6. Atsushi Yokotani, “Surface modification technology of the plastic by vacuum ultraviolet rays” in Japanese, Comber tech, No.421, p.110-113, Apr.2008
7. Shinriki Teii, “Plasma fundamental engineering” in Japanese, Uchidarokakuho
8. The Japan Society of Plasma Science and Nuclear Fusion Research, “Generation and diagnosis of plasma” in Japanese, Koronasya
9. Hideo Sugai, “Electron energy distribution function and radical composition” in Japanese, The Japan Society of Plasma Science and Nuclear Fusion Research, Vol.77, No.7,p.660-665
10. Nobuyuki Haraki, Saiensu Nakao, Shigeru Ono, Shinriki Teii: “ Oxygen radical density measurement in O2-N2 gas mixture plasma by means of a thin platinum wire ”, Electrical Engineering in Japan, Vol.149, No.4, p.14-20 (2004)

In-situ FTIR-ATR spectroscopic investigations of atmospheric-pressure plasma modification of polyolefin thin films – where are the primary amino groups?

Zohreh Khosravi, Alena Hinze, Claus-Peter Klages

Institut für Oberflächentechnik, Technische Universität Braunschweig, Bienroder Weg 53, 38108 Braunschweig, Germany

Abstract

Surface treatment of polyolefines by atmospheric-pressure dielectric barrier discharges (DBDs) in virtually oxygen-free nitrogen-containing gases was studied *in situ* by Fourier transform infrared spectroscopy in the attenuated total reflection mode (FTIR-ATR) in order to follow the plasma-chemical generation of chemical functional groups and their further temporal development in the presence of inert or reactive atmospheres.

Polyolefin thin films of thicknesses between 50 and 200 nm were prepared directly on ZnS ATR crystals by spin-coating from hot solutions of linear low-density polyethylene (LLDPE), low density polyethylene (LDPE), or polypropylene (PP) in hydrocarbons solvents like xylene or decalin. After the exposure to the afterglows of DBDs in N_2 or in mixtures of N_2 with H_2 or NH_3, infrared spectra were taken *in situ* under inert conditions and after controlled exposure to various reagents, resp., such as water vapor or oxygen. In order to unravel the complex spectra which are generally due to several functional groups with overlapping vibrational bands, exchange reactions with vapor of heavy water (D_2O) was applied in order to identify groups which are known to exhibit a rapid H/D exchange like >N=H (imine), -NH_2 (prim. amine), >NH (sec. amine), -CO-NRH (prim. or sec. amide), using characteristic ratios of wavenumber ratios for corresponding vibrational bands in the deuterated and the protonated moiety.

In addition, reactions of the plasma-treated surface with vapors of 4-(trifluoromethyl)-benzaldehyde (TFBA) or 4-(trifluoromethyl)phenyl isothiocyanate (TPI) were studied by FTIR-ATR *in situ*. Based on these experiments, tentative assignments of the observed vibration bands to imino, amino, and amido groups are made and interpreted in terms of feasible or probable chemical mechanisms.

Keywords: Dielectric barrier discharges, polymer surface modification, in situ, FTIR-ATR, derivatization

Introduction

Hollahan and Stafford in 1969 [1] and Courval et al. in 1976 [2] were probably the first to investigate the effects of low-pressure radio-frequency (RF) and atmospheric-pressure dielectric-barrier ("corona") discharges (DBD), resp., in nitrogen or nitrogen-containing gases on surfaces of polyethylene, polypropylene, and other polymers. In both cases the formation of amino groups on the polymer surfaces was inferred – either from the adsorption of negatively charged molecules to quaternary N sites formed by alkylation [1] or by the absorption of acidic dyes [2], resp. In later detailed XPS studies by Foerch et al. [3] and Gerenser [4], the presence of primary and secondary imino groups, C=N-H and C=N-R, on the freshly plasma-treated surface was detected, in parts undergoing hydrolysis upon contact with humid air according to the equations

$R\text{-}CH{=}N\text{-}H + H_2O \rightarrow R\text{-}CH{=}O + NH_3$ and
$R\text{-}CH{=}N\text{-}R' + H_2O \rightarrow R\text{-}CH{=}O + H_2N\text{-}R'$.

In the recent two decades many more papers were published about the plasma treatment of polymer surfaces in nitrogen-containing gas atmospheres. XPS analysis, frequently combined with chemical derivatization, has become a standard tool for characterization of the resulting surfaces. Everhart and Reilley had in 1991 [5] introduced derivatization with pentafluoro-benzaldehyde (PFB) to analyze nitrogen-plasma treated LDPE, assuming that PFB would react with "primary and secondary (!) amines and hydrazines but is not expected to react with amides, imines, nitriles, or nitrogen-containing heterocyclics". Fally et al. [6] used PFB and 4-(trifluoromethyl)benzaldehyde (TFBA) for "primary amine derivatization" to analyze plasma polymers obtained from primary amines as precursors[1]. In the recent years it has become standard to assume that TFBA reacts only with $-NH_2$ groups of plasma-modified surfaces.

From a chemical point of view this assumption cannot be justified. Quite generally aldehydes may react - among many others - with compounds containing nitrogen-hydrogen bonds [7] and in some cases the product of the first addition reaction, for example of a secondary amine (leading to a hemi-aminal), can be isolated:

$R\text{-}CHO + R'\text{-}NH\text{-}R'' \rightarrow R\text{-}CHOH\text{-}NR'R''$

In case of primary amines the subsequent elimination of H_2O generally furnishes secondary imines (aka Schiff bases or azomethines) as products. But aldehydes can also react with imines which are known to be a major product of plasma treatment of polymers in N-containing gases, see above. Aromatic aldehyde may react according to the following scheme, exchanging the aldehyde component of the aldimine [8]:

$Ar\text{-}CHO + R\text{-}CH{=}N\text{-}R' \rightarrow R\text{-}CHO + Ar\text{-}CH{=}N\text{-}R'$

The uncatalyzed exchange of amine and carbonyl components between imines under moderate conditions has recently gained considerable interest in the field of dynamic covalent chemistry (DCC) as one tool to generate combinatorial substance libraries [9].

Also primary imines $R\text{-}CH_2\text{-}CR'{=}N\text{-}H$ are expected to react with aldehydes because they are in equilibrium with an enamine:

$R\text{-}CH_2\text{-}CR'{=}N\text{-}H \Leftrightarrow R\text{-}CH_2{=}CR'\text{-}NH_2$, most probably forming an α,β-unsaturated imine:

$R\text{-}CH_2{=}CR'\text{-}NH_2 + Ar\text{-}CH{=}O \rightarrow R\text{-}CH_2{=}CR'\text{-}N{=}CH\text{-}Ar$

These considerations show that it is not unreasonable to expect a reaction with TFBA or another aromatic aldehyde also in case of nitrogen-plasma treated surfaces which are virtually free of $-NH_2$ groups - if only imine functionalities are present, for example.

In fact, in our experiments using *in situ* FTIR-ATR study of LDPE thin films during remote DBD plasma treatment with $N_2 + H_2$ we are so far unable to find the expected vibrations of primary amino groups and nevertheless we observe a reaction with TFBA, introducing the $4\text{-}C_6H_4\text{-}CF_3$ group to the films.

Experiments

The experimental setup is shown schematically in Figure 1: FTIR-ATR measurements were done on a Nicolet 5700 FT-IR spectrometer with series measurement capability, equipped with an MCT detector and a ZnS ATR crystal (length x height x width = 80 x 4 x 10 mm^3, θ = 45°, from *Korth Kristalle GmbH*, Hamburg, Germany,) using unpolarized light with 4 cm^{-1}

[1] The authors noted some reactivity of both aldehydes with secondary amino groups of model compounds.

spectral resolution. LDPE thin films with thicknesses between 50 and 200 nm were obtained by spin coating from hot solutions of purified LDPE (*Goodfellow GmbH*, Bad Nauheim, Germany) in decalin on the preheated ZnS crystal. Polymer purification was done by dissolution in hot xylene and precipitation in isopropanol.

The remote plasma treatment was achieved by a DBD reactor made from glass with an active volume of 70 x 50 x 1 mm^3, mounted beyond the ZnS crystal so that the gas flow (N_2 + 4% H_2) of typically 16 l/min STP could pass the discharge and reach the polymer surface within a few millisecond after leaving the plasma zone. Gases were purified by an ALPHAGAZ purifier from *Air Liquide*. The discharge was powered by a commercial generator 7010 R from *SOFTAL electronics GmbH*. The voltage and frequency were typically 25 kV (ignition voltage 13.0 kV) and between 20 and 30 kHz, respectively.

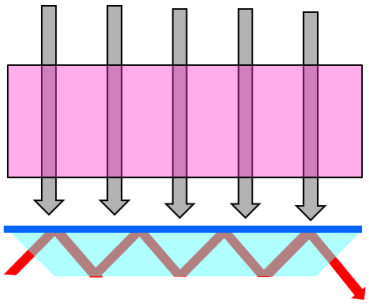


Figure 1. Schematic view of experimental setup: Light blue: ZnS crystal, dark blue: polymer film, violet: discharge zone, grey arrows: gas stream, red arrow: IR light.

First results and preliminary conclusions

The following three figures show the spectral changes observed (i) before, during, and after 30 s remote plasma treatment (Fig. 2, reference: untreated PE), (ii) after several consecutive H→D and D→H exchanges, resp. (Fig. 3, reference: spectrum S_H or S_D before exchange), and (ii) before (red) and after (black) 30 min reaction of the plasma-treated surface with TFBA vapor in N_2 and 20 min dry N_2 purge (Fig. 4, reference: untreated PE).

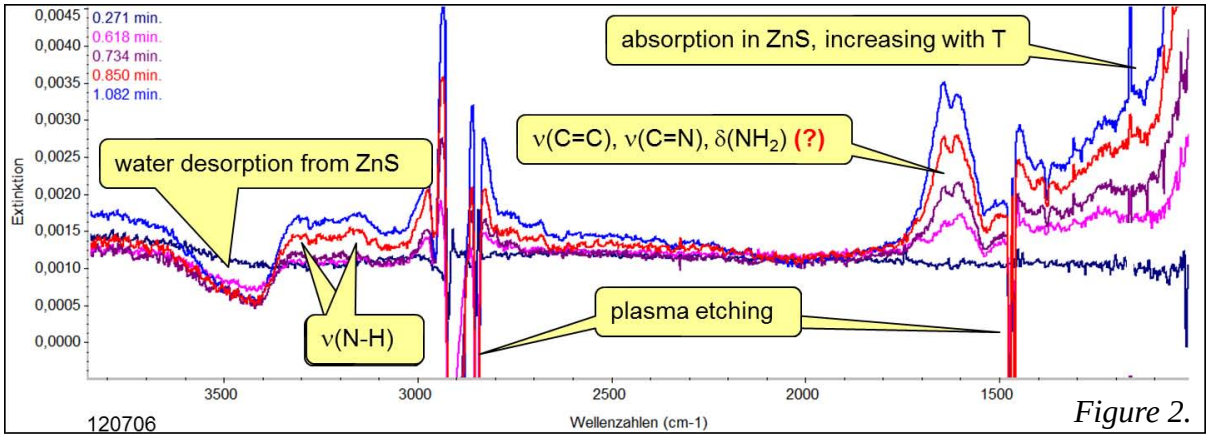


Figure 2.

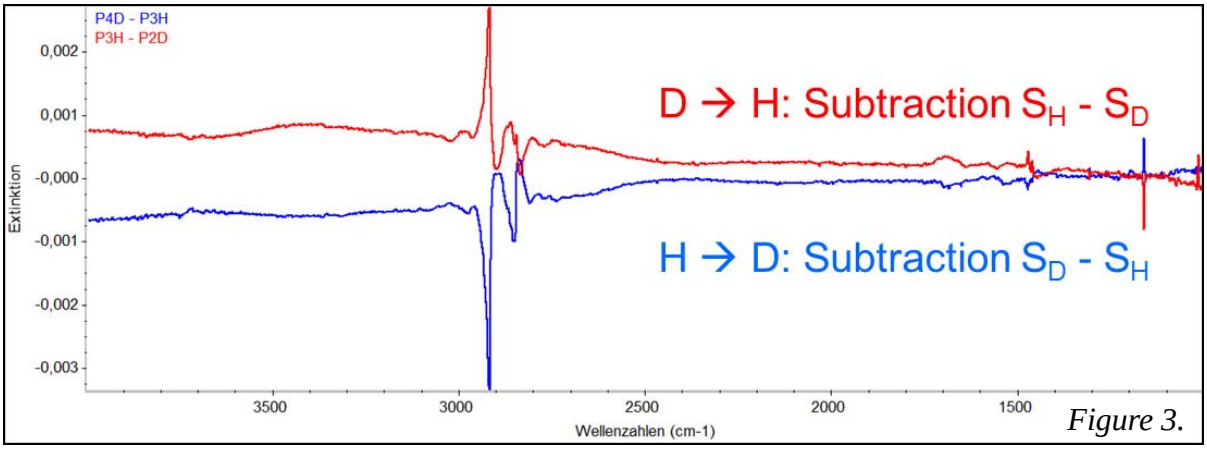


Figure 3.

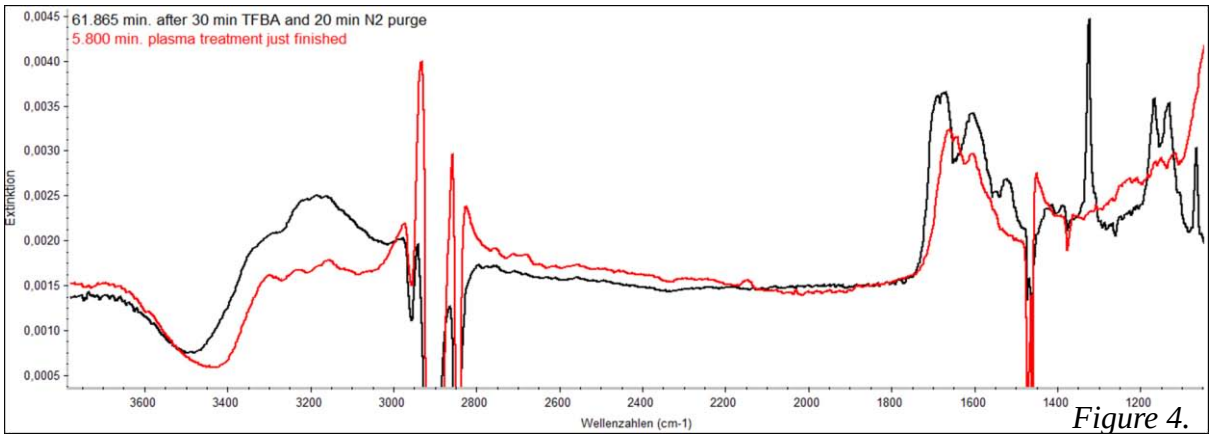


Figure 4.

The following observations can be made:

- During plasma treatment at least four vibrational bands appear in the region of double bond stretching and NH_2 deformation vibrations between 1550 and 1700 cm^{-1}. Beyond 3000 cm^{-1} ν(NH) bands are developing.
- H→D and D→H exchanges show vanishing ν(NH) (+ possibly ν(OH)) and appearance of deuterated groups and vice versa. There are minor effects in the region between 1700 and 1400 cm^{-1}, probably due to C=NH and amides. There is no significant indication of the presence of amine NH_2 (expected around 1620…30 cm^{-1}) or ND_2 groups (expected around 1225…35 cm^{-1}) within the experimental error range. Expected band areas for 1 NH_2/nm^2 (1 ND_2/nm^2), based on integral intensity values [10] are 0.006 (0.003) cm^{-1}.
- The reaction with TFBA does not proceed along the usually adopted "standard" scheme $R–NH_2$ + O=CH-Ar → R-N=CH-Ar: At least three new strong bands are developing between 1500 and 1720 cm^{-1} instead of a single imine vibration expected near 1650 cm^{-1} (ν(C=N) as measured after adding model primary alkyl amine and TFBA in hexadecane).
- Using isothiocyanate TPI instead of aldehyde TFBA for derivatization (no figures shown here), the amount of bonded reagent is roughly doubled[2]. This may be due to a major role of secondary amines on the surface, smoothly forming thioureas with the reagent.[3]

From an applicational point of view the presented results do not impair the high value of DBD-based "plasma-amination" of polymer surfaces for subsequent processes such as metallization, printing, gluing, coating or covalent coupling of (bio)molecules. Quite the contrary they give valuable clues how to adapt the subsequent processing in order to exploit the chemical surface functionalities provided by the plasma treatment even more efficiently.

References

[1] J. R. Hollahan, B. B. Stafford, J. Appl. Polym. Sci. **1969**, *13*, 807.
[2] G. J. Courval, D. G. Gray, D. A. I. Goring, J. Polym. Sci, Polym. Lett. Ed. **1976**, *14*, 231.
[3] R. Foerch, N. S. McIntyre, R. N. S. Sodhi, D. H. Hunter, J. Appl. Polym. Sci **1990**, *40*, 1903.
[4] L. J. Gerenser, J. Adhes. Sci. Technol. **1993**, *7*, 1019.
[5] D. S. Everhart, C. N. Reilley, Anal. Chem. **1981**, *53*, 665.
[6] F. Fally, C. Doneux, J. Riga, J. J. Verbist, J. Appl. Polym. Sci. **1995**, *56*, 597.
[7] O. Beyer, „Houben-Weyl - Methoden der organischen Chemie – Vol. 7,1 Aldehyde", Thieme-Verlag, Stuttgart, New York 1975.
[8] S. Patai, ''The chemistry of the carbon-nitrogen double bond", Interscience Publishers, London 1960, pp. 82 and 264.
[9] P. Kovaříček, J.-M. Lehn, J. Am. Chem. Soc. **2012**, *134*, 9446.
[10] M. R. Yagudaev, Yu. N. Sheinker, Dokl. AN SSSR **1962**, *144*, 179.

[2] This was generally observed in recent labeling experiments with TFBA and TPI on N-DBD-treated polyolefin surfaces, also after direct microplasma treatments ("plasma printing").
[3] Imines >C=N-H probably show an analogous reaction. OH groups are not expected to react.

FUNCTIONAL COATINGS FOR POLYMER COMPOSITES

A. Babik[1], L. Hoferek[1], D. Janova[2], V. Cech[1]

[1]*Institute of Materials Chemistry, Brno University of Technology*
Purkynova 118, CZ-61200 Brno, Czech Republic
[2]*Dept. of Structural and Phase Analysis, Brno University of Technology*
Technicka 2896/2, CZ-61669, Brno, Czech Republic

ABSTRACT

The development of high-performance polymer composites is tightly bound with the functional surface modification of reinforcements. A new method, based on the principle of the fiber-bundle pull-out test, was used to analyze the interfacial properties between the long fibers in the form of a bundle and the polymer matrix. The pull-out test can be used for a relative comparison of different surface modifications if the bundle geometry is unknown. Glass fibers coated by plasma polymer films of tetravinylsilane were tested to determine the interfacial shear strength as a function of RF power and film thickness that was varied from 50 nm to 10 μm. SEM micrographs of pulled-out (debonded) fiber bundle were used to characterize adhesion at the interlayer/fiber and polymer/interlayer interfaces.

KEYWORDS

Thin films, plasma-enhanced chemical vapor deposition (PECVD), polymer composites, scanning electron microscopy (SEM)

1. INTRODUCTION

New helical coupling plasma system for continuous surface treatment and modification of fiber bundles has been developed using the RF (13.56 MHz) pulsed plasma of glow discharge technique [1]. The pulsed mode means, that plasma was controlled by changing the ratio of time, when plasma was switched on (t_{on}) to the time when plasma was switched off (t_{off}). Afterwards we can define the effective power $P_{eff} = t_{on}/T \times P_{total}$, where the period was defined as $T = t_{on}+t_{off}$ and the total power of generator was $P_{total} = 50$ W [2].

Low-temperature plasma is a suitable technique used for surface modification of materials [3] and plasma-enhanced chemical vapor deposition (PECVD) is a useful technique able to prepare engineered interlayers on surface of composite reinforcements [4].

The surface of reinforcements has to be modified to improve wettability and adhesion to the matrix for sophisticated composites. The surface modification of reinforcements is a useful way to influence the chemical and physical structures of their surface layer, tailoring fiber-matrix stress transfer, but without influencing their bulk mechanical properties [5]. Silane coupling agents are applied to glass fiber surface to promote their adhesion to the polymer matrix. However, modern surface analytical studies have shown that the coatings are usually heterogeneous, with thickness varying from less 10 nm to more than 1μm [6]. The formed siloxane bonds are hydrolytically unstable, which results in worsening of mechanical properties of the composite in the presence of water and, eventually, in failure of the material. This problem may be resolved with plasma surface modification [7].

2. EXPERIMENTAL

Plasma polymer films were deposited on a bundle of unsized glass fibers (GF) using tetravinylsilane monomer (TVS, purity 97%, Sigma Aldrich) at different powers

ranging from 0.1 to 10 W using RF (13.56 MHz) pulsed-plasma system and film thicknesses that ware varied from 50 nm to 10 microns.

Glass fibers (E type, 1200 tex, 19 μm diameter) were used as reinforcements and polyester resin was the matrix. This polyester resin was cured from oligomers on the base of isophtalic acid with mixture of styrene, initiators, stabilizer and separator. Curing was carried out in the oven with programmable temperature regime at 140 °C.

The composite samples were tested by fiber-bundle pull-out test [8] to determine the interfacial shear strength. The bundle was terminated by the disk at the bottom side and by a polymer dumb bell (ISO 527) at the other side. Such a specimen was subjected to a tensile test using a universal testing machine (Z010/TH2A, Zwick). The dumb-bell-shaped part of the specimen was hold by grips and the disk was hold by a test fixture using a specific edge. The experiment consists of an increasing normal force, which is applied to the fiber bundle in order to pull it out of the polymer disk. The design of the sample was constructed with respect to results of finite element analysis (FEA). The tensile test was employed to evaluate adhesion at the fiber-matrix interface. The maximum applied load, P_{max}, corresponds to a debonding of the fiber bundle embedded in the polymer disk; the contact area between the bundle and the disk can be expressed through the disk height, h, and the bundle perimeter, πd, where d is the bundle diameter. In a similar manner to the microbond technique, the interfacial shear strength can be calculated as the maximum applied load divided by the contact area using the relation:

$$\tau_{int} = P_{max} / (\pi h d) \ . \qquad (1)$$

The coated fibers and pull-out bundles were observed by scanning electron microscopy (SEM) to investigate film uniformity, and characterize adhesion of plasma polymer interlayer to the surface of glass fibers and polymer matrix.

3. RESULTS AND DISCUSSION

Unsized glass fibers and fibers with plasma coatings were observed by SEM to investigate film uniformity. The deposited plasma coatings on fibers were uniform (Figure 1) unlike industrially sized fibers using wet chemical processes. Surface of plasma coated GF is smooth without impurities and defects. In the detail (Figure 2), an evident rupture of the coating is observed on the fiber surface close to the cut fiber end. This means that the plasma coating is spread on the whole surface area of GF.

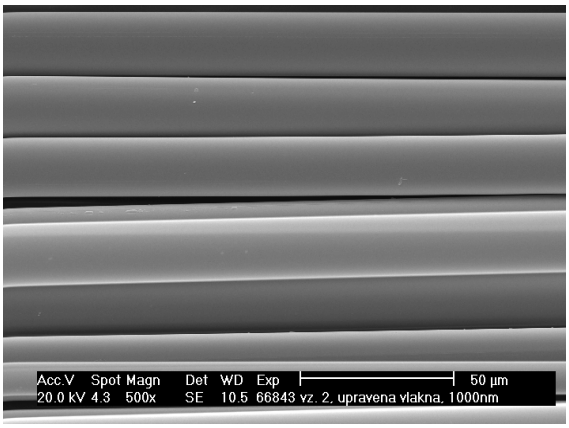


Figure 1. Deposited plasma coatings on glass fibers.

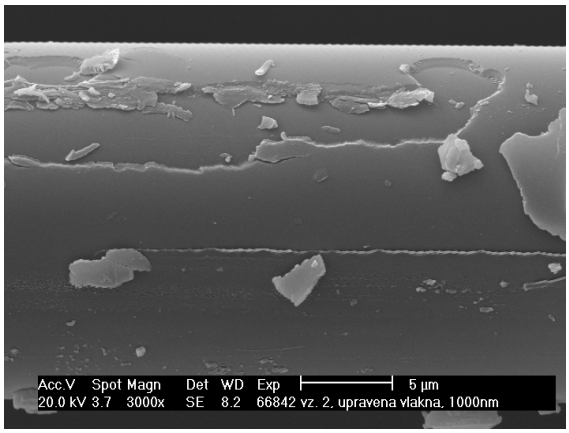


Figure 2. Rupture of the coating on surface of glass fiber.

Prepared composite samples with unsized and plasma modified glass fibers were tested by universal testing machine. Displacement rate was 1 mm per minute and the force response was measured. The tensile test was ended when the bundle of glass fibers was pulled-out from polymeric disk of composite sample.

Results of fiber-bundle pull-out test for composite samples with unsized fibers and plasma coated reinforcements at different powers ranging from 0.1 to 10 W are given in Table 1.

Table 1. Results of fiber-bundle pull-out test.

RF power (W)	h (mm)	P_{max} (N)	P_{max}/h	τ_{int} (MPa)
Unsized	4.90	235	48	17.0
0.10	4.91	354	72	24.1
0.50	4.90	331	68	23.9
2.5	4.94	343	69	24.4
5.0	4.93	339	69	24.5
10.0	4.92	385	78	27.6

(h is the height of polymeric cylinder, P_{max} is the maximum applied load for pulling-out the bundle of tested glass fibers from disk, and τ_{int} is the interfacial shear strength calculated using equation (1)).

Results of fiber-bundle pull-out test for composite samples with unsized and plasma coated fibers at the film thickness that was varied from 50 nm to 10 μm are given in Table 2.

Table 2. Results of fiber-bundle pull-out test.

Thickness (nm)	h (mm)	P_{max} (N)	P_{max}/h	τ_{int} (MPa)
Unsized	4.90	235	48	17.0
50	4.99	293	59	20.8
100	4.96	340	69	24.4
500	4.95	375	76	27.0
1000	4.94	343	69	24.4
5000	4.89	452	93	32.9
10000	4.86	534	110	38.9

Pull-out bundles were observed by SEM to characterize adhesion of TVS interlayer to surface of glass fibers and to polymer matrix. In SEM micrographs, we observe that the fibers are coated by thin polymer film and covered by cured polyester resin. A good adhesion of polymer matrix to the glass fiber and no signs of cracks are evident in micrographs (Figure 3). In the detail, we can observe the rupture of the coating on GF surface evidencing the cohesion failure (Figure 4).

4. CONCLUSION

Plasma surface modification is an effective technique to influence physical and chemical properties of interphases in fiber reinforced polymer composites. The tensile strength of single fibers is sensitive to both the plasma treatment and plasma polymerization. Strong adhesion is promoted by increasing the surface energy of fibers, as a result of plasma modification, decreasing contact angle of the matrix, and thus the wettability of fibers by the polymer matrix is improved. The organosilicon plasma polymers are widely recognized for preparation controlled interphase in composites. The functional coating serves as suitable interlayer to

improve compatibility between the glass fiber and the polymer matrix resulting in enhanced composite performance. The composite samples were tested by fiber-bundle pull-out test to determine the interfacial shear strength as a function of RF power and film thickness that was varied from 50 nm to 10 microns. A significant increase of the interfacial shear strength by 102% was found for the increased film thickness and a weak descent by 10% was related to the enhanced power. SEM micrographs of pulled-out (debonded) fiber bundle were used to characterize adhesion at the interlayer/fiber and polymer/interlayer interfaces.

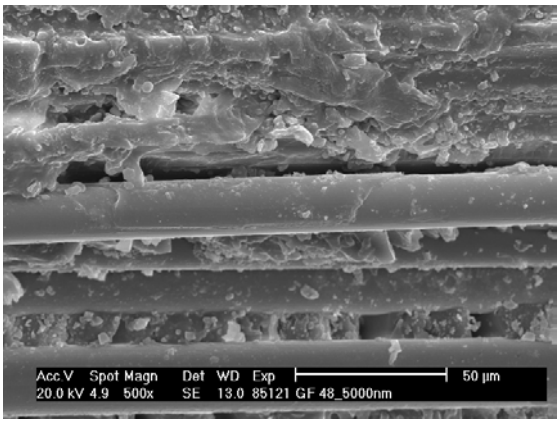


Figure 3. Micrograph of plasma modified glass fibers embedded in polyester resin after fiber-bundle pull-out test.

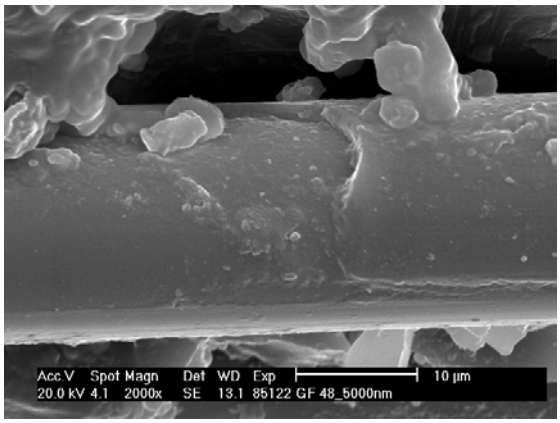


Figure 4. Detail of plasma coated glass fiber embedded in polyester resin using SEM image.

Acknowledgements: This work was supported in part by the Czech Science Foundation, grants no. P106/11/0738, P205/12/J058 and 104/09/H080, the Czech Ministry of Education, grant no. ME09061 and the Technology Agency of the Czech Republic, grant no. TA01010796.

REFERENCES

[1] V. Cech, N. Inagaki, J. Vanek, R. Prikryl, A. Grycova and J. Zemek, Thin Solid Films 502, 181 (2006).
[2] V. Cech, J. Studynka, N. Conte, V. Perina, Physico-chemical properties of plasma-polymerized of tetravinylsilane, Surface & Coating Technology 201, 5512 (2007).
[3] N. Inagaki, *Plasma Surface Modification and Plasma Polymerization.*
Lancaster : Technomic Publishing Company, Inc., 1996.
[4] V. Cech, Compos. Interfaces 14, 321 (2007).
[5] J-K. Kim and Y-W. Mai, *Engineered Interfaces in Fibre Reinforced Composites*, Amsterdam, Elsevier, 1998.
[6] D. W. Dwight, Glass Fiber Reinforcement, in: *Comprehensives Composite Materials*, Amsterdam: Elsevier, 2000, Ed. Kelly A., Zweiben C. Volume 1. p 231 – 261.
[7] V. Cech, New Progress in Composite Interphases: A Use of Plasma Technologies. In *Proceedings of FRC 2000.* 2000. Newcastle, GB: Woodhead Publishing Ltd, s. 246.
[8] V. Cech, P. Janecek, T. Lasota, J. Bursa, Compos. Interfaces 18, 309 (2011).

Applications of Low Pressure Plasma in High-tech Textiles

Rubel Alam[1], Gaffar Hossain[1], Günter Grabher[1], Mokbul Hossain[2]

[1]V-Trion GmbH Textile research, Schwefelbadstr. 2, A-6845 Hohenems, Austria
[2]Sefar AG, Töberstr. 4, CH-9425 Thal, Switzerland

Introduction

The textile and clothing industries especially in developed countries are facing now-a-days some big challenges largely because of the globalization process. Therefore, the market of a high-functional, added value and technical textiles is deemed to be essential for their sustainable growth. The growing environmental and energy-saving concerns will also lead to the gradual replacement of many traditional wet chemical-based textile processing by various forms of low liquor and dry-finishing processes. The main reason for the increasing interest is that industrially well-established surface finishing processes suffer considerably from environmental demands such as large amount of water, energy and effluents. Plasma technology, when developed at a commercially viable level, has strong potential to offer in an attractive way to obtain new functionalities in textiles.

The synthetic fibres such as polypropylene (PP), polyester (PES), Aramid (AR) etc. are widely used in apparel and home furnishings due to their good physical and chemical properties. The demand of these fibres increases greatly for high performance applications such as smart textiles, technical textiles, operation clothing etc. and more recently, for their potential applications in electronic textiles [1-2]. But these fibres often reveal hydrophobic nature due to the lack of polar functional groups. The hydrophobic nature of such fabrics limits their application to the above mentioned areas. In addition, adhesion is fundamentally a surface property, often governed by a layer of molecular dimensions, which necessarily required for coating, bonding and printing of synthetic textiles. The low surface energy of hydrophobic polymeric materials results in intrinsically poor adhesion.

On the other hand, some natural fibres (e.g. cotton, wool, linen) and synthetic fibres (e.g. rayon, viscose, acetate, spun nylon) exhibit to be hydrophilic in nature due to their polar functionalities. Hydrophilicity of such fibres may act as a barrier for their applications in many areas where liquids repellent is necessary. It is a wide-reaching technical effect that is sought after in several industry sectors, from biosciences, healthcare and electronics to industrial filtration, sports and active wear [3-4]. In addition to water repellency, other liquids such as oils, inks and alcohols repellency often required. Liquids are constantly in use around us, in the majority of cases in the form of rain water and food and beverages. Arguably, the most noticeable, unfavorable interactions of these liquids are with textile products such as clothing, carpets and upholstery, so added value can be provided by protecting these items from interacting with the liquids, enabling the liquids to roll off or be dabbed away, leaving the underlying material unchanged. Furthermore, hydrophobicity of textiles is frequently associated with self-cleaning properties. When a water droplet rolls off the surface, the surface impurities such as dust get carried away by the droplet resulting in a self-cleaning effect [5].

Using plasma technology to modify textile surfaces with precision cleaning, etching, chemical priming for lowering or raising surface energy can be used to obtain a desirable property of an end product. The plasma technology, a dry and eco-friendly technique, avoids waste water production which is a unique advantage over the wet-chemical processes [6-7]. This benefit

extends into all market areas, where the end product can undergo the plasma enhancement process to provide properties such as adhesion, hydrophilic, liquid-repellent etc. However, to transfer this technology from laboratory into industry, both the scale-up and economic aspects have to be regarded.

Main objective of this work is to study the possibility of substituting plasma processes for the traditional wet chemical methods using an industrial plasma reactor aiming to produce wash permanent super-hydrophilic, super-hydrophobic textile surfaces.

Experimental

Plasma reactor

The Nano-Plasma-Coater BAG at V-Trion GmbH is one of the biggest low pressure plasma reactor in Europe and offers a wide range of surface functionalisation, nanoscaled coatings etc. The semi-continuous reactor has a capacity of treating materials up to 4000 and 1.60 meter in length and width, respectively, and the material speed up to 40 meters per minute. The machine is capable of running for three shifts with a monthly production of about 400,000 meter (depending on material speed / coating thickness).

Durable plasma-nanocoatings

Depending on the plasma power and gas feed the modification of textile surface can alter over a wide range of properties such as hydrophilicity, hydrophobicity, adhesion promoter etc. The use of gaseous mixtures facilitates crosslinking. For instance, the Ar/O_2 plasma produces better hydrophilicity and wettability, as compared to Ar/CO_2 and N_2/O_2 plasmas. But, plasma-activated fabric surfaces were not durable over time due to the reorganization processes on the surface [8-9]. Therefore, the deposition of plasma coatings is required to obtain a permanent surface functionalisation. Generation of new reactive sites by plasma functionalisation promotes adhesion strength. The adhesion strength between PA / polyurethane (PU) and between PES / PU polymer is investigated at ambient condition as well as at 80ºC in water for a long time of period (up to 30 days) according to standard test (DIN 53539).

The possibility of substituting plasma process for the traditional waterproof finishing of fabrics was further studied in this work. A good water repellent finish could be obtained using silane plasma by a plasma-enhanced chemical vapor (PECVD) method. Furthermore, a wash permanent super-hydrophobic and oleophobic coating was obtained by a plasma pretreatment using non-polymerized gases followed by a grafting with perflouracrylates. This coating has an excellent washing durability (ISO 6330, 80 washing cycles) and has very good water repellency which is tested with a spray test (AATCC 22) as well as Bundesmann test method.
The permanency of the plasma hydrophilic coating has been recorded measuring sinking time after 50 times washing and after aging. The mechanical stability of the coating was also evaluated according to Martindale test (SN 198514, 60,000 rubbing cycles).

Results

The formation of plasma polymers from organic molecules is a technologically attractive way to deposit functional ultrathin films with unique properties. Appropriate combinations of gas mixtures and plasma parameters, a rather broad range of surface functionalities can be incorporated to the fibers. Wettability of the surface and adhesion properties varies according to the nature of the plasma treatment. In particular, the adhesion with PU material with PA and PES surfaces was improved greatly by plasma pre-treatment. As can be seen in Fig. 1, the pull-off strength can be increased by 130% for PA and by 110% for PES compared to the untreated

fabric. The aging study shows that more than 80% of their initial values can be retained after 30 days of immersion in water at 80ºC. The mechanism that leads to the improved adhesion of the plasma treated polymer surfaces may be due to the surface cleaning, mechanical interlocking, the increase of inter-diffusion, the increase of wettability and the polar interaction at the interface.

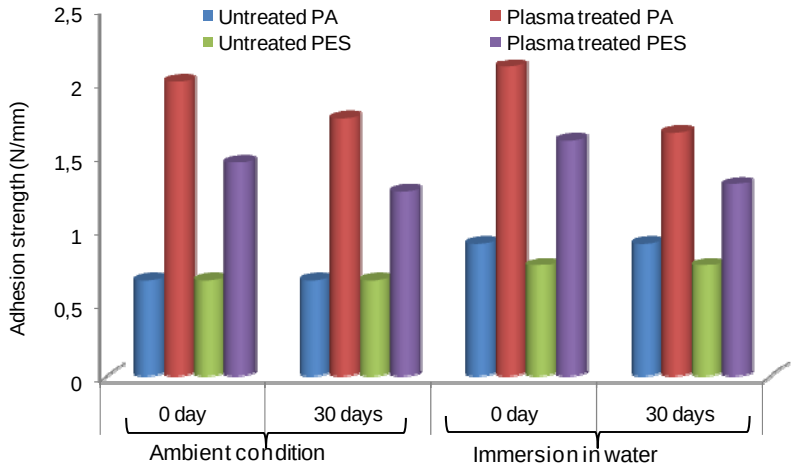


Fig.1. Adhesion and pull-off strength test (DIN 53539) of plasma-treated and untreated PA and PES fabrics

The water contact angle (CA) reflects the surface hydrophilicity / hydrophobicity by measuring how much a droplet of water spreads on a surface. The lower the contact angle, the more hydrophilic the surface is. The time-dependent spreading of a water drop on AR and PES samples are shown in Fig. 2 (data for PA is not shown). Since water drop disappeared very quickly on the plasma coated hydrophilic AR and PA surfaces, CA could be given to zero, whereas untreated AR and PA fabric show a water contact angle of ~ 110° and 76°, respectively. The durability of these plasma coatings was observed with a minor alteration in sinking time by the aging test up to one year for 50 times washed AR samples. The incorporation of polar groups increases the surface energy of polymers concomitantly improves the wettability of the surface. Due to the covalent bonding and their polar chemical nature, the functionalized films adhere well to the substrate which was also proved by the abrasion tests. It was evident that no changes were detected on the coated surface even after 60,000 rubbing cycles indicating the permanency of the novel coating against industrial washing (ISO 6330/2A, 60°C).

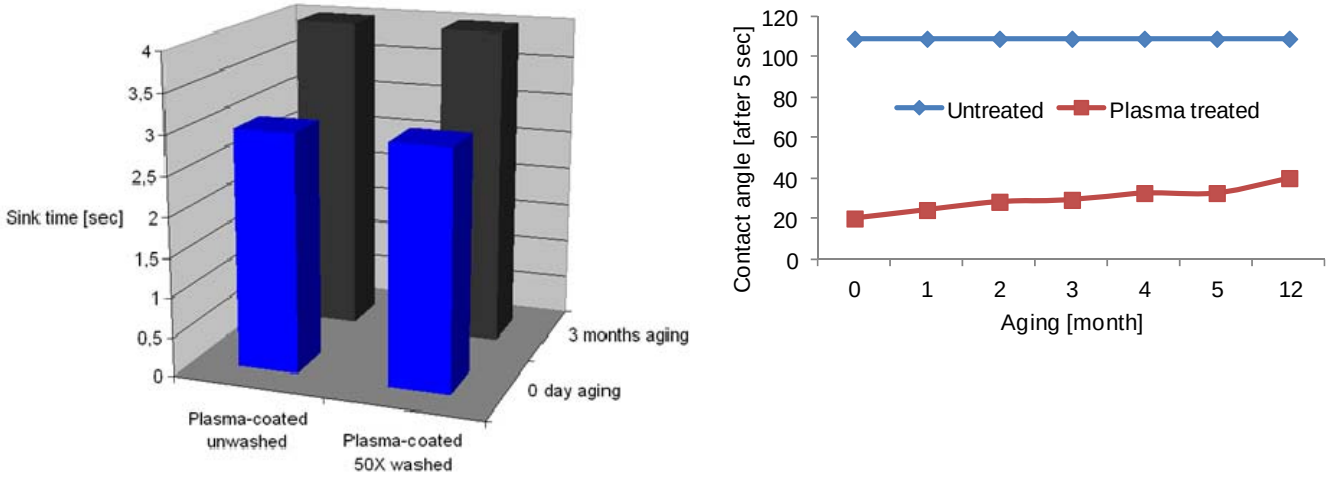


Fig. 2. The wash durability of the plasma-coated AR (left) and aging of untreated and plasma treated PES (right)

A super-hydrophobic surface with a very large CA was obtained by the plasma pretreatment with non-polymerized gases and followed by a grafting of perflouracrylates. Wash permanency of the hydrophobic coating has been characterized by the Bundesmann test measuring the lotus effect, water penetration and water pick up% (Tab.1). An excellent water repellency (grade 100) was obtained according to spray test even after 80 washing cycles. Oil repellency behavior has also been observed up to grade 7. Permanent modification of the textile surface can be attributed to the strong covalent bond of fluorocarbon to the plasma functionalized surface.

Treatment	Spray test grade (after 80 washes)	Contact angle (CA)	Bundesmann test (after 20 Washing cycles)			
			Lotus effect	Water penetration (ml)	Pick up (%)	g (water)/m^2
Untreated PA	0	76	1	> 400	45	.139.
Untreated PES	0	109	1	> 400	49	..135
Plasma treated PA	100	145	4	40	20	58
Plasma treated PES	100	150	5	9	4	3

Tab.1. Water repellency test by contact angle, spray test and Bundesmann test of untreated and plasma- treated fabric

Conclusion

Low pressure plasma processes have been successfully developed using an industrial plasma reactor to produce permanent hydrophilic, hydrophobic and oleophobic surfaces for the application in high-tech textiles. Plasma coating provides high density of polar groups which yield a super-hydrophilic textile surface. Durability of the hydrophilic coating has been confirmed by the aging test up to one year with a minor alteration. Bundesmann test coupled with standard spray test after 80 washing cycles indicate the wash permanency of the super-hydrophobic coating. Thus, plasma-coated textiles are able to support excellent adhesion to subsequent wet chemical processes.

References

[1] Hossain M.M, Hegemann D., Textile dyeing, In Tech, Chapter 9, 173-194.
[2] Hossain, M.M., Hegemann, D., Herrmann, A.S., Plasma Process. Polym. 2006, 3, 299.
[3] Berzowska, J., J. Cloth. Culture2005, 3, 58.
[4] Hossain, M.M., Hegemann, D., Herrmann A.S., Chabrecek P., J. Appl. Polym. Sci. 2006, 102, 1452.
[5] Hossain, Kh.M.G., Maria D.G, Guillem R.L., Tzanko T, J. Biotech. 2009, 141, 58.
[6] Hossain M.M., Hegemann D., Herrmann A.S., Plasma Process. Polym. 2007, 4, 135.
[7] Hossain M.M., Grabher G., Melliand International 2011, 3, 149.
[8] Hegemann D., Hossain M.M., Balazs D.J., Progress Org. Coat., 2007, 58, 237.
[9] Höcker H., Pure Appl. Chem. 2002, 74(3), 423.

POLY(ACRYLIC) NANOCOATINGS DEPOSITED BY AP-PECVD PROCESSES ON PAPER SUBSTRATES FOR PACKAGING APPLICATIONS

José Manuel García, Jordi Mota, Laia Crespo, Meritxell Martínez, Laurent Aubouy, Llorenç Bautista

R&D Department, Leitat Technological Center, C/Innovació 2, 08225, Terrassa, Spain.

Abstract

Poly(acrylic acid) coatings on paper substrates have been prepared by atmospheric pressure plasma enhanced chemical vapor deposition (AP-PECVD). The structure/properties relationships of the samples were studied in dependence of the plasma experimental conditions. Acrylic acid monomer/helium ratio and treatment speed clearly influences the wettability properties of the paper substrate: advancing contact angle values were reduced to the half (around 60 º) if compare to non-treated paper (120 º approximately). The surface morphology of the films did not greatly vary with the plasma polymerization treatment.

Keywords: acrylic acid, atmospheric pressure plasma enhanced chemical vapor deposition, paper substrate, hydrophilic character

1. Introduction

In the last decades, thin functionalized plasma-polymerized films has received increased attention because plasma processes allows surface modification of materials attributing different properties but without affecting their bulk. On the other hand, this technique allows not only the deposition on a wide variety of substrates [1,2] but also tuning the surface properties by varying the experimental conditions [3,4]. All these characteristics together with the unique properties of the obtained coatings (i.e. the films are generally amorphous, free from pinholes, highly cross-linked, resistant to heat and corrosion and very adhesive to a variety of substrates) makes them ideal candidates to be applied in a wide variety of fields: mechanics, optics, electronics, biotechnology or biomedicine [5,6]

Up to day, plasma deposition has been revealed successful to obtain coatings with different chemically reactive moieties (primary amine (-NH_2), carboxyl (-COOH) or hydroxyl (-OH) groups). Among those, carboxylic group containing films are one of the most studied layers [7,8]. Acrylic acid is typically used as a monomer to grow such films. Plasma-deposited acrylic acid thin films can be obtained using various plasma techniques. The most common which enables a good control of the surface chemistry is radiofrequency low pressure glow discharge fed with acrylic acid vapor [9,10]. However, the main drawbacks of these plasmas are the need for expensive vacuum systems and the low deposition rate. Atmospheric pressure plasma-enhanced chemical vapor deposition (AP-PECVD) has thus recently received increasing attention to grow plasma-polymer films [11].

In this paper, acrylic acid is used as a monomer to prepare plasma polymerized films on paper substrate using AP-PECVD technique. Acrylic acid was chosen for this study because it is known that this plasma polymer can served as an adhesion-promoting interlayer for packaging applications. Moreover, from a scientific point of view, acrylic acid can be easily polymerized by conventional polymerization processes. The influence of the preparation conditions (applied potential, speed, carrier gas/monomer ratio,…) on the final properties of the deposited coating will be reported.

2. Materials and Methods

2.1. Materials

Acrylic acid (AA) was purchased from Sigma Aldrich and used without further purification. Helium was used as a carrier and was purchased from Air Liquid. Premium office paper 100% recyclable, 80 g/m2, EU Ecolabel PT/11/02 was used as substrate.

2.2. Plasma treatments

Paper samples were coated in continuous mode using an Atmospheric Pressure Glow Discharge (APGD) equipment,

model PLATEX 600 – LAB VERSION, from the Italian company Grinp, S.r.l. The two-planar electrode equipment operates at low frequency (20-45 kHz) to partially ionize gases and/or vapors of precursors. In this work the monomer/gas carrier ratio (0.1/0, 0.1/1 and 0.1/3 l/min), power of discharge (1-2 kW) and treatment speed (1-10 m/min) have been varied while keeping constant the electrode temperature (160ºC) and distance between electrodes (1.2 mm).

Surface morphology was examined with a Hitachi H-4100 FE field emission scanning electron microscope (FE-SEM) after depositing a carbon nanocoating to make the samples conductive.

Wettability properties have been analyzed using contact angle measurements. In order to measure the dynamic contact angle of plasma-treated fabrics, a Krüss K100 MK2 tensiometer was employed. Wilhelmy method has been applied on 20 mm x 20 mm samples. An average value of contact angle has been calculated by measuring four replicates of each sample. All measurements were determined at 65 ± 2 % of relative humidity and 20 ± 0.5 ºC (ISO 139:2005).

Surface characterization of poly(acrylic acid) film-coated papers have been done by FTIR-ATR and XPS spectroscopies. FTIR-ATR (Nicolet 710 FTIR – Diamond crystal, Pike®, Miracle™) spectra were recorded between 500 and 4000 cm^{-1}. Mean spectra of 32 scans and normalization to the maximum peak have been carried out using IR solution software (Shimadzu, Japan). X-ray photoelectron spectroscopy (XPS) measurements were performed with a PHI 5600 multitechnique system. The binding energies (BE) of the XPS signals of all species have been corrected by assuming C1s signal at 285.0 eV

3. Results and Discussion

3.1. Wettability properties

3.1.1. Influence of the acrylic acid/He ratio and power of discharge

The first step of this work was to study the influence of the discharge power in the wetting properties of the treated paper for the 3 different acrylic acid/helium ratios used. Figure 1 shows the variation of the advancing water contact angle with the applied power. As it can be observed, no influence of the power discharge on the contact angle is detected when no helium is used (Figure 1A). However, under the presence of a small proportion of helium contact angle decreases but only at high discharge powers (Figure 1B). A decrease in the contact angle was observed at lower discharge powers when the proportion of He in the fed mixture increased (Figure 1C). The reason could be an activation process of the gas carrier which made easier the polymerization of acrylic acid monomer on the substrate: the higher the He content, the higher the activation and the better the polymerization. On the other hand, no important differences were detected when discharge power increased up to 2 kW.

3.1.2. Influence of treatment speed

Other important parameter that may affect the wettability of the films is the treatment speed. Treatment speed influences on the time the substrates resides between the two electrodes, in other words, the lower the treatment speed is the higher the plasma treatment time is. Figure 2 shows how the treatment speed can influence on the contact angle of the tested films prepared with the higher He content. As it can be observed, the wettability of the paper decreases as the treatment speed increases, which could be attributed to a thinner deposited poly(acrylic acid) film.

Based on the previous results, the films with the better wettability properties were obtained from the mixture with the acrylic acid monomer/helium ratio 0.1/3 l/min at a treatment rate of 1 m/min. Power discharge slightly influenced the contact angle value: 60.3 º (± 5.5º) at 1 kW and 72.5º (± 4.1º) at 2 kW.

3.2. Surface Characterization

The surface morphology of non-treated and plasma-polymerized paper substrates with the better wettability properties were analyzed FE-SEM microscope. Figure 3 the SEM images in which it can be observed cellulose fibers and the inorganic charge typical of printing papers. Looking specifically at the cellulosic fibers, no significant differences

were detected between treated and non-treated samples at low magnifications (Figure 3A-C). However, higher roughness seems to be observed after plasma polymerization at high magnifications (Figure 3D-E), results in agreement with those presented by Amorosi *et al.* [12].

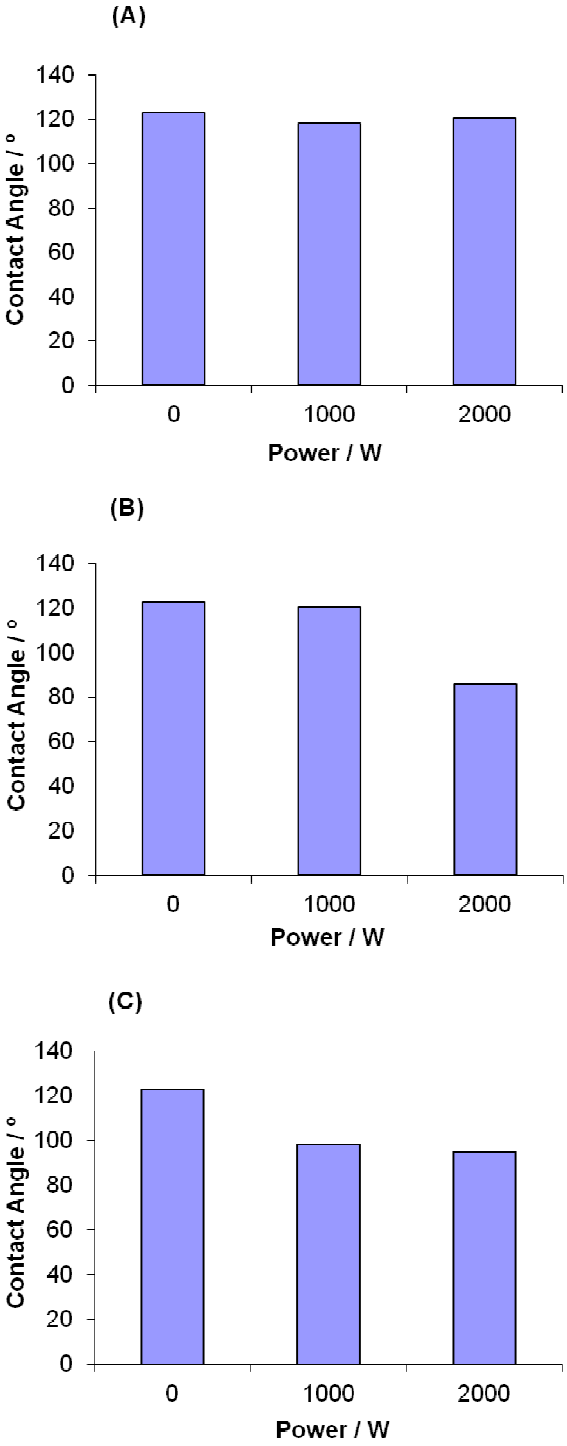


Figure 1. Influence of the power discharge on the contact angle for different acrylic acid/He ratios. A) Only Acrylic acid, B) 0.1/1 l/min and C) 0.1/3 l/min.

FTIR-ATR spectra of non-treated and plasma-treated samples confirm the cellulosic nature of the substrates studied in this work. However, FTIR-ATR technique is not able to differentiate surface modifications associated to plasma polymerization treatments. This suggests that the chemical modification on the paper surface is at nanometric level, not at micrometric level. On the other hand, preliminary XPS studies reveal the presence of carboxyl groups attributed to the polymerization of acrylic acid monomer by atmospheric pressure plasma.

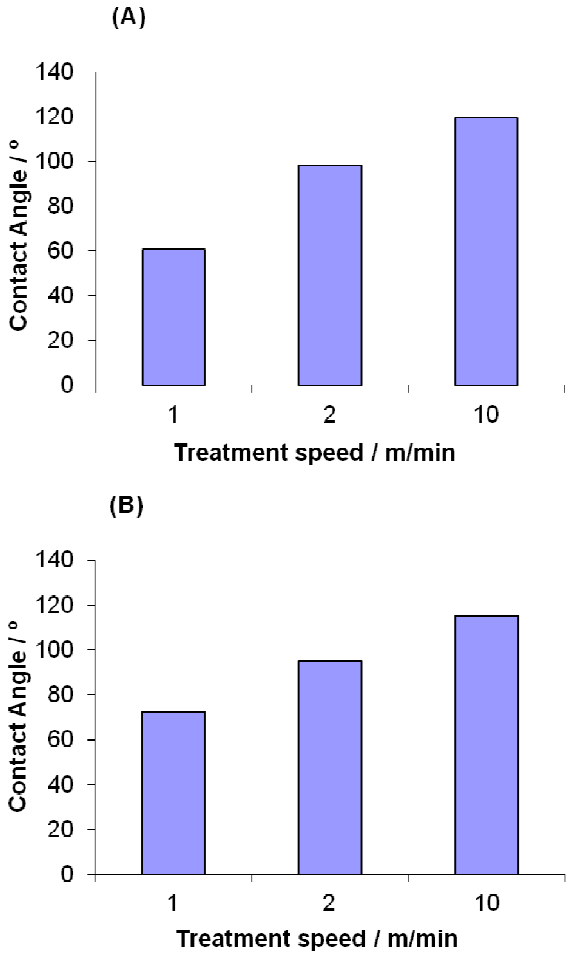


Figure 2. Influence of the treatment speed on the contact angle of the plasma-polymerized poly(acrylic acid) films obtained from the mixture with the higher He content at the different power dicharges. A) 1000 W and B) 2000 W.

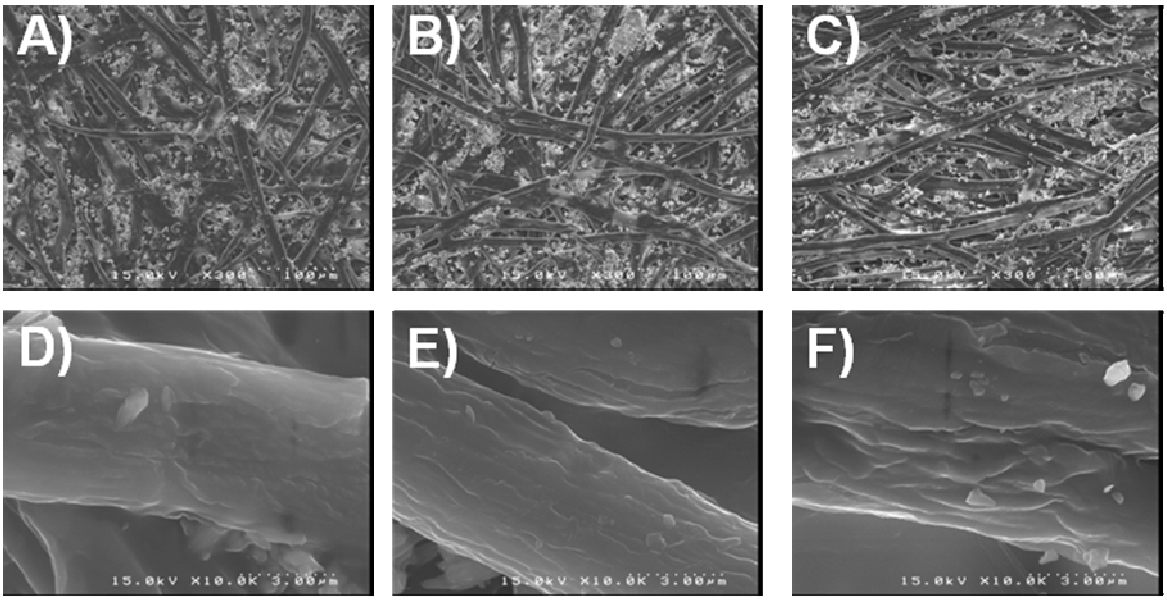


Figure 3. SEM images of non-treated (A,D) and treated samples with acrylic acid/He ratio 0.1/3 l/min at different treatment speed: 1 m/min (B,E) and 2 m/min (C,F).

4. Summary

In the present work, nanocoatings made from acrylic acid via AP-PECVD processes were prepared. Depending on the conditions of the process, the wettability properties were significantly modified: the helium content in the fed mixture as well as the treatment speed greatly influenced on the contact angle. Contact angle values of 60 º approximately were obtained after plasma-polymerized paper substrates. Moreover, surface morphology of cellulosic fibers was slightly roughened by the plasma process. Summarizing, plasma polymerization parameters have to be carefully adjusted in order to control the film characteristics such as wettability or morphology.

Acknowledgements

This work has been achieved thanks to the support of ACCIO (Generalitat of Catalunya) in the framework of the BIP project TECCOL11-1-0001 co-financed by FEDER fundings.

References

[1] M.R. Alexander, T.M. Duc, *J. Mater. Chem.* 8, 1998, 937.

[2] F. Arefi, V. Andre, P. Montazerrahmati, J. Amoroux, *Pure and Applied Chemistry* 64, **1992**, 715.

[3] T.P. Kasih, S.Kuroda, H. Kubota, *Plasma Process. Polym.* 4, **2007**, 648.

[4] Y. Sawada, S.Ogawa, M. Kogoma, *J. Phys. D: Appl. Phys.* 28, **1995**, 1661.

[5] K.S. Siow, L. Britcher, S. Kumar, H. J Griesser, *Plasma Process. Polym.* 3, **2006**, 392.

[6] D.S Kumar, Y. Yoshida, *Surf. Coat.Technol.* 169-170, **2003**, 600.

[7] A. Fahmy, R.Mix, A. Schönhals, J.F. Friedrich, *Plasma Process. Polym.* 8, **2011**, 545.

[8] P.Hamerli, *Biomaterials*, 24, **2003**, 3989.

[9] L. Detomaso, R. Gristina, R. d'Agostino, G.S. Senesi, P. Favia, *Surf. Coat. Technol.* 200, **2005**, 1022.

[10] P.Rossini, P. Colpo, G. Ceccone, K. D. Jandt, F. Rossi, *Mater. Sci. Eng. C* 23, **2005**, 1022.

[11] O. Carton, D.B. Salem, S. Bhatt, J. Pulpytel, F. Arefi-khonsari, *Plasma Process. Polym.* DOI: 10.1002/ppap. 201200044.

[12] C. Amorosi, T. Fouquet, V. Toniazzo, D. Ruch, L. Averous, *Reactive&Funct. Polym.* 72, **2012**, 341.

Atmospheric Plasma surface treatment of Styrene-Butadiene Rubber

Cátia A. Carreira[1,2], Ricardo Silva[3], Vera V. Pinto[3], Maria José Ferreira[3], Fernando Sousa[2], Fernando Silva[1], Carlos M. Pereira[1]

[1]Faculdade Ciências Universidade Porto, Porto, Portugal; [2]CEI – Companhia Equipamentos Industriais Lda, S. João Madeira, Portugal; [3]CTCP – Centro Tecnológico Calçado Portugal, S. JoãoMadeira, Portugal

c.carreira@zipor.com

Introduction

Thermoplastic rubbers are widely used in a large number of applications (e.g. footwear, adhesives manufacturing, molded or extruded goods). Due to the non-polar nature of these rubbers, poor adhesion is achieved with polar polyurethane (PU) adhesive thus, a surface treatment is required to chemically modify the rubber surface and produce suitable joints.

Surface treatments have been demonstrated to be suitable for the improvement of adhesion and wettability properties of non-polar synthetic rubbers. Over the last two decades progresses in adhesion of rubber were achieved by changing of the ingredients in rubber composition or by modifying surfaces by the use of a chemical agent (halogenation, cyclization, etc.) or using high energy irradiation such as bombarding the surface by electron beam or gamma irradiation.

Actually, wet-chemical treatments are not well acceptable because of environmental and safety considerations and question on uniformity and reproducibility. Plasma surface treatment process was been proposed as an environmentally friendly and have gained large acceptance because it can be easily integrated into existing production lines and because their effectiveness in the treatment of several materials with different shapes and sizes.

The effectiveness of plasma treatment on enhancement of adhesion depends on the gas used to generate the plasma and also on the formulation of the rubber. Vulcanized rubbers like, styrene-butadiene rubber (SBR), are especially difficult to bond due to low molecular weight ingredients in their formulation that may migrate to the rubber surface limiting its interaction with the adhesive.

This study attempts to find an alternative treatment to improve the adhesion of SBR surface and PU adhesive. Plasma treatments were performed in an air plasma system from Acxys and were selected three types of SBR rubbers with different percentages of styrene-butadiene which were provided by Procalçado. The effect of experimental variables such as distance, speed and scan number on the adhesion of PU adhesive was evaluated and compared with halogenated SBR rubbers.

Keywords: SBR Rubbers; Surface treatment; Atmospheric Plasma; Adhesion; Aging

Experimental

The wettability of the as-received and surface treated SBR rubber was evaluated by contact angle measurements using a home-made goniometer. Drops of deionized water (18 MΩ.cm) were placed on the surface rubber using a microsyringe (Hamilton Instruments). Contact angle values were measured immediately after plasma treatment. Contact angles were obtained after digital image treating using image J.

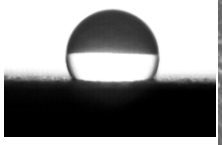
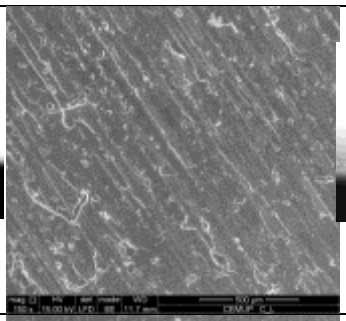
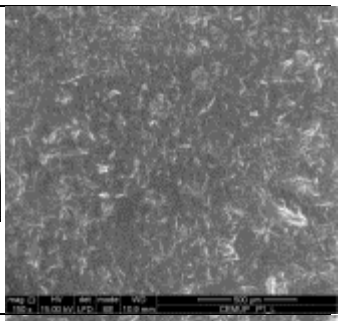
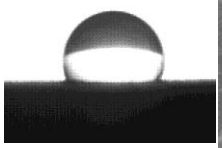
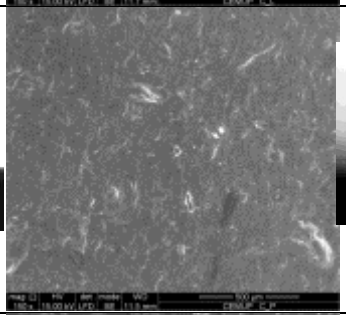
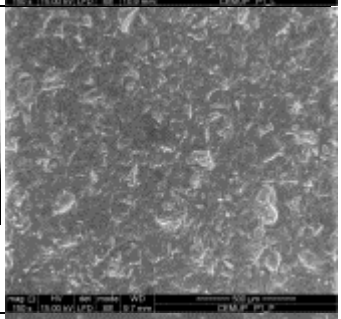
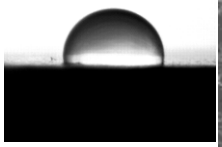
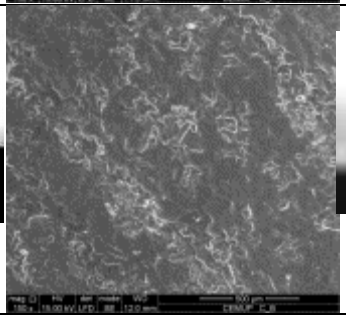
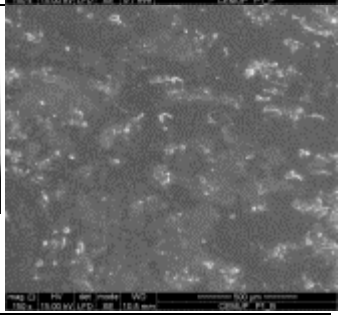
SBR rubber/PU adhesive/leather joints were made use two test pieces with the same dimensions. The leather surface was roughened and then, was treated with a primer solution

and 30 minutes later, PU adhesive was applied with brush on the rubber treated and leather. After 60 minutes, the PU adhesive was reactivated at 80 °C for 5 seconds and the adhesive-coated rubber and adhesive-coated leather were immediately placed into contact at a pressure of 5 bar for 10 seconds. Adhesive joints were conditioned for 72 hours at room temperature. The adhesive strength of the treated surfaces is evaluated by T-peel tests.
The T-peel strength measurements were performed using a Jupiter instrument, at a peeling rate of 0.1 $m.min^{-1}$ performed according to ISO 17708:2003. Each reported adhesive strength value is the median of three bonded samples.
The morphological modifications produced on the treated SBR rubbers were analyzed using a JEOL JSM-840 Scanning Electron Microscope (SEM) using a 20 kV electron beam.

Results and discussion

The plasma treatment produce a decrease in contact angle values compared to as-received SBR rubber as shown in data displayed in table I indicating improved wettability of the surfaces after plasma treatment.

Table I. Contact angle and SEM images of the rubber samples used in this work, before and after plasma treatment.

	As-received rubber		After plasma treatment	
	Contact angle	SEM micrographs	Contact angle	SEM micrographs
SBR 1	 (110 ± 4)°		 (39 ± 7)°	
SBR 2	 (104 ± 2)°		 (41 ± 2)°	
SBR 3	 (101 ± 2)°		 (47 ± 6)°	

The improved wettability can be ascribed to chemical and morphological surface modifications on the SBR rubber produced by the plasma treatment.

The SEM micrographs (x150) of the as-received SBR rubber show a homogeneous flat surface with some patches likely due to paraffin wax. When SBR rubber was treated with plasma, the surface morphology is rougher.

After optimization of the experimental parameters the aging of the plasma treated surfaces was studied for 30 days in order to monitor the effectiveness of the plasma treatment.

Figure 1 shows the effect aging effect of plasma treatment, for three different rubbers, on the T-peel strength results.

The SBR rubber surface was effectively modified by air plasma treatment and the adhesion properties were greatly improved. After to 2 days of treatment, the T-peel strength values were higher than the specification to footwear adhesion and the trend of the T-peel strength values shows that one month after plasma treatment, there is no signal of treatment degradation.

This study shows that plasma treatment is a viable alternative to improve adhesion strength of SBR rubber and can easily substitute the halogenation process.

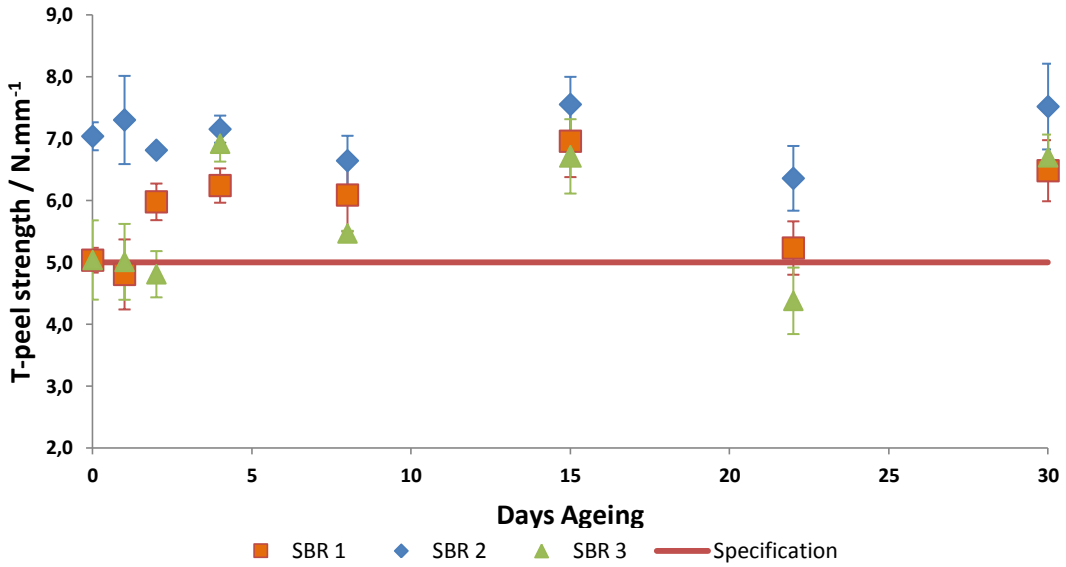


Figure 1. Effect of time, after plasma treatment of different rubbers, on the T-peel strength results.

References:

J. Tyczkowski, I. Krawczyk-Kłys, S. Kuberski, P. Makowski, European Polymer Journal 46 (2010) 767–773

J. Tyczkowskia, I. Krawczyka, B. Wożniakb, Surface and Coatings Technology 174 –175 (2003) 849–853

J.M. Martín-Martínez, M.D. Romero-Sánchez, Eur. Phys. J. Appl. Phys. 34 (2006) 125–138

María D. Romero-Sánchez, José Miguel Martín-Martínez, International Journal of Adhesion & Adhesives 26 (2006) 345–354

Maryline Moreno-Couranjou, Patrick Choquet, Jerôme Guillot, Henri-Noël Migeon, Plasma Process. Polym. 6 (2009) 397–S400

Acknowledgements:

Financial support from Portuguese Program “Programa Operacional Factores de Competitividade” under “Sistema de incentivos à Investigação e Desenvolvimento Tecnológico - Projectos Mobilizadores”, Grant number 13850, Project Newalk and FCT for the PhD grant no. SFRH/BDE/51087/2010 (Cátia A. Carreira) are acknowledged.

Plasma-generated nanostructure formation on polymer surfaces depending on the polymer type

P. Munzert, C. Praefke, U. Schulz, N. Kaiser
Fraunhofer Institute for Applied Optics and Precision Engineering
*peter.munzert@iof.fraunhofer.de

Introduction

To produce functional elements for optical applications, the components often have to be coated or joined together. Low adhesion is usually caused by different polarity or surface chemistry of the individual components [1]. Therefore, measures have to be taken to modify the respective interfaces to improve the adhesion. In the case of highly transparent polymers (e.g. PC, PMMA, COC, PA) this turns out to be problematic due to the demands on the optical properties. Many methods for adhesion promotion, as etching with chemicals or mechanical roughening, lead to a significant deterioration in the transparency of such components [2]. In many cases a plasma treatment alone has no sufficient effect on improving the adhesion [3]. The Fraunhofer Institute in Jena (IOF) is working several years now on the nano-structuring of polymer surfaces by plasma etching [4-6]. Except for antireflection purposes, such a structure can also be used to promote adhesion. However, large structure depths and high aspect ratios are necessary therefore. In the experiments carried out here the self-organizing formation of such nanostructures on various polymer types was studied.

Experimental procedure

For the experiments, test samples with a diameter of 55 mm and a thickness of 1 mm were used. These samples were injection-molded by Jenoptik Polymer Systems GmbH from the materials shown in Table 1.

Polymer	Trade name	Supplier
Polycarbonat PC	Makrolon Al2647	Bayer Material Science
Cycloolefinpolymer COP	Zeonex E48R	Zeon Nippon
Polyamid PA	Trogamid CX7323	Evonik Industries AG
Polyethylenterephthalat PET	Melinex ST504	Du Pont

Tab.1: Polymer materials used for the experiments

Plasma etching was performed in a vacuum evaporation system (APS 904 from Leybold Optics). For the etching experiments the plasma ion source (Advanced Plasma Source, APS) of the coating plant was used. The operating mode of this plasma source has been described elsewhere [7]. The plasma gases were argon and oxygen in a 1:2 ratio, resulting in a total pressure of 5×10^{-4} mbar. Argon and oxygen ions are accelerated by a self-bias voltage to impinge on the substrates with an energy distribution maximum at about 120 eV. Etching times were fixed at 300 s, 600 s and 1000 s. The topography of the patterned surfaces was investigated by scanning electron microscopy with a Zeiss Sigma FE-SEM. Due to the temperature sensitivity of some plastic samples the acceleration voltage must be reduced to values less than 3 kV. In order to visualize the material removal as well as the structures depth, the samples were partially masked before etching. Micrographs of this generated etching rim were acquired for an inclination angle of 45° using the microscopes SE detector. To avoid charging effects of the polymer surface, the samples were sputtered with a gold layer of approximately 20 nm thickness prior to the SEM examination.

Results and Discussion

Experiments for structuring the polymer materials indicated that for the various polymer types very different structural depths occur despite identical plasma etching conditions. In Fig.1, image sections from the scanning electron micrographs show the etching ledge and a region of the resulting structure. For the Zeonex sample (Fig. 1 on top) it is obvious that a homogeneous ablation of the material takes place without the formation of a deep texture. Elongated etching times only contribute to an increased erosion but the resulting structure still has a low aspect ratio. For PET the situation is completely different. As shown in Figure 1 (bottom), knob-like structures with a depth of ~200 nm are formed at already 300 s etching time. For longer etching times not only the ablation, but also the depth of the nanostructures became significantly greater.

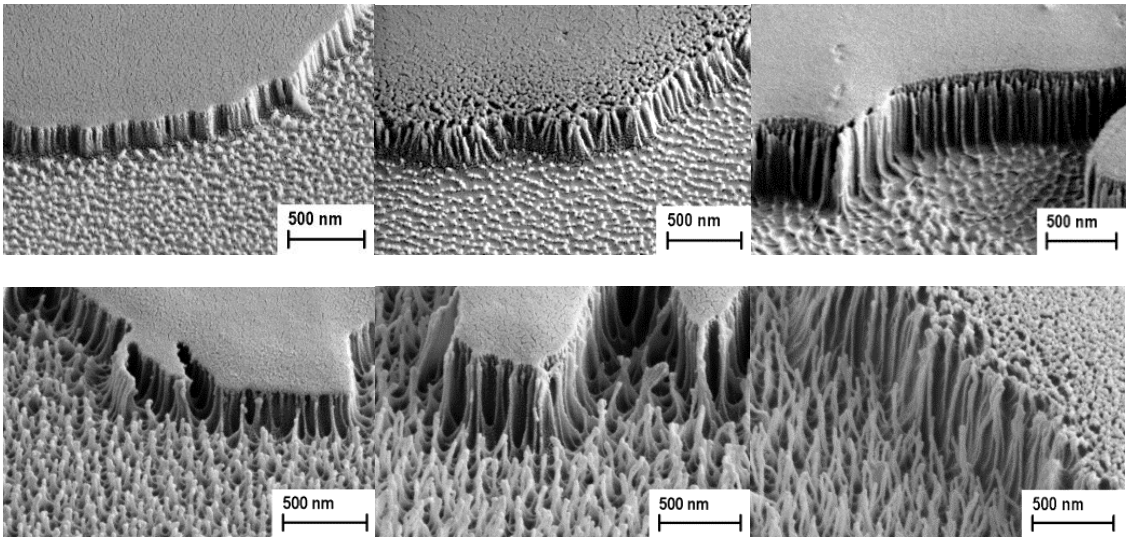


Fig.1: Scanning electron micrographs of nanostructures etched on Zeonex (top) and PET (bottom) for different plasma etching times: 300 s (left), 600 s (middle) and 1000 s (right)

If we plot the homogeneous surface ablation and the resulting structure depth in diagrams as a function of the etching time (see Figure 2) it becomes obvious that also on polymers not exhibiting a distinctive structure growth (Zeonex and Makrolon in Fig.2 right) homogeneous ablation occurs. In the case of the Zeonex material the ablation is as high as for the PET (see Figure 2 left) where deep structures can be generated. Of course the entire material erosion (and thus the etching rate) is higher for the PET because the material in between the structure features also becomes removed and must be added to the homogeneous ablation. Nevertheless the etching rate for PC and Zeonex is far from zero, so an explanation for the absence of structure formation can not be a lack of ablation.

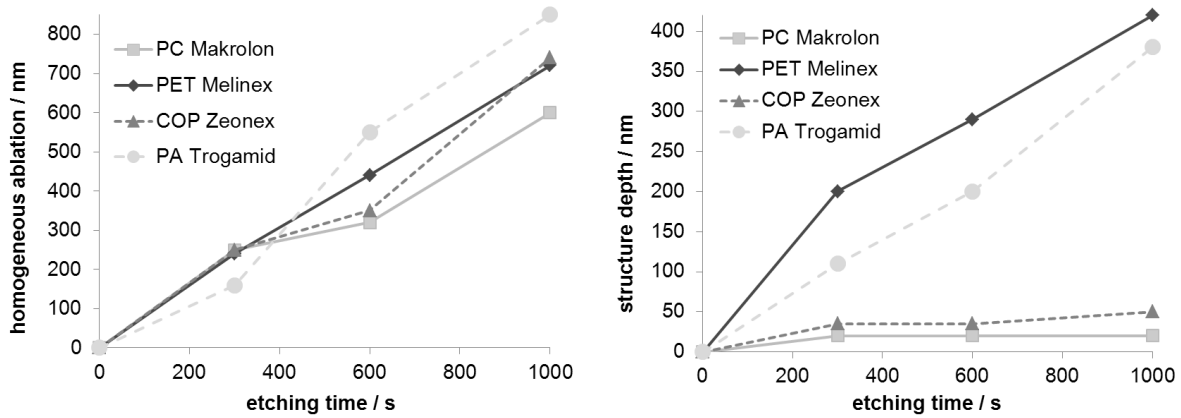


Fig.2: Homogenous ablation (left) and resulting structure depth (right) on various polymers as a function of the etching time

Summary and conclusions

Experiments were carried out to investigate the importance of the polymer type on the self-organizing formation of nanostructures on a plastic surface. This nano-texture should be generated by plasma etching and act as an effective and highly transparent adhesion promoter for subsequently applied wet-chemical laquers. It was found that a formation of up to 400 nm deep structures takes place on some polymers while on others no texture growth at all can be observed despite absolute identical etching conditions. Considering the ablation rates of the individual polymers no significant correlation to the nanostructure formation became obvious. So, the polymers chemistry and internal structure must have a crucial role in the formation of such nanostructures. This approach will be the subject of further investigations.

References

[1] K.L. Mittal, A. Pizzi; *Adhesion Promotion Techniques*, Marcel Dekker Inc., New York (2002)

[2] C. Harper; *Handbook of Plastics, Elastomers and Composites*, 2nd Ed. McGraw Hill, New York (1992)

[3] E.M. Liston, L. Martinu, M.R. Wertheimer; *Plasma surface modification of polymers for improved adhesion: a critical review*, J. Adhesion Sci. Technol., 7 (1993) 1091-1127

[4] Munzert, P., Uhlig, H., Scheler, M., Schulz, U., Kaiser, N.; *Method for reducing boundary surface reflection of plastic substrates and substrate modified in such manner*, WO04024805C1 (2005)

[5] Kaless, A., Munzert, P., Schulz, U., Kaiser, N.; *Nano-motheye antireflection pattern by plasma treatment of polymers*, Surface & Coating Technology, 20 1-4 (2004) 58-61

[6] U. Schulz, P. Munzert, R. Leitel, I. Wendling, N. Kaiser, A. Tünnermann; *Antireflection of transparent polymers by advanced plasma etching procedures*, Optics Express, 15 (2007) 13109-13113

[7] S. Pongratz, A. Zöller; *Plasma ion assisted deposition: A promissing technique for optical coatings*, J. Vac. Sci. Techn., A10 (1992) 1897-1904

Plasma Directed Assembly: Process Issues, Materials and Applications

Dimitrios Kontziampasis, Athanasios Smyrnakis, Vassilios Constantoudis, Evangelos Gogolides.

N.C.S.R. "Demokritos", Aghia Paraskevi, Greece.

dkontz@imel.demokritos,gr

The modern trend in nanofabrication is the use of self or directed assembly methods to form periodic or semi-periodic patterns in the nanoscale. Block copolymer lithography and colloidal lithography are used mostly to create these patterns. Our group [1, 2] has shown that oxygen plasma can direct the formation of organized nanodots on the surface of PMMA films (Fig. 1) and then transfer the pattern to a subsequent Silicon substrate.

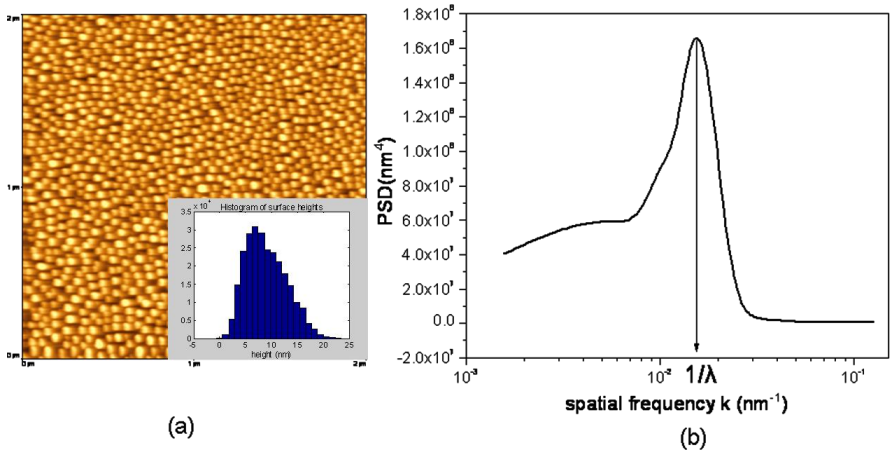


Figure 1. Plasma Directed Organization of Nanodots on a PMMA surface. a) 2x2μm AFM image of an initially 750 nm thick PMMA film etched for 1min in Oxygen plasma at the following conditions (1900 W top power, O V bias, 0.75 Pa, 65^{o}C, 1min etch, etching rate 600nm/min). Notice the formation of ordered nanodots on the surface of the film. b) PSD of the AFM image shown in (a). The peak wavenumber corresponds to a period of ~66 nm, and the peak sharpness quantifies the extent of order formation. The histogram of surface heights is shown as an inset in Fig. 1a and reveals a distribution with skeweness=0.44 and kyrtosis=2.60)

With the use of a cryogenic plasma etching process we create high aspect ratio silicon nanowires or nanopillars. A schematic of the process flow is shown in Fig. 2a. Etching a polymeric film for a few tens of seconds to a few minutes, results in the formation of ordered nanodots. These nanodots may serve as a mask when they reach the substrate. For the pattern transfer to the substrate, the same plasma reactor is used by switching the discharge chemistry and conditions. Fig. 2b shows the top-down 2D morphology and embedded 3D zoomed view of periodic nanodots which develop on a PMMA film. A high density helicon plasma reactor is employed.

For the pattern transfer to a subsequent silicon layer and the creation of high aspect

ratio silicon nanopillars, we developed a cryogenic silicon etching process. It is a clean anisotropic process that uses a SF_6/O_2 gas mixture at cryogenic temperature (T<−100 °C) which forms a SiO_xF_y passivation layer on the sidewalls that inhibits lateral etching. Having high etch selectivity to silicon over the polymeric nanodots mask, the cryogenic process was optimised in the nanoscale leading to the formation of silicon nanopillars with a diameter in the range of 40-100 nm and aspect ratio up to 20:1 (Fig. 2c). These nanopillars can find possible application for silicon solar cells or as molds for nanoimprint lithography.

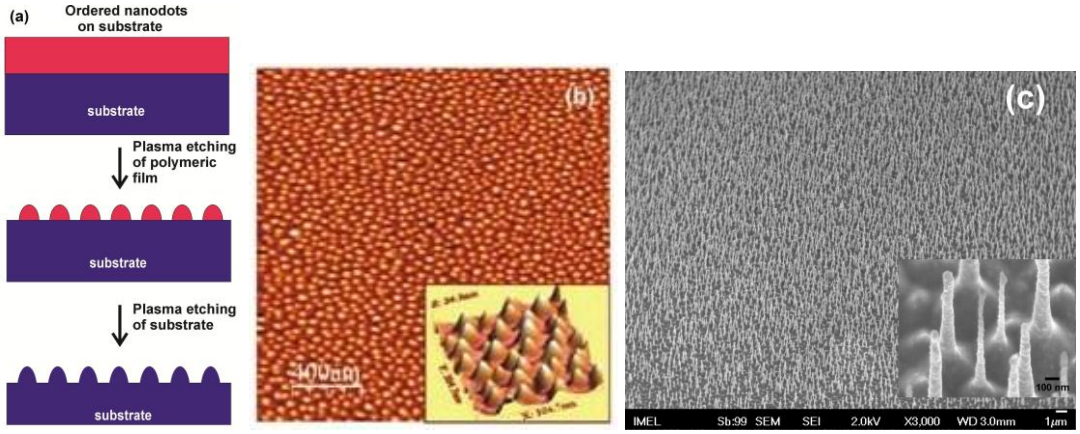
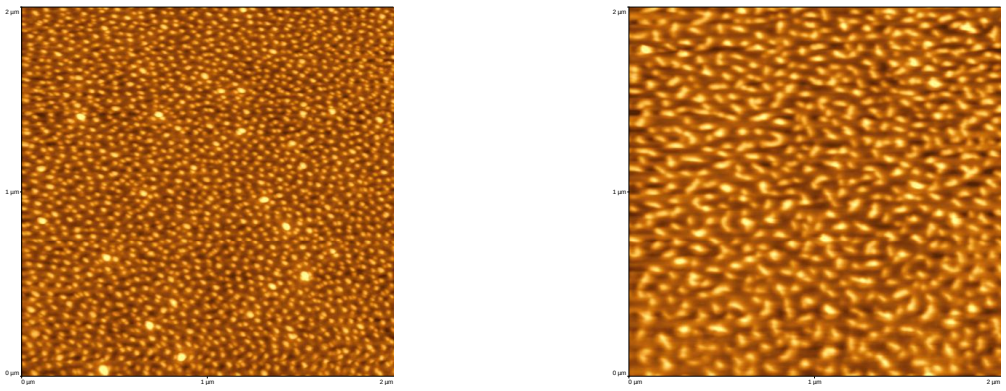
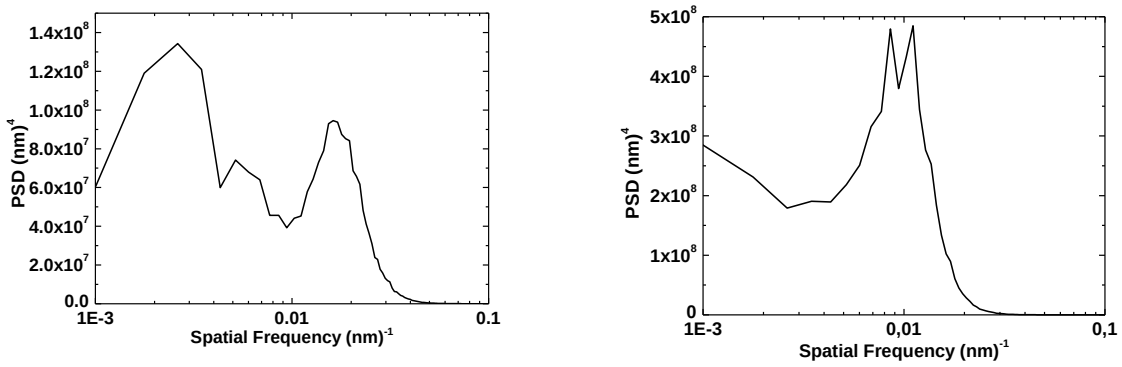


Figure 2. (a) Process flowchart showing direct pattern transfer to the substate using plasma etching. (b) 2×2 um^2 AFM image of a PMMA film surface after O_2 plasma etching down to Si substrate (c) tilted SEM image of Si nanopillars fabricated by the cryogenic etching process (a zoomed part of the image is embedded).

In this work, we also examine the generality of the phenomenon by looking if plasma directed assembly applies in other polymers. We study Polystyrene, a thermoplastic polymer more resistant to Oxygen plasma etching than PMMA, and PET a thermoplastic polymer which is widely used in food industry (it was chosen for potential future biological applications) and compare their morphology and dot characteristics with those of PMMA, thus generalizing our previous finding of plasma directed nanodot formation on PMMA [2]. The glass transition temperature of the polymer is proposed to play a role in the size and height of the created nanodots.



(a) (b)



(c) (d)

Figure 3. Plasma Directed Organization of Nanodots on PS and PET. (a) 2x2μm^2 AFM image of a ~ 1200 nm thick PS film etched for 2 min with Oxygen plasma (conditions similar to Fig. 1, except etching rate which was ~ 350 nm/min, almost half the etching rate of the PMMA polymer). (b) 2x2μm^2 AFM image of a PET plate etched for 1 min with Oxygen plasma (conditions similar to Fig. 1, except etching rate which was 680 nm/min.) (c) PSD of the 2d PS surface shown in (a). (d) PSD of the PET 2d surface shown in (b).

Processing (etching) time was also examined as to how it affects nanodot formation, along with the size of the features created and their order. We observed a second mechanism emerging after a few minutes of processing time and a transition from a small size ordered nanodots to a bigger size mounds with embedded nanodots on their surface. The emergence of this second scale topography on the etched surface affects the homogeneity of dot heights and widths resulting in much taller and wider features, which in some cases seem to form a rhomb-like network. [3]

In Figure 4, we can see the effects of the emergence of that second scale topography on vertical roughness parameters. For etching times less than 5 min, rms value remains almost unaltered with only a slight increase at 4 and 5 min. However, afterwards a dramatic change appears and rms increases very fast with a rate ~2.5nm/min. This crossover in rms behavior is also manifested in the time dependences of skewness and kyrtosis. As one can see in Figures 4b and 4c, skewness exhibits a shift from values less than 1 to values close to 2, while kyrtosis presents an abrupt increment from values around 3 to much higher ones about 6. Both changes can be attributed to the emergence of the second scale topography and the subsequent selective enhancement of the height and width of some dots since it increases the asymmetry of height distribution (upwards shift of skewness) and makes its peak steeper (increment of kyrtosis).

That emergence of the second, low frequency scale and the concomitant degradation of order and homogeneity of nanodots can be also detected in the evolution of the shape of PSDs as shown in Figure 5. For times shorter than 8 mins, the PSD is characterized mainly by the presence of a peak at frequency fp~0.016nm-1 the inverse of which at λ~65nm provides an estimation of the mean spacing between nearby dots. This peak widens progressively with time affecting the low frequency part of PSD, whereas at high frequencies (f>fp) the spectrum remains almost unaltered even for t=8min. After passing the crossover time of 8min, the low frequency part exhibits an abrupt increase (notice the log scale of PSD axis in Figure 5) and a second power law appears for $0.002<f<fp$ with the simultaneous formation of a wide peak at very low

frequency. This power law quantifies in frequency terms the emergence of the second scale topography associated with low frequency fluctuations in surface morphology.

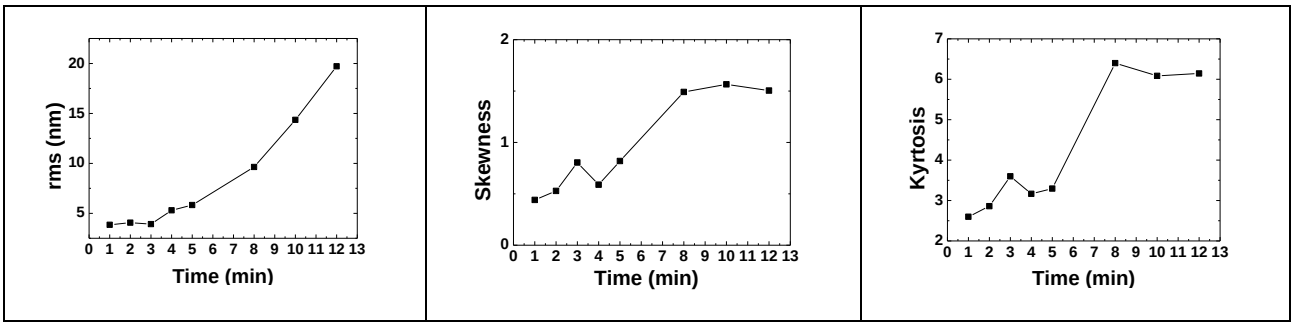


Figure 4. Evolution of the surface morphology metrics with oxygen plasma etching time. Vertical roughness parameters are shown versus time: rms (a), skewness (b) and kyrtosis (c).

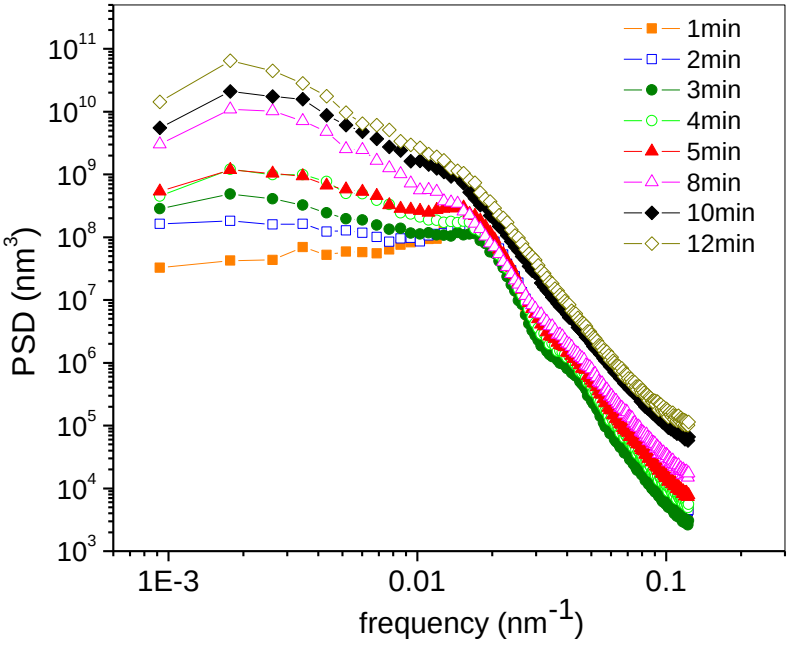


Figure 5. Circularly averaged Power Spectral Density (PSD) of etched surfaces versus etching time. Notice the importance of low frequency at long etching times, and the transition taking place between 5min and 8min of etching.

References:

[1] E. Gogolides, et. al.; PCT/GR2009/000039, WO/2009/150479.

[2] N. Vourdas, et. al.; Nanotechnology 21 (2010) 08530.

[3] D. Kontziampasis, et. al.: Plasma Proc. Polym., DOI: 10.1002/ppap.201100163

DC Discharge Plasma Polymerization of 1-Naphthylamine

M. Yablokov[1], A. Gilman[1], N. Surin[1], M. Augustyniak-Jablokow[2], K. Tadyszak[2], A. Kuznetsov[1]

[1] *Enikolopov Institute of Synthetic Polymer Materials Russian Academy of Sciences, Moscow, Russia*
E-mail: plasma@ispm.ru
[2] *Institute of Molecular Physics Polish Academy of Sciences Poznan, Poland,*
E-mail*: aldona@ifmpan.poznan.pl*

Naphthalene and their derivatives such as 1-naphthylamine are very promising blocks for building high-quality conducting polymers due to the extended π-electron systems in their molecules [1], and plasma polymerization is of undoubted interest in this regard, since it allows for the synthesis of polymers in the form of thin films and coatings [2, 3]. There are some chemical and electrochemical methods for producing polymer from 1-naphthylamine [4 – 7].

In this work thin polymer films from 1-naphthylamine have been obtained for the first time by polymerization at the cathode and anode in DC discharge and studied the chemical structure and properties of this polymer.

1-naphthylamine (NA) was purified by recrystallization from ethanol prior to use, and its purity was checked by measuring the melting temperature (T_m=50°) using differential scanning calorimetry.

The setup and procedure for DC discharge plasma polymerization of compounds that are solid at room temperature are described by us elsewhere [8, 9]. A polymer from NA (PPNA) was obtained by DC discharge in the form of thin film on an aluminum foil, conducting single-crystalline silicon, or fused silica substrate. The process conditions were as follows: a temperature in the reaction chamber of 40°, an NA vapor pressure of 40 Pa, a discharge current of 5 mA, and a reaction time from 60 s to 420 s. The films thickness was measured by interferometry. The PPAN films neither dissolved nor swelled in ethanol, acetone, heptane, at all, but the films obtained at the cathode were easy detached from the aluminum foil

substrate with ethanol. Kinetics of the formation of polymer films obtained by the DC discharge at the cathode has been investigated, and it is shown that the growth rate of polymer films increases from 3 nm/s to 6 nm/s with the film thickness from 100 nm to 1 μm; then, the growth rate becomes constant. The morphology of polymer films synthesized under various conditions was examined by SEM and AFM. It was shown that the films have granular structure and a size of these granules is ~ 50 nm. The presence of micron-size aggregates composed from granules was also established. The value of the surface roughness calculated from roughness profile obtained by AFM was increased from 4±1 nm for the film with the thickness of 90 nm to 35±12 nm for the film with the thickness of 1.5 μm. These data are in agreement with the results obtained in [5].

The elemental composition of PPNA was studied by pyrolysis chromatography using a Carlo-Erba IA 1108 CHNS analyzer. It is evident that the relative amount of hydrogen and nitrogen in polymer is lower than that in NA, and oxygen appears as well. Calculation of the empirical formula for C_{10} shows the amount of nitrogen in PPNA is reduced to 0.7 as compared to 1.0 in the initial compound.

Fig. 1 shows the FTIR absorption spectra of (***1***) NA and (***2***) PPNA obtained at the cathode.

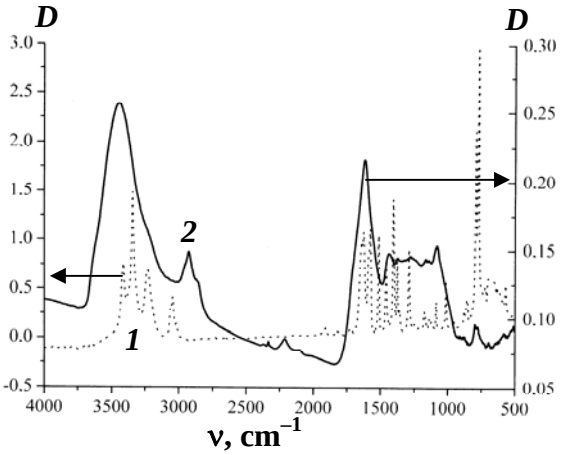


Fig. 1. FTIR absorption spectra of (*1*) NA and (*2*) PPNA synthesized at the cathode.

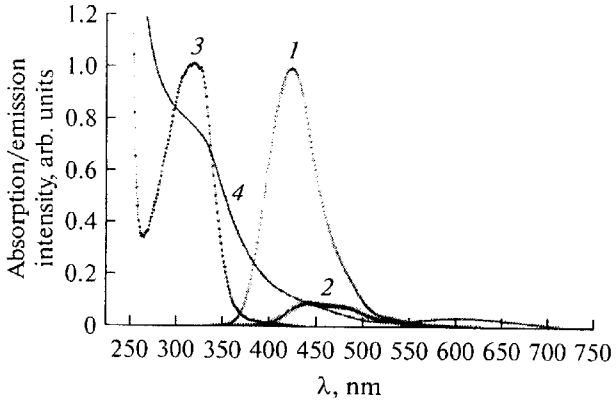


Fig. 2. Matching the (*1*, *2*) luminescence and (*3*, *4*) absorption spectra of (*1*, *3*) NA and (*2*, *4*) PPNA.

The broad band at 3370 cm^{-1} is associated with stretching vibrations of secondary amines, and the band at 1630 cm^{-1} is apparently due to stretching vibration of the imine group. The absorption bands at 1378 and 1260 cm^{-1} are associated with C–N stretching, and the absorption band peaked at 1141 cm^{-1} indicates the presence of the imine and secondary amine groups, i.e., benzenoid and quinonoid conjugated moieties in polymer chain. The absorption bands at 1445 and 1520 cm^{-1} correspond to C=C skeletal vibration of the aromatic rings, and the absorption bands at 720 and 879 cm^{-1} apparently indicate attachment of aromatic rings in the 1,4-position [7].

The luminescence spectra of NA in ethanol and (*2*) PPNA are shown in Fig. 2, as well (*3*) the monomer and (*4*) polymer absorption spectra. It is seen that the spectrum of (*2*) PPAN exhibits maximums close in position to the 240- and 325-nm peaks of (*1*) the NA spectrum and new maximums at 440 and 615 nm. In the case of excitation at a wavelength of 325 nm, week luminescence of the polymer at 400-600 nm is observed, roughly coinciding with the monomer luminescence. A comparison of the absorption spectra of PPNA and NA leads to the conclusion that this may be aminonaphthalene nucleus luminescence strongly attenuated by the 440-nm polymer absorption band (inner filter effect).

The data of FTIR and UV spectroscopy show that the PPNA chain is apparently made of units with two different structures. In one case, NA units are joined together without breaking the double bonds, as confirmed by the long-wavelength absorption and the absence of luminescence. In the other case, NA units are linked to one another by a spacer with broken conjugation.

The TGA measurements were shown that PPNA loses less than 20% of mass in an argon atmosphere when heated to 400°C, whereas the polymer undergoes oxidative degradation in air: a 50% of mass loss is observed upon heating to ~410°C and further heating leads to a rapid loss (up to 90% at ~470°C), and then slowly to the gradual complete degradation of the sample at 800°C. These data resemble those reported in [7] for the polymer synthesized by the chemical method.

Polymer synthesized by the DC discharge was investigated by ESR method. The typical ESR spectrum of PPNA is shown in Fig. 3.

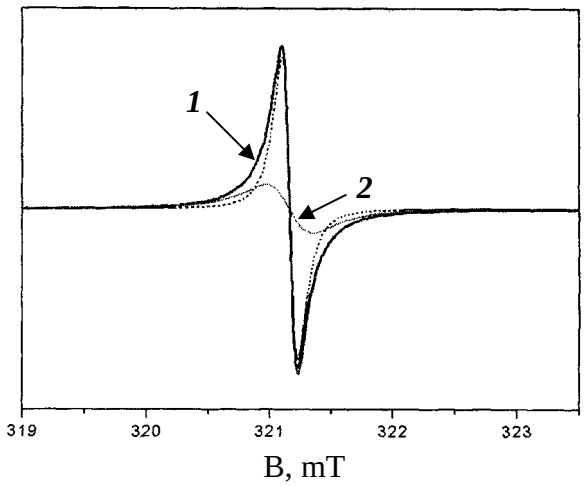


Fig. 3. A typical ESR spectrum of PPNA and its resolution on spectra of (***1***) long and (***2***) short polymer chains.

It is presumed that this spectrum is a sum of signals from radicals located on the polymer chains of different length. Fig 3 shows the resolution of PPNA spectrum on 2 spectra of (***1***) long and (***2***) short polymer chains. It is found that the spin concentration is equal to ~ 10^{19} spins/g, the line width at 300 K is equal to ΔB = 0.13 mT, and g factor is equal to 2.0020±0.0002. The data obtained confirm the presence of aromatic free radicals localized near nitrogen atoms [10].

Acknowledgements. This work was supported by the Russian Foundation for Basic Research, project no. 10-03-00772-2a.

References

1. Kim, J.-E., Son, S.-H., Bae, J.-S., Lee, Y.-G., Kim , K.-K, Lee, J.-C., Jang< J.-G., and Im, S.-G., US Patent 7604874, 2009.
2. Yasuda H., *Plasma polymerization.* Missouri: Academic, 1985.
3. Friedrich J. // *Plasma Process. Polym*. 2011, ***8***, 783-802..
4. Moon, D-K., Osakada K., Maruyma T., Kubota K., and Yamamoto T. // *Macromolecules,* 1993, ***26***, 6992-6997.
5. Riaz U., Jahan R., Ahmad S., and Ashraf S.V. // *J. Appl. Polym. Sci.* 2008, ***108***, 2604-2610
6. Schmitz, B.K., and Euler, W.B. // J. Electroanal. Chem. 1995. ***399***, 47-53
7. Ciric-Marjanovic G., Marjanovic B., Stamenkovic V., Vitnik Z., Antic V., and Juranic I. // *J. Serb. Chem. Soc.* 2002, ***67***, 867-877.
8. Drachev A., Gilman A., Obolonkova E., and Kuznetsov A. // *Synth. Met.* 2004, ***112***, 35- 40.
9. Yablokov M., Gilman A., Surin N., Semenov I., Kuznetsov A., and Chmutin I. // High Energy Chem. 2010, ***44***, 431-435.
10. Gong X., Dai L., Mau A.W.H., and Griesser H.J. // *J. Polym. Sci. Part A: Polymer Chemistry,* 1998, **36,** 633-643.

Polymerization of Acrylic Acid by a 4kJ plasma focus device

Morteza Habibi, Reza Amrollahi, MHS Alavi
Amirkabir University of Technology, Fusion Lab., Tehran, Iran

Abstract

The most conventional way for polymerization of acrylic acid on different substrates is using RF devices and introducing of other devices is under way. In this work we have a new study on formation of polymer Acrylic Acid using APF plasma focus device. The formation of plasma polymer acrylic acid is discussed using results obtained from attenuated total reflectance infrared spectroscopy (ATR). The results show that after 15 shots, nitrogen pulses performed polymerization on the specimens and the main peaks of ATR spectra assured poly acrylic acid formation on SBR substrate.

Keywords: Plasma polymerization, APF Plasma focus device, Acrylic acid, ATR-FTIR

1. Introduction

Plasma polymerization is one of the well-known techniques for depositing thin layers on different substrates without affecting their bulk properties [1-4]. Generally, plasma polymerization is accomplished by introducing different types of monomer precursors (vapour or aerosol) into a plasma reactor chamber leading to the deposition of so-called plasma polymers. The –COOH group in figure.1 plays the main role in ppAAs and the main goal in this area of research is to gain a surface with high density carboxylated surfaces which can be used for immobilization of bio-molecules, high retention of carboxylic acid groups, improving hydrophilicity and wrinkle recovery angle of some textile surfaces [1, 3]. We used SBR (Styrene-Butadiene-Rubber) (figure.2) as substrate and nitrogen as medium gas. Plasma can be used as a means of providing hydrophobicity to rubber [4,5]. SBR is one of the most important synthetic rubbers. It accounts for about 40% of the total synthetic elastomer production [6], so it can be a good candidate for investigation in this study.

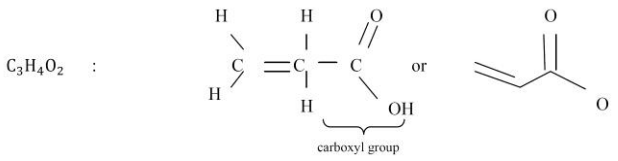


Figure 1. Chemical structure of acrylic acid

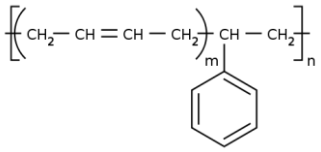


Figure 2. Chemical structure of SBR

Although some other devices like DBD (Dielectric Barrier Discharge) was introduced for polymerization of acrylic acid [4], but our device characteristic is more similar to RF reactors/generators in case of pressure (both continuous and pulsed [7]) ranging from 3-50 Pa (23-375 mTorr) [1-3, 8-10] which are commonly used in recent studies.
In pulsed discharges of the plasma focus device, the accelerated current sheath forms a dense (10^{25}–10^{26} m^{-3}) short lived (~100ns), and high temperature (1-2keV) plasma pinch column [11]. Due to m=0 instability the plasma pinch is broken and the resulting induced electric field accelerates electrons and ion beams (V ≥ 10^7 cm/s). The details of the plasma focus device have been published earlier [12-16]. Nitrogen plasmas and their characteristics, suggest that they provide significant plasma densities and populations of reactive species for effective plasma treatments on a variety of materials [17]. As it shown in figure.3, the ions in the plasma help breaking C=C bonds to C-C preparing the acrylic acid to form poly acrylic acid.

In the present work, we investigated formation of ppAA by APF device. After 15 shots, nitrogen pulses performed polymerization on the specimens and the main peaks of ATR spectra assured poly acrylic acid formation on SBR substrate.

2. Experiments

The APF is a 4 kJ plasma focus of Mather type. The condenser bank consists of a single low inductance capacitor of 36 μF capacitance, 30nH inductance, and maximum potential of about 16kV. The measured total external inductance of the device is 115nH [18]. A parallel plate spark gap with a swinging cascade configuration was used as a high voltage switch. The experimental set up is shown in figure.4. The gas (nitrogen) was fed to the discharge tube by using a needle valve and pressure is read with a pirani gauge.
After adjusting the working pressure, transfer of energy from the capacitor to coaxial electrodes is made by a rail gap switch.
Since the goal of this study is the formation of ppAA regardless of thickness of layers, instead of introducing acrylic acid to the chamber we carefully coat our substrate with thin layer of acrylic acid (99%, Merck KGaA). Commercial SBR substrates are cut and prepared to stand in the holder. Specimen (size 20×15×10 mm^3) were introduced into the plasma focus chamber and mounted axially above the anode at a distance of 8 cm. Neither bias voltage nor auxiliary heating is applied to the specimen. Schematic diagram of plasma focus electrodes configuration is illustrated in figure.4.
Throughout the experiment, the filling gas pressure is kept at 2 Torr to obtain strong focusing action. The focusing efficiency is monitored using Rogowski coil, Farady cup and scintillation detector. After 15 shots ppAA was produced on the substrate.

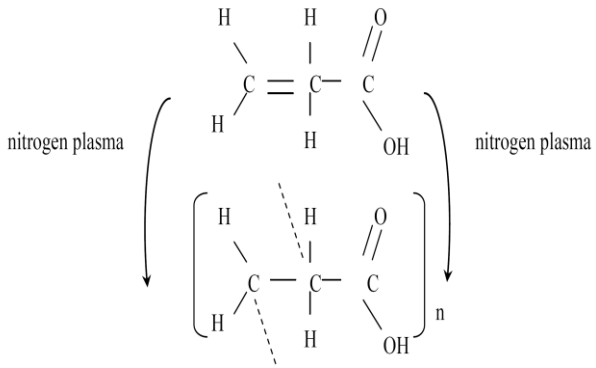


Figure 3. Acrylic acid polymerization

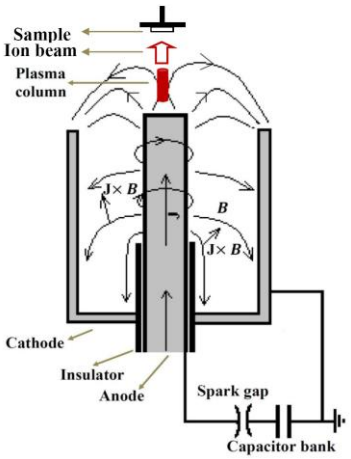


Figure 4. Sketch of APF plasma focus device

The chemical composition of plasma-polymerized coating is obtained using Fourier transform infrared spectroscopy (FTIR) on a Bruker Equinox 55 equipped with ATR accessory with 0.4 cm resolution and 32 scans for each spectrum in the range between 600- 4000cm^{-1}.

3. Results and discussion

ATR-FTIR Results

To confirm the polymerization of acrylic acid and before this analysis one should know assignments of FTIR-ATR of each chemical band for both before and after of polymerization of main specimen [19] and also probable reaction which may occur. Since except C=C band all other bands are the same in both acrylic and poly acrylic acid the full spectrum in references would be useful [20, 21] to distinguish between them. Assignments for main absorption bands and potential

C-N band are shown in table 2. More accurate analysis can be done by knowing the peaks of each specimen using references and comparing the full spectra which are also may be available in some FTIR-ATR devices libraries. In this case we introduced some main peaks (without mentioning their band) of SBR, acrylic and poly acrylic acid in table 3.

Type of vibration	Wave number (cm^{-1})
OH broad band	2800-3500
CH stretch band	2800-3000
C=O	1695-1725
OH deformation	910-950
C=C	1617-1634
CH2 bending	1430
C-O vibration	1167-1250
C-N stretch band	1055-1175

Table 2. Assignments of FTIR-ATR absorption bands (excluding SBR)

Compound	Wave number (cm^{-1})
Poly acrylic acid	*2940*,*1715*,*1420*,*1400*,1250,*1190*
Acrylic acid	2992,1704,1637,1617 1435, 1299,*1060*,985
SBR	2900,2800,1650,1480,1440,*960*,900,700

Table 3. Compounds main peaks wave number (actual data may vary. italic numbers observed) [20, 21]

To investigate the uniformity of polymerization we shall discuss ATR spectrum of ppAA layers on SBR substrate at the centre and the edge of a typical substrate in figures 6 and 7 respectively. In figures 6 and 7 some main peaks that illustrate formation of poly acrylic acid are as follows. CH stretch band between 3000-2800cm $^{-1}$ which is more intensive at the edge of the substrate, CH2 bending band approximately in 1453cm $^{-1}$ at the centre and 1442cm $^{-1}$ at the edge of the substrate, C-O band in about 1173cm $^{-1}$ at the centre and 1181cm $^{-1}$ at the edge, C=O band in about 1719cm $^{-1}$ at the centre and 1725 cm $^{-1}$ at the edge, and small OH deformation peak in around 912 cm $^{-1}$ for both of them. These peaks are the main peaks to assure formation of poly acrylic acid.

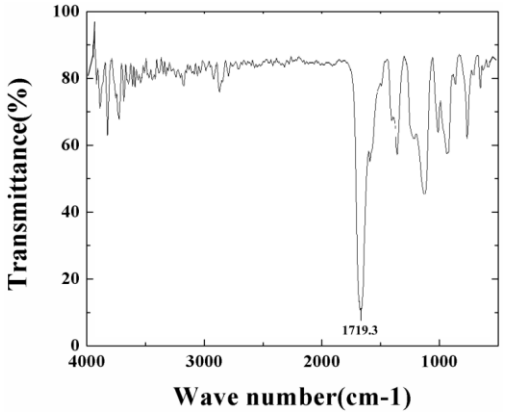


Figure 6. ATR spectra of ppAA layers at the centre of SBR substrate

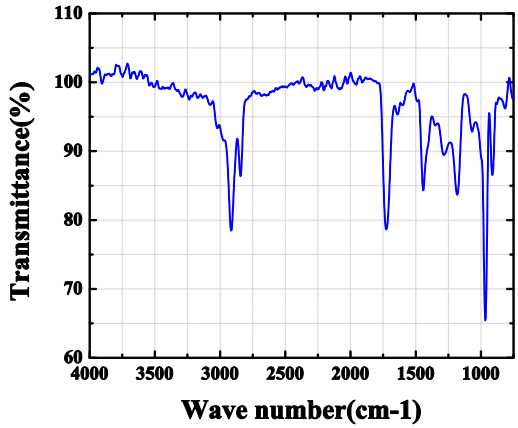


Figure 7. ATR spectra of ppAA layers at the edge of SBR substrate

To assure the formation of polymer in the centre, the centre spectra is checked with device ATR library in figure.8 which is well matched.

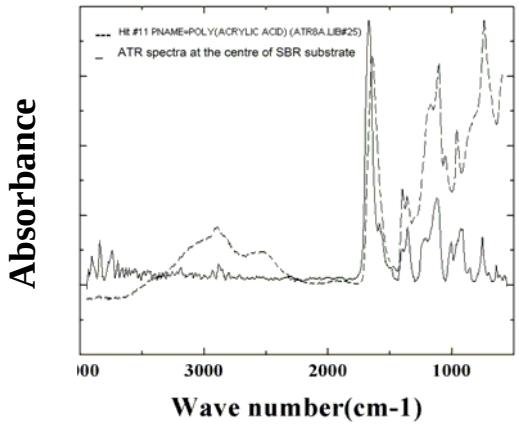


Figure 8. Comparison of experimental spectrum of specimen at the centre with one obtained from ATR device library

4. Conclusions

This paper provides new information about formation of plasma polymer acrylic acid by APF device. Setting the device for most optimum ion charachteristics lead us to plasma polymer acrylic acid after few shots on discharge energy of about 1.8kJ. Optimum number of shots to achieve stable polymers without side effects is one of the concerns. Styrene-Butadiene-Rubber used as substrate and nitrogen puffed into the chamber as medium gas. After 15 shots, nitrogen pulses performed polymerization on the specimens and the main peaks of ATR spectra assured poly acrylic acid formation on SBR substrate. Increasing the plasma treatments to more than 30 shots give an enhanced adhesion and sputtered Cu layers on SBR substrate obsereved.

References

[1] Hegemann D, Korner E and Guimond S. 2009, Plasma Process Polymer,6: 254
[2] Robert D. Short and David A. Steele. 2010, Plasma Process Polymer,7: 370
[3] Zanini S, Ziano R, Riccardi C. 2009,Plasma Chem. Plasma Process,29:535
[4] Morent R, Nathalie De Geyter, Sandra Van Vlierberghe,et al. 2009,Plasma Chem. Plasma Process,29:103
[5] M Mercedes Pastor-Blas, Jose Miguel Martin-Martinez,Dillard G J.1998, Surface and Interface Analysis, 26:385
[6] Gerardo Martinez Delfa, Olivieri A,Carlos E Boschetti.2009,Computers and Chemical Engineering 33:850
[7] Sciarratta V, Vohrer U, Hegemann D, et al. 2003,Surface and Coatings Technology, 174: 805
[8] Gupta B, Saxena S,Ray A. 2008, Journal of Applied Polymer Science , 107:324
[9] Jiang Z, Jiangb Z J, Shi Y, et al. 2010, Applied Surface Science, 256: 6473
[10] Basarir F, Choi E Y,Moon S H , et al. 2005,Journal of Membrane Science, 260:66
[11] Mather J W. 1965, Physics of Fluid , 8,2 :366
[12] Mather J W. 1971, Methods of Experimental Physics. Academic Press: New York
[13] Srivastava M P, Mohanty S R , Annapoorni S,et al. 1996, Phyisics Lett., A 215:63
[14] Piekoszewski J, et al. 1988, Journal of Applied Physics, 64:2648
[15] Stygar W, Gerdin G, Venneri F, et al. 1982, Nucl. Fusion 22:1161
[16] Mehboob S, Ahmad S, Waheed A ,et al. 2006, Plasma Sources Sci. Technology, 15:295
[17] Grace J M and Gerenser L J.2003, Journal of Dispersion Science and Technology ,24: Issue 3: 305
[18] Habibi M, Amrollahi R, Attaran M. 2009 Journal of Fusion Energy, 28:130
[19] Bellamy L J.1975, The infra-red spectra of complex molecules. Chapman and Hall: London
[20] Pouchert C J. 1981, The Aldrich library of infrared spectra. Aldrich Chemical Co.: Milwaukee
[21] Pachler K G R, Matlok F, Gremlich H U. 1988, Merck FT-IR atlas: a collection of FT-IR spectra. VCH: Weinheim, New York

Synthesis and characterization of Nanostructured thin films by reactive triode sputtering

Chahinez Saied and Abdelouahad Chala

Laboratoire de Chimie Appliquée, Université de Biskra, BP 145 RP, 07000 Biskra, Algeria

Abstract
The present work deals with structural, mechanical and tribological charaterization of nanostructure of nitrides based films (ZrN, TiN) for cutting tool applications. Coatings are deposited by reactive magnetron sputtering from metallic targets (Ti, Zr and B) on static substrate holders with RF or DC bias.
Thermo chemical treatments by plasma nitrided have been held on steel substrates for eventual duplex applications.
The influence of plasma parameters (nitrogen partial pressure and substrate bias) on mechanical properties of ZrN an TiN is studied. In order to improve its mechanical properties, bore is then introduced to TiN and ZrN thin films. The fraction of bore into the coatings is then increased in order to achieve the formation of ZrBN and TiBN nanocomposite. Chemical, mechanical, tribological and structural properties are studied as a function of bore content using XPS, FTIR and nano-indentation, Scratch tests, XRD, SEM and TEM techniques. C-BN and h-BN phases are detected from 1 at.% of bore by XPS measurements.
An increase of the hardness is observed while adding bore to nitrides with two maximum at 5 and 10 at.% of bore. The resistance corrosion is also studied as function of deposition conditions.
Keywords: reactive magnetron sputtering, thin films, mechanical properties, tribological properties, TiN, ZrN, TiBN, ZrBN, nancomposites, corrosion.

Introduction

Cubic BN presents a variety of mechanical, thermal, electrical and optical properties [1] highly desirable for thin-film applications. The main problem for its industrial application is that c-BN films peel off from substrate even for low thickness (0.1 - 0.2μm). This delamination of c-BN films is attributed to high compressive stress, which is believed to arise from the intense energetic ion bombardment [2,3]. Many attempts have been made to improve the adhesion of c-BN films such as the introduction of intermediate buffer layers and the increase of the substrate roughness [4]. It was shown [5] that boron, boron-rich and boron carbide/B-C-N gradient layers increase c-BN film adhesion.
Nevertheless, these interfaces may be detrimental to some potential applications of c-BN films. Another way was to increase the deposition temperature. Taylor *et al.*[6] obtained thick adherent c-BN films at temperatures up to 1000 °C. But such a high temperature limits the number of possible substrate materials for c-BN growth. A third way was to decrease the stress level by post- deposition annealing or ions implantation. Kim *et al.* reported a stress decrease down to 3 GPa after 40 min annealing in nitrogen at 800°C [7]. Widmayer et *al*. [8] also observed a reduction of stress level, a graphitization and a resputtering of the films during ion implantation at high energy (50-100 keV).
Recently, some studies have shown that growing conditions are different from nucleation ones [9] and stress models of thin films deposited under ion bombardment predicts stress variation with ion energy and flux. [10, 11] What is generally called c-BN film is, in fact, a multilayer structure, which consists of an amorphous BN layer at the film/substrate interface, followed by a textured h-BN layer and the thick c-BN layer. Finally, at the top a very thin h-BN layer is observed [3]. In a previous paper [12], we have shown that a peak of stress of about 15 GPa is

observed in the h-BN basal layer, and that the occurrence of the cubic phase leads to a stress relaxation as expected from the conversion of the h-BN into a denser structure [12]. We may conceive to decrease the stress level, and thereby improving the adhesion, if we maintain a low value of stress by reducing the ion bombardment after the nucleation of the cubic phase. Bi-step procedure, where we have differentiated between the nucleation and growth conditions, has been used in order to decrease the stress level and improve the film adhesion. The results show a significant improvement of film adhesion. In fact for the films deposited by changing the ion fluxes, there were no delamination and no cracks in the film even after a long period. Scratch tests have been conducted and critical loads up to 5 N have been measured. Despite the adhesion improvement no stress relaxation was observed and the stress level remains as high as 10 GPa [13].
The purpose of the present work is to decrease the stress in the films by depositing a ternary compound like ZrBN. The addition of a third element like zirconium can be a means for achieving this goal and therefore improving in a significant manner the adhesion of the coating without an important decrease of its hardness thanks to the intrinsic hardness of ZrN.

Experimental Part

Triode Sputtering System (TS) was the deposition methods used in this study. It consists of a chamber pumped down to 5×10^{-5} Pa by a diffusion pump. An emitting filament and a plate anode create the plasma discharge. Two magnetic coils assure a high rate of ionization that enables to work at pressures down to 0.05 Pa. The target was dc biased, while the substrate holder was biased by a rf generator. A ZrB_2, nitrogen and argon gases were used [14]. For both the deposition techniques, silicon <100> substrates were used. The structural investigations of the deposited films were performed by IR absorption spectroscopy using a FTIR spectrophotometer (Biorad FTS 6000). The transmission spectra were recorded at normal incidence in the range of 400 to 4000 cm^{-1}. The hexagonal phase (h-BN) of boron nitride is characterized by the two infrared active TO modes which give a strong and asymmetrical absorption band E1u at approximately 1380 cm^{-1}, attributed to B-N-B bond in plane stretching, and a weaker band A2u near 800 cm^{-1} due to an out-of-plane B-N-B bond bending mode [3]. The zinc blend phase (c-BN) exhibits a single absorption band near 1065 cm^{-1} attributed to the infrared active TO mode. X-ray diffraction analyses using glancing angle with Co Ka radiations were performed to determine the structure of films.The mechanical stress was calculated from substrate curvature measurements.
The substrate Curvature and film thickness were measured by Dektak 3030 profilometer and gravimetry measurements were carried out using Sartorius Supermicro S4 microbalance. SEM and TEM observations were performed to determine the morphology and the microstructure of the coatings.

Results and discussion

The morphology of selected coatings deposited on low alloy steel is shown in the SEM photograph in Fig. 1.a. The Zr-B-N coatings exhibit a very dense structure. No columns nether grains were observed. Fig. 1.b. shows the microstructure of the films obtained by TEM. It reveals some ZrN crystallites in amorphous matrix.
Fig. 2 presents the X-ray diffraction patterns with 2θ scanning from 20 to 70 degrees as function of nitrogen flow and substrate bias voltage. It is clear that the preferred orientation is always (220). With increasing nitrogen flow (Fig. 2. b.) crystalline films growth slightly favoured with respect to amorphous growth. The transition from an amorphous to crystalline structure occurs in the nitrogen flow range from 12 to 19 sccm. Fig.2. a. shows the influence of the substrate bias voltage in the XRD patterns at a constant flow rate (12 sccm). The film structure changes from amorphous to crystalline with increasing substrate bias voltage. The

increasing of bias voltage and thus the higher ion energy during film growth enhances the activity of condensing particles resulting in an increased activity for the formation of the Zr B-N phase. Substrate bias voltage and nitrogen flow are the main parameters to obtain c-BN nucleation by triode sputtering system. Substrate bias voltage was firstly scanned from 0 to 150 V. fig. 3. a. shows the evolution of IR spectra for ZrBN films growths in pure nitrogen vs. bias voltage. T2 (1095-1100 cm^{-1}) peak of c-BN and E_{1u} (1395-1400) peak of h-BN were observed. Increasing substrate bias voltage is accompanied with decreasing of the intensity of h-BN peak and increasing of c-BN one. The maximum amount of c-BN found (79 %) was obtained in the range of 75-100 V bias voltage. Fig.3. b. shows the FTIR spectra of Zr-B-N films prepared with different flow of nitrogen. It can be clearly seen that with increasing nitrogen flow rate the transmission peak corresponding to c-BN phase becomes stronger. This implies that B-N bonding were formed in zirconium boron nitride films. The maximum of c BN formed in this case was about 98 % and it was obtained in the range of 25-50 %.
The evolution of the stress within the films was calculated by the Stoney equation from the inverse of the curvature radius and the corresponding thickness. The calculated stress values obtained from each film are reported in Fig. 4. The internal stress is max at -100V, which is the optimum bias for max c-BN content. The level of stress is decreased by almost an order of magnitude.

Conclusion

ZrBN films have been deposited on silicon and low alloy steel substrates by triode sputtering of ZrB_2 composite target. The conditions of deposition were successfully controlled and the properties of the layers are defined as function of the nitrogen flow and the negative bias voltage. Bi step procedure enables to increase the adhesion of the c-BN films but it appears no relaxation of the internal stress. Compressive stress in BN appears to be more related to the c BN content than to the deposition conditions. Thick (2 μm), dense films constituted of nanocristallites of ZrN has been observed.
Narrow window of experimental conditions lead to c-BN phase is observed and the maximum is obtained for 75 % N_2 and -100 V bias voltage.

References:

[1] L. Vel, G. Demazeau and J. Etourneau, Mater. Sci. Eng. 1991, B10, 149.
[2] D.J. Kester, K.S. Ailey, D.J. Lichtenwalner, R.F. Devis. J. Vac. Sci. Technol. 1994, A12, 3074.
[3] P.B. Mirkarimi, K.F. McCarty, D.L. Medlin. Mater. Sci. Eng. 1997, R21, 47.
[4] R. Freudenstein, S. Reinke, W. Kulisch, R. Fischer, J. Zweck, A. Bergmaier, G. Dollinger, Mater. Sci. For., 1998, 259, 287.
[5] M. Keunecke, K. Yamamoto and K. Bewilogua, 7th Int. Conf. on Plasma Surface Engineering, Garmisch-Partenkirchen, Sept. 2000.
[6] C.A. Taylor and R. Clarke, Mat. Res. Soc. Symp. Proc. 1996, 423, 265.
[7] I.-G. Kim, S.-H. Kim and K.-B. Kim, J. Vac. Sci. Technol. 1998, A 16 (4), 2295.
[8] P. Widmayer, P. Ziemann, S. Ulrich and H. Ehrardt, Diamond Relat. Mater., 1997, 6, 621.
[9] H. Hofsäss, H. Feldermann, M. Sebastian, C. Ronning, Phys. Rev. B 1997, 55 (19), 13230.
[10] C.A. Davis, Thin Solid Films 1993, 226, 30.
[11] H. Windischmann, J. Appl. Phys. 1987, 62(5), 1800 .
[12] M.-A. Djouadi, V. Mortet, S. Khandozhko, P.Y. Jouan, G. Nouet, surf. Coat. Technol. 2001, 142-144, 899.
[13] M. A. Djouadi, O. Banakh, A. Soltani, R. Sanjines, F. Levy, Thin Solid Films 2001, 398-399, 205.

[14] M. Ben El Mekki, M.-A. Djouadi, V. Mortet, E. Guiot, G. Nouet, N. Mestres, Thin Solid Films 1999, 355-365, 89.

Figure captions :
Fig. 1. SEM observation (a) and TEM microstructure (b) of the Zr-B-N coating
Fig. 2. XRD patterns of ZrBN films prepared under 12 sccm nitrogen flow as function of the bias
voltage (a) as function of the flow of nitrogen (b) (bias voltage = -100 V)
Fig. 3. IR spectra for ZrBN films as function as nitrogen percentage (a) and bias voltage (b)
Fig. 4. Compressive stress of ZrBN films vs nitrogen flow (a) and substrate bias voltage (b)

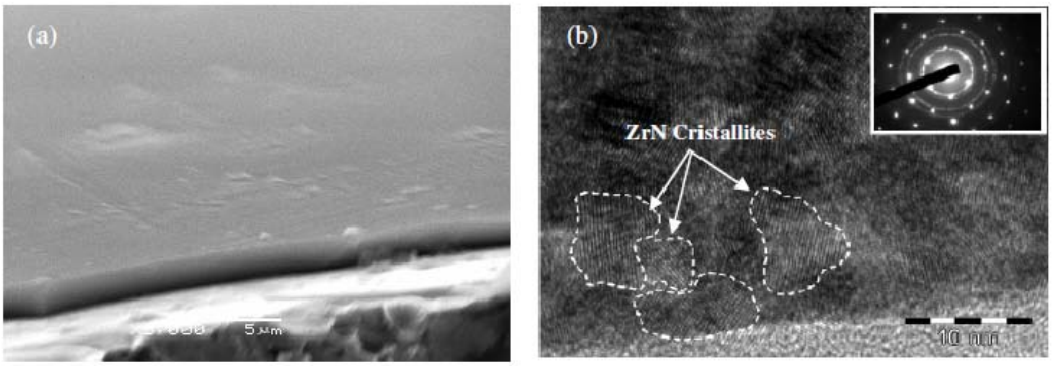


Figure 1

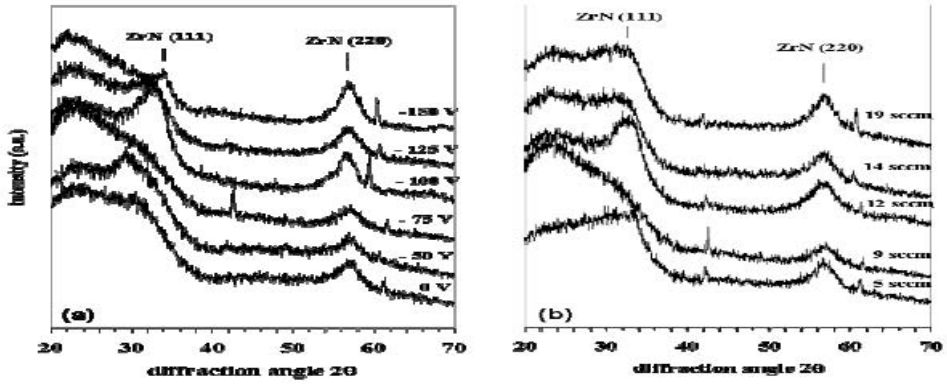


Figure 2

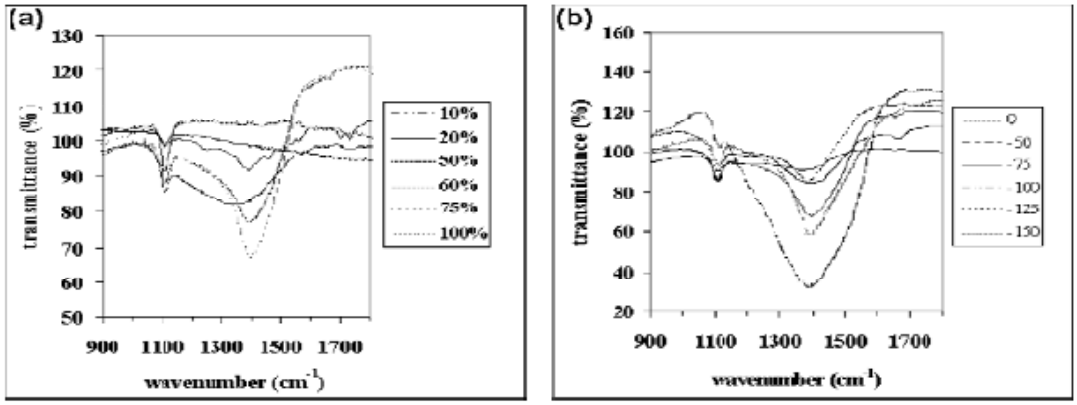


Figure 3

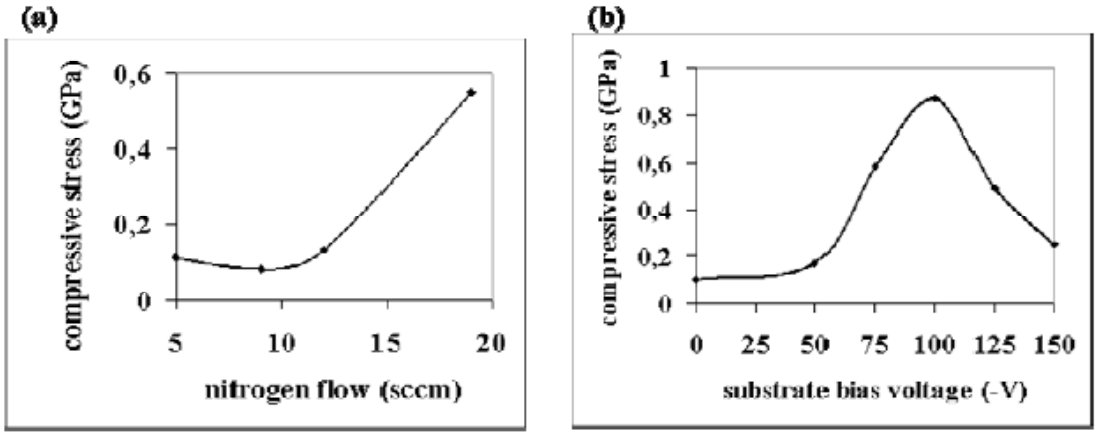


Figure 4

The Improved Friction Properties of Bonded MoS_2 Films By MAO Treating of Al Substrates

Hu Hanjun, Zhou Hui, Zheng Yugang, Sang Ruipeng， Zhang Kaifeng,Wan Zhihua
Lanzhou Institute of Physics, China Academy of Space Technology, Lanzhou 730000, PR China

Abstract
The bonded MoS_2 films is widely used as solid lubricants in aerospace mechanisms due to their excellent tribological properties. Traditionally, the MoS_2 was directly bonded on the Al substrate that was only treated by the technique named of sandblast. For improving the tribological properties of MoS_2 films, micro arc oxidation(MAO) instead of sandblast was introduced as a new technique for treatment of Al substrate. In this article, the tribological properties of MoS_2 films bonded on different surface of Al substrate as mentioned above was discussed, respectively. It is concluded from the test results that the MoS_2 films bonded on substrate treated by MAO have better tribological properties than the ones treated by sandblast, and the endurance life against abrasion of the former is as high as twenty times than the latter by the stand test method of ball on disk using the UMT Multi-Specimen Test System. This test results can be illustrated by the following reasons. One point is the porous microstructures of MAO ceramic coatings on the Al substrate. The coatings have numerous pits to be good at increasing the binding force with the MoS_2 films, and the pits can also provide a MoS_2 lubricants reservoir during processes of friction. Both of them improved the MoS_2 film's ability of wear-protective. Otherwise, naturally the MAO coatings' hardness is higher than the Al, and this ensures well wearing resistance, especially in practical application to big load-supporting moving parts, such as bearing, gear, etc…

Keywords: MoS2; Micro arc oxidation; Tribology; Wear; Endurance life

1. Introduction

The bonded MoS_2 films were widely used as excellent lubricants at aerospace moving parts in flight hardware for many years, and its tribological properties in vacuum are unique [1]. Some research departments in the worlds included NASA, ESA, etc.., were interested in the study of bonded MoS_2 films and paid lots of attention to extend its endurance life [2, 3]. According to the research results of the former, it was generally conceived that the substrate surface with a proper roughness was good for increasing the bonding strength between the substrate and the MoS2 films. For example, the Lyndon B considered that the MoS2 films were mechanically bonded to metal surfaces, and this surface must be roughened to promote lubricant adhesion by increasing the contact area [4]. Traditionarily, the usual method for roughening the substrate surface was abrasive blasting or glass bead blasting. Novelly, in this article a smart technology named MAO (micro arc oxidation) was introduced as a method instead of the abrasive blasting for roughening the metal substrates. MAO was a distinguished technique to fabricate a ceramic coating with lots of pores on light alloys such as Al, Mg, Ti and their alloys, by arc discharge at high voltage on the anodic surface under the cooperating effects of thermochemistry, plasma chemistry and electrochemistry reaction[5,6,7]. The pores with different sizes promoted the bonding force between the MoS_2 films and the ceramic substrates. Additionaly, the pores can act as 'reservior' of lubricants for further improving the endurance life of bonded MoS_2 films[8]. The following paragraph of this article would discuss the properties of bonded MoS_2 films which substrates surface was treated by MAO technology.

2. Experimental

2.1 Aluminum substrate surface treated by MAO

Aluminum alloy substrate was selected for preparing bonded MoS_2 films, and was treated by MAO skill under different processing parameters. As the power pulse frequency increased, the ceramics thickness and roughness synthesized on the substrates surface were also increased. In order to show the effects of MAO methods better or not, one of the substrate was treated by abrasive blasting for contrast. The information of the substrate surface treated by different processing parameters or methods was listed in Table 1.

Table 1 The different substrate surface

Sample No.	Processing parameter	thickness	roughness	method
1#	50v,6%,1000Hz,120s	3.27um	0.29um	MAO
2#	550v,6%,800Hz,120s	10.95um	1.06um	MAO
3#	550v,6%,500Hz,120s	20.59um	2.76um	MAO
4#	550v,6%,100Hz,120s	29.74um	4.18um	MAO
5#	—	—	2um	abrasive blasting

2.2 MoS_2 films bonded on the aluminum substrates

Firstly, using ethanol solvent cleaned the substrates surface through any technique capable of removing particulate and organic surface contamination. Secondly, the expoxy-bonded MoS2 films were prepared on the substrate surface via a metallic muzzle (this is the key step for deciding the thickness and roughness of lubricant films. Because the substrates listed in Table1 were processed in the same batch at this step, all of the samples in this article have the same lubricant films but different substrate surfaces.).

2.3 Testing and characterizing

Testing: The tribological behaviors of the samples were evaluated using a ball-on-disc tester (CETR UMT-2 Friction-Wear Tester) under dry sliding conditions. GCr15 ball with a diameter of 8 mm and a surface roughness smaller than 0.05μm was used as the counter face material. The measurement of the friction coefficient was performed at the load of 5 N and the sliding speed of 300 rpm. The endurance life of the lubricant films was evaluated by the total testing times before the friction coefficient sharply changed and got to the point of 0.3. All the tests were conducted at ambient lab conditions (25 °C and relative humidity of 50%).

Characterizing: Lots of charactering technologies were used for analyzing samples. The MAO thickness was measured by

using MINITEST-4100 eddy current thickness tester. The MAO roughness was measured by Nano-scratch tester (NST, CSM) at constant load 5mN, scanning length 3mm. The MAO surface morphology was observed by using Light Microscope/CCD Camera (PEC3010, CSM). The microstructure of MAO was observed by SEM.

3. Results And Discussion

3.1 Surface morphology

Fig.1 and Fig.2 show the surface morphology of different samples as listed in table 1, which Fig.1 and Fig.2 belonged to the samples with the processing of abrasive blasting and with MAO coatings, respectively. As showed in Fig.1, it could be observed clearly that the surface of Al substrate was properly modified. Some of the metal sheets and pits existed on the

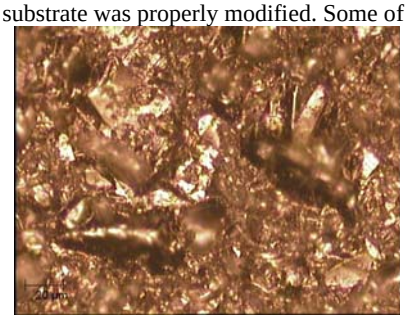


Fig. 1 Surface morphology of 5#

surface were formed to be good at extending the interface and improving the binding strength.

As is shown in Fig.2, it could be observed that the sizes of surface micro-pores were increased gradually from 1# to 4#. Contrarily, the amounts of micro-pores were reduced. The reason for the different surface morphology may be attributed to the MAO processing parameter with different pulse frequency. With decrease of impulse frequency, the total thermal energy for synthesizing MAO coatings was increased at the same processing time, the relationship between the thermal energy and frequency can be inferred from formula 1(the thermal energy is direct proportioned with impulse width.). With increase of thermal energy, more fusing objects of oxide were sintered or deposited in the surrounds of the micro-pores, and the lots of pores with small sizes were fused for forming big pores, and the thickness and roughness of the MAO coatings were also increased as showed in table 1.

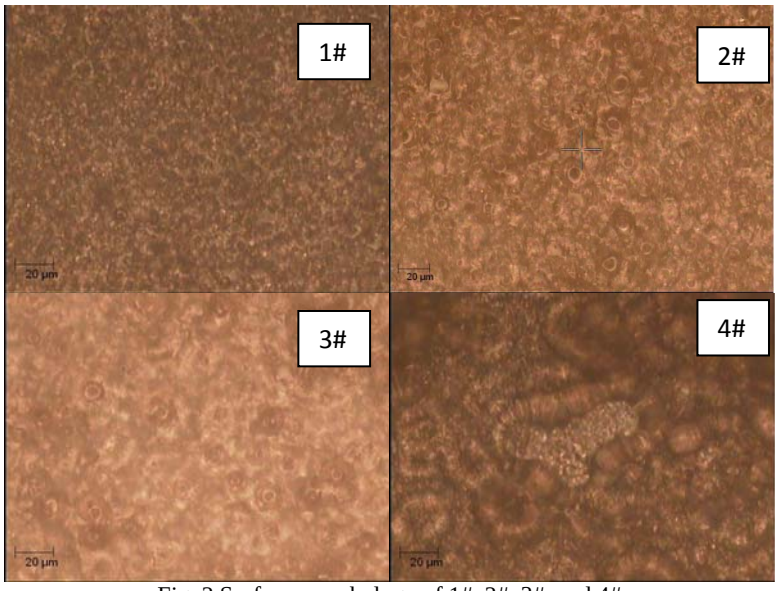


Fig. 2 Surface morphology of 1#, 2#, 3#, and 4#

$$T \times \phi = \frac{1}{f} \times \phi = T_{on} \qquad (1)$$

T: cycle F: frequency,
Φ: duty cycle T_{on}: impulse width

Otherwise, making contrast among the pictures, the MAO coatings could also help to reach the purpose like the abrasive blasting processing as showed in Fig.1, furthermore, the MAO coating may more adapt to improving the friction property of bonded MoS2 films, for its powerful binding strength with Al substrates and lots of pores with different sizes on the surface. For more clearly observed the micro-pores of MAO coatings, Fig.3 shows the microstructure of MAO coating surface. As Fig.3a showed, lots of micro-pores and protuberance were uniformly dispersed on the surface of coating, and no micro cracks existed .Fig.3b was one of the open micro-pores existed on the surface. These open micro-pores may effect as a ‘reservoir’ and be filled with some lubricants.

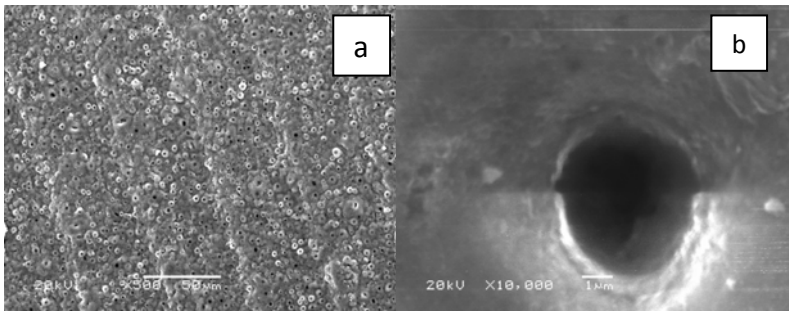


Fig.3 The microstructure of MAO coating with micro-pores

3.2 Microstructure of section

Fig.4 shows the sectional microstructure of MAO coating, and it included MAO coating and Al substrate. It was obvious that there was more than 10um thickness MAO coating naturally growing on the Al substrate, and there wasn't clear interface between the coating and the substrate, which mean the MAO coating tightly combined with Al substrate. Otherwise, it was also observed that the structural density of MAO coating was big even more than Al substrate, which ensured the excellent load-supporting ability of the coating.

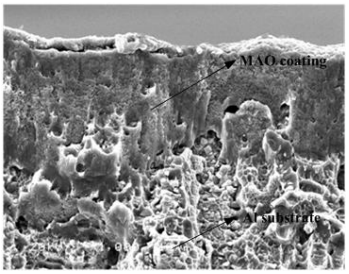


Fig.4 The sectional micro-morphology of MAO coating

Fig.5 showed the sectional microstructure of MAO coating with bonded MoS_2 film after friction test. Fig.5a showed the entire sectional micro-morphology of samples, which included substrate, MAO coating and MoS_2 film. The MoS_2 film was wore out, and transited to small pieces of MoS_2 arranged along the direction of friction test. Fig.5b was the high

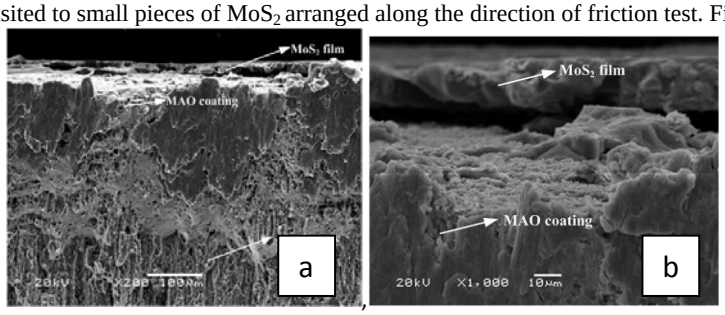


Fig.5 The sectional sectionmicro-morphology of MAO coating with bonded MoS2 films

magnifying section of MoS_2 film and MAO coating. As display of the Fig.5b, the small pieces of MoS_2 was gathered and coated on the tribological orbital local of MAO coating, and the edge of MoS_2 film didn't flaked away in the manner of great pieces, which all of this illustrated the good bonding force of the interface.

3.3 Friction properties

Fig.6 shows the frictions coefficient (COF) of different samples. It was observed from the curves that the COF was about 0.2 at the start stage, and it would increased step by step along with the prolongation of friction test time. For friction test, it was defined that the endurance life of the samples were the time when the friction coefficient arrived at 0.3. Fig.7 shows the endurance life of different samples. As shows in Fig.7, the 3# sample with roughness of 2.76um has the longest endurance life up to 30h, and the 5# sample treated by abrasive blasting has the shortest endurance life less than 1.5h. The former is as longer as twenty times of the latter. All of the samples treated by MAO have the longer endurance life than the 5#. These results expressed that the endurance life of bonded MoS_2 film can be improved by MAO treating of substrate, even more than 20 times than before, and this may attribute to the porous microstructures of MAO ceramic coatings on the Al substrate as showed in Fig.3. The coatings have numerous pores and pits to be good at increasing the binding force with the MoS_2 coatings, and the pores can also act as a MoS_2 lubricants reservoir during processes of friction. Both of them improve the MoS_2 film's ability of wear-protective. Otherwise, naturally the MAO coatings' hardness is higher than the Al, and this ensure well wearing resistance.

Fig.7 also shows that the proper roughness of MAO coating is very important for the tribological properties of bonded MoS_2 film. With the increase of roughness of MAO coating, the binding force between MAO coating and MoS_2 film is also enhanced. Nevertheless, when the roughness came high to certain point and the pores changed, the surface roughness and inner stress of bonded MoS_2 film would also get higher, which would finally deteriorate the tribological properties the films, therefore, by adjusting the processing parameter of preparing MAO coating could get the proper roughness for preparing the bonded MoS_2 film with excellent tribological properties and longer endurance life.

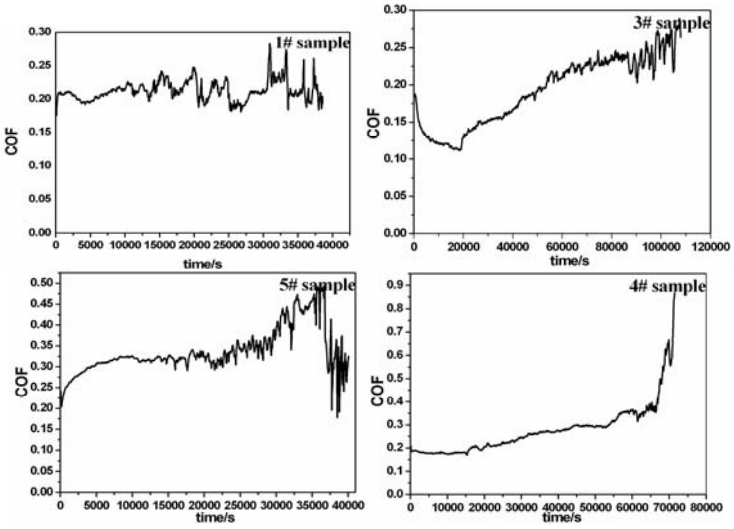


Fig.6 The friction coefficient of different samples

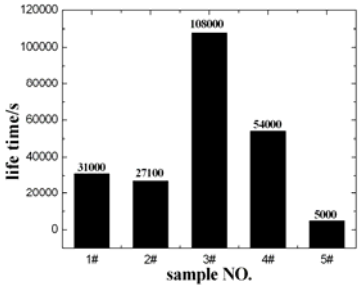


Fig.7 endurance life of different samples

4. Conclusion

The surface of MAO coating existed a lot of pores with different sizes, and this surface morphology was good for enhancement of binding force between the bonded MoS2 films and substrate. The MAO coating naturally grown on the Al substrate, and there wasn't clear interface between the coating and the substrate. The MoS_2 films bonded on substrate treated by MAO have better tribological properties than the ones treated by sandblast, and the endurance life against abrasion of the former is as high as twenty times of the latter by the stand test method of ball on disk using the UMT Multi-Specimen Test System. The main reason for above results of endurance life was the special structural characteristics of MAO coating, in especial of rough and porous structure. By adjusting the processing parameter of preparing MAO coating could get the proper roughness and pores for preparing the bonded MoS2 film with excellent friction properties and longer endurance life.

Acknowledgements

The authors would like to thank China Aerospace Academe for its great fund supports with this research and experts in Lanzhou Institute of physics for their unselfish guidance. We would also like to thank teacher Wang for its SEM analyse.

References

[1] ESR Technology Ltd., SPACE TRIBOLOGY HANDBOOK, 4th edition, 2007:216-228

[2] K. Miyoshi, M. Iwaki, K. Gotoh, S. Obara, K. Imagawa, Friction and Wear Properties of Selected Solid Lubricating Films, Part 1: Bonded and Magnetron-Sputtered Molybdenum Disulfide and Ion-Plated, Silver Films, NASA/TM-1999-209088/Part 1, October 1999.

[3] L. Rapoport, A. Moshkovich, V. Perfilyev, A. Gedanken, Yu. Koltypin, E. Sominski,G. Halperin, I. Etsion, Wear life and adhesion of solid lubricant films on laser-textured steel surfaces, Wear 267(2009) 1203-1207

[4] Lyndon B. ,Process Specification for Dry-Film Lubricant Application, Johnson Space Center, NASA, 4, 2010

[5] , F.P. Wang, et al, Effect of Current Density on Al Alloy Microplasma Oxidation, J Mater. Sci. Technol, 2001, 17(6): 657-660

[6] S.G Xin, Z.H. Jiang, F.P. Wang, et al, Effect of Current Density on Al Alloy Microplasma Oxidation, J Mater. Sci. Technol, 2001, 17(6): 657-660

[7] W.Krysmann, P.Kurze, K.H.Dittrich, et al. Process characteristics and parameters of anodic oxidation by spark discharge (ANOF). Crystal Research and Technology, 7(1984):973-979.

[8] Jin F Y, Chu P K, Tong H H, etal. Improvement of surface porosity and properties of alumina films by incorporation of Fe micrograins in micro-arc oxidation[J]. Applied Surface Science, 2006, 253: 863-868.

Self-lubricating W-S-C-Cr tribological coatings deposited by r.f. magnetron sputtering

Joao Vitor Pimentel[1*], Manuel Evaristo[2], Tomas Polcar[3], Albano Cavaleiro[2]

[1]Czech Technical University in Prague, Prague, Czech Republic

[2]SEG-CEMUC - Department of Mechanical Engineering, University of Coimbra, Coimbra, Portugal

[3]nCATS, Engineering Sciences, University of Southampton, Southampton, United Kingdom

[*]Corresponding author: j.v.bernatel@gmail.com

Introduction

Tribological coatings composed of transition metal dichalcogenides (TMD) have long been studied for their excellent self-lubricant properties. However, they exhibit low load-bearing capacity, and their performance tends to deteriorate significantly in the presence of humidity. In previous works, doping disulfides and diselenides of tungsten and molybdenum has proven to be a way of greatly improving the tribological performance of this class of films in different environments.

In this work, thin films were deposited by r.f. magnetron sputtering on silicon and steel samples, using two targets (carbon and chromium) and tungsten disulfide pellets. The final composition was controlled by the number of WS_2 pellets and the ratio of the power applied to the targets. The carbon content was fixed at approximately 40 at.% in all depositions. The chromium content in the coatings was varied in the range 0 – 13.5 at.% and the S/W ratio was approximately 1.25 in all compositions in the series. The coatings were characterized in regard to their hardness, adhesion, chemical composition and bonding, microstructure and morphology, as well as their tribological behaviour.

Characterization

Tribological tests were performed in humid air using a pin-on-disk tribometer. The applied contact load was varied and the wear tracks were examined, particularly by Raman spectroscopy and 3D profilometry. An adaptation of the equipment allowed the in-situ monitoring of the evolution of the wear tracks, by optical microscopy and Raman spectroscopy. The results of characterization and tribology evidenced improvements in hardness and wear resistance associated with the dopants.

Hardness values increased with Cr content, up to 7.1 GPa. With 0 at.% Cr (i.e., W-S-C only) the hardness was approximately 5 GPa, lower than that obtained previously with anther W-S-C system [1]. Nonetheless, these results evidence an improvement of more than one order of magnitude compared to undoped WS_2 films and are consistent with previous studies on doped TMD films [1,2].

The friction coefficients decreased with increasing load, indicating that the sliding under high contact pressure leads to the formation of a TMD-rich tribolayer. Raman spectroscopy showed a clear decrease in the contribution to the spectra of peaks corresponding to carbon. Analyses of the wear tracks indicated that the tribolayer consisted mainly of amorphous tungsten and chromium oxides with platelets of WS_2 in small areas. Below the outermost surface, however, a thin layer of well oriented WS_2 was found at the interface between tribolayer and coating [3].

The in-situ analyses yielded interesting results regarding the tribolayer formation during running-in and the sliding process. Although it was not possible to carry out a full measurement of the wear track profile, the optical analysis showed that the wear track widened rapidly in the first tens of cycles. By the 100^{th} cycle, the width of the wear track was already about 90% of the final width at steady state.

It was also observed during running-in the formation of rather large particles of debris, as well as scratches produced very early on which remained for tens of cycles or more. In some cases,

we were able to directly relate events in the friction curves with the presence of large debris or localized spots where the film was worn out. In previous studies with TMDs and results obtained with patterned samples (yet to be published), we have found that small areas where the substrate is exposed are very often filled up with tribomaterial during the sliding process, in a self-healing process.

References

[1] J.V. Pimentel, T. Polcar, M. Evaristo, A. Cavaleiro, Tribol. Int. 47 (2012) 188-193.

[2] T. Polcar, A. Cavaleiro, Surf. Coat. Technol. 206 (2011) 686-695.

[3] T. Polcar, F. Gustavsson, T. Thersleff, S. Jacobson, A. Cavaleiro, Faraday Discuss. 156 (2012) 383-401.

Figures

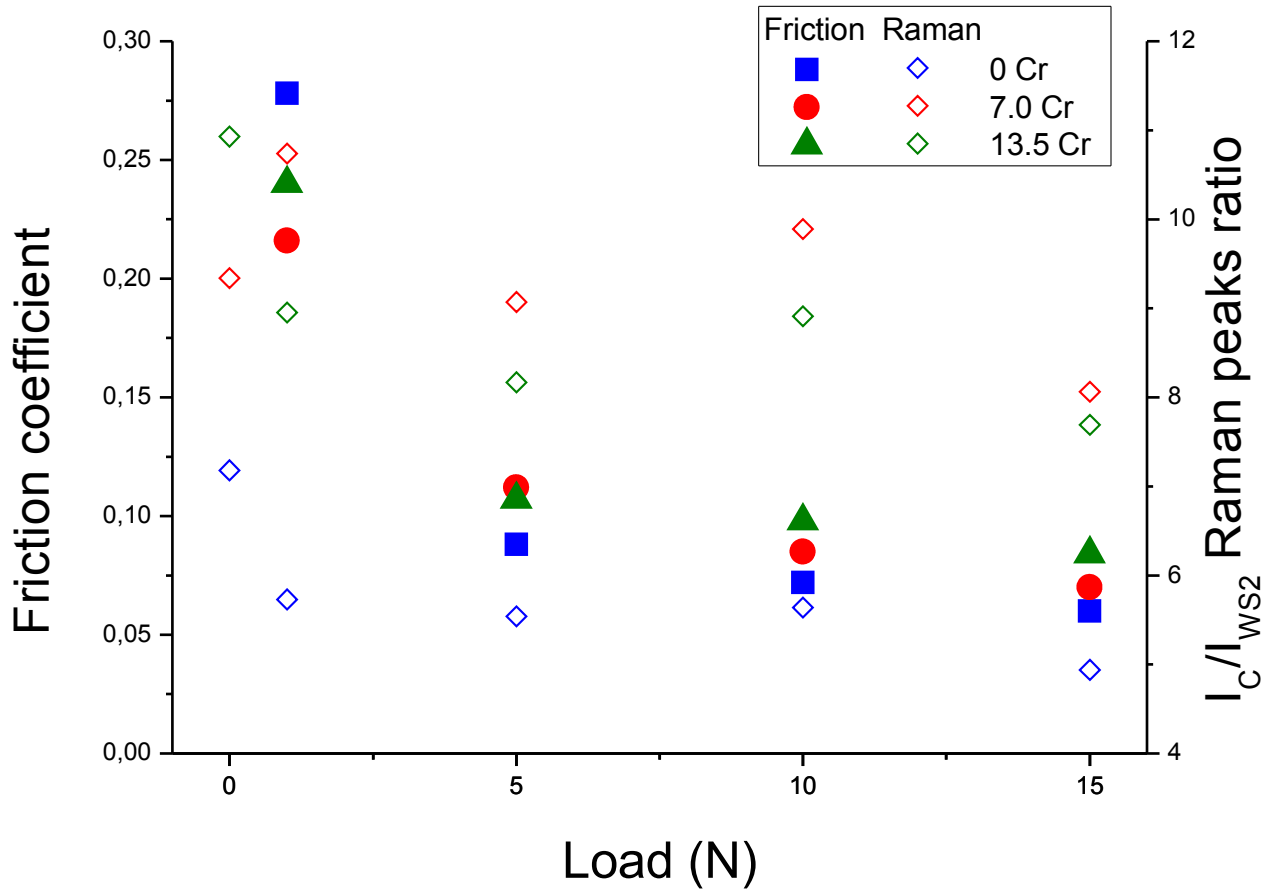


Fig. 1 Friction coefficient and Raman peak ratio for different loads

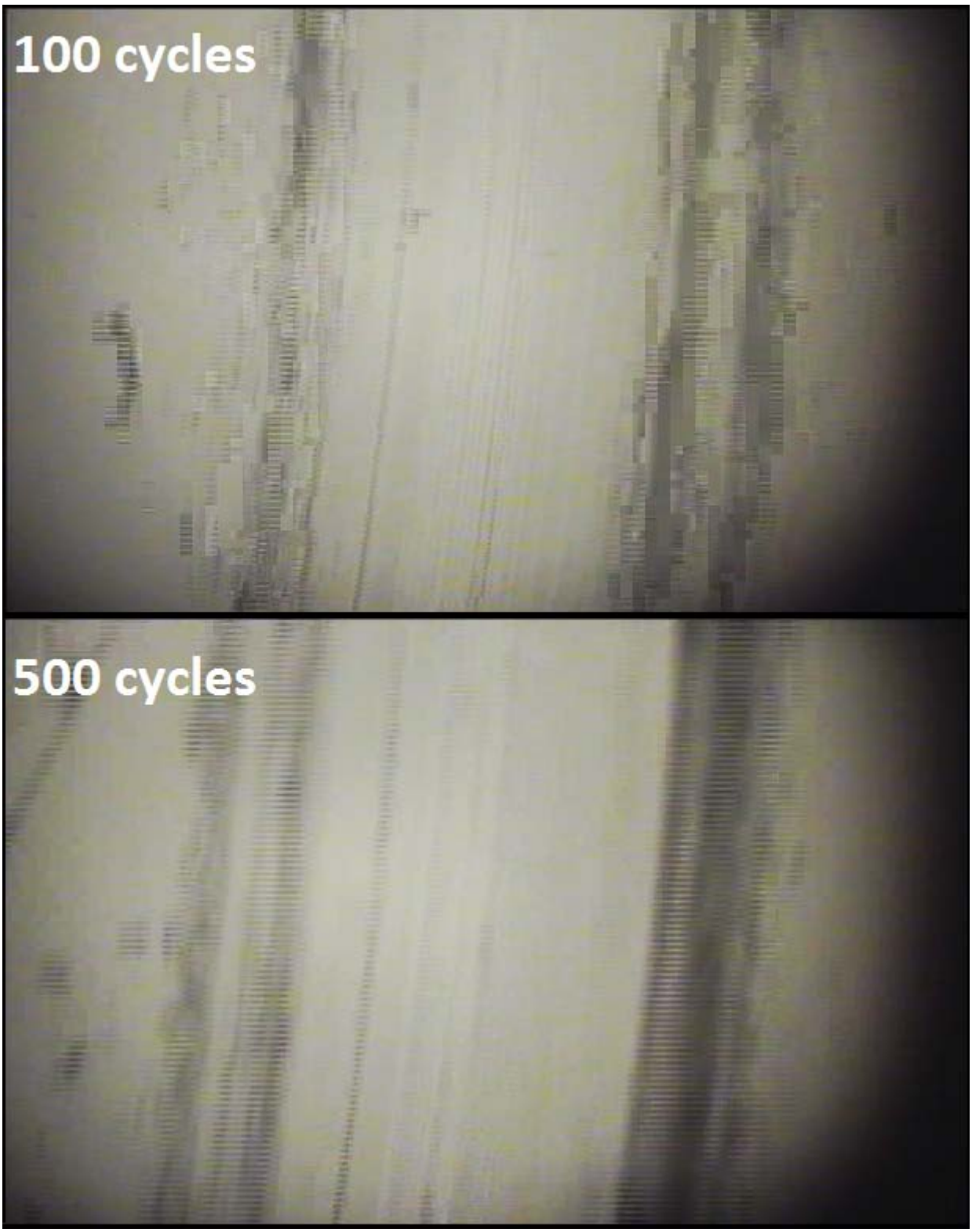


Fig. 2 Wear track during sliding, after 100 (above) and 500 cycles (below).

Wear Properties of AISI 4140 Steels Modificated By Using Pulse Plasma Technique

Y.Y.Özbek , M.Durman

yyarali@sakarya.edu.tr

Sakarya University, Metallurgical and Materials Engineering Department

Esentepe Campus, 54187, TURKEY

Abstract

In this study, the microstructure and wear properties of pulse plasma treated AISI 4140 steel was investigated. The surfaces of the samples were modified by using plasma pulse technique. The only one battery capacities (800mF) and two different sample plasma gun nozzle distances of 50mm, 60mm, 70mm, 80mm and different number of pulse were chosen for surface modification. XRD analyses were done for all samples. Wear test was done in CSM-linear wear test machine with 0.15 m/s constant sliding speed under 5N, 7N, and 9N loads for 200 m. It was observed that friction coefficient and wear value were changed in accordance with load. Friction coefficient values of modified specimens were lower than that of non-modified ones. Wear resistance was increased in modified samples. Worn surfaces of specimens were studied by SEM, EDS analyses techniques. Modification layer was formed on surface (in Fig.1a).

Key words: Pulse-plasma, surface modification, wear resistance

2. Introduction

It is known that the treatment of metals and alloys by high intensive ion, electron, plasma and laser flows is accompanied by surface heating (often higher than melting temperature) with subsequent rapid cooling of surface layer with approximately 10^{10} K/s rate. The appearing temperature gradients and doping of target during treatment procedure lead to structure-phase transformation in near-surface layer and to corresponding changes of mechanical properties such as hardness, wear resistance, corrosion resistance[1-3]. The using of compression plasma flows has a number of advantages: high plasma parameters in the flow, the possibility of surface layer doping by plasma working substance, short treatment duration, thick (up to 60 mm) modified layer.

In pulse plasma, an increase in the diffusion coefficients at a highrate elasto-plastic deformation is caused by an increase in the mean concentration of vacancies, which is in excess of the equilibrium one [4].

The pulsed-plasma technology allows a simultaneous, in one treatment pulse, realisation of different methods of affecting the workpiece surface: elasto-plastic deformation, impact by sound and pulsed magnetic field, heat and electric-pulse treatment, and deformation of metals and alloys during reversible ($\alpha+\gamma$) transformations. High power density of the flow (up to 10^7 W/cm^2 at the point of contact with the workpiece surface) makes it possible to perform

treatment in air atmosphere with no surface preparation. Treatment with a high-energy density flow of alloying elements causes no changes in geometric sizes of workpieces.

Depending upon the composition of the high-energy density flow, the surface layer can have high anti-friction properties, as well as high heat, wear and corrosion resistance. However, Pulse plasma has no line-of-sight restriction and retained dose problem characteristic of conventional ion beam implantation. It is therefore an excellent surface modification technique to treat complex-shaped industrial components [6].
In this study, cheaper and more heavily used in industrial surface properties of AISI 4140 steel with improved pulse plasma system you find in expensive and difficult availability of steel instead of groups investigated.

We have done wear tests: to 200m, 0.15 m/s speed 5N, 7N, 9N load device and a linear abrasion wear tests were performed under the CSM. Change of the load applied to samples after the abrasion test has changed the amount of the friction coefficient and wear was observed. The friction coefficient decreased 2-fold increase in wear resistance of steels was modified surfaces.

3.Experimental Procedure

In this study, AISI 4140 steel industry has a large surface area of use has been modified with pulsed plasma technology aims to improve the surface properties of. Surface properties of this steel type commonly used in a long, laborious without further heat treatment is cost-effective to develop the selected target. The chemical composition of the AISI 4140 steel in Table1, CNC machines in the cylindrical rod 22cm in diameter 10mm in height so that all the specimens cut from the same extent. Pulse plasma samples prior to any pre-treatment was applied. Pulse plasma process conditions applied in Table 2. " W" (tungsten) is used as the consumable electrode in this study.

Tablo 1.Chemical composition of 4140 steel

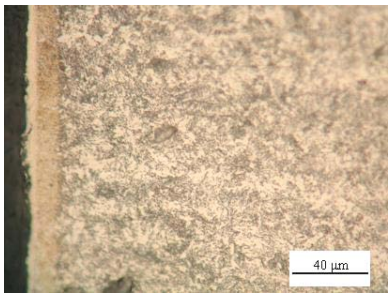
%	C	Si	Mn	P	S	Cr	Mo
AISI 4140	0.40	0.30	0.70	0.035	0.035	0.98	0.27

Tablo2. Pulse plasma parameters

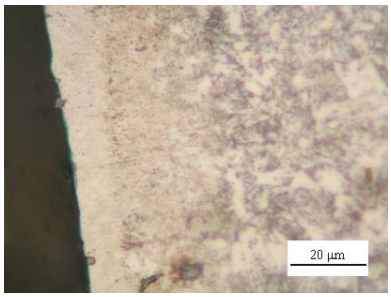
Sample No	h (mm)	Between the nozzle and samples(mm)	Number of pulse	Battery capacity, (mf)
1	10	70	15	800
2	10	70	10	800
3	10	70	5	800
4	10	80	15	800
5	10	80	10	800
6	10	80	5	800
7	10	60	15	800
8	10	60	10	800
9	10	60	5	800
10	10	50	15	800
11	10	50	10	800
12	10	50	5	800

Pulse plasma modified surfaces of the specimens in the method of linear wear device with CSM 0.15m/sn speed for the road 200m 5N, 7N, 9N wear test was performed for loads. The average air temperature 32°C during the experiments. Humidity is around 50-60%. Both the wear surfaces and wear products, SEM (different magnifications) and EDS analysis was conducted. Later, calculations and interpretations to help you wear a Perthometer MAHR surface roughness were measured with the specimens after wear.

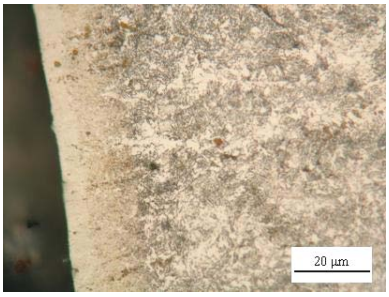
3. Results and Discussion



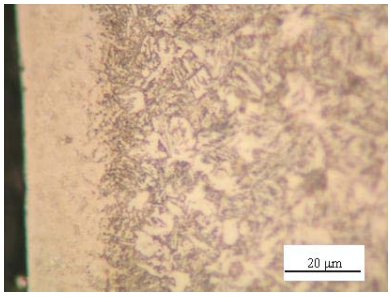
a)



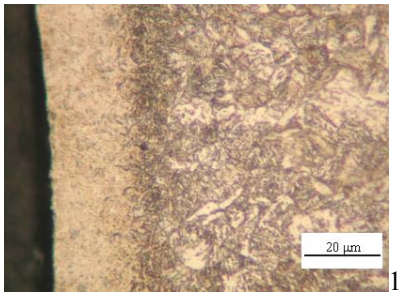
b)



c)



d)



11

e)

Fig1.Micrograph cross-section of modified samples a)2, b)5, c)7, d)8, e)11

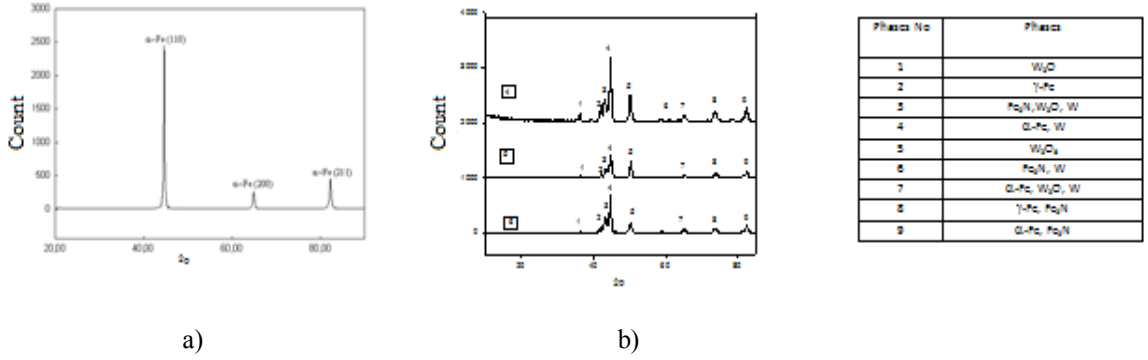
Fig. 1 shows optic micrograph cross-sections of the modified AISI 4140 steel sample. Evidence of severe plastic deformation is present in the treated surface layer, where microstructural morphology differs from that in the matrix. It was obvious from the microstructural examination that the modification layer, the diffusion layer and, at the bottom, the substrate can easily be seen due to contrast of light. The modification layer can be detected due to contrast of light.When the specimen-nozzle distance increases, the thickness of modificated layer decreases due to decreasing effect of plasma as seen in the results.

Another cause for this decrease is the ionized gasses exhausted from nozzle and they cannot reach to surface of specimen clearly and homogeneously[7-9].

Fig. 2 shows X-ray diffraction profiles of the untreatment and modified samples by pulse plasma technology. The Bragg diffraction peaks of the modified layer were broadened compared to that of the matrix, which can be attributed to the grain refinement effect and the lattice distortion on the atomic-level. Samples contained strong diffraction peaks for the Fe phase,as well as weak diffraction peaks of $Fe_{2-3}N$ and Fe_4N.

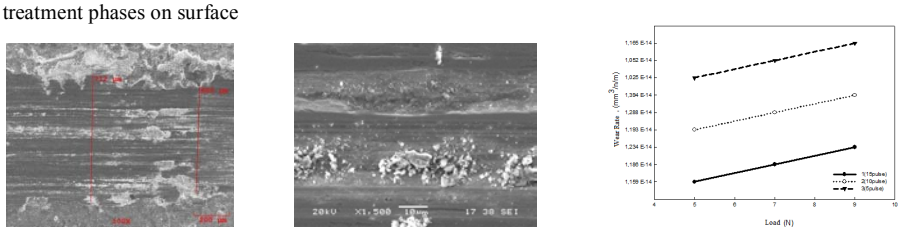
In addition, the pulse plasma technique can clearly improve the surface hardness. The surface microhardness value of the modified AISI 4140 steel was measured to be 1000HV0.05, which equals 5 times the associated value of the untreated substrate.

Fig.3. The compound layer can be identified easily under metallographic examination. The detailed thickness of the modified layers for different proses parameters. As the number of pulse and increased, the compound layer thickness increased.



a) b)

Fig 2.a) X-ray diffraction pattern obtained from the surface of the pulse –plasma treatment phases on surface, b) after pulse plasma treatment phases on surface



a) b) c)

Fig.3 a)after wear testing, wear scar on surface, b) SEM of worn surface, c) pulse effect to wear rate

After wear testing, SEM analyses were done all of samples surface. Especially, the plastic deformation was done in worn surface in Fig 3b. The groove was occurred in surface. The number of pulse affected to wear rate of samples surface. The wear resistance modified samples increased.

Results

The new phases were occured in modified surface by pulse plasma treatment. The hardness values of specimens exposed to modification treatment are 4 to 6 times greater than that of untreated specimens. Also, the wear resistance 2-3 times increased.

Atmospheric pressure plasma treatments inside meander-like cavities

Antje Quade, Katja Fricke, Klaus-Dieter Weltmann

Leibniz Institute for Plasma Science and Technology (INP Greifswald e.V.),
Felix-Hausdorff-Straße 2, 17489 Greifswald, Germany

Non-equilibrium atmospheric pressure plasma is used in a variety of applications related to surface treatment [1]. Most of all materials, intended for biomedical application, which must provide specific surface properties (e.g. enhanced wettability, biocompatibility) are exposed to plasma to improve for instance the efficiency of medical devices or the acceptance of implants. Atmospheric pressure plasma jets have reached an increasing importance in many plasma processing applications which is based on their ability to provide enhanced gas phase chemistry without operating at elevated gas temperatures [2]. Furthermore, an important feature of plasma jets is their capability to penetrate into small structures, such like cavities, gaps, crevices, and tubes which enables the treatment of complex geometries (e.g. scaffolds). For this purpose, a three-dimensional (3D) polycarbonate module was used to demonstrate the capability of jet plasmas, driven at atmospheric pressure, to penetrate into small cavities.

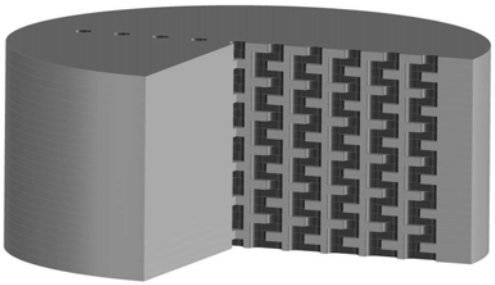


Figure 1:
Schematic drawing of the 3D module with meander-like cavities in a stack of perforated PC-layers.

The 3D module (Fig. 1) consists of perforated PC slices (∅ 24 mm) creating a porous 3D corpus. The slices themselves were laser-cut and the number of slices and the entire geometry is variable according to requirements. The holes of adjacent slices are interconnected in a vertical direction. The vertical pore sequence results in a meander-like single channel configuration throughout the 3D construct. Each slice was 0.5 mm in height, and a stack of 24 slices generates pore channels of an overall longitude of around 1.2 cm. A more detailed description of this newly generated 3D module and its application for cell culture investigations were published by

Bergemann *et al.* [3]. Due to the requirements for osteoblast ingrowth the pore sizes were chosen to be 500 µm in diameter [4].

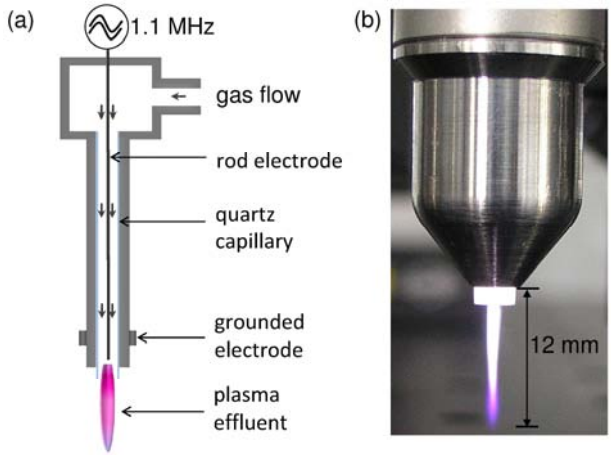


Figure 2: a) Schematic setup of the plasma jet (kINPen09®), b) photograph of the plasma effluent with a length of 12 mm using 5 slm argon gas.

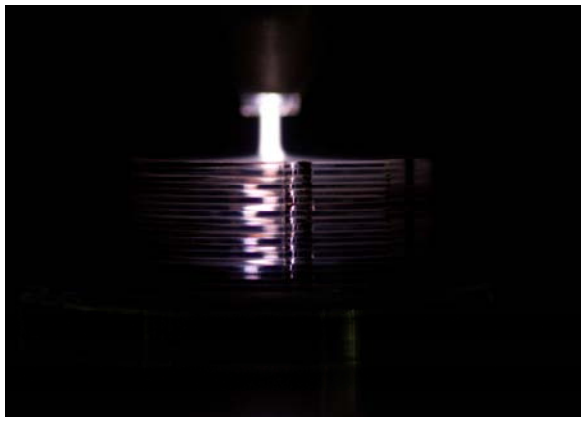


Figure 3: Plasma treatment through meander-like cavity in a stack of 24 PC-slices.

The atmospheric pressure plasma jet (kINPen09®) used in this study is shown in Figure 2. It consists of a hand-held unit for the generation of the plasma jet at atmospheric pressure, a DC power supply and a gas supply unit. In the continuous working mode, used here, a high frequency voltage is coupled to the pin-type electrode. The plasma is generated from the top of the centred electrode and expands to the surrounding air outside the nozzle [5]. As feed gases 5 slm argon (labelled as “Ar-jet”) or 5 slm argon mixed with 0.05 slm molecular oxygen (labelled as “Ar/O_2-jet”) were applied. The plasma treatment through the meander-like cavity (see Fig. 3) was carried out locally at a distance of 2 mm to the nozzle outlet. To study the penetration capability of the atmospheric pressure plasmas, the height of the stack was varied. For the experiments a short plasma treatment time of 30 s and a long-time plasma treatment of 300 s were chosen.

For the examination of the plasma-induced depth effect X-ray photoelectron spectroscopy (XPS) was applied. The surface analysis was performed on the surface of a non-perforated end-layer (made of polycarbonate (PC)), which was layered under the stack. The changes in elemental surface composition were analyzed using an AXIS Ultra DLD electron spectrometer (Kratos Analytical, Manchester, U.K.). The spectra were recorded as a line scan á 0.5 mm with a spot size of ~250 µm at the surface of the end-layer. The O/C ratios of the polycarbonate surfaces exposed to Ar and Ar/O_2 plasma for 30 s and 300 s, respectively, using a stack height of 2 mm (comprised of 4 layers) are depicted in Fig. 4.

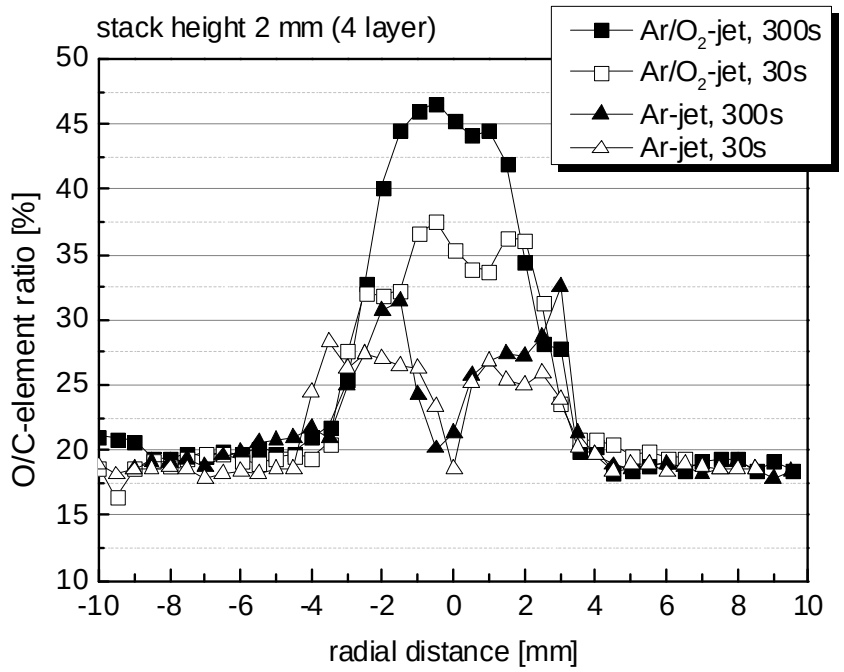


Figure 4:
XPS-O/C-elemental ratio at the PC-end-layer after plasma jet treatment through meander-like cavity with a height of 2 mm in dependence on time and operating gases.

As shown in Fig. 4, a functionalization, marked by an increased O/C ratio, of the PC-end-layer via a meander-like channel in a 4-layer stack can be observed. In dependence on treatment time and operating gases the O/C-element ratio varies. For 30 s Ar/O_2-jet treatment the O/C ratio was increased up to 20%, whereas after 30 s Ar-jet plasma treatment even less O-incorporation was noticed (lower O/C ratio). The highest amount of oxygen (O/C ratio of ~47%) was detected after a treatment time of 300 s by using the Ar/O_2-jet. Without oxygen admixture the O/C ratio was increased up to ~30% after long-time plasma treatment. This relatively high O/C ratio obtained by Ar-jet plasma is based on plasma-activated oxygen of the ambient air as well as post plasma oxidation.

Furthermore, along the O/C-curve shapes of the Ar-jet treated samples a distinct decrease of the O/C ratio directly on-axis of the jet can be seen. At this point no additional O-incorporation was detected. A possible explanation might be the low influence of oxygen of the surrounding air in the meander-like cavity due to the high Ar gas flow, which probably generates and operates in its own localized Ar atmosphere.

Since plasma-generated species can lose its reactivity over long distances, the impact of the different process gases on a stack comprised of 24 layers was investigated which is shown in Fig. 5.

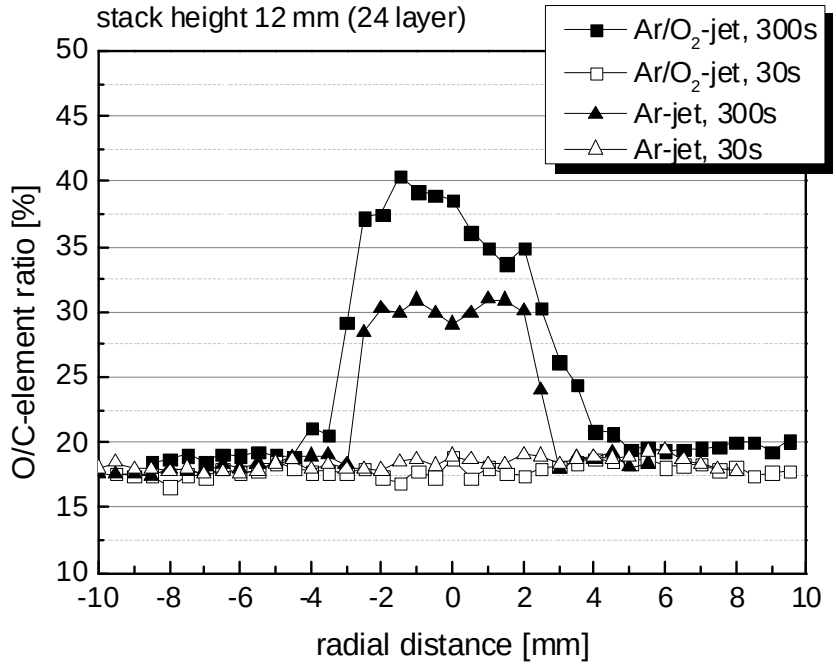


Figure 5:
XPS-O/C-elemental ratio at the PC-end-layer after plasma jet treatment through meander-like cavity with a height of 12 mm in dependence on time and operating gases.

Through a 12 mm long meander-like cavity a significant increase of the O/C ratio at the surface of the end-layer was detected, even though, the O-incorporation depends mainly on the time of the plasma jet treatment (see Fig. 5). A remarkable increase of the O/C ratio of 40% was observed after 300 s Ar/O_2 plasma. Whereas after the short Ar/O_2 plasma treatment of 30 s no oxygen functionalization was detected at the end-layer. In terms of Ar plasma, the O/C ratio was increased to a value of 30% after the long time treatment of 300 s. In accordance to Ar/O_2 plasma, the short time plasma treatment had no influence on the elemental composition of the end-layer.

Summarizing, the ability of an atmospheric pressure plasma jet to create oxygen-functionalities in small cavities in complex 3D geometries was demonstrated. The investigations about the dependence of the functionalization on the applied process gas and treatment time revealed that long-time treatments and Ar/O_2 gas mixtures provide the highest O/C ratio. Furthermore, it was shown, that the surface functionalization can be achieved at high distances.

References

[1] A. B. Gil'man, *High Energy Chem.* **2003**, *37*, 17
[2] M. Laroussi and T. Akan, *Plasma Process Polym* **2007**, *4*, 777
[3] C. Bergemann, A. Quade, F. Kunz, S. Ofe, E.-D. Klinkenberg, M. Laue, K. Schröder, V. Weissmann, H. Hansmann, K.-D. Weltmann, B. Nebe, *Plasma Process Polym* **2012**, *9*, 261
[4] E. Pamula, L. Bacakova, E. Filova, J. Buczynska, P. Dobrzynski, L. Noskova, L. Grausova, J. *Mater. Sci.: Mater. Med.* **2008**, 19, 425
[5] K. D. Weltmann, E. Kindel, T. von Woedtke, M. Hähnel, M. Stieber, R. Brandenburg, *Pure Appl. Chem.* **2010**, *82*, 1223

Optimization of APS Process Parameters Using a Design of Experiment for CSZ (Y_2O_3- CeO_2 Stabilized Zirconia) Coatings

[1-2]Ekrem Altuncu [2]Fatih Ustel
altuncu@kocaeli.edu.tr

Kocaeli University, Vocational School of Asim Kocabiyik, Machine-Metal Tech. Dept. -Hereke Borusan Campus, 41800 Kocaeli/ Turkey,

Sakarya University, Eng. Fac., Thermal Spray Technology R&D Center, Serdivan Esentepe Campus,54187, Sakarya/ Turkey

Abstract

Air Plasma Sprayed (APS) Ceria Stabilized Zirconia (CSZ) coatings have been extensively used as alternative material yo Yttria Stabilized Zirconia (YSZ) in the gas turbine industries due to the good mechanical properties and hot corrosion resistance at an elavated temperatures. Due to the high velocity and temperature gradients in the plasma jet, any changes in the process parameters can result in significant changes in the particle properties and consequently in the microstructure of the coating. For increasing coating quality,operational primer process parameters as plasma gas flow rates, plasma current, spray distance must be optimized. The statistically designed taguchi experiments and regression analysis are used to determine the effects of processing parameters on mechanical and microstructural properties of coatings. The effect of changing the processing parameters on properties such as density, thickness, deposition efficiency and the amount of porosity in the coatings has been investigated in this study. Results showed that the CSZ has a higher deposition efficiency and denser microstructure than the YSZ systems.

Keywords: Plasma Spraying, Stabilized Zirconia, Coating Quality, Process Optimization, Deposition Efficiency

1. Introduction

Yttria stabilized zirconia (YSZ) has been usually chosen for the thermal barrier coating material because of its high coefficient of thermal expansion (CTE), which closely matches that of the Inconel substrate and low thermal conductivity. However, other researches indicate that the Ceria and Yttria stabilized zirconia (CSZ) coating was superior to the YSZ coating due to its phase stability at high temperature, improved thermal insulation, higher CTE and good corrosion resistance [1-4]. The fundamental of the air plasma spray process is heating up the powders above their melting point in a plasma stream and accelerate them toward a substrate. The microstructure of plasma sprayed coatings is a lamellar type structure. Microstructural features are also affected by defects such as pores, unmelted particles and microcracks. Due to the high velocity and temperature gradients in the plasma stream, any changes in the process parameters can result in significant changes in the particle properties

and consequently in the microstructure of the coating. For increasing coating quality, operational process variables must be optimized [5-6]. The effect of changing the processing parameters on properties such as, density, deposition efficiency, thickness, and the amount of porosity in the coatings has been investigated in this report.

2. Experimental Study

Inconel 738 superalloy was used as the substrate with the diameter 30mm and thicknes 4mm. The spray powders were commercial NiCoCrAlY powder (Amdry962 Sulzer Metco, 38–75 mm) as bond coat and ZrO_2–8 wt%Y_2O_3 (YSZ:204NS, Sulzer Metco, 50-62 μm), ZrO_2 –25 wt% CeO_2–2.5 wt%Y_2O_3 (CSZ: 205NS, Sulzer Metco, 45-58μm) and were deposited by Multicoat robot controlled air plasma spraying(APS) system with F4MB spray gun (**Fig 1**). Argon gas was the primary plasma gas and hydrogen gas was added as the secondary gas. The microstructure of as sprayed coatings was observed using a scanning electron microscope (SEM), supplied with energy dispersive spectroscopy (EDS) was used.. The phase was analyzed using X-Ray diffractometer (40kV,40mA, CuKα radiation).

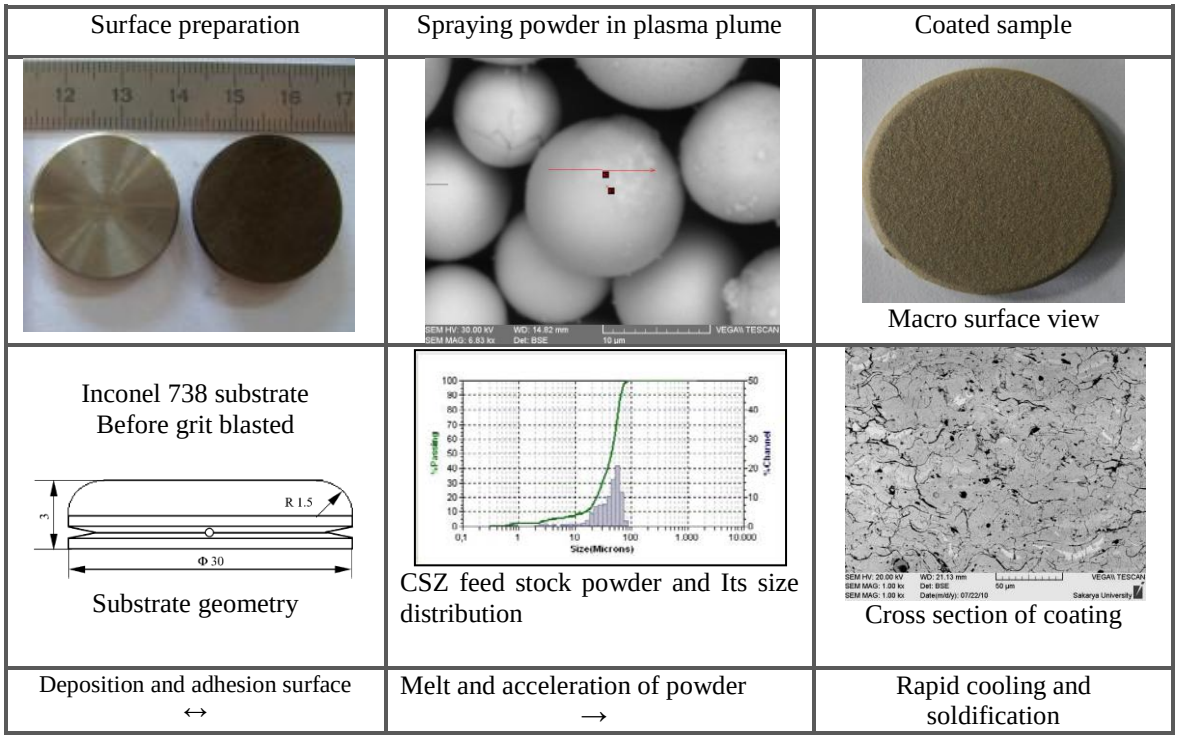


Fig.1 Experimetal materials

Design of experiment (L9 Taguchi design) has been used to obtain the spray parameters in the minimum possible number of experiments. For finding the range of various parameters selected such as plasma current, spray distance, plasma gases flow rate, some preliminary experiments have been performed. In order to carry out varied characterization for a given type of experiment, a number of samples have been made (**Table 1**.).

Table 1. Spray parameters (Plan for Taguchi design of experiment, L9)

Variab.	Plasma Current (Ampere)			Primar gas flow rate Ar (nlpm)			Secondar gas flow rate H_2 (nlpm)			Spray Distance (cm)		
Level	1	2	3	1	2	3	1	2	3	1	2	3
Value	575	600	625	35	45	55	7.5	10	12.5	10	15	20

Input:Spray materials and selected factors → Process (APS) F4MB plasma gun → Output (Deposition Eff., Porosity)

3. Primary Results and Discusssion

Deposition efficiency is defined as the ratio of the weight of coating deposited on the substrate to the weight of the expended feedback. The deposition efficiency of coatings has a strong dependence on spray distance, primar gas flow rate, plasma current respectively among the spray parameters. Increasing porosity decreases the deposition efficiency. DE of the CSZ is higher than the DE of YSZ coatings.

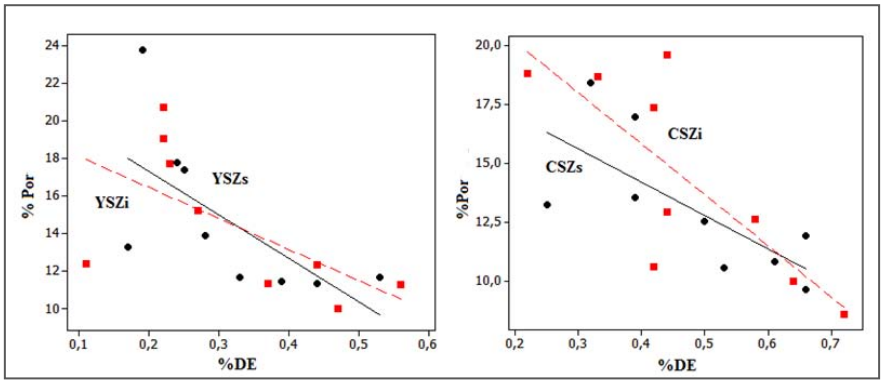


Fig. 2. Deposition Efficiency vs Porosity graphics for YSZ and CSZ based coatings

References

[1] YQ. Wang, G. Sayre, Commercial thermal barrier coatings with a double-layer bondcoat on turbine vanes and the process repeatability, Surf Coat Tech.,203 (2009), pp. 2186–2192.

[2] B. Ma, Y. Li, K. Su, Characterization of ceria–yttria stabilized zirconia plasma-sprayed coatings, Appl Surf Sci, 255 (2009), pp. 7234–7237.

[3] JH. Lee, PC. Tsai, CL. Chang, Microstructure and thermal cyclic performance of laser-glazed plasma-sprayed ceria–yttria-stabilized zirconia thermal barrier coatings, Surf Coat Tech., 202 (2008), pp. 5607–5612

[4] WB Gong, CK Sha, DQ Sun, WQ. Wang, Microstructures and thermal insulation capability of plasma-sprayed nanostructured ceria stabilized zirconia coatings , Surf Coat Tech., 201 (2006), pp. 3109–3115.

[5] P. Fauchais, Understanding Plasma Spraying, Institute of Physics Publishing, J. Phys. D, 2004, 37, p 86-108.

[6] S. Sampath, X. Jiang, A. Kulkarni, J. Matejicek, D.L. Gilmore, and R.A. Neiser, Development of Process Maps for Plasma Spray: Case Study for Molybdenum, Mater. Sci. Eng. A, 2003, 348, p 54-66.

Microstructure and Mechanical Behaviour Relationship of Plasma Sprayed Mullit+YSZ Coatings

Yıldız Yaralı Özbek[1], Ekrem Altuncu[2], Fatih Üstel[1]

[1]Sakarya University, Metal and Mats. Eng. Dept.,Sakarya, Turkey
[2]Kocaeli University, Machine-Metal Tech.,Kocaeli, Turkey
yyarali@sakarya.edu.tr, altuncu@kocaeli.edu.tr

Abstract

The YSZ/mullite composite coatings have been given an impression for improved high temperature resistance over YSZ coatings under severe service conditions and should be investigated further for its possible use in thermal barrier coating (TBC) systems. In this study, a composite thermal barrier coating made from a combination of YSZ and mullite (wt%25 to 50) was investigated. Powders of each powders were mechanically mixed together and then sprayed on superalloy substrates. Microstructure and mechanical behaviour relationship of these composite coatings were investigated. Crystallinity and phase ratios were determined by XRD analysis. Results showed that mullite addition improved the mechanical behaviour of YSZ coating under high temperature conditions.

Keywords: YSZ-Mullite Coating, Plasma Spray, Durability, Thermal barrier

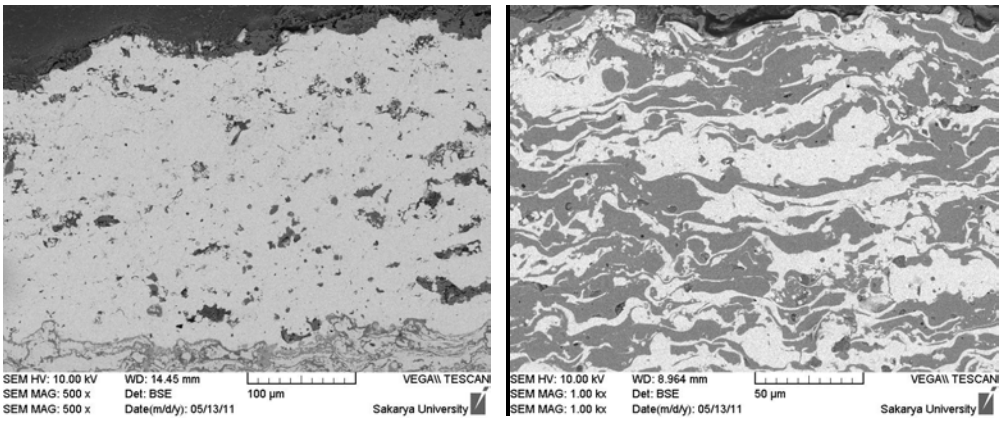
Introduction

TBCs have been extensively developed for aero gas turbines operating in clean environments. Because of their promise to improve engine efficiency and component life, TBCs are expected to be widely used in the future in industrial gas turbines or diesel engines. In industrial gas turbines or diesel engines, hot corrosion resistance over extended exposures (20000 h) in 'dirty' fuel is another key durability issue. Dirty fuels may contain higher levels of sulfur plus additional contaminants such as sodium, vanadium and phosphorous, accelerating the degradation of YSZ TBCs.

Experimental Details

YSZ/mullite composite coatings were fabricated by air-plasma spraying (APS). Spray-dried 7-8 wt.%Y_2O_3-ZrO_2, fused and crushed mullite, and a mechanically mixed combination of the two powders onto stainless steel plate. Coatings were sprayed using with a Metco F4MB plasma torch.

A Na_2SO_4 was selected as corrosive salt. Corrosive salt was spread over the surface of the coatings in a concentration of 25 mg/cm^2. The specimens were set in an electric furnace with air atmosphere at 950 ◦C for 40 h and then cooled down inside the furnace. The coatings were inspected periodically after each of 10 h. The microstructure, morphology and chemical compositionof the surface and the cross-section of the coatings were examined by scanning electron microscopy (SEM) equipped with energy dispersive spectrometer (EDS). X-ray diffraction (XRD) was used to determine the crystalline structure of the coatings and hot corrosion products.



a.Standard YSZ Coating b.YSZ+Mullite Composite Coating

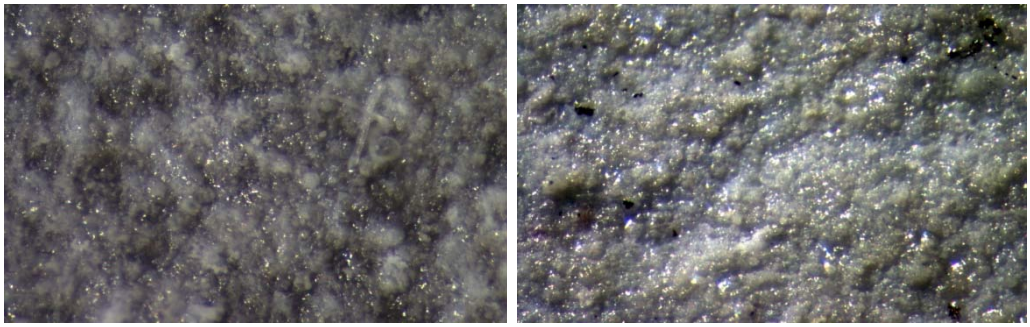
Fig.1. As Sprayed coatings

Results and Disscusions

In this study influences of the mullite addition to YSZ was investigated. Mullite addition improved the hot corrosion resistant. Mullite ($3Al_2O_3$-$2SiO_2$) addition to YSZ provided excellent resistance to molten salt attack in hot corrosion furnace tests. TBCs with mullite showed higher life than standard YSZ. There was no evidence of salt causing any damage to the YSZ, YSZ/ TGO or TGO/bond coat interfaces. No chemical reaction was reported between sodium sulfate and mullite. Stabil Al_2O_3 layer between TGO and top coat had effective role in prevention for top coat deterioration. In Fig.1, After corrosion testing, micrograph cross-section of samples 3.



Fig.2. After corrosion testing, micrograph of sample 3



a) b)

Fig.3 Surface of "sample 3" a)before corrosion test, b)after corrosion test

The amount of coating cracks at increasing the amount of mullite increased after the experiment, so it reduces the resistance of the coating were observed with high-temperature corrosion. In addition to being much thicker than the coating cracks and pores generated within a larger structure (Fig.3).

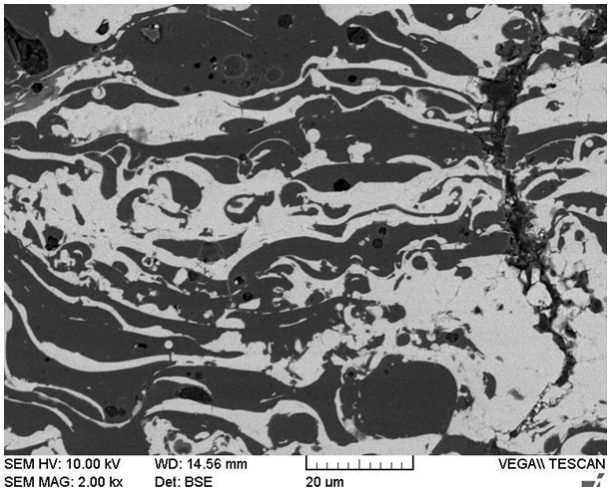


Fig.4.SEM analyses of sample 3 after corrosion test

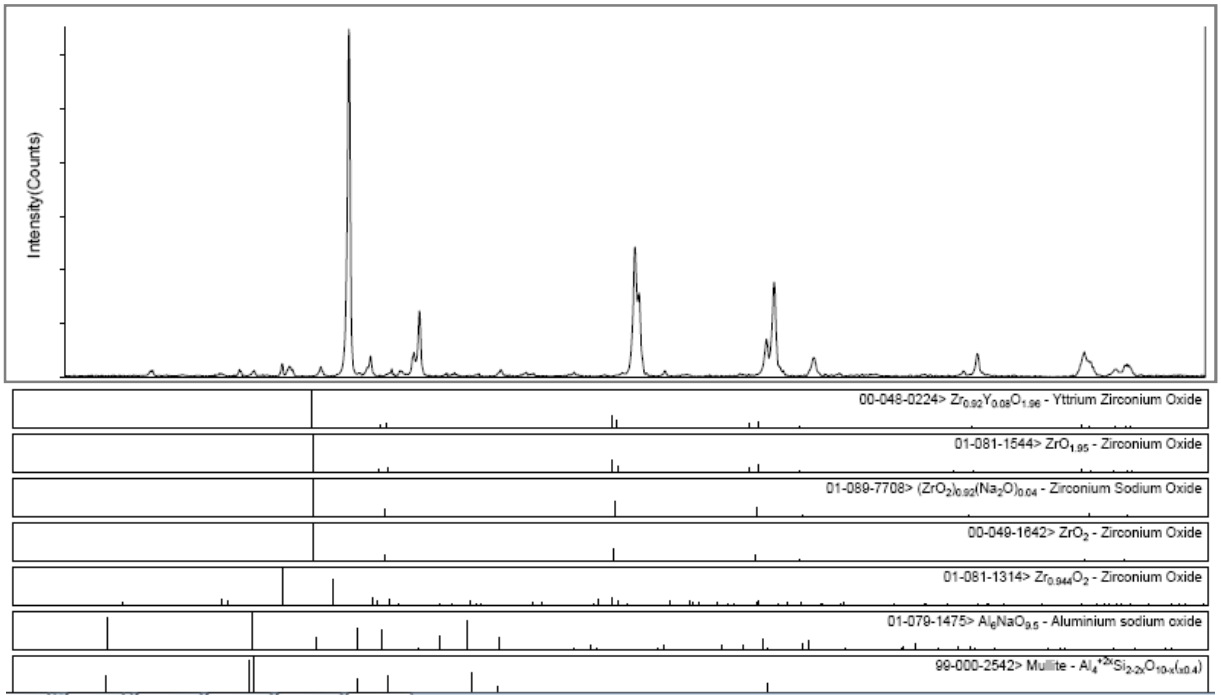


Fig. 2. XRD pattern after hot corrosion test at 950 ◦C for 10 h

The effectiveness of prevailing plasma spray conditions in the synthesis of protective coatings

Vitas Valinčius, Viktorija Grigaitienė, Pranas Valatkevičius, Liutauras Marcinauskas
Lithuanian Energy Institute, Plasma Processing Laboratory, Kaunas, Lithuania
vitas@mail.lei.lt

Introduction. Protective and catalytic coatings of different composition are widely used in diverse fields of industry including a modification of surface layers of constructional materials. Mechanisms of film formation in plasma spray processes are not investigated thoroughly. It is not determined how the parameters of process influence the quality, specific surface area, thickness and adhesion of coatings [1,2]. Therefore the investigation of the influence of formation technology on structure and properties of protective ceramic coatings is the main objective of present work.

Experimental equipment. Coatings in the present study were deposited employing a specific plasma spray technique with a linear, sectional plasma generator (PG) 50-70 kW of power generating non-equilibrium plasma jet at atmospheric pressure. Plasma stream reactor was connected to the plasma torch exhaust nozzle.

The main parts of the equipment are: plasma torch with electricity supply, gas supply, cooling, operation control and data monitoring systems. Power supply system consists of direct current (DC) power source capacity up to 1 MW with smooth current tuning, rheostat and arc excitation facility. The gas supply system contains pressure vessels containing compressed gas, air compressor, pipelines and high accuracy mass-flow controllers. Clean dry air was used as plasma forming gas. The mass flow rate of gas was controlled by valves and monitored by diaphragms and critical nozzles.

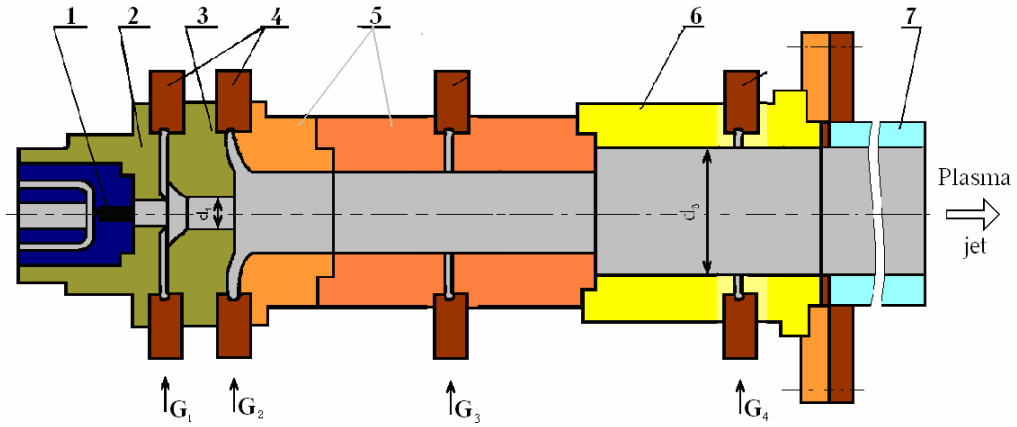


Fig.1. The schematic presentation of a linear sectional DC plasma torch. 1 – cathode with hafnium emitter; 2 – cathode junction; 3 – arc ignition ring, 4 – insulating rings with holes for feeding of plasma forming gas G_1, G_2, G_3 and G_4; 5,6 – step-formed anode; 7 – circular exhaust nozzle

The PG arc current varied in the range of 150–200 A. The voltage drop depended on the gas flow rate and ranged from 300 to 450 V. The operating gas was injected at the cathode (G_1) and anode (G_2) side. The substance in the form of dispersed particles less than 50 micrometers in diameter were injected via tangential holes made in insulating rings (G_3 and G_4) together with a small amount of carrying gas (air). The total air flow rate through the PG was $G = G_1+G_2+G_3+G_4 = (5–8)\cdot10^{-3}$ kg·s^{-1}. Experiments were performed at the mean plasma flow temperature 3000–4000 K and the mean velocity 500–550 m·s^{-1}.

During the experiments on the effect of PG operating regime, coatings were deposited with intermediate layers of Al powder on stainless steel substratum supplying outside the reactor into exhaust plasma jet at the distance x/d=0.5 from the exhaust nozzle. Aluminum hydroxide particles up to 50 μm of diameter were mixed with copper oxide particles up to 50 μm using mass ratio 10:1. 75% of initial powder was injected via blowholes into the reactor and 25% outside the reactor. Experiments were conducted at three regimes of PG changing arc current from 180 A at the constant flow

rate of plasma forming gas (Table 1). The power supply of this plasma torch was P = 50–70 kW. A similar plasma source is described in detail elsewhere [3]. Depending on plasma process regime (arc current and voltage), films of 30 – 70 micrometers in thickness were formed from $Al(OH)_3$, TiO_2 and CuO containing powder mixtures on the metal strips. The similar coatings were deposited using other ceramic based powder containing dolomite and quartz sand mixture. Depending on demand, practically any metal oxides such as iron, cobalt, nickel, etc. were added to the mixture. The structure of coatings was evaluated from the top-view and cross-sectional scanning electron microscopy (SEM) observation and the surface phase composition was analyzed by X-ray diffractometer.

Table 1. Plasma spraying regimes for ceramic coatings deposition

Spray regime	1	2	3
Arc current, A	180	190	200
Arc voltage, V	320	325	322
Power, kW	57.5	61.7	64.5
Total gas flow rate, 10^{-3} kg·s^{-1}	5.03	5	5.03
Exhaust mean velocity, m·s^{-1}	510	530	550
Exhaust mean temperature, K	3560	3650	3820
Spray distance, mm	120	120	120

Results and discussion. It was determined, that during plasma spray process the powder was partially melted and spheroidized whereas the initial ceramic based dolomite and sand mixture powder were in the form of agglomerates. It has been found, that the shape and size of the grains on the coating depend on characteristics of the plasma source and gas flow rate. Under high plasma forming gas flow rate and low temperature in plasma chemical reactor, the feeding dispersed particles does not melt fully in the same time and may be carried out as partly melted and agglomerated granules [4]. The small amount of hydrogen improved the deposition efficiency and increased the energy transfer.

The dependence of spraying parameters on the structural changes of aluminum hydroxide coatings was studied from SEM micrographs and is shown in Fig. 2. The microstructure of coatings contains certain amount of pores and voids. However, it is seen, that proper choose of deposition regime has a direct influence on the coating quality. The structure of the coating deposited at lower temperature (regime 1) is characterized by porous nature (Fig. 2, b). The distribution of pores is quite homogeneous. Reduced porosity is specific to the coatings deposited at higher temperature, but these coatings are qualified by finer structure and increased density (Fig. 2, c). X-ray diffraction analysis of plasma-sprayed $Al(OH)_3$, quartz sand and dolomite mixture shows the domination of amorphous substances with a small amount of crystalline phases of mullite, corundum, quartz, cristobalite in all the products obtained. The presence of amorphous or crystalline phase or other properties of the product may be regulated also by means of variation of mean plasma parameters.

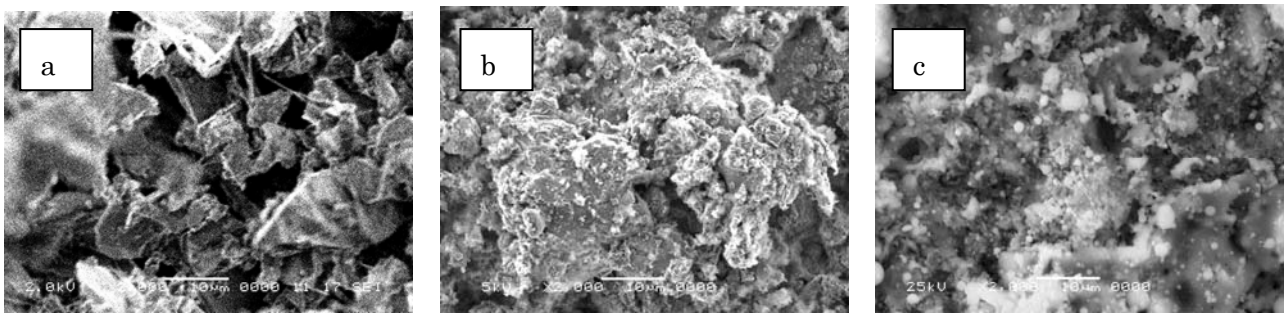


Fig. 2. SEM image of coatings produced of $Al(OH)_3$ and 10% CuO mixture at different plasma source regimes showed in Table 1: a – initial powder; b – regime No1; c – regime No3

By XRD patterns the dominated phase of the initial powder is rutile and the second phase is anatase (Fig. 3, 1). In the XRD patterns of plasma-sprayed titanium there is no new phase. It was observed that the peak intensities present some difference according the plasma process regime. As the process temperature was increased (Table 1, regime 3), the intensity of the main peaks is increased indicating an increased degree of crystallographic texture in the plasma deposited titanium. X-ray analysis of $Al(OH)_3$ coatings doped with metal oxides shows the presence of α-Al_2O_3 and γ-Al_2O_3 phases. It is shown that the ratio of phase fraction depends on the substrate temperature. Pure α-Al_2O_3 is obtained if the substrate temperature exceeds 760 ^oC.

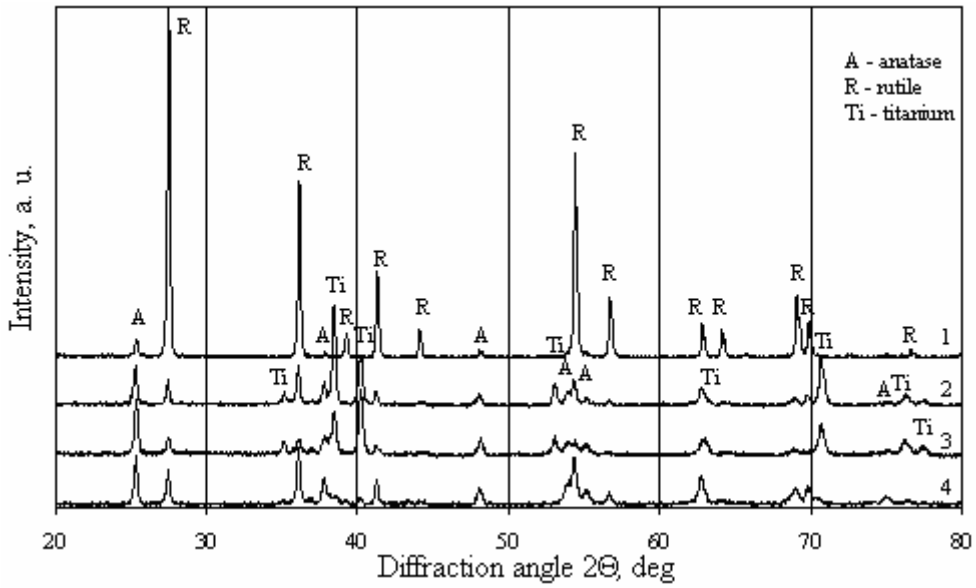


Fig. 3. The XRD patterns of titanium at different plasma source regimes in table 1: 1 – initial powder; 2 – regime No 2; 3 – regime No 1; 4 – regime No 3

With the increasing temperature, the pore size decreases. This means that increasing arc current in the plasma source, the particles on the coating became more porous because of plasma spray pyrolysis process [5] which may occur in certain conditions during the interaction of particles with the plasma jet. However, after the injection of small amount of hydrogen, the temperature may become as the most important parameter. Besides, for the reason of high temperature, the dispersed particles in the jet is fully melted and partly evaporated before they reach the substratum. Since deposited coatings have a good adhesion and mechanical strength, however their porosity and specific surface area is rather low (Fig. 4). Such coatings are suitable in tribological application, however is inapplicable in the catalysis.

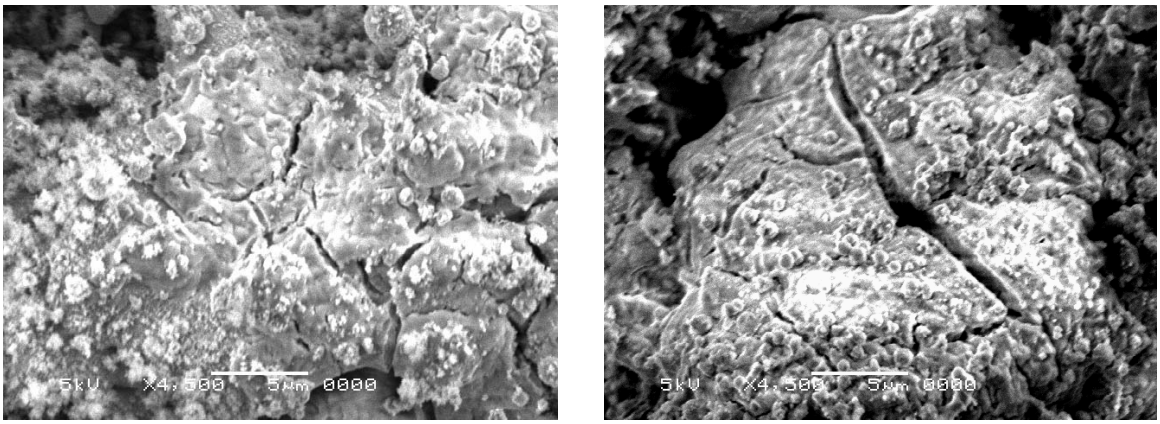


Fig. 4. SEM micrographs of plasma-sprayed aluminum hydroxide powder injected directly into reacting arc zone before arc spot: left – regime No 1, right – regime No 3

In all other cases, the surface structure of the coatings in the SEM observation shows that the coatings deposited using the plasma spraying are of good quality, thick, rough and homogeneous. Randomly distributed pores of different sizes are observed. The average coating thickness evaluated by cross-sectional SEM observation was from 35 μm to 50 μm and more. By the results, all plasma sprayed metal oxide coatings are well adhered to the substrate. The coating thickness depends mainly on the spray duration.

The plasmas generally can be produced by the application of a sufficient high level of energy, e.g., in the form of arcs, sparks, glow discharges, flames or shock waves. It is the activated state of medium where the individual types of particles, e.g. ions, electrons and neutral particles (in the form of non-excited and excited atoms, molecules and radicals), can be grouped in accordance with different temperatures. Thanks those properties, atmospheric pressure arc plasma in touch with material stands out series properties, which are not possible to receipt at using another method of deposition [6,7]. The most important property is high power density, which is supplied to the material, its income up to 1 $kW \cdot cm^{-2}$ for continuous radiation and – uniquely to 1 $kW \cdot cm^{-2}$ (and even more) for pulse radiation.

Since constructional materials working temperature is up to 800 ^{o}C, the plasma-sprayed coatings were heat treated at this temperature for 10 hours. Microscopic analysis showed no substantial changes when compared to the not heat-treated samples. Post-treated coatings are qualified by finer and reduced porosity and increased density due to grain growth and sintering.

Conclusions

The use of the non-equilibrium plasma spraying technology at atmospheric pressure demonstrates the ability to obtain coatings with controlled characteristics for special applications. The prevailing properties of the final product obtained in plasma may be modified by the plasma source operational parameters and plasma jet characteristics.

Ceramic coatings have excellent characteristics such as fine and narrow size distribution, pure phase and spherical morphology. By the results, all plasma sprayed coatings are thick, porous, homogeneous and well adhered to the substrate. No substantial changes in the coatings microstructure were observed after the thermal annealing. Properties of prepared coatings (thickness, density, etc.) depend mainly on the precursor‘s chemistry, plasma jet parameters and exposure time, the plasma torch construction and optimal parameters.

Acknowledgement

This study has been partly supported by the European Union (European Regional Development Fund) PlasTEP | # 033 | KST 770123

References

[1] P. Fauchais. Understanding plasma spraying. J. Phys. D: Appl. Phys., 37 (2004) R86-R108.
[2] Thermal Spray 2004 – Advances in Technology and Application: Proceedings of the International Thermal Spray Conference, Osaka, Japan, 10–12 May 2004.
[3] V. Valinčius, et al. Plasma Sources Sci. Technol., 13 (2004) 199–206.
[4] V. Valinčius, et al. J. of High Temp. Mat. Proc., 10, (2006) 365–375.
[5] V. Valinčius, et al. Surf. Coat. Technol., 205 (2011) S359–S363.
[6] M. I. Boulos et al., "Thermal Plasmas - Fundamentals and Applications", Plenum Press, New York (1994), isbn 0-306-44607-3.
[7] G..Leofanti, M. Padovan., G.. Tozzola., B. Venturelli. Catalysis Today 41 (1998) 207-219.

A Comparative Study of Wear Effect on the Microstructures Behavior of CoNiCrAlY Coatings fabricated by APS, HVOF and CGDS Coatings

Mustafa Sabri Gok[1], Abdullah Cahit Karaoğlanlı[1], Azmi Erdoğan[1], Ahmet Türk[2]
[1]Bartin University, Bartin, Turkey
[2]Sakarya University, Sakarya, Turkey

Abstract

This work focuses on the micro-abrasion wear and microstructural properties of CoNiCrAlY coatings fabricated on nickel based super alloy substrates by using the atmospheric plasma spraying (APS), high-velocity oxygen fuel (HVOF), cold gas dynamic spraying (CGDS) methods. Tribological tests were performed on the samples in order to understand the wear mechanism of thermally sprayed coatings and influence of the coating microstructure on wear mechanism. The microstructures of as sprayed and weared coatings were investigated by scanning electron microscopy. Initial surface topography was examined by surface profilometer. Coating hardness measurements were performed with a micro-hardness tester. The micro-abrasion tests were carried out with some different durations. The lateral fracture was observed as wear mechanism on the specimens. The wear surface resistance have changed with coating process and surface features of specimens depending on the coating process.

Keywords: Wear, CoNiCrAlY, CGDS, HVOF, APS, Surface roughness, Bond coat

1. Introduction

Coating methods are generally used to improve the performance of industrial parts. There are different coating methods according to the application. There are many different types ranging from hard, high wear resistance coatings to soft lubricating coatings or applications where low wear ratio is needed [1]. Thermal spray coating method has long been used in aviation industry to produce coating that can resist erosion and wearing [2]. Powders with 10-100 µm dimension have been applied to, by widely studying, metallic and ceramic materials to create a more wear resisting surface layers [3]. While choosing the metallic abradable material that will be used in high temperature applications, coatings need to have high oxidation and erosion resistance in service temperatures during use [4]. One of the most important coating structures to protect turbine seal applications, blades, duct segments, turbine sections of aircraft jet engines and such materials from high temperature oxidation, heat corrosion and erosion damages is the MCrAlY material [5-6]. Bond coatings that are used on substrate material are typically produced with APS, LPPS, VPS and HVOF methods [7-8]. One of the biggest disadvantages of usage area in application is that high temperature that takes place in production of methods cause oxide inclusions in coating microstructure and crack-like formations [7]. Coatings with superior properties with regard to dense coating structure and mechanical properties and that has no oxide index can be produced when plastic deformation dependant production is performed instead of heat effect's being an active parameter in coating production with the use of the method that is called CGDS and has been used in bond coating production in recent years [9]. CGDS coating method works in lower temperatures than other thermal coating processes, produces coating depending on the high kinetic energy and plastic deformation that happens later on [10]. In the method, powder particles are accelerated and are undergone plastic deformation on substrate with supersonic flow speed and as a result coating is produced [7]. Ball crater micro abrasion test, also known as micro abrasion test method, is a method that is used to identify the abrasive wear resistance of coating and materials. The method is based on the application of wear process and rotation of a spherical ball with its own weight on the specimen in the presence of an abrasive. Wear volume can be identified with optical or profilometric methods [11-13]. In this study, CoNiCrAlY powders were deposited onto Inconel 600 substrates by APS, HVOF and CGDS methods. Wear performance of the MCrAlY coatings has been investigated. Coatings with CoNiCrAlY that are produced with CGDS method show more superior wear performance than coatings produced with other methods after the tests.

2. Experimental

2.1 Material and methods

The samples consisted of a CoNiCrAlY bond coat (BC) and CoNiCrAlY powder with a particle size range of 5-37 µm was used as starting materials. The substrates, Inconel 600 Nickel based super alloy coupons in the form of 25x25x3.5 mm, were grit blasted to clean and roughen the surface to increase the resulting coating adherence. After grit blasting the samples were cleaned ultrasonically in ethanol. In this study, APS, HVOF and CGDS techniques were used to produce CoNiCrAlY coating layers. The used spraying systems were a GTV K2 HVOF system, a Plasma Giken CGDS system and a GTV F6 APS system. All powders were standard thermal spray powders and delivered by Sulzer Metco. All spraying parameters are shown in the Table 1. The thicknesses of the CoNiCrAlY coating layers were about 100-140 µm.

Table 1. APS, HVOF, CGDS spray parameters for bond coats powder deposition

APS CoNiCrAlY Bond Coatings		
Arc Current	Electrical power	Argon flow rate
600 A	40 kW	65 slpm
Hydrogen flow rate	Powder feed rate	Stand-off distance
14 slpm	30 g/min	140 mm

HVOF CoNiCrAlY Bond Coatings		
Combustion medium	Powder Carrier Gas	Powder Feed Rate
O_2 (880 slpm) and kerosene (25 l/h)	Argon (15 slpm)	50g/min
Powder feed gas flow	Stand-off distance	
12 slpm	330 mm	

CGDS CoNiCrAlY Bond Coatings		
Spray Pressure	Gas Temperature	Working gas
3 Mpa / 30 bar	600 °C	Nitrogen (1000 slpm)
Gun speed rate	Stand-off distance	
20 mm/sn	15 mm	

After grit blasting, average surface roughness values were obtained through measurements that are carried out at different points on each specimen ranging between 5 and 10 points in accordance with the standard of DIN EN ISO 3274 norm on surface roughness measurement values of substrate, bond and top coating. Micro-hardness measurement of coatings has been carried out with Duramin brand test devices in accordance with DIN EN ISO 4516 norm. Measurements have been carried out under 100 g weight for 15 seconds with Vickers indenter tip**.** Ball rotating micro-abrasion experiments were conducted with one ball made of AISI 52100 steel (nominal chemical composition of 1.04 wt.% C, 0.35wt.% Mn, 0.25 wt.% Si, 1.45 wt.% Cr, bal. Fe), which presented a diameter (*D*) of 25.4mm (1 inch). The abrasive used was black silicon carbide (SiC) with average particle size of 5-10 µm. The abrasive slurry was prepared as a mixture of 25% of SiC and 75% of distilled water, in volume. Conventional characterization techniques, such as scanning electron microscopy (SEM), microhardness, and profilometer analyses were employed to study the microstructure of the abraded and coating zone. Micro abrasion test parameters are given in Table 2.

Table 2. Micro abrasion test parameters for whole coating systems

Coating Methods	APS, HVOF and CGDS techniques		
Test condition for CoNiCrAlY coatings	1	2	3
Test time (min)	3	5	7
Sliding distance (m)	36.72	61.2	85.68
Shaft rotational speed (rpm)	160	160	160
Ball rotational speed (rpm)	102,5	102,5	102,5
Ball tangentinal sliding velocity (m/s)	0,136	0,136	0,136
Drop time (s)	20	20	20
Repetitions	3	3	3

3. Results and Discussions

3.1 Characterizations of the coatings

When the microstructure properties are analysed after coating production, APS bond coatings are seen to have oxide content and discontinuities crack-like gaps and low amount of unmelted particle structure because of process production. HVOF bond coatings have low porosity content in local areas as well as having a dense coating structure. In CGDS bond coatings, this situation has dense coating structure and local porosity content because the coating method is based on plastic deformation. Surface roughness measurements are applied as after grit blasting, after bond coating and after top coating of the specimen. Surface roughness measurement of the grit-blasted substrate as well as all as-sprayed coatings are summarized in Table 3.

Table 3. Average surface roughness values of the substrate and the as-sprayed coatings

Materials	R_a (µm)	Materials	R_a (µm)	Materials	R_a (µm)
Inconel 600 (grit-blasted)	4.34	Inconel 600 (grit-blasted)	4.80	Inconel 600 (grit-blasted)	4.93
APS-BC	5.27	HVOF-BC	5.56	CGDS-BC	6.75

The microhardness values of coatings are shown in Table 4.

Table 4. Microhardness average values of TBCs

Coating abbreviation	Microhardness (Hv)
APS - CoNiCrAlY	340± 25
HVOF - CoNiCrAlY	440± 30
CGDS - CoNiCrAlY	490± 50

4. Wear Results

Figure 1 shows the volume loss at coating layer volume that are produced with 3 different surface coating method depending on the sliding distances of the ball. As it can be seen in surface profilometers, materials whose surface has been coated with CGDS method show the lowest wear crater depth at the end of micro abrasion test that is performed at 160 rpm for 7 minutes, and specimen that are coated with HVOF and APS method follow it respectively. The reason for this can be associated with the hardness of the specimen. Because specimen coated with CGDS method show the highest surface hardness among the specimen and specimen coated with HVOF and APS method follow it respectively (Table 4). When the roughness values of the specimens are studied, it is seen that CGDS has the highest roughness value and HVOF and APS follow it respectively. Although CGDS that has high roughness value in initial time wear has high volume loss, the layers wear resistance increased when the hard and brittle rough is cleaned. It is possible to say this also for the other specimen. When evaluated as coating methods, coatings produced with HVOF and APS methods follow CGDS coatings respectively. As mentioned in micro-structure properties, this situation is closely associated with coating production methods.

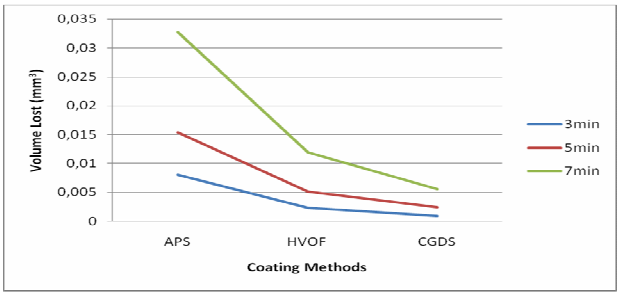


Figure 1. Volume losses as a result of erosion according to coating method

Typical surface profiles of the substrate and coatings wear tested against both types of balls are presented in Fig. 2-4.

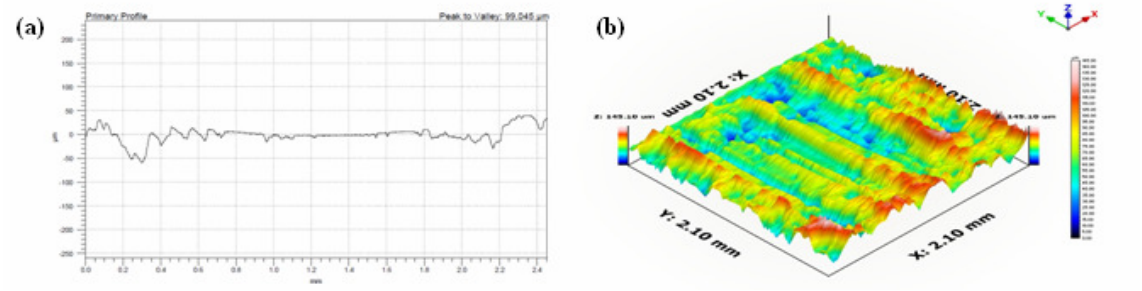


Figure 2. Surface profile of CoNiCrAlY coatings produced by CGDS wear tested against (a) substrate, and (b) surface topography of the worn coating

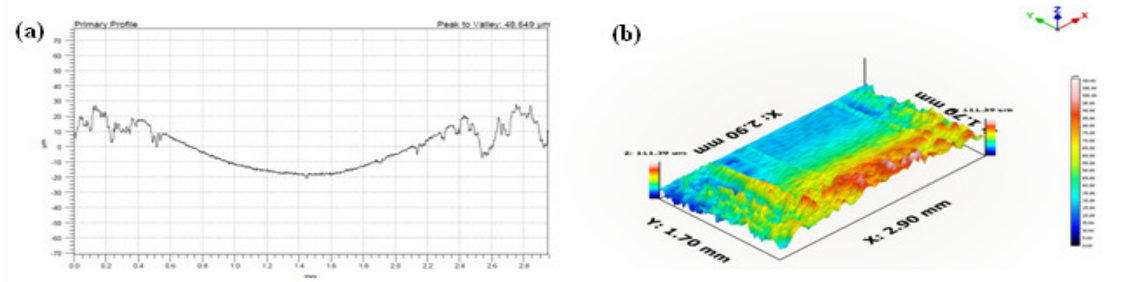


Figure 3. Surface profile of CoNiCrAlY coatings produced by APS wear tested against (a) substrate, and (b) surface topography of the worn coating

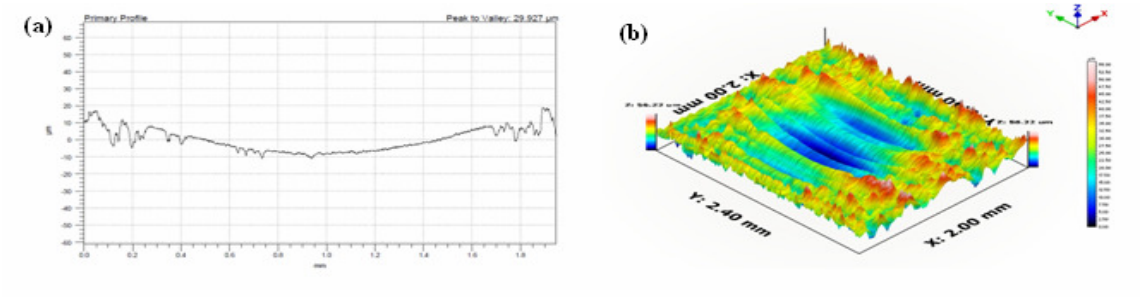


Figure 4. Surface profile of CoNiCrAlY coatings produced by HVOF wear tested against (a) substrate, and (b) surface topography of the worn coating

Micro abrasion SEM wear surface picture of the specimen are shown in Fig. 5 (a-c) respectively. Lateral fracture type abrasion is seen as wear mechanism. There is no important difference between wear mechanisms of specimens.

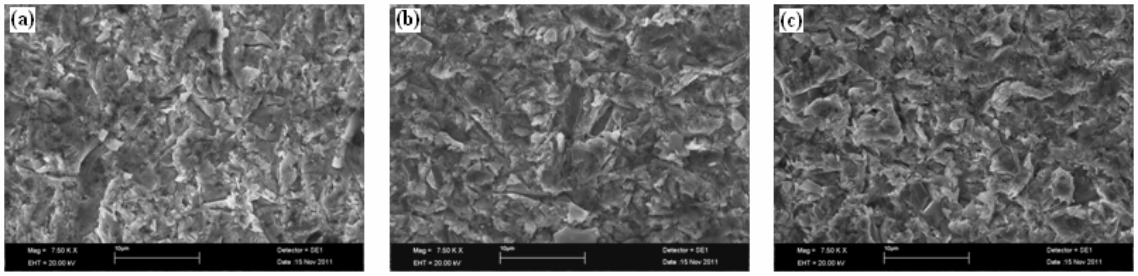


Figure 5. SEM micrograph of the wear track on the CoNiCrAlY coatings; (a) APS- CoNiCrAlY coatings, (b) HVOF- CoNiCrAlY coatings, (c) CGDS- CoNiCrAlY coatings

4. Conclusions

This study has investigated the wear performance and microstructural characterization of CoNiCrAlY bond coatings that were produced by APS, HVOF and CGDS, respectively.

The major results are summarized as follows:

1) Specimen produced with CGDS method show the highest surface hardness among the specimen and specimen produced with HVOF and APS method follow it respectively.
2) The highest roughness value is seen at the coating specimen produced with CGDS method and coating specimens produced with HVOF and APS methods follow it respectively. When the wear performances of coating systems during the early states are evaluated, CGDS coatings are seen to have lower performance than coatings produced with HVOF and APS methods. This situation is the result of surface roughness effect's being the operative mechanism in the erosion's starting period. Because of the loss of surface roughness effect depending on erosion, dense structure and high hardness of coating layer, CGDS coatings show the best performance in abrasion performances in progressive processes of wear (last state and later on).
3) The lowest volume loss is seen in coating specimen produced with CGDS method among the specimens and specimen that are abraded with HVOF and APS follow it respectively.

References

[1]. P. Cosemans, X. Zhu, J.P. Celis, M. Van Stappen, Development of low friction wear-resistant coatings, Surface and Coatings Technology 174 –175 (2003) 416–420.
[2]. R.G. Bonora, H.J.C. Voorwald, M.O.H. Cioffi, G.S. Junior, L.F.V. Santos, Fatigue in AISI 4340 steel thermal spray coating by HVOF for aeronautic application, Procedia Engineering 2 (2010) 1617–1623.
[3]. J.F. Li, H. Liao, X.Y. Wang , B. Normand , V. Ji , C.X. Ding , C. Coddet, Improvement in wear resistance of plasma sprayed yttria stabilized zirconia coating using nanostructured powder, Tribology International 37 (2004) 77–8.
[4]. S. Wilson; D. Sporer; M. R. Dorfman, Technology Advances in Compressor and Turbine Abradables, ITSC 2008, 330-335.
[5]. E. Lugscheider, J. Zwick, Aachen/D, M. Hertter, München/D, and D. Sporer, Sonthofen/D, Control of Coating Properties of Abradable Seals by On-Line Process Diagnostics, International Thermal Spray Conference 2005, Thermal Spray connects: Explore its surfacing potential, Basel, Switzerland, May 2 - 4, 2005, 610-614.
[6]. A.C. Karaoglanli, E. Altuncu, I. Ozdemir, A. Turk, F. Ustel Structure and durability evaluation of YSZ+Al_2O_3 composite TBCs with APS and HVOF bond coats under thermal cycling conditions. Surface & Coatings Technology 205 (2011) 369–373.
[7]. P. Richer , M. Yandouzi, L. Beauvais, B. Jodoin, Oxidation behaviour of CoNiCrAlY bond coats produced by plasma, HVOF and cold gas dynamic spraying, Surface & Coatings Technology 204 (2010) 3962–3974.
[8]. W. Brandl, D. Toma, H.J. Grabke, The characteristics of alumina scales formed on HVOF-sprayed MCrAlY Coatings, Surface and Coatings Technology 108–109 (1998) 10–15.
[9]. I. Burlacov, J. Jirkovsky, L. Kavan, R. Ballhorn, R.B. Heimann, Cold gas dynamic spraying (CGDS) of TiO2 (anatase) powders onto poly(sulfone) substrates: Microstructural characterisation and photocatalytic efficiency, Journal of Photochemistry and Photobiology A: Chemistry 187 (2007) 285–292.
[10]. L. Ajdelsztajn, B. Jodoin, J.M. Schoenung, Synthesis and mechanical properties of nanocrystalline Ni coatings produced by cold gas dynamic spraying, Surface & Coatings Technology 201 (2006) 1166–1172.
[11]. K.I. Schiffmann, R. Bethke, N. Kristen, Analysis of perforating and non-perforating micro-scale abrasion tests on coated substrates, Surface & Coatings Technology 200 (2005) 2348– 2357.
[12]. D.B. Luo, V. Fridrici, Ph. Kapsa, Relationships between the fretting wear behavior and the ball cratering resistance of solid lubricant coatings, Surface & Coatings Technology 204 (2010) 1259–1269.
[13]. Y Kusano, K Van Acker, I.M. Hutchings, Methods of data analysis for the micro-scale abrasion test on coated Substrates, Surface and Coatings Technology 183 (2004) 312–327.

Oxygen effect in Magnetron Sputtered Aluminum doped Zinc oxide films.

Saad Rahmane[1], Mohamed Abdou Djouadi[2], Mohamed Salah Aida[3] and Nicolas Barreau[2]

1-Laboratoire de Chimie Appliquée, Université de Biskra, BP 145 RP, 07000 Biskra, Algérie.
E-mail: rahmanesa@yahoo.fr
2-Institut des Matériaux Jean Rouxel IMN UMR 6502, Université de Nantes, 2 rue de La Houssinière BP 32229, 44322 Nantes Cedex France.
3-Laboratoire des Couches minces et Interfaces, Université Mentouri, 25000 Constantine, Algérie.

Abstract:

In this work, polycrystalline transparent conductive aluminum doped zinc oxide (ZnO:Al) films, have been successfully grown on glass and silicon substrates by rf magnetron sputtering technique at room temperature. The effect of oxygen content in plasma on the structural, optical and electrical properties of the films was systematically studied. The growth rate was fond to decrease with the increase in O_2 content. The crystal structure of ZnO:Al films deposited on glass is hexagonal with C-axis preferential orientation, while for film deposited on silicon substrate, the preferred orientation of crystallite shifts from (002) to (100) direction with the increase in O_2 content. Intrinsic stress increases with an increase of oxygen content, and near stress-free film was obtained at 0 % O_2 content. Low resistivity ($\rho = 1.25 \times 10^{-3}$ Ωcm) associated to high transmittance (T>92 %) in the visible regions, were obtained for ZnO:Al film deposited at room temperature without oxygen content in the deposition chamber. From the optical characterization, we deduced that the band gap shifts towards lower energy with an increase of oxygen content.

Keywords: magnetron sputtering, Al doped ZnO, O_2 content, properties.

1. Introduction:

II-VI compound semiconductor zinc oxide (ZnO) has attracted much attention because of its interesting properties and its unique combination of electrical, optical, piezoelectric and acoustical properties. ZnO thin films have found many applications namely solar cells, energy windows, varistors, gas sensors [1-3], short wavelength light emitting diodes [4] and transparent electrodes [5].This is due to their important properties characterized by a high transparency, and conductivity, a good thermal stability against the hydrogen plasma, non toxic and easy fabrication [6].

The physical properties of ZnO films prepared by rf magnetron sputtering depend mainly on the sputtering parameters such as sputtering power, argon gas pressure, substrate temperature and the target-substrate distance. In this paper, thin films of ZnO:Al are prepared by magnetron sputtering system. The mutual dependence of structural, optical and electrical properties of the samples as function of oxygen gas content is investigated.

2. Experimental procedure:

ZnO:Al films were deposited in magnetron sputtering system using a ZnO target (diameter 7.5 cm) mixed with 2 wt.% Al_2O_3. Prior the deposition, the base pressure in the chamber was 5×10^{-7} mbar. The target-substrate spacing, the sputtering power, and argon gas pressure were kept constant at 2.6 cm, 200 W and 2×10^{-3} mBar respectively. All the films were deposited at room temperature on glass and monocrystalline silicon (100) substrates. In order to investigate the influence of oxygen content in plasma on the ZnO:Al properties, the oxygen gas content in the deposition was varied from 0 % to 40 %.

Film thickness and substrate curvatures were measured with a stylus profilometer DEKTAK 3030. As most commonly used, the stress in our films has been calculated by the bend-bending method, where the radius of the coated substrate curvature is determined and used to calculate the residual stress. The internal stress in the

deposited film is calculated from the change in the substrate curvature from $1/R_0$ for the uncoated substrate to $1/R_e$ after film deposition, with the following Stoney's formula [9]:

$$\sigma = [(E_s e_s^2) / (6(1-\nu_s)e)][(1/R_e)-(1/R_0)]$$

where R_0 is the radius of curvature of the Si substrate, R_e is the curvature radius after film deposition, E_s and ν_s are, respectively, the Young's modulus and Poisson ratio of the substrate, e_s and e are the thickness of the substrate and the film, respectively. The crystal structure of the films was studied by x-ray diffraction technique using a Siemens D 5000 system with Cu K_α (λ= 0,15406 nm). The structural investigation was also performed using high-resolution Transmission Electron Microscopy (HRTEM), a HF2000-FEG having 0.23 nm resolution and Jeol 6400 Scanning Electron Microscope (SEM). EDS (Energy Dispersive Spectroscopy associated to Jeol 5400 SEM) was used to determine the chemical composition of the films. A CARRY UV-Vis-NIR scanning spectrophotometer was used to record the optical transmittance.

The dc electrical resistivity measurement is achieved at room temperature with four-point probe, with the appropriate correction factors.

3. Results and discussions

ZnO:Al films deposited on glass and silicon substrates, were physically stable and had a good adherence to the substrates. The deposition rate was estimated from the film thickness and the corresponding time. The higher oxygen content resulted in lower growth rate of ZnO:Al films, as shown in figure 1. With a fixed total gas pressure, an increase in oxygen content in the gas chamber reduces the number of incident argon ions; the later are responsible for the target sputtering. Therefore, the growth rate decreases with increasing oxygen content. A high rates (114 nm/min on silicon and 106 nm/min on glass) are obtained at 0 % oxygen concentration, in some cases, this value is higher than the existing bibliographical references [10,11].

In EDS typical spectra shown in figure 2, peaks were appeared at 518, 1109 and 1496 eV, they are assigned to O-K_α, Zn-L_α and Al-K_α respectively. The estimated concentration of zinc, oxygen and aluminium was 50.5 at.%; 47.5 at.% and 2at.%, respectively. A clear variation of the concentration of the elements upon the oxygen content in plasma was not found. Due to the limitations of EDS technique, it must be considered that these results giving only an idea of the composition of the films.

XRD patterns of the ZnO:Al films deposited at different oxygen concentration on glass substrates are shown in figure 3(a). For all films, only the (002) diffraction peak at about 34 (°) appears in the spectra, which indicates the ZnO:Al films are of hexagonal wurtzite crystal structure and that film growth is achieved along the C axis perpendicular to the substrate surface. It is noted that no diffraction peak from other phase is detected. At 0 % oxygen content, the diffraction intensity of the (002) direction is very high and the FWHM corresponding is 0.21(°). With a further increase of the oxygen content, the diffraction intensity of the (002) direction decreases and the FWHM increased as can be seen in figure 4. The highest intensity and the smallest FWHM value of 0.21(°) for the film deposited at 0 % oxygen content, indicate that the crystallinity of the resulting films is improved when prepared with low O2 content. This behaviour can be understood, by the decrease in the kinetic energy of the reactive particles in the plasma when oxygen concentration in the chamber is increased, which limits the surface diffusion of the growing atoms. This yields to the decrease in the films thickness and thus degrades the films quality.

By considering the (002) peak position in the standard data as reference position, we found that the peak position shifts towards lower angle value, this indicates the clear evidence of the existence of compressive stress in the film network, especially in the films deposited at high oxygen content. Figure4 shows the stress versus the oxygen content, the stress is compressive and varies from 1.1 (GPa) to nearly free of stress when the oxygen concentration decreases from 40 % to 0 %. This is attributed to the improvement in crystallinity. A similar value of stress was reported in the literature [12, 13]. The increase in the film stress with increasing oxygen can be due to the fact that, the oxygen atoms in excess will occupy interstitial sites which cause network distortion.

Figure 3(b) displays XRD patterns of ZnO:Al films deposited on silicon substrate at different O_2 concentration. It can be seen that with the increase in oxygen content, the intensity of (100) plane increases. However, the intensity of (002) plane shows a decreasing trend and disappears completely for high O_2 content. Furthermore, with increasing oxygen content, the FWHM of (100) plane becomes narrower which indicates an improvement in the structural order of ZnO:Al films. The most attractive feature is that by increasing the oxygen concentration, the preferred orientation of crystallite shifts from (002) to (100) directions. However, as reported above, in the case of glass substrate the growth plane remains preferentially (002). This discrepancy in

the preferential orientation with the nature of the used substrate may originate from the growth process involved during film growth, especially at the earlier stage of growth, i.e the nucleation step. Further study is necessary to elucidate this difference. Regardless the deposition technique, it is generally reported that ZnO thin films grow with the (002) direction [14-17] which correspond to the growth along the direction c normal to the substrate surface. This preferential orientation is believed to be due to the low energy of this plane [18]. With increasing the deposition temperature or film doping, the preferential growth direction disappear and other plane emerge in the diffraction pattern, namely (100) and (101) [19-21].
The influence of the deposition condition on the occurrence or not of a privileged direction can be linked to the films growth mechanism and the role played by the deposition conditions.

Despite the numerous works on ZnO thin films there are no much publications describing the growth mechanism. Indeed, the deposition mechanism of ZnO thin films passes through the nucleation and the subsequent growth. The growth direction is governed by the «survival of the fastest» as proposed by Drift [22]. The nucleation with various orientations can be formed at the initial stage of the deposition and each nucleus competes to grown. It was reported in sputtered ZnO that at high deposition rate the less density packed atomic planes are preferentially oriented [23]. The less densely packed orientation (100) ($5.91\ 10^{14}$ atm/cm^2) rather than the plane (002) ($10.93\ 10^{14}$ atm/cm^2), this can be explain the shift of the preferred orientation of crystallite from (002) to (100) directions.

The films surfaces were analysed by SEM, figure 5 presents a typical surface and cross-sectional SEM image of the film deposited with oxygen content 0 %. The film displays a granular surface, uniform grain size and void free. From the cross-sectional image, it is seen that the film is composed with columnar structures, which is consistent with the highly (002) texture growth evidenced by XRD analysis. The columnar morphology of our films is confirmed by the micrograph of TEM shown in figure 6.

In figure 7 we have reported the optical transmittance spectra for ZnO:Al films deposited at various oxygen content, the fluctuation in the spectra is principally due to the interface effect owing the reflexion at interfaces. Sharp fundamental absorption edges are observed in all the spectra corresponding to the ZnO:Al films. These films have a high transmittance (>92%) in visible regions and high absorption (near 100%) in ultraviolet regions. As the oxygen content is above to 0 %, the average transmittance of the films reduces slightly. It would be noted that the film deposited at 0 % oxygen content becomes nearly opaque to near infrared region. This is due to the highest carrier concentration, which absorb photons [24]. Figure 8 shows the variation of band gap and Urbach tail as a function of oxygen concentration. The blue shift of the absorption edge with decreasing oxygen content is mainly attributed to the Burstein-Moss effect [25,26], since the absorption edge of degenerate semiconductor is shifted to shorter wavelength with increasing carrier concentration [27]. This decrease in the band gap energy with increasing oxygen content is confirmed by the decrease in band tail width. The variations of E_g and E_U can be explained by the decrease in growth rate with the increase in oxygen concentration. The value of E_U obtained for undoped ZnO prepared by sol-gel [28] and CVD techniques [29] is reported to be in the range of 0.07 – 0.10 eV. The larger values of E_U (0.15 – 0.18 eV) obtained in the present study indicates the presence of a large concentration of localised donor states in the band gap.

Low films resistivity (~1.25×10^{-3} Ωcm) can be achieved without oxygen in the deposition chamber. Also the resistivity increases significantly with increase in oxygen content. This variation of resistivity is ascribed to the change in carrier concentration and/or mobility which are the characteristic parameters reflecting the films structure. It can be seen that at the position of the stress minimum corresponds the minimum in the measured resistivity. This indicates the clear evidence of the correlation between intrinsic stress and electrical parameters of ZnO:Al films. Low mechanical stress, i.e., a low concentration of crystallographic defects leads to better electrical properties.

4. Conclusion:

In summary, highly transparent and lower resistive ZnO:Al films were deposited at room temperature on silicon and glass substrates using rf magnetron sputtering technique. A systematic study was made on the influence of oxygen content in plasma, on the structural, optical and electrical properties of our films.

X-ray diffraction studies indicated that the films deposited on glass were polycrystalline in nature with (002) orientation axis perpendicular to the substrate surface. The FWHM of the films decreased to 21° with increasing oxygen content. For ZnO:Al films deposited on silicon we have found that by increasing the oxygen

concentration, the preferred orientation of crystallite shifts from (002) to (100) directions, this could be due to the nucleation process during film formation.

The film stress is compressive, it decreases from 1.1 (GPa) to nearly stress free with reducing oxygen content in the deposition chamber. The decrease in the intrinsic stress is probably the raison for the observed improvement of film crystallinity.

All films have a high transmission greater than 90% in visible region > However, the film deposited without oxygen in the deposition chamber is nearly opaque in near infrared region. This is due to photons absorption by the large concentration of free electron present in film network; this is consistent with the low measured electrical resistivity (~$1.25x10^{-3}$ Ωcm) in film deposited without adding oxygen in the chamber. The optical band gap shifts towards lower energy with an increase of oxygen content.

References

[1] Chopra K L, Major S and Pandya D K 1983 Thin Solid Films **102** 1.
[2] Aranovich J J, Golmaya D, Fohrenbruck A L and Bube R H 1980 J. Appl. Phys. **51** 4260.
[3] Olvera M L, Maldonado A, Asomoza R, Komagai M and Azomosa M 1993 Thin Solid Films **229** 196.
[4] Tang Z K, Wong G K L, Yu P, Kawasaki M, Ohtomo A, Koinuma H and Y. Segawa 1998 Vacuum **72** (25) 3270.
[5] Hoffman R L, Norris B J and Wagera J F 2003 Appl. Phys. Lett. **82** 733.
[6] Jin Z C, Hamberg J and Grangvist C G 1988 J. Appl. Phys. **64** 5117.
[7] Abdallah B, Chala A, Jouan P-Y, Besland M P and Djouadi M A 2007 Thin Solid Films **515** 7106.
[8] Jeong S H and Boo J H 2004 Thin Solid Films **447-448** 105.
[9] Lee J, Lee D, Lim D and Yang K 2007 Thin Solid Films **515** 6094.
[10] S. Rahmane, M.A. Djouadi, M.S. Aida, N. Barreau, B. Abdallah, N. Hadj Zoubir, Thin Solid Films 519 (2010) 5–10.
[11] Hinze J and Ellmer K 2000 J. Appl. Phys. **88** 2443.
[12] Lokhand B J, Patil P S and Uplane M D 2000 Mater.Lett. **57** 573.
[13] Mass J, Bhattacharya P and Katiyar R S 2003 Mater.Sci. and Eng. B **103** 9.
[14] Ondo-Ndong R, Pascal-Delannoy F, Boyer A, Giani A and Foucaran A 2003 Mater.Sci. Eng.B **97** 68.
[15] Nakanishi Y, Miyake A, Kominami H, aoki T, Hatanaka Y and Shimaoka G 1999 Appl.Surf.Sci.**142** 233.
[16] Shu Y, Water W and Liaw J T 2003 J.Eur.Ceram.Soc. **23** 1593.
[17] Zhang C, Li X, Bian J, Wu W and Gao X 2004 Sol.Stat.Commun.**132** 75.
[18] Nunes P, Fortunato F and Martins R 2001 Thin Solid Films **383** 277.
[19] Goyal D J, Agshe C, Takwale M G, Bhide V G, Mahamuni S and Kulkarni S K 1993 J.Mater.Res.**8** 1052.
[20] Van der Drift A 1967 Philips Res.Rep.**22** 267.
[21] Murti D K and Bluhm T L 1982 Thin Solid Films **87** 57.
[22] Timothy J. Coutts, David L.Young, and Xiaonan Li 2000 MRS BULLETIN 58.
[23] Burstein E 1954 Phys. Rev. **93** 632.
[24] Moss T S 1954 Proceedings of the physical Society London B**76** 775.
[25]3 Lee G H, Yamamoto Y, Kourogi M and al. 2001 Thin Solid Films **386** 117.
[26] Natsume Y, Sakata H 2000 Thin Solid Films **372** 30.
[27] Natsume Y, Sakata H and Hirayama T 1995 Phys. Stat. Solid. (a) **148** 485.

Figures Caption

Figure 1: Variation of deposition rate versus oxygen content.
Figure 2: EDS spectrum for ZnO:Al film deposited at 10 % O_2 content.
Figure 3: X- ray diffraction patterns of ZnO:Al films prepared at different oxygen content (a) on glass and (b) on silicon.
Figure 4: Variation of FWHM and intrinsic stress with oxygen content in the deposition chamber.
Figure 5: SEM images showing the (a) cross-sectional and (b) surface of ZnO:Al film grown at 10 % oxygen content.
Figure 6: TEM Micrograph of ZnO:Al film.
Figure 7: Optical transmittance of ZnO:Al films deposited at various oxygen composition in the deposition gas.
Figure 8: Variation of band gap and band tail width on oxygen content in the deposition chamber.

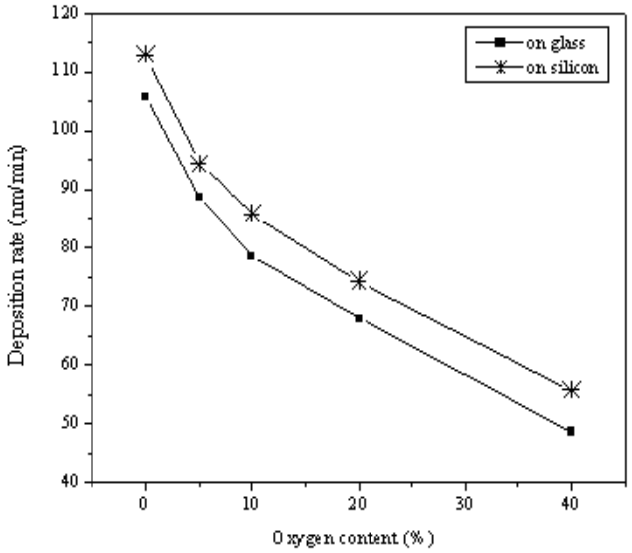


Figure 1

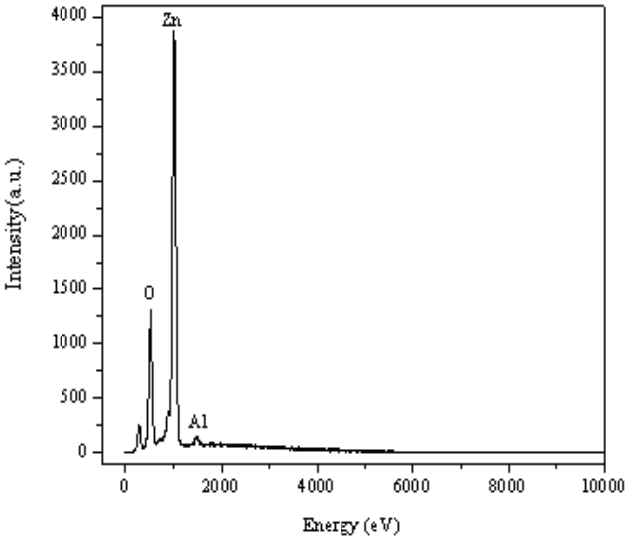


Figure 2

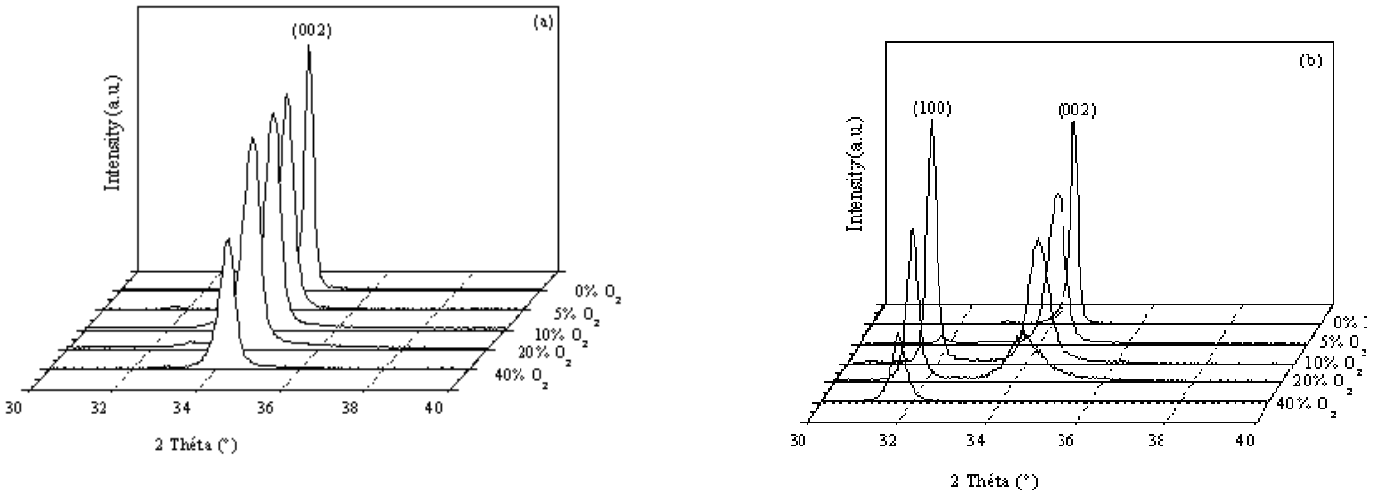


Figure 3

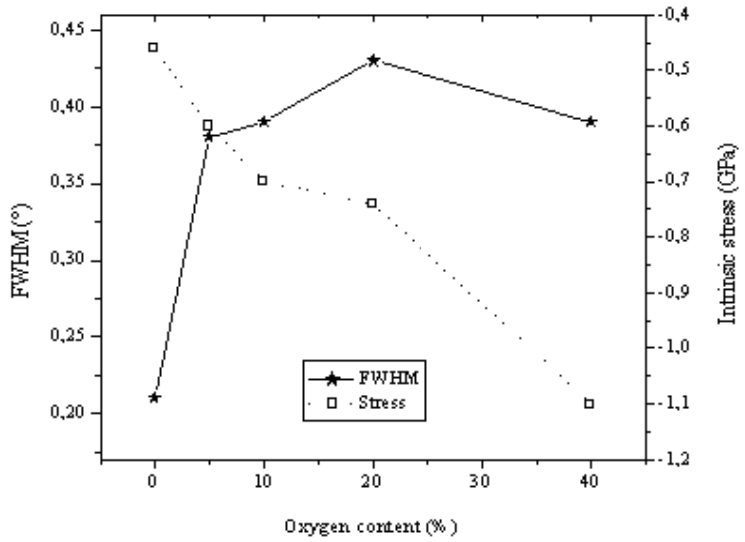


Figure4

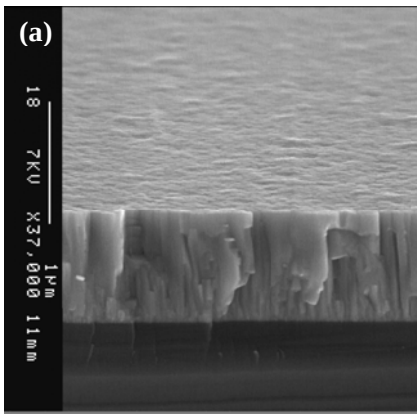
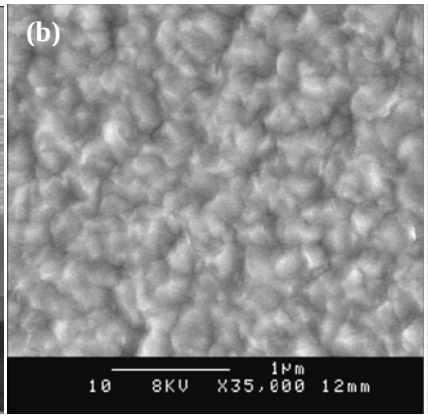


Figure5



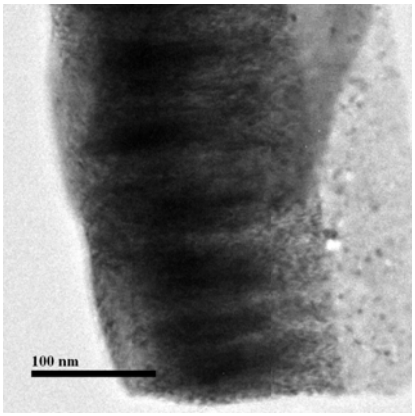


Figure 6

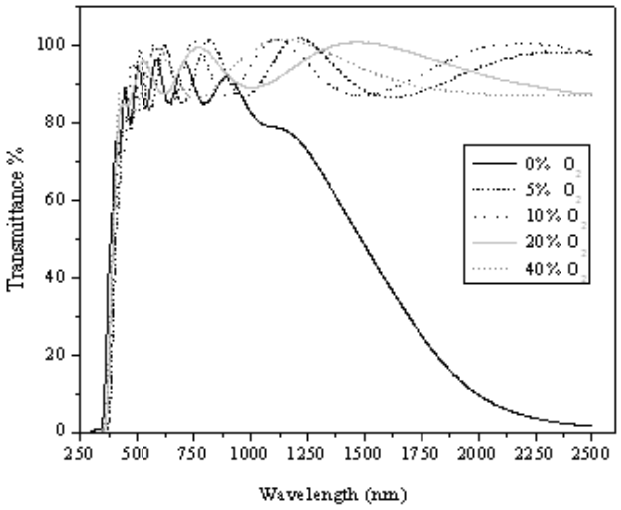


Figure 7

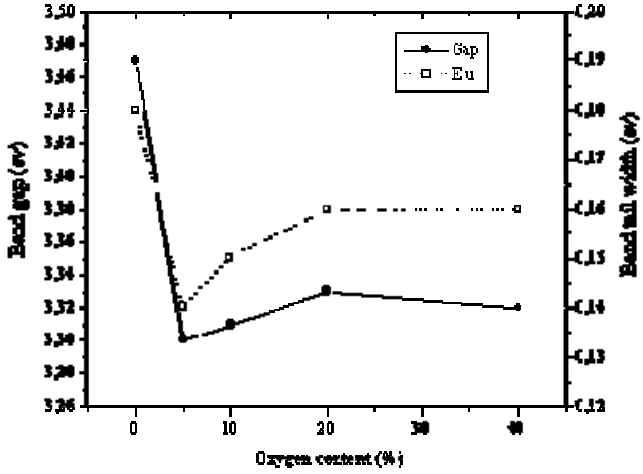


Figure 8

Photocatalytic, hydrophilic titanium dioxide prepared by direct current magnetron sputtering

Authors: Falk Bernsmann[*] [†], Udo Grabowy[*]

Keywords: titanium dioxide, photocatalysis, magnetron sputtering, antimicrobial activity, hydrophilia

Hygienic surfaces are required for many industrial processes, for example production of food, cosmetics or pharmaceuticals, as well as in healthcare facilities. Often these surfaces are not sufficiently cleaned by conventional methods. Self-cleaning surfaces can improve hygienic safety by degradation of organic contaminants using photocatalysis.

The photocatalytic activity of Titanium dioxide (TiO_2) was first described by Fujishima and Honda[1]. Due to its band gap of 3.2 eV (in anatase crystal structure) TiO_2 absorbs only ultraviolet (UV) light of a wavelength below 390 nm. The electrons and holes generated this way can completely degrade organic surface contaminations[2] either by direct redox-reactions or by generation of highly reactive oxygen compounds like superoxide anions ($O_2^{-\bullet}$), hydroxyl radicals ($OH^{\bullet}$), hydrogen peroxide (H_2O_2) and peroxide radicals ($HO_2^{\bullet}$)[3].

TiO_2 surfaces can also exhibit photo-induced super-hydrophilicity[4]: Under illumination the contact angle with water decreases to zero. Hydrophilic surfaces are easy to clean because water can penetrate below dirt particles to remove them. Additionally it has been shown that hydrophilic surfaces improve bone ingrowth of medical implants[5]. Therefore TiO_2 can be an ideal surface for implants since it decreases the risk of contamination by photocatalysis and favours bone ingrowth by hydrophilicity.

We have developed a TiO_2 coating obtained by direct current magnetron sputtering of titanium targets in an argon-oxygen-atmosphere. The coating can be applied to a wide range of materials (metals, ceramics, glasses) of various shapes at a process temperature of 285 °C, and it forms a smooth, homogeneous, optically transparent layer. A typical coating time of four hours leads to a thickness of 0.4 µm. Furthermore the coating resists well to mechanical and chemical treatments.

Elastic recoil detection analysis (ERDA), using gold ions with 200 MeV of kinetic energy as probes, reveals a homogeneous composition of the coating over the whole coating thickness. Atomic fractions are 59 % oxygen, 38 % titanium, 3 % hydrogen and 1 % carbon (Figure 1).

[*] NTTF Coatings GmbH, Maarweg 32, D-53619 Rheinbreitbach http://www.nttf-coatings.de
[†] Tel.: +49 22 24 96 88 81, e-mail: falk.bernsmann@nttf-coatings.de

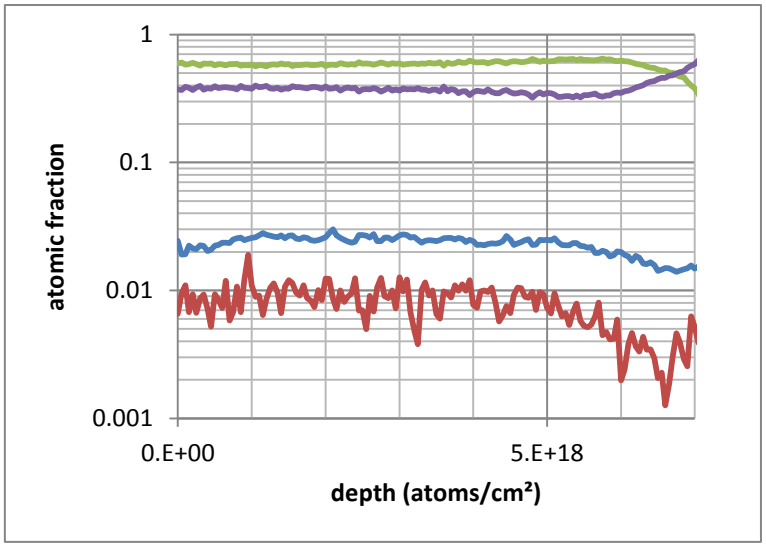


Figure 1: Atomic fraction of oxygen (green), titanium (violet), hydrogen (blue) and carbon (red) depending on depth in the coating obtained by ERDA. At a depth of $7 \cdot 10^{18}$ atoms/cm² the titanium substrate is reached.

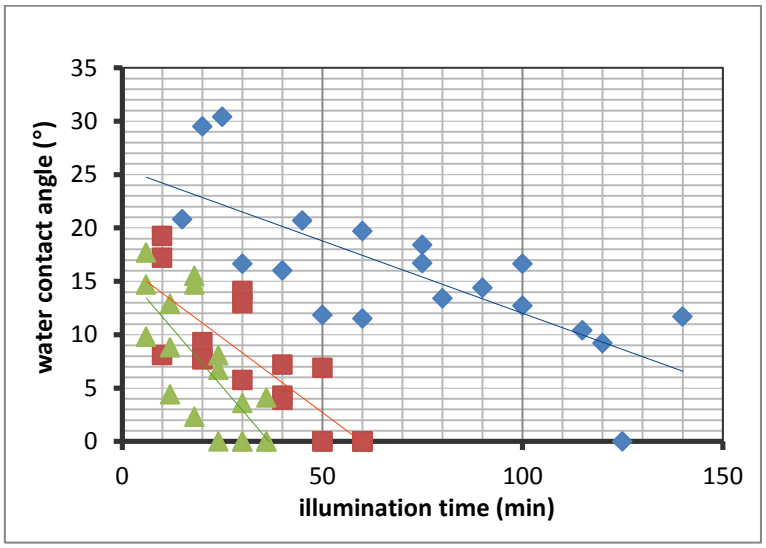


Figure 2: Water contact angle on TiO_2 coatings dependent on illumination time at wavelength 370 nm and intensity 5 W/m² (diamonds), 16 W/m² (squares) or 22 W/m² (triangles). For each intensity three independent experiments are combined in the graph. Lines are a guide to the eye.

The as prepared surface is super-hydrophilic with water contact angles below 3°. In ambient air the contact angle starts to increase after some hours of storage due to surface contamination. This effect can be reversed by UV irradiation. Under moderate UV-intensity corresponding to a Central-European summer day (16 W/m²) super-hydrophilicity is re-established within about an hour depending on the degree of surface contamination. This delay is shortened by illumination with higher intensity (Figure 2). For practical applications, for example on implant surfaces, it is important to preserve the hydrophilicity of the coating during storage. Therefore we have compared different storage conditions (Figure 3). When coated samples are stored in the dark at room temperature in physiologic saline solution, their surface remains super-hydrophilic for at least five months.

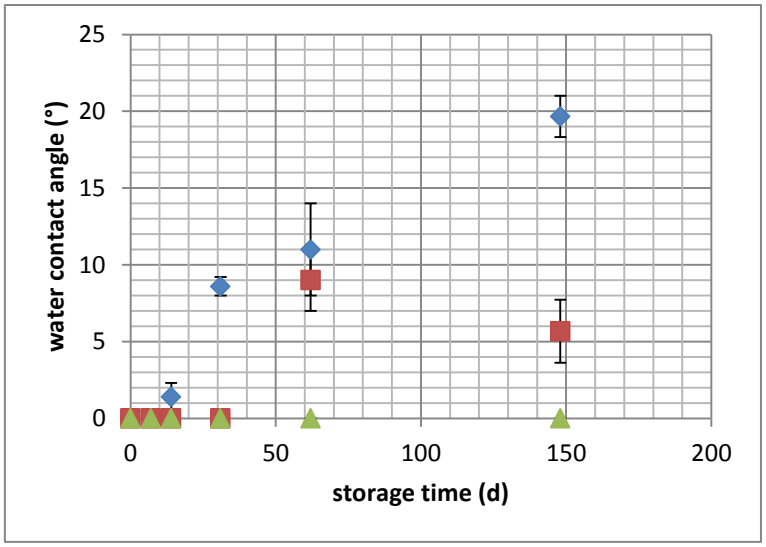


Figure 3: Water contact angle on TiO_2 coatings dependent on storage time in nitrogen gas (blue diamonds), distilled water (red squares) or physiologic saline (green triangles). Each point represents the mean value and standard deviation of three replicate samples.

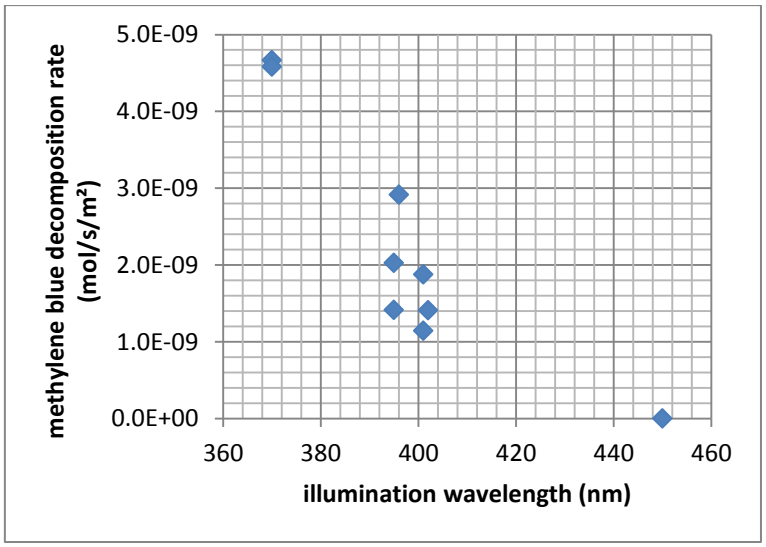


Figure 4: Methylene blue decomposition rate depending on illumination wavelength for comparable intensities (10 W/m² at 370 nm, about 10 W/m² at 400 nm, about 60 W/m² at 450 nm)

Photocatalytic activity of the coatings is shown by UV-light-induced photodegradation of methylene blue in an aqueous solution with an initial concentration of $2 \cdot 10^{-5}$ mol/L. Methylene blue is commonly used to examine the degradation of organic compounds due to its simple photometric quantification. For illumination at a wavelength of 370 nm and an intensity of 10 W/m² methylene blue is degraded at a rate per sample surface area of $5 \cdot 10^{-9}$ mol/(m² s) corresponding to an apparent quantum yield of $2 \cdot 10^{-4}$. There is also significant photocatalytic activity in case of illumination at a wavelength of 400 nm (Figure 4). Thus it is possible to exploit the photocatalytic activity using visible light of short wavelength, which is present for example in conventional indoor lighting.

The light-induced antimicrobial activity of the coatings is assessed under simulated daylight with small UV intensity (0.03 W/m²). This intensity can be found indoors with-

in 2 m of a window during daytime[6]. *Kocuria rhizophila* is chosen as test organism, because it is a ubiquitous airborne cause of food spoilage and highly resistant against drying, radiation and high salt concentrations. Using an initial surface concentration of $(6.3 \pm 1.3) \cdot 10^4$ CFU/cm^2 the concentration of colony-forming units (CFU) was reduced by a factor of 300 compared to an uncoated surface within 24 h of illumination. Therefore even small UV intensities found indoors contribute to the decontamination of coated surfaces. Rapid sterilization of coated surfaces would be achieved using lamps of high UV intensity.

The hardness of the coatings obtained by the Vickers indentation method is 1000 HV 0.005/30. This corresponds to the highest values reported for natural TiO_2 crystals[7]. Due to its hardness and good adhesion to various substrates, the TiO_2 coating is suitable for surfaces exposed to severe mechanical treatments, for example during cleaning.

In summary we present a thin, transparent, chemically and mechanically stable TiO_2 coating with photocatalytic, anti-bacterial and super-hydrophilic properties. It can be applied for example to instruments and devices in food processing or healthcare facilities for easier disinfection and cleaning. The small UV fraction of daylight suffices to trigger the photoinduced effects at a low level. Higher activity can be obtained by exposure to direct sunlight or lamps of higher UV intensity. Most applications benefit from the unlimited repeatability of the photoinduced effects assuring a long functional lifetime of TiO_2 coatings. Yet TiO_2 coatings can also improve products as a single-use surface. For example medical implants can be rendered sterile and hydrophilic just before placement in the body to decrease the risk of infection and improve ingrowth.

Part of this work was funded by the German “Bundesministerium für Bildung und Forschung” (projects “Photokat”, FKZ 01RI0637M and “Titosan”, FKZ 03X0095A).

---

[1] Fujishima, A., & Honda, K. (1972). Electrochemical Photolysis of Water at a Semiconductor Electrode. Nature, 238(5358), 37–38. doi:10.1038/238037a0

[2] Jacoby, W. A., Maness, P. C., Wolfrum, E. J., Blake, D. M., & Fennell, J. A. (1998). Mineralization of Bacterial Cell Mass on a Photocatalytic Surface in Air. Environmental Science & Technology, 32(17), 2650–2653. doi:10.1021/es980036f

[3] Fujishima, A., Rao, T. N., & Tryk, D. A. (2000). Titanium dioxide photocatalysis. Journal of Photochemistry and Photobiology C: Photochemistry Reviews, 1(1), 1–21. doi:10.1016/S1389-5567(00)00002-2

[4] Wang, R., Hashimoto, K., Fujishima, A., Chikuni, M., Kojima, E., Kitamura, A., Shimohigoshi, M., et al. (1997). Light-induced amphiphilic surfaces. Nature, 388(6641), 431–432. doi:10.1038/41233

[5] Junker, R., Dimakis, A., Thoneick, M., & Jansen, J. A. (2009). Effects of implant surface coatings and composition on bone integration: a systematic review. Clinical Oral Implants Research, 20, 185–206. doi:10.1111/j.1600-0501.2009.01777.x

[6] ISO 27447. (2009). Test method for antibacterial activity of semiconducting photocatalytic materials. International Organization for Standardization, Technical Committee ISO/TC 206 Fine ceramics.

[7] John W. Anthony, Richard A. Bideaux, Kenneth W. Bladh, and Monte C. Nichols, Eds., Handbook of Mineralogy, Mineralogical Society of America, Chantilly, VA 20151-1110, USA. http://www.handbookofmineralogy.org/

PHOTOCATALYTICALLY ACTIVE TITANIA PRODUCED BY MOCVD PLASMA PROCESSES

Eva Maria Moser [1,*], Sidney Chappuis [1], Javier Olleros [2]

[1] *University of Applied Sciences of Geneva, rue de la Prairie 4, CH-1202 Geneva, Switzerland*
[2] *University of Applied Sciences Northwest Switzerland, Gründenstrasse, CH-4132 Muttenz, Switzerland*

(*) Corresponding author: eva-maria.moser@hesge.ch

Abstract

The deposition of photocatalytically active titania layers at ambient temperature was developed using the plasma enhanced metal organic chemical vapour deposition (PE-MOCVD) method at low and atmospheric pressure. An increase of the photo-activity in the near ultraviolet (UV) and blue light irradiation was achieved by doping the titania layers using the elements nitrogen and/or carbon.

Investigation of the chemical and structural features of the titania layers was carried out by x-ray photoelectron spectroscopy, atomic force microscopy, and Raman. The optical energy bandgap and photocatalytic activity at 365/428 nm for various titania layers were analyzed using ellipsometry and the methylene blue dye bleaching according to ISO 10678:2010, respectively. The reduction of the aqueous methylene blue solution was similar for the two categories of titania layers. However, the photo-induced properties such as the mineralization of stearic acid for investigating anti-fingerprint effects evidenced a weaker interaction between the mostly hydrophobic PE-MOCVD titania surfaces than for the hydrophilic and rougher PVD produced titania layers when irradiated under UV light.

The observed differences were related to the chemical and structural features since the hydrophobic PE-MOCVD produced titania layers were amorphous and nitrogen and carbon incorporation into TiO_2 led to an enhanced photocatalytic ability by a factor of two regarding the dye tests, whereas the energy bandgap remained at about 3.2 eV. Substitutional and interstitial doping of nitrogen and/or carbon was evidenced by XPS. An additional benefit regarding the adhesion and abrasion resistance was observed for the tailored doping of titania layers.

Results and Discussion

For heat or plasma sensitive substrates the deposition by the PE-MOCVD technique is advantageous. In addition, the deposition rate is increased up to 300 nm/min and to more than 1000 nm/min for processes carried out at atmospheric pressure [1]. As far as the titania layers produced by PE-MOCVD are concerned, the illumination under near UV at 365 nm and blue light at 428 nm exhibits a remarkable increase in the photo-activity if carbon and nitrogen were incorporated into the amorphous TiO_2 lattice according to the dye tests. Surprisingly, the optical energy bandgap and the refractive index were not affected strongly and varied only by $\pm$ 0.1 eV. However, the absorbance in the UV vis spectra is clearly red-shifted for the nitrogen-doped PE-MOCVD-N and nitrogen/carbon-doped PE-MOCVD-N/C samples, being responsible for the yellowish tint of some layers which is due to N_s-doping [2]. In Tab. 1, the optical properties and photo-activities of the titania layers produced by PE-MOCVD are summarised.

For all coatings, XPS data revealed the incorporation of carbon and nitrogen by forming O-Ti-NC sites at a binding energy of 287 eV for the C (1s) core level and 398.7 eV for the corresponding N

(1s) core level. The clearly distinctive additional peak at 284.2 eV is observed just for the co-doped layer and is tentatively assigned to interstitially integrated carbon (C_i) since the binding energy of graphitic carbon is typically in this region.

Table 1: Photocatalytic activity and optical properties of selected titania layers produced by PE-MOCVD at reduced and atmospheric pressure compared to a PVD TiO_2 layer and a commercial Pilkington sample.

Titania layer on Si (100) and glass	Thick-ness (*nm*)	Rough-ness[a] (*nm*)	Refractive index[a] *(633 nm)*	E_{gap}[a] (*eV*)	Photo-activity[b] *(μmol/m^{2}h)*	CIF[c] (*365 nm*)	CIF[c] *(428 nm)*
PE-MOCVD	230	1.1	1.79	3.48	4.5	4.5	1.3
PE-MOCVD-N	339	0.5	1.71	3.27	3.9	3.4	1.7
PE-MOCVD-C	276	0.9	1.76	3.33	6.4	7.0	2.2
PE-MOCVD-N/C	237	1.0	1.79	3.39	6.6	7.3	3.1
PE-MOCVD-AP[d]	200	n.a	n.a.	n.a.	3.1	2.6	1.7
PVD	200	3.4	2.18	3.29	5.4	4.9	1.3
Pilkington	30	n.a.	n.a.	n.a.	1.3	1.5	-

Remarks: [a] Roughness, refractive index and optical energy gap (E_{gap}) were analysed by ellipsometry; [b] photo-activity was measured according to ISO 10678:2010; [c] CIF (catalytic improvement factor); [d] PE-MOCVD-AP was produced at atmospheric pressure

For all deposition processes, nitrogen was entering the partly or completely amorphous TiO_2 lattice and substituting an oxygen site (N_s at 396 eV) or stationing itself interstitially (N_i at 400 eV) [2]. Nitrogen was substituting the oxygen site in the TiO_2 network to a larger extend than carbon did. As a result, the N_s concentration reached up to 9.6 at% and nitrogen reacted also with carbon and formed Ti-NC sites.
Despite the fact that predominant N_s incorporation is observed for all produced titania thin films, the different insertion of the doping elements, their combination possibilities, and the resulting formation of oxygen vacancies contributes in a complex way to the observed photo-induced properties. However, a higher concentration of N_i and N_s seems to be necessary to affect the functional properties of our amorphous titania layers than the concentration of 0.1 at% for N_i in anatase TiO_2 as explored by Dunnill [3].

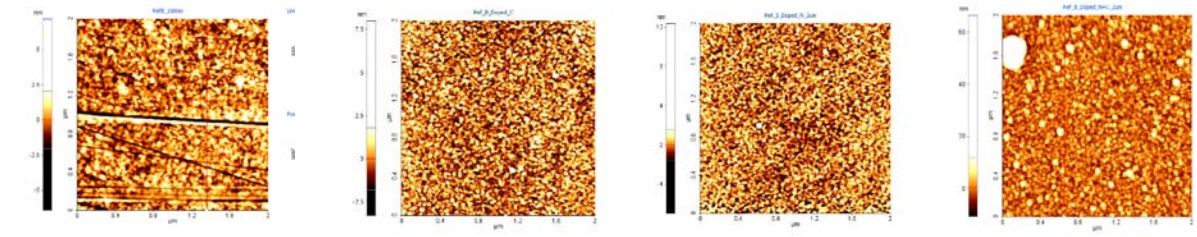
Table 2: Photo mineralization of stearic acid (UV and blue light), roughness, water contact angle, surface energy, the inactivation and attachment of E. coli of selected PVD and PE-MOCVD produced titania layers.

Titania layer on Si(100) / glass	Stearic acid *(mmol/h @ 365 nm)*	Stearic acid *(mmol/h @ 428 nm)*	WCA[a] *(°)*	Surface energy[b] *(mN/m)*	Ra[c] *(nm)*	Antibacterial[d] *(inactivation/ removal)*	Color[e] *(visual)*
PE-MOCVD	0.1	0.03	62	47.4	0.6	good	yellowish tint
PE-MOCVD-N	0.1	n.a.	60	40.8	0.6	excellent	yellowish tint
PE-MOCVD-C	0.1	n.a.	63	40.7	0.8	excellent	yellowish
PE-MOCVD-N/C	0.5	0.02	86	36.5	1.9	excellent	transparent
PE-MOCVD-AP	2.9/0.1	n.a.	48/66	50/43	28/12	n.a.	transparent
PVD	4.8	0.08	4	76.0	3.6	good	transparent

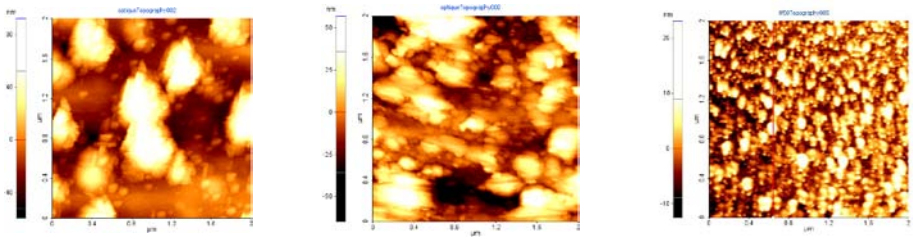
Remarks: a : Water contact angles (WCA) were after exposure to UV radiation for 24 hours
b: The surface energy was analysed after radiation with UV light at 365 nm for 24 hours
c: The roughness Ra was investigated using atomic force microscopy Park System XE-100 in non contacting mode
d: The inactivation and attachment of E. coli were analysed by applying several methods
e: The colour of the titania layers were compared by visual inspection

The surface topography of the TiO_2-layers was investigated using atomic force microscopy AFM in the non contacting mode and is presented in Figure 1. An area of 2 μm x 2 μm was scanned

for all titania layers in order to compare the grain sizes and roughnesses (Tab. 2). Titania coatings produced at atmospheric pressure and PVD-TiO_2 are rougher and show a more open surface than PE-MOCVD TiO_2 layers whose roughness is typically < 1 nm.



a) PE-MOCVD b) PE-MOCVD-N c) PE-MOCVD-C d) PE-MOCVD-N/C



e) PE-MOCVD-AP f) PE-MOCVD-AP' g) PVD

Fig. 1: AFM images (2 μm x 2 μm) of the titania layers with a thickness of about 200 nm; e) thickness of 100 nm; f) thickness of 200 nm

Conclusions

Collectively, the PE-MOCVD thin films are Raman amorphous, hydrophobic, and show smooth and closed surface topographies. All PE-MOCVD titania coatings deposited at ambient temperature exhibit a high photocatalytic activity in bleaching the aqueous methylene blue solution when irradiated under near UV (365 nm) and blue light (428 nm). The response to the UV/vis irradiation is improved by incorporation the non-metallic elements nitrogen and/or carbon into the titania lattice. The most photo-active titania layer for reducing methylene blue is the transparent co-doped PE-MOCVD-N/C layer.

The mechanical removal of the deposited stearic acid was straight forward for the hydrophobic and smooth PE-MOCVD surfaces. The reaction of the hydrophobic PE-MOCVD produced TiO_2 layers with the stearic acid is weaker than for the PVS-layer when irradiated under UV light. However, the PE-MOCVD and PVD titania layer showed similar reaction ability towards stearic acid when irradiated with blue light, while the characteristic attachment of the stearic acid is independent of the illumination. Furthermore, E. coli inactivation and/or removal is more efficient for the PE-MOCVD than for the rougher and hydrophilic PVD titania surface.

For the amorphous PE-MOCVD-N/C titania layer, XPS data reveal concentrations of 6.1 at% and 2.1 at% for substitutional N_s and C_s, respectively and 1.4 at% and 2.1 at% for interstitial N_i and C_i, respectively. The substitution of oxygen sites due to the formation of Ti-NC-like species (1.9 at%) is also observed. The non-doped titania PVD layer consists of > 50 % anatase grains embedded in the amorphous matrix and is superhydrophilic.

PE-MOCVD-AP titania layers produced at atmospheric pressure show a slightly reduced photo-activity compared to the coatings deposited at reduced pressure. However, their functional features combine nicely the advantages of the above described hydrophilic PVD TiO_2 layer and the PE-MOCVD titania thin films produced at low pressure.

It can be concluded that TiO_2 layers produced by plasma deposition techniques at ambient temperature operate as a photocatalyst and respond to the illumination under near UV and visible light which proves them to be a potential candidate for a wider application field since many white/visible light sources do have a minimal UV component. The observed different photo-

induced features such as antimicrobial, anti-fingerprint, easy-to-clean, and self-cleaning effects enable to tailoring the manufacture of the titania layers towards the demanded specifications of the product.

References

[1] Chappuis S., Campiche A, Gilliéron D., Moser E.M., Lausmaa J., Reller A., Plasma Process Polym, 6, 440-445 (2008)

[2] Dunnill CW, Aiken ZA, Kafizas A, Pratten J, Wilson M, Morgan DJ, Parkin IP. White light induced photocatalytic activity of sulfur-doped TiO2 thin films and their potential for antibacterial application. *J. Mater. Chem.* 2009;**19**:8747-8754

[3] Dunnill CW, Parkin IP. Nitrogen-doped TiO_2 thin films: photocatalytic applications for healthcare environments. *Dalton Trans.* 2011;**40**:1635-1640

Plasma Nitriding Performed under Atmospheric Pressure using Pulsed-Arc Plasma Jet

R. Ichiki[1], H. Nagamatsu[1], Y. Yasumatsu[1], M. Yoshida[2], S. Akamine[1] and S. Kanazawa[1]

[1]*Oita University, Oita 870-1192, Japan*
[2]*Shizuoka Institute of Science and Technology, Fukuroi 437-8555, Japan*
E-mail ryu-ichiki@oita-u.ac.jp

Abstract: Plasma nitriding is achieved by spraying the nitrogen pulsed-arc plasma jet under atmospheric-pressure N_2/H_2 mixture. The quality of nitriding is found to depend on the H_2 flow rate, which has an optimal value. We propose a simple mechanism of this dependence. Moreover, the amount of H_2 necessary for best nitriding can be decreased to 1/20 by changing the way of H_2 addition.

Keywords: nitriding, surface hardening, atmospheric-pressure plasma, plasma jet

Plasma nitriding is one of the surface-hardening technologies utilized for a number of mechanical products such as automobile components, dies, and cutting tools [1-6]. As the treatment requires a vacuum system in conventional plasma-nitriding methods, the treatment is performed as a batch process and the capital cost becomes very high. To eliminate these shortcomings, we are developing a new plasma nitriding using atmospheric-pressure plasma technologies. As far as the authors know there are only a few literatures on successful surface hardening by atmospheric-pressure plasma nitriding, e.g., nitriding with a dielectric barrier discharge [4]. Of a wide variety of atmospheric-pressure plasmas, we have adopted the pulsed-arc (PA) plasma jet for the following two reasons [7]. First, the plume temperature of the PA discharge is suitable for nitriding. Second, the PA discharge can produce relatively high density reactive species.

Up to now, we have demonstrated that local nitriding is feasible with spraying the PA plasma jet onto a steel surface, provided that H_2 gas is added to the ambient N_2 atmosphere [8]. Here, we report the detail of H_2 addition influencing the quality of nitriding. Moreover, a new method of H_2 supply is described in which the H_2 amount necessary for nitriding can be decreased drastically.

The jet nozzle is composed of a coaxial cylindrical electrode system as shown in Fig. 1. The grounded external electrode is 35 mm in inner diameter and has an orifice of 4 mm in diameter at the tip. The tip of the internal electrode has a curvature

radius of 4 mm. The electrode gap, between the internal electrode tip and the inner wall of the external electrode near the orifice, is 18 mm. N_2 gas of 99.99% in purity is introduced into the gap at 20 L/min. The low-frequency voltage pulse (4-5 kV in height and 21 kHz in repetition as shown in Fig. 2) is applied to the inner electrode using a high voltage power supply. The maximum of the discharge current is ca. 1 A. The afterglow of the generated PA plasma is spewed out from the orifice, forming the jet plume.

Nitriding is performed in a closed cylindrical container. The jet nozzle is inserted into the container from the upper end. Prior to the generation of plasma jet, the N_2 gas flow from the nozzle purges residual O_2 inside the container. Note that it is necessary for performing nitriding to add H_2 gas. Our conventional way is to add H_2 to the N_2 atmosphere through a container port (the atmosphere H_2 mode) [8]. Here we newly tried an alternative H_2 supply, i.e., to add H_2 through the jet nozzle with the working N_2 gas (the nozzle H_2 mode). The N_2/H_2 gas mixture flows out through the exhaust ports mounted at the lower end. The container is not fitted with any pumping system so that the N_2 pressure inside the container is kept at 1 atm.

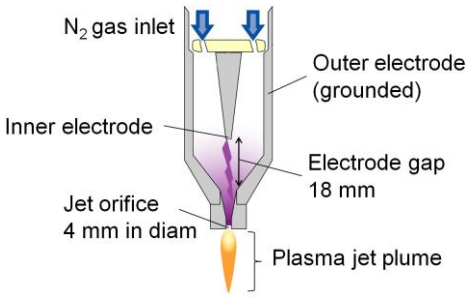


Fig. 1 Schematic of pulsed-arc plasma jet nozzle.

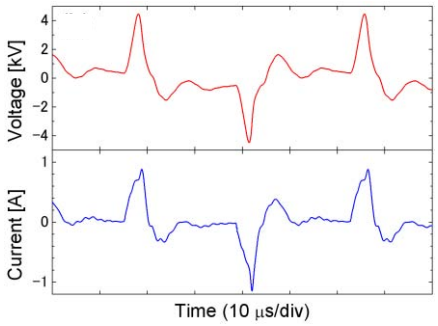


Fig. 2 Typical voltage and current waveforms.

The nitriding response is examined by spraying the jet plume onto the surface of disk-shaped samples (20 mm in diameter and 4 mm in thickness) of die steel JIS SKD61 which is frequently used to benchmark nitriding [3,6]. The sample is put on a ceramic heater to control the treatment temperature. The distance between the nozzle tip and the sample surface is 15 mm, The treatment temperature is 530°C. The treatment duration is 2 h. The visible jet plume covers the entire surface of the sample during the treatment.

Fig. 3 shows a typical metallographic structure of a treated sample cross-section. The white layer is

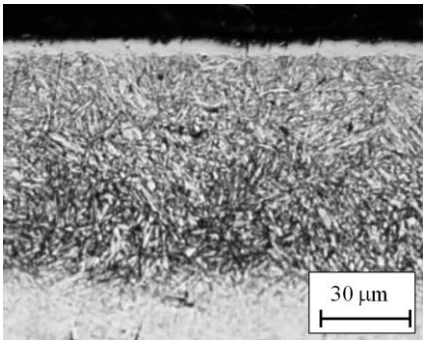


Fig. 3 Metallographic section of sample surface.

the compound layer, which is mainly composed of ε-$Fe_{2-3}N$ phase. The dark zone beneath the compound layer corresponds to the diffusion layer. The hardness profile is shown later. Fig. 4 shows the nitrogen distribution of the cross-section obtained with EPMA. We can see that the compound layer of less than 10 μm contains a dense nitrogen and the diffusion layer (down to 70 μm here) also has a considerable amount of nitrogen. This indicates that the hardening is truly attributed to N atoms diffusing into steel surface.

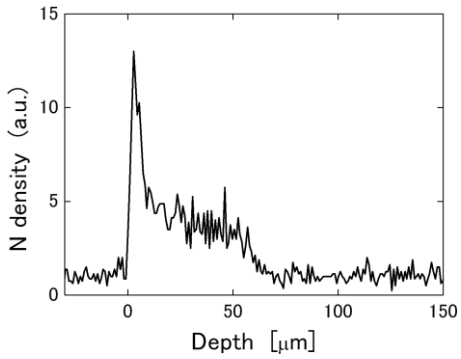
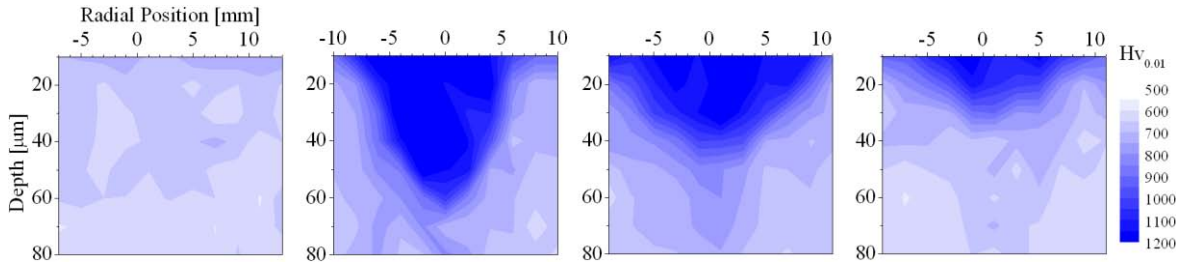


Fig. 4 Relative nitrogen density profile as a function of the depth from surface.

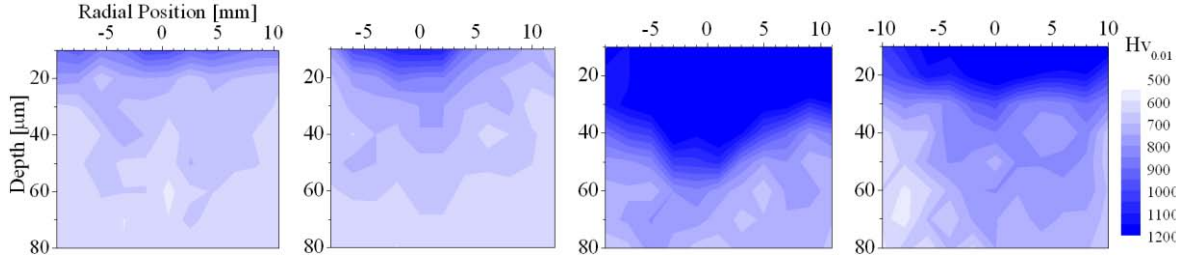
Fig. 5 shows the hardness profile of nitrided cross-section for several H_2 flow rates under the atmosphere H_2 mode. The results indicate that the quality of nitriding is low when the H_2 flow rate is too low, or too high. That is, there exists an optimal H_2 flow rate to provide the deepest hardened layer. In our experiments, the optimal value is 4 L/min. On the other hand, Fig. 6 shows the hardness profiles for the nozzle H_2 mode. One notices that this mode also gives a qualitatively same dependence on the H_2 flow rate. However, the flow rate necessary for nitriding is much lower than that for the atmosphere H_2 mode. The optimal H_2 flow rate, 200 mL/min, proves to be 1/20 of that for the atmosphere H_2 mode.

The optical emission spectroscopy revealed that the intensity of the NH radical is most prominent in the both H_2 modes. Fig. 7 shows the NH emission intensity as a



0.4 L/min 4 L/min 7 L/min 15 L/min

Fig. 5 Hardness profile of nitrided samples treated under the atmosphere H_2 mode.



20 mL/min 100 mL/min 200 mL/min 500 mL/min

Fig. 6 Hardness profile of nitrided samples treated under the nozzle H_2 mode.

function of the H_2 flow rate. It can be predicted from the result that a low H_2 flow rate provides a high-density NH radicals and the density decreases with increasing H_2 flow rate under the both H_2 mode. This dependence might be due to that a high H_2 flow rate leads to the production of NH_3 rather than NH. It should be emphasized here that a substantially analogous NH emission intensity is obtained under the nozzle H_2 mode although the horizontal scale for this mode is 1/40 of that for the other mode. The effective NH production under the nozzle H_2 mode is most likely caused by the direct supply of H_2 to the discharge region involving active chemical reactions.

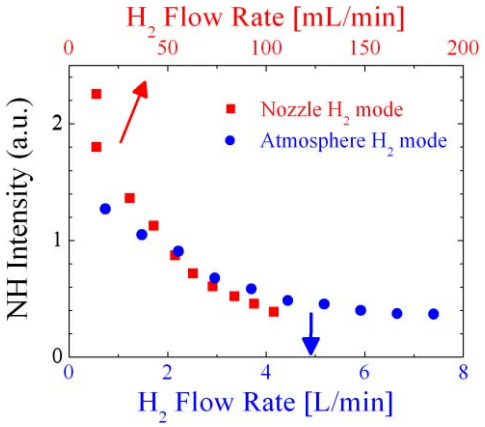


Fig. 7 NH emission intensity as a function of H_2 flow rate in the both H_2 mode.

By considering the presented results comprehensively, we construct a likely mechanism of the plasma-jet nitriding as follows:

(A) The HN radicals play a role of supplying N atoms to the sample surface.

(B) The low-quality nitriding for too high H_2 flow rate under the both H_2 mode is due to the lack of N supply to the surface.

(C) The low-quality nitriding for too low H_2 flow rate is caused by the surface oxidization by residual O_2 ramaining because of a low H_2 reduction ability.

(D) The efficient production of NH radicals under the nozzle H_2 mode provides the decrease in the H_2 amount necessary for nitriding to 1/20.

We hope that the PA plasma jet nitriding will offer an easy-to-use, economical hardening method to industrial and scientific fields.

[1] Y. Sun and T. Bell, Mater. Sci. Eng. **A 140**, 419 (1991).

[2] T. Czerwiec, H. Michel, and E. Bergmann, Surf. Coat. Technol. **108-109**, 182 (1998).

[3] R. Ichiki and T. Hara, Jpn. J. Appl. Phys. **48**, 076001 (2009).

[4] L. Yan, X. Zhu,J. Xu,Y. Gao,Y. Qin, and X. Bai, Plasma Chem. Plasma Process. **25**, 467 (2005).

[5] T. Hassel, C. Birr, and F. W. Bach, Key Eng. Mater. **438**, 147 (2010).

[6] O. Salas, J. Oseguera, N. Garcí, and U. Figueroa, J. Mater. Eng. Perform. **10**, 649 (2001).

[7] Y. Takemura, Y. Kubota, N. Yamaguchi, and T. Hara, IEEE Trans. Plasma. Sci. **37**, 1604 (2009).

[8] R. Ichiki, H. Nagamatsu, Y. Yasumatsu, T. Iwao, S. Akamine, and S. Kanazawa, Mater. Lett. **71**, 134 (2012).

Effect of Plasma Nitriding and Nitrocarburising Process on the Corrosion Resistance of Grade 2205 Duplex Stainless Steel

Subroto Mukherjee[1] , Alphonsa Joseph[1], Ghanshyam Jhala[1], Satyapal M[2], A. S. Khanna[2], Pratipal Rayjada[1], Narendra Chauhan[1], Raja V. S.[2]

[1]Institute for Plasma Research, Gandhinagar, India
[2]Indian Institute of Technology, Bombay, India

Corresponding author
Dr. S. Mukherjee,
Institute for Plasma Research,
Bhat, Gandhinagar, Gujarat, India.
Phone: +91-79-23269011, 23269000
Fax No. : +91-79-23269000
E-mail: mukherji@ipr.res.in; dr_mukherjee@yahoo.co.in

Abstract:
Grade 2205 duplex stainless steel is a type of stainless steel possessing a nearly equal amount of the ferrite (α-Fe) and austenite (γ-Fe) phases as a matrix. Since this steel has a relatively low hardness of 256 HV0.1, an attempt has been made to improve its hardness and wear properties without compromising the corrosion resistance by plasma nitriding and nitrocarburising process. Plasma nitriding and plasma nitrocarburising process was performed with 80% nitrogen and 20% hydrogen gas and 78% nitrogen, 20% hydrogen and 2% acetylene gas respectively at 350, 400, 450 and 500 ^{o}C for 4 hours. The temperature played an important role in the distribution of nitrogen and carbon in the original austenite and ferrite phases present in the bulk material. As a result there was an improvement in microhardness and corrosion properties after these treatments. It was observed that plasma nitrocarburising process performed better than plasma nitriding process in improving the corrosion properties due to the presence of carbon.

Keywords

Duplex steel; Plasma Nitriding; Nitrocarburising; Hardness; Corrosion

Introduction

The ferritic-austenitic Duplex Stainless Steel (DSS), possesses good mechanical properties and high corrosion resistance. For this reason they are frequently used in chemical engineering, oil refining, food processing, dyeing, tanning and the paper industry [1]. The most common duplex grade used today is EN 1.4462 or 2205 (UNS S31803/S32205), which has a nominal composition of 22% Cr, 5%Ni and 3% Mo [2]. However, even in the DSS, there is still the necessity to increase surface hardness in order to obtain higher wear resistance without loss of corrosion resistance [3]. Plasma Nitriding process seems to be a reasonable method to improve the wear resistance of this steel but unfortunately it decreases the corrosion resistance properties due to chromium nitride precipitation. It was found that in case of austenitic steel when plasma nitriding was conducted at temperature below 500 °C it was possible to maintain high corrosion resistance due to formation of so called “expanded

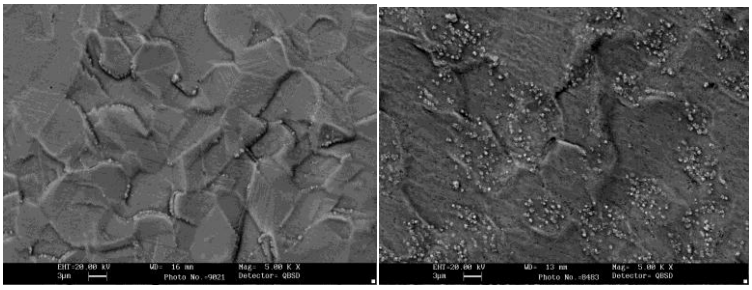
austenite" (named also γN , S-phase). Few works on plasma nitrided duplex steel confirmed the formation of this phase also. In a recent work by A. Triwiyanto eta al, the effect of carbon and nitrogen was investigated at 460 ^{o}C indicating an increase in surface hardness due to the presence of expanded austenite [4]. Till now, corrosion resistance properties have not been investigated after plasma nitriding and nitrocarburising process for this steel. In the present study, a comparison of both structural and corrosion properties have been made after plasma nitriding and plasma nitrocarburising process on 2205 grade duplex stainless steel.

Experimental details:

Circular disc of dimensions of 3cm diameter and 5mm thickness of 2205 grade duplex stainless steel (C 0.026%, Ni 4.6%, Cr 22.06%, Si 0.69%, Mn 1.74%, S 0.008%, P 0.025% and Mo 2.580% by weight, with Fe being the balance). The samples were mechanically polished up to 1 μm diamond paste and 0.5 micron alumina paste in order to obtain a final mirror finish of a mean roughness Ra value better than 0.01microns, and cleaned in acetone. The plasma nitriding and plasma nitrocarburizing processes with a gas mixture (80% nitrogen and 20% hydrogen) and (78% nitrogen, 20% hydrogen and 2% C_2H_2) respectively were performed at 5mbar. Prior to plasma processing surface cleaning was done at 250 °C/1 h by using pure H_2 atmosphere. The working temperature was controlled by monitoring a J- type thermocouple and adjusting the voltage as needed in order to maintain the substrate temperature of 350, 400, 450 and 500 °C for 4 hours. After plasma nitriding, the samples were cooled down to 180 ^{o}C in a nitrogen gas atmosphere to avoid oxidation before removing them from the vacuum chamber. The phases formed were identified using glancing angle X-ray diffractometer collected between 35 °≤2 θ <80° with Cu–Kα radiation (λ =1.5406 Å), at a step size of 0.06°. Surface morphology of the treated samples were observed under Scanning Electron Microscopy (SEM). Microvickers Hardness Tester was used to measure surface hardness with 100 grams load. Potentiodymanic studies were done with 3.5% NaCl solution using Gamry make Potentiostat.

Results:

a) Surface Roughness:



(a) (b)

Fig. 1: Surface morphology of Duplex 2205 at (a) plasma nitrided at 500 ^{o}C b) plasma nitrocarburised at 500 ^{o}C.

The surface roughness of duplex 2205 stainless steel samples increases with temperature after plasma nitriding and plasma nitrocarburising process. The increase in surface roughness after plasma nitrocarburising process at high temperatures is due to the presence of nitrides. This is

evident in fig. 1b where small microparticles are present in austenite phases after plasma nitrocarburising compared to plasma nitriding processs as observed in fig.1 a.

b) Surface hardness

The experimental results demonstrated that the surface hardness of plasma nitrided specimens is significantly affected by nitriding. Very high microhardness values were found on the surface of samples treated at temperatures ≥450 °C as shown in Fig. 2. The initial hardness of Duplex 2205 is 250HV0.10. The maximum values measured from the 500 °C/4 h treated sample is 1326 HV0.10, which is about 5 times as hard as the untreated material. However, the surface hardness was lower after plasma nitrocarburising compared to plasma nitriding process due to low diffusion rate of carbon than nitrogen ions in 2205 duplex steel.

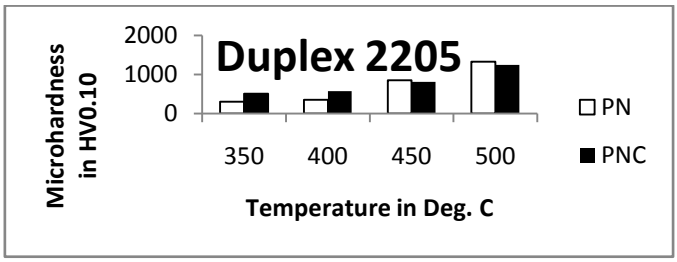


Fig. 2: Surface hardness after plasma nitriding and plasma nitrocarburising of Duplex 2205 steel at different temperatures

c) Phase Analysis:

The GIXRD of untreated duplex 2205 steel shows the presence of both ferrite and austenite phase. After plasma nitriding at 350 ^{o}C, there is a formation of expanded austenite and ferrite phase. The expanded austenite peaks are broad and shift towards the lower 2 theta angles. With increase in temperature i.e. 400 ^{o}C, there is presence of expanded austenite and ferrite but the shifts of expanded austenite phase are lower than that formed at 350 ^{o}C. With further increase in temperature the expanded austenite dissociates to form chromium nitride and ferrite along with iron nitrides (Fig. 3a). In case of plasma nitrocarburising at 350 and 400 ^{o}C the shifts of expanded austenite is more compared to that after plasma nitriding mainly due to the presence of carbon nitrogen supersaturated expanded austenite phase. At higher temperature there is presence of iron nitrides and chromium nitrides (Fig.3b).

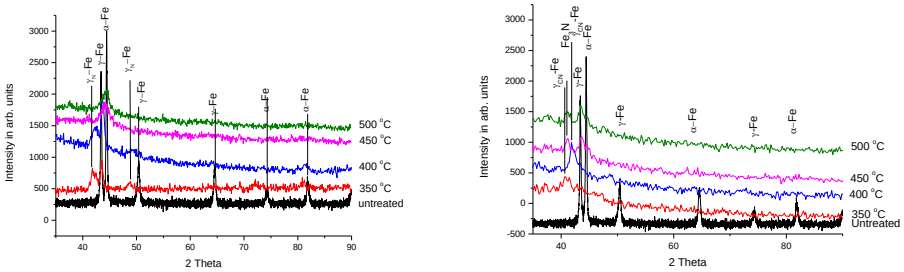


Fig. 3: GIXRD pattern of Duplex 2205 steel a) plasma nitrided b) Plasma nitrocarburised at different temperatures.

d) Potentiodynamic studies:

Fig. 4 shows the potentiodynamic polarization curves for both untreated and treated duplex samples at different temperatures studied using 3.5 wt% NaCl environment. The

corrosion current density of plasma nitrided samples at 350 ^{o}C was more positive than other samples including the untreated sample (fig.4a). This improvement is due to the presence of γ_N phase formed at 350^{o}C. Whereas the samples treated at 450 & 500 ^{o}C nitriding temperature are more susceptible to corrosion due to the formation of CrN phases.

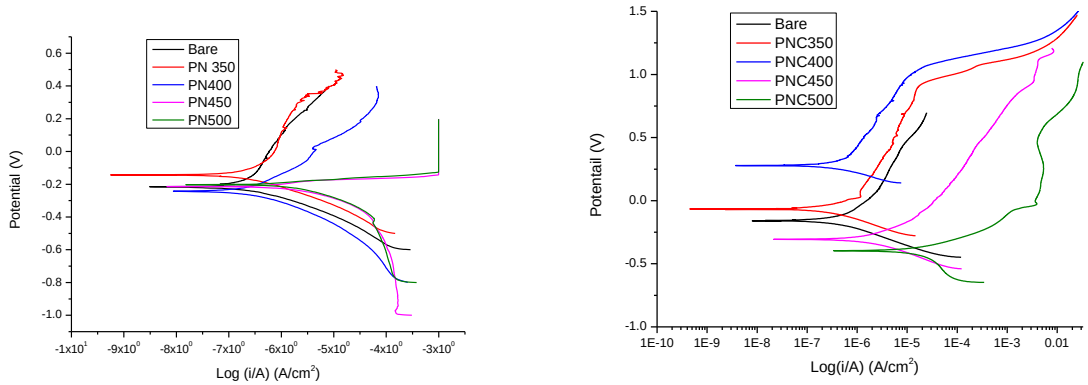


Fig.4 Potentiodynamic curves of a) plasma nitrided b) plasma nitrocarburisied duplex steels in 3.5% NaCl solution

After plasma nitrocarburising process it was found the the corrosion current density was the lowest for duplex samples treated at 350 ^{o}C as shown in figure 4b. Also the corrosion rate obtained from these curves is lower than plasma nitrided samples indicating that the improvement in corrosion resistance is due to the presence of carbon-nitrogen supersaturated expanded austenite phase.

Conclusion:

It was concluded from this investigation that both surface hardness and corrosion resistance of duplex steels can be enhanced by plasma nitriding and plasma nitrocarburising process. It was observed that the duplex samples treated at 350 ^{o}C exhibited better corrosion resistance then samples which were treated at higher temperatures. Moreover, samples treated by plasma nitrocarburising process performed better than plasma nitrideing process due to the presence of carbon which was responsible in forming carbon nitrogen supersaturated expanded austenite phase.

References:

[1] Rim Dakhlaoui, Chedly Braham, Andrzej Baczma´nski, Mechanical properties of phases in austeno-ferritic duplex stainless steel—Surface stresses studied by X-ray diffraction, Materials Science and Engineering A 444 (2007) 6–17.

[2] Iris Alvarez-Armas, Duplex Stainless Steels: Brief History and Some Recent Alloys, Recent Patents on Mechanical Engineering 1 (2008) 51-57.

[3] H. Dong, “S-phase surface engineering of Fe-Cr, Co-Cr and Ni-Cr alloys,” Int. Mater. Rev., vol. 55, no. 2, (2010) 65–98.

[4] A.Triwiyanto1, P. Hussain2, M. Che Ismail, Behavior of Carbon and Nitrogen after Low Temperature Thermochemical Treatment on Austenitic and Duplex Stainless Steel, Applied Mechanics and Materials Vols. 110-116 (2012) 621-62.

WEAR PROPERTIES OF PLASMA NITRIDED INCONEL 718 SUPERALLOY

Halim Kovacı[1], Hojjat Ghahramanzadeh ASL[1], Çiğdem Albayrak[2], Akgün Alsaran[1]
[1]Ataturk University, Erzurum, Turkey
[2]Erzincan University, Erzincan, Turkey
halim.kovaci@atauni.edu.tr

Abstract:

Inconel 718 is a nickel-based superalloy that is extensively used in a broad range of applications such as turbine blades, power generation, petroleum and nuclear reactor technology due to its good mechanical properties at intermediate and high temperatures. Contrast to its wide range of usage, high plasticity and good corrosion resistance, poor wear resistance of Inconel 718 limits its usage in some applications. In order to improve the wear resistance of Inconel 718 several surface treatment methods are used. One of the most important methods, that is used to prevent the metal from wear is to modify the surface with a nitride layer by plasma nitriding. In this study Inconel 718 super-alloy was plasma nitrided in different parameters and the wear mechanism of plasma nitrided Inconel 718 was investigated using a pin-on-disk wear tribotester. Microstructure and phase components of Inconel 718 were investigated using SEM and XRD before and after plasma nitriding process.

Keywords: Wear, Superalloy, Plasma nitriding, Inconel 718

Introduction:

Inconel 718 is a nickel-based superalloy that is extensively used in a broad range of applications such as turbine blades, power generation, petroleum and nuclear reactor technology due to its good mechanical properties at intermediate and high temperatures [1-3]. Although it has good corrosion and oxidation resistance, it is subjected to high wear levels where materials are slide one part to another and wear of alloy can cause the failure [4]. In the literature, there are different studies which examine the wear characteristics of treated and untreated Inconel 718 [1, 4, 5].

Plasma nitriding is a thermochemical surface treatment method, which bases on the nitrogen diffusion into the material surface in a plasma environment, used to enhance the wear, corrosion resistance and fatigue properties of ferrous and non-ferrous materials [1, 6-9] and the wear resistance of a nitrided material depends on the hardened layer formed on the surface after nitriding [10]. The aim of this study is to determine the effect of different nitriding times and temperatures on wear mechanisms and structural properties of Inconel 718 and to find out the best nitriding condition. For this aim, Inconel 718 substrates have been nitrided at different parameters and the treated samples have been investigated by pin-on-disk wear test, SEM, XRD and microhardness test.

Material and Method:

Inconel 718 alloy substrates chemical composition is tabulated in Table 1 [11] were used for plasma nitriding. Before the nitriding process, the specimens, whose dimensions are 15x11 mm^2 and with a thickness of 1 mm, were polished by using SiC emery paper with 1200-mesh grit and an alumina having 3µm grain size, respectively. After cleaning with alcohol, the specimens were placed into the plasma nitriding chamber and specimens were cleaned from surface contaminations by hydrogen sputtering for 15 minutes under a voltage of 500V and a pressure of $5x10^2$Pa. Then, the plasma nitriding processes were performed with DC voltage under a pressure of $5x10^2$ Pa.

Table 1. Chemical composition of Inconel 718 (% weight, max.)

C	Mn	Si	Cr	Co	Mo	Nb+Ta	Ti	Al	Fe	Cu	Ni
0.08	0.35	0.35	21.0	1.00	3.30	5.50	1.15	0.80	Balance	0.30	55.00

The specimens were nitrided at 400°C, 500°C and 600°C with times 1 and 4 hours (In this article, the specimens

were coded as nitriding temperature-time like 400-1). After nitriding processes, X-ray analyses were performed by Rigaku diffractometer at 30 kV and 30mA with CuKa radiation. The hardness values of treated and untreated specimens were measured by using a STRUERS ODURAMIN 5 microhardness tester with a load of 10 g and a loading time of 10 second with Vickers method. The wear tests were performed by using Turkyus pin-on-disk tester under a load of 5N at 3000 seconds and a distance of 150 m. The wear tests were performed by using WC pin with a diameter of 6 mm. The diameter of wear tracks was measured as 8 mm for all specimens. After wear tests, the worn surfaces were examined by ZEISS EVO SEM. In order to calculate wear rate, the wear profiles and surface roughness values were recorded using Mahr M1 profilometer and then, the wear rates were calculated by using the equation of W=V/(DF)-mm^3/N.m [10].

Results and Discussion:

XRD patterns of untreated and nitrided Inconel 718 were shown in Fig. 1. When the XRD patterns were examined, untreated specimen showed Inconel peaks. After the nitriding processes, the reaction of Cr and nitrogen was given rise to the formation of CrN. In the meantime, the substrate peaks were shown in all nitrided specimens because of the thin nitride layer. CrN peaks were obtained at angles of 38 and 64 and this result is accordance with the another study [5].

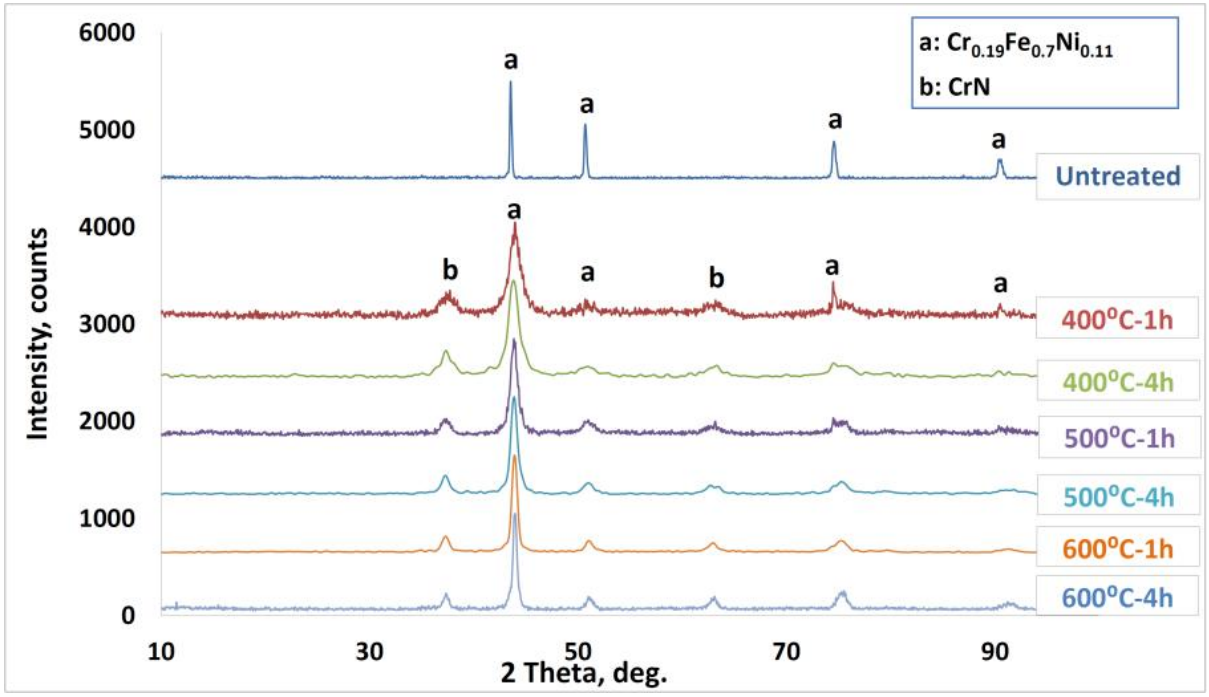


Fig. 1. XRD patterns of specimens

The microhardness and wear rate values were shown in Fig. 2. The hardness of untreated specimen was measured approximately as 500 $HV_{0.01}$. The increase of nitriding time and temperature provided 2-5 times hardening. The maximum hardness was obtained from specimen 600-4, roughly 2600 $HV_{0.01}$, among the nitrided specimens. Also, it was inspected that the increase of hardness was depends on the increment of process time and temperature. When the wear rates were investigated (Fig. 2.), it was observed that the maximum wear rate was obtained from the untreated specimen and the increase of nitriding time and temperature causes to the decrease of wear rates. There was an inverse proportionality between hardness and wear rate and the minimum wear rate was obtained from 600-4.

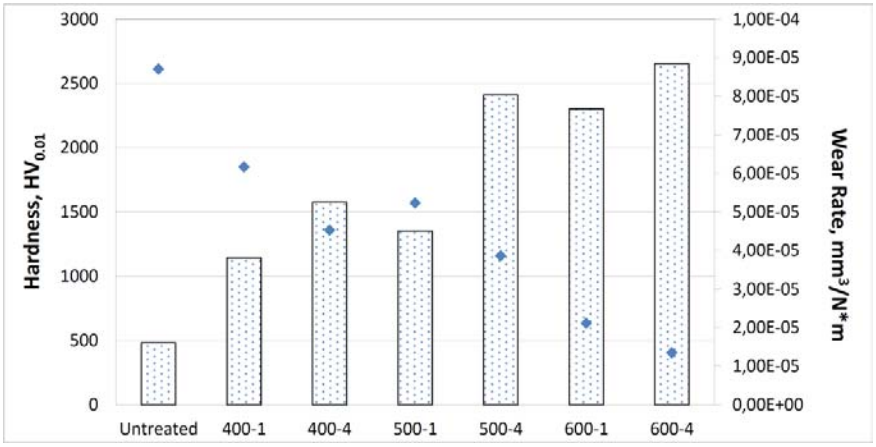


Fig. 2. Microhardness values of untreated and nitrided specimens

The surface roughness values are tabulated in Table 2 and as shown in table; it was found that the roughness values increased with the increase of nitriding time and temperature. The reason of the increase at the surface roughness was the effect on increasing ion bombardment. The specimens were more exposured to the ion bombardment at high temperatures and times.

Table 2. Roughness values at different nitriding conditions

Nitriding Parameters	Surface Roughness, µm
Untreated	0.030-0.035
400-1	0.050-0.550
500-1	0.062-0.065
600-1	0.086-0.900
400-4	0.122-0.126
500-4	0.134-0.139
600-4	0.175-0.178

The friction test results were shown in Fig. 3 and 4. When the figures were examined, it was found that the friction coefficients reduced correspondingly with the increase of hardness after the nitriding processes and the lowest friction coefficient was obtained from 600-4, which has the highest surface hardness. Depending on the increase of surface hardness, the contact area was decreased and this has provided the obtaining the lower friction coefficients in comparison to the untreated specimen. As shown in figures, the friction coefficients have the waviness form. The reason of that was the breakage and detachment of hard nitride layer from the surface during the sliding and this case caused the abrasive effect on the wear behavior. Also, this case was supported with the wear images.

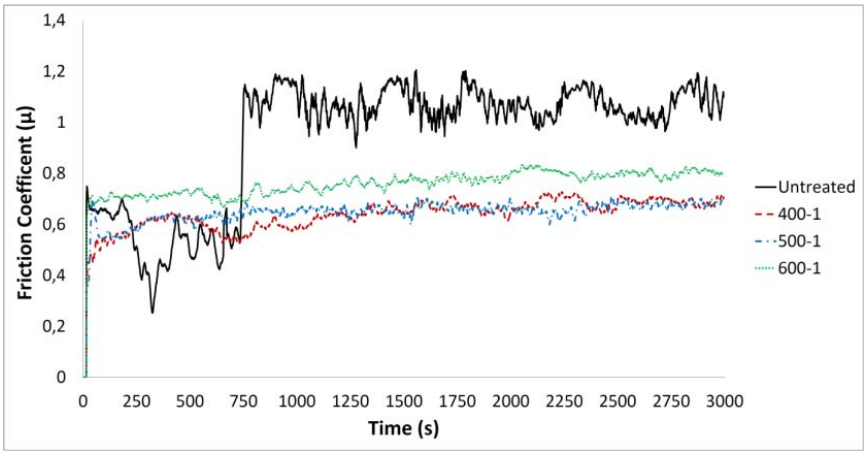


Fig. 3. The change of friction coefficient versus time at 1 h and different temperatures

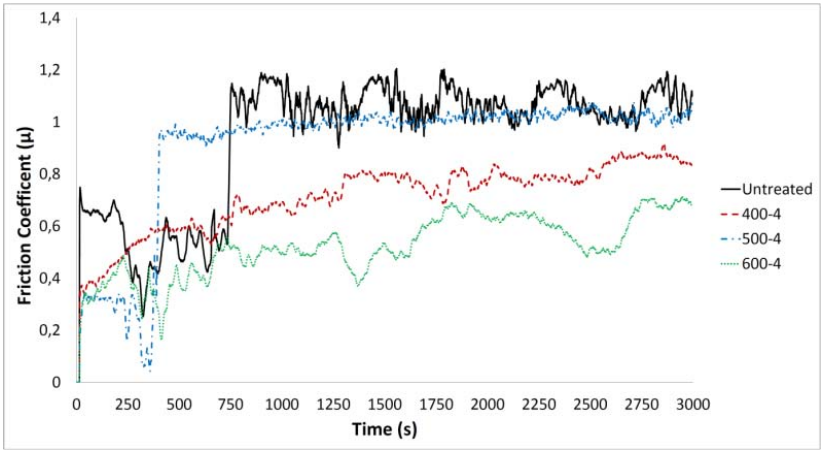


Fig. 4. The change of friction coefficient versus time at 4 h and different temperatures

The SEM images after the wear test were shown in Fig. 5 and 6. When the SEM images were investigated, it was observed that the untreated specimen was subjected to severe wear (Fig. 5-a). However, the increase of nitriding temperature and time caused the decrease of wear tracks. The lowest wear track width was obtained from 600-4, which has the highest hardness. When the SEM images were examined, it was found that the nitriding process significantly increased the wear resistance.

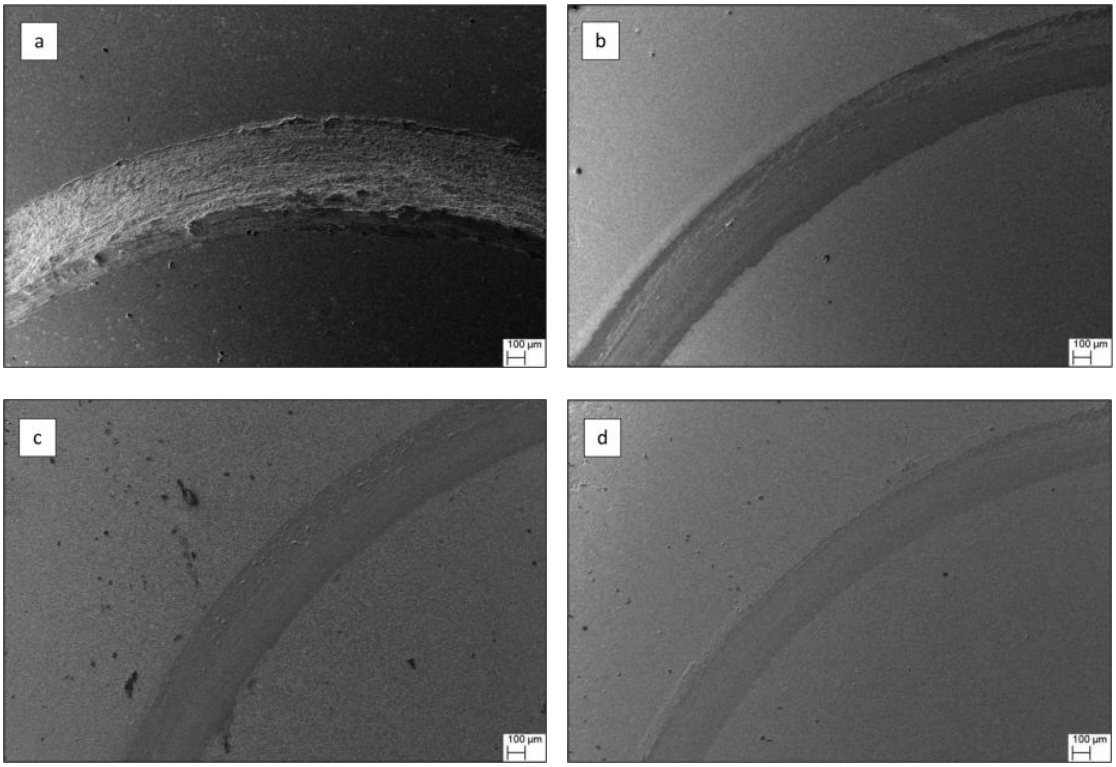


Fig. 5. SEM images obtained from different nitriding conditions; untreated specimen (a), 400-4 (b), 500-4 (c), 600-4 (d)

The cracks, which were occurred after the wear tests, at the nitride layer were clearly seen in Fig. 6. Also, it was found that the cracks occurred 400-4 and 500-4 were less than the 600-4 because of that the hardness and thickness of nitride layer for 600-4 were higher than the others. The detachment or crack wasn't observed at 600-4 and this case reveals that the optimum condition for selected nitriding parameters was 600-4 in terms of tribological investigations.

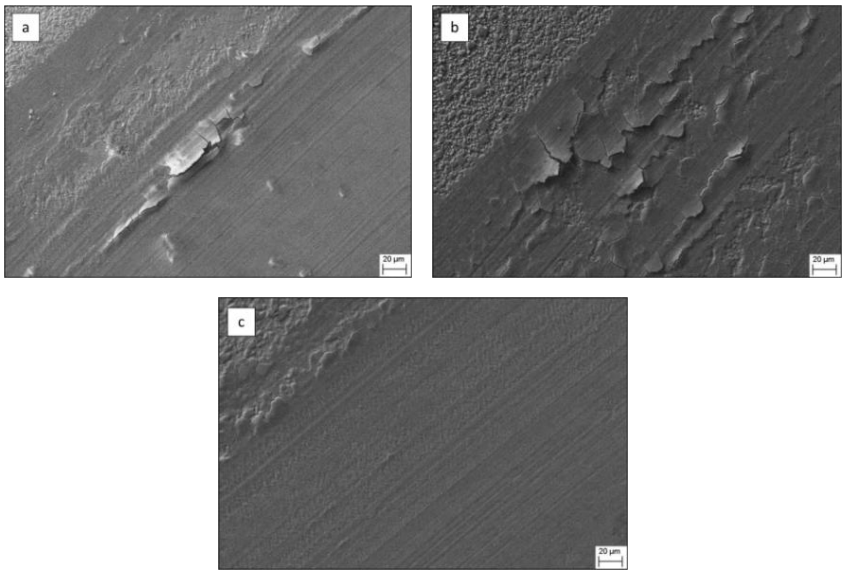


Fig. 6. Detailed SEM images obtained from different nitriding conditions; 400-4 (a), 500-4 (b), 600-4 (c)

Conclusions:

In this study, Inconel 718 was nitrided at various nitriding parameters and the nitride layer composed from CrN was formed on the surface. The nitrided specimens were investigated as structural and tribological. In consequence of these investigations, the obtained results were listed as bellows:

- ✓ It was observed that the increase of hardness was depending on the increment of process time and temperature. The maximum hardness was obtained from the specimen 600-4.
- ✓ The surface roughness increased with the increment of the nitriding time and temperature.
- ✓ The plasma nitriding process considerably reduced friction coefficient. The friction coefficients were improved with the increasse of the nitriding time and temperature.

As a result, it was found that the optimum condition for selected nitriding parameters was 600-4 in terms of tribological investigations.

References:

1. Aw, P., A. Batchelor, and N. Loh, Failure mechanisms of plasma nitrided Inconel 718 film. Wear, 1997. 208(1-2): p. 226-236.
2. Bhatt, A., et al., Wear mechanisms of WC coated and uncoated tools in finish turning of Inconel 718. Tribology International, 2010. 43(5-6): p. 1113-1121.
3. Smith, W.F., Structure and properties of engineering alloys. 1993.
4. Houghton, A., et al., Characterising and reducing seizure wear of inconel and incoloy superalloys in a sliding contact. Wear, 2011. 271(9-10): p. 1671-1680.
5. Aw, P., A. Batchelor, and N. Loh, Structure and tribological properties of plasma nitrided surface films on Inconel 718. Surface and Coatings Technology, 1997. 89(1): p. 70-76.
6. Alsaran, A., et al., A repair process for fatigue damage using plasma nitriding. Surface and Coatings Technology, 2004. 186(3): p. 333-338.
7. MATSUDA, F., et al., Surface Hardening of Ni Alloys by Means of Plasma Ion Nitriding (PIN) Process (Report II) t. 1987.
8. Yildiz, F., et al., Plasma nitriding behavior of Ti6Al4V orthopedic alloy. Surface and Coatings Technology, 2008. 202(11): p. 2471-2476.
9. Edenhofer, B., Physical and Metallurgical Aspects of Ionitriding. Pt. 1. Heat Treatment Metals, 1974(1): p. 23-28.
10. Yildiz, F. and A. Alsaran, Multi-pass scratch test behavior of modified layer formed during plasma nitriding. Tribology International, 2010. 43(8): p. 1472-1478.
11. ASTM, ASTM B637 - 12, Standard Specification for Precipitation-Hardening and Cold Worked Nickel Alloy Bars, Forgings, and Forging Stock for Moderate or High Temperature Service. ASTM, 2012. 02.04.

Effects of ion-beam bombardment on the physical properties of 100Cr6 steel

R. Droppa Jr[1], H. Pinto[2], J. Garcia[3], E. Ochoa[4], M. Morales[4], S. Cucatti[4], and F. Alvarez[4]

[1]Centro de Ciências Naturais e Humanas - Universidade Federal do ABC, Santo André, Brazil
[2]Escola de Engenharia de São Carlos - Universidade de São Paulo, São Carlos, Brazil
[3]Sandvik Machining Solutions, Stockholm, Sweden
[4]Instituto de Física ‘‘Gleb Wataghin" - Universidade Estadual de Campinas, Campinas, Brazil

Abstract

The effect of ion-beam bombardment on the physical properties of 100Cr6 steel is reported. The energy dependence of the in-depth stress and the pattern formation are presented. The modified region by the relative low energy (< 1keV) ions extend orders of magnitude deeper than the stopping region of the projectiles. The formation of peculiar patterns on the treated surface is explained by the current model of surface instability created by preferential sputtering and surface diffusion in metals.

Keywords: Surface modification, ion-beam bombardment, Internal stresses

1. Introduction

The development of new processes to improve the adhesion and wear resistance of hard coatings in cutting tools and moulds is a challenging task. Such processes aim to modify the surface of the substrate at atomic level by forming new phases, controlling internal stress, and/or tailoring the surface topography. The pre-treatment of steel surfaces by using heavy ions bombardment and posterior N^+ ion beam nitriding process could thus be used to get surfaces suitable prepared for hard coatings deposition improving the well-known “duplex” process. This paper focuses the research on the stress and topography generated by heavy ions bombardment of different energies on 100Cr6 steel.[1] The in-depth stress study shows that the bombardment effect extend much deeper than the damaged region. Changes from compressive to tensile stress are also observed.

2. Experiments

The 100Cr6 steel is a high carbon, chromium containing low alloyed steel used in ball bearings or other applications where resistance to fatigue is demanded. The studied samples are 20 mm diameter disks, 2 mm thick, sliced from the same rod (C:1.00; Si 0.25; Mn 0.35; Cr 1.50 %wt) and mirror polished. The studied samples were bombarded perpendicularly to the free sample surface with Xe^+ ions at different kinetic energies (0.2 keV to 1.0 keV). The bombardment of the samples was performed in an IBAD system with x-ray electron spectroscopy (XPS) for *in situ* studies. Details of the apparatus are reported elsewhere.[2] Prior to Xe^+ bombardment, the samples were sputter cleaned by Ar^+ ion bombardment (0.6 keV) during 5 minutes. This ensured identically starting substrates surface. The Xe^+ bombardment treatment was performed at room temperature during 30 minutes. The sample temperature was monitored by a thermocouple fixed in the sample holder and maintained below 300°C. The base pressure of the chamber was $<1.1 \times 10^{-4}$ Pa and the working pressure maintained at $\sim 1.2 \times 10^{-1}$ Pa during ion bombardment. The Xe concentrations underneath the samples surfaces were obtained *in situ* by XPS analysis. The layer probed is around ~5Å depth.[3] Ion implantation simulation using TRIM shows that the average projectile penetration region is

around 11-18 Å, i.e., approximately the same range probed by XPS.[4, 5] The samples were further analyzed by Grazing Incidence X-ray Diffraction (GIXD) at different incident angles in order to obtain information about the average residual stress gradient induced by the bombardment treatment. These measurements were performed at the XRD1 beamline of the Brazilian Synchrotron Light Laboratory (LNLS). The x-ray wavelength used in the experiment was 1.7701 Å. A Ge (111) crystal analyzer was used on the 2θ diffractometer arm to improve the instrument resolution and to make the measurements insensitive to small sample misplacements as well as to possible geometrical aberrations.[6] The residual stress depth profiling was performed by using the $\sin^2\psi$ method in the asymmetric multi-reflection mode (fixed grazing incidence angle).[7] The effective penetration depth for each x-ray incidence angle was calculated according to Noyan[8], assuming a layer of material contributing to 63% to the diffracted intensity. Atomic force microscopy (AFM) was utilized in the analysis of the surface patterning.

3. Results and analysis

3.1 Structure

Figure 1, left, shows the XRD diffractogram of the 100Cr6 steel pristine sample. The characteristic reflections associated to α-Fe (ferrite) and Fe_3C (cementite) are indicated.

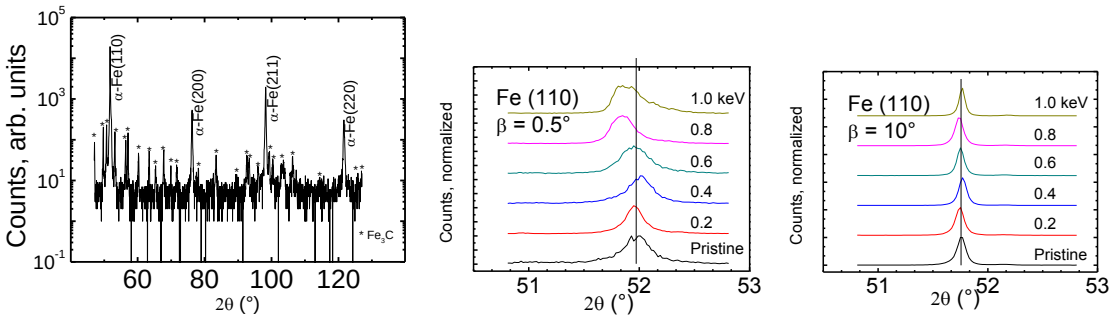


Figure 1. Left: θ–2θ diffractogram of a typical sample. Middle: α-Fe (110) x-ray diffraction peak for different Xe beam energies, taken at incident beam angle β=0.5°. Right: incident beam angle β=10°.

Figure 1 (middle and right) shows examples of the α-Fe (110) diffraction peak profiles of each sample after Xe^+ ion bombardment taken at two incident x-ray beam angles β (0.5° and 10°). The curves show a shift of the diffraction lines after ion energy bombardment relative to the non-bombarded sample. This is compatible with a non-uniform lattice deformation as a function of the projectile energy. The shift to the right, corresponding to a lattice shrinking, is found only at 0.4 keV ion bombardment energy, i.e., just the energy giving the highest Xe concentration retained in the samples as obtained from the XPS analysis (Figure 2, inset). For all other bombardment energies the lattice is stretched, as the diffraction lines shift to lower reflection angles. For an incident angle of β=0.5° the depth probed by the x-rays is ~ 0.2 μm. This corresponds to a layer whose thickness is much larger than the stopping distance of the projectiles (≤18 Å).

We note that for the highest bombardment energies the reflections associated with the most external atomic layers (≤ 0.2 μm) display asymmetric profiles suggesting the formation of a new distorted phase. These asymmetries also appear in the diffractograms for other reflections associated with the α-Fe phase (not shown). On the other hand, for an incident angle of β=10° the depth probed by the x-ray is ~ 3.4 μm. As observed in Figure 1 (right) the reflection lines

are practically not affected by the bombardment, in opposition to the top most layers, where the Xe^+ ion bombardment generates strong strain/stress (Figure 1 left).

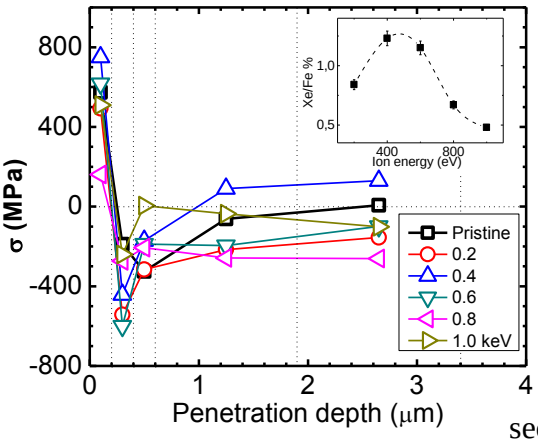


Figure 2. In depth stress distribution in the steel samples. The dotted vertical lines indicate the layers according to the model of constant average stress discrete layers used to deconvolute the stress profile. Here, each point represents the average stress in the respective layer. Inset: Xe/Fe (%) ratio for each bombarded sample as a function of ion energy.

Figure 2 shows the deconvoluted stress profile for the studied bombardment energies. As observed, all samples show a ~ 0.2 μm layer under tensile stress. Beneath this layer there is a second layer of same thickness under compressive stress. In agreement with the results discussed above, the maximum tensile stress is obtained for the sample bombarded with 0.4 keV and having the maximum Xe/Fe ratio retained in the material. Furthermore, for all bombardment energies, there is the formation of a thin compressive stressed layer just below the top most surface layer.

3.2 Morphology

The surface patterns and roughness of the bombarded samples are also affected by the bombardment as illustrated by the AFM micrographs (Figure 4, left). For the sake of clarity only the micrographs of a particular sample is displayed. As observed in Figure 4 (right) the Xe^+ ion bombardment also increases the roughness, generating a characteristic pattern on the material surface. For the highest studied bombardment energy the roughness and the sputtering yield seems to decrease. Nevertheless, more experimental data are necessary to confirm this result. Also, Figure 4 (right) suggests that there is a slope change for higher energies than 0.4 keV, just the energy where the Xe/Fe ratio is maximum (Figure 2, left).

The treated surfaces show characteristic patterns at different bombardment energies. It is particularly interesting the 1.0 keV case where pyramidal patterns are observed (Figure 4, left). This peculiar topology appears in some grains on the treated surface suggesting that they own similar crystallographic orientations relative to the ion beam.

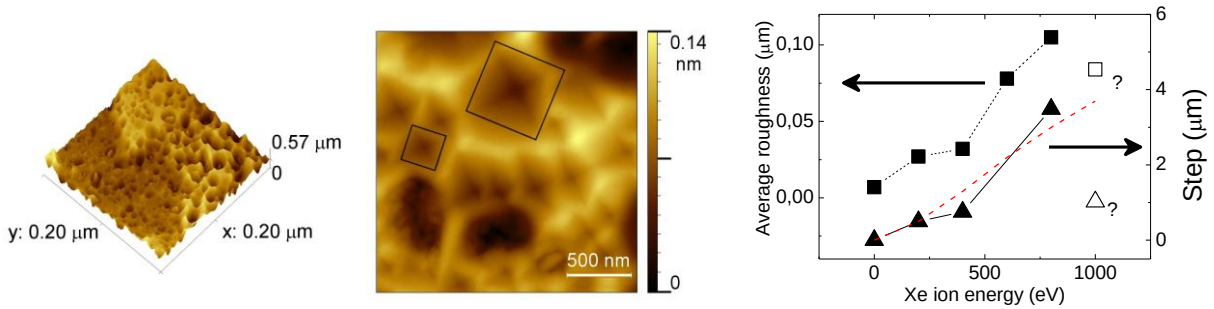


Figure 4. Left: AFM micrographs from the 1 keV bombarded sample. The pyramidal groove patterns are distinguished. Right: Roughness (squares) and step (triangles) formed on the bombarded surfaces as a function of Xe energy. The red dashed curve is the theoretical calculation for step formation according to the Xe sputtering yield for 100Cr6 steel.

This behavior is explained by the roughening instability model due to Ehrlich-Schwoebel diffusion barriers in metal.[9] Roughly speaking, the regular pattern stems from essentially two mechanisms inducing surface instability. The first one is related to the surface curvature dependence of the ion sputtering and the second one is due to the presence of an energy barrier to diffusing adatoms to descend step edges. Also, the 4-fold symmetry of the patterns suggests that these grains are oriented in the <100> direction.

4. Conclusions

X-ray experiments show that the bombarded Fe matrix changes from tensile to compressive stress in a layer close to the bombarded surface (< 400 Å) but much more profound than the stopping range of the projectiles (< 18 Å). In this region, also, a lattice crystalline deformation and the upsurge of new phase(s) is (are) noticeable. At deeper distance from the material surface, the stress diminishes and extends at least up to ~3.4 μm. The only peculiar behavior is observed in the samples bombarded with 0.4 keV switching from compressive to tensile stress again. It is remarked that at this particular energy the sample retains the highest relative Xe atoms concentration. Moreover, at this energy, the projectiles induce the maximum strained/stressed surface structure observed in this study. In conclusion, the generated compressive stress depends on the projectile energy and it extends orders of magnitude deeper than the stopping range of the ions being ~11-18 Å. The process of sputtering and surface diffusion probably explains the formation of patterns as those reported in noble gases metals bombarding studies.[9]

The roughness increasing on energy of Xe^+ ions bombardment augments the sample surface effective area. This effect probably contributes to increase nitrogen retention in nitriding experiments influencing the diffusion process by augmenting the chemical potential at the sample surface. The surface modification to atomic level by ion bombardment to improve hard coatings adhesion could be a route to increase cutting tools performance.

Acknowledgements

Part of this work was supported by FAPESP, project 05/53926-1. FA and EO are CNPq fellows. The authors are indebted to C. Piacenti for technical help. The XRD measurements were performed at the XRD-1 beamline of LNLS. The AFM measurements were performed at the Multiuser Experimental Center of UFABC.

References

[1] Standard ASTM A 295/1994.
[2] P. Hammer, N. M. Victoria, F. Alvarez, J. Vac. Sci. Technol. A 16, 2491 (1998).
[3] D. Briggs and M. P. Seah, *Practical Surface Analysis*, 2nd ed. Willey,New York, **1** (1993).
[4] J.P.B. Biersack, G. L. Haggmark, Nucl. Instrum. Methods 174 (1980) 257.
[5] E.A. Ochoa, C.A. Figueroa, T. Czerwiec, F. Alvarez, Appl. Phys. Lett., **88** (2006) 254109.
[6] P. J. Withers, M. Preuss, P. J. Webster, D. J. Hughes, A. M. Korsunsky, Mat. Sci. Forum 404-407, 1 (2002).
[7] Quaeyhaegens, C., Knuyt, G. & Stals, L. M. Surf. Coat. Technol. 74–75, (1995) 104–109.
[8] I.C. Noyan, J.B. Cohen, Residual Streess-Measurement by Diffraction and Interpretation, Springer-Verlag, Berlin, 1987.
[9] See W. L. Chana and E. Chason, J. of Applied Phys.**101** (121301) 2007 and references there in.

Mechanism of Ti99.2 titanium unconventional ion nitriding

Tadeusz Fraczek[1], Jerzy Michalski[2], Michal Olejnik[1], Jaroslaw Jasinski[1]

[1] Czestochowa University of Technology, Materials Science Institute, Czestochowa, Poland .
[2] Institute of Precision Mechanics, Warsaw, Poland

Various surface engineering methods are used to form the mechanical and exploitation properties of the metallic materials surface layer. Currently, the fastest developing surface engineering methods include: nitriding, vacuum and low-temperature plasma heat treatment and thermochemical treatment and plasma or laser methods [1].
The modification of titanium and titanium alloys surface layer by gas nitriding process considerably inhibits their passivation. Compact TiO_2 oxide layers form, which hamper the diffusion of the atoms into the substrate. Therefore, a costly operation of oxide film removal is used before gas nitriding of these materials to preliminarily activate the surface [2]. The ion nitriding process in compare to gas nitriding allows to form superior quality layers [3].

Moreover ion nitriding enables the oxide films to be removed already at the initial stage of the process, while eliminating the need for preliminary surface activation [4]. Surface activation by cathode sputtering involves the bombardment of the surface with low-energy ions. However energy level of these ions must be higher than the threshold energy value of surface atom sputtering [5]. The present study concerns the effect of an unconventional Grade 2 titanium nitriding method using an active screen in different glow discharge areas. The analysis of the investigation results has enabled to study the development of a model for the ion nitriding process.

Titanium, Grade 2, was ion nitrided in a temperature range of 803 ÷ 863 K for a duration from t = 18 ks to t = 61,2 ks, in an atmosphere of 25 % H_2 + 75 % N_2, at pressure of 150 Pa. Four variants of positioning the nitrided elements in the ion nitriding device chamber were assumed, either:

- directly on the cathode,
- in the plasma potential – area isolated from the anode and the cathode,
- on the cathode using an active screen,
- in the plasma potential using an active screen.

The active screens used had the purpose of intensify the surface phenomena due to the local temperature increase and the increase in the energy of active plasma components.

The XRD analysis was performed on a DRON-2 X-ray diffractometer using filtered cobalt anode tube radiation.The element distribution analysis was made on a GDS GD PROFILER HR glow-discharge optical emission spectrometer. The observation of the obtained structures was performed on specimens, either etched or not etched, using a Carl-Zeiss Jena Axiovert 25 metallographic microscope.
The analysis of the investigation results has shown that the previously established and adopted conventional ion nitriding process models might not be appropriate for active screen nitriding. The earliest model developed by Kölbel [7] assumes that the transfer of nitrogen requires iron atoms to be sprayed from the cathode surface and then passed to the plasma. In that case, the iron atoms react with the nitrogen to form FeN nitrides that are sprayed onto the substrate surface. The FeN nitrides are metastable and transform to $Fe_{2÷3}N$ and Fe_4N nitrides on the steel substrate surface. At the same time nitrogen atoms diffuse into the substrate material.

Study has found that the active screen changes to a considerable extent the course of phenomena under glow discharge conditions [9]. The Kölbel model does not fully allow for the characteristics of the physical phenomena occurring in this process. It only considers the sputtering and redeposition phenomena. Therefore, a different model of nitriding under an active screen has been proposed, especially for the initial process stage, which takes into

account the following phenomena: cathode sputtering, physical desorption (releasing atoms, ions or molecules), diffusion and spraying. In addition, study [10] has assumed that the cathode sputtering and then re-spraying play the most important role in nitriding using the active screen. The remaining phenomena need also to be taken into account.

The analysis of literature data shows that the conventional glow discharge nitriding process is adequately characterized in many studies. However, this is only true for individual phenomena and their effect on the process kinetics, but there is no comprehensive analysis of the process.

The results of our investigation into active screen glow discharge nitriding of titanium and its alloys enable us to claim that:

- the use of the active screen intensifies the nitriding process and increases its temperature;
- the active screen changes primarily the voltage characteristics, both quantitative and qualitative ones (Figure 1). Additional voltage pulses form under the active screen. The values of those voltages are greater by several times than the voltage values occurring during cathode nitriding. The time of these voltage pulses causes the ions and other active plasma components to gain a high velocity. This velocity corresponds to a high kinetic energy of the order of several hundred electron volts. The active plasma components are implanted into the substrate material. They form a disequilibrium nitrogen-supersaturated zone in the surface layer. The high nitrogen concentration facilitates the nitrogen diffusion into the substrate;

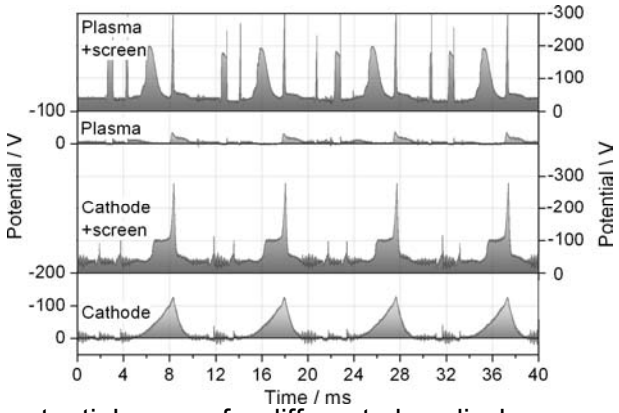


Figure 1. Oscilloscopic potential curves for different glow discharge regions

- increasing the temperature of titanium and titanium-alloy substrates in the active screen cathode nitriding process causes the nitrided layer to form both on the surface in the plasma environment and on the surface adjacent to the cathode. This indicates the presence of molecular nitrogen, despite the low-temperature nature of this nitriding process;
- the ion bombardment and cathode sputtering phenomena have a great effect on the nitriding process kinetics, the phase composition and the morphology of the microstructure phase constituents of the layers forming; hence, in the nitriding process as effected either on the cathode and using the active screen, nitride zones form in the surface layer, which have a high nitrogen concentration compared to the plasma potential nitriding process resulting in the formation of a layer composed solely of a diffusion layer;
- the process of nitriding in the nitrogen and hydrogen mixture atmosphere proceeds involving NH radicals capable of bonding hydrogen to form active NH_2 radicals. Reducing the nitrogen concentration in the mixture reduces the quantity of NH radicals. Therefore, with a low nitrogen content, no cathode nitriding effect is found, but the cathode sputtering intensity increases.

The presented investigation results provide a basis for developing a new model for glow discharge nitriding of Grade 2 titanium, depending on the position in the direct current glow discharge region, while allowing for the active screen effect (Figure 2). It has been found that the TiN nitride, formed at the initial stage of the Grade 2 titanium nitriding process under glow discharge conditions, undergoes transformation to the Ti_2N nitride and a free nitrogen atom diffusing into the substrate material. At the further stage of the process, the nitride decomposes following the reaction:

$$2TiN \rightarrow Ti_2N + N\downarrow \quad (1)$$
$$Ti_2N \rightarrow 2Ti + N\downarrow \quad (2)$$

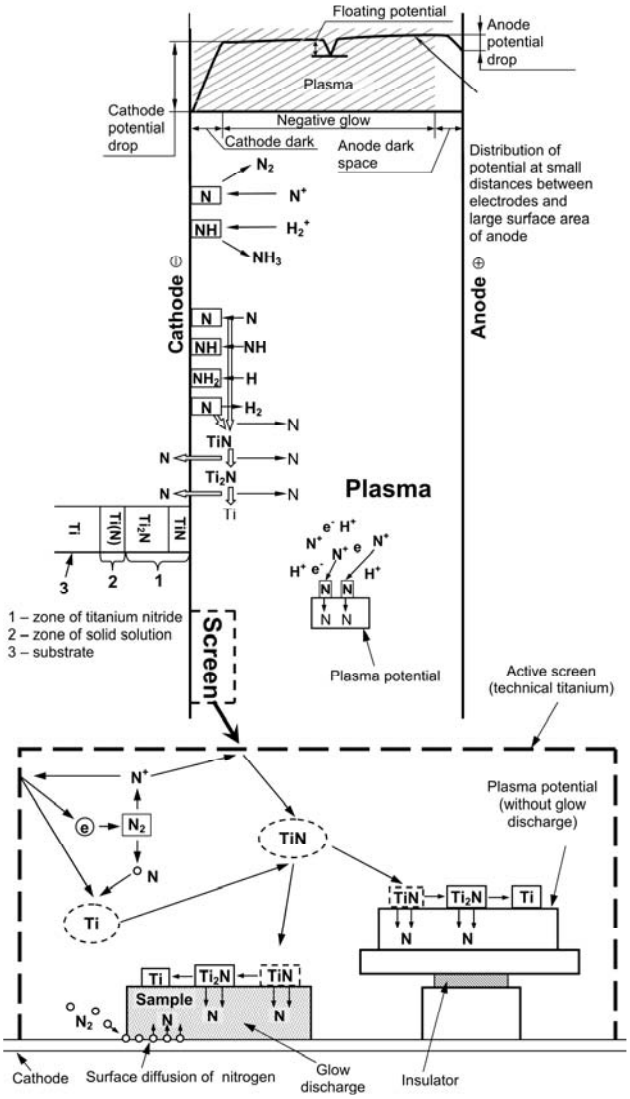


Figure 2. The model of Grade 2 technical titanium ion nitriding in different glow discharge regions

The nitrided layer on the substrate of titanium and its alloys, in the following glow discharge plasma regions: I – the cathode, II – the plasma potential + the active screen, III – the cathode + the active screen, has a zonal structure (Figure 4a). The following zones are distinguished: the TiN nitride zone; the Ti_2N nitride zone; and the deepest positioned zone of grains of the solid solution of nitrogen in α titanium, Tiα(N).

In contrast, in the case of the substrate isolated from the cathode and the anode – nitriding in the plasma potential – no presence of nitrides was found. In that case, grains of the solid solution of nitrogen in titanium, Tiα(N), occur in the microstructure. The reason for this is the low energy of ions for the given process conditions. Moreover, these ions are

characterized by a negative polarization relative to the plasma – approx. 20 V (Figure 1 – plasma). Hence the small effect of the sputtering phenomenon [3]. The low ion energy is also insufficient for driving metal atoms out from the base, which would then react with nitrogen atoms to form nitrides. For these conditions, only the nitrogen ion desorption phenomenon occurs, whereby the nitrogen ions diffuse to the iron crystal lattice to form grains of the solid solution of nitrogen in titanium, Tiα(N).

Noteworthy is the fact that the process of nitriding on the cathode with the use of the active screen, even for such a low temperature as the one used in the experiment, results in the formation of a nitrided layer on the surface screened from the glow discharge on the surface adjacent to the cathode - the bottom of the element being nitrided (Figure 4b). Literature data suggests that it is possible to produce a nitrided layer on such a surface at a temperature much higher than the temperature used in the experiment under consideration. In that case, titanium nitrides form as a result of reaction between the base titanium and the molecular nitrogen [11].

REFERENCES

[1] Burakowski T., Wierzchoń T.: Inżynieria Powierzchni, WNT, Warszawa, 1995.
[2] Christiansen Th., Somers M.A.J.: Characterisation of low temperature surface hardened stainless steel. Struers Journal of Metallography, 2006, No 9, s. 1-17.
[3] Michalski, D.C. glow discharge in a gas under lowered pressure in ion nitriding of Armco iron Journal of Materials Science Letters, 19, (2000), s. 1411-1414.
[4] T. Frączek, J. Michalski, Rola potencjału plazmy w warunkach wyładowania jarzeniowego prądu stałego w procesie azotowania stali EJ96, Inżynieria Materiałowa, (2002), (Nr 5), s. 299-301.
[5] Tsujikawa M., Yamauchi N., Ueda U., Sone T., Hirose Y.: Behavior of carbon in low temperature plasma nitriding layer of austenitic stainless steel. Surface & Coatings Technology 193 (2005). s. 309– 313.
[6] Frączek T.: Niekonwencjonalne niskotemperaturowe azotowanie jarzeniowe materiałów metalicznych. Wydawnictwo WIPMiFS, Seria: Monografie Nr 13, Częstochowa 2011.
[7] Kölbel J.: Die Nitridschichtbildung bei der Glimmentladung. Forschungsbericht des Landes NW (Nordhein-Westfalen), Nr. 155, Westdeutscher Verlag, Köln, Opladen, 1965.
[8] Keller K.: Schichtaufbau glimmnitrerter Eisenwerkstoffe, Härterei–Technische-Mitteilung (HTM) 26, 1971, Heft 2, S. 120 – 130.
[9] Zhao C., Li C.X., Dong H., Bell T.: Study on the active screen plasma nitriding and its nitriding mechanism. Surface & Coatings Technology 201, 2006, 2320-2325.
[10] Gallo S.C., Dong H.: On the fundamental mechanism of active screen plasma nitriding. Vacuum 84, 2010, 321-325.
[11] Roliński E.: Azotowanie jonowe tytanu i jego stopów, Prace Naukowe Politechniki Warszawskiej, Mechanika, z. 118, 1988.

EVALUATION OF THE MECHANICAL BEHAVIOUR OF A DLC FILM ON PLASMA NITRIDED AISI 420 WITH DIFFERENT SURFACE FINISHING

Sonia Brühl[1], Raúl Charadia[1], Eugenia Dalibón[1], Vladimir Trava Airoldi[2], Amado Cabo[3]

[1]Universidad Tecnológica Nacional, Concepción del Uruguay, Argentina.
[2]Instituto Nacional de Pesquisas Espaciáis, São José dos Campos - SP, Brazil.
[3]IONAR S.A., San Martín, Buenos Aires, Argentina

sonia@frcu.utn.edu.ar

Introduction

Diamond-like-carbon films (DLC) are hard coatings with a very low friction coefficient, a high wear resistance and chemically inert. However, these coatings have adhesion problems on metallic substrates, because the high residual stresses in the DLC films cause failure of the interface between the film and the substrate. Different methods have been tested to improve the adhesion: deposition of interlayers, multilayer coatings between the substrate and the DLC film have been used as interface, chemical and physical modifications of the carbon coating or diffusion treatments of substrate surface [1-3].
Plasma nitriding is a well-established method to harden stainless steels and can act as a pre-treatment to increase adhesion and improve tribological behaviour of the DLC coating. Hopwever, the characteristics and phases of the nitrided layer can influence on the adhesion and the mechanical behaviour of the system [4-6].
In this work, the mechanical behaviour of a DLC film deposited over non-nitrided and nitrided martensitic stainless steel with two different surface finishing is studied.

Experimental

The AISI 420 steel was heat treated, but two different surface finishing were accomplished previous to the nitriding process: paper grinding until grit 1000 (named GN) and polishing with 0.5 µm diamond powder (named PN). Another group of samples was coated without nitriding (named C). The nitriding process was carried out in a DC pulsed discharge for 10 hours at temperature of 390 ºC using a gas mixture composed of 20 % N_2 and 80 % H_2. The DLC film was deposited by the PACVD process, with an asymmetrical bipolar DC pulsed discharge described in a previous work [7], using methane and hydrogen as precursor gases. Hardness on the surface was measured with a Vickers microindenter, 50 g load. Both the nitrided layer and film were observed with optical microscope and SEM. The film composition was analysed by Raman Spectroscopy. Adhesion was tested with the methods of Rockwell C Indentation and Scratch Test with loads of 1500 N and 35 N respectively.
The mechanical behaviour was analysed in both linear and rotational reciprocating sliding wear tests. The linear reciprocating sliding tests were performed in a self-made machine using a WC ball 5mm in diameter as counterpart with 12 N load. The amplitude was set in 0.5 mm and the frequency in 11.7 Hz. The rotational sliding wear tests were carried out in a pin on disk tribometer, with the same WC ball as counterpart and 5 N load. The track radius was set in 5 mm, the tangential velocity in 10 cm/s and the total wear length was 500 m.

Results and discussion

The hardness of the DLC film reached 1400 $HV_{0,05}$. This value corresponds to a composite hardness because the indentation depth exceeds 10% of the film thickness. The films had about

20% hydrogen content, typical of these CVD processes. In the Raman Spectrum for the DLC films (not shown) the two bands known as D and G bands well positioned could be observed, indicating a good quality film as already reported by some of the authors [7]. The film thickness varied between 2.6 and 3 microns (Figure 1) with a regular interface with the previous nitrided layer. The nitrided case did not seem to affect the film growth, since it had the same width on the three types of samples.
Regarding the nitriding process, in the polished samples with a roughness of 0.026 µm, the layer thickness was about 11 µm (Figure 2) and only 8 µm in the grounded ones which had a roughness of 0.033 µm. It seems that the polished sample allowed better nitrogen diffusion even though the surface hardness was almost the same for both samples, 1150 $HV_{0,05}$.

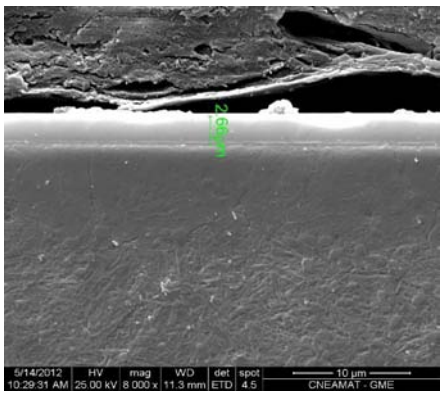


Figure 1. SEM micrograph of the coating on the GN sample

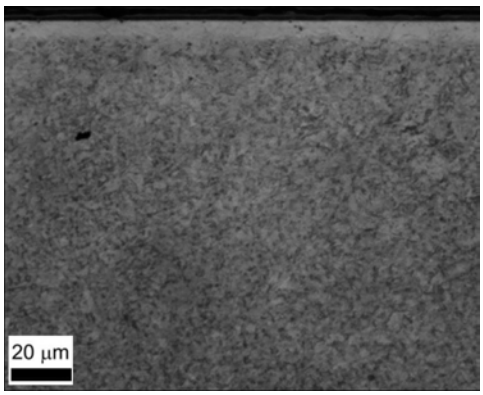
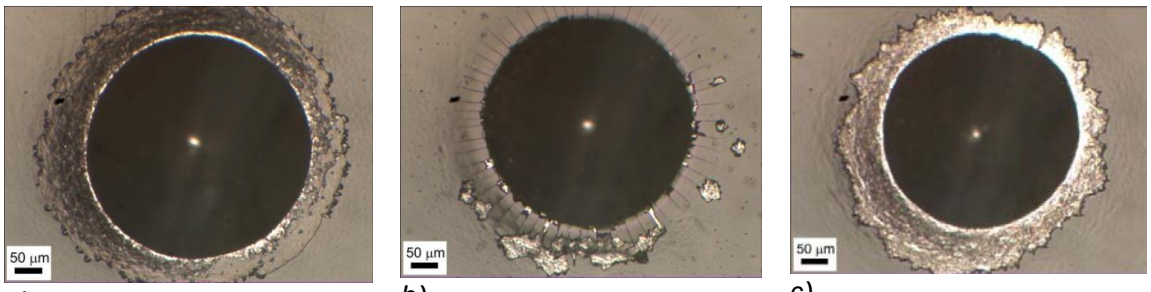


Figure 2. Optical micrograph of the nitrided layer in the PN nitrided sample

The adhesion quality of the DLC film on the PN sample resulted better than on the C sample and the GN sample (Figure 3). In the PN sample, the adhesion was acceptable according to the VDI standard, eventhough radial cracks can be observed in the coating around the indentation and the film was detached in small regions. This was expected because the nitrided layer acts as a hardness gradient between the soft substrate and the hard film. The reason for the bad adhesion on the grinded and nitrided sample -almost as bad as the non nitrided and coated sample- could be related to the minimization of interfacial energy on sharp convex surfaces, or the presence of surface oxides and contaminants which were removed after polishing, according to other researchers [8].

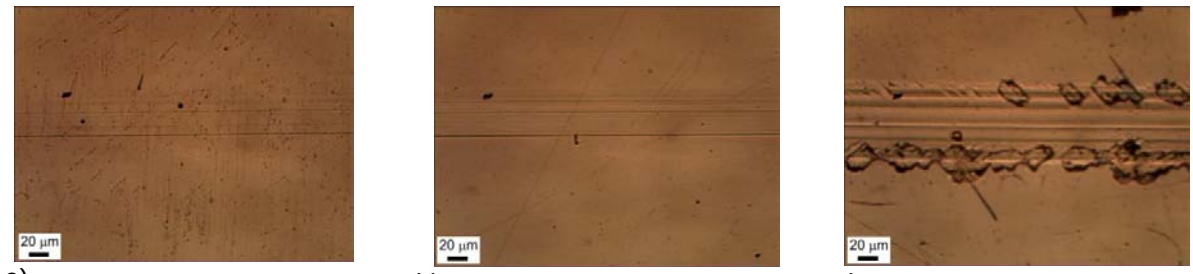


a) *b)* *c)*

Figure 3. Optical micrographs 100x of the Rockwell C indentation on the samples: (a) C, b) PN, c) GN.

In the scratch test, with a minor load, the film on both GN and PN samples showed better adhesion than on the only coated sample (Figure 4). In the C sample, the failure mode could be described as recovery spallation. This mode is associated with the elastic recovery that occurs

when the indenter is moved over the coating surface, and it depends on the plastic deformation in the substrate and the cracking that appears in the coating [9].



a) b) c)

Figure 4. Optical micrographs 200x of the scratch test tracks: a) PN, b) GN and c) C samples.

In the linear reciprocating sliding wear test, the wear loss was smaller in the coaetd samples (PN, GN and C) compared with a nitrided sample without coating, as it can be seen in the wear track profiles in Figure 5. But the two duplex samples PN and GN had a slightly better wear behaviour than the C sample. As it is well known this is because the nitrided layer improves the load capacity of the coating and thus its wear resistance. Anyway, there is no difference between the nitrided samples grounded until grit 1000 (GN) and the others polished with 0.5 µm diamond powder (PN). This can be explained by the fact that in the region next to the surface, the hardness profile of the two nitrided layers is similar, as it is shown in Figure 6.

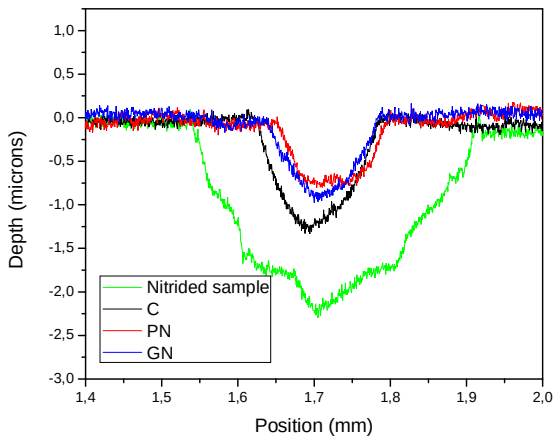


Figure 5. Depth profile of the linear sliding wear tracks.

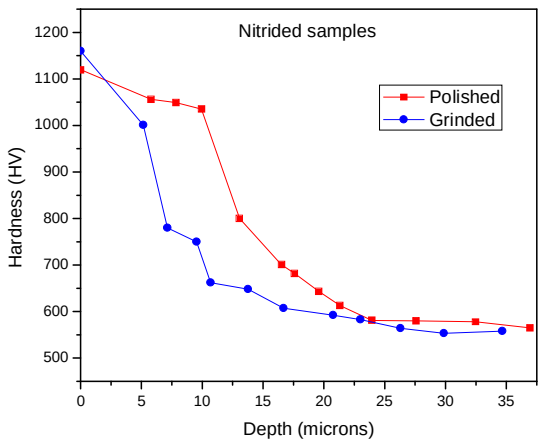


Figure 6. Hardness depth profile of the two nitrided samples.

In the pin on disk tests, with 5 N load, the wear track was almost invisible over the three coated samples, and thus the wear loss was impossible to calculate. The friction coefficient was registered during the test and it is shown in Figure 7. It can be observed that a steady value was reached after a few minutes and all the values are under 0.15. In the same experiment over the nitrided sample without coating μ_D was about 0.8. It can also be observed, the coated sample C has the lowest coefficient with a mean value of 0.08. This can be attributed to the roughness previous to the DLC deposition, which was smaller in the non nitrided sample, because the DC nitriding process always produces a rougher surface due to ion bombardment. After the CVD process it was measured that the film copied the surface roughness.

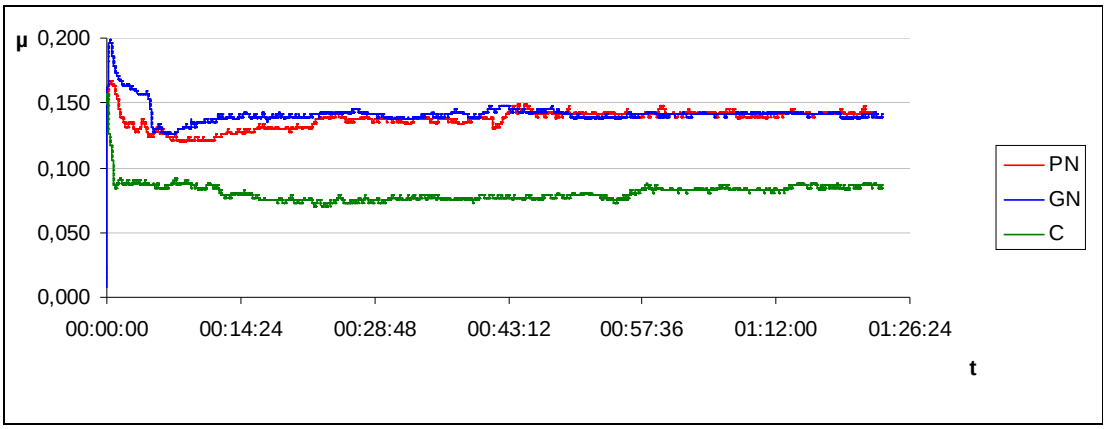


Figure 7. Friction coefficients registered in the pin-on-disk tests for the three coated samples

Conclusions

The results of the tribological tests showed that the coating improves wear resistance compared to the nitriding process alone. The friction coefficient against WC was lowered from 0.08 to 0.15. A comparison between the three coated samples showed that the nitriding pre-treatment of the steel substrates improved even more the wear resistance in the evaluated conditions. The nitrided layer proved to be a good interface that increased the substrate hardness and provided a suitable interlayer. But the adhesion quality was better in the PN sample than that in the grinded sample. The nitrided layer was also wider on the polished samples which proved to allow better nitrogen diffusion.

References

1. D. A. Lima-Oliveira, R. P. Castro Costa, G. Valdete Martins, E. J.Corat, V. J. Trava-Airoldi, A. Oliveira Lobo, F. R. Marciano. Open Journal of Metal, 2, 1-7, 2012.
2. M. Azzi, P. Amirault, M. Paquette, J. E. Klemberg-Sapieha, L. Martinu. Surface and Coatings Technology 204, 3986–3994, 2010.
3. J. Choi, K Soejima, T. Kato, M. Kawaguchi, W. Lee. Nuclear Instruments and Methods in Physics Research B 272, 357–360, 2012
4. M. M. Morshed, B.P. Mc. Namara, D. C. Cameron, M.S.J. Hashmi. Surface and Coatings Technology 163 –164, 541–545, 2003.
5. D. Chicot, E. S. Puchi-Cabrera, X. Decoopma, F. Roudet, J. Lesage, M. H. Staia. Diamond & Related Materials 20, 1344–1352, 2011.
6. N. G. Shang, Z.F. Zhou, C.S. Lee, I. Bello, S. T. Lee. Diamond and Related Materials 10, 1506-1510, 2001.
7. V. J. Trava-Airoldi, L. F. Bonetti, G. Capote, L. V. Santos, E. J. Corat. Surface and Coatings Technology 202, 549–554, 2007.
8. Y. Fu, B. Yan, N. L. Loh. Surface and Coatings Technology 130, 173-185, 2000.
9. S. J. Bull, Tribology International 30, 491-498, 1997.

Nanocomposite nitride thin films for hard coatings: Application to wear and corrosion resistance

Abdelouahad Chala, Chahinez Saied and Hanane Ghelloudj

Laboratoire de Chimie Appliquée, Université de Biskra, BP 145 RP, Biskra, Algeria

Abstract
New simple and duplex coatings were elaborated by triode sputtering and ionic nitriding, imposed to low alloy steel and characterized by the mean of various experimental techniques (EDS, XPS, XRD, SEM, TEM, FTIR, …). Their ability to protect substrate against corrosion and wear has been evaluated.
These deposits are either CrN or ZrN monolayer, or nanocomposite deposits formed by the dispersion of BN into ZrN matrix.
The experiments show the good physical, chemical and mechanical properties of the films. The tribological analysis permitted us to define the optimal conditions of triode sputtering and the ionic nitriding ones used in the duplex treatments. A great amelioration in the tribological properties was observed and was explained by the good stress repartition into the layers.
Simples and duplex treatments were imposed to low alloy steel cutting tools. Their application in peeling of wood and corrosion shows their efficiency.

Keywords: triode sputtering, nitriding, duplex, nanocomposite, microstructure, tribology, peeling, corrosion.

1. Introduction

The nitride coatings deposited by Physical Vapour Deposition (PVD) techniques have some excellent properties, such as high hardness, good wear resistance, chemical stability, corrosion resistance and attractive colours, and therefore, are widely used in industry [1-5]. These coatings are mainly based on the nitrides and carbides of the transition metal elements. Recently, increasing interest is laid on the corresponding borides [5]. However, even if the coatings allowed increasing the service life of tools, their adhesion is not sufficient [6]. This could be a limit to their employment. Nevertheless, the solution to increase the adhesion of the films was to realise a previous nitriding treatment before the deposition [6]. That means to make a duplex treatment.
Nitriding is a thermochemical process that is typically used to diffuse nitrogen into ferrous materials. This treatment can improve the surface hardness, fatigue strength, wear and corrosion resistance [6-9]. Plasma nitriding owing to a number of advantages such as a lower process temperature, a shorter treatment time, minimal distortions and low energy use compared to conventional techniques has found increasing applications in industry [6, 7].
However the formation of porous compound layers affect the wear and corrosion resistance. Relatively little works have been done concerning the combination of nitriding and PVD coatings to remove these disadvantages.
The aim of the present study is to investigate the corrosion resistance of 32CDV13 low alloyed steel duplex treated by using ion nitriding and PVD triode process. The effect of the different parameters of nitriding and coating is evaluated.

2. Experimental

A series of experiments have been carried out to investigate the plasma nitriding and triode PVD sputtering responses of 32CDV13 low alloyed steel. The chemical composition of 32CDV13 is: 0.3% C; 0.31% Si; 0.5% Mn; 3.25% Cr; 0.44% Mo; 0.11% Ni; 0.1% V. This steel commonly used for nitriding, presents a good toughness and provides the ability of hardness gradient from the treated surface layer down to the bulk.

The substrate surface was prepared and polished with 1 μm diamond paste. Specimens were nitrided in a vacuum furnace pumped down to low pressure (10^{-3} mbar) to minimise the oxygen contamination. The temperature of samples is followed thanks to a thermocouple very closed to them. The nitriding parameters were fixed referred to previous works [6, 10]. The morphology of samples surfaces, nitrided layers and thin films were observed by Jeol 5900 Scanning Electron Microscope (SEM). X-ray diffraction analyses with Co K_α radiations were performed to determine their structure.

The ZrBN films were deposited by reactive triode sputtering. The deposition parameters are defined in a previous works [10, 11].

The corrosion tests were carried out in a neutral aqueous NaCl (30 g L^{-1}) solution, naturally aerated. The test device was composed of an EGG 273 potentiostat and a 1 L cell containing electrolyte, into which three electrodes were plunged: the calomel reference electrode saturated in KCl (SCE), the graphite counter electrode and the specimen as the working electrode. Stirring was carried out at 250 rev.min^{-1} using rotating electrode. In order to determine the corrosion behaviour of a specimen immersed in electrolyte, the curves *i(E)* are plotted from -100 mV versus the corrosion potential up to 400 mV in the anodic side, using a sweep rate of 10 mV min^{-1}.

Prior to electrochemical tests, the specimens were ultrasonically cleaned in acetone. The potentiodynamic polarization tests were performed on all specimens: plasma nitrided, ZrBN coated and duplex treated ones. An untreated sample was also used as reference.

3. Results and discussion

Figure 1 presents cross sections of 32CDV13 steel plasma nitrided at 500°C in 80%N_2+20%H_2 gas mixture during 8 hours. The top of the sample corresponds to the nitrided layer, indicating a thickness of about 5 μm (Fig. 1.b). It appears to be bright under optical microscope (Fig. 1.a). EDS microanalysis showed that the nitrided layer contains a high amount of nitrogen in the surface and the nitrogen concentration is gradually reducing with increasing distance from surface until the substrate value at a depth of about 100-150 μm. The compound layer formed on the surface does not contain micropores which is good for corrosion resistance.

The morphology of selected coatings deposited on low alloyed steel is shown in the SEM photograph (Fig. 2). It appears that Zr-B-N coatings exhibit a very dense structure, without columns or grains. Mitterer and al. [12] obtained similar results using non reactive and reactive d.c. magnetron sputter deposition.

The XRD analysis shows that the compound layer of the plasma nitrided specimens consists in ε-$Fe_{2-3}N$ and γ'-Fe_4N phases (Fig. 3.a). The ZrBN films were also examined by glancing angle X-Ray diffractometry and the results for a 2θ range between 20° and 100° are shown in Fig. 3.b. Owing to the fact that boron nitride may be not crystallised and is almost transparent to X rays at thicknesses down to 1 μm, the spectrum is expected to reflect only ZrN reflection peaks as reported by Gibson et al. [13] for the Ti-B-N system.

Indeed, a major peak at an angle 2θ ≈ 34° characteristic of ZrN (111) reflections appears, which can be attributed to $ZrN_{1-x}B_x$ compounds. In addition, minor signals from ZrN, corresponding to (220) and (311) orientations, are also detected.

Figure 4 shows the surface morphology of the specimens after corrosion tests in NaCl 30 g.L^{-1} solution. The pictures (Fig. 4) clearly delineate the increase of corrosion resistance from ZrBN coated sample (Fig. 4.a) to the plasma nitrided sample (Fig. 4.b) and to the duplex treated one (Fig. 4.c).

ZrBN coated steel samples reveal defects, which appear as craters or droplets. M. Ürgen et al. [14] have also observed that the Zr-B-N layers on steel substrate exhibited various types of defect which decreased the protective properties of the coating. A recent study conducted on arc PVD TiN and CrN coatings showed that the droplets were identified as important defect sites [5].

Potentiodynamic curves for nitrided steel surfaces and duplex treated ones, recorded after immersion in the corrosive solution, are shown in Fig. 5. The plasma nitriding considerably changed the polarisation properties of 32CDV13 steel as can be seen in Fig. 5.a. Firstly, the corrosion potential E_{corr} was shifted to higher values, e.g. from -610 mV/SCE for the untreated sample to -350 for 80%N_2+20%H_2 plasma nitrided sample. Moreover, the latter part denotes from a passive interesting behaviour, on more than 200 mV. Secondly the current densities were reduced e.g. I_{corr} was decreased from 8 $\mu A/cm^2$ for the untreated sample to 0.7 $\mu A/cm^2$ for 80/20 nitrided one. These results are in good accordance with those of A. Alsaran et al. [9] who had studied the corrosion behaviour of plasma nitrided AISI 5140 steel and found that the dense compound layer formed after plasma nitriding can significantly improve the corrosion characteristics. In the same way, enhanced protection properties were also reported by Steyer et al. for gas nitrided steels [15]. Nevertheless, some authors [2] found that when plasma nitriding is carried out at high temperature, e.g. 500 °C, chromium nitrides may form in the nitrided layer so that the bulk of the nitrided case had very poor corrosion resistance. In our case, this phenomena was not observed, probably owing to the steel composition.

ZrBN coated samples indicates the same potentials value as substrate one (Fig. 5.b), which confirm the fact that it does not cover totally steel part (Fig. 4.a). Nevertheless, despite of an unfavourable anodic/cathodic (steel/coating) areas ratio, ZrBN coating affords a beneficial effect on corrosion protection, by decreasing, of more than one decade, the corrosion rate of steel. This result is in accordance with [14, 16-17].

The duplex treated samples showed far better electrochemical corrosion behaviour when compared with the plasma nitrided or the ZrBN coated ones by decreasing the active corrosion rate and the current density. The specimens duplex treated shows higher corrosion potential (-338 mV) than the plasma nitrided specimen. A lower anodic currents (~ 0.13 $\mu A/cm^2$) are also observed. The nobler electrochemical behaviour of duplex treated specimens can be explained by a conjunction of the good properties of ZrBN films and the protection of the nitride layer which eliminates the drawbacks due to the droplets and the discontinuities of the ZrBN coating.

Conclusion

The corrosion behaviour of plasma nitrided, ZrBN coated and duplex treated 32CDV13 low alloyed steel was studied using potentiodynamic techniques in NaCl solution. The results obtained can be summarized as follows:

- After plasma nitriding, the compound layer corresponds mainly to $Fe_{2-3}N$ and Fe_4N iron nitrides, which present good corrosion properties. This layer is dense and contains little defects.
- ZrBN layers on steel exhibit various types of defect (droplets, physical discontinuities) which decrease the protective properties of the coating. Moreover, due to a galvanic effect, the small anodic area (steel exposed through open porosities) against the large cathodic one (ZrBN film) may provoke severe localized corrosion.
- The corrosion protection properties depend on the porosity of the protective layer. The conjunction of nitriding and deposition processes enables to overcome the drawbacks of the two techniques and mainly the porosity of the deposited films. Therefore, the duplex treated specimens (nitriding + ZrBN coating) present the better corrosion protection, with, in addition, passive ability.

Acknowledgements

The authors would like to thank Professor Ji Vincent from ENSAM of Paris for its very valuable experimental collaboration.

References

[1] W.J. Chou, G.P. Yu, J.H. Huang, Corrosion Science 43 (2001) 2023-2035
[2] C.X. Li, T. Bell, Corrosion Science 46 (2004) 1527-1547
[3] V.A. Alves, C.M.A. Brett, A. Cavaleiro, Surf. Coat. Techno. 161 (2002) 257-266
[4] M.A.M Ibrahim, S.F. Korablov, M. Yoshimura, Corrosion Science 44 (2002) 815-828
[5] C. Mendibide, P. Steyer, J-P. Millet, Surf. Coat. Techno., (2005) Article in Press.
[6] L. Chekour, C. Nouveau, A. Chala, M.A. Djouadi, Wear 255 (2003) 1438-1443
[7] P. Steyer, J-P. Millet, S. Anderbouhr, P. Jacquot, Surf. Eng. 17 (2001) 327-331
[8] K.H. Lee, K.S. Nam, P.W. Shin, D.Y. Lee, Y.S. Song, Materials Letters 57 (2003) 2060-2065
[9] A. Alsaran, H. Altun, M. Karakan, A, Celik, Surf. Coat. Techno. 176 (2004) 344-348
[10] A. Chala, L. Chekour, C. Nouveau, C. Saied, M.S. Aïda, M.A. Djouadi, Surf. Coat. Techno., (2005) Article in Press.
[11] A. Chala, PhD thesis, n° 07-2005, Université de Biskra, Algérie (2005)
[12] C. Mitterer, R. Ebner, Surf. Coat. Techno. 60 (1993) 571-576
[13] P.N. Gibson, W. Gissler, J. Haupt, T. Freisen, R. Falcon, Vide les couches minces 48 (1992) 297.
[14] M. Ürgen, A.F. Cakir, O.L. Eryilmaz, C. Mitterer, Surf. Coat. Tachno. 71 (1995) 60-66
[15] P. Steyer, J-P. Millet, J-P. Peyre, P. Jacquot, D. Hertz, Surf. Eng. 19-3 (2003) 173-178
[16] W.J. Chou, G.P. Yu, J.H. Huang, Surf. Coat. Techno. 167 (2003) 59-67
[17] G. Yang, L. Ying, L. Haichao, Corrosion Science 43 (2001) 397-411

Figure captions

Fig. 1: Cross sections of the 500 °C plasma nitrided low alloyed steel (80%N_2+20%H_2 gas mixture; 8h) (a) optical micrograph; (b) SEM image.
Fig. 2: Microstructure of ZrBN Coating (f(N_2)=12 sccm; substrate bias voltage = -100 V).
Fig. 3: XRD patterns of plasma nitrided layer (80%N_2+20%H_2; 8h; 500 °C) (a) and ZrBN coating layer (b).
Fig. 4: The surface morphology after potentiodynamic test in NaCl 30 g/L of ZrBN coated part (a), plasma nitrided (80%N_2+20%H_2; 8h; 500 °C) steel (b) and duplex treated steel (c).
Fig. 5: Potentiodynamic polarization curves in NaCl 30g/L for nitrided samples (a), ZrBN coated and duplex treated parts (b).

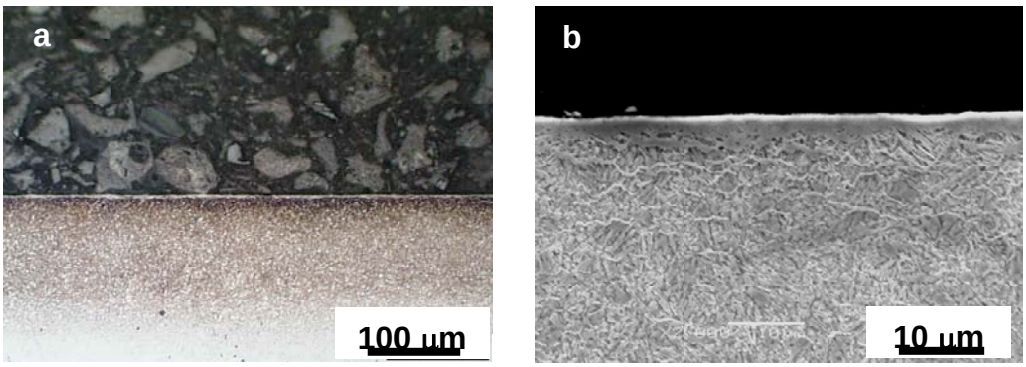


Figure 1

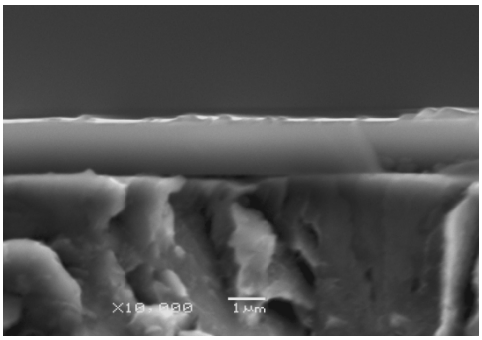


Figure 2

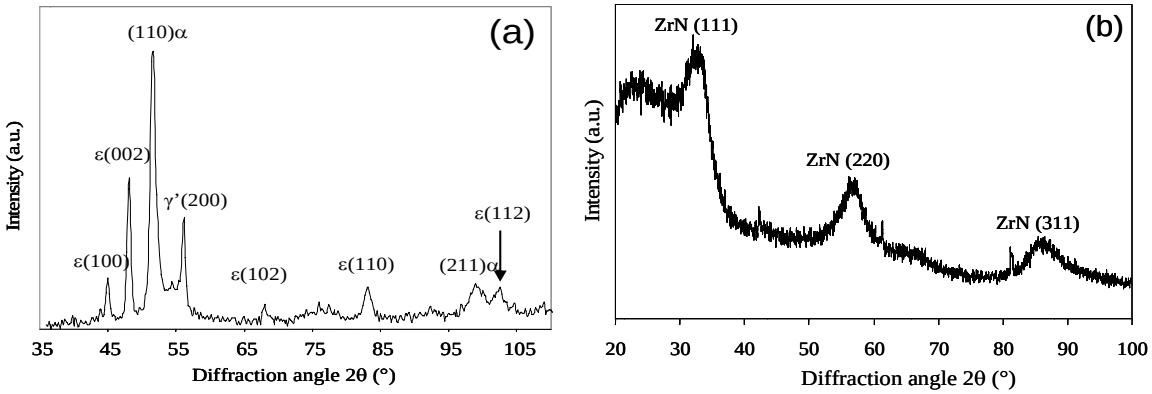


Figure 3

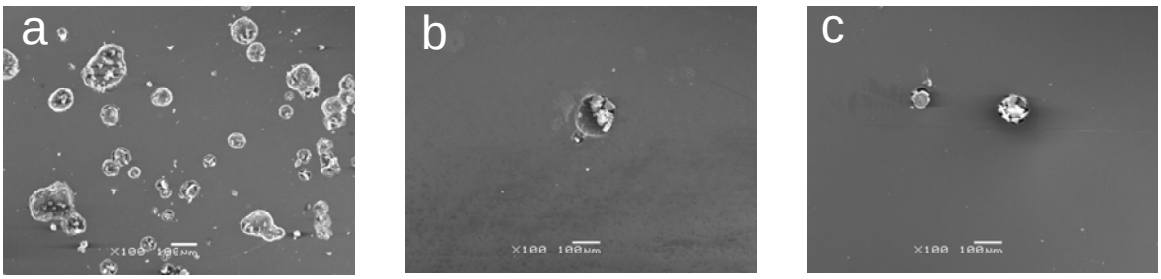


Figure 4

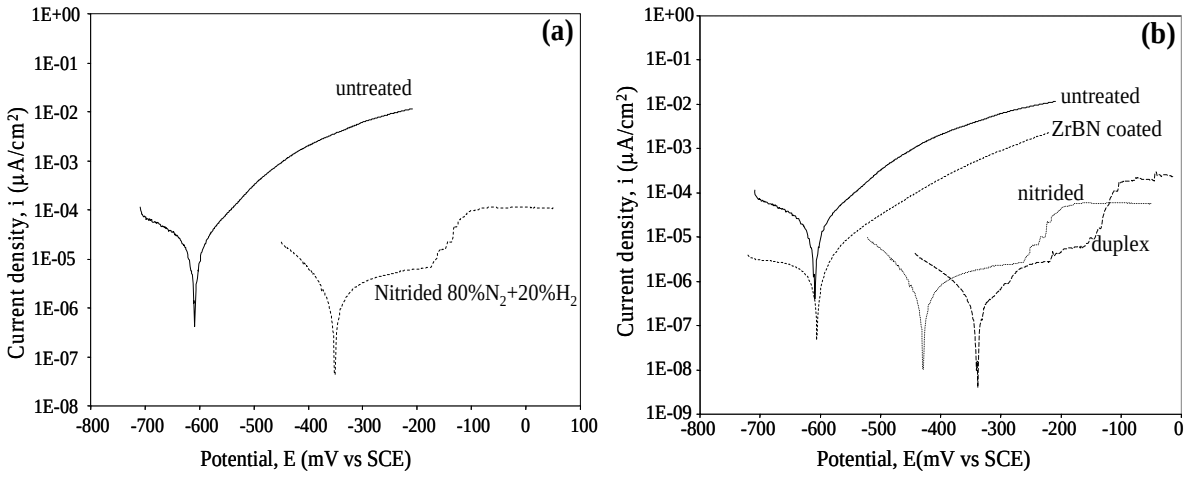

(a)
untreated
Nitrided 80%N2+20%H2
Current density, i (µA/cm²)
Potential, E (mV vs SCE)
(b)
untreated
ZrBN coated
nitrided
duplex
Current density, i (µA/cm²)
Potential, E(mV vs SCE)

Figure 5

Wear behaviour of PN+CrN, PN+CrAlN and PN+AlCrTiN layer composite during ball-on-disk tests in higher temperature

Joanna Kacprzyńska [1], Jerzy Smolik [1], Adam Mazurkiewicz [1]

[1)] Institute for Sustainable Technologies – National Research Institute,
Pułaskiego 6/10, 26-600 Radom, Poland

Extended Abstract

One of the most perspective directions of the development of surface engineering is related to hybrid technologies, which best fulfil the expectation of the industry concerning obtaining expected properties of the surface of tools and machine components. The mostly known and widely used surface treatment hybrid technology is a combination of gas or glow-discharge nitriding process with the process of deposition of hard antiwear coatings by means of PVD methods. The effect of the hybrid technology with such a configuration is a layer composite, consisting of a nitrided layer and a PVD coating deposited directly on it, which can be use for increase of durability of tools working in high mechanical and temperature loads, e.g. forging dies or moulds for pressure casting of aluminium. One of the main important parameters of the PN+PVD layer composite is the wear resistant in higher temperature.

This paper presents the results of materials investigations and ball-on-disk wear test of three different layer composites PN+CrN, PN+CrAlN and PN+AlCrTiN. The designed layer composites were obtained with the use of the hybrid technology, which consist of plasma nitriding (PN) followed by arc-evaporation coating deposition. Technological processes for the production of coating composites (plasma nitriding process and PVD process) were realised by means of hybrid, multi-stage method of surface treatment in continuous cycle, in the vacuum device produced by the Institute for Sustainable Technologies – National Research Institute (ITeE-PIB) in Radom, Poland (Fig. 1).

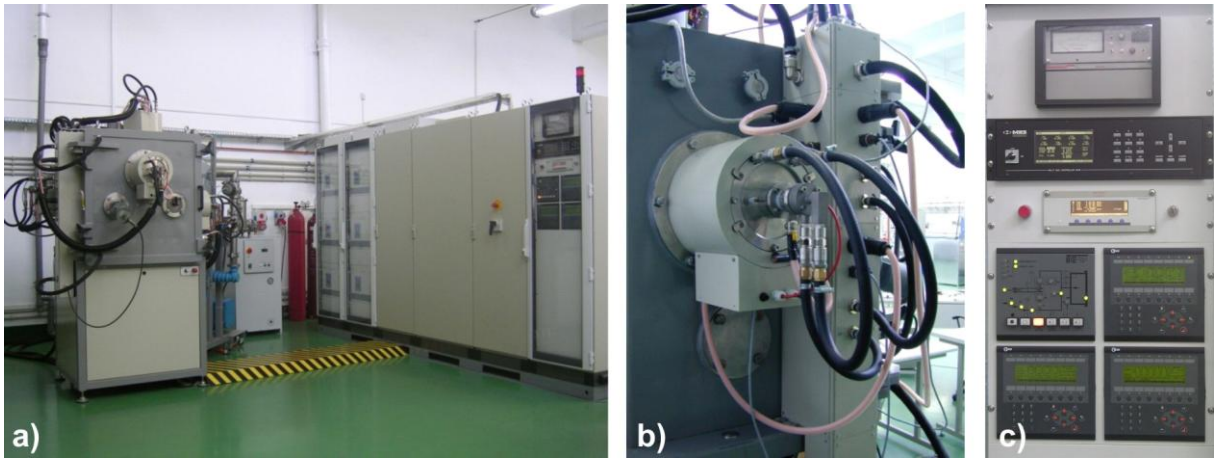


Fig.1. Device for the realisation of hybrid surface treatment processes a) entire technological system, b) arc plasma source, c) computer control system.

For all created layer composites the material properties like adhesion (Scratch test) and mechanical properties (Nano Hardness Tester) , chemical composition (GDOES method) – Table 1, microstructure (FIB+STEM technique) – Fig.2 were investigated.

Table 1. The material properties of three different PVD coatings which were investigated

Materials properties	CrN	AlCrN	AlCrTiN
Thickness [μm]	4.5	3.7	4.0
Hardness [HV]	2100÷2500	2100÷2650	2550÷3000
Young modulus [GPa]	260÷310	255÷380	315÷350
Friction coeficient	0.32	0.40	0.48
Rougness [μm]	R_a=0.43	R_a=0.40	R_a=0.29
	R_z=1.16	R_z=3.06	R_z=2.28
	R_t=1.92	R_t=4.49	R_t=3.40
Adhesion [N]	Fc_1=46	Fc_1=71	Not observed
	Fc_2=60	Fc_2=83	Fc_2=83
	Fc_3=103	Fc_3=124	Fc_3=110
Chemical composition [% at.]	N=46	N=44	N=47
	Cr=54	Cr=29	Cr=23
	-	Al=27	Al=22
	-	-	Ti=8

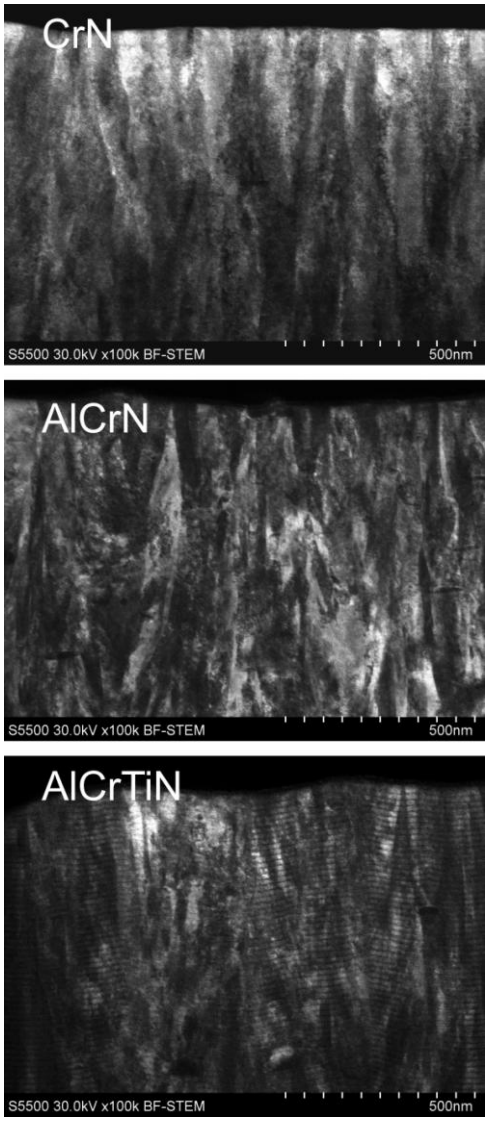


Fig.2. The results of microstructure investigations obtained by Scanning Transmission Electron Microscopy with used the Focus Ion Beam method for preparation of samples.

The microstructure investigations obtained by Scanning Transmission Electron Microscopy (Fig.2), proved that the CrN and AlCrN are typical monolayer coatings with columnar microstructure, whereas in the AlCrTiN coating the nanomultilayer microstructure was observed. The reason for nanomultilayer microstructure of AlCrTiN coating was the used of two different types of targets, i.e. AlCr and AlTi, placed in two opposite walls of vacuum chamber.

The ball-on-disk tribological tests, for cylindrical samples made of EN X32CrMoV3.3 hot working steel covered by investigated layer composites, were carried out in the range of temperatures $25^oC \div 600^oC$. The tribometer from CSM Instruments and the following parameters: linear velocity – 0.1 km/min, load – 10 N, the radius of wear track – 10mm, ball – made of Si_3N_4 ϕ = 6mm were used. After the test, the wear track geometry was measured by non contact 3D profiler type: Talysurf CCI from Taylor Hobson and the volume of removed material of coating *(V)* was calculated. The methodology of ball-on-disk tribological tests is presenting on Fig.3.

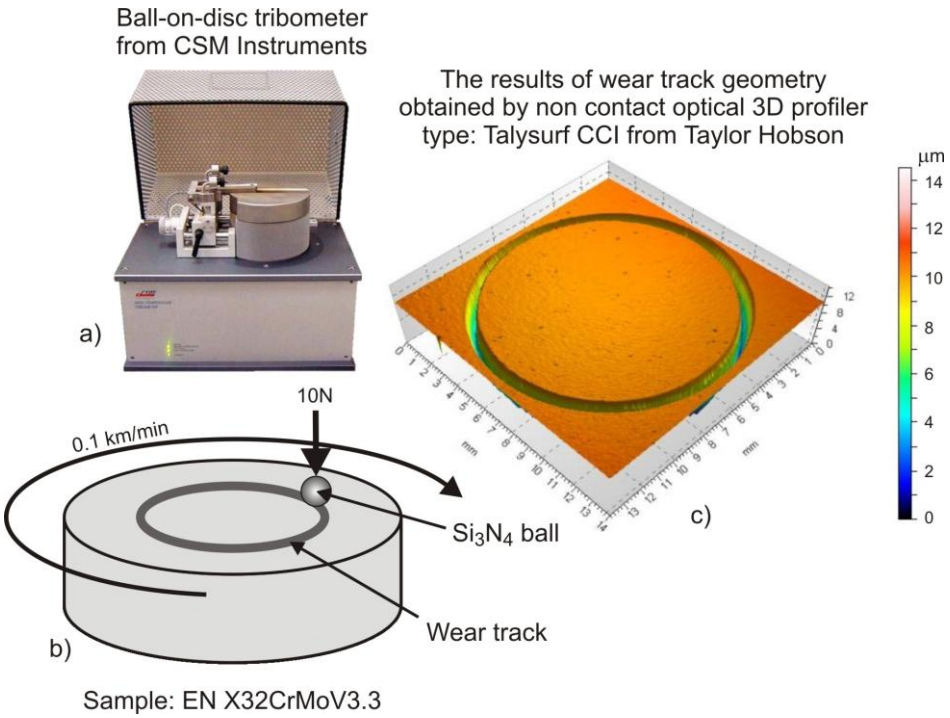


Fig.3. Realisation of ball-on-disc tribology tests: a) ball-on-disc tribometer from CSM Instruments, b) ball-on-disc tribology system, c) wear track geometry obtained by non contact optical 3D profiler.

In the next step according to the formula: $W = V / F \cdot S$, the value of Wear index *(W)* was calculated; V – volume of removed material of coating, F – load of the ball on sample, S – length of wear track. The results of changes of wear index *(W)* with the increase of temperature of sample in the ball-on-disc tribology tests are presenting in the Fig.4.

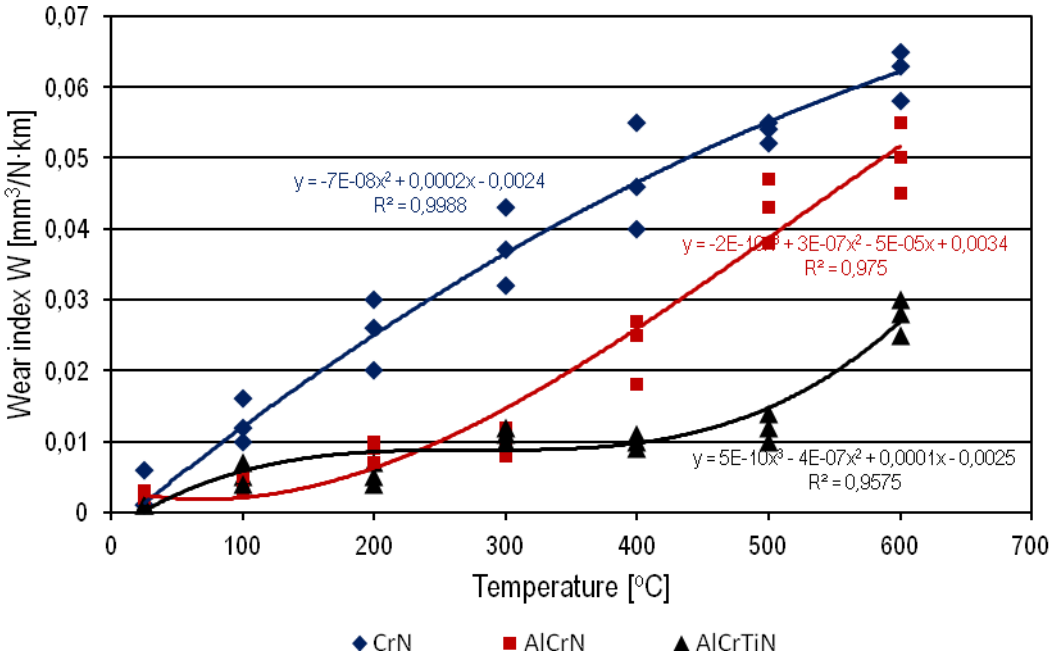


Fig.3. The results of ball-on-disc tribology tests obtained for three different investigated layer composites: PN+CrN, PN+CrAlN and PN+TiCrAlN.

Basing on the obtained results authors proved that the proper chemical composition and microstructure of thin PVD coatings, is the effective way for increase of stability of wear resistant of layer composites type “PN+PVD coating” in high temperature. The most important role in this process fulfil the participation of different metals in deposition process. It increase the possibility of creation of multicomponent nitrdes, i.e. Cr-Al-N, Ti-Al-N, Ti-Cr-N and Al-Cr-Ti-N, which characterized higher hardness and higher stability in high temperature.

Nitrogen effect and thermal stability of Cr and CrN thin films deposited by HiPIMS

Axel Ferrec[1], Frédéric Schuster[2], Pierre-Yves Jouan[1], Mohamed Abdou Djouadi[1]

[1]Institut des Matériaux Jean Rouxel, CNRS UMR 6502, Nantes, France
[2]Laboratoire Commun MATPERF CEA-Mecachrome, Vibraye, France,

Keywords

HiPIMS, Chromium, Chromium nitride (CrN), thin films, reactive sputtering, annealing treatment.

Introduction

The chromium nitride thin films are studied since several years and are widely use in mechanical applications as corrosion barrier. It has already been established that magnetron sputtering can improve by many ways the chromium nitride properties such as hardness, adhesion, oxidation resistance. A new development of this process, named HiPIMS (High Power Impulse Magnetron Sputtering), allows enhancing coating properties.

In the first part, the objective of this study is to check the influence of the nitrogen content in the gas mixture on the CrN thin film (on the structure, the morphology). And next, the annealing treatment was investigated to study their behavior at high temperature.

Experimental

Chromium and chromium nitride thin films were deposited by reactive magnetron sputtering from a pure chromium target (99,99 %). The nitrogen content in the gas mixture was varied between 0 and 50%. Cr and CrN were deposited using HiPIMS generator (HIP3 Solvix 5K) at floating potential without heating during deposition. The on-time was set at 30 µs and the frequency was 1000Hz. To obtain films with the same thickness, deposition time was adjusted with nitrogen content injected in the gas mixture.

The thickness of the film was measured by profilometry. The film crystallinity was analyzed by X-ray diffraction. From the XRD diagrams, the crystallite size is calculated using the Scherrer formula.

In order to study the thermal stability, we performed annealing tests from 400°C to 900°C in heater for 1 hour in air.

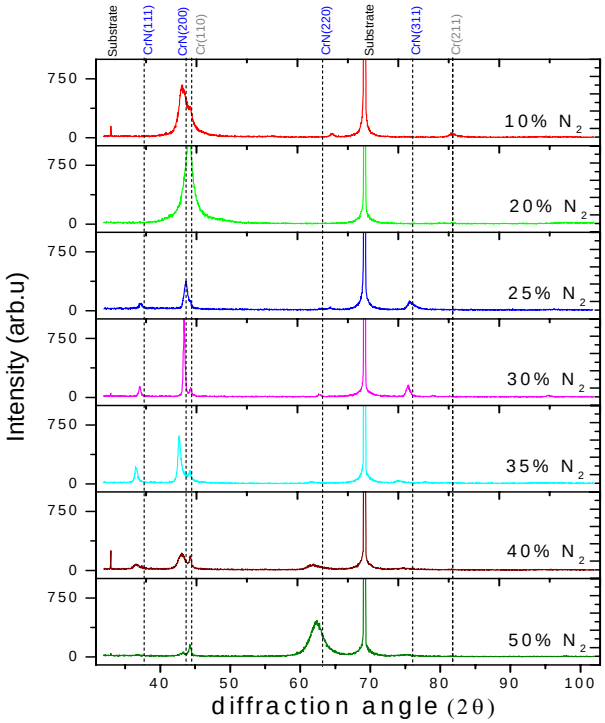


Figure 1, *XRD pattern of CrN thin films with different discharge nitrogen contents*

Results

In this part, the amount of nitrogen in the discharge was varied between 0 and 50%. As we can see on Figure 1, the structure evolves from (110) Cr to (220) CrN phase.

On each diagrams, we can see a Cr peak, it comes from the adhesion layer. The introduction of small nitrogen quantity leads to formation of Cr-CrN phase, reduces the crystallinity and the peaks are broader. Face centered cubic polycrystalline CrN thin films (JCPDS 11-0065) can be obtained with 25%. As the nitrogen increases, the crystallinity increases up to 30%. At this percentage, the film presents a strong (200) preferential orientation to minimize the surface energy.

If one increase further the nitrogen content up to 50% the crystallinity declines and the preferential orientation changes from (200) to (220). In the same time, we can observe the broadening of the XRD peaks.

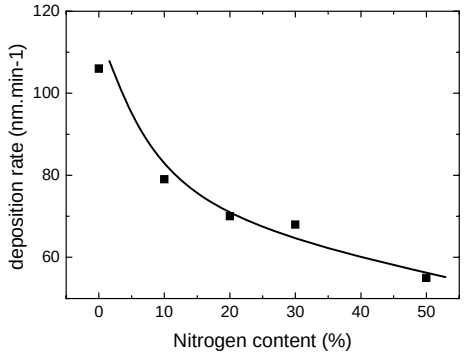


Figure 2, *Deposition rate evolution with various discharge nitrogen contents*

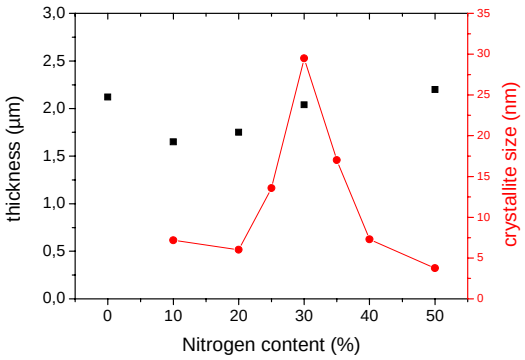


Figure 2, *Thickness and crystallite size with various discharge nitrogen contents*

With similar thickness, the calculations of the grain size from the Scherrer formula (Figure), reveals crystallite sizes around 5-10 nm except between 25% and 35% of nitrogen. In this region, their sizes reach a maximum of 30 nm at 30% of nitrogen. Below 30%, the CrN films are metal rich and above, the nitrogen tends to amorphized the layer.

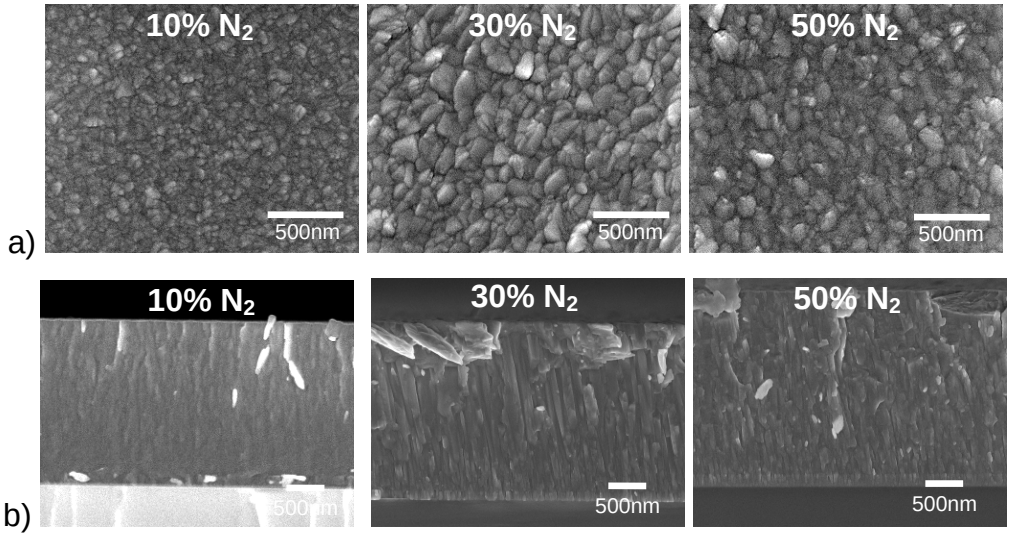


Figure 3, *a) Surface and b) cross-sectional scanning electron micrographs of CrN thin films deposited with various nitrogen contents*

The SEM micrographs show that column tops in surface tends to be bigger at 30% of nitrogen (Figure 3). This observation is in good agreement with calculations. At 10% of nitrogen, the film is featureless and very dense. At 30 and 50% of nitrogen, cross-section images reveal columnar structures. Nevertheless, with more nitrogen (50%)

the coating seems to be denser. As expected, the XRD measurements (not showed) from the chromium and the chromium nitride thin films show an increase of the crystallinity and the texture with the annealing temperature.

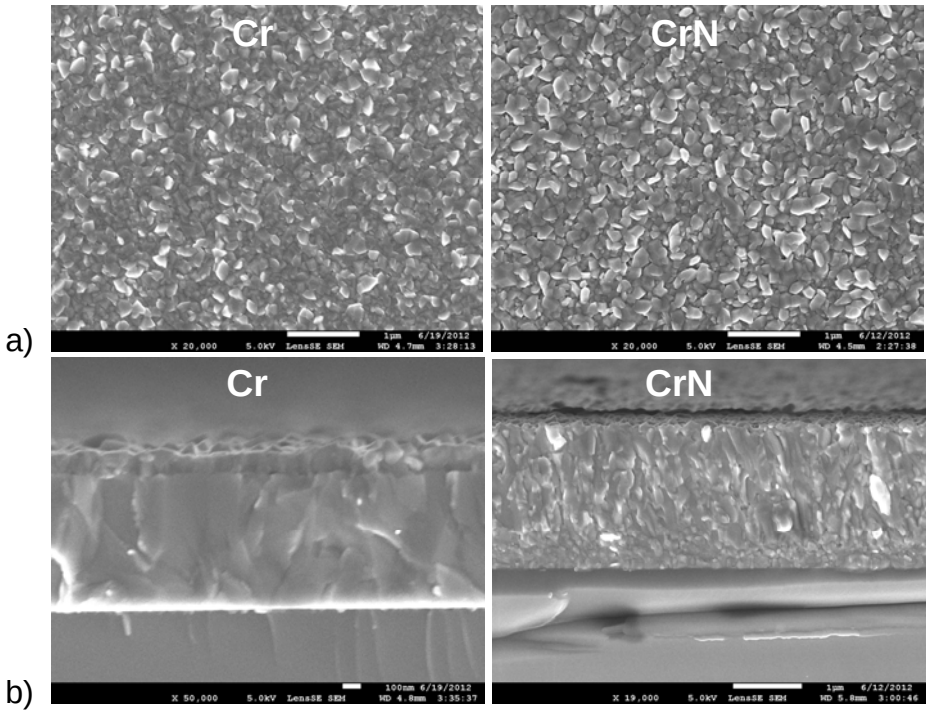


Figure 4, *a) Surface and b) cross-sectional scanning electron micrographs of Cr and CrN thin film annealed at 700°C*

The CrN was deposited with 30% of nitrogen. Film oxidation evaluated by XRD, reveals a Cr_2O_3 phase from 700°C in the two cases. The crystallite size increases continuously with the temperature. The SEM pictures from the surface and the cross-section confirm this tendency. On the other hand, the Cr_2O_3 layer in surface seems to be thicker in chromium deposition (Figure 4).

To summarize, the chromium thin films are well crystallized, stable up to 700°C with a slight change of the morphology. Whereas the chromium nitride coatings are also more crystallized but the morphology is unchanged at this temperature (stable at 900°C).

Acknowledge

We thank the CEA and the Région des Pays de Loire for their financial support.

Effect of low temperature air plasma treatment on physico-chemical properties of kaolinite

Lubomir Lapcik[1,2], Ivo Krasny[2], Ivana Kupska[2], Barbora Lapcikova[1,2]

[1]Center of Polymer Systems, Tomas Bata University in Zlin, Faculty of Technology, Nam. T.G. Masaryka 5555, Zlin, Czech Republic
[2]Tomas Bata University in Zlin, Faculty of Technology, Dept. Food Technology and Microbiology, Nam. T.G. Masaryka 275, Zlin, Czech Republic
Email: lapcik@ft.utb.cz

Keywords: kaolinite, air plasma, wetting, powder rheology, crystal lattice.

Abstract

It was found in this study that air plasma treatment of particular kaolinite has led to the change of its wettability. This was reflected in the decreased values of water contact angles of wetting. There were determined yield locus and flow function dependencies at different stress levels for virgin and different time plasma treated samples (flow index - *ffc*, effective angle of internal friction - phi*e*, unconfined yield strength - *sigmac*). It was found that by plasma treatment the character of the flow was shifting from region of very cohesive (*ffc* = 2.39) to the cohesive (*ffc* = 3.19). For untreated samples effective angle of internal friction was decreased with increasing applied consolidation stress, while for plasma treated kaolinite it was increased.

Introduction

Granular materials occupy a prominent place in our culture, the worldwide annual production of grains and aggregates of various kinds reaching approximately ten billion metric tons [1]. They are used in many different applications and industries, such as basic construction materials, agriculture, synthetic polymers fillers, cosmetic, pharmaceutical, processing and food industry. Many practical engineering applications involve handling, flow and storage of bulk solids (e.g. pelletizing, particle size reduction, tableting, mixing, packaging etc.) require knowledge and understanding of the particular solids flow properties and surface energy

distribution. For example, the compaction of particular solids may be defined as a reduction in the total volume of an assembly of solid particles by the application of stress. The formation of a coherent body from such an assembly can be then described in terms of the stresses required to overcome cohesion, internal friction and the yield criterion of particular material. The strength of a bulk solid is used to determine the ability of the material to form cohesive arches, as well as to correlate process behaviour to material properties.

Methods

Air plasma treatment of studied powder was performed in Diener Femto (Diener Electronic, Germany) capacitively coupled plasma reactor operating at 13.56 MHz frequency for 10, 20 and 30 minutes. Kaolinite powder was placed into the rotating rectangular parallel piped glass reactor chamber (borosilicate glass cylinder of 320 mm length and 150 mm diameter), which was placed inside the plasma reactor. The processing reactor conditions were as follows: generator power 100 W, air flow rate 5 cm^3/min, processing pressure 35 Pa. The latter construction configuration enables high uniformity of the surface modification of treated powder samples.

Shear cell tester measurements were performed on untreated and air plasma treated kaolinite powder samples using a ring shear cell tester (RST-XS, Dr. Dietmar Schulze, Germany) at laboratory ambient temperature 24°C. Tested powders were of 0.27 w.% moisture content and were kept for 48 hours prior to the measurement at constant humidity conditions in desiccators. Powders were distributed into the shear cell under gentle vibration in order to achieve a similar packing state for each sample under study. The samples were tested using different pre-loads of 8.6; 13; 22; 33 and 43.5 kPa. Calculated experimental error was less than 1 %.

Kaolinite particles ζ-potential and effective diameter were determined on ZetaPlus instrument (Brookhaven Instruments Corporation, USA) in 0.001 M KCl at 24°C. Prior to each measurement the vial was kept in ultrasonic bath for 5 minutes to destroy all possible conglomerates.

Contact angle measurements of wetting of studied kaolinite powders were performed on Krüss K12 Tensiometer apparatus (Krüss, Germany) by means of Washburn method [8], where the porous solid was treated as a bundle of cylindrical capillaries with mean or equivalent radius. Each measurement was repeated for 5 ×. Measurements were performed at ambient laboratory temperature of 24°C. Re-distilled water, ethylene glycol, ethyl alcohol,

dimethyl sulfoxide and diiodomethane were used as testing liquids (ACS grade, Sigma-Aldrich, USA).

Inverse gas chromatography was conducted using a Surface Energy Analyser (SEA) (Surface Measurement Systems, UK). Samples were placed in 4 mm (internal diameter) columns, to give a total surface area of approximately 0.5 m^2. Specific surface area measurements were made using a Micromeritics TriStar 3000 surface area and porosity analyser (USA), using the nitrogen BET technique. All reagents were obtained from Fisher Scientific (USA), and were of analytical grade. The following eluent vapours were passed through the column: Nonane, Octane, Hexane, Heptane. The injection of vapours was controlled to pass a set volume of eluent through the column to give pre-determined fractional coverage of the sample in the column. The retention time of the vapours by the particles gives an indication of the surface properties of the material, including the surface energy. By gradually increasing the amount of vapour injected, it is possible to build up a surface heterogeneity plot [9,18-20].

FT-IR spectra were recorded on FTIR- 8601PC spectrometer (Shimadzu, Japan) by means of KBr disk method. The resolution of the instrument was set to ± 2 cm^{-1}. A mixture of the studied kaolinite and dried KBr (1.3 mg kaolinite/160 mg KBr) was grand and pressed using a pellet die under pressure to obtain transparent disk. During dressing, the press was connected to the vacuum pump to remove water moisture. Analytical grade potassium bromide (Aldrich, USA) was used for disk preparation.

Conclusions

It was found in this study that the air plasma treatment of particular kaolinite has led to the increased wettability, which was reflected in the observed decreasing values of contact angles of wetting. Due to the fact, that contact angle measurements are best suited mainly for low surface energy solids, there were used the inverse gas chromatography measurements for determination of both the dispersive surface energy distributions as well as dispersive surface energy profiles for virgin and plasma treated samples. Results of these measurements confirmed our assumption, that air plasma treatment activates surface energy of the crystal planes of the kaolinite as reflected in the broadened dispersive surface energy distribution after 10 minutes treatment time. However with prolonged 30 min treatment time the dispersive surface energy distribution profile was decreased. We assume, that the latter decrease reflects the distorsion of the crystal lattice of the kaolinite. Calculated dispersive surface free energy for 24 % surface coverage was increased from original 35 mJ/m^2 to 40.3 and 40.8 mJ/m^2 for 10 and 30 minutes treatment times. Plasma treated samples show higher

average surface energies in the wide range of coverage regimes in comparison to the virgin samples. Observed changes of the surface properties of studied kaolinite samples were reflected also in decrease of the negative values of electrokinetic ζ-potential in 0.001 M KCl aqueous solutions from -8.0 mV to -11.0 mV. By means of FT-IR analysis there was confirmed the fact, that air plasma treatment is changing internal structure of the kaolinite crystal lattice most probably due to the ongoing initial stages of the internal disintegration process as reflected in changes of Si-O-Si and Al_2O-H infra red characteristic spectral regions. With respect to the characterization of macroscopic powder flow behaviour, yield locus and flow function dependencies at different stress levels for virgin and different time plasma treated samples were determined. It was found that by plasma treatment the character of the flow was shifting from region of very cohesive (ff_c = 2.39) to the cohesive (ff_c = 3.19). For untreated samples effective angle of internal friction was decreased with increasing applied consolidation stress, while for plasma treated kaolinite it was increased. However, the latter mentioned changes of the φ_e values for materials under study were not changed significantly.

Acknowledgements

This article was created with support of Operational Program Research and Development for Innovations co-funded by the European Regional Development Fund (ERDF) and national budget of Czech Republic within the framework of the Centre of Polymer Systems project (reg. number CZ.1.05/2.1.00/03.0111).

References

[1] L. Lapcik, B. Lapcikova, I. Krasnz, I. Kupska, R.W. Greenwood, K.E. Waters: “Effect of low temperature air plasma treatment on wetting and flow properties of kaolinite powders”. Plasma Chem. Plasma Process (2012) 32:845-858.

Biocompatible thin films obtained from heparin-methane plasma process

R. P. Mota[1], I. A. Perrenoud[1], R. Y. Honda[1], M. A. Algatti[1], M. E. Kayama[1], K. G. Kostov[1], T. Sadahito China[1], N. C. Cruz[2]

[1]FEG-DFQ-UNESP, Av. Ariberto Pereira da Cunha 333, 12516-410, Guaratinguetá, SP, Brazil

[2]UNESP Campus Experimental de Sorocaba, Av. Três de Março 511, 18087-180, Sorocaba, SP, Brazil

E-mail: rmota@feg.unesp.br

Abstract. Heparin is an appropriate molecule to suppress the thrombus formation in the initial stages of blood contact with an artificial material. Therefore the covering of a synthetic material with heparin-like molecules is a great importance issue in biomaterial science and engineering. In order to reach this goal this paper deals with the plasma deposition of thin heparin-like films on microscope slides from RF-excited heparin/methane low pressure plasmas. Plasma were excited by a RF-power supply operating on 13.56 MHz at a fixed power of 50 W. Heparin was diluted in ethanol and fed into the plasma chamber in mixtures of 50% of CH_4 (in pressure) at 10 Pa. Film's molecular structure was characterized by Fourier transform infrared spectroscopy (FTIR here in). Molecular spectra presented absorption bands due C-H, O-H and C-O stretching and bending modes. Film's surface wettability was investigated by contact angle measurements. The experimental results show values varying from 65^0 to 20^0. Surface's optical microscopy showed the occurrence of heparin islands distributed almost uniformly over the film. The blood's coagulation time placed in contact with glass substrate covered by plasma deposited heparin/methane films was measured by thrombosis time and activated thromboplastin.

1. Introduction

In the early 80's it appeared that biomedical engineering had achieved the goal of a workable total artificial human heart [1,2]. Although the heart met mast of the stringent mechanical requirements it had a fatal how. The material that contacted the blood, although in many ways the best available material did not have the necessary biocompatibility. Blood coming into contact with a segmented polyurethane would recognize it as a foreign surface and form thrombi. In human patients anticoagulants were administered chronically to inhibit clotting and thrombosis but this practice subsequently created much more problems. Despite the use of anticoagulants the patients suffered frequent strokes, believed to result from embolus of thrombi formed on the material surface. Recent efforts have led to a much greater applications of the number and complexity of processes involved in blood coagulations on foreign surfaces (5 mm). Researches shown that synthetic vascular grafts, made of Dracon^{TM} or expanded Teflon, are widely used to replace occluded or diseased arteries in humans. When used in large-diameter applications, synthetic vascular grafts, show satisfactory patency rates. In small-diameter applications (inner diameter less than 5 mm), however, graft performance is disappointing due

to stenosis and thrombus formation [3-5]. Endothelial cell seeding is an accepted approach to improve small-diameter graft performance. For successful endothelial cell seeding, a suitable substrate is required, which, is not provided by Dracon^{TM} or expanded Teflon grafts. Otherwise, it is important to mention that thermoplastic polyurethanes and plasticized poly-vinyl chloride have been widely used for various biomedical applications due to their excellent mechanical properties and proper blood compatibility [6,7]. Surface modification is an effective approach to improve the blood compatibility being the size, shape and mechanical properties of the original material maintained. Many studies have been performed on producing a blood-compatible surface by tailoring with poly-ethylene glycol, heparin, heparin-like, phospholipid polymer, and so on [6,7]. However, the aqueous solubility of some materials make them unsuitable for many biomedical applications. Good results have been obtained with plasma treatment or deposition. This work reports the production of heparin-like films using plasma polymerization process. This technique allows one to obtain materials which do not dissolve in strong acidic and basic and present physical and chemical attractive properties.

2. Experimental

Heparin diluted in isopropanol/methane mixtures (50 % in pressure) discharges were generated by a 13.56 MHz RF power supply operating in 50 W at a fixed pressure of 10 Pa. Plasmas were generated within a pyrex cylindrical reactor 190 mm of inner diameter and 150 mm long. The vacuum inside the plasma chamber is monitored by pirani^{TM} (thermocouple) and penning^{TM} (inverse magnetrom) gauges. The diffusion pump is coupled to the chamber through a gate valve and is used for cleanness purposes. The pressure is pumped down to 10^{-3} Pa, being the chamber purged with argon several times before each running of the experiment. The plasma chamber walls were heated with a temperature controlled belt in order to minimize the heparin-isopropanol condensation as well as the humidity. Heparin-isopropanol was placed inside a stainless steel bottle and was fed into the plasma chamber through a needle valve. Methane was fed into plasma chamber through needle valves and mass-flow controllers. The wettability of plasma polymerized films was investigated by contact angle measurements using a Ramé-Hart goniometer model 100 and water and diiodomethane (CH_2I_2)as probe liquids. Film's thickness were measured using an Alpha Step Tencor 100^{TM}. The film's structure was investigated by FTIR spectroscopy using a Perkin-Elmer Lambda 25^{TM} spectrometer. Surface smoothness was probed by optical microscopy. Surface's blood compatibility was evaluated by determination of platelets density, fibrinogen and prothrombin (PT), activated partial thromboplastin (APTT) and coagulation times (Tc) of a pool of eight samples of freshly collected human blood kept in contact with different samples for 2.5 hours.

3. Results and discussion

FTIR spectra of methane plasma polymer (1), heparin-isopropanol methane plasma polymer (2), sodic heparin (3) are shown in figure 1. For comparison, the principal bands of the heparin are present in the heparin-isopropanol methane plasma polymer. It suggests the preservation of the heparin structure in the films. It is important to mention that the overlapping of bands derived from bonds in the methane and isopropanol molecules do not allow the precise identification of the structure of the heparin-isopropanol methane plasma polymer. Characteristic absorption bands can be observed at 3500 to 3200 cm^{-1} (assigned to O-H stretching), 2950 to 2850 cm^{-1} (C-H stretching), 1630 cm^{-1} (O-H bending), 1440 cm^{-1} (C-H bending), 1380 cm^{-1} (C-H bending), 1280 cm^{-1} (C-O stretching), 1230 cm^{-1} and 1040 cm^{-1} (symmetrical and asymmetrical stretching of S-O in SO_3 heparin groups, respectively. The band near 1700 cm^{-1} is due to the presence of C=O groups. These results are consistent with the features of FTIR spectra of plasma polymer films deposited from methane and isopropanol discharges. The action of plasma on a material surface can promote changes in their surface energy and contact angle.

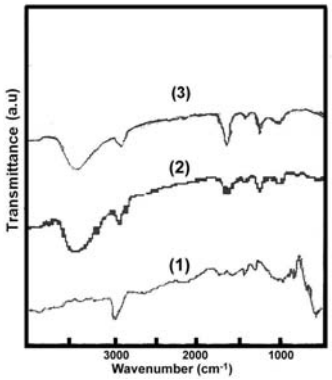


Figure 1. FTIR spectra of (1) methane plasma polymer , (2) heparin-isopropanol methane plasma polymer, (3) sodic heparin

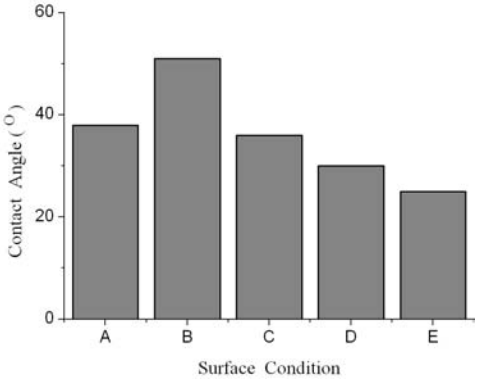


Figure 2. Contact angle of plasma deposited films for different conditions: (A) cleaned glass substratum, (B)methane plasma film, (C) heparin-isopropanol methane plasma film 40 nm thick, (D) same as (C) 10 nm thick, (E) heparin-isopropanol methane plasma film over glass covered by sodic heparin

Figure 2 shows water contact angles values for glass covered at different conditions. In (A), the glass was only cleaned in ultrasonic medium with petroleum ether and ethyl alcohol. In (B), the sample has been coated by thin films from methane plasma polymer (at 50 W and 10 Pa). In (C), the glass substrate was exposed to heparin-isopropanol methane (50% to 50%) plasma at 50 W and 10 Pa. Film thickness is approximately 40 nm. In (D) the same film as in (C) 10 nm thick. In (E), the glass substrate was covered with sodic heparin diluted in isopropanol and finally coated by heparin-isopropanol methane plasma polymer. As can be seen in this figure, the plasma treatment was profitable for obtaining hydrophilic surfaces. The different surface produced by plasma deposition have a distinctive influence on the haemocompatibility of the samples. This results can be illustrated in figure 3 that shows the measurements of coagulation times Tc. The results indicate that among all the conditions evaluated, the glass coated with methane plasma polymer and pristine glass substrate are the least haemocompatible materials. The coagulation times of these materials were up to 44% smaller than the average coagulation time of fresh blood. Figure 3 also shows that the surface produced by plasma polymerization of heparin-isopropanol methane 40 and 10 nm thick (C,D) presents quite equal coagulation times. These results are 10% lower in comparison with those obtained for fresh blood. On the other hand the surface of the sample (E), presents coagulation time higher than fresh blood.

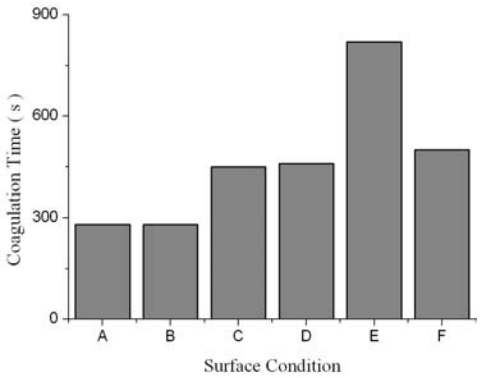


Figure 3. FTIR spectra of (1) methane plasma polymer , (2) heparin-isopropanol methane plasma polymer, (3) sodic heparin

This result can be attributed to the presence of islands of heparin on the surface of the sample that were not completely covered by the thin film from heparin-isopropanol methane plasma (micro-graphs not shown in this paper). These islands are dispersed on the surface and have irregular shapes. Another important result is also showed in this figure. The coagulation times of blood in contact of samples (C) and (D) (glass coated with heparin-isopropanol methane plasma polymers 40 and 10 nm thick respectively) are near fresh blood coagulation time. These aspects are important because they indicate an improvement in the performance of the materials most widely used nowadays in devices that operate in contact with blood. However , the material (E) (substrate coated by sodic heparin and polymer from heparin-isopropanol methane plasma) despite having high coagulation time, it is not suitable for use because it may induce or cause haemorrhages and cardiovascular complications.

4. Conclusions

It was shown that heparin-isopropanol methane plasma process could improve the haemocompatibility of glass substrates. The best results were obtained with heparin-isopropanol methane plasma polymers 40 and 10 nm thick. The coagulation times of blood in contact with such modified glass increased up to 65% compared to the values measured with pristine glass surface and glass coated by methane plasma polymer. Therefore one may conclude that the plasma surface treatment was successful for obtaining haemocompatible surfaces.

Acknowledgements

Authors would like to thank FAPESP, CAPES and CNPq for financial support.

References

[1] 2008 *Advanced plasma technology* eds R D'Agostino, P Favia, Y Kawai, H Ikagami, N. Sato and N. Arefi-Khonsari (Weinheim: Wiley-VCH)
[2] 2008 *Low temperature plasmas: fundamentals, technologies, and techniques* ed R Hippler, H Kersten, M Schmidt and K Shoenbach (Weinheim: Wiley-VCH)
[3] Lelah M. D., Cooper S. L. eds. 1986 *Polyurethanes in Medicine* (Boca Raton: CRC Press Inc)
[4] Ward R. A., Wellhausen S. R., Dobbins J. J., Johnson G. S., De Vries W. C. eds 1987 *Blood in contact with natural and artificial surfaces Ann. N. Y. Acad. Sci.* **516** 638
[5] Andrade J. D. ed 1985 *Surface and Inter facial Aspects of Biomedical Polymers* **1** (New York: Plenum Press)
[6] Balakrishnan B., Kumar D. S., Yoshida Y., Jayakrishnan A. 2005 *Biomaterials* **26** 3495
[7] Lee H. J., Park K. D., Park H. D. 2000 *Coll. and Surf. B* **18** 355

Analysis of the aging of cell-adhesive plasma-polymer coatings on titanium

F. Hempel[1], J. Schäfer[1], H. Rebl[2], J.B. Nebe[2], K.-D. Weltmann[1], B. Finke[1]

[1] *Leibniz-Institute for Plasma Science and Technology e.V. (INP), Felix-Hausdorff-Straße 2, D-17489 Greifswald, Germany*
[2] *University Rostock, Biomedical Research Center, Department of Cell Biology, Schillingallee 69, D-18057 Rostock, Germany*

A crucial factor for titanium implant performance is the rapid acceptance of osteoblastic cells just after implantation. It could be shown that the aging of microwave plasma deposited allylamine polymer films on polished titanium surfaces has no influence on cell adhesion and spreading.

Keywords: Pulsed plasma polymerization, amino functionalization, thin layer, aging, cell behavior

1. Introduction

Plasma polymer deposition is the method of choice for the finishing of metallic implant materials like titanium with nitrogen-containing bioactive coatings. The deposited cell-adhesive plasma polymer films have to possess special properties such as homogeneity, film stability on air as well as in different media, sufficient density of functional groups and the appropriate surface charge. But also the knowledge of long-term stability is essential for the application as implant surface. Therefore, aging studies of plasma polymer coatings on titanium surfaces are important to detect the changes of surface chemistry over a longer time period. For this purpose, results of physicochemical surface diagnostics were combined with adequate tissue culture experiments. The objective of this paper was to measure surface chemical characteristics of thin plasma polymerized allylamine (PPAAm) coatings on polished titanium with the main focus on FT-IR studies over a time period of one year and to correlate these data with the adhesion of human MG-63 osteoblastic cells.

2. Materials and Methods

Polished titanium disks (Ti-P) (R_a=0.4 µm), 11 mm in diameter were used as substrates for the chemical functionalization. The preparation was carried out in two steps:

(1) Disks were decontaminated and activated by cw oxygen plasma, followed by

(2) Plasma polymerization of the monomer allylamine using a micro-wave (MW) excited (2.45 GHz, 500 W) pulsed (duty cycle of 0.15 at a pulse length of 2 s) low pressure (p = 50 Pa) gas-discharge plasma for 144 s [1, 2].

The elemental chemical surface composition and chemical binding properties were determined by high-resolution scanning X-ray photoelectron spectroscopy (XPS). The Axis Ultra spectrometer (Kratos, UK) runs with the monochromatic Al K_α line at 1486 eV (150 W)

Corresponding author: Dr. Frank Hempel
e-mail: hempel@inp-greifswald.de
Tel.: +49-3834-554359; fax: +49-3834-554301

implemented charge neutralization and a pass energy of 80 eV for estimating the chemical elemental composition or 10 eV for highly resolved C1s spectra. The C-C/C-H component of the C1s peak was adjusted to 285.0 eV. Amino groups were labelled by reaction with 4-trifluoromethyl-benzaldehyde (TFBA) at 40 °C in a saturated gas phase for 2 h [1].

Additionally, the PPAAm-films were investigated by Fourier-Transform-Infrared Spectroscopy (FT-IR) using the diamond attenuated total reflection (ATR)- or the IR-reflection-absorption spectroscopy (IRRAS)- unit of a Spectrum One (Perkin-Elmer, Germany) spectrometer.

Water contact angles were measured by the sessile drop method (drop volume ~0.5 µl) using the measuring system OCA30 (Data Physics Instruments GmbH, Germany).

Human osteoblastic cells (MG-63 cells, ATCC) were cultured under serum-free conditions to avoid masking of the amino-functionalized Ti-P surfaces with adsorbed proteins [1, 2].

3. Results and Discussion

As expected, XPS and FT-IR (ATR and IRRAS) measurements demonstrate the oxidation of the PPAAm film by post plasma processes [3], initiated by surface free radicals during sample storage on air. XPS elemental analysis showed a closed pinhole–free polymer film since no Ti signal was observed. The N/C ratio was found to be at 27.2±0.2 % (19.2±0.5 %) and O/C at 5.6±0.4 % (16.2±0.3 %), measured after preparation and one year´s storage (in brackets). The theoretical value for the precursor allylamine is N/C=33.3 %, no O/C. Amino groups, determined from the XPS elemental ratio F/C, are present with a density of about 2.5±0.5 % (0.20±0.07 %), after preparation and one year´s storage (in brackets). About 70 % of primary amino groups have been lost within the first 30 days of storage, while the nitrogen content remains nearly stable. The loss of primary amino groups (CF_3-peak at 292.7 eV) is accompanied by an oxidation to acid amides at 288.2 eV and increasing oxygen functional groups (C-O, C=O peaks at 286.6 eV and 287.5 eV).

The PPAAm surface shows remarkable amounts of -C-NH_2 bonds and thus can counterbalance the existing negatively charged oxygen functional moieties. This should lead to a positive surface charge in aqueous environment. The zeta-potential of a freshly prepared [1,4] and also an aged PPAAm surface was found to be slightly positive [4].

FT-IR studies confirmed a high retention of the structural properties of the monomer allylamine [5] for the deposition method used here. Basic structures of the monomer are dominant: the stretching vibrations of the aliphatic C-H groups, ν-$CH_{2,3}$ at 2980-2880 cm^{-1}, the deformation vibration, δ-$CH_{2,3}$ at 1465-1375 cm^{-1}, and deformation vibrations of amines, δ-NH at 1650-1510 cm^{-1}. Also ν-NH stretching vibrations between 3380-3200 cm^{-1} are

clearly visible. Typical plasma and also aging effects can be observed as e.g. significantly broadened, disappearing or arising bands. Here, amino groups were partially transformed into amide, imine or nitrile functional groups by the plasma process. An indication for that is the band between 2300-2200 cm^{-1} associated with stretching vibrations of nitrile and ethine groups, ν-CN, ν-CC. FT-IR spectra of the PPAAm-surface after preparation and aging on air for 7 days are compared in **Fig. 1**.

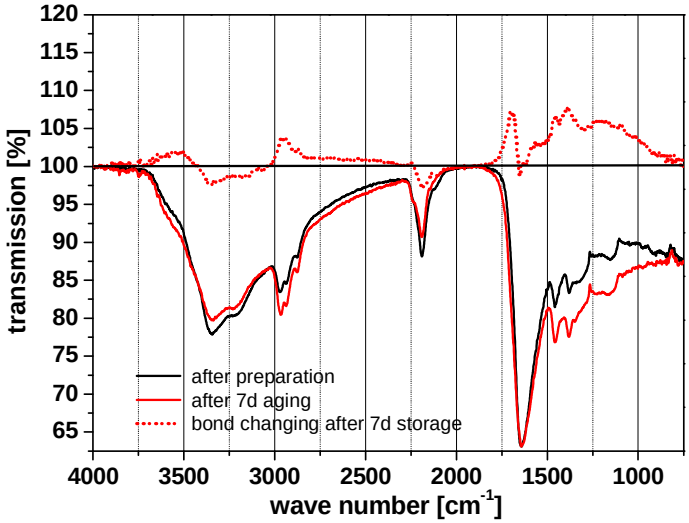


Figure 1: FT-IR ATR spectra of PPAAm surfaces after preparation and storage on air over 7 days

Characteristic changes due to ageing already after 7 days (dotted graph in Fig. 1) are: the formation of O-H vibrations near 3700-3200 cm^{-1} by water absorption, the formation of acid amides at 1700-1680 cm^{-1} [6], a degradation of nitrile and ethine groups, ν-CN and ν-CC at about 2200-2150 cm^{-1}.

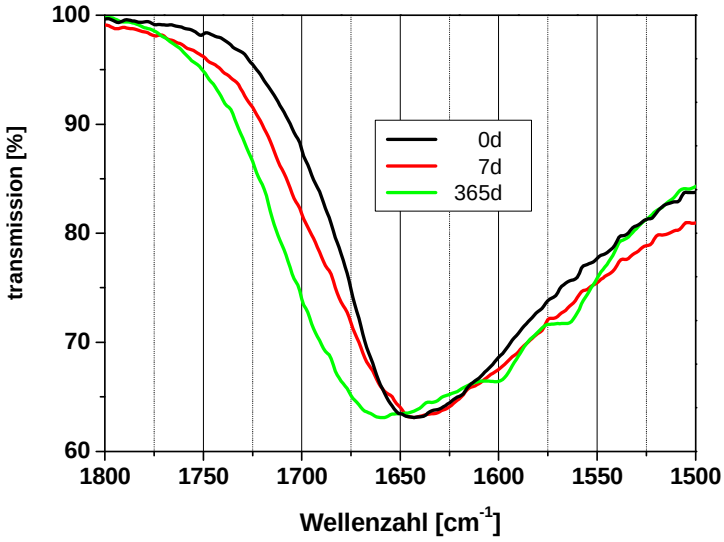


Figure 2: FT-IR IRRAS spectra of PPAAm surfaces after preparation and storage on air up to 365 days

The analyses of the ν-N-H vibration band around 1750-1500cm^{-1} shows the broadening by the oxidation process, the shifting of this band and also substructures during the aging process. First signs for the broadening can be observed after 7 days (Fig. 2) already.

Different water contact angle were detected (PPAAm 48±3^{o}, untreated Ti-P 87±3^{o}). The water contact angle for PPAAm decreased to 36±2^{o} after 360 days storage on ambient air. Thus, advantageous medium hydrophilicity still exists. This means that the wettability of PPAAm covered titanium is optimum for cell adhesion even after one year storage [7].

Cell culture experiments with MG-63 human osteoblast-like cells demonstrated a significantly enhanced adhesion and spreading on a PPAAm coated Ti-P substrate not only immediately after preparation as already observed [1,2,4, 8-10] but also independent of the storage duration up to one year.

In fact, not only primary amino groups but also other N-functional groups as e.g. acid amides or imides seem to play a role for initial cell functions [11]. Furthermore the examined plasma polymer coating PPAAm enables the cells to exhibit a very flattened and widespread phenotype indicating a strong cell-surface contact for improved implant ingrowth. Our newest results demonstrate that this long-time stable PPAAm-nanolayer has an impressive impact versus the titanium surface topography on osteoblast orientation [12].

Acknowledgements

This work was supported by the Federal Ministry of Education and Research of Germany (grant no. 13N9779, 13N11188, Campus PlasmaMed) as well as by the program TEAM of Mecklenburg-Vorpommern and the Helmholtz Association in Germany (UR 0402210, VH-MV1). We appreciate the technical support of U. Kellner, G. Friedrichs, U. Lindemann from the INP Greifswald and S. Staehlke (Biomedical Research Centre), W. Labs (EMZ) from the University of Rostock.

References

[1] B. Finke, F. Lüthen, K. Schröder, P.D. Müller, C. Bergemann, M. Frant, A. Ohl, B.J. Nebe, Biomaterials 28 (2007) 4521.
[2] B. Nebe, F. Lüthen, B. Finke, C. Bergemann, K. Schröder, J. Rychly, K. Liefeith, A Ohl,. Biomol Eng 24 (2007) 447-454. doi: 10.1016/j.bioeng. 2007.07.004.
[3] B. Finke, F. Hempel, H. Testrich, A. Artemenko, H. Rebl, O. Kylián, J. Meichsner, H. Biederman, B. Nebe, K.-D. Weltmann, K. Schröder, Surf. Coat. Technol.205 (2011) S.520.
[4] H. Rebl, B. Finke, J. Rychly, K. Schröder, JB. Nebe, Advanced Biomat 12/8 (2010) 356-364.
[5] K. Schröder, B. Finke, A. Ohl, F. Lüthen, C. Bergemann, B. Nebe, J. Rychly, U. Walschus, M. Schlosser, K. Liefeith, H.G. Neumann, K.D.Weltmann, J. Adh. Sci. Technol. 24 (2010) 1191.
[6] J. Kim, D. Jung, Y. Park, Y. Kim, D.W. Moon, T.G. Lee, Appl. Surf. Sci. 253 (2007) 4112.
[7] I. Gancarz, J. Bryjak, G. Pozniak, W. Tylus, Eur. Polym. J. 39 (2003) 2217.
[8] H. Rebl, B. Finke, K. Schroeder, JB. Nebe, Int J Artif Organs 33 (2010) 738-748.
[9] JB. Nebe, H. Jesswein, A. Weidmann, B. Finke, R. Lange, U. Beck, S. Staehlke, K. Schroeder, Mater Sci Forum, Vols. 638-642 (2010) 652-657.
[10] B. Finke, F. Hempel, H. Testrich, A. Artemenko, H. Rebl, O. Kylián, J. Meichsner, H. Biederman, B. Nebe, K-D. Weltmann, K. Schröder, Surface & Coatings Technology 205, Suppl. 2 (2011) pp. S520-S524
[11] T.R. Gengenbach, R.C. Chatelier, H.J. Griesser, Surf. Interface Anal. 24 (1996) 611.
[12] H. Rebl, B. Finke, R. Lange, K-D. Weltmann, B. Nebe, Acta Biomaterialia 2012, DOI 10.1016/j.actbio.2012.06.015

COMPARISON OF SURFACE PROPERTIES OF DLC AND ULTRANANOCRYSTALLINE DIAMOND FILMS WITH RESPECT TO THEIR BIO-APPLICATIONS

Miroslav Jelinek[1,2,*], Alexandra Voss[3], Tomáš Kocourek[1,2], Mahsa Mozafari[3], Veronika Vymětalová [2], Marketa Zezulová[1,2], Petr Písařík [1,2], Cyril Popov[3], and Jan Mikšovský[1,2]

[1] Institute of Physics ASCR v.v.i., Na Slovance 2, 182 21 Prague 8, CZECH REPUBLIC
[2] Czech Technical University in Prague, Faculty of Biomedical Engineering, nám. Sítná 3105, Kladno, CZECH REPUBLIC
[3] Institute of Nanostructure Technologies and Analytics, University of Kassel, Heinrich-Plett-Str. 40, 34132 Kassel, GERMANY

* Corresponding Author's E-mail: jelinek@fzu.cz

Keywords: diamond-like carbon, ultrananocrystalline diamond films, surface properties antibacterial tests

Introduction

DLC layers are entirely amorphous or contain micro- or nanocrystalline diamond or graphite and possess a disordered structure with a mixture of carbon bonding configurations. Furthermore, DLC can be hydrogen free (a-C) or containing hydrogen (hydrogenated amorphous carbon (a-C:H)). DLC films exhibit excellent physical and chemical properties, as well as high level of biocompatibility [1]. The films are dense, mechanically hard, smooth, abrasion resistant, IR transparent, chemically inert, resistant to attack by both acids and bases, have a low coefficient of friction, low wear rate, and are biocompatible and thromboresistant [2-3]. DLC coatings can be adherent on various biomaterials; neither toxicity toward certain living cells nor inflammatory response or loss of cell integrity were reported [4]. DLC shows an excellent hemocompatibility, a decreased tendency of thrombus formation and coated heart valves and stents are already commercially available [5]. The properties of the DLC coatings depend strongly on the hydrogen content and sp^3/sp^2 ratio which, in turn, depend on the deposition process and its parameters. The range of the properties of the DLC produced by different methods and under different process parameters is considerable.

Diamond is a material with quite a number of excellent properties [6], like extreme hardness, high elastic modulus, high wear resistance, optical transparency in a broad spectral range, resistivity controllable by the level of dopants, etc. which make it a promising candidate for diverse applications. Due to its outstanding electrochemical properties, superior chemical inertness and biocompatibility, artificially grown diamond has been recognised as an extremely attractive material for both (bio-)chemical sensing and as an interface to biological systems. This holds for all forms of diamond: monocrystalline (natural or artificial) and poly- (PCD), nano- (NCD) and ultrananocrystalline (UNCD) films.

In the current work the surface and antibacterial properties of DLC and UNCD films including the nature of the surface bonding and termination, wettability, surface energy and tests with Gram-positive and Gram-negative bacteria were studied and discussed.

Experimental

Deposition: The DLC layers were prepared by pulsed laser deposition (PLD) with a KrF excimer laser with energy densities from 4 $J \cdot cm^{-2}$ to 14 $J \cdot cm^{-2}$ and PLD combined with simultaneous bombardment of the growing film with argon ions of various energies. The number of the laser pulses on the rotating graphite target (0.5 Hz) was adjusted to reach approximately the same layer thickness (80 nm for layers on Ti-6Al-4V substrates (ISO 5832-3) and 100 nm on Si (111) substrates) and were between 2000 and 4000. Before deposition the substrates were RF cleaned (13.56 MHz) in 5 Pa argon for two minutes [7, 8]. The DLC films were deposited at room temperature in argon ambient (0.01-0.15 Pa) .In case of bombardment with Ar^+, an ion gun eH200 (Kaufman and Robinson, Inc.) was applied with parameters adjusted to reach a maximum value of sp^3 bonds [9], i.e. working argon pressure of 0.01 - 0.1 Pa, cathode current of 0.5 A

and 0.15 A, and ion energy of 40 eV. The ion gun regulated the gas flow needed to maintain constant cathode current and ion energy.

For the deposition of the UNCD films microwave plasma enhance chemical vapour (MWCVD) deposition was used. The process gas mixture contained 17% methane in nitrogen with a total flow of 300 sccm, leading to a pressure of 2.3 kPa. The substrate temperature was kept at 600°C and the input MW power at 800 W. The deposition time was 360 min in order to achieve UNCD films with thicknesses of ca. 1 µm. They were deposited on monocrystalline (100) Si wafers, ultrasonically pretreated in a suspension containing 80 mg ultradisperse diamond powder (mean grain size 3-5 nm) and 50 mg nanocrystalline diamond powder (mean grain size 250 nm) in 75 ml n-pentane. The pretreatment provided a nucleation density of about 10^{10} cm^{-2} allowing the deposition of closed and uniform films.

The schemes of the deposition systems are shown in Figure 1; the deposition parameters are summarized in Table 1.

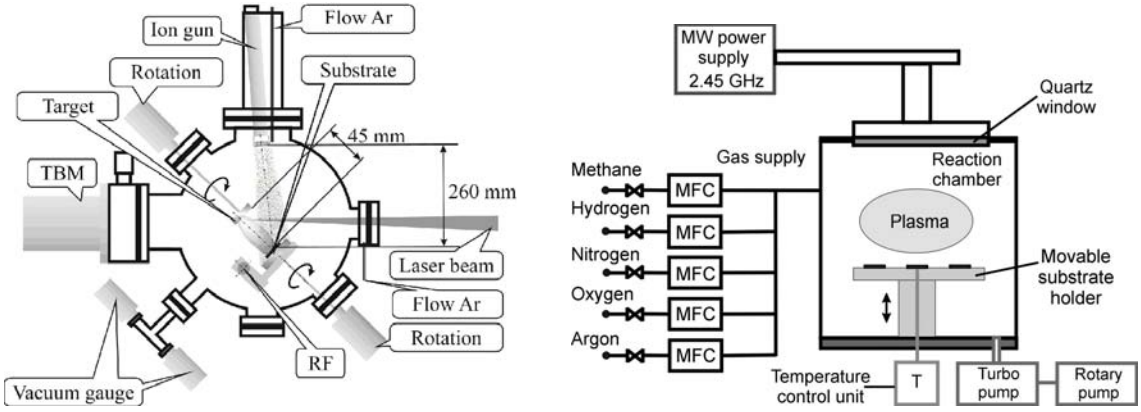


Figure 1: Scheme of PLD deposition system with ion bombardment (left) and MWCVD (right)

Table 1: Deposition conditions, composition, bonding nature and rms roughness of DLC and UNCD films

Sample	Laser energy density [J cm-2]	Ion energy [eV], ion current [A]	Composition			Bonds [%]		Roughness rms [nm]
			C [at%]	O [at%]	N [at%]	sp^2	sp^3	
DLC4	4	-	-	-	-	42	58	0.3
DLC8	8	-	-	-	-	35	65	-
DLC10	10	-	-	-	-	32	68	0.3
DLC10 0.15 A	10	40 and 0.15	92.7	6.1	1.2	19	81	0.2
DLC10 0.5A	10	40 and 0.5	91.2	8.2	0.6	29	71	4.2
DLC10 1A	10	40 and 1.0	94.1	5.9	0.0	27	73	-
DLC14	14	-	-	-	-	-	-	0.6
UNCD	-	-	98,1	1,2	0,7	10	90	9-14

Characterization: The morphology and topography of the DLC and UNCD films were investigated by scanning electron microscopy (SEM, Hitachi S-4000) and atomic force microscopy (AFM, Nanoscope Dimension 3100).

The content of diamond (sp^3) and graphitic (sp^2) bonds were determined by X-ray photoelectron spectroscopy (XPS) applying an ADES-400 spectrometer (VG Scientific, U.K.) with Mg Kα radiation (1253.6 eV) and a hemispherical electron energy analyzer. The photoelectron spectra were recorded with a pass energy 100 eV or 20 eV for survey scan and for the narrow scans of C1s and O1s core spectra, respectively. The inelastic electron background was subtracted using the Shirley`s procedure [10].

Wettability studies were performed by static contact angle measurements using a contact angle meter (DSA100, Krüss Co.) with three test liquids: distilled water, diiodomethane and ethylene glycol. The measurement was performed at room temperature by the sessile drop method with a drop volume of approximately 1±0,2 µl. The surface free energy with its dispersive (γ^d) and polar (γ^p) components was

calculated using the Fowkes method. The component γ^d related to van der Waals and induced dipole forces, while γ^p describes short-range dipole-dipole interactions, hydrogen bridge bonds, acceptor-donor and acid-base interactions.

The antibacterial properties of DLC and UNCD films were investigated using two representative bacteria typically used in antimicrobial testing, i.e. strain *Bacillus subtilis* and *Escherichia coli*. *Bacillus subtilis* is a Gram-positive bacterium commonly found in soil, while *Escherichia coli* is a Gram-negative bacterium found in large intestine of mammals. Microbial cells *E. coli* were grown in nutrient media LB Broth (Luria/Miller), microbial cells *B. subtilis* in nutrient media MPB (pepton, beef extract, NaCl, pH 7,0). For preparation of the solid media, the nutrient media was supplemented with 2% bacteriological agar as solidifying agent. The tested thin films were placed into sterile chambers and covered with 1 ml of the overnight cultures *E. coli* or *B. subtilis* diluted to cell concentration of 10^6 CFU/ml. The sterile chambers were cultivated at 35°C and aliquots of 100 µl were taken and diluted up to 10^{-6} after 8 hours. 100µl of each diluted sample were spread over the agar plates, incubated for 48 hours and then the number of growing colonies was counted.

Results and Discussion

The morphology and topology of the films were studied by scanning electron microscopy (SEM) and atomic force microscopy (AFM), which revealed closed, uniform and homogeneous DLC and UNCD coatings. The DLC layers are extremely smooth with rms roughness between 0.2 and 0.6 nm; only DLC 10, 0.5 A shows higher rms roughness of 4.2 nm, probably due to the higher energy of the bombarding ions used during the deposition. The rms roughness of UNCD layers was on the order of 9 - 14 nm.

The XPS survey spectra reveled only carbon and oxygen peaks for the DLC films. The O concentration (6 - 9%) was the same for all samples under investigation. The percentage of sp^2 and sp^3 hybridized carbon atoms in them was estimated by peak-fitting of the high resolution C1s core spectra using Gaussian functions. It was found that depending on the laser energy density and the energy of the bombarding Ar^+ the amorphous films contained from 58% to more than 80% of sp^3 bonds (see Table 1). The ion bombardment increased in general the content of the sp^3 bonds due to increased mobility of the condensing atoms and implantation of atoms under the surface [9, 11]. The UNCD films were composed of diamond nanocrystallites (3-5 nm in diameter) embedded in an amorphous carbon matrix, containing up to 30% sp^2 bonds, also determined by deconvolution of the C1s core spectra. The ratio of the crystalline and amorphous fractions is closed to 1.

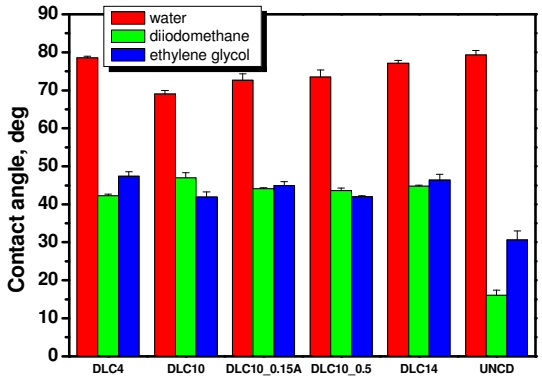


Figure 2: Wettability of DLC and UNCD films with water, diiodomethane and ethylene glycol

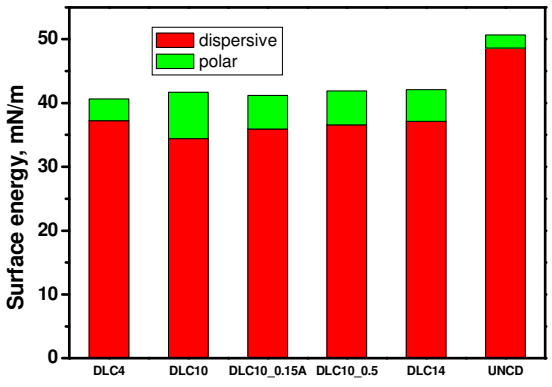


Figure 3: Total surface energy γ of DLC and UNCD films shown with dispersive γ^d and polar γ^p components

Contact angle measurements were used to probe the wettability of the DLC and UNCD films. The water contact angle for all DLC films was between 69° and 79°, for UNCD it was 79° (Fig. 2). In a similar way the contact angles for the other two test liquids, ethylene glycol (less polar than water) and diiodomethane (non-polar) do not differ substantially for all DLC films, while they are lower for the

UNCD films. In this case the surface is hydrogen terminated, as shown in previous studies, which determines the wettability. Based on these data, the surface energy of the DLC and UNCD was calculated. The total surface energy γ can be described as the sum of a dispersive γ^d and a polar γ^p component.There are not significant changes in the surface free energies for DLC layers deposited under different conditions. However, the surface energy of the UNCD layers is slightly higher, with higher disperse and lower polar component (Fig. 3)

The bactericidal efficacy of different diamond-like-carbon thin films on *E. coli* and *B. subtilis* strain was estimated according the formula:

$$\text{(bactericidal efficacy) (\%)} = \frac{\text{(alive number in reference group)} - \text{(alive number in experiment group)}}{\text{(alive number in reference group)}} \times 100\ \%$$

All DLC and UNCD films under investigation showed very good antibacterial efficiency as shown in Figure 4.

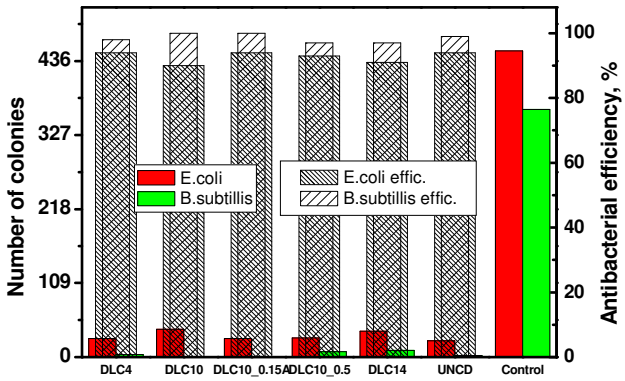


Figure 4: Number of *E. coli* and *B. subtillis* colonies on DLC and UNCD films and the respective antibacterial efficiency

Conclusions: DLC and UNCD films under investigation exhibit high antibacterial efficiency which could be related to their surface properties including high smoothness, hydrophobicity and high dispersive component of the surface energy.

Acknowledgements: The authors gratefully acknowledge the Institutional research plan AV010100522, grant of the Czech Technical University in Prague SGS12/167/OHK4/2T/17 and the Ministry of Education, Youth and Sports of the Czech Republic for grants COST LD12069.

References

[1] C. Dumkum, D.M. Grant, I.R. McColl, Diamond and Related Materials 6, 802 (1997)
[2] H.S. Tran, M.M. Puc, C.W. Hewitt, D.B. Soll, S.W. Marra, V.A. Simonetti, J.H. Cilley, A.J. DelRossi, Journal of Investigative Surgery 12, 133 (1999)
[3] J. Robertson, Surface and Coatings Technology 50,185 (1992)
[4] F.Z. Cui, D.J. Li, Surface and Coatings Technology 131, 481 (2000)
[5] R. Hauert, U. Muller, Diamond and Related Materials 12, 171 (2003)
[6] P. May, Philosophical Transactions of the Royal Society London A 358, 473 (2000)
[7] T. Kocourek, M. Jelínek, V. Vorlíček, J. Zemek, T. Janča, V. Žížková, J. Podlaha, C. Popov, Applied Physics A 93(3), 627 (2008)
[8] M. Jelínek, T. Kocourek, J. Remsa, J. Mikšovský, J. Zemek, K. Smetana, B. Dvořánková, T. Luxbacher, Applied Physics A 101 (4), 583 (2010)
[9] M. Jelínek, P. Písařík, T. Kocourek, J. Zemek, J. Lukeš, Applied Physics A- in print
[10] D.A. Shirley, Physical Reviews B 5(12), 4709 (1972)
[11] J. Robertson, Diamond and Related Materials 2 (5-7), 984 (1993)

PO 3043: New methods for reprocessing of medical devices based on plasma treatment

Jörg Ehlbeck, Uta Schnabel, Manfred Stieber, Jörn Winter, Martin Polak, Udo Krohmann, Klaus-Dieter Weltmann
Leibniz Institute for Plasma Science and Technology, Felix-Hausdorff-Str. 2, 17489 Greifswald, Germany

Introduction

The rapid progress in the development of new devices for minimal invasive surgery leads to more complex and fragile instruments including a mixture of different materials most of them thermo labile. In consequence these instruments become more and more expensive which increases the demand for reuse. By now, the manufacturer are obligated to specify the reprocessing procedure which may be a restriction in the development of new products. Therefore, there is a real need for new reprocessing procedures.
Especially, plasma processes are commonly discussed as a promising alternative although only few plasma based techniques are currently commercial available.

Three examples for plasma based reprocessing are discussed in detail:

1. Classical gas sterilization device: Based on commercial steam sterilizers of low temperature and formaldehyde (LTSF). The formaldehyde unit is replaced by plasma gas generator based on the PLexc® technology developed at INP. This plasma based decontamination technique was tested on long tubes similar to biopsy channels of endoscopes.
2. Atmospheric pressure plasma coating with nanoparticles in order to generate antimicrobial acting surfaces. With a special treatment unit based on the principle of a dielectric barrier discharge the inner surfaces of tubes are coated with nanoparticles.
3. "Plasmoscope": using special plastic tubes, which include a helical electrode structure it is possible to manufacture endoscopes which allow plasma operation in their biopsy channel. This plasma can either used for decontamination, a reprocessing or under modified operation condition also for therapeutically applications. To simulate the complete reprocessing procedure the "plasmoscope" can be integrated in a reprocessing demonstrator allowing the combination of cleaning and decontamination steps.

Classical gas sterilization device

The prime father of all plasma gas decontamination devices was the ozone tube invented in 1857 from Werner von Siemens. In 1898 the company Siemens&Halske delivers first industrial scale water plants to the waterworks of Wiesbaden-Schierstein and Paderborn in Germany [1, 2] based on this technology and up to now the main application of ozone is drinking water purification. But the generation of ozone is only one example to use the process gases of plasma for decontamination applications. According to the gas temperature the composition of the plasma changes and with increasing temperature the dominant decontaminating species changes from reactive oxygen (ROS) to reactive nitrogen species (RNS). As DBD and Corona discharges are good choices for generating ROS, microwave discharges become interesting for the generation of RNS.

For the generation of ROS and RNS the atmospheric pressure region is preferred due to higher species densities and lower equipment costs. Unfortunately, microwave plasma sources at atmospheric pressure suffer from two kinds of difficulties:

1. Stable ignition is a problem because of the low electrical field strengths generated by the applied microwave field [3, 4]
2. Wall burning: the microwave plasma has the tendency to move towards the source of radiation which usually destroys the device within short time [5]

To a certain extend these problems are solved by the special plasma source PLexc® developed by INP, s. Figure 1. This plasma source is described in details elsewhere, e.g.[6].

In order to apply this technique to a complex reprocessing problem endoscopic biopsy channels are chosen as a critical object. These channels are made of thermo labile materials as e.g. PTFE, and their typical dimensions are length of 1m and an inner diameter of 2 mm. Therefore the specimen are chosen in the same dimensions.



Figure 1: microwave excited plasmasource PLexc® developed by INP

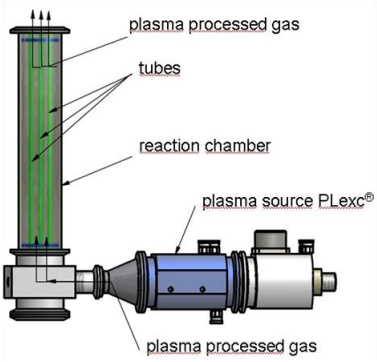


Figure 2: PLexc® gas treatment device for plastic tubes

The treatment of the specimen is performed in a tube which has a length of 1.1 m and an inner diameter of 50 mm and serves as process chamber. The size of the chamber allows the simultaneously treatment of up to 3 specimen. The plasma treated gas is supplied from the bottom as depicted in Figure 2. The plasma device was operated for 10 s to ensure a complete gas exchange in the process chamber. The overall incubation time was set to 30 min in order to allow the gas to diffuse into the lumina of the specimen. The results are shown in Figure 3. This technique is now integrated into a commercial available formaldehyde sterilizer by removing the formaldehyde system and implementing the PLexc® source instead, see Figure 4. For more details see [7].

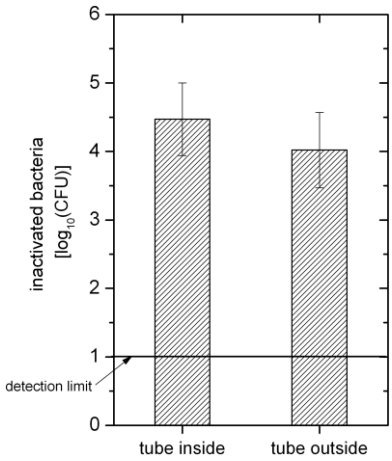


Figure 3: results of plasma gas treatment of PTFE tubes as specimen for biopsy channels of flexible endoscopes



Figure 4: commercial sterilizer with integrated PLexc® plasma source

Atmospheric pressure plasma coating with nanoparticles

Antimicrobial surface, as can be achieved by e. g. coatings, can act as an alternative or addition to classical inactivation processes. These coatings are especially helpful in cases where reprocessing is known to be critical, such as biopsy channels of flexible endoscopes. The coating is based on nanoparticles, see [8], which have to be fixated by a plasma process in order to withstand the shear forces in a biopsy channel.

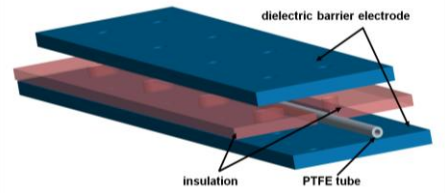


Figure 5: Scheme of DBD setup



Figure 6: Photograph of realized setup

"Plasmoscope": using special plastic tubes, which include a helical electrode structure

The reprocessing of flexible endoscopes is mandatory due to the high costs of these devices. Unfortunately the reprocessing is difficult because of two reasons:

1. The devices are made of a complex mixture of sensitive materials. e. g. plastic tubes several kinds of glue, optics etc.. In most cases they a thermo labile and scratch sensitive due to the necessary high bending properties.
2. The flexible endoscopes have a complex geometry, especially the long fine lumen of the biopsy channels which is highly contaminated after the usage.

All gas sterilization processes, as e. g. ethylene-oxide- (EtO), low-temperature-steam-and-formaldehyde- (LTSF) or hydrogen-peroxide-sterilizers suffer from the transportation problem which is without any special equipment limited by diffusion. The new idea is to implement the plasma directly into the endoscope so that the antimicrobial effect is generated directly where it is needed and without a change in the essential bending properties.

This can be achieved by a modification of the tube used for the endoscope channel, as shown in [9].

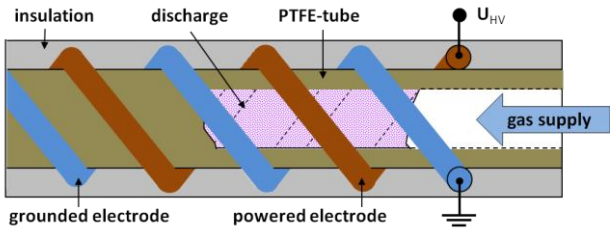


Figure 7: Scheme of the bifilar setup

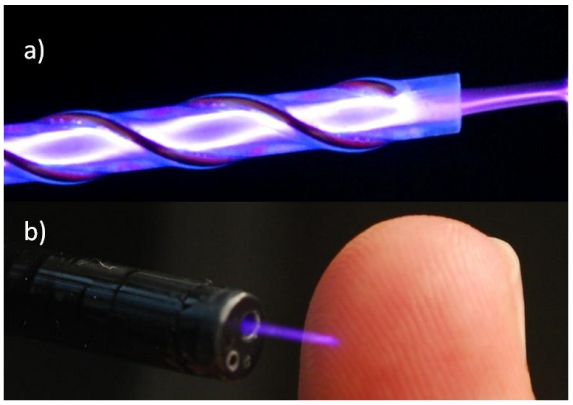


Figure 8: Photographs of a tube with the bifilar electrode structure a) and the realization of this technique in an endoscope b)

For the complete reprocessing of endoscopes equipped with this technique special reprocessing equipment is needed. In order to simulate the reprocessing process a demonstrator is build up which is capable of different cleaning and plasma inactivation steps, see Figure 9.



Figure 9: Demonstrator for a reprocessing unit for endoscopes equipped with bifilar plasma generator

Acknowledgement

The work is partly supported by the BMBF under the contract acronyms and numbers: Endoplas 13N9320 and Nanogiene 13N11358.

Key words (5 words)
non-thermal plasma; atmospheric pressure plasma; plasma coating plasma decontamination; nanoparticles

Literature

[1] Roeske, Wolfgang; Ritter, Klaus: *Trinkwasserdesinfektion : Grundlagen, Verfahren, Anlagen, Geräte, Mikrobiologie, Chlorung, Ozonung, UV-Bestrahlung, Membranfiltration, Qualitätssicherung*. 2. Aufl. /. Aufl. München: Oldenbourg Industrieverlag, 2007

[2] Kogelschatz, U.; Eliasson, B.; Egli, W.: From ozone generators to flat television screens: history and future potential of dielectric-barrier discharges. *Pure and Applied Chemistry* 71 (1999) 10, 1819-1828

[3] Rackow, K.; Ehlbeck, J.; Krohmann, U.; Baeva, M.: Microwave-based characterization of an atmospheric pressure microwave-driven plasma source for surface treatment. *Plasma Sources Science & Technology* 20 (2011) 3

[4] Pipa, A. V.; Andrasch, M.; Rackow, K.; Ehlbeck, J.; Weltmann, K. D.: Observation of microwave volume plasma ignition in ambient air. *Plasma Sources Science & Technology* 21 (2012) 3

[5] Baeva, M.; Luo, X.; Schafer, J. H.; Uhlenbusch, J.; Zhang, Z.: Experimental and theoretical studies of a pulsed microwave excited Ar/CF4 plasma. *Plasma Chemistry and Plasma Processing* 18 (1998) 4, 429-446

[6] Ehlbeck, J.; Schnabel, U.; Polak, M.; Winter, J.; von Woedtke, T.; Brandenburg, R.; von dem Hagen, T.; Weltmann, K. D.: Low temperature atmospheric pressure plasma sources for microbial decontamination. *Journal of Physics D-Applied Physics* 44 (2011) 1

[7] Weltmann, Klaus-Dieter; Winter, Jörn; Polak, Martin; Ehlbeck, Jörg; Woedtke, Thomas; Machala, Zdenko; Hensel, Karol; Akishev, Yuri: *Atmospheric Pressure Plasmas for Decontamination of Complex Medical Devices Plasma for Bio-Decontamination, Medicine and Food Security.* Springer Netherlands, 2012, S. 3-15

[8] Gerold Lukowski, Martin Polak, Jörn Winter, Christian Lösche, Klaus-Dieter; Weltmann, Ulrike Lindequist, Jörg Ehlbeck: Nanostructured coating of endoscopes against MRSA contamination using atmospheric plasma sources (PSE, Garmisch Patenkirchen, 2012)

[9] Polak, M.; Winter, J.; Schnabel, U.; Ehlbeck, J.; Weltmann, K. D.: Innovative Plasma Generation in Flexible Biopsy Channels for Inner-Tube Decontamination and Medical Applications. *Plasma Processes and Polymers* 9 (2012) 1, 67-76

FABRICATION AND PLASMA MODIFICATION OF POLYMER SCAFFOLDS FOR REGENERATIVE AND REPLACEMENT MEDICINE.

Victor N. Vasilets[1,2], Valentina A. Surguchenko[1,3], Viktor I. Sevastianov[1,3],
vnvasilets@gmail.com
[1]Academician V.I. Shumakov Federal Research Center of Transplantology and Artificial Organs
Moscow, Russia
[2]Institute for Energy Problems of Chemical Physics, Russian Academy of Sciences
Chernogolovka, Russia
[3]Institute of Biomedical Research and Technology, Moscow, Russia

Introduction

Materials that serve as analogues for the native extra-cellular matrix (ECM) can be used in medicine to aid in either the reconstruction or regeneration of damaged tissue and organs. Polymer matrices have been used for regeneration of bone, liver, pancreas, skin and other tissues [1]. Macroporous. biodegradable polymer scaffolds have been prepared by numerous techniques including solvent casting/salt leaching, phase separation, solvent evaporation, and fiber bonding to form a polymer mesh.

The main goal of this research was to apply novel physical processing techniques to fabricate and modify highly porous implantable biodegradable scaffolds. More specifically, this involves fabricating scaffolds using electrospinning, piezoelectric printing, gel sublimation techniques and finally modification of matrixes by plasma treatment in order to control chemical structure and morphology of scaffolds.

Materials and Methods

Poly(oxybutirate-co-valerate), POB (Aldrich, USA) and collagen containing heterogenic biopolymer hydrogel (HBH) (BIOMIR service, Russia) obtained from hydrolyzate of farm animal tissues [2] , were used for preparation of polymer scaffolds and 2D predefined structures by electrospinning, piezoelectric printing and gel sublimation methods.

The homemade apparatus used for electrospinning included a pump driven by stepping motor, a high voltage power supply and a syringe as the reservoir for the polymer solution to which an blunt-end needle was attached. The stainless plate (10.0 cm * 8 cm * 0.5 cm) was used as the collection target. All electrospinning parameters including applied voltage (10 – 25 kV), distance between the needle and grounded plate (10 – 25 cm), solution dispensing rate (0.2 - 2mL/min) and concentration of polymer in methyl chloride (5 -15 %). could be changed to optimize the morphology of scaffolds. Three milliliters of solution was electrospun for each matrix.

Piezoelectric ink jet printing is a thermally constant process that can be carried out at room temperature or in a localized cold environment. The piezoelectric printhead consists of a piezoelectric transducer, nozzles, manifolds, ink pumping chambers, and fluid inlet passages. When a voltage is applied to the lead zirconate titanate (PZT) piezoelectric transducer, the transducer deforms and creates mechanical vibrations. For example, the ink jet cartridge in the Dimatix Materials Printer DMP 2831 used in these experiments is powered by a thin piezoelectric unimorph, which is constructed in the plane of the wafer. This structure consists of patterned PZT bonded to a silicon diaphragm. Actuation of the PZT piezoelectric transducer is in the plane of the wafer (bender mode). A die consists of 16 individually addressable jets

that release drops perpendicular to the wafer from an array of inline nozzles that are spaced 254 μm apart. The effective diameter of the nozzle is 21.5 μm, which provides a drop in the ~10 pL range.

Gel sublimation at low temperature was used for the fabrication of scaffolds from the cooled mixture of POB with two solvents: acetic acid and carbon tetrachloride. Due to the different crystallization parameters of these solvents a two dimensional porous structure was formed in the process of pumping the mixture and removing the solvents at low temperature. The morphology of the matrix could be varied by changing the relative concentration of the solvents and pumping temperature.

After fabrication polymer scaffolds were placed between the electrodes of dielectric barrier discharge (DBD) in atmospheric air (22kV, 5μs pulse duration) in order to modify their surface chemical composition and improve biocompatibility. ATR FTIR spectroscopy was used to analyze surface chemical composition before and after plasma treatment. The morphology of polymer scaffolds was investigated by AFM and SEM techniques

Biocompatibility of polymer scaffolds was estimated by different biological tests: hemolysis, cell toxicity and cell proliferation experiments. Fibroblast cells NIH 3T3 were used for cell toxicity and cell proliferation testing experiments.

Results and discussion

Figure 1 shows SEM pictures of polymer scaffolds fabricated from POB by electrospinning technology. By variation the main parameters of the electrospinning process listed above it was possible to change the fibers diameter in the range 0.1 -10 microns and verify porous size in the range 10 – 50 microns.

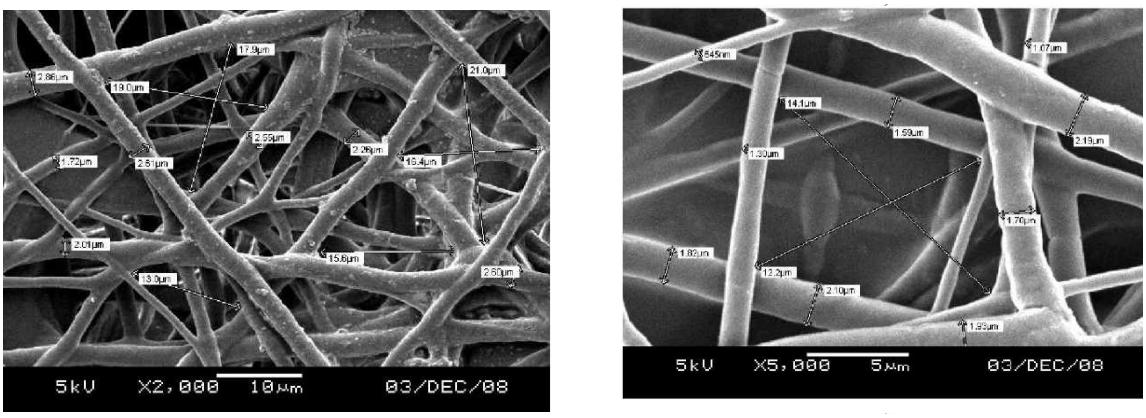


Figure 1. SEM pictures of polymer scaffolds fabricated by electrospinning technology from POB

The matrix presented at Figure 1 was fabricated after optimization of electrospinning parameters to obtain homogeneous and free of defects structure for the POB concentration 15%wt. The optimized structure for this concentration was obtained at the distance between the needle and grounded plate 10 cm and applied voltage 25 kV. The diameter of the fibers in this matrix was in the range 2 – 3 microns and the distance between fibers was 15 – 20 microns approximately. Estimated porosity of this scaffold was in the range 95 – 97%.

The optimum viscosity for jettable fluids in piezo drop-on-demand printheads is ~8–14 mPas (8–14 cps). However, most biological materials including collagens exhibit very low viscosities (0.1–1 cps) and very high surface tension values (58–60 cps dynes/cm). As a result, it is important to be able to adjust the operating parameters of the ink jet printhead to successfully jet low viscosity fluids. In our experiments it was possible to adjust the frequency of the waveform, the voltage to individual nozzles, and the structure of the waveform that drives the movement of the PZT piezoelectric transducer for Dimatix Materials printing system. The collagen containing solution of HBH (in 1.5% acetic acid) was dissolved in phosphate buffer saline (PBS) to the concentration 1mg/ml. Tween 80 surfactant (0.1%; Fisher Scientific, Fair Lawn, NJ, USA) was added to prevent aggregation of collagen. The protein solution was maintained at 28°C, purged through the printhead for uniform droplet formation and then calibrated at a constant velocity of 0.58 m/s for all nozzles prior to deposition. The solution of HBH was printed directly on poly(ethyleneterephthalate) (PET) substrates to develop microscale 2D patterns of materials for possible medical and biological applications. The patterned materials have been examined using several characterization techniques, including optical microscopy, atomic force microscopy, and electron microscopy. Figure 2 shows the optical pictures of the predefined porous structure printed from HBH on PET substrate..

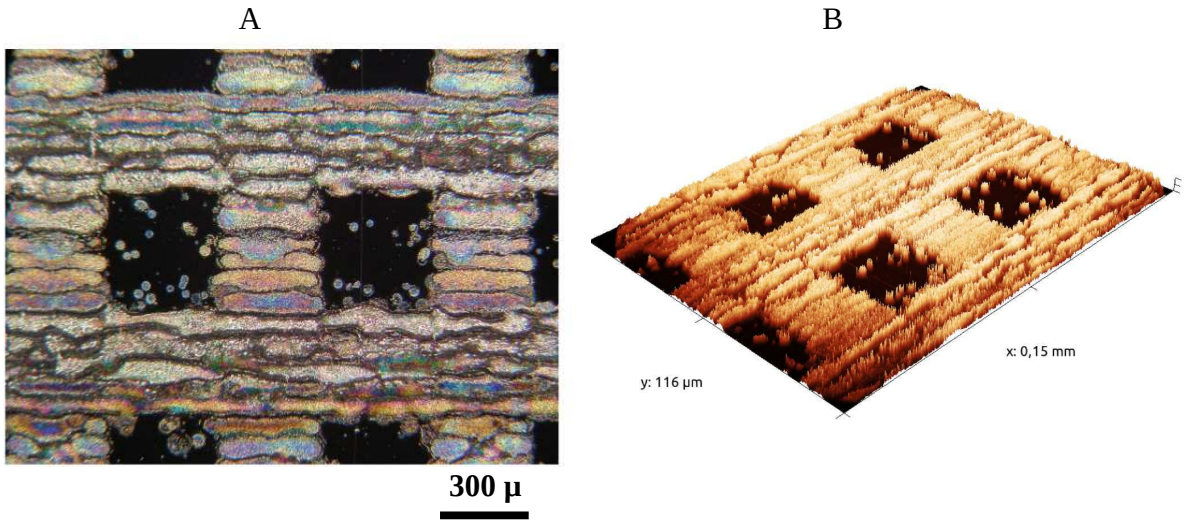


Figure 2. Optical pictures of predefined structures printed from hydrolyzed collagen solution on PET film (A), 3D reconstruction of optical images

The structure with the thickness about 50 microns was obtained after 20 layers printing of collagen containing HBH. According to the computer template used for printing, the structure contains rectangular holes with the size 300 *300 microns. These images presented on Figure 2 (A,B) demonstrate that high resolution microscale features may be obtained for collagen containing structures using piezoelectric ink jet digital fabrication technology.

The porous structure with bi-modal controllable distribution function was fabricated from POB by gel sublimation method. Depending on the relative concentrations of acetic acid and carbon tetrachloride solvents different porous structure was obtained after pumping the binary solution of POB in vacuum chamber. The process of gel sublimation technique consists of the

few stages. At first the mixture of POB with acetic acid and carbon tetrachloride was cooled to the frozen temperature -25 - -30C and stored in the refrigerator for 24 hours. After that the frozen sample was placed in vacuum chamber and pumped at the pressure about 100 Torr for 2-3 hours to remove the solvents and fabricate a porous structure.

As shown in Figure 3 the bi-modal porous structure is fabricated by this gel sublimation method.

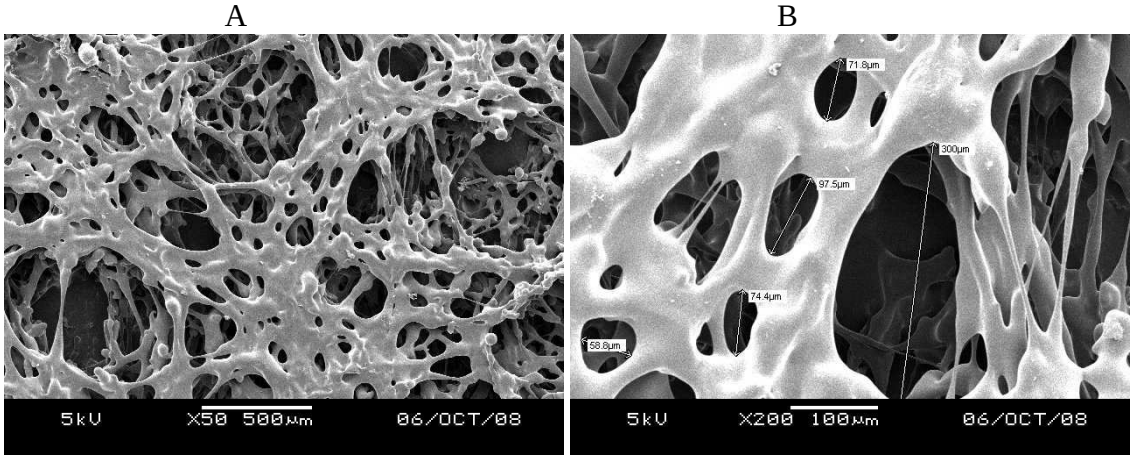


Figure 3 SEM pictures porous structure obtained by gel sublimation method at different magnifications x50 (A) x200 (B)/

The two types of pores are formed as a result of elimination of two differently crystallized solvents. The size of small pores is varied in the range of 5 – 30 microns, while the size of large pores is ranged in 100 – 300 microns.

In order to improve hydrophilicity and biocompatibility of scaffolds obtained by electrospinning and gel sublimation techniques the POB porous structures were treated by atmospheric pressure DBD discharge at different dosages. Plasma treatment leads to the formation of carboxylic groups and provides the increase of polymer surface energy and hydrophilicity as it was proved by ATR FTIR and contact angle measurements [3]. According to various biological testing procedures polymer scaffolds obtained by new fabrication technologies and treated by DBD plasma at optimal conditions have shown no toxic reactions and improve cell proliferation .behavior.

Conclusions

Polymer scaffolds obtained by electrospinning, piezoelectric printing or gel sublimation technologies and treated by atmospheric pressure DBD discharge could provide the attachment and proliferation of various cells and may be used as pre-defined scaffolds in various tissue engineering applications.

References

1. Sevastianov V.I., Vasilets V.N., Agapov I.I., Rare Metals, v. 28, Spec. Issue, p. 84, 2009.
2. Patent of Russian Federation, 2011, № RU 2433828.
3. Vasilets V.N., Kuznetsov A.V., Sevastianov V.I., High Energy Chem., v.40, N 2, p. 79, 2006.

The corrosion properties of zirconium and titanium load-bearing implant materials with protective oxide coatings

Anna Zykova[1,2*], Vladimir Safonov[2], Jerzy Smolik[3], Renata Rogowska[3], Vladimir Luk'yanchenko[4], Oleg Vyrva[5], Stas Yakovin[6]

[1]Institute of Surface Engineering, Kharkov, Ukraine
[2]National Science Centre „Kharkov Institute of Physics and Technology", Kharkov, Ukraine
[3]Institute for Sustainable Technologies, National Research Institute, Radom, Poland
[4]Inmasters Ltd, Kharkov, Ukraine
[5]Sytenko Institute of Spine and Joint Pathology, Kharkov, Ukraine
[6]Department of Physical Technologies, Kharkov National University, Kharkov, Ukraine

Abstract. At present study the comparative analysis of parameters for oxide Al_2O_3 and ZrO_2 films deposited by reactive magnetron sputtering (RMS) method on the load-bearing implant materials such as titanium-based (Ti4Al6V) and Zr has been made. The corrosion examinations of anodic polarization by potentiodynamic method, Tafel and Stern curves and also impedance method at SBF solution were presented.

Keywords: Corrosion protection; Magnetron sputtering; Biocompatibility.
PASC: *81.65.Kn; 87.85.jj*.

1. Introduction

Good mechanical properties, coupled with excellent biocompatibility and corrosion resistance properties have made titanium and alloys the most popular materials for various biomedical applications. But more demanding expectations for orthopedic and trauma defects reconstruction are driving the development of alternative bearing materials. Zirconium and alloys are presented as alternative to other load-bearing materials in order to increase the biocompatibility for needs of metal sensitive (Ti, V, Al) patients.

Novel functional coatings are widely applied in different industrial areas due to the high hardness and wear resistance properties [1]. However, many of such applications require the high stability in an aggressive and corrosive environment.

Corrosion is one of the major processes that cause problems when metals and alloys are used as implants in the body [2]. Corrosion of implants in the aqueous medium of body fluids takes place via electrochemical reactions [3]. The body fluid environment may well decrease the fatigue strength of the metal implant and enhance the release of iron, chromium, nickel, titanium ions and these ions are found to be powerful allergens and carcinogens [4]. The presence of titanium in the surrounding tissues of these implants in the form of titanium compounds and subsequent failure of implants due to fatigue, stress corrosion cracking and poor wear resistance have been reported [5,6]. Release of metal ions into the tissues adjacent to the implants results in accumulation of harmful products at tissue and internal organs of animals [7]. The comparative analysis of corrosion properties of zirconium and titanium materials with novel oxide coatings deposited by reactive magnetron sputtering method (RMS) is of great interest for next biomedical applications

2. Materials and Methods

The substrates for deposited coatings were the popular load-bearing implant materials such as titanium-based alloy (Ti4Al6V) and Zr samples. The substrates were ultrasonically cleaned in acetone, ethanol and deionised water in sequence and next were dried in dryer.

The oxide Al_2O_3 and ZrO_2 (RMS) coating deposition was performed in high vacuum pumping system with the base pressure about 10^{-5} mBar. The main details of the magnetron

* Corresponding author. E-mail: zykova.anya@gmail.com
Tel.: +38 066 776 5852

and ion source in the sputtering chamber were demonstrated at [8]. The magnetron discharge power was 1-4 kW, power of activated oxygen source up to 1 kW, coating deposition rate 8 μm/hour. There was the problem of target oxidation during deposition process. At the excessive oxygen flow conditions the process shifts to the target passivation regime (lower part of. volt-ampere characteristics (VAC) curves Fig.1) The sputtering process should be made in the regimes far from the target passivation areas both for aluminum and for zirconium target materials for next oxide coatings deposition with highly stoichiometric composition. Also, such deposition conditions allow to avoid micro-arcs and micro-drops formation increasing the corrosion resistance properties. The optimum conditions were realized for the upper part of VAC curves of magnetron discharge in argon with oxygen both for aluminum and zirconium target materials (Fig. 1 a, b).

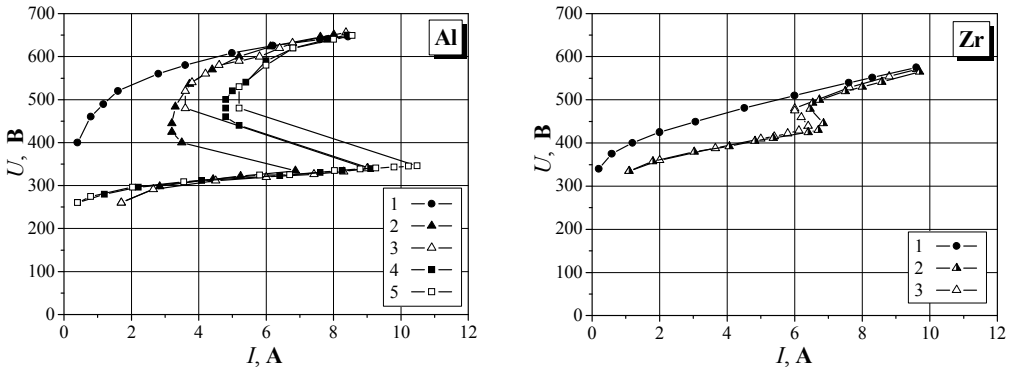


Fig.1. Volt-ampere characteristics of magnetron discharge in argon with oxygen a) aluminum target, b) zirconium target. The pressure Ar was 6 10^{-2} Pa, oxygen flow 1-q=0 sm^3/min, 2,3 –q=17 sm^3/min, 4,5-q=26 sm^3/min for aluminum target material and 1-q=0 sm^3/min, 2,3 –q=35 sm^3/min for zirconium target material.

The coatings adhesion properties, hardness and elastic modulus, were evaluated by standard methods with the use of Revetest (CSEM) and the Rockwell indenter with the tip radius 200 μm, within the load range 200N [9].

The comparative analysis of corrosion parameters for oxide Al_2O_3 and ZrO_2(MS) coatings has been made. The corrosion examinations of anodic polarization by potentiodynamic method at the potential range -1.0V-+2.0V with scanning rate 1mv/s, Tafel -0.050V - +0.050V and Stern - -0.020V-+0.020V range curves and also impedance method for frequency range 100 kHz – 10 MHz at SBF(NaCl-8,035, $NaHCO_3$-0,355, KCl-0,225, K_2HPO_4 $3H_2O$-0,231, $MgCl_2$ $6H_2O$-0,311, $CaCl_2$-0,292, Na_2SO_4-0,072 at pH=7.4 and temperature 37^{o}C) solution were made by Potentiostat PARSTAT 2263 (AMETEK, USA).

Electrochemical Impedance Spectroscopy (EIS) is a powerful analysis technique, which can provide a lot of information on the corrosion reactions, the mass transport and electrical charge transfer characteristics of coated materials in various solutions. The impedance spectrum reflects dielectric behaviour, oxidation-reduction reactions and mass migration, which are determined by the electrical and chemical properties of the corrosion medium and the electrode materials. Over a frequency bandwidth of interest the impedance was presented in various ways by both the Nyquist and Bode plots. EIS spectra describe the electrical charge transfer kinetics and details of physical and electrochemical corrosion characteristics of substrate/coating interface. EIS measurements were obtained at SBF solution. Platinum and Ag/AgCl wires were used as counter and reference electrodes, respectively between the frequency ranges 100 kHz-10 MHz at constant 5mV amplitude and 250mV initial potential for all measurements. The impedance parameters $|Z|$, polarization resistance R_p and capacitance C_d were calculated from Nyquist and Bode plots. The surface topography and corrosion failure after corrosion test was investigated by means of Interferometric Microscope Talysurf CCI (Taylor Hobson) and AFM (Quesant Instrument Corporation, USA).methods.

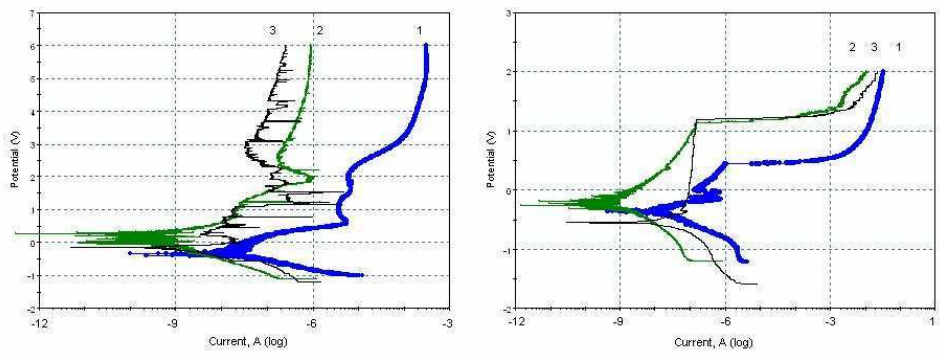
3. Results and Discussion

The mechanical parameters of the oxide Al_2O_3 and ZrO_2(RMS) coatings deposited on the Ti and Zr substrates were presented in the Table 1.

Table 1.
Mechanical and tribological characteristics of oxide coatings Al_2O_3 and ZrO_2

Material/	Mechanical parameters (average results 10 tests)			
Coating type	Hardness Hv	Hardness H [Mpa]	Young Modulus [Gpa]	Adhesion [N]
Zr/ZrO_2	755.5	7831.5	167.7	28.5
Zr/ Al_2O_3	782.0	8115.2	184.4	27.1
Ti/ZrO_2	767.5	8072.4	172.3	38.4
Ti/ Al_2O_3	953.6	8289.9	197.0	40.3

The corrosion tests of anodic polarization by potentiodynamic method at the potential range -1.0V-+2.0V with scanning rate 1mv/s were presented in Fig.2a for Ti, Ti/Al_2O_3, $Ti//ZrO_2$ and Fig. 2b for Zr, Zr/Al_2O_3, Zr/ZrO_2 coatings at SBF solution and by Tafel -0.050V - +0.050V and Stern - -0.020V-+0.020V range curves, The impedance spectra of all samples were

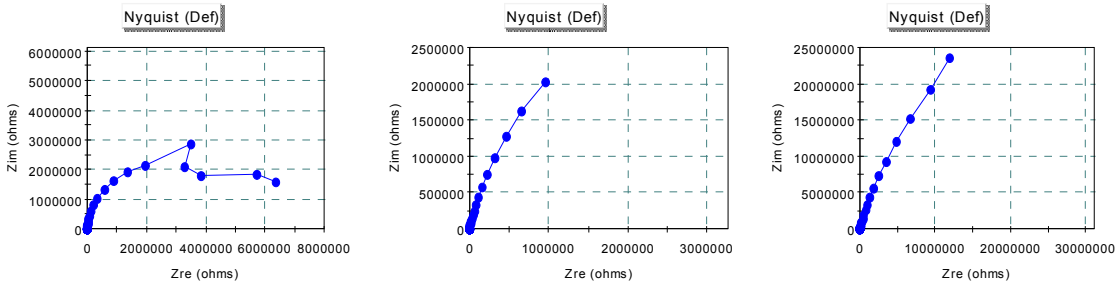


a) b)

Fig. 2. The anodic polarization curves for a) 1-Ti, 2-Ti/ZrO_2, 3-Ti/Al_2O_3, and b) 1-Zr, 2-$Zr//ZrO_2$, 3-Zr/Al_2O_3 coatings at SBF solution

recorded before and after polarization conditions, to evaluate the performance of the coatings under equilibrium conditions and after the onset of the corrosion process respectively.
The Nequist plot of impedance was obtained from real ($Z_{re}= R_s+R_p/(1+\omega^2R_p^2C_d^2)$) and imaginary ($Z_{im}= \omega R_p^2C_d /(1+\omega^2R_p^2C_d^2)$) impedance at different frequencies to determine charge-transfer kinetics (R_s is electrolyte solution resistance, R_p is polarization resistance and C_d is capacitance at interface). Fig. 3. show the Nyquist plots for Zr, Zr/ Al_2O_3 and Zr/ZrO_2 coatings respectively at SBF solution.

.



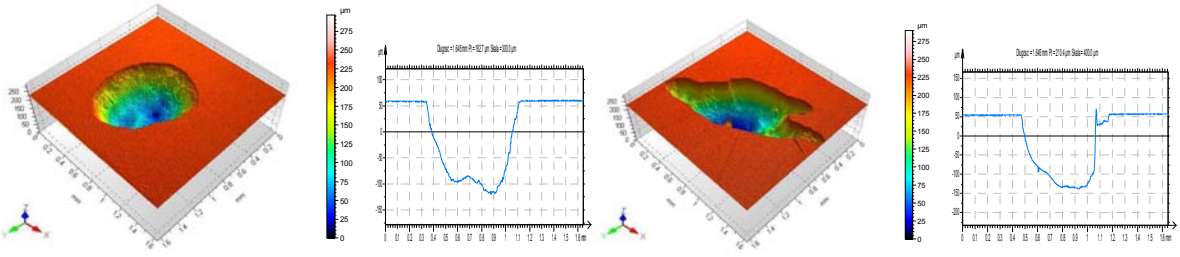
a) b) c)

Fig. 3. Nyquist plots for a.)Zr, b.)Zr/ Al_2O_3, c.)Zr/ZrO_2 materials at SBF solution

The data show that coating deposition had improved charge-transfer kinetic performance in counter electrode-electrolyte interfaces. The surface with ceramic oxide coatings has strong capacitive response due to their electrically inert properties and high dielectric constants. The surface topography and corrosion failure after corrosion tests was investigated by Interferometric Microscope Talysurf CCI and AFM methods

The Figure 4 demonstrate the images of surface failure after corrosion test at SBF solution and the data further confirmed the main results of polarization curves and EIS measurements.

.



a) b)

Fig. 4. The surface topography and failure after corrosion test at SBF solution by IM:

a) Zr/ Al_2O_3, b) Zr/ZrO_2 coatings

4. Conclusion

The technology is developed allowing to obtain the highly stoichiometric oxide coatings deposited by means of RMS method with hardness parameters up to 9 GPa, adhesion up to 40N and improved corrosion resistance properties both on titanium and zirconium substrate materials. The results show that the best corrosion resistance characteristics at SBF solutions have the oxide coated Ti/ Al_2O_3 and Zr/ZrO_2 ceramic materials. Zirconium with oxide coatings demonstrates the excellent protective properties and presents as alternative load-bearing material for various biomedical applications.

References

[1] A. P. Serro, C Completo, R Colaco, F dos Santos, C. Lobato da Silva, J M S. Cabral H.Araujo, E. Pires and B. Saramago, Surf. Coat. Techn. 203 (2009) 3701-3707.

[2] E. Eisenbarth, D. Velten, K. Schenk-Meuser, P. Linez, V. Biehl, H. Duschner, J. Breme, H. F. Hildebrand, Biomol. Eng. 19 (2002) 243-49.

[3] L. Dion, F. Bordenave, R. Lefebvre, C. V. Boreille, J.Mat. Sci.- Mat. Med. (1994) 18.

[4] D. J. Kim, M. H. Lee, D. Y. Lee and J. S. Han, J. Biomed. Mat. Res. 53 (2000) 438-43.

[5] B. D. Ratner, J. Biomed. Mat. Res. 27 (1993) 837-850.

[6] D. Velten, V. Biehl, F. Aubertin, B. Valeske, W. Possart, J. Breme, J. Biomed. Mat. Res. 59 (2002) 18-28.

[7] A. V. Zykova, V. V. Luk'yanchenko, V. I. Safonov, Surf. Coat. Techn 200 (2005) 90.

[8] A. Zykova, V. Safonov, V. Luk'yanchenko, J. Walkowicz, R. Rogovska, S.Yakovin, J. Phys.: Conf. Series 113 (2008) 1-5.

[9] A. Zykova, V. Safonov, V. Luk'yanchenko, et al. Probl. At. Sci. Technol.- Plasma Physics 15 (2009) 156-158.

Extended Abstract of the Thirteenth International Conference on Plasma Surface Engineering 2012, PO-3054

High rate PECVD of a-C:H coatings in a hollow cathode arc plasma

Burkhard Zimmermann[a], Fred Fietzke[a], Heidrun Klostermann[a],
Jan Lehmann[b], Frans Munnik[b], Wolfhard Möller[b]

[a] Fraunhofer-Institut für Elektronenstrahl- und Plasmatechnik FEP, Winterbergstraße 28, 01277 Dresden, Germany

[b] Institut für Ionenstrahlphysik und Materialforschung, Helmholtz-Zentrum Dresden-Rossendorf, Bautzner Landstraße 400, 01328 Dresden, Germany

Abstract

Amorphous carbon films deposited by plasma-based processes are of increasing importance for tribological applications, e. g. as protective coatings on components or in order to reduce their friction. However, most plasma-activated CVD and PVD techniques suffer from their poor deposition rate and low economic efficiency. At Fraunhofer FEP, a hollow cathode-based plasma source has been established as a versatile, reliable, and highly efficient tool for plasma pretreatment, plasma-enhanced PVD processes, and reactive gas activation in large volumes. As a further application field, this plasma source has been evaluated for PECVD of amorphous hydrogenated carbon films (a-C:H).

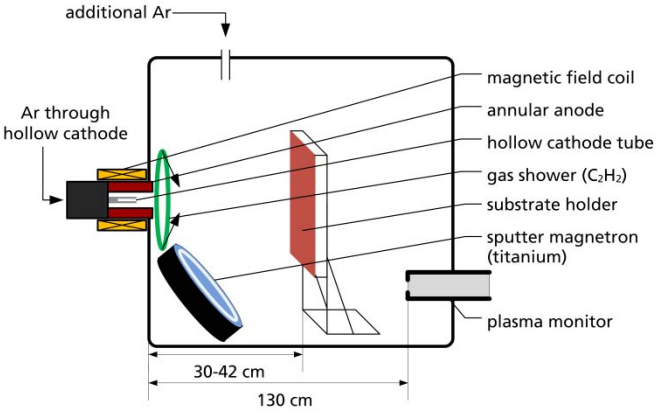
Acetylene has been introduced into the hollow cathode plasma as a precursor gas. The plasma composition has been characterized by an energy-resolved ion mass spectrometer. Intense ionization, dissociation, and polymerization effects have been observed, which strongly increase when the argon gas flow rate through the hollow cathode tube is reduced. Moreover, the ion energy distributions show high energy tails up to 100 eV in dependence of the spatial distribution of ion generation.

a-C:H films have been deposited on stainless steel and silicon substrates with growth rates up to 1000 nm/min. Nanoindentation measurement of the a-C:H coatings reveal hardness up to 18.2 GPa. In this paper, film properties and compositions will be discussed and related to the corresponding plasma conditions obtained by energy-resolved ion mass spectrometry.

1. Introduction

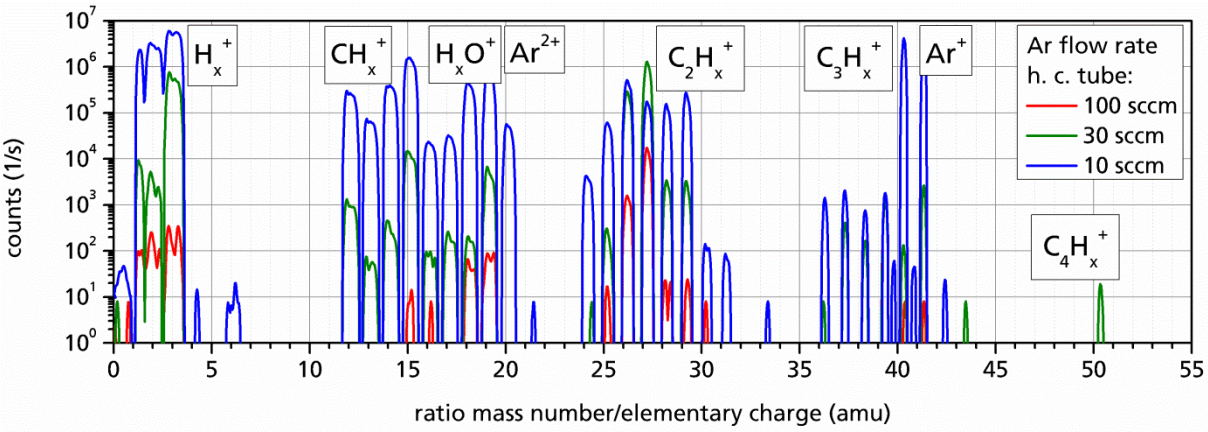
At Fraunhofer FEP, a magnetically enhanced arc hollow cathode has been established as a large volume plasma source (plasma density of 10^{10} -10^{12} cm^{-3} in a volume of several 100 l) for applications such as plasma etching, plasma-assisted evaporation (e. g. Al) as well as reactive magnetron sputtering (e. g. CrN) [1,2]. The magnetic field allows for drastic reduction of the working gas flow rate through the hollow cathode resulting in strongly increased plasma density and range [3]. In this paper, the hollow cathode arc plasma has been evaluated for plasma-enhanced chemical vapor deposition (arcPECVD) of amorphous hydrogenated carbon (a-C:H) films with very high rates up to 1 µm/min. a-C:H coatings can exhibit polymeric, graphitic, or diamond-like properties and are typically used as tribological coatings reducing wear or friction of components, or as biocompatible coatings e. g. on implants [4].

2. Experimental setup



The hollow cathode consists of a tantalum tube (length 75 mm, inner and outer diameter 4 and 12 mm, respectively) which is surrounded by a cylindrical anode. The discharge current was 100 A throughout the presented investigations. A magnetic field coil produces a magnetic field, which is axial within the cathode tube, where it reaches typically 60 mT. Whereas the working gas argon flows through the hollow cathode tube, the PECVD precursor acetylene (C_2H_2) is injected by a gas shower into the hollow cathode plasma. Furthermore, additional argon can be introduced into the vacuum chamber to maintain a certain argon partial pressure when reducing the gas flow through the hollow cathode.
Below the hollow cathode plasma source, a sputter magnetron PPS5 equipped with a titanium target is installed. The substrates are mounted on a water-cooled substrate holder face-to-face with the orifice of the hollow cathode tube. The plasma has been characterized by an energy-resolved mass spectrometer (plasma process monitor PPM 422, Balzers Instruments).

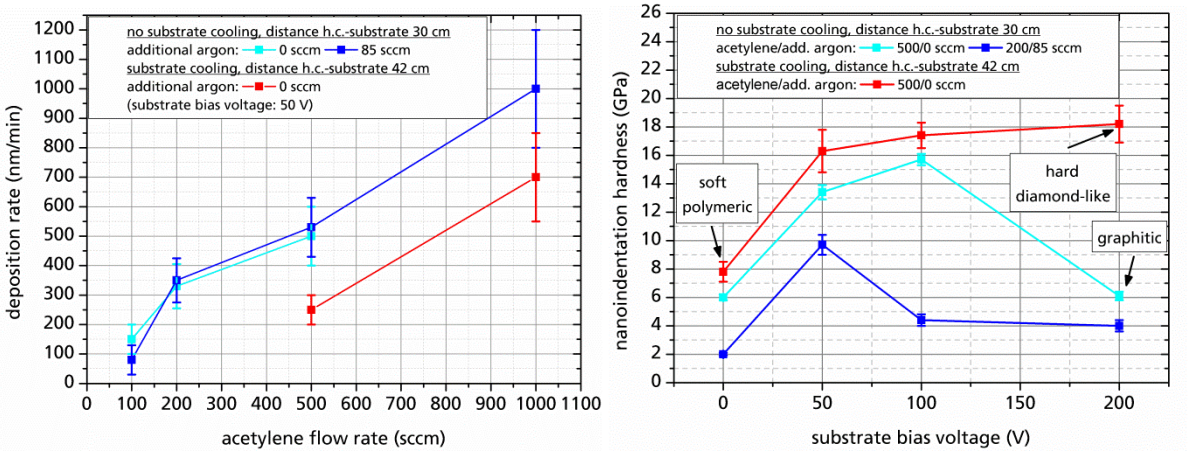
3. Plasma characterization



The reduction of the working gas flow rate (argon through hollow cathode tube) leads to enhanced energies of the electrons emitted by the hollow cathode and generating the plasma [3]. In the case of arc-PECVD, working gas flow rate reduction resulted in strongly increased acetylene dissociation. In the mass spectrum depicted above, signals recorded at three different values of gas flow rate through the hollow cathode tube are shown. Signals of dissociation and polymerization products as well as of hydrogenated residual gas and working gas can be identified (constant total argon flow rate of 100 sccm, acetylene flow rate of 200 sccm). The signal intensity increases with decreasing flow rate through the hollow cathode.
The ion energy distributions (see poster) consist of a low energy peak and high energy tails up to 100 eV. The low energy peak dominates the energy distribution of polymerization products and is related to the bulk plasma potential. In contrast, the high energy tails are based on ions generated in the vicinity of the hollow cathode plasma source at elevated potential, and have been mainly observed for products of acetylene dissociation. It can be derived that whereas dissociation is stimulated by high energy electrons near to the hollow cathode orifice, polymerization predominantly takes place in the bulk plasma.

4. Deposition and analysis of a-C:H films

a-C:H films have been deposited on glass, stainless steel, and n-doped silicon substrates. After hollow cathode-based plasma treatment, a 100-200 nm titanium sublayer has been sputtered in order to enhance the a-C:H layer adhesion. As a third step, arcPECVD of a-C:H (argon flow rate through the hollow cathode tube: 15 sccm) with different additional argon and acetylene flow rates as well as varied substrate bias voltage has been carried out.



The deposition rate is found to depend on the acetylene gas flow rate and reaches values between 100 and 1000 nm/min. Various analysis techniques have been applied for film characterization. The highest nanoindentation hardness of 18.2 GPa has been reached in the case of substrate cooling and high substrate bias voltage (diamond-like a-C:H, substrate temperature up to 290°C). The content of hydrogen measured by elastic recoil detection analysis and Rutherford backscattering spectrometry (ERDA/RBS, with 1.7 MeV He^+ ions, H content ca. 31 at.-%) as well as of the sp^3 sites obtained by Raman spectroscopy has been found to be medium. Scanning electron microscopy (see poster) reveals a dense microstructure and a smooth surface of the coatings.
Without substrate bias, soft polymer-like films have been produced with high hydrogen and sp^3 contents, respectively, as the hydrogen atoms are predominantly bonded by sp^3 sites to carbon atoms. Without substrate cooling, high substrate temperatures of about 500°C were reached due to thermal load at high bias voltages resulting in graphitic film properties. The values of hardness, hydrogen and sp^3 content are low in this case.

5. Conclusions

arcPECVD has been found to be a versatile PECVD technique with very high deposition rates and simple technological assembly. Energy-resolved mass spectrometry reveals plenty of dissociation and polymerization products in the argon acetylene plasma; the energy distribution of the ions depends on the spatial distribution of their origin. a-C:H layers with a film hardness up to 18.2 GPa have been deposited. First deposition experiments on small components treated as bulk good have been carried out successfully and will be published elsewhere. The presented results will be described in detail in a paper submitted to *Surface and Coatings Technology*.

References

[1] F. Fietzke, H. Morgner, S. Günther, Plasma Process. Polym. 6 (2009) S242
[2] B. Zimmermann, F. Fietzke, W. Möller, 54th SVC Ann. Tech. Conf. Proc. (2011) 337
[3] B. Zimmermann, F. Fietzke, W. Möller, Surf. Coat. Technol. 205 (2011) S393
[4] J. Robertson, Mater. Sci. Eng. R 37 (2002) 129

Growth of Carbon Materials on Gold Substrate by Plasma Enhanced CVD

Jiří Šperka[1,2], Lenka Zajíčková[1,2], Ondřej Jašek[1,2], Annapurna Pamreddy[1] and Josef Havel[1]
Masaryk University[1] and CEITEC[2], Kotlářská 2, CZ-61137 Brno, Czech Republic
sperka@physics.muni.cz

Jan Schäfer, Rüdiger Foest
INP Greifswald e.V., Felix-Hausdorff-Str. 2, D-17489 Greifswald, Germany
jschaefer@inp-greifswald.de

1 Introduction

Carbon is a versatile building element of many interesting materials that have already find practical applications in the form of thin films (diamond, DLC) or potential applications in the form of nanostructures (fullerenes, carbon nanotubes, graphene). For electronics or sensors, it is important to provide a very good contact to the functional structures. Gold is the best choice taking into account its inertness, i. e. oxidation resistance. From this point of view the investigation of the growth of carbon materials on gold is important. The carbon-gold interaction plays an important role in different fields of electronics such as atomic force microscope lithography [1], bioelectronics [2] or semiconductor industry. Research in this field is developing rapidly e. g. the modification of interface structure and contact resistance between a CNT and gold electrode was recently modified by Joule melting and amorphous C-Au nanocomposite thin films were deposited by dc magnetron co-sputtering [3].

Herein we report on the preparation and characterization of the carbon nanocomposites which were synthesized on gold substrate from methane precursor using low pressure thermal chemical vapor deposition technique and two different plasma-enhanced chemical vapor deposition (PECVD) methods. The former one PECVD proceeded in microwave reactor at low pressure and the latter one was carried out using non-thermal atmospheric pressure plasma jet (ntAPPJ). Presented approach is based on the deposition of carbon material on gold instead of the deposition of gold on carbon material which is more common. Surprisingly, we didn't find similar studies dealing with the synthesis of carbon nanocomposites using direct deposition from hydrocarbon precursor on the gold thin film. The surface morphology was studied by high resolution scanning electron microscopy (HRSEM). Depth-structure profile including the film thickness was observed using the focused ion beam ablation. Energy-dispersive X-ray spectroscopy (EDX), infrared reflection absorption spectroscopy (IRRAS) and laser desorption-ionization time of flight mass spectrometry (LDI-TOF MS) were used to study the chemical properties. Gold and carbon related clusters were observed by means of mass spectrometric study.

2 Experimental section

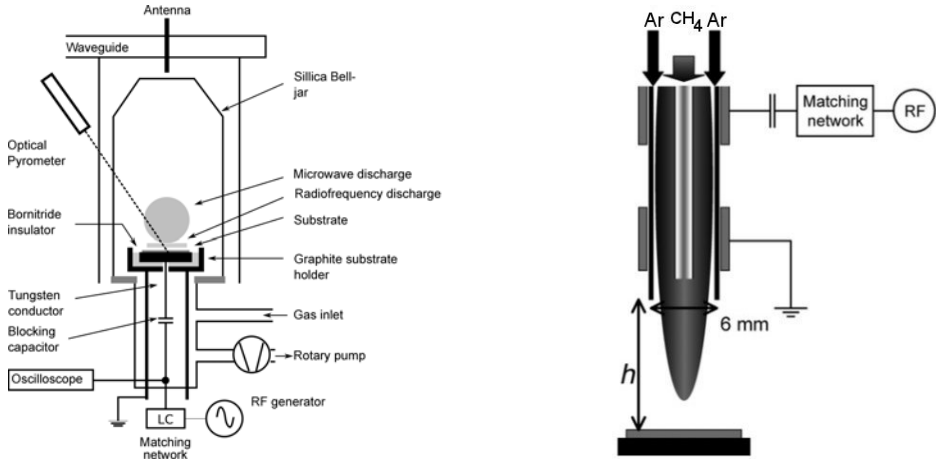
The silicon was covered with 100 nm thick gold layer using thermal evaporation. The substrate was then processed employing chemical vapor deposition using methane as precursor. Corresponding deposition conditions are listed in Tab. 1. The thermal CVD proceeded in the center of horizontal furnace inside quartz glass tube (1 m long, inner diameter 45 mm and hot zone length of 150 mm) terminated with flanges. The furnace deposition temperature was measured by K type thermocouple. The microwave low pressure PECVD proceeded in the conventional silica bell jar ASTeX-type reactor (Fig. 1a) operating at the frequency of 2.45 GHz. The power supplied to the plasma was 850 W. On the graphite holder of the substrate was applied 13.56 MHz RF 35 W power to ignite capacitively coupled discharge and to maintain negative self-bias voltage about 70 V on the substrate holder during deposition. The deposition started by the introduction of methane. The substrate temperature was measured using optical pyrometer and was about 900°C [4].

The radio frequency PECVD has been carried out by a miniaturized non-thermal atmospheric pressure plasma jet (Fig. 1b) [5]. The design of this plasma source features two outer copper ring electrodes (width $w = 4.0$ mm,

distance $d = 4.9\,\mathrm{mm}$) attached to the outer quartz capillary ($D_{out} = 6.0\,\mathrm{mm}$, $D_{in} = 4.0\,\mathrm{mm}$). The electrodes are RF shielded by a grounded metal enclosure. The upper electrode is capacitively coupled to the RF generator (27.12 MHz, DTG2710, Dressler) over a matching network and the power supplied to the plasma was 9 W. The lower electrode is connected to ground potential. Inside the outer capillary a inner capillary ($D_{out} = 1.85\,\mathrm{mm}$) is positioned to provide the thin film precursor during film deposition experiments. Downstream of the active plasma zone (between the electrodes) a chemically reactive effluent develops [6]. During the experiments reported here, the outer channel was fed with argon and the inner channel was fed with methan. The deposited area was a circle with the diameter of 6 mm.

Sample	Method	I (sccm) CH4	I (slm) next gas	Pressure (bar)	Deposition time (min)
1	Thermal	7.6	0.3 H_2	0.08	20
2	MW	7.6	0.3 H2	0.08	40
3	AP	1.5	1 Ar	1	60

Table 1: Deposition conditions



(a) MW reactor (b) APPJ

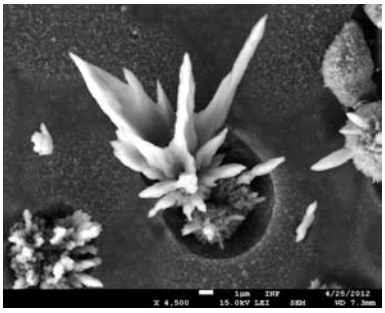
Figure 1: Deposition devices

3 Results

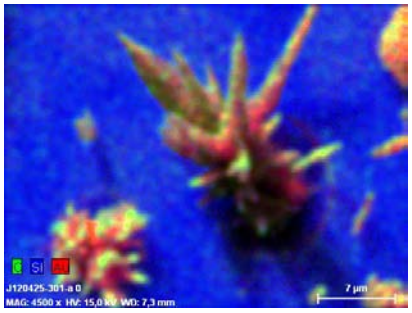
The 3D mesoscopic structures were prepared on the sample 1 using thermal low pressure CVD in CH_4/H_2 atmosphere. Figure 2a shows detailed SEM picture of one of these structures. Similar anisotropic gold mesostructures with complex shapes have been recently reported and are called mesoflowers [7]. Mesoflowers consist of a large number of stems, which are growing outward from the core making the mesoflower 3D. Their number is different for each mesoflower. Recently published mesoflowers were prepared through seed-mediated growth using oligoaniline-capped Au seed nanoparticles and were composed of pure gold [8]. In contrast to this, in the present study, the mesoflowers have been produced differently by thermal CVD. The spatially resolved EDX image of the mesoflower that is shown in Fig. 2a gives an evidence on the chemical composition of the mesoflower. The EDX signal shows that prepared mesoflowers are mainly composed of gold and partially of carbon.

The carbon layer on gold of the sample 2 which was synthesized during microwave low pressure PECVD in CH_4/H_2 atmosphere shows detailed SEM image (Fig. 3a). After high temperature annealing which takes place during this type of deposition process re-structuring of gold takes place. Spatially resolved EDX analysis in Figure 3b shows gold islands which were created by melting of the origin gold layer. The inner structure of this layer was estimated using FIB ablation. This method showed that about 120 nm thick carbon layer was deposited over gold. The island-formation of gold was also observed on the cross-section of this layer.

The thin homogenous a-C:H film was prepared on the gold surface of the sample 3 by means of ntAPPJ. Small spherical particles have been sporadically observed on the film (Figure 4a). The size (about one micron) of these particles is in agreement with carbon spheres that were prepared earlier in the radio frequency plasma [9]. Spatially resolved EDX analysis in Figure 4b demonstrates the chemical homogeneity of the distribution of carbon and gold on the sample. In this case, in addition to the formation of gold clusters, gold carbides and gold silicides were detected by LDI-TOF MS measurement and the stoichiometric formulas of gold carbides $Au_mC_n^+$ and other clusters identified are shown in Figure 5. Intensities of Au carbides and silicides reach about 20-30 percent of the intensities of Au-clusters. The results proof that the formation of carbides is significant. Recently, laser ablation synthesis of various gold carbides from the carbon obtaining materials has been published [10, 11, 12].

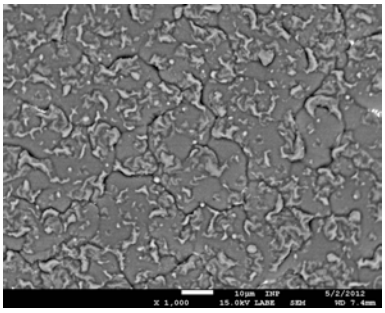


(a) SEM picture.

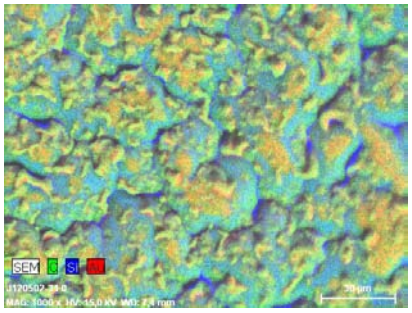


(b) Spatially resolved EDX.

Figure 2: Growth of the mesostructures during low pressure thermal CVD (sample 1).

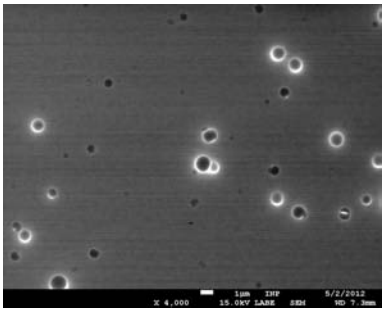


(a) SEM picture.

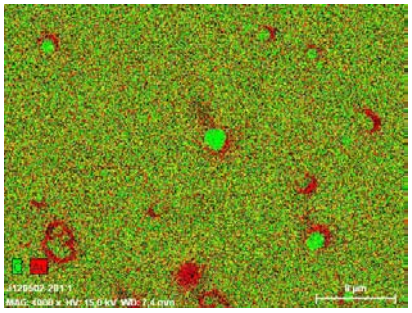


(b) Spatially resolved EDX.

Figure 3: Carbon layer on gold created during low pressure microwave PECVD (sample 2).



(a) SEM picture.



(b) Spatially resolved EDX.

Figure 4: Carbon spheres generated on gold during atmospheric pressure radiofrequency PECVD (sample 3).

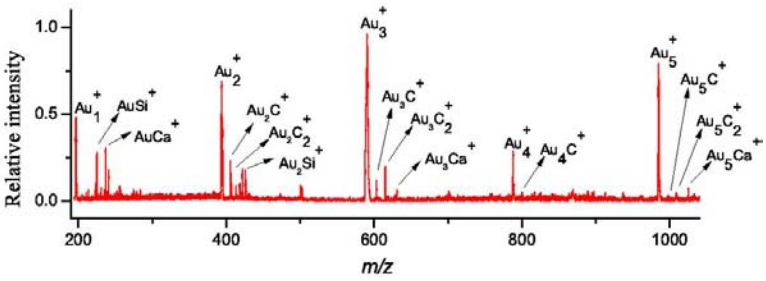


Figure 5: LDI-TOF MS of sample 3, positive ion mode, 5 laser shots used at laser energy 140 a.u.

4 Conclusions

Three different CVD deposition techniques of the carbon deposition on gold have been investigated. Gold mesoflowers were prepared by low pressure thermal CVD in CH_4/H_2 atmosphere. To the best of our knowledge we are not aware that someone has used the thermal CVD for growth of these structures before. We propose a growth mechanism which consists of local melting, renucleation and aggregation of gold in the form of islands, self-assembling of gold and further growth of mesoflower. Homogenous a-C:H film has been deposited using ntAPPJ and various $Au_mC_n^+$ clusters were detected after the laser ablation of corresponding sample using mass spectrometry.

References

[1] Y. Kahng, J. Choi, B. Park, D. Kim, J. Choi, J. Lyou, S. Ahn, Nanotechnology 19 (2008) 195705.

[2] M. Lockett, S. Weibel, M. Phillips, M. Shortreed, B. Sun, R. Corn, R. Hamers, F. Cerrina, L. Smith, Journal of the American Chemical Society 130 (27) (2008) 8611–8613.

[3] K. Asaka, M. Karita, Y. Saito, Applied Surface Science 257 (7) (2011) 2850–2853.

[4] J. Schäfer, R. Foest, A. Quade, A. Ohl, K. Weltmann, Journal of Physics D: Applied Physics 41 (2008) 194010.

[5] J. Schäfer, R. Foest, A. Quade, A. Ohl, M. J., K. Weltmann, Eur. Phys. J. D 54 (2009) 211.

[6] J. Schäfer, R. Foest, A. Ohl, K. Weltmann, Plasma Phys. Control. Fusion 51 (2009) 124045.

[7] P. Sajanlal, T. Pradeep, Nano Research 2 (4) (2009) 306–320.

[8] P. Sajanlal, T. Pradeep, The Journal of Physical Chemistry C 114 (38) (2010) 16051–16059.

[9] G. Chen, V. Stolojan, S. Silva, H. Herman, S. Haq, Carbon 43 (4) (2005) 704–708.

[10] E. Peña-Méndez, J. Hernández-Fernaud, R. Nagender, J. Houška, J. Havel, Chem. Listy 102 (2008) s1394–s1398.

[11] J. Houška, N. Panyala, E. Peña-Méndez, J. Havel, Rapid Communications in Mass Spectrometry 23 (8) (2009) 1125–1131.

[12] Y. Cohen, V. Bernshtein, E. Armon, A. Bekkerman, E. Kolodney, The Journal of chemical physics 134 (2011) 124701.

Cr-DLC films deposited by dual pulsed laser ablation

Petr Písařík [1,2,*], Miroslav Jelínek [1,2], Tomáš Kocourek [1,2], Jan Mikšovký [1,2], Karel Jurek [2]

[1] Institute of Physics ASCR v.v.i., Na Slovance 2, 182 21 Prague, Czech Republic
[2] Czech Technical University in Prague, Faculty of Biomedical Engineering,
nam. Sitna 3105, 272 01 Kladno, Czech Republic
[*] e-mail: petr.pisarik@fbmi.cvut.cz

Abstract - Diamond-like carbon (DLC) and Cr doped diamond-like carbon (Cr-DLC) layers were studied for potential medical applications. DLC and Cr-DLC were deposited on silicon and titanium substrate by dual pulsed laser ablation using two KrF excimer lasers and two targets (graphite and chromium). The topology of layers was studied using scanning electron microscopy (SEM). The composition was analyzed using wavelength-dependent X-ray spectroscopy (WDS). Ethylene glycol, diodomethane and deionized water were used to measure their contact angles, which were used to evaluate the surface free energy.

Keywords - Chromium, Diamond-like carbon, Thin films, Surface morphology, Dual Pulsed laser deposition

1. INTRODUCTION

Diamond-like carbon (DLC) is thin film with high hardness, low friction coefficient, optical transparency in the visible and infrared regions, high electrical and thermal conductivities and high wear resistance [1--6]. DLC is a biocompatible material than can be used in prostheses or biological implant [3--6]. However, the practical applications of DLC films have been limited because of low adhesion on biomedical alloys and high internal stress. Several studies have shown that the internal stress in DLC films can be relieved reduced and their adhesion can be increased by doping elements into the DLC films.

One of the possibilities is doping with chromium. Cr-DLC layers were prepared by various techniques, mostly hybrid systems - radio frequency plasma enhanced chemical vapor deposition (RF-PECVD) and thermal evaporation techniques [7], plasma-assisted vapor/chemical vapor deposition (PVD/CVD) and magnetron sputtering [8, 9], linear ion source and DC magnetron sputtering [10, 11], intensified plasma-assisted processing and magnetron sputtering [12], dual-magnetron sputtering [13], dual-target cathodic art evaporation system [14].

The layers thus prepared were studied and effects of chromium doping on the mechanical properties (adhesion, hardness, Young's model, wear, friction coefficient) [7, 10--12, 15--20], optical properties (transmission) [7], structure (FTIR [7, 14], XPS [10--12, 14--16, 19], XAES [17], Raman [11, 15, 18, 21]) and electrical properties [7], surface morphology (AFM) [10, 11, 21] and contact angle [11, 22] were evaluated.

Adhesion of DLC films to biomedical alloy substrates (Ti-6Al-4V, Co-Cr-Mo and stainless steel) is poor [3, 23]. It is caused by stress in the layer due to different hardness and different coefficient of thermal expansion of substrate and layer. Sheeja found [24] that the critical load of the DLC films to silicon substrate was about 2.5 N. Similar results were presented Baragetti [25]. DLC films on aluminium alloy exhibited critical load about 3.5 N

[25]. One option to improve the adhesion is use of doping layer. Dai et al.'s study [15] revealed that the critical load of the Cr-DLC films is much higher than the DLC film. One the other hand, the hardness Cr-DLC films presented in [12] was increased by ~ 10 % by incorporating Cr into the DLC films, respectively ~ 30 % in [10]. On other hand, the results in [19] show that incorporation of Cr into DLC causes the hardness reduction.

In our contribution we concentrated on synthetize and study of DLC film and Cr-DLC films.

2. EXPERIMENTAL

2.1 Deposition

Silicon (100) wafers, titanium alloy (Ti-6Al-4V) and were used as substrates, which were cleaned ultrasonically in acetone, toluene, ethanol, then just cleaned with ethanol and dried in air before being put into the vacuum chamber. Cr-DLC films were prepared by dual PLD using a two KrF excimer laser (λ = 248 nm, τ = 20 ns). First laser beam was focused onto a high purity graphite target with energy densities of 8 J·cm^{-2} with repetition rate from 4 Hz to 12 Hz and second laser beam was focused onto a chromium target with energy densities of 5 J·cm^{-2} with repetition rate from 2 Hz to 10 Hz – see Table 1. Figure 1 shows the schematic diagram of the system used to prepare the Cr-DLC film samples. The numbers of pulses were adjusted to reach approximately the same layer thickness (350±50 nm) and different atomic chromium content 0-18 %. Substrate was in a distance of 45 mm from the targets. The targets were rotated (0.5 Hz). The Cr-DLC films were created at room substrate temperature. The base vacuum of the coating system was 5x10^{-4} Pa. The films were deposited in argon ambient (0.25 Pa) [4, 6].

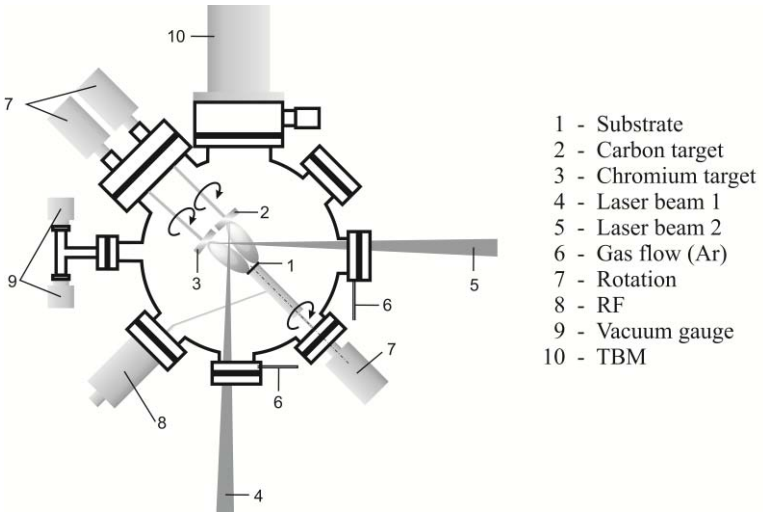


Figure 1 The scheme of dual PLD deposition system

2.2 Characterization of layers properties

The composition of Cr-DLC thin layers was determined by an electron microprobe using a wavelength dispersive X-ray spectroscopy (WDS). WDD was performed with JEOL 840. The energy of primary electrons was kept at 5 keV to minimize their penetration depth and the absorption of emitted X-rays. For this energy, an electron spot diameter was estimated to be in the range 1-2 μm, which gives information at a depth of about 0.5 μm. The accuracy of the measurement of Cr and C, using STRATA program [26] was better than 5 %. The surface morphology was observed at a magnification of 400.

Wettability studies were performed by static contact angle measurement. Using a contact angle meter (DSA100, Krüss Co.) and with combination of three liquids: demineralized water, diiodomethane and ethylene glycol. Measurement was arranged at room temperature and

humidity 20 ± 5 % by the sessile drop method with drop volume approximately 0.75±0.25 µl. Surface free energy was calculated using the Fowkes method and dispersive (γ^{LW}) and polar (γ^{AB}) components were obtained. The component γ^{LW} summarizes long-range Lifshitz - van der Waals forces, and γ^{AB} describes short-range polar interactions.

3. RESULTS AND DISCUSSION

Cr-DLC films were synthesized using dual PLD of C and Cr target. In dependence with deposition conditions the Cr content moved from 0 at % to ~ 18 at % - see Table 1. The layers were generally smooth with rare droplets, see Fig. 2.

Contact angle (CA) of Cr-DLC for all liquids (ethylene glycol, diodomethane and deionized water) was higher compared the DLC film ($CA_{Deionized\ water}$ = DLC ~70°, Cr-DLC ~90°; $CA_{Diodomethane}$ = DLC ~41°, Cr-DLC ~52°; $CA_{Ethylene\ glycol}$ = DLC ~43°, Cr-DLC ~65°). Our measured for contact angles for water had the same trend as Cr-DLC layers reported by Ali [22]. Contact angles were used to evaluate the surface free energy (SFE). SFE of Cr-DLC for all liquids was lower than the DLC film (SFE_{Total} = DLC ~43 mN/m, Cr-DLC ~33 mN/m; $SFE_{Disperse\ component}$ = DLC ~37 mN/m, Cr-DLC ~31,5 mN/m; $SFE_{Polar\ component}$ = DLC ~6 mN/m, Cr-DLC ~1,5 mN/m).

Table 1 Deposition conditions of Cr-DLC films created by dual-PLD

Sample (Substrate)	Laser 1 - Carbon	Laser 2 - Chromium	WDX
	Repetition rate (Hz)	Repetition rate (Hz)	Chromium (at. %)
DLC (Si 100 + Ti6Al4V)	12	0	0
Cr-DLC-1 (Si 100 + Ti6Al4V)	12	2	2.2
Cr-DLC-2 (Si 100 + Ti6Al4V)	9	3	4.1
Cr-DLC-3 (Si 100 + Ti6Al4V)	10	7	8.2
Cr-DLC-4 (Si 100 + Ti6Al4V)	4	7	17.9

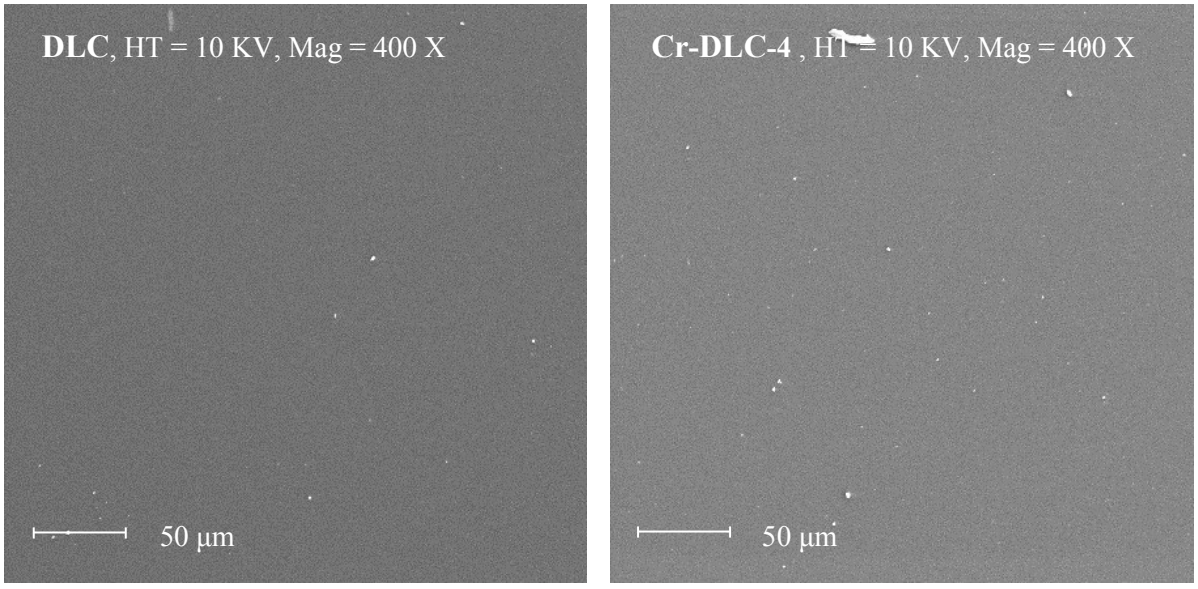


Figure 2 SEM micrographs showing surface DLC and Cr-DLC-4

4. CONCLUSIONS

This paper focuses on DLC and Cr-DLC films on silicon and biomedical alloy substrate (Ti-6Al-4V). The layers were prepared using dual Pulsed Laser Deposition (PLD) using two targets (graphite and chromium). The Cr content increased from 2.2 to 17.9 at. %. The layers were generally smooth with rare droplets. The contact angle measurements for water showed that the contact angle of Cr-DLC films (90°) was higher than DLC film (70°) and surface free energy of Cr-DLC films (43 mN/m) was lower than DLC film (33 mN/m).

ACKNOWLEDGMENTS

We thank the Institutional research plan AV010100522, grant of the Czech Technical University in Prague SGS12/167/OHK4/2T/17 and SGS12/088/OHK4/1T/17, and the Ministry of Education, Youth and Sports of the Czech Republic for grants COST LD12069.

REFERENCES

[1] J. Robertson: Mater. Sci. Eng. R. **37**(4-6), 129 (2002)
[2] A. Grill: Diamond Relat. Mater. **8**(2-5), 428 (1999)
[3] R. J. Narayan: "Functionally Gradient Hard Carbon Composites for Improved Adhesion and Wear," Mater. Sci. Eng. NCSU_doctoral_2002_08_06 (2002)
[4] T. Kocourek, M. Jelínek, V. Vorlíček, J. Zemek, T. Janča, V. Žížková, J. Podlaha, C. Popov: Appl. Phys. A **93**(3), 627 (2008)
[5] M. Jelínek, K. Smetana, T. Kocourek, B. Dvořánková, J. Zemek, J. Remsa, T. Luxbacher: Mater. Sci. Eng. B **169**(1-3), 89 (2010)
[6] M. Jelínek, T. Kocourek, J. Remsa, J. Mikšovský, J. Zemek, K. Smetana, B. Dvořánková, T. Luxbacher: Appl. Phys. A **101**(4), 579 (2010)
[7] N. Dwivedi, S. Kumar, C. M. S. Rauthan, O. S. Panwar: Plasma Process. Polym. **8**(2), 100 (2011)
[8] J. A. Colón Santana, V. Singh, V. Palshin, E. M. Handberg, A. G. Petukhov, Y. B. Losovyj, A. Sokolov, I. Ketsman: Appl. Phys. A-Mater. Sci. Process. **98**(4), 811 (2010)
[9] J. A. C. Santana, R. Skomski, V. Singh, V. Palshin, A. Petukhov, Y. B. Losovyj, A. Sokolov, P. A. Dowben, I. Ketsman: J. Appl. Phys. **105**(7), art. no. 07A930 (2009)
[10] W. Dai, P. Ke, A. Wang: *Vacuum* **85**(8), 792 (2011)
[11] W. Dai, H. Zheng, G. Wu, A.Wang: *Vacuum* **85**(2), 231 (2010)
[12] S. K. Pal, J. Jiang, E. I. Meletis: Surf. Coat. Technol. **201**(18), 7917 (2007)
[13] Y. Xiang, W. Cheng-biao, L. Yang, Y. De-yang, F. Zhi-qiang: Surf. Coat. Technol **200**(24), 6765 (2006)
[14] J.-Y. Jao, S. Han, L.-S. Chang, C.-L. Chang, Y.-C. Liu, H.C. Shih: Appl. Surf. Sci. **256**(24), 7490 (2010)
[15] W. Dai, G. Wu, A. Wang: Diamond Relat. Mater. **19**(10), 1307 (2010)
[16] J. Y. Jao, S. Han, L. S. Chang, Y.-C. Chen, C.-L. Chang, H.C. Shih: Diamond Relat. Mater. **18**(2-3), 368 (2009)
[17] H. Renondeau, R. I. Taylor, G. C. Smith, A. A. Torrance: Proc. Inst. Mech. Eng. Part J.-J. Eng. Tribol. **222**(3), 231 (2008)
[18] A. Czyzniewski: Plasma Process. Polym. **4**(SUPPL.1), S225 (2007)
[19] V. Singh, J. C. Jiang, E. I. Meletis: Thin Solid Films **489**(1-2), 150 (2005)
[20] D.-Y. Wang, K.-W. Weng, S.-Y. Hwang: Diamond Relat. Mater. **9**(9), 1762 (2000)
[21] Y.-Y. Chang, D.-Y. Wang: Surf. Coat. Technol **200**(10 SPEC. ISS.), 3170 (2006)
[22] N. Ali, Y. Kousar, T. I. Okpalugo, V. Singh, M. Pease, A. A. Ogwu, J. Gracio, E. Titus, E. I. Meletis, M. J. Jackson: Thin Solid Films **515**(1), 59 (2006)
[23] S. J. P. Laube, A. A. Voevodin, K. D. Keener, S. R. Leclair: Eng. Appl. Artif. Intell. **11**(5), 649 (1998)
[24] D. Sheeja, B. K. Tay, S. P. Lau, X. Shi, J. Shi, Y. Li, X. Ding, E. Liu, Z. Sun: Surf. Coat. Technol. **127**(2-3), 247 (2000)
[25] S. Baragetti, L. Lusvarghi, G. Bolelli, F. Tordini: Surf. Coat. Technol. **203**(20-21), 3078 (2009)
[26] J. L. Pochou, F. M. A. Pichoir, D. Boivin: Proc. 12th Internat. Conf. X-ray Optics Microanalysis, Cracow, Poland, Polish Academy of Mining and Metallurgy Printing House, 52 (1990)

Comparison of the wear particle size distribution of different a-C coatings deposited by vacuum arc

Ying Ren[1]*, Ingo Erdmann[1], Victoria Khlopyanova[2], Friederike Deuerler[1], Volker Buck[2]
[1]Faculty D-Department of Mechanical Engineering, University of Wuppertal, 42119, Wuppertal, Germany

[2]Thin Film Technology Group, Faculty of Physics and CENIDE, University Duisburg-Essen, 47057, Duisburg, Germany

Abstract

For biomedical application in the field of artificial hip joints diamond-like carbon (DLC) coatings have been widely studied due to their excellent mechanical, tribological and biological properties. The wear particles as the main factor limiting the life expectancy of hip joints have attracted more and more interest, not only the number of them, but also the distribution of their size. In this study we have deposited DLC coatings on stainless steel (P2000) by a vacuum arc adjustable from anodic to cathodic operation mode. To improve the adhesion of the DLC coating on P2000, titanium as a metallic interlayer was deposited by cathodic vacuum arc evaporation. The frequency distribution of wear particles generated using a disc-on-disc test was measured by a particle size analyzer. It was shown that the maximum of the frequency distribution e.g. at —1000 V bias can be shifted to below 1 µm with increasing anode/cathode diameter ratio d_a/d_c.

1. 1.Introduction

Many methods have been developed for the deposition of DLC coatings in biomedical applications. In this study, the vacuum arc deposition which can be adjusted from anodic to cathodic operation mode was used to deposit the DLC coatings to be applied in artificial hip joints. What's more, different DLC coatings can be deposited by controlling the anode-cathode diameter ratio of d_a/d_c. The purpose of this study was to compare the wear particles size distribution of DLC coatings with different d_a/d_c, which was also important in the evaluation of life time of implants, not only the number of wear particles.

2. Materials and method

Discs as substrates with diameter of 31 mm and thickness of 4 mm, were made of stainless steel (P2000). Titanium was chosen as interface layer to improve the adhesion of the DLC film to P2000. The friction and wear tests were carried out using a disc-on-disc tribometer (Wazau TRM 1000) in deionized water as lubricant under a normal force of 120 N, and a sliding velocity of 0.01 m/s was chosen. After tribological tests, the wear particles generated were measured using the particle size analyzer Horiba LA-950 with 17 channels per decade. Due to the properties of coatings, the sliding time in these experiments was varied in order to get more wear particles.

3. Results

Here the volume density distribution $q_3(x)$ was chosen to characterize the size of particles, which represents the amount of particles of a given particle size x relative to the entire particles size distribution, as shown in Fig. 1.

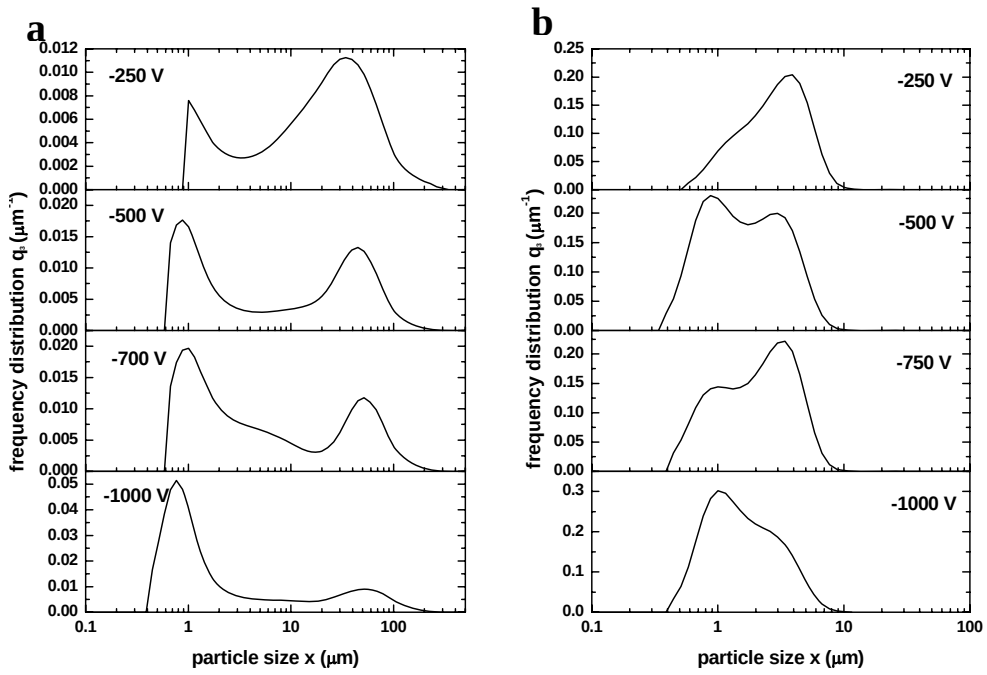


Fig. 1 Volume density distribution $q_3(x)$ at the DC bias from —250 V to —1000 V with the anode-cathode diameter ratio of (a) d_a/d_c = 3/1 and (b) d_a/d_c = 1/1

The modal value x_{mod}, the particle size at which the density distribution $q_3(x)$ exhibits a maximum, can be determined that characterize the particle collective from the measured size distribution $q_3(x)$. Fig. 1 (a) showed that when the DLC coatings were deposited with d_a/d_c = 3/1, the wear particles collected were in the range of 0.3 to 200 µm which was observably different from the DLC coatings with d_a/d_c = 1/1, 0.3 to 10 µm as shown in Fig. 1 (b).

However, there were two peaks in volume density distribution no matter which anode-cathode diameter was used. One peak was distributed at ~ 1 µm ($x1_{mod}$) for d_a/d_c = 3/1 and d_a/d_c = 1/1, another at ~ 50 µm ($x2_{mod}$) for d_a/d_c = 3/1 and ~ 5 µm for d_a/d_c = 1/1. That means that most particles were distributed in the range of smaller particles and larger particles. In Fig. 1 (a), it was found that two peak heights representing the density distribution of $x1_{mod}$ and $x2_{mod}$, $q(x1_{mod})$ and $q(x2_{mod})$, respectively changed with the bias. Fig. 1 (b) showed that the curve had the same tendency with the bias when the DLC coatings were deposited at d_a/d_c = 1/1, just the maximum of the curve was shifted from ~ 1 µm to ~ 5 µm when the bias was increased from —500 V to —750 V. According to the previous work, the concentration of wear particles at —1000 V with d_a/d_c = 1/1 was distributed more equally in a whole range.

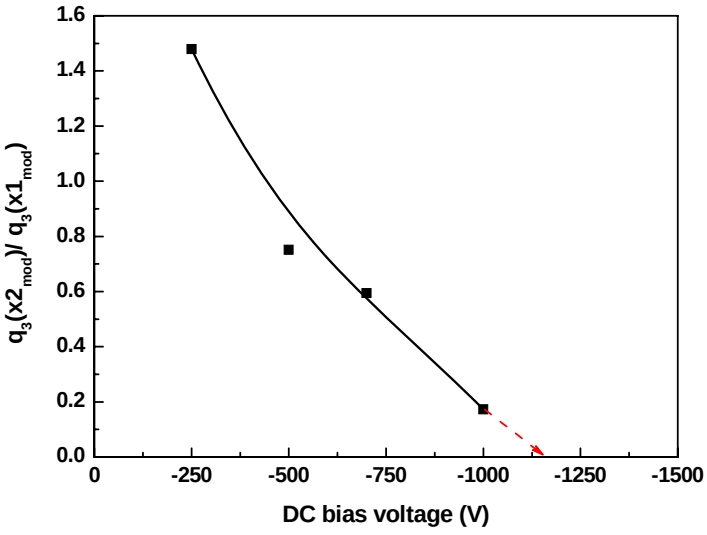


Fig. 2 Variation of $q_3(x2_{mod})/q_3(x1_{mod})$ ratio with DC bias voltage

The relative density distribution ratio of x2mod and x1mod is shown in Fig. 1. From Fig. 2 it is obvious that the ratio of $q_3(x2_{mod})$ and $q_3(x1_{mod})$ decreases from 1.5 to 0.15 regularly with

increasing bias from —250 V to —1000 V; fitting with a curve of Bezier indicated that the maximum of the frequency distribution can be shifted to below 1 µm at higher bias. According to Bezier curve equation, one can try to get the approximation of bias at which the $q_3(x2_{mod})/q_3(x1_{mod})$ ratio eventually nears zero; from this extrapolation it can be expected that the wear particle size could be reduced and the frequency distribution would be downshifted to below 1 µm when the bias is slightly lower than —1100 V (see red line in Fig. 2).

4. Conclusion

Amorphous carbon (a-C) films were synthesized on P2000 substrates by vacuum arc technique using an anode-cathode diameter ration of d_a/d_c = 3/1 with the application of a DC bias to the substrate from —250 V to —1000 V. The influence of d_a/d_c and the substrate bias on the wear particle size distribution were investigated. When the films were deposited with d_a/d_c = 1/1, all particles generated were smaller than 10 µm. However, the wear particle size of a-C coatings deposited with d_a/d_c = 3/1 is distributed in the range of 0.3 to 200 µm. The maximum of the frequency distribution can be downshifted gradually with increasing bias to below 1 µm at voltages lower than —1000 V bias. It is estimated that all wear particles can be distributed in the range of ~ 1µm when the bias is slightly lower than approximately —1100 V.

Oxidation behaviour of RuAl thin films: influence of the diffusion barrier

M. A. Guitar & F. Mücklich

Functional Materials, Materials Science Department, Saarland University, Saarbrücken D-66123, Germany

RuAl is a B2-structured intermetallic material with high melting point (2050ºC) which possesses outstanding thermodynamical stability in high-temperature aqueous environments. Moreover, RuAl presents good oxidation-resistance up to at least 1200ºC and strength at high temperatures. The good oxidation and corrosion resistance is due to the formation of a slow-growing protective Al_2O_3 layer, which has been found to be dense and compact even after oxidising during 100 hours at 1000°C. Furthermore, the RuAl thermal expansion coefficient (CTE) is nearly equal to that of Al_2O_3 in a wide temperature range, which makes this intermetallic optimal as a protective coating material in applications that demand oxidation resistance (e.g. working layers for moulding dies).

The present work describes the study of the oxidation behaviour at elevated temperatures on nanocrystalline RuAl thin films. Stainless steel (SS) was selected as substrate due to its technical relevance. The RuAl thin films were synthesized from high-purity (99.99%) Al and Ru targets using a PVD magnetron sputtering. A Ti-adhesion layer (50 nm) was deposited onto the substrate previous to the Ru-Al deposition in order to improve the adhesion. To study the oxidation behaviour of this SS/RuAl thin film system, isothermal oxidation treatments were carried out in ambient air at 750°C and 900°C for short times (up to 1h) and the subsequent analysis of the oxide scale was performed using STEM and X-ray diffraction. Moreover, the oxidation kinetics and oxide layer growth morphology was studied with and without diffusion barrier so as to determine how the Fe affects the intermetallic performance.

Oxidation tests showed the formation of a dense, compact and well adhered oxide scale. However, the presence of diffused Fe and Cr at the grain borders from the substrate in the RuAl films was also observed in the oxidised samples. To avoid this effect, an Al_2O_3 and W diffusion barrier was deposited between the subtrate and the RuAl film. Coating detachment was observed by depositing first Al_2O_3 onto the substrate and oxidizing at 900°C.

RuAl thin films exhibit parabolic oxidation kinetics. The surface colour and reflectivity did not change with the oxidation time and also no apparent increasing in roughness was observed after oxidation at 750°C.

The importance of analyzing the oxidation behaviour of these thin films lies on the fact that usually, bulk intermetallics show different oxidation rates compared to those of thin films and therefore, new studies in the aforementioned intermetallic system are needed.

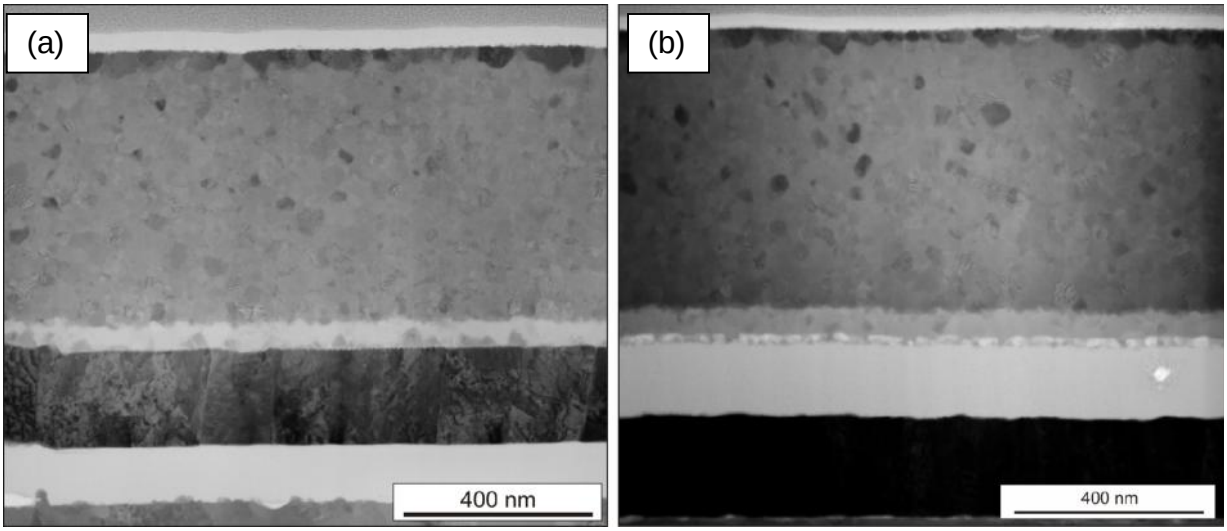


Figure 1: RuAl thin films oxidised at 750°C for 45 minutes using (a) Al_2O_3 + W and (b) W + Al_2O_3 as diffusion barriers.

PRODUCTION AND CHARACTERIZATION OF SELF-HEALING PROPERTIES OF B4C+SIC ADDED TBC

Fatih Üstel, Ahmet TÜRK, Garip Erdogan

Sakarya University Eng. Fac. Materials, Sakarya/Serdivan, Turkey

ustel@sakarya.edu.tr

Abstract

Thermal barrier coatings have significant interest for protecting of the effect of high temperature the materials used under high temperature. To coat the materials used under high temperature such as gas turbine liners, is considerably important. Yttria stabilized zirconia (YSZ) is the most common material used for that purposes in commercial applications. Thermal barrier coatings damage due to the thermal expansion and internal stress, formed by the temperature variation. The micro and macro cracks, which are formed under service life of the coating, causes the coating failures such as spallation by developing crack network. In this research SiC and B4C powders added into commercial YSZ powder to improve thermal shock resistance. Two different powder ratio were prepared as %25(%12,5 SiC +B4C) %75 YSZ and %50(%25 SiC +B4C) %50 YSZ. After preparing powders coatings were manufactured using F4 plasma gun. Coated samples were subjected to thermal shock test in burner rig testing equipment and as well oxidation tests were carried out as well for 10h, 20h and 50h at 1000°C. TG and XRD analysis were used to investigate self-healing products. Scanning Electron Microscope and Optical Microscope were used to examine microstructural properties of SiC and B4C added YSZ.

Introduction

Gas turbine's hot section liner materials and space and aircraft hot section materials, rockets and satellites are protected with a Thermal Barrier Coating (TBC) system from high temperature effects. (1,2,3,4). In order to protect materials from high temperature oxidation TBCs are manufactured consisting two different layers. In present high-temperature systems, a thermal barrier coating (TBC) is applied as a top coating on diffusion or connection coating to lower metal surface temperatures. In combination with internal cooling of the component, a temperature gradient of 100–150◦C can be acquired through the thickness of the TBC (Peters et al. 2001). Today's TBC's are prepared of yttria stabilized zirconia (ZrO2 with 6–8 wt%Y2O3) and deposited by plasma spraying or EB-PVD (5). In the high-temperature TBC coating system, the diffusion or overlay coating, often referred to as bond coating (BC), provides the protection against high-temperature oxidation. In this case, the oxide layer that forms between the BC and the TBC is referred to as the thermally grown oxide (TGO) layer.

Failure of the high-temperature TBC coating systems is limited mainly to the surrounding of the TGO layer, although cracks initiated at the TGO layer can run vertically through the TBC and reach its free surface (6). The fragile TBC experiences cracks that run predominantly parallel to the TGO layer.

Self-healing concept is to fill the cracks by using reaction products of the additives in the top coat during service condition. Wim G. Sloof (7) reported self-healing properties of high

temperature properties of coatings at high temperature. Guo, et al.(8) has reported the B4C has self-healing properties as coating on SiC/C composite. In this work, The self-healing properties of B4C and SiC added YSZ top coat was studied.

Experimental

In this work, B4C and SiC powders were mixed with commercial Ytria Stabilized Zirconia (204NS-Sulzer Metco, Switzerland) Figure 1 shows the powder's size distributions and SEM images. %12,5 B_4C and %12,5 SiC %75 YSZ and %25 B4C %25 SiC %50 YSZ powders were ball milled for 1 hour with zirconia balls with 3mm diameters for powder / ball ratio 1/10. Figure 2 shows the SEM images of the %12,5 and %12,5 SiC added powders. It can be seen in Figure 3 SEM image of %25 B4C and %25 SiC added YSZ powder

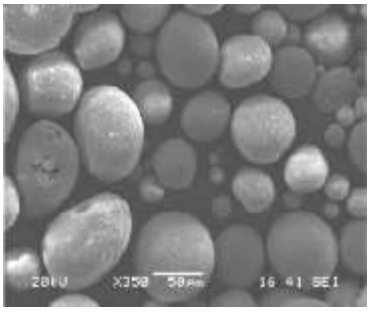
NiCrAlY and B4C and SiC added YSZ powders were sprayed onto 316 stainless steel specimen with a Sulzer Metco F4 MB gun to manufacture the coatings by using the parameters given in Table 1 for both top coat and bond coat. Coated specimens were heated to 1000°C for 10h, 20h, 50h and 100h. Moreover thermal shock tests were implemented with burner rig equipment as well. Burner rig tests were carried out as 5 min. heating and 2 min. cooling.

Table 1 Plasma Spray Parameters

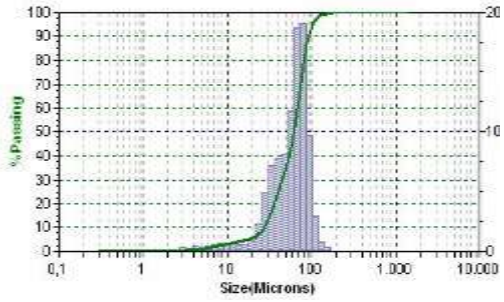
Coating	Argon Flow (NLPM)	Hydrogen Flow (NLPM)	Current	Voltage	Spray Distance	Powder Flow
Bond Coat	40	10	575A	70V	150mm	35 gr/min
Top Coat	38	12	540A	65	120mm	40gr/dk

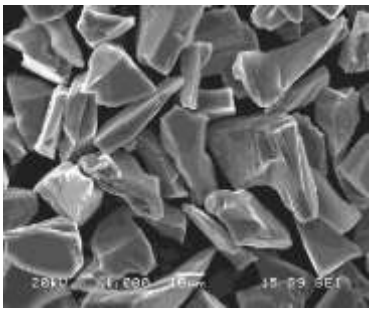
Fig. 4 shows that the as coated situation of the sample produced %75 YSZ powder. It can be seen some B4C and SiC particles were impregnated into top coat. Fig 5 shows the SEM images of coating produced from %50 YSZ powder. It is clear from both images SiC and B4C impregnated into top coat. Furthermore it can be seen from Fig. 6.

In Fig. 7 A SEM image of the coating manufactured using %75 YSZ (%12,5 B4C and %12,5 SiC) powder. It can be seen vertical crack interior of the top coat body. In Fig. 8 %50 YSZ (%25 B4C and %25 SiC) It can be seen that there is not any spallation after 20h oxidation at 1000°C.

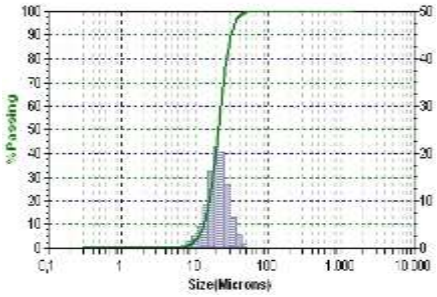


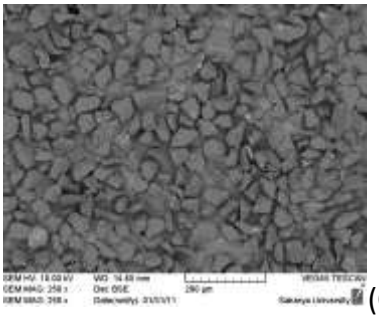
(A)





(B)





(C)

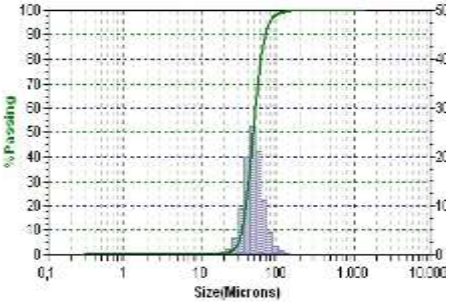
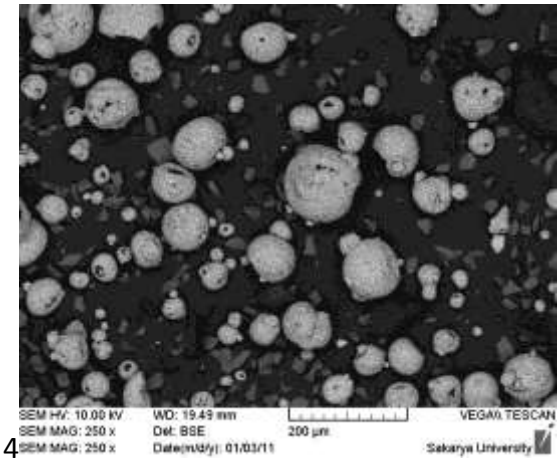
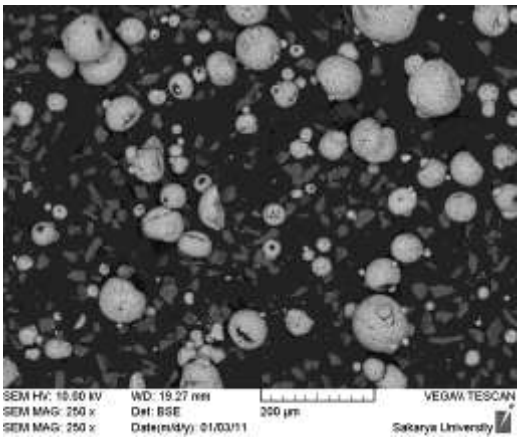


Figure 1 Powders SEM images and size distrubitions a) YSZ b) SiC c) B4C



4

Figure 2 SEM image of %12,5 B4C and%12,5 SiC added YSZ



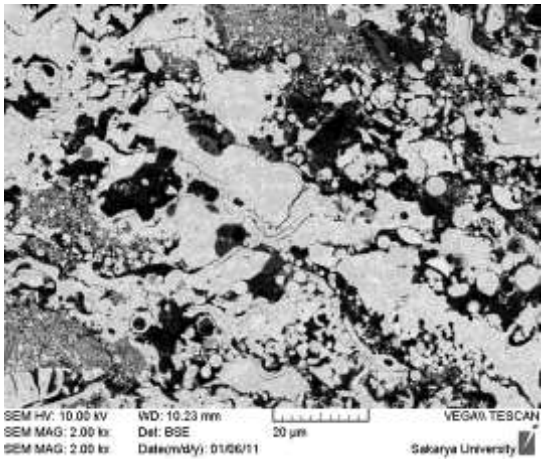
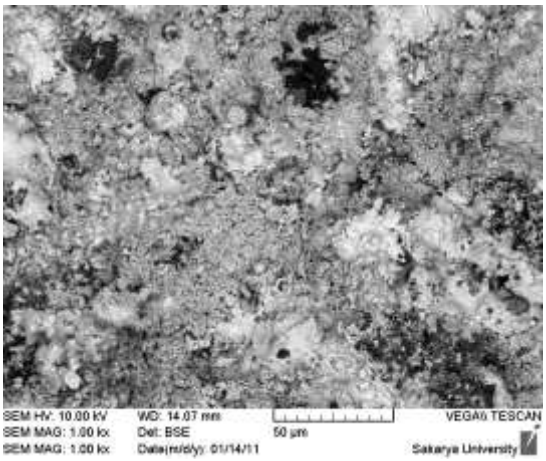


Figure 3 SEM image of %25 B4C and %25 SiC added YSZ powder



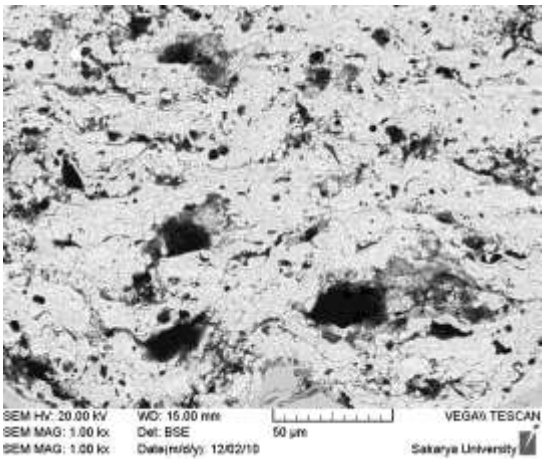


Figure 4 As coated sample produced %75 YSZ powder

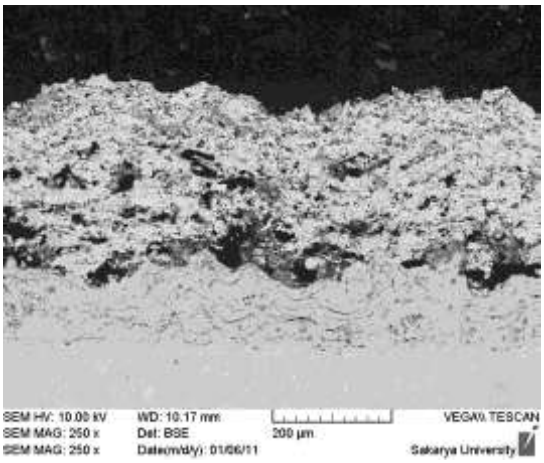
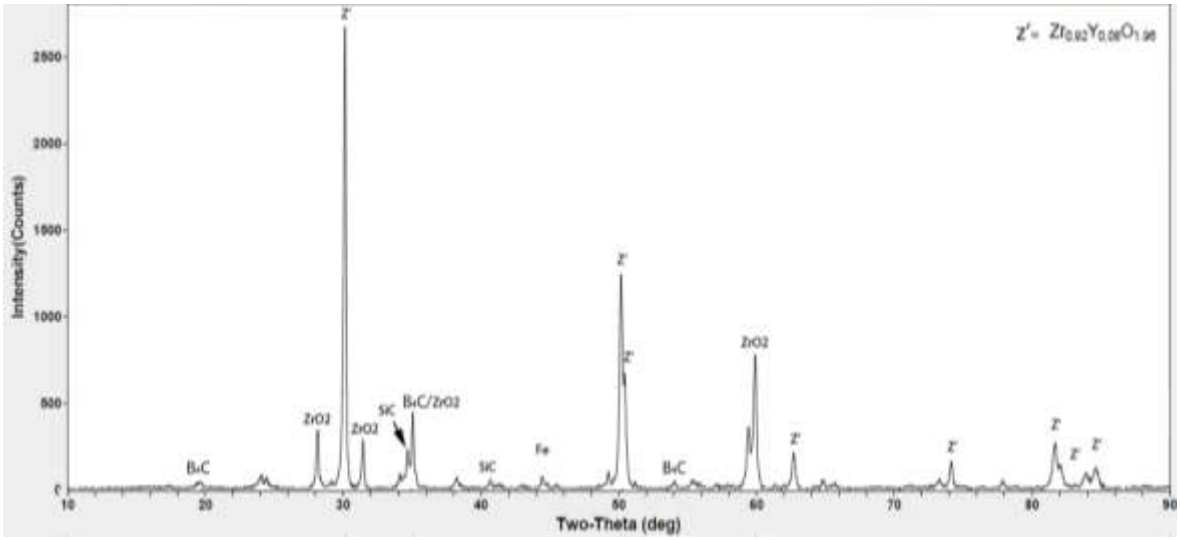
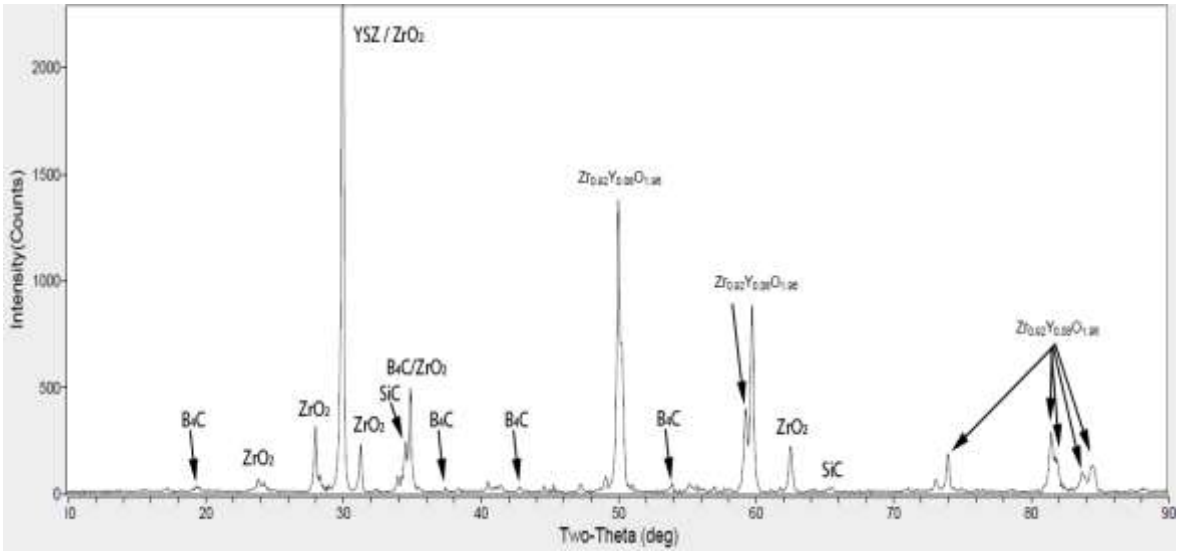


Figure 5 Fig 5 shows the SEM images of coating produced from %50 YSZ powder.



(a)



(b)

Figure 6 XRD patterns of as coated samples a) %75 YSZ b)%50 YSZ

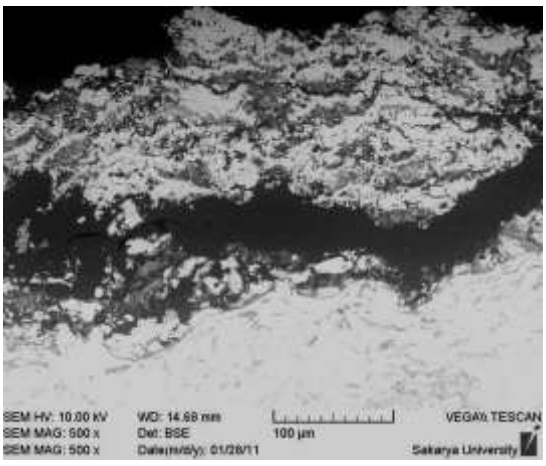
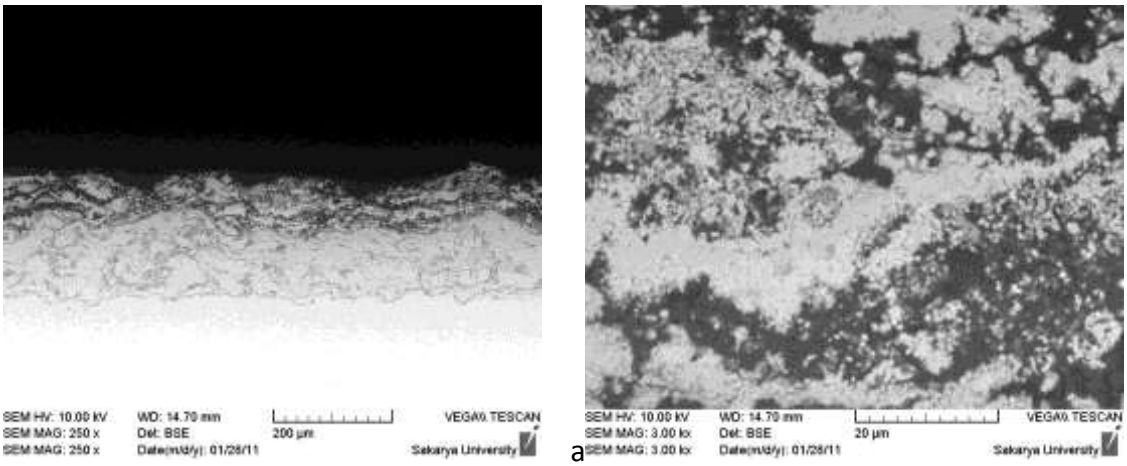


Figure 7 SEM images of %75 YSZ coating after 20h 1000°C



a

Figure 8 SEM image of %50 YSZ coating after 20 hour oxidation at 1000°C

Figure 9 shows that SEM image of top surface of %75 YSZ coating after 50h oxidation. From EDX analysis some boron oxide can be observed

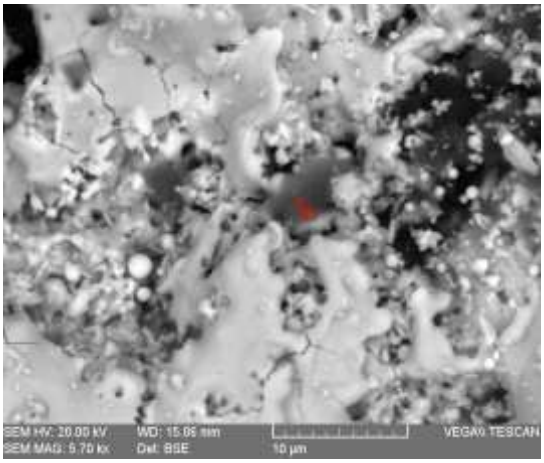


Figure 9 Top Surface SEM image of %75 YSZ after 50h oxidation.

Figure 10 shows the DSC-TGA graph of %75 coating. It can be seen there is a weight change over 700°C . From DSC –TG analysis ıt can be thought that there is clear oxidation after 700°C.

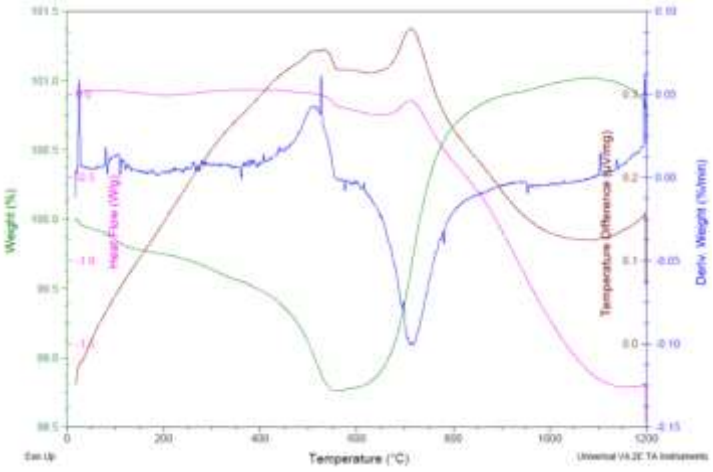


Figure 10 DSC-TG analysis of %75 YSZ coating.

It can be observed some reaction products after 200cycle burner rig tests from top surface SEM image given in Figure 11.

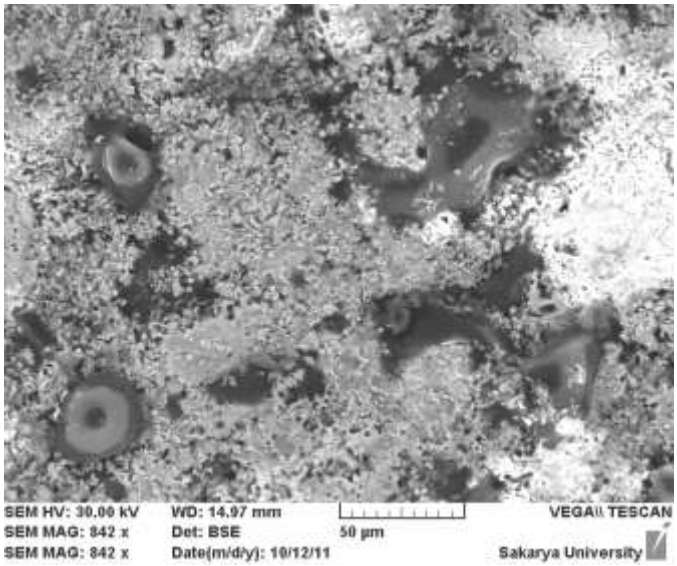


Figure 11 Top Surface SEM image of %50 YSZ coating after 200 cycle in burner rig.

Conclusions

Two different powder mixture were prepared and isothermal oxidation and thermal burner rig test were carried out in order to understand the self – healing behaviour of the coatings. Several silicon oxide and boron oxide phases were observed after both isothermal oxidation and burner rig tests.

References

1. ÜSTEL F., Plazma Sprey Kaplama Teknolojisi, (Plasma Spray Coating Technology), Master in Science Dissertation Istanbul Technical University Natural Science Institute. (1992).
2. KARAALİ İ., E., Termal Bariyer Kaplamalarını Termal Şok Özelliklerinin İncelenmesi(Investigation of Thermal Shock Properties of TBCs) , Master in Science Dissertation Sakarya University Natural Science Institute., (2008).
3. J. KITAMURA, S. Usuba, Y., Kakudate, H. Yokoib, K. Yamamoto, A. Tanaka, S. Fujiwara, “Formation of boron carbide coating by electromagnetically accelerated plasma spraying”, Surface and Coat. Techn. 169-170, pp. 324–327, (2003).
4. . KLOOLLOOS, Schouten M.J.W., “Thermal testing of low porosity microcracked thermal barrier coatings, National Aerospace Laboratory, NLR,(2002).
5. V.K Tolpygo, D.R Clarke, Morphological evolution of thermal barrier coatings induced by cyclic oxidation, Surface and Coatings Technology, V. 163–164, 30 January 2003, P. 81-86
6. D.R. Mumm, A.G. Evans, I.T. Spitsberg, Characterization of a cyclic displacement instability for a thermally grown oxide in a thermal barrier system, Acta Materialia, Volume 49, Issue 12, 17 July 2001, p 2329-2340
7. Sloof, G. Wim, -Healing in Coatings at High Temperatures, Self-Healing Materials, Publisher: Springer Netherlands Isbn: 978-1-4020-6250-6 (2008)
8. GUO Q, Song J, Liu L.,Zhangb., Factors Influencing Oxidation Resistance of B_4/C Composites With Self-Healing Properties”, Carbon Vol. 36, No. 11, pp. 1597–1601, (1998).

Effects of Production Method and Heat Treatment on the Adhesion Strength and Microstructural Behavior of MCrAlY Coatings

H. Dikici [a, *], A. C. Karaoglanli [b], T. Grund [c], T.Lampke [c], Y. Kucuk [d]
[a] Department of Mechanical Engineering, Kocaeli University, 41380, Kocaeli, Turkey
[b] Department of Metallurgical and Materials Engineering, Bartin University, 74100, Bartin, Turkey
[c] Institute of Materials Science and Engineering, Chemnitz University of Technology, 09107, Chemnitz, Germany
[d] Department of Mechanical Engineering, Bartin University, 74100, Bartin, Turkey

Abstract

Thermal barrier coatings (TBCs) are widely-used as protective and insulative coatings on hot section components of gas turbines and their applications, like blades and combustion chambers, power generation. TBCs are used to allow higher service temperatures hot section of turbines and thus higher turbine efficiencies. TBCs generally consist of a metallic bond coating (BC) usually MCrAlY, a ceramic top coating (TC) usually ZrO_2+Y_2O_3 and a thin oxide ceramic inter-layer (TGO) that forms under service condition within the bond coat / top coat interface. In this study, CoNiCrAlY powders were deposited on stainless steel substrate. High velocity oxy-fuel (HVOF) and Atmospheric plasma spraying (APS) techniques were used to produce two different types of bond coats. The ceramic top layers on both BC types were produced by APS. TBC specimens were subjected to heat treatment tests. Heat treatment tests was carried out in standard atmosphere at 550 °C, 650 °C and 750 °C for 1 and 2 hours. The microstructure and adhesion strength for top coat / bond coat interface of as sprayed and heat treated samples were investigated. Besides, the mechanical and microstructure behaviors of the produced layers in TBCs with heat treated and without heat treated samples were characterized and evaluated by SEM and optical microscope (OM). The results show the heat treatment of the coatings in different temperatures caused changes in microstructure and increase in adhesion strength properties of the coatings.

Key words: Thermal barrier coatings, heat treatment, adhesion strength, high velocity oxygen fuel (HVOF), atmospheric plasma spraying (APS)

1. Introduction

Thermal barrier coatings (TBCs) are applied for protection of metallic components that are supposed to high thermal gradients in applications such as gas turbines, diesel engines and jet engines [1–5]. To ensure high engine efficiency, TBCs' durability should be maintained at higher working gas temperatures without increasing component temperatures [6]. To obtain low thermal conductivity, TBCs are generally implemented onto a superalloy substrate and composed of a metallic bond coat and a ceramic top coat. A typical metallic bond coat, which is used as an oxidation resistance layer, consists of a MCrAlY composite (M: Co and/or Ni) and it is normally applied by implementing several spraying techniques such as Air Plasma Spraying (APS), Low Pressure Plasma Spraying (LPPS) or Vacuum Plasma Spraying (VPS). The High Velocity Oxygen Fuel (HVOF) technique has recently being used to obtain denser bond coats [1, 7-10]. As for ceramic top coat, TBCs have monolithic ceramics such as yttria stabilized zirconia (YSZ) as a heat insulating layer [11] and two general spray techniques are applied for ceramic top coating, i.e. Electron Bean assisted Physical Vapor Deposition (EB-PVD) and APS. APS and HVOF techniques have mostly been preferred due to having low cost alternative among spraying techniques mentioned above [12]. In APS process, coating material is used as powder particles and injected into a plasma flame. After melting the powder particles injected, the droplets occurred are accelerated towards the substrate. So, the droplets transform to a flat and solid coating layer as a result of impact onto the substrate surface [13]. HVOF thermal spray process provides better microstructure and adhesive strength for forming bond coats in TBCs compared with the APS process [14-17]. However, HVOF technique requires the high temperatures. Therefore, it leads to forming an oxidation environment during spraying process. The oxidation of the bond coat results in the formation of a thermally grown oxide (TGO), which leads to the early spilling of the TBC at the top/bond coat interface. Increasing in thickness of the TGO causes more internal stresses and, as a result of this, the early failure of TBC [7].TBCs should maintain their integrity against thermal gradients. Local heat changings on part surfaces lead to changes in the residual stress field and on the microstructure of the coating/substrate interface region due to thermo-mechanically induced metallurgical transformations in the coating and/or the substrate, such as solid state diffusion, phase transformations, grain growth, precipitation, coalescence of second phase particles, segregation and dislocation rearrangements [18]. Upon affecting these effects on mechanical and metallurgical properties of coating/substrate interface, the adherence of the TBC may be negatively affected and this situation should be taken into account in specific conditions that will occur during the service time. The adhesion between the interfaces in which top coat/bond coat and bond coat/substrate, directly affects the quality and further performance of TBCs. Adhesive bonding is highly related to several mechanisms i.e., mechanical keying, physical, chemical and diffusion [19-20]. Some other parameters having significant effects on coating adhesion can be classified as substrate-coating materials, cleaning and blasting of substrate, process type and parameters of coating application and environmental conditions [1]. Isothermal oxidation, which is occurred via the heat treatments, leads to an increase in the adhesion of the TBC compared to the as-sprayed condition [21]. In literature, it is seen that a lot of study have been carried out to determine the thermo mechanical and metallurgical properties of TBCs. However, in these studies performed, superalloys were frequently considered as a substrate and so, there is not much enough study to evaluate the characteristics and adhesion properties of TBCs after applying heat treatments when the stainless steel was selected as substrate. In this study, the austenitic stainless steel was selected as substrate due to its chemical composition and thermal conductivity features for TBC application. As for process type used, APS process was implemented for both the bond and top coats of TBC while the HVOF thermal spraying process was only applied for bond coat.

2. Experimental procedure

CoNiCrAlY powder with a particle size range of 5-37 µm, ZrO_2–8% Y_2O_3 with a particle size range of -45+20µm and were used as starting materials. The substrates, austenitic stainless steel coupons in the form of 25x28x3.5 mm, were grit blasted to clean and roughen the surface to increase the resulting coating adherence. After grit blasting the samples were cleaned ultrasonically in ethanol. The TBC samples consisted of a CoNiCrAlY bond coat (BC) and a ZrO_2–8%Y_2O_3 top coat (TC). In this study, HVOF and APS technique were used to produce bond coats. The ceramic top coatings were produced by APS method in both cases. HVOF K2 and GTV F6 APS systems were used to deposit coatings. All powders were standard thermal spray powders and delivered by GTV. All spraying parameters are shown in the Table 1. The thicknesses of the bond and top coats were about 100 µm and 300 µm, respectively.

Table 1. HVOF and Plasma spray parameters for bond and ceramic top coat powder deposition

YSZ Top Coatings			
Arc Current	Electrical power	Argon flow rate	
630 A	40 kW	44 slpm	
Hydrogen flow rate	Powder feed rate	Stand-off distance	
13 slpm	25 g/min	90 mm	
APS CoNiCrAlY Bond Coatings			
Arc Current	Electrical power	Argon flow rate	
600 A	40 kW	65 slpm	
Hydrogen flow rate	Powder feed rate	Stand-off distance	
14 slpm	30 g/min	140 mm	
HVOF CoNiCrAlY Bond Coatings			
Combustion medium		Powder Carrier Gas	Powder Feed Rate
O_2 (880 slpm) and kerosene (25 l/h)		Argon (15 slpm)	50 g/min
Powder feed gas flow		Stand-off distance	
12 slpm		330 mm	

The microstructures of TBC systems were investigated by optical (Olympus GX51) and scanning electron microscopy (SEM, LEO 1455VP). The constituent phases of the bond and top coats of the TBCs were analyzed by X-ray diffractometry (Siemens D5000). The porosity of the coatings was measured using an optical image analysis software (Olympus a4i). The oxidation behavior of TBC systems were investigated by Nabertherm high temperature furnace. Grit-blasted substrate and as deposited bond and top coatings surface roughness values were investigated by contact stylus instrument (statistical determination according to DIN EN ISO 3274). The microhardness of the coatings was measured by means of Vickers indentation (using an Duramin microhardness. tester) at a loading of 100 g for 15 s. The adhesion strength tests of the TBC samples were carried out regarding DIN EN 582 using FP-100 testing machine from Heckert (Germany). The adhesion tests applied to both of coating systems. Disc shaped samples with a diameter of 25X25X50 mm were used as substrate. Uncoated counter adhesion samples were grit blasted with aluminum oxide and the samples were ultrasonic cleaned by acetone and ethanol. The bonding of the samples was performed using a HTK Ultra Bond100 adhesive afterward the samples put into the furnace at 150 ° C with a holding time of 90 min. For each TBC system, at least three samples were subjected to the adhesion strength test.

3. Results and Discussions

3.1 Microstructure of the TBC systems

The cross section of the samples was observed under the Optical microscope and SEM (Fig. 2 a-d). The as-sprayed TBC samples showed a typical APS microstructure, with crack network and porosity in the bond and top coat. The as-sprayed TBC samples showed a typical HVOF microstructure, with high density and low porosity in the bond coat. The investigations of TBC system after 1h and 2 hours of heat treatment in air showed changes in the microstructure in area between BC and YSZ. After several heat treatment time, number of cracks occured both of TBC systems. These cracks became rather long at the ceramic/bond coat interface. Metallographic examinations of cross section showed presents not only horizontal cracks but also long vertical macro-cracks especially in area of ceramic top coat.

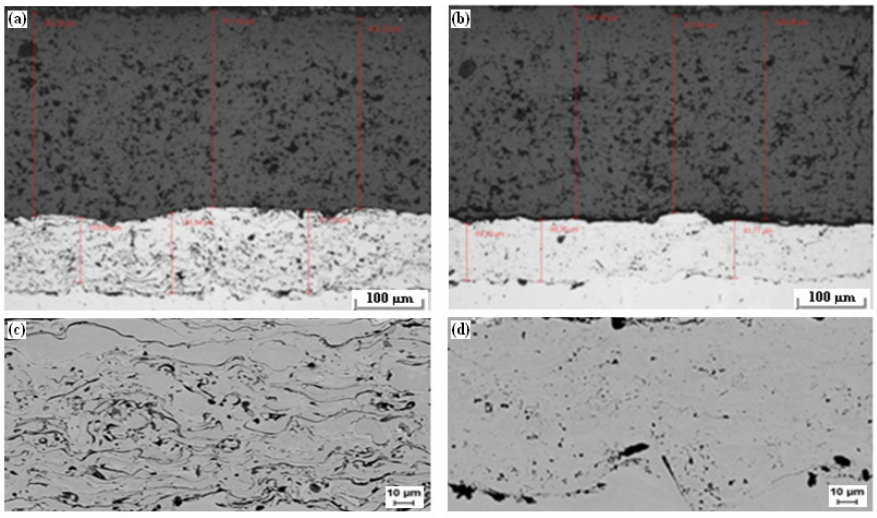


Figure 2. Optical cross-sectional and SEM bond coating microstructures of TBC samples; (a)-(c) APS-TBC, (b)-(d) HVOF-TBC

3.1. Surface roughness measurement of the coatings

Surface roughness measurement of the grit-blasted substrate as well as all as-sprayed coatings are summarized in Table 2.

Table 2. Average surface roughness values of the substrate and the as-sprayed coatings

Materials	**R_a (µm)**	**Materials**	**R_a (µm)**
Stainless Steel (grit-blasted)	6.14	Stainless Steel (grit-blasted)	6.30
HVOF-BC	4.57	APS-BC	5.15
APS-YSZ	5.24	APS-YSZ	5.16

3.2. Effect of heat treatment on adhesion strength and mechanical properties of APS and HVOF coatings

The average bond strength of the HVOF bond coat with APS top coat thermal barrier coating is superior to that of the APS bond coat with APS top coat thermal barrier coating. The bond strength of as-sprayed APS BC/ APS TC coating was 23.2 MPa whereas that of the HVOF BC/ APS TC coating was 25.5 MPa. Tensile adhesion strength measurement results of the as sprayed as well as all heat treated coatings are summarized in **Figure 3.**

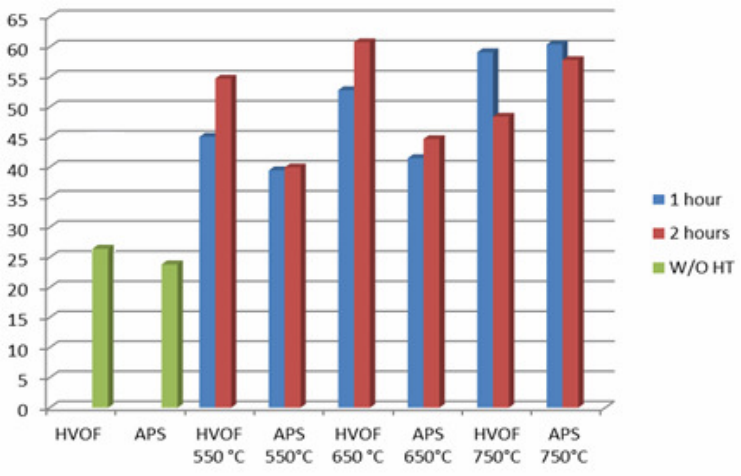


Figure 3. Tensile adhesion results of the coating systems from DIN EN 582 test

Fracture surfaces of a TBC systems after DIN EN 582 tensile test showing the bond coat ceramic interface of the all heat treated coatings are summarized in Figure 4.

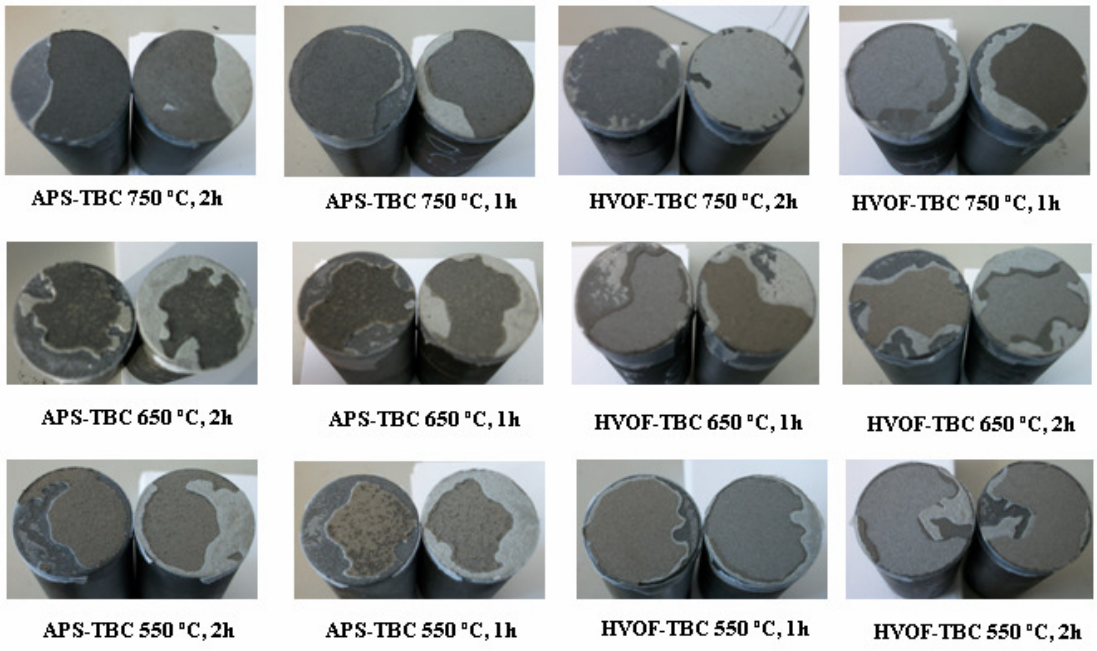


Figure 4. Fracture surfaces of a TBC systems after tensile tests

The microhardness of the coatings was measured by means of Vickers indentation (using an Duramin microhardness. tester) at a loading of 100 g for 15 s. The microhardness of substrate stainless steel is found to be in the range of 270-320 Hv. The microhardness values of all of bond and top coatings are shown in Figure 5 and 6.

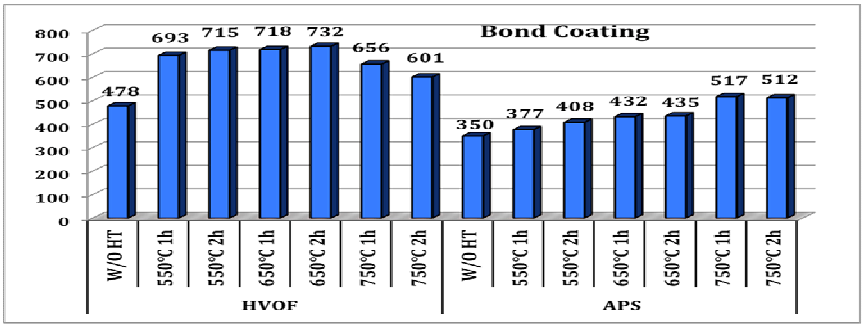


Figure 5. Microhardness results of the bond coatings for heat treated and without heat treated coatings

Microhardness values of TBC, which has HVOF bond coating showed generally increase that depends on time and temperature untill 750 ºC, but after 750 ºC values has decreased gradually. Microhardness values of TBC which has APS bond coating, showed generally increase depending on temperature and time.

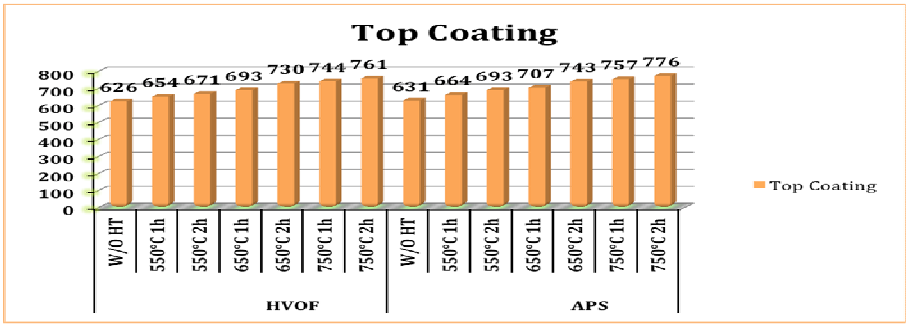


Figure 6. Microhardness results of the top coatings for heat treated and without heat treated coatings

Microhardness values of TBCs, which have top coating of HVOF and APS with bond coating, showed generally increase depending on temperature and time.

4. Conclusions

In this study, CoNiCrAlY powders deposited on stainless steel substrate. HVOF and APS techniques are used to produce different types of bond coats. On all samples, ceramic top layers are to be produced by APS. The produced TBC specimens were subjected to heat treatment tests that are to be carried out in natural atmosphere at 550 °C, 650 °C and 750 °C for 1 and 2 hours, respectively. Heat treatment procedure, which is applied depending on temperature and time parameters, in mechanical (hardness adhesion strength values), microstructural properties of TBCs, that are produced with different bond coating method has been observed changes. It was observed that rising temperature and time variables cause a increase in the adhesion strength and hardness of the coatings. These increases have taken place with a higher ratio in TBC systems with HVOF bond coatings. The microstructural investigations of TBC system after 1h and 2 hours of heat treatment in air showed changes in the microstructure in area between BC and YSZ. After several heat treatment time, number of cracks occured both of TBC systems.

References

[1]. C.R.C. Lima, J.M. Guilemany (2007) Adhesion improvements of Thermal Barrier Coatings with HVOF thermally sprayed bond coats, Surface & Coatings Technology 201 (2007) 4694–4701
[2]. W. Beele, G. Marijnissen, A. Lieshout, Van, The evolution of thermal barrier coatings—status and upcoming solutions for today's key issues, Surf. Coat. Technol. 120–121 (1999) 61–67.
[3]. A.G. Evans, M.Y. He, J.W. Hutchinson, Mechanics-based scaling laws for the durability of thermal barrier coatings, Prog. Mater. Sci. 46 (2001) 249–271.
[4]. A. Uzun, I. Cevic, M. Akcil, Effects of thermal barrier coating on a turbocharged diesel engine performance, Surf. Coat. Technol. 116–119 (1999) 505–507.
[5]. G.W. Goward, Progress in coatings for gas turbine airfoils, Surf. Coat. Technol. 108–119 (1998) 73–79.
[6]. J.A. Nesbitt, Thermal modeling of various thermal barrier coatings in a high heat flux rocket engine. Surface and Coatings Technology 130 (2000) 141-151
[7]. A.C. Karaoglanli, E. Altuncu, I. Ozdemir, A. Turk, F. Ustel Structure and durability evaluation of YSZ+Al2O3 composite TBCs with APS and HVOF bond coats under thermal cycling conditions. Surface & Coatings Technology 205 (2011) 369–373
[8]. Y. Itoh, M. Saitoh, M. Tamura, J. Eng. Gas Turbine Power 122 (2000) 43.
[9]. P. Vuoristo, S. Ahmaniemi, S. Tuurna, T. Mantyla, E. Cordano, F. Fignino, G.C. Gualco, Proceedings of ITSC 2002 — International Thermal Spray Conference and Exposition, Essen, Germany, vol. 1, ASM-International/DVS, Dusseldorf, Germany, 2002, p. 470.
[10]. V.V. Sobolev, J.M. Guilemany, J. Nutting, High Velocity Oxy-fuel Spraying: Theory, Structure–Property Relationships and Applications, Maney Publishing, London, 2004, 397 pp.
[11]. S. Rangaraj, K. Kokini Estimating the fracture resistance of functionally graded thermal barrier coatings from thermal shock tests. Surface and Coatings Technology 173 (2003) 201–212
[12]. A.G. Evans, D.R. Mumm, J.W. Hutchinson, G.H. Meier, F.S. Pettit, Prog.Mater. Sci. 46 (2001) 505.
[13]. P. Bengtsson, C. Persson, Modelled and measured residual stresses in plasma sprayed thermal barrier coatings. Surface and Coatings Technology 92 (1997) 78-86
[14]. N.J. Simms, P.J. Kilgallon, C. Roach, J.E. Oakey, D. Renusch, H. Echsler, M. Schutze, Mater. High Temp. 20 (4) (2003) 519.
[15]. Kh.G. Schmitt-Thomas, H. Haindl, D. Fu, Surf. Coat. Technol. 94– 95 (1997) 149.
[16]. F. Tang, L. Ajdelsztajn, G.E. Kim, V. Provenzano, J.M. Schoenung, Surf. Coat. Technol. 185 (2004) 228.
[17]. S.J. Bull, R.I. Davidson, E.H. Fisher, A.R. McCaber, A.M. Jones, Surf. Coat. Technol. 130 (2000) 257.
[18]. J. Lesage, M.H. Staia, D. Chicot, C. Godoy, P.E.V. De Miranda, Effect of thermal treatments on adhesive properties of a NiCr thermal sprayed coating. Thin Solid Films 377-378 (2000) 681-686
[19]. A.W.S., Thermal Spraying: Practice, Theory and Application, American Welding Society, Miami, FL, 1985.
[20]. V.V. Sobolev, J.M. Guilemany, J. Nutting, J.R. Miguel, Int. Mater. Rev. 42 (3) (1997) 117.
[21]. R. Eriksson, H. Brodin, S. Johansson, L. Östergren, X.-H. Li, Fractographic study of adhesion tested thermal barrier coatings subjected to isothermal and cyclic heat treatments. Procedia Engineering 10 (2011) 195–200.

Oxidation Behavior of Thermal Barrier Coatings With Cold Gas Dynamic Sprayed CoNiCrAlY Bond Coats

A. C. Karaoglanli [a,*], A. Turk [b], İ. Ozdemir [a], F.Ustel [b]
[a] Department of Metallurgical and Materials Engineering, Bartin University, 74100, Bartin, Turkey
[b] Department of Metallurgical and Materials Engineering, Sakarya University, 54187, Sakarya, Turkey

Abstract:

The paper presents the results of investigation into the oxidation resistance and thermally grown oxide (TGO) of thermal barrier coatings (TBC). TGO occurred during in service affect the lifetime of the component by introducing several kinds of degradation mechanisms such as decreasing bonding strength, initiation of stress concentration and thermal stresses which lead to crack initiation and propagation associated with delamination or spallation failure. Therefore, TGO plays important role on TBC durability. In this study, TBCs that consist of a typical bond layer / top layer system (CoNiCrAlY bond layers and YSZ top layers) are deposited on Inconel 718 superalloy substrates. The metallic bond coatings are applied via Cold Gas Dynamic Spraying (CGDS); the ceramic top coatings via Atmospheric Plasma Spraying (APS). Investigations are done concerning the oxidation behavior of this TBC system at 1100 °C in normal atmosphere for 8h, 24h, 50 h and 100 hours. The oxidation behaviour and microstructural properties during the oxidation test were evaluated and compared, and TGO growth behavior was also investigated under high temperature oxidation. The microstructural features and oxidation behaviours were characterized by scanning electron microscopy and energy dispersive X-ray spectroscopy. Phase stability of TBCs were evaluated by means of X-ray diffraction method.

Keywords: Thermal barrier coatings; Oxidation; Thermally grown oxide; Cold Gas Dynamic Spraying

1. Introduction

Due to their insulating property, thermal barrier coatings (TBC) are used in protection of hot section components against high temperature working environment in gas turbine engines. A TBC used in gas turbines typically consists of a superalloy substrate, a metallic bond coat with oxidation resistance (BC), a ceramic top coat (TC) and a thermally grown oxide (TGO) layer that forms between TC and BC by oxidation of BC due to high temperature and oxidizing environment [1-2]. It is widely stated that TGO structure and thickness have important role in failure of TBC system [1,3-4]. There is a general acception that the desired TGO is alfa alumina since this type of oxide has the lowest growth rate, higher top coat adhesion etc. [1,5-6]. In many studies relation between TGO formation and BC composition and microstructure is explained by applying the BC with different processes (such as APS, HVOF etc.) and exposing the coating to isothermal oxidation [7-9]. APS has a very high process temperature and melts the powder prior to deposition. As a result the produced BC is high in process induced oxides and Al content in some regions of such BCs is suggested to be low due to preferential oxidation of Al during process. [8,10]. Hence the alumina formation is deteriorated due to lack of Al at the interface. In HVOF sprays since the process temperatures are relatively low compared to APS, the powders to be deposited are usually semi-molten and undergo a plastic deformation during deposition. Thus, resulting BC is lower in oxide content and is denser. As a result, the BC is higher in Al content and TGO is higher in alumina compared to TGO forming on APS BCs [10-11]. Recent developments in CGDS, has made production of the superalloys employed in TBC possible with that process. The main advantage in this spray type is that almost no process induced oxide is involved and the resulting composition of the BC can be very close to feedstock powder [2,8]. Due to that property of CGDS process, the TGO of the BC is expected to be superior to those forming on other spray process BCs. To examine the oxidation behavior, CoNiCrAlY bond layers are deposited on an Inconel 718 substrate. After BC deposition with CGDS, YSZ top layer is deposited by APS. The resulting TBC is isothermally oxidized at 1100 °C in normal atmosphere for 8 h, 24 h, 50 h and 100 h periods. The compositional and microstructural properties of TGO and BC are evaluated via use of scanning electron microscopy (SEM) and X-ray diffraction.

2. Experimental

2.1 Material and methods

Inconel 718 nickel based superalloy disc shaped samples with a diameter of 25.4 mm and thicknesses of 5 mm, were used as substrate. CoNiCrAlY (Sulzer-Metco USA, Amdry 9951, 5-37 μm) and ZrO_2/Y_2O_3 (GTV Germany, -45+20 μm) powders were used as the feedstocks for the deposition of the bond and top coats. The thickness of the bond and ceramic top coats were measured as 100 μm and 300 μm, respectively. The used spraying systems were a Plasma Giken CGDS system and a GTV F6 APS system.

The oxidation behavior of TBC systems were investigated by Protherm high temperature furnace. All spraying parameters are shown in the Table 1.

Table 1. CGDS and Plasma spray parameters for bond and ceramic top coat powder deposition

YSZ Top Coatings		
Arc Current	Electrical power	Argon flow rate
630 A	40 kW	44 slpm
Hydrogen flow rate	Powder feed rate	Stand-off distance
13 slpm	25 g/min	90 mm
CGDS CoNiCrAlY Bond Coatings		
Sprey pressure	Gas temperature	Working gas
3.0 MPa	600 °C	Helium
Gun speed	Stand-off distance	
20 mm/sec	15 mm	

3. Results and Discussions

3.1 Microstructure of the As-Deposited TBC

CGDS and its top coatings, cross-sectional microstructure of SEM bond/top coating interface that are produced with APS method is shown in Figure 1.

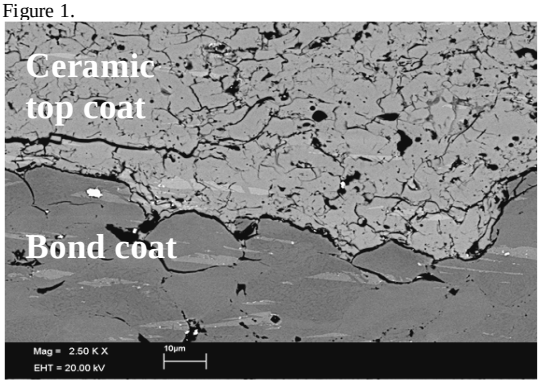


Figure 1. An image of the cross-sectional microstructure of TBC produced with CGDS method

It is seen that bond coating microstructure of TBC produced with CGDS method have gaps and porosity that can be seen with naked eye. The presence of these gaps and porosity on bond coating structure are thought to be caused by insufficient local plastic deformation of the particles that crash each other during accumulation and this situation's causing small gaps between two adjacent particles.

3.2. Oxidation behavior of coatings

CoNiCrAlY bond layer produced with CGDS method consists of bcc structure β-(Co,Ni)Al precipitates and fcc structure γ-matrix (Ni,Co) phases. β- precipitates structure that is rich in Al shows formation depending on oxidation and disappears as a result of decreasing of Al concentration in time. After oxidation tests that are carried out at 1100 °C and different time processes, TGO layer formed on bond and top coating interface as a result of oxygen penetration from top ceramic coating and this formation structure can also vividly be seen in microstructures in Figure 2.

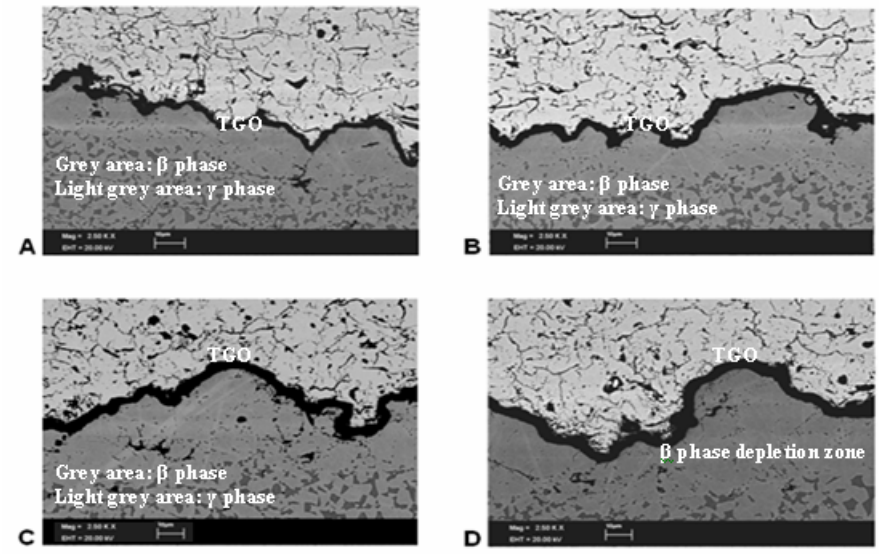


Figure 2. Oxidation SEM cross-sectional microstructures of TBC samples at 1100 °C that have CGDS CoNiCrAlY bond and APS YSZ top coating: (a) 8 hours, (b) 24 hours, (c) 50 hours and (d) 100 hours

The thickness of formed TGO structure shows an increase depending on time. Al_2O_3 layer formed at interface as a result of the increase of oxygen and aluminum concentration at ceramic top coating and bond coating interface. Generally, at first stages of oxidation, Al_2O_3 form does not undergo a structural change and have a more decisive structure, however, mixed oxide structures (light grey colored) are seen to form on Al_2O_3 form depending on the increasing time. CoNiCrAlY bond layer consists of β-(Co,Ni)Al precipitates and γ-(Ni,Co) matrix micro-structure. β- precipitates structure that is rich in Al shows formation depending on oxidation and disappears as a result of the decreasing of Al concentration depending on time. At 1100 °C after 50 hours oxidation, it is seen that β- precipitates decreases starting at TGO level and forms at depletion zone. Micro-structures with some cracks and non-continuous gaps are also seen on top ceramic coating structure. Different discontinuities, porosity and crack-like formations are present at interface zones of coatings. As it can vividly be seen in the micro-structure and elemental distribution in Figure 3. TGO oxide structure that form between bond and top coating have Al and O elements and formation of mixed oxide structures on the interface are seen, as well. Besides Al and O elements density is high in TGO zone, mixed oxides are seen at light grey areas outside the Al_2O_3 oxide layer.

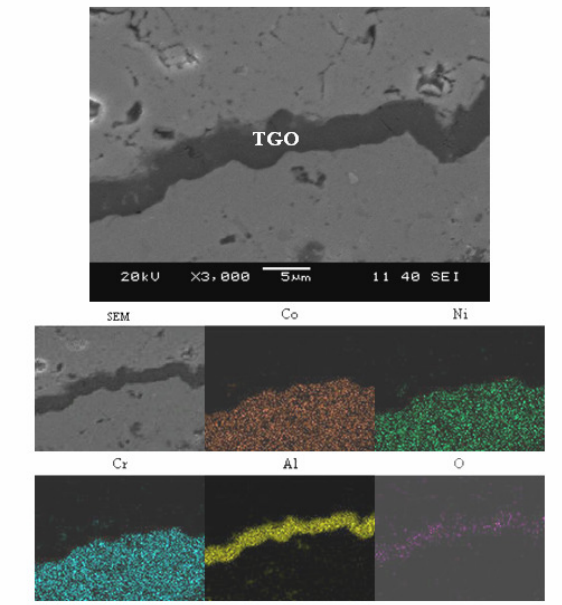


Figure 3. SEM image and EDS elemental mapping showing the surface oxide morphology of TBCs with CGDS bond coating following 100 h of oxidation at 1100 ℃

3.3. XRD analysis

XRD analysis results of bond coating, produced with CGDS method at 1100 ℃ and 100 hours and XRD analysis results of TBCs, that have bond coating produced with CGDS method, at 1100 ℃ temperature and 8, 24, 50 and 100 hours are shown in Figure 4 and Figure 5.

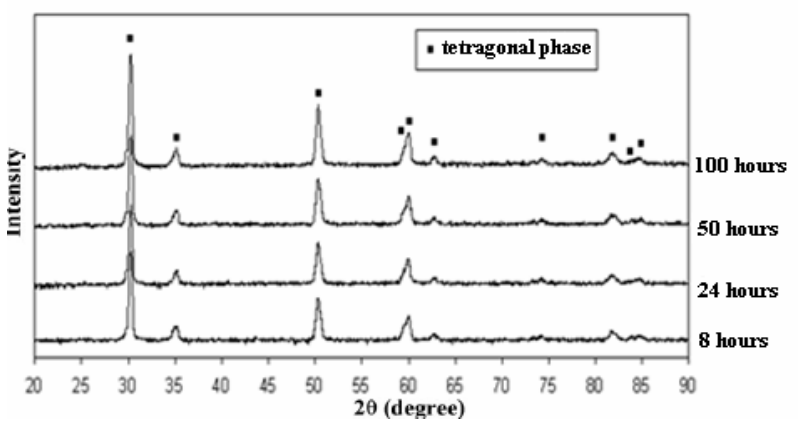


Figure 4. XRD patterns of TBCs after various oxidation times at 1100 ℃

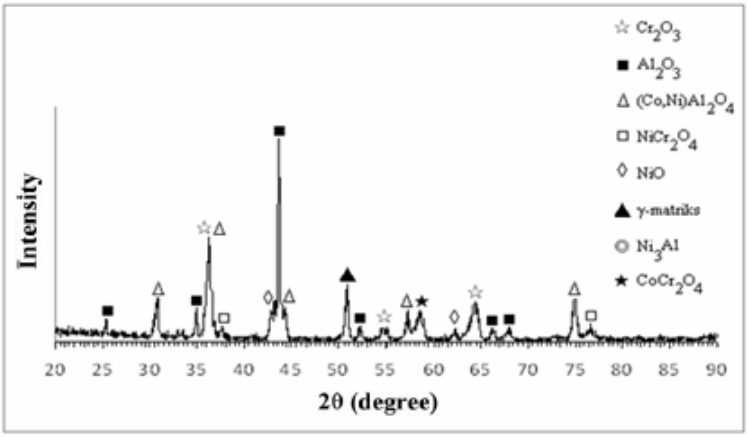


Figure 5. XRD patterns of CGDS CoNiCrAlY coatings following 100 h of oxidation at 1100 ℃ temperature

When XRD analysis results of bond coatings produced with CGDS method are investigated, Al_2O_3 phase is generally seen to be stable position. Mixed oxides as NiO and spinel phase structures are seen to form on bond coating.

3.4. TGO growth behavior of TBC

After 8, 24, 50 and 100 hour oxidation processes of TBCs whose bond coating are produced with CGDS method, thickness change of TGO layer in tme is shown in Figure 6. at TGO layer thickness counts whose measurement has been done on SEM micro-structure views that are taken at 2500X magnification, measurements are done on 4 micro-structure photos for each specimen and measurements, changing between 10 and 20 in the average, are taken for each micro-structure. Measurements are done on areas where TGO remains its continuity and unity. Measurements are done at a point where TGO layer, which lies parallel to bond/top coating interface, growth direction, namely vertical to bond coating surface.

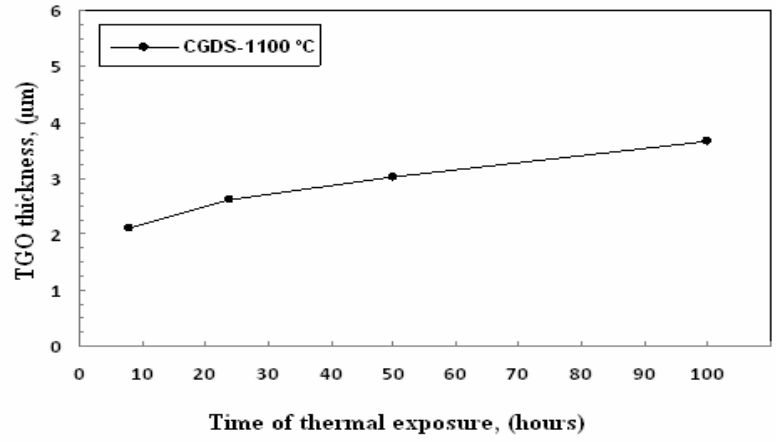


Figure 6. TGO growth in TBC with a CDGS-CoNiCrAlY bond coat at 1100 ºC for 8, 24, 50 an 100 hours

It can be seen in Figure 4 that the thickness of TGO structure that forms in TBC system shows increase depending on the increasing time.

4. Conclusions

In the present work, oxidation behaviour and micro-structural characterization were studied in TBC system with CGDS bond coats during high temperature oxidation for different times. It is seen that as-sprayed TBC coating structure is generally uniform and in a dense structure, local gaps form in bond coating structure as a result of insufficient local plastic deformation of particles that crash each other during accumulation. It is seen that ceramic top coating structure produced with APS method have high porosity because of process production conditions and crack and many similar imperfect formation structures. At the micro-structure inspections after oxidation, it is seen that CoNiCrAlY bond layer that is produced with CGDS method consists of bcc structure β-(Co,Ni)Al precipitates and fcc structure γ-matrix γ-(Ni,Co) matrix phases. β- precipitates, which is rich in Al, structure disappears as a result of the decrease of Al concentration depending on time, by showing formation depending on oxidation. After oxidation tests that are carried out at 1100 ºC temperature and different time processes, TGO layer is seen to form on the bond and top coating interface as a result of top ceramic coating's oxygen penetration and TGO thickness increased depending on the increasing oxidation time. In the XRD inspections after coating oxidation; it is seen that other mixed oxide formations besides Al_2O_3 phase exist in coating structure. Consequently, that coating structure undergoes change depending on the increasing oxidation, TGO oxide layer forms in BC/TC interface and thickness increases because of increasing oxidation and other mixed oxide layers form in the interface as a result of Al_2O_3 structure, which forms TGO, losing its unity are seen as a result of micro-structural inspections and XRD analysis.

5. Acknowledgment
This work partially supported by The Scientific and Technological Research Council of Turkey (TUBITAK, 111M265).

References
[1]. EVANS A.G., MUMMA D.R., HUTCHINSON J.W., MEIERC G.H., PETTIT F.S., Mechanisms controlling the durability of thermal barrier coatings, Progress in Materials Science, 46 (5), 505–553, 2001.
[2]. LI Y., LI C.J., ZHANG Q., YANG G.J., LI C.X., Influence of TGO composition on the thermal shock lifetime of thermal barrier coatings with cold-sprayed MCrAlY bond coat, Journal of Thermal Spray Technology, 19 (1-2), 168-177, 2010.
[3]. RABIEI A., EVANS A.G., Failure Mechanisms Associated with the Thermally Grown Oxide in Plasma-Sprayed Thermal Barrier Coatings, Acta mater, 48, 3963–3976, 2000.
[4]. VaßEN R., GIESSEN S., STOVER D., Lifetime of Plasma-Sprayed Thermal Barrier Coatings: Comparison of Numerical and Experimental Results, Journal of Thermal Spray Technology Volume, 18(5-6), 835-845, 2009.
[5]. MERCIER D., KAPLIN C., GOODALL G., KIM G., BROCHU M., Parameters influencing the oxidation behavior of cryomilled CoNiCrAlY, Surface & Coatings Technology, 205 (7), 2546-2553, 2010.
[6]. PUETZ P., HUANG X., YANG Q., TANG Z., Transient Oxide Formation on APS NiCrAlY After Oxidation Heat Treatment; Journal of Thermal Spray Technology, 20 (3), 621-629, 2011.
[7]. BRANDL W., TOMA D., KRUGER J., GRABKE H.J., MATTHAUS G.,The oxidation behaviour of HVOF thermal-sprayed MCrAlY coatings, Surface & Coatings Technology, 94-95, 21-26, 1997.
[8]. RICHER P., YANDOUZI M., BEAUVAIS L., JODOIN B., Oxidation behaviour of CoNiCrAlY bond coats produced by plasma, HVOF and cold gas dynamic spraying; Surface & Coatings Technology, 204, 3962–3974, 2010.
[9]. YUAN F.H., CHEN Z.X., HUANG W Z.W, WANG Z.G., ZHU S.J., Oxidation behavior of thermal barrier coatings with HVOF and detonation-sprayed NiCrAlY bondcoats, Corrosion Science, 50, 1608-1617, 2008.
[10]. CHEN W.R., WU X., MARPLE B.R., LIMA R.S., PATNAIK P.C., Pre-oxidation and TGO growth behaviour of an air-plasma-sprayed thermal barrier coating; Surface & Coatings Technology, 202 3787–3796, 2008.
[11]. CHEN W.R., WU X., MARPLE B.R., NAGY D.R., PATNAIK P.C., TGO growth behaviour in TBCs with APS and HVOF bond coats, Surface & Coatings Technology, 202, 2677–2683, 2008.

Thermal stability of TiZrAlN films deposited by a reactive magnetron sputtering method

G. Abadias[1], I. A. Saladukhin[2], V.V. Uglov[2], S. V. Zlotski[2]

[1]*Institut P', Université de Poitiers-CNRS-ENSMA, SP2MI, Téléport 2, F86962 Chasseneuil-Futuroscope, FRANCE, gregory.abadias@univ-poitiers.fr*

[2]*Belarussian State University, 4 Nezavisimosti ave., 220030 Minsk, BELARUS, solodukhin@bsu.by*

Introduction

Quaternary TiZrAlN films are:

• perspective for both oxidation and wear resistance applications and expectant substitution for TiN, (Ti,Al)N and (Ti,Zr)N hard films [1-4];

• capable to possess by the unique properties due to possibility of nanocomposite structure formation during their synthesis [3, 5].

The aim of the present work is to study the thermal stability, under vacuum and air annealing, of quaternary transition metal nitride films, namely $(Ti,Zr)_{1-x}Al_xN$, with emphasis on the role of Al content on the structure and phase formation.

Coating growth conditions

$(Ti,Zr)_{1-x}Al_xN$ films with thickness of 300 nm have been deposited onto Si (001) wafers by a reactive unbalanced magnetron sputtering method. Titanium, zirconium and aluminum targets were co-sputtered under mixed $Ar+N_2$ plasma discharges at a total pressure in the working chamber equal to 0.20 Pa. Varying the RF power of the Al target from 20 to 200 W resulted in a concentration of aluminum x_{Al} in the films to increase from 2.6 to 36.4 at.%, while the Ti:Zr concentration ratio was kept constant to ~1.0.

Influence of Al concentration on phase formation and structure of as-deposited $(Ti,Zr)_{1-x}Al_xN$ films

Results of the XRD analysis on as-deposited films indicate the formation of (Ti,Zr,Al)N solid solution. However, with rising Al concentration, the structure changes from nanocrystalline to nanocomposite and then it turns into the amorphous state. This structural evolution is accompanied with a transition from (111) to (200) texture at low Al concentrations and by a subsequent displacement of the (Ti,Zr,Al)N diffraction peak to area of hexagonal AlN mononitride at the aluminum concentration $x_{Al} \geq 13.8$ at.%.

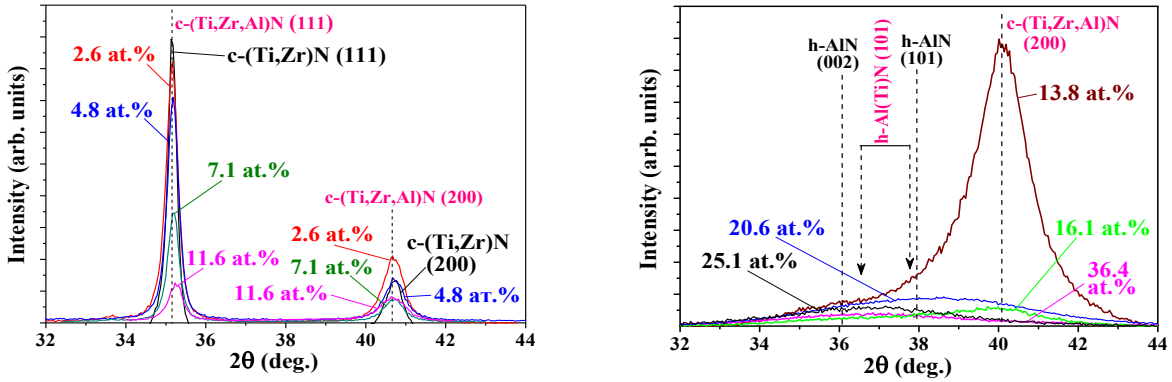


Fig. 1. Evolution of XRD patterns with Al content

Thermal stability of $(Ti,Zr)_{1-x}Al_xN$ films during annealing in air

Annealing under air atmosphere of the samples coated by $(Ti,Zr)_{1-x}Al_xN$ films was carried out for temperature intervals ranging from 400 to 950°C using in situ temperature XRD.

Corresponding to the (Ti,Zr,Al)N solid solution the diffraction lines disappear at T=600°C. At the same temperature (600°C), the initiation of a film oxidation process is observed. However, the intensive formation of orthorhombic $(ZrTi)O_4$ oxide phase occurs only at the temperature of 780°C.

Increase in x_{Al} up to 25.1 at.% leads to oxide formation reduction that can be explained by the passivating role of the Al_2O_3 surface layer.

Al target RF power supply (W)	[Ti] / ([Ti]+[Zr])	[Al] / ([Al]+[Ti]+[Zr]) (%)
30	0.52	4.8
60	0.52	11.6
80	0.52	16.1
120	0.51	25.1
200	0.50	36.4

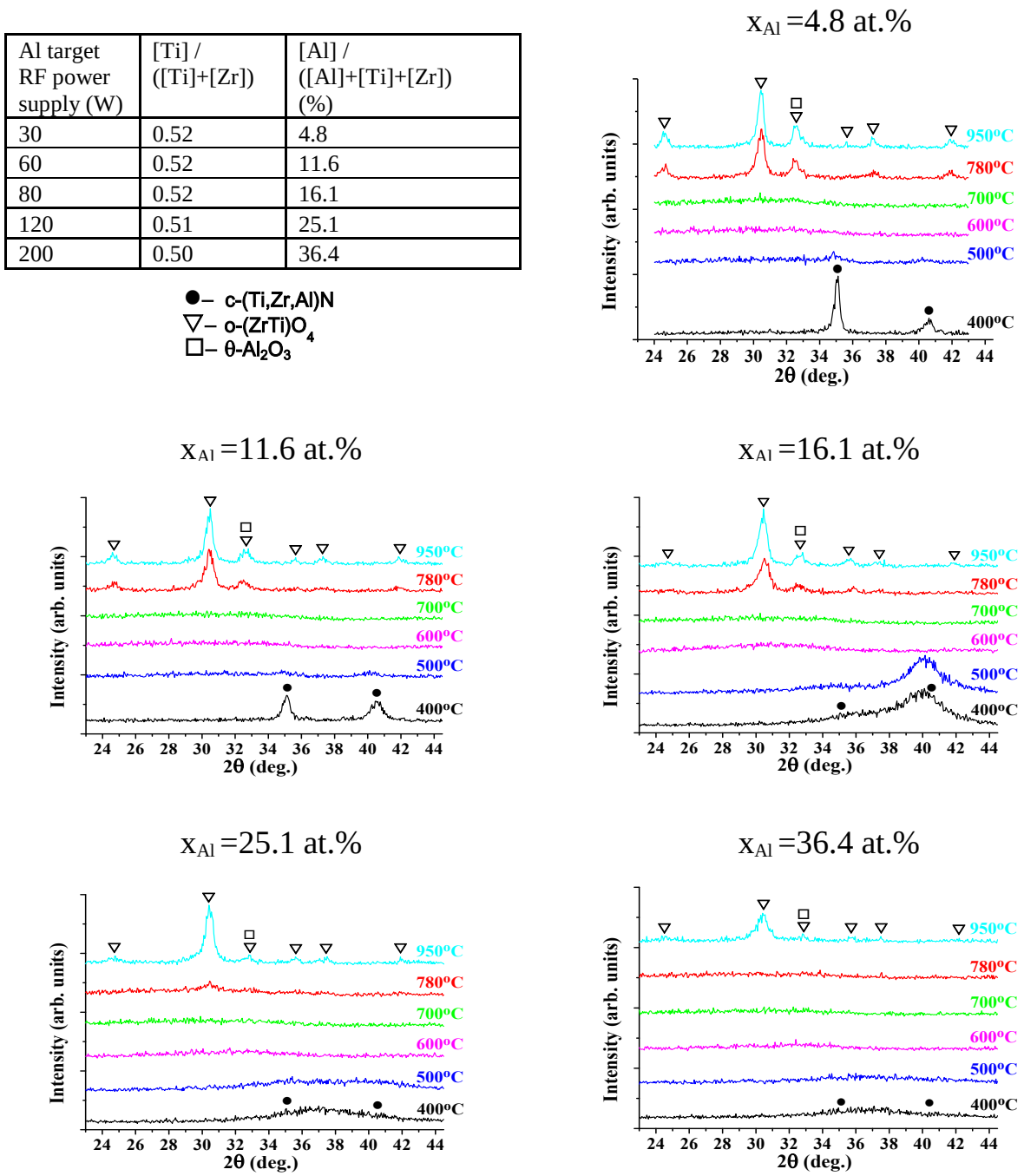


Fig. 2. Evolution of XRD patterns with annealing temperature increase

Thermal stability of $(Ti,Zr)_{1-x}Al_xN$ films under annealing in vacuum

Annealing in vacuum (~10^{-4} Pa) at the temperature of 600°C does not cause any essential change of (Ti,Zr,Al)N solid solution structure.

After annealing in vacuum at 950°C, the structure of the films depends essentially on the aluminum content. At the smaller Al concentrations, the (Ti,Zr,Al)N solid solution remains stable.

The TiN and ZrN mononitride phases become dominating when $x_{Al} \geq 13.8$ at.%. At the same time, aluminum is apparently included substitutionally into these phases by forming the solid solutions of TiAlN and ZrAlN type.

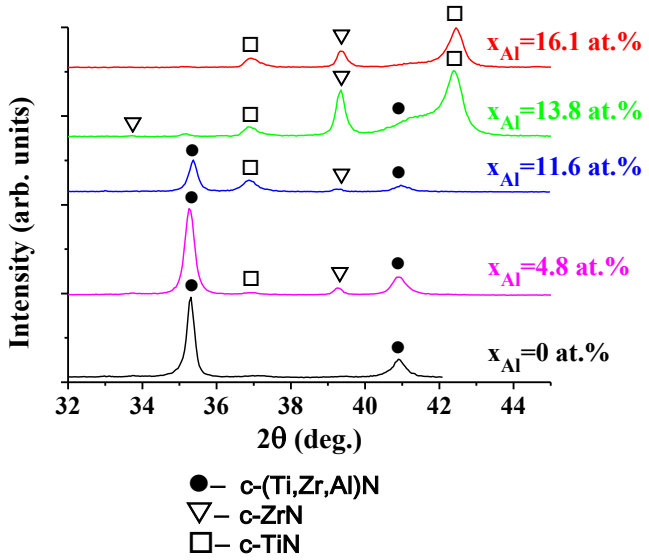


Fig. 3. Phase composition of $(Ti,Zr)_{1-x}Al_xN$ films after annealing in vacuum (950°C)

Conclusions

- With the increase of the Al concentration (x_{Al}) the structure of $(Ti,Zr)_{1-x}Al_xN$ films changes from nanocrystalline (c-(Ti,Zr,Al)N) to nanocomposite (c-(Ti,Zr,Al)N + + h-Al(Ti)N) and then to the amorphous state (a-(Ti,Zr,Al,N))
- Under annealing in air the films in a-(Ti,Zr,Al,N) state ($x_{Al} \geq 25.1$ at.%) are characterized by the highest oxidation resistance
- Under annealing in vacuum the (Ti,Zr,Al)N solid solution remains stable (at $x_{Al} \leq 4.8$ at.%) when the temperature changes from 600 to 950°C, and it decomposes onto mononitrides at higher Al concentration when the temperature reaches 950°C

References

1. L.Chen et al. Thin Solid Films **519** (2011) 5503
2. J. Zhang et al. Thin Solid Films **517** (2009) 4830
3. Y.J.Kim et al. Thin Solid Films **516** (2008) 3651
4. V.P.Tabakov et al. Russian Engineering Research **30/1** (2010) 84
5. G.Abadias et al. Reviews to Nanomeeting, Minsk, 24-27 May 2011, pp. 458-461.

Lifetime Assessment and Shock Behavior of TBC in Gas Turbine Blades: Experimental and Numerical Investigations

Yaşar Kahraman, İmdat Taymaz.*
Sakarya University, Engineering Faculty, Adapazari, Turkey

taymaz@sakarya.edu.tr

ABSTRACT

In this study, the thermal shock behaviour of a thermal barrier coating system of a gas turbine engine's turbine blade of the space and aircrafts are evaluated. The thermal shock behaviour of the thermal barrier coating system was investigated. Computer-assisted thermal (ANSYS) and crack growth (FCPAS) analyses were carried out with the help of the obtained information. Thermal barrier coating system consists of nickel based superalloy substrate, ytria stabilized zirconia (%8 YSZ) ceramic top coat and NiCrAlY bond coat. Plasma spray method was used for coatings. Damages that occurred in the specimens were assessed according to cycle numbers, thermal stress and heating time. With the aid of the experiments, stress analyses of the modelled TBC were performed. The crack profiles and crack progression rates were determined. Finally the coating life was determined.

1. Introduction

To protect turbine blades in hot working conditions from thermal stresses and other effects, TBC was applied on to the structure of the blade. Different types of coating technologies are widely used for turbine blades. Thermal barrier coating (TBC) systems, consisting of yttria partially stabilized zirconia (YSZ), thermally grown oxide (TGO) and a metallic bond coat, are used in applications for thermal protection of hot-section parts in gas turbine engines [1-5].

The interface regions undergo high stresses due to the mismatch of thermal expansion between BC and TBC. Additionally, growth stresses due to the development of thermally grown oxide (TGO) at the interface and stresses caused by interface roughness are superimposed. Stress relaxation generally leads to a reduction in stress levels at high temperature, but can also give rise to enhanced stress accumulation after thermal cycling, which results in early crack initiation at the bond coat/alumina interface and spallation failure afterwards [6-12].

It is clear that thermal barrier coatings have an important role in current applications and in the new generation of engines that are being designed. In addition to this, durability and reliability limits the benefits of thermal barrier coatings. Due to the lack of a reliable lifetime assessments, full use of the potential of these coatings is not possible. Proper understanding of damage mechanisms in thermal barrier coatings is a key factor for increasing the durability and reliability of the coating. [13].

In this study, cracks that formed on the coatings due to thermal stress were investigated experimentally, and a finite element model was developed based on the results obtained from the experiments. For the base blade material, Nickel base alloy substrate was used. As a bond coating material NiCrAlY was preferred. YSZ was selected for the top coating layer. See

table 1 for materials' details. For the TBC used geometry, the turbine blade was covered with a 150 micron thickness of a super alloy bond coating (NiCrAlY). For over the bond coating layer, 350 micron thickness of YSZ (ytria stabilized zirconia) was used as a top coating.

Table 1: Material properties of substrate, bond coat and top coating

Material	Thermal Conductivity [W/m°C]	Thermal Expansion 10-6 [1/°C]	Density [kg/m3]	Specific Heat [J/kg°C]	Poisson's ratio	Young's Modulus [GPa]
Ni-base alloy	19	15	8190	575	0,3	18
NiCrAlY	20,7	15,4	7710	567	0,25	16,8
YSZ	1	10.8	5240	582	0,25	50

2. Experimental Study

In the literature, for thermal and structural analysis of the turbine blade, a small segment of the turbine blade is obtained and subjected to thermal shock tests. The front surface temperature of the test sample was raised to 1250°C and maintained at this temperature for 5 minutes. While heating, the rear side of the test sample was cooled with a high flow of air to obtain a controlled temperature gradient. In this way, the temperature of the base was maintained at 800°C. After completing the heating process, burning gas was removed automatically from the coating surface which was then cooled from both sides with pressurized air for 2 minutes.

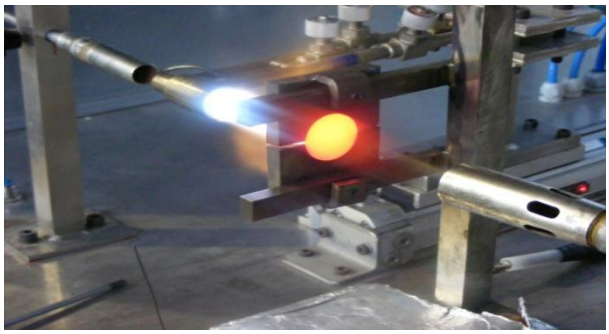


Figure 1.Sample view at the time of experiment

The samples were taken for macro evaluation at the end of every 50 cycle, and for micro evaluation at the end of every 500 cycles. Samples for micro analysis were obtained by cutting the cross-sections, and cracks that formed were identified with the aid of a Scanning Electron Microscope (SEM).

3. Modelling and analysis

The "Solid-90" used for thermal analysis and the "solid-186" element type used for structural analysis were generated by sweep meshing the hexagonal shape that provided the best result. Mesh was performed in a sequential and correct manner according to material characteristics

and element type that were entered to the finite element model formed on ANSYS. All parameters necessary for thermal and structural analysis were entered to the crucial points formed after meshing. Data was formed on the FCPAS program using the results obtained from these analyses. FCPAS is an interface, based on finite elements method that can perform the three dimensional breaking analysis for engineering materials and crack progression analysis for cylindrical models with a plate. By using ANSYS in the crack progression analysis, the horizontal cracks in the three dimensional coating were modelled, parametric macros were generated under thermal loads, and individual analysis were performed.

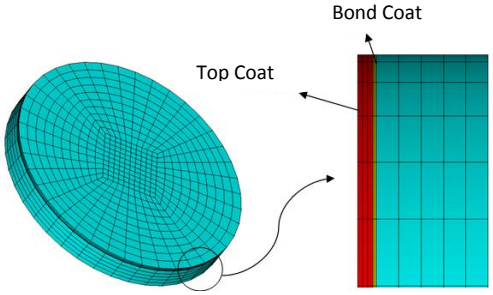


Figure 2. Finite element model of the experimental sample

4. Results and discussion

In the experiments, the sample heating rate was 20 ºC/s, and cooling rate was 10 ºC/s. İt was determined that the experimental data and numerical results for the heating and cooling times overlapped with1.2% deviation. As a result of the analyses that were performed, it was calculated that when the upper surface temperature reached 1232 ºC, the base temperature was 990 ºC. It was hence determined that the TBC with YSZ provided 19.6% thermal protection by reducing the base temperature by 242 ºC.

In the life estimates that were performed, it was calculated that, as shown in Figure 3, the crack size progressed 1 mm from the side towards the center at the end of 1500 cycles, 1.45 mm at the end of 1750 cycles, and 2.6 mm at the end of 2000 cycles. At the end of 2300 cycles, the crack size reached 20% of the radius, which corresponds to 3 mm. It was observed that the experimental data and numerical results overlapped with 3.6% deviation at most.

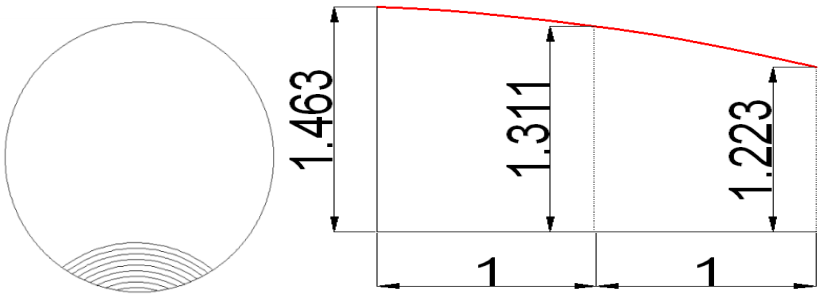


Figure 3. Graph of crack length according to the number of cycles obtained experimentally and numerically

As seen on Figure 4, it was determined that the crack profile is epileptic and that it overlaps with the numerical results with a 1% deviation.

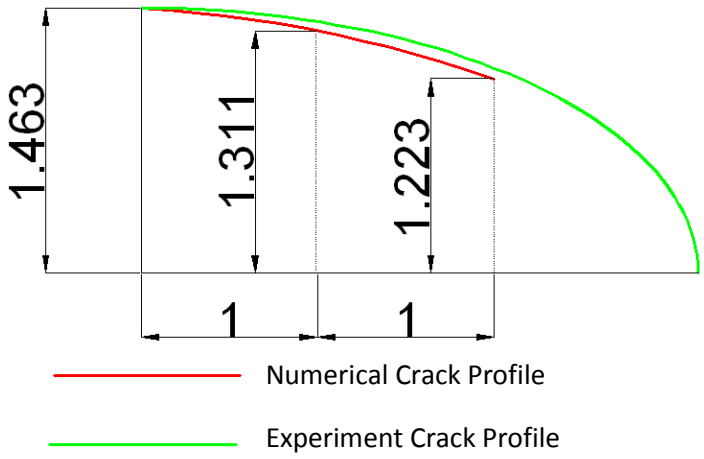


Figure 4. Crack profiles obtained experimentally and calculated numerically

References

[1] R.A. Miller, Surf. Coat. Technol. 30 (1987) 1.

[2] D.J. Wortman, B.A. Nagaraj, E.C. Duderstadt, Mater. Sci. Eng.A 121 (1989) 433.

[3] S.M. Meier, D.M. Nissley, K.D. Sheffler, T.A. Cruse, J. Eng.Gas Turbines Power Trans. Am. Soc. Mech. Eng. 114 (1991)258.

[4] R.T. Jones, Thermal barrier coatings, in: K.H. Stern (Ed.),Metallurgical and Ceramic Protective Coatings, Chapman &Hall, London, 1996, p. 194.

[5] R.D. Jr. Sisson, E.Y. Lee, Y.H. Sohn, in: K.S. Shin, J.K. Yoon, S.J. Kim (Eds.), Proceedings of the 2nd Pacific Rim InternationalConference on Advanced Materials and Processing, TheKorean Institute of Metals and Materials, 1995, p. 1203.

[6] A.G. Evans, D.R., at all, Prog. Mater. Sci. 46 (2001) 505.

[7] G. Fleury, F. Schubert, Anisotrope Stoffgesetze für dasviskoplastiche Verformungsverhalten der einkristallinen Superlegierung CMSX-4, Dissertation, RWTH Aachen, Jül-3436 (1997) ISSN 0944-2952.

[8] F. Schubert, G. Fleuri, T. Steinhaus, Modelling of the mechanical behaviour of the SC

alloy CMSX-4 during thermomechanical loading, Modelling Simul. Sci. Eng. 8 (2000) 947

[9] F. Schubert, G. Fleuri, T. Steinhaus, Modelling of the mechanical behaviour of the SC

alloy CMSX-4 during thermomechanical loading, Modelling Simul. Sci. Eng. 8 (2000) 947.

[10] T.B. Thoe, D.K. Aspinwall, N. Killey, J. Mater. Proc. Technol. 92–93 (1999) 323.

[11] M. Miao Jr., C.-Y. Wu, Int. J. Heat Mass Transfer 49 (2006) 919.

[12] K.T. Voisey, T.W. Clyne, Surf. Coat. Technol. 176 (2004) 296.

[13] VaBen, R., Kerkhoff, G., Stöver, D., Mater. Sci. Eng.A, 100-109, (2001), 303.

Novel Nanometer Thin Films On Magnesium Alloy Prepared By Ultra-Shallow Nitrogen Implantation Using PECVD Method

Marcin Grobelny[1*)], Małgorzata Kalisz[1, 2)], Robert Mroczyński[2)], Magdalena Szymańska[1, 2)]

1) Motor Transport Institute, Centre for Material Testing and Mechatronics, Jagiellońska 80, Str. 03-301 Warsaw, Poland
2) Institute of Microelectronics and Optoelectronics, Warsaw University of Technology, Koszykowa 75, Str.00-662 Warsaw, Poland
**E-mail: marcin.grobelny@its.waw.pl*

The low density of magnesium alloys makes them especially attractive especially for the automotive, electronic and aeronautical industries. Unfortunately, magnesium alloys have a strong susceptibility to atmospheric, galvanic and pitting corrosion and need to be protected with anticorrosive coatings. Traditionally magnesium and magnesium alloys have been protected with chromium-based coatings with the consequent problem of pollution by Cr(IV) ions. The development of new corrosion resistant coatings, by using clean and environmentally friendly processes is very important and strategic for the European industry due to environmental, health and economic considerations.

In this context plasma technology, including: Plasma Enhanced Chemical Vapor Deposition (PECVD) are becoming increasingly popular.

In this paper, magnesium alloys AZ91 were treated using nitrogen plasma (N_2 and NH_3) generated in PECVD reactor. Then, some of magnesium alloys samples were oxidized in oxygen plasma, and for some magnesium alloys samples SiO_2 layer was deposited (in PECVD reactor).

The obtained coatings were investigated using various characterization methods. Electrochemical properties were based on analysis of the voltammetric curves and electrochemical impedance spectroscopy, the microscopic examination was performed by using the techniques of SEM / EDS.

Key words: *corrosion resistance, plasma process, electrochemical methods, magnesium alloys, PECVD.*

Introduction

In the researches on new materials for applications in automotive and aviation industries and aerospace engineering the light metal alloys are widely used, especially magnesium alloys. The advantages of Mg alloys are: low specific gravity and yield strength and modulus of elasticity, allowing the transfer of great loads. The ratio of strength to weight of castings and good machinability are also advantageous. Despite of many strong points, these alloys also have drawbacks. The most important of these is the low corrosion resistance and susceptibility to pitting corrosion even in the presence of small concentrations of other metals. In order to increase the corrosion resistance, magnesium and its alloys are subjected to the processes of both physical and chemical surface treatment, which are aimed to create a barrier layer between the metal and the surrounding environment. Typical examples of such coatings include chromate coatings. However, due to the high toxicity of their main component, namely Cr (VI), they can no longer be used and are replaced with the other coatings and layers to increase the corrosion resistance. However, new technologies for improving the corrosion resistance of Mg alloys are not sufficiently effective. Therefore, it is necessary to modify the existing ones or develop new methods to improve the corrosion properties of magnesium alloys. One of the widely developed methods is coating the Mg surface with the layer of SiO_2 in the "sol-gel" process" [1] and anodic oxidation leading to generation of an oxide layer. However, the plasma technologies enable deposition of SiO_2

layers, and also the surface oxidation of Mg alloys. These methods also lead to improved corrosion resistance of magnesium alloys [2-4].

The paper presents the properties of magnesium alloy AZ91 after the process of implantation with nitrogen molecules before the formation of SiO_2 layer in the process of plasma deposition and before plasma oxidation. The SiO_2 layer and plasma oxidation were performed by PECVD (Plasma Enhanced Vapor Deposition) technique. Nitrogen was introduced to the Mg alloy surface by a process of ultra-shallow implantation with radio-frequency plasma (13.56 MHz) in the PECVD reactor. Plasma generated in the gases N_2 or NH_3 was used in the implantation process.

Materials and Methods

PECVD plasma technologies, are the processes during which the solid layer formation takes place on any substrate from the reactants, which react each other in the reactor chamber, under vacuum and in volatile phase. The substrate, in such a process, fulfills the role of a mechanical carrier. Working gases containing appropriate reactants are introduced into the reactor where the chemical reaction proceeds between them in plasma. The product of this reaction is a solid, which forms a new layer on the surface of the mechanical carrier. The advantage of plasma layers is a low temperature (below 350^{o}C) of their generation, high purity of the process (under vacuum) and the ability to free control of the chemical composition and thickness of the produced layer using the process parameters (composition of working gases, temperature, time, power and pressure). Plasma reactors also allow you to conduct multistage processes, such as cleaning the surface of the samples, ultra-shallow ion implantation to the surface of the sample, deposition of the proper layer and annealing, without contacting the sample with the environment.

Before the formation of SiO_2 layers and before the plasma oxidation the surface of samples was cleaned and then subjected to nitrogen implantation process. Implantation was carried out with radio-frequency plasma in the PECVD reactor using N_2 or NH_3 gas. The parameters of the surface treatment processes of AZ91 alloy are shown in Table 1.

All processes were carried out on the plasma stand Oxford Plasmalab 80 Plus, with PECVD method using radio-frequency plasma (13.56 MHz).

***Table 1. The main parameters the processes of plasma deposition and plasma oxidation*.**

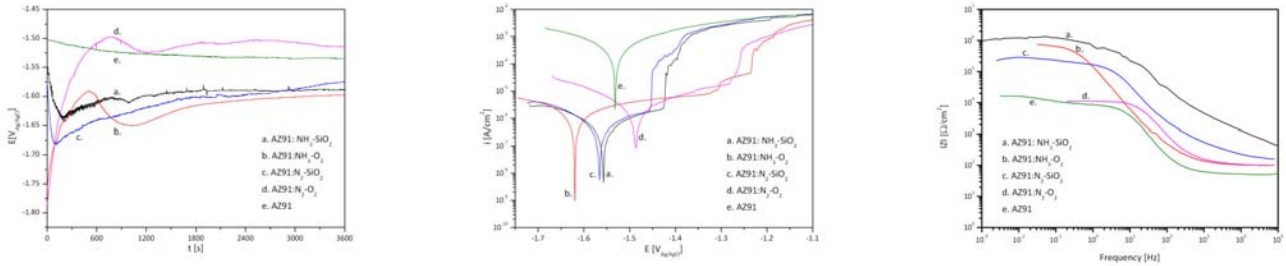
Sample No.	Implantation	Plasma deposition				Plasma oxidation				Thickness [nm]
		Power [W]	Temp. [^{o}C]	Gas flow [ml/min]	Time [min]	Power [W]	Temp. [^{o}C]	Gas flow [ml/min]	Time [min]	
1	NH_3	80	300	SiH_4=150 N_2O=100	10	--	--	--	--	30
2	NH_3	--	--	--	--	100	300	O_2=50	10	14
3	N_2	80	300	SiH_4=150 N_2O=100	10	--	--	--	--	44
4	N_2	--	--	--	--	100	300	O_2=50	10	20

Voltametric measurements were carried out with a scan rate of 1 mV/s within the range of -150 mV to 1000 mV versus open circuit potentials and polarization curves corresponding to every examined material were recorded. Prior to each polarization experiments, the samples were immersed in the electrolyte solution 0.5M/l NaCl for 1 h while monitoring the open circuit potential to establish steady state conditions. A three-electrode cell arrangement was applied using the Ag/AgCl electrode as reference electrode and a platinum wire as the auxiliary electrode (counter electrode). The measurements were carried out by means of EcoChemie System of AUTOLAB PGSTAT 302N with relevant software. The impedance (electrochemical impedance spectroscopy, EIS) data was obtained

at the open circuit potential with a Princeton Applied Research model VersaStat 3 system. The frequency range analysed, went from 10^6 Hz up to 10^{-3} Hz, with the frequency values spaced logarithmically (ten per decade). The amplitude of sinusoidal voltage signal applied to the system was 10 mV rms (root-mean-square). Prior to the beginning of the measurements, the specimens were maintained for 1.5 h in sodium sulphate (VI) solution Na_2SO_4 of 0.5 M/l (pH=6.0) for stabilisation of an open – circuit potential. The chemical composition of the layers obtained on magnesium alloys was examined using secondary ion mass spectrometer - MiniSIMS.

Results

Electrochemical measurements



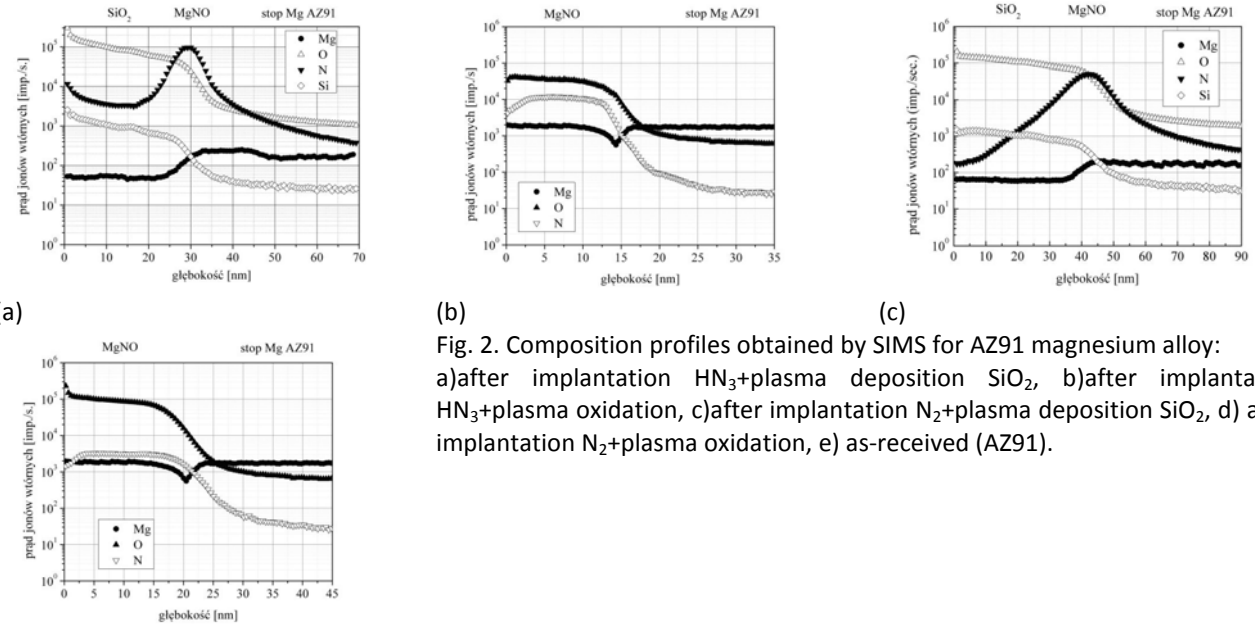
(a) (b) (c)

Fig. 1. Open circuit potentials (a), voltametric curves (b) in 0.15M NaCl and impedance modulus (c) in 0.5 M Na_2SO_4 for magnesium alloy AZ91: a)after implantation HN_3+plasma deposition SiO_2, b)after implantation HN_3+plasma oxidation, c)after implantation N_2+plasma deposition SiO_2, d) after implantation N_2+plasma oxidation, e) as-received (AZ91).

Table 2. Electrochemical corrosion parameters of the samples obtained from polarization curves.

Sample	E_{corr} [$V_{Ag/AgCl}$]	i_{corr} [$\mu A/cm^2$]	E_{pitt} [$V_{Ag/AgCl}$]	E_{corr}- E_{pit} [$V_{Ag/AgCl}$]
As-received (AZ91)	-1.531	700.0		
implantation HN_3+plasma deposition SiO_2	-1.558	3.0	-1.426	-0.132
implantation HN_3+plasma oxidation	-1.620	6.3	-1.323	-0.297
implantation N_2+plasma deposition SiO_2	-1.566	2.4	-1.456	-0.110
implantation N_2+plasma oxidation	-1.487	5.0	-1.283	-0.204

Surface composition



(a) (b) (c)

(d)

Fig. 2. Composition profiles obtained by SIMS for AZ91 magnesium alloy: a)after implantation HN_3+plasma deposition SiO_2, b)after implantation HN_3+plasma oxidation, c)after implantation N_2+plasma deposition SiO_2, d) after implantation N_2+plasma oxidation, e) as-received (AZ91).

Conclusions

1. Plasma processes occurring on the surface of magnesium alloy AZ91 influenced its corrosive properties. For the samples with a layer produced in the process of plasma deposition and after plasma oxidation compared to the pure alloy a significant decrease in corrosion currents was observed as well as significant increase of impedance modulus.
2. The smallest values of i_{corr} and greatest values of impedance modulus, and thereby the highest corrosion resistance, were characteristic for the samples with the layer produced in the plasma deposition process.
3. The corrosion resistance of AZ91 magnesium alloy after the process of implementation of nitrogen molecules with radio-frequency plasma in the PECVD reactor using N_2 or NH_3 gas and after formation of the layer in the plasma deposition or plasma oxidation process was similar. However, it should be noted that for the samples after the oxidation process the thickness of the generated layer was 14-20 nm and was smaller than the layer produced in the process of plasma deposition (30-40nm).
4. For the samples with a layer generated in the plasma oxidation process the greatest difference of corrosion potential and pitting corrosion potential was observed. These samples were characterized by the greatest resistance to the occurrence of local corrosion processes (pitting corrosion).

References

1. V. Barranco, N. Carmena, J.C. Galván, M. Grobelny, L. Kwiatkowski, M.A. Villegas, Electrochemical study of tailored sol–gel thin films as pre-treatment prior to organic coating for AZ91 magnesium alloy, Progress in Organic Coatings, vol. 68, 4, 2010
2. M. Kalisz, M. Grobelny, B. Dytkowicz, An application of oxide coatings SiO_2 and SiOxNy to increase corrosion resistance of magnesium alloys, Corrosion Protection, vol. 54, 4-5, 2011
3. M. Grobelny, M. Kalisz, B. Dytkowicz, An application of oxide coatings type SiO_2 to improve corrosion resistance of magnesium alloy AZ91, Corrosion Protection, vol. 5, 6, 2011
4. M. Kalisz, M. Grobelny, B. Dytkowicz, Preparation of SiO_2 coatings, by using PECVD technique, for magnesium alloys to improve corrosion resistance, Corrosion Protection, vol. 5, 6, 2011

Effect of nitrogen incorporated into oxide layer, formed on the magnesium alloys by using r.f. PECVD process, on their corrosion resistance

Małgorzata Kalisz [*, 1)], Marcin Grobelny[1)], Barbara Dytkowicz [1)]
[1)] Motor Transport Institute, Jagiellonska 80, Str., Warsaw
[*)] malgorzata.kalisz@its.waw.pl

Summary

This paper presents the changes in corrosion resistance of SiO_2 coatings generated in the plasma process PECVD (Plasma Enhanced Chemical Vapour Deposition), using RF plasma (13.56 MHz), under the influence of the introduction of nitrogen to their volume. Two magnesium alloys AZ32 and AZ91 were put under the tests. On each of Mg alloys the coating of SiO_2 was made with a thickness of 1000 nm, and the coatings of SiO_xN_y (oxynitride) with a thickness of 60 nm and 500 nm. The obtained results were compiled with the reference samples of these alloys. The corrosion properties of the tested coatings were determined based on the analysis of voltammetric curves. The obtained results show that the introduction of nitrogen to a volume of a thin layer of plasma produced SiO_2, which is the formation of the layer of SiO_xN_y improves the corrosion resistance of both examined magnesium alloys. With a much smaller thickness of SiO_xN_y layer in relation to the thickness of SiO_2 oxide layer the similar corrosion current density decreases were obtained.

Keywords: *corrosion resistance, plasma process, electrochemical methods, magnesium alloys*

Introduction

In a study of new materials for applications in automotive, aviation and aerospace industry the application of light metal alloys, especially magnesium alloys, is still increasing. Among their undeniable advantages are their low specific gravity and yield strength as well as modulus of elasticity, allowing the transfer of great loads. The ratio of strength to weight of castings is also advantageous as well as good machinability. Despite many advantages, magnesium alloys have also drawbacks. The most important of these is the low corrosion resistance and susceptibility to pitting corrosion even in the presence of small concentrations of other metals. In order to increase the corrosion resistance, magnesium and its alloys are subjected to the processes of both physical and chemical surface treatment, which aim is to create a barrier coating between the metal and the surrounding environment. Typical examples of such coatings include chromate coatings. However, due to the high toxicity of their main component, namely Cr (VI), they can no longer be used and are replaced with the conversion coatings generated with using other technologies. Unfortunately, these coatings are much less effective. Therefore, the new technologies for generation and modification of corrosion properties of layers, in order to obtain the best protection against corrosion for light metal alloys, including magnesium, are still researched. In this context, the plasma technologies, ie: thin film deposition (PECVD - Plasma Enhanced Vapor Deposition [1,2] or PACVD Plasma Assisted Chemical Vapour Deposition) [3] and etching (RIE - Reactive Ion Etching), are becoming increasingly popular [4].

The plasma technologies, including the PECVD technologies, are the processes during which the production of a solid layer on any substrate from the reactants takes place, which react each other in the reactor chamber, under vacuum and in a volatile phase. The substrate, in such a process fulfills the role of the mechanical carrier. Working gases containing appropriate reagents are introduced into the reactor where the chemical reaction between them takes place in plasma. The product of this reaction is a solid, which creates a new layer on the

surface of mechanical carrier. The advantage of plasma layers is a low temperature of their production (below 350 ^{o}C), high purity of the process (under vacuum) and the ability to control freely the chemical composition and thickness of the generated layers by means of the plasma process parameters, namely: the choice of working gases, the process temperature, time and pressure.

The influence of nitrogen introduced into the volume of SiO_2 coatings produced in the PECVD plasma process, with using RF plasma, on the corrosion properties of magnesium alloys AZ32 and AZ91 is presented in this paper. On each of the two types of alloys the two types of coatings were deposited: SiO_2 coating with a thickness of 1000 nm and SiO_xN_y coatings with a thickness of 60 nm and 500 nm. For comparative purposes, the tests were also performed on the reference samples of each of the Mg alloys. The corrosion properties of the tested coatings were determined based on the analysis of voltammetric curves.

Description of the experiment

For the experiment, four samples were prepared for each of the tested magnesium alloys AZ32 and AZ91. Prior to plasma deposition processes, the surface of each sample was ground and polished, and then cleaned using the standard RCA microelectronic procedure (SC1 + SC2 + buffered HF). On the samples marked with a number 1 the SiO_2 layer with a thickness of 1000 nm was deposited on the plasma stand type Oxford Plasmalab 80 Plus by the PECVD method using RF plasma (13.56 MHz). On the samples marked with the numbers 2 and 3 the layer of SiO_xN_y was deposited by the same method, with the thicknesses of 60 nm and 500 nm. The samples marked with the number 4 were not protected with any of the above mentioned coatings. In this way, we had the reference samples, for each of the examined magnesium alloys. The parameters of the performed plasma deposition processes PECVD are presented in Table 1.

Table 1. The main parameters of PECVD plasma processes carried out under this work.

<table>
<tr><th rowspan="2">Sample No</th><th colspan="5">PECVD plasma deposition processs</th><th rowspan="2">Coating thickness [nm]</th></tr>
<tr><th>Temperature [°C]</th><th>Plasma power [W]</th><th>Pressure in reactor [Pa]</th><th>Time of deposition process [min.]</th><th>Gas flow [ml/min]</th></tr>
<tr><td>1</td><td>350</td><td>15</td><td>46,6</td><td>55</td><td>SiH_4 = 50; N_2O = 50</td><td>1000</td></tr>
<tr><td>2</td><td rowspan="2">350</td><td rowspan="2">10</td><td rowspan="2">38,8</td><td>2,30</td><td rowspan="2">SiH_4 = 150; N_2O = 24; NH_3 = 32</td><td>60</td></tr>
<tr><td>3</td><td>55</td><td>500</td></tr>
</table>

Thickness of the deposited layers was measured using single-wavelength ellipsometer (λ = 632.8 nm). Ellipsometry measurements were carried out immediately after the PECVD plasma deposition processes.

The examinations of corrosion properties of magnesium alloys were performed by voltammetric technique [5] [6]. For this purpose, the current density-potential curves (polarization curves) were recorded at the rate of change of the potential of 1mV/sw in the environment of the electrolyte consisting of 0.15M NaCl. Before performing the polarization curves the corrosion potential of the samples was recorded during 1h. The measurements were done in non-thermostated, three-electrode vessel with Ag / AgCl electrode as the reference electrode. The AUTOLAB PGSTAT 302N potentiostat with GPES software was utilized in the tests.

Test results.

Figures 1 and 2 show the polarization curves recorded for the tested coatings and for magnesium alloys without coating. Among the tested coatings the lowest value of corrosion current density was obtained for the SiO_2 layer with a thickness of 1000 nm generated on AZ32. In this case, the value of i_{kor} was 0.08 μA/cm^2. It should be noted that for a 500nm thick layer formed on the same alloy, but containing nitrogen atoms (SiO_xN_y coating) the value of the corrosion current is slightly higher and amounts to 0.10 μA/cm^2. In the case of magnesium alloy AZ91 a similar phenomenon was also observed, ie, the corrosion current density values for the SiO_2 coating with a thickness of 1000 nm are slightly lower than the corrosion current density values obtained for the SiO_xN_y coating, however with a thickness of 500 nm. The i_{kor} values amount to 0.19 μA/cm^2 for SiO_2 coating and 0.27 μA/cm^2 for SiO_xN_y coating.

Table 2. Electrochemical parameters of corrosion processes obtained from voltametric curves.

Material	AZ32			AZ91		
	E_{kor} (V)	i_{kor} (μA/cm^2)	E_{pit} (V)	E_{kor} (V)	i_{kor} (μA/cm^2)	E_{pit} (V)
Pure alloy	-1.504	8.47	-1.375	-1.531	1537	--
1000nm SiO_2	-1.441	0.08	-1.384	-1.485	0.19	-1.391
60nm SiO_xN_y	-1.379	3.72	-1.204	-1.500	2.08	-1.355
500nm SiO_xN_y	-1.469	0.10	-1.374	-1.558	0.27	-1.451

Pitting corrosion was observed only in the case of AZ91 alloy without coating. A lack of pitting corrosion can be associated with high intensity of corrosion processes (high value of corrosion current density, Table 2) on the surface of the tested sample, leading to the formation of the sealed oxide layer. Among the other tested materials the greatest difference of potentials: corrosion potential (E_{kor}) and pitting corrosion potential (E_{pit}) were characteristic for SiO_xN_y coatings for which these differences were 175 mV for the coating with a thickness of 60nm on AZ32 and 145 mV for the coating of 60 nm on AZ91.

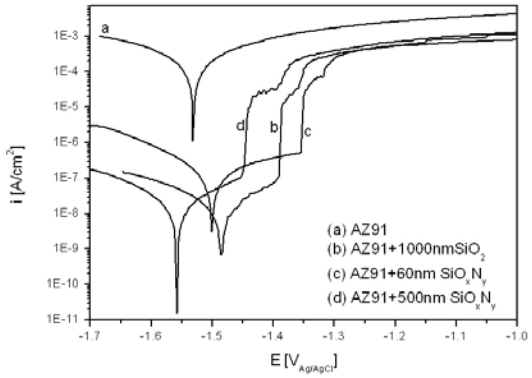


Fig. 1. Voltametric curves for magnesium alloy AZ91: a) as-received, b) with 1000nm SiO_2, c) with SiO_xN_y 60nm, d) with SiO_xN_y 500nm.

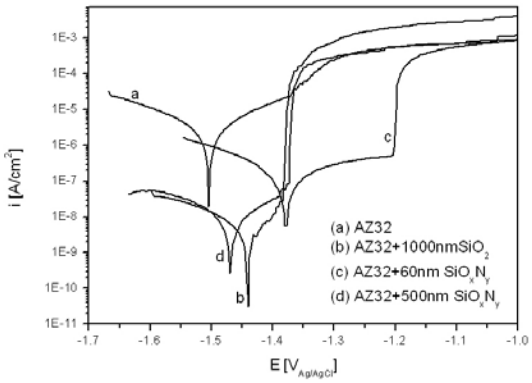


Fig. 1. Voltametric curves for magnesium alloy AZ32: a) as-received, b) with 1000nm SiO_2, c) with SiO_xN_y 60nm, d) with SiO_xN_y 500nm.

Summary

On the basis of experiments carried out in this work, it was found that the process of plasma deposition of SiO_2 and SiO_xN_y layers from RF plasma (PECVD) is suitable for surface modification of Mg alloys to increase their corrosion resistance.

In this paper we examined the protective properties of plasma deposited coatings SiO_2 and SiO_xN_y (using the method of PECVD) on the magnesium alloys AZ32 and AZ91. The lowest corrosion current density values were obtained for the SiO_2 coating with a thickness of 1000 nm (for alloy AZ32 $i_{kor} = 0.08$ μA/cm^2, for AZ91 $i_{kor} = 0.19$ μA/cm^2). It should be noted that the corrosion current density value obtained for SiO_xN_y coating with a thickness of 500 nm, for both magnesium alloys is close to the value of this parameter obtained for the SiO_2 layer with a thickness of 1000nm. For the AZ32 alloy the corrosion current density value obtained for the coating SiO_xN_y (500nm) is higher by 0.02 μA/cm^2 compared to the value of this parameter obtained for the coating SiO_2 (1000nm). For the AZ91 alloy, the i_{kor} value for the coating SiO_xN_y (500nm) is higher by 0.08 μA/cm^2 compared to the value of this parameter obtained for the coating of SiO_2 (1000nm).

The results obtained show that the introduction of nitrogen to a volume of a thin plasma deposited layer of SiO_2, ie. generation of SiO_xN_y layer, considerably increases its resistance to the corrosive environment (for both magnesium alloys). For SiO_xN_y coating with a thickness of 500nm the similar decreases of corrosion current density were obtained as for the oxide layer SiO_2 with a thickness of 1000nm.

Bibliography

1 Y.T. Kim et al., „PECVD SiO_2 and SiON films dependant on the rf bias Power for low-loss silica waveguide" Thin Solid Films 475, 271-274 (2005)

2. A. Boogaard, "Plasma-enhanced chemical vapour deposition of silicon dioxide: Optimizimg dielectric films through plasma characterization" Ph.D Thesis, MESA+ Institute for Nanotechnology (2011)

3 J. Olivares Roza et al., "Plasma assisted chemical vapour deposition silicon oxide films grown from SiH4 + NH3 + O2 gas mixtures" Journal of Vacuum Science and Technology A, 16, 2757-2761 (1998)

4 M. Jagadesh Kumar et al., "Selective Reactive Ion Etching of PECVD silicon nitride over amorphous silicon in CF4/H2 and nitrogen containing CF4/H2 plasma gas mixtures" Solid State Electronics 39, 1, 33-37 (1996)

5. X.L. Zhang, Zh.H. Jiang, Zh.P. Yao, Y. Song, Zh.D. Wu, Corrosion Science, 51, 3, (2009) 581

6. S. D. Cramer, S. B., Covino Jr., ASM Handbook: Corrosion : Fundamentals, Testing, and Protection, ASM International, 2003

Application of the dusty plasma technology for diamond ceramics production

Alexander Pal[1], Evgeny Ekimov[2], Alexander Ivanov[3], Nikolay Borovikov[2], Andrey Rusinkevich[3], Alexey Ryabinkin[4], Alexander Serov[4], Andrey Starostin[5], Vladimir Fortov[6], Elena Gromnitskaya[2]

[1]Naco technologies, Riga, Latvia; [2]IHPP RAS, Troitsk, Russian Federation; [3]Kurchatov Institute, Moscow, Russian Federation; [4]MSU SINP, Moscow, Russian Federation; [5]TRINITI, Troitsk, Russian Federation; [6]JIHT RAS, Moscow, Russian Federation; apal@triniti.ru

One of the most widespread industrial methods for producing diamond compacts and two-layer plates (a diamond layer on a substrate from a hard alloy WC-Co) is sintering the diamond in the presence of an activating additive – cobalt. Cobalt is a solvent for carbon and a catalyst in the transformation of graphite to diamond, which stimulates the sintering of diamond and the formation of a hard diamond frame (matrix). However, the presence of cobalt in the final product has a rather negative effect upon the diamond thermo-stability in the processes of production and use of the instrument. The difference in a thermal expansion of the matrix and its inclusions results in a formation of cracks and, finally, in a short life or even a failure of the operation part of the instrument. Cobalt is usually incorporated into a diamond powder either by being infiltrated or by previously mixing reagents. However, this technique does not allow homogeneous distribution of cobalt in the sintered mixture when the cobalt density becomes less than 5 in volume percent, especially if the size of sintered diamond particles is less than 5 μm. Therefore deposition of thin Co layers upon the surface of micron diamond particles with content 1–3 vol. (2–6 mass. percentage) in the charge mixture may become a promising approach to sintering of thermo-resistant diamond ceramics.

To deposit cobalt nanolayers upon individual diamond particles we used a plasma-dusty method. The idea of such method for depositing metal coatings upon the surface of microparticles having the size of about 1–10 μm was proposed in [1, 2]. The method for depositing coatings is based on particles' levitating in the particular area of plasma, that is, in plasma-dusty traps. A coating is deposited upon the surface of levitating particles by an atom flow created by a magnetron sputtering system. The particles in plasma acquire great negative charges, which prevents the particles' agglomeration. This method was practically used in [2], where the performance of a powder with a nano-sized coating production was several cm^3/hour.

In Fig. 1 there is a scheme of the reactor, which was used in present work, for plasma-dusty deposition of cobalt coatings upon diamond microparticles. A reactor was placed in a vacuum chamber. Inside the reactor there is RF plasma in which there forms a plasma-dusty trap

containing a dusty cloud with the particle density up to 10^6 cm^{-3}.

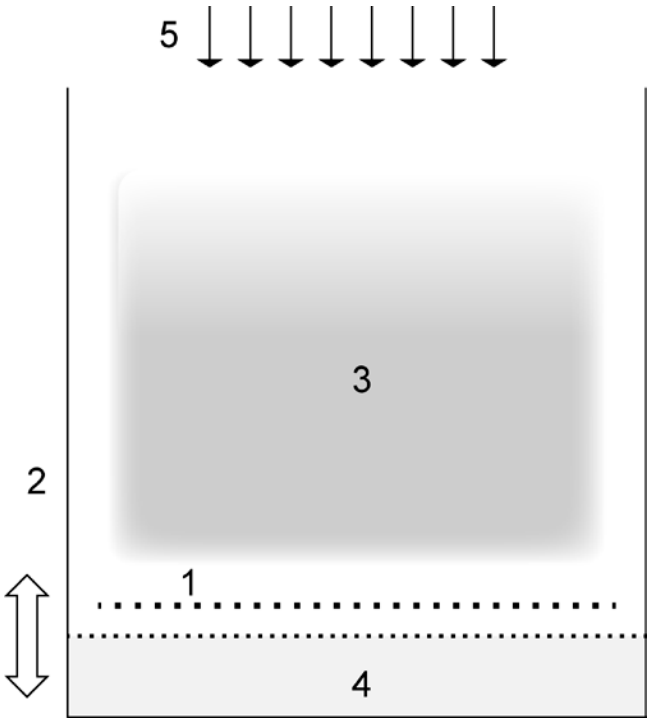


Fig. 1. Scheme of the reactor: 1 – the RF electrode, 2 – the reactor wall, 3 – the plasma-dusty cloud, 4 – the system for dispersion and collection of the powder, 5 – flow of Co atoms from a magnetron sputter. The arrows in the lower area of the figure point out to the direction of the reactor vibration in a powder dispersion process.

Powder particles from the inertial dispersion system in the lower part of the reactor enter the plasma area where they are coated by a flow of atoms from the magnetron sputtering system through the hole in the upper part of the reactor. Levitating particles are exposed to a cobalt atom flow from the sputtering system, after which they enter the dispersion system again. Such scheme decreases the probability for the formation of particle agglomerates in the final product in case of an incomplete dispersion.

Powders were produced with various (1–3) mass. percentage of cobalt which were then used for fabrication of compacts (with the thickness of 3 mm and the diameter of 4 mm) by sintering the diamond powder with the cobalt coating under the pressure of 8 GPa in high pressure chambers of the “toroid” type. Heating the reaction area up to the temperature of 2000–2100 K (it is higher than the melting temperature of Co under the pressure of 8 GPa) was performed under the pressure of 8 GPa with the rate of 50–100 ^{0}C/s. On being exposed to the constant P and T for 5–120 seconds, the specimens were cooled under a constant pressure.

In Fig. 2 there is a microstructure of diamond particles with a cobalt coating under the mean cobalt density in the powder about 3 mass percent. It is seen that cobalt is relatively homogeneous over the surface of diamond grains. Most interesting results are for the diamond powder in which the maximal cobalt density about 3 mass percent was achieved. In the Table there are physical properties of the produced compacts. For comparison there are literature data for the properties of the best diamond compacts produced according to the traditional methods of a binder injection.

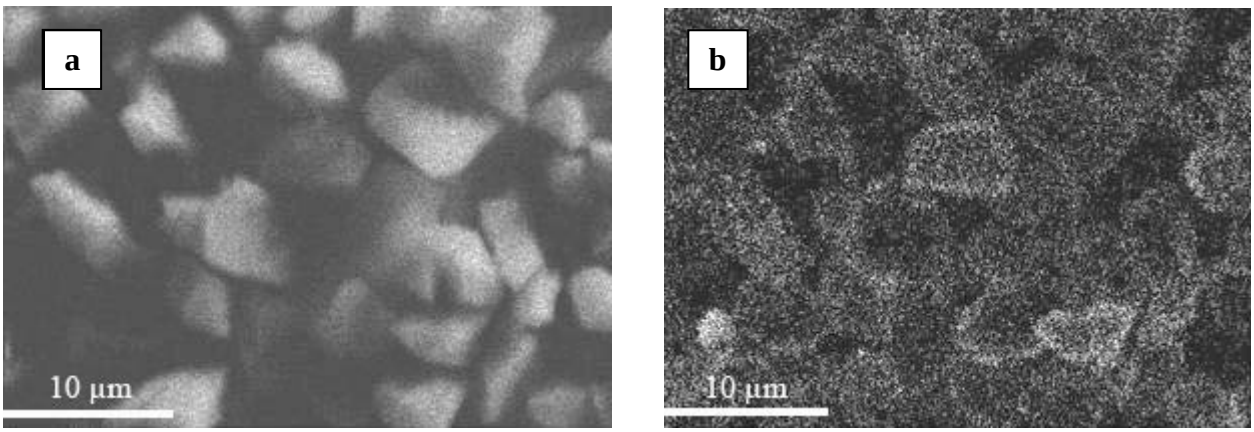


Fig. 2. Microstructure of the diamond powders with a cobalt coating. X-ray point images corresponding to carbon (a) and cobalt (b) demonstrate relatively homogeneous distribution of cobalt on diamond particles.

Table 1. Physical properties of diamond compacts (ρ is the density, V_l and V_t are the longitudinal and transverse velocities of sound, K_s is the volume modulus of elasticity, E is the modulus of elasticity, μ is the Poisson coefficient). The sintering temperature is 2050 K.

N of speci-men	T_{anneal} (K)	Pressure and sintering duration	ρ (g/cm^3)	V_l (km/s)	V_t (km/s)	E (GPa)	K_s (GPa)	μ
37-2	900	8–9 (GPa), 5(s)	3.6	16.612	10.259	917	495	0.19
37-3	970	7–8 (GPa), 20(s)	3.6	14.470	9.291	717	340	0.15
37-12	870	7–8 (GPa), 10(s)	3.6	13.968	7.958	575	399	0.26
			4.0 [3]	13.0–16.5 [4]		890 [3]		

It is seen that mechanical properties of the specimens produced in the first set of experiments are of extreme values in comparison with the corresponding literature data. Studying a microstructure specimens' shows relatively homogeneous distribution of cobalt over the specimen (Fig. 2 b) under the mean cobalt density of about 3 mass percent, this agrees with the cobalt percentage in the sintered powder. On the whole, the close intergrowth of diamond grains is typical for specimens (Fig. 3), which provides unique properties of compacts in spite of the presence of submicron-sized metal particles in the sintered material.

Fig. 3 demonstrates diamond grains intergrowth (a) and rather homogenous distribution of cobalt among diamond grains (b).

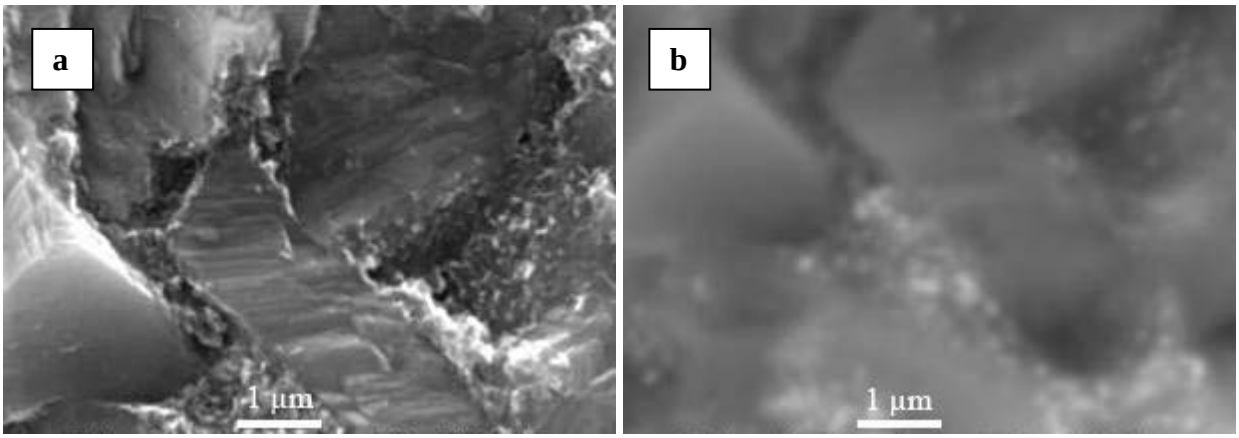


Fig. 3. Microstructure of diamond compact N 37-2 in the secondary (a) or reflected (b) electrons.

Conclusions

A method for magnetron deposition of nano-sized cobalt coatings upon diamond particles confined in the plasma-dusty trap was developed. A diamond powder with the particle size of 3–7 μm with a cobalt coating was sintered under the temperatures within 2000–2100 K and the pressure of 8 GPa. The produced compacts had high values of the Young's modulus 917 GPa and the modulus of dilatation 495 GPa, which indicated the formation of the solid bond among diamond particles.

References:

[1] Kersten, H., et al., New Journal of Physics, 2003, **5**, 93.1.

[2] Ivanov A.S., et. al, in *Plasma Processes and Polymers*, edited by R. d' Agostino, P. Favia, C. Oehr, and M. Wertheimer (Wiley-VCH Verlag GmbH & Co. KGaA, Weinheim, 2005), pp. 455–464.

[3] P. D. Gigle. Proceedings of the Sixth AIRAPT International High Pressure Conference Boulder, July 1977, ed. by K. D. Timmerhause and M. S. Barder (Plenum, New York, 1979), **1**, 914.

[4] P. A. Bex, D. C. Roberts. Industrial Diamond Review, 1979, **1**, 1.

Effect of the rapid thermal annealing on the structural properties of TaO_xN_y thin films deposited by reactive magnetron sputtering

F. Zoubian[1,2], E. Tomasella[1,2], A. Bousquet[1,2], J. Cellier[1,2], T. Sauvage[3]

[1]Clermont Université, Université Blaise Pascal, Institut de Chimie de Clermont-Ferrand, BP 10448, F-63000 CLERMONT-FERRAND

[2]CNRS, UMR 6296, ICCF, BP 80026, F-63171 AUBIERE

[3]CNRS/CEMHTI Site Cyclotron, 3A rue de la Férollerie 45071 Orléans Cedex 2 France.

Keywords: magnetron sputtering, tantalum oxynitride, XRD, phase transition, structure, morphology.

Abstract. Tantalum oxynitride thin films are deposited by radio-frequency magnetron sputtering using a pure tantalum target under argon/oxygen/nitrogen gas mixture. The argon flow is kept constant while the oxygen and nitrogen flows are changed simultaneously in a way to keep constant the total flow of these reactive gases. We succeed to deposit TaO_xN_y films with stoichiometry ranging between those of TaN and Ta_2O_5. All films are deposited at room temperature without any biasing. A thermal annealing in a RTA furnace was applied to all the films in a nitrogen atmosphere. A phase transition was detected by XRD investigations and SEM scanning from as deposited to annealed films, noticing the crystallisation of all films which depends on the composition of each film.

1. Introduction

The integration of antireflective coatings in optical applications has made an important improvement in their performance. The simplest antireflective coating consists of a single layer of transparent material with an optimum refractive index. The efficiency is improved by a multilayer structure formed by a succession of layers with graded refractive indices. These films are the essential component of electroluminescent devices used particularly in lighting applications (panel backlighting to liquid crystal displays) providing good illumination by consuming relatively little electric power, and frequently used as protective and antireflection coating in eyeglass lenses and solar panels. Tantalum pentoxide (Ta_2O_5) is used as gate dielectric in electronics, optical devices and in antireflective coatings due to its high transparency, high dielectric constant [1, 2], large band gap and its large refractive index (~2.3 at 632.8 nm) [3]. Tantalum nitride (TaN) is a hard material, resistant to the corrosion and chemically inert, is used for hard and wear resistant coatings [4], as diffusion barrier [5], as well as film resistors since its electrical resistance is very stable [6] and it possesses metallic behavior. Combining the useful properties of oxide and nitride allows obtaining all the qualities in oxynitride material supervised by controlling the process parameters. Tantalum oxynitride films are promising candidates for applications as electroluminescent devices, decorative coatings, dielectric layers [7] diffusion barriers [8] and antireflective coatings due to the wide range of variation of their refractive index between 2.3 and 3.8.

The reactive magnetron sputtering represents a good candidate to deposit optical and electrical structures on sensitive substrates due to the lower work temperatures. The possibility of variation of several deposition parameters such as pressure, gas flows, target, power, etc. allows obtaining a wide range of film stoichiometry; thereby it permits to deposit layers with graded composition.

In this work we deposit TaO_xN_y thin films by reactive magnetron sputtering from a pure tantalum target with $Ar/O_2/N_2$ plasma. We focus our interest on the investigation of the annealing effect on the structural properties of our films and what advantage could this annealing provide to the optical properties which will be published later on.

2. Experimental details

TaO_xN_y thin films were deposited at room temperature by radio-frequency magnetron sputtering in an Alcatel A450 vacuum chamber, using a pure tantalum target (99.99%) under argon/oxygen/nitrogen gas mixture. A constant power density of 3.18 $W.cm^{-2}$ was applied. Initially, the chamber was evacuated to a base pressure of $5x10^{-4}$ Pa. The work pressure varied between 1 and 1.2 Pa. Prior to film deposition, target

was cleaned in Argon plasma for 15 minutes. The argon supply was kept constant while oxygen and nitrogen were varied simultaneously in a way to keep a constant total flow of these reactive gases which is presented by the $R_F=F_{O2}/(F_{O2}+F_{N2})$ ratio. The choice of the total reactive gases value gives us the opportunity to deposit films with large variation of stoichiometry without being in a completely poisoned mode. Below this value all the films had a metallic appearance, with composition very rich on tantalum, and above this value only nitride-like and oxide-like films were obtained. In this study, we deposit the thin films on different substrates: quartz, silicon, and vitreous carbon. All the substrates were ultrasonically cleaned in ethanol (10 min). Rapid thermal annealing of the films was realised in a JIPELEC JETFIRST furnace at 900°C under nitrogen atmosphere after pumping the furnace chamber to eliminate the maximum of residual oxygen. The chemical composition was investigated by RBS at CEMHTI (Orléans-France), using 2 MeV alpha particles. The experimental results were correlated with numerical simulations made by SIMNRA code. Structural properties of as deposited and annealed films were studied by X-ray diffraction employing a PHILIPS X'PERT Diffractometer using CuK_α radiation. Typical patterns were recorded in 10°- 70° 2θ range. Surface morphology of the films was observed by scanning electron microscopy SEM using a ZEISS SUPRA 55VP, with an acceleration voltage of 50 kV.

3. Results and discussion

3.1 Chemical composition

Figure 1 shows the ratio of O/O+N content of the films as a function of R_F before and after annealing. We notice that tantalum content on the films before and after annealing varies only between 27 and 33 at. %. A wide variation of stoichiometry between those of TaN and Ta_2O_5 was obtained by controlling plasma composition in oxygen and nitrogen. The annealed films show a little increase of oxygen content in their composition; In fact, even in a pure nitrogen atmosphere, some residual oxygen persists on the chamber of the furnace. During the annealing, atoms will reorganized and the residual oxygen benefits to incorporate in the structure. This is due to the fact that oxygen atoms have a stronger affinity to tantalum atoms than that of nitrogen [9].

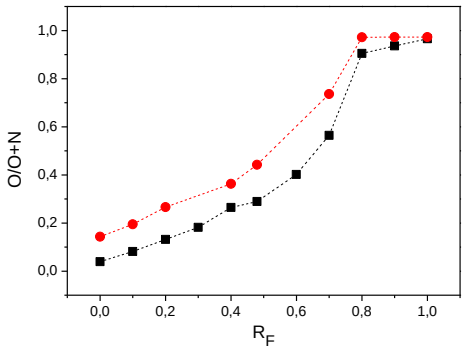


Figure 1. Oxygen and nitrogen content in the films as a function of R_F for as deposited (square) and annealed (circle) films.

3.2 Structure and morphology

XRD patterns of the as deposited films (figure 2) exhibit a variation of the structure with the deposition conditions. Films deposited in a nitrogen/argon plasma (R_F=0), exhibit 4 diffraction peaks which correspond to the cubic phase of TaN, same structure was obtained by other authors [10]. This crystallite structure is well seen by the granular surface showed by SEM image (figure 3,a). To assume, the grain size calculated using the Debey Sherrer's formula from the diffraction peaks and that estimated from the SEM image are in coherence (between 3.2 and 5.4 nm). For oxynitride films, the diffraction peaks disappear and a large peak remains around 2θ=34°, it could be assigned to a quasi-amorphous structure with nanocrystallites embedded in an amorphous matrix [11] which leads to a smoother surface showed by SEM (figure 3.b). For oxygen-rich films (R_F>0.48), no diffraction peaks were observed in the diffraction patterns and the SEM image (figure 3.c) shows a completely smooth surface which puts in evidence the amorphous structure of these films.

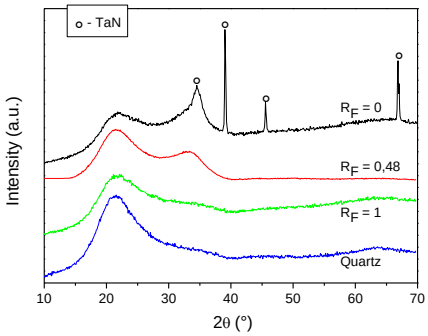


Figure 2. XRD patterns for as deposited films at RF = (b) 0; (c) 0.48 and (d) 1.

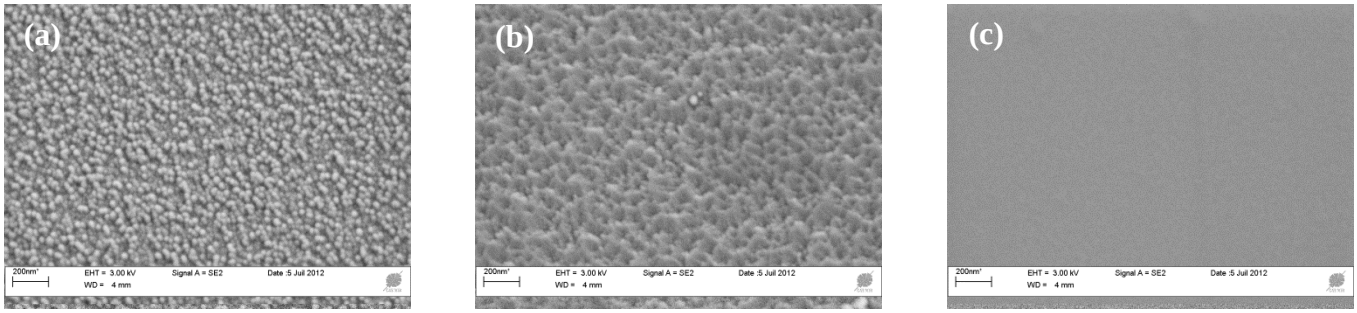


Figure 3. SEM images for as deposited films at RF = (a) 0; (b) 0.48 and (c) 1.

Figure 4 shows the XRD patterns of the films after rapid thermal annealing. We note a variation on the structure for all films after annealing. Nitrogen-rich film (R_F=0) shows three peaks at 2θ = 35; 36 and 61° associated to the Ta_3N_5 orthorhombic phase. Its SEM image (figure 5.a) shows granular surface with some pores. Film with intermediate composition (R_F=4.8) exhibits crystalline TaON peaks with monoclinic structure. Its SEM image (figure 5.b) shows granular surface with some pores and a crack due to the thermal stress in the film. Upon increasing the oxygen content, orthorhombic Ta_2O_5 thin films have been formed after annealing for films deposited at R_F=1, with islands of grains surrounded by well-defined grain boundaries (figure 5.c)

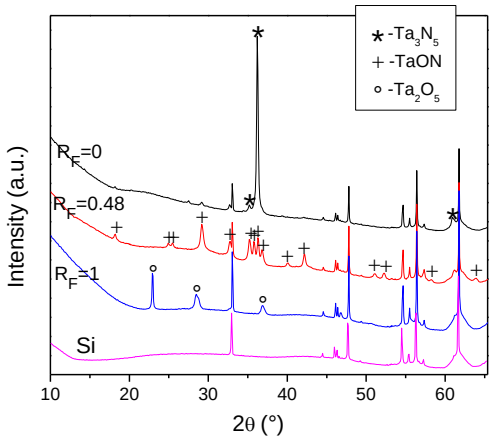


Figure 4. XRD patterns for films deposited at RF = (b) 0; (c) 0.48 and (d) 1 after RTA annealing at 900°C.

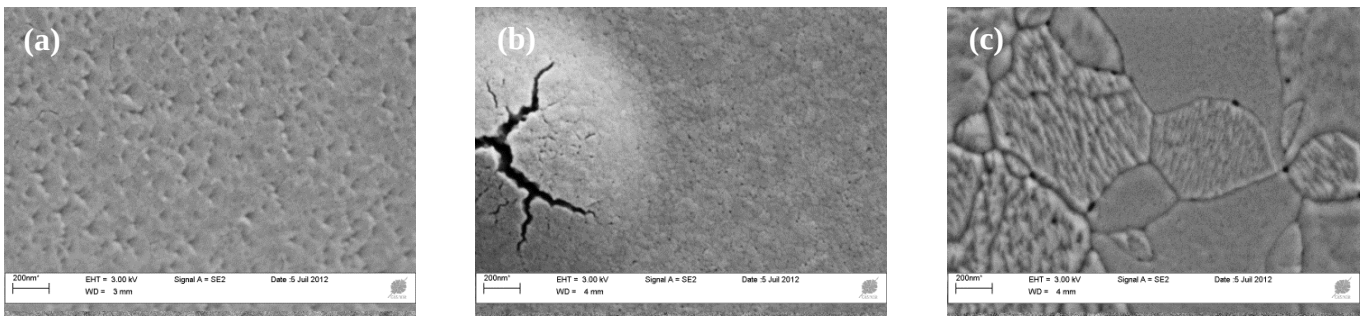


Figure 5. SEM images for films deposited at RF = (a) 0; (b) 0.48 and (c) 1 after RTA annealing at 900°C.

4. Conclusion

Thin TaO_xN_y films were deposited by reactive magnetron sputtering in an $Ar/O_2/N_2$ atmosphere. Wide variation of stoichiometry spanning the range between tantalum nitride and tantalum oxide was obtained by controlling the plasma composition. Rapid thermal annealing under nitrogen atmosphere leads to a little increase of oxygen content due to the residual oxygen in the furnace chamber but conserve the wide variation of stoichiometry. Structural and morphological variations were investigated for three types of films before and after RTA. As deposited TaN_x films shows a cubic TaN structure which transforms to orthorhombic Ta_3N_5 after annealing. TaO_xN_y films with intermediate composition show, before annealing, amorphous structure with nanocristallytes embedded on an amorphous matrix which is transformed into monoclinic TaON structure after annealing. And films with high oxygen content, TaO_x-like films, exhibit an amorphous structure which became orthorhombic Ta_2O_5 structure after annealing. The controlled variation of film's stoichiometry as well as the variation of the structure with the annealing gives us the opportunity to study their effects on the optical properties in view of their use as antireflective graded layers.

5. References

[1] A. J. Waldorf, J. A. Dobrowolski, B. T. Sullivan, and L. M. Plante, Applied Optics 32 (1993) 5583.
[2] F. Rubio, J. M. Albella, J. Denis, and J. M. Martinez-Duart, Journal of Vacuum Science and Technology 21 (1982) 1043.
[3] C.-A. Jong and T. S. Chin, Materials Chemistry and Physics 74 (2002) 201.
[4] Y. M. Lu, R. J. Weng, W. S. Hwang, and Y. S. Yang, Thin Solid Films 398–399 (2001) 356.
[5] T. Oku, E. Kawakami, M. Uekubo, K. Takahiro, S. Yamaguchi, and M. Murakami, Applied Surface Science 99 (1996) 265.
[6] E. K. M. T. T. Y. U. T., IEEE transactions on microwave theory and techniques 38 (1990) 1949.
[7] H. K. S. Masahiko, O. Atsushi, US Patent US5786078 (1998)
[8] O. Banakh, P. A. Steinmann, and L. Dumitrescu-Buforn, Thin Solid Films 513 (2006) 136.
[9] J. H. Hsieh, C. C. Chang, J. S. Cherng, and F. Y. Hsu, Thin Solid Films 517 (2009) 4711.
[10] S. Venkataraj, H. Kittur, R. Drese, and M. Wuttig, Thin Solid Films 514 (2006) 1.
[11] C. K. Chung, T. S. Chen, and N. W. Chang, Thin Solid Films 519 (2011) 5099.

The Structure-Phase Compositions of Ni - Cr and Co–Cr Based Powder Alloys Coatings Deposited by Plasma-Detonation on Steel Substrates

Darya L. Alontseva[1], Alexander D. Pogrebnjak[2], Galina Klassen[3]

[1]East Kazakhstan State Technical University, 69 Protazanov St., 070004, Ust-Kamenogorsk, Kazakhstan, dalontseva@mail.ru

[2] Sumy State University, 2R-Korsakov St., 40007, Sumy, Ukraine, alexp@i.ua

[3]Technische Universitaet Dortmund, August-Schmidt-Str. 4, 44227, Dortmund, Germany

Key words: plasma detonation coatings, structure-phase composition, transmission electron microscopy

Abstract. This paper presents new results of transmission electron microscopy (TEM), X-ray diffraction (XRD) and atomic force microscopy (AFM) investigation of the structure-phase compositions of thick (150 μm) coatings on the base of Ni–Cr and Co–Cr deposited by plasma-detonation on steel substrates. The phase structures and morphology of precipitation from solid solution are defined. The microstructure model of a thick plasma detonation coating on steel substrate is developed. The main aim of carrying out these investigations is developing science based recommendations for modification of plasma-detonation coatings by plasma-jet or e-beam.

1. Introduction

The plasma detonation method is recent; it allows obtaining coatings from high-melting metal powder in air medium. One of the main problems of plasma detonated thick coatings (100-500 μm thick) is their porosity, lack of homogeneity on account of poor agglomeration of powder particles, high roughness of surface and low adhesion to substrate. These result in insufficient corrosion and wear resistance of such coatings. Practical experience of the use of combined technologies of coating deposition by plasma detonation with the subsequent modification by e-beam or plasma jet allows to claim that the mechanical properties of such coatings of metals and alloys (microhardness, nanohardness, wear resistance, and corrosion resistance) are very high. However, we should clearly constitute the structure-phase coating composition for coatings with expected properties by added irradiation. There are not enough published TEM data about structure-phase composition of coatings deposited by plasma detonation. The conditions of plasma-detonation depositing (heating at high speed, pressure, and short exposure to high temperatures) justify the formation of nanostructures and amorphous areas in coatings.

The goal of the research is to empirically establish the structure-phase compositions and mechanical properties of PG-19N-01 and AN-35 (Russia Industrial Standard) powder composite coatings deposited on steel by plasma detonation and to scientifically justify the modes of additional irradiation by plasma-jet or e-beam.

2. Materials and Experiment Methods

An “Impulse-6” plasma detonation unit was used to form 150 μm thick protective coatings of powder alloys on steel substrate (St 3: Fe – base, C - 0.25 %, Mn - 0,8 %, Si - 0,37 %, P < 0,045 %). For the coatings we used the PG-19N-01 Ni-based powder alloy with additives of Cr (8…14%), B (2,3%), Si (1,2-3,2%), Fe (5%), C (0,5%) and the AN-35 Co-based powder alloy with additives of Cr (8…32 %); Ni (≤ 3%), Si (1,7…2,5%), Fe (≤ 3%); C (1,3…1,7%) and W (4…5%). The powder fractions varied from 56 to 260 μm in size. The substrates were 20x30x10 mm^3 steel samples with the surface pre-treated by sandblasting.

Plasma-detonation powder coatings were deposited in air using the following modes: the distance from the sample to the plasma jet nozzle edge – 60 mm; sample travel speed – 360 mm/min; pulse frequency - 4 Hz; powder consumption – 21,6 g/min.. Pulse duration is 10^{-5} seconds, the shape of impulse is square, the diameter of a plasma jet on a sample is 25 mm. Propane, oxygen and air were used as combustible and orifice gases. Mo was selected as a plasma-jet eroding electrode material. The coating was deposited at the Sumy Institute for Surface Modification (Sumy, Ukraine).

Experimental methods of analysis: AFM by JSPM-5200 (“JEOL”, Japan) and by NT-206 (Belorussia), TEM by JEM-2100 (“JEOL”, Japan), SEM by JSM-6390LV (“JEOL”, Japan) with EDS

("Oxford Instruments", Great Britain), XRD by X'Pert PRO ("PANalytical", the Netherlands). The foils for TEM were prepared by the Ar ion sputter etching method using the PIPS facility ("Gatan", USA). For a more detailed analysis of the coating it was mechanically cut off the surface of the substrate to examine the structure at different distances from the coating surface. We used the method of arbitrary secant line to define the volume fraction of phases according to TEM-images and data [9-11] and Crystal Maker software to define the parameter of crystal-lattice according to TEM-diffraction pattern. Microhardness is measured on the coatings' angle laps by PMT-3 microhardness meter (LOMO, Russia) with an indentation load of 2, 5, and 10 N. Concurrently we measured the sizes of corresponding grains.

3. Experiment Results

The roughness of plasma-detonation coatings is very high. The average number of roughness coefficient Ra is 100 nm for AN-35, and 121nm for PG-19N-01. We observed X-Ray halo in the field of low-angle area at the X-ray diffractogram, which allows assuming surface amorphization. The XRD analysis results of coating phase structure are presented in Table 1.

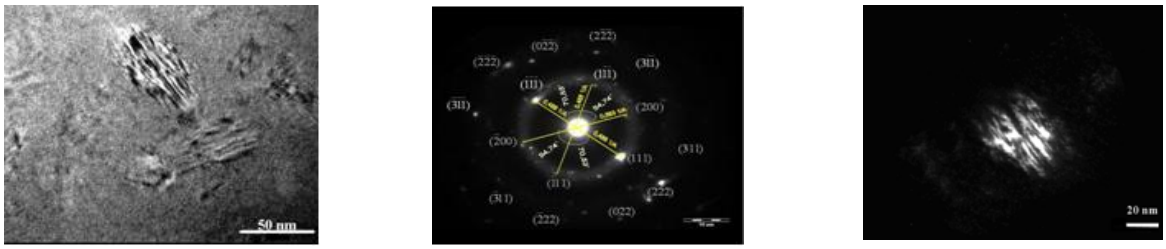
Table 1. Phase composition of the Ni-Cr and Co-Cr based coatings (the thickness of analyzed layer is about 50 μm)

Material and the field of analysis	Volume concentration. Chemical formula. Crystal system. Space group. Space group number. Parameters (Å)
Ni-Cr based coating	
PG-19N-01 base powder	75 % - solid solution on Ni-base (γ-phase) - Cubic, Fm3m, 225, *a* =3,55 25% - Cr_{13} Ni_5 Si_2- Cubic, Pm-3m, 221, *a* =6,1180
coating PG-19N-01, 0-50 μm from the surface	60 vol. % -solid solution on Ni-base (γ-phase) - Cubic, Fm3m, 225, *a*=3,535..3,540 15 vol. % Cr_3 Ni_5 Si_2 – Cubic, Pm-3m, 221, *a*=6,1180 15 vol. % Cr Ni_3 -Cubic, Fm-3m, 225, *a*=3,552 10 vol. % NiO_2 - Cubic, Fm-3m, 225, *a*=4,2
coating PG-19N-01, 150-200 μm from the surface	70 vol. % - solid solution on Ni-base (γ-phase) - Cubic, Fm3m, 225, *a*=3,525...3,500 10 vol. % Cr Ni_3 -Cubic, Fm-3m, 225, *a*=3,552 20 vol. % Fe_7Ni_3 – Cubic, Im-3m, 229, *a*=2,861
Co-Cr based coating	
AN-35 base powder	20 vol.% - Co –based solid solution, hexagonal (hcp) 70 vol% - Co –based solid solution, Cubic (fcc) 10%- $CoCr_2O_4$, Cubic (fcc), Fm-3m (225), *a*=8,2990
coating AN-35, 0-50μm from the surface	60 vol. % - Co-based solid solution, Cubic (fcc), Fm-3m, 225, *a* =3,55…3,54 20 vol. % - $Co_{0.8}Cr_{0.2}$, hexagonal, P63/mmc,194 , *a* =2,52; *в* = 2,52; *c* = 4,062 10 vol. % $FeCr_2O_4$- Cubic (fcc), Fm-3m, 225, *a* =8,3780 10 vol. % $CoCr_2O_4$ - Cubic (fcc), Fm-3m, *225*, *a*=8,2990
coating AN-35 150-200 μm from the surface	50 vol. % - Co-based solid solution, Cubic (fcc), Fm-3m, 225, *a* =3,52-3,53 15 vol. % - Co0.8Cr0.2 , hexagonal, P63/mmc,194, a =2,52; в = 2,52 ; c = 4,062 35 vol. % CoFe– Cubic, Pm-3m, 221, *a* =2,8570

The coatings have differences in the phase structure with depth (see table 1).We noted the reduction of γ-phase parameter *a* in the coatings and relative increase of the γ-phase peak (220), (422), (440) intensity with depth. In general the γ-phase peaks spread. In the coating layers that contact substrate the volume concentration of Fe–based phases rises (Fe is the basic component of a substrate), and the oxides disappear.

According to the data of the XRD the material of the substrate contains a Fe -based bcc-lattice phase (cubic, Im-3m, 229) with the parameter *a*=2,8662 Å. It was proven by TEM that the base through-thickness layer of plasma detonation coatings is a mixture of crystallographically differently oriented nanograins of austenitic γ-phase with the size of 1-2 nanometers and lamellas of intermetallic phases up to 50 nanometers long (Fig. 1a, Fig. 2a). Though in electron diffraction pattern all reflexes of face-centered cubic lattice are observed, yet the planes with zone axis <111> give brighter reflexes. It is indicative of texture. Every indexed reflex of intermetallic phases (Fig. 1b and Fig. 2b) was tested by the dark field method (Fig. 1c and Fig. 2c). According to the XRD data the PG-19N-01 coating contains a Ni-based fcc-lattice phase with the parameter *a* = 3,525…3,540 Å (Table 1). In accordance with the

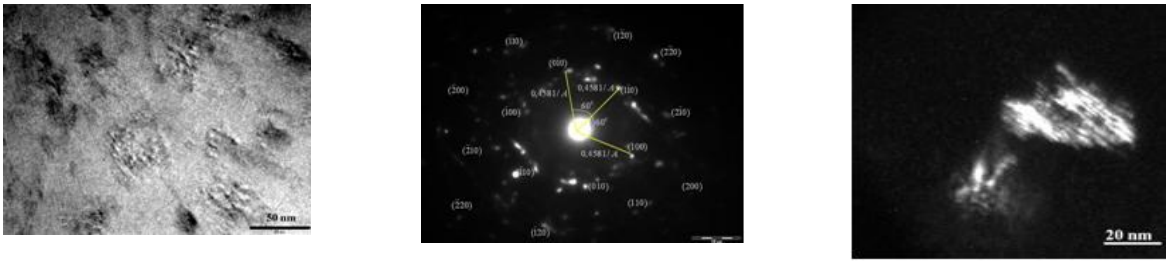
estimated electron-diffraction pattern this parameter makes 3,53 Å. The estimated fcc-lattice parameter of $CrNi_3$ (Fig. 1b) in the coating made a= 3,58 Å (the interplane distance is 2,05 Å), which is very close to the XRD data (Table 1). The volume ratio of $CrNi_3$ in the coating PG-19N-01, as defined by TEM images, makes about 20%.



(a) (b) (c)

Fig. 1. TEM - images of PG-19N-01 coating: the $CrNi_3$ particle (bright field) (a); the electron diffraction pattern of a $CrNi_3$ particle, the zone axis is $[0\bar{1}1]$ (b); the $CrNi_3$ particle (dark field) shot in point reflex (111) (c)

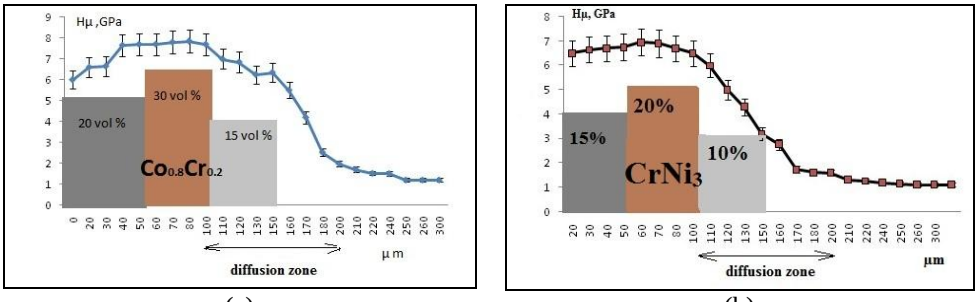
In accordance with the estimated electron-diffraction pattern (Fig. 2b) the parameters of $Co_{0.8}Cr_{0.2}$ - phase are: a =$в$ = 2,5 Å and c = 4,0 Å. The volume ratio of $Co_{0.8}Cr_{0.2}$ in the coating AN-35, as defined by TEM images, makes about 30 %. These nanosize intermetallic phases ($CrNi_3$ and $Co_{0.8}Cr_{0.2}$) may be called strengthening as the highest microhardness of a coating corresponds to those places where the volume concentration of these phases is the highest (Fig.3). In the contact with the substrate layer the coatings are deformed.



(a) (b) (c)

Fig. 2 TEM - images of AN-35 coating: the $Co_{0.8}Cr_{0.2}$ particle (bright field) (a); the electron diffraction pattern of a $Co_{0.8}Cr_{0.2}$ particle, the zone axis is [001] (b); the $Co_{0.8}Cr_{0.2}$ particle (dark field) shot in point reflex $(0\bar{1}0)$ (c)

The analysis of dependence of microhardness at some distance from the surface shows that the coating microhardness is considerably higher than that of the steel substrate (fig.3). The steel microhardness on the average is 1,4 GPa. The maximum microhardness of AN-35 is 8,0 GPa and of PG-19N-01 is 7,0 GPa. It is observed in the coatings at the depth of 60 μm from the surface. The width of the transitional from a coating to a substrate layer with the increased microhardness is estimated as 100 microns, the analysis of its structurally-phase composition (Tab. 1) allows to name it a diffusion zone.



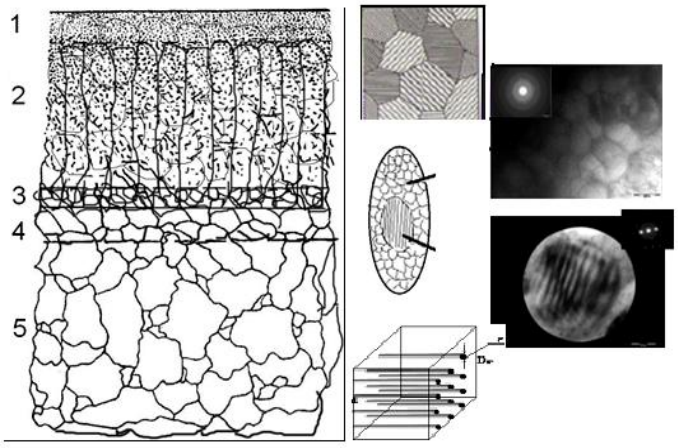
(a) (b)

Fig. 3 Coating microhardness variation according to the distance from the surface and to the volume concentration of the intermetallic phase: AN-35 (a), PG-19N-01 (b)

4. Discussion

We think that the structure-phase state of a coating is defined by the following factors: the deformational impact of a plasma jet, the temperature profile distribution in the coating material, and the inhomogeneous concentration of the elements in the coating. The formed structures are stable at room temperature, no reduction of strength properties is observed.

We consider that the nanocrystalline patterns found in these coatings are distinctive for all the coatings deposited by the plasma detonation method, and partially characteristic for the substrate layer next to the coating. One of the reasons is high micro structure defectiveness conditioned by the plasma jet impact action on the surface and steep temperature gradient in the coating, which may lead to a great deformation in a coating. As a result, in order to relieve the stresses in a coating there is formed a substructure of nanograins of a different crystal lattice orientation with high and continuous disorientation, which is proved by distinctive ring electron-diffraction patterns. When the foils in a goniometer are oriented randomly, the characteristics of polycrystal features of diffraction contrast are absent, namely, the changes of its intensiveness on the boundaries, necessary for defining grain edges. We assume that we observe the pattern similar to a fragmented one, with fragment – nanograin – disorientation being analogous to the one of crystal polygonization. The validation of this assumption for the coatings is some diffusion of the peaks and lowering of their intensiveness on the X-Ray diffractograms. Occurrence of a fiber texture with the zone axis perpendicular to the coating surface is connected with the direction of a heat current at heating by a plasma jet at deposition and the subsequent cooling of the coating. The results of research of the microstructure, phase structure and the microhardness of plasma detonation coatings at depth from the surface helped to develop the scheme of their structure (Fig.4).



(a) (b)

Fig. 4 The scheme of the structure of coatings on Ni - Cr and Co–Cr based powder alloys deposited by plasma-detonation on the steel substrates (a) with explanatory drawings and images: the nanograins and intermetallic phase precipitation with their electron diffraction pattern and the scheme of cubic grain (b), where: 1- amorphous layer with oxides and carbides; 2 - textured layer (solid solution on Co-base or Ni-base with an intermetallic phase) and unmelted particles of the coating powder; 3 - intermediate coating layer (coating-substrate) with deformed and broken particles of coating; 4-intermediate substrate layer with the fine-grained microstructure; 5-substrate with large grains. The strokes (a) show precipitation of lamellas of the intermetallic phase in the cubic grains of the γ-phase (b).

This scheme was used at working out the model of the temperature profile distribution in these coatings under irradiation by a plasma jet or an e-beam. The choice of additional irradiation modes is based on the calculations of irradiation modes leading to heating of the upper thin layer of a coating to the Co or Ni melting point, respectively, and heating the coating across the entire thickness with the aim of its homogenization. The numerical experiment to determine the temperature profiles during irradiation was carried out by mathematical simulation methods.

Synthesis of intermetallic compounds in the surface layer of eutectic silumin by dense plasma impact

Nikolai Cherenda[1], Natalya Bibik[1], Vladimir Uglov[1], Valentin Astashynski[2], Anton Kuzmitski[2]

[1]Belarusian State University, Minsk, Belarus
[2]Institute of Physics, Minsk, Belarus

cherenda@bsu.by

Particles reinforced metal matrix composites are one of the prospective groups of novel materials and they are widely used nowadays. Aluminium alloy matrix composites attract considerable attention due to their low density and low cost. At present transition metals trialuminides like Al_3Ti are considered as reinforcing particles in aluminium composites. Al_3Ti has a relatively high melting point (~1350 C), a low density (~3.3 g/cm^3) and a low coarsening rate at elevated temperatures. Thus, aluminium matrix composites reinforced by Al_3Ti particles could be used in conditions of more intense mechanic and thermal loads.

A large number of investigations were carried out in the area of synthesis of bulk aluminium matrix composites reinforced by metals trialuminides. At the same time many applications require good exploitation properties only of the materials surface layer. In this case techniques providing synthesis of composites in the surface layer are of interest. Treatment of a coating/substrate system by high energy particles ($\geq 10^6$ W/cm^2) is one of such techniques that allow to alloy the surface layer of a substrate with coating elements. Such treatment provides enough energy to melt a coating and the surface layer of a substrate. Convection in the melt leads to mixing and homogenization of elemental composition in the melted layer. A high cooling rate results in the formation of a disperse structure having submicron or nanocrystalline grains and phases. The change of the coating thickness and energy absorbed by the surface layer allows to control the concentration of coating elements in the mixed layer thus giving an opportunity to regulate phase composition and volume fraction of the synthesized phases. This approach was used to form the surface composite layer reinforced by Al_3Ti intermetallic particles in the Al-Si piston alloy and was realized by treating Ti coated alloy samples with compression plasma flows (CPF).

The samples used were made of a eutectic silumin alloy (12,9 Si; 3 Mg; 0,7 Cu; 0,4 Ni; 0,1 Fe; at.%, Al - balance). The titanium coating was formed using cathodic arc vapour deposition with the following process parameters: arc current of 100 A, bias voltage of -120 V, deposition time 10 and 20 min (the corresponding coating thickness 2.5 and 5.5 μm).

CPF were obtained using a gas-discharge magneto-plasma compressor of compact geometry. CPF treatment was performed in a ‘‘residual gas’’ mode in which the vacuum chamber was filled with nitrogen up to the preset pressure of 400 Pa. The plasma flow parameters were as follows: pulse duration ~100 μs, flow velocity $(5\div6)\cdot10^6$ cm/s and electron concentration $(4\div7)\ 10^{17}$ cm^{-3}. The discharge duration in the MPC amounted to ~ 100 μs. Treatment of the formed Ti/silumin system was carried out by three pulses. The energy density (Q) absorbed by the surface layer varied in the range of 4-19 J/cm^2 per pulse.

Element composition was analyzed by means of the Rutherford backscattering analysis of He^+ ions with the energy of 2 MeV. Phase composition of the samples was investigated by the X-ray diffraction analysis (XRD) in Bragg- Brentano geometry and Cu Kα radiation using a DRON 4-13 diffractometer. Surface and cross-section morphology as well as element composition were analyzed by means of scanning electron microscopy (SEM) using a LEO1455VP device equipped with an energy-dispersive X-ray Röntec detector. Microhardness

of the samples was tested by means of a Wilson Instruments 402MVD microhardmeter with a Vickers indenter under the load ranging from 0.1 to 1 N.

The data of the phase composition analysis showed that plasma impact with $Q \geq 7$ J/cm^2 led to melting in the Ti (2.5 μm) /silumin system, mixing of components and as a result – the formation of Al-Ti intermetallic phases (Fig. 1). The formation of $AlTi_3$ phase was found at Q=7 J/cm^2. The increase of Q up to 13 J/cm^2 resulted in additional formation of Al_3Ti compound with a tetragonal $D0_{22}$ structure. At Q=19 J/cm^2 the surface layer contained only Al_3Ti compound. Such a change of phase composition can be explained by the decrease of Ti concentration in the surface layer with the growth of Q. Treatment with Q=4 J/cm^2 did not lead to melting of the surface layer. At Q=7-13 J/cm^2 nonuniform mixing in the surface layer was observed by SEM. Local areas with a different concentration of titanium atoms were found thus resulting in the formation of different types of Al-Ti intermetallic phases during crystallization. The growth of the energy absorbed by the surface layer leads to the increase of the melted layer thickness and to the growth of the melt existence time. In case of a constant coating thickness the whole volume of the coating element will be distributed in the melted layer of a greater thickness resulting in the decrease of the alloying element concentration. That is consistent with the data of the elemental composition analysis. According to the energy-dispersive analysis Ti mean concentration in the layer with the thickness of ~1μm changes from 31±2 at.% at Q=13 J/cm^2 to 9±1 at.% at Q=19 J/cm^2. The increase of the melt existence time provides more uniform distribution of Ti atoms in the melt. Thus, at treatment parameters providing the highest energy absorbed by the surface layer only Al_3Ti was found.

The lattice parameters of Al_3Ti derived from the diffraction pattern are less than those of the standard (a=0.3853 nm and c=0,8583 nm). Q increase led to diminishing the Al_3Ti lattice parameters. At Q=19 J/cm^2 they were equal to: a=0,3792 nm and c=0.8488 nm. It is known that in Al_3Ti compound up to 15 % of Al atoms can be substituted by Si atoms thus leading to diminishing lattice parameters. It is seen from Fig. 1 that Q increase also resulted in diminishing Si diffraction lines intensity. Thus, some part of Si atoms can take part in precipitation from the melt of Al-Ti intermetallic phase which can be identified as $(Al,Si)_3Ti$.

Si atoms can also form an oversaturated solid solution on the aluminium basis crystallized in conditions of a high cooling rate thus resulting in the shift of Al diffraction lines to the region of greater diffraction angles (Fig. 1).

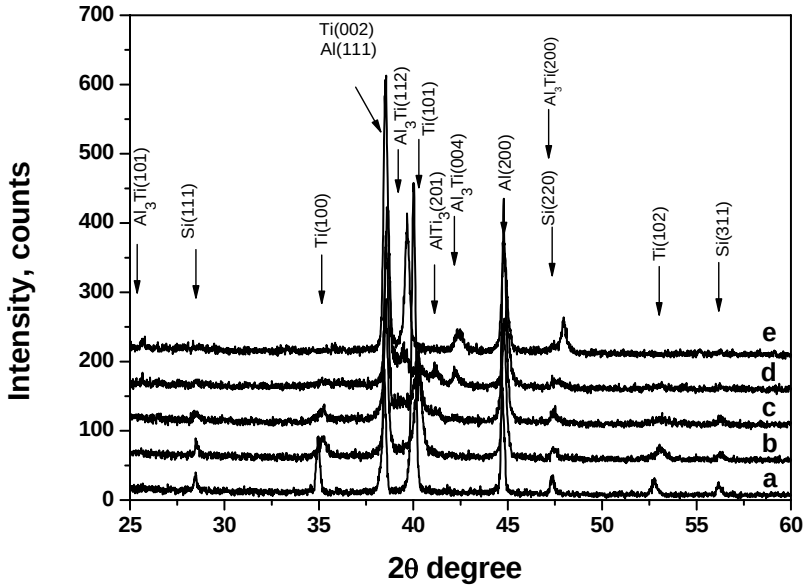


Fig. 1 XRD diffraction patterns of the Ti (2.5 μm) /silumin system samples before (a) and after CPF treatment with the energy density of 4 J/cm^2 (b), 7 J/cm^2 (c), 13 J/cm^2 (d), 19 J/cm^2 (e).

Similar dependencies were observed in the samples of the Ti (5.5 μm) /silumin system treated by CPF at Q=7-19 J/cm^2 but Al_3Ti or $(Al,Si)_3Ti$ was the only intermetallic phase observed (Fig. 2).

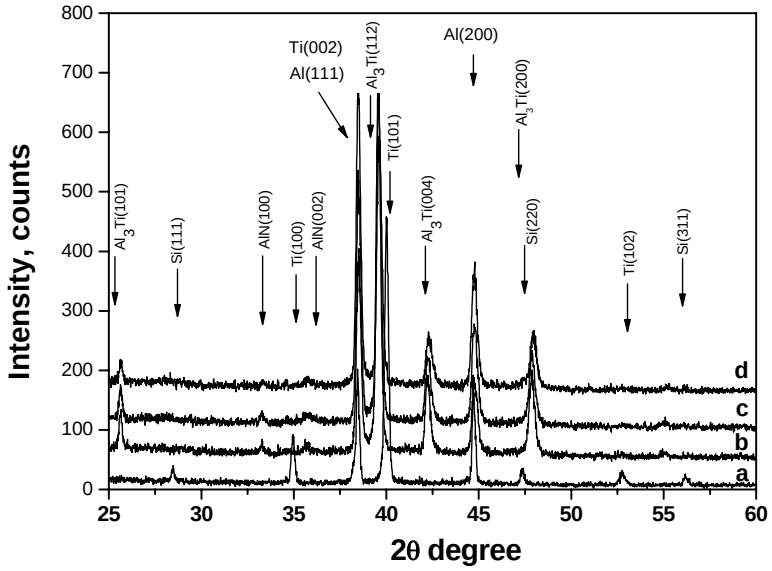


Fig. 2 XRD diffraction patterns of the Ti (5.5 μm) /silumin system samples before (a) and after CPF treatment with the energy density of 7 J/cm^2 (b), 13 J/cm^2 (c), 19 J/cm^2 (d).

The investigation of cross-section morphology showed that the thickness of the composite layer in the system Ti (5.5 μm) /silumin treated by CPF at Q=19 J/cm^2 was 50-60 μm (Fig. 3). The energy-dispersive analysis along the cross section showed homogeneous distribution of Ti and Si in the melted layer (assuming resolution limit ~ 1μm). One can see that $(Al,Si)_3Ti$ precipitates have relatively uniform distribution in the composite layer.

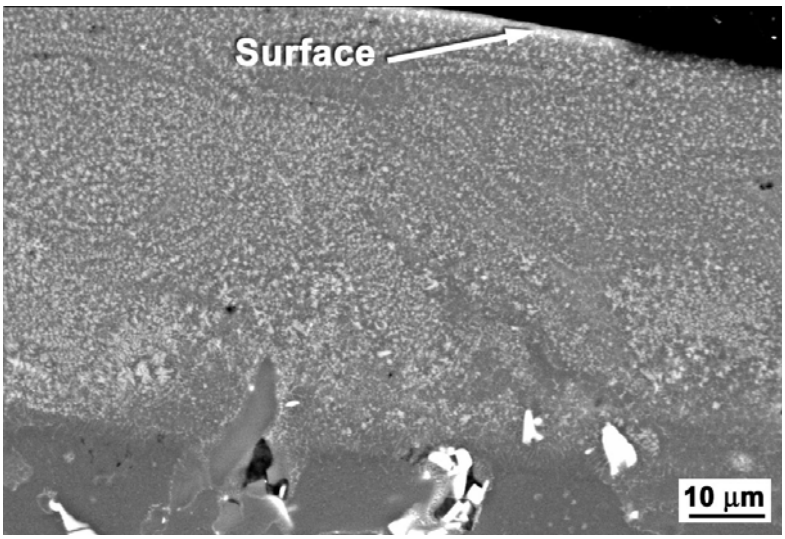


Fig. 3 Cross-section morphology of the Ti (2.5 μm) /silumin system sample after CPF treatment with the energy density of 19 J/cm^2 (e).

$(Al,Si)_3Ti$ precipitates grew in the form of dendrites due to high undercooling (Fig. 4a). Their size varied in the range of 0.2 – 1 micrometers depending on plasma parameters for the samples with 2.5 μm Ti coating. The increase of the Ti coating thickness up to 5.5 μm allowed to

form a surface layer consisting only of intermetallic phase dendrites with the size up to 4 μm after CPF treatment at Q=7 J/cm^2 (Fig. 4b).

a)

b)

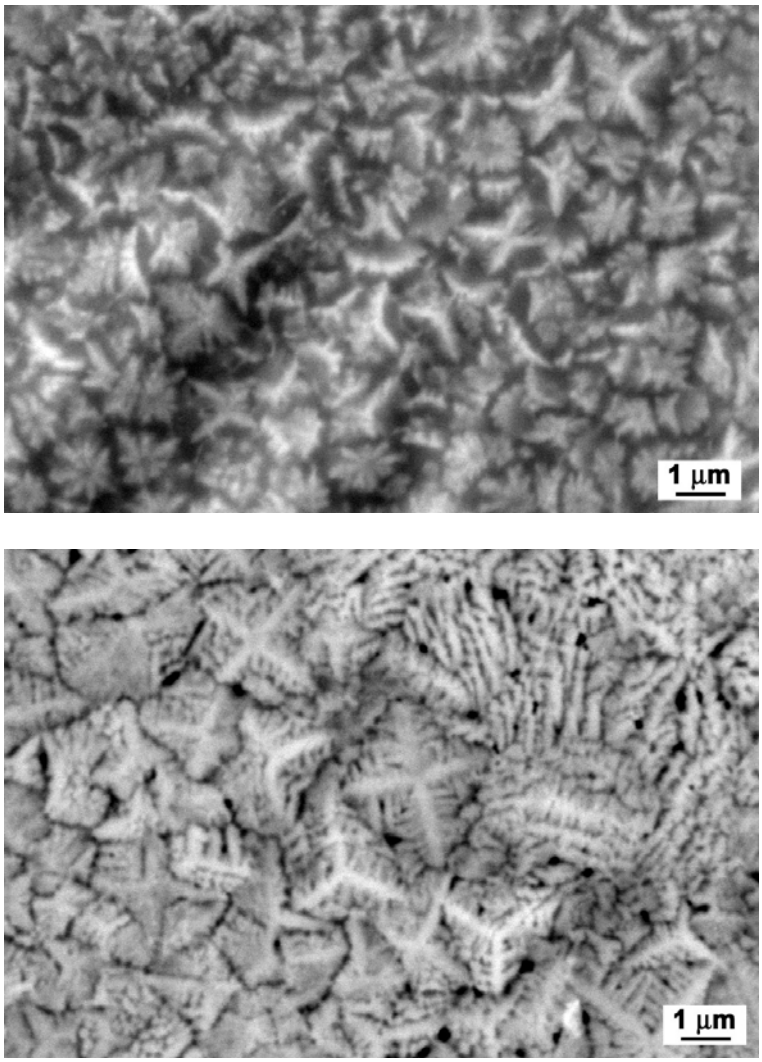


Fig. 4 Cross-section morphology of the Ti (2.5 μm) /silumin system (a) and Ti (5.5 μm) /silumin system samples after CPF treatment with the energy density of 19 J/cm^2 (a) and 7 J/cm^2 (b).

The microhardness tests showed that CPF treatment resulted in the surface microhardness increase from 1.3 GPa (for the initial silumin sample) to 2.2 GPa (for the Ti (2.5 μm) / silumin system sample treated at Q=19 J/cm^2) and to 4.4 GPa (for the Ti (5.5 μm) / silumin system sample treated at Q=7 J/cm^2). The latter value lies in the range attributed to microhardness of bulk Al_3Ti, which agrees with the data of SEM investigations (Fig. 4b).

The results of this work demonstrate that compression plasma flows treatment of Ti pre-coated silumin samples allows to form a surface composite layer with the thickness up to 60 μm reinforced by $(Al,Si)_3Ti$ intermetallic particles. The size of intermetallic precipitates (mainly dendritic-like) varies in the range of 0.2 – 4 micrometers depending on treatment parameters and Ti coating thickness. Plasma treatment also results in dissolution of primary silicon crystals and formation of a Al(Si) supersaturated substitutional solid solution. The change of treatment parameters and Ti coating thickness allows to control Ti atoms concentration and volume fraction of reinforced particles providing a substantial microhardness increase up to 4.4 GPa.

EVALUATION OF THE PVD AND CVD COATINGS' STRUCTURE USING THE MODIFIED METHOD OF SPHERICAL METALLOGRAPHIC MICROSECTION (BALTEST-M)

Marek Betiuk

betiuk@imp.edu.pl

Instytut of Precision Machanics, Warszawa, Poland

ABSTRACT

The Baltest-M testing method developed at the Institute of Precision Mechanics allows a precise metallographic analysis of the structures of the coating and substrate materials subject to a strong local plastic strain. The material structure of locally strained areological systems (coating: PVD, CVD – substrate: steel, carbides) is revealed on precise spherical polished sections. The essence of this new testing method is the fact that the spherical polished sections are made in the area of indentations formed during hardness testing (HB, HRC, HV, HK of the surface) of the areological system. Material structures of substrate and coating in the indenter strain area are analysed quantitatively and qualitatively. The Kulotester test rig with a high-quality optical system, a rotary x-y bench for a sample holder and a microprocessor controller allows a precise preparation of polished sections within the indentations formed during the hardness test.

INTRODUCTION

The Baltest-M testing method is related to the research conducted at the Institute of Precision Mechanics on hybrid surface strengthening technologies. One of topics investigated during this research is the research on the areological systems obtained using the hybrid disjoint technology [1,3]. The areological system is formed as a result of gas or ion nitriding of tool steels and independent synthesis of coatings, such as TiN, TiAlN, CrN, CrAlN, using the PAPVD methods. Modern, multifunctional coating materials have a complex multilayered structure. [1-3]

One of the key criterions which determine the quality of the PVD coatings on the surface of tools and machine parts and allow them to be used in industrial environments are good results of hardness tests, adhesions tests and fracture resistance tests. Qualitative and quantitative evaluation criteria result from correlations associated with wear and tear [1-4].

A popular adhesion and cohesion test of coating materials is a standardized test of elastic and plastic strain implemented using the spot method as described in the VDI 3198 German industry standard (Bechichten von Werkzeugen der Kaltmassivumformung CVD- und PVD-Verfahren) [4]. This test is recommended for quenched and tempered hot- and cold-work tool steels (steel hardness > 52 HRC) and for sintered carbides covered with 1÷5 um TiN, CrN, TiC, TiAlN coatings. The method involves evaluation of the deformed surface and corresponding classification of surface quality on a six-point scale [4].

Being spot and static, the Rockwell test method (VDI 3198) does not give information about the behaviour of material structures in their volume (i.e. in cross-section). Other tests of the quality of areological systems involve spot dynamic tests [14], [16]. They allow to obtain the fatigue evaluation of the system and its resistance to cracking, spalling and chipping. The features of damage, i.e. evolution of fractures and delamination depend, among other things, on geometrical parameters of the coating structure, thickness in case of multilayered coatings, coating modulation parameter [4-12].

The new Baltest-M method of evaluation of the substrate-coating system conforms to strict quality evaluation standards of industrial coating materials. The Baltest-M method is a combination of two available testing techniques: hardness measurement (e.g. HV, HRC, HK) and a precise spherical polished section in the plastic strain area of the coating around the indentation. A precise spherical polished section in the indentation area, formed e.g. during the HRC hardness test, is used to perform a metallographic analysis of strained structures of the substrate and coating materials. The method allows a quick and precise evaluation of the quality of PVD, CVD coatings with a complex multilayered structure. A precise spherical polished section in the hardness test indentation area is made on the Kulotest test rig designed at the Institute of Precision Mechanics.

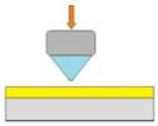
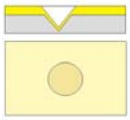
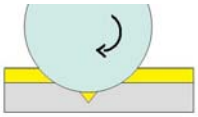
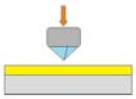
DESCRIPTION OF THE *Baltest-M* TESTING METHOD

The essence of the Baltest-M testing method is combination of two standard available testing techniques:

- hardness measurement (e.g. HV, HRC, HK), and
- a precise spherical polished section in the indentation area.

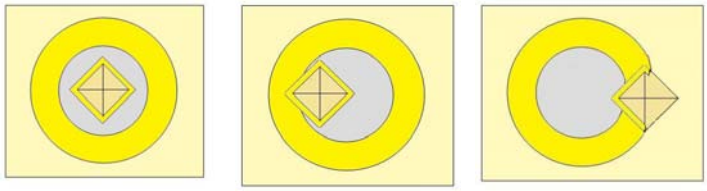
The diagram of the method used for coatings and layers on flat surfaces is presented in a table 1.

TABLE 1. Sequence of technological operations in the Baltest-M method, flat surfaces

I - Make an indentation with the hardness tester	II - Elastic and plastic strain of coating and substrate	III - Make a precise spherical polished section	IV - Microscopic analysis of revealed structures
			
Rockwell HRC indenter			
			
Vickers HV indenter			

Correct application of this technique to evaluate the structure of layers and coatings requires:

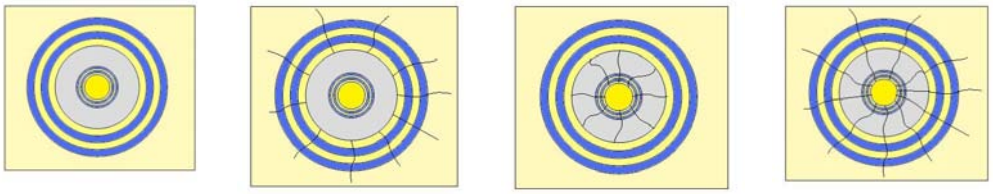
- a hardness measurement using one of the methods, e.g. HB, HRC, HV, with parameters allowing the plastic strain of the coating,
- an analysis of the coating material structure around the indentations, at the edge and inside,
- making a precise spherical polished section in the indentation area – in the indentation axis (Fig.1a) or asymmetrically (Fig.1 b, c).
- an analysis and quantitative evaluation of the revealed coating and substrate material structures on spherical polished sections using optical or electron microscopes.



a b c

Fig. 1. Structures revealed on the spherical polished section surface in various positions in relation to the Vickers hardness indentation: a – centrally, b – from side inwards, c – from side outwards

During the coating material quality evaluation using the Rockwell hardness test (VDI 3198), in case of the best adhesion quality classes HF1 and HF2, Baltest-M allows to obtain more detailed description. The description relates to the fracture propagation structure inside the substrate and coating materials. The diagram of the proposed classification for Rockwell indentations is presented in Fig. 2. The cases B I – B IV correspond to the following situations:



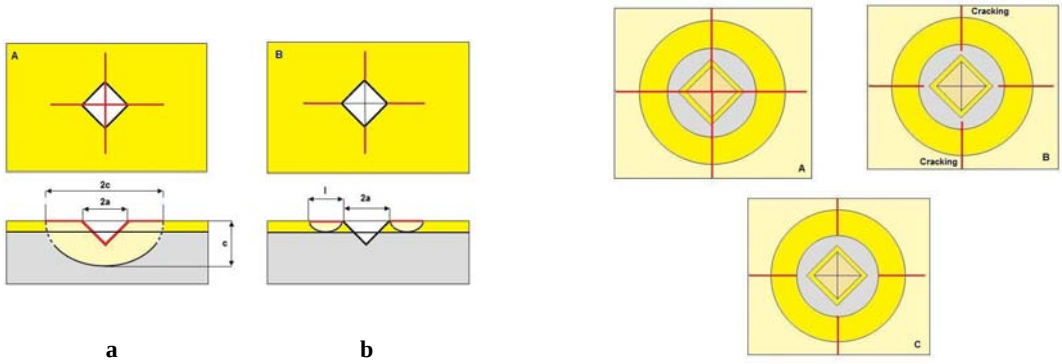
B I **B II** **B III** **B IV**

Fig. 2. Structures revealed on the spherical polished section surface of the substrate + multilayered coating areological system in the Rockwell indentation axis: B I – absence of fractures, B II – fractures in the coating, B III – fractures in the substrate, B IV – fractures in the substrate and the coating

- B I shallow, very short fractures, or absence of fractures, in the coating and the substrate,
- B II propagating fractures in the coating,
- B III propagating fractures in the substrate,
- B IV propagating fractures in the coating and the substrate.

The fractures can be linear, curvilinear or mixed, singular or propagating to a number of smaller fractures.

A spherical polished section in the area of indentation formed during the Vickers hardness test, with fractures in the corners visible on the coating surface, allows to observe the character of the fracture propagation in the volume and in the substrate material, Fig. 3, 4.



a **b**

Fig. 3. Propagation of dry cracking initiated by a spot strain of the areological system (substrate + coating) by the Vickers indenter: a – fracture propagation in the substrate and coating material, b – fracture propagation in the coating material

Fig. 4. Structures revealed on the spherical polished section surface of the substrate + multilayered coating areological system in the Vickers indentation axis: a – fractures propagating in the substrate and coating material, b – fractures propagating partially in the substrate and in the whole coating, c – fractures propagating in the coating material

The fractures' propagation analysis gives a possibility of unambiguous determination of their route. A fracture can propagate in the entire volume of areological system (Fig. 2a, Fig. 3a) or only in the layer and coating material (Fig. 2b, Fig. 3b). The obtained data can be used as a basis to find the methodology of determining the *KIc* factor (Fig. 6) for coating materials based on the length measurements of fractures formed in the corners of the Vickers indentations.

This data is necessary to test the resistance to the layer dry cracking in order to choose the methodology of determining the K_{1c} factor [15], [19].

Figure 4 presents three diagrams of the coating structure around the Vickers indentation revealed on the spherical polished section.

- the first one corresponds to the fracture propagation through the indentation corners, the maximum fracture depth h_c (Fig. 3a) is greater than the indentation depth h_{HV} ($h_c > h_{HV}$) (Fig.4a.)
- the second one illustrates a situation where the fractures are located in the substrate and the coating, the maximum fracture depth is less than the indentation depth ($h_c < h_{HV}$) Fig. 4b.
- the third one shows a situation where the fractures (Fig. 3b) are located only in the coating Fig. 4c.

Application examples of the Baltest-M testing method

Analysis of the TiN coating – HSS steel areological system in the area of Rockwell (HRC) and Vickers (HV5) indentations with the spherical polished sections in order to illustrate the Baltest-M testing method.

Strain made using the Rockwell HRC indenter

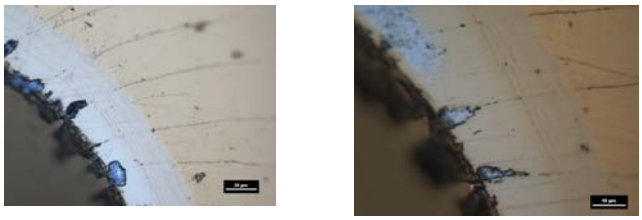
The analysis was performed on the TiN coating - SW7M steel areological system. The 4 µm titanium nitrides coating was made using the magnetron technique (Fig. 5, Fig. 6). The coating has a gradient structure with varying nitrogen concentration (Fig7). The fractures visible on the surface around the Rockwell indentation seen on the spherical polished section propagate only in the TiN coating (Fig.5 b). The fracture propagation within the coating is linear. Very small local chipping on the substrate-coating boundary are visible in the indentation edges area (Fig.7 a, b). Such a behaviour of the coating material proves its good adhesion.



a **b** **a** **b**

Fig. 5. Rockwell indentation on the surface of the SW7M (1.3343) steel with the TiN coating: a-micro-fractures around the indentation edge, b- spherical polished section within the Rockwell indentation revealing fracture propagation in the coating

Fig. 6. Spherical polished section within the Rockwell indentation edge revealing the TiN coating structure and the fracture propagation features: a – polished section in the indentation axis, - offset in relation to the indentation axis



a **b**

Fig. 7. Spherical polished section within the Rockwell indentation SW7M (1.3343) steel edge with the multi-gradient TiN coating: a- fracture propagation inside and on the coating, b- fracture propagation in the TiN coating initiated on the substrate-local micro-chipping boundary

Strain made using the Vickers HV5 indenter

Strain of the areological system made using the Vickers HV5 indenter is less invasive. The load range can be adapted to control the indenter penetration depth and corresponding strain size. Examples of surface defect structures and the cross-section of a multi-gradient TiN coating on the spherical polished section is shown in Fig. 8 and Fig. 9. The HV5 coating strain generates numerous fractures in the indentation corner and parallel to its edge Fig.8 b. The coating structure revealed in the corner area does not show distinct fractures and chippings (Fig.9b) which proves its good fracture resistance in the conditions of the generated HV5 load.



a **b** **a** **b**

Fig. 8. Defects of the TiN coating on the SW7M (1.3343) steel around the indentation after the HV5 hardness test: a - fractures and micro-chipping of the TiN coating on the indentation edge, b – coating fractures propagating in various directions

Fig. 9. Structure of the multi-gradient TiN coating in the HV indentation area revealed on the spherical polished section surface: a – coating structure, b – brittle fracture propagating in the coating in the Vickers indentation corner

CONCLUSIONS

The Baltest-M method allows to evaluate the behaviour of the internal structure of the coating and substrate materials subject to a strong elastic and plastic strain generated during the HB, HRC, HV hardness tests.
The coating materials structure revealed on the spherical polished section allows a precise analysis of material cracking and chipping phenomena in the areological system, particularly in its cross-section.
The Baltest-M testing method requires further research, especially in the area of its systematic qualitative and quantitative description.

LITERATURA

[1] Burakowski T.: Areologia , Instytut Technologii Eksploatacji -PIB, Radom 2007.
[2] Dobrzański L.: Significance of materials science for the future development of societies. “Journal of Materials Processing Technology” 175 (2006) pp 133-148.
[3] Verein Deutscher Ingenieure Normen, VDI 3198, VDI-Verlag, Dusseldorf (Coating (CVD, PVD) of cold forging tools) 1991.
[4] Mathias C,. Ernst G., Fleischmann W, Christian H. Konrad, Schuetz A., Glatzel U.: Abrasion resistance of oxidized zirconium in comparison with CoCrMo and titanium nitride coatings for artificial knee joints. “Journal of Biomedical Materials Research B”: applied biomaterials 2010 vol 93B, 24 pp 4 -251.
[5] Taktak S., Tasgetiren. S.: Identification of delamination failure of boride layer on common Cr-rased steels. “Journal of Materials Engineering and Performance”. Volume 15(5) October 2006, pp. 570-574.
[6] Wiklund U., Hedenqvist P., Hogmark S.: Multilayer cracking resistance in Bendig. “Surface and Coatings Technology”, 97 (1997) pp 773-778.
[7] Stallard J., Poulat S., Teer D.: The study of the adhesion of a TiN coating on steel and titanium alloy substrates using a multi-mode scratch tester. “Tribology International”, 39 (2006) pp.159-166.
[8] Harris S., Doyle E.D., Vlasveld A.C., Audy J., Quick D. A.: Study of the wear mechanisms of Ti1−*x*Al*x*N and Ti1−*x*−*y*Al*x*Cr*y*N coated high-speed steel twist drills under dry machining conditions. “Wear” 254 (2003) 7 pp 23-734.

Measurements of SiH_4/H_2 VHF Plasma Parameters with Heated Langmuir Probe

Tsukasa Yamane [1], Sachiko Nakao[1], Yoshiaki Takeuchi [1], Hiroshi Muta [2], Ryuta Ichiki[3], Kiichiro Uchino[2] and Yoshinobu Kawai [2]

[1] Solar Power Department, Mitsubishi Heavy Industries Ltd., Isahaya, Nagasaki, 854-0065, Japan
[2] Interdisciplinary Graduate School of Engineering Sciences, Kyushu University, Kasuga, Fukuoka 816-8580, Japan
[3] Department of Electrical and Electronic Engineering, Oita University, Oita, 870-1192, Japan

E-mail: kawai@aees.kyushu-u.ac.jp

Abstract

The parameters of S_iH_4/H_2 VHF plasma were measured as a function of silane gas concentration with a heated Langmuir probe. When the sailane gas concentration was increased, the nagative ion density increased. The negative ion density was estimated from the reduction of the electron saturation current. In addition, the dependence of the sheath potential on the silane gas concentration agreed with the theoretical values derived from the Bohm sheath equation including negative ions.

Keywords VHF plasma, negative ions, silicon thin film, sheath potential, multi-rod electrode

1. Introduction

Microcrystalline silicon has been widely investigated using VHF plasmas in order to reduce production costs of silicon thin film solar cells [1]. Recently, higher deposition rate of microcrystalline silicon was achieved by a short gap discharge at high pressure [2-4]. Microcrystalline silicon is deposited by introducing a small amount of SiH_4 gas into H_2 plasmas. As well known, negative ions are produced in S_iH_4 plasma [5]. The cross section of electron attachment is much lower than that of ionization. However, negative ions are confined in plasma without diffusing to electrodes, leading to high negative ion density. Thus, it is an important subject in solar cell development to investigate S_iH_4/H_2 plasma parameters including negative ions. The simplest method to estimate the negative ion density is to use Langmuir probe characteristics. The negative ion density n_- normalized to the ion density n_+ is in the following:

$$n_-/n_+=1-I_{es}/I_{es0} \quad (1)$$

where I_{es} and I_{es0} is the electron saturation current with negative ions and without negative ions, respectively. Thus, the negative ion density is easily estimated from the reduction of the electron saturation current. Note that this method includes the assumption that the ion density is kept constant even when negative ions increase [6].

The sheath potential is one of key parameters in plasma CVD because it corresponds to ion bombardment energy. According to the Langmuir probe theory [7], the sheath potential V_w is in the following

$$V_w \approx \frac{\kappa T_e}{2q} \ln\left(\frac{2M_+}{\pi m}\right) \quad (2)$$

Here κ, q, m and M_+ is Boltzman constant, electron charge, electron mass and ion mass, respectively. As seen from Eq. (2), the sheath potential is estimated from the electron temperature Te if there are not negative ions. That is, the comparison between measured sheath potentials and those calculated using Eq. (2) provides information about existence of negative ions. In this paper, we measured the parameters of VHF S_iH_4/H_2 plasma with a heated Langmuir probe and discussed the VHF S_iH_4/H_2 plasma characteristics from the Langmuir probe *I-V* curve. We found that there are a lot of negative ions in SiH_4/H_2 VHF plasma.

2. Experimental

The experimental apparatus consisted of a stainless steel vacuum vessel (height: 420 mm, width: 1350 mm, depth: 470 mm), a multi rod electrode [8] of 1200 mm x 114 mm and a VHF power supply. The distance between the multi rod electrode and the glass substrate was 34 mm, where a punched electrode (stainless- steel- disk plate) of 1200 mm x 114 mm was used as a substrate holder to look at plasma uniformity. The VHF power source with frequency of 60 MHz was used and the power was150 W, where

we used a balanced power feeding method [9] to produce a stable VHF plasma. Here the forward and reflected RF power was measured with a power meter. The gas flow rate was 50-150 sccm. The plasma parameters were measured with a heated Langmuir probe [10]. In order to reduce the disturbance of the Langmuir probe to the plasma, a tungsten wire of 0.3 mm in diameter was used as the heated Langmuir probe. Before measuring S_iH_4/H_2 VHF plasma parameters, the current range not disturbing plasma generation due to heating was confirmed and calibration for the surface area of the heated probe was performed by measuring argon and hydrogen plasma using an ordinary Langmuir probe.

3. Experimental results and discussion

We produced a VHF S_iH_4/H_2 plasma and measured the plasma parameters as a function of silane gas concentration (=$[SiH_4]/[S_iH_4]+[H_2]$) for 500 mTorr. The results are shown in Fig.1 It was found that both the ion saturation current I_{is} and the electron saturation current I_{es} decrease with increasing S_iH_4 gas. On the other hand, the electron temperature Te tends to increase when $[S_iH_4]/[S_iH_4]+[H_2]$ is increased. Here we estimated the negative ion concentration n_-/n_i from Eq. (1) for different gas flow rates. Fig. 2 indicates that when the silane gas concentration is increased, the negative ion concentration rapidly increases and tends to saturate at a certain silane gas concentration. This is consistent with the increase of the electron temperature, that is, Te begins to increase when negative ions are produced.

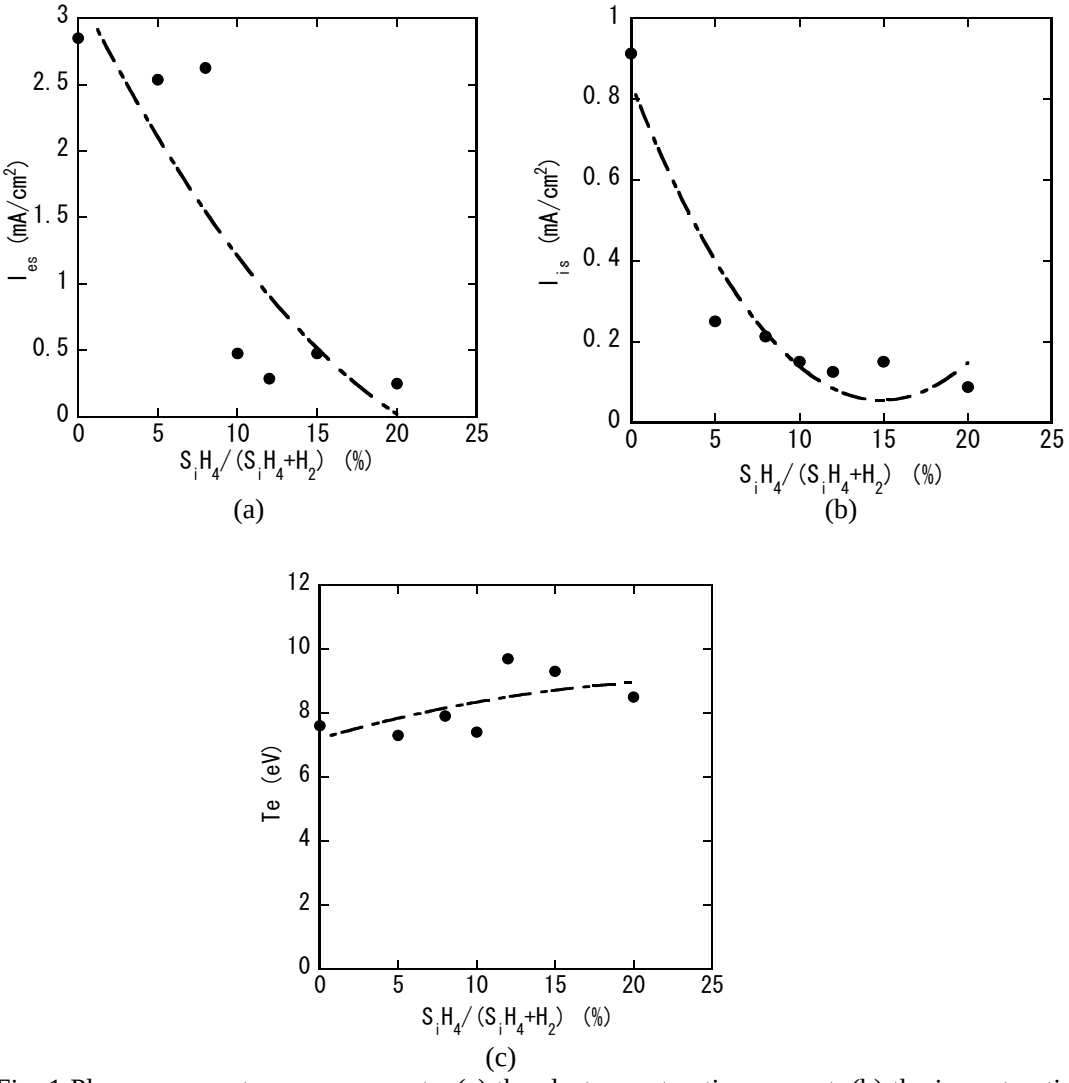


Fig. 1 Plasma parameter measurements: (a) the electron saturation current, (b) the ion saturation current and (c) the electron temperature.

Fig. 3 shows the dependence of the sheath potential on silane gas concentrations. Here the solid lines are the theoretical sheath potentials calculated using the sheath equation derived by Shindo and Horiike [11]:

$$n_e \exp(-\frac{eV}{kT_e})(\frac{kT_e}{2\pi m})^{1/2} + n_- \exp(-\frac{eV}{kT_-})(\frac{kT_-}{2\pi M_-})^{1/2} =$$

$$\{\frac{2(kT_+ + eV_B)}{M_+}\}^{1/2}\{n_e \exp(-\frac{eV_B}{kT_e}) + n_- \exp(-\frac{eV_B}{kT_-})\} \quad (3)$$

$$n_e \exp(-\frac{eV_B}{kT_e})\{\frac{1}{kT_e} - \frac{1}{2(kT_+ + eV_B)}\} + n_- \exp(-\frac{eV_B}{kT_-})\{\frac{1}{kT_-} -$$

$$\frac{1}{2(kT_+ + eV_B)}\} = 0 \quad (4)$$

Here n_e and V_B is the electron density and the Bohm criterion voltage, and T_+ and T_- is the temperature of ions and negative ions, respectively. In this calculation, we assumed $T_+=T_-$. Note that there are theoretically two solutions [11]. The comparison between the experimental results and the theoretical ones indicates qualitative agreement.

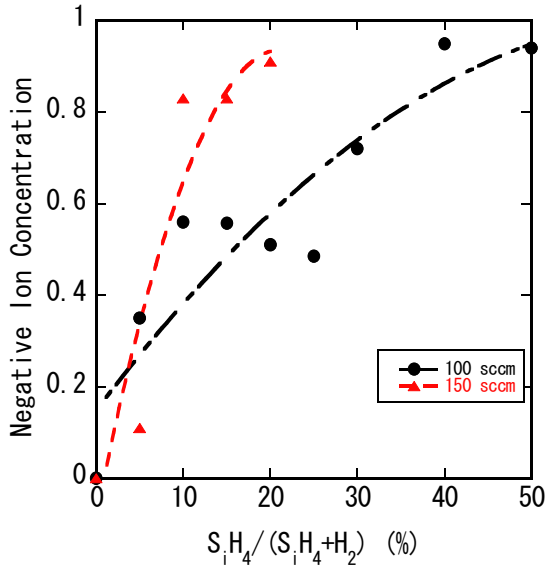


Fig. 2 Negative ion concentration.

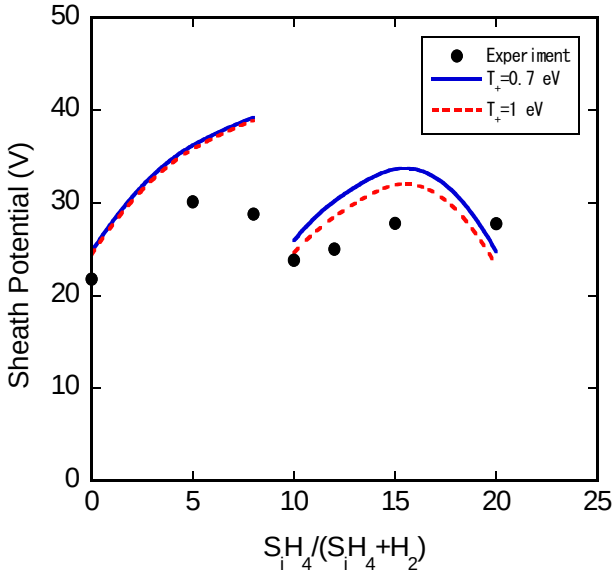


Fig. 3 Sheath potentials.

Fig. 1(b) shows that the ion saturation current decreases when the silane gas is increased. As well known, when there are negative ions, the sheath thickness becomes broad and as a result the ion saturation current decreases [12]. Thus, the observed reduction of the ion saturation current is understood by the change of the sheath thickness.

4. Conclusion

We measured the plasma parameters of S_iH_4/H_2 VHF plasma as a function of silane gas concentration with a heated Langmuir probe and estimated the negative ion density from the reduction of the electron saturation current. It was found that observed sheath potentials agree qualitatively with the theoretical values calculated using the sheath equation derived by Shindo and Horiike [11].

References

[1] A. Shah, J. Meier, A. Buechel, U. Kroll, J. Steinhauser, F. Meillaud, H. Schade and D. Domine: Thin Solid Films, **502**,(2006) 292
[2] M. Kondo, M. Fukawa, L. Guo and A. Matsuda: J. Non-Cryst. Solids, **266-269**, (2000) 84
[3] M. Isomura, M. Kondo and A. Matsuda: Jpn. J. Appl. Phys., **41** (2002) 1947

[4] U. Graf, J. Meier, U. Kroll, J. Bailat, C. Droz, E. Vallat-Sauvain and A. Shah: Thin Solid Films, **427** (2003) 37
[5] A. Matsuda and K. Tanaka: Thin Solid Films**, 92** (1982) 171
[6] M. Shindo, S. Uchino, R. Ichiki, S. Yoshimura and Y. Kawai: Rev. Sci. Instrum., **72** (2001) 2288
[7] W. Lochte-Holtgreven, *Plasma Diagnostics*, Chap.11 (North-Holland, 1968)
[8] Y. Kawai, M. Yoshioka, T. Yamane, Y. Takeuchi and M. Murata: Surf. Coatings Technol., **116-11**9 (1999) 662
[9] T. Nishimiya, Y. Takeuchi, Y. Yamauchi, H. Takatsuka, T. Shioya, H. Muta, Y. Kawai: Thin Solid Films, **516** (2008) 4430
[10] Y. Takeuchi, H. Mashima, M. Murata, S. Uchino and Y. Kawai: Jpn. J. Appl. Phys., **40** (2001), 3405
[11] H. Shindo and Y. Horiike: Jpn. J. Appl. Phys., **30** (1991)161
[12] H. Shindo and Y. Horiike: Jpn. J. Appl. Phys., **32** (1993) 5109

Systematic evaluation of thin electrically insulating layers on common engineering materials

F. Schmaljohann, D. Hagedorn, F. Löffler
Physikalisch-Technische Bundesanstalt, Bundesallee 100, 38116 Braunschweig
frank.schmaljohann@ptb.de

Abstract:

Thin insulating layers are often required for typical engineering materials, e.g. steel, alumina, titanium and the respective alloys. A very dense insulating layer for subsequent conducting layers acting as electrical paths is crucial. Experiments have shown, however, that the electrical insulation of such substrates is often not sufficient or fails completely and is seldom repeatable.
To determine the most important influences regarding the insulation, a systematic evaluation based on a screening design of experiments for the variation of ten parameters is introduced. The films were deposited using a radiofrequency magnetron sputter system and a non-reactive process as well as a SiO_2 target for the deposition of the insulation.
A thin layer of a Cu-Ni-alloy was successively deposited through a mask on top of the insulating layer. The resistance between the substrate material and the conducting layer was investigated to determine the major influencing parameters with respect to the quality of the insulation layer.
Based on the results, further experiments on film thickness variations with less parameters were carried out and Al_2O_3 layers were compared to those utilising SiO_2.

Keywords: thin-film insulation, sputtered insulation layer, steel substrate, titanium substrate

1. Introduction

In today's semiconductor technology thin electrical insulation layers are commonly used and are essential for its functionality. Typical materials for insulating layers are SiO_2 and Al_2O_3 respectively [1]. They have, therefore, been widely investigated when applied to Si-wafers serving as the substrate material.
Nevertheless, there is a variety of applications, where the use of thin insulating layers is needed and typical engineering materials, e.g. steel, alumina, titanium and their alloys, have to be used. Even more as certain materials are given by fixed standards, as this is often the case especially in the field of metrology, the National Metrology Institute's main task.
As an example, sensors comprising thin conducting films are applied directly onto the component to be measured and microstructured by distinct photolithographic steps. Results have proven very promising for precision measurement technology in the future [2, 3]. Besides the possibility of sensor fabrication on a large scale, achieving more precise sensors with a higher spatial resolution and accuracy than conventional sensors is of foremost interest. To achieve a low impact on the measurement, insulating layers as thin as possible are to be found.
However, experiments have shown electrical insulation layers being not sufficient or failing completely when applied to common engineering materials. Therefore, we analysed thin SiO_2 layers thoroughly on titanium alloy Ti6Al4V and 1.3505 steel (100Cr6) substrates, utilising different surface roughnesses.

2. Electrically insulating layers – deposition and quality determination

The insulating layers presented in this paper are being deposited by a magnetron sputtering system (*Von Ardenne – LS320S*) using a non-reactive sputtering process. The system is equipped with two 13.56 MHz generators connected to the target and the substrate which allows the deposition of insulating materials.
Layer thickness is determined by spectroscopic reflectometry *(Micropack NanoCalc-VIS)* which is connected to a microscope for a small spot size and is capable of measuring layers even on rough surfaces. Additionally, the substrate surface and the layer quality were examined using SEM.
The samples used are made of Ti6Al4V and 1.3505 steel (100Cr6) and have a diameter of 30 mm, allowing the sputtering of three samples in one batch. The surface facing towards the target is either turned ($Ra < 0{,}7$ µm) or polished. Polishing was done with a *"Struers LaboPol"*, achieving a surface roughness of $Ra < 15$ nm by using a colloidal silica suspension in the last polishing step.
The most important factor is the determination of the electrical insulation capability of the layer to the substrate itself. Electrical insulation is normally tested by a voltage ramp until a disruptive discharge occurs. This method is not applicable for these layers as, firstly, this would destroy the layer and secondly, the normal operating voltage for the conducting layers on top of the insulating layer (e.g. thin-film sensors) is below 10 V. Hence, the insulating capabilities are tested by measuring the resistance to the substrate.
Experiments have shown that a simple contact of the layer with a conventional measuring tip is not sufficient as small defects in the layer will not be recognised and only a very small spot is inspected. Another possible solution is to contact the layer's surface with a liquid electrolyte. Yet the best and most demanding way to test the insulation is to deposit a conducting layer on top of the insulation and, therefore, have a test scenario similar to the intended use of the layer. If there are pin-holes in the insulation layer, they are most likely to be detected by using this method.
At first, the thin insulating layer of SiO_2 is sputtered, followed by a layer thickness measurement. Next, a 150 nm



Fig. 1: Samples with spot mask for conducting layer

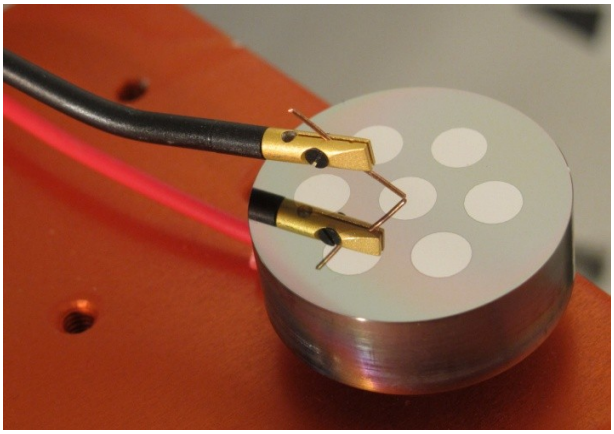


Fig. 2: Probe head contacting one spot

layer of CuNi is sputtered through a mask, to obtain seven spots with a diameter of 5 mm each, evenly distributed over the sample's surface (compare fig.1). The spot size and their positions ensure contrastable results with an even layer thickness distribution (differences below 10 %). For the resistance measurement, one terminal of the multimeter is connected to the uncoated reverse side of the sample, the other one to a probe head with its small tip located on one of the conducting spots. With this setup the contact force is comparable for all measurements (see fig. 2). To evaluate the single resistance value of the spots and to improve comparability, a point rating system was introduced which is shown in tab. 1.

Subsequently, the single values were added which results in the insulating capability of the whole sample, weighted between 0 (best) and 21 (worst).

Resistance value	Rating point
< 1000 Ω	3
< 1 MΩ	2
< 100 MΩ	1
> 100 MΩ	0

Tab. 1: Point rating system

3. Design of experiment

Prior to the start of the investigations the influencing factors on the system consisting of substrate material and preparation, surface, layer material and deposition were analysed. Out of the vast number of factors, the ten most interesting ones were chosen for further investigation.

By variation of only one factor at a time, the standard experiment design, 2^{10} = 1024 test runs are required. Therefore, a proper design needs to be selected. As the determination of the most influencing factor on the insulation is the main goal at first, a screening design of experiment (DoE) was chosen. With this design, one can reduce the amount of experiments to a total of 16: every factor has one low and one high level setting only and multiple factors are changed at the same time [4, 5]. The results need to be interpreted by using statistical evaluation methods afterwards. It has to be remarked that nonlinear processes cannot be appraised by this kind of experimental setup.

Tab. 2 lists the chosen influencing factors with their corresponding low and high level setting and a short description of the same. These are the values used for the screening experiment and, hence, for the results given below. One setting of each factor is the standard value (marked with a star) already used prior to these investigations, the other one is, therefore, the modified value.

Factor	Level low / high		Description
Material	Ti6Al4V	1.3505	Titanium alloy or steel as substrate
Surface	Turned	Polished *	Turned surface Ra < 0,7 µm Polished surface Ra < 15 nm
Preheating	No *	Yes	Heating was done under vacuum at 150 °C
Target distance	40 mm *	60 mm	Distance between sputter target and substrate
Sputter time	2 h	4 h *	Total time of sputter process
Interruptions	0	2 *	Number of interruptions (1 h each) of the sputter process
Sputter power	150 W	200 W *	Supplied power to target
Sputter pressure	8e-3 mbar	10e-3 mbar *	Sputter gas pressure during the sputter process
Oxygen supply	0 sccm *	3 sccm	Inlet of supplementary oxygen
Bias voltage	0 V *	50 V	Bias voltage on substrate

Tab. 2: Influence factors and the corresponding low and high level settings

4. Systematic evaluation – results and discussion

For validation of the DoE and the statistical methods, the influencing factors on the sputtering rate and, thus, on the layer thickness were analysed as these are generally known and, therefore, comparable. The values of the samples' layer thicknesses of the according influence factor level are totalled and averaged:

$$d_{avg,x} = \sum_{i=1}^{16} d_{x,i}$$

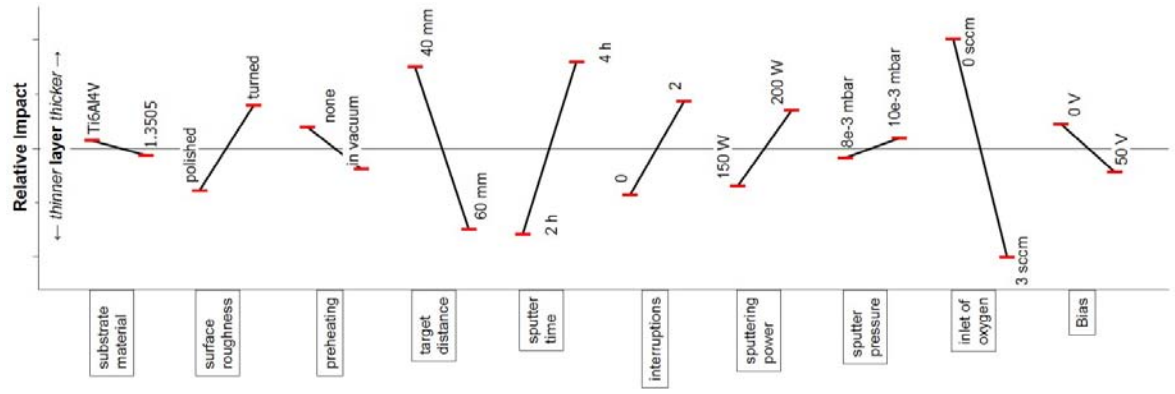


Figure 3: Relative impact of each factor on layer thickness

The highest influence can be determined by the biggest difference between the low and high level setting of each factor, the relative impact, as displayed in the diagram in fig. 3.
Factor number 9 – supplementary oxygen – has the biggest influence, obtaining a thinner layer with oxygen influx. This is followed by the sputter time and the substrate to target distance. All three values are reasonable, not only in magnitude, but also in orientation, and are a validation for the statistical method.
Using the point rating system described above (compare tab. 1), the same calculations were being performed for the insulation values of the samples and drawn into the diagram depicted in fig. 4.
The major influence on the quality of insulation is the substrate material. Insulation of Ti6Al4V substrates was considerably better than those utilising 1.3505. Another significant influence factor is the bias voltage, with an improved insulation if turned off.
The very small difference in insulation with respect to surface roughness modification, however, is misleading. Ti6Al4V samples with a polished surface have considerably better insulation values than their turned counterparts, whereas the turned samples of 1.3505 are better than the polished ones. Therefore, the results relating to the different surface roughnesses interfere with each other, which cannot be resolved by the screening experiment.
For the identification of the main influence on the layer thickness and on the quality of insulation, the chosen design of experiment has proved to be suitable. The insulating layer is influenced considerably by the substrate material and its pre-treatment (i.e. surface roughness) and less by variation of the sputter parameter. Nevertheless, the results reveal that further investigations are necessary with respect to surface roughness and layer thickness. If there is a direct dependency, thicker layers should have a better insulation capability, especially on rough surfaces and also in the case of steel substrates. However, for the application in sensor systems, thick layers have a negative impact on the accuracy of measurement.

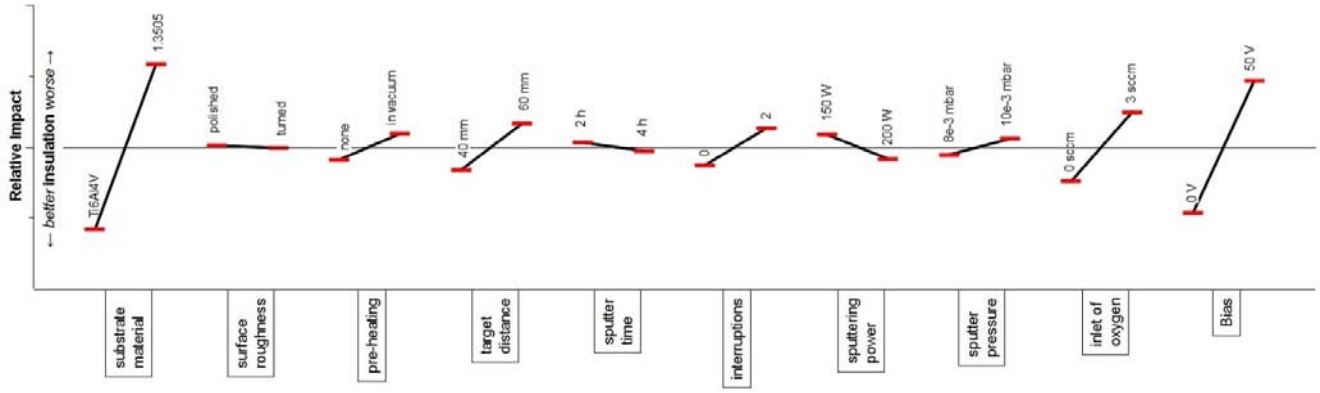


Figure 4: Relative impact of each factor on electrical insulation

5. Follow-up investigations

For the following investigations, the sputter parameters were initially changed to achieve a higher sputtering rate. The standard settings as shown in tab. 2 were altered to a sputtering power of 300 W, a pressure of 8e-3 mbar, no oxygen and 0 V bias voltage. As a result, the rate increased from 1,5 µm/h to 2,2 µm/h, whilst the quality of insulation did not change.
For the investigation of different surface roughnesses and layer thicknesses and their influence on the insulation, a variation of the sputtering time and, therefore, the layer thickness was carried out. Every batch consists of three samples: Ti6Al4V (polished), 1.3505 (turned and polished). As shown in fig. 5 (left) the layer thickness was varied between 600 nm and 3500 nm in six steps.
The samples made of Ti6Al4V show good insulation values throughout the experiment and, thus, a layer thickness of about 600 nm has found to be sufficient. For the 1.3505 samples with a turned surface the insulating capability is not sufficient at first but reaches the level of the titanium alloy at about 2000 nm thickness. The polished samples

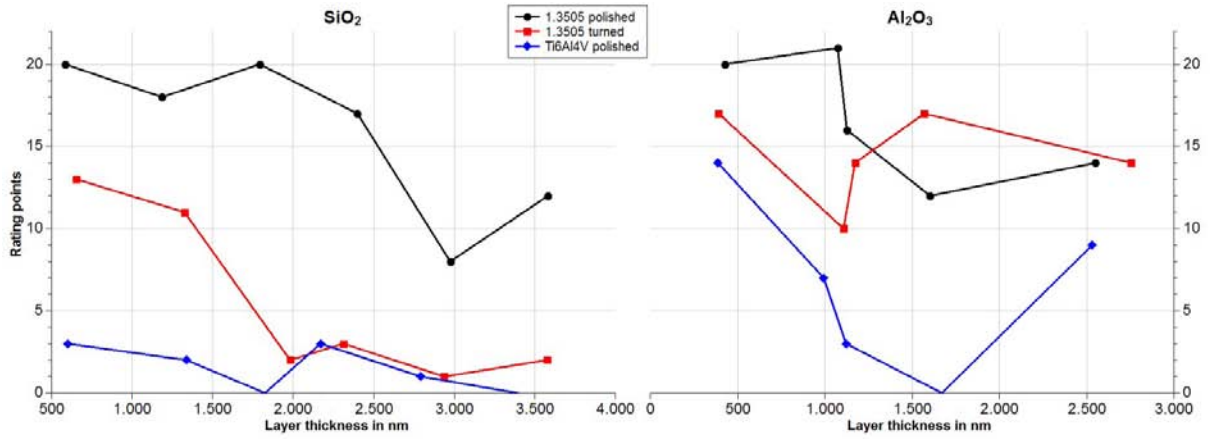


Figure 5: Insulation rating against layer thickness of SiO_2 (left) and Al_2O_3 (right)

have bad results for thin layers, but improve with layers thicker than 2000 nm. Still, these samples only reach a fair level of insulation.

Electrical insulation utilising thin SiO_2 layers is, as a rule, better for Ti6Al4V than for 1.3505 steel. As shown, the surface does have a major influence on the insulation, too, but cannot be described by surface roughness alone. Instead, we have found it to be caused by the composition of surface structure of the material itself.

For the evaluation of the comparability to other insulating materials, a contrastable experiment using an Al_2O_3 target instead of SiO_2 was carried out. Besides a higher sputtering power of 400 W, other parameters remained the same. We were able to achieve a sputtering rate of up to 1,6 µm/h. The layer thickness was varied in five steps from 400 nm to 2700 nm. The results of the insulation rating plotted against the layer thickness are shown in figure 5 (right).

Similar to the results with SiO_2 thin-films, it seems that there is a dependency between the layer thickness and the insulating capability, recognisable for the polished Ti6Al4V sample. However, this is not clearly visible for the 1.3505 samples, sticking to a poor level of insulation, regardless of layer thickness and surface roughness in the investigation range. Further experiments are necessary to ensure the results with Al_2O_3 and for the evaluation of thicker layers.

6. Conclusions and Outlook

Prior investigations revealed that the electrical insulation of common engineering materials by thin-films was scarcely reproducible. Therefore, thorough research on sputtered insulation layers, especially on SiO_2 was carried out and presented.

From influencing factors on the substrate-layer system, ten of the most important ones were selected. A screening design of experiment was introduced to reduce test runs and for the identification of the main influence factors by means of systematic evaluation.

These experiments showed that the major influence on the quality of insulation is given by the substrate material and its surface roughness. Thus, further investigations were carried out in terms of layer thickness variation on different substrates with turned and polished surfaces. The results strengthen the outcome of the screening experiment and point to a dependency between insulation quality and film thickness. Furthermore, the insulation does not depend on the surface roughness alone, but also on the surface structure itself.

Finally, the first experiments utilising Al_2O_3 as an insulation layer are presented and compared. Further investigations are needed in terms of insulating capability and to evaluate the applicability and possible advantages or disadvantages of Al_2O_3 against SiO_2.

Layers, thicker than about 3 µm could be investigated for their insulation capabilities in the future. Nevertheless, for the intended use of the layer system, e.g. for high precision sensors, thinner layers are preferred as they potentially have less influence on the measurand and better adhesion.

The use of other sputtering techniques, as in pulsed sputtering systems, with potentially denser thin-films is projected.

[1] Frühauf, J.: *Werkstoffe der Mikrotechnik*. Hanser Verlag 2005

[2] Schmaljohann, F.; Hagedorn, D.; Buß, A.; Kumme, R.; Löffler, F.: *Thin-film sensors with small structure size on flat and curved surfaces*, 2012 Meas. Sci. Technol. 23 074019 doi:10.1088/0957-0233/23/7/074019

[3] Schmaljohann, F.; Hagedorn, D.; Buß, A.; Kumme, R.; Löffler, F.: *Entwicklung von Dünnschichtsensoren mit kleiner Strukturbreite auf dünnen isolierenden Schichten*. MikroSystemTechnik - Kongress 2011, Darmstadt, pg. 764-767

[4] NIST/SEMATECH *e-Handbook of Statistical Methods*, http://www.itl.nist.gov/div898/handbook/, 2011

[5] Siebertz, K.; Van Bebber, D.; Hochkirchen, T.: *Statistische Versuchslpanung – Design of Experiments (DoE)*. Springer-Verlag 2010

Ultra-shallow fluorine implantation from r.f. plasma as a method for improvement of electro-physical properties of MIS structures with PECVD gate dielectric layers

M. Kalisz[1,2]; R. Mroczyński[1]
[1] Institute Microelectronics and Optoelectronics Warsaw University of Technology, Koszykowa 75, Str. Warsaw
[2] Motor Transport Institute, Jagiellońska 80, Str.,Warsaw

Introduction

In this work a comprehensive analysis of changes in electrical and reliability parameters, which are introduced by the presence of a fluorine-rich layer in the gate structure based on MOS ($Al/SiO_2/Si$) and MIS ($Al/SiO_xN_y/Si$) system, has been carried out. The surface of silicon substrates prior to the test structure execution was subjected to the processes of ultra-shallow ion implantation from CF_4 plasma, different, than those usually found in the literature. To this end, the conventional plasma reactors were utilized to carry out a plasma enhanced chemical vapour deposition process PECVD and reactive ion etching RIE. To perform gate dielectric layers the PECVD method was used. The conducted analysis of the electrical properties was complemented by spectroscopic measurements (SIMS), which allowed the identification of causes and effects of observed changes in electro-physical parameters.

Experiment

To perform the test structures the NMOS technology with a non-self-aligned metal gate was selected. For the experiment the silicon plates type p were prepared with a crystal orientation <100> and resistivity of 4-10 Ωcm. The substrates cleaned using the RCA method were subject to the processes of manufacturing the passivating dielectric, which protects the silicon surface during the process of ultra-shallow implantation from the RF plasma. In the case of the structures with the gate dielectric in the form of silicon oxide (SiO_2), passivation was performed by high-temperature silicon oxidation process. The resulting thermal oxide thickness was about 15 nm. In the case of the structures with the gate dielectric in the form of silicon oxynitride (SiO_xN_y), the passivating oxide was prepared in PECVD process. The thickness of deposited oxide was about 7 nm. Then, the fluorine ion implantation process was carried out in CF_4 plasma through the passivating oxide. To carry out the process of implantation of fluorine the plasma reactors type PlasmaLab 80 + system manufactured by Oxford Instruments were utilized. To this end, both the reactor for carrying out dry etching process (RIE) and the reactor for plasma enhanced chemical vapour deposition process – PECVD were used.

Table 1 Technological parameters of processes performed in the course of this work.

	Parameters of ultra-shallow fluorine implantation				Layer deposition						Ann.
	CF_4 flow	Pressure	RIE power	PECVD power	Temp.	Pressure	Power	Gas flow			Temp.
								SiH_4	N_2O	NH_3	
	[ml/min]	[mTorr]	[W]		[°C]	[mTorr]	[W]	[ml/min]			[°C]
SiO_2	50	200	160		350	600	10	70	120	-	1100
SiO_xN_y			80			500		150	24	32	

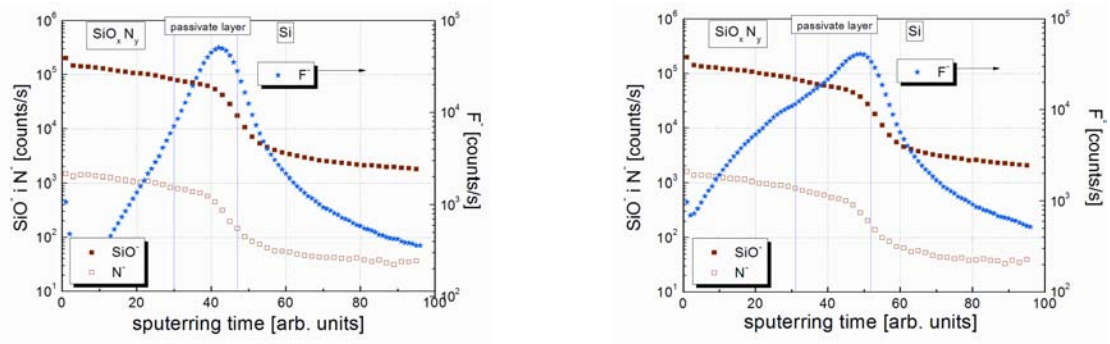
In the next technological step the layers of gate dielectrics, SiO_2 (13 nm) and SiO_xN_y (7 nm), were deposited by PECVD method on the passivating layer generated on the surface in the result of the ultra-shallow implantation process. In addition, the structures with gate dielectrics were made, which were subjected to high-temperature annealing process in a standard quartz furnace under Ar atmosphere at

1100 °C for 30 min. This experiment allowed to check the thermal stability of fluorine in the gate dielectric/passivating layer/silicon structure. Additionally, the reference structures without modifying the silicon substrate in a CF_4 plasma were prepared. All parameters of the performed technological processes are specified in Table 1.

Ellipsometry measurements were carried out immediately after technological processes. The thicknesses of the layers obtained were measured using a single-wavelength ellipsometer (λ = 632.8 nm). The analysis of spectroscopic measurements SIMS (Secondary Ion Mass Spectroscopy) was also carried out, which allowed to determine the chemical composition and the profiles of distribution of fluorine atoms in the resulting structures.

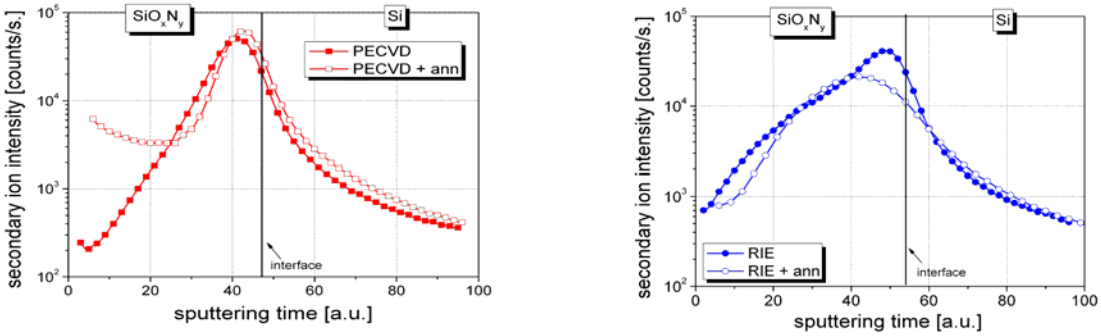
The results obtained from spectroscopic measurements (SIMS)

Application of plasma deposition technology PECVD to form the gate dielectric layer (SiO_2 or SiO_xN_y) on the passivating layer generated by ultra-shallow implantation from CF_4 plasma, leads to the formation of the system of following layers: gate dielectric layer/passivating layer/silicon [12].



a) b)

Fig. 1 Comparison of SiO^-, N^- and F^- profiles within the silicon oxynitride layers after modification of silicon substrate in PECVD (a) and RIE (b) reactor.



a) b)

Fig. 2 Thermal stability of fluorine concentration within the SiO_xN_y layers after modification of silicon substrate in PECVD (a) and RIE (b) reactor.

Figure 1 shows the comparison of profiles of fluorine, nitrogen and oxide phase in the layer of silicon oxynitride after modification of the silicon substrate surface in PECVD (Figure 1a) and RIE (Figure 1b) reactors. Analysis of the profiles indicates that, regardless of the type of reactor, in which the process of ultra-shallow implantation of fluorine ions from RF plasma was carried out, the maximum concentration of fluorine differs insignificantly. It is worth mentioning that the construction of both plasma reactors is essentially different. The main difference is the different geometry of the electrodes, which has a significant impact on the energy and density of ions in the RF plasma. The maximums of the concentration of fluorine in case of silicon oxynitride, are located very close to the semiconductor / passivating layer (rich in fluorine) interface. Only in the case of silicon surface modification in the RIE

reactor, you may notice the increased concentration of fluoride in the volume of the gate dielectric layer, in relation to the concentration of fluoride in the layer modified in the PECVD reactor. Figure 2 shows the comparison of the profiles of fluorine atoms before and after the high temperature annealing of dielectric layers. As is apparent from the profiles presented in Figure 2, in contrast to the results described in other papers connected with implantation of fluorine [eg 13]the fluorine from the passivating layer, covered with a layer of plasma-deposited SiO_xN_y is thermally stable. Fluorine atoms under the influence of the structure annealing at 1100 °C are not removed from it. What's more, it seems that the dose of fluorine deposited at the interface after annealing is very similar to the dose before annealing. There are very small changes: under the influence of high temperature of the process the fluorine concentration value at the maximum of its distribution, in the case of modification at the PECVD reactor slightly increases, and for modifications in the RIE reactor - slightly diminishes (see Figure 2a and 2b). In the case of the plasma silicon oxide layer, the obtained results are very similar to those obtained for SiO_xN_y layers. This is confirmed by fluorine profiles shown in Figure 3. It may be noted that the high temperature (1100 °C) annealing of silicon oxide layer does not affect significantly the value of the maximum concentration of fluoride.

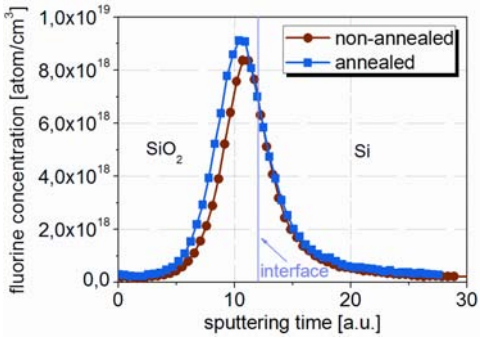
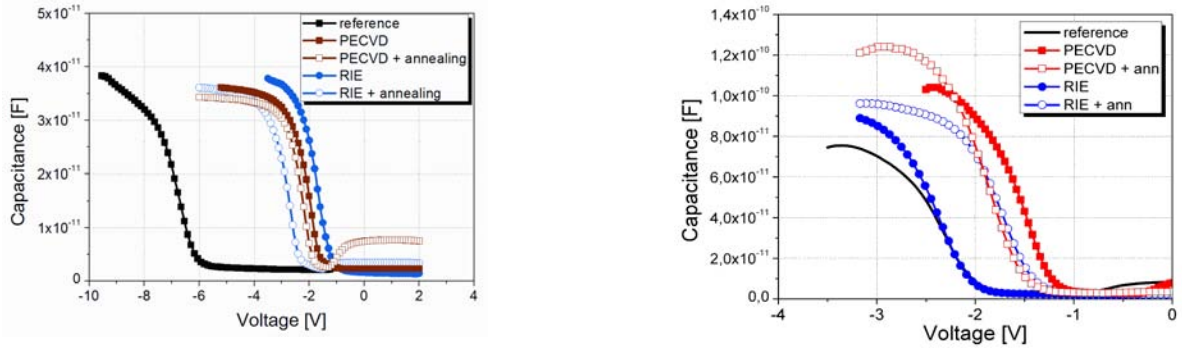


Fig. 3 Thermal stability of fluorine concentration within the SiO2 layer after modification of silicon substrate.

The analysis of electrical characteristics of MOS (MIS) test structures with gate dielectrics produced by PECVD method.

Figures 4a-b show the comparison of the C-V characteristics (1 MHz) obtained for the MOS capacitors (Fig. 4a) with the gate dielectric in the form of silicon oxide, and MIS (Fig. 4b) with the gate dielectric in the form of silicon oxynitride (SiO_xN_y), after the silicon surface modification processes in reactors for PECVD and RIE. For comparison, the drawings show also the characteristics of MOS and MIS reference structures.



a) b)

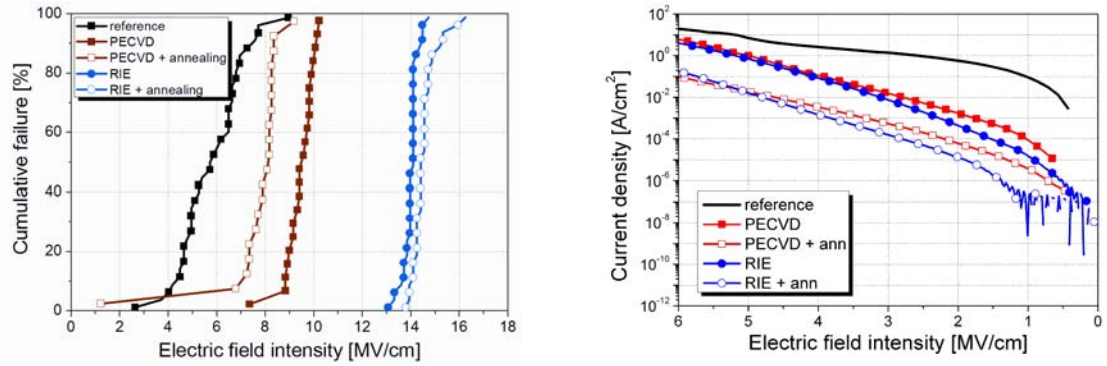
Fig. 4a Comparison of C-V characteristics of a) MOS structures; b) MIS structures, fabricated on modified silicon substrates; C-V characteristics of reference structure was also shown.

The analysis of the capacitance-voltage (C-V) characteristics of the prepared MOS (MIS) test structures has shown that the systems: semiconductor/passivating layer/gate dielectric produced on the modified silicon substrates, are characterized by smaller values (in absolute value) of flat-band voltages (U_{FB}) and effective load (Qeff) compared to the reference structures. However, the density of surface states in the middle of the silicon forbidden energy band (D_{itmb}) does not change significantly (see Table 2). The introduction of fluorine in the interface area of MOS (MIS) structures also results in the slight reduction of the electric permittivity of dielectric layers produced by PECVD, which can be utilized in the technology of intermetallic layers of integrated circuits.

Table 2 Basic electro-physical properties of PECVD silicon dioxide and PECVD SiO_xN_y (in the brackets) layers.

	reference	PECVD	PECVD + ann.	RIE	RIE + ann.
thickness [Å]	130 (70)	122 (46)	108 (42)	156 (61)	130 (54)
electric permittivity	3,8 (4,3)	3,3 (3,9)	2,8 (4,2)	4,6 (4,5)	3,5 (4,1)
D_{itmb} [$ev^{-1}cm^2$]	3,2 x 10^{12} (6,3 x 10^{12})	3,2 x 10^{12} (8,7 x 10^{12})	3 x 10^{12} (9 x 10^{12})	5 x 10^{12} (6,7 x 10^{12})	4,6 x 10^{12} (7 x 10^{12})
Q_{eff}/q [cm^{-2}]	7,9 x 10^{12} (4,2 x 10^{12})	1,8 x 10^{12} (3,4 x 10^{12})	1,5 x 10^{12} (3 x 10^{12})	8,6 x 10^{12} (4,1 x 10^{12})	2,6 x 10^{12} (2,6 x 10^{12})

The analysis of current-voltage characteristics (I-V) (see Figure 5a and 5b) of MOS and MIS test structures showed that the structures produced on the substrates, which have been subjected to the processes of fluorine implantation from CF_4 plasma, are characterized by dramatically increasing uniformity of breakdown voltage.



a) *b)*

Fig. 5 Cumulative failure of a) MOS structures; b) MIS structures, investigated in the course of this work

Results

Based on the technological experiments and spectroscopic measurements (SIMS) carried out in this work it was stated clearly that the processes of ultra-shallow implantation of fluorine ions from CF_4 plasma, performed in the classical plasma reactors (PECVD and RIE), are ideal for surface modification of silicon substrates by introducing a high concentration of fluoride into their subsurface area.

The results of this study show that the developed technology of ion implantation of fluorine in CF_4 plasma can be safely used in self-aligned CMOS technology, as well as in technology with extremely low thermal budget, such as on strained substrates (SiGe).

Bibliografia

[1] M. Kalisz et al., Vacuum 2008, 82: 1040-1045; [2] Endo K, T. Tatsumi, J Appl Phys 1995, 78:1370; [3] M. Kalisz et al., J Telecomm Inf Technol 2007, 2-3: 5-9

Laminated composite on the basis of plasma modified PTFE films and thin aluminum layers

M. Yablokov, A. Gilman, A. Kechek'yan, A. Kuznetsov

Enikolopov Institute of Synthetic Polymer Materials Russian Academy of Sciences,

Moscow, Russia 117393 ul. Profsoyuznaya 70 +7(495) 332 5865,

+7(495) 7183404

E-mail: plasma@ispm.ru

The treatment in low-temperature plasma is an effective method of the improvement of adhesive strength of the polymer/metal interface. It is well known what PTFE has unique chemical and physical properties: it neither swells nor dissolves in common solvents; is resistant toward oxidants, acids, and alkalis and exhibits good dielectric properties over wide temperature and frequency ranges. However, some applications concerning the use of PTFE as an engineering material demand the improvement of the contact properties. This task is highly important in practice. Earlier we showed that the modification of the PTFE films under conditions that ensure the separation of the discharge active species acting on the polymer materials make it possible to achieve substantially lover values for the contact angle and higher values for the surface energy than the case of other modes of discharge [1]. For example, θ value of water was 33° or 49° after modification at the anode or cathode, respectively, and the total surface energy increases from 13.18 to 61.5 or 50.7 mJ/m^2, respectively. These findings open the possibility for resolving the applied problem of manufacturing multilayer composite materials, including nanosized metal layers and thin PTFE films, which is important for electrical engineering and electronics.

PTFE films of 50 μm thickness (RF State Standard 24222-80) were used. The procedure for film modification in dc discharge is detailed in [2]. Film samples of 40 x 120 mm dimensions were mounted on the anode and treated on both sides in the alternating mode. The processing was run in the flow mode at a working gas

(air) pressure of ~ 20 Pa and a discharge current of 50 mA for 60 s. TO prepare a multilayer composite material, aluminum layers (of 100 nm thickness) were deposited by vacuum evaporation onto both sides of plasma-modified PTFE film in a VUP-4 device according to the scheme depicted in the figure. The thickness of the coating was controlled by varying the deposition time, and a calibration curve for determination of the Al layer thickness was obtained by the goniometric technique using a MII-4 microinterferometer.

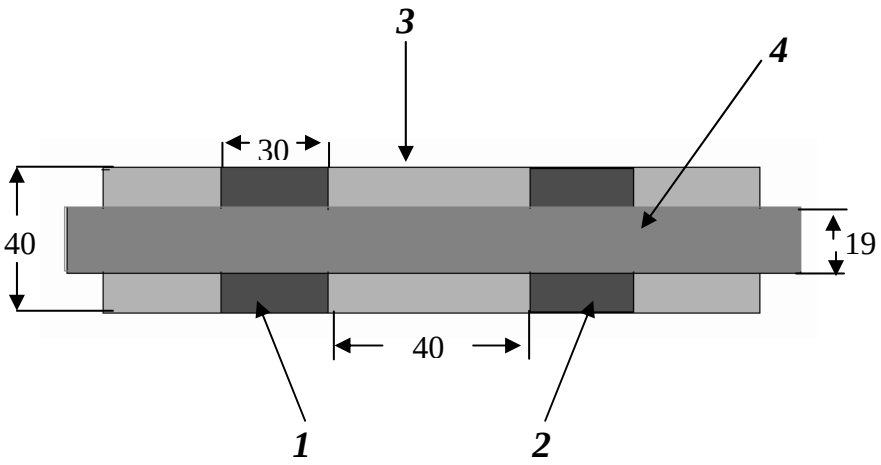


Figure. Schematic of the specimen for the measurement of adhesion (top view): (*1*, *2*) Al layers deposited by vacuum evaporation, (*3*) PTFE film modified at the anode in dc discharge, and (*4*) Scotch®810 tape.

To appreciate the adhesion characteristics of the laminated composite material, we developed a peel resistance (***A***) measurement procedure, the T-peel test with the use of a Scotch® 810 adhesive tape (ASTM D3359-02) [3]. The T-peel testing of the obtained composite samples was performed on a Shimadzu Autograph AGS-10 KNG universal testing machine at a crosshead speed of 100 mm/min. As a result of the experiments, a curve reflecting a change in the peel resistance (***A***) along the sample length was obtained. Peeling was performed successively on one (layer 1/PTFE) and the other (PTFE/layer 2) side of the composite material. The experimental data were averaged over 3 sets of 5 specimens each; the results are given in the table.

Peel resistance (***A***) for specimens of the 100-nm Al (layer 1)/PTFE/100-nm Al (layer 2) multilayer composite material

Set	Joint measured	***A***, N/m		
		(1)-(4)*	(2)-(4)*	(3)-(4)*
I	Layer 1/PTFE	312±8	304±6	188±6
	PTFE/Layer 2	390±9	384±9	243±5
II	Layer 1/PTFE	315±5	321±8	190±5
	PTFE/Layer 2	380±6	370±11	208±5
III	Layer 1/PTFE	294±11	306±5	198±8
	PTFE/Layer 2	363±7	368±8	271±9

* The numbers refer to the joints as shown in the figure.

It was established that the ***A*** value for the first peel (layer 1/PTFE) is smaller than that for the second one (PTFE/layer 2), and the values of ***A*** averaged over all runs of the 3 sets are 308±12 and 377±13 N/m, respectively.

However, according to the concept of adhesive-layer failure mechanism [4], the peel resistance must be identical in the first and second cases despite the fact that the Scotch® 810 tape (55 μm thickness) is peeled off the PTFE/ Scotch® 810 composite (105 μm thickness) in the former case and from the PTFE films (50 μm thickness) in the latter case. The reason for the real resistance to be identical in both cases is that the thickness of the adhesive layer is the same. The results obtained in this study can be explained in terms of formation of charged states under the peeling of composite material [4]. Therefore the charge generation during the first peeling leads to the polarization of PTFE/layer 2 contact and to the increase of ***A*** value during the second peeling of layer 2 from PTFE film.

Thereby the DC discharge modification of PTFE film surface make it possible to obtain laminated composites on the basis of plasma modified PTFE films and thin aluminum layers with high interlaminar adhesion.

References

[1] A. Gil’man, M. Piskarev, N. Shmakova, M. Yablokov, A. Kuznetsov // Materials Science Forum. 2010. vol. 636-637. pp 1019-1023.

[2] M. Piskarev, A. Gilman, N. Shmakova, A. Kuznetsov // High Energy Chemistry. 2008. vol. 42. pp. 137-140.

[3] M. Yablokov, A. Kechek’yan, A. Bazhenov, A. Gil’man, M. Piskarev, A. Kuznetsov // High Energy Chemistry. 2009. vol. 43. pp. 512-515.

[4] M. Yablokov, A. Kechek’yan, A. Gil’man, A. Ozerin // Nanotechnika. 2011. no. 2. pp. 83-86.

THE FORMATION OF SUPERHARD COATINGS ≥ 48 GPa IN TI-HF-N (Fe) AND ANALYSIS OF THEIR STRUCTURE AND PROPERTIES.

A. D. Pogrebnjak[1], A. G. Ponomarev[2], M. V. Kaverin[1], D. A. Kolesnikov[3], V. M. Beresnev[4], F.F. Komarov[5], S. S. Mel'nik[5].

[1]Sumy State University, 2, Rymsky Korsakov Str., 40007 Sumy, Ukraine, alexp@i.ua
[2] Institute of Applied Physics, NAS of Ukraine, 58, Petropavlivska Str., 40030 Sumy, Ukraine
[3]Belgorod State University, 85, Pobeda Str., 308015 Belgorod, Russia
[4]Kharkiv National University, 21, Frunze Str.,61002 Kharkiv, Ukraine
[5]Belarusian State University,4, Nezavisimosti Ave., 220030 Minsk, Republic of Belarus

Abstract

Superhard nanostructured Ti–Hf–N(Fe) coatings are prepared. The formation of local regions of (Ti, Hf)N, FeN, and Hf is detected using μ-PIXE (ion microbeam). It is revealed that the synthesized coatings have a nanohardness of 48 ± 1 GPa and are composed of nanograins with a size of 4.8–10.6 nm, which are enveloped by finer entities of other phases (Ti, Fe)N and FeN. There is a good correlation between the results derived by XRD, TEM, AFM, and SEM and microanalysis, which in turn are complemented by the analysis results obtained using an ion microbeam and PIXE.

Keywords: Superhard, nanostructured, Ti–Hf–N(Fe), μ-PIXE, ion microbeam, nanohardness.

I Introduction

It is known that the unique properties of nanostructured nanocomposite coatings are a high volume fraction of the interfaces and their strength, the absence of dislocations inside the crystallites, the possibility of changing the ratio of fractions of the crystalline and amorphous phases, and the mutual solubility of the metallic and nonmetallic components [1–3]. The strength of the interface contributes to an increase in the strain resistance of nanostructured coatings, and the absence of dislocations inside the crystallites increases the elasticity of the coatings. Therefore, it is a high priority problem of materials science and solid state physics to study the physical causes of the high physicomechanical properties of nanostructured materials (coatings). Ti–Hf–N(Fe) films with a thickness of 1.5 μm were deposited on steel samples with a diameter of 20 and 30 mm and a thickness of up to 3 mm in a vacuum chamber using a vacuum arc source in a high-frequency (HF) discharge and employing a Ti–Hf(Fe) cathode (sintered by an electron gun in an Ar atmosphere). The deposition parameters are listed in the table 1.

Experiment and discussion

To analyze the properties of the Ti–Hf–N(Fe) coatings, we used a scanning nuclear microprobe based on an electrostatic accelerator designed at the Institute of Applied Physics, National Academy of

Sciences of Ukraine [3]. Analysis was performed using Rutherford backscattering (RBS) and proton induced characteristic X-ray emission (PIXE and μ-PIXE) at an initial energy of *Ep* = 1.5 MeV, a beam size of 2-4 μm, and a current of $\approx 10^{-5}$ A [5]. The total PIXE spectrum was analyzed using the GUPIXWIN software, which provided information on the quantitative content of elements and stoichiometry. To compare the elemental composition and to analyze the morphology, we used a Quanta 200 scanning electron–ion microscope with an EDS detector. A Bulat-3T vacuum arc source with an HF generator was used [5]. A bias potential was applied to the substrate from the HF generator, which generated decaying oscillation pulses at a frequency of ≤1 MHz, Ti–Hf–N(Fe) coating deposition parameters; crystallite sizes and hardness for different sets of samples. A pulse duration of 60 μs, and a repetition frequency of 10 kHz.

Table 1 – Deposition parameters and coatings characteristics of Ti–Hf–N(Fe).

No.	P, nitrogen pressure in the chamber, Pa	Substrate potential, V	Nanohardness, GPa	Average crystallite size, nm
7(direct) 11(separated)	0,3 0,5	-200 -200	41.82 47.17	6.4 4.8

The negative substrate auto-bias voltage, owing to the HF diode effect, was 2–3 kV. In addition, we used an RBS scheme with 1.3-MeV He^+ ions, a registration angle of θ = 170°, and a detector resolution of 16 keV. The dose of helium ions was ≈5 μs [5]. XRD analysis of the nanostructured films was carried out using two diffractometers: DRON-4 and X'Pert PANlytical (Holland) with a step size of 0.05° at a tube voltage of *U* = 40 V and a current intensity of *I* = 40 mA; the emitter was copper Cu*Kα*. The analysis of morhology, structure, and elemental composition on the cross sections of the coatings was performed using a Quanta 200 3D scanning electron–ion microscope. The mechanical properties i.e., hardness, nanohardness, and elastic modulus were studied using two Nanoindentor G 200 instruments (MES System, United States) employing Berkovich and Vickers pyramids; in addition, we employed a Rockwell C indenter with a radius of curvature of about 200 μm. Figure 1 shows the distribution maps for the elements in the coating, which were obtained using an ion microbeam, depending on color (dark regions with a low concentration, lighter regions with a high concentration of elements).

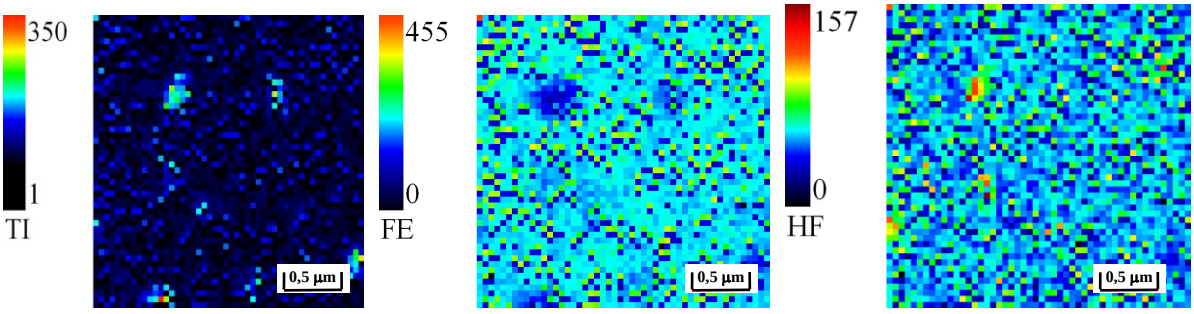


Fig. 1. Element (Ti; Hf; Fe) distribution maps derived for the steel samples with a deposited Ti–Hf–N(Fe) coating. In particular, there are local regions with sizes of from 2–4 to 6–10 μm that consist of Hf and Ti inclusions, in which the concentration of Fe greatly decreases.

The PIXE-derived quantitative analysis and its stoichiometry are represented in Fig. 2. The results (the concentration integrated over depth is about 2 μm) show that a thin AlC film is formed on the surface, which is probably the result of exposure to a proton beam, and the main concentration of the elements is as follows, at %: Fe ≈ 77, Ti ≈ 11, Hf ≈ 11.05, Mn ≈ 0.9, and Cr =0.01; the last-mentioned elements apparently are part of the substrate.

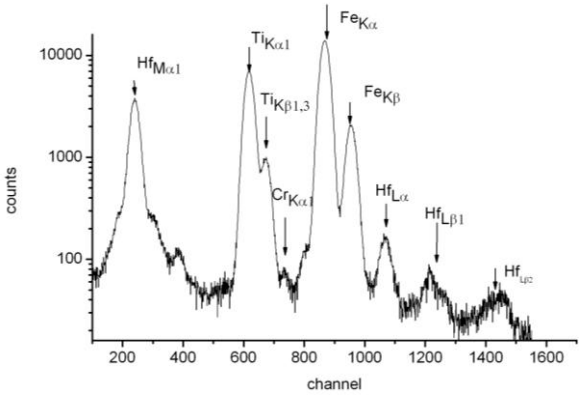
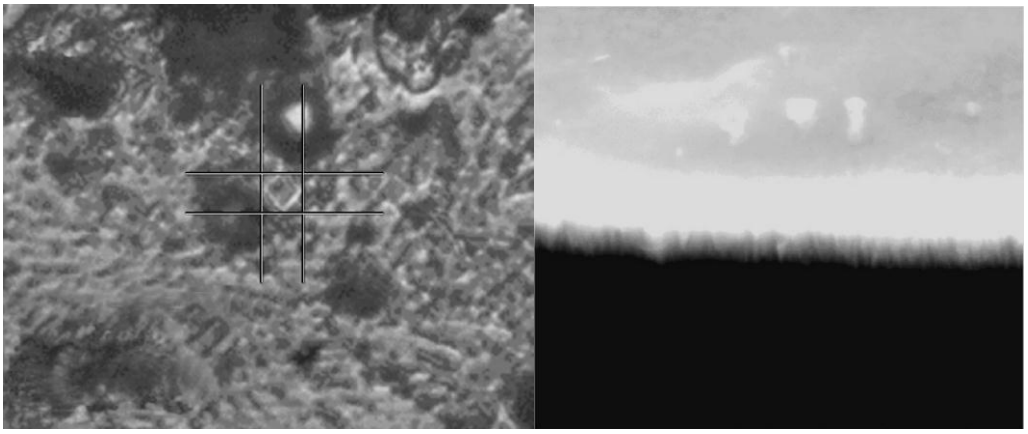


Fig.2 Total PIXE spectrum (in a logarithmic scale) derived from the sample with an Hf–Ti–N–Fe coating in the analysis using a 1.5-MeV proton beam (the spectrum was recorded using a silicon detector).

Figure 3b depicts an image of a region of the surface area of the coating with the imprint of the indenter, which is equivalent to the nanohardness of 48 ±1 GPa; this nanohardness value is very high about 50 GPa and, according to the modern classification scheme, corresponds to a superhard coating [6, 7]. At the same time, the nanohardness of the coating measured using a Vickers pyramid is 36.4 GPa, because a softer steel substrate is located under the coating (Fig. 3b). The XRD analysis results obtained for the samples with this coating type show that the coatings are composed of at least two phases (Ti, Hf)N, (Ti, Hf)N, or FeN and the nanograin sizes determined from the diffraction peak widths by the Debye–Scherrer technique are 4.8–10.6 nm. In addition, by changing the coating deposition parameters, we can specify the stoichiometry (composition) of the film; that is, by changing the substrate potential of 0–100, and –150 to –200 V, at the same pressure of nitrogen (or an Ar/N mixture), we can change the coating structure from columnar (Fig. 3a) at low pressures to nanograin at a high potential. Three dimensional islands on the surface of the films with a columnar structure emerge on the surface of the faces of individual grains (Fig. 3a). Surface undulation is attributed to the growth mechanism and the formation of individual islands on the surface (Volmer–Weber mechanism). In addition, measurement of the XRD spectra in the coating in the θ–2θ geometry and the $\sin_2\varphi$ method revealed compression microstresses, which are formed in nanograins and correspond to a

compression value of ≈2.6%. The compression stresses that occur in the film growth plane, which were measured according to the position of the diffraction line peaks by the $\sin_2\varphi$ method, were ≈2.78%.



a) b)

Fig. 3. (a) Cross section of the Hf–Ti–N–Fe coating with a columnar structure; (b) imprint of a four-sided Vickers pyramid on the Ti–Hf–Fe–N coating with a nanohardness of H_V = 36.4 GPa.

The represented distributions of elements over the coating surface and to a depth of 2 μm show that, in fact, the segregation process has not been completed; therefore, the derived hardness values of ≈50 GPa can be increased (by 15–25%) owing to rapid diffusion and the completion of the spinodal segregation process [4, 5]. That is, we can state that the "self-hardening" effect in superhard coatings can lead to an increase in nanohardness up to 60–65 GPa. The μ-PIXE results imply that, apparently, it will be possible to control the self-hardening process or the grain-boundary diffusion acceleration and, thereby, to in situ control the spinodal segregation and the distribution of elements.

Acknowledgments.

Authors thank O.V. Sobol' (Kharkiv Technical University) for help in interpreting the XRD analysis results. This work was supported by the State Foundation for Basic Research of Ukraine (project F-41/20-2011) and the Belarusian Republic Foundation for Basic Research (project T11K-058).

REFERENCES

1. A. D. Pogrebnyak, A. P. Shpak, V. M. Beresnev, and N. A. Azarenkov, Usp. Fiz. Nauk **179** (1), 35 (2009).

2. R. A. Andrievskii and A. M. Glezer, Usp. Fiz. Nauk **179** (4), 337 (2009).

3. O. G. Ponomarev, Doctoral Dissertation in Mathematical Physics (Kharkiv, 2011).

4. R. F. Zhang, A. S. Argon, and S. Veprek, Phys. Rev. **79**, 245 426 (2009).

5. A. D. Pogrebnyak, A. G. Ponomarev, A. P. Shpak, and Yu. A. Kunitskii, Usp. Fiz. Nauk **182** (3), 287 (2012).

6. R. F. Zhang, S. H. Shing, and S. Veprek, Appl. Phys. Lett. **91**, 031 906 (2007).

7. A. D. Pogrebnyak, A. P. Shpak, V. M. Beresnev, et al., Tech. Phys. Lett. **37** (7), 636 (2011).

Electrochemical and mechanical properties of low friction nc-CrC/a-C:H and nc-WC/a-C:H coatings on construction materials deposited by magnetron sputtering.

Marcin Grobelny[1*], Dariusz Rudnik[1], Marcin Makówka[2], Katarzyna Włodarczyk-Kowalska[2], Piotr Nolbrzak[2], Wojciech Pawlak [2]

1) Motor Transport Institute, Centre for Material Testing and Mechatronics, Jagiellońska 80, 03-301 Warsaw, Poland
2) Lodz University of Technology, Institute of Materials Science and Engineering Stefanowskiego 1/15, 90-924 Lodz, Poland
**marcin.grobelny@its.waw.pl*

The increased focus on the natural environment protection, the increasing fuel prices and the will to reduce the costs of machines' maintenance - all that obliges us to search for innovative engineering solutions that would both limit the use of conventional lubricants and enhance the machines' efficiency. To fulfil this challenging goal, the parts of machines are coated with special low friction and high wear resistant materials more and more often. The PVD methods play a great role in this field. As the examples of coatings deposited by a PVD method and assuring the above mentioned goals may serve the nc-CrC/a-C:H and nc-WC/a-C:H.

This research focuses on the electrochemical and mechanical studies of low friction nc-CrC/a-C:H and nc-WC/a-C:H coatings deposited by magnetron sputtering on two kind of construction materials: Vanadis 23 steel and oxygen hardened Ti-6Al-4V alloy.

The obtained coatings were investigated using various electrochemical and mechanical methods. The following parameters of coatings were determines: electrochemical (corrosion resistance), micro-mechanical (nanohardness, Young's modulus) and tribological (wear resistance, friction coefficient).

The results presented in this paper have been obtained within the project "KomCerMet" (contract no. POIG.01.03.01-00-013/08 with the Polish Ministry of Science and Higher Education) in the framework of the Innovative Economy Operational Programme 2007-2013.
***Keywords**: nanocoatings, electrochemical properties, corrosion, mechanical properties*

Materials and testing

Coatings were deposited using magnetron sputtering of three graphite targets (Ø 107x10 mm) and one of pure metal Cr or W (Ø 107x10 mm) for nc-CrC/a-C:H or nc-WC/a-C:H, respectively in atmosphere of Ar+H_2. The coatings were deposited onto bulk hardened HS steel Vanadis 23 (Ø25x6mm), diffusion hardened Ti6Al4V alloy (Ø25x6mm), silicon wafers (10x10x0,55 mm) and 0H18N9 steel plates (10x10x1 mm).

Metal substrates were grinded using abrasive papers with fraction from 80 to 1200 and polished using diamond powder (1µm) with lubricant. After polishing substrates were washed in mixture of water and detergent, after that using acetone in sonic bath. Silicon substrates were cleaned using only water mixture with detergent and acetone. After cleaning substrates were mounted on holder inside vacuum chamber of B-90 deposition unit. The exact preparation of samples, processes of deposition and schema of B-90 unit were presented in [1-2].

Tribological properties were measured using ball-on-disc method using High Temperature Tribotester CSM with use fi1/4" 100Cr6 counterbodies under load of 10 N with linear speed 0.1 m/s on radius of friction path 10 mm, friction path was 1000 m. Humidity during tribological test was 25±6%. The friction force, temperature, humidity and vertical displacement were measured during tribological tests. Mechanical properties like nanohardness and Young modulus were measured using Nanoindenter G-200 based on CSM (Continuous Stiffness Measurement). Chemical composition and thickness were measured using Hitachi S-3000N with EDS module. Quality of adhesion of coating to steel and hardened titanium alloy was measured using Daimler-Benz test.

The impedance (electrochemical impedance spectroscopy - EIS) data was obtained at the open circuit potential with a Princeton Applied Research model VersaStat 3 system. The frequency range analysed, went from 10^6 Hz up to 10^{-3} Hz, with the frequency values spaced logarithmically (ten per decade). The amplitude of sinusoidal voltage signal applied to the system was 10 mV rms (root-mean-square). Prior to the beginning of the measurements, the specimens were maintained for 1.5 h in 0.5 M/l NaCl for stabilisation of an open – circuit potential.

The investigation of the coated oxygen hardened Ti-6Al-4V alloy and VANADIS 23 steel nano/microstructure was carried out by scanning- and transmission electron microscopy (SEM, TEM) and high resolution TEM (HRTEM). Phase identification was performed by means of selected area electron diffraction (SAED), XRD and GIXRD measurements. The SAED and fast Fourier transformation FFT patterns were interpreted with the help of Java Electron Microscopy Software (JEMS) [3].

Results

Electrochemical properties

a) **b)**

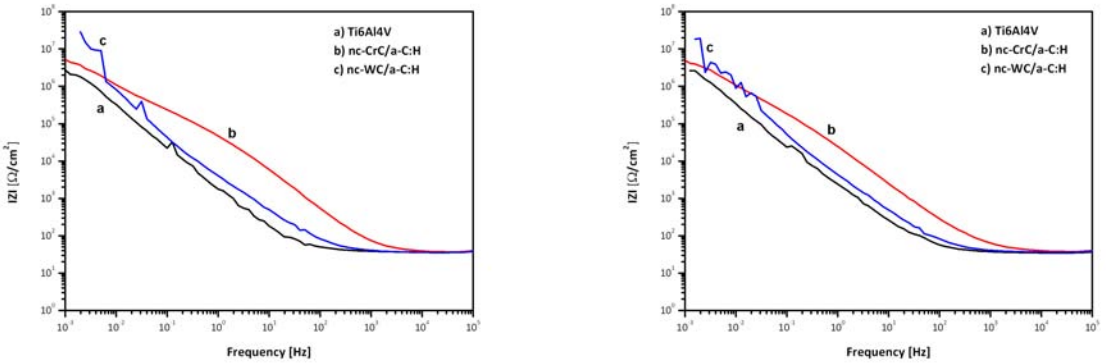


Fig. 1. Impedance modulus for Ti6Al4V with and without nanocomposite coatings after 1h (a) and 48h (b) immersion in 0.5 M NaCl.

a) **b)**

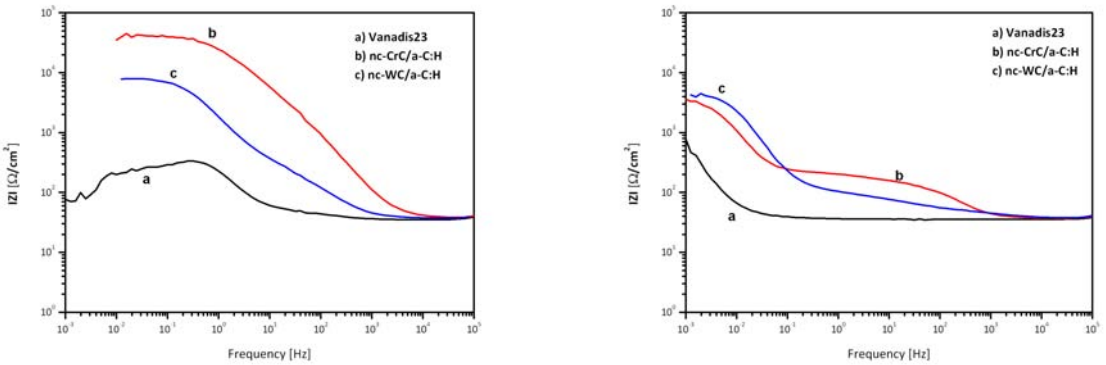


Fig. 2. Impedance modulus for Vanadis 23 steel with and without nanocomposite coatings after 1h (a) and 48h (b) immersion in 0.5 M NaCl.

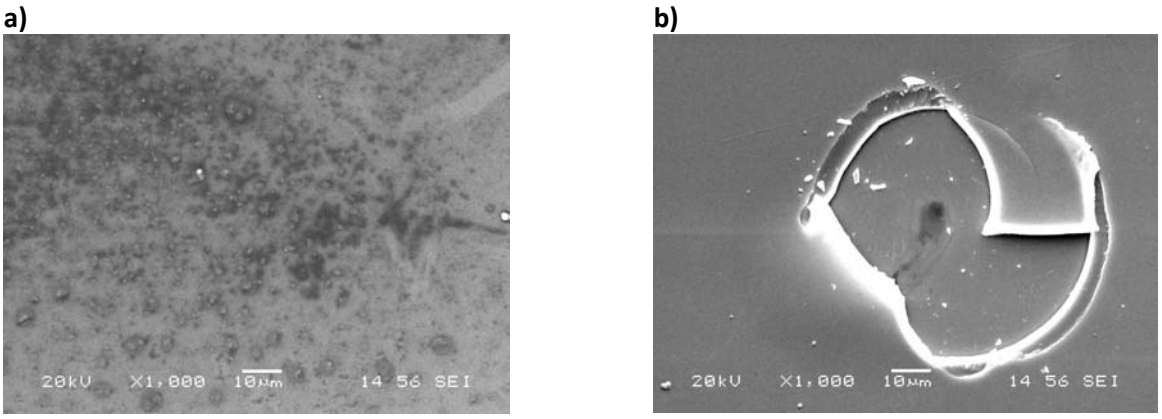


Fig. 3. SEM images of Ti6Al4V with nc-CrC/a-C:H (a) and nc-WC/a-C:H (b) coating after 48h immersion in 0.5M NaCl.

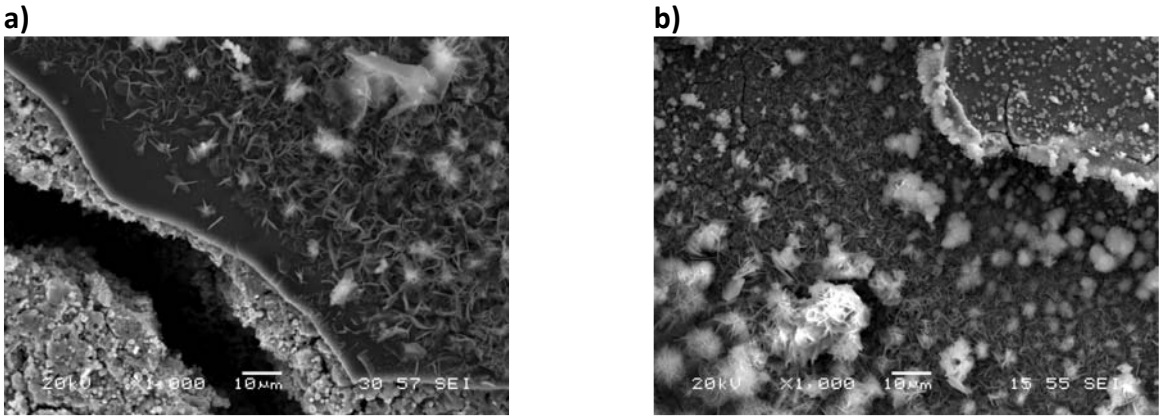


Fig. 4. SEM images of Vanadis 32 with nc-CrC/a-C:H (a) and nc-WC/a-C:H (b) coating after 48h immersion in 0.5M NaCl.

Mechanical properties

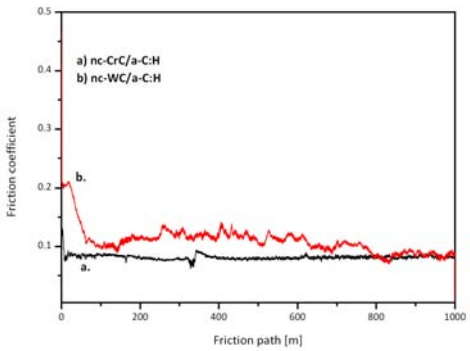


Fig. 5. Friction coefficient in function of friction distance for a) nc-CrC/a-C:H and b) nc-WC/a-C:H deposited onto Vanadis 23.

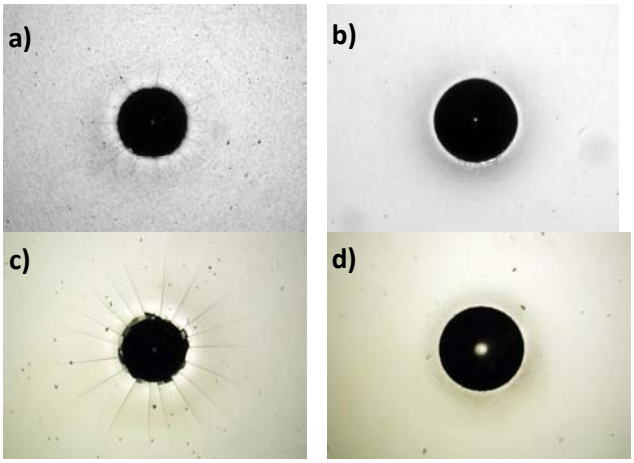


Fig. 6. View of coatings surface after Daimler-Benz test of a)nc-WC/a-C:H on Ti6Al4V, b) nc-WC/a-C:Hon Vanadis 23, c) nc-CrC/a-C:H Ti6Al4V d) nc-CrC/a-C:H Vanadis 23.

Microstructure

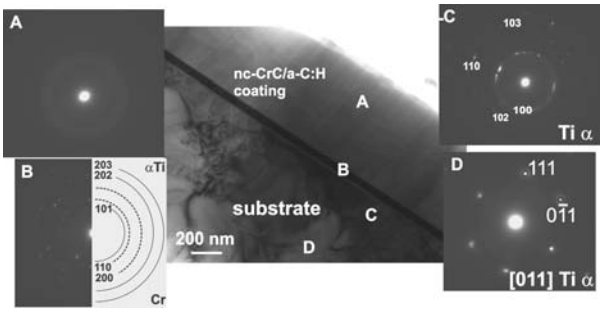


Fig. 7. Microstructure of the nc-CrC/a-C:H coating on oxygen hardened Ti-6Al-4V alloy as well as SAED patterns taken from the areas A-D marked in the figure and their identification; TEM cross-section thin foil.

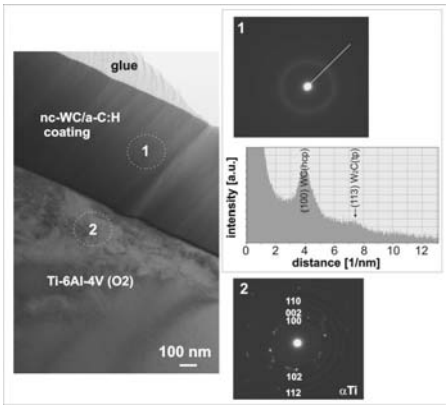


Fig. 8. Microstructure of the nc-WC/a-C:H coating on oxygen hardened Ti-6Al-4V alloy as well as SAED patterns taken from the areas marked on the figure and their identification; an intensity profile of the SAED patterns taken from the coatings are presented; TEM cross-section thin foil.

Conclusions

Obtained nc-CrC/a-C:H and WC/a-C:H coatings have very good adhesion also to bulk hardened and tempered steel substrates and to diffusion hardened Ti6Al4V alloy. Mean values of friction coefficients between coatings on steel substrates and hardened titanium alloy was 0.08 for nc-CrC/a-C:H and 0.1 for nc-WC/a-C:H. This is a very good result and in connection with good quality of adhesion to those substrates, allows to use low friction nanocomposite coatings based on amorphous matrix and nanocrystalites of transition metals to enhance tribological properties of elements made of steel or titanium alloys working as friction couples in temperatures up to 200 ºC. Especially in aviation and car industry as parts of engines and power transmissions and as a coating on machining tools, also for hard-to-machining materials like Ni, Ti and Co. In spite of low values of hardness and Young modules the coatings have very good wear resistant which are most important for low friction coatings than mechanical properties.

Corrosion properties of nanocomposite coatings mainly depend on the substrate material. In the case of steel Vanadis 23 coatings caused a significant increase of corrosion resistance, even after 48 hours in a chloride solution.

However, in the case of titanium alloy tested coatings also increased corrosion resistance. However, this increase was not as significant as in the case of steel Vanadis 23.

References

1. K. Włodarczyk, M. Makówka, P. Nolbrzak, B. Wendler: Low friction and wear resistant nanocomposite nc-MeC/a-C and nc-MeC/a-C:H coatimgs, Journal of Achievements in Materials and Manufacturing Engineering, 37 (2), 2009
2. M.Makówka, T.Moskalewicz, K.Włodarczyk, B.Wendler: Niskotarciowe i odporne zużycie nanokompozytowe powłoki typu nc-CrC/a-C oraz nc-CrC/a-C:H, Material Engineering, 4 (176), 2010
3. P. Stadelmann: JEMS Java Electron Microscopy Software, 2004, http://cimewww.epfl.ch

Effect of time in plasma electrolytic oxidation process on titanium substrate with addition nano alpha alumina powder in electrolyte and investigate wear behavior of coating

S. Sarbishei [a], M.A. Faghihi-Sani [a], M. Mohammadi [a], F.Einkhah[a]

[a] Sharif University of Technology, Tehran, Iran

1. Introduction

Titanium and its alloys have wide applications in industry and recently researches have been expanded in this area. The main reasons are unique features of titanium such as biological behavior, corrosion resistance and high strength to weight ratio . The fundamental problem of titanium is low wear resistance that leads to be worn in industrial applications.

Plasma electrolytic oxidation(PEO) is a novel method to create ceramic coatings on metals and improve wear resistance. Base of this method is similar to electrochemical coating methods with difference the high voltage discharge phenomenon. In this research hard nano alpha-alumina particles (hardness of 9 Mohs) were added to the electrolyte for improving wear properties of titanium.

2. Experimental Details

Pure Titanium discs with 28mm diameter and 5mm thickness were used as substrate. System includes power supply, magnetic stirrer, cooling copper pipe, cathode(stainless steel) and anode(titanium sample). Wear tests were done according to ASTM G99-05 standard by alumina pin, 6.21N vertical force, 0.27m/s speed and 70m route. Table 1 shows components and concentrations of electrolyte.

Table 1.Electrolyte components and concentrations

Component	Concentration (gr/lit)
Sodium Silicate	15
Nano alpha alumina powder	6
potassium hydroxide	3
sodium phosphate	2
Triethanolamine (TEA)	0.048

Three samples with 10, 20 and 30 minutes process times and constant parameters of current density, frequency and duty cycle were prepared. Nano

alpha alumina powders with average 80nm particle size were added to electrolyte.

Table 2. PEO parameters during process

Sample name	Time (min)	Current density (A/cm2)	Duty cycle (%)	Frequency (Hz)
S1	10	0.2	50	50
S2	20	0.2	50	50
S3	30	0.2	50	50

SEM (model VEGA\\TESCAN-XMU), EDS, eddy current tests and optic microscope were used to study the microstructure, chemical composition, thickness and wear route of coatings, respectively.

3. Results and Discussion

3.1.Coating mechanism with presence of nano particles in electrolyte

Coating mechanism with nano particles in electrolyte is combination of cataphoretic effect and spark ignition. Since isoelectric point of alumina is 6-7 and electrolyte has pH=12, alumina particles get negative charge and related to cataphoretic effect absorb to substrate that has positive charge(anode) .PEO process is based on Spark ignition, that causes melting substrate during electrical discharge channels and sintering nano particles to the surface. According to Fig 1 nano alpha alumina particles and discharge channels are seen that confirm cataphoretic and spark ignition mechanisms.

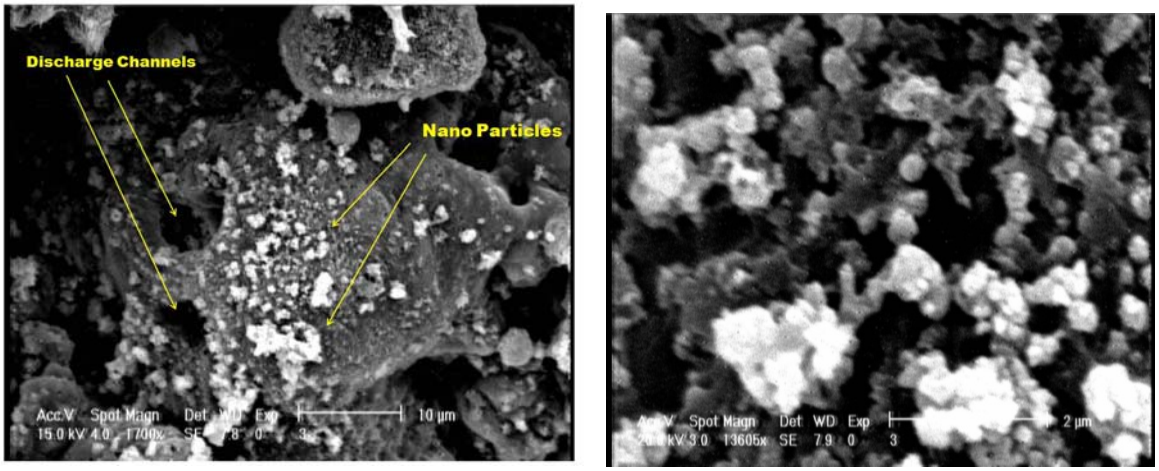


Fig 1. SEM image of sample S3

3.2.Microstructure and chemical composition of coating

Fig2 (a,b,c) shows SEM images of samples. It can be seen that by increasing process time, small pores are filled by nano particles and large pores get larger. Time of process has important role in absorbing nano particles to the surface by cataphoretic and spark ignition mechanisms.EDS analysis of samples shows that aluminum and silicium element percent is increased and decreased,respectively by increasing process time, due to more absorption of nano particles by sintering time and reduce in silicium elemet of paste background (table3).

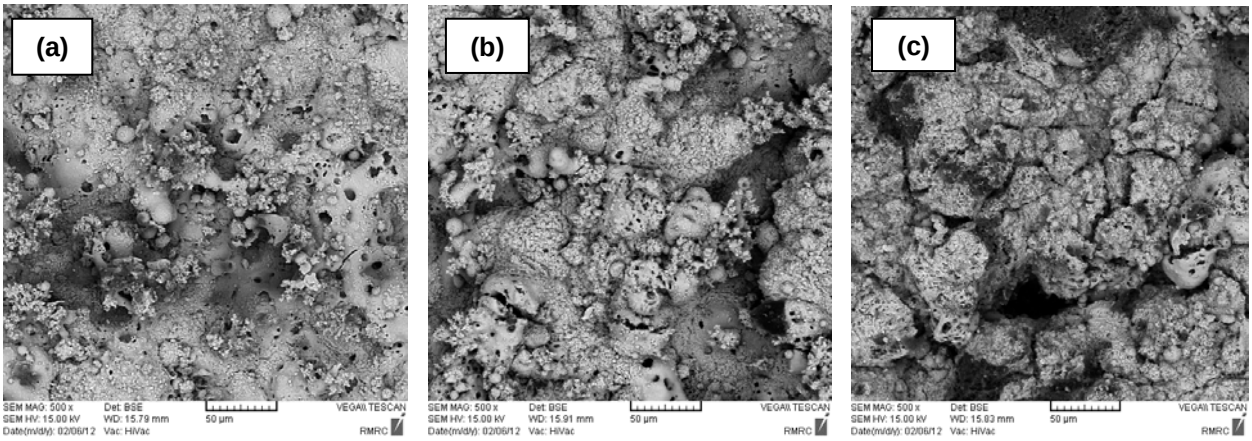


Fig 2. SEM images of samples :(a) S1 (b)S2 (c)S3

Table 3. Element percent composition of samples by EDS analysis of surface

Sample name	O	Si	Al	Na	K	Ti
S1	65.56	23.10	5.86	3.51	1.36	0.61
S2	66.14	22.94	7.06	2.22	0.98	0.66
S3	65.89	19.74	8.34	3.78	1.4	0.85

3.3.Wear behavior of coating

Wear mechanism is combination of adhesive and abrasive mechanisms. There is adhesive force between surface of alumina pin and coating(adhesive mechanism). Alumina pin can cut the materials of coating by passing on surface and makes debris (silicon and alumina particles) that playing role of three-body abrasive mechanism. Fig3 shows weight loss of samples after wear test. Also fig 4 shows wear tracks on coating that confirm sample S3 has worn less than other samples.

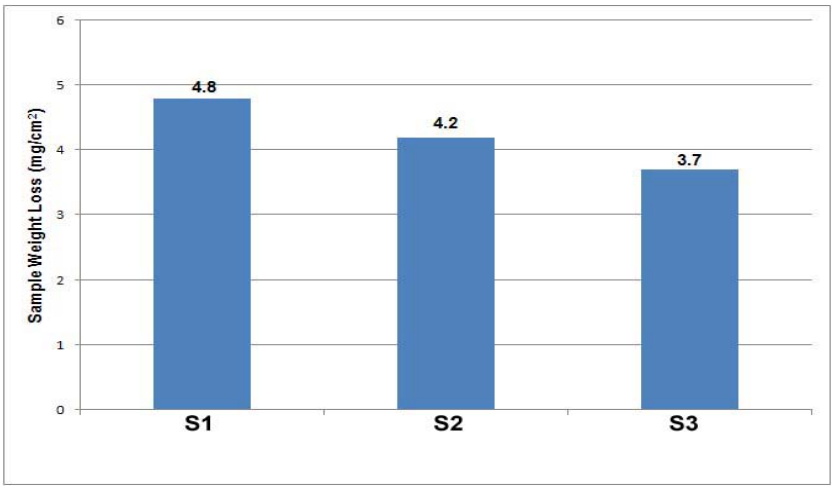


Fig 3.weight loss of samples after wear test

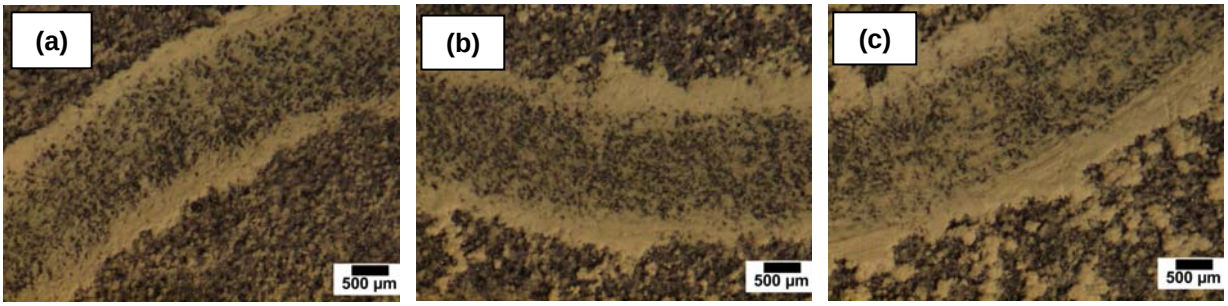


Fig 4. Optic microscope images of wear tracks on coatings: (a) S1, (b) S2, (c) S3

4. Conclusion

Coating mechanism via plasma electrolytic oxidation with nano particles in electrolyte is combination of cataphoretic effect and spark ignition. Nano alpha alumina particles with high hardness have significant role in imroving wear resistance of coating. With increasing time of PEO process nano particles adhere more to the surface due to more sintering time and wear resistance is increased. Coefficient of friction is increased by rising process time due to increase in amount of alumina nano particles in the coating and increase in surface roughness.

FATIGUE BEHAVIOR OF COATED AND UNCOATED CEMENTED CARBIDE INSERTS INVESTIGATED BY IMPACT TEST AT THE CUTTING EDGE VICINITY

K.-D. Bouzakis, M. Batsiolas, G. Skordaris, N. Michailidis, F. Stergioudi

Aristoteles University of Thessaloniki, Thessaloniki, Greece.

Fraunhofer Project Center for Coatings in Manufacturing, Aachen , Germany and Aristoteles University of Thessaloniki, Laboratory for Machine Tools and Manufacturing Engineering, Thessaloniki, Greece

Introduction

The cutting edge wear due to fatigue affects directly the overall coated tool performance. In the present work, a quick assessment of the cutting edge fatigue behavior of uncoated and coated cemented carbide inserts is investigated by impact tests near the cutting edge. Substrates with various grain sizes, surface roughness and heat treatment were tested concerning the cutting edge fatigue endurance load. The FEM simulation of the test procedure at various distances from the inserts' cutting edge provided insight in the occurring stress fields. The developed test method facilitates a rapid quality control of both coated and uncoated cutting inserts at loading conditions, close to those encountered during their cutting operation.

Development of the experimental setup

In order to examine the fatigue failure of cemented carbide inserts' cutting edges, an appropriate feature was integrated into an existing impact tester [1, 2]. The developed arrangement controls accurately the positioning of the coated insert to the ball indenter spindle. This procedure is supervised by the impact tester control unit. In this way, the fixed specimen on a 2-axis linear guide system can be accurately displaced for attaining impact imprints at a certain distance from the cutting edge. The specimen movement to the impact tester spindle axis is monitored, as it is presented in figure 1. An appropriate graphical user interface, based on the platform of LabVIEW v.8.6 software, supports this procedure. In this way, the application of repetitive impacts at predetermined distances from the specimens' cutting edge was enabled.

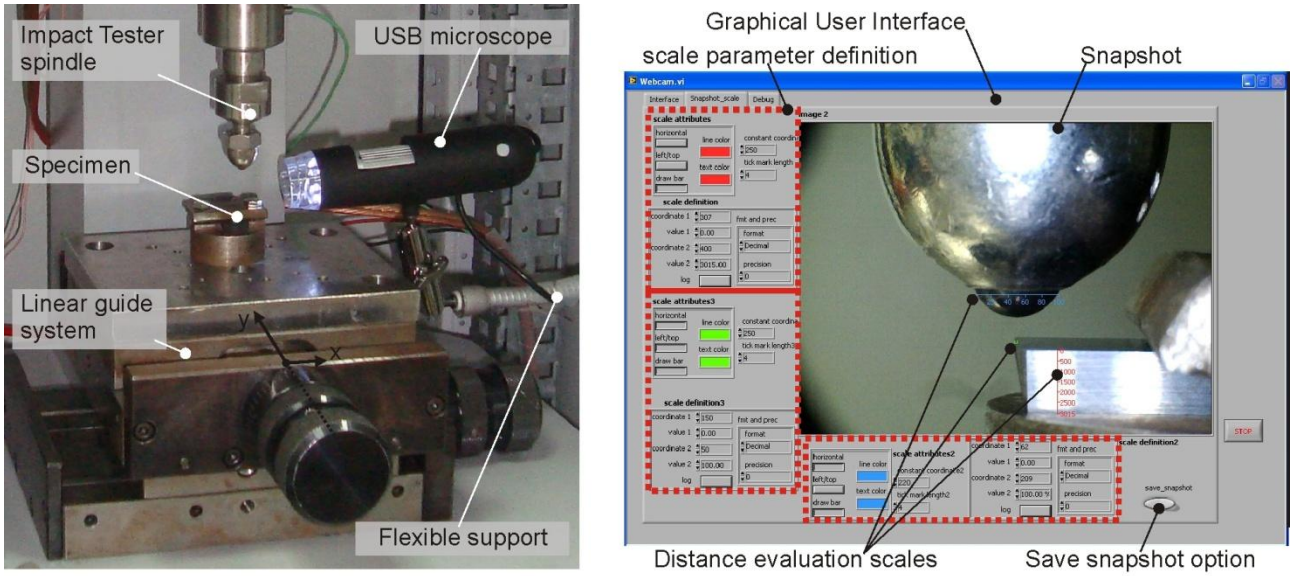


Figure 1: The developed experimental setup and graphical user interface.

The developed FEM model for describing the experimental procedure

The geometry of the specimen's edge affects significantly the stress distribution and failure initiation in the cutting wedge region. A 3-dimensional, plane-symmetric simulation model of the ball indenter penetration into the substrate was developed with appropriate boundary conditions and finite element discretization (see upper part of figure 2). This FEM model was modified accordingly, for calculating the related deformations and stress fields at various loading distances from the cutting edge. The plane symmetry that was exploited for restricting computational time and the meshing network for a penetration at a distance of 50 μm from the cutting edge are displayed. In the diagram at the lower figure part, the imprint load and the corresponding distances from the cutting edge for achieving a constant maximum stress of 5.3 GPa in the cutting edge region are exhibited. At this stress level, cutting edge breakages occur at distances lower than 100 μm after one million or less impacts. The photos illustrate the developed craters. These results indicate that loading proximity to the cutting edge leads to edge failure at lower loads for the same equivalent stress levels. Based on calculation results, this was attributed to tensile principal stress components that facilitate crack propagation under dynamic loading. The loading distance of 100 μm from the cutting edge does not lead to cutting edge fracture at a force of 27.5 daN after one million impacts for the fine-grained substrate with ground rake surface.

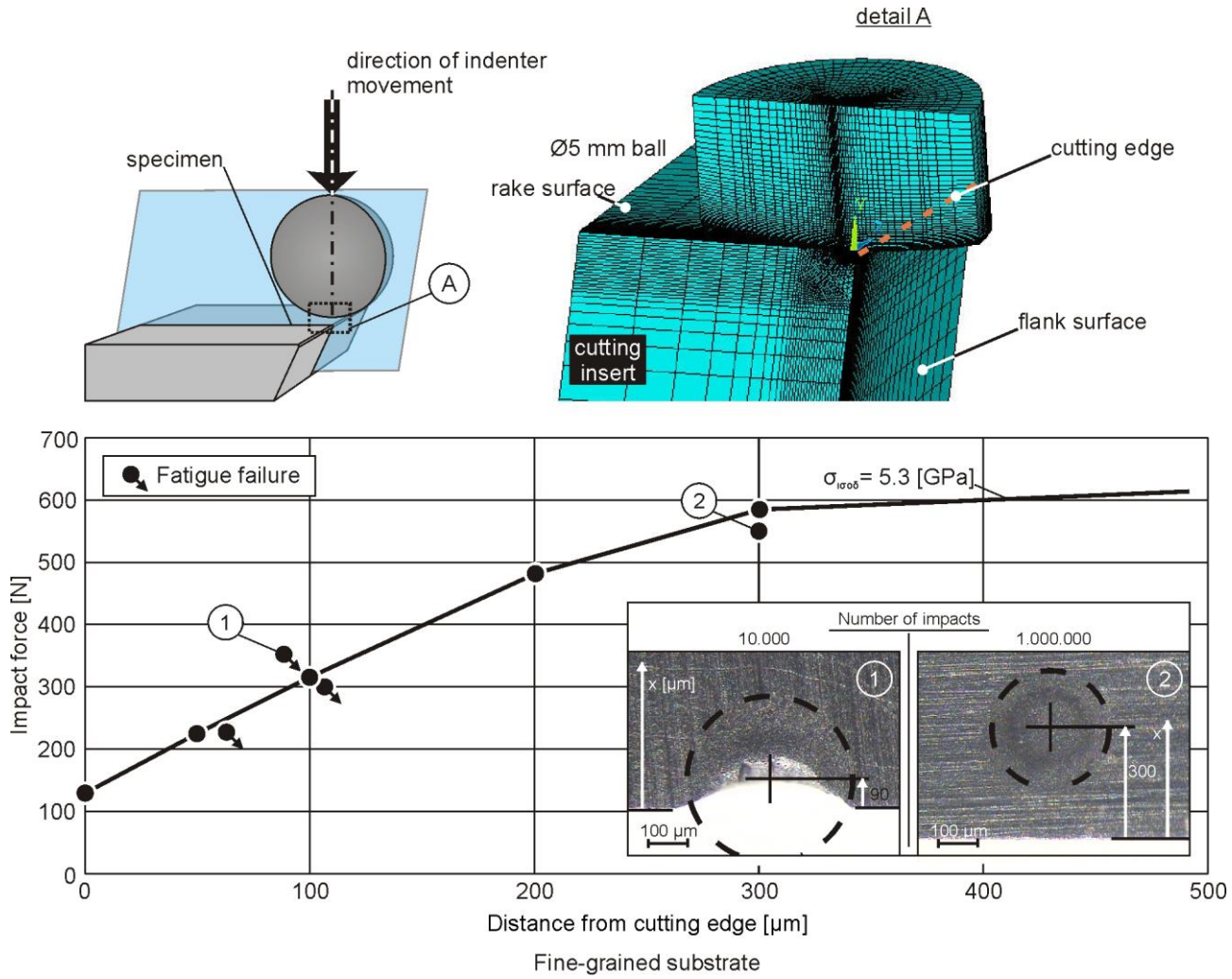


Figure 2: 3D-FEM model and selected experimental results for corresponding equivalent von Mises stress levels.

Effect of grain size, surface roughness and annealing temperature on experimental fracture load

In the described investigations, among others, fine-grained and ultrafine grained substrate grades were examined in relation to their fatigue endurance load, keeping the imprint distance from the cutting center constant and equal to 100 µm (see figure 3). The diminishing of substrate grain size increases the load for avoiding cutting edge fatigue failure after one million impacts. Moreover, the effect of heat treatment, for 4 h at various temperature levels in vacuum, on the maximum fracture load was also examined. A diminishing trend was revealed regarding the load that the substrate can withstand for one million impacts, with the annealing temperature augmentation.

By the introduced impact test procedure, the fatigue endurance of cutting edges can be effectively evaluated at various coated and uncoated specimens data.

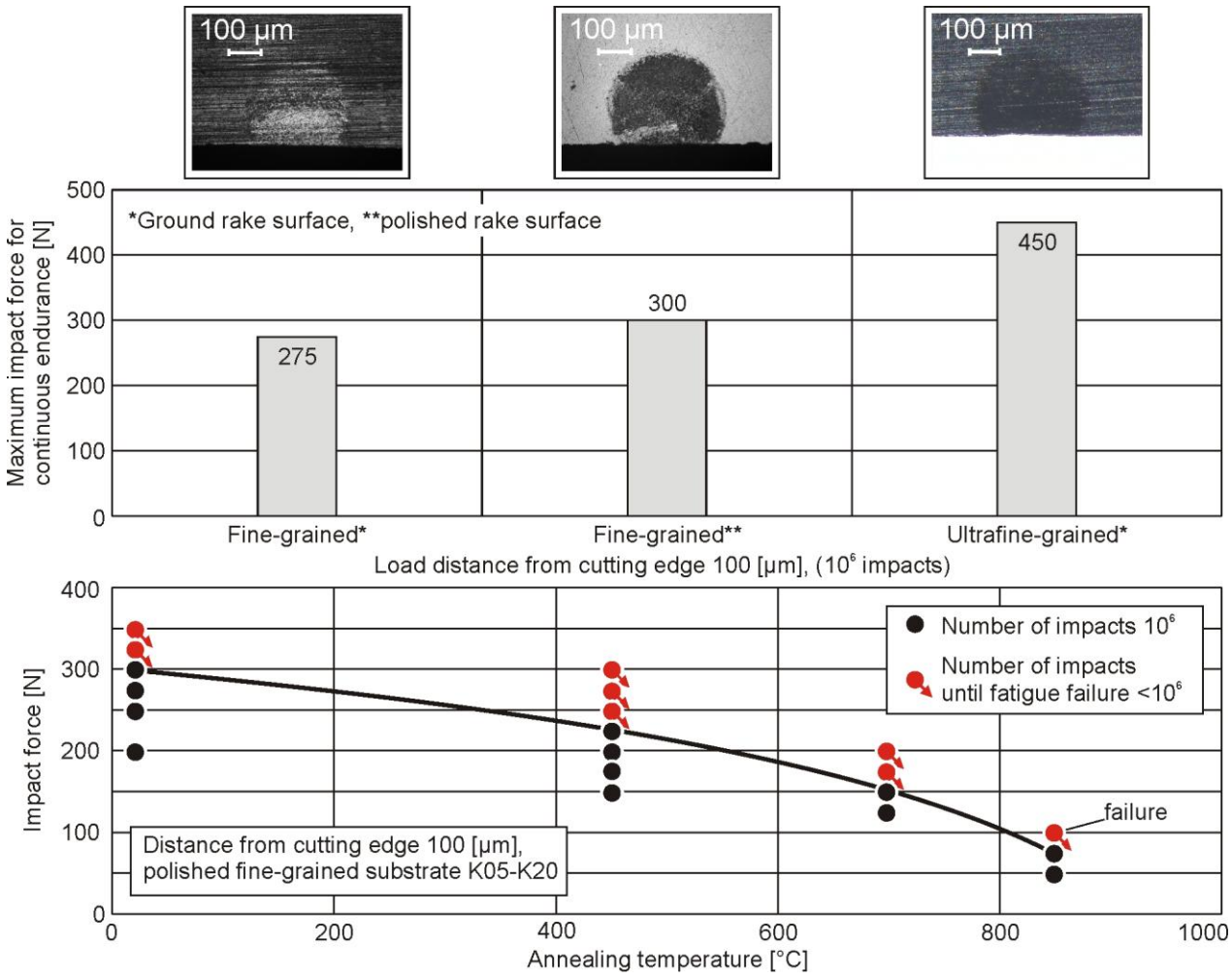


Figure 3: Comparison between experimental and FEM-calculated imprint depths versus the number of impacts

References

[1] K.-D. Bouzakis, N. Michailidis, A. Lontos, A. Siganos, S. Hadjiyiannis, G. Giannopoulos, G. Maliaris, T. Leyentecker, G. Erkens, Characterization of Cohesion, Adhesion and Creep-Properties of Dynamically Loaded Coatings through the Impact Tester, Zeitschrift fuer Metallkunde, 92 (2001) 1180-1185.

[2] Batsiolas M., Development of experimental arrangements and methodologies for the characterization of fatigue and cohesion properties of thin hard coatings at various temperatures, Aristotle University of Thessaloniki, Thessaloniki, 2012, PhD Thesis.